The Dissertation Committee for Leonel Augusto Gomez Torres certifies that this is the approved version of the following dissertation:

Characterization of the Spacial Arrangement of Opening-Mode Fractures

Committee:

_____
Randall Marrett, Supervisor

_____
Sharon Mosher

_____
Charles Kerans

_____
Julia F. Gale

_____
Jon T. Holder

_____
Rolf Ackerman

Characterization of the Spatial Arrangement of Opening-Mode Fractures

by

Leonel Augusto Gomez Torres, B.Sc.

Dissertation

Presented to the Faculty of the Graduate School of

The University of Texas at Austin

in Partial Fulfillment

of the Requirements

for the Degree of

Doctor of Philosophy

The University of Texas at Austin

May 2007

Dedication

A mi mamá, quién con su ejemplo de dedicación y compromiso a la educación universitaria me mostró el camino de la curiosidad científica.

Acknowledgements

I am thankful to Dr. Randall "Randy" Marrett for sharing his knowledge and experience in all areas of scientific expertise. Randy's breadth and depth of knowledge is truly remarkable and is accompanied by a keen eye to find the important details in an outcrop or in a graph plotted on a piece of paper. I can only wish that Randy will one day realize deep in his heart and mind the large impact that his decisions have on student's lives, and how important is to communicate openly with his students.

John "the dude" Hooker was the best classmate both in the field and at the office; I just wish I could be half as "cool" as John. Perhaps our differences in age and musical taste prevented me to become closer to John, but those differences helped me expand my view of the American culture.

I have an immense debt of gratitude to Dr. Steve Laubach and Dr. Julia Gale at the Fracture Research and Application Consortium (FRAC) at the Bureau of Economic Geology (BEG), they challenged my knowledge and cherished my ideas, provided me with the financial support needed to complete my degree and with needed professional and personal advice. Even though they were my superiors and clearly have more experience and knowledge that I do, I always felt I was working with them and not for them.

Orlando (Dr. Orlando Ortega), gracias por tus palabras en tiempos de crisis y por compartir tus conocimientos y experiencias de una manera tan desinteresada. La generosidad y el compañerismo de Faustino Monroy-Santiago siempre estara conmigo. No hay palabras que expresen suficientemente la gratitud que tengo hacia Orlando y Faustino.

Tip Meckel, Katy Herrell and Brad Reid were the best office mates and friends one can wish for, I just wish we could get jobs in the same corner of the world! Thanks to Dr. Robert Reed at FRAC/BEG for enduring my nagging questions with remarkable stoicism and for half-jokingly giving birth to the name of the fracture quantification spreadsheet that I developed as part of my dissertation work.

I could have not defended my dissertation before the end of 2006 without the great effort of Dr. Charles Kerans, Dr. Sharon Mosher, Dr. Jon Holder, and Dr. Rolf Ackermann, who read my dissertation in a remarkably short amount of time. Dr. Sharon Mosher was also a model of scientist and professor that will always carry with me. I am very thankful to Dr. Sharon Mosher and Dr. Mark Cloos for the financial support that they provided me in the last semester at UT-Austin. The help of Dr. Jon Olson was fundamental in increasing my understanding of subcritical fracture propagation. Although my interaction with the late Dr. Robert "Bob" Goldhammer was relatively small, I have a great debt of gratitude for him.

Thanks to Erik Leuro for sharing his sharing his knowledge in geophysical techniques that I used to know. I greatly benefited from interacting with Kira Tushman, Meghan Ward, Edgar Pinzon at FRAC/BEG. The difficult circumstances of my last semester at UT-Austin were mitigated by sharing living quarters and talking about the Sierra Madre Oriental with Dr. Younis Altobi. I am sure I am forgetting people that at one moment or another of my time during the course of my PhD helped me, to all of them, my sincere thanks. Finally, words cannot express my gratitude to Melissa "Missy" Halick for sharing my life during the good and bad times of finishing up my dissertation.

Characterization of the Spatial Arrangement of Opening-mode Fractures

Leonel Augusto Gomez Torres, PhD.

The University of Texas at Austin, 2007

Supervisor: Randall Marrett

In spite of the abundance of opening-mode fractures in the earth's upper crust, knowledge about their spatial arrangement remains limited. The spatial arrangement of fractures refers to the patterns of fracture positions in space. On one-dimensional analyses, fracture position can be obtained by combining fracture apertures, spacings, and their sequence along a one-dimensional scanline. Previous approaches failed to account for fracture position and fracture size, thus a new technique, normalized correlation count (NCC), was used to overcome these limitations. This technique was designed to distinguish random from non-random (fractal, inherited/imposed, periodically arranged fractures, or periodically arranged clusters) spatial arrangements of fractures. In addition, another method to quantify the attributes of microfractures in rock samples larger than a thin section was developed and used to quantify their spatial arrangements.

NCC indicated that where statistically significant (non-random) clusters exist, large fractures are more clustered than small ones. Differential clustering according to fracture size was detected in data sets from different lithologies at outcrop and rock-

sample scale, suggesting that this phenomenon is related to development of fracture systems as opposed to host rock lithology and scale. Fracture clusters with power-law variation of spatial correlation with length scale are not strictly natural fractals because clusters occur in cascades at discrete values of length scale and not in a continuous fashion. Some statistically significant clusters with a power-law of spatial correlation are formed by smaller clusters with a power-law of spatial correlation that are also periodically arranged.

Fractures from the Cupido Fm. in the Monterrey salient were grouped in three categories based on their trace morphology, cement composition, and timing of fracture cements with respect to fracture opening. Fractures at outcrop scale in two of the categories exhibit low percentages of synkinematic cement and random arrangements, whereas fractures in the remaining category exhibit large amounts of synkinematic cement and periodically arranged clusters. An evolutionary model of fracture development based on subcritical propagation is proposed. This model suggests that mechanical layering increases during cluster development, explaining the non-random clustering within interclustering domains at outcrop scale and implies that cluster spacing increases with mechanical layering but decreases during evolution towards cluster saturation.

Table of Contents

Chapter 1: Introduction

Fractures are ubiquitous in the earth's upper crust. They can be found through a wide range of scales, from thin section, to geologic map and are present in all rock types. Fractures can greatly influence the flow and storage of valuable natural resources like water (Sharp, 1993; Adler and Thovert, 1999) and hydrocarbons (Nelson, 2001), and fracture-enhanced permeability is also important for waste repositories (Barton and Hsieh, 1989) and hydrothermal mineral deposits (Sanderson et al., 1994). A hallmark of fracture-controlled permeability in aquifers and hydrocarbon reservoirs is tremendous heterogeneity in well productivity, with differences of several orders of magnitude between adjacent wells being common. The heterogeneous effect that fractures have on fluid flow in part reflects their spatial arrangement.

The spatial arrangement of fractures in a fracture set is defined by how fractures are positioned relative to one another in space, where each set groups all fractures with common characteristics (e.g., timing, orientation and cement fill) and genesis (e.g., Twiss and Moores, 1992; Davis and Reynolds, 1996). However, fractures that belong to a single set do not need to be comparable in size. A fracture cluster can be defined as a domain of a fracture set where fractures are unusually abundant.

In the absence of substantial matrix porosity, fracture connectivity is perhaps the dominant influence on the ability of a fractured rock volume to transmit fluid effectively (Renshaw, 2000). If all fractures of a set were planar and had exactly the same orientation, connectivity between fractures would require more than one fracture set. Although natural fractures in rock are commonly approximately planar (Pollard and Aydin, 1988), variations in orientation are visible at all scales, both along individual fractures and between different fractures of a set. For a given variation in fracture

orientation, increasing the spacing between two fractures will increase the minimum lengths required for the fractures to intersect, and therefore, lower the probability of intersection. Consequently, closely spaced fractures (i.e., inside a fracture cluster) are more likely to be connected than fractures spaced farther apart (i.e., outside a fracture cluster). The ability to quantitatively describe fracture arrangement has direct implications for predicting or modeling natural fracture patterns, especially how well connected fractures may be (Adler and Thovert, 1999).

Because fractures commonly start from flaws randomly distributed inside a rock mass (e.g., Rives et al., 1992; Olson, 2004), many authors have investigated the hypothesis that fractures are randomly arranged in space (Priest and Hudson, 1976; Rives et al., 1992). From a scientific standpoint, knowing the spatial arrangement of a fracture set facilitates understanding the origin, growth and evolution of fractures in rock. For instance, non-randomly arranged fractures may indicate operation of a process (e.g., self-organization) during growth that organized fractures from initial flaws having random arrangement.

Although fracture clustering is a useful intuitive concept, it has remained poorly studied and resistant to meaningful quantification. The fact that five structural geology textbooks published in English since 1990 lack a definition or explanation of a fracture cluster illustrates how fracture clustering is not considered an important characteristic of fractures. However, without quantification of fracture clustering, it is impossible to make rigorous comparisons of spatial arrangements between fracture sets in different rock units or between natural and modeled fractures.

1.1 USING MICROFRACTURES FOR FRACTURE CHARACTERIZATION

Although the main focus of my dissertation is the spatial arrangement of fractures, two chapters show research conducted on the prediction of macrofracture orientation

(Chapter 3), and intensity (Chapter 4) using genetically related microfractures (Laubach, 1997) from subsurface samples. The inclusion of Chapters 3 and 4 serves two goals. The first goal is to illustrate the limitations in sampling when studying subsurface fracture networks and some approaches and methodologies used to overcome these limitations. The approach is the use of microfractures as proxy for the characterization of genetically related macrofractures (Laubach and Milliken, 1996; Laubach, 1997). Following this approach, microfractures were measured in scanlines along coordinated sets of thin sections using a methodology I developed (Gomez and Laubach, 2006). The spatial arrangement of microfractures was used to study the relationship between fracture size and the spatial arrangement of fractures (Chapter 7), and to investigate whether or not the phenomenon of fracture clustering transcends outcrop scale towards smaller scales (Chapter 8). The methodologies include the orientation of rotary-drilled sidewall cores using sedimentological and mechanically induced features (Chapter 3), and the use of cathodoluminescence images to detect microfractures typically invisible under a petrographic microscope (Chapters 3 and 4). The second goal is to illustrate that other attributes (e.g., aperture) are needed characterize fracture arrays in addition to spatial arrangement.

1.2 DISSERTATION ORGANIZATION

This dissertation contains nine chapters grouped in four sections. Section one contains an introduction to research in the spatial arrangement of fractures (Chapter 1). Section one also contains a summary of the terminology used throughout this dissertation, descriptions about the methodology used to collect fracture data along scanlines, and a summary about the geology of the two main areas where fracture data were collected (Chapter 2). Section two (Chapters 3 and 4) focuses on the use of microfractures (as defined by Laubach, 1997) for the prediction of attributes of

genetically related macrofractures (as defined by Laubach, 1997). Section three (Chapters 5 and 6) describes the methodologies I developed, or collaborated in developing, for the quantification of the spatial arrangement of fractures. Finally, section four (Chapters 7, 8, and 9) studies different aspects of the spatial arrangement of fractures that could not be studied properly before the development of the techniques explained in section 3. Among these topics are the relationship of clustering with fracture size (Chapter 7), the internal structure of fracture clusters (Chapter 8), and the influence of diagenetic processes on how fractures are spatially arranged (Chapter 9).

1.2.1 Section One

This chapter of my dissertation describes the organization of the dissertation, the objectives of this study and the significance of studying the spatial arrangement of fractures. Chapter 2 includes four parts. The first part establishes terminology that will be used throughout this document. Because uniformity is lacking in the structural geology community about some of the terms used in the study of fractures, it is important that the reader know what terms signify in my dissertation. The second part of Chapter 2 explains how data were collected for one-dimensional (1D) studies of the spatial arrangement of fractures, and provides a summary of the data sets used for this research. The last two parts of Chapter 2 contain a summary of the geology of the two regions where fracture data were acquired for the study of the spatial arrangement of fractures: the Monterrey salient of the Sierra Madre Oriental (SMO) and Pedernales Falls State Park.

1.2.2 Section Two

Section two of my dissertation includes Chapters 3 and 4. These two chapters are studies that do not address the spatial arrangement of fractures, but instead quantify the attributes (e.g., orientation, intensity) of microfractures in order to quantitatively predict the same attributes for genetically related macrofractures in subsurface oil reservoirs

where fractures contribute an important component of permeability. Each chapter contains a paper that was peer-reviewed and published during the course of my doctoral studies. Chapter 3 discuss a study that successfully predicted the orientation of two distinct fracture sets in a West Texas oil reservoir using only rotary-drilled sidewall cores (Gomez et al., 2001). Gomez et al. (2001) served as seed for two additional publications, Gomez et al. (2003b) and Gale and Gomez (in review). Chapter 4 describes a study that predicted the intensity of macrofractures along a horizontal core of the Cozzette Sandstone by extrapolating the intensity of microfractures measured in thin sections from several samples along the horizontal core (Gomez et al., 2003a), using the scaling of fracture apertures described in Marrett et al. (1999).

1.2.3 Section Three

Section three of my dissertation includes Chapters 5 and 6. Chapter 5 explains a method that I developed to rapidly and efficiently quantify the attributes (including spacing) of microfractures detected in digital microscopic images that extend beyond a single thin section (Gomez and Laubach, 2006). The method presented in Chapter 5 is currently the preferred method for quantifying fracture attributes of microfractures at the Fracture Research and Application Consortium of the Bureau of Economic Geology (S. Laubach, personal communication, 2006).

In contrast to Chapter 5, which focuses on a method to obtain measurements of fracture spacing at thin section scale, Chapter 6 focuses on how to quantitatively analyze measurements of fracture spacing at any (e.g., thin section, outcrop) scale. Chapter 6 is composed of five parts, all of them dedicated exclusively to techniques for the study of the spatial arrangement of fractures. The first part establishes the difference between the concept of fracture spacing and the concept of spatial arrangement of fractures. The second part of Chapter 6 examines the limitations of techniques traditionally used to

study fracture spacing and the spatial arrangement of fractures (Gomez and Marrett, in review). The third part of Chapter 6 introduces the reader to a new technique for quantifying the spatial arrangement of fractures. Normalized correlation count (NCC) addresses the limitations of previous techniques and is not biased to a particular type of spatial arrangement of fractures (Marrett et al., in review). The fourth part of Chapter 6 also illustrates the different types of spatial arrangement of fractures, as defined by Marrett et al. (in review), mostly using data sets measured for my dissertation. The fifth, and last, part of Chapter 6 explores how unbiased estimation of cluster width by NCC provides a better estimation of fracture intensity along scanlines that can be made traditionally.

1.2.4 Section Four

Section four of my dissertation includes Chapters 7, 8 and 9. Chapter 7 studies differential clustering of fractures according to fracture size and explores the relationship between fracture position and fracture size using both traditional crossplots of fracture aperture versus fracture spacing and also NCC. Natural fracture data sets from different lithologies, with different types of spatial arrangements (as established by Marrett et al., in review), and at different scales were used in Chapter 7. Initially, Chapter 7 studies the validity of using crossplots of fracture aperture versus fracture spacing for the study of the relationship between fracture size and fracture spatial arrangement. Later, NCC analysis of subsets of natural data sets with varying ranges of fracture aperture is used to study variations of spatial arrangement of fractures with varying fracture size.

Two main approaches were used in Chapter 8 to explore the internal structure of fracture clusters. One approach compared the spatial arrangement of natural fractures at outcrop and rock sample scales. For this first approach, rock samples were extracted from layers with outcrop-scale scanline measurements, and using the method described in

Chapter 5, fractures were measured along scanlines in thin sections. Based on availability, rock samples from different domains (i.e., intracluster versus intercluster domains) along a scanline were studied from layers with different lithologies, and with fractures that exhibit different types of spatial arrangements. A second approach studied the spatial arrangement of fractures located exclusively inside clusters of selected outcrop-scale fracture data sets.

In Chapter 9, I explore the relationship between different diagenetic processes and the spatial arrangement of fractures of the Cupido Fm. Using the paragenetic sequence developed by Monroy-Santiago (in preparation) I established a categorization of fractures based on fracture characteristics in addition to orientation, such as fracture trace morphology, composition of fracture cements (e.g., quartz, calcite), and timing of fracture cements with respect to fracture opening (i.e., prekinematic, synkinematic, or postkinematic). Then, I proceeded to study the spatial arrangement of fractures (using NCC) from data sets of different categories in order to explore which diagenetic processes influenced the development of a recognizable spatial arrangement.

Finally, six appendices compile all the data and supporting information generated during the course of my dissertation research. Appendix 1 encloses a set of digital templates needed to quantify fractures in new digital image collages as explained in Chapter 5 (Gomez and Laubach, 2006). Appendix 1 also contains all the files generated during the quantification of fractures in microscopic images taken in a coordinated set of thin sections from a dolostone layer in the SMO (Chapter 5, Gomez and Laubach, 2006). Appendix 2 contains the digital files (software, input and output files and Excel® template) used to calculate and display NCC results (Chapter 6). Appendix 3 compiles all the quantitative (e.g., orientation, unedited field aperture and spacing measurements, cumulative frequency distributions of fracture spacing, graph of fracture location vs.

aperture, NCC results) and qualitative (e.g., location, outcrop photo) data for each data set measured in outcrop (Chapters 7, 8 and 9). Appendix 4 is similar to Appendix 3 but compiles data from measurement in coordinated sets of thin sections from rock samples (Chapters 7 and 8). Among the data included in Appendix 4 are the NCC results for coordinated sets of thin sections (for both logarithmic and linear graduations of length scales) used in Chapters 7 and 8. Appendix 5 groups all the Excel® files containing the NCC results for fracture data sets (from both outcrop and rock sample) with different aperture thresholds used in Chapter 7.

1.3 RELEVANCE OF RESEARCH CONCERNING FRACTURE SPATIAL ARRANGEMENT

Because of the internal complexity of fractured aquifers and reservoirs and our limitations on viewing subsurface rocks, subsurface fracture systems are more difficult to characterize and less understood than aquifers or reservoirs where the permeability is mainly due to primary porosity. Subsurface fracture networks are difficult to characterize because most dimensions of a macrofracture (length, height) are typically larger than the diameter of a wellbore, and also because the probability is small that a vertical well will intersect macrofractures that are commonly vertical and widely spaced.

There are both practical as well as scientific motivations for reaching a better understanding of the spatial organization of natural fractures. From a practical standpoint, the spatial arrangement of fractures impacts subsurface fluid flow. Fractures are much more efficient conduits if they are interconnected, and connectivity within a fracture set partly reflects the degree to which fractures are closely spaced (or clustered). A fracture cluster can be defined as a domain of a fracture set where fractures are unusually abundant. In addition, the minimum length required for a horizontal well to be economically feasible may depend on the spatial arrangement of fractures, especially if fractures are clustered (Gale, 2002). Fractures arranged in wide cluster that are closely

spaced will require a shorter horizontal wellbore than narrow clusters that are widely spaced.

My dissertation provides quantitative descriptions of the geometry of different natural fracture networks. Comparing the descriptions with synthetic fracture networks can provide new constraints on mechanical models of fracture development. For example, fracture growth by linkage between initially distinct fractures influences the size distribution of a fracture population (Cladouhos and Marrett, 1996) and the variation of aperture along a fracture (Moros, 1999). Because linkage depends on the spatial arrangement of fractures, it is likely that the study of how fractures are spatially organized will also increase knowledge of how other fracture attributes evolve through time. A more realistic quantitative portrayal of the spatial arrangement of a subsurface fracture system could guide numerically created fracture systems (Gillespie et al., 1993) used to simulate fluid flow in fractured reservoirs.

Chapter 2: Terminology, Geologic Setting and Fracture Data Collection

Fractures used in this research were measured in three types of locations: in layers that crop out, in rock samples obtained from outcrop or subsurface cores and from wellbore images. With one exception, all fracture data sets measured in outcrop were obtained in the Monterrey salient, Sierra Madre Oriental, NE Mexico. The only exception is a data set that was measured in a layer of the Marble Falls Limestone that crops out at Pedernales Falls State Park, Central Texas. The data set from Pedernales presented here is an extended version of the data set in Marrett et al. (1999). Of the data sets measured in the Monterrey salient, the majority were veins measured in carbonate layers of the Lower Cretaceous Cupido Formation while one data set of veins was measured in a sandstone layer of the Upper Triassic-Lower Jurassic La Boca Formation (Davis, 2005). In addition, two data sets of joints were measured in siltstone layers of the Upper Tamaulipas Formation (Aptian-Albian) and the Agua Nueva Formation (Upper Cretaceous).

The fracture data sets obtained from the subsurface came from two different geologic regions within the continental US. The first group of fracture data sets from the subsurface is composed of 76 rotary-drilled sidewall cores and 125 m of wellbore images from three wells that penetrated the Barnhart field, a reservoir in the Ellenburger Group (Lower Ordovician) located about 16 km southeast of the town of Big Lake, Texas (Gomez et al., 2001). The second group of subsurface fracture data sets were measured from 35 m of subhorizontal core drilled across the Cozzette Sandstone (Cretaceous) from the Slant Hole Completion Test (SHCT-1) well in northwestern Colorado (Gomez et al., 2003a). Fracture data sets were measured along the entire core and in five rock samples obtained from the core.

In this chapter, I present definitions and some generalities about how fracture data were acquired. This is followed by a summary of the stratigraphy and structural geology of the two regions where outcrop fracture data were collected and some qualitative information about the fractures. Quantitative information about each data set will be provided in subsequent chapters. A summary of the regional geology where the subsurface fracture data were acquired will be provided in the chapters where subsurface fracture data are analyzed (Chapters 3 and 4).

2.1 FRACTURE TERMINOLOGY

A fracture is any mechanical discontinuity along which rocks have lost cohesion. Current practice in structural geology distinguishes two kinds of fractures depending on the relative motion between the two fracture walls: opening-mode (or mode I) and shear-mode (modes II and III) fractures (Pollard and Aydin, 1998). The relative motion across opening-mode fractures is perpendicular to the fracture while for shear fractures the relative motion is parallel to the fracture. The volume of an opening-mode fracture is formed by motion in which the two fracture walls have moved apart (Twiss and Moores, 1992). As stated by Kulander et al. (1990), there are no restrictions to the term fracture due to scale or directions of applied stress. A fracture set (e.g., Twiss and Moores, 1992; Davis and Reynolds, 1996) groups all fractures genetically related and with common characteristics (timing, orientation, cement fill). I use fracture array as a general term for a group of sets of natural fractures. Fractures can also be classified as macrofractures (fractures visible without any magnification aid) or microfractures (fractures visible only under magnification), with microfractures typically being much more common and therefore more likely to be sampled effectively in small volumes of rock (Laubach, 1997; Marrett et al., 1999; Laubach, 2003).

Using the absence or presence of mineral cements, opening-mode fractures can be further classified as joints (Figure 2.1a) or veins (Figure 2.1b), respectively. Alternatively, it can be alleged that joints lack cohesion at this time whereas veins lacked cohesion at least temporarily during growth (R. Marrett, personal communication, 2005). Both joints and veins display evidence for exclusively or mostly opening displacement.

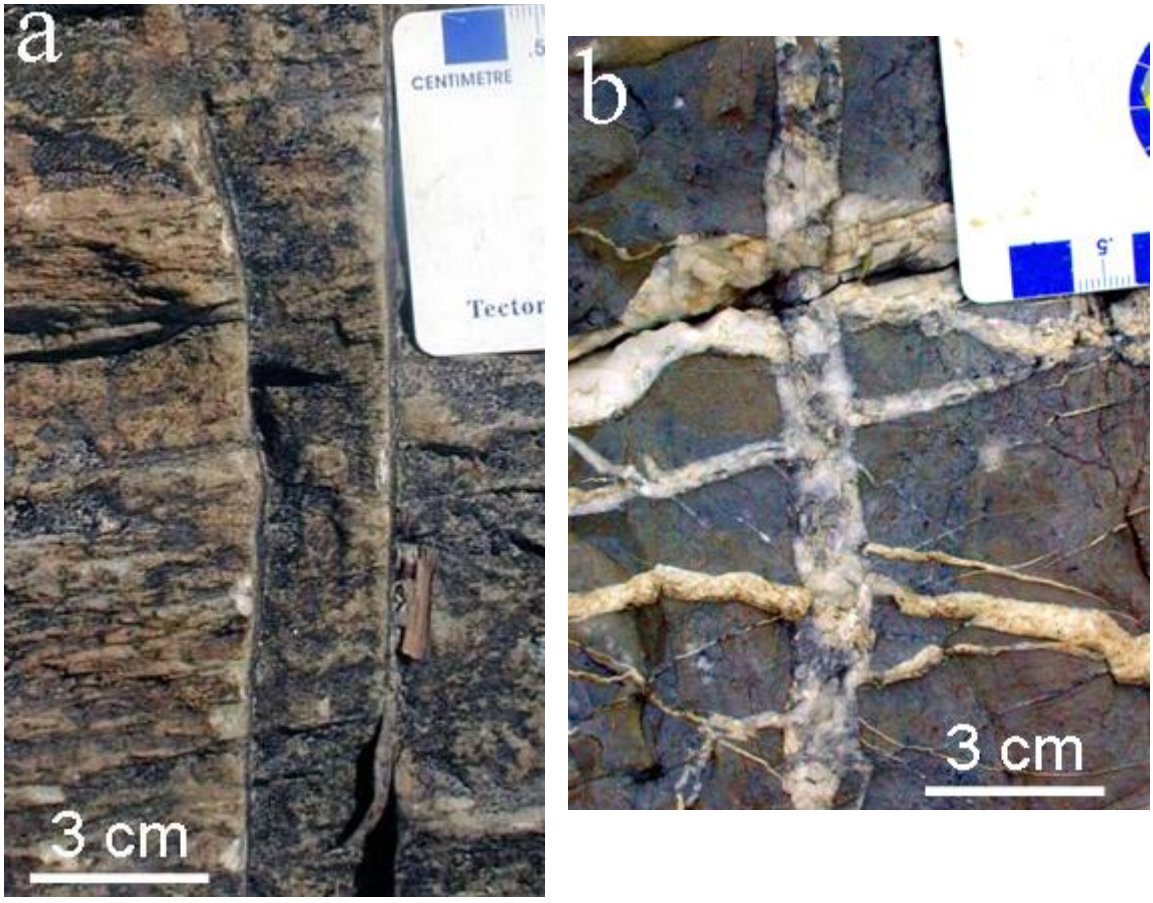

Figure 2.1 Outcrop photographs of typical joints (a) and veins (b). (a) Photo was taken in a siltstone layer of San Felipe Fm. between Escalera and Palmas canyons. (b) Photo was taken in a carbonate layer of the Cupido Fm. in Los Chorros canyon.

Cements inside fractures can also be classified based on timing of fracture opening relative to cement precipitation (Laubach, 2003; Laubach et al., 2004).

Prekinematic and postkinematic cements precipitate before or after fracture opening, respectively (Laubach, 1997; Laubach, 2003). In contrast, synkinematic cements precipitate concurrently with fracture opening (Laubach, 2003). The terms pre-, syn-, and postkinematic indicate the relationship between fracture opening history and diagenesis of rock and fracture. These terms also highlight how fracture timing relative to the diagenetic history of a rock can influence the preservation of porosity (Laubach, 2003).

Although a joint is commonly defined as an opening-mode fracture with little or no displacement (Hodgson, 1972; Narr and Suppe, 1991; Twiss and Moore, 1992) and without any mineral cement, I agree with the assessment of Pollard and Aydin (1988) that if a joint exists then there must have been some displacement. An opening-mode fracture having an aperture that is small compared to fracture length and lacking cement is also typically classified as a joint (Pollard and Aydin, 1988). Opening-mode fractures that have been filled with one or more minerals precipitated from an aqueous solution in the fracture are typically called veins (van der Pluijm and Marshak, 1997).

I avoided any size qualification and use only the presence (veins) or absence (joints) of cement as the criteria to distinguish joints from veins, because a classification that uses fracture size will be problematic for the commonly found opening-mode fractures that have characteristics of the two categories. For example, opening-mode fractures with apertures as small as one-tenth of a millimeter could be classified as joints based on the small amount of displacement between the fracture walls yet they can be completely filled with cement (Marrett et al., 1999).

2.2 FRACTURE DATA COLLECTION

The most important observable features of a single opening-mode fracture are its orientation, aperture, length, height, position relative to other fractures, stratigraphical and structural location, fracture wall roughness, minerals precipitated on fracture walls

and timing relative to other features. Being approximately planar structures, fractures require three mutually orthogonal measurements to fully quantify their size.

For fractures oriented perpendicular to layering in sedimentary rocks, fracture length and fracture height are typically defined with respect to bedding planes. Fracture height is the distance between fracture tips as measured normal to bedding whereas fracture length is measured in a direction parallel to bedding. The third measurement, kinematic aperture, is defined as the distance between fracture walls measured in a direction perpendicular to the fracture walls (Figure 2.2), regardless of the presence (or absence) of mineral fill occupying the fracture (Marrett et al., 1999). The definition of kinematic aperture includes any cement precipitated inside a fracture; partly or totally filling the pore space created by fracture opening.

Cement that partially or completely fills a vein would difficult reduction in fracture aperture due to variations in the local stresses. In contrast, the lack of cement inside joints makes them more susceptible to reductions in aperture. Therefore, kinematic aperture of veins quantifies more reliably the cumulative opening displacement of a fracture throughout its geologic history.

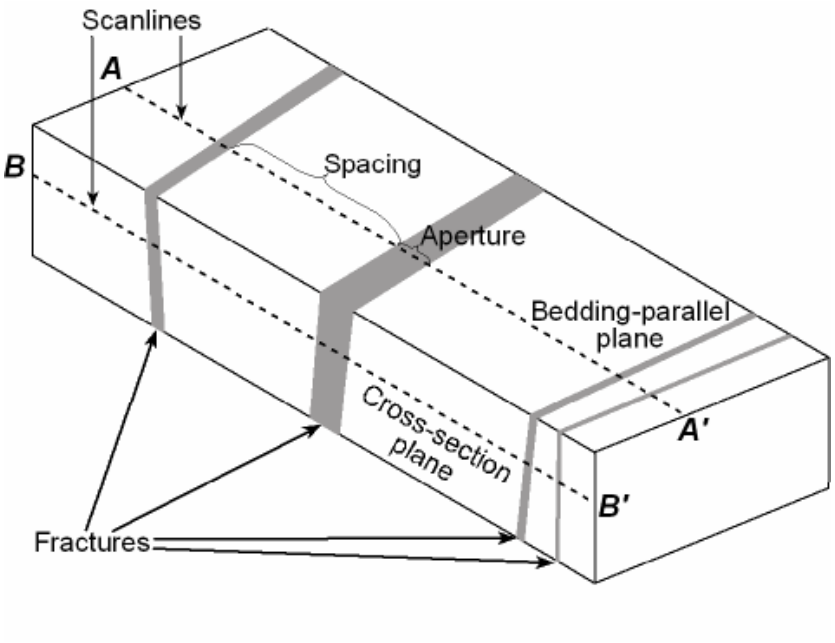

Figure 2.2 Isometric sketch depicting a set of opening-mode fractures that are perpendicular to layering. Fracture-perpendicular scanlines can be located on bedding-parallel (A-A') or cross-section exposures (B-B').

2.2.1 One-dimensional Scanline Data

Although fractures are truly three-dimensional structures, quantification of the spatial arrangement of fractures has been done almost exclusively in 2D or 1D terms because of the difficulties in observing fractures in three dimensions. To fully quantify the properties of a fracture array in a 2D fashion, a map containing the traces of fractures visible in a surface (e.g., an exposed bedding plane) must be drawn, whereas for 1D studies, only the positions of fractures intersected by a line of observation, commonly known as a scanline, are required (Figure 2.2). When measuring fractures with apertures that span several orders of magnitude or more (Marrett et al., 1999), the extra time required to take a study from 1D to 2D would be extremely large because, in order to measure 2D data, fracture apertures would have to be measured at numerous places along each fracture trace to fully represent the variability of fracture aperture along fracture

trace (Moros, 1999). Sedimentary rock exposures suitable for 1D investigation of fractures (on surfaces parallel or transverse to bedding) are more abundant than for 2D studies (typically parallel to bedding). Adequate outcrops need to be, as much as possible, continuous and free of superficial irregularities like vegetation or erosional channels that cause difficulties in data acquisition and impose errors. Also, 1D analyses of fracture arrays are readily applicable to borehole data from core or image logs without stereological corrections, and are topologically similar.

Scanline data cannot represent the complexity of fracture arrangements in three dimensions. However, in principle, if a scanline is positioned in a representative portion of the fracture array, then it can distinguish between regularly spaced or clustered arrangements of fractures (Priest and Hudson, 1976). In addition, a scanline needs to be long enough to capture the characteristic of the spatial arrangement under study. For example, to detect the distance between clusters a scanline needs to cross at least two clusters.

To measure fracture attributes in a 1D fashion, a scanline is simply oriented in a direction perpendicular to the average orientation of the fracture set under study; this is feasible because fractures commonly have consistent orientations in domains of several hundred meters or more in length (e.g., Cruikshank and Aydin, 1995) but occasionally of up to 100 km (e.g., Engelder and Geiser, 1980). Scanline orientation is determined a priori to minimize geometric distortions created by non-normal intersection of fractures along the scanline, and I located the scanlines using criteria that were independent of the fractures (e.g., based on outcrop quality and continuity) so that the resulting sample is as random as possible. If more than one fracture set was recorded, each set with a distinct orientation, the orientation of the scanline could not be perpendicular to all measured fracture sets. In those cases, fracture apertures and spacings were trigonometrically

corrected to compensate for the non-perpendicularity between fracture and scanline orientation. Along a scanline, consecutive values of kinematic aperture and fracture spacing or position are measured for fractures that are larger than a pre-determined size threshold. This threshold is typically the minimum size that can be measured in the field (Ortega et al., in review) or in petrographic images (Gomez et al., 2003a) without risk of omitting some fractures.

In practice, obtaining fracture data along a scanline is accomplished by measuring first the distance between the beginning of the scanline and the near wall of the first fracture. Second, the distance between the two walls (kinematic aperture) of the first fracture is measured. Third, the distance between adjacent walls of the first and second fractures is measured and recorded as the fracture spacing between the first two fractures (Figure 2.3). These last two steps are repeated along the entire length of the scanline for each fracture reaching the size threshold. When needed, information about the type(s) of fracture cement(s) present inside the fractures and fracture orientation was also acquired simultaneously and used later to separate fractures into sets. Although fracture orientation is a fracture attribute that cannot be measured in a strictly 1D line, it was acquired (or at least estimated) by following a fracture outside the scanline.

Fracture data along a scanline can be acquired at any scale, in air photos (Huang and Angelier, 1989; Gillespie et al., 2001), outcrops (Huang and Angelier, 1989; Narr and Suppe, 1991), physical models (Rives et al., 1992; Spyropoulos et al. 1999), petrographic images (Gross and Engelder, 1995; Gomez, 2004), and scanning electron microscope images (Marrett et al., 1999; Gomez et al., 2003a). However, for this research fracture data were acquired only in outcrops and on images from petrographic and scanning electron microscopes.

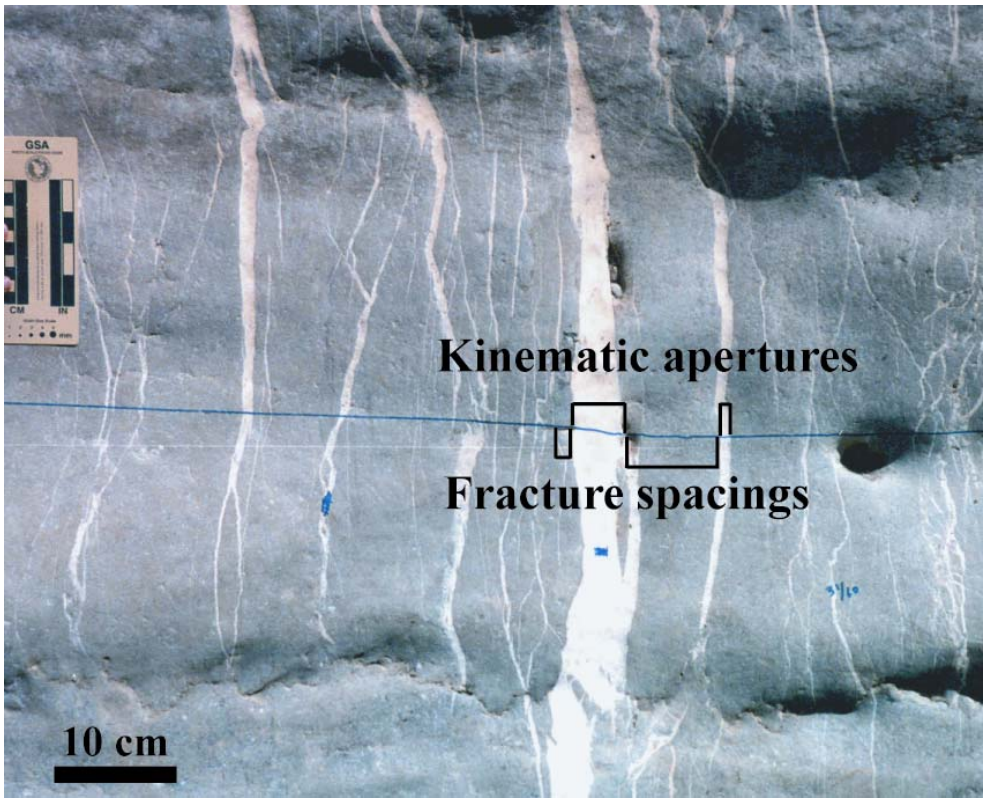

Figure 2.3 Outcrop photograph of a scanline in a cross-section exposure of Layer 13 at Palmas Canyon, Cupido Formation (Lower Cretaceous), NE Mexico.

To measure both kinematic aperture and fracture spacing with the greatest possible accuracy in outcrops, I used a hand lens and a logarithmically graduated comparator (Ortega et al., 2006). This combination of tools allows collection of fracture aperture or spacing data down to approximately 0.05 mm. The comparator contains lines with increasing width from 0.05 to 5 mm, which allows rapid measurement of fracture apertures or spacings while maintaining consistent accuracy across a broad range of fracture sizes. The increments in line width are such that they represent approximately uniform multiples of each other and thus are evenly spaced when plotted on a logarithmic axis. In this way, aperture and spacing sizes were measured with consistent accuracy as viewed in a log-log graph (Marrett et al., 1999; Ortega et al., 2006). If fracture apertures

or spacings were larger than 5 mm, they were measured with a millimetric ruler. The attributes of fractures on images from petrographic and scanning electron microscopes were measured using the method described in detail in Chapter 5.

2.2.2 Summary of Data Measured

Fracture spacing along scanlines has been measured in numerous lithologies, such as granite (Rouleau and Gale, 1985), quartzite (Simpson, 2000), chalk (Priest and Hudson, 1976; Gale, 2002), chert (Narr and Suppe, 1991; Gross, 1993), limestone (Huang and Angelier, 1989; Rives et al., 1992; Gillespie et al., 2001), dolostone (Gross and Engelder, 1995; Gomez, 2004), and sandstone (Priest and Hudson, 1976; Huang and Angelier, 1989; Gillespie et al., 1993). For this dissertation, the spacings between 6110 fractures were measured along a total of 142.2 m of scanline in outcrops of sedimentary rocks in the Monterrey salient. Of those fractures, the apertures of only 5088 were measured (Table 2.1). In some data sets, fractures (a total of 1,010) having apertures slightly smaller than the aperture threshold, and therefore the two spacings around such fractures, were measured even though the apertures could not be reliably measured. Outcrops were selected for measurement if they displayed a smooth surface that allowed a reliable measurement of fracture aperture and spacing, and if they were long enough for the measurement of a representative portion of the fracture array. The Monterrey salient offered abundant outcrops either perpendicular (cross-section) or parallel to bedding (Figure 2.2, Table 2.1) with excellent quality due to the polishing of rocks on canyon walls caused by flash floods. Although most of the data sets were acquired with the smallest line width on the comparator (0.05 mm), aperture thresholds of 0.095, 0.14, 0.215 and 0.265 mm were used in four data sets (Table 2.1).

Table 2.1 Summary of geologic information and statistics for all the outcrop fracture data sets acquired for this study. Although two layers (Escalera OO12 and OO1) were previously studied by Ortega (2002), data used in this dissertation are new because only fracture apertures were collected in previous work.

Data Set	Geographic and Political Area	Structure Name	Structural Position	Geologic Unit	Lithology	Fracture type	Outcrop Type	Number of Fractures		Aperture Threshold	Scanline Length	Strain
								Aperture				
								Measured	< Threshold			
								All Sets		mm	m	%
Escalera OO12	Escalera Canyon SMO, Mexico	San Blas Anticline	Anticline forelimb	Cupido Fm.	Dolostone	Veins	Cross section	1095	48	0.05	3.56	20.4
Escalera OO1								1160	480		3.20	13.3
Escalera 3			Anticline backlimb					293	0	0.095	6.93	4.46
Escalera 2								614	46	0.05	6.15	7.73
Escalera 1							Bedding surface	460	0		7.03	7.02
Escalera Joints				Aurora Fm.	Siltstone	Joints		707	286		35.83	0.385
Palmas 12	Palmas Canyon SMO, Mexico		Anticline forelimb	Cupido Fm.	Dolomitic limestone	Veins	Cross section	316	0	0.265	6.14	12.7
Palmas 13								459	0	0.14	5.43	9.16
Oliverio Anticline	Chorros Canyon SMO, Mexico	Arteaga Anticline	Forelimb and backlimb of minor folds	Cuesta del Cura Fm.	Limestone			214	102	0.05	1.72	3.55
Claxon Syncline								150	39		0.84	9.48
Huasteca - Set A	Huasteca Canyon SMO, Mexico	Muertos Anticline	Anticline forelimb	Cupido Fm.	Dolostone	Veins		581	0	0.215	16.59	5.74
Muertos			Anticline backlimb	San Felipe Fm.	Siltstone	Joints	Bedding surface	61	9	0.05	48.82	0.0282

Total number of fracture spacings measured = 6110

Total number of fracture apertures measured = 5088

Total scanline length measured = 142.24 m

In addition to the data sets I collected, several other data sets acquired by other members of the Jackson School of Geosciences were available for analysis (Table 2.2). One of the data sets is the only one measured in a sandstone layer inside the Monterrey salient (Ward, in preparation), at a locality that was called “San Pablo” and “Rancho Alomar” by Wilson (1990) but for this research the name of Tranquitas (Davis, 2005) is adopted.

As mentioned in Chapter 1, the spatial arrangement of fractures (mainly microfractures) from coordinated sets of thin sections was also studied (Table 2.3). Because intragranular microfractures (Types Ib, Ic, and Id of Laubach, 1997) could be confused with inherited microfractures (Type III of Laubach, 1997), only transgranular microfractures (Type Ia+ of Laubach, 1997) were used for the study of the spatial arrangement of fractures in thin sections (Gomez, 2004). Selecting only transgranular microfractures reduced the number of fractures available for study from 1432 to 1315 (Table 2.3).

Table 2.2 Summary of geologic information and statistics for all the outcrop fracture data sets acquired by others but made available for this study. JG = Julia Gale, MW = Meghan Ward, FRAC = Randall Marrett, Celinda Kelsey, Julia Gale, Chris Hare and Leonel Gomez.

Data Set (Acquired by)	Geographic and Political Area	Structure Name	Structural Position	Geologic Unit	Lithology	Fracture type	Outcrop Type	Number of Fractures		Aperture Threshold	Scanline Length	Strain
								Aperture				
								≥ Threshold	< Threshold			
								All Sets		mm	m	%
Palmas 11 LR (JG)	Palmas Canyon SMO, Mexico	San Blas Anticline	Anticline forelimb	Cupido Fm.	Dolostone	Veins	Cross section	262	0	0.95	21.11	4.59
Palmas 11 HR (JG)								575	0	0.075	2.49	7.62
Tranquitas (MW)	Galeana area SMO, Mexico	Huizachal - Peregrina Anticlinorioum	Anticline crest	La Joya Fm.	Sandstone		Bedding surface	496	0	0.05	31.09	1.30
North Disppointment Draw (OO)	Uinta Mountains Colorado, USA	Not Applicable	Gently tilted bed on monocline	Weber Sandstone	Sandstone			362	0	0.10	208.59	1.26
Grove Creek (JG)	Near Waxahachie, North Central Texas, USA	Not Applicable	Sub-horizontal	Austin Chalk	Chalk			136	0	0.05	246.40	0.15
Pedernales (FRAC)	Llano uplift, Texas, USA	Not Applicable	Gently tilted bed	Marble Falls Limestone	Limestone			916	83	0.05	58.96	0.53

Total number of fractures apertures measured = 2747

Total number of fracture spacings measured = 2825

Total scanline length measured = 568.62 m

Table 2.3 Summary of geologic information and statistics for all the fracture data sets measured in thin sections. All thin sections are approximately parallel to bedding. SEM = Scanning Electron Microscope, CL = Cathodoluminescence.

Corresponding Outcrops	Sample		Number of Consecutive Thin Sections	Thin Section Sizes	Microscope Type	Imaging			Scanline Information			Transgranular Fracture Aperture		
	Name	Location in Outcrop		(in)		Individual Images	Magnification	Image Collages	Scanline Length (mm)	Number of Fractures	Number of Transgranular Fractures	Minimum (μm)	Maximum (μm)	Strain (%)
Escalera Joints	02LG2	Along scanline	1	2 x 3	Petrographic	18	5X	1	24.33	39	3	25.1	189	1.02
Escalera OO1	02LG11	Outside cluster Along scanline	1			47		2	65.44	60	52	3.59	3795	9.82
	02LG12	Inside cluster Outside scanline Layer base	2			85		4	110.61	94	94	1.50	1299	13.2
			1		SEM	69 (only CL)	150X	2	45.88	35	29	2.77	1254	14.4
Escalera OO12	02LG13	Inside cluster	4		Petrographic	101	5X	7	148.74	484	484	0.63	12355	20.0
Palmas 12	02LG15	Along scanline	2			88		4	101.45	31	29	8.06	8590	14.6
Palmas 13	02LG16	Along scanline	5			186		10	290.32	208	175	4.55	4023	8.08
Huasteca	03LG26	Contains part of a cluster	2			77		2	121.54	38	34	3.60	136	0.918
Palmas 11	PA11JG	Outside cluster	2	1 x 2		43		2	63.72	156	156	3.50	424	14.6
			1	2 x 3		N.A.	2.5X	1	38.25	86	86	20.2	377	15.6
Tranquitas	04GA01LG	Inside cluster	8	1 x 2	SEM	660 (only CL)	150X	16	229.77	201	173	0.48	632	2.59

Total number of thin sections = 29

Total number of digital images = 1374

Total scanline length measured = 1.24 m

Total number of fracture apertures measured = 1432

Total number of transgranular fractures used for spatial arrangement analysis = 1315

2.2.3 Wellbore Image Data

A common tool used in the oil industry to study fractured reservoirs is image logs (Nelson, 2001). The most common type of image log detects fractures by measuring the differences in resistivity between rock matrix and fracture; because the tools are oriented and their depth is known, the detected fractures can be located and oriented (Ekstrom et al., 1987). If image logs are acquired in wells that are approximately perpendicular to fractures (typically requires a horizontal well), then it would be possible to study the spatial arrangement of fractures along the wellbore (Lofts et al., 1997).

The spatial arrangement of a few fracture data sets obtained from wellbore image logs was analyzed using the Normalized Correlation Count (NCC) technique (see Section 6.3). Most of these data sets were provided by oil companies that are members of the Fracture Research and Application Consortium of the University of Texas at Austin (Bureau of Economic Geology).

Unfortunately none of the data sets available fulfilled all the conditions required for an ideal analysis of the spatial arrangement of fractures in subsurface fractured reservoirs. Because this would have been the first time that the spatial arrangement of subsurface macrofractures was studied with NCC, the conditions that an ideal data set must have are quite stringent. In order of importance those conditions are: First, regardless of the well orientation with respect to bedding, the imaged section of the well (typically only the horizontal) should remain in the same layer. Because fractures are commonly limited to individual beds, using fracture data from multiple layers would risk mixing fractures from mechanically different layers and with different spatial arrangements (Chapter 8). Second, fractures should have been mapped with a quality index. Without an indication of quality of interpretation of each fracture, some planar

features analyzed might be geologic structures different than fractures (e.g., cross bedding) or artifacts generated during log acquisition or processing (Lofts and Bourke, 2000). The inclusion of such planar features could alter the signal of the spatial arrangement of fractures. And third, the images should have uniform detection threshold for fractures along entire wellbore. If drilling or logging conditions changed during the acquisition of wellbore images, fractures that otherwise would be detected could go unnoticed. This would result in some segments of the wellbore having artificially low fracture intensity, which in turn would make other sections display abnormally high fracture intensity, the signature of a cluster.

All of the data sets from wellbore images displayed an arrangement of fractures that was indistinguishable from random. Because no data set complied with the conditions stated above, it is possible that some of the data sets are not randomly arranged but instead comprise inadequate data. However, the potential for understanding the spatial arrangement of fractures in the subsurface using image logs remains high.

2.3 SIERRA MADRE ORIENTAL

The Sierra Madre Oriental (SMO) is a fold-thrust mountain belt in northeastern Mexico (Figure 2.4) that mostly exposes Mesozoic sedimentary strata uplifted during the Laramide orogeny (Late Cretaceous to Paleogene). The SMO trends approximately northwest to southeast in northern Mexico. Between the cities of Torreón and Ciudad Valles the trend of the SMO changes, where deformation affected rocks farther out into the foreland than in adjacent areas, forming a segment of the fold-thrust belt about 600 km wide known as the SMO salient (Marrett and Aranda-García, 2001). Structures trend approximately to the north on the eastern side and to the west on the northern side of the SMO salient (inset in Figure 2.4).

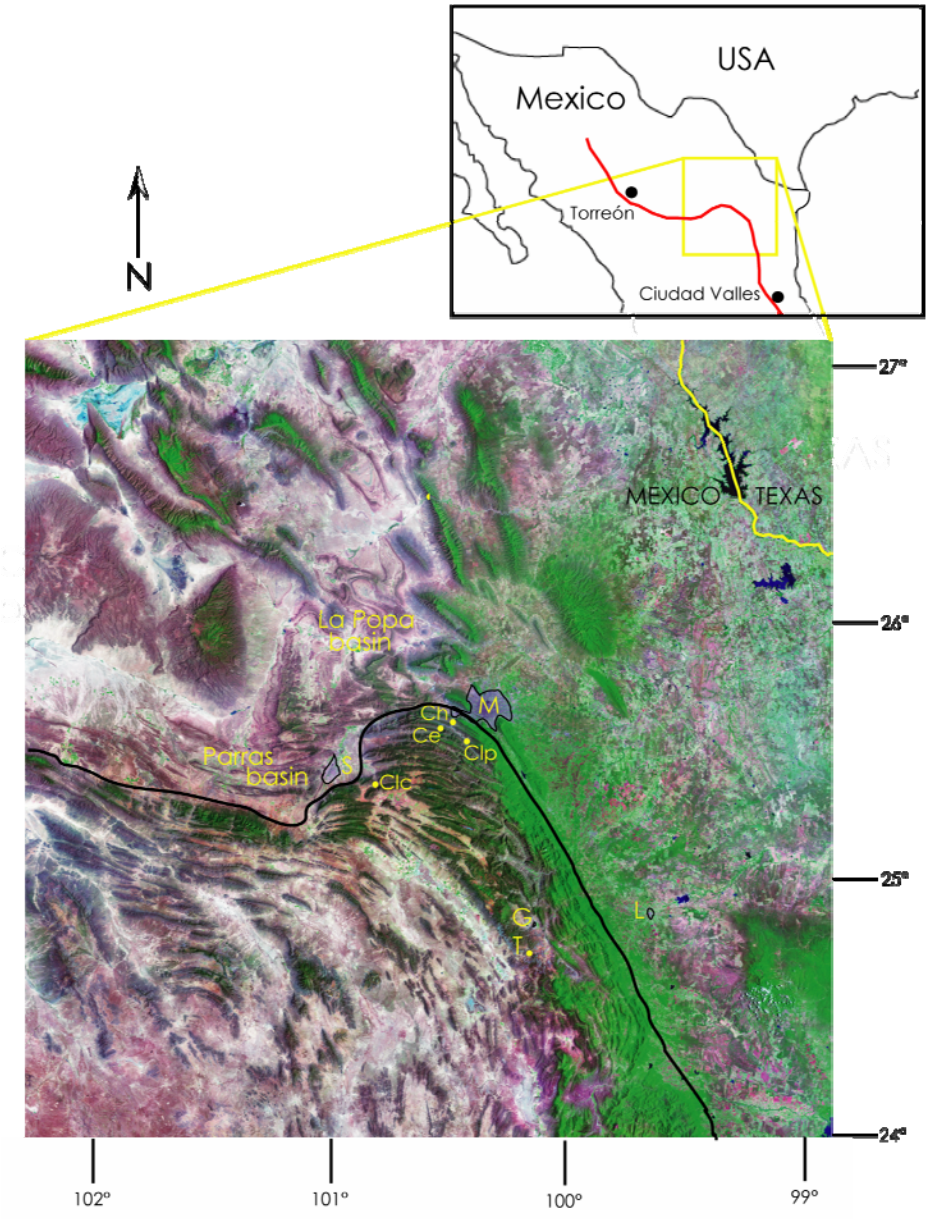

Figure 2.4 Satellite image of part of the Sierra Madre Oriental (SMO), including the Monterrey salient. Yellow line marks the international boundary between Mexico and the USA. Thick and continuous black line approximates the deformation front, as delimited by laterally continuous exposure of Jurassic-Cretaceous carbonate strata. M – Monterrey, S – Saltillo, L – Linares, G – Galeana, Ce – Escalera Canyon, Ch, Huasteca Canyon, Clc – Chorros Canyon, Clp – Palmas Canyon, T – Tranquitas locality. Also shown are the Parras and La Popa Basins. Modified from Hooker, 2004.

Between the cities of Linares and Saltillo, at the apex of the SMO salient, the fold belt shows locally enhanced curvature in the Monterrey salient (Eguiluz de Antuñano, 1991). Fracture data used for this study were acquired in the Monterrey salient, near the cities of Monterrey and Galeana (Nuevo León state) and Saltillo (Coahuila state).

Horizontal shortening in the SMO was, like in the Rocky Mountains, attained mainly through thrust faulting with associated folding (Dickinson and Snyder, 1977; Marrett and Aranda-García, 2001). However, shortening in the Monterrey salient was dominated by colossal (multi-kilometer arc length) folds. Faults, where present, provide only a minor contribution to the total strain (Avenius, 1982).

2.3.1 Stratigraphy

The majority of the rocks cropping out in the SMO range in age from Upper Jurassic (Kimmeridgian, Olvido Formation) through Upper Cretaceous (Santonian, San Felipe Formation). Outcrops of younger (Parras Shale and Difunta Group, Campanian to Maastrichtian) rocks are present in the foreland of the SMO in the Parras and La Popa Basin (Figures 2.4 and 2.5). These sedimentary sequences were deposited after the opening of the Gulf of Mexico rift basin and during subsequent passive-margin sedimentation, representing four major (second-order, supersequence) sea-level transgression-regression cycles, each roughly 15 m.y. in duration (Goldhammer and Johnson, 1991).

Major second-order supersequences are defined as large-scale basin fill cycles marked by regionally correlative facies patterns of retrogradation and progradation. The entire sedimentary package has a thickness of approximately 3000 m and can be regionally correlated with sequences throughout the Gulf of Mexico (Todd and Mitchum, 1977; Goldhammer et al., 2001; Lehmann et al., 2000).

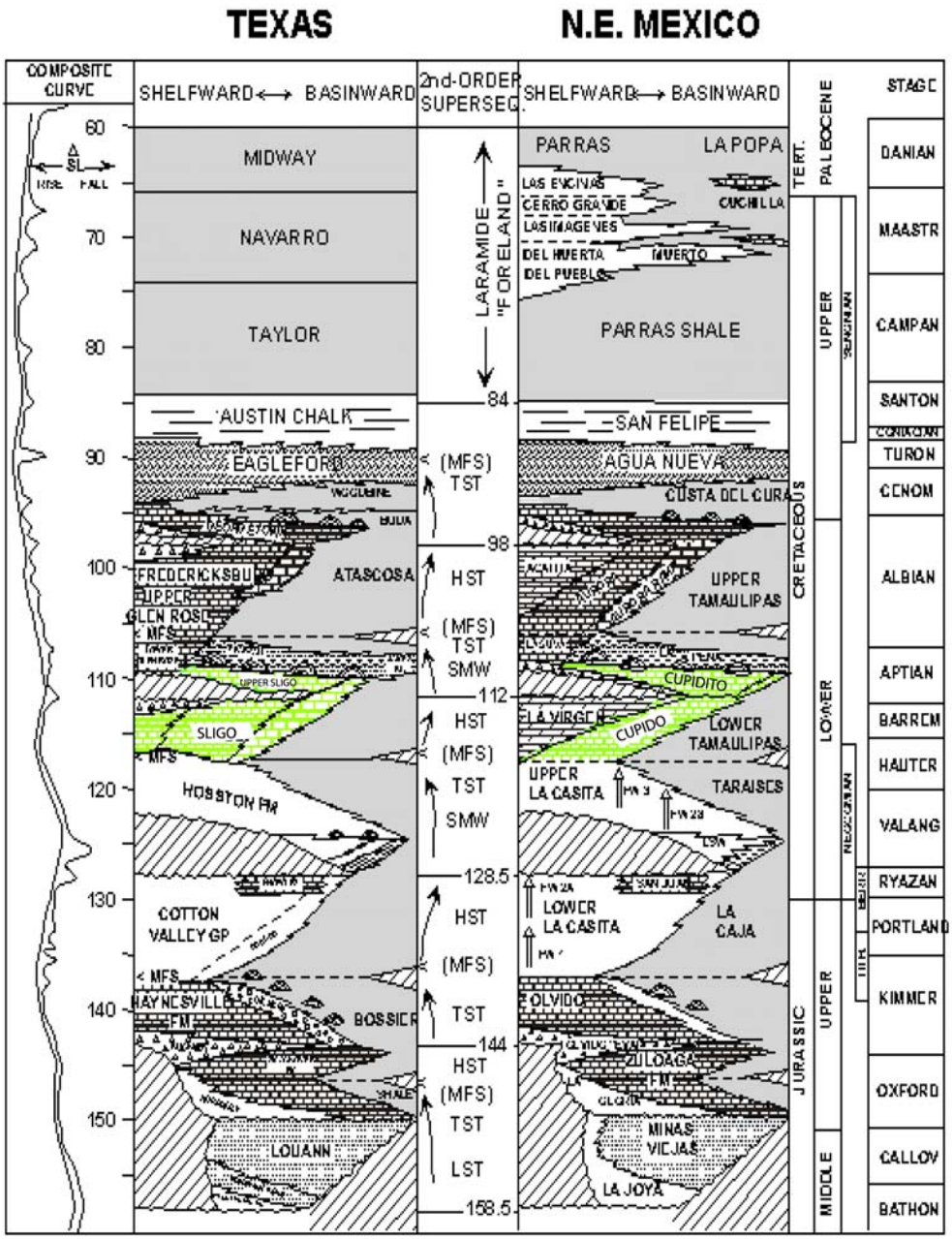

Figure 2.5 Chronostratigraphic charts for northeastern Mexico and Texas Gulf Coast showing second-order supersequences as interpreted by Goldhammer et al. (1991).

However, in a comparatively small part of the Monterrey salient near the town of Galeana (Figure 2.4) there are outcrops of two additional geologic units, one deposited

during (syn-rift) and another immediately after (post-rift) the opening of extensional to transtensional basins associated with opening of the Gulf of Mexico (Barboza-Gudino et al., 1999), known respectively as La Boca (late Triassic-early Jurassic) and La Joya Formations (Goldhammer and Johnson, 1991).

The oldest sedimentary rocks used for this dissertation in the Monterrey salient are conglomeratic sandstones of fluvial-alluvial origin of La Boca Formation (Davis, 2005). They are overlain by upward fining siliciclastic rocks (La Boca Formation) and by a polymictic cobble conglomerate of alluvial origin that marks the base of the La Joya Formation (Barboza-Gudino et al., 1999; Davis, 2005). In the locality of Tranquitas, La Joya sandstones have intercalated evaporites suggestive of a lacustrine-marginal evaporitic depositional setting (Davis, 2005).

Immediately above the La Joya Formation are evaporites and limestones of the Minas Viejas, Zuloaga and Olvido Formations (Oxfordian-Kimmeridgian), deposited shortly after the rifting phase of the Gulf of Mexico (Goldhammer and Johnson, 1991) and marking the beginning of a marine carbonate system that would dominate deposition for the entire Cretaceous period (Figure 2.5). Overlying the Olvido Formation is the La Casita Formation (Neocomian), formed in an open marine environment and derived from exposed land masses to the north and from the Coahuila Peninsula to the northwest (Goldhammer and Johnson, 1991).

A large portion of the fracture data analyzed in this study was acquired in rocks of the Barremian-Aptian Cupido Formation. The Cupido Formation is a limestone-dolostone highstand-regressive sequence defined as the platformal carbonate formation above the Taraises Formation and below the La Peña Formation, and is the most erosionally resistant formation in the stratigraphic section. The Cupido Formation is the equivalent of the Sligo Formation of the Texas Gulf Coast (Goldhammer, 1999). The Cupido

Formation has an estimated thickness between 500 and 800 m with the uppermost ~100 m designated as the transgressive Cupidito member, which is not formally recognized as distinct from the Cupido Formation (Humphrey and Diaz, 2003).

The Cupidito member was introduced by Wilson and Pialli (1977) to designate the Upper Cupido transgressive interval immediately underneath the La Peña Formation. The Cupidito member is a passive-margin carbonate shelf deposit (Figure 2.6) and is separated from the remainder of the Cupido Formation by the 120 Ma second-order supersequence boundary (Lehmann et al., 2000), which has been correlated around the SMO and is characterized in outcrop by a solution-collapse breccia (Goldhammer et al., 1991). The Lower Tamaulipas Formation is the basinal equivalent of the platformal Cupido Formation (Figure 2.5), and was deposited to the south and east of the platform.

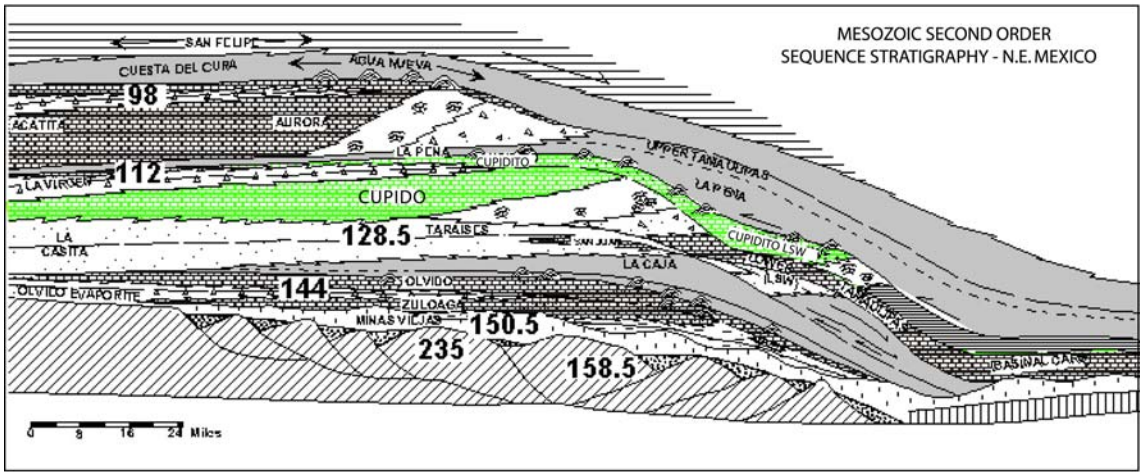

Figure 2.6 Schematic dip-oriented regional stratigraphic cross-section trending north-northwest to south-southeast. Major second-order supersequence boundaries are shown (approximate ages in Ma). After Goldhammer et al. (1991).

The Cupido carbonate factory was flooded during the Aptian and draped by the calcareous La Peña Shale, in association with global sea level rise (Tinker, 1985). Deposition in shallow carbonate platforms returned during the Albian forming the

regressive Aurora Formation, which is overlain by the transgressive Cenomanian Cuesta del Cura Limestone (Goldhammer and Johnson, 1991). The Cuesta del Cura Limestone is overlain by the further transgressive deep marine carbonates of the Agua Nueva (Cenomanian-Turonian) and San Felipe (Santonian) Formations. The sedimentary sequence in the SMO is capped by the Campanian Parras Shale and the Maastrichtian Difunta Group (Goldhammer and Johnson, 1991).

2.3.2 Structural Geology

The SMO is the geologic expression in northeastern Mexico of Laramide-age orogeny that uplifted and horizontally shortened the upper crust throughout western North America (Lopez-Ramos, 1983). The term Laramide has been used to represent a specific tectonic event from late Cretaceous to early Tertiary, which is the significance of the term used here. However, it also has been used to denote the thick-skinned, fault dominated style of deformation that characterized the orogenic activity (Dickinson and Snyder, 1977; Gray et al., 2001) throughout most of north Mexico and southwest USA.

In the Monterrey salient (Figure 2.7) shortening occurred mainly by the development of giant (6-9 km arc length and 2-3 km amplitude) folds (Padilla y Sanchez, 1985). The folds are approximately isoclinal and lack coherent vergence. The limbs of the folds are locally overturned but more commonly are near vertical (Marrett and Aranda-García, 2001).

Although shortening in the SMO reached up to 50% in magnitude where thrust faulting dominated, the Monterrey salient was shortened only about 30% (Marrett and Aranda-García, 2001). The variation in style of Laramide-age deformation along strike of the SMO is believed to be associated with the presence of evaporite strata of Oxfordian-Kimmeridgian age (Olvido Formation). Areas of fold-dominated deformation are associated with thick evaporite strata (Marrett and Aranda-García, 2001). Evaporites are

much weaker than limestone at depths of 1-2 km or more, because they are capable of crystal plastic flow (Davis and Engelder, 1985). In the SMO salient, evaporites acted as a decollement and flowed into the cores of anticlines as they developed (Figure 2.8) allowing folds to develop with relatively little faulting (Stewart, 1996). However, evaporites later had to evacuate the anticline cores near the end of fold development. In contrast, the style of Laramide-age shortening is fault-dominated outside of the SMO salient, where evaporites are absent (Marrett and Aranda-García, 2001).

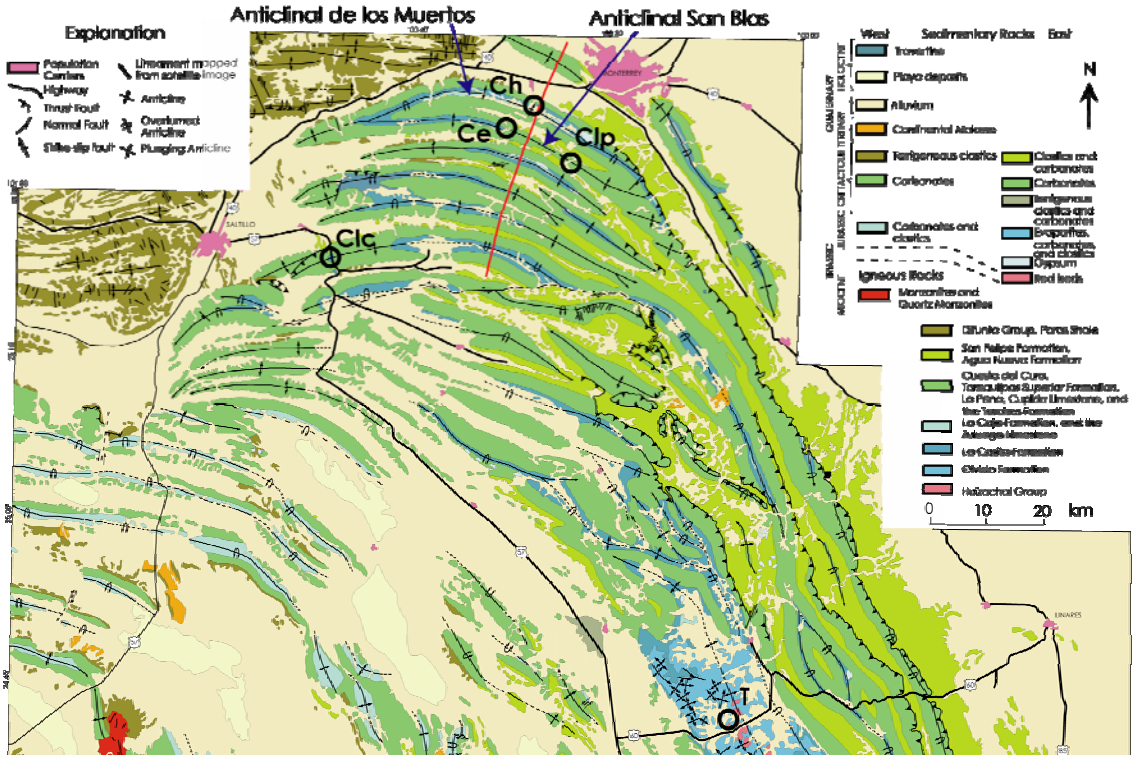

Figure 2.7 Geologic map of the Monterrey salient from Padilla y Sanchez (1985). Ce – Escalera Canyon, Ch – Huasteca Canyon, Clc – Chorros Canyon, Clp – Palmas Canyon, T – Tranquitas locality.

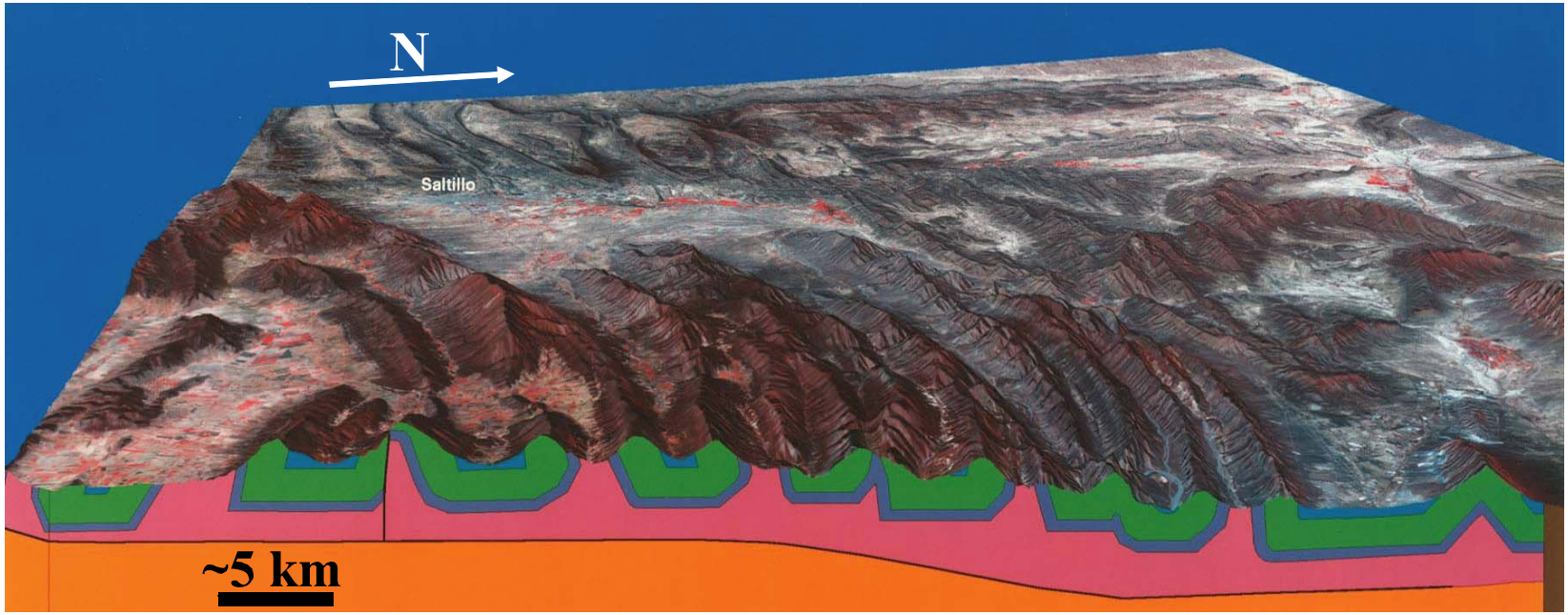

Figure 2.8 Generalized cross-section through the Monterrey salient, from Marrett and Aranda-García (2001), with oblique view of Digital Elevation Model (DEM) painted with Landsat TM image. Unfolded older rock, presumably rift-related and crystalline basement, in orange, Jurassic evaporites in pink, and folded Jurassic and Cretaceous sedimentary rock above. Note resistant topography in Cretaceous outcrops; the green interval represents the Taraises Formation, the Cupido Formation, and the Aurora or Upper Tamaulipas Formation.

The absolute age of the orogenic activity that generated the SMO salient is not tightly constrained. Some studies (Weidie and Murray, 1967; Vega-Vera et al., 1989) estimate that most of the folding occurred between late Paleocene and Early Eocene using unconformities in the Difunta Group (the youngest geologic unit affected by Laramide-age deformation in the Monterrey area) as well as foreland structures that are kinematically coherent with structures in the Monterrey salient to refine timing estimates. However, based on clastic drowning of the carbonate platforms Marrett and Aranda-García (2001) inferred that regional deformation initiated during the Cenomanian to the SW of the city of Monterrey, Mexico.

Another group of recent studies have investigated meso- and microscopic structures like veins, stylolites and calcite twins in the giant folds of the SMO salient in order to constrain fold development. For instance, Camerlo (1998) studied the San Blas and San Juan Bautista anticlines in the Monterrey salient (Figure 2.7) and concluded that flexural slip was the most important mechanism in folding, that pressure solution was locally important, and that calcite twinning and opening-mode fractures contributed only a small amount to the total strain. Rico's (1999) conclusions in her study of San Miguel anticline were generally in accordance to those of Camerlo (1998). The most recent study concluded that the giant folds developed by a combination of the rotating limb and migrating hinge fold models. Fischer and Jackson (1999) proposed a three-stage structural evolution for the Paleogene folds, consisting of first, bedding-parallel shortening. Second, fold initiation by hinge-directed shearing as suggested by bedding-parallel veins, sheeted vein complexes and cleavage particularly in argillaceous units. And third, late-stage fold tightening and hinge-parallel extension as indicated by suitably oriented, early cross-fold veins that were reactivated as minor faults and by rotated cleavage in mudstone intervals (into near parallelism with bedding).

These last three studies implicitly assumed that mesoscopic and microscopic structures are genetically associated with the Laramide-age folding in the Monterrey salient. However, this assumption does not seem to encompass all the veins in the Monterrey salient. Marrett and Laubach (2001) proposed that many veins likely formed before the Laramide orogeny. Their evidence includes veins that are cross-cut by syn-depositional features like solution-collapse breccias or early burial features like bedding-parallel stylolites. It also includes vein sets indicating opening directions that systematically trend perpendicular to the slope of the Cupido platform (Lu, 2000), as opposed to being oriented consistently with respect to fold axes or limbs. Hooker (2004) explored the timing of shear fractures (faults) and also concluded that many faults that cut across bedding are syn-depositional in origin and that they were probably developed as the result of down-slope gravitational spreading.

2.3.3 Vein Attributes

Ortega (2002) studied the variation of fracture intensity with facies, bed thickness and degree of dolomitization in the Cupido Formation and found that only the degree of dolomitization is a valuable predictor of fracture intensity. Ortega (2002) also pointed out that the degree of dolomitization was in turn closely related to the stratigraphic position of beds within fifth-order sequence stratigraphic cycles.

In addition, the normalized fracture intensity data presented by Ortega (2002) for carbonate rocks of the Sierra Madre Oriental rejects the well-known bed thickness-fracture spacing hypothesis. This long-standing paradigm in structural geology proposes a linear increase in the average fracture spacing with simultaneous increase in bed thickness (e.g., Twiss and Moores, 1992; Davis and Reynolds, 1996). Ortega (2002) suggested that the consistent bed thickness to average spacing could result from an artifact in the traditional method of measuring and calculating average fracture spacing.

To understand the relationship between fracture evolution and carbonate diagenetic processes, Monroy-Santiago (in preparation) developed a methodology that combines three types of analyses. First, he differentiated the main fracture sets with field observations. Second, petrographic analyses are used to detect the main diagenetic episodes and the relative timing of diagenetic and fracturing events. And third, the possible origin of fractures is constrained by conditions of fracture-filling cement precipitation based on stable isotope analysis ($\delta_{13}C$ and $\delta_{18}O$). Preliminary results of stable isotope analysis are available in Monroy-Santiago et al. (2001). Monroy-Santiago (in preparation) used this newly developed methodology to obtain a diagenetic history (paragenetic sequence) that includes not only diagenetic processes like cementation, but also the timing of fracturing events relative to those processes. A preliminary version of the above mentioned paragenetic sequence is shown in Figure 4 of Monroy-Santiago et al. (2001).

2.4 PEDERNALES FALLS STATE PARK

One fracture data set for my dissertation was obtained from veins at Pedernales Falls State Park (Figure 2.9), which is located approximately 60 km west of Austin, Texas (Wermund and Barnes, 2003). The Pedernales River exposes gently dipping limestone strata of the Upper Member of the Marble Falls Limestone (Figure 2.10a). Upper Marble Falls facies are more fine-grained than those from the Lower Member and comprise mainly phylloidal algal mounds, skeletal grainstones, siliceous (spiculitic) limestones and shales (Erlich and Coleman, 2005). Although the thickness of Upper Member can be up to 150 m in the subsurface, the maximum thickness measured in outcrop is 82 m with an estimated additional 10 m of section eroded (Erlich and Coleman, 2005).

At Pedernales Fall, the Marble Falls Limestone is characterized locally by its very fine grain, gray color, abundant crinoids, and two different fracture sets (Wermund and Barnes, 2003). The erosional action of the Pedernales River has generated polished bedding planes large enough to facilitate the acquisition of fracture data along a 59 m scanline.

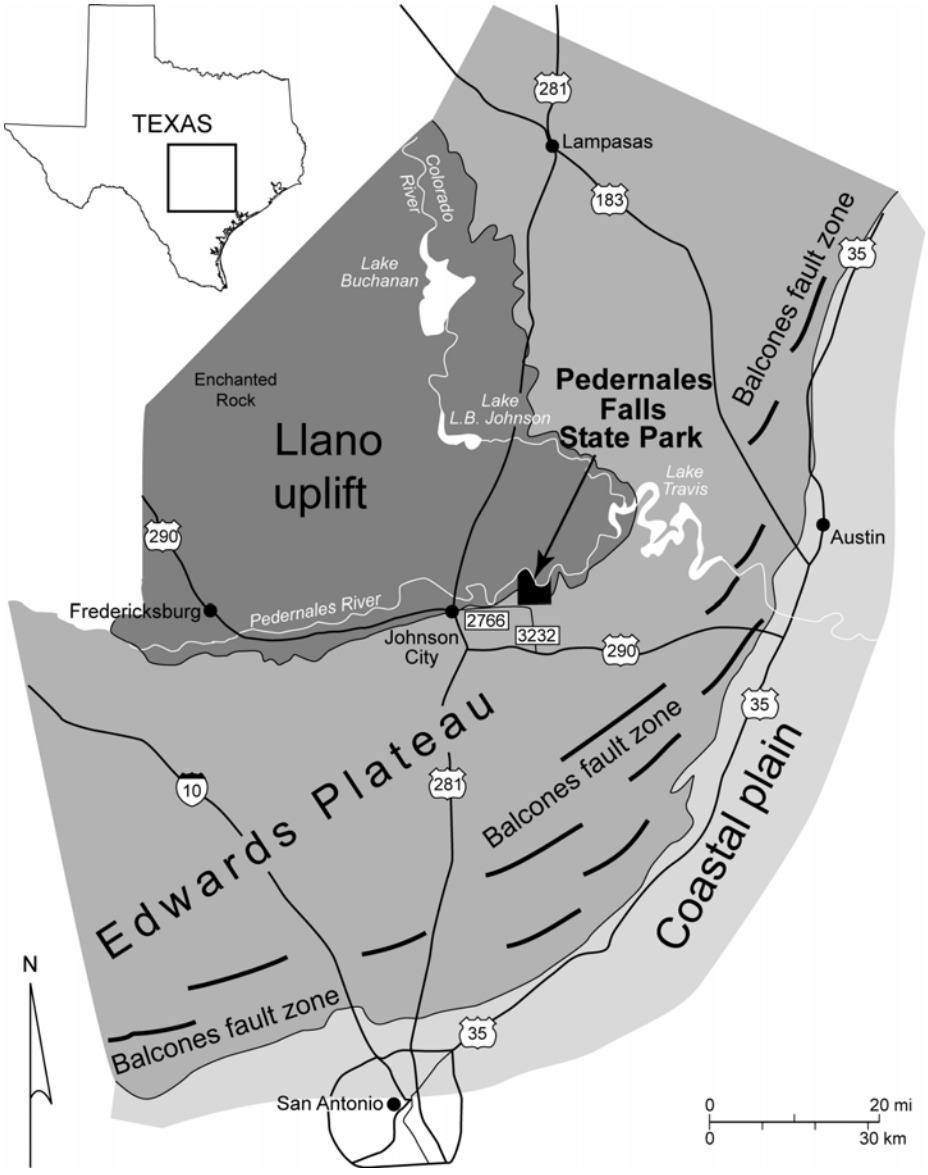

Figure 2.9 Location map of Pedernales Falls State Park. Modified from Wermund and Barnes (2003).

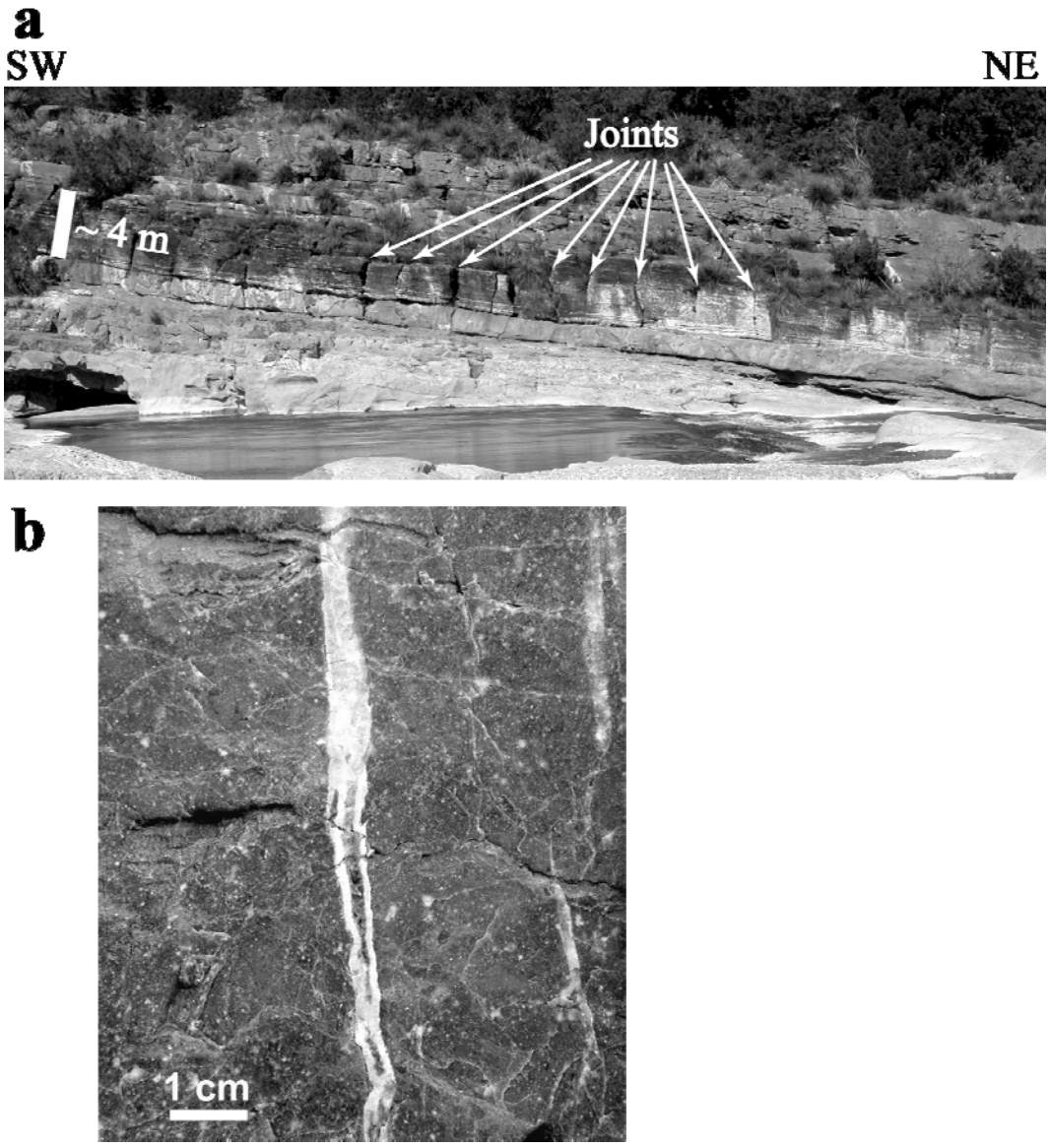

Figure 2.10 Outcrop photographs of Marble Falls Limestone at Pedernales. a) Chert-rich layer with joints. Most joints in (a) span the entire layer thickness. Joints display approximately regular spacing. b) Detailed photograph showing a cross-section (layer perpendicular) view of a calcite-filled vein. There are at least two types of cement inside the vein.

Both fracture sets are subvertical and approximately perpendicular to bedding, which is marked by layer-parallel stylolites. One fracture set consists of joints with a NNE strike (Figure 2.11). Joints tend to be barren of mineral fill, end at bedding planes, locally crosscut layer-parallel stylolites, are more abundant in chert-rich layers and tend to be regularly spaced (Figure 2.10a). Although the strike of joints is sub-parallel to the nearby Tertiary-age Balcones fault zone (Figure 2.9) there is no certainty that they are genetically related (Ferrill et al., 2000).

The second fracture set comprises veins with roughly E-W strike (Figure 2.11). Veins are older and more abundant than joints and are completely filled with authigenic calcite that, based on differences in color and texture of mineral fill, precipitated during at least two different phases of cementation (Figure 2.10b). In contrast to joints, veins at Pedernales tend to cross multiple layers, are cross-cut by layer-parallel stylolites, occur in clusters (Figure 2.12) and exhibit both left and right stepping en echelon patterns.

Two alternative interpretations about vein genesis can be hypothesized. They might have formed during the Marathon-Ouachita-Appalachian orogeny or they might have a much earlier origin, perhaps during burial, based on layer-parallel stylolites that crosscut the veins. Where they intersect, joints cross-cut the calcite-filled veins, and are therefore interpreted as being younger. Because a comprehensive study of the evolution of the fractures at Pedernales is beyond the scope of this research, no systematic data that might elucidate the timing of the different fractures were acquired. Although the mechanical thickness at Pedernales could not be precisely determined, Hare and Marrett (in review) suggested that is in the order of 100 m. In addition, veins at Pedernales were observed to have heights of at least a few meters and to cross bedding parallel stylolites.

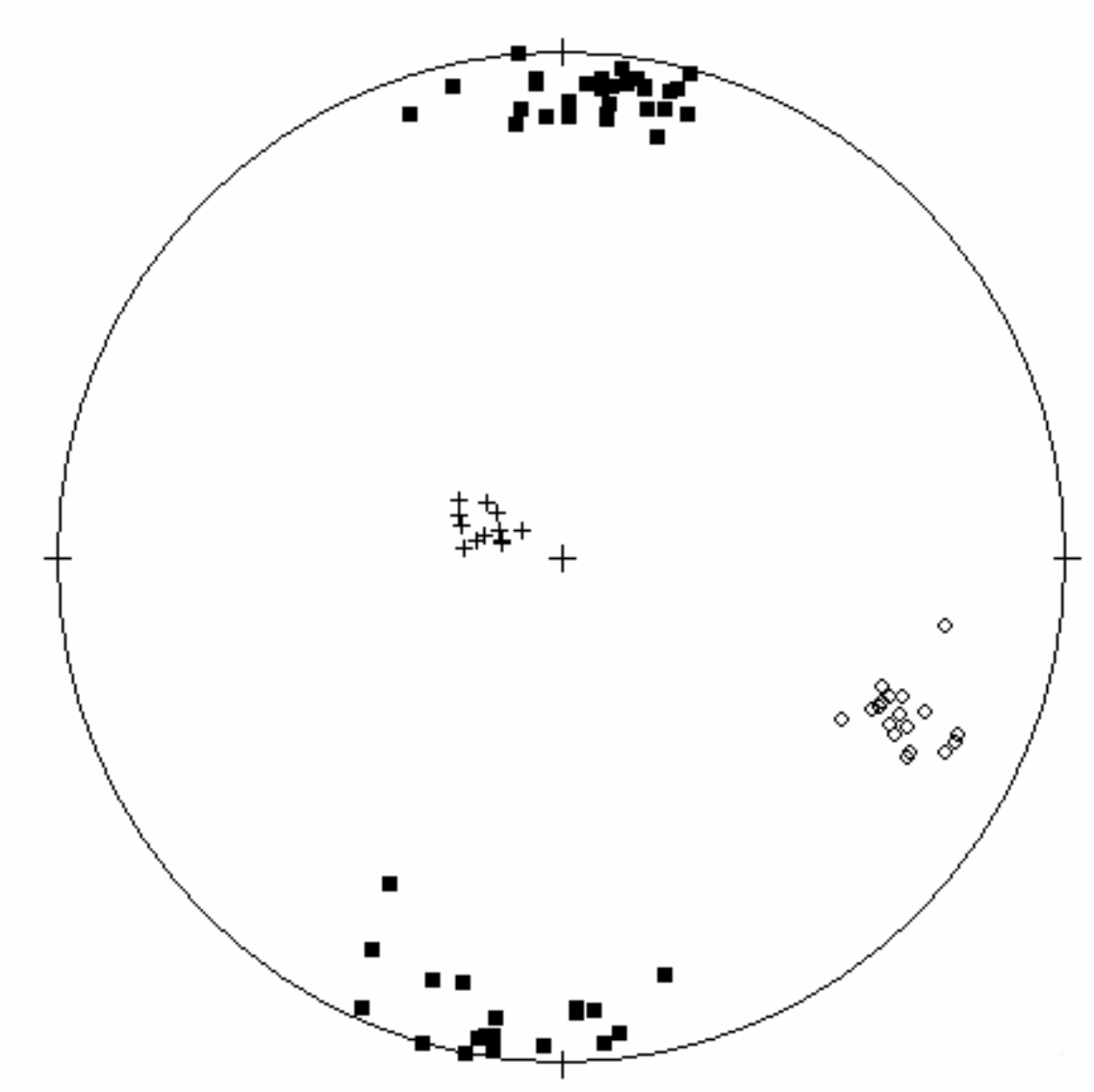

Figure 2.11 Lower hemisphere equal-area stereogram of poles to veins (filled squares, 50), joints (open diamonds, 19) and bedding planes (crosses, 12) measured at Pedernales.

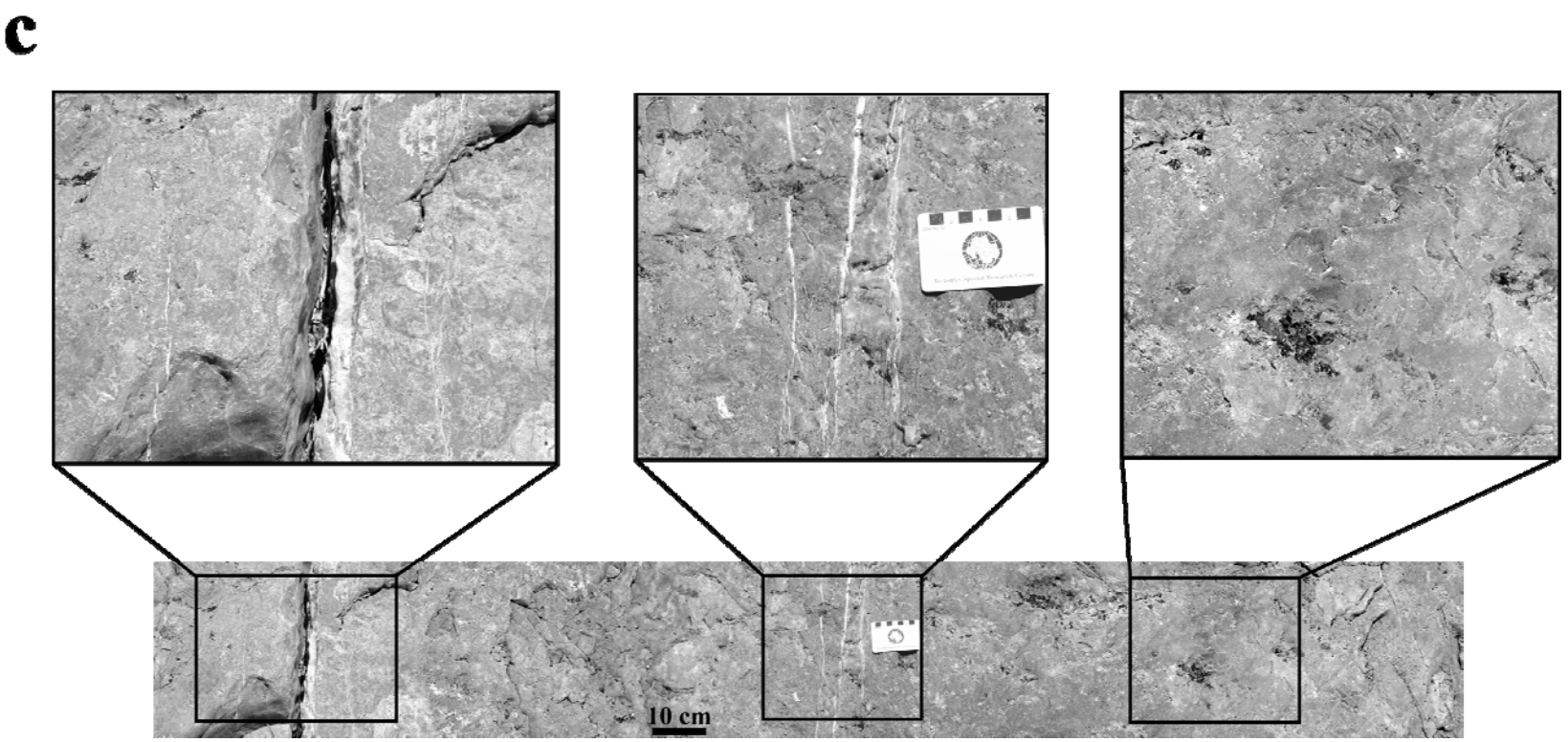

Figure 2.12 Outcrop photograph of veins within Marble Falls Formation at Pedernales. Lower image corresponds to a photograph taken with its long dimension perpendicular to vein strike. There are two clusters of veins in this image (visible in the center and left enlargements) and there are also regions of the image where no visible fractures are present (right enlargement). This illustrates the irregular spatial arrangement of vein

Chapter 3: Fracture characterization using rotary-drilled sidewall cores: an example from the Ellenburger Group, West Texas.

ABSTRACT

New techniques that use microfractures to predict orientation and fill of macrofracture sets have been successfully applied using rotary-drilled sidewall cores. The sidewall cores were drilled from open-hole intervals in two ≥ 45-year-old wells in the Ellenburger dolomite in West Texas. The new techniques allowed measurement of 17 fractures in one well, grouped into two distinct, steeply dipping sets, striking NE-SW and NW-SE. These data give a much more robust indication of dominant fracture orientations than the four moderately dipping possible fractures discernible on 116 ft of image logs, which in isolation could give no clear indication of dominant fracture orientation, and which alone might have been interpreted as artifacts. Fractures observed in core and image logs from a recently drilled vertical well are consistent with the two orthogonal fracture sets identified using sidewall cores. The NW-SE-trending set is dominant in most horizons, although fracture orientation varies with depth. Petrographic analysis and SEM-based cathodoluminescence observations of horizontal and vertical thin sections from sidewall cores indicate a history of dolomite and later calcite precipitation in fractures. Hydrocarbons are also present in and around fractures, with migration probably postdating earlier cements. Information about the relationship between fracturing and diagenetic events is not obtainable from image logs.

3.1 INTRODUCTION

Understanding of fluid flow in fractured hydrocarbon reservoirs is hindered by low data density that prevents effective fracture-attribute mapping. Sparse sampling of large fractures is unavoidable, and collection of meaningful, systematic data at the

wellbore and extrapolation into the interwell volume are significant challenges. New techniques that use microfractures to predict orientation and fill of macrofracture sets have been successfully applied using rotary-drilled sidewall cores. Relationships between cements and microfractures are combined with orientation data to produce a fracture evolution model.

Microfracture orientations have been found to be reliable predictors of macrofracture orientations in the same set (Laubach, 1997; Ortega and Marrett, 2000). In addition, aperture sizes of fracture populations have been found to follow power-law distributions (Marrett et al., 1999), allowing microfracture data sets to be used to predict the intensity of larger aperture fractures (e.g., macrofractures).

Fractures may be open or sealed by mineral cements. Observations of cements on the thin-section scale can provide information for predicting whether large fractures are open, even if those large fractures have not been observed directly (Laubach and Milliken, 1996). This approach provides an alternative, or complementary, method for fracture orientation analysis. It is advantageous over image logs in that the fracture cementation history and potential for fluid flow can be assessed more fully than with image log data alone. It can be utilized in cases where whole core is not available for technical or economic reasons, and generally provides data on many more fractures than is usual for studies of macrofractures.

The techniques for orienting rotary-drilled sidewall cores were developed by Laubach and Doherty (1999) in the absence of an orienting device on the sidewall core drill. This technique and evidence that small fractures are valid guides to large fractures have meant that sidewall cores can be used to collect meaningful fracture data, even though large fractures may not be sampled.

3.2 ELLENBURGER GROUP STUDY

3.2.1 Setting

Data for this study were collected from sidewall cores in the Barnhart field, an Ellenburger reservoir located in southeast Reagan County about 10 mi southeast of the town of Big Lake, Texas (Figure 3.1). Discovered in 1941, Barnhart field (Figure 3.2) has produced 16,248,093 barrels of oil from the Ellenburger as of December 31, 2000, from a depth of about 9,000 ft (Figure 3.3). Although the field produced at high rates during its early years, production rates and reservoir pressure fell sharply through the 1950's and 1960's, with production falling to less than 1,000 bopd by 1956 (Figure 3.4). In 1968, a pilot waterflood program was instituted in the field to reverse pressure decline and increase production. This program met with only limited success, and most of the wells in the field, which totaled about 80, were abandoned. By 1974, only a few producing wells remained. Production in 2001 from the field was at less than 21,000 barrels per year from six active wells.

The Ellenburger reservoir in the Barnhart area is composed of shallow-water, lower Ordovician carbonates containing both dolostone and limestone (Holtz and Kerans, 1992) (Figure 3.5). These rocks, which were assigned to the Ellenburger Ramp Carbonate subplay by Holtz and Kerans (1992) (Figure 3.1), typically contain low permeabilities and high initial water saturations despite relatively high porosity.

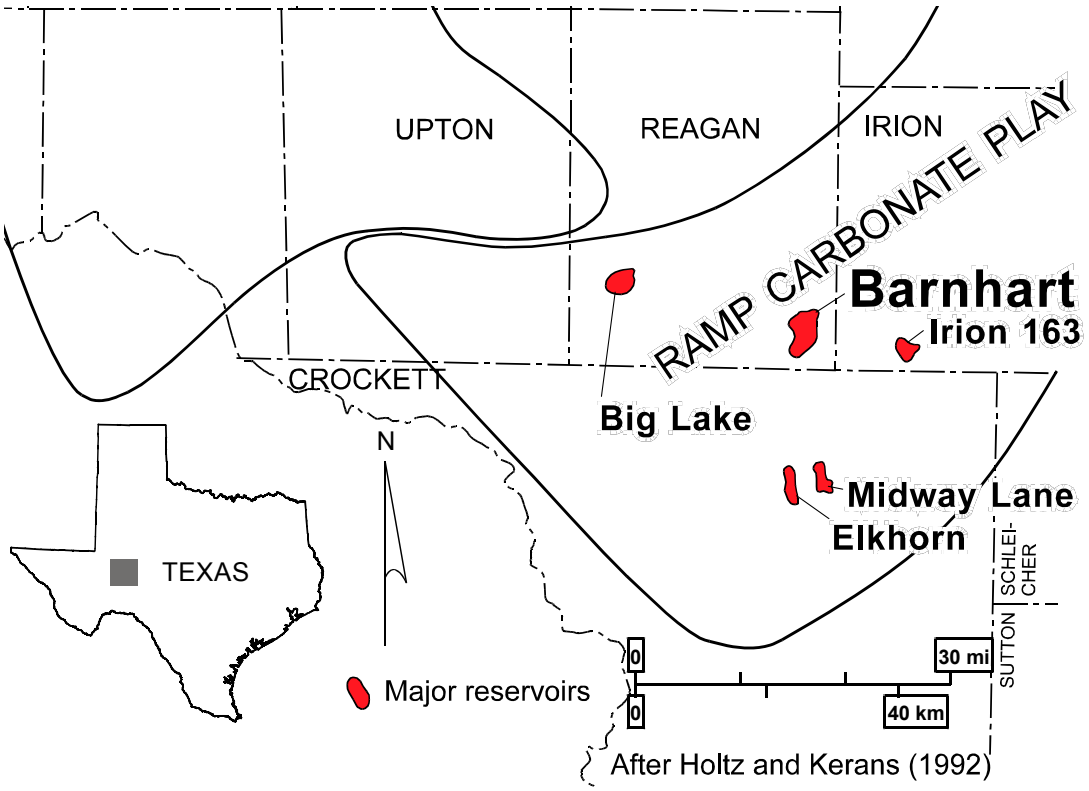

Figure 3.1 Regional map of the Permian Basin showing major Ellenburger fields on University Lands and the location of Barnhart field. After Holtz and Kerans (1992).

Preliminary studies of new cores in Barnhart field suggest that the Ellenburger is dominated by karst-related processes and is highly fractured. The current study is part of a reservoir characterization study undertaken by the Bureau of Economic Geology in cooperation with the current operator, Goldrus Producing Company, and The University of Texas System to develop new approaches for the recovery of the large remaining oil resource in the field. The study is focused on the southern half of the field, which lies on University Lands (Figure 3.2).

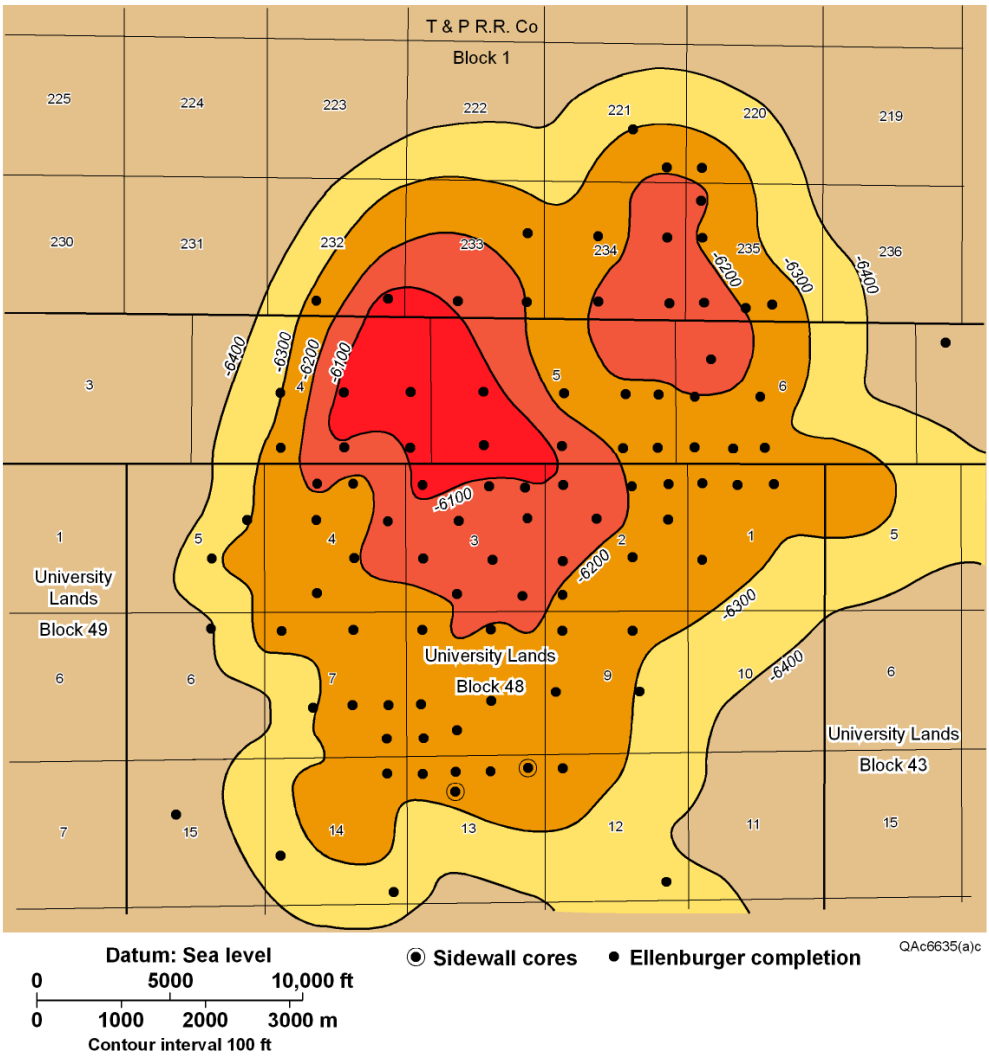

Figure 3.2 Map of Barnhart field showing structure at the top of the Ellenburger reservoir and distribution of University leases. After Cotton (1966).

Extrapolation of studies by Tyler et al. (1991) indicates that the recovery efficiency from this part of the Barnhart reservoir is less than 17%. This leaves a remaining resource of more than 26 million barrels of unrecovered mobile oil on University leases as a target for incremental production. A potential key to the recovery of this resource is an improved understanding of the distribution and orientation of fractures in the reservoir.

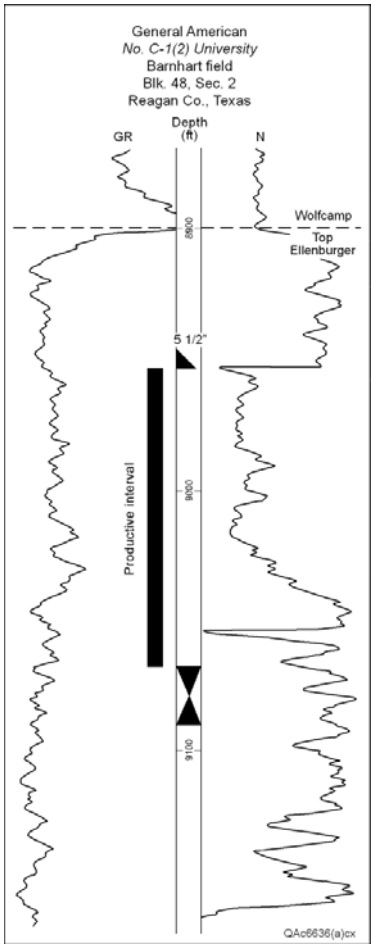

Figure 3.3 Type log of the Ellenburger reservoir in Barnhart field. After Cotton (1966).

Hoak et al. (1998) worked on the distinction between karst-related fractures and tectonic fractures in the Ellenburger Group, concluding that the two could be distinguished in whole core through careful analysis of the regional depositional, diagenetic, and tectonic framework. This paper demonstrates that in cases where whole core is not available, fracture characterization is possible using microfractures in rotary-drilled sidewall cores.

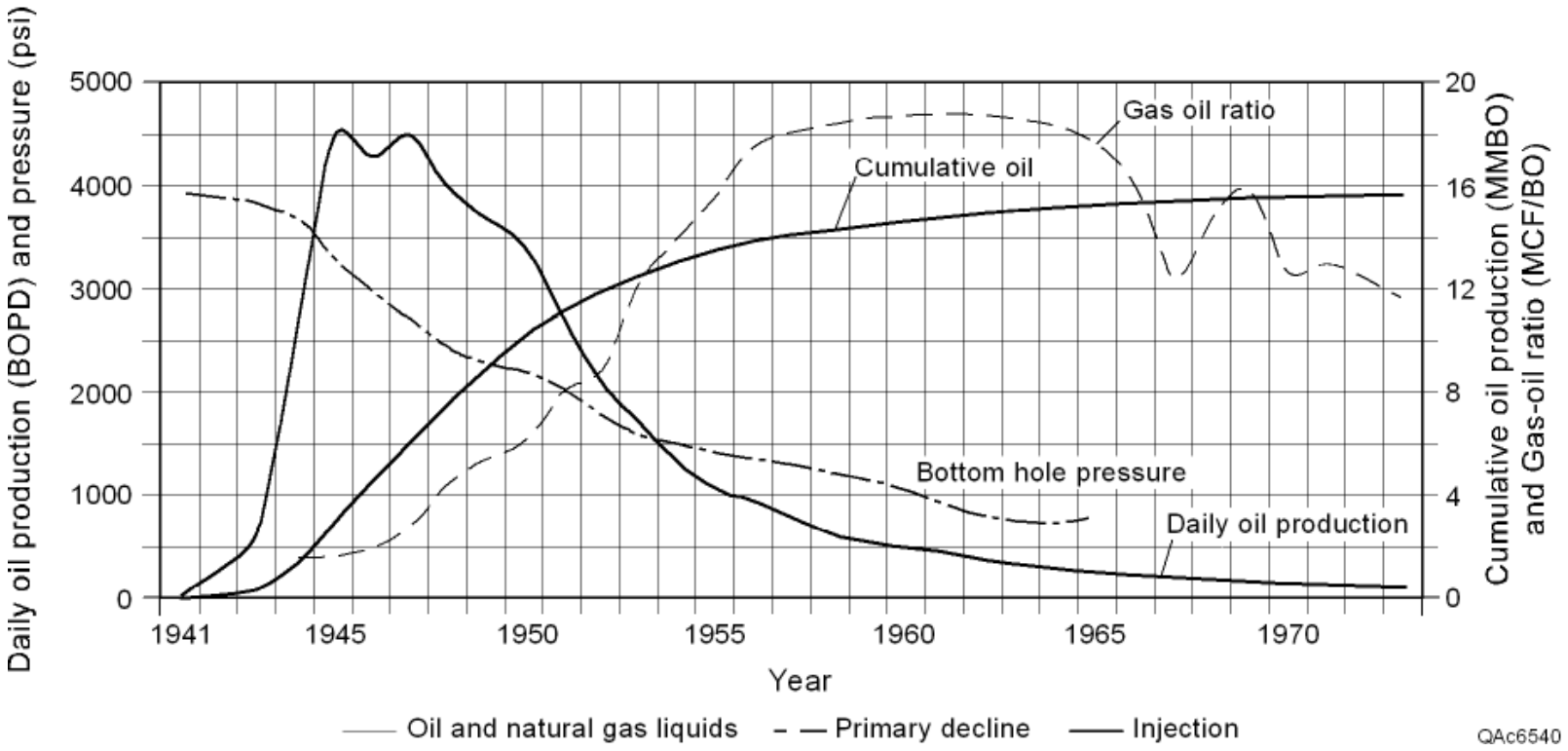

Figure 3.4 Production history of the Ellenburger reservoir at Barnhart field. Data were obtained from Texas Railroad Commission.

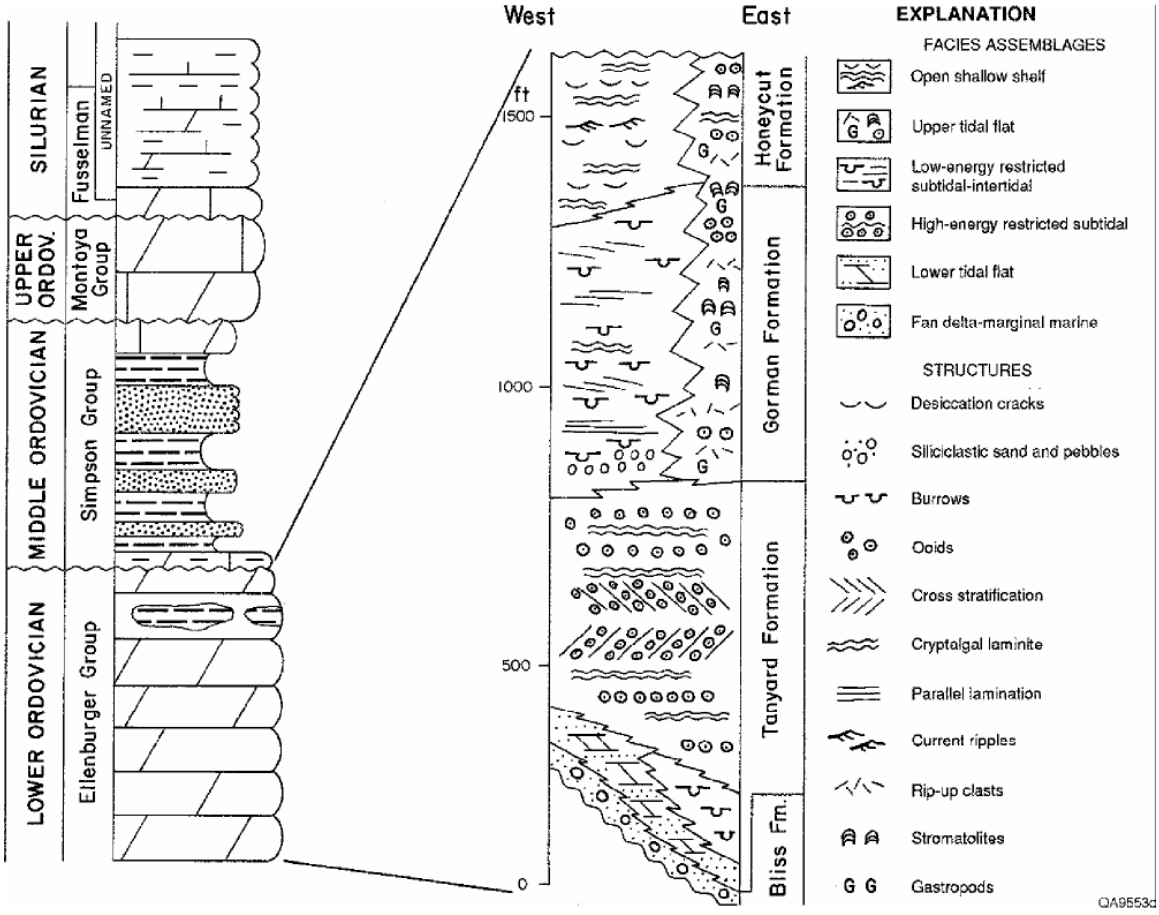

Figure 3.5 Schematic representation of depositional systems in West Texas compared with formalized Ellenburger stratigraphy in the Llano area. Total thickness of complete section is approximate. After Kerans (1990).

3.2.2 Sidewall core orientation

Fracture characterization of the Ellenburger at Barnhart field is based on 75 sidewall cores, drilled from open-hole intervals, in two reentered ≥ 45-year-old wells, A and B. The orientation procedure (Laubach and Doherty, 1999) makes use of sedimentological features in the cores, mechanical features induced by the original well drilling and rotary sidewall drilling, and evidence of core facing direction from image logs. Sidewall cores are generally detected successfully using image logs, so that azimuth is frequently known with good to excellent accuracy. The main challenge in orienting

sidewall cores is usually identifying the "up" direction for the core cylinder. For each orientation result, a degree of certainty is attached using a numerical ranking scheme. For example, the certainty for an azimuth based on an image log can take a range of 0 to 4, with 0 being zero certainty. The orientation procedure was first to determine core azimuths, then to distinguish core ends, and lastly to determine core tops. Once cores were oriented, fractures in those cores could also be oriented.

Core azimuths from well A were measured on an image log run after the cores were taken (Figure 3.6). The wellbores, which had received several acid treatments, were badly pitted, resulting in poor-quality image logs. This makes it easy to distinguish the borehole end of the sidewall core from the formation end (Figure 3.7). Unfortunately, logs in well B were run prior to coring, so no image log was available for orientation.

With azimuths and ends of the cores known, the remaining orientation to be determined is the core top. The most reliable indicator of up is a sedimentary structure; but it is rare for these structures to be captured in such small cores. In the absence of such structures Laubach and Doherty (1999) found that mechanical indicators, resulting from the drilling and break-off of rotary-drilled sidewall cores, could be used. A lip, dimple, and smear may be present on one side of the formation end of the core, (Figure 3.8) and together with the remnant curvature of the borehole end, the certainty of each observation can be assigned a rank (Figure 3.8). To test the core top identification procedure samples were analyzed from both wells, although core orientation for well B was precluded by the sequence in which cores and logs were collected.

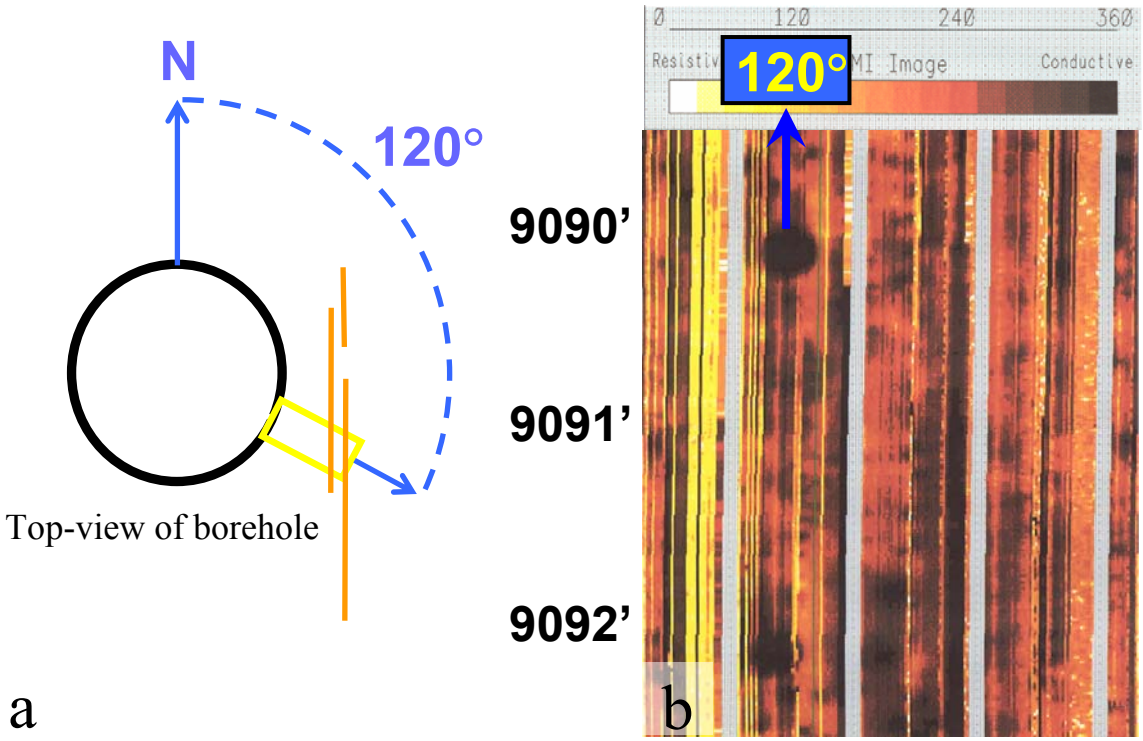

Figure 3.6 (a) Schematic diagram of sidewall core azimuth measurement. (b) Four feet of electric borehole image log from well A. Two sidewall cores drilled at an azimuth of 120° from geographical north appear as low-resistivity elliptical areas (highlighted with white dashed ellipses). The poor quality of the electric image log is apparent, and only four possible fractures could be interpreted from 116 ft of image log.

The highest possible numerical scores for all core-top indicators totals 24. A score in this range would indicate an overdetermined core orientation, with all possible, in some cases redundant, core orientation indicators giving data. In general a core rank of 3 to 5 gives acceptable core orientation reliability. The number of cores with core -top rank greater than 3 was 33% in well A and 44% in well B (Table 3.1); the greatest rank attained by an individual core was 6.

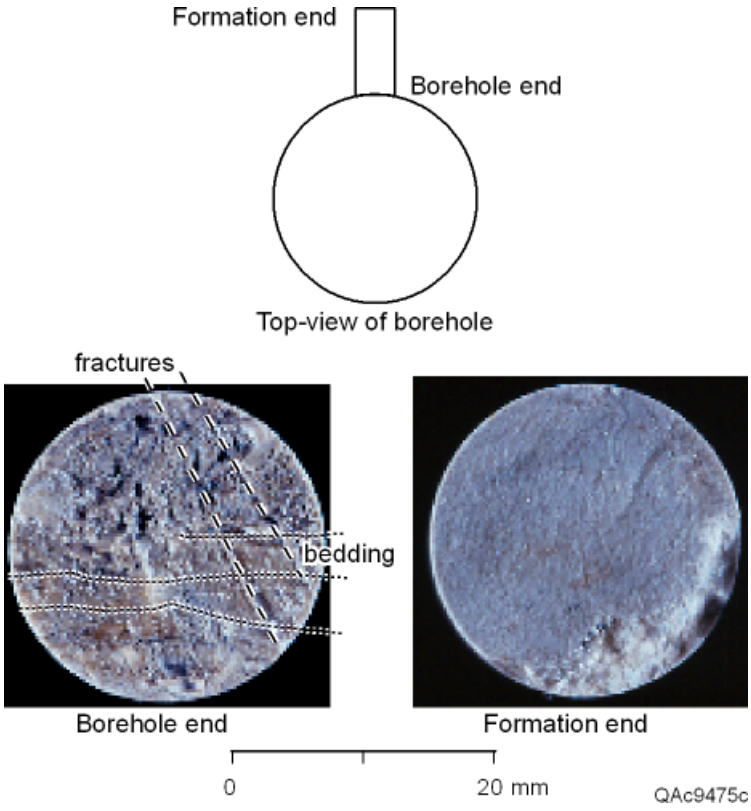

Figure 3.7 Comparison of the borehole and formation ends of a sidewall core. The borehole end is pitted and etched because of acid treatments to the well. This process enhances fractures and bedding traces. The formation end has a smooth surface except for the lip produced by mechanical break-off of the plug (bottom right).

To facilitate the orientation of sidewall cores, I developed a template that records all features (e.g., bedding, lip, fractures) of an individual sidewall core (Figure 3.9). All recovered cores, with the exception of those composed of only rubble had their features recorded on this template.

	Well A	Well B
Drilled	45	34
Recovered (complete, partial core or rubble)	44 (98%)	32 (94%)
Observed on borehole image logs	38* (85%)	0
With top-core rank ≥ 3	15 (33%)	14 (41%)
With one or more fracture sets	22 (49%)	23 (68%)
Compliant with all four conditions	8 (18%)	0

*Image log collected prior to coring

Table 3.1 Number of sidewall cores from wells A and B that comply with one or all of the selection criteria: complete recovery; azimuth located on borehole image; top-core-rank ≥3; and presence of macroscopic fractures.

The strategy for deciding which sidewall cores to use for fracture orientation analysis was to select those cores that complied with four conditions (Table 3.1): the core must be intact, at least partly; it must be visible on the image log; it must have a top indicator rank of ≥ 3; and it must contain fractures. Of the 45 sidewall cores drilled in well A, 38 could be identified on the image log. Natural fractures, visible with a hand lens, were present in 22 cores in well A and 23 cores in well B, and orientations were measurable in 15 of the cores. Only eight cores, all in well A, were compliant with all four conditions. Fractures in cores having low orientation certainty, or unorientable cores, were examined petrographically but were not included in the orientation analysis. These samples can also potentially provide useful information on fracture quality and scaling.

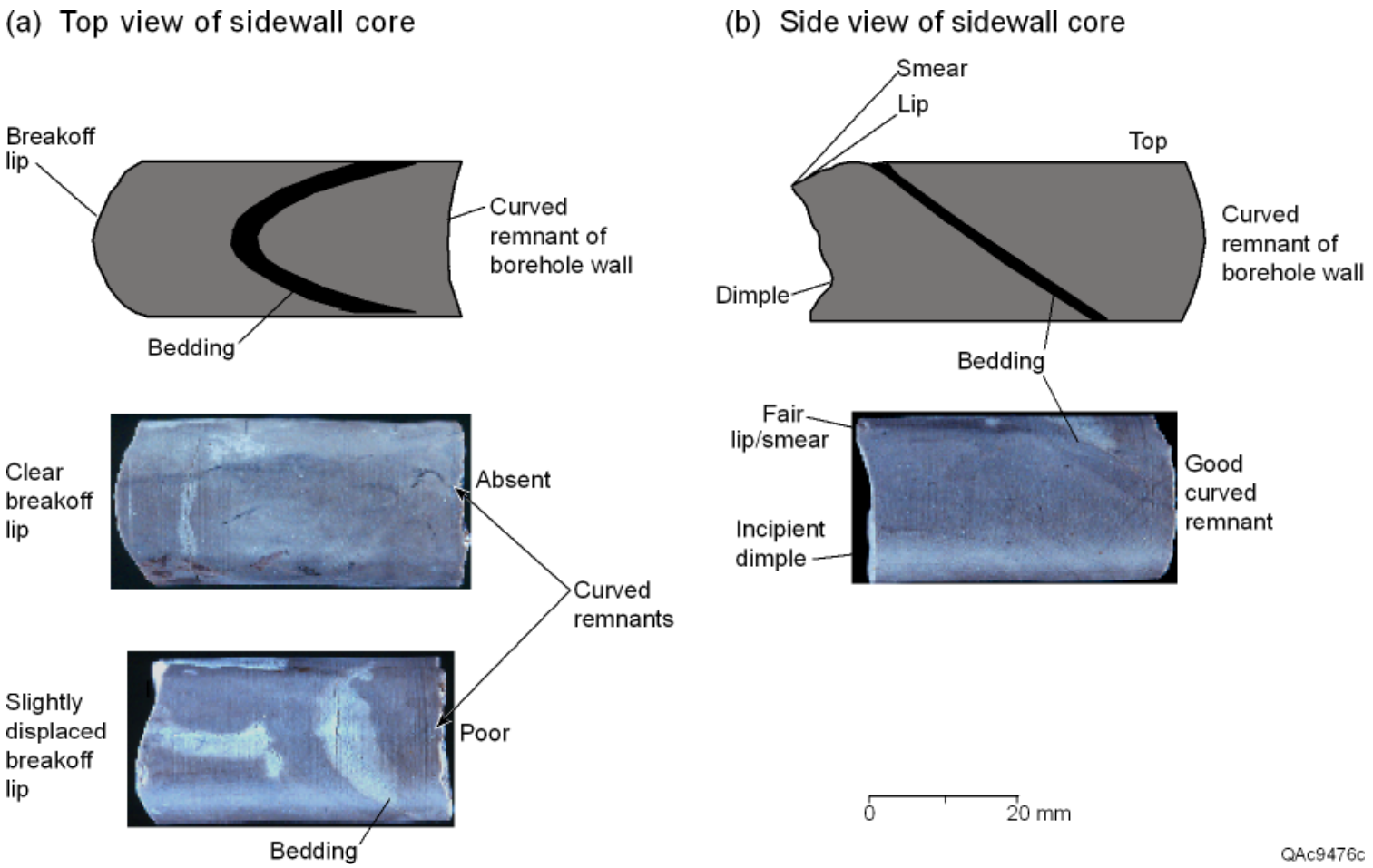

Figure 3.8 (a) Schematic diagram and photographs of mechanical indicators observed on a top view of a sidewall core. (b) Schematic diagram and photograph of mechanical indicators observed on a side view of a sidewall core.

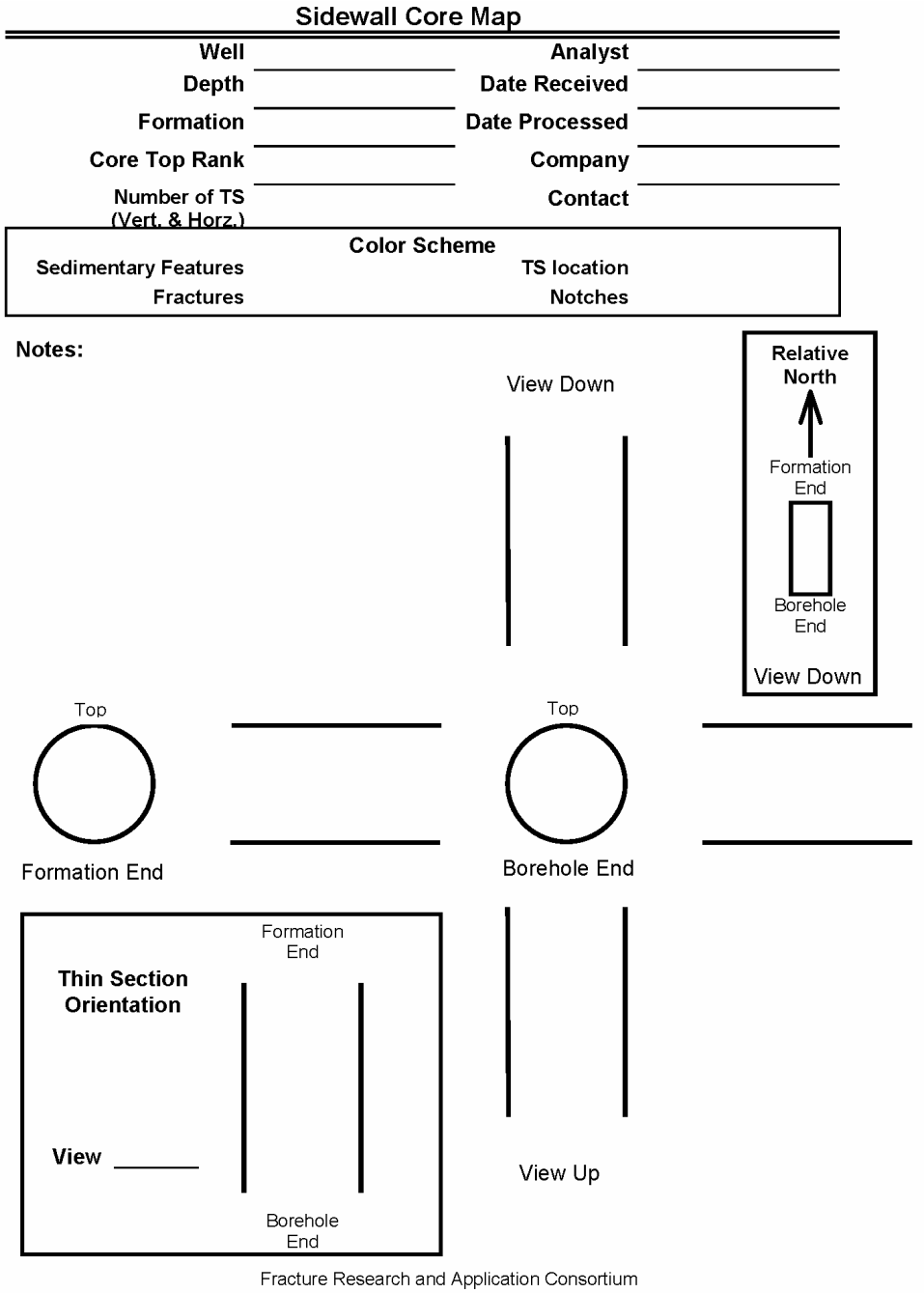

Figure 3.9 Template designed to record the sedimentological (e.g., bedding) and mechanical (e.g., dimple) features of a sidewall core.

3.2.3 Fracture orientation

Two sets of steeply dipping fractures, striking NE-SW and NW-SE, can be recognized on a stereographic projection of 17 oriented fractures measured in the sidewall cores (Figure 3.10a). Fractures observed on image logs, taken over 180 ft of a recently drilled vertical well, through an equivalent interval (well C), are consistent with these two orthogonal fracture sets (Figure 3.10b, c). The image logs for wells A and B are poor quality, however, in part because of the condition of the wellbores (Figure 3.6b). Fractures are difficult to pick on these logs, and on the 116 ft of image log obtained in well A only four fractures are discernible, and these fractures have no consistent orientation (Figure 3.10a).

Fracture strikes for different subsets of data from well A are plotted on rose diagrams (Figure 3.11). The plot of all strike data shows the dominant set to be NE-SW trending and other fractures trending NNW-SSE and NW-SE (Figure 3.11a); however, some of these fractures are moderately dipping. A plot of vertical fractures only reveals dominance of the NW-SE set, with a smaller number trending in the NW-SE quadrant (Figure 3.11b).

It is possible to encounter changes in the dominant fracture orientation from layer to layer in a sedimentary succession, and a bed-by-bed orientation analysis is desirable. In this case, although image log data are poor, the sidewall cores provide some information. Fracture strikes from three different depths are shown in Figures 3.11c-e. At 9,030 ft the dominant orientation is NE-SW (Figure 3.11c), whereas at 9,049 to 9,050 ft the dominant orientation is NW-SE (Figure 3.11d). For both depths there are fracture strikes in the quadrant normal to the dominant set. At depths ≥ 9,086 ft fractures strike NNW-SSE and NE-SW with equal frequency (Figure 3.11e).

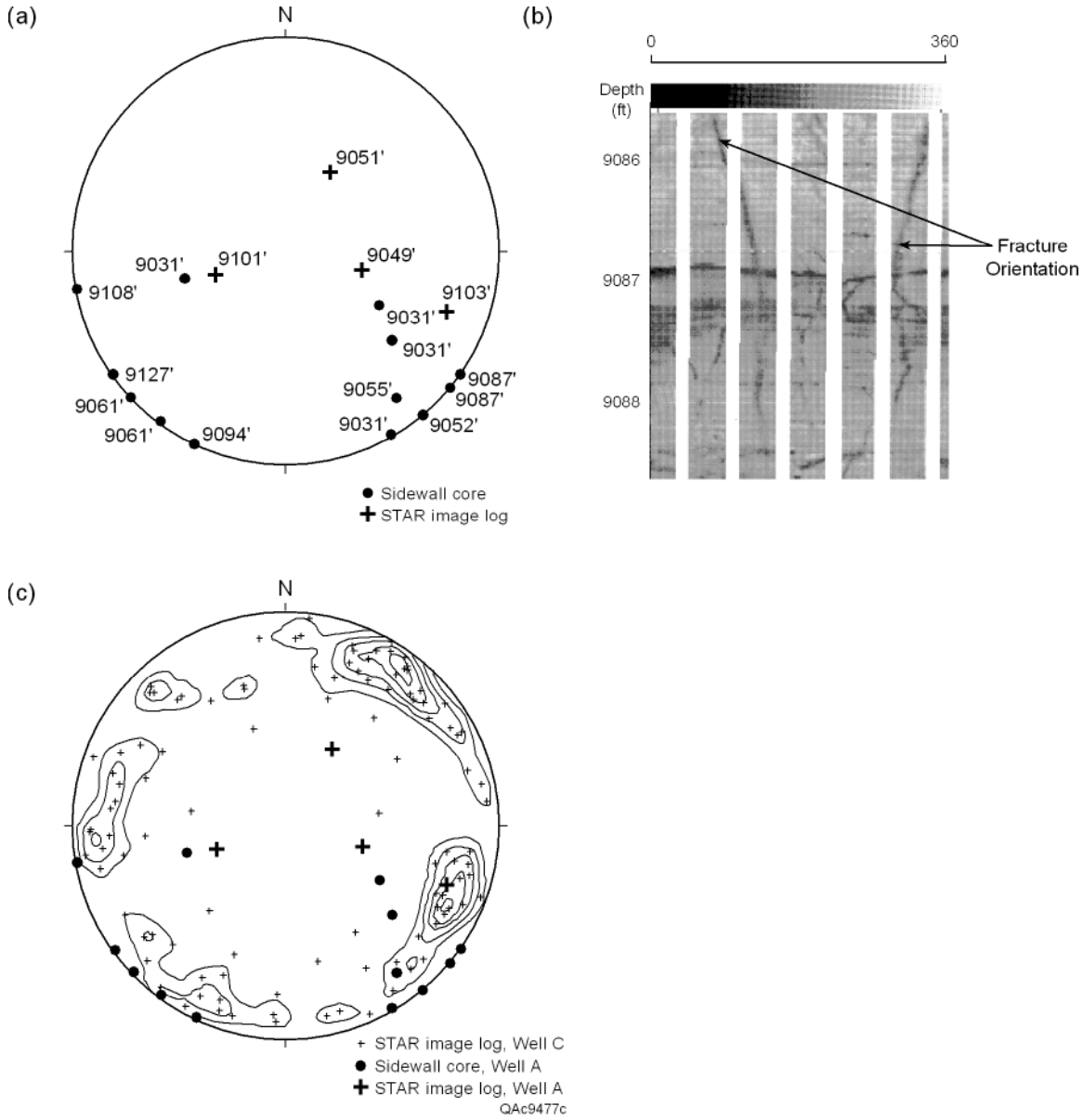

Figure 3.10 (a) Lower hemisphere equal-area projection of oriented fractures from well A, showing poles to fracture planes from oriented sidewall cores (n = 17; dots) and poles to fracture planes from borehole images (n = 4; crosses). (b) Representative 4-ft section of image log from well C showing fractures. (c) Lower hemisphere equal-area projection with 1% area contours for poles to fracture planes (n = 111; small crosses) from borehole images of well C, superimposed on data from Figure 3.10a. The orientations of fractures detected using oriented sidewall cores coincide with orientations of fractures interpreted from good-quality borehole images from well C.

Finally, fractures in well B are more abundant than fractures in well A, and there is a subhorizontal fracture set in well B that is not observed in well A.

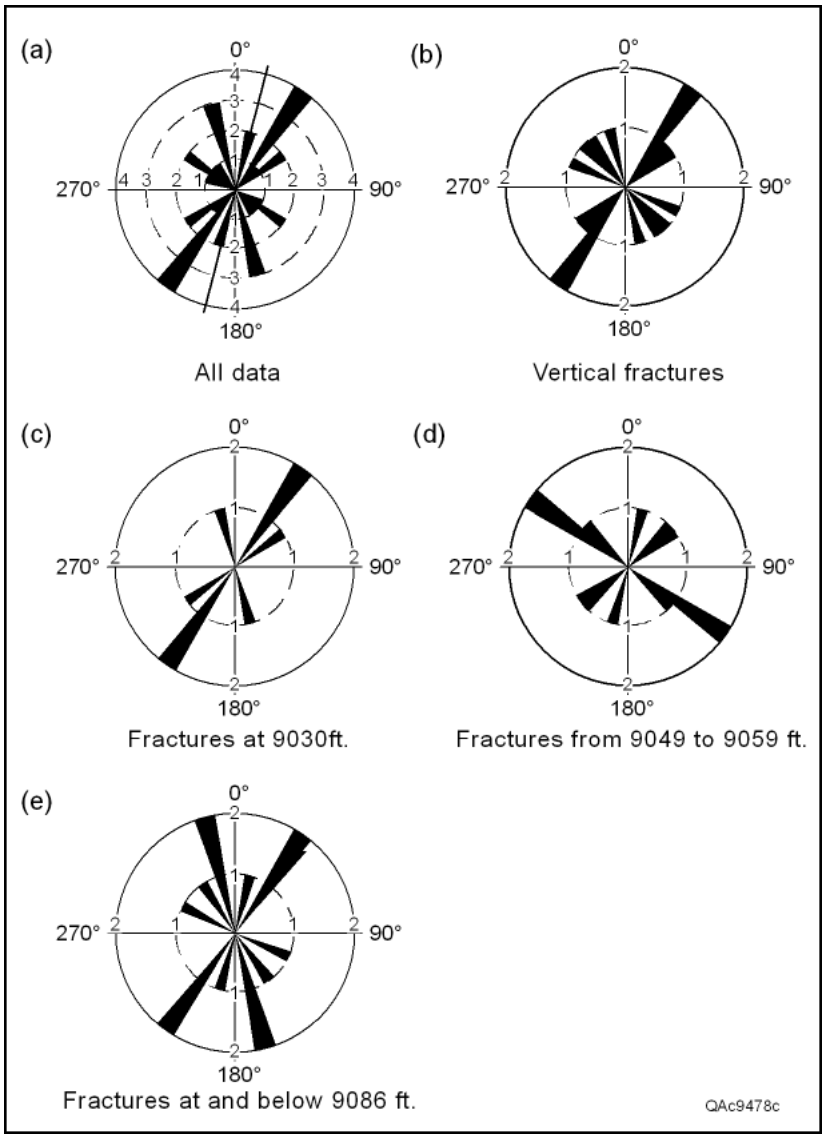

Figure 3.11 Rose diagrams of fracture strikes for different subsets of data from well A

3.2.4 Petrographic analysis

A combination of conventional petrography, Scanning Electron Microscope based cathodoluminescence (SEM-CL), and SEM -based energy dispersive spectral analysis (EDS) was used to establish the nature and relative timing of the mineral cements in the fractures and the host rock. Some fractures are wholly or partly filled with dolomite and calcite. Dolomite forms local mineral bridges and may have precipitated contemporaneously with fracture opening. Calcite is more abundant and precipitated in areas between dolomite bridges, suggesting it postdates dolomite cement. Open fractures crosscut dolomite and calcite-filled fractures and represent a late fracturing event. Many of these late fractures are associated with "halos" of wall rock where qualitative visual inspection suggests hydrocarbon abundance is lower. Possibly these halos represent leaching of matrix hydrocarbons adjacent to open fractures (Figure 3.12). Late fractures commonly track earlier fractures for distances of a few millimeters, although they are not always subparallel (Figure 3.12). In both wells A and B parts of some fractures are filled with solid hydrocarbons, and in other fractures the walls are coated with, or are surrounded by, hydrocarbon accumulations (Figure 3.12). The proportion of fractures in well A filled with dolomite or calcite is approximately equal to those filled with solid hydrocarbon.

Most well B fractures have hydrocarbon fills, but a few have dolomite or calcite cement. SEM-CL images reveal sealed microfractures, less than 50 mm in aperture, that were not observed using standard optical microscopy and show that different phases of dolomite are present in the samples (Figure 3.13). The dolomite crystals forming the host rock are pale gray in Figure 3.13a. Some of these crystals are zoned, with a dark-gray overgrowth forming the outer layer. The larger fracture (Figure 3.13a) is partly filled, and the small fracture is completely filled with the dark-gray dolomite cement. This dolomite

is also present in the centers of some of the pores of the host rock. The cause for the different luminescence of the two dolomites has not been established. Element mapping reveals no compositional difference between them. Some of the dark-gray cement crystals are overgrown by later cement that is very dark gray, almost black, in the image. Element mapping shows that this cement is more iron rich than the dark-gray centers of these crystals.

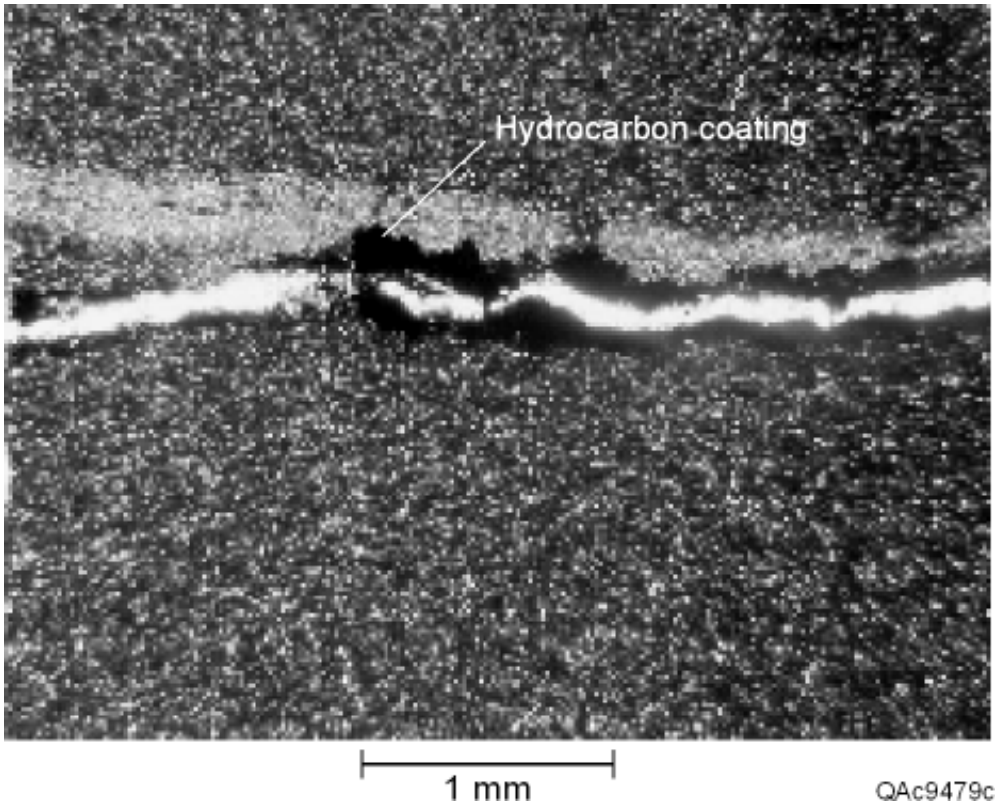

Figure 3.12 Photomicrograph of fractures in a sidewall core from well A at 9 031 ft. The lower fracture is lined with small dolomite crystals and filled with calcite. The hydrocarbon coating appears to partly fill and partly surround this fracture. A second fracture, with an aperture of just 0.02 mm and a pale halo surrounding it, is subparallel to the first and becomes coincident with the lower fracture toward the right of the image. It is mostly oil filled but is open in places.

Fracture walls, at the boundary between the dark and pale dolomite crystals, have a very irregular shape, and opposite sides of the fractures do not match. There is no evidence of straight-sided fracture walls, and it is not possible to perform a simple opening-mode restoration for these fractures. In addition, there is no evidence of crack seal. Although two fracture sets were observed in several cores, no clear consistent crosscutting relationships were observed in thin sections that would indicate which set is older.

3.3 DISCUSSION

This study has shown that sidewall cores may be taken from old wells and used for fracture characterization. The orientation of sidewall cores requires that delicate mechanical features be preserved, but this is possible if care is taken to protect the core ends at the time of sampling. The core azimuths may be determined with an image log run after coring, even if the image log quality is generally poor. The total number of fractures that can provide information on fracture population attributes is maximized if cores are sectioned and examined using SEM-based techniques because microfractures that are part of the same population as visible macrofractures are included in the analysis.

Timing of cements with respect to fracture opening is difficult to determine. Although mineral bridges are commonly composed of cement precipitated at the time of fracture opening, a more reliable indicator is crack-seal texture (Laubach and Milliken, 1996). There are no clear examples of crack seal in dolomite in the SEM -CL images from the sidewall cores, and fracture walls are indistinct in many fractures. The irregular shape of microfracture walls (Figure 3.13a) may have been caused by fractures propagating preferentially around, rather than through, the host-rock dolomite grains. This is a common phenomenon in subcritical fracture growth (Holder, J., personal communication).

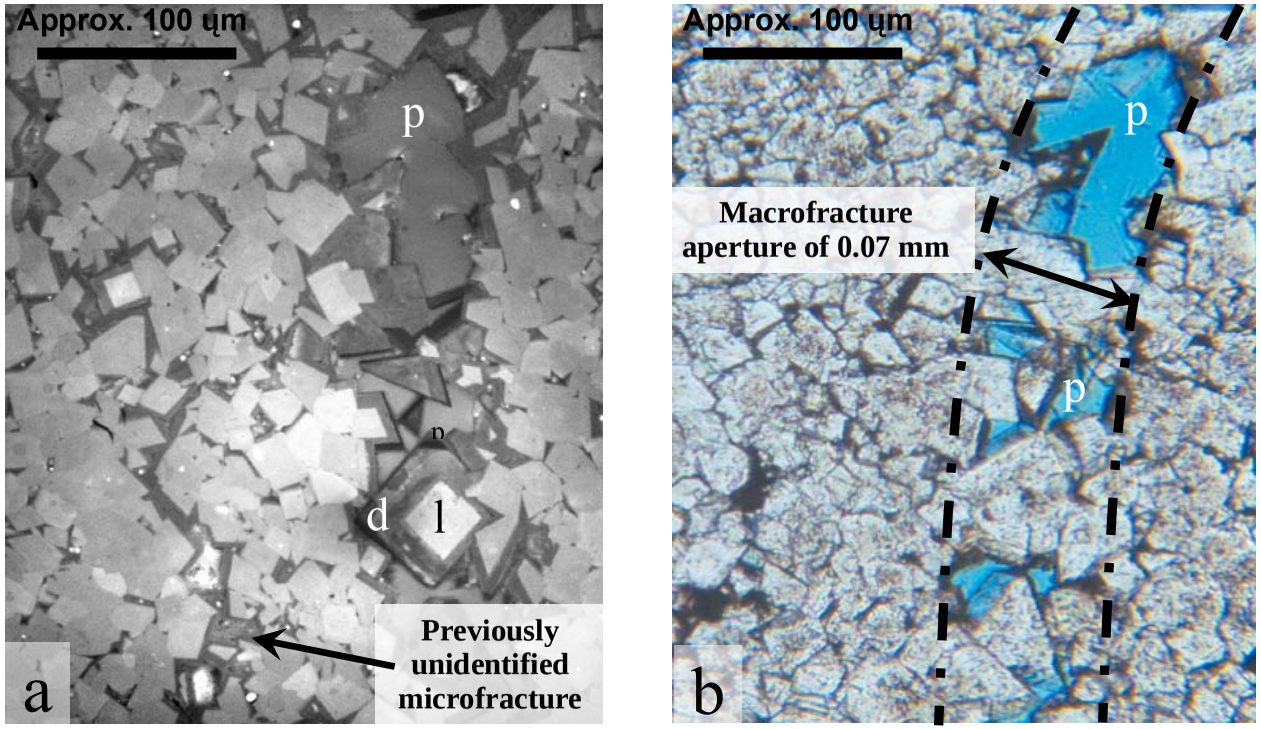

Figure 3.13 Micrographs of fractures from a well B sidewall core comparing SEM-based imagery with conventional petrography. (a) SEM-based cathodoluminescence image of pale -gray dolomite (l) forming the rock matrix and dark-gray dolomite (d) partly filling the large fracture, sealing the small fracture (newly identified fracture) and filling some pores in matrix. A very dark, almost black, iron-rich dolomite may be seen in the large fracture, forming the outer zone of some dark-gray crystals. Fracture porosity (p) is present in the large fracture. (b) Plane polarized light photomicrograph of the same area as in (a). Note the small fracture is not visible, and there is no distinction between the different dolomite cements.

Fracture cementation progressed sufficiently to occlude most of the porosity in fractures having apertures smaller than 50 mm, but fractures 100 mm wide or more have open pores. These large open fractures are the potential fluid pathways within the rock.

3.4 CONCLUSIONS

Two sets of steeply dipping fractures, striking NE-SW and NW-SE, were characterized using rotary-drilled sidewall cores in two reentered ≥45-year-old wells. The 17 orientable fractures from one well provided a much more reliable indication of fracture orientation than an image log from the same well, on which only 4 possible fractures were imaged. The fracture orientations were subsequently confirmed with whole core and image logs from a new well.

Petrographic analysis and observations of horizontal and vertical thin sections from the cores indicate that dolomite cement, forming mineral bridges, was followed by calcite cement in some fractures. The dolomite cement is zoned, the outer zones being more iron rich than the inner zones and dolomite in the host rock. Hydrocarbons are concentrated around sections of these fractures. A later set of fractures with pale halos postdate calcite- and dolomite-filled fractures. These may have been pathways for hydrocarbon movement during emplacement or production. Fractures with apertures ≥100 mm are bridged with dolomite but locally retain porosity and could act as conduits for fluid flow, whereas smaller fractures are sealed with cements.

Chapter 4: Quantifying Fracture Intensity: An Example from the Piceance Basin

ABSTRACT

Fracture intensity, the number of fractures per unit length, area, or volume, is an essential attribute of fracture patterns. Inherent problems in sampling subsurface fractures limit the effectiveness of conventional core and log analysis for measuring fracture intensity, so we are investigating scaling of microfracture populations as a surrogate to predict the intensity of large fractures. Using five microfracture datasets from 35 m (116.4 ft) of subhorizontal Cretaceous Cozzette Sandstone core from the Slant Hole Completion Test (SHCT-1) well in northwestern Colorado, we measured populations of microfractures having kinematic aperture sizes ranging from 0.0002 to 0.04 mm with a high-resolution SEM-based cathodoluminescence detector. Microfracture abundances vary in the samples measured, but intensities are unrelated to proximity to macrofractures, suggesting that microfracture populations in the Cozzette Sandstone are suitable for predicting macrofracture abundance regardless of the presence or absence of nearby macrofractures. Power laws adequately describe aperture-size distributions. Scaling analysis predicts 0.46 large (>1 mm), open fracture per meter of 2 5/8-inch core, which is close to the intensity of 0.37 fracture per meter measured in the horizontal core. These results suggest that size-cognizant fracture intensity measurements using microfractures can extend fracture intensity predictions to areas where conventional methods yield no data.

4.1 INTRODUCTION

Successful exploration and development of hydrocarbon deposits in rocks in which natural fractures potentially contribute to producibility are impaired by inadequate

data on fracture abundance. Accurate information about fracture intensity and spatial distribution of large, open fractures would be useful for well placement and stimulation planning, interpretation of hydrocarbon production and water encroachment patterns, and resource assessment. Yet sampling imposes fundamental limits on subsurface fracture intensity measurements. Direct measurement of spacing of large fractures is usually impossible to obtain with vertical wells simply because large fractures typically are more widely spaced than the diameter of a borehole. The probability of encountering any large fractures in a given layer is small (Terzaghi, 1965; Narr, 1991), and direct evidence of fracture spacing is typically lacking. Nevertheless, probabilistic methods have had success in predicting fracture spacing (Narr, 1996). The method we propose does not measure fracture spacing directly, but it does provide a prediction on the basis of layer-specific fracture observations.

Microfractures may identify macrofracture strikes (Laubach, 1997; Ortega and Marrett, 2000) and timing (Laubach, 2003). We define macrofracture as a fracture that can be observed with the unaided eye, whereas a microfracture requires magnification greater than ×10 to detect. Likewise, microfracture intensity is related to macrofracture intensity in many cases (Marrett et al., 1999; Ortega and Marrett, 2000; Ortega et al., in press). A scale-independent method to measure fracture intensity is to treat abundant microfractures as proxies for related, but unsampled, macrofractures in the same rock volume. Fracture intensity is defined here as the number of fractures present in a given length, area, or volume of rock. In this study we collected fracture intensity data from small areas of thin sections (2-D sample) and along scanlines normal to fracture trend (1-D sample). Intensities are therefore expressed in terms of fractures per unit length or per unit area. Because fractures of different sizes are present in the same rock it is essential to indicate the size range of fractures for each intensity measurement (Ortega et al., in

press). For example, in a given rock sample of unit area, suppose there are 100 fractures just a few micrometers wide, 10 fractures 1 mm wide, but only 1 fracture 1 cm wide. The intensity could be reported as 1 fracture/unit area for fractures ≥1 cm wide, or 111 fractures/unit area for fractures ≥1 μm wide. Average spacing of fractures is the inverse of intensity and, again, is dependent on the size of fractures being considered.

This approach relies on systematic measurement of fracture dimensions in samples retrieved from the subsurface, but it is not required that fractures be large enough to be visible to the unaided eye. In other words, apparently unfractured core can be used to deduce fracture intensity, allowing unconventional categories of samples, such as drilled sidewall cores, to be used for structural analysis (Laubach and Doherty, 1999; Gomez et al., 2001). The conceptual underpinnings of this work are described in the literature (Marrett, 1996; Marrett et al., 1999; Gillespie et al., 2001, Ortega et al., in press).

The purpose of this study is to apply fracture attribute scaling to a Cretaceous sandstone that has been sampled by horizontal core. Using microstuctural surrogates, we predict the orientation, degree of mineral fill, and intensity of large fractures, with a focus on intensity. To test the effects of macrofracture proximity on microfracture intensity we use several samples from the same sandstone at the same depth. We present a preliminary comparison of predictions and observations of macrofracture intensity in the horizontal core, a test not normally available where samples are from vertical wells.

4.2 GEOLOGIC SETTING AND METHODS

4.2.1 Local Geology and Well History

This study was conducted on core of the Upper Cretaceous Cozzette Sandstone Member of the Iles Formation (Mesaverde Group) from the Piceance Basin of northwestern Colorado, a Late Cretaceous to early Tertiary sedimentary basin defined by

a series of Late Cretaceous/early Tertiary uplifts. The basin contains a thick Cretaceous sedimentary sequence. Although much of the Upper Cretaceous Mesaverde Group is nonmarine, fluctuations between nonmarine and marine conditions occurred frequently during its deposition. The Cozzette Sandstone has been interpreted to be a marginal marine sandstone, possibly shoreface or offshore-bar facies grading upward into barrier or strandplain facies (Lorenz, 1983, Dutton et al., 1993 and references therein).

Most Cozzette sandstones are classified as sublitharenites and consist primarily of quartz, with minor amounts of chert and rock fragments (Hansley and Johnson, 1980). Locally, mica and detrital dolomite content are high, and the sandstones are litharenites. Texture is very fine to medium sandstone having detrital silt and clay, and it is typically poorly sorted. Grain size determined using transmitted light microscopy is a maximum value because quartz grains and cement overgrowths are not readily distinguished. Cements include quartz, the major cementing agent, and clay and carbonate minerals.

The study was conducted on thin sections from Cozzette Sandstone core from the Slant-Hole Completion Test (SHCT-1) well, which was drilled as part of a DOE project to evaluate tight gas sandstones in the Piceance Basin. The surface location of the SHCT-1 well is 700 ft south of the DOE Multiwell Experiment (MWX) site in section 34, T6S, R94W, in Garfield County, Colorado (Figure 4.1) (see Pitman and Sprunt, 1986; Lorenz and Hill, 1991 for MWX and SHCT-1 references).

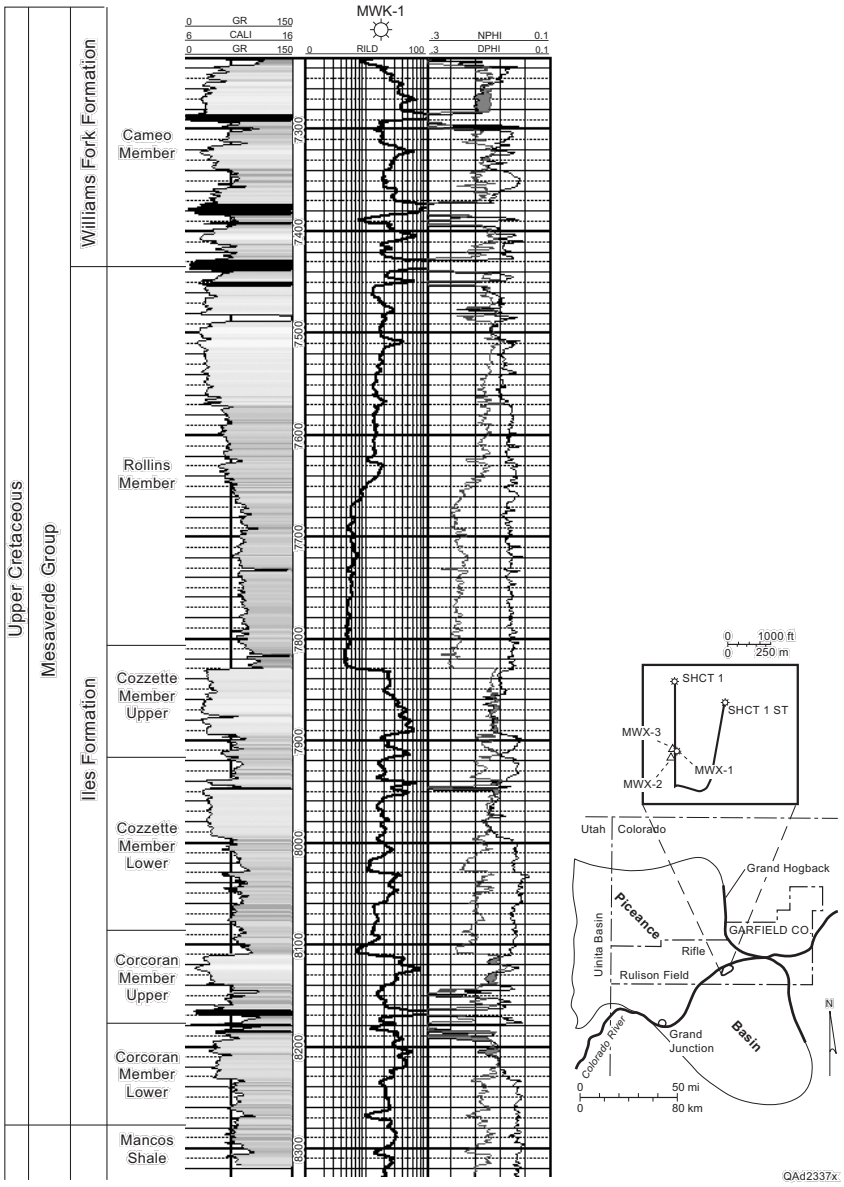

Figure 4.1 Type log (from MWX-1 well) and location map and well trajectories (inset) near the SHCT-1 well, Piceance Basin, Colorado. Cozzette Sandstone Member near the SHCT-1 is the middle of three marine regressive cycles of the Iles Formation. The Iles Formation overlies the marine Mancos Shale and is overlain by nonmarine coastal plain and fluvial deposits of the Williams Fork Formation. The Upper Cozzette is uniformly about 60 ft thick near the SHCT-1 well. Sandstone maximum thicknesses trend northeast, and regional mapping shows that this trend parallels the paleoshoreline of the Cozzette. Location map modified from Lorenz and Hill (1991).

The Cozzette Sandstone from the MWX-1 core lies below the Cozzette Sandstone interval from SHCT-1, but core taken in the MWX-2 vertical well partly overlaps the SHCT-1 cored interval by 12 ft (Lorenz and Hill, 1991, their Figure 3). Fractures in MWX cores from the overlying Mesaverde Group dominantly strike west-northwest, and the SHCT-1 wellbore was positioned to drill perpendicular to this fracture trend.

The well was spudded on April 10, 1990, and reached TD of 9,466 ft measured depth (7,910 ft TVD) in the Cozzette on August 4, 1990. The well drilled the Cameo Coal Member of the Williams Fork Formation and the Rollins Sandstone at a wellbore deviation of about 60° from vertical and proceeded north to intersect the upper Cozzette at a deviation of about 85°. The well then drilled at a maximum angle of 85°, within a few degrees of bedding dip, for a distance of 410 ft (Figure 4.2).

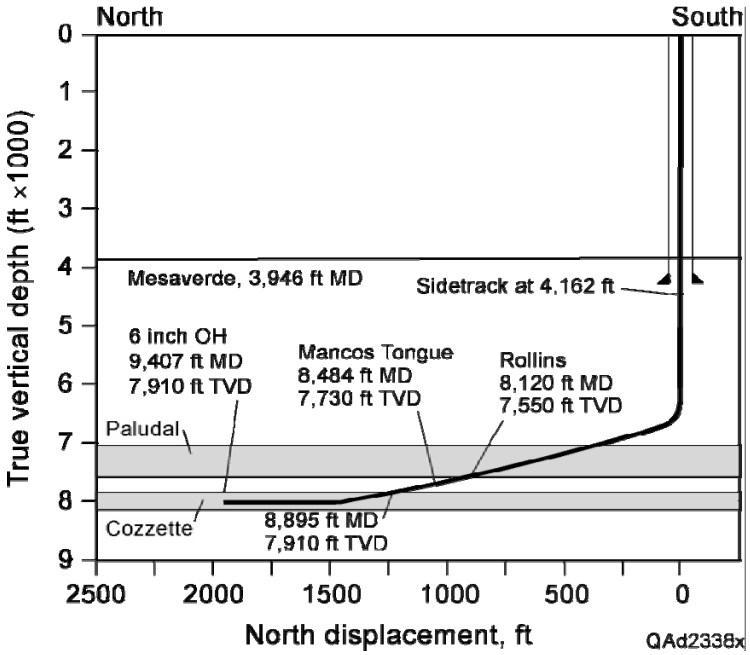

Figure 4.2 SHCT-1 well diagram showing location of sampled core interval.

Four cores aligned approximately parallel to bedding were taken in the Cozzette Sandstone from 8,990 to 9,108 ft (Figure 4.3). During drilling, gas kicks were observed in naturally fractured intervals of the Cozzette Sandstone (Lorenz and Hill, 1991, 1992). Rock permeability is typically 0.1 to 2 microdarcies in restored-state laboratory measurements (Lorenz and Finley, 1989). Well tests, however, calculate permeabilities that are two or three orders of magnitude higher owing to natural fractures (Lorenz and Hill, 1994).

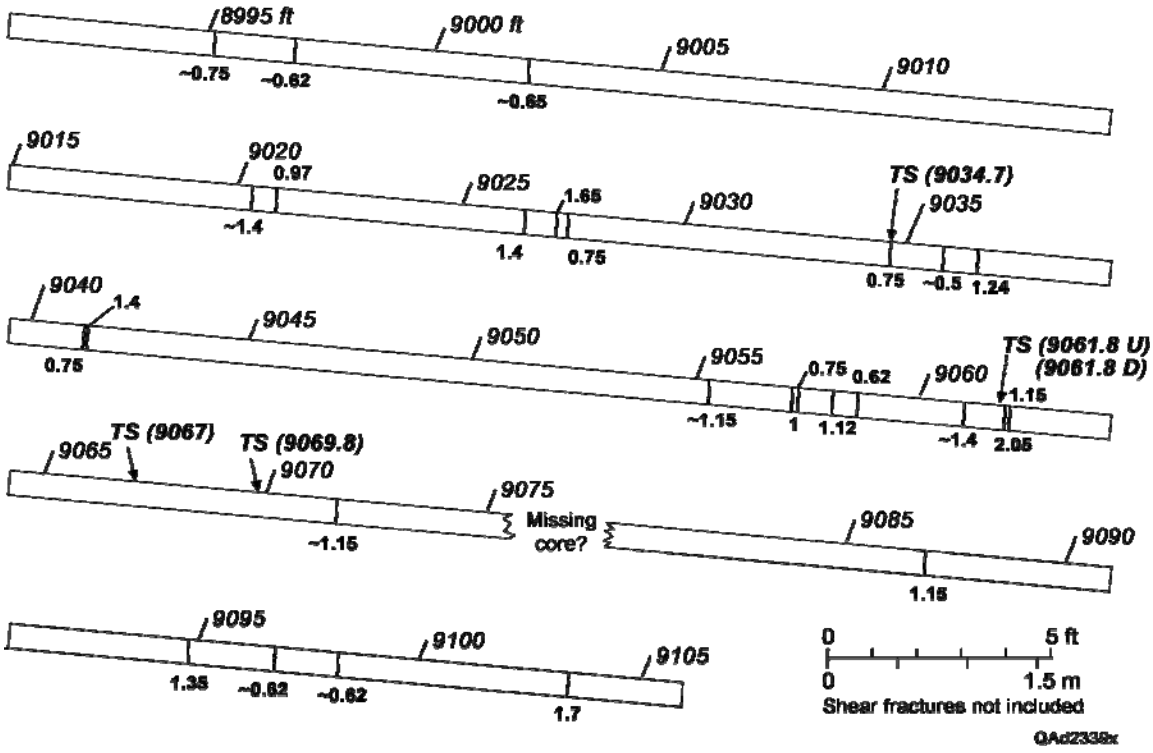

Figure 4.3 Location of macrofractures and samples in SHCT-1 core. Macrofractures are marked by thin vertical lines, TS marks thin-section locations for scaling, and bold numbers adjacent to core diagram are macrofracture kinematic apertures in millimeters. Macrofracture locations based on core description by L. Gomez and Lorenz and Hill, (1991, their Figure 5).

The subsequent history of the SHCT-1 well provides evidence of the effect on fluid flow and producibility of the large fractures encountered. Mechanical problems occurred while cementing the liner in the Cozzette interval, eventually resulting in loss of the lower part of the initial SHCT-1 hole from which the core had been obtained. Sidetrack operations began April 26, 1991, and a second Cozzette lateral was drilled to a total depth of 9,407 ft. The horizontal part of the hole penetrated about 300 ft of net upper Cozzette pay, was completed open hole, and flow tested at rates up to 15 MMCFD during a 3-hour test before a temporary plug was set. The sidetrack was put on production on January 16, 1992, and tested until June 3, 1992.

The well began making water in February, and water production increased to about 400 BWPD in mid-March when the well was shut in. Water production dropped after shut-in periods but increased during flow periods. Because the nearby MWX-1 well had produced from the Cozzette with little water, and oxygen activation logs indicated water movement behind pipe, water from the Rollins Sandstone was suspected. The lower Rollins was perforated, and cement was squeezed to try to shut off this water. Nevertheless, when the Cozzette was tested from April 12, 1993, to June 1, 1993, water production reached rates of more than 400 BWPD, and no further production was attempted.

4.2.2 Sampling

Within the Cozzette Sandstone cored interval, we collected four samples from locations close to and away from macrofractures in the SHCT core. All samples were made into thin sections 1 by 2 inches in size with the long side of the sample oriented parallel to the core axis. All thin sections were cut parallel to bedding. The name of the thin section reflects its measured depth in the core. Two datasets (9061.8 U and 9061.8 D) were obtained from a single thin section prepared from a sample from 9,061.8 ft.

These datasets contain the same macrofracture. Dataset 9061.8 U was imaged from the uphole side of the macrofracture, and 9061.8 D was imaged on the downhole side. A second thin section (9067) was prepared from a sample located halfway between macrofractures at 9,061.8 ft and 9,071.8 ft. The third thin section (9069.8) was obtained from a sample located close to the macrofracture at 9,071.8 ft but does not contain any macrofractures. A fourth thin section (9034.7) was made from a sample that contains a macrofracture (Figure 4.3). We also collected a separate suite of samples for diagenesis studies and for description of macrofracture attributes.

4.2.3 Microstructure Imaging

High-resolution microstructure imaging using scanning electron microscope (SEM)-based cathodoluminescence (scanned CL) allows efficient high-magnification (as much as 2,000□) examination of silicate minerals having low levels of luminescence over large specimen areas (Milliken and Laubach, 2000). Sensitive photomultiplier-based CL systems, high magnification, and stable SEM observing conditions provide clear resolution of cement-filled microfractures that cut grains and/or cement, permitting construction of accurate microstructure maps that delineate grain and fracture boundaries and cement growth textures within fractures.

Differences in CL intensity arise from slight variations in trace-element content or defect structure that characterize quartz of various origins (Milliken and Laubach, 2000 and references therein). Under conventional transmitted light microscopy, these minute fractures are generally invisible because quartz cement in fractures has grown in optical continuity with quartz grains in the fracture walls. However, microfractures could be partly visible as trains of inclusions (Figure 4.4a, b).

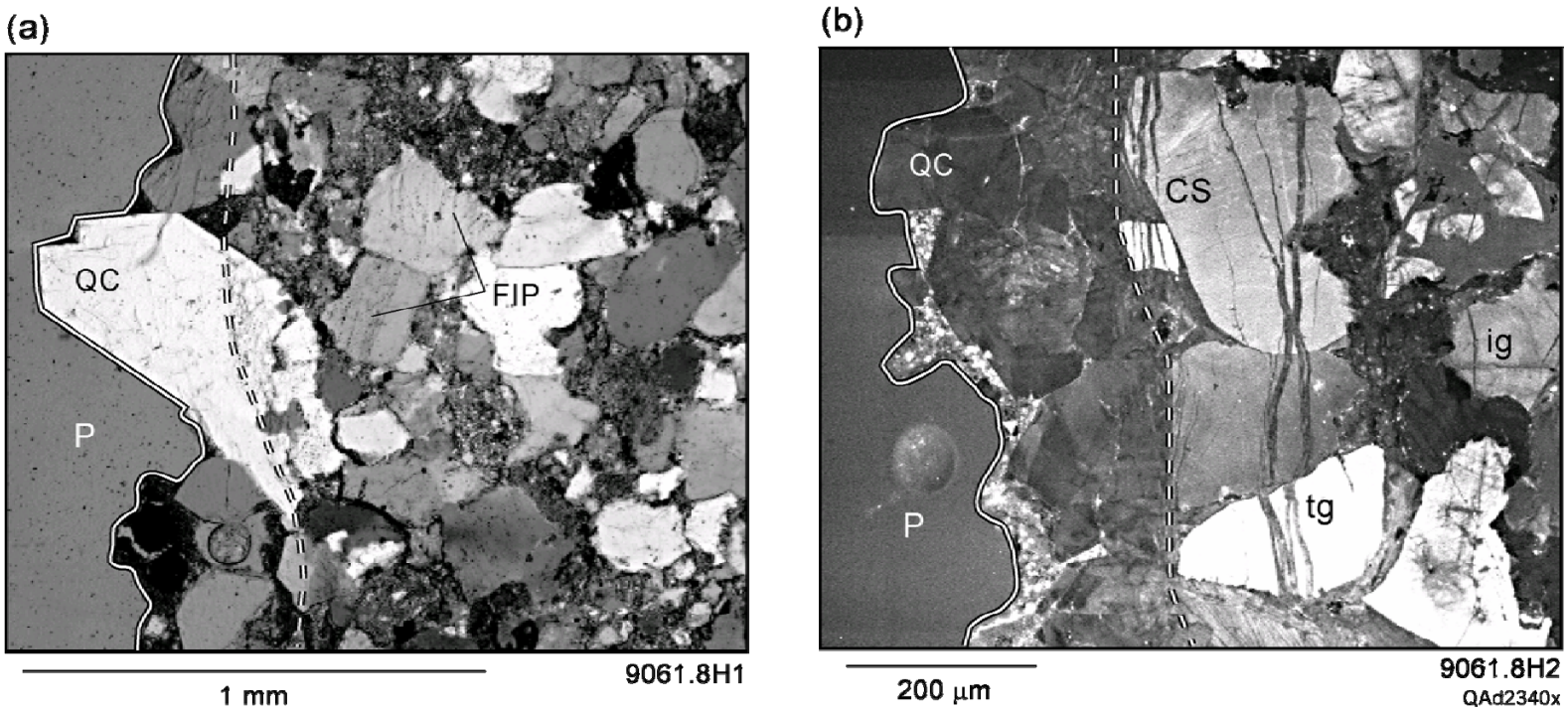

Figure 4.4 Comparison of typical microstructures near a fracture wall, imaged by optical microscopy and SEM-based cathodoluminescence. Both images are from the same fracture but from adjacent thin sections; one was stained for carbonates (9061.8H1), and the other one was polished for SEM use (9061.8H2). Dashed lines indicate the approximate location of the macrofracture wall. Crystals located between the dashed and solid lines have precipitated on the fracture wall. (a) Transmitted light photomicrograph of a typical fracture wall with euhedral quartz cement growing (QC) into the fracture porosity (P). Quartz-sealed microfractures are only partly visible as lines of inclusions (FIP). The apertures of these microfractures cannot be measured accurately. (b) Scanned CL image of fracture wall showing euhedral quartz cement (QC), fracture porosity (P), and crack-seal texture (CS). Transgranular microfractures (tg) cross more than one detrital grain and cement and are approximately parallel to the macrofracture present in the sample. In contrast, intragranular microfractures (ig) do not extend beyond boundaries of a single grain.

The detectors and processing used for these images record CL emissions in the range of ultraviolet through visible into near infrared and convert them to gray-scale intensity values. All images were acquired using an Oxford Instruments MonoCL2 system attached to a Philips XL30 SEM operating at 15 kV.

Microstructures were imaged on thin sections cut parallel to bedding. Scanned CL photographs were taken in traverses several millimeters in length, and stitched electronically into mosaics (Figure 4.5). Typically, a mosaic of 30 to 40 individual images at a scale of 1:150 is required to record a continuous CL image along the short side of a 1-by-2-inch thin section. To increase the likelihood of intersecting microfractures genetically related and parallel to macrofractures, mosaics were oriented perpendicular to known macrofracture strike (Terzaghi, 1965; Marrett et al., 1999). However, the mosaic from a sample located 2 ft away from a macrofracture (at a depth of 9,069.8 ft) was acquired approximately parallel to macrofracture strike. Most microfracture trace lengths are two to three times shorter than the narrow dimension of the image mosaics, so the aspect ratio or the orientation of the image mosaics may not be important.

On a CL mosaic, fractures were identified and classified on the basis of their shapes and crosscutting relations with respect to pore-filling, grain overgrowth, and fracture-filling cements. We further classified all microfractures into those that extend beyond individual grain boundaries (transgranular) and those that are confined within individual grains (intragranular). Orientation and size were mapped electronically using commercially available software by defining four points: the two fracture tips and two opposite points on the fracture walls at the widest aperture.

Figure 4.5 Microfracture trace map, 9,067 ft, SHCT-1 well. Panchromatic black-and-white CL images are acquired along a linear trajectory perpendicular to macrofracture strike. Individual images are acquired with a small overlap to ensure mosaic continuity. Box outlined on trace map indicates location of a single uninterpreted CL image (bottom) and its corresponding fracture trace map (center). Fractures visible in the CL image that are not indicated on the trace map were interpreted as inherited or compaction-related fractures.

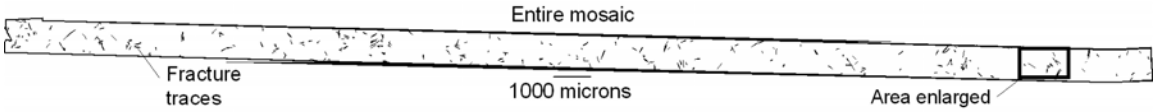

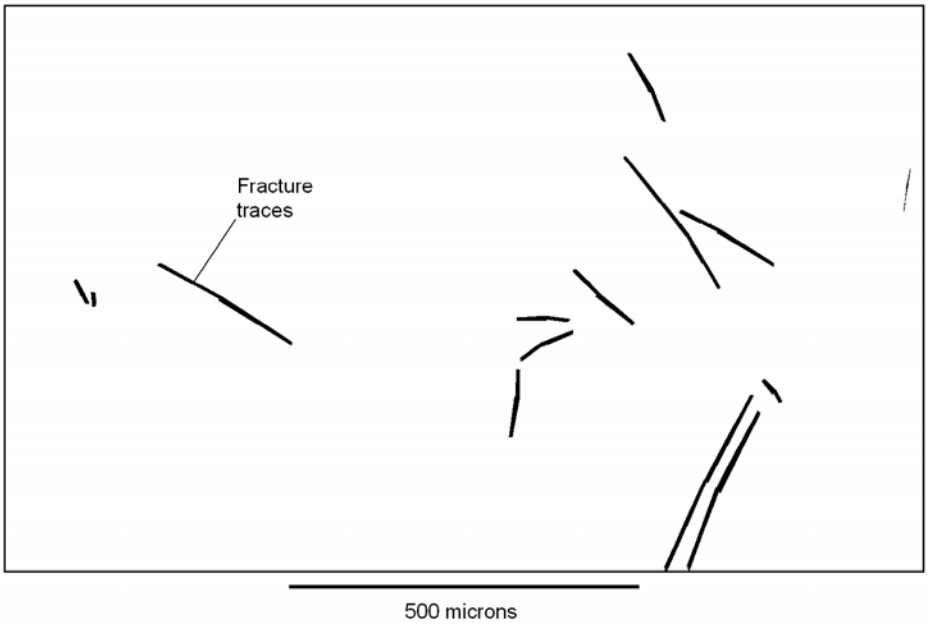

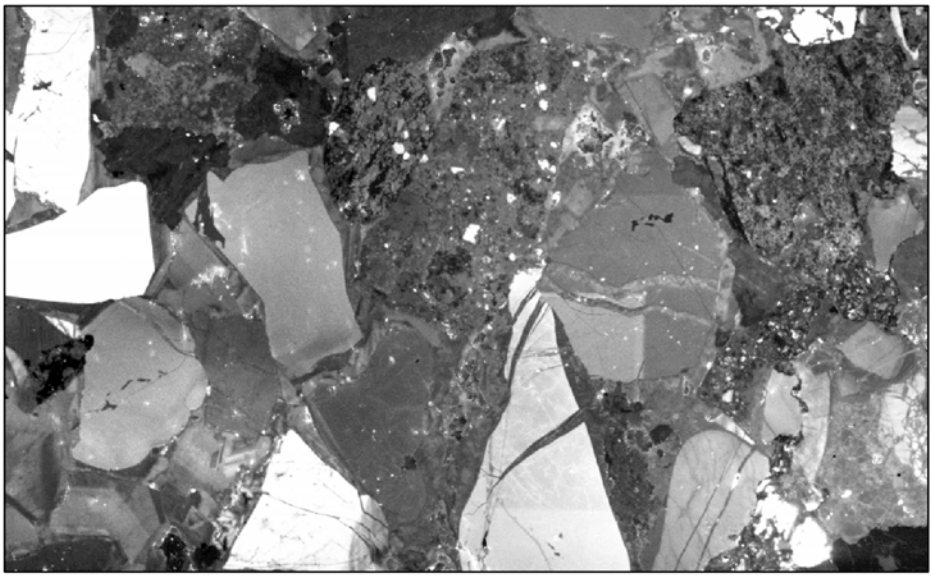

CL image QAd2342x

Fracture attributes were measured and compiled using in-house software that uses the digitized parts of the four points to calculate length, aperture, and orientation (Ortega, 2002). The area of the CL mosaic is also calculated using image-processing software.

4.3 SCALING METHODS

In addition to the sampling limitations imposed by typical well configurations, methods of fracture intensity measurement such as counting the number of fractures encountered in the observation domain (core, outcrop, thin section) divided by the dimension of observation domain, or calculating the average spacing between fractures, are inadequate if they ignore the wide spectrum of fracture sizes, from micrometer to meter scale, found in nature. Apparent fracture intensity varies with minimum fracture size chosen for fracture intensity measurement; therefore, in order to compare fracture intensity, it is essential to define the size-range of fractures being considered (Ortega et al., in press).

A potential solution to subsurface fracture sampling limitations for fracture intensity is scaling analysis using the population statistics of small fractures to predict the sizes and abundance of large fractures important to fluid flow. Fractures in sandstone may range from less than a micrometer to more than a meter in width. Small and large opening-mode fractures that have the same orientation may be different size fractions of the same fracture sets. Power-law aperture-size distributions ranging over five orders of magnitude have been reported in sandstone and limestone (Marrett et al., 1999) and over three orders of magnitude in dolomites (Gale et al., in press).

Power-law descriptions of fracture aperture populations take the form: $F = ab\text{-}c$, where F is cumulative fracture frequency, a is the coefficient, b is the fracture aperture, and c is the exponent of the power-law relationship. Where these parameters can be delineated for microfracture size distributions, the equations can be used to predict the

distribution of sizes of macrofractures in the same volume of rock (Marrett, 1996). Power-law distribution coefficients may be thought of as a measure of fracture intensity at a given size. For example, if b = 1, then the equation simplifies to F = a. Exponents reflect the slope of the power law on a log-log plot.

Scaling results can be used to estimate the distance a hydraulic fracture or horizontal well would need to penetrate a given horizon perpendicular to natural fracture strike in order to encounter fractures of a given size (Gale, 2002). Results can also be used to predict fracture porosity and permeability (Marrett, 1996).

Fractures occupy a three-dimensional (3-D) volume of rock, but samples having lower topology such as one-dimensional (1-D) and two-dimensional (2-D) samples can capture essential parts of fracture population attributes (Marrett, 1996). Microfracture studies of rocks are typically either 1-D scanline studies or 2-D trace map studies. For 1-D analysis, kinematic apertures and the spacing between fractures are measured along scanlines constructed normal to fracture strike. Kinematic aperture is defined as the distance between fracture walls measured normal to the fracture trend regardless of the presence or absence of fracture porosity. For 2-D analysis, apertures of all fractures occurring in the imaged area are measured. Aperture data are presented as cumulative frequency plots of fracture apertures, normalized to scanline length or fracture mosaic area.

The data commonly display truncation and censoring artifacts (Marrett, 1997 and references therein). Artifacts produce deviations from a linear trend in a log-log graph. Truncation bias at the small-scale end of the plot is produced by limits in either imaging or recognizing and recording progressively narrower fractures. Censoring bias of large fractures occurs because these fractures are inadequately sampled in the area of observation. We use a regression model to obtain the power-law distribution (straight

segment on a log-log graph) for sampled microfractures. The model fits all data by recursive calculations (R. Marrett, written communication, 2000) so that artifacts and an underlying power-law equation are honored.

Sampling of non-uniformly distributed fractures, however, may lead to bias in the microfracture sample and over- or under-prediction of macrofracture intensity. The SHCT-1 core provides an opportunity to investigate whether the location of samples used for microfracture analysis, relative to macrofractures, affects the power-law distribution function and, therefore, accuracy of macrofracture intensity prediction. In addition, macrofractures present in the core allow us to test the microfracture predictions.

4.4 FRACTURE DESCRIPTION

4.4.1 Macrofracture Apertures and Spacing

The horizontal Cozzette core contained 35 subvertical west-northwest-striking opening-mode fractures (Lorenz and Hill, 1991) that are lined and partly filled with quartz and, locally, traces of calcite (Figure 4.3). The dimension of large fractures that can be measured in the core is kinematic aperture. Macrofracture apertures range between 0.5 and 2.15 mm. This spectrum of sizes includes small macrofractures that are nearly completely filled with quartz. Unless the core breaks along these fractures, they are difficult to perceive with a hand lens because of the rough external whole core surface, although they may be obvious in a polished rock sample or thin section, and a few were found in thin sections selected from apparently unfractured core. This shows that some fractures at the small end of the macrofracture aperture range were missed during conventional core analysis.

Fracture width (or kinematic aperture; hereafter, aperture) was measured using a logarithmically graduated comparator (Ortega and Marrett, 2000; Ortega et al., in press).

This tool together with a hand lens allows measurement of fracture apertures in core as small as ~0.05 mm if fractures are clearly visible.

Previous sampling of the SHCT-1 core removed rock containing eight fractures. Of the 27 remaining fractures, an aperture measurement was obtained on all but one. Our macrofracture analysis used only those 26 fracture aperture measurements. The SHCT-1 core is broken along some macrofractures. Aperture of broken fractures was estimated from the heights of crystals present along one or both macrofracture walls and from relict bridges, introducing some uncertainty into the macrofracture data. Two shear fractures (possible sheared opening-mode fractures) were also identified but not included in the analysis.

Fracture spacing ranges from 9 mm to 5.4 m, and the arithmetic mean spacing is 1.3 m. Macrofractures in the core are not evenly spaced, however, and may be clustered in swarms (c.f. Lorenz and Hill, 1991, 1994; Laubach, 1991).

4.4.2 Fracture Diagenesis

Quartz is present in both microfractures and macrofractures, and over the entire sampled size range, quartz is the first cement precipitated on fracture walls. Scanned CL evidence of quartz cement appearance, fracture orientation, and crosscutting fracture/cement relations is consistent with micro- and macrofractures having formed contemporaneously. Microfractures tend to be entirely sealed, whereas fractures larger than about 1 mm aperture are mostly open, having fracture walls lined by faceted quartz crystals that grew into open fracture pore space. Size dependence of open fractures with respect to quartz cement, where wider fractures are less likely to be completely filled with quartz cement, was noted in the initial fracture description (Lorenz and Hill, 1991).

Quartz also forms mineral bridges in large microfractures and several macrofractures (Figure 4.6). These bridges are typically oriented normal to, and connect

opposite, fracture walls. Bridges contain crack-seal texture that records repeated fracturing and local sealing by quartz precipitation. Unlike crack-seal textures described from metamorphic veins, where the entire fracture is commonly filled with cement (e.g., Ramsay, 1980), these fractures can have extensive porosity and only a thin veneer of cement that deposited synchronous with fracture growth on areas of the fracture wall between bridges (Laubach, 1988; Lander et al., 2002; Laubach, 2003). Crack-seal texture shows that fracture porosity and bridges evolved concurrently.

Crack-seal texture results from repeated small increments of extension (microfractures) with new cement spanning the fracture between widening increments. Sharp-sided boundaries between broken grains and cement record individual opening and sealing events. The growth increments of fracture bridges are recorded by the width of the microfractures that form the crack-seal texture. In the Cozzette Sandstone, microfracture width in crack seal ranges from 5 to 20 μm.

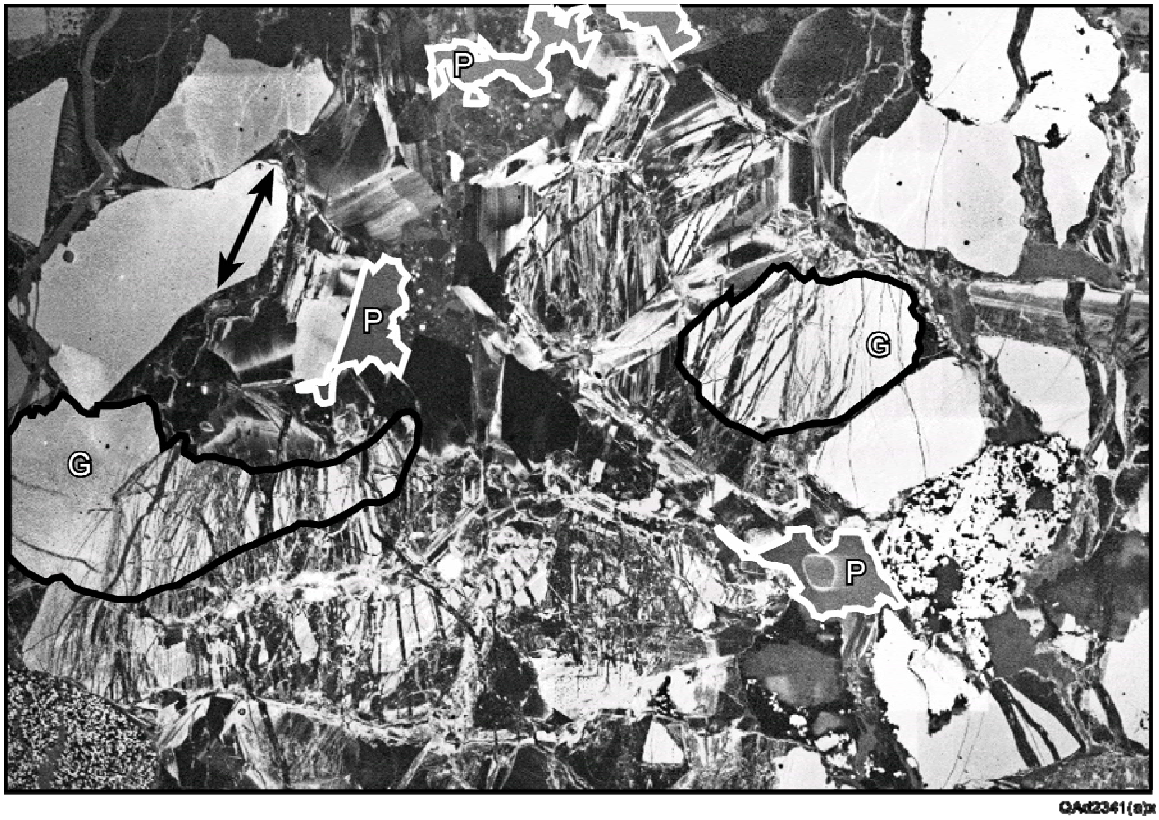

Figure 4.6 Quartz cement bridge within macrofracture having crack-seal texture (scanned CL). Arrow indicates the approximate trend of the macrofracture. P indicates fracture porosity. The boundaries of two quartz grains (G) that have been strained by crack seal are highlighted.

Crack-seal texture suggests a mechanism by which micro- and macrofractures develop in the same fracturing episode and therefore are part of the same fracture population. Abundant flaws are likely to trigger the generation of many microfractures, some of which may seal before the next extension increment, preventing them from opening further. Others may not completely seal before the next extension increment and reactivate repeatedly, thereby becoming macrofractures. Because both macrofractures and microfractures are being formed at the same time by the same stresses, they have similar orientations.

According to Lander et al. (2002), crack-seal bridges arise when (1) increase in fracture aperture is small for individual fracture events (e.g., micrometers); (2) rate of aperture increase integrated over geologic timescales is less than rate of precipitation along the direction of fastest growth rate, but greater than that of the slowest growth rate (R. Lander, L. Bonnell, and R. Larese, unpublished test results, 2000); and (3) new anhedral nucleation surfaces are periodically created by fracturing of quartz crystals. Patterns in Cozzette fracture bridges, in the SHCT-1 well and in other wells, are consistent with this model of fracture and bridge growth.

The significance of crack-seal textures in bridges is that they explain why data on sealed microfractures can be relevant to predicting the intensity of large fractures that might be open (Lander et al., 2002). Interaction of the geochemical process of cement precipitation with progressive fracturing is such that many small fractures initiate, but few grow. Most small fractures probably vanish, in a mechanical sense, as cement fills them. On the other hand, some large fractures widen faster than cement can fill them. Unless geochemical conditions change, cementation processes like quartz precipitation require protracted deep burial to seal these fractures.

Other diagenetic processes can seal large fractures. For example, many fractures in core from the Williams Fork Formation are lined and bridged with quartz but are filled with late calcite and other minerals (Pitman and Sprunt, 1986; Cumella et al., 2002). Macrofractures in the Cozzette horizontal core are mostly open, with a veneer of quartz cement on fracture surfaces, as predicted by methods outlined by Laubach (2003). These surrogate methods for predicting preservation of fracture porosity in large fractures correctly predicted the open character of large fractures in the Cozzette Sandstone (unpublished data and Cumella et al., 2002).

4.4.3 Microfracture Categories and Strike

We recognize three categories of microfractures on scanned CL mosaics on the basis of shape, patterns, and crosscutting relations with respect to cement and grains (Laubach, 1997). Category I fractures have straight traces and may cross grains and cement. These are the microfractures we interpret to be genetically related to macrofractures. Category II microfractures have shapes and patterns with respect to cement and nearby grains that are consistent with formation as a result of grain-grain interaction (possibly compaction), and category III microfractures are those inherited from source rocks of detrital grains.

Our analysis uses only category I microfractures, although it is inherently difficult to classify the smallest microfractures unambiguously (length less than grain size). We subdivided category I microfractures on the basis of their observed crosscutting relations with cement. Microfractures crossing multiple grains and intervening cement, and those that cross from grains into cement, are termed transgranular. Microfractures contained within grains are termed intragranular and are the most difficult to interpret. We distinguished them from grain crushing- or inheritance-related fractures on the basis of fracture patterns, shapes, and crosscutting relations with cement.

More than 2,600 microfractures were measured. The area of image mosaics ranges from 8.27 to 28.4 mm2, and the number of microfractures interpreted in a single mosaic ranges from 521 to 714. Category I microfractures represent between 34 and 70% of the entire microfracture population, with 4 to 10% being transgranular. Category II microfractures range from 6 to 15%, whereas those in category III range from 19 to 51%. These results show that the type of microfracture suitable for scaling studies is common in these rocks.

In-house software (Ortega, 2002) was used to record and plot fracture orientation from digital microfracture trace maps (Figure 4.5). Rose diagrams of microfracture strike were generated (Figure 4.7). We defined microfracture strike using both equal-area and length-weighted rose diagrams. Length-weighted rose diagrams of fracture orientation generally allow improved grouping of genetically related microfractures to identify dominant strikes, but in this case there was little difference in the result between plot types.

Fracture strike orientations for transgranular fractures alone (Figure 4.7a, left column) and transgranular and intragranular fractures combined (Figure 4.7a, right column) are similar. The dominant microfracture strike is west-northwest. This trend coincides with orientations of macrofractures (Figure 4.7b), although there is greater dispersion in the microfracture data owing to inclusion of intragranular fractures. Some subsets of the microfracture data suggest that subsidiary northwestward and northeastward trends are also present. We selected fractures trending 65° to 135° as falling within the same set as the macrofractures (Figure 4.7c). Although the 70° window is rather wide, it separates fractures of the west-northwest trend from those of the northwest and northeastward trends and allows for variations in microfracture orientation caused by grain-scale perturbations. Of 1206 Category I microfractures, 642 belong to the west-northwest set. All intensity and spacing analyses are confined to these 642 fractures, of which 87 are transgranular.

Figure 4.7 Rose diagrams of microfracture and macrofracture orientation data. (a) Length-weighted transgranular microfractures (left column) and transgranular and intragranular microfractures (right column). (b) Macrofractures (not length-weighted). Data from Lorenz and Hill (1991). (c) Orientation window used to select microfractures of west-northwest-trending set.

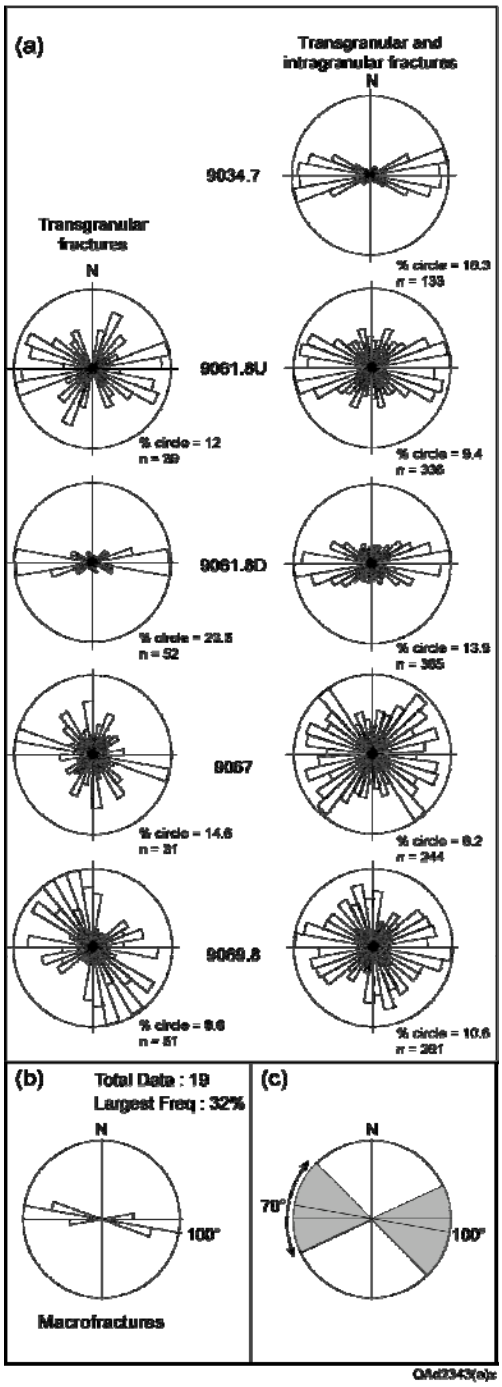
(a)
Transgranular and intragranular fractures
N
9034.7
% circle = 16.3
n = 133
Transgranular fractures
N
9061.8U
% circle = 12
n = 39
% circle = 9.4
n = 336
9061.8D
% circle = 22.5
n = 52
% circle = 13.9
n = 365
9067
% circle = 14.6
n = 31
% circle = 8.2
n = 244
9069.8
% circle = 9.6
n = 51
% circle = 10.6
n = 281
(b)
Total Data : 19
Largest Freq : 32%
N
100°
Macrofractures
(c)
N
70°
100°

4.4.4 Aperture-Size Distributions

4.4.4.1 Macrofractures

Macrofracture apertures from the SHCT-1 core (Figure 4.3) are presented in a cumulative frequency log-log plot (Figure 4.8). To obtain a cumulative frequency plot, apertures are sorted in decreasing size and cumulative numbers counted for all aperture sizes. Cumulative numbers were divided by the cross-sectional area of the SHCT-1 core to generate a 2-D cumulative frequency that could be compared directly with 2-D microfracture data.

Macrofracture aperture data were fit to a curve, termed a bias model function, which fits all data by recursive calculations (R. Marrett, written communication, 2000) so that artifacts (truncation and censoring) and an underlying power-law equation are honored. This function is composed of two curved segments (truncation and censoring) and one straight segment (power law). The power law implies scale-invariance of the attribute examined. The power-law segment for the SHCT-1 macrofracture aperture data ranges between 1.12 and 1.65 mm, the truncation segment ranges from 0.5 to 1.12 mm, and the censoring segment ranges from 1.65 to 2.15 mm. The narrowest macrofracture measured in the core is 0.5 mm, and the widest is 2.15 mm. The kinematic aperture of 1.12 mm is significant in two ways. It is approximately the minimum aperture value where fracture porosity was detected, and it was used as the specific fracture size for comparisons of measured and predicted fracture intensities.

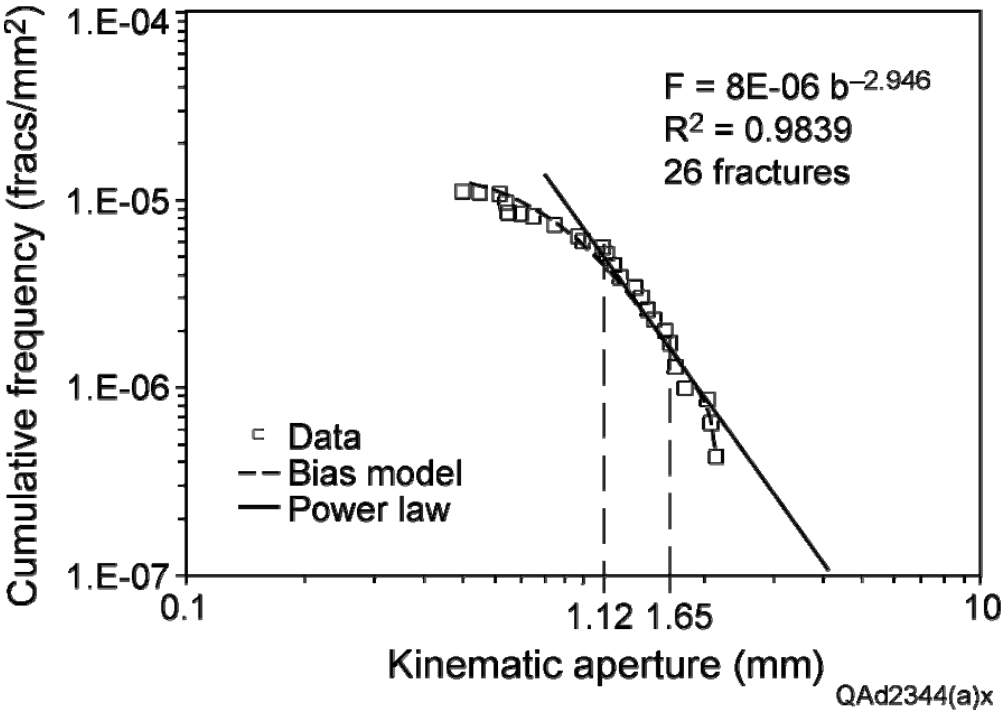

Figure 4.8 2-D cumulative frequency of macrofracture apertures, SHCT-1 well (8,990 to 9,106.4 ft) from apertures of 26 fractures measured using a comparator (Ortega and Marrett, 2000). A bias model function that includes all data points is indicated by a dashed line. This function includes truncation, power-law, and censoring segments of the dataset. Further details of this function are explained in the text. The correlation coefficient refers to the bias model fit. The continuous line and the equation correspond to the power-law segment of the bias model. The power-law segment is located approximately between kinematic apertures of 1.12 and 1.65 mm, but the power-law line in the figure was extrapolated to higher and lower values of kinematic aperture.

4.4.4.2 Microfractures

Aperture sizes of microfractures in the west-northwest-trending set, measured in CL mosaics, range over approximately two orders of magnitude, from 0.00028 mm (0.28 μm) to 0.039 mm (39 μm). Most microfracture apertures, however, lie within one order of magnitude, between 0.001 and 0.01 mm. Microfracture lengths range approximately

from 0.007 to 0.68 mm. Microfracture data are from areas 10 to 30 mm2 measured in thin sections; macrofracture data are from SHCT-1 core (equivalent area approximately 2.E+06 mm2).

4.4.4.3 Using microfractures to predict macrofracture intensity

Transgranular and intragranular microfracture apertures are combined in a cumulative frequency log-log plot (Figure 4.9). Microfracture aperture-size distributions can also be described using the bias model function with its power-law segment. On each plot the power-law segment was extrapolated to the scale of the macrofracture aperture data. The extrapolated power-law segment would pass through the peak of macrofracture data if it were an accurate prediction of macrofracture intensity.

The difference between the measured macrofracture intensity and the predicted intensity (from extrapolation of microfracture population) was included on each plot. This difference was calculated in terms of macrofractures of 1.12 mm aperture or wider per meter of core. Although the difference could have been expressed in fractures per square millimeter, it is more meaningful to express it in fractures per meter of core.

The difference in fracture intensity in units of fractures per square millimeter was multiplied by the width of the core in millimeters, 66.675 mm (2 5/8 inches) to give a measure of fracture intensity in units of fractures per millimeter of core, which was then converted into fractures per meter. Some datasets underpredicted (9034.7 and 9069.8) and others overpredicted (9061.8U, 9061.8D and 9067) the macrofracture intensity. However, two datasets (9034.7 and 9061.8U) generated an excellent prediction of macrofracture intensity.

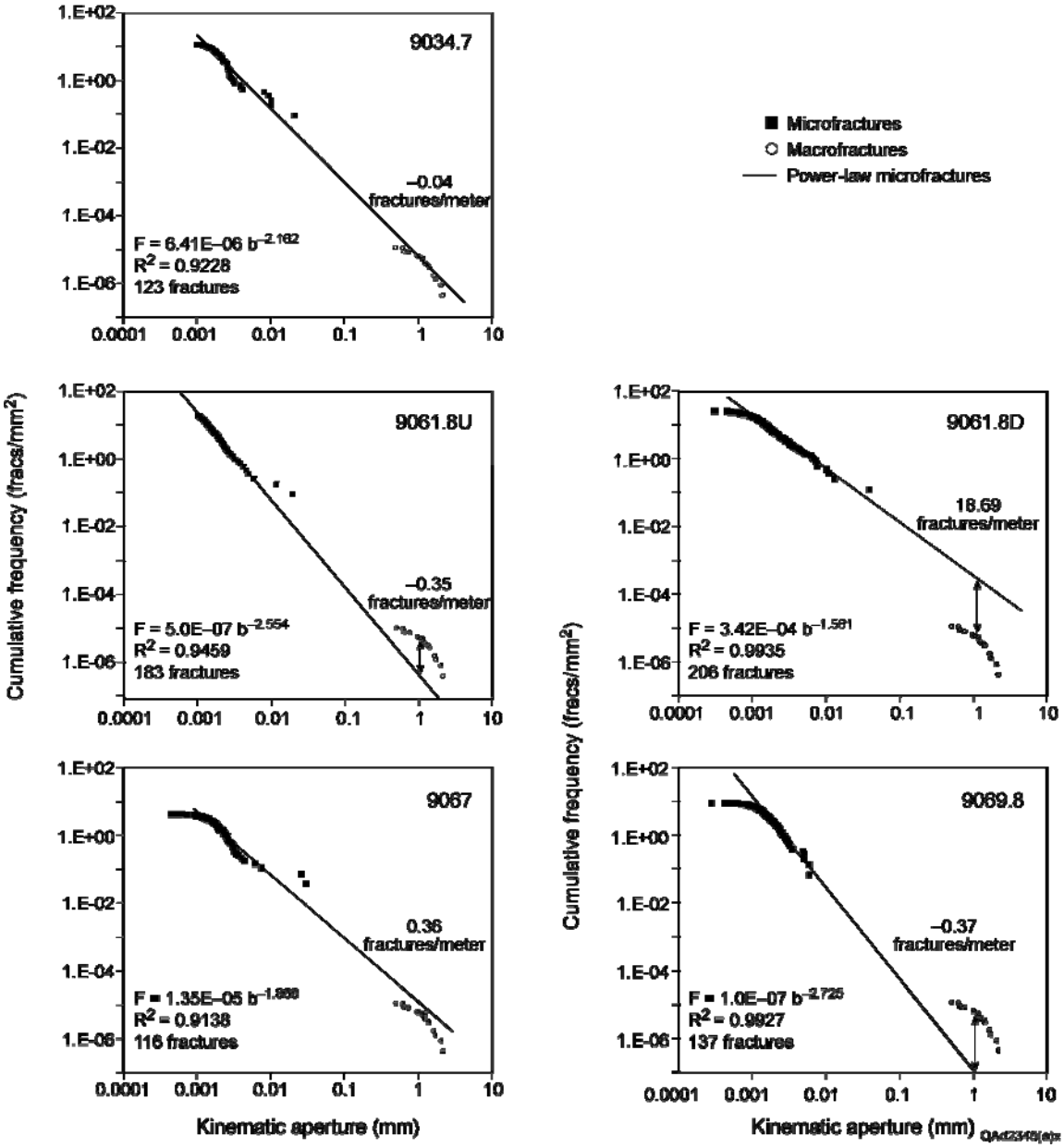

Figure 4.9. 2-D aperture cumulative frequency plots for transgranular and intragranular microfractures. Each plot contains microfracture (squares) and macrofracture (circles) populations. The macrofracture data on each plot (lower right corner) correspond to the data in Figure 8. Solid lines are power-law fits to microfracture data only, and their equations and correlation coefficients are shown. Arrows and numbers in units of fractures per meter indicate the difference between the measured and predicted macrofracture intensity for fractures with aperture of 1.12 mm or wider.

We combined the transgranular microfractures from all samples into a single cumulative frequency plot (Figure 4.10a). We also combined the transgranular and intragranular microfractures into a second cumulative frequency plot (Figure 4.10b). Bias model functions were fit to the data, and power-law segments were extrapolated to the macrofracture data as for Figure 4.9. The difference between measured and predicted intensities was calculated. Transgranular fractures produced a poor prediction of macrofracture intensity. Following the conversion of fracture intensity from units of fractures per square millimeter to units of fractures per meter of core, the difference was calculated to be 39.44 fractures per meter. In contrast, when all fractures were combined (Figure 4.10b) the predicted intensity was very close to that measured. The predicted fracture intensity was 0.37 fracture per meter, and the measured intensity was 0.46 fracture per meter; therefore, the difference was only 0.09 fracture per meter of core.

4.5 2-D FRACTURE INTENSITY

Power-law distribution coefficients and exponents of microfractures were plotted against distances between sample and nearest macrofracture (Figure 4.11). If microfractures were concentrated around macrofractures, coefficients would be higher in samples closest to macrofractures. It is less clear how exponents would vary because their value depends on relative number of fractures of different sizes. There is no consistent relationship between coefficient and proximity to macrofractures (Figure 4.11a); neither is there any relationship between exponent and proximity to macrofractures (Figure 4.11b). We interpret this to mean that in the Cozzette Sandstone, microfractures do not necessarily concentrate around macrofractures. The spatial arrangement of microfractures appears to be at least partly independent of the spatial arrangement of macrofractures.

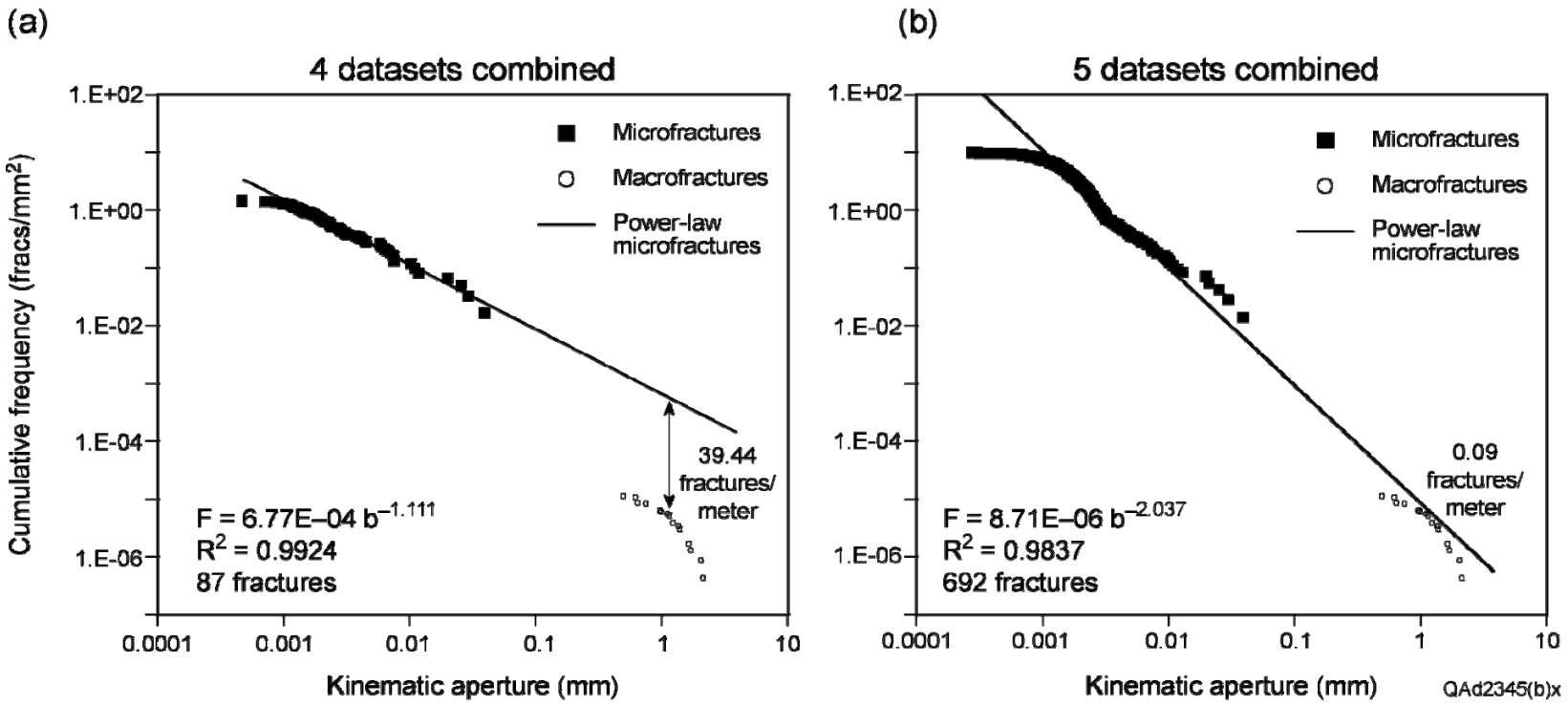

Figure 4.10 2-D aperture cumulative frequency plots for (a) combined transgranular microfractures from four datasets (9061.8U, 9061.8D, 9067, and 9069.8) and (b) combined transgranular and intragranular microfractures from five datasets (9034.7, 9061.8U, 9061.8D, 9067, and 9069.8). Each plot contains aperture data for microfractures (squares) and macrofractures (circles). The macrofracture data in the lower right corner correspond to the data in Figure 4.8. As in Figure 4.9, the power-law segment of a bias model function generated from the microfracture population was extrapolated to the scale of the macrofracture aperture data. The value of the difference between the measured macrofracture intensity and the predicted is indicated by the arrows and numbers in units of fractures per meter.

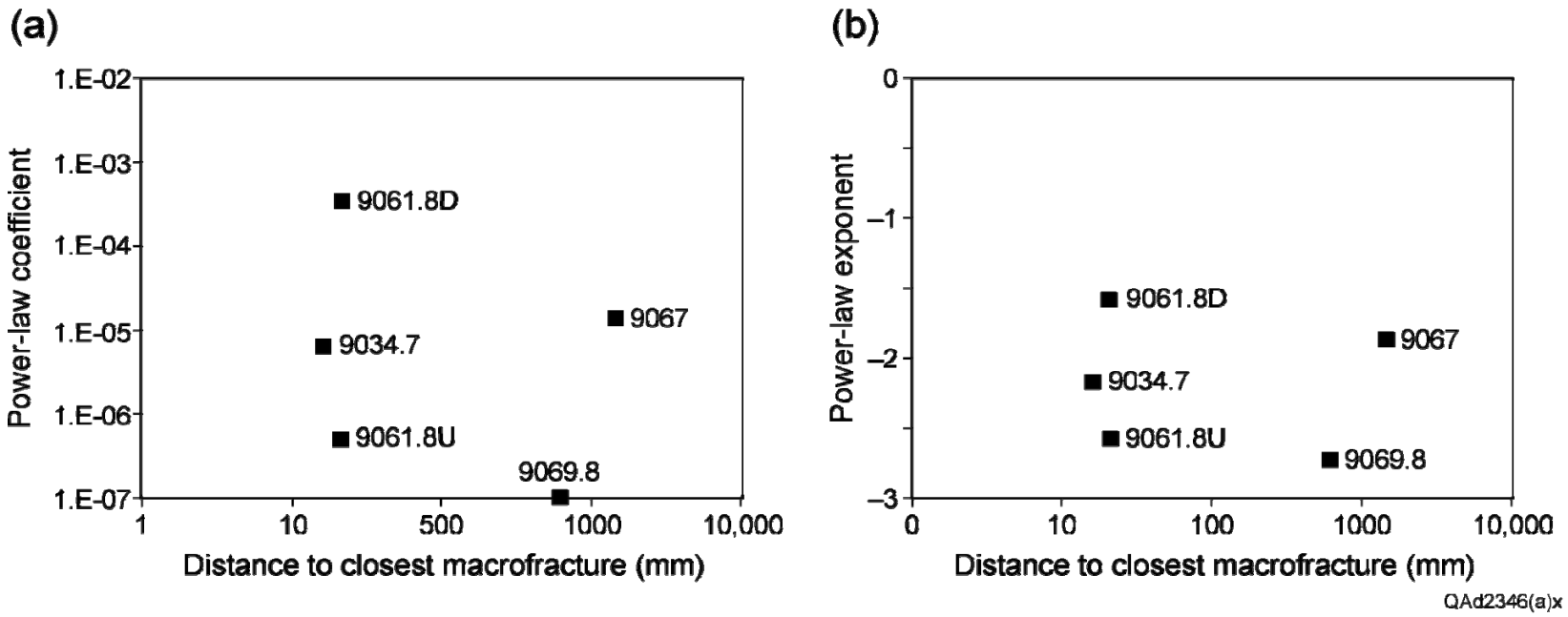

Figure 4.11 Power-law coefficients (a) and exponents (b) of all datasets available with respect to distance to macrofracture for transgranular and intragranular microfractures. Values for this figure were obtained from the power-law functions displayed on each plot in Figure 4.9. Sample numbers are displayed next to each data point. No trend is evident on either plot, suggesting that for the Cozzette Sandstone, microfracture intensity is not affected by macrofracture proximity.

The macrofracture aperture-size distribution is shown on the same plots as microfracture data by normalizing frequency to data acquisition area (Figure 4.9). Power-law equations for microfractures are extrapolated to the aperture size of macrofractures, allowing predictive accuracy of the extrapolation to be evaluated. Although power-law exponents vary over less than one order of magnitude, when extrapolated to the macrofracture scale this small variation in power-law slope has a considerable effect on predicted fracture intensities.

To quantify the accuracy of the prediction we calculated the difference between the predicted and measured intensities for macrofractures 1.12 mm or wider and expressed the difference as the number of fractures per meter of core greater or less than the measured frequency (Figure 4.9). We selected fractures 1.12 mm or wider for prediction evaluation because the aperture-size distribution power law for the macrofractures (Figure 4.8) is well defined for a range of apertures from approximately 1.12 to 1.65 mm.

Differences between measured and predicted fracture intensities were plotted against size of mosaic area (Figure 4.12a) and the distance between a sample and its closest macrofracture (Figure 4.12b). This was done to investigate whether mosaic area influences prediction accuracy and how prediction varies with distance between sample and the nearest macrofracture. There is no consistent relationship between mosaic area and accuracy of the prediction (Figure 4.12a). There is also no relationship between prediction accuracy and the distance between the sample and the nearest macrofracture (Figure 4.12b).

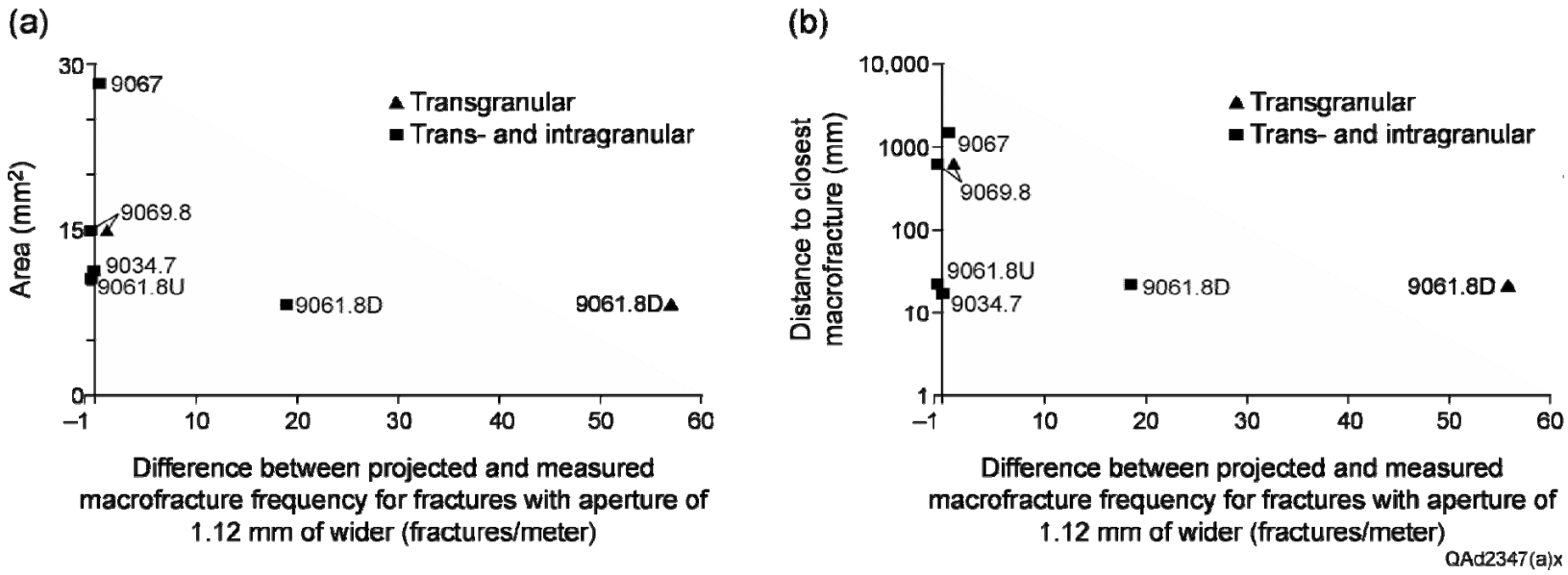

Figure 4.12. Difference between predicted and measured macrofracture intensity, (for apertures 1.12 mm or wider) plotted against (a) mosaic area from which microfracture aperture data were obtained and (b) distance between sample and the nearest macrofracture. Difference was calculated in terms of macrofractures per meter of 2 5/8-inch core. Values for this figure were calculated using the data displayed on each plot in Figure 9. High differences indicate poor predictions of macrofracture intensity, whereas an ideal prediction would lie on the y-axis of the plot.

4.6 FRACTURE SPACING

The previous analysis resulted in an estimate of number of fractures per unit length, but fracture spacing is a more conventional way of representing fracture intensity and is more readily comparable to horizontal core data. Inspection of macrofracture patterns in the core suggests clustering of fractures possibly in swarms, although we have no rigorous definition of the term swarm (Laubach, 1991; Olson et al., 2001).

Lorenz and Hill (1994) determined the average distance between swarms in outcrop to be ~1 m (3.4 ft) and in the SHCT-1 core to be 1.8 m (6 ft). Average spacing does not convey information about the degree of fracture clustering and may not be ideal for defining flow behavior of fractures, but it is a conventional starting point for fracture intensity comparison (Narr, 1991). A full treatment of the spatial distribution of fractures is outside of the scope of this paper, but calculations of average spacing give some indication of overall fracture intensity.

From a fracture mechanics perspective, the spacing of fractures that vertically span a mechanical layer is an appropriate reference frame for identifying the fractures to measure, but it is rarely possible to measure mechanical layer thickness directly in core. Cumella et al. (2002) speculated, on the basis of bed thickness patterns in vertical cores, that mechanical layer thickness in the Cozzette might be in the range of 1 to 2 m for the lower Cozzette and 4 to 6 m for the upper Cozzette, but compelling evidence of mechanical (or fracture) stratigraphy is lacking (Lorenz and Hill, 1991).

We used two methods to calculate average macrofracture spacing and then compared them. In the first method we calculated the arithmetic mean of spacings of all macrofractures above a threshold size of 1.12 mm in the core. The arithmetic mean for spacings is 2.7 m (35 m of core, 13 fractures of 1.12 mm and above). Minimum and

maximum spacing is 9 mm and 7 m, respectively. In the second method, we computed average spacing by taking the inverse of the fracture intensity predicted using microfracture aperture-size distribution (Figure 4.10b). The predicted fracture intensity is 0.46 fracture per meter, which gives an average fracture spacing of 2.2 m.

Our measurements of spacing give results that are slightly different from previously reported measurements from this core for two reasons associated with the choice of which fractures to measure. We regard both sets of results as valid but use our own data for comparison with our prediction mainly because we chose to make the comparison for fractures 1.12 mm wide or more. Lorenz and Hill (1991, 1994) measured average spacing in the SHCT-1 core, Cozzette interval, to be 0.92 m (3.0 ft), and individual spacings ranged from 30 mm to 5.4 m (0.1 to 17.8 ft). Their average spacing was calculated using all fractures (smallest aperture 0.5 mm) and would be expected to be smaller than our spacing calculation because more fractures were included. Also, our results differ because some fractures documented as being present in the core by Lorenz and Hill (1991) are now missing owing to sampling. Because their apertures are unknown, we could not include them in our calculation.

4.7 DISCUSSION

Our study shows that site-specific information about the intensity of large, open fractures can be derived from minute microfractures that are sealed with quartz cement. In the Cozzette interval of the SHCT-1 core, microfractures are part of a fracture population that includes large fractures that retain porosity, and the dominantly west-northwest strike of these structures is a good proxy for macrofracture strike. The hypothesis that micro- and macrofractures are part of the same population is supported by evidence that small and large fractures share a common orientation, that fractures formed at about the same time in the diagenetic history of the rocks, and that they can be

described by aperture-size distributions that follow the same power-law functions. In all cumulative frequency distribution plots there is an aperture-size gap between the microfracture and the macrofracture populations. We think fractures in this aperture range exist but were not observed in the core because these fractures are obscured by the rough external whole core surface and because the matrix and fracture fill are both quartz. These fractures were not observed in thin sections because the likelihood of encountering them is very small given their low intensity at that scale of observation.

Our results suggest 2-D microfracture populations in the Cozzette Sandstone are suitable for predicting macrofracture intensity. Yet microfracture abundances are far less than those found in highly microfractured sandstones that have been the focus of previous micro- and macrofracture comparisons (Ortega and Marrett, 2000). Cozzette Sandstone samples provide a test of scaling methods in rocks having relatively low microfracture intensities.

There is topological dissimilarity between micro- and macrofracture datasets, and there is also variation in sampling topology within a dataset (Marrett, 1996). For fractures that cross a sample area completely (macrofractures in core and large microfractures in mosaics) the sampling topology approaches 1-D, whereas the sampling topology for smaller fractures in the same dataset is 2-D. We have treated the core as a 2-D set for comparison with 2-D microfracture datasets even though it has a width of only about 6.5 cm (2 5/8 inches) and a length of 35 m, and macrofractures pass all the way through it. For future work it would be desirable to control the sampling topology of all datasets that are to be compared directly.

The presence or absence of nearby macrofractures apparently does not have a consistent effect on accuracy of prediction. For example, the two samples from depth 9,061.8 ft are both adjacent to a macrofracture yet give results that are markedly

different. One slightly underpredicts large fracture abundance (9061.8 U), whereas the other overpredicts large fracture abundance (9061.8 D), although we have not yet determined whether these curves are rigorously different. There is no consistent relationship between size of individual mosaic area and accuracy of prediction. One might expect a larger mosaic area, with larger fracture abundance, would correspond to a more accurate prediction, but we suspect that because the difference between individual mosaic areas is small an effect was not observed.

We are not yet able to distinguish between mosaic size and topology, and macrofracture proximity as controls on microfracture intensity, although no one factor appears dominant. It is likely that a combination of factors including local microfracture clustering, sample area, aspect ratio and orientation all affect prediction accuracy. These variations seem to cancel out if several mosaics are combined (Figure 4.10b) perhaps because the combined dataset encompasses the variations in proximity to macrofractures, mosaic area, and mosaic orientation shown by individual datasets. Given the assumptions in how fracture intensities were calculated, the uncertainties in these values are probably large but have not yet been adequately quantified. The apparent agreement of the combined dataset is encouraging, given the large extent of the extrapolation.

The combined mosaic area is only 72 mm2, and this is substantially smaller than the area covered by a single thin section. In a vertical, 4-inch-diameter core there is easily sufficient material to collect a representative sample of microfractures on a bed-by-bed basis. We used only a tiny part of the rock volume that would be available for microanalysis in a vertical core, or even a sidewall core, but more efficient image capture and processing are needed to exploit this data source.

Owing to the presence of fracture clustering and other issues, the best use of an average spacing prediction is not so much to provide specific fracture-spacing numbers as

to identify high, medium, and low fracture intensity of larger fractures without having to sample those large fractures in a horizontal well. Comparison of predicted and observed average spacings in the SHCT-1 Cozzette interval suggests that our prediction underestimates average spacing. However, the major source of error in our measured spacings is due to the fractures we did not count because of missing core; including them would decrease measured average spacing to a value very close to that predicted. Sources of error in calculated spacings include the small image areas we used, the topology of macrofracture versus microfracture data, and the use of intragranular microfractures, some fraction of which may be inherited fractures that should have been excluded. Use of longer scanlines or larger mosaics where data could be restricted to more readily interpreted transgranular fractures might reduce these errors.

Power-law distributions of aperture sizes reflect self-organization processes during fracture growth, probably in part a result of interaction among mechanical and chemical processes over time (Cladouhos and Marrett, 1996; Gillespie et al., 2001; Lander et al, 2002; Olson, in press). Although the origin of such patterns is beyond the scope of this discussion, evidence of interaction of cement precipitation and fracture growth is widespread in Cozzette macrofractures and Cretaceous sandstones of the western United States (e.g., Figure 4.6), and similar patterns of fracture organization are probably present in other diagenetically altered, fractured sandstone gas reservoirs.

We might use our results to make a prediction about the intensity of fractures potentially open to fluid flow (aperture >1 mm) in the sidetrack well (SHCT-ST, Figure 4.1), which penetrated 300 ft (91.4 m) of net upper Cozzette pay and which was not cored. Using the 2-D microfracture analysis we would predict 0.46 fracture per meter of core. For 91.4 meters of 2 5/8-inch core (equivalent to the SHCT-1 core) the number of fractures with apertures of 1.12 mm or greater would be 42.

4.8 CONCLUSIONS

Population statistics of sealed microfractures in Cretaceous tight gas sandstone can be measured on small rock samples using widely available SEM-based microscopy techniques. These statistics may then be used to predict macrofracture attributes—notably, the intensity of large, open fractures. Microfracture intensity does not vary systematically with distance of samples from macrofractures, so it is valid to use samples to predict fracture intensity irrespective of their location relative to macrofractures.

For the west-northwest-trending set, macrofracture intensity derived from microfracture aperture-size data extrapolated over two orders of magnitude comes remarkably close to direct measurement of fracture intensity in the SHCT-1 horizontal core. The closest prediction of macrofracture intensity comes from a combined dataset of all microanalysis samples, giving the largest possible subset of microfractures present in the SHCT-1 core, but even the combined dataset is derived from a sample area that is small compared with the volume of rock available in a typical vertical core.

Many questions remain about the theory and practice of collecting and interpreting this type of fracture intensity data, and this paper is merely a progress report on an ongoing study. Yet the value of this approach is that it may provide a method to measure and compare fracture intensities that is not limited by macrofracture observation, which would be a significant advance in fracture analysis. These initial findings on typical Rocky Mountain tight gas sandstone, combined with the results of other recent studies (Marrett et al., 1999; Gillespie et al., 2001; Gale et al., in press; Ortega et al., in press), are encouraging.

Chapter 5: Rapid Digital Quantification of Microfracture Populations

This chapter contains a paper that I wrote together with Dr. S. Laubach. This paper was submitted for peer-review in March of 2005 to Journal of Structural Geology and published in the March issue of 2006. The paper describes a method that I developed while working as research assistant for the Fracture Research and Application Consortium (FRAC) of the Bureau of Economic Geology. This method was initially conceived to rapidly measure fracture aperture and spacing along scanlines longer than a single thin section on mosaics of digital images.

ABSTRACT

Populations of microfractures are a structural fabric in many rocks deformed at upper crustal conditions. In some cases these fractures are visible in transmitted-light microscopy as fluid-inclusion planes or cement filled microfractures, but because SEM-based cathodoluminescence (CL) reveals more fractures and delineates their shapes, sizes, and crosscutting relations, it is a more effective structural tool. Yet at magnifications of 150 to 300×, at which many microfractures are visible, SEM-CL detectors image only small sample areas (0.5 to 0.1 mm^2) relative to fracture population patterns. The substantial effort required to image and measure centimeter-size areas at high-magnification has impeded quantitative study of microfractures. We present a method for efficient collection of mosaics of high-resolution CL imagery, a preparation method that allows samples to be any size while retaining continuous imagery of rock (no gaps), and software that facilitates fracture mapping and data reduction. Although the method introduced here was developed for CL imagery, it can be used with any other kind of images, including mosaics from petrographic microscopes. Compared with manual measurements, the new method increases several fold the number of

microfractures imaged without a proportional increase in level of effort, increases the accuracy and repeatability of fracture measurements, and speeds quantification and display of fracture population attributes. We illustrate the method on microfracture arrays in dolostone from northeast Mexico and sandstone from northwest Scotland. We show that key aspects of microfracture population attributes are only fully manifest at scales larger than a single thin section.

5.1 INTRODUCTION

Observation of structural fabrics on the millimeter to centimeter scale is a central technique in structural analysis. In many tectonites, light or scanning-electron (SEM) microscopy at the thin-section scale produces useful results. Examples include many types of cleavage and certain fault fabrics. For these rocks, the size of a meaningful fabric sample is small compared with the size of the rock volume available within a single thin section. Although the size of an individual element of a structural fabric (e.g., one gouge particle, one microfracture) is typically smaller than the rock available within a single thin section, quantitative studies of fabrics sometimes requires measurement having at least one dimension (length or width) larger than an individual thin section. In these cases, and where time-consuming measurements at high resolution over large areas are required for meaningful analysis, machine-assisted workflows are increasingly used. An example is documentation of crystallographic preferred orientation patterns (van Daalen et al., 1999). We define microfracture as a fracture that can only be detected with magnification (Laubach, 1997).

Microfractures are a widespread but underutilized structural fabric. They can be used as paleostress indicators (Laubach, 1989; Lespinasse, 1999), strain gauges, and markers of deformation timing (Laubach, 2003). In sedimentary rocks, description of microfracture populations that have been fossilized by authigenic cements is another type

of analysis that involves time-consuming, high-magnification measurement (Laubach, 1997; Marrett et al., 1999; Ortega and Marrett, 2000). For example, in many sandstones quartz-sealed microfractures are visible using SEM-based cathodoluminescence (SEM-CL, Figure 5.1b) but are invisible under petrographic microscopy (Milliken and Laubach, 2000; Laubach et al., 2004).

Owing to the configuration of most SEM-CL detectors (Kearsley and Wright, 1988), an individual image at the requisite magnification is a minute fraction of the area of a typical thin section (e.g., about 0.3 mm^2, or 0.01 percent of the typical amount of rock in a 50- × 75-mm thin section at a magnification of 200×). Yet for fracture patterns and population statistics to be adequately documented, image areas of cm2 are commonly required (Gomez et al., 2003a). Clearly a machine-assisted workflow is needed for effective collection and processing of this type of structural fabric data over more than one thin section.

Here we illustrate a method of rapid digital quantification of microfracture populations consisting mostly of sample-preparation methods, software, and mapping procedures we developed but also involving adaptations of commercially available hardware and software. The workflow includes a new method of producing sequential thin sections along continuous rock traverses without gaps (missing rock) and that are suitable for use in SEM's.

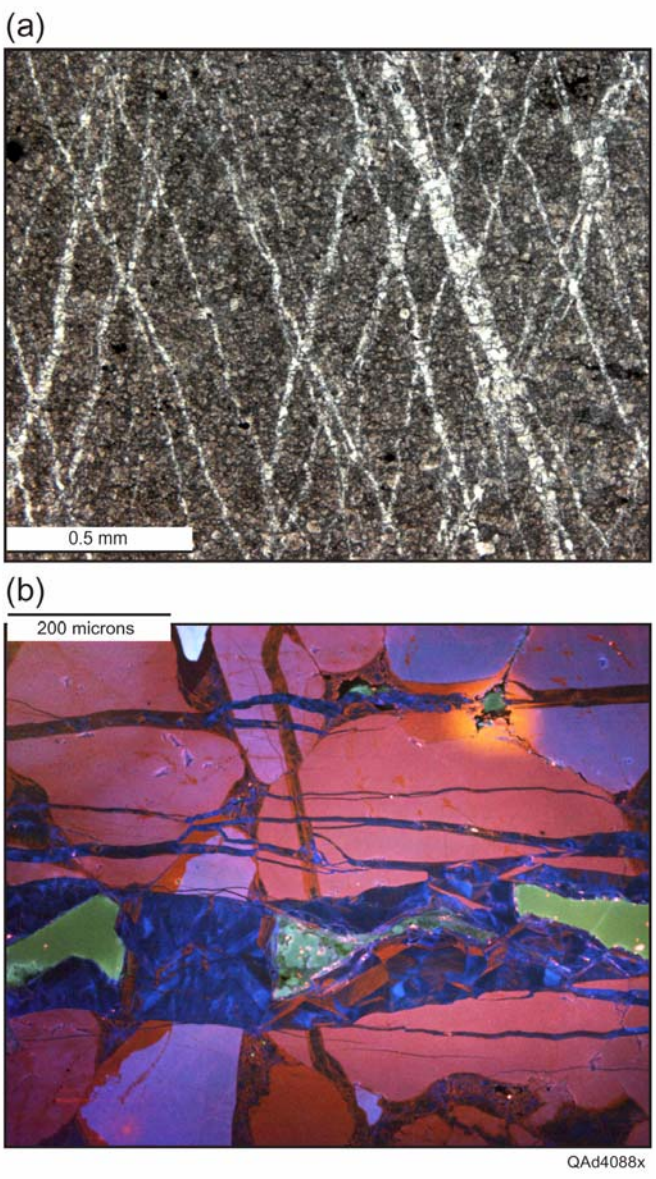

Figure 5.1 Photomicrographs and SEM-CL images of microfractures. (a) Transmitted-light image of microfractures in Cretaceous Cupido dolostone, Mexico. Fractures are lined with dolomite and filled with calcite and show mutually crosscutting relations. (b) Two sets of quartz-sealed microfractures, Cambrian Eriboll Formation sandstone, Dundonnell Bridge, Scotland. Early fractures (red quartz) are crosscut by later fractures (blue quartz). SEM-CL synthetic color from superposing multiple panchromatic CL images captured using red, green, and blue filters (image, R. Reed). In transmitted light, some microfractures are visible as fluid-inclusion planes.

We take advantage of existing automation software for SEM's to create CL mosaics that are as long as the available sample. To map and measure fractures efficiently on images, we combine commercial digitizing software for mapping fractures and spreadsheet-based software that we created for data reduction and analysis.

The method presented herein comprises four main steps. First, a thin section or polished slab is generated. If a continuous area larger than that of an individual thin section is desired, a suite of consecutive thin sections is prepared using a procedure described later. Second, images are acquired using software that drives an SEM stage. However, other types of imagery, including images collected using transmitted-light microscopes, can also be used. Third, we digitize microfractures using commercial digitizing software and export fracture coordinates to a spreadsheet. Fourth, our spreadsheet-based software quantifies and displays attributes of all or part of the fracture population. In this paper we describe each step, then illustrate its application to microfracture arrays in dolostone from NE Mexico (petrographic imagery) and in sandstone from NW Scotland (SEM-CL imagery). Our method makes microfracture analysis more accessible and effective. We show that key aspects of microfracture population attributes are only fully manifest at scales larger than a single thin section. Together with the scaling methods of Marrett et al. (1999), our results can be used for quantitative extrapolation of fracture attributes from fractures on a thin-section scale (microfractures) to larger scales (macrofractures).

5.2 SAMPLE PREPARATION AND MOSAIC ACQUISITION

The first step in microfracture analysis is preparation of suitable samples and subsequent thin sections. Because we are measuring fractures that are mostly filled with cement, no special handling designed to preserve or measure open fractures is needed (Kranz, 1983). The second step is to image the rock. For many applications, it involves

collecting images at high magnification then stitching the images together into a mosaic. Although this is the rate-limiting step for the entire process, automated image collection can greatly reduce researcher's time.

For one-dimensional (1-D) inventories of fracture populations, we measure fracture attributes along a line (commonly known as scanline) normal to dominant fracture strike (Marrett, 1996). To accomplish such 1-D analysis, we acquire a strip of contiguous images and generate a long and narrow image mosaic. For two-dimensional (2-D) analysis and quantification of fracture length, an equidimensional mosaic is needed. Long, narrow image mosaics require less effort to create, but they are biased toward sampling fractures at a high angle to the scanline and commonly have censoring of fracture lengths. Nevertheless, if they are long enough to capture a representative population of fracture sizes, 1-D scanlines in thin sections can provide useful information on fracture strain, aperture scaling, orientation, and spacing (Marrett et al., 1999; Gomez, 2004). The examples we present later are based on 1-D scanline analysis.

5.2.1 Consecutive thin sections

A special problem of 1-D analysis occurs when the desired scanline length is much longer than that of a single thin section. To properly study all microfractures in a sample larger than one thin section requires more than just several adjacent thin sections. It demands consecutive thin sections prepared in such a way that there is no sample gap between them.

There are at least three reasons why such large continuous samples are needed. First, in many rocks, the number of transgranular microfractures detected in a scanline across an individual thin section may not be large enough to generate a reliable cumulative frequency distribution of any fracture attribute (Gomez et al., 2003a). For example, half of the samples of Gross and Engelder (1995) did not have enough

microfractures to quantify the relative abundances of large and small fractures, expressed as the exponent of the power-law distribution of fracture apertures.

Second, gaps made during preparation of consecutive thin-sections can have systematic locations and vary widely in size. Gaps that are not randomly located can have effects on the statistics of the fracture population that are difficult to estimate or predict. Cumulative frequency distributions of fracture attributes such as aperture or spacing should be generated, with data measured along a continuous scanline or inside a continuous area (Marrett et al., 1999; Ortega and Marrett, 2000; Gillespie et al., 2001). Gaps can introduce errors into analysis of fracture spatial arrangement, particularly where fractures are clustered. For example, not knowing the exact size of the sample gap will introduce an inaccuracy in the scanline length; if fractures were present in that gap, their absence would also have an unpredictable impact on the fracture population.

And third, some fracture clusters are wider than the dimension of a single thin section. Therefore, only by accurately measuring the spacing between microfractures along groups of consecutive thin sections without sample gaps between them it would be possible to quantify the spatial arrangement of microfractures inside the cluster (Gomez, 2004).

Consequently, we developed a method outlined in Figures 5.2 and 5.3 that allows the generation of consecutive thin sections of conventional size (currently as many as seven 50- × 75 mm) while eliminating loss of sample between sections caused by sawing during sectioning. To generate consecutive thin sections the first step is to obtain suitable rock samples that lack any breaks or discontinuities.

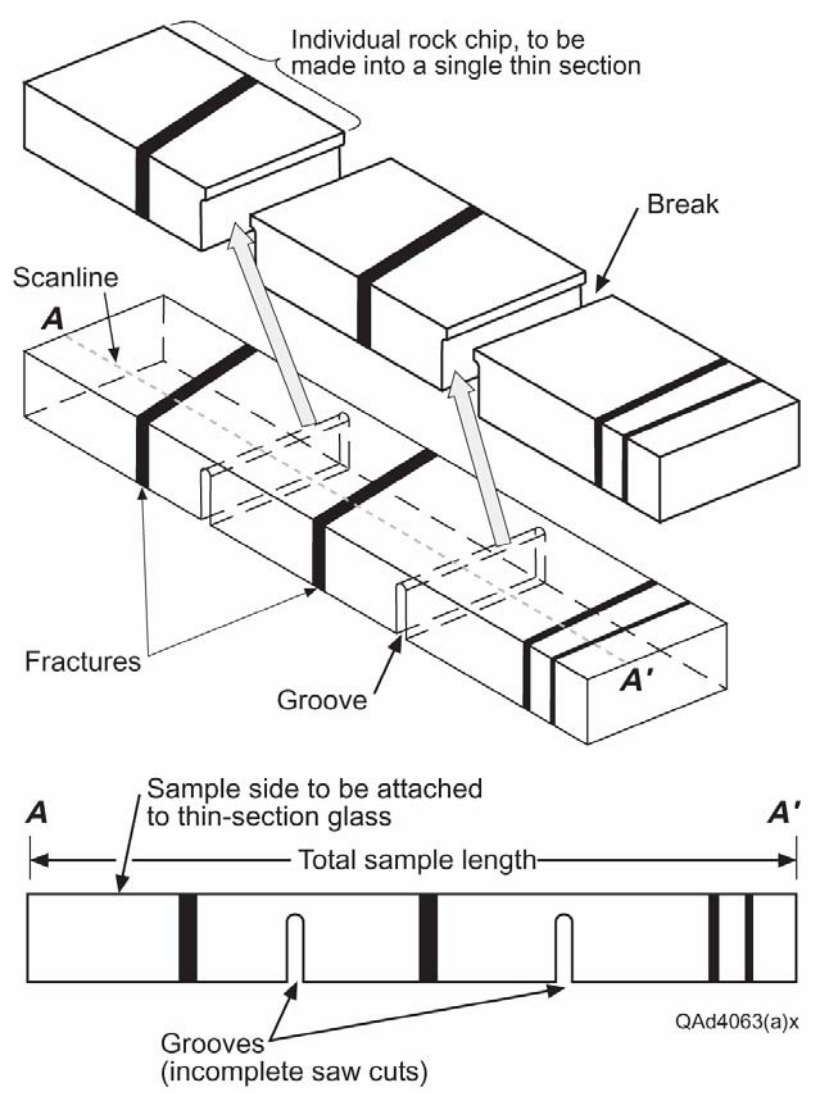

Figure 5.2 Procedure for preparing consecutive thin sections having no sample gap between them. Long side of rock slab is perpendicular to fractures (black lines). Middle (block diagram) and lower (cross section) sketches show grooves (incomplete saw cuts, dashed lines) that stop short of crossing the slab. Upper sketch shows sample broken at grooves. Conventional thin-section preparation involves use of a trim saw (approximate kerf 1 mm) to cut slab into thin chips. All of these cuts remove material from between adjacent sections. Our technique preserves this material.

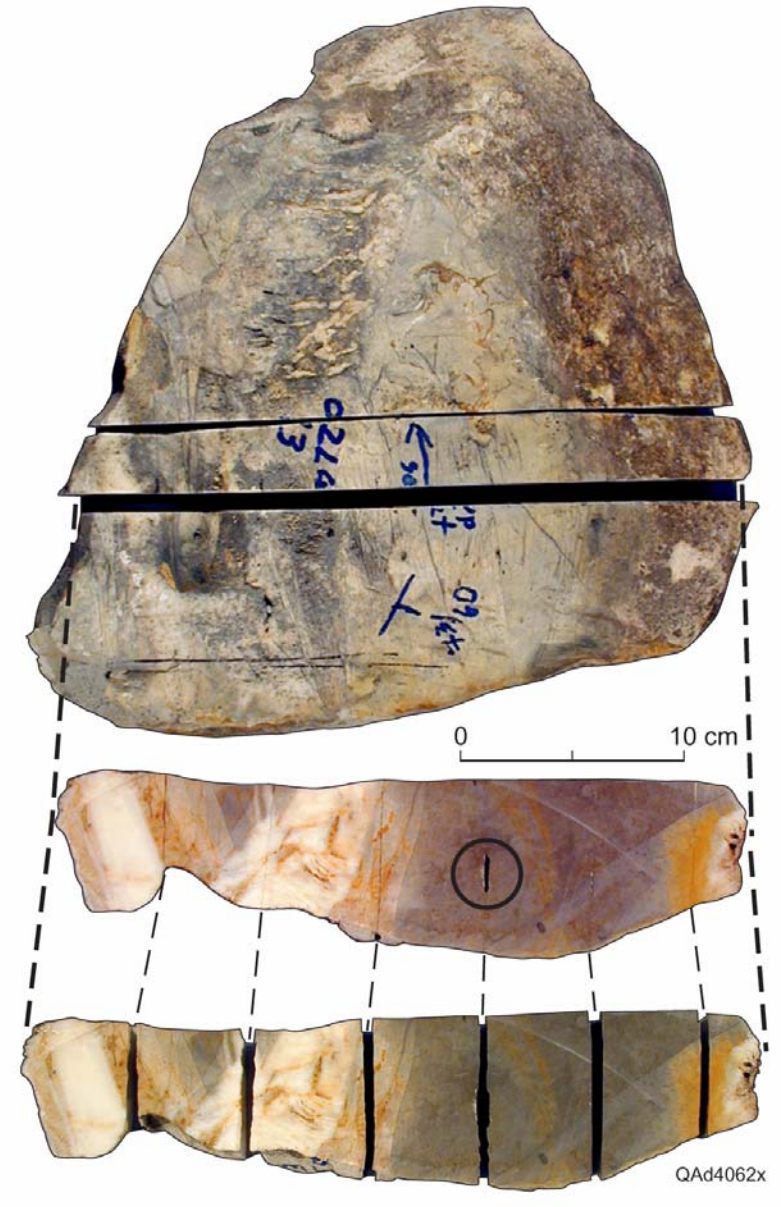

Figure 5.3 Progression from intact sample to consecutive thin sections, Cupido dolostone. Top image shows excision of slab sample. Notice gaps caused by slab saw. Middle image shows rock slab on continuous sample face broken into seven contiguous chips. Incomplete saw cuts (dashed lines) are on opposite side of sample. Note rock continuity except area marked by circle that shows where a saw cut penetrated the continuous face, illustrating how much rock is lost owing to saw cuts. Lower image shows sample separated along incomplete saw cuts. If the rock sample is oriented, it is important to record the orientation of the rock slab and each thin section with respect to geographic north.

The next step is to define the plane where the consecutive thin sections are going to be located and to cut the rock sample into a relatively thin (typically as much as 30 mm thick) slab parallel to that plane. Generally it is possible to define a plane that is approximately perpendicular in 3D to most of the fractures belonging to the set under scrutiny (Figure 2).

We preserve rock continuity between adjacent thin sections by modifying how the rock slab is separated into thin-section-size chips. This modification is accomplished by preventing the trim saw from cutting entirely across the slab (Figures 5.2, and 5.3). By stopping the cut in the back of the sample (the side opposite to where the thin sections will be placed) a few millimeters before it crosses the slab, the sample can be broken using gentle pressure. The resulting rupture mostly preserves continuous rock, and continuity can be achieved with a little practice. Our newly developed method complements previous sample preparation methods (i.e., Chapter 10, Passchier and Trouw, 1998). Although in our experience, rock samples larger than one thin section have a better chance of properly quantifying a fracture population, in many instances there will not be sufficient sample, time, or resources to obtain a suite of consecutive thin sections. With the exception of how to prepare a suite of consecutive thin sections, all other methods presented herein are suitable for individual thin sections.

5.2.2 Transmitted-light imaging

In some rocks, cement-filled microfractures are readily visible using transmitted-light microscopy (Figure 1a). The method we present can be applied to mosaic images generated using petrographic microscopes and a digital camera. We use a graduated mechanical stage to make controlling the position of the thin section easier, facilitating alignment and proper overlap of individual images for image stitching. Having a digital or paper copy of an entire individual thin-section image helps register features on

adjacent thin sections. The area of individual images typically varies between 5.5 (30×) and 0.3 (125×) mm^2, the equivalent of 0.24 to 0.01 percent of the rock available in a typical 50- × 75-mm thin section. Image collection using petrographic microscopes could be automated, but at typical magnifications used for microfracture quantification (30 to 125×), the number of images per thin section is small enough (around 30 images at 50× along 45 mm of sample) that the manual approach is practical. Such is not the case for most scanned-CL image mosaics, where as a result of the restricted field of view, at 200×, approximately 85 images would be required to cover the same length. Because rock usually does not extend to the edges of a thin section, those 45 mm could correspond to the scanline length along the short side of a typical 50- × 75-mm thin section.

5.2.3 SEM-based cathodoluminescence (SEM-CL)

SEM-CL imaging of microfractures is a useful structural technique because it delineates fracture shapes, sizes, and crosscutting relations that otherwise would be difficult or impossible to discern (Figure 1b). Yet at 150 to 300×, where many fractures are visible, SEM-CL detectors image only small sample areas (0.5 to 0.1 mm^2—the equivalent of 0.02 to 0.003 percent of the rock available in a typical 50- × 75-mm thin section). This is a small area relative to fracture-population patterns, and the effort required to image a representative area of the sample at these magnifications impedes use of microfractures. Image collection and stage-control-automation software for SEM's helps remove this impediment.

Electron-beam-excited photons detected and used for CL microscopy reflect subtle chemical and structural differences (Pagel et al., 2000, and references therein). In quartz, for example, luminescence variations result from differences in trace-element composition and mineral structure. SEM-CL imaging allows detection of quartz-lined microfractures that are not readily visible using transmitted light or cold-cathode CL

microscopy (Milliken and Laubach, 2000). Owing to the stable observing conditions, high magnifications, and sensitive light detection that characterize this detection method (Kearsley and Wright, 1988), SEM-CL permits rapid collection of images having higher resolution than those of conventional light-microscope-based CL systems.

Images in this study were acquired using an Oxford Instruments MonoCL2 system attached to a Philips XL30 SEM operating at 15 or 20 kV. Detectors and processing record CL emissions in the range of ultraviolet through visible into near infrared (185 to 850 nm) and convert them to gray-scale intensity values (Figures 5.1b and 5.4). Apart from moving between image locations manual acquisition of a single SEM secondary electron image (SEI) takes about 2 minutes, whereas a single CL image takes between 3 (typical sandstone) and 6 minutes (typical carbonate rock). A mosaic of SEM images collected manually forces the operator to wait until one image is acquired, save that image, move the stage to its new position, and start collection of the contiguous image. It is a cumbersome process that makes poor use of the operator's time. The solution is automation of stage movement and image collection.

The SEM mosaics used in this study were collected using Oxford Instruments' Autostage software (part of its ISIS analytical and imaging system). We also collect image mosaics using Scandium® stage control and image collection, an SEM-specific version of analySIS software from Soft Imaging Systems Inc. This software guides both SEM stage and imaging system so that we can acquire consecutive digital images along a predetermined line (or other prescribed area) without subsequent operator input. The SEM user controls start point, end point, and distance between images. Sample geology and study objectives govern the optimal images area size and shape. For example, in coarse sandstone we collect larger mosaics to encompass the larger grain size.

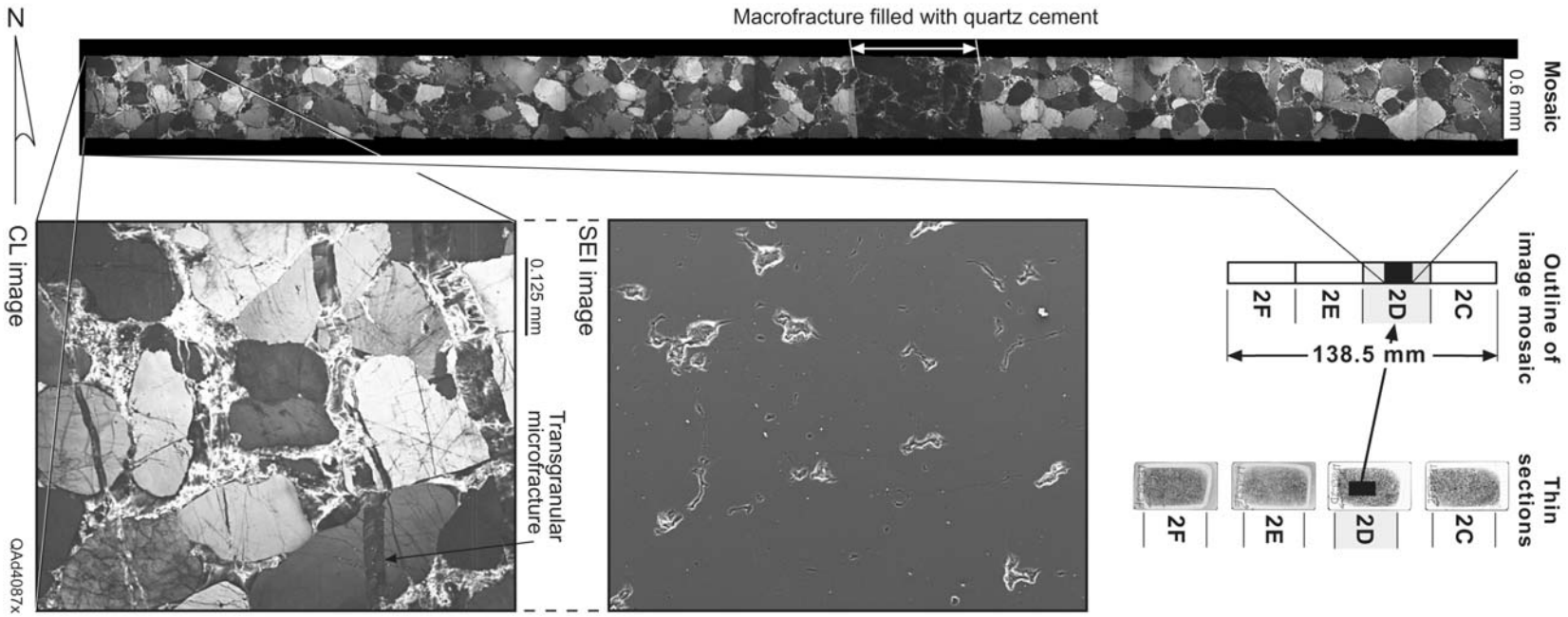

Figure 5.4 Part of SEM-based CL mosaic from consecutive thin section suite of sandstone. Plane of section is parallel to bedding. Length of image mosaic shown covers about two-thirds of a 25- × 46-mm thin section. Entire CL mosaic is 138.5 mm long and was imaged at 150×. Expanded view shows an individual CL image and matching SEI image. Note transgranular, north-northwest-striking fractures. Inset shows area of image (box) compared with the area of four thin sections without gaps between them. Sample is Cambrian Eriboll Formation sandstone, near Lochan Fada, Wester Ross, Scotland (National grid reference: NH045704).

At a magnification of 200×, a distance between image centers of 530 microns allows for about 10 percent image overlap, which is needed to effectively stitch contiguous images in mosaics. Typically at least 10 to 15 images can be acquired in a single automatic run before focus is lost owing, mainly, to nonplanarity of imaged surface. At 200×, a scanline across the rock in a typical 50-mm-wide thin section (about 45 mm) would need 85 pairs of SEI and CL images, which would require about 10 hours of SEM time but only about 2 hours of SEM-operator time.

Without automation, generation of image mosaics larger than one thin section is prohibitive. It took about 32 hours of SEM time but only 8 hours of the operator's time to acquire SEI and CL images on the long dimension of four 25- × 46-mm thin sections (138.5 mm) of a quartz-cemented sandstone using SEM automation software. In contrast, manual acquisition of the same number of images would have taken at least the same number of hours of SEM time and effectively the same amount of SEM-operator time. Automation makes acquiring mosaic images that extend beyond a single thin section practical.

5.2.4 Mosaic stitching

Once individual images are collected from either a petrographic microscope or a SEM (Figure 1) and adjusted to enhance structural features, they must be stitched into mosaics (Figure 4), which can be done manually using image-editing software, such as Photoshop®, or image-stitching software, such as Panavue®. Because the electron beam causes changes in luminescence as CL images are acquired, auto-stitching programs may not match adjacent CL images accurately because of beam-induced luminescence differences in the image overlap zone. These luminescence variations may need to be adjusted manually. Some image-acquisition programs will also stitch images automatically, which is the procedure we currently use with Scandium® stage control

and image collection. To facilitate manual stitching or to verify the accuracy of image mosaics stitched automatically, we recommend that each thin section be scanned in a single digital file. We co-register SEI and CL images in layered image files in order to better identify the location of pores on CL images (Figure 5.4). This co-registration necessitates doubling the number of images collected per mosaic. Color imaging using filters increases threefold the number of CL images required. Although two orthogonal scale bars will facilitate the calibration of each image mosaic, one scale bar will suffice.

On the SEM, we used automated image collection systems to create mosaics at 150 to 300× that have areas of as much as 89 mm^2 (0.64- × 138.5-mm). Our largest mosaic of scanned CL contains 191 images, but it documents only 2 percent of the rock available. On the petrographic microscope, we manually acquired long and narrow image mosaics (1-D analysis) at magnifications of 50× that have areas of as much as 388 mm^2 (1.4- × 277-mm). Our largest mosaic from transmitted-light microscopy contains 194 images, and it also documents only 2 percent of the rock available. These two long mosaics were derived from sequential thin sections prepared from consecutive thin-section suites having no gaps (Figures 5.2 and 5.3).

5.3 FRACTURE-MAPPING PROCEDURE AND QUANTIFICATION

The next steps in microfracture analysis are to map and quantify the microfracture attributes. Procedures for microfracture mapping must be capable of efficiently recording numerous microfracture attributes for thousands of fractures at micron resolution. For patterns having multiple fracture sets or other variability, the procedure should also be capable of easily separating digitized fractures into subsets on the basis of fracture type (Laubach, 1997) and other criteria such as orientation (Gomez et al., 2003a). For our goal of scaling analysis (i.e., Marrett et al., 1999; Ortega and Marrett, 2000), we also need to look at both scanline (1-D) and area (2-D) samples. Currently, automated fracture picking

from SEM-CL images is not feasible owing to the complexity of gray-scale textures of pores, grains and cements versus those from fractures. Finally, we sought digitizing and spreadsheet software that is readily available, Quantifying and plotting fracture attributes in familiar spreadsheet software means that adding new types of analysis or displays is straightforward.

5.3.1 Fracture mapping

Although any graphic software that allows image scale calibration and coordinate export would be adequate to map fractures, we selected Didger® 3 because it allows us to assign an ID to each drawn object. This ID can be used later to separate fractures into subsets having the same classification (e.g., transgranular or intragranular; Gomez et al., 2003a). If the digitizing software does not have this capability, each fracture type can be mapped independently (each one in a different file), but doing so makes the process slower.

The following is our procedure for mapping fractures present on an image mosaic:

(i) Import image mosaic into the digitizing software.

(ii) Calibrate the image mosaic. Calibration commonly involves locating a coordinate origin and assigning a length scale (e.g., pixels per millimeter) in both X and Y directions using a line of known length as a guide.

(iii) Draw the scanline (1-D analysis) or the area (2-D analysis) of the image mosaic where fractures are going to be mapped.

(iv) Digitize each fracture with a closed polygon composed of four anchor points. The first and third points should always represent the fracture tips. The second and fourth points must represent the aperture (Figure 5.5). If wanted, assign an ID (fracture type) to each fracture. If a fracture extents beyond the width of the image mosaic, the fracture tip would be represented by the intersection of the fracture with the

image boundaries (Figure 5.5) and the length of that particular fracture would be censored.

(v) Export coordinates of the four points of all fractures (leftmost fracture on Figure 5.6) in a format that can be easily read by spreadsheet software, say Excel®.

Although there are some commercial digitizing programs that, once calibrated, can quantify length or angles of drawn objects, we prefer to calculate fracture attributes in a spreadsheet instead of within the digitizing program to keep control of how those attributes are calculated and displayed. It also gives us the ability to compile and display attributes of fracture subsets and to generate many kinds of diagrams, including cumulative frequency diagrams of fracture attributes like aperture or length. Spreadsheets also allow calculation of distances between digitized objects, in this case fracture spacing (Gomez, 2004).

For 1-D quantification of fracture attributes, the aperture of a fracture is the distance between the two walls along the scanline (Marrett et al., 1999). In a 2-D study, the aperture is the distance between fracture walls measured at its largest value. In our method, there are four possible ways that a fracture can be digitized with four points (Figure 5.6); any of them would be adequate, as long as points 1 and 3 are located on the fracture tips, and points 2 and 4 are used to measure fracture aperture.

When all fractures are mapped, their IDs and the coordinates of the points that define them can be exported in a format that can be read by spreadsheet software (we used Excel®). Didger® 3 can export coordinates in a file format called Atlas Boundary format (BNA).

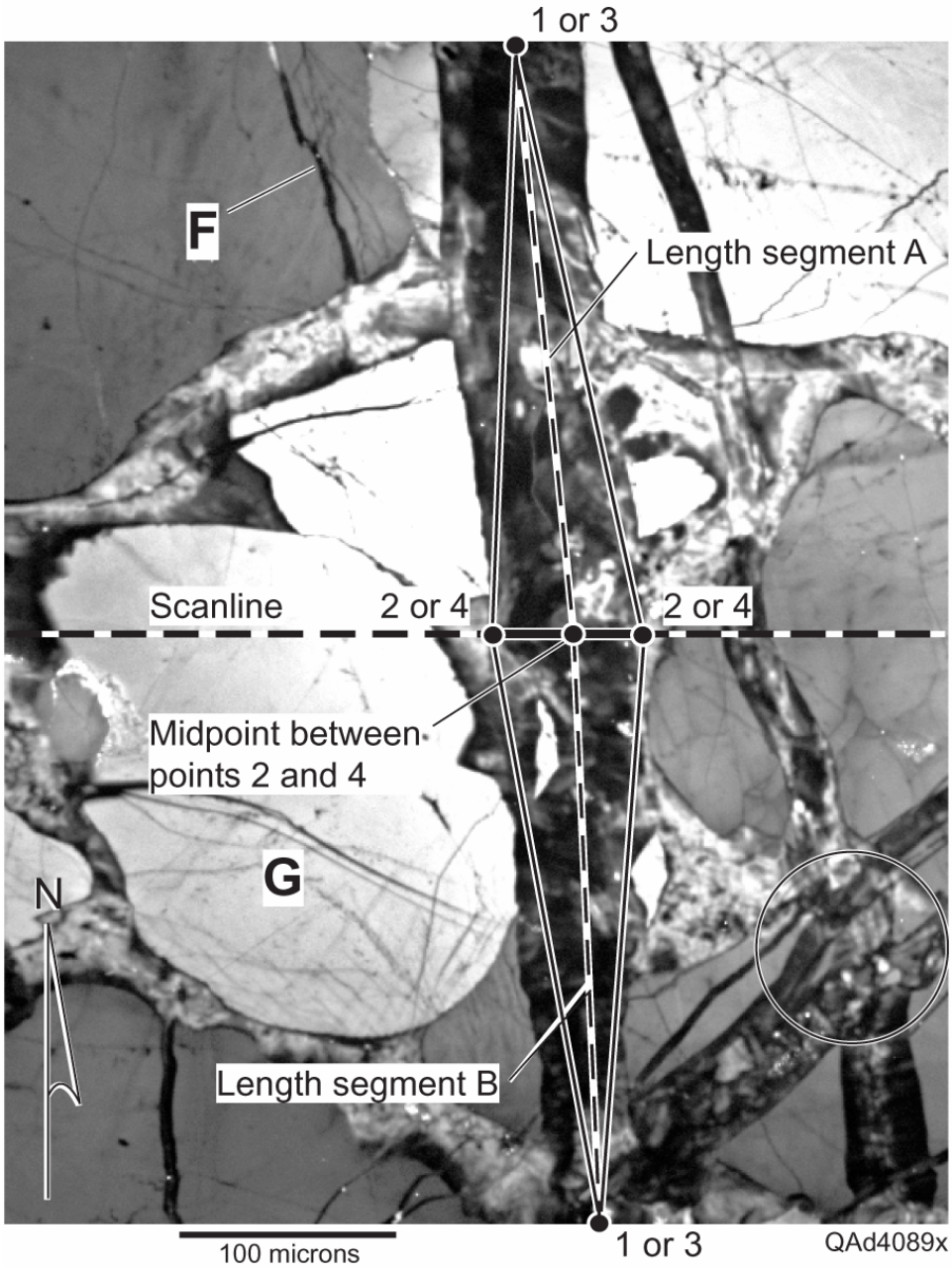

Figure 5.5 Fracture mapping convention. Diagram shows fracture aperture measured along scanline (dashed line). Background is bedding-parallel CL image, Cambrian Eriboll Formation sandstone. Note that in this example, fracture length is severely censored owing to fracture tips extending outside image area. G, grain; F, quartz-filled fractures. Circle shows north-striking fracture crosscut by two northeast-striking fractures.

Atlas Boundary files are ASCII format files that contain the coordinates of polygons, points or lines and their corresponding IDs. Although we selected a specific file format for transferring coordinates and ID's of fracture objects to a spreadsheet, any format is adequate, provided that the exported data is transformed into a BNA-equivalent format before is imported into the spreadsheet.

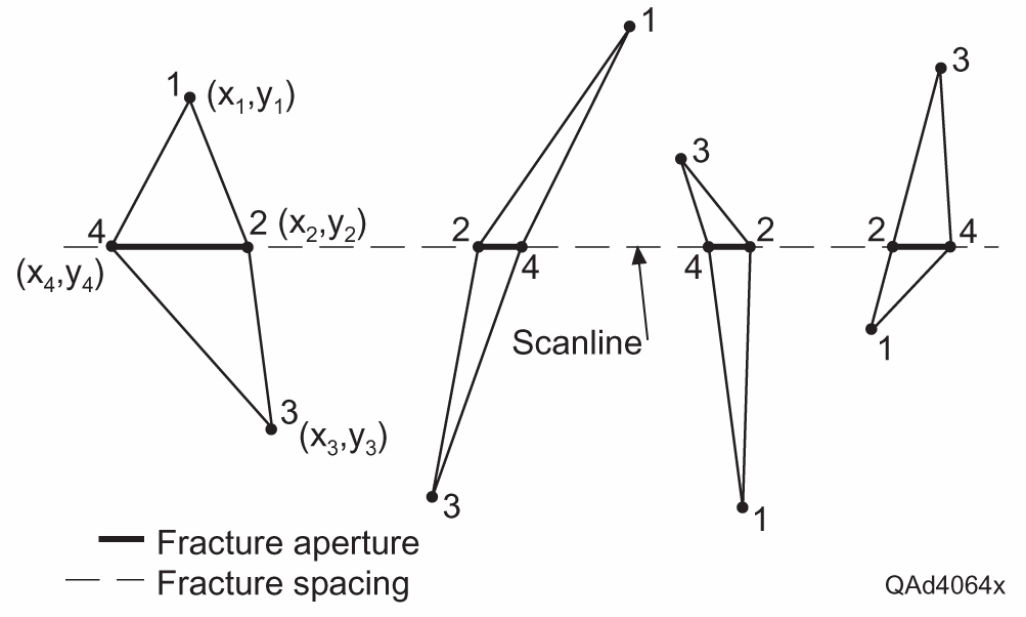

Figure 5.6 Fracture aperture and spacing measured along a scanline and mapping protocol showing four possible ways a fracture can be digitized with four points. In our method, any of them would be adequate, as long as points 2 and 4 are located along the scanline (used to measure aperture) and points 1 and 3 represent the fracture tips. With our software, if the four points that define a fracture are digitized in the wrong order, all values of fracture properties will be wrong.

5.3.2 Quantification of fracture attributes

Although fracture quantification was greatly facilitated by in-house software written in C++ (Ortega, 2002), this program was linked to commercial software that became obsolete. The new GoMezure™ template, on the other hand, uses a common platform. One advantage of using spreadsheet software instead of in-house software

specifically written (using a programming language such as C++) is that in a spreadsheet, equations are visible and variables of those equations are easily traceable by—instead of invisible to—the user.

The GoMezure™ spreadsheet template was designed to quantify fracture length, strike, aperture, and spacing and calculates fracture length-weighted strike and fracture strain. In addition, GoMezure™ can generate displays or calculate descriptive statistics (e.g., arithmetic mean) of fracture attributes for all digitized fractures or for a group of fractures having a common identity. GoMezure™ is organized in worksheets (individual spreadsheet of an Excel® file), with each worksheet designed to quantify and display a particular fracture attribute.

One worksheet is exclusively dedicated to receiving input from digitizing software. Fracture attributes are calculated and compiled, and mapping errors are identified and flagged. We programmed GoMezure™ cells where tests are performed to change color and to write a descriptive message briefly explaining why a test failed. The data-quality tests performed in GoMezure™ include checking that all fractures are digitized using only four points (Figure 5.5), verifying that four points that represent each fracture are digitized in the proper order (Figure 5.6) by comparing fracture length and fracture aperture (typically, transgranular fracture length is much greater than fracture aperture), and verifying that the scanline length or area of study is entered. One of these two last values must be present if cumulative frequency distributions are to be generated.

The advantage of representing fractures as four-point polygons is that fracture attributes can be reduced to distances between points (e.g., length, aperture) and angles (strike). These distances or angles can easily be calculated using trigonometric calculations. For instance, using the Pythagorean Theorem, fracture aperture can be calculated as follows (leftmost fracture, Figure 5.6):

$$\text{Fracture Aperture} = \sqrt{(X_2 - X_4)^2 + (Y_2 - Y_4)^2} \quad (1)$$

Although 1-D scanlines are biased against oblique fractures, if azimuth of an individual fracture is not perpendicular to the azimuth of the 1-D scanline, the aperture measured is an apparent aperture. True apertures could be recovered using a trigonometric correction (Terzaghi, 1965) incorporated in GoMezure™.

Ortega (2002) calculated fracture length as half the perimeter of the digitized four-point polygon. However, this calculation is reliable only when the aperture of a fracture is several times smaller than its length, which may not be the case for 1-D analysis because narrow mosaics censor fracture lengths close to and larger than the width of the image mosaic. Alternatively, we calculate fracture length as the distance between point 1 and the midpoint between points 2 and 4 (segment A of Figure 5.5), plus distance between point 3 and the midpoint between points 2 and 4 (segment B of Figure 5.5).

The strike of an individual fracture can be calculated as the azimuth of a line joining points at the tips of a fracture (Ortega, 2002). To preserve more information and to account for curved fractures, we calculate instead the azimuth of an individual fracture as a length-weighted azimuth of segments A and B (Figure 5.5). Because geographic north could be located in any direction, the strike of an individual fracture is calculated with respect to a hypothetical north located toward positive values along the Y axis. If the orientation of the thin section is known, it will possible to calculate the true strike of all digitized fractures.

Rose diagrams of strike of the entire fracture population or a subset are calculated using circular statistics. The visual quality of rose diagrams from our spreadsheet software is satisfactory for on-screen analysis. If a more appealing rose diagram or any other kind of fracture orientation diagram is needed, all the values of fracture strike can

be extracted easily. Using petrographic or CL images, we need mutually orthogonal thin sections to specify fracture dip in addition to fracture strike.

To avoid imposing limitations on the order in which individual fractures are digitized, the initial step to calculate fracture spacing along a scanline is to sort all fractures in decreasing value of the X coordinate of point 2 (Figures 5.5 and 5.6). The next step is a nested conditional statement for calculating fracture spacing (distance between nearest-neighbor fractures), regardless of which of the four possible ways of digitizing a fracture is used (Figure 5.6).

Cumulative frequency distributions of fracture attributes are commonly used to quantify properties of a fracture network (Marrett et al., 1999; Gillespie et al., 2001; Gale et al., 2004). However, when the number of fractures is great and their classification is intricate (sets organized by strike, aperture, type of crystalline cement, etc.), the analyst is faced with the time-consuming task of creating individual cumulative frequency distributions for each set of fractures. The method presented here automates creation and display of cumulative frequency distributions for as many as four individual fracture sets or up to three combined fracture sets. We analyze cumulative frequency rather than cumulative number because doing so allows comparison of data sets collected at different scales or predictions of fracture attributes across a wide range of scales (Marrett et al., 1999; Ortega and Marrett, 2000).

Most spreadsheets, including Excel®, can group calculations and tasks into scripts, called macros, which can be executed without having to execute the tasks individually. The following are tasks recorded in all macros designed to generate cumulative frequency distributions of fracture attributes:

(i) Copy from the first worksheet (where attributes for each fracture are calculated and compiled) values of the fracture attribute to be studied and respective primary ID for all fractures.

(ii) If the primary ID of a fracture matches criteria entered by the user, then copy the value of the fracture attribute to the next column.

(iii) Sort the output from step ii from largest to smallest. In a contiguous column, starting with a value of one, assign increasing numbers (increments of one) to the fractures. This value is called cumulative number, which indicates how many fractures have an attribute equal to or larger than the corresponding value of fracture attribute.

(iv) From sorted values of fracture attribute, copy values of the fracture attribute that are not duplicates and their corresponding cumulative numbers to the next two columns. For fractures with duplicated fracture attributes only the one with the largest cumulative number should be copied.

(v) In an additional column, divide the consecutive number (for the values of fracture attribute that are not duplicates) by the length of the scanline (1-D analysis) or the area (2-D analysis) of the image where fractures were digitized. The resulting value is the cumulative frequency.

Although retention of duplicate values of fracture attributes would not significantly affect the appearance of a cumulative frequency distribution, it is required for an accurate calculation of the equation of a probability distribution (e.g., negative exponential). To study subsets of the data, we use conditional statements prior to sorting the data (step iii) to select fractures of the same type on the basis of classifications applied during mapping. Fractures can also be segregated by user-defined ranges of strike.

5.4 EXAMPLES: FRACTURES IN NE MEXICO AND NW SCOTLAND

5.4.1 Dolostone – Petrographic images

The Monterrey Salient of the Sierra Madre Oriental of Mexico has large outcrops of the Lower Cretaceous Cupido Formation (Goldhammer, 1999). Excellent exposure, together with abundant fractures, makes the Cupido Formation a good place to test analytical techniques (Marrett et al., 2004; Ortega et al., 2006), and to study the attributes of natural fractures (e.g., spatial arrangement; Gomez, 2004). In the Cupido Formation, fractures are abundant in dolostone layers and may have formed prior to regional folding (Marrett and Laubach, 2001; Ortega 2002). Our test sample is from one of these dolostones. Fractures are filled mainly by crystalline calcite that contrasts with the dolomitic rock mass such that most microfractures are visible using a transmitted-light microscope.

Macroscopically visible fractures and microfractures are present in a large (320 × 350 × 70 mm) sample that covers most of a fracture cluster (Figure 5.3). The sample was cut into seven contiguous thin sections, 50- × 75 mm in size (Figure 5.3). From these samples, a long (194 images) and narrow (1 image) digital mosaic at a magnification of 50× was acquired using a petrographic microscope. The aperture and spacing between 712 fractures were measured on a 277-mm-long scanline crossing the short dimensions of the rectangular thin sections. Although the scanline length on each thin section is about the same size, the heterogeneity in spatial arrangement of fractures causes individual thin sections to have different numbers of microfractures along the scanline (between 51 and 147 fractures).

The cumulative frequency of fracture aperture of one of those seven thin sections extends for about 3 orders of magnitude of aperture and does not display a common power-law distribution with the population of genetically related macrofractures

measured in outcrop (Figure 5.7a). In contrast, cumulative frequency of microfractures measured on the seven contiguous thin sections varies over 4.5 orders of magnitude of fracture aperture—a large range compared with published aperture distributions (Marrett et al., 1999)—and shows a power-law scaling over 2 orders of magnitude (Figure 5.7b). Typically an increase in number of fractures corresponds with an increase in range of fracture property values. In contrast to the microfracture population for a single thin section, the microfracture population from the seven thin sections (entire sample) displays a common power-law distribution with the macrofractures measured in outcrop (Figure 5.7b).

By providing a scanline larger than a single thin section, we obtained a representative population of the microfractures, which allowed us to quantify the size and spacing of microfractures in a way that would not be apparent from a sample of smaller size (Figures 5.7b and 5.8). In addition, only a scanline larger than a single thin section would have allowed us to use the cumulative frequency distribution of microfracture aperture to predict the intensity of genetically related macrofractures (Marrett et al., 1999; Ortega et al., 2006). For instance, a single thin section inside one microfracture cluster (60 to 95 mm, Figure 5.8) would have overestimated the fracture intensity of the entire microfracture population and the clustering of the microfracture population would have remained undetected. Owing to the scale of non-random fracture clustering, quantitative spacing analysis of this microfracture population successfully predicted some characteristics of the spatial arrangement of genetically related macrofractures (Gomez, 2004).

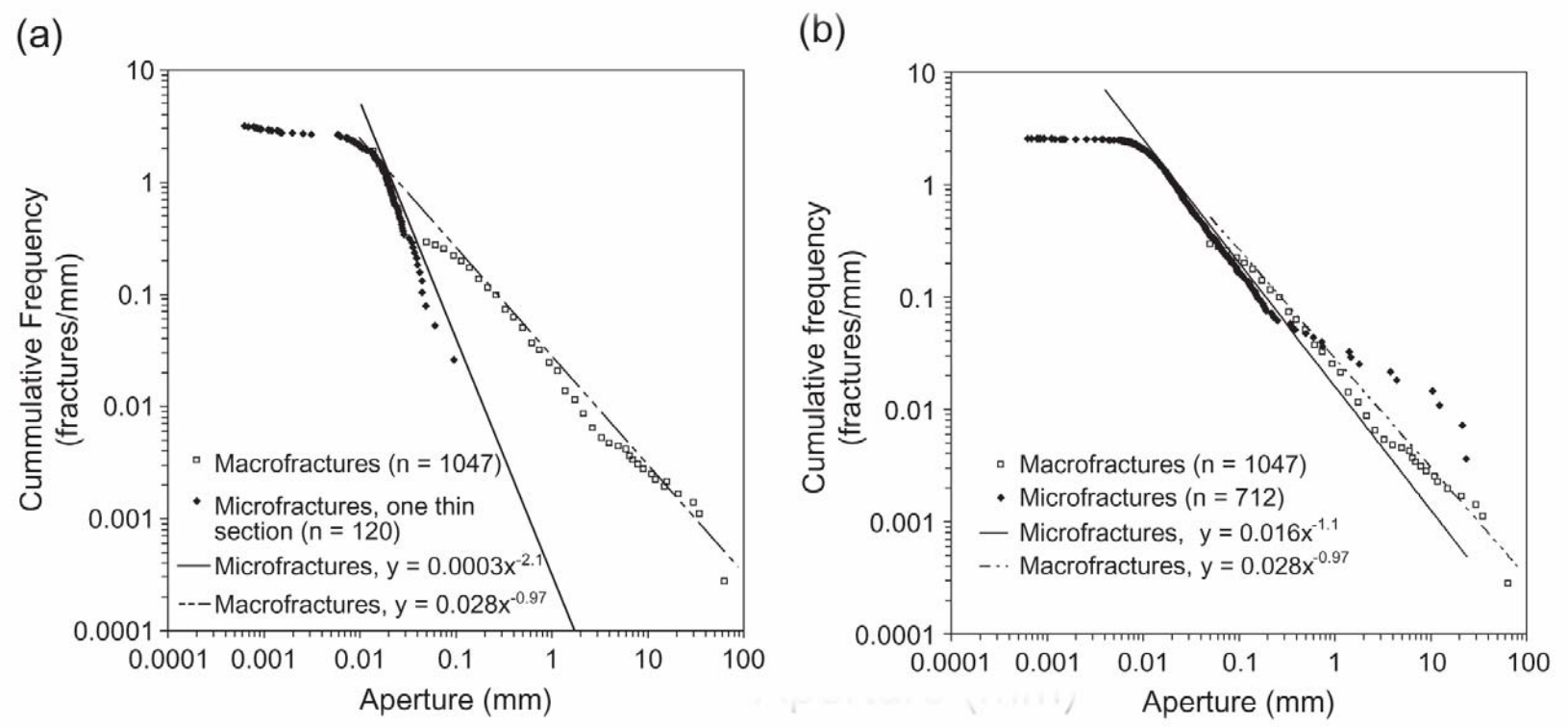

Figure 5.7 Fracture attributes of sample from Cupido dolostone, NE Mexico. (a) Cumulative frequency distribution of fracture aperture for only one of the seven contiguous thin sections. Also shown are macrofractures and a power-law regression to the macrofracture population. Microfractures and macrofractures do not share a similar aperture distribution. (b) Cumulative frequency distribution of fracture aperture for seven consecutive thin sections having no gaps between them. Microfractures display a power-law scaling over 2 orders of magnitude (0.01 to 1 mm). Also shown are macrofractures and separate power-law regressions to micro- and macrofracture populations. Microfractures and macrofractures can be described by similar power-laws. We interpret deviation of apertures below 0.01 mm from power-law to be a truncation artifact.

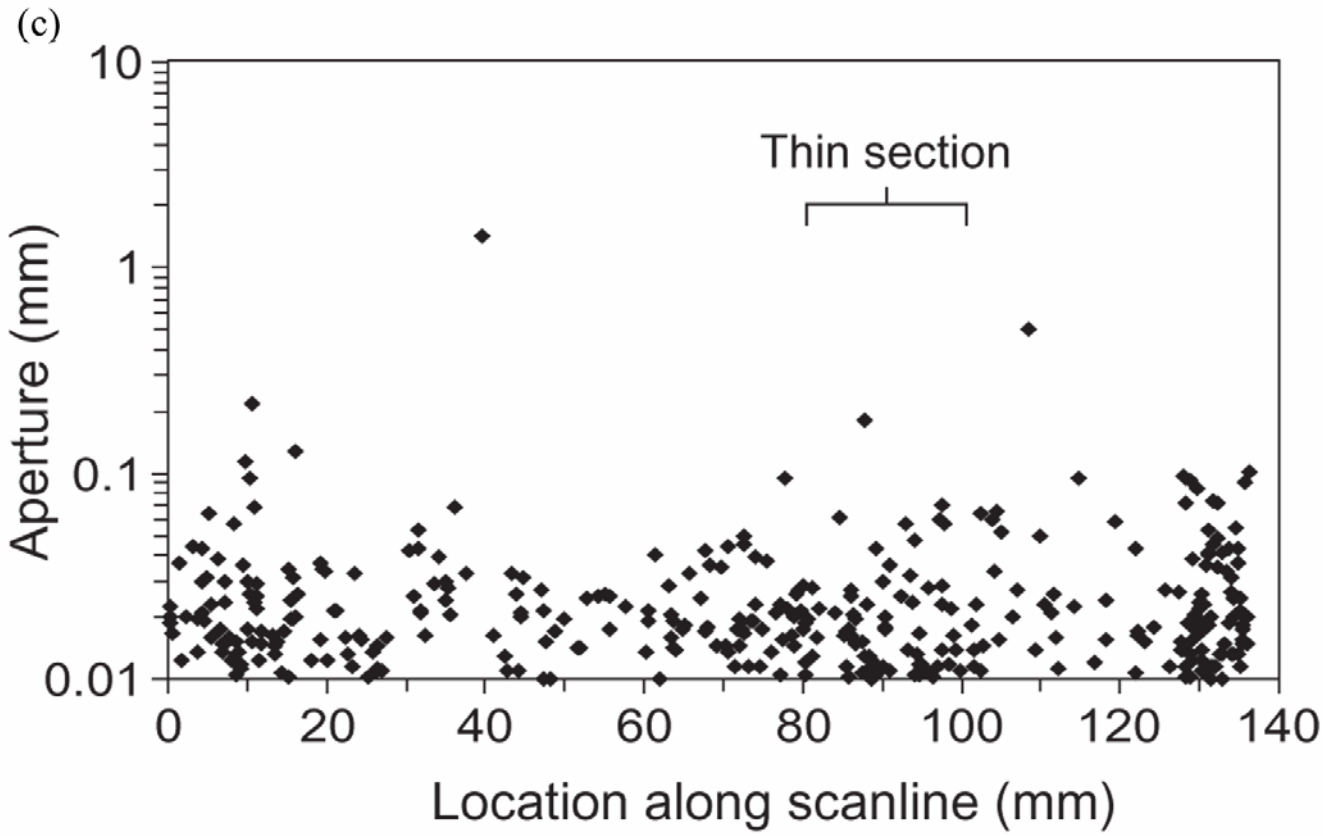

Figure 5.8 Fracture attributes of sample from Cupido dolostone, NE Mexico. Aperture versus location for microfractures along four of the seven contiguous thin sections (scanline of 135 mm). Note the variation in the fracture intensity along the scanline; a noticeable increase in fracture intensity corresponds to a microfracture cluster (5 to 15, 65 to 100 and 128 to 135 mm).

5.4.2 Sandstone – SEM-CL images

As part of an ongoing fracture and diagenesis study (Diaz-Tushman et al., 2005), we have extensively sampled Cambrian Eriboll Sandstone in the footwall of the Moine thrust zone in northwestern Scotland (Strachan et al., 2002). The rock is quartz cemented, it has very low porosity, a grain size of about 100 μm, and contains numerous quartz-filled opening-mode microfractures only partly visible petrographically as fluid-inclusion planes. We selected a 20-cm-long sample from a tilted but otherwise structureless bed for testing our method. We focus on a bed-parallel mosaic and scanline oriented normal to one of the fracture sets in this sample. We used the method previously to collect four 25- × 46-mm thin sections having no gaps between them (Figure 5.2). The scanline followed the long dimension of the thin sections (Figure 5.4). Microfractures are parallel to macrofractures, and both are arranged in two sets having distinct orientations regionally (Figures 5.1b, and 5.5).

The 138.5-mm-long mosaic consists of 191 pairs of registered panchromatic CL and SEI images collected in automated mode (Figure 5.4). The scanline intersected 2,095 microfractures, 325 of which are transgranular (Gomez et al. 2003a) and therefore more reliable guides to the attributes of genetically related macrofractures (Laubach, 1997). Individual thin sections display 346, 413, 660 and 676 microfractures of which 61, 62, 105 and 97 are transgranular respectively.

Microfracture strike has been used to correctly predict the strike of genetically related macrofractures (Laubach, 1997; Ortega and Marrett, 2000). A diagram of microfracture strike for transgranular and intragranular microfractures in one of the four thin sections that compose the entire scanline displays only one preferred orientation (Figure 5.9a).

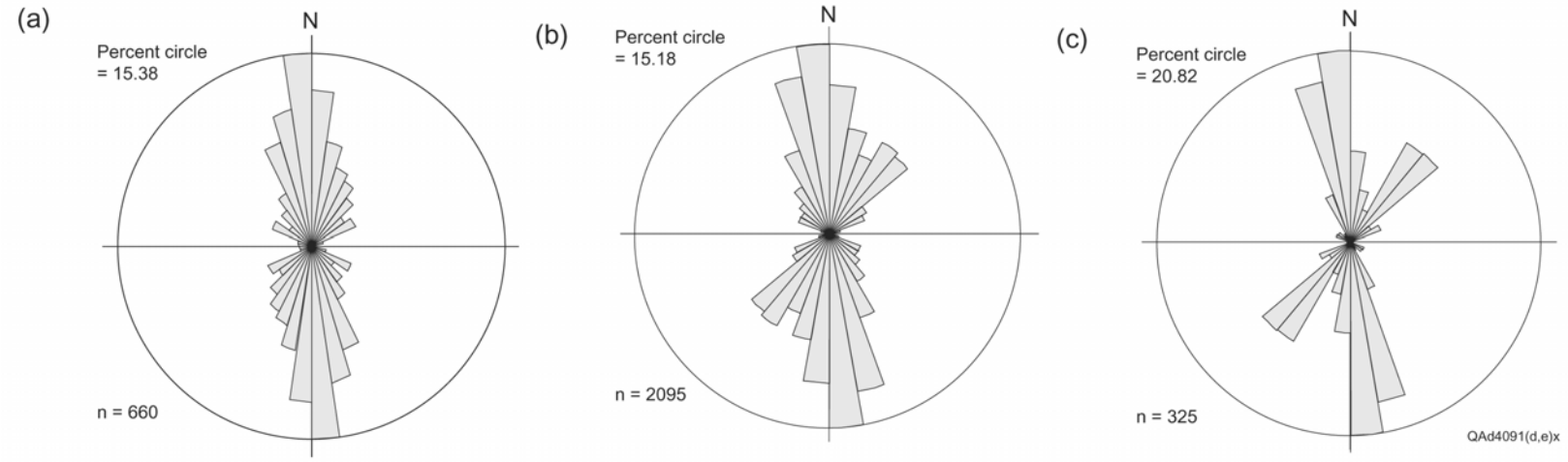

Figure 5.9 Length-weighted, equal-angle rose diagrams of microfracture strike collected along a scanline; quartz-sealed microfractures; Cambrian Eriboll Formation sandstone, Scotland. (a) Transgranular and intragranular fractures, scanned-CL mosaic of 37-mm-long from one thin section. (b) Transgranular and intragranular fractures, scanned-CL mosaic of 138.5-mm-long continuous sample, four thin sections. (c) Transgranular fractures only, scanned-CL mosaic of 138.5-mm-long continuous sample, four thin sections. North and northeast striking preferred orientations of these two sets differ in strike by about 50°. Crosscutting relations indicate that the north-striking set is older.

In contrast, transgranular and intragranular microfractures from all four thin sections have two distinct preferred orientation maxima (Figure 5.9b). Two directions are also present in the subset of only transgranular microfractures for all four thin sections (Figure 5.9c), and this pattern matches that of macroscopic fractures in outcrop.

The scanline we drew along the center of the image mosaic intersected 2,095 microfractures, which ranged in aperture from 0.00031 to 0.98 mm (Figure 5.10). Cumulative apertures along the scanline record strain of 4.9 percent. Microfracture strain measurements using SEM- CL have greater accuracy than would be possible using cold-cathode CL methods because the resolution of SEM-CL reveals more small fractures more clearly and these small fractures represent much of the rock's deformation. CL results are far more accurate than strain estimates from fluid-inclusion size (Onash, 1990), because CL shows that fluid-inclusion diameter is commonly much smaller than aperture and not a good proxy for fracture width.

The large size of the image mosaic and the numerous fractures, together with the flexibility of the spreadsheet software, allows rapid, systematic description of all or part of the fracture population. The shape of the image mosaic results in severe censoring of fracture lengths above 0.65 mm, which is about the width of an individual CL image at 150× (Figure 5.5). We therefore focused on analysis of kinematic apertures of fractures and spatial arrangement of those fractures.

Inspection of the image mosaic shows that there are many more small microfractures than large (Figure 5.4). Cumulative frequency plots of aperture show evidence of power-law scaling, particularly in the transgranular fracture population (Figures 5.10a and 5.10b). The population that includes all microfractures shows two slopes (Figure 5.10b), which may result from mixing of fracture populations, including inherited fractures (Laubach, 1997). Separating transgranular fractures produces a

population that is well fit by a power-law across approximately 2 orders of magnitude, but further subdividing this population by strike gives a result that is geologically more meaningful (Figures 5.10a, and 5.10b). We know from crosscutting relations, after all, that transgranular fractures compose two sets that formed at different times and have different orientations (Figures 5.1b, and 5.5). However, in one of the thin sections there are only eight microfractures with a northeastward strike, not enough fractures to generate a reliable distribution (Figure 5.10a). In contrast, a scanline that spanned four contiguous thin sections detected 48 microfractures with the same northeastward strike, a stronger signal of the true fracture pattern (Figure 5.10b).

Unraveling the intriguing patterns in these plots is beyond the scope of this paper. Mapping and manipulating the measurements of a population of more than 2,000 fractures allows us to explore these patterns efficiently. For instance, the pattern of the combined strike and type population may differ in fracture intensity, as defined by cumulative frequency of aperture (Figure 5.10b), yet the two sets are similar in length to aperture ratio (Figure 5.10c).

Key evidence for fracture attributes, including numbers of fracture sets, strike, crosscutting relations, strain, the volume of cement sequestered in microfractures, and meaningful data on microfracture population statistics are only fully manifest at scales larger than a single thin section. For example, plots of aperture versus distance along scanline show qualitative evidence of fracture clustering (Figure 5.10d). The clustering pattern would not be evident without a scanline that extended beyond a single thin section. This data set also illustrates why the method to generate consecutive thin sections without gaps between them is needed for microfracture-spacing analysis. No data zones (gaps) would corrupt spacing data beyond the first kerf, and with every additional gap the error in fracture spacing data would increase (Figure 5.10d).

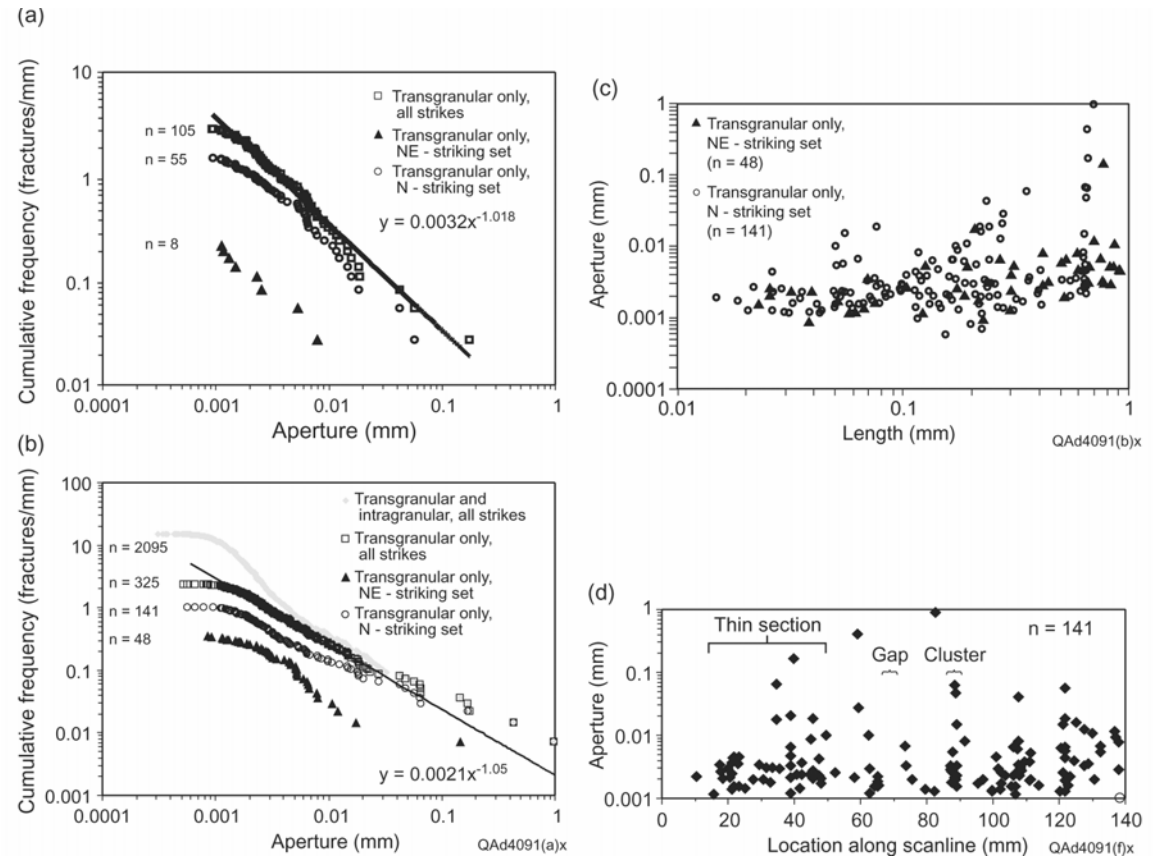

Figure 5.10 Fracture attributes, Eriboll Formation sandstone, NW Scotland sample. (a) Cumulative frequency, fracture aperture from one thin section. Curves show microfracture population for transgranular fractures only subdivided by strike (all strikes, NE-striking, 30° to 50°, and N-striking, 160° to 190°). North-striking set is older, judging by crosscutting relations. Regression is power-law for transgranular microfractures only, all strikes. (b) Cumulative frequency, fracture aperture for four thin sections. Curves show microfracture population subdivided by fracture type (transgranular versus transgranular and intragranular fractures combined) and/or strike (NE-striking, 30° to 50°, and N-striking, 160° to 190°). Transgranular and intragranular fractures of all strikes show two slopes. (c) Aperture versus length, transgranular fractures of N- and NE-striking sets. (d) Aperture versus location of one set of transgranular fractures along scanline; 138.5-mm-long continuous sample; open circle marks end of scanline. Note gaps at 25, 55, 70, 93 and 117 mm and clusters at 20, 40, 65, 108 and 123 mm (two are labeled).

5.5 DISCUSSION

Although an issue in many types of textural and crystallographic studies (e.g., Trimby and Prior, 1999) the advantages of texture studies over wide sample areas are well illustrated by studies of fault rocks, where most published observations are restricted to image areas smaller than a thin section despite fault rocks heterogeneities that extend over larger scales (e.g., Marone and Scholz, 1989; Biegel et al., 1989; Sammis et al., 1987). All these studies of structural fabrics in thin sections were limited by the largest magnification of the tool(s) selected and assuming there was no limit on the size of sample, these studies were also bounded by the size sample that they could image. Some studies are restricted to individual images at different magnifications (Marone and Scholz, 1989) while others used one-dimensional (Biegel et al., 1989) or two-dimensional (Sammis et al., 1987) mosaics but always without exceeding the rock sample available in a single thin section. Because fault fabrics are to some extent penetrative, even individual images provide some information. The same is not true for many fracture populations, where individual fractures are distributed throughout the rock.

Because of the distributed character of microfractures, there is no guarantee that an individual microscopic image or an image mosaic with one dimension as long as an individual thin section will have a large enough population to meaningfully quantify the population attributes. Many rocks have lower overall fracture intensity than samples illustrated in this paper or in Marrett et al. (1999). For example, in a study of microfracture intensity in Cretaceous sandstones Gomez et al. (2003a) found that it was only possible to obtain a meaningful population (87 transgranular microfractures detected in about 110 mm of SEM-CL scanline) that accurately predicted macrofracture intensity in a horizontal core by combining transgranular microfractures detected in image mosaics from five separate thin sections.

The rocks of Gross and Engelder (1995) and Gomez et al. (2003a) have about 90 and 63 percent lower transgranular microfracture intensity, respectively, than the Eriboll Sandstone samples described above (Figure 5.10b). Although intensely fractured, Eriboll Sandstone samples required a scanline larger than an individual thin section to detect the two sets of transgranular fractures having distinct orientation maxima (Figures 5.9b and 5.9c) and microfracture clustering (Figure 5.10d). We expect that the larger microfracture populations that could be obtained from samples larger than an individual thin section would better define the aperture distributions of the rocks studied by Gross and Engelder (1995) and Gomez et al. (2003a).

Although it is possible to increase the number of fracture measurements from a single thin section by using serial parallel scanlines, it is likely that many fractures in the thin section would intersect more than one scanline. Multiple measurements of some fractures produces artifacts that can only be explicitly accounted for by understanding aperture variations with fracture length, which is neither simple nor consistent (Moros, 1999). Of course if multiple orientation sets are present, then additional scanlines may be needed.

Image areas of square centimeters are needed to measure microfracture populations effectively in many slightly deformed rocks. A prohibitively large amount of time—days of imaging time—is required to manually acquire even 1-D image mosaic strips having lengths in centimeters at 150×. Yet for many applications, large rectangular (2-D) mosaics are preferable, for example, because of bias in fracture orientation statistics and censoring of fracture lengths in 1-D image strips. The methods presented here largely overcome these challenges.

A key step in the overall process is automation of image collection and stitching. The procedure we describe uses about 75 percent less SEM-operator time than manual

SEM image collection for the same amount of machine time. We can generate SEM-based mosaics of paired-CL and SEI images at a rate of about 3.5 minutes per millimeter of scanline at 150×. Nevertheless, the CL mosaics we describe cover only about 2 percent of the area we desire to image. Our longest SEM-CL mosaic imaged less than 1 cm2 (<89 mm^2). This area is reasonable for 1-D microfracture analysis, but for 2-D analysis, larger image areas are needed that use a greater percentage of the sample. On the other hand, we have not yet fully exploited the capabilities of commercially available automation software. Further improvements in the rate-limiting step of CL image acquisition will undoubtedly allow us to accomplish 2-D imaging of thin-section scale areas.

New software greatly improves the efficiency of mapping, data reduction, and display of structural fabric data. Together, image automation and these efficiencies in data reduction allow us to use much larger samples, which in turn provide much richer microfracture data sets. Using the new method to create continuous samples larger than one thin section, we were able to document fracture population patterns that would not have been apparent in a smaller sample. The same method can be used successfully, regardless of rock type, on mosaic images from scanned-CL or petrographic microscopes. These improvements over manual methods make systematic documentation and quantification of microfracture fabrics in many rocks practical.

5.6 CONCLUSIONS

Microfractures have been used to estimate the orientation, and spatial arrangement of genetically related macrofractures. Microfractures that follow a power-law distribution of sizes have also been used to estimate the intensity of macrofractures that can control fluid flow but that are commonly challenging to sample in the subsurface. For these types of analyses, large populations of microfractures are vital.

Effective methods of measuring fossilized microfracture systems therefore have utility in structural analysis.

Microfracture populations contain much information that is only fully manifest at scales larger than a single thin section. This makes rapid digital imaging and quantification vital for analysis of such populations. We show that in examples from two different lithologies (dolostone and sandstone) using different type of microscopic images (petrographic and SEM-CL respectively), this approach provides key evidence for numbers of sets, strike, crosscutting relations, strain, the volume of microfracture-sequestered cement, and meaningful data on microfracture population size and spacing patterns that would not be evident otherwise.

Chapter 6: Techniques for the Analysis of the Spatial Arrangement of Fractures

1. INTRODUCTION

This chapter is divided in four parts. The first part explains the difference between the widely known concept of fracture spacing and the concept of the spatial arrangement of fractures. This explanation is required because the following part reviews previously used techniques for analyzing fracture spacing and evaluates their strengths and weaknesses in quantifying the spatial arrangement of fractures (Gomez and Marrett, in review). In the third part of the chapter, the reader is introduced to a new technique called Normalized Correlation Count (NCC). NCC was developed to quantify the spatial arrangement of fractures without the limitations or the biases of previously used techniques (Marrett et al., in review).

The second and third parts of this chapter use the same fracture data set (measured at Pedernales Falls State Park, Texas). This data set is available in Hare (2002) and is an expanded version (30% more fractures) of the data set used in Marrett et al. (1999). Using the same data set should facilitate comparison between the different techniques used to characterize fracture spacing and the spatial arrangement of fractures. The quantitative characteristics of the Pedernales data set will be introduced in this chapter whereas the qualitative characteristics of the fractures at Pedernales Falls State Park were described in Chapter 2. Finally, in the fourth part of the chapter the reader is introduced to the different types of spatial arrangement of fractures, as defined by Marrett et al. (in review), mainly using data sets measured by the author for this dissertation. The NCC analyses presented in the fourth part of this chapter are performed using both logarithmic and linear graduation of length scales (Marrett et al., in review).

The current chapter is based on two peer-reviewed papers on which I am coauthor (Gomez and Marrett, in review; Marrett et al., in review) that were submitted to Journal of Structural Geology. The first paper, Gomez and Marrett (in review) was accepted for publication with only minor changes, whereas the second paper, Marrett et al. (in review) received some suggestions that will be address in the coming months.

1.1 Fracture spacing versus spatial arrangement of fractures

Fracture spacing is the distance between two immediately adjacent fractures (nearest neighbors) of the same set along a straight line perpendicular to the fractures, as shown in Figure 2.2 (e.g., Priest and Hudson, 1976; Rives et al., 1992; Gross et al., 1995). In contrast, the concept of spatial arrangement of fractures refers to the presence, or absence, of patterns in fracture positions in space (Priest and Hudson, 1976). For example, a fracture set where the small spacings are grouped (forming a fracture cluster) is qualitatively different from a set lacking systematic sequence of fracture spacings or having regular spacings between fractures. As mentioned in Chapter 1, a fracture cluster can be defined as a domain of a fracture set where fractures are unusually abundant. The position of fractures can be obtained by combining the fracture apertures and spacings and the sequence in which they are located along a one-dimensional (1D) scanline. Alternatively, knowing the position of each fracture along a scanline allows calculating the spacings between fractures and their corresponding sequence.

This section focuses on evaluating two of the most traditionally used methods to analyze one-dimensional (1D) fracture spacing (i.e., descriptive statistics and frequency distributions) and identifying their shortcomings for characterization of fracture spatial arrangement. The main limitations of the traditional methods are: First, the most widely used traditional methods ignore a fundamental component of spatial arrangement of fractures, namely their positions with respect to all the other fractures in the same set,

which can be expressed as the sequence of fracture spacings along an observation line. Although some methods of spacing analysis in some cases can distinguish if observed fractures are more clustered or more regularly spaced than a random arrangement, they do not always succeed. Even when successful, they fail to characterize the form of organization within clusters (e.g., fractal) or between clusters (e.g., periodically arranged clusters). Second, the traditional methods of spacing analysis ignore the wide range of sizes of natural fractures.

1.1.1 Ignoring Fracture Position

A synthetic 1D fracture data set illustrates the first limitation (ignoring the sequence of spacings) of analytical techniques that only address fracture spacing. By ignoring the sequence of fracture spacings, these techniques cannot distinguish different spatial arrangements having the same values of fracture spacing (Figs 6.1a and 6.1b). Fractures with negligible aperture and random positioning along a line show regions where fractures are more closely spaced than others (Figure 6.1b) and constitute clusters. However, the clusters of Figure 6.1b do not represent statistically significant organization (i.e., departure from randomness) so their sizes and locations are coincidental (Priest and Hudson, 1976). The same values of fracture spacing (and therefore the same number of fractures) can be systematically sequenced in position along the scanline to generate a completely different spatial arrangement of fractures (Figure 6.1a) that contains two statistically significant clusters, each having nearly half of the fractures in Figure 6.1b. Changing the sequence of fracture spacings (Figures 6.1a versus 6.1b) changes the spatial arrangement. Any method for analyzing spatial arrangement that relies solely on the values of fracture spacings, regardless of their sequence, will be incapable of distinguishing between the two different spatial arrangements and, consequently, will be unable to discriminate between random and non-random clustering. Techniques that

ignore the sequence of spacings also cannot characterize or quantify the organization within or between clusters, for instance the width of and the distance between the two clusters of Figure 6.1a.

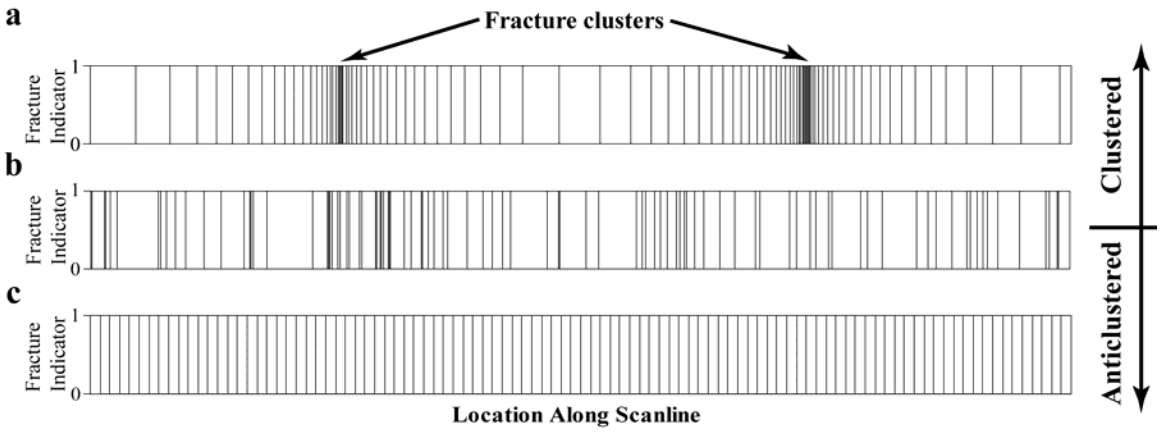

Figure 6.1 Fracture indicator series of three synthetic data sets with identical numbers of fractures (100) and scanline lengths. The indicator series equals 1 (black) where a fracture is present along the scanline and 0 (white) where there is no fracture. All fracture apertures are equal and infinitesimally small and therefore can be ignored. (a) Randomly located fractures show several places where fractures are more closely spaced (clusters) but the clusters are not statistically significant. (b) A synthetic data set with the same values of fracture spacing as in (a) but sorted in such a way that two statistically significant fracture clusters are present. The spacings between fractures systematically increase away from the center of each cluster. c) Regularly spaced fractures. The average fracture spacing is equal to the spacing between any pair of nearest neighbor fractures.

1.1.2 Ignoring Fracture Size

The second limitation of techniques that analyze fracture spacing is that, by ignoring fracture size, some techniques implicitly assume all fractures are the same size whereas natural fractures commonly display a wide range of sizes. Apertures in a fracture set can vary at least four orders of magnitude (Marrett et al., 1999), from fractures that can be measured easily with the naked eye to fractures that can only be seen with

microscopy. Likewise, fracture lengths can vary at least three orders of magnitude (Ortega and Marrett, 2000).

Ignoring fracture size has negative practical implications. For laminar fluid flow in ideally connected fractures, the permeability contribution of an individual fracture to a rock mass is proportional to the cube of its aperture (Warren and Root, 1963). Because natural fractures have a wide range of apertures, the fractures with the largest apertures (typically also longest and most likely to be connected with other fractures) dominate the permeability of the set (Marrett, 1996). In addition, it has been demonstrated that in poorly connected fractures, the longest fractures dominate permeability (Philip et al., 2005). Therefore, characterizing the spatial arrangement of fractures without taking fracture size into account (or assuming that all fractures have the same size) will fail to recognize patterns in the location of large fractures, the ones most likely to control fluid flow.

In addition, ignoring fracture size conveys the impression that all fractures were detected and measured, but predictably the observational tools used impose limits on the size of fractures that can be measured. For instance, without differential erosion along fractures, currently available satellite imagery cannot resolve any but the very largest aperture fractures (e.g., 61 cm resolution for QuickBird satellite). Although many more fractures can be measured with visual observation of outcrops, still more fractures are too small to measure without microscopy (Laubach, 1997). By embracing fracture sizes when studying the spatial arrangement of fractures, it is possible to investigate the preferential positioning of fractures of a particular size range in specific regions of the spatial arrangement (e.g., clusters; Marrett et al., in review).

1.2 Quantitative Characterization of Veins at Pedernales

A 1D data set of veins measured at Pedernales Falls State Park was described will be used throughout this chapter to compare the different techniques used to analyze fracture spacing and the spatial arrangement of fractures. A qualitative description of the veins at Pedernales was presented in Chapter 2.

The consistency in orientation of the veins (Figure 2.12) allowed measuring kinematic apertures of and spacings between 916 veins along a 59 m scanline parallel to a bedding plane. The minimum value of aperture measured was 0.05 mm while the largest was 18.0 mm (Figure 6.2a). The minimum fracture spacing was 0.08 mm while the largest was 2,260 mm or 2.26 m (Figure 6.2b). Because of the large difference (more than four orders of magnitude) between the minimum and maximum fracture spacings, the range (defined as the difference between the maximum and minimum fracture spacings) is almost identical to the maximum value (Figure 6.2b). The measured strain due to fracture opening was 0.53%. For fractures with apertures of 0.05 mm and larger, the average spacing is 64.0 mm, the median is 15 mm, the standard deviation is 156 mm and the geometric mean is 14.4 mm. The dimensionless coefficient of variation (standard deviation divided by average) equals 2.43.

A histogram indicates that about 85% of fracture spacings are less than or equal to 100 mm (Figure 6.3). As previously reported by Marrett et al. (1999), cumulative frequency of kinematic apertures at Pedernales (number of fractures with aperture greater than or equal to a particular aperture value, normalized by scanline length) follows a power-law size distribution (Figure 6.2a). In contrast, fracture spacings closely follow a log-normal distribution (Figure 6.2b).

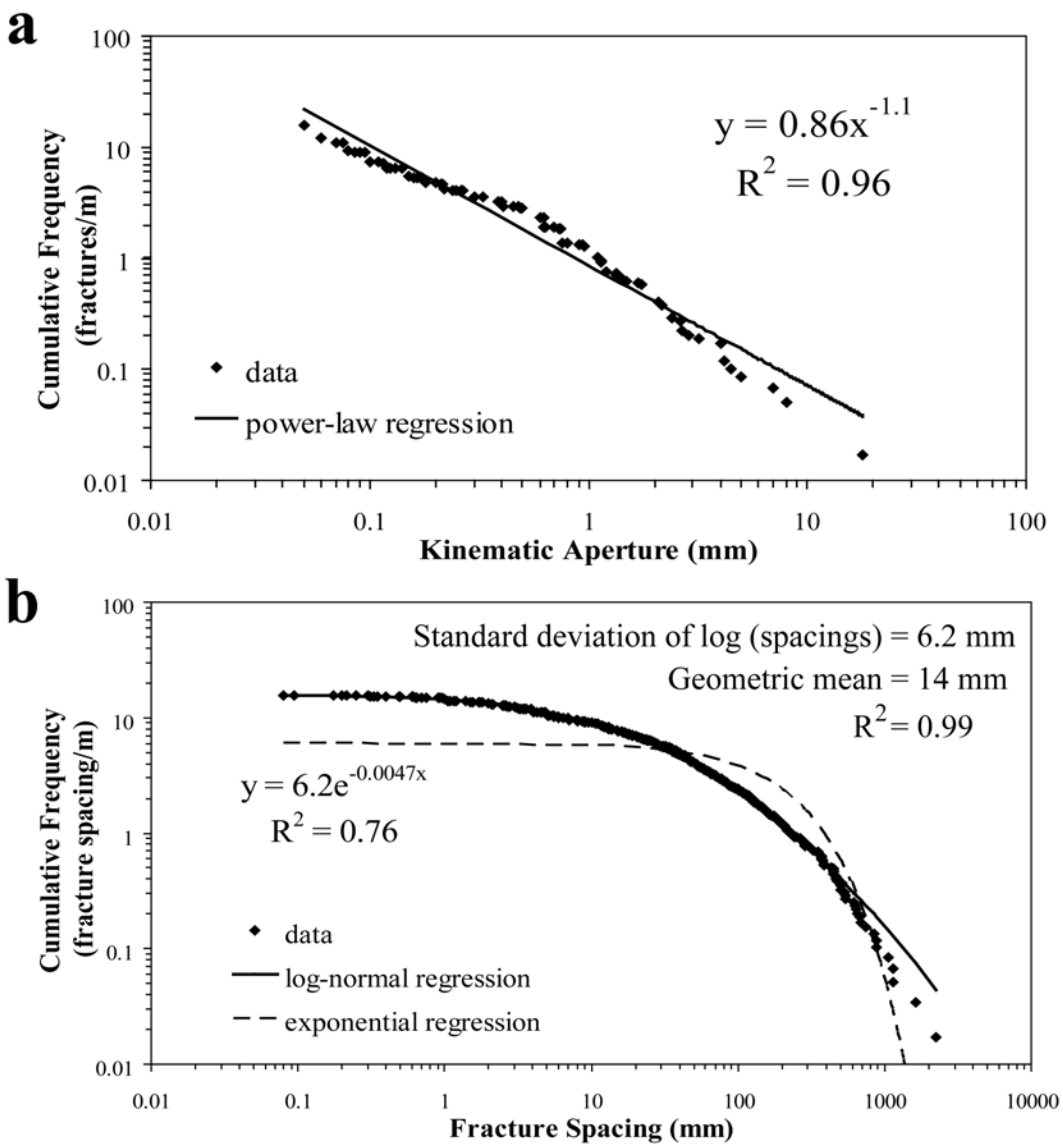

Figure 6.2 Cumulative size distributions of kinematic aperture (a) and fracture spacing (b) for veins at Pedernales. The best fitting distributions (largest R^2 coefficient) are power-law for apertures and log-normal for spacings. Visual inspection and a smaller R^2 coefficient indicate that the negative exponential distribution of fracture spacings (dashed line, Figure 6.2b) is of inferior quality than the log-normal distribution (continuous line, Figure 6.2b).

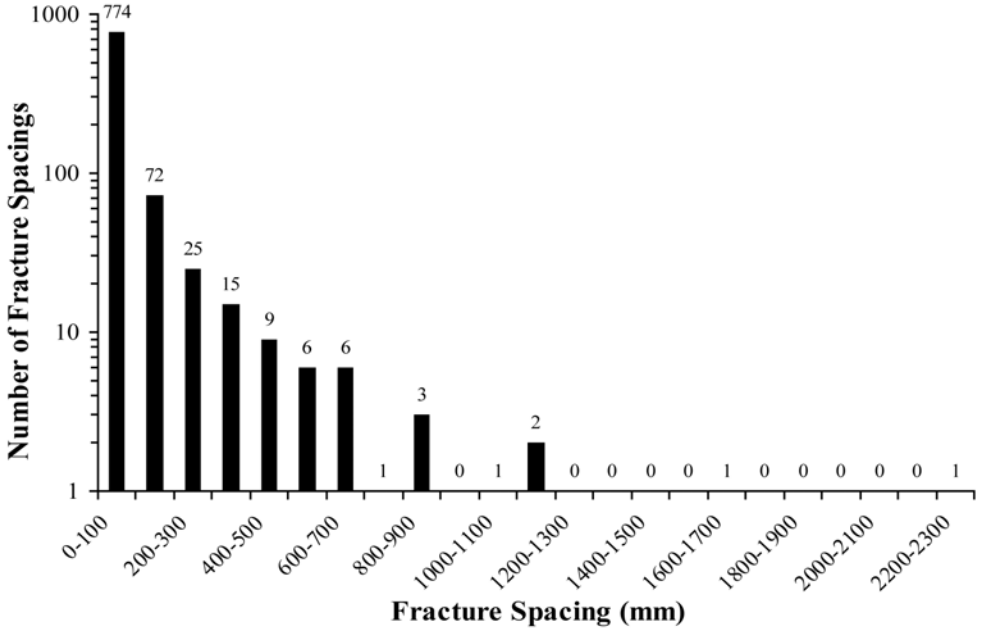

Figure 6.3 Histogram of fracture spacings for veins at Pedernales having apertures greater than or equal to 0.05 mm. Annotations indicate number of fracture spacings in each category.

Veins at Pedernales are heterogeneously arranged (Figure 2.13). Qualitatively speaking, there are at least three clusters along the scanline (Figure 6.4a). The clusters are not only regions where vein spacings are smaller than elsewhere, but also where the largest veins occur; this is clearly seen in the three largest clusters of veins (Figure 6.4a). Randomly relocating the fractures illustrates how the observed spatial arrangement of veins differs from a random arrangement (Figure 6.4b). Clusters are less dominant and there is no evident pattern in the positions of large-aperture fractures along the randomized scanline. Because the definition of a fracture cluster is qualitative and scale dependent, there are no clear rules for identifying the boundaries of a cluster. It is unlikely that a reader would disagree with us about the presence of clusters, but the same reader might disagree with our choice of boundaries (Figure 6.4a).

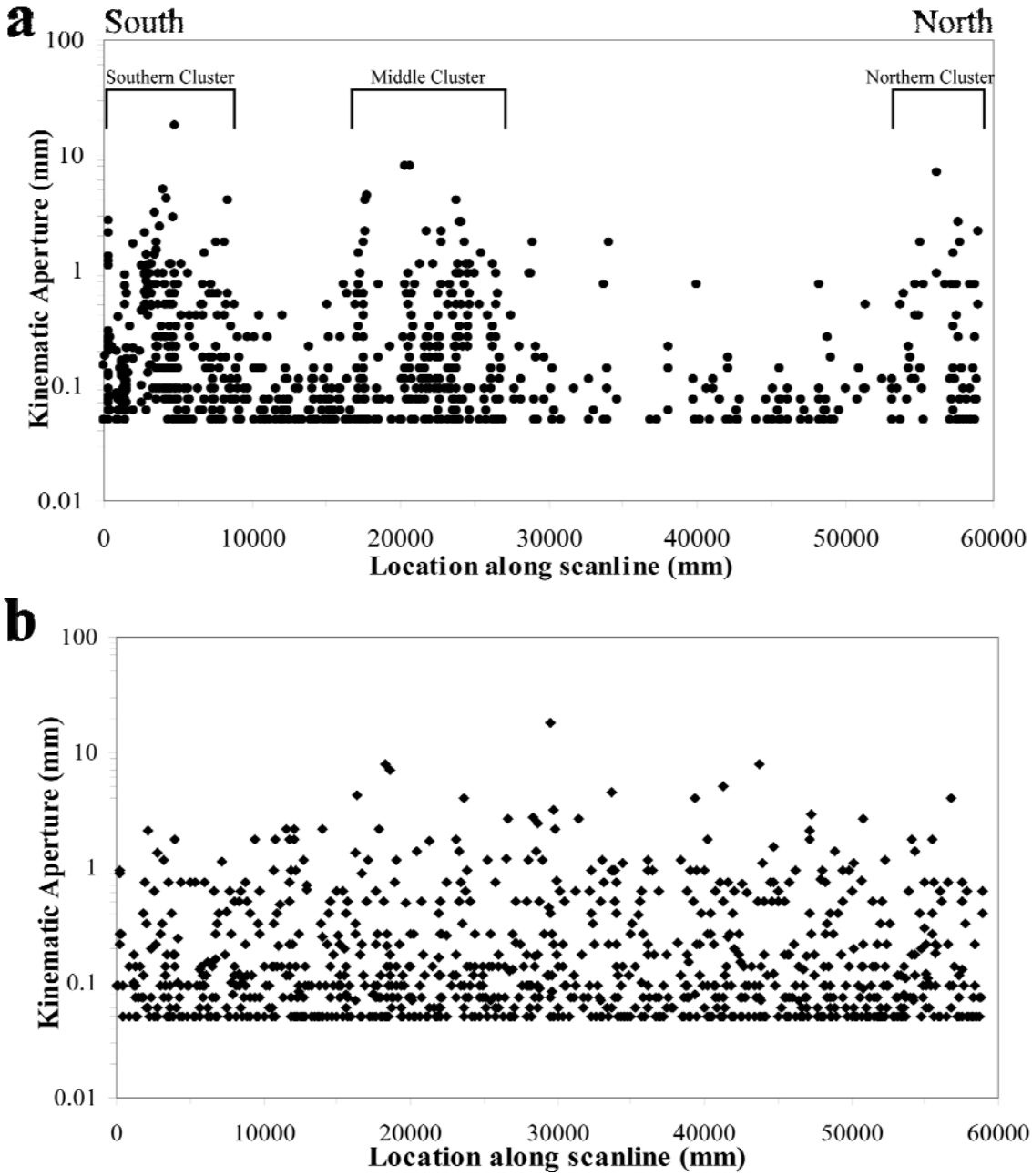

Figure 6.4 Plot of kinematic aperture versus location along scanline for observed (a) and randomly located (b) veins at Pedernales. The use of a logarithmically graduated axis for kinematic apertures allows visualization of the entire range of vein sizes measured. In randomization, vein apertures were not changed but observed vein positions were replaced by random locations along the scanline. Clusters can be qualitatively identified in (a) but can not clearly detected in (b).

2. PREVIOUSLY USED TECHNIQUES FOR CHARACTERIZING FRACTURE SPACING

This part of Chapter 6 focuses on evaluating techniques traditionally used to analyze one-dimensional (1D) fracture spacing and explaining their shortcomings for characterization of fracture spatial arrangement.

2.1 Descriptive Statistics

Descriptive statistics is a branch of statistics that denotes any of the many techniques used to numerically summarize and describe a set of data (population or sample) without any effort to test a particular hypothesis (e.g., Burt and Barter, 1996; Salkind, 2004). Descriptive statistics measure the central tendency (e.g., arithmetic mean, median) and the variability or dispersion (e.g., standard deviation, coefficient of variation) of a set of numbers. Although descriptive statistics of a fracture data set can be calculated easily from scanline data, as will be explained below, the information they provide about spatial arrangement of fractures is severely limited except when fractures are regularly spaced.

2.1.1 Arithmetic Mean (Average or Mean)

Perhaps the most commonly used statistic, the average, mean or more correctly arithmetic mean, is an estimate of the 'typical' or 'central' value of a set of data (e.g., Salkind, 2004). However, the average spacing only carries this meaning when the data follow a symmetrical (e.g., normal) distribution (Burt and Barber, 1996).

Average spacing ($\overline{S}$) is calculated by summing all the spacings between nearest-neighbor fractures (S_i) and dividing by the total number (n) of fracture spacings (e.g., Narr, 1996):

$$\overline{S} = \frac{\sum_{i=1}^{n} S_i}{n} = \frac{L - \sum_{i=1}^{n} b_i}{n} \approx \frac{L}{n} \qquad (1)$$

The sum of spacings also equals the length of the scanline (L) minus the sum of all apertures (b_i), or approximately L if strain due to fracture opening is small. As can be deduced from Equation (1), the average spacing depends only on the sum of all fracture spacings and the number of fracture spacings measured, regardless of the sequence of fracture spacings or their individual values, so it ignores the position of each fracture with respect to fractures other than its nearest neighbors. For instance, the three synthetic fracture sets of Figure 6.1 have identical average fracture spacing, even though they have very different spatial arrangements. The average spacing of fractures can indicate the typical value of fracture spacings, but not how the observed spatial arrangement compares with regularly spaced, randomly arranged, or systematically clustered fractures. The closer a spatial arrangement of fractures is to a regularly spaced set of fractures, however, the more representative the average spacing is.

The significance of the average fracture spacing is also limited by the fact that it ignores the wide spectrum of fracture sizes found in many natural fracture sets. As mentioned earlier in this chapter, apertures can range up to at least four orders of magnitude and lengths up to at least three orders of magnitude. The implicit assumption, almost never fulfilled in estimation of average fracture spacing, is that all fractures along the scanline were detected. In fact there will be a fracture-size threshold, below which fractures are sampled incompletely or not at all. Therefore, most natural fracture sets will not have a unique value of average fracture spacing, but instead average spacing will vary depending on the aperture threshold used during data acquisition or later analysis.

For the veins at Pedernales, average spacing increases with increasing aperture threshold (Figure 6.5a), where aperture threshold is the minimum aperture of fractures included in analysis. The variation in average fracture spacing with aperture threshold follows a power law with an exponent near one. Namely, for every order of magnitude

increase in the aperture threshold, there is an increase of approximately one order of magnitude in the average spacing (Figure 6.5a). This increase of average spacing with increasing aperture threshold can be inferred from the graph of cumulative frequency of kinematic aperture, because average spacing is simply the inverse of cumulative frequency (Figure 6.2a).

To avoid unnecessary difficulties when comparing different fracture sets, Ortega et al. (2006) recommended the use of cumulative frequency distributions of fracture aperture to estimate average fracture spacing. This is accomplished by inverting the value of cumulative frequency (number of fractures above the aperture threshold per unit length of scanline) using a common value of aperture for all data sets. Although, this approach explicitly accounts for fracture size, it does not overcome the fundamental limitation of average fracture spacing as a statistic, in that it ignores the spatial position of fractures and cannot distinguish between random and non-random spatial arrangements.

Although average fracture spacing is typically calculated using 1D data, it has also been calculated using two-dimensional (2D) data by dividing the area under study by the sum of fracture lengths (Wu and Pollard, 1995). However, 2D average fracture spacing suffers the same limitations of its 1D counterpart; namely, it ignores both fracture sizes and positions.

2.1.2 Median

In descriptive statistics, the median (S_m) is the middle value when a data set is arranged in order of size; it is the number that separates the largest half of a sample or a population from the smallest half (e.g., Salkind, 2004). This implies that in order to calculate the median spacing, no information about the position of individual fractures in the scanline or about the sequence of fracture spacings is required.

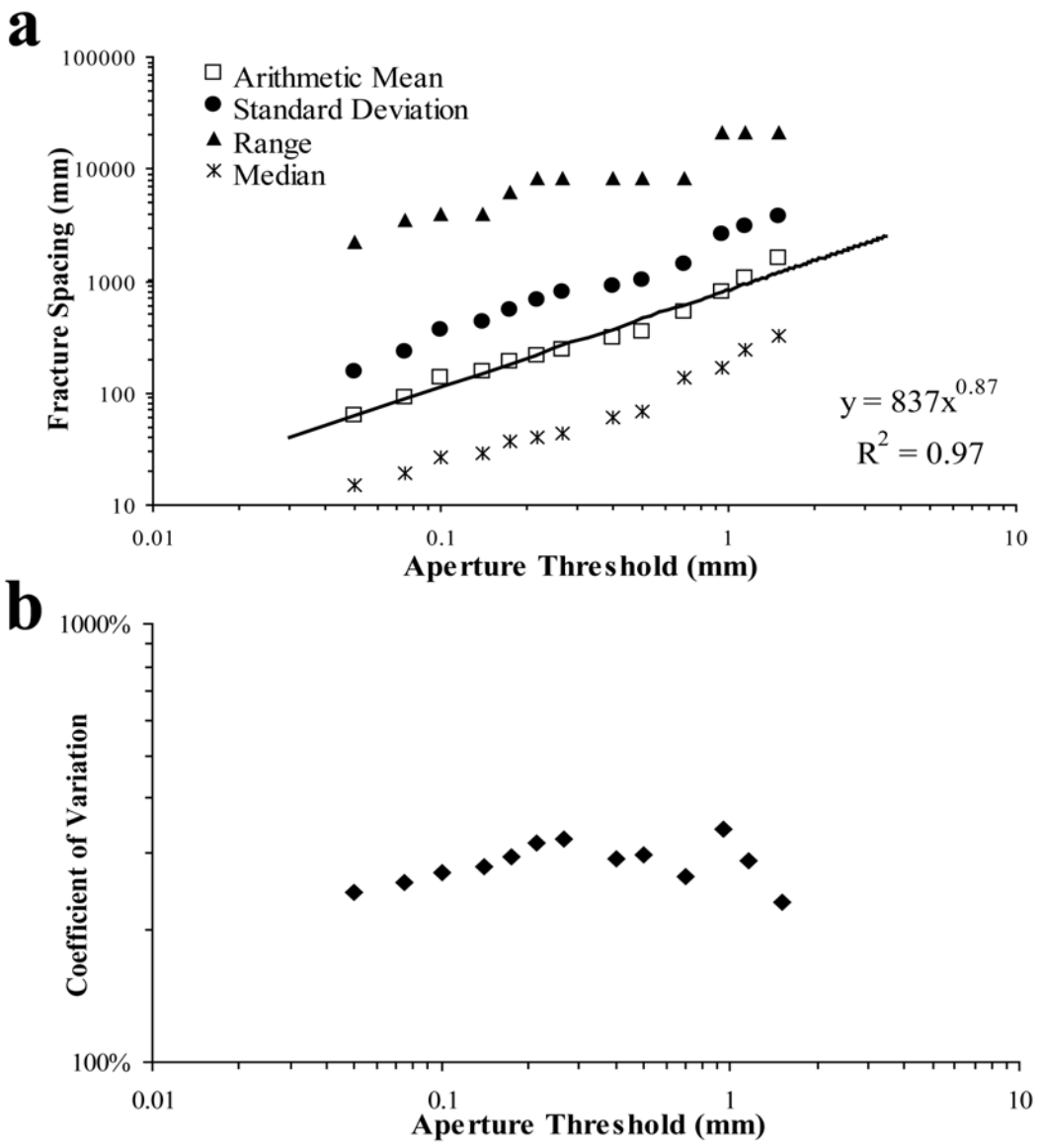

Figure 6.5 Plot of kinematic aperture threshold versus different measures of fracture spacing, (a), and coefficient of variation (b) for veins at Pedernales. The best fitting distribution (power-law) to average spacing and standard deviation are similar whereas coefficient of variation is nearly constant.

In the case of a random arrangement of fractures:

$$S_m = \bar{S} \ln 2 \approx \frac{L}{n} \ln 2 \qquad (2)$$

The median has not been used directly to quantify the spacing between nearest-neighbor fractures along a scanline but instead it has been used through what Narr (1991) called the fracture spacing index (FSI), the slope to the regression line of jointed-layer thickness vs median joint spacing (Narr and Suppe, 1991; Gross, 1993; Gross et al., 1995). The reason for using the median instead of the arithmetic mean (as used by Narr and Lerche, 1984 to calculate their version of FSI) for fracture characterization was stated by Narr and Suppe (1991) and illustrated by Figure 12 of Gross et al. (1995): "The median is a better and more stable estimator of the center of these asymmetric (log-normal) populations of joint spacing than is the arithmetic mean".

However, the fact that fracture spacing values commonly show large dispersion indicates that no single number, including the median, can represent many fracture sets in a meaningful way. The 916 veins with apertures of 0.05 mm and larger at Pedernales have spacing values that range more than four orders of magnitude (0.08 to 2260 mm) and have a median of 15 mm. Randomizing the positions of fractures at Pedernales 100 times (e.g., Figure 6.4b) allows calculation of median spacing for each randomization (average of 44.5 mm and 95% confidence interval of 3.12 mm). The median for observed fracture spacings at Pedernales (15 mm) is less than expected for a random arrangement (44.6 mm from Equation 2), nominally indicating that the veins at Pedernales are more clustered than random.

Like average spacing, the median spacing ignores the position of each fracture with respect to fractures other than its nearest neighbors. The median only indicates the central value of the statistical sample, regardless of the range and arrangement of fracture spacings. For example, the fractures of Figures 6.1a and 6.1b have significantly different spatial arrangements and yet their median is the same. Another limitation of the median is that it varies with the size threshold for fracture measurement or analysis (Figure 6.5a).

For the veins at Pedernales, the median increases with increasing values of aperture threshold in approximate proportion to the average spacing and the standard deviation (Figure 6.5a). This is emblematic of the fact that there is not a unique median of fracture spacings; rather it is inherently scale-dependent.

2.1.3 Standard Deviation and Coefficient of Variation

The standard deviation (σ) is the most commonly reported measure of variability or dispersion in a set of data. The more widely the values vary, the larger the standard deviation. The definition for the standard deviation is (e.g., Burt and Barter, 1996):

$$\sigma = \sqrt{\frac{\sum_{i=1}^{n}(S_i - \overline{S})^2}{n-1}} \tag{3}$$

In the case of a random arrangement of fractures (Gillespie et al., 2001):

$$\sigma = \overline{S} \approx \frac{L}{n} \tag{4}$$

The standard deviation has an undesirable feature; like the mean, one or two extreme values in a statistical sample can significantly influence the standard deviation. Although the standard deviation can be used directly to characterize the variability of fracture spacings (e.g., Salkind, 2004), it can also be expressed in proportion to the mean to yield the coefficient of variation (C_v). For a random arrangement of fractures:

$$C_v = \frac{\sigma}{\overline{S}} = 1 \tag{5}$$

In probability theory and statistics, the coefficient of variation is a measure of dispersion of a probability distribution. For fracture spacing analysis, the coefficient of variation is a dimensionless number that allows comparison of data sets having

significantly different average spacings. The C_v in practice scales the standard deviation by the size of the mean, making it possible to compare fracture data sets acquired at different places and/or at different scales.

Gillespie et al. (1999; 2001) appropriately proposed using the coefficient of variation to quantify the degree of clustering for a fracture data set. For randomly arranged fractures, the mean and the standard deviation are equal, therefore $C_v = 1$ (Equation 4). If fractures are more clustered than random, then the arrangement of fractures will have a large σ compared with the corresponding $\overline{S}$, with small spacings located inside the clusters and large spacings between the clusters, making $C_v > 1$. In contrast, if fractures are anti-clustered (i.e., more regularly spaced than random) then σ will be small compared with $\overline{S}$ and therefore $C_v < 1$ (Gillespie et al., 1999). Indeed, 100 randomized versions of the veins at Pedernales (e.g., Figure 6.4b) yield an average C_v of 1.06 and a 95% confidence interval of 0.06. In contrast, the C_v of observed vein spacings at Pedernales is 2.43, suggesting that the veins are more clustered than a randomly arranged data set.

Although in some cases C_v can distinguish a fracture spacing data set from random, it cannot determine how many clusters there are, what cluster spacing is, what kind of organization (e.g., fractal) the clusters have, because C_v ignores the spatial position of fractures. For instance, the fracture sets of Figures 6.1a and 6.1b have the same C_v and yet they display distinctively different spatial arrangements. This illustrates that C_v cannot distinguish all non-random arrangements from random.

Like the other two descriptive statistics considered, the coefficient of variation ignores the wide range of fracture sizes. However, C_v does not change systematically with increasing values of aperture threshold at Pedernales (Figure 6.5b), so it might be less scale-dependent than other descriptive statistics.

2.2 Frequency Distributions

In statistics, a frequency distribution is an inventory of the values that a variable takes in a sample (e.g., Salkind, 2004). Statistical samples of fracture attributes, including fracture spacing, have been analyzed both as discrete (Table 6.1) and cumulative frequency distributions (Table 6.2). Discrete frequency distributions tabulate the number of times (frequency) an event or item of a value (or a range of values) occurs in a data set whereas cumulative frequency distributions quantify the number of times an event or item larger (or smaller) than a particular value occurs in a data set.

In addition, frequency distributions of fracture attributes can be compared to a predetermined model that has a known algebraic expression describing the relative frequency for every possible value in the statistical sample. Such a model (commonly known as probability model or probability distribution) attempts to capture the essential structure of a frequency distribution as if an infinite number of fracture measurements were taken with infinite precision. Such a model is called a probability distribution because it is a mathematical function that assigns to each measurable event in a sample the probability that the event will occur. The quality of the fitting of a particular probability distribution to a fracture spacing data set is typically expressed using goodness-of-fit tests like R^2 or χ^2 (Figures 6.2b and 6.6a). It is typically interpreted that a particular data set follows the probability distribution with the best goodness-of-fit (highest R^2 or lowest χ^2 coefficient) as shown is Figure 6.2b. The most common probability models for the spacings between natural fractures in rocks are: log-normal, negative exponential, negative logarithmic, normal, and power-law (Tables 6.1 and 6.2).

Table 6.1 Compilation of the main characteristics of some of the most commonly cited studies about fracture spacing using only discrete frequency distributions. G. = gamma, L.N. = log normal, N = normal, N.E. = negative exponential, N.L. = negative logarithmic, and P.L. = power law.

Publication	Type of Fractures	Rock Type or Material	Number of Fractures	Scale	Spacing Distribution	Comments
Priest and Hudson (1976)	Rock discontinuities	Chalk, sandstone, limestone	4884, 249	Outcrop (tunnels)	N.E.	Different orientations were included in a single analysis.
Rouleau and Gale (1985)	Fractures	Granite	1324	Outcrop (tunnel) and core	L.N.	Examined spacings for each fracture set.
Huang and Angelier (1989)	Tension tectonic joints	Limestone	800	Outcrop	G. and apparent N.E.	N.E. due to limitation in measuring small spacings in air photos.
		Calcareous sandstone	400, 107			
Villaescusa and Brown (1990)	Joints	Siliceous, pyretic ores	304		N.E.	
Narr and Suppe (1991)	Rock joints	Chert, dolostone, porcelanite	596	Outcrop	L.N.	Spacing normalized by the median spacing for each set.
Rives et al. (1992)	Joints	Limestone, shale, mudstone, siltstone	320 (outcrop), 314 (model)	Outcrop, physical and numerical models	L.N., N.E. and N.	Evolve from N.E. to L.N. and N. with increasing strain.
Gross (1993)	Cross joints	Chert	710	Outcrop	G.	
Gross and Engelder (1995)	Veins	Dolostone	70, 155 (outcrop), 37, 47 (thin section)	Outcrop and thin sections	L.N and P.L.	Distributions differ for outcrop (L.N. and P.L.) and thin sections (P.L.).

Table 6.2 Compilation of the main characteristics of some of the most commonly cited studies about fracture spacing using cumulative frequency distributions. G. = gamma, L.N. = log normal, N = normal, N.E. = negative exponential, N.L. = negative logarithmic, and P.L. = power law.

Publication	Type of Fractures	Rock Type or Material	Number of Fractures	Scale	Spacing Distribution	Comments
Cumulative Frequency Distributions						
Gillespie et al. (2001)	Veins	Limestone	160, 103	Digitized air photos	P.L.	Veins and joints in same outcrops.
	Joints		120, 202, 52		L.N.	
Gale (2002)	Veins	Chalk	136, 51, 204	Outcrop and core	N.L. and L.N.	
Discrete and Cumulative Frequency Distributions						
Gillespie et al. (1993)	Joints	Sandstone	92, 390	Outcrop	N., P.L. and N.E.	Combining different fracture sets gives a N.E. distribution.
Simpson (2000)	Veins	Sandstone, phyllites, quartzites	114, 200	Outcrop	L.N.	

2.2.1 Discrete Frequency Distributions

Discrete frequency distributions are one of the most popular analytical techniques used to quantify the attributes, including spacing, of fractures (Table 6.1). Graphs of discrete frequency distributions are commonly shown in the form of histograms (e.g., Salkind, 2004). A histogram is a bar graph of a frequency distribution in which the heights of the bars are proportional to the interval frequencies. In practice, a frequency distribution is typically generated by dividing the range (covering the minimum and maximum values that the variable takes) of a data set into a set of mutually exclusive (non-overlapping) intervals of equal width, listing them in increasing order and assigning to each interval the number of measurements (frequency) that fall in each interval.

There are two different ways to express frequency with the same data. One uses the number of measurements per interval (e.g., Figure 6.3), while the other uses the number of measurements per interval divided by the total number of measurements, which yields an estimate of the probability that a measurement in a statistical sample will fall into a particular interval (e.g., Figure 6.6). Another variation in the way frequency distributions are graphed uses points (or a line connecting the points) located where the tops of the bars would plot in a histogram (e.g., Figure 6.6a).

Perhaps the most widely known inadequacy of discrete frequency distributions is the fact that changing the size of the intervals can change the appearance of the histogram and possibly the conclusions that one may draw from it. For instance, Figures 6.6a and 6.6b represent the same data set and, although the graphs look similar, the difference in the interval sizes affects the exponential regression that best fits the data set (Rives et al., 1992). In general, it is not possible to obtain an ideal interval size that avoids any bias.

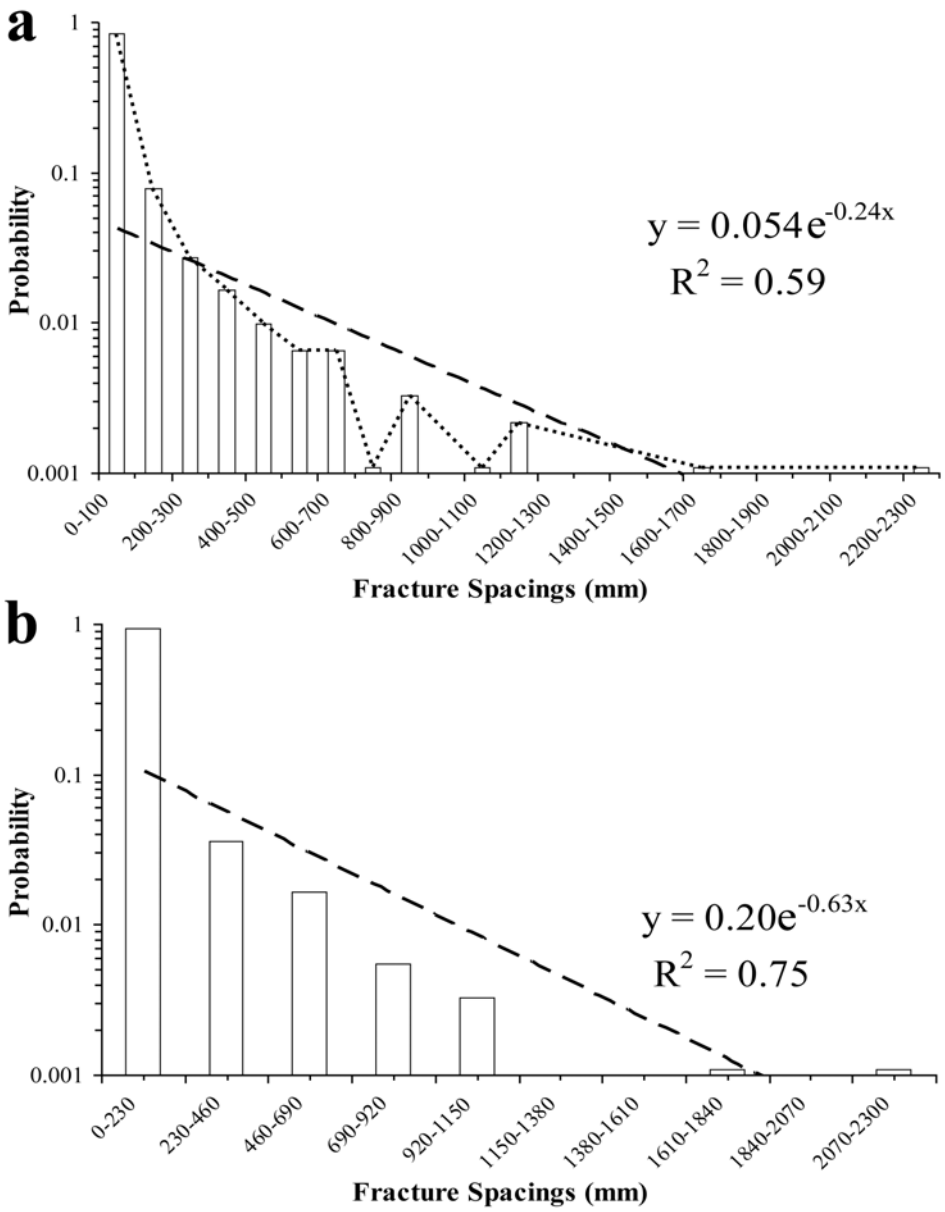

Figure 6.6 Plot of fracture spacing versus probability of veins at Pedernales with apertures equal or larger than 0.05 mm. Dashed line is negative exponential distribution fitted to the data. (a) Probability is plotted as bars and a dotted line. Intervals are 100 mm. (b) Probability is plotted only as bars. Intervals are 230 mm, more than double in size of those of (a). Changing the size of the intervals changes the equation of the probability distribution (power-law exponent increased 37%) even though both regressions are fitted to the same underlying data.

Discrete frequency distributions also have two other important limitations. First, discrete frequency distributions suffer from the fact that they ignore the sequence of fracture spacings (Figures 6.1a and 6.1b). To construct a histogram of fracture spacings, individual values of fracture spacing are assigned to an interval that matches its size regardless of where the spacings occur along the scanline. Second, logarithmic axes commonly cannot be used because of the zero values commonly present for some intervals (Gillespie et al., 1993). Logarithmic axes are frequently desirable to adequately display the large ranges of fracture spacing (typically the X axis) or interval frequencies (typically the Y axis).

A random arrangement of fractures will generate a negative exponential probability distribution of fracture spacings (Priest and Hudson, 1976; Dershowitz and Einstein, 1988). To estimate the discrete frequency distribution for randomly arranged fractures, the only parameters needed are the total number of spacings in the data set (n), the length of the scanline (L), and the minimum ($S_{\min}$) and maximum ($S_{\max}$) spacings that define an interval in the distribution:

$$N = n\left[e^{-S_{\min}\frac{n}{L}} - e^{-S_{\max}\frac{n}{L}}\right] \tag{6}$$

Negative exponential distributions of fracture spacing, as expected for random arrangements, have been detected using discrete frequency distributions (Priest and Hudson, 1976; Villaescusa and Brown, 1990; Rives et al., 1992). Although random fracture locations along a scanline will indeed generate fracture spacings that closely follow a negative exponential distribution, it is false that all negative exponential distributions must derive from random positioning of fractures. For example, the sets of Figures 6.1a and 6.1b, both have the same values of fracture spacings, and therefore follow the same frequency distribution (a negative exponential), and yet only one of them

has fractures that are randomly located (Figure 6.1a). Therefore, a discrete frequency distribution of fracture spacings that follows a negative exponential distribution only suggests that the fracture spacing data set might be a result of random fracture locations.

2.2.2 Cumulative Frequency Distributions

In 1D analyses, cumulative frequency is used to determine the number of observations that are greater than or equal to a particular value in a data set per unit of scanline length. Although uncommon in the literature of fracture characterization (Table 6.2), another version of cumulative frequency distributions displays how many fractures per unit of scanline length (cumulative frequency) have an attribute less than or equal to the corresponding value of fracture attribute.

The first step to generate a cumulative frequency distribution of a fracture attribute of interest (e.g., aperture, length, spacing) is to sort all measurements of the fracture attribute from largest to smallest, and then calculate the cumulative number by assigning increasing numbers (increments of one) to each measurement of fracture attribute. Secondly, duplicate values of the fracture attribute should be distilled so that only the largest value of cumulative number is retained. This creates a table with pairs of values of fracture attribute (e.g., spacing) and cumulative number. The cumulative number indicates how many fractures in the sample have an attribute greater than or equal to the corresponding value of fracture attribute. Although retention of duplicate values of fracture attributes would not significantly affect the graphical appearance of a cumulative frequency distribution, it is required for correct calculation (e.g., least squares regression) of the equation of a probability distribution (e.g., power law in Figure 6.2a). The third step is to divide the cumulative number by the scanline length to obtain the cumulative (spatial) frequency of the fracture attribute under study (e.g., Figure 6.2).

Normalization to calculate cumulative frequency is similar to the one commonly used for histograms (Figure 6.6) but instead of normalizing by the total number of measurements, it is done using the scanline length (e.g., Figure 6.2). Such charts of cumulative frequency allow comparison of data from different observational scales through normalization to the sizes of the scanline studied at each scale. For example, Marrett et al. (1999) used graphs of cumulative frequency of kinematic aperture to demonstrate that veins measured in thin sections and in outcrops of carbonate rocks of the Marble Falls Limestone at Pedernales share a common probability distribution. Gomez et al. (2003) did the same for veins measured in thin sections and horizontal core of the Cozzette Sandstone in the Piceance Basin, NW Colorado.

Cumulative frequency distributions have two distinct advantages over discrete frequency distributions. First, there is no need to select an interval size, which minimizes the possibility of bias in the interpretation of the frequency distribution and in the calculation of a probability distribution (Figure 6.2). Second, because there are no values of cumulative frequency equal to zero, logarithmic axes can be used to display large ranges of fracture attributes (Figure 6.2). Cumulative frequency distributions are also smoother than their discrete counterparts, an inevitable result of the procedure used to calculate the cumulative numbers.

However, like discrete frequency distributions, cumulative frequency distributions ignore the sequence of fracture spacings and spatial position. Information about the spatial position of fractures is crucial to distinguish spatial arrangements that are different (Figures 6.1a and 6.1b) but have the same probability distribution. As a consequence, cumulative frequency distributions cannot distinguish between stochastic clustering caused by random fracture locations (Figure 6.1a) and systematic clustering caused by other processes (Figure 6.1b).

To estimate the cumulative frequency distribution for randomly arranged fractures, the only parameters needed are the total number of fracture spacings (n) and the length of the scanline (L):

$$N = n\, e^{-S_N \frac{n}{L}} \tag{7}$$

The cumulative frequency distribution of spacings between the 916 veins measured at Pedernales most closely (highest R^2 coefficient) follows a log-normal distribution (Figure 6.2b). As with discrete frequency distributions, a negative exponential probability distribution only suggests that fractures might have random locations. Mathematical proof (Priest and Hudson, 1976) and numerical modeling (Rives et al., 1992) demonstrate that negative exponential distributions of fracture spacing are generated by randomly arranging fractures and that any other distribution is evidence of a non-random arrangement. This is confirmed by randomizing the positions of the fractures at Pedernales 100 times (Figure 6.7a). The average cumulative frequency for the 100 randomized versions follows a nearly perfect (R^2 almost equal to one) negative exponential distribution, whereas the spacings of observed veins at Pedernales follow a log-normal distribution that almost entirely plots outside the 95% confidence interval of the 100 randomized versions (Figure 6.7a). Therefore, the cumulative frequency distribution demonstrates that veins at Pedernales are not randomly arranged (Figure 6.2b).

Log-normal distributions of fracture spacing have been reported using cumulative frequency distributions (Simpson, 2000; Gillespie et al., 2001; Gale, 2002). Currently, no quantitative model for a physical or geological process quantitatively explains log-normal distributions of fracture spacing.

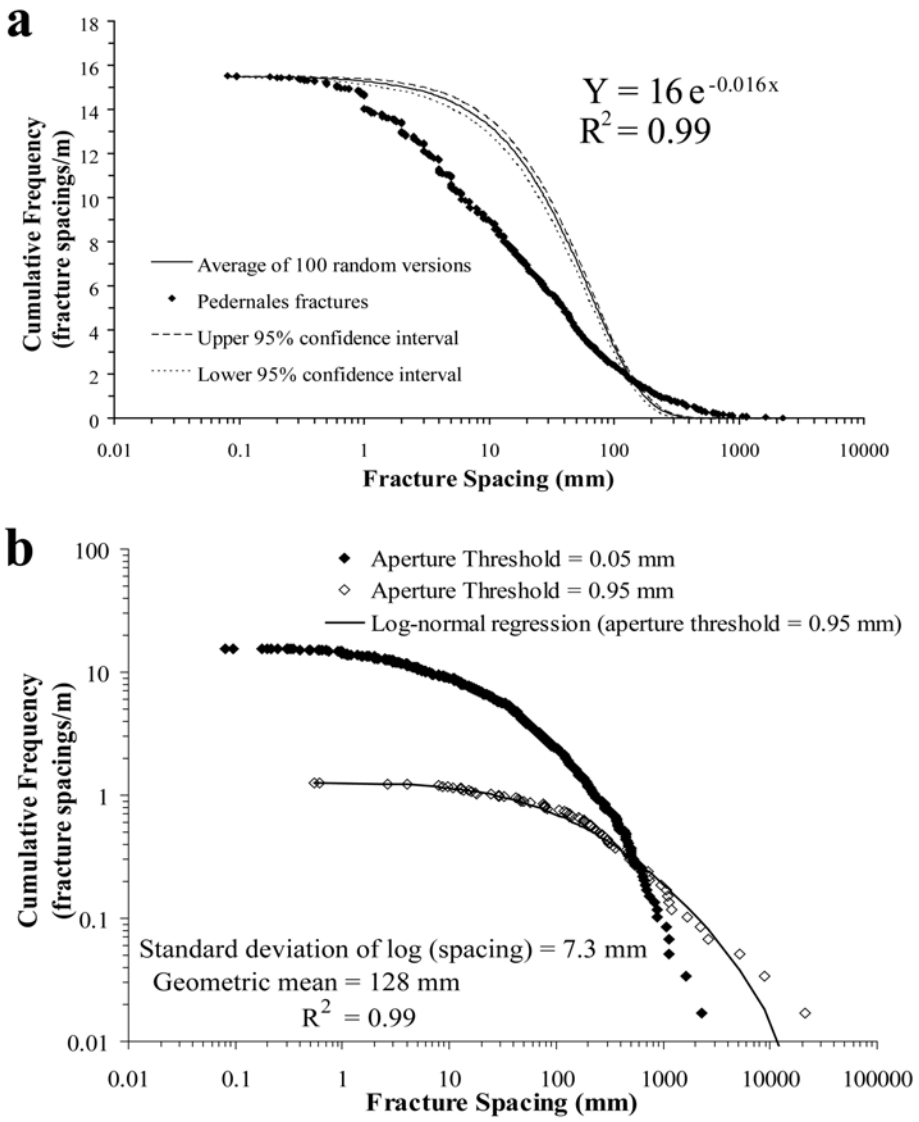

Figure 6.7 Plot of fracture spacing versus cumulative frequency for the veins at Pedernales with apertures equal or larger than 0.05 mm (filled diamonds). (a) Also includes the average cumulative frequency (and corresponding 95% confidence intervals) for 100 versions of randomly located fractures at Pedernales. The negative exponential regression is calculated from the average cumulative frequency of randomized fracture locations. (b) Also includes the cumulative frequency of fracture spacings at Pedernales but with an aperture threshold of 0.95 mm (open diamonds). By changing the aperture threshold, the number of fractures reduced from 916 (0.05 mm) to 75 (0.95 mm). Although both data sets follow a log-normal distribution, the parameters of the distributions differ (compare with Figure 6.2b).

With a qualitative mechanical rationalization, Rives et al. (1992) suggested that during the evolution of a fracture set, spacings would evolve from a negative exponential to a log-normal distribution. Rives et al. (1992) proposed that the initial negative exponential distribution would reflect the random arrangement of flaws, from which fractures nucleated, while the log-normal distribution would result from increasing interaction between fractures and their corresponding stress shadows. Simpson (2000) used simple numerical models to show that the fluid-pressure drop inside a fracture, caused by fracture opening, might create a zone in the adjacent rock which is driven into a critical stress state and help localize fracture initiation around existing fractures. Although the numerical model of Simpson (2000) leads to a degree of clustering higher than randomly arranged fractures, the model did not generate the commonly observed log-normal distribution of natural fracture spacings and also ignores the mechanical interaction between fractures that grow simultaneously, which has been demonstrated to influence the spatial arrangement of fractures (Olson, 2004).

Cumulative frequency graphs for fracture spacings of natural fractures can also be affected by limitations in the range of fracture sizes that can be measured. Due to sampling limitations and the large range of fracture apertures present in nature (Marrett et al., 1999; Gillespie et al., 2001), only a limited range of apertures can be detected and measured. Changing the aperture threshold for Pedernales veins modifies not only the number of fractures (Figure 6.2a) and most of the descriptive statistics of fracture spacings (Figure 6.5a), but also the cumulative frequency distribution of spacings (Figure 6.7b). Therefore, the attributes of a statistical sample of fracture spacings depend on the range of apertures measured, which in turn is controlled by the resolution (aperture threshold) and the length of the scanline (maximum aperture).

2.3 Critique of Previously Used Techniques for Characterizing Fracture Spacing

2.3.1 Position of Fractures along a Scanline

The most important limitation of all analytical techniques considered above, is that they ignore the position of fractures along a scanline. Fracture spacings alone, without information on sequence of fracture spacings, are insufficient for understanding some fundamental aspects of the spatial arrangement of fractures. Namely, descriptive statistical techniques characterize fracture spacing with a single value, which is generated by applying arithmetical operations to all fracture spacings under consideration. These operations effectively synthesize information about the magnitudes of individual fracture spacings but completely ignore where they were located along the scanline. Although frequency distributions represent individual values of spacing in results, by grouping spacings according to their magnitude (discrete frequency distributions) or sorting them (cumulative frequency distributions), all information about the sequence of spacings is permanently lost.

2.3.2 Type of Spatial Arrangement

Sketches of fracture networks in the literature, such as those used to explain different methodologies for studying fracture spacings, typically imply that the methodologies were designed to quantify regularly spaced arrangements of fractures (e.g., Figures 3 and 5 in Narr and Lerche, 1984; Figure 1 in Gross, 1993; Figures 1b and 1c of Narr, 1996). Schematic diagrams and photographs of fracture networks and the accompanying text in some structural geology textbooks also suggest that fractures tend to be regularly spaced (e.g., Figures 6.2 and 6.9 in Suppe, 1985; Figures 2.1, 9.3, and 14.21 in Price and Cosgrove, 1990; Figures 3.3 and 3.12 in Twiss and Moores, 1992; Figures 7.6, and 7.11 in Van der Pluijm and Marshak, 1997).

Indeed, all of the descriptive statistical techniques evaluated in this paper (average, median and coefficient of variation) generate quantitative results that usefully describe regularly spaced arrangements of fractures. Techniques that generate a graphical output (e.g., frequency distributions) are also capable of quantifying regularly spaced fractures.

Observations of natural fractures in rocks, together with convincing evidence in the literature (e.g., Gillespie et al., 1993; Rives et al., 1994), show that approximately regularly spaced fracture sets exist in nature. But their existence does not mean that this is the only kind of spatial arrangement of fractures found in nature or even that it is the most common arrangement. In our experience, fractures commonly deviate in significant ways from approximately regular spacing (e.g., Gillespie et al., 2001; Marrett et al., in review).

To their credit, authors have commonly warned readers that their techniques to analyze fracture spacings are designed to work or were tested with fracture data sets that are, at least in a qualitative fashion, regularly spaced. For example, Narr and Lerche (1984): "In stratified rock, they are generally perpendicular to bedding and occur with systematically spaced, parallel fractures to form a set". "These attributes —systematic spacing of parallel bedding-normal fractures—are the ones that the technique described in this paper is dependent on." Or Gross et al. (1995): "joints are confined solely to the light colored siliceous layers and display a regular spacing". However, admonitions that previous techniques were developed, tested and aimed to study regularly spaced fractures were perhaps not explicit or abundant enough to be heeded by the scientific community.

As we have demonstrated with the set of veins at Pedernales, some of the techniques presented here might quantify some aspects of non-regularly spaced fractures (i.e., C_v and interval counting can distinguish some types of clustering from random), but

we have lacked a technique that can quantify other important characteristics of spatial arrangement, such as cluster width or the distance between clusters. The most useful techniques should be able to quantify clustered or anti-clustered (regularly spaced) fractures and distinguish both from statistically random arrangements (Marrett et al., in review).

2.3.3 Number of Fractures

Because the essence of this section is to evaluate quantitative techniques that address the spatial arrangement of fractures, it is important to examine the number of fractures required in order to quantify the spatial arrangement of a specific fracture set. Some authors have already recognized that an inadequate number of measurements can limit accuracy in the quantification of spatial arrangement of fractures. For instance, Narr and Suppe (1991) measured a maximum of 50 fractures in an individual layer and stated "our measurements of joint spacing in any single layer are generally insufficient to describe a joint spacing distribution with confidence" (Tables 6.1 and 6.2).

For rocks that crop out, the most important causes for sparse data are probably the limited extent of outcrops and the limited visibility of fractures (outcrop quality or resolution of remote sensing images). Moreover, the study of fractures in subsurface rocks is mainly limited by the low probability of wellbores intersecting macrofractures (Laubach, 1997). To circumvent these limitations, several authors have used microfractures (as defined by Laubach, 1997) to predict the orientation (Laubach, 1997) and fracture intensity (Ortega et al., 1998; Marrett et al., 1999; Gomez et al., 2003) of genetically related macrofractures. Gomez (2004) measured the spacing between microfractures along a scanline spanning several thin sections (following the method described in Gomez and Laubach, 2006) to predict some attributes of the spatial

arrangement of the macrofractures present in the outcrop from where the rock sample was obtained.

The minimum number of fractures that must be measured in order to quantify the spatial arrangement of fractures depends on the type of spatial arrangement. In principle, only two adjacent fractures (one value of spacing) would be sufficient to determine the spacing for fractures with perfectly regular spacing. On the other hand, if most fractures of a set are inside clusters, the only way to detect and quantify a cluster would be to measure a representative number of the fractures inside at least one cluster and to cover part of the region between clusters. If the organization among clusters is under study, fractures from at least two clusters must be measured in order to estimate the distance between clusters. Whenever possible, we recommend that each fracture set under study be qualitatively assessed and sampled in such a way that fractures from all the qualitatively different domains of the set (e.g., clusters) are represented along a continuous scanline.

2.3.4 Fracture Sizes

Descriptive statistics, except for C_v, generate results that change significantly depending on the fracture size threshold (Figure 6.5). For example, reducing the aperture threshold (i.e., increasing resolution) will increase the number of fractures measured. If more fractures are quantified but the scanline length remains unchanged, the average and median spacings will decrease (Equations 1 and 2, Figure 6.5a). Although cumulative frequency distributions of fracture size (Marrett et al., 1999; Gillespie et al., 2001) do not change with varying size threshold (e.g., aperture; Figure 6.2a), changing fracture size threshold has an important impact on the cumulative frequency distribution of fracture spacing (e.g., Figure 6.7b).

Techniques that do not account for fracture positions (e.g., average, median, and frequency distributions) are sensitive to changes in size threshold. For instance, a reduction in size (e.g., aperture in 1D analysis) threshold will include new fractures with smaller sizes in the data set. For each newly included fracture, one fracture spacing will be removed from the population and subdivided into two new smaller spacings. In contrast, newly included fractures do not change the position (or the distances between non-neighbor pairs of fractures; Marrett et al., in review) of previously included fractures.

It is interesting that although C_v does not account for fracture position, it does not vary significantly with size threshold (Figure 6.5b). Lack of systematic variation in C_v indicates that σ and $\bar{S}$ change in approximately the same proportion (Figure 6.5a). We interpret this as evidence that the degree of clustering is similar across most of aperture range of the Pedernales fracture data set.

Techniques that ignore the size and position of fractures intersected along a scanline have at best a limited utility to quantify the spatial arrangement of fractures. However, this problem is exacerbated when results are presented without any information about the fracture sizes measured (Figures 6.2b and 6.7b). As explained by Ortega et al. (2006) using graphs of cumulative frequency of fracture aperture, comparison of fracture intensity between different layers is only meaningful when common thresholds of fracture size are used. Because a fracture size threshold is inevitable in data from natural fractures, it is imperative that, regardless of the technique used, any quantification of the spatial arrangement be qualified by the range of fracture sizes considered.

2.3.5 Fracture Clustering

Because randomly arranged fractures display some degree of clustering (Priest and Hudson, 1976), distinguishing random (Figure 6.1a) from non-random arrangements (Figure 6.1b) can be done by comparing a quantification of clustering (Marrett et al., in

review). Distinguishing if fractures along a scanline are randomly arranged in space or not has implications for the understanding of fracture evolution. If the flaws from which fractures are assumed to grow are randomly arranged, detecting a random arrangement of fractures might indicate that the fractures did not self organize during their evolution (Dershowitz and Einstein, 1988; Rives et al., 1992).

Only one technique (C_v) can determine if a fracture set is more or less clustered than an equivalent (in terms of number of fractures and scanline length) arrangement with randomly positioned fractures. However, it cannot quantify several other attributes of a clustered spatial arrangement: fracture arrangement inside clusters (e.g., fractal; Marrett et al., in review), arrangement among clusters (e.g., periodic; Marrett et al., in review), cluster width, and cluster spacing.

The arithmetic mean and the median of fracture spacings fail to quantify the clustering of fractures in any way, because they disregard the individual values of spacings and the sequence of those spacings along a scanline. Consequently, they are unable to differentiate between random and non-random arrangements of fractures (Figures 6.1a and 6.1b). The other descriptive statistic studied here, C_v, is capable of detecting some random arrangements of fractures because it relates the mean to the standard deviation (σ), which quantifies the dispersion of fracture spacings.

Although frequency distributions do not disregard individual values of fracture spacing, they ignore the sequence of fracture spacings and therefore do not address fracture position. For instance, they do not distinguish between small spacings that are concentrated in clusters and those that are nonsystematically arranged (Figures 6.1a and 6.1b). Frequency distributions can recognize when fracture spacings follow a negative exponential distribution (Narr and Suppe, 1991; Gillespie et al., 2001), the kind of distribution that derives from randomly arranged fractures (Priest and Hudson, 1976;

Rives et al., 1992). However, non-random arrangement of fractures can also generate negative exponential distributions (Figure 6.1b). Therefore, detecting a negative exponential distribution can only establish that the fractures under study might be, but not necessarily are, randomly arranged (Rouleau and Gale, 1985).

3. NORMALIZED CORRELATION COUNT (NCC)

Normalized Correlation Count (NCC) is a new technique (Marrett et al., in review) that quantifies the spatial arrangement of fractures while overcoming two major limitations of traditional techniques: the fact that they do not account for the sequence of fracture spacing values (a proxy for the spatial position of fractures) and that they ignore fracture sizes (Gomez and Marrett, in review). Although NCC was not the only technique evaluated by Marrett et al. (in review), it was more robust and faster computationally than the other two techniques (normalized semivariogram and correlation sum). An important strength of NCC is that it can quantify both fractal and periodic arrangement of fractures (Marrett et al., in review).

3.1 Fundamentals of NCC

Unlike other techniques that address only the spacing between nearest neighbor fractures and ignore the sequence of fracture spacings (Gomez and Marrett, in review), NCC uses the distance between all pairs of fractures, implicitly addressing the sequence of spacings, a proxy for the study of the spatial arrangement of fractures (Marrett et al., in review). In summary, NCC is a technique that quantifies the number of pairs of fractures (or other discrete structures like deformation bands) as a function of distance between fractures (length scale), normalized by the number of fracture pairs for an equivalent (in terms of number of fractures, fracture strain and scanline length) random arrangement of fractures. Normalization by an a priori expression for randomness yields a measure of fracture organization that is referred to as spatial correlation (Marrett et al., in review).

Variation of spatial correlation with length scale provides more meaningful characterization of spatial arrangement than any single statistic can.

NCC generates quantitative measures of spatial arrangement as a function of length scale by analyzing fracture positions. Fracture spacings combined with their sequence are used to calculate fracture positions along a scanline, which provide the same information as fracture spacings combined with their sequence along a scanline. NCC is discrete technique in the sense that the spatial correlation is estimated independently for each range of length scales. Different graduations of length scale can be used to study different types of spatial arrangement. For instance, logarithmic graduations of length scale are most effective at detecting fractal arrangement of fractures inside clusters, whereas linear graduations of length scale are typically used to identify periodic arrangements (Marrett et al, in review).

Normalization using an analytical calculation of the fracture pairs for a random arrangement of fractures allows quantification of the spatial arrangement of fractures relative to randomly arranged fractures (Marrett et al., in review). Therefore, a spatial correlation equal to 1 indicates that the fracture data set under analysis has the same number of fracture pairs separated by distances within a given range of length scales as an equivalent data set with randomly arranged fractures. Likewise, a spatial correlation larger or smaller than 1 indicates that the fracture data set under analysis has more or less, respectively, fracture pairs separated by distances within a given range of length scales than an equivalent data set with randomly arranged fractures.

Normalization of the correlation count is done using an analytical equation for a random arrangement of fractures (Marrett et al, in review). To verify the validity of this equation, the number of fracture pairs separated a given range of length scales is independently determined for a number (typically at least 100) of randomized versions

(position along scanline for each fracture is randomly assigned) of the data set under analysis. Then, the average number of fracture pairs is calculated for each length scale considered. Then, the average is also normalized by the above mentioned analytical equation. If the resulting average spatial correlation of the randomized data sets approximately follows a value of 1, then the equation used for the spatial correlation of a random arrangement of fractures is validated (Marrett et al., in review).

In addition, the spatial correlations of the randomized versions of the data set are also used to calculate a 95% confidence interval (Marrett et al., in review) around the average spatial correlation for all the random arrangements. At a given length scale, a spatial correlation larger than 1 plus the 95% confidence limit indicates that the number of fracture pairs is significantly larger than expected for a random arrangement of fractures. Likewise, at a given range of length scales, a spatial correlation smaller than 1 minus the 95% confidence limit denotes a data set with a number of fracture that is significantly smaller than expected in a random arrangement (Marrett et al., in review).

3.2 Definition of NCC

This section is dedicated to explain step-by-step how NCC is calculated with the aim of facilitating the understanding of NCC plots (spatial correlation vs. length scale) using the Pedernales data set (Table 2.2) as example. NCC is the difference between two values of correlation sum normalized to a statistically equivalent random fracture arrangement (Marrett et al., in review).

3.2.1 Correlation Sum

The correlation sum (also known as the two-point correlation integral) is a technique that has been used to study the spatial arrangement of fractures in a 2D fashion (e.g., Bour and Davy, 1999; Bonnet et al., 2001) by measuring the distances between the center points of fracture traces in a plane. One of the advantages of the correlation sum

technique, and consequently of the correlation count technique, is that fracture size data are not required although they can be used. Two-dimensional use of the correlation sum concentrated on the measurement of the so-called correlation dimension (i.e., the slope on a log-log plot of the correlation sum versus length scale). The NCC defined by Marrett et al. (in review) is based on a 1D version of the correlation sum that analyzes the distances between fractures along a scanline.

To calculate the correlation sum of fractures along a scanline, each fracture is described by the distance from the start of the scanline to the near (x_i) and far (y_i) fracture walls. Although the aperture of the ith fracture can be determined ($y_i - x_i$), it is ignored for the computation of correlation sum. The correlation sum (C) is the fraction of all fracture pairs ($N^2/2 - N/2$) for which the fracture separation ($x_j - y_i$) is less than the length scale (λ_k) under consideration (Marrett et al., in review):

$$C(\lambda_k) = \frac{2}{N(N-1)} \sum_{i=1}^{N} \sum_{j=i+1}^{N} H\left[\lambda_k - \left(x_j - y_i\right)\right] \qquad (10)$$

where N is the total number of fractures and H is the Heaviside step function, which yields a value of 0 for negative arguments (length scale ≤ fracture separation) or a value of 1 for positive arguments (length scale > fracture separation).

For $i = 1$, Equation 10 counts the number of fracture pairs formed by the first fracture with all other fractures along the scanline ($N - 1$) that are separated by a distance less than a given length scale (λ_k). This occurs because when the length scale is greater than fracture separation ($x_j - y_i$), the Heaviside step function will yield a value of 1 (Equation 10). Subsequently, $i = 2$ and the same count will be executed but between the second fracture along the scanline and all the remaining fractures between the second fracture and the end of the scanline. The nested sum operators will generate the number

of fracture pairs for which the fracture separation is less than the length scale under consideration. Multiplying this fracture count by the inverse of the total number of fracture pairs will yield the fraction of all fracture pairs for which the fracture separation is less than the length scale under consideration. Finally, the entire calculation is repeated for the next value of length scale (λ_{k+1}) within a graduation (logarithmic or linear) of length scales (e.g., Pedernales data set, Figure 6.8).

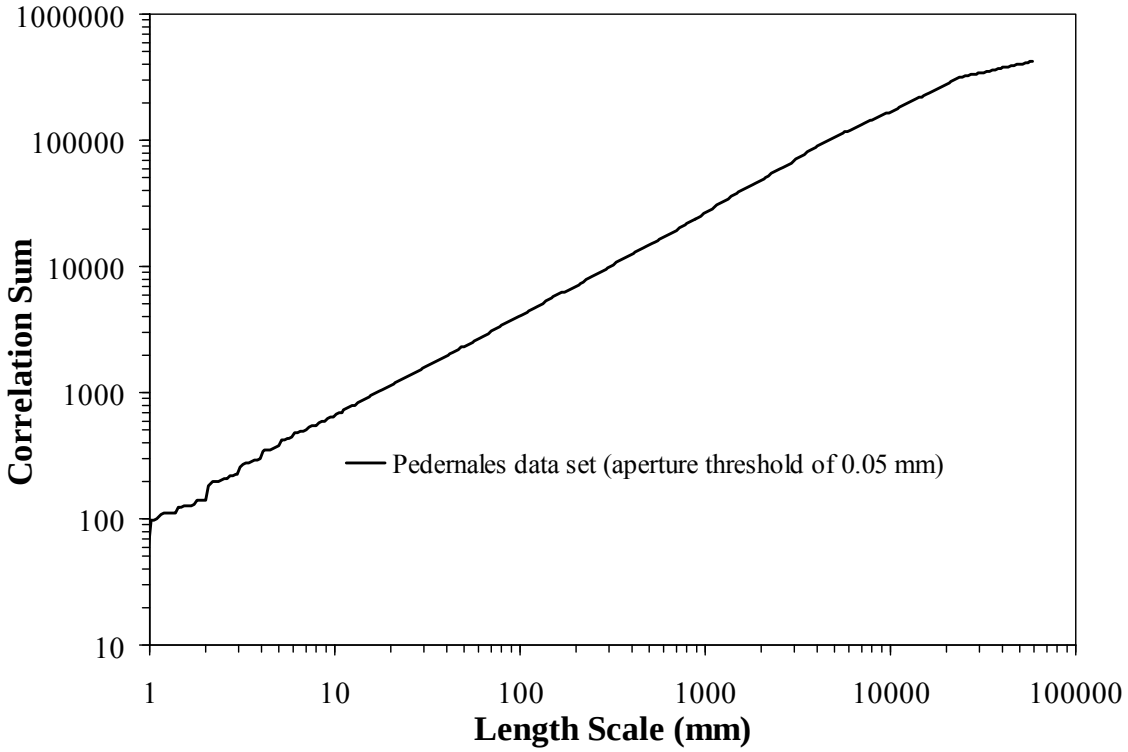

Figure 6.8 Graph of correlation sum (C) versus logarithmic graduation of length scales (λ_k) for veins at Pedernales with an aperture threshold of 0.05 mm.

3.2.2 Correlation Count

Marrett et al. (in review) defined the correlation count (c) as the difference between two values of correlation sum (C):

$$c(\lambda_k) = C(\lambda_{k+m}) - C(\lambda_{k-m}) \quad (11)$$

where m can be adjusted to avoid null results. Therefore, the correlation count is the fraction of all fracture pairs for which the fracture separation is less than λ_{k+m} but greater than λ_{k-m}.

The correlation count amounts to a binned version of the correlation sum, with the index m expressed in terms of number of graduations of length scale. The calculated correlation count for a given range of length scales (λ_{k-m} to λ_{k+m}) is plotted at the center of the above mentioned length scale range (λ_k). The width of the range of length scales (also called length-scale bin) used to calculate the correlation count is equal to 2m + 1 graduations of length scale with m graduations of length scale larger than λ_k and m graduations of length scale shorter than λ_k.

The correlation count for the Pedernales data set is qualitatively similar to the correlation sum of the same data set, although it is smaller and is more variable (Figure 6.9). The correlation count can increase and decrease with increasing length scale, whereas the correlation sum (Figure 6.9) can only increase (Marrett et al., in review). Using logarithmic graduations of length scale, both correlation sum and correlation count for Pedernales data follow a power law (straight line in a log-log plot) with similar exponent for most of the length scale range. This indicates that correlation count and correlation sum are equally useful regarding assessment of fractal scaling (Marrett et al., in review).

Although the correlation sum can also be normalized, the normalized correlation sum is inadequate to characterize periodic behavior, such as regular spacing of fractures, because the integral/summation operator cancels positive correlation with anti-correlation at progressively longer length scales (Marrett et al., in review).

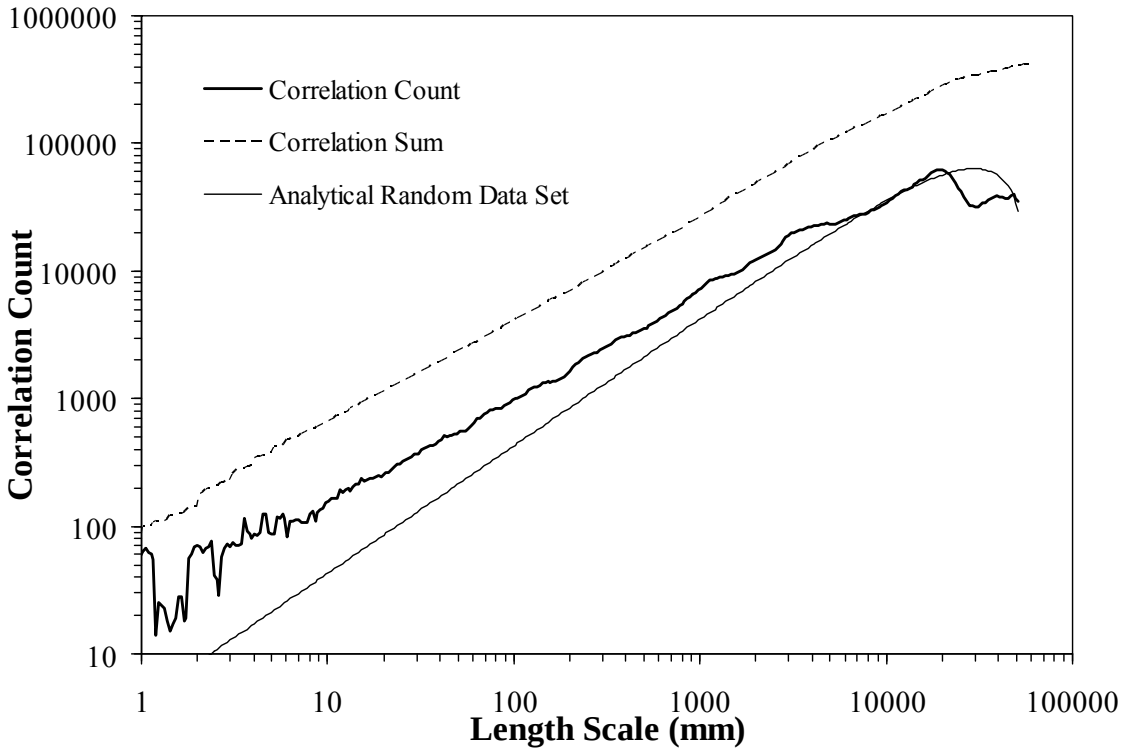

Figure 6.9 Graphs of correlation count (c, thick continuous line), correlation sum (C, dashed line) and analytical random data set (thin continuous line) versus logarithmic graduation of length scales (λ_k) for veins at Pedernales with an aperture threshold of 0.05mm. Width of length-scale bin is 9 graduations of length scale ($m = 4$).

Normalization of the correlation count by the expected correlation count for randomly located fractures (Marrett et al., in review; their Appendix A):

$$c_{random}(\lambda_k) = \frac{\lambda_{k+m} - \lambda_{k-m}}{L}\left(2 - \frac{\lambda_{k+m} + \lambda_{k-m}}{L}\right) \qquad (12)$$

allows the resulting spatial correlation to be directly compared with an equivalent random arrangement of fractures (e.g., Pedernales data set, Figure 6.10). Namely, if spatial correlation is significantly higher than 1 for a given range of length scales centered at λ_k (λ_{k+m} to λ_{k-m}), the fractures under study have more fracture pairs separated by more

than λ_{k-m} but less than λ_{k+m}, compared with an equivalent (in terms of number of fractures and scanline length) random arrangement of fractures. Conversely, if the spatial correlation is significantly lower than 1 for a given range of length scales centered at λ_k the fractures under study have less fracture pairs in the range (λ_{k+m} to λ_{k-m}) than an equivalent random arrangement of fractures.

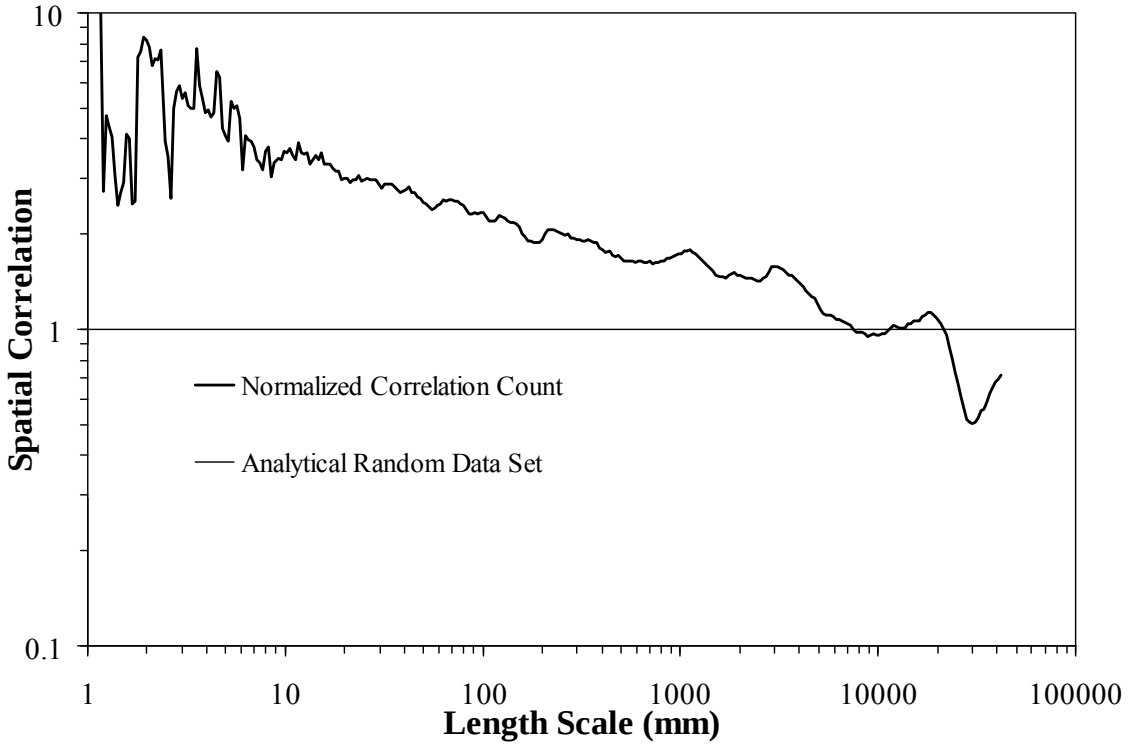

Figure 6.10 Graphs of spatial correlation versus logarithmic graduation of length scales for veins at Pedernales with an aperture threshold of 0.05 mm (thick line) and analytical solution of randomly arranged fractures with an equivalent number of fractures and scanline length as veins at Pedernales (Equation 12, thin line). Width of length-scale bin is 9 graduations of length scale (m = 4).

Due to normalization, randomly arranged fractures yield a spatial correlation of 1 for all values of length scale. The NCC for veins at Pedernales yields a spatial correlation larger than one for at least 4 orders of magnitude below 10 m (Figure 6.10). However, a more meaningful result for NCC is available when the spatial correlation of a particular

data set is compared with the average spatial correlation of 100 randomized versions of the data set under study (Figure 6.11).

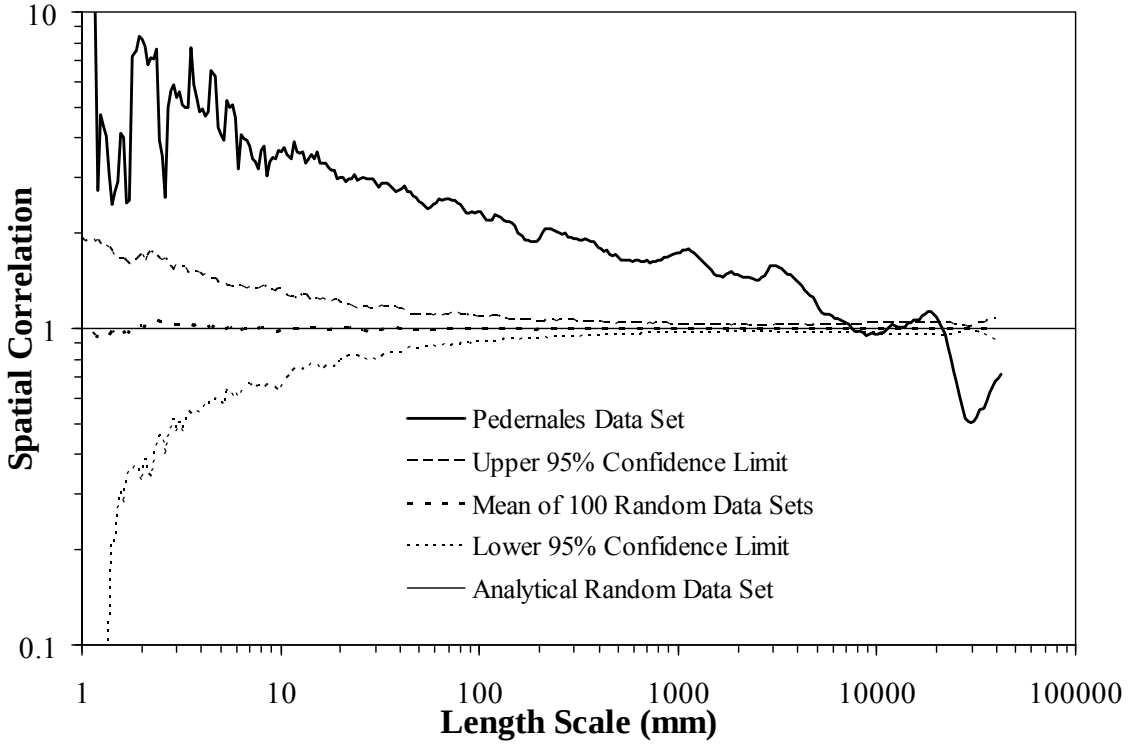

Figure 6.11 Graphs of spatial correlation versus logarithmic graduation of length scales for veins at Pedernales with an aperture threshold of 0.05 mm (thick line), analytical solution of randomly arranged fractures with an equivalent number of fractures and scanline length as veins at Pedernales (thin line), average spatial correlation for 100 randomized data sets (short-dashed line), and upper (long-dashed line) and lower (dotted line) 95% confidence intervals. Width of length-scale bin is 9 graduations of length scale ($m = 4$).

To make this comparison, a number of random versions of the data set under study can be generated (typically 100, Marrett et al., in review). For each randomized version, fracture apertures and scanline length remain unchanged from the measured data set and only fracture position is randomized (Marrett et al., in review). Then, the correlation count for each randomization is individually generated and an average correlation count and 95% confidence interval for each bin of length scale λ_k are

calculated for the ensemble of all randomizations. As with the correlation count for a particular data set, the average correlation count and 95% confidence intervals for all randomized data sets are normalized by the analytical correlation count expected (Equation 12) for a random arrangement of fractures (Figure 6.11).

The average spatial correlation curve for the randomized versions of the Pedernales data set approximately follows the analytical solution of randomly arranged fractures (spatial correlation = 1, Figure 6.11), validating the equation used for the spatial correlation of a random arrangement of fractures (Marrett et al., in review). As expected, the spatial correlation curve for an example randomized set lacks a consistent pattern and does not go significantly outside the 95% confidence interval (short-dashed line, Figure 6.12).

By including the 95% confidence interval about random in the graph of spatial correlation versus length scale, it is possible to detect if a natural data set displays a statistically significant pattern (e.g., power law), which is indicated by a curve that systematically reaches outside the 95% confidence interval. As mentioned before, the veins at Pedernales display a spatial correlation significantly larger than one for at least four orders of magnitude (Figures 6.10 to 6.13). Across three orders of magnitude in length scale (~8.5 to 8550 mm), the spatial correlation of Pedernales veins follows a power-law pattern outside the 95% confidence interval (Figures 6.12, and 6.13), indicating that the veins at Pedernales display a fractal arrangement that is statistically significant.

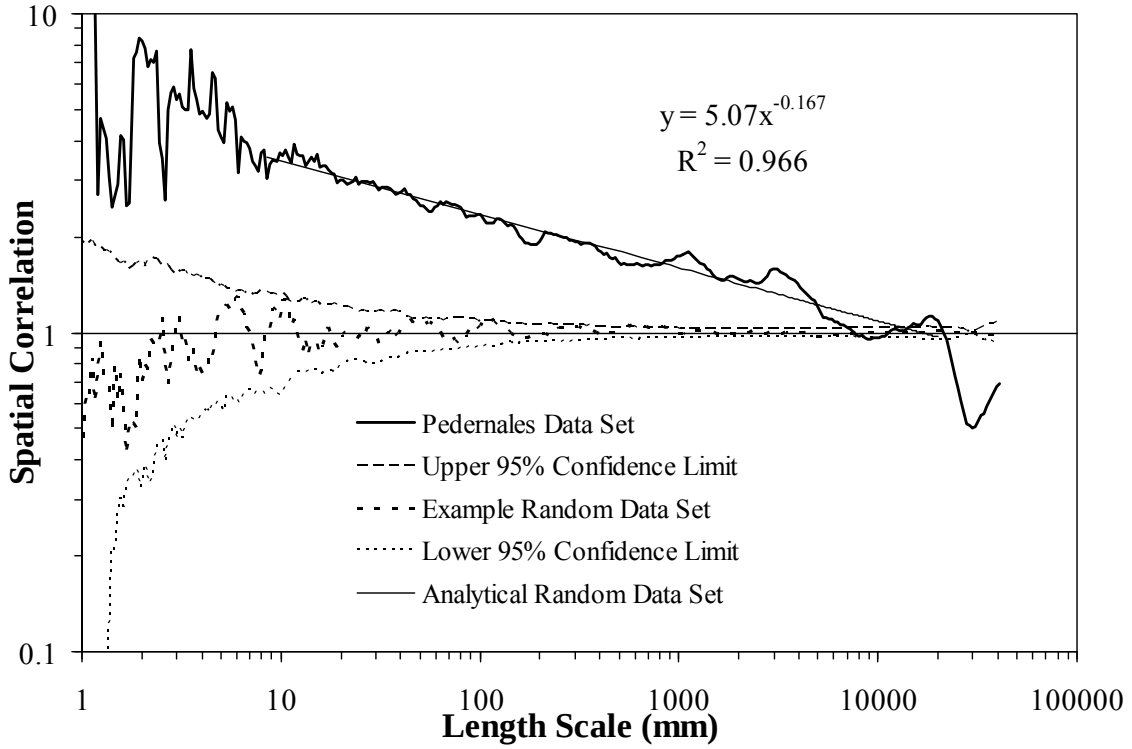

Figure 6.12 Graphs of spatial correlation versus logarithmic graduations of length scale for veins at Pedernales with an aperture threshold of 0.05 mm (thick line), analytical solution of randomly arranged fractures with an equivalent number of fractures and scanline length (thin line), spatial correlation for an example randomized data set (short-dashed line), and upper (long-dashed line) and lower (dotted line) 95% confidence intervals. Width of length-scale bin is 9 graduations of length scale (m = 4).

Increasing the width of the length-scale bin (Equations 11 and 12) typically reduces the local variability of the spatial correlation curves (natural and randomized) displayed in a typical NCC plot and also can subtly change the regressions calculated. For instance, there is a negligible change in the power law regression shown in Figures 6.12 and 6.13 in spite of a 50% reduction (from 9 to 5) in the width of the length-scale bin.

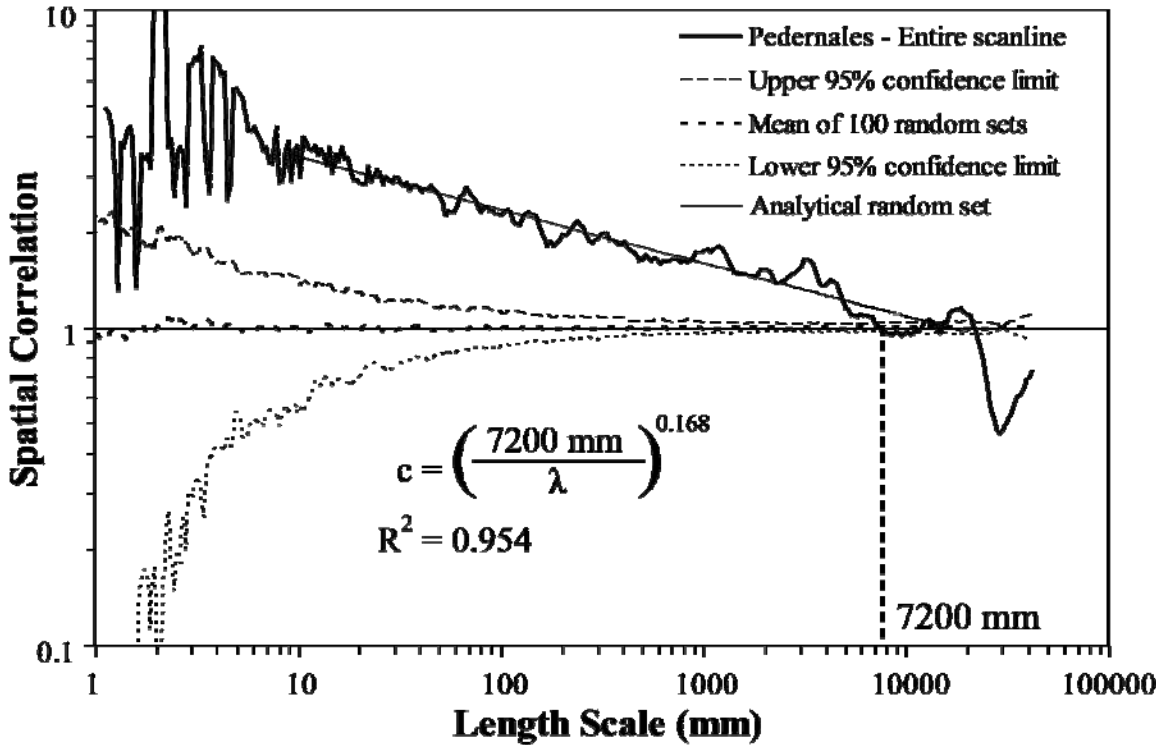

Figure 6.13 Graphs of spatial correlation versus logarithmic graduations of length scale for veins at Pedernales with an aperture threshold of 0.05mm (thick line), analytical solution of randomly arranged fractures with an equivalent number of fractures and scanline length as veins at Pedernales (thin line), average spatial correlation for 100 randomized data sets (short-dashed line), and upper (long-dashed line) and lower (dotted line) 95% confidence intervals. Width of length-scale bin is 5 graduations of length scale (m = 2), about half of the size used in Figure 6.12.

Of the three techniques evaluated by Marrett et al. (in review), NCC was most effective for detecting fractures with periodic arrangements. For example, using a linear graduation of length scales, veins of the Palmas 11 LR data set display (Figure 6.14) a pattern of spatial correlation comprising periodic peaks (spatial correlation > 1) and troughs (spatial correlation < 1).

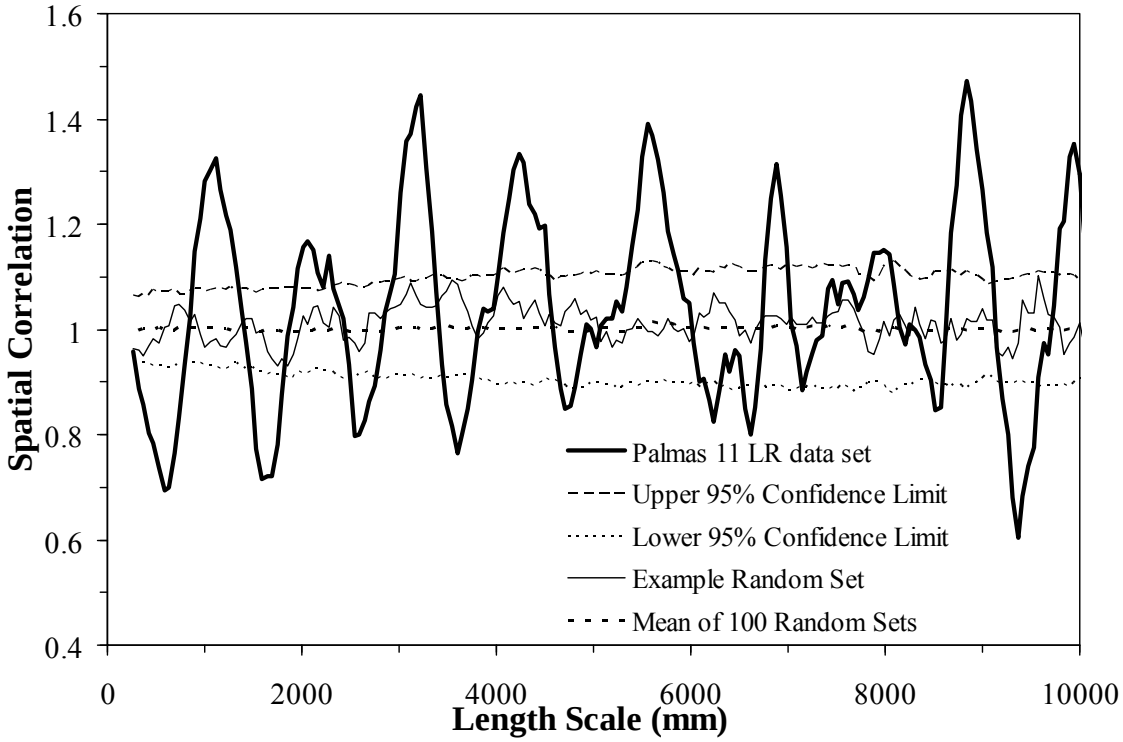

Figure 6.14 Graphs of spatial correlation versus linear graduations of length scale for veins of the Palmas 11 LR data set with an aperture threshold of 0.95 mm (thick line), an example randomized set generated with an equivalent number of fractures and scanline length (thin line), average spatial correlation for 100 randomized data sets (short-dashed line), and upper (long-dashed line) and lower (dotted line) 95% confidence intervals. Linear axis of spatial correlation (instead of logarithmic) was used to facilitate the detection of patterns in curves with small differences in spatial correlation. Width of length-scale bin is 9 graduations of length scale (m = 4). Maximum length scale shown is about half of the total scanline measured.

Peaks of spatial correlation occur at a length scale corresponding to the dominant cluster spacing and its multiples, and troughs occur at intermediate length scales. With one exception, all peaks and troughs are outside the 95% confidence interval and therefore represent statistically significant clusters with a periodic arrangement (Figure 6.14).

As with logarithmic graduations of length scale, the spatial correlation curve for the average of 100 randomized versions approximately follows the analytical solution for randomly arranged fractures when linear graduations of length scale are used (spatial correlation = 1, Figures 6.14, and 6.15), validating the equation used for spatial correlation of a random arrangement of fractures (Marrett et al., in review). Also, the spatial correlation curve for an example randomized set lacks a consistent pattern and does not go significantly outside the 95% confidence interval (thin line, Figure 6.14). Marrett et al. (in review) also noticed that the amplitudes of peaks and troughs decrease with increasing length scale, partly due to imperfect periodicity and partly due to a finite range effect.

4. DIFFERENT TYPES OF SPATIAL ARRANGEMENT OF FRACTURES

Marrett et al. (in review) recognized five types of spatial arrangement of fractures based on patterns in curves of spatial correlation versus length scale and also provided the physical meaning of some of those patterns. These types of spatial arrangements were recognized much earlier by Shepherd et al. (1981), but their proposed method for quantification was not free of interpreter's bias.

4.1 Indistinguishable from Random

The first type of fracture arrangement, indistinguishable from random (Figures 6.15a and 6.15e), is indicated when the spatial correlation of a data set under analysis approximately follows the flat pattern (or varies in a non-systematic fashion) of a random arrangement (spatial correlation = 1, Figures 6.15a and 6.15e) and consistently stays within the 95% confidence interval with logarithmic (Figures 6.16a, and length scales < 40 mm in Figure 6.17a) or linear (Figure 6.16b) graduations of length scale. A fracture arrangement that is indistinguishable from random means that fractures retained the

random arrangement of flaws from which they are assumed to have originated (Ackermann and Schlische, 1997; Olson, 2004).

4.2 Self-organized Cluster

A second type of spatial arrangement of fractures is what Marrett et al. (in review) called a self-organized cluster (Figure 6.15b). This type of arrangement is indicated by a pattern of power-law variation (straight line in a log-log plot) of spatial correlation with length scale outside the 95% confidence interval (typically using logarithmic graduations), which suggests self-organization of fractures inside clusters (e.g., Figures 6.11 to 6.13, and 6.18a). As discussed by Marrett et al. (in review), clustering is fractal in the sense that clusters are formed by groups of smaller clusters, which are formed by still smaller clusters (Chapter 8; Hare and Marrett, in review).

For power law patterns of spatial correlation with length scale, Marrett et al. (in review) interpreted the length scale at which the power-law has a spatial correlation = 1 (analytical random arrangement of fractures) as the width of observed clusters (Figures 6.15b, 6.17a and 6.18a). Marrett et al. (in review) also interpreted the slope (exponent) of the power-law pattern as a scale-independent measurement of the degree of fracture clustering (Figures 6.15b and 6.18a), with steeper slopes indicating more intense clustering (i.e., more fractures in clusters at the expense of inter-cluster regions).

Figure 6.15 Patterns of spatial correlation versus length scale, as defined in Marrett et al. (in review). Each pattern indicates a distinct spatial arrangement. Using logarithmic graduations of length scale, three spatial arrangements can be distinguished (left column): (a) a flat-line pattern of spatial correlation (slope = 0; correlation = 1) indicates no statistically significant organization, or indistinguishable from random, (b) a power-law pattern of spatial correlation (slope ≠ 0), which indicates fractal clustering (self-organization), (c) a plateau pattern of spatial correlation (slope = 0; correlation ≠ 1), which indicates statistically significant clustering due to some process other than self organization (e.g., externally imposed control or inherited faulting or folding). Using linear graduations of length scale, three different spatial arrangements can be distinguished (right column): (e) a flat-line pattern of spatial correlation similar to (a), indicating an arrangement that is indistinguishable from random, (f) periodically arranged fractures and (g) periodically arranged clusters, which are characterized by a pattern of periodic peaks and troughs. Combinations of any or all of these patterns can occur (d), with different patterns characterizing different ranges of length scale.

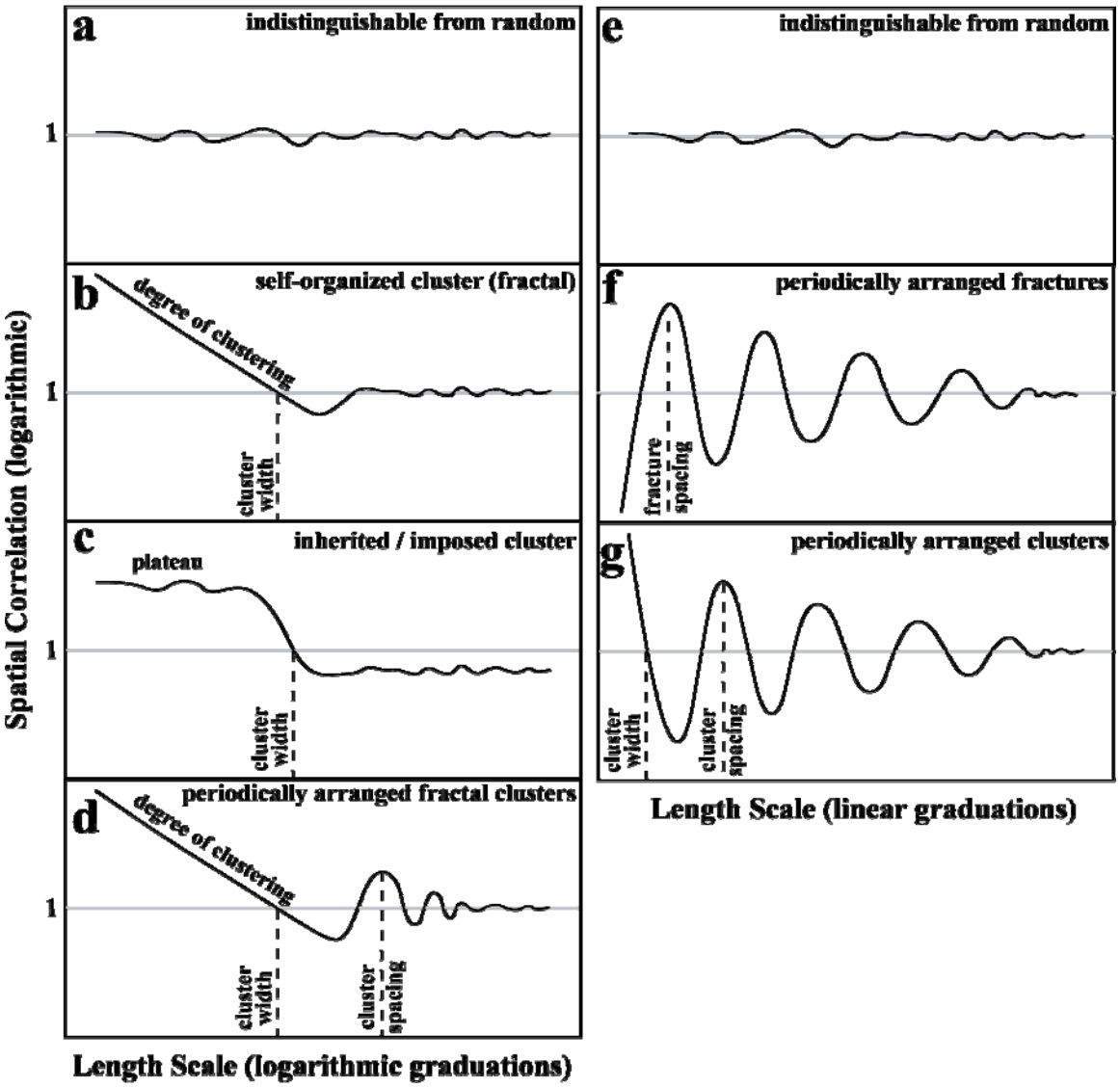
a
indistinguishable from random
1
b
self-organized cluster (fractal)
degree of clustering
cluster width
c
inherited / imposed cluster
plateau
cluster width
d
periodically arranged fractal clusters
degree of clustering
cluster width
cluster spacing
Spatial Correlation (logarithmic)
Length Scale (logarithmic graduations)
e
indistinguishable from random
f
periodically arranged fractures
fracture spacing
g
periodically arranged clusters
cluster width
cluster spacing
Length Scale (linear graduations)

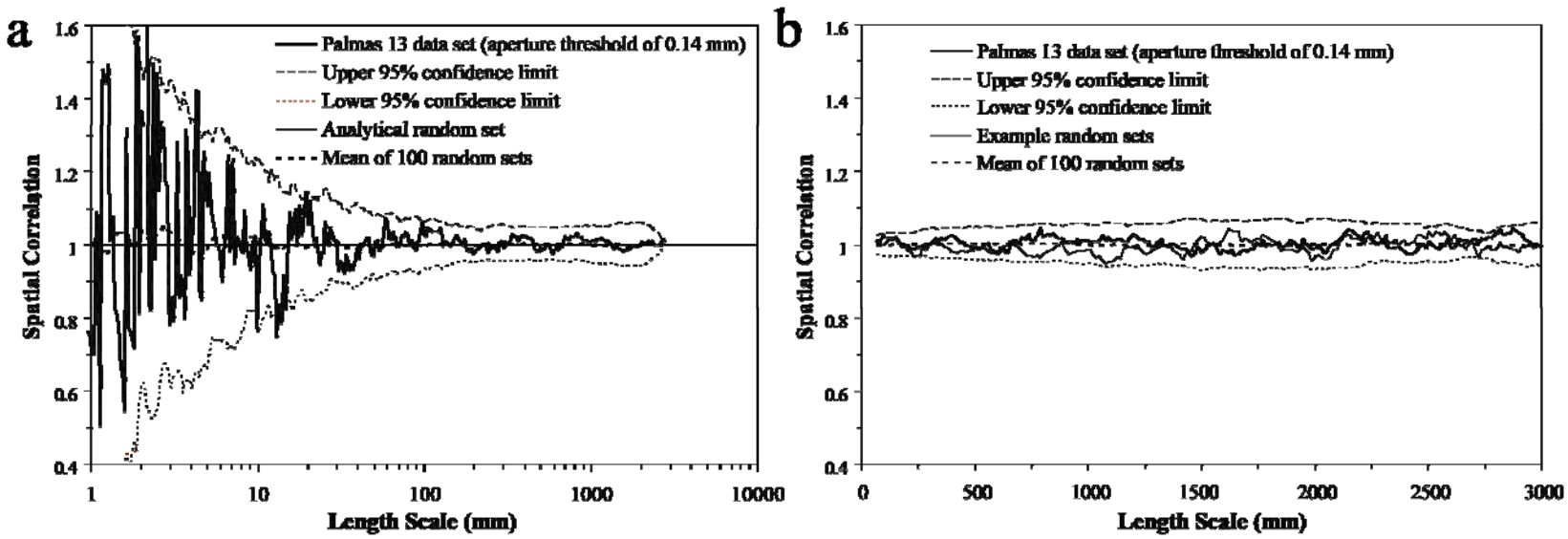

Figure 6.16 Graph of spatial correlation vs. (a) logarithmic graduations of length scale and (b) linear graduations of length scale for the Palmas 13 data set (all fractures measured, aperture threshold = 0.14 mm, thick continuous line). The thin discontinuous (long dashes) line represents the upper 95% confidence interval while the thin discontinuous (short dashes) line represents the lower 95% confidence interval. Thin dotted line corresponds to the mean of 100 randomized data sets. Linear axis of spatial correlation (instead of logarithmic) was used to facilitate the detection of patterns in curves with small differences in spatial correlation. Width of length-scale bin is 7 graduations of length scale (m = 3).

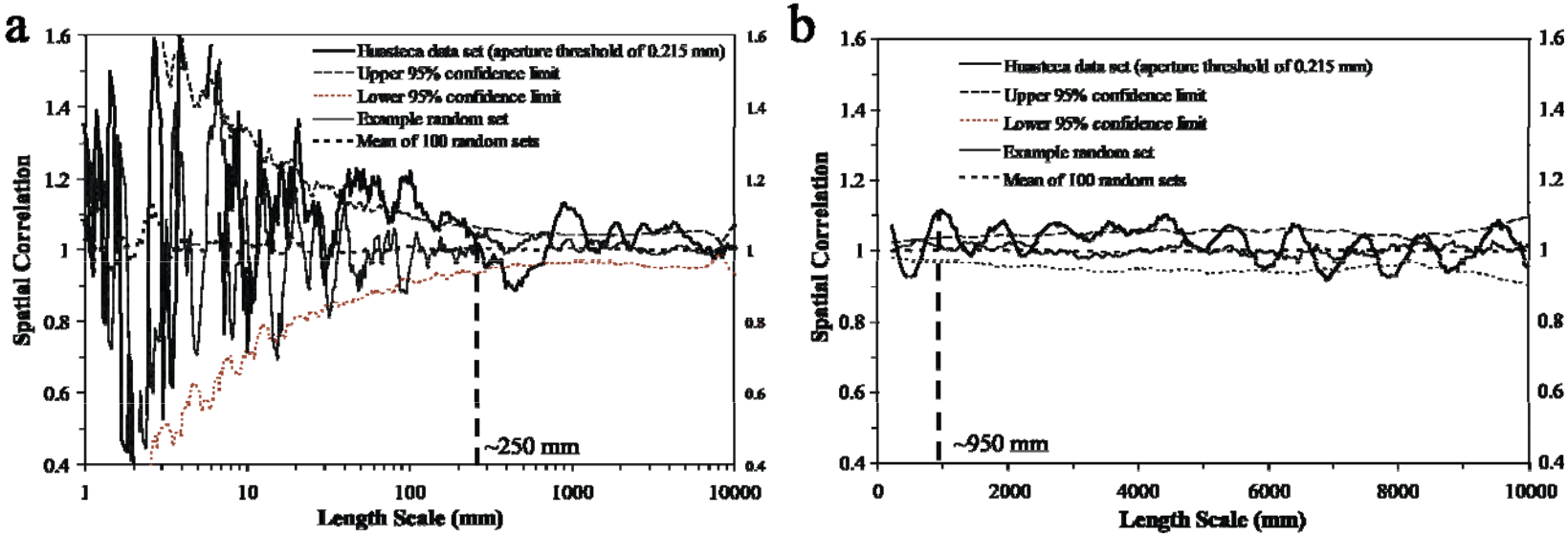

Figure 6.17 Graph of spatial correlation vs. (a) logarithmic graduations of length scale and (b) linear graduations of length scale for the Huasteca data set (set A only, 581 fractures measured, aperture threshold = 0.215 mm, thick continuous line). Analytical solution of randomly arranged fractures with an equivalent number of fractures and scanline length as veins at Huasteca (thin line). The thin discontinuous (long dashes) line represents the upper 95% confidence interval while the thin discontinuous (short dashes) line represents the lower 95% confidence interval. Thin dotted line corresponds to the mean of 100 randomized data sets. Linear axis of spatial correlation (instead of logarithmic) was used to facilitate the detection of patterns in curves with small differences in spatial correlation. Width of length-scale bin is 7 graduations of length scale (m = 3).

4.3 Periodically Arranged Fractures or Periodically Arranged Fracture Clusters

A periodic (regularly-spaced) arrangement of fractures or fracture clusters is best detected using linear graduation of length scales (Figures 6.15e and 6.15g). This type of spatial arrangement produces a pseudo-sinusoidal pattern with approximately evenly spaced peaks and troughs of spatial correlation that are outside the 95% confidence limits and reflects self organization that is opposite of fractal clustering. (Marrett et al., in review).

As mentioned by Marrett et al. (in review), the peak at the shortest length scale indicates the dominant spacing and multiples of the dominant spacing are marked by additional peaks which are separated by intervening troughs (Figure 6.14). Patterns of alternating peaks and troughs of spatial correlation with peaks at length scale multiples of the first peak indicate periodically arranged fractures (Figure 6.15f) or periodically arranged clusters (Figure 6.15g). The key to differentiate periodically arranged fractures from periodically arranged fracture clusters is the trend of the curve of spatial correlation at length scales smaller than the dominant spacing. Decreasing spatial correlation for most length scales smaller than the first peak of spatial correlation indicates periodically arranged fractures (Figure 6.15f) whereas periodically arranged clusters (e.g., Figures 6.14, 6.17a, and 6.18a) exhibit increasing spatial correlation for most length scales smaller than cluster spacing (Figure 6.15g).

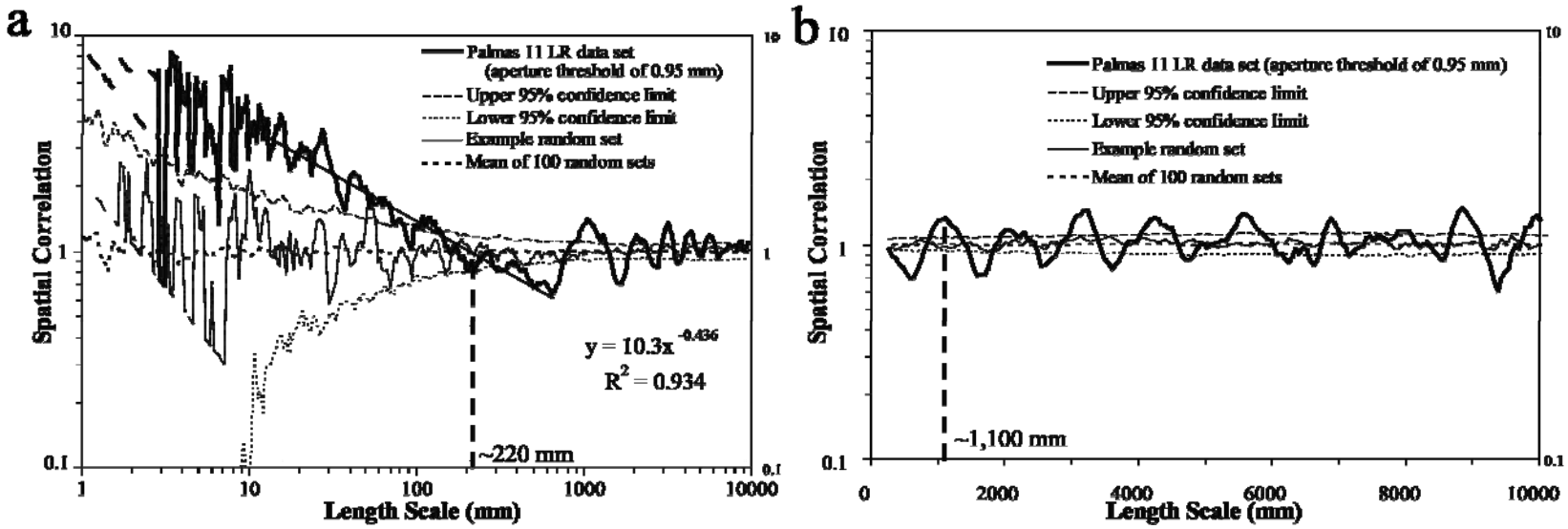

Figure 6.18 Graph of spatial correlation vs. (a) logarithmic graduations of length scale and (b) linear graduations of length scale for the Palmas 11 LR data set (262 fractures measured, aperture threshold = 0.95 mm, thick continuous line). Analytical solution of randomly arranged fractures with an equivalent number of fractures and scanline length as veins at Palmas 11 LR (thin line). The thin discontinuous (long dashes) line represents the upper 95% confidence interval while the thin discontinuous (short dashes) line represents the lower 95% confidence interval. Thin dotted line corresponds to the mean of 100 randomized data sets. Power law in (a) was calculated using spatial correlation of Palmas 11 LR data set between length scales of 12 and 664 mm. Width of length-scale bin is 5 graduations of length scale (m = 2).

4.4 Inherited Cluster

A fourth type of spatial arrangement (Figure 6.15c) was interpreted as an inherited/imposed cluster by Marrett et al. (in review). This type of spatial arrangement generates a plateau pattern that differs from the power law pattern in that the straight line in a log-log plot of spatial correlation versus length scale has a slope equal or close to 0 and has spatial correlation above the upper 95% confidence interval (Figure 6.19a). For inherited/imposed clusters, the length scale intercept with a spatial correlation of 1 also indicates the width of such a cluster. In addition, the elevation of the plateau increases with an increase in the ratio of fracture intensity within the cluster to inter-cluster fracture intensity, or with a decrease in the ratio of cluster width to scanline length (Marrett et al., in review).

Marrett et al. (in review) argued that the plateau pattern is the result of externally driven processes that dominate fracture arrangement. Such processes can be active before or during fracturing. For instance, the spatial distribution of diagenetic fluids might produce lateral variability in the mechanical attributes of rocks (e.g., more cement could make the rock more brittle). Later deformation might result in areas with higher fracture intensity, which reflect the distribution of diagenetic cements rather than self organization of fractures (Marrett et al., in review). Also, externally imposed variations of strain magnitude, such as in different domains of a fold, might facilitate the development of fractures in certain areas more than in others. The resulting variation in fracture intensity would reflect the folding rather than self organization by fractures (Marrett et al., in review).

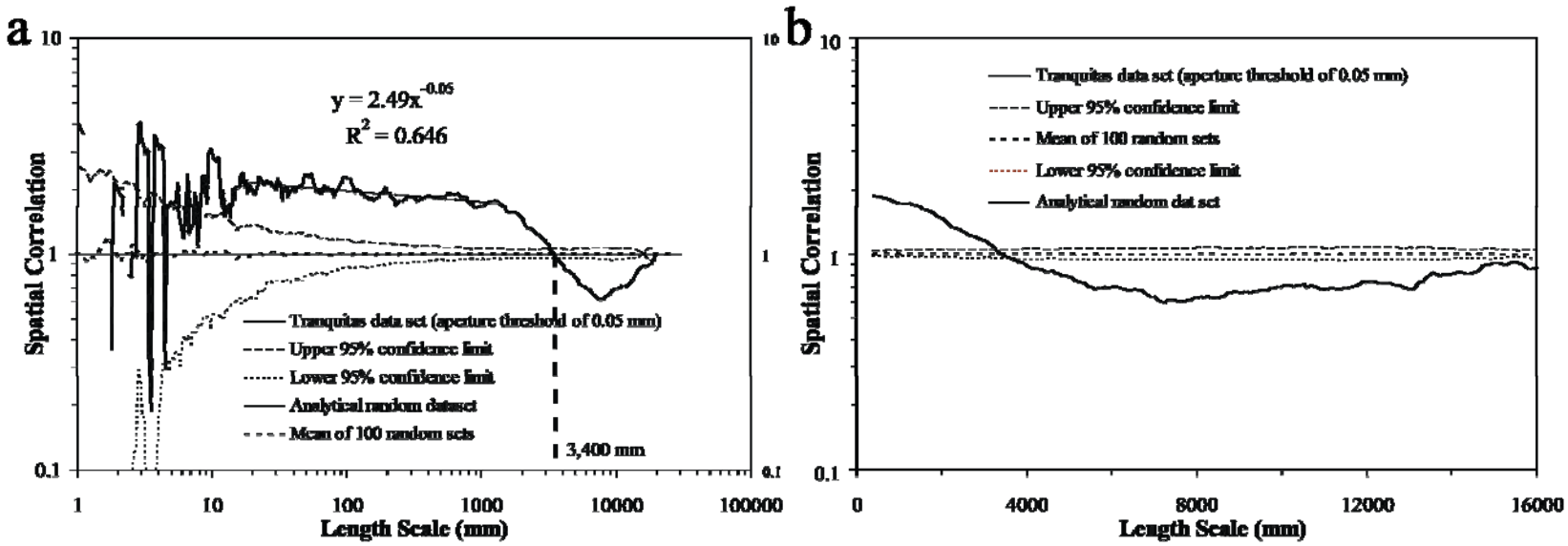

Figure 6.19 Graph of spatial correlation vs. (a) logarithmic graduations of length scale and (b) linear graduations of length scale for the Tranquitas data set (496 fractures, aperture threshold = 0.05 mm, thick continuous line). Analytical solution of randomly arranged fractures with an equivalent number of fractures and scanline length as veins at Tranquitas (thin line). The thin discontinuous (long dashes) line represents the upper 95% confidence interval while the thin discontinuous (short dashes) line represents the lower 95% confidence interval. Thin dotted line corresponds to the mean of 100 randomized data sets. Power-law in (a) was calculated using spatial correlation of Tranquitas data set between length scales of 16 and 1,410 mm. Notice the low exponent of the power law, indicative of an almost horizontal line. Width of length-scale bin is 7 graduations of length scale (m = 3).

4.5 Combination

Finally, combinations of patterns have been detected. Namely, a single fracture set can have different arrangements at different ranges of length scale (Marrett et al., in review). For instance, fractures inside clusters can have a fractal arrangement (Figures 6.18a and 6.17a for length scales > 40 and < 250 mm), whereas clusters of fractures can be periodically arranged (Figures 6.17b and 6.18b).

5. METHODOLOGY TO CALCULATE FRACTURE INTENSITY

In 1D quantitative studies of fractures, fracture intensity is a measure that quantifies how many fractures are per unit of length (Nelson, 2001). A similar measurement to fracture intensity is fracture density. Although fracture intensity and fracture density have the same units, fracture intensity is calculated by counting the number of fractures over a distance whereas fracture density is typically calculated by dividing the fracture length measured on a wellbore image over the wellbore area imaged (W. Narr, personal communication, 2004).

Although it is possible to quantify the fracture intensity of an entire fracture set by simply dividing the number of fractures by the scanline length (1D study) or the area (2D study) over which the fractures were measured, this calculation does not take into account fracture size (Ortega, 2002). And, as shown by Ortega et al. (2006), calculations of fracture intensity that ignore fracture size cannot be used to compare different fracture sets (Ortega et al., 2006). But even if fracture size is considered, a single value of fracture intensity for an entire scanline will not be able to characterize (cluster width, location, spacing) the clustering in a particular data set (Gomez and Marrett, in review).

However, by calculating the fracture intensity in a fraction (window size) of the entire scanline and repeating the calculation at evenly spaced (window step) locations along the scanline, it is possible to generate a curve of fracture intensity that varies with location along scanline, which in turn can be used to detect peaks and troughs of fracture intensity, with peaks indicating the location of clusters and troughs indicating the separation between clusters. However, the two parameters needed for the calculation of fracture intensity (window size and window step) impose a bias that can affect how clustering (e.g., location and width of clusters) is interpreted from a curve of fracture

intensity (e.g., Figure 6.20). An unbiased way of calculating fracture intensity has not been published yet. Typically, a fracture researcher change the window size and the window step until he or she obtains a curve of fracture intensity that generates peaks that match with the location of clusters detected by qualitative observation of the fracture data set (Wayne Narr, personal communication, 2004).

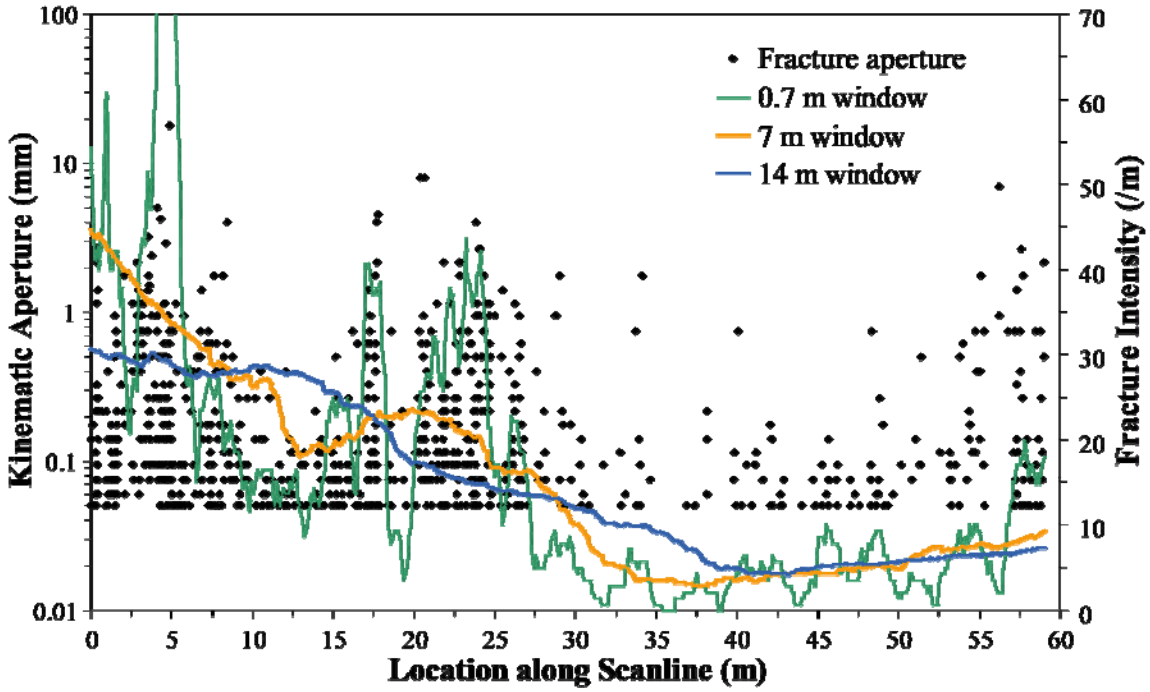

Figure 6.20 Kinematic aperture and fracture intensity versus location along scanline for the Pedernales data set. Three curves of fracture intensity were calculated, each curve with a different window size but the same window step of 0.1 m. A window size of approximately the size of cluster width (7 m, orange line), as estimated by NCC (Figure 6.13), displays two peaks of fracture intensity which match the location of qualitatively detected clusters centered approximately at 3 and 22 m. A window size equal to a tenth of cluster width (0.7 m, green line) displays several peaks of fracture intensity, several of which are inside a single cluster. In contrast, a window size twice the size of cluster width does only detect correctly the cluster at the end of the scanline, but wrongfully suggested a cluster at 12.5 m along the scanline.

Moreover, NCC can be used to induce a more systematic approach in the calculation of fracture intensity along a scanline (Figures 6.20 and 6.21). In the case of fractures with a fractal arrangement inside clusters, NCC can be used to estimate cluster width (Marrett et al., in review), which in turn can be used as window size for the calculation of fracture intensity. A window size equal to cluster width should enhance the detection of clusters because when the window for calculating fracture intensity is positioned over a cluster, the number of fractures (and therefore the fracture intensity) will be the highest along the scanline. A window size smaller than cluster width will generate an irregular curve that reflects heterogeneities smaller than cluster width, whereas a window size larger than cluster width will always include fractures inside and outside a cluster, which will reduce the size of the peak of fracture intensity and will likely generate a smooth curve that might not exhibit all the clusters in the data set. Therefore, whenever fracture intensity is calculated for data sets with a fractal arrangement of fractures inside clusters, a window size equal to cluster width will be used.

For instance, Pedernales data set has a cluster width of approximately 7 m (Figure 6.13), and when the window size is equal to cluster width (orange curve, Figure 6.20), the curve of fracture intensity display three peaks at 0, 21 and 59 m along the scanline, which roughly matches the location of the qualitatively detected clusters (Figure 6.20). In contrast, a window size equal to a tenth of the cluster width generates peaks of fracture intensity within the qualitatively detected clusters making it more difficult to estimate the number and width of clusters (green curve, Figure 6.20). Also, a window size equal to two times the cluster width exhibits two peaks of fracture intensity, with one of them (12.5 m along the scanline) located between the two clusters qualitatively detected (blue curve, Figure 6.20).

In the case of randomly arranged fractures inside clusters, there is no statistically meaningful cluster width (Marrett et al., in review), and therefore there is no particular window size that would contain more fractures per unit length. For instance, the Palmas 13 data set displays randomly arranged fractures inside (Figure 6.16a) and between (Figure 6.16b) clusters and therefore does not exhibit a statistically meaningful cluster width. When fracture intensity is calculated for the Palmas 13 data set using three different window sizes spanning one order of magnitude, the three curves mimic each other and the only difference is the smoothness of the curve, with the largest window size having the smoother curve (Figure 6.21). Additionally, in contrast to window size, window step does not affect greatly the curve of fracture intensity as long as the window step is small enough to generate an adequate amount of data points that can represent the clustering (R. Marrett, personal communication, 2006). Finally, whenever possible throughout my dissertation, curves of fracture intensity will be generated using a window size equal to the cluster width estimated using NCC.

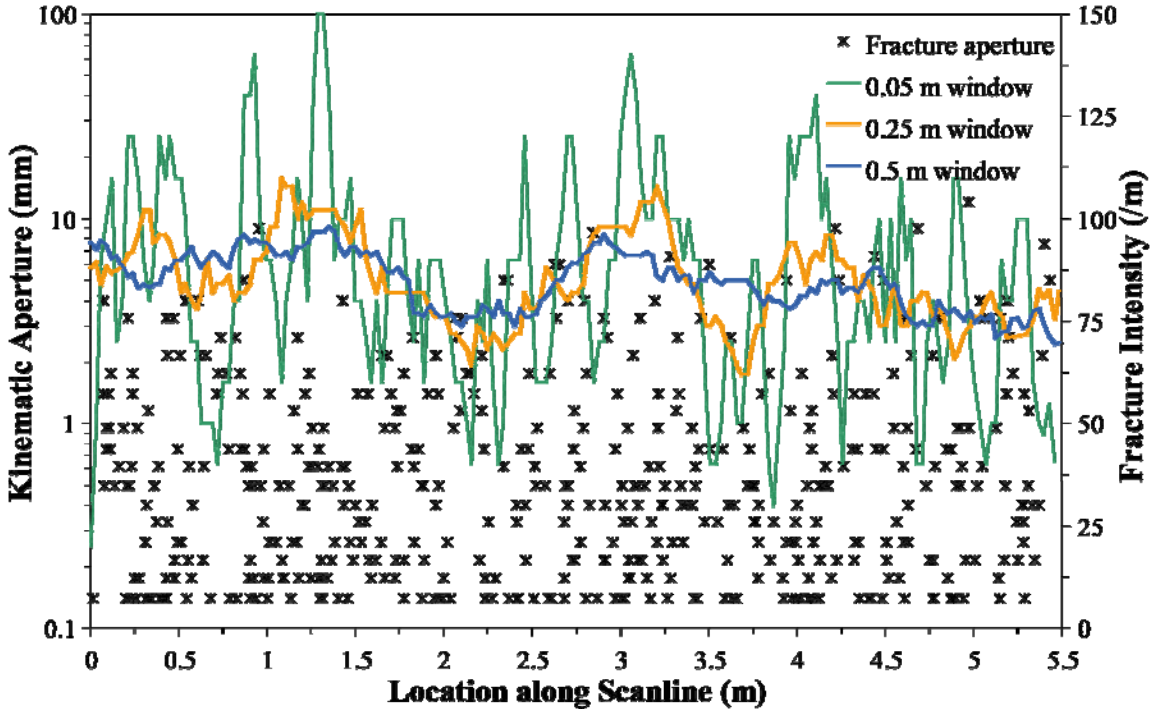

Figure 6.21 Kinematic aperture and fracture intensity versus location along scanline for the Palmas 13 data set. Three curves of fracture intensity were calculated, each curve with a different window size but the same window step of 0.03 m. In contrast to the Pedernales data set (Figure 6.20), the Palmas 13 data set does not have a statistically meaningful cluster width (Figure 6.16a). Curves of fracture intensity for window sizes ranging one order of magnitude (0.05 to 0.5 m) yield peaks at the same locations (1.25, 3, and 4.5 m, approximately). However, the curve with the largest window size (blue line, 0.5 m) is smoother compared with the other two curves.

Chapter 7: Differential Clustering According to Fracture Size

The research presented in this dissertation goes beyond independent quantification of size (aperture) scaling (Chapters 3 and 4) and the spatial arrangement of fractures. Chapter 7 attempts to bring the two issues together by exploring possible relationships between the size and position of a fracture. This chapter is divided in five sections. The first section introduces the hypothesis to be tested, presents the methodologies to be used, and reviews published work on the relationship between fracture aperture and fracture spacing. The second section presents seven data sets used to quantify relationships between fracture size and position. The third section explores the relationship between fracture size and fracture spacing using traditional techniques. The fourth section tests the significance of fracture size in spatial organization by treating size as an additional independent variable in normalized correlation count (NCC) analyses. Finally, the fifth section discusses the results of the previous two sections and describes a set of conclusions.

7.1. INTRODUCTION

Field observations (e.g., Figures 7.1 and 7.2) suggest that opening-mode fractures with the largest apertures are almost exclusively present inside clusters in some arrays (Gomez and Marrett, 2006), the opposite of what Ackermann and Schlische (1997) observed for shear-mode fractures (faults). Because the permeability of a fracture network is dominated by the few largest aperture fractures (Marrett, 1996), understanding the relationship between spatial organization and fracture size potentially can improve fluid-flow modeling of fractured reservoirs and planning of horizontal wells (Gale, 2002). In addition, increased knowledge of the relationship between fracture size and fracture position could validate synthetically modeled fracture networks (e.g., Olson, 2004).

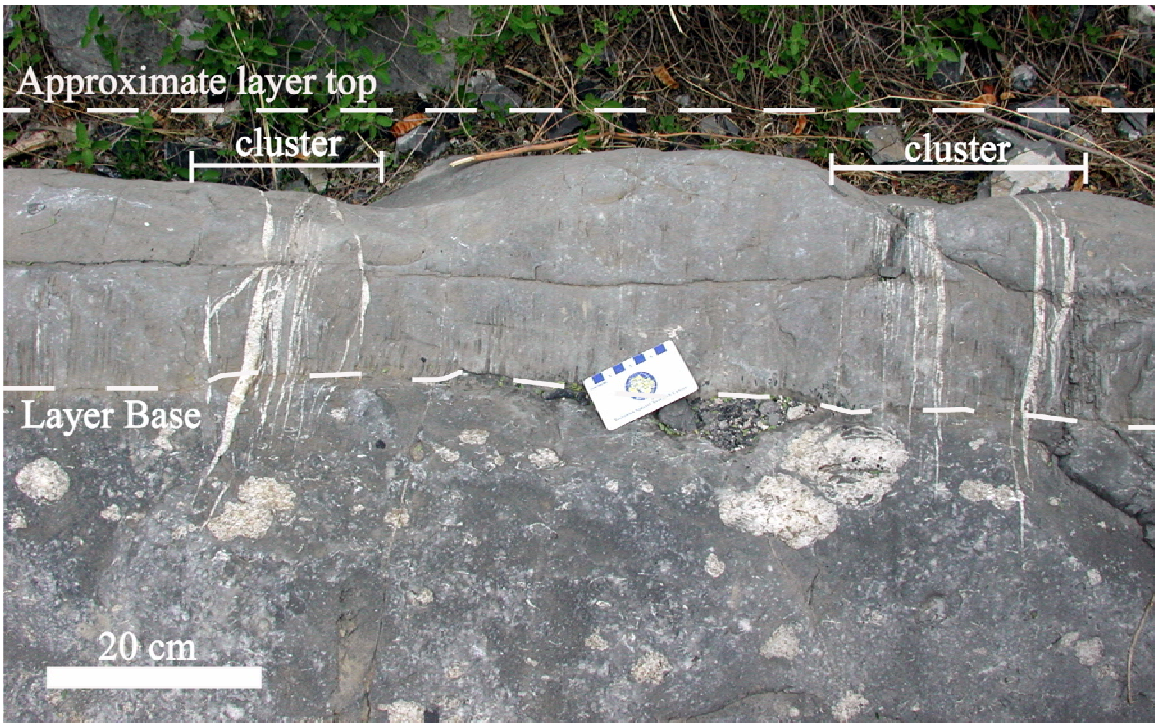

Figure 7.1 Photograph of two clusters of macrofractures in cross-sectional exposure of layer 11 from Palmas canyon (Cupido Formation). Scanline was located approximately half-way between top and base of layer. Notice how fractures with large apertures occur only in clusters. Most fractures are confined inside layer or narrow rapidly in lower layer.

Chapter 7 tests the hypothesis that in fracture sets with statistically significant clusters in scales ranging from outcrop to rock-sample, large fractures are more strongly partitioned into clusters than small fractures and that randomly arranged fractures (with clusters that are not statistically significant) lack a relationship between fracture position and fracture size. Namely, for non-randomly clustered fractures, large fractures are more concentrated inside clusters than small fractures. The hypothesis implies that for fracture sets with statistically significant clusters (Marrett et al., in review) the aperture of a fracture can be statistically related to its position.

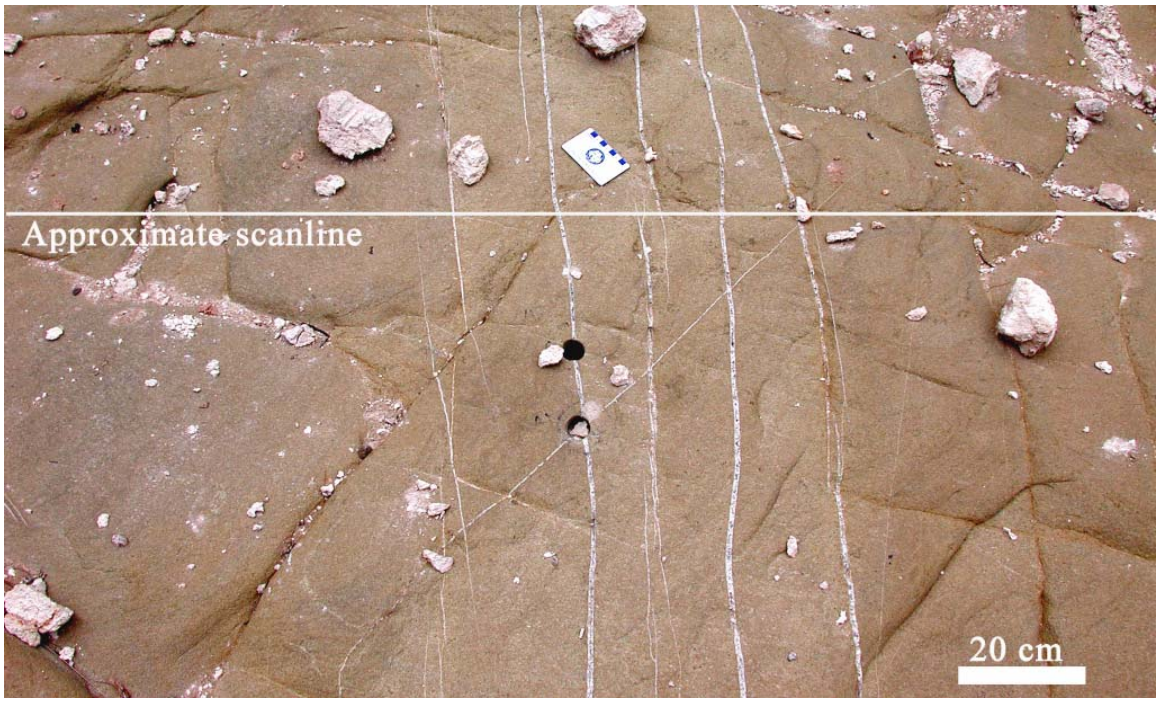

Figure 7.2 Photograph of a cluster of macrofractures in bedding-parallel exposure of layer in Tranquitas location (La Boca Formation). Scanline was approximately perpendicular to macrofracture cluster. Notice the absence of large fractures outside of the cluster.

If the hypothesis is correct for fractures that exhibit statistically significant clusters, then calculations about the horizontal well trajectory needed to reach a permeability threshold should not use the average spacing between large fractures but instead the cluster spacing. In addition, if the hypothesis is correct, then synthetic models of fluid flow (e.g., oil, water and/or gas) in reservoirs should take into account the fact that clusters are not only preferential conduits of fluids because there are more fractures in them, but also because the most permeable fractures, the largest ones, are more clustered than small ones. In the case of modeling the evolution of natural fracture networks, knowing that large fractures are more clustered than small ones should serve as one of the calibration points to validate the resulting modeled fracture networks.

7.1.1 Hypothesis

Chapter 7 will test the hypothesis that large fractures are more partitioned into statistically significant clusters than small fractures, and therefore that a relationship between fracture size and fracture position exists when fractures exhibit non-random clustering. The hypothesis will be tested in rocks with different lithologies (limestone, dolostone and sandstone), different ages (Early Pennsylvanian, Lower Cretaceous and Jurassic), different geologic provinces with different tectonic histories (Forth Worth Basin, above and below the anhydrite decollement in the Sierra Madre Oriental of Mexico), and different scales (outcrop and rock sample). Four approaches will be used to test the hypothesis that large fractures are more partitioned into statistically significant clusters than small fractures.

A crossplot of fracture aperture versus fracture spacing is the simplest and most used approach to study the relationship between fracture size and fracture spacing. The first approach will generate crossplots of fracture aperture versus fracture spacing (or variations of fracture spacing) and search for trends using natural fracture data sets that exhibit different types of spatial arrangements as defined by Marrett et al. (in review). Later, the efficacy of such crossplots in observing a relationship between fracture size and position will be evaluated using the concepts of clustering and spatial arrangement discussed in previous chapters.

The second approach will study NCC results from different subsets of fractures of a single data sets, in which subsets are defined by variable aperture thresholds. By comparing the NCC results (spatial correlation variation with length scale) of fracture subsets with different ranges of fracture aperture it will be possible to describe variations in the spatial correlation according to fracture size. For instance, if there is no variation in the spatial correlation between subsets with different aperture ranges, then clustering is

comparable for large and small fractures. On the contrary, if spatial correlation increases or decreases at length scales corresponding to cluster spacing, then it can be said that different fracture sizes are clustered differently. Two different methods will be used to generate different subsets of fractures. The first method involves using increasingly larger aperture thresholds, resulting in progressive removal of smaller fractures. The second method to generate fracture subsets involves separating fractures that are larger than or equal to an aperture threshold from fractures that are smaller than the same aperture threshold.

The third approach will compare the NCC results of the measured data set with corresponding results of an equivalent (in terms of scanline length, number of fractures and values of fracture aperture) data set with randomly arranged fractures. Randomization of fracture position implies that the values and sequence of spacings along the scanline change but fracture apertures remain unchanged.

The fourth approach to assess the possibility that large fractures are more partitioned into clusters than small fractures will compare the spatial correlation of the observed scanline with the spatial correlation of a version in which fracture locations have been randomized, but to randomize fracture locations in a way that conserves the values and sequence of spacings along the scanline. Namely, fracture positions remain unchanged but the sequence in which different values of aperture are encountered will be randomized. Consequently, the fracture at a position between clusters (intercluster region) has the same probability of being one of the largest observed apertures as a fracture within a cluster. The resulting randomized scanline will be statistically equivalent to the observed scanline, except that there will be no differential clustering according to fracture size.

Selected combinations of the four approaches explained above will also be performed. For instance, NCC results from versions of the observed data set with increasingly larger aperture threshold will be compared with similar results from versions with increasingly larger aperture threshold for randomly arranged fractures (changed spacing values and sequence of spacings). In addition, the hypothesis under question will be tested with fracture data sets that represent all recognized types of spatial arrangement that exhibit clustering (Figure 7.3), as defined by Marrett et al. (in review). By comparing the results of different types of spatial arrangement it will be possible to determine which spatial arrangements display differential clustering according to fracture size. For instance, are large fractures more partitioned into clusters than small ones in both statistically significant and statistically insignificant (Poissonian) clusters? A possible outcome of the test is that both statistically significant and statistically insignificant clusters exhibit differential clustering according to fracture size, which would imply that differential clustering occurs for most conditions of fracture development. Another possible outcome is that only statistically significant clusters display differential clustering according to fracture size. If the statistically significant clusters are periodically arranged and/or exhibit fractal arrangement of fractures inside clusters, then differential clustering might reflect the same self-organization processes that guided the development of these two types of spatial arrangement. If the statistically significant clusters that display differential clustering according to fracture size are only in an inherited/imposed type of spatial arrangement, then differential clustering might only arise from processes that drive fracturing such as folding or faulting. On the contrary, if differential clustering according to size is detected only in statistically insignificant (randomly arranged) clusters, then differential clustering might be a phenomenon present

early in the evolution of fractures from randomly arranged flaws, evolution that did not lead to self-organization of fracture positions.

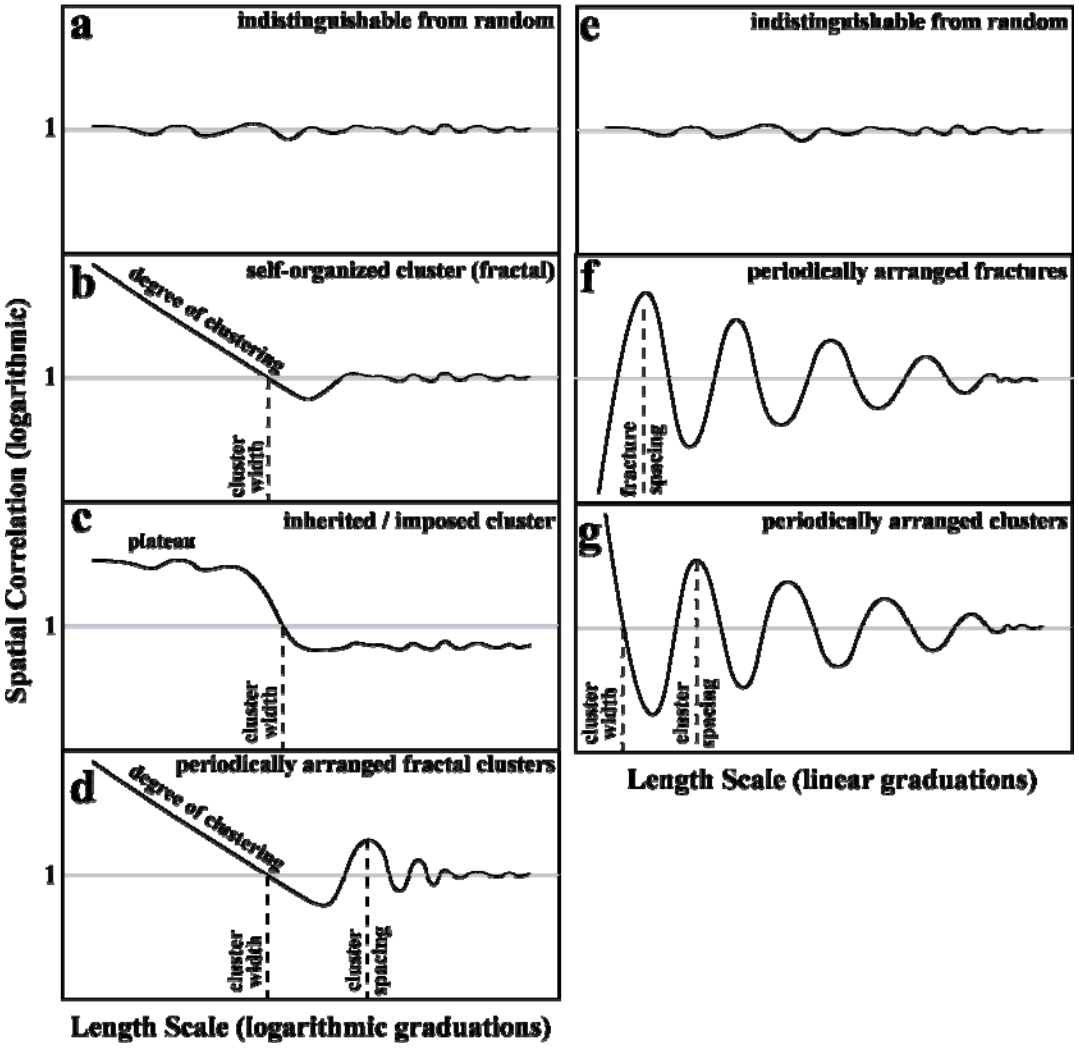

Figure 7.3 Patterns of spatial correlation versus length scale, as defined in Marrett et al. (in review). Each pattern is indicative of a distinctive spatial arrangement. Using logarithmic graduations of length scale (left column), three spatial arrangements can be distinguished: (a) indistinguishable from random, (b) fractal clustering (self-organization), (c) inherited or imposed clustering due to some process other than self organization (e.g., folding or faulting). Using linear graduations of length scale (right column), three different spatial arrangements can be distinguished: (e) indistinguishable from random, (f) periodically arranged fractures, (g) periodically arranged clusters. Combinations of any or all of these patterns can occur (d), with different patterns characterizing different ranges of length scale.

7.1.2 Fracture Size

In Chapter 7 of my dissertation the terms large and small fracture size do not refer to specific sizes. Large and small qualify the relative size of a fracture in regards to the scale on which the measurements of fracture size were made. For instance, in typical outcrop data sets the smallest measured fracture size is a fraction of a millimeter (Ortega et al., 2006) and the largest a few centimeters (Table 7.1). But in a scanline measured in a thin section the smallest fracture might be as small as 0.0005 mm and typically the largest fracture is only a few millimeters (Chapter 5, Gomez and Laubach, 2006). Therefore, what would be considered a small fracture at one scale would be considered large at another scale. For instance, a fracture with 0.1 mm of aperture would be considered small at outcrop scale and large at rock-sample scale.

7.1.3 Domains and Length Scales along Fracture Scanline

A fracture cluster is defined as a domain where fractures are unusually abundant. Statistically significant clusters contain more fractures than equivalent (in terms of scanline length and number of fractures) randomly arranged fractures (Marrett et al., in review). Namely, statistically significant clusters exhibit systematic patterns of spatial correlation outside the 95% confidence interval. If a fracture data set exhibits statistically significant clusters (red fractures, Figure 7.4), as quantified by NCC (Chapter 6), an intracluster domain of a scanline corresponds to part or all of an entire cluster (Figure 7.4). An intercluster domain refers to a part of the scanline located outside clusters and flanked by clusters (green fractures, Figure 7.4). The cluster-to-cluster length scale represents a distance that is larger than the intercluster domain width and smaller than the distance resulting of adding the width of two clusters (one on each end) plus intercluster width (Figure 7.4). The presence of statistically significant clusters implies that fractures are unusually scarce between clusters (green fractures, Figure 7.4). Although minor

clusters might be located in intercluster domains, such clusters lack statistical significance with regards to the entire scanline. In addition, spatial arrangements that are indistinguishable from random also exhibit clusters, but they are not statistically significant (Marrett et al., in review).

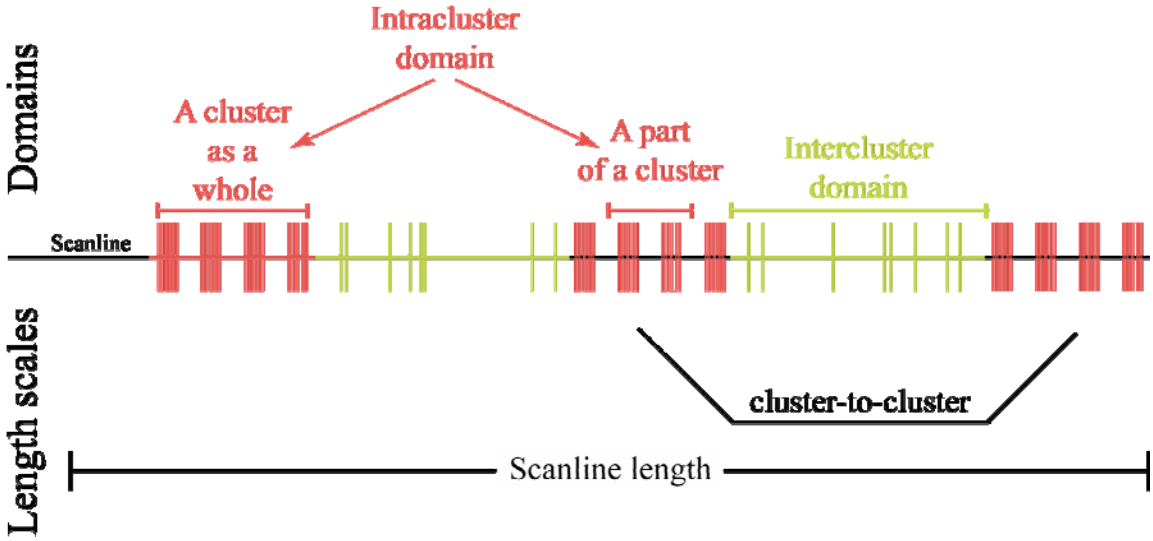

Figure 7.4 Sketch illustrating two different domains of a fracture scanline (above scanline) and two different length scales (bellow scanline). Fractures are represented by vertical lines of equal thickness. Data set shows three clusters (red fractures) that are regularly spaced separated by intercluster domains (green fractures). See text for definitions of terminology.

7.1.4 Methodologies for Subset Generation

The aperture of individual sets of natural opening-mode fractures has been detected ranging up to four orders of magnitude (Marrett et al., 1999). Globally, veins in sandstones have apertures at least as large as two meters (Ortega, 2002) and at least as small as a few microns (Gomez et al., 2003). This wide range of apertures typically makes it infeasible to measure the entire range of apertures of a natural fracture set in a single scale of observation and with a single tool. For instance, apertures of macrofractures (Laubach, 1997) that are 0.05 mm or larger can be efficiently measured in

outcrop using the comparator (Ortega et al., 2006). The resulting scanline will not contain the microfractures (Laubach, 1997) that most likely are present but are too small to be detected or measured efficiently. In addition, logistical reasons (e.g., time availability) might compel researchers to impose an aperture threshold that is larger than the smallest measurable aperture (observational threshold). For instance, the Palmas 11 LR data set was acquired with an aperture threshold of 0.95 mm even though fractures with apertures as small as 0.1 mm could be measured (Table 2.2). Consequently, most data sets of natural fractures will have an observational or artificial aperture threshold and are therefore decimated. The word decimated does not imply that only one in every ten fractures is present but simply that not all fractures are present and therefore every data set is incomplete. In spite of omitting fractures smaller than the aperture threshold, decimated data sets can characterize distinct spatial arrangements (e.g., fractal inside clusters, periodic arrangement of clusters) using NCC (Marrett et al., in review). Therefore, further decimating a data set by increasing the aperture threshold will not necessarily hinder the ability of NCC to quantify spatial arrangement of fractures.

Two variations of an important test to be performed for my dissertation is to compare NCC results (spatial correlation variation with length scale) from different subsets of fractures, in which subsets are defined by variable aperture threshold. One involves generating fracture subsets with increasingly larger aperture thresholds, calculating independently the spatial correlation in a range (logarithmically or linearly graduated) of length scales, and then studying variations in spatial correlation for increasingly larger fractures. Increasing the aperture threshold implies that fractures are progressively removed, which implies large fractures are present in more subsets than small fractures. The second variation of this test involves comparing two subsets of fractures, one subset with fractures larger than or equal to a specified aperture threshold

and another subset with fractures smaller than the same threshold. Although no data set measured or facilitated for my dissertation contains the entire range of fracture sizes, and therefore all data sets are decimated; in order to differentiate the artificially decimated subsets from the measured data set (with the smallest aperture threshold), the measured data sets will be titled *original* or *undecimated*.

7.1.4.1 First Method for Subset Generation - Increasingly Larger Aperture Threshold

To investigate variations in the clustering of increasingly larger fracture sizes, fracture data sets will be progressively decimated of small fractures by using an increasingly larger aperture threshold (Figure 7.5) and analyzed by applying NCC techniques independently to the original data set and each subset. Although some fracture spacings change during decimation, positions of remaining fractures and scanline length remain unaltered (Figure 7.5).

7.1.4.2 Second Method for Subset Generation- Mutually Exclusive Data Sets

To compare two mutually exclusive subsets of the same fracture data set, fractures with apertures smaller than a specified threshold are separated from fractures that have apertures larger than or equal to the same threshold (Figure 7.6). Fracture positions in each subset remain unchanged compared to the original data set, which implies that although some spacings change, scanline length remains the same (Figure 7.6). The number of fractures in the two mutually exclusive subsets should add to the number of the fractures in the original data set.

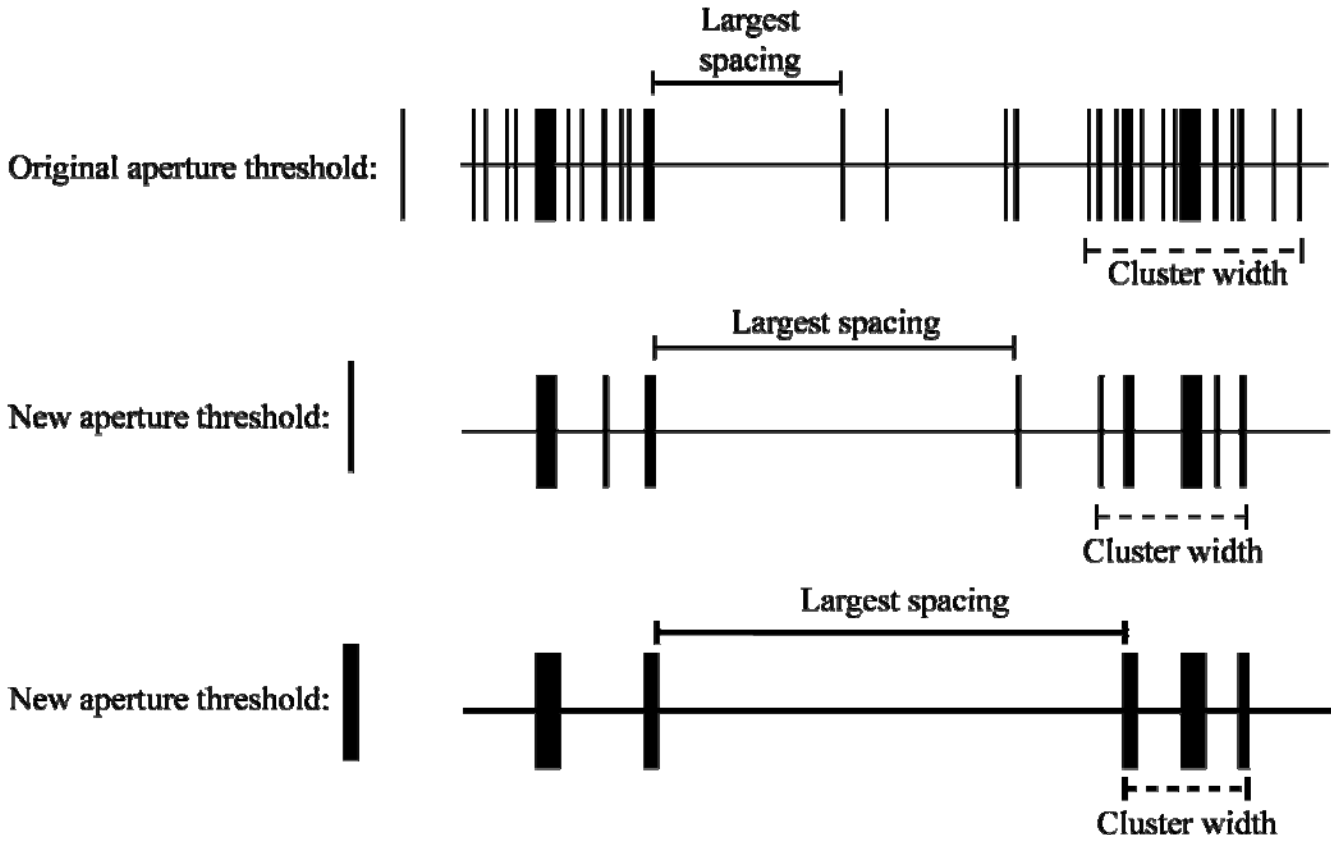

Figure 7.5 Sketches of method utilized to reduce the number of fractures using increasingly larger aperture thresholds. Fracture data set with the original aperture threshold (upper sketch) contains all measured fractures. When a new aperture threshold is imposed, fractures with apertures smaller than that threshold are removed (middle and lower sketches). Fractures with apertures larger than or equal to the specified threshold remain in the same position, and spacings between remaining fractures are recalculated. Solid and dashed brackets show how the largest spacing and widest cluster, respectively, change when progressively smaller fractures are removed.

Figure 7.6 Sketches of method utilized to obtain two mutually exclusive data sets, one with fractures smaller than and other with fractures larger than or equal to a specified aperture threshold. Fracture data set with the original aperture threshold (upper sketch) contains all (28) measured fractures. Fractures with apertures smaller than threshold (middle sketch) are separated from fractures with apertures larger than or equal to the same threshold (lower sketch). Fracture position is not changed for any fracture, but fracture spacings for each subset are recalculated. Solid and dashed brackets show how the largest spacing and widest cluster, respectively, change depending on which fracture subset is examined.

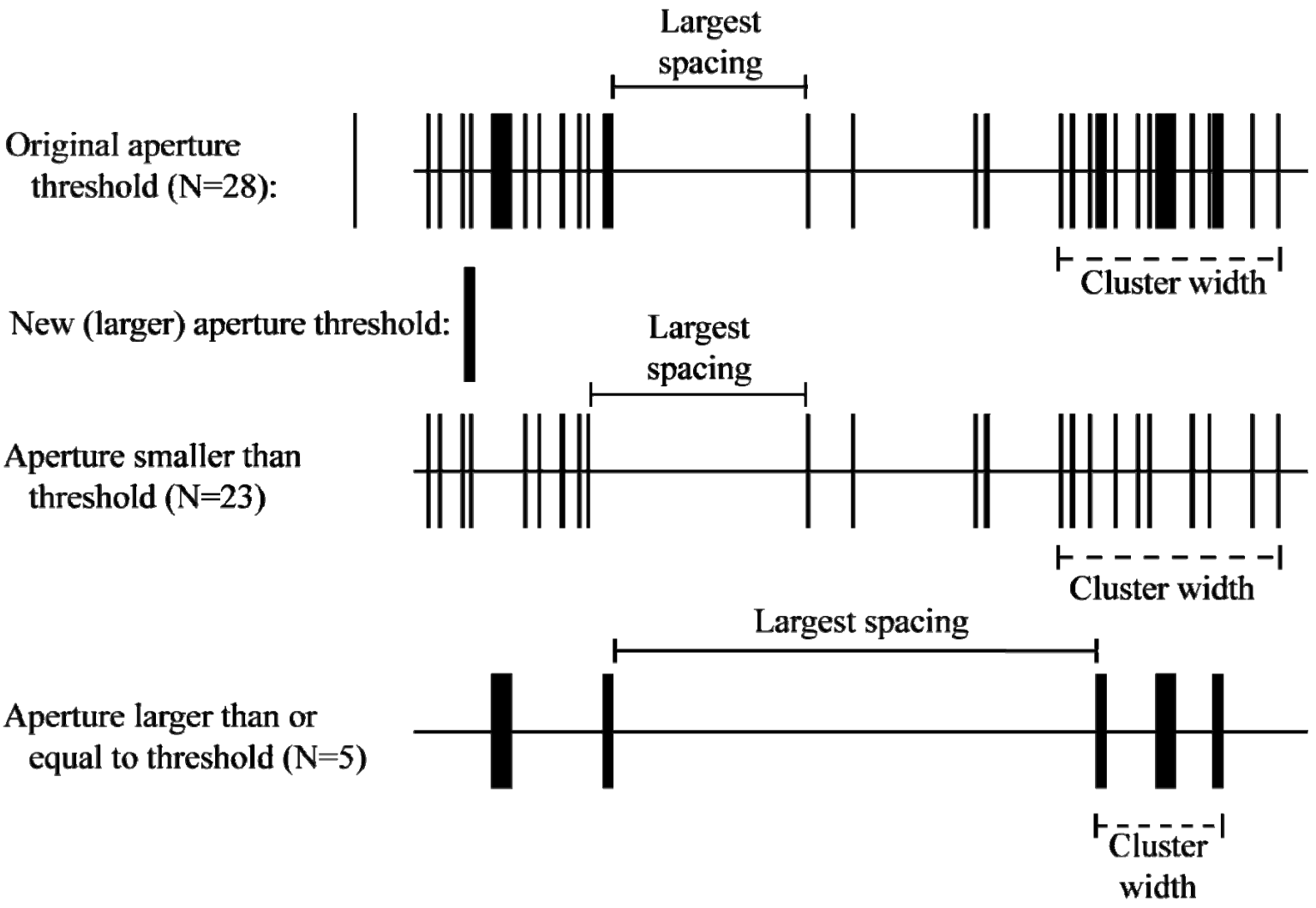
Largest
spacing
Original aperture
threshold (N=28):
Cluster width
New (larger) aperture threshold:
Largest
spacing
Aperture smaller than
threshold (N=23)
Cluster width
Largest spacing
Aperture larger than or
equal to threshold (N=5)
Cluster
width

7.1.5 Fracture Cements

In addition to a mineralogical classification (e.g., quartz, calcite), cements inside fractures can also be classified based on timing of fracture opening relative to cement precipitation (Laubach, 2003; Laubach et al., 2004b). Prekinematic and postkinematic cements precipitate before or after fracture opening, respectively, whereas synkinematic cements precipitate concurrently with fracture opening (Laubach, 1997; Laubach, 2003). Synkinematic cements commonly develop bridges, which can assist the preservation of fracture porosity and fracture permeability, whereas postkinematic cements can greatly reduce fracture porosity and fracture permeability by occluding porosity left after fracture opening. Bridges are defined as "cement deposits that span fractures and that are surrounded by fracture porosity or by later cements" (Laubach et al., 2004b).

To quantify the percentage of synkinematic (or postkinematic) cement inside a fracture, individual thin sections were scanned at high resolution. The resulting images were imported and calibrated in digitizing software such as Didger®. Later, the trace of every fracture intersected by the scanline was digitized and the area of each fracture was automatically calculated by Didger®. Then, the area of the fracture occupied by either synkinematic of postkinematic cement was also digitized and calculated, allowing estimation of the percentage of each fracture occupied by both synkinematic and postkinematic cements.

7.1.6 Previous Studies

Some published studies have observed or modeled clustering (e.g., Gillespie et al., 1993) or anticlustering (e.g., Ackermann and Schlische, 1997; Bour and Davy, 1999) of small shear fractures (faults) near large shear fractures. Regarding opening-mode fractures, there are abundant studies on the relationship of fracture aperture with length,

most of which interpreted this relationship as a power-law distribution (e.g., Moros, 1999; Ortega, 2002). In contrast, most studies have treated the spacing of opening-mode fractures to be independent of other fracture attributes like aperture or length. For instance, Gross and Engelder (1995) used discrete frequency distributions, one of the most common techniques to quantify fracture attributes (Chapter 6; Gomez and Marrett, in review), to independently investigate probability distributions for aperture and the spacing of veins in dolostones. In a similar example, Rouleau and Gale (1985) also used discrete frequency distributions to independently investigate probability distributions for length and the spacing of fractures in granite. However, both of these studies neglected to consider possible correlations between fracture size and spacing.

Gillespie et al. (1999) differentiated stratabound from non-stratabound fractures sets in terms of coefficient of variation for spacings (C_v), cumulative frequency distributions of aperture and spacing, and graphs of location along scanline versus cumulative aperture (staircase plots). According to Gillespie et al. (1999), stratabound fractures have $C_v < 1$, smooth staircase plots and non-power-law aperture distributions, whereas non-stratabound fractures have $C_v > 1$, power-law distribution of apertures, log-normal distribution of spacings and irregular staircase plots. However, other studies have shown that stratabound fractures can follow power-law distributions of fracture aperture (Gale et al., 2004; Marrett et al., 2004) and $C_v > 1$. In addition, Gillespie et al. (1999) created synthetic data sets with independent distributions of fracture spacing and fracture aperture. Gillespie et al. (1999) interpreted natural stratabound fractures to be best mimicked by periodic/normal and random/normal (spacing/aperture) models in terms of staircase plots and cumulative frequency distributions. However, cumulative frequency distributions do not take into account the spatial position of fractures (Chapter 6, Gomez

and Marrett, in review) and therefore only provide a limited basis from which to infer spatial organization (e.g., random arrangement).

A few studies, however, have attempted to study the relationship between size and spacing of opening-mode fractures. For instance, Belfield (1997) calculated what he called the distance ratio (spacing to the nearest neighbor fracture in one direction divided by spacing to the nearest neighbor fracture in the opposite direction) of 2500 fractures measured along a horizontal well in the Austin Chalk. To incorporate fracture aperture in his analysis, Belfield (1997) started with the two largest fractures in the scanline and incrementally incorporated fractures with progressively smaller apertures, calculating the distance ratio of every fracture that was added to the scanline (Figure 1 of Belfield, 1997). Belfield (1997) also determined that the variance of the log of the distance ratio for the fracture data set decreases with decreasing aperture while the variance for randomly located fractures does not change with aperture (Figure 4 of Belfield, 1997). Based on that finding, Belfield (1997) concluded that the spatial arrangement of fractures is not independent from aperture, but he failed to establish the relationship between fracture position and aperture and to quantify the spatial arrangement of fractures.

In another example, Jolly et al. (1998) found that cumulative frequency of fracture aperture for clastic dikes conforms best to a log-normal distribution whereas dike spacing shows a good correlation to a power-law distribution. These findings for clastic dikes are opposite of what have been reported for joints and veins. Apertures of opening-mode fractures typically follow power-law distributions whereas spacings most commonly follow either log-normal or negative-exponential distributions (Tables 6.1 and 6.2; Gomez and Marrett, in review). Jolly et al. (1998) also generated graphs of dike aperture (called thickness by Jolly et al., 1998) versus the average (Figure 7.7a) and minimum (Figure 7.7b) distance from a dike to its two nearest neighbors. They did not find a

correlation between aperture and average spacing (Figure 7.7a). However, their graph of dike aperture versus minimum dike spacing shows a weak pattern indicating that thin dikes have smaller values of minimum spacing then thick dikes (Figure 7.7b). Jolly et al. (1998) concluded that thin dikes are preferentially located inside clusters. This finding is opposite of what has been qualitatively inferred for other kinds of opening-mode fractures (e.g., Figures 7.1 and 7.2). Jolly et al. (1998) proposed that preferential positioning of thin clastic dikes inside clusters occurs because of branching of thin dikes from larger dikes (Jolly et al., 1998).

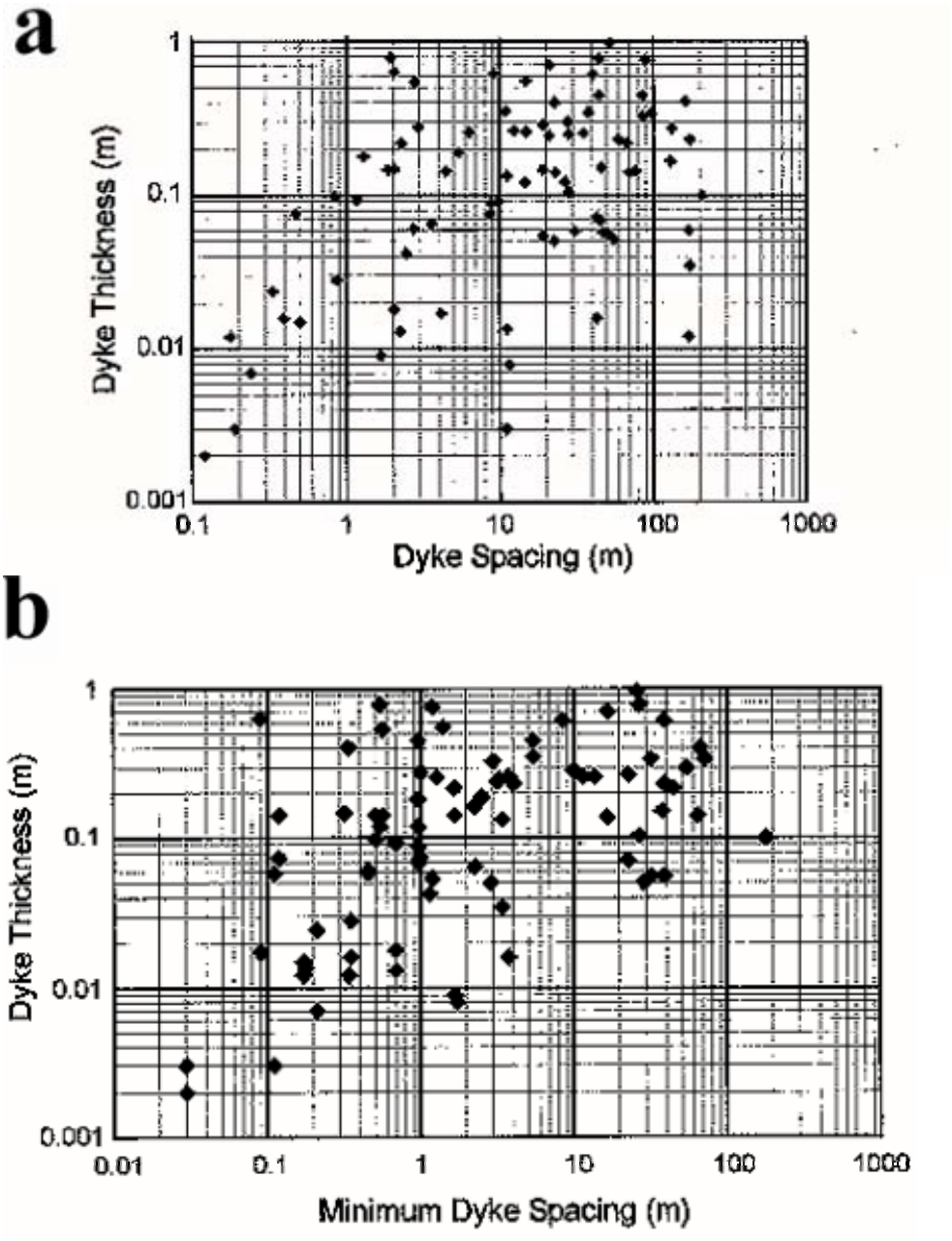

Figure 7.7 Graphs of dike thickness (aperture) versus (a) dike spacing and (b) minimum dike spacing. Graphs from Jolly et al. (1998). There is a weak positive correlation between minimum dike spacing and dike thickness in (b).

7.2. DATA SETS

Of all the data sets measured for my dissertation (Table 2.1) or measured by others but made available to me (Table 2.2) I selected six data sets at outcrop scale (Table 7.1) and one data set at rock sample scale. Two data sets at different scales (outcrop and rock sample) come from the same layer (Tranquitas). The six data sets at outcrop scale were selected because they represent a range of geologic histories, lithologies, ages, strain magnitudes, and types of spatial arrangement (Marrett et al., in review). Two different geologic regions, each with a distinct geologic history, are represented by the data sets. Marble Falls Limestone in Central Texas is represented by the Pedernales data set (Figure 2.9). Rocks above (Cupido Fm.) the anhydrite decollement in the Monterrey Salient (Figures 2.4 to 2.8) are represented by the Huasteca, Palmas 11 LR, Palmas 11 HR, and Palmas 13 data sets, whereas rocks below (La Boca Fm.) the above mentioned decollement (Figures 2.4 to 2.8) are represented by the Tranquitas data set. A variety of lithologies are also represented by the data sets, with one data set measured in a limestone (Pedernales), four (Huasteca, Palmas 11 LR, Palmas 11 HR, and Palmas 13) data sets measured in dolostones and one (Tranquitas) in sandstone. The seven data sets represent rocks of different ages: Early Pennsylvanian (Pedernales), Jurassic (Tranquitas) and Lower Cretaceous (Huasteca, Palmas 11 LR, Palmas 11 HR, and Palmas 13). In addition, the data sets cover a range of fracture strain magnitudes (Table 7.1), with Pedernales having the smallest value (0.53%) and Palmas 13 the highest (9.16%).

Table 7.1 Quantitative attributes of fracture data sets at outcrop scale. Cumulative frequency distributions (e.g., power law, negative exponential, etc.) were selected based on the best coefficient of determination. A perfect distribution has a χ^2 coefficient of zero. N.A = Not Available.

Outcrop data sets	Huasteca – Set A	Palmas 11 LR	Palmas 11 HR	Palmas 13	Tranquitas	Pedernales
Outcrop type)	Cross section	Cross section	Cross section	Cross section	Bedding surface	Bedding surface
Geologic Unit	Cupido Fm.	Cupido Fm.	Cupido Fm.	Cupido Fm.	La Boca Fm.	Marble Falls Fm.
Lithology	dolopackstone	lime dolowackstone	lime dolowackstone	dolowackstone	Sandstone	Limestone
Layer Thickness (cm)	70	27	27	24	N.A.	~10000
Number of Fractures	581	262	575	614*	496	916
Length of Scanline (m)	16.59	21.1	2.49	5.43	31.09	58.96
Fracture Strain (%)	5.74	4.59	7.62	9.16	1.3	0.53
Aperture Threshold (mm)	0.215	0.95	0.075	0.14	0.05	0.05
Maximum Aperture (mm)	15	42	17.5	12	14	18
Range of Fracture Aperture (orders of magnitude)	1.8	1.6	2.4	1.9	2.5	2.5
Cumulative Frequency Distribution of Apertures (fractures/mm)	Power-law $y = 0.15\ b^{-2.2}$	Power-law $y = 0.015\ b^{-1.2}$	Power-law $y = 0.0126\ b^{-1.15}$	Power-law $y = 0.022\ b^{-0.7}$	Power-law $y = 0.003\ b^{-1.42}$	Power-law $y = 0.0011\ b^{-1.2}$
Chi square (χ^2)	0.1064	0.0885	0.035	0.101	0.040	0.018
Range of Fracture Spacings	0.4 – 427.3	0.075 – 806	0.095 – 115	0.175 – 66.5	0.46 – 603	0.08 - 2260
(mm, orders of magnitude)	3.0	4.1	3.1	2.5	3.2	4.3
Average Fracture Spacing(mm)	27.01	76.73	4.01	10.85	61.87	14.38
Coefficient of Variation	1.39	1.72	1.67	0.93	1.39	2.43
Cumulative Frequency Distribution of Spacings (R^2)	Log-normal 0.9952	Log-normal 0.981	Log-normal 0.998	Negative exponential 0.998	Log-normal 0.998	Log-normal 0.997
Average Spacing for fractures with apertures ≥ 0.95 mm(mm)	59.26	80.6	5.18	40.6	277.6	786.1

For each data set, a scanline was positioned in a representative portion of the fracture array with a length long enough to capture the characteristic of the spatial arrangement under study. For example, to quantify the spatial arrangement of the fractures traversing from top to bottom in Figure 7.2 a scanline was positioned perpendicular to the average fracture orientation. Fractures in other orientations such as the ones in Figure 7.2, were either measured or ignored depending on whether they were believed to be genetically related or unrelated, respectively, to the fractures under study.

All seven data sets quantify only cement-filled opening-mode fractures with negligible shear displacement (Figures 7.1, 7.2 and 7.8), namely veins. The apertures and spacings of the fracture data sets at outcrop scale were measured along scanlines using a logarithmically graduated comparator (Ortega et al., 2006) for measurements between 0.05 mm and 5 mm, and a millimetrically graduated ruler for measurements larger than 5 mm. The data set at rock sample scale was obtained using the method described in Chapter 5 (Gomez and Laubach, 2006).

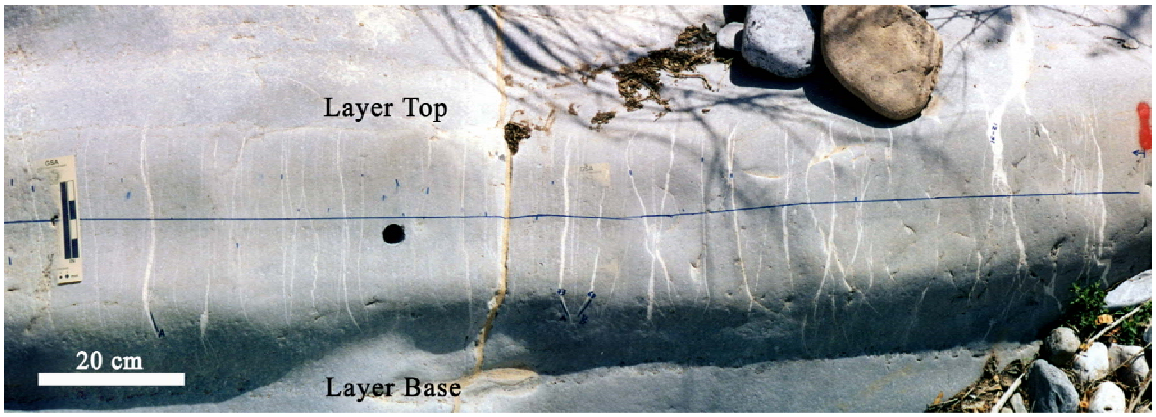

Figure 7.8 Photograph of the first 1.5 meters of scanline in cross-sectional exposure of layer 13 from Palmas canyon (Cupido Fm.). Scanline was located approximately half-way between top and base of layer. Notice that most fractures are confined between layer boundaries and that obvious fracture clusters are lacking.

7.2.1 Pedernales Falls State Park (Pedernales)

The Pedernales data set was measured in a bedding-parallel outcrop of limestone in the Early Pennsylvanian Marble Falls Formation (Erlich and Coleman, 2005; Gomez and Marrett, in review). The Pedernales data set was obtained by several people (Table 2.2) and is available in Hare (2002). Part of the Pedernales data set was introduced in Marrett et al. (1999) and later expanded for Hare (2002) and Marrett et al. (2004). Using an aperture threshold of 0.05 mm, 916 calcite-filled veins were measured along a scanline of approximately 59 m with a fracture strain of 0.53% (Table 7.1). This data set was analyzed by Marrett et al. (in review) using NCC, which demonstrated that fractures at Pedernales have a fractal arrangement inside clusters (Figure 7.9a) with a cluster width of 7200 mm. However, the Pedernales data set displays statistically significant clusters that might or might not be periodically arranged (Figure 7.9b). The periodicity of the clusters of the Pedernales data set is in question because fractures at Pedernales do not exhibit the pattern of alternating peaks and troughs that is interpreted to indicate periodically arranged clusters (Figure 7.3g) with peaks at length scales multiple of the length scale for the first peak (cluster spacing). The uncertainty in interpreting periodically arranged clusters at Pedernales might be caused by the relatively short length of the scanline (59 m) compared with the cluster spacing (19 m) and cluster width (7.2 m), which only allowed three clusters that are not regularly spaced to be measured (Figure 7.10a).

Pedernales veins display a heterogeneous arrangement in space (Gomez and Marrett, in review) with at least three clusters centered approximately at 3, 22 and 58 m as indicated by fracture intensity (Figure 7.10a). Randomizing fracture apertures without any change in fracture position will not change the curve of fracture intensity, because fracture intensity only depends on fracture position. However, randomizing fracture apertures makes it more difficult to detect clusters using fracture apertures (Figure 7.10b).

For instance, most fractures with aperture of 0.95 mm or larger are located inside clusters in the observed Pedernales data set (Figure 7.10a), whereas fractures of the same size are more evenly arranged along the randomized scanline (Figure 7.10b). This qualitatively suggests a relationship between fracture size and fracture position for the Pedernales data set; namely, that large apertures are more clustered than small ones. In addition, it could indicate that the relationship between fracture size and fracture position in fractures at Pedernales is unlikely to simply reflect a random arrangement of fractures.

Figure 7.9 Graphs of spatial correlation (thick continuous line) vs. length scale for (a) logarithmic graduations and (b) linear graduations for the entire Pedernales data set (59 m of scanline, 916 fractures, aperture threshold of 0.05 mm). In (a) and (b) the thin discontinuous line represents the upper 95% confidence limit while the thin dotted line represents the lower 95% confidence limit, and the thick discontinuous line corresponds to the mean of 100 randomized data sets. In (a) the thin continuous line represents the analytical solution of randomly arranged fractures with the same number of fractures and scanline length. In (b) the thin continuous line represents an example randomized set generated with the same number of fractures and scanline length. Width of length-scale bin in (a) and (b) is 9 (m = 4) graduations of length scale. Spatial correlation in (a) follows a power-law pattern. Power law equation in (a) was calculated using spatial correlation between length scales of 9 and 17000 mm. The power-law pattern is statistically significant (outside the 95% confidence interval) for about 3 orders of magnitude of length scale, which indicates that the interpreted fractal arrangement is statistically significant. Cluster width is estimated at 7200 mm, as shown in (a) and (b). Two statistically significant peaks at 13000 and 18000 mm are shown in (b).

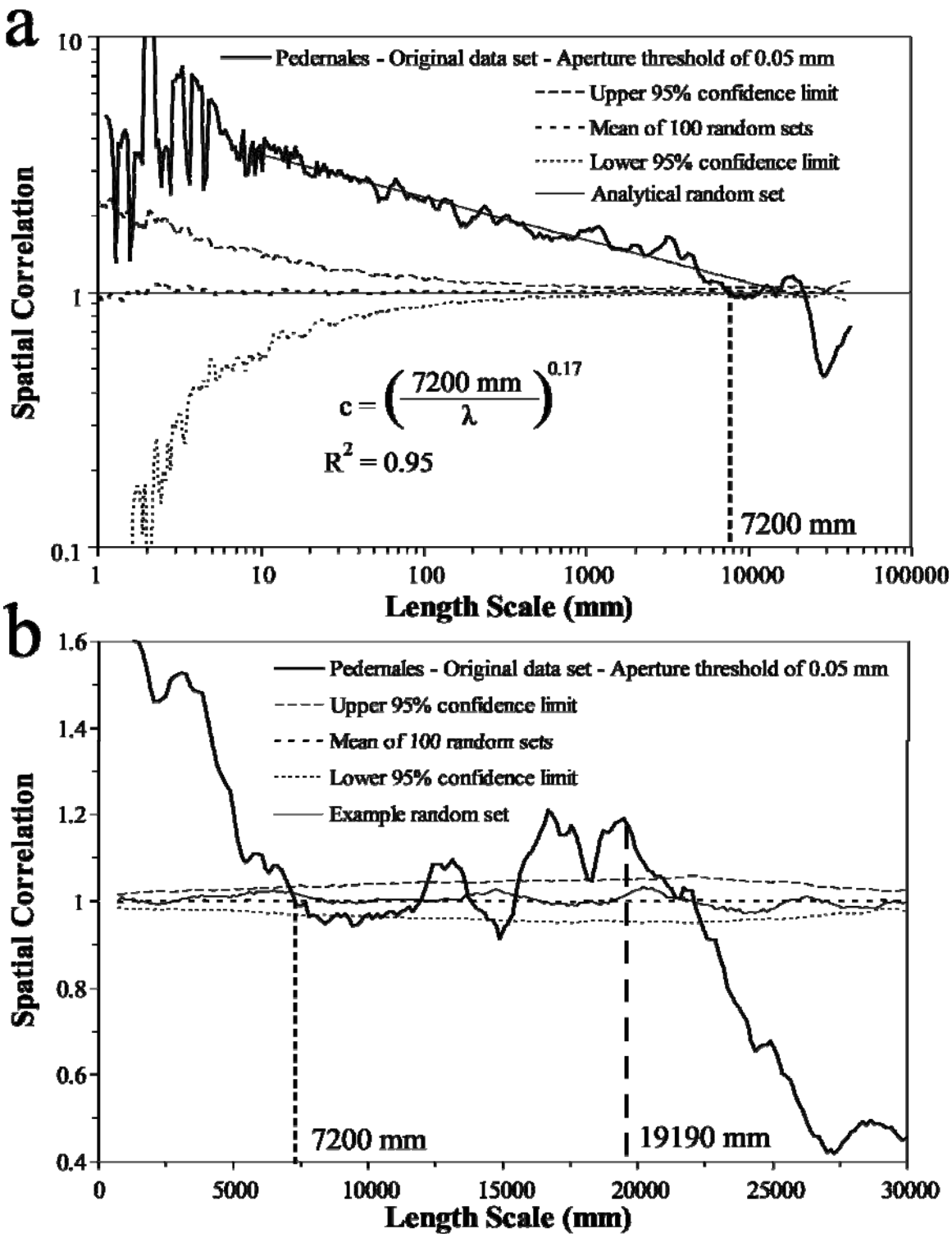
a
Pedernales - Original data set - Aperture threshold of 0.05 mm
Upper 95% confidence limit
Mean of 100 random sets
Lower 95% confidence limit
Analytical random set
Spatial Correlation
10
1
0.1
$c = \left(\frac{7200\ mm}{\lambda}\right)^{0.17}$
$R^2 = 0.95$
7200 mm
1
10
100
1000
10000
100000
Length Scale (mm)
b
Pedernales - Original data set - Aperture threshold of 0.05 mm
Upper 95% confidence limit
Mean of 100 random sets
Lower 95% confidence limit
Example random set
Spatial Correlation
1.6
1.4
1.2
1
0.8
0.6
0.4
7200 mm
19190 mm
0
5000
10000
15000
20000
25000
30000
Length Scale (mm)

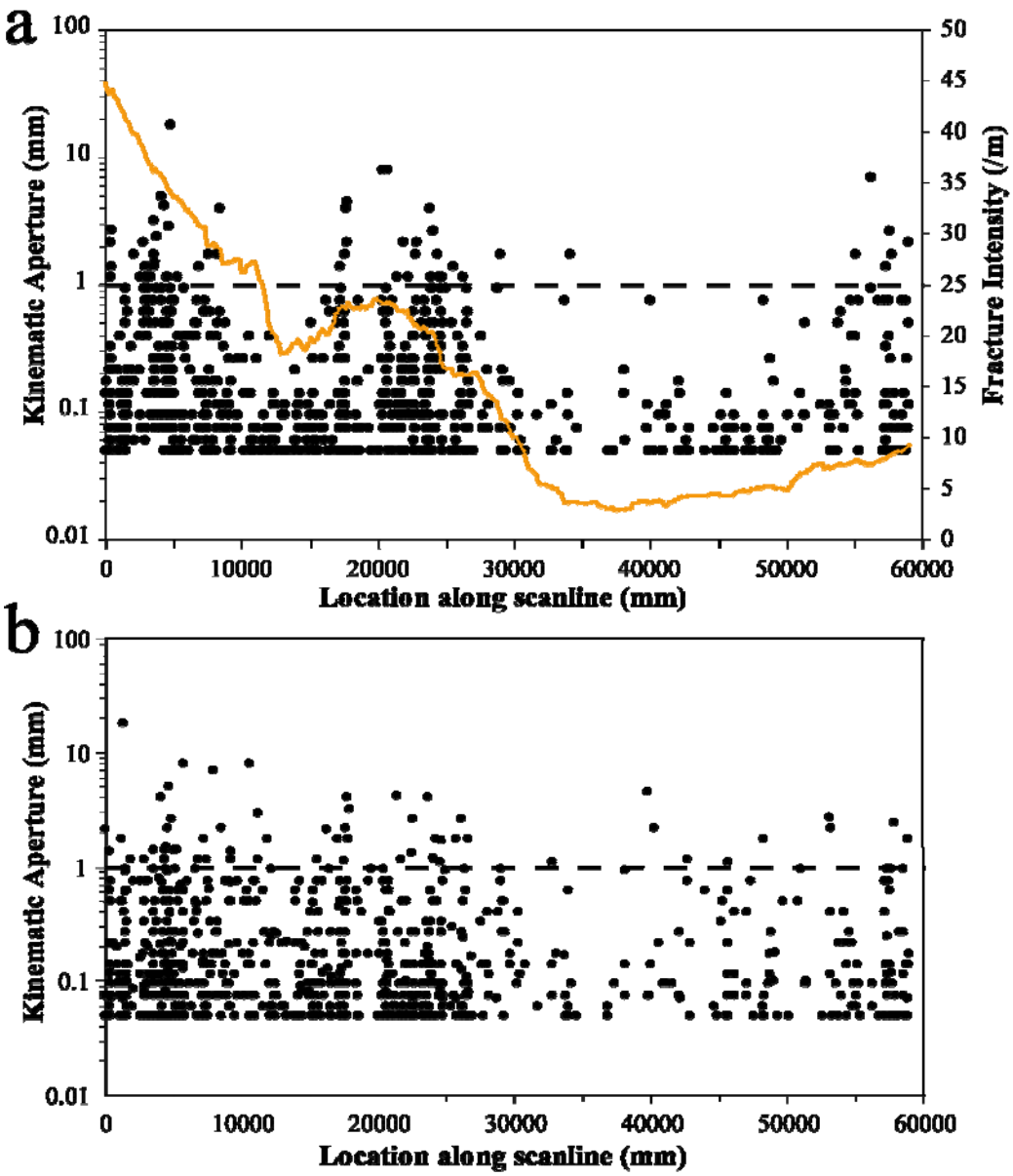

Figure 7.10 Kinematic aperture and fracture intensity versus location along scanline for a) Pedernales data set and b) Pedernales fractures with randomized apertures (unchanged positions). Fracture intensity was calculated inside a window with length (window size) equal to 7 m (approximate equal to cluster width, Figure 7.9) that was moved in increments (window step) of 0.1 m. High fracture intensity indicates the location of fracture clusters. Cluster boundaries are more visible in fracture aperture data of a) because intercluster regions contain more large fractures (e.g., apertures larger than 0.95 mm, dashed line) in b). Note that only the kinematic aperture axis uses logarithmic graduations.

7.2.2 Data sets at Layer 11 in Palmas Canyon

As with all the data sets from the Cupido Formation studied in this dissertation, the two data sets from Layer 11 at Palmas canyon were measured in isoclinal folds of the Sierra Madre Oriental, Mexico, near the city of Monterrey. Two overlapping data sets (High Resolution, or HR, and Low Resolution, or LR) with different aperture thresholds (0.075 and 0.95 mm, respectively) were measured in layer 11 at Palmas canyon, which is located near the top of the Cupido Formation. These two data sets were measured by Dr. J. Gale, and made available for my dissertation (Marrett et al., 2004). Palmas 11 is a 27 cm thick lime dolowackstone that suffered dedolomitization. Although fractures in Palmas 11 layer exhibit both synkinematic and postkinematic cements, the majority (~100%) is synkinematic (Chapter 9).

7.2.2.1 Low Resolution Data set (Palmas 11 LR)

The Palmas 11 LR data set represents 262 calcite-filled veins measured in a cross-sectional outcrop of a dolostone layer and records a strain of 4.59% (Figure 7.1 and Table 7.1). As with the Pedernales data set, Palmas 11 LR data set also displays a heterogeneous arrangement of fractures in space, as shown in Figure 7.11a (Marrett et al., 2004). The Palmas 11 LR data set displays periodically arranged fracture clusters (Figures 7.3g and 7.11b), which in turn display a fractal arrangement of fractures (Figures 7.3b and 7.11a), a combination of spatial arrangements called periodically arranged fractal clusters (Figure 7.3d; Marrett et al., in review). Although the small width of the clusters (220 mm, Figure 7.11a), compared with the entire scanline length (21 m, Table 7.1), obscures somewhat qualitative detection of clustering of fractures in the Palmas 11 LR data set (Figure 7.12a), a detailed view of a segment of the scanline reveals that large fractures are almost exclusively located inside clusters (Figure 7.12b). In addition, a continuous curve of fracture intensity indicates the presence of at least 14 clusters (Figure

7.12a) with approximately periodic spacing of about 1.1 m (Figure 7.11b). The first two clusters (approximately at 0.15 and 1.4 m, Figure 7.12a) are also included in the Palmas 11 HR data set (Figure 7.13a).

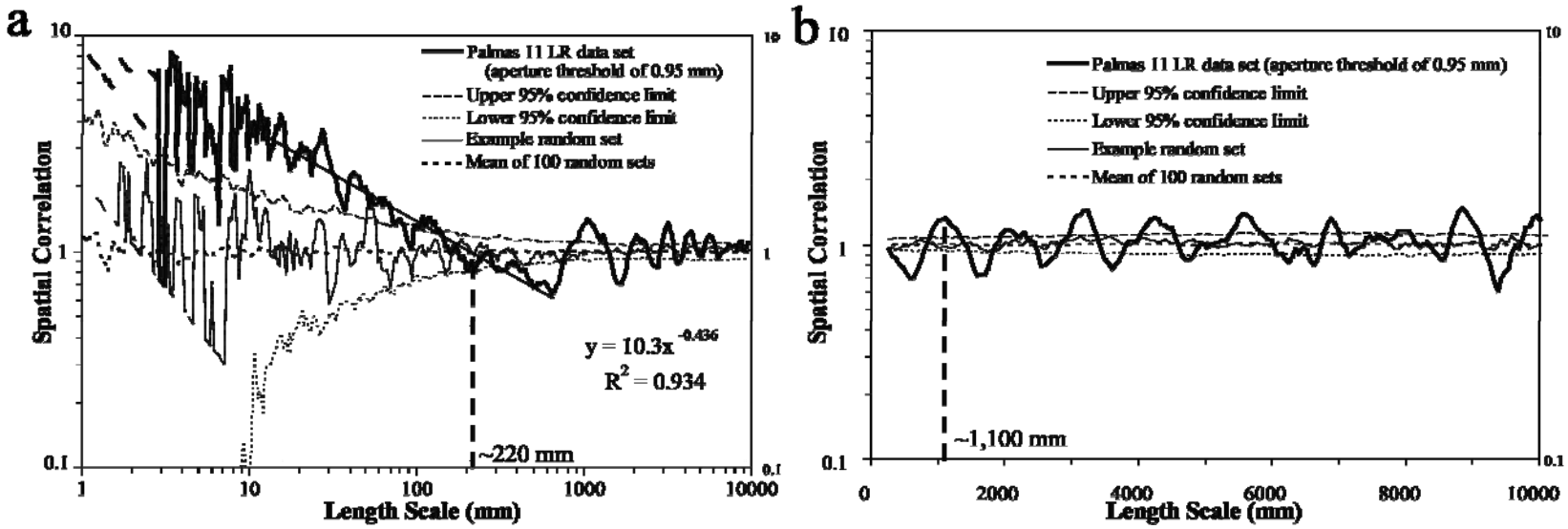

Figure 7.11 Graph of spatial correlation vs. (a) logarithmic graduations of length scale and (b) linear graduations of length scale for the Palmas 11 LR data set (262 fractures measured, aperture threshold = 0.95 mm, thick continuous line). Analytical solution of randomly arranged fractures with an equivalent number of fractures and scanline length as veins at Palmas 11 LR (thin line). The thin discontinuous (long dashes) line represents the upper 95% confidence interval while the thin discontinuous (short dashes) line represents the lower 95% confidence interval. Thin dotted line corresponds to the mean of 100 randomized data sets. Width of length-scale bin in (a) and (b) is 5 graduations of length scale (m = 2). Power law pattern of spatial correlation in (a) was calculated between length scales of 12 and 664 mm. Power-law pattern of spatial correlation in (a) is indicative of a fractal arrangement of fractures. Cluster width is approximately 220 mm, as shown in (a). Spatial correlation in (b) shows alternating peaks and troughs with peaks at length scale multiples of first peak of length scale (1100 mm). Cluster spacing is approximately 1100 mm, as shown in (b).

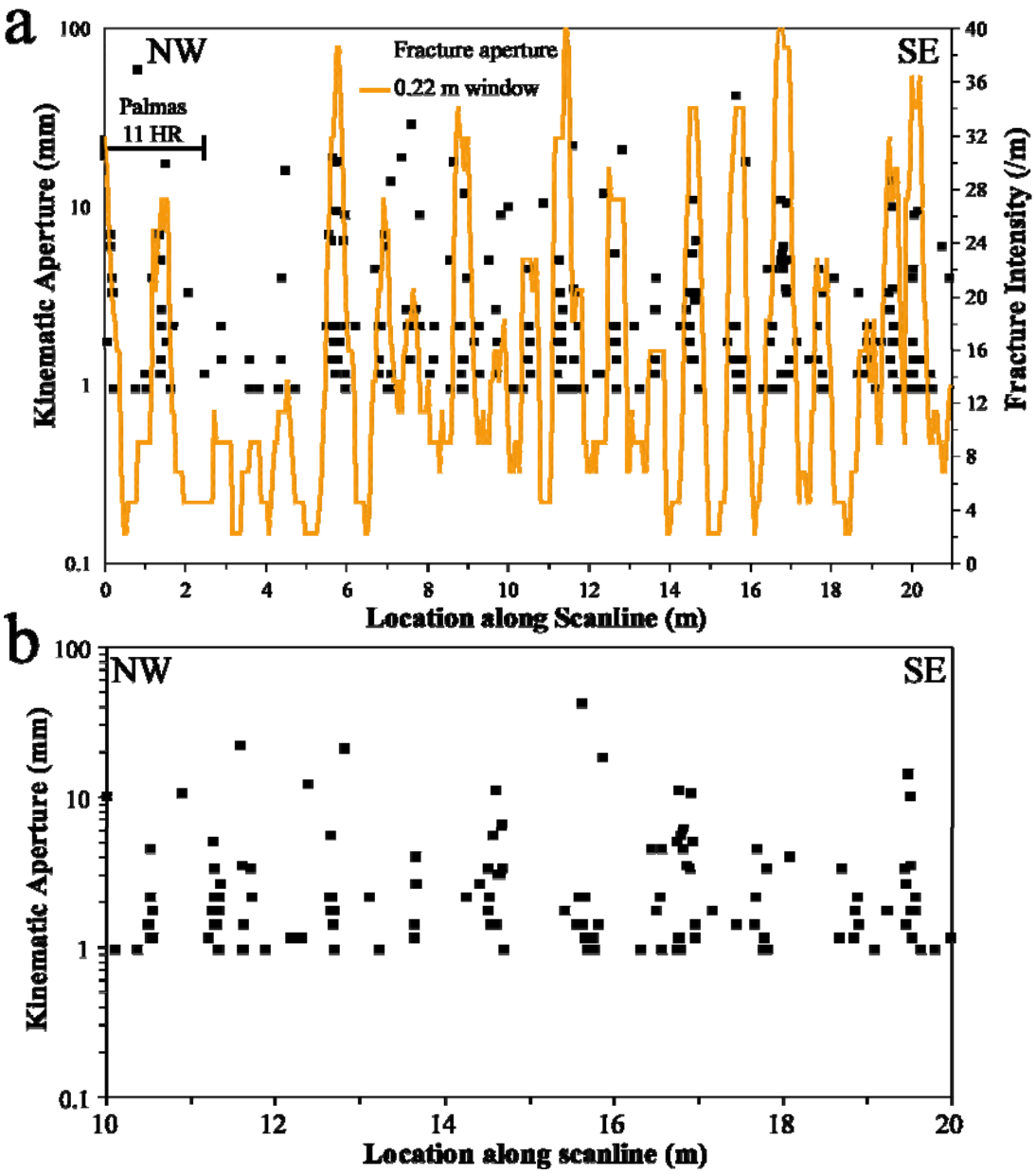

Figure 7.12 Kinematic aperture and fracture intensity versus location along scanline for all (a) and part (b) of the Palmas 11 LR data set. Fracture intensity was calculated inside a window with length equal to cluster width as estimated by NCC (0.22 m, Figure 7.11a) that was moved in increments equal of 0.05 m. Please note that only the kinematic aperture axis use logarithmic graduations. Line at the beginning of the scanline in (a) indicates location of Palmas 11 HR data set. Clusters are more easily detected in (b) than in (a) because cluster width is larger compared with the plotted scanline.

7.2.2.2 High Resolution Data set (Palmas 11 HR)

The Palmas 11 HR data set represents 575 calcite-filled veins measured in scanline 2.5 m long and records a strain of 7.62% (Table 7.1). The relatively high aperture threshold of Palmas 11 LR data set (0.95 mm) facilitated acquisition of a scanline with numerous clusters. However, the resulting data set contains a very limited number of fractures in intercluster regions (Figure 7.12b), which precludes meaningful randomization of fracture apertures (without change in fracture position) like the one performed for Pedernales data set and displayed in Figure 7.10b. Nevertheless, meaningful randomization of fracture apertures can be performed with the Palmas 11 HR data set, because the aperture threshold (0.075 mm) allowed recording of fractures in both intracluster and intercluster regions of the scanline (Figure 7.13a). Fracture apertures in the Palmas 11 HR indicate the location of clusters (Figure 7.13a). For instance, most fractures with aperture of 0.95 mm or larger are located inside the clusters detected in the Palmas 11 HR data set (Figure 7.13a) whereas fractures of the same size are more evenly arranged along the scanline when apertures are randomized (Figure 7.13b). As with Pedernales data set, this qualitatively suggests a relationship between fracture size and fracture position for the Palmas 11 data set. Namely, large apertures are more clustered than small ones.

Fractures of the Palmas 11 HR scanline exhibit clusters that might be regularly spaced (Figure 7.13a). Spatial correlation for logarithmically graduated length scales for the original version (all fractures measured in field) of Palmas 11 HR data set displays a power-law pattern, which is indicative of a fractal arrangement of fractures inside clusters (Figures 7.3b and 7.14a) with a cluster width of approximately 70 mm. Spatial correlation for linearly graduated length scales for the original Palmas 11 HR data set displays a pattern of peaks and troughs of spatial correlation some of which are statistically

significant (Figure 7.14b). Pattern of spatial correlation of Figure 7.14b can be interpreted as indicative of periodically arranged fracture clusters (Figure 7.3g) with a cluster spacing of 353 mm. Combination of the two spatial arrangements of Palmas 11 HR data set was label by Marrett et al. (in review) as periodically arranged fractal clusters (Figure 7.3d).

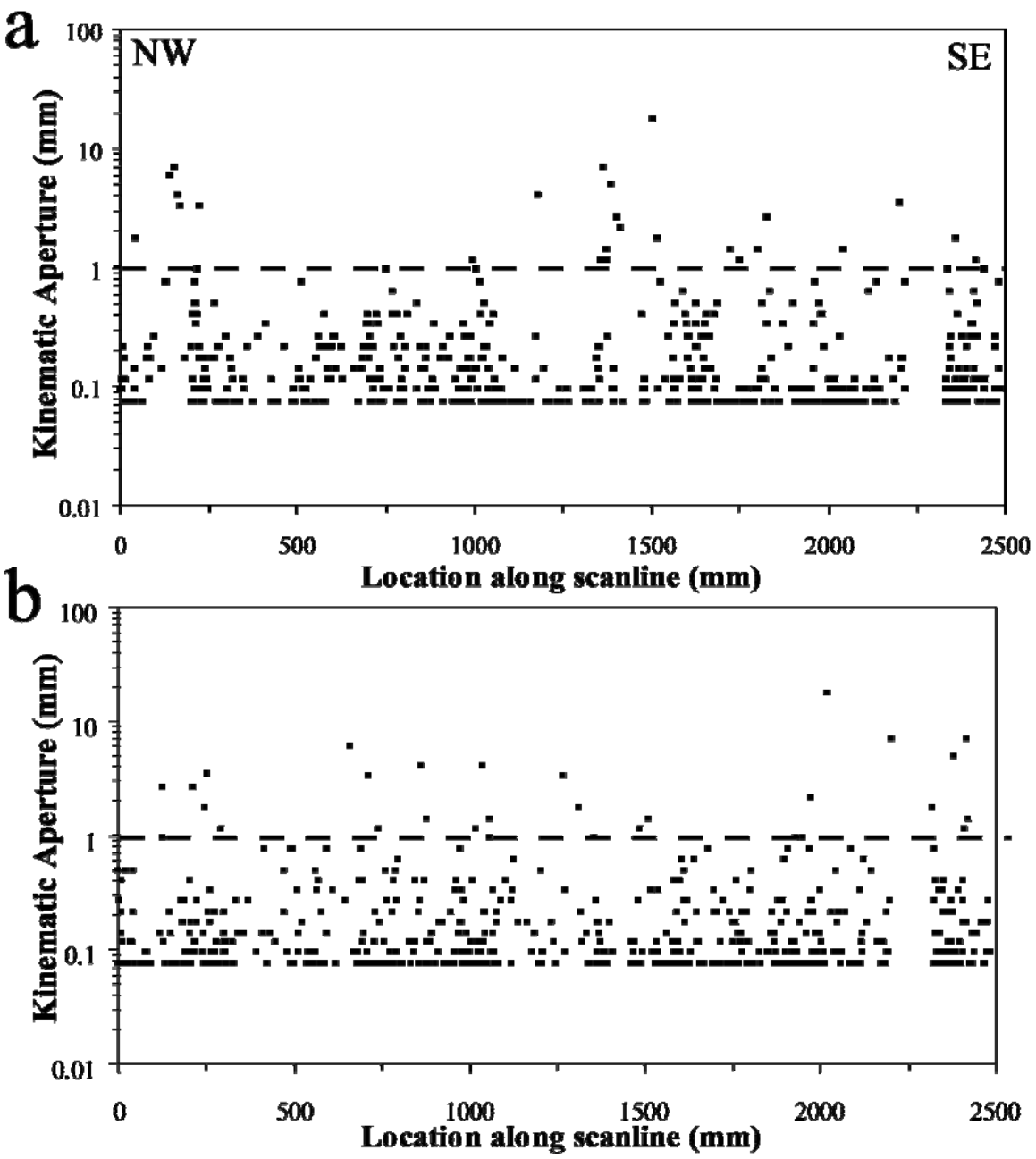

Figure 7.13 Kinematic aperture versus location along scanline for the (a) unmodified and (b) modified version with randomized apertures (unchanged positions) of the Palmas 11 HR data set. The clusters centered at 160 and 1400 mm (detected by the curve of fracture intensity in Figure 7.12a) contain the majority of the large fractures (e.g., larger than 0.95 mm, dashed line), as shown in (a). However, when apertures are randomized (b), large fractures (e.g., apertures larger than 0.95 mm, dashed line) are more evenly arranged.

Figure 7.14 Graphs of spatial correlation (thick continuous line) vs. length scale for (a) logarithmic graduations and (b) linear graduations for the entire Palmas 11 HR data set (2.5 m of scanline, 575 fractures, aperture threshold of 0.075 mm). In (a) and (b) the thin discontinuous line represents the upper 95% confidence limit while the thin dotted line represents the lower 95% confidence limit, and the thick discontinuous line corresponds to the mean of 100 randomized data sets. In (a) the thin continuous line represents the analytical solution of randomly arranged fractures with the same number of fractures and scanline length. In (b) the thin continuous line represents an example randomized set generated with the same number of fractures and scanline length. Width of length-scale bin in (a) is 21 (m = 10) and in (b) is 9 (m = 4) graduations of length scale. Power law equation in (a) was calculated using spatial correlation between length scales of 5 and 90 mm. Power-law pattern in (a) is statistically significant (outside the 95% confidence interval) for about 1 order of magnitude of length scale, which indicates that the interpreted fractal arrangement is also statistically significant. Evenly spaced lines every 353 mm in (b) match approximately peaks of spatial correlation, which display a regularly spaced pattern, indicative of periodically arranged clusters.

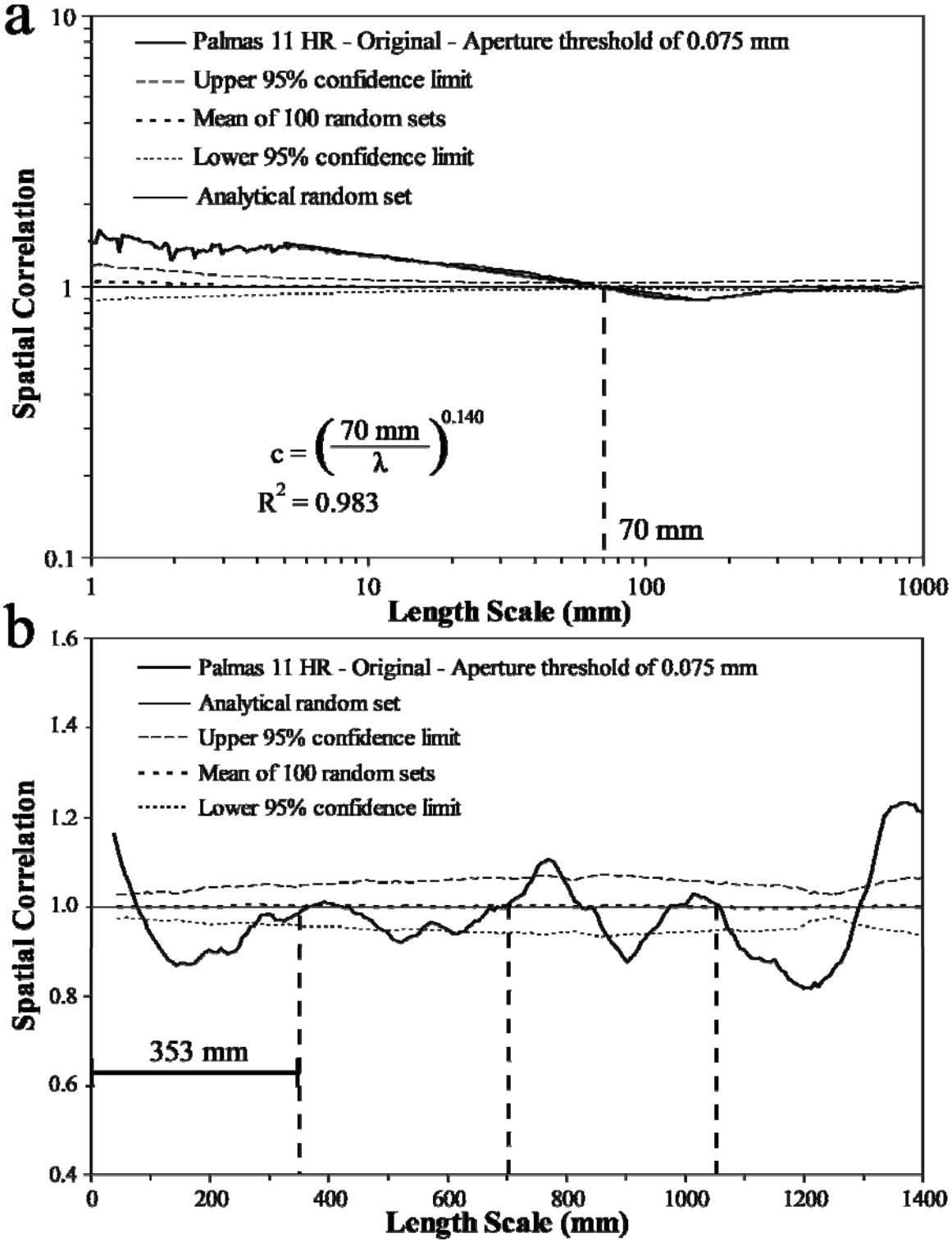
a
Palmas 11 HR - Original - Aperture threshold of 0.075 mm
Upper 95% confidence limit
Mean of 100 random sets
Lower 95% confidence limit
Analytical random set
Spatial Correlation
10
1
0.1
$c = \left(\frac{70\ mm}{\lambda}\right)^{0.140}$
$R^2 = 0.983$
70 mm
1
10
100
1000
Length Scale (mm)
b
Palmas 11 HR - Original - Aperture threshold of 0.075 mm
Analytical random set
Upper 95% confidence limit
Mean of 100 random sets
Lower 95% confidence limit
Spatial Correlation
1.6
1.4
1.2
1.0
0.8
0.6
0.4
353 mm
0
200
400
600
800
1000
1200
1400
Length Scale (mm)

7.2.3 Tranquitas

7.2.3.1 Outcrop-scale Data Set

The Tranquitas data set I analyzed resulted from merging the A1 and A2 scanlines of Ward (in preparation), which were measured in what Laubach and Ward (2006) called the Canyon outcrop. The Tranquitas data set was obtained in a bedding-parallel outcrop of a sandstone layer from La Boca Fm. by M. Ward (Table 2.2) for her M.Sc. thesis (Ward, in preparation) and was graciously provided for my dissertation. The Tranquitas outcrop is located in the Sierra Madre Oriental, approximately 100 km south of the Monterrey Salient, near the town of Galeana (Davis, 2005). La Boca Fm. deposited during Middle Triassic to Lower Jurassic and is part of Huizachal Group Red Beds deposited in extensional to transtensional basins associated with opening of the Gulf of Mexico (Barboza-Gudino et al., 1999). La Boca Fm. lies beneath the regional evaporite decollement that separates two different structural domains; gigantic isoclinal folds (that affected the Cupido Fm.) above the decollement and open folds with faults and basement involvement below (Marrett and Aranda-Garcia, 2001). In the Tranquitas are, La Boca Fm. is affected by an open, basement involved fold (Zhou et al., 2006) and are affected by numerous small normal and reverse faults (Davis, 2005).

The Tranquitas data set represents 496 quartz- and calcite-filled veins measured along a scanline of approximately 31 m and with a total strain of 1.3% (Figure 7.15; Table 7.1). Veins at the Tranquitas location are partially or completely filled with synkinematic quartz and, locally, postkinematic calcite (Ward, in preparation).

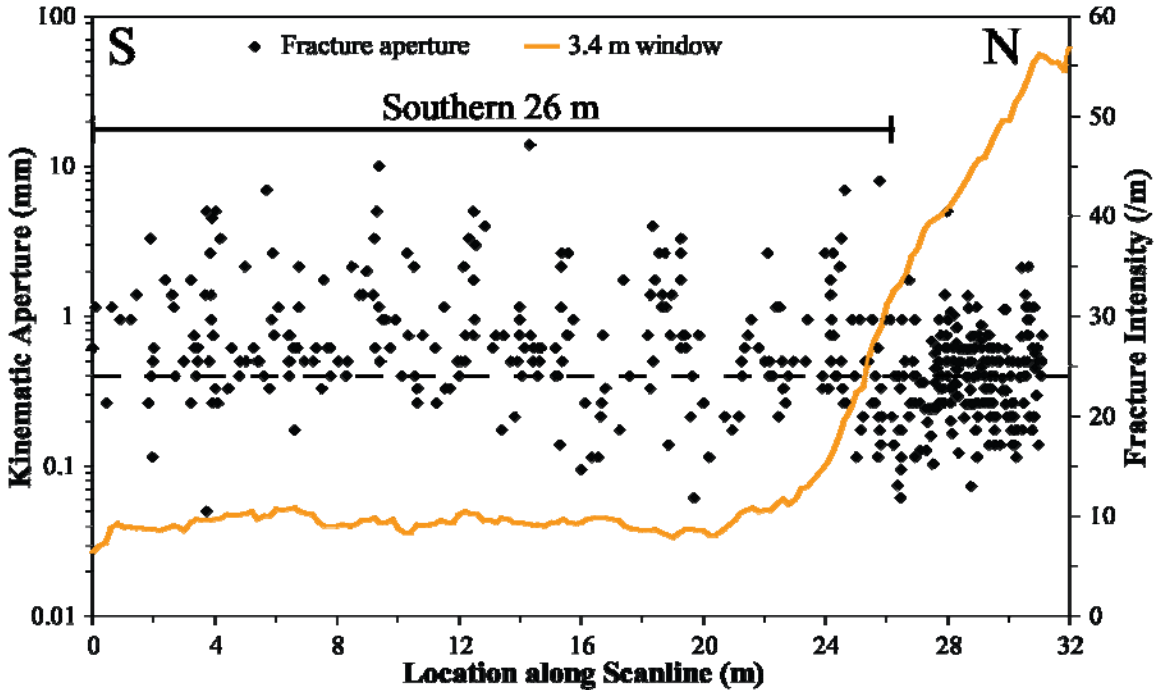

Figure 7.15 Kinematic aperture and fracture intensity versus location along scanline for all the Tranquitas data set. Fracture intensity was calculated inside a window with length (window size) of 3.4 m, the cluster width as measured by NCC (Figure 7.16a) that was moved in increments (window step) 0.2 m. Small fractures (e.g., apertures smaller than 0.4 mm, dashed line) are more abundant in the northern 5 m of scanline. In contrast, large fractures (e.g., apertures larger than 1 mm) are more abundant in the southern 26 m of scanline. Note that kinematic aperture axis uses logarithmic graduations.

Spatial correlation for logarithmically graduated length scales for the original Tranquitas data set at outcrop scale displays a plateau pattern that can be interpreted as inherited or imposed clustering for about two orders of magnitude of length scale and with a cluster width of about 3400 mm (Figures 7.3c and 7.16a). Although spatial correlation for linearly graduated length scales is outside the 95% confidence interval, it does not exhibit a recognizable pattern, suggesting an arrangement that cannot be determined (Figure 7.16b).

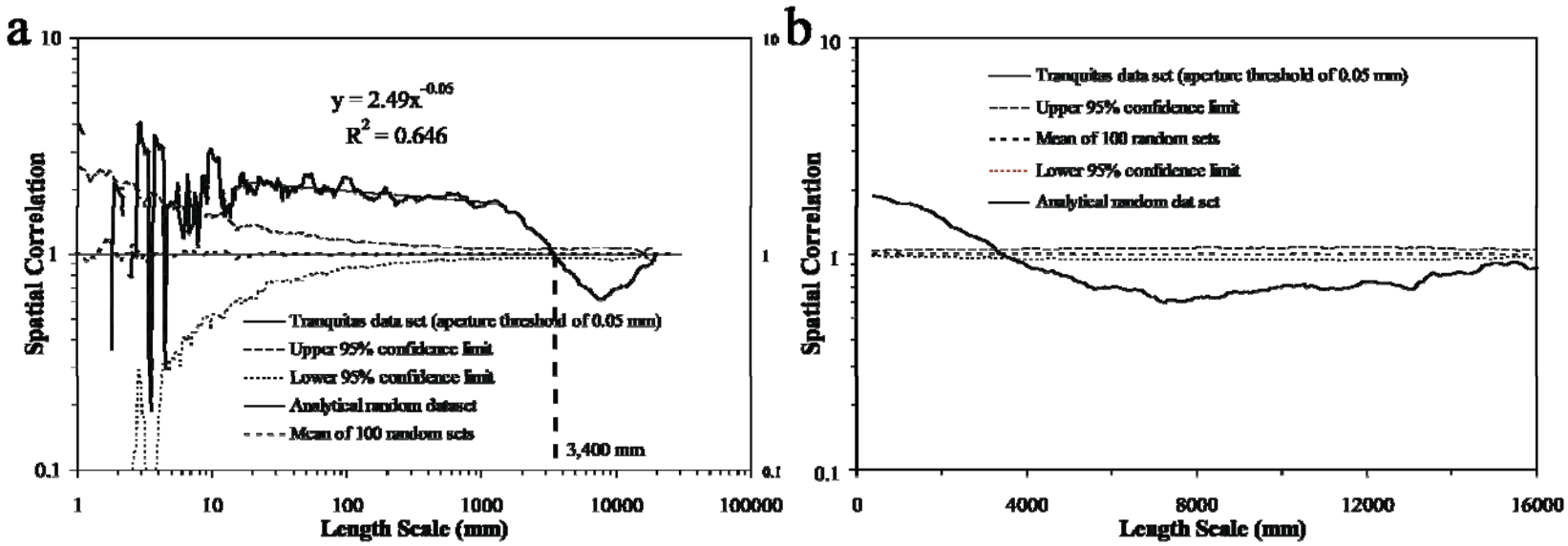

Figure 7.16 Graph of spatial correlation vs. (a) logarithmic graduations of length scale and (b) linear graduations of length scale for all the Tranquitas fractures (496 fractures, aperture threshold = 0.05 mm, thick continuous line). Analytical solution of randomly arranged fractures with an equivalent number of fractures and scanline length as veins at Tranquitas (thin line). The thin discontinuous (long dashes) line represents the upper 95% confidence interval while the thin discontinuous (short dashes) line represents the lower 95% confidence interval. Thin dotted line corresponds to the mean of 100 randomized data sets. Width of length-scale bin in (a) and (b) is 7 graduations of length scale (m = 3). Power-law in (a) was calculated using spatial correlation of Tranquitas data set between length scales of 16 and 1410 mm. Cluster width is estimated in (a) as approximately 1400 mm. Notice the low exponent of the power law, indicative of an almost horizontal line.

As with the three previously described outcrop data sets, Pedernales (Figure 7.10a), Palmas 11 LR (Figure 7.12), and Palmas 11 HR (Figure 7.13a), the Tranquitas data set at outcrop scale displays a heterogeneous arrangement of fractures in space (Figure 7.15). Although all previously mentioned data sets exhibit clusters, only the Tranquitas data set exhibits clusters with a different width and different minimum fracture aperture. A graph of fracture aperture versus location along scanline for the entire Tranquitas data set shows one wide cluster in the most northern 5 m, whereas in the southern 26 m there are several narrower clusters (Figure 7.15). In addition, there is an unusual abundance of small fractures (e.g., apertures smaller than 0.4 mm, dashed line in Figure 7.15) and the scarcity of large fractures (e.g., apertures larger than 1 mm, Figure 7.15) in the northern 5 m of scanline compared with the southern 26 m. Because the differences between the southern 26 m and the northern 5 m might indicate differences in the spatial arrangement of fractures, these two regions of the Tranquitas scanline will be analyzed separately using NCC.

7.2.3.1.1 Outcrop Scale – Southern 26 m of Tranquitas

The southern 26 m of the Tranquitas data set represents 256 fractures with a total fracture strain of 1.1%. Qualitative analysis of the fracture intensity curve indicates 8 clusters that seem to be regularly spaced with a cluster spacing of 3 m (Figure 7.17a). In addition, large fractures (e.g., apertures larger than 1mm, dashed line in Figure 7.17a) seem to be more abundant inside clusters than in the intercluster region. Moreover, compared with the Pedernales data set (Figure 7.10a, clusters are harder to detect at southern 26 m of Tranquitas (Figures 7.17a) because the number of fractures and the range of measured fracture apertures inside clusters at Tranquitas is smaller than at Pedernales (Table 7.1). Nevertheless, fracture clusters in the southern 26 m of the Tranquitas scanline seem regularly spaced, with a spacing of about 3 m, as indicated by

fracture intensity in Figure 7.17a. Randomizing fracture apertures without any change in fracture positions does not make a recognizable difference in the position of large fractures inside clusters (Figure 7.17b). Although this finding suggests the lack of a qualitative relationship between fracture position and fracture size (large apertures are more clustered than small ones), vigorous testing of the hypothesis requires quantitative analysis, which will be described in subsequent sections of this chapter.

Spatial correlation for logarithmically graduated length scales for the southern 26 m did not yield a systematic pattern outside the 95% confidence interval, suggestive of an arrangement that is indistinguishable from random (Figures 7.3a and 7.18a). Spatial correlation for linearly graduated length scales for the southern 26 m of Tranquitas data set displays a pattern of alternating peaks and troughs, indicative of periodically arranged fracture clusters (Figures 7.3g and 7.18b). Cluster spacing and cluster width are estimated in Figure 7.18b to be 1500 and 500 mm respectively (Figures 7.3g).

Figure 7.17 Kinematic aperture and fracture intensity versus location along scanline for the southern 26 m of a) Tranquitas data set and b) Tranquitas data set with randomly located apertures (unchanged positions). Fracture intensity was calculated inside a window with window size of 0.5 m and window step of 0.2 m. Fracture intensity indicates clusters approximately located at 3.8, 6.6, 9.5, 12.3, 15.2, 19, 22.3, and 24.5 m, which yields a qualitative periodic arrangement of clusters with an approximate cluster spacing of 3 m. Qualitative comparison of (a) and (b) does not suggest that large fractures (e.g., apertures larger than 1 mm, dashed line) are more concentrated in clusters in (a) than in (b). Note that only the kinematic aperture axis uses logarithmic graduations.

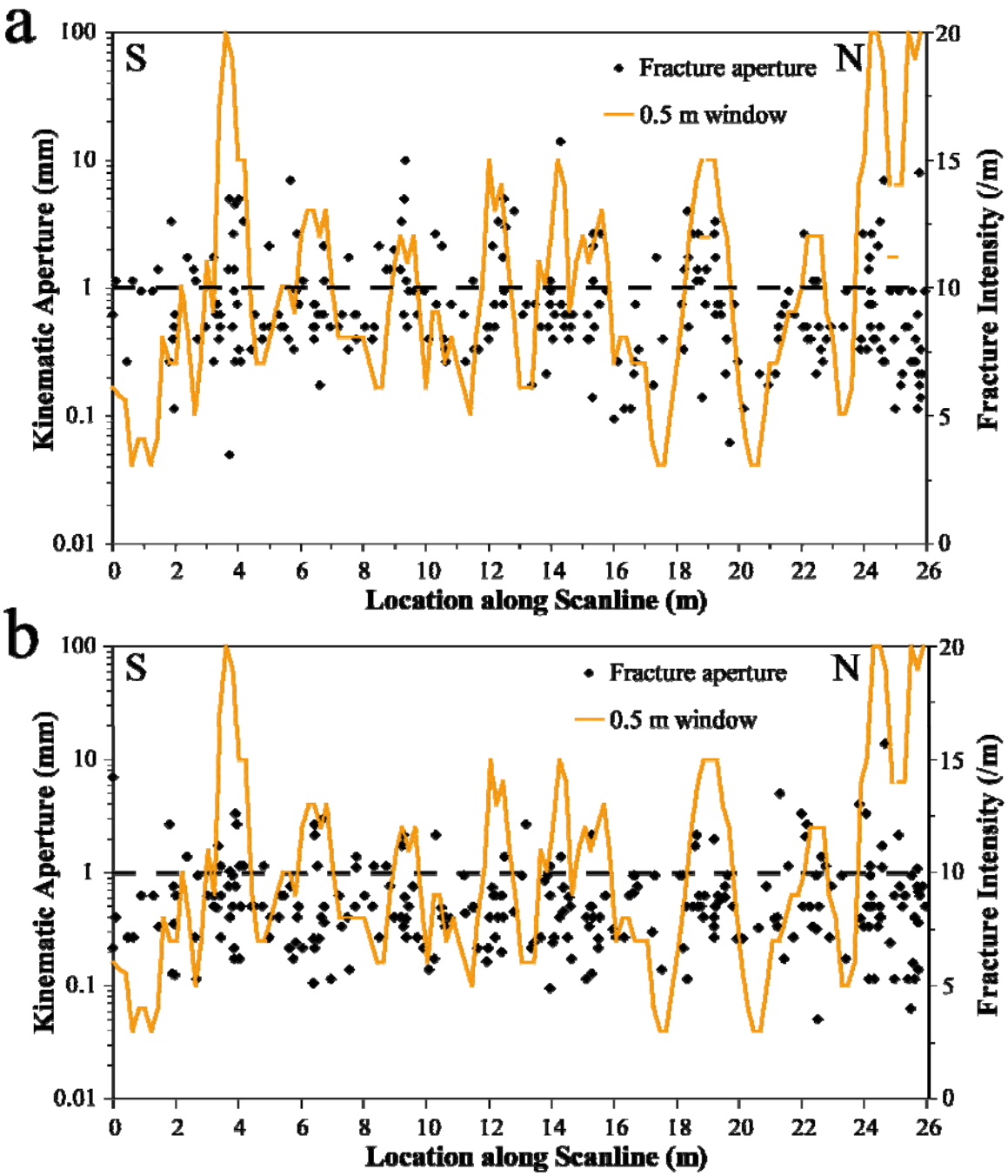
a
S
N
Fracture aperture
0.5 m window
Kinematic Aperture (mm)
Fracture Intensity (/m)
Location along Scanline (m)
b
S
N
Fracture aperture
0.5 m window
Kinematic Aperture (mm)
Fracture Intensity (/m)
Location along Scanline (m)

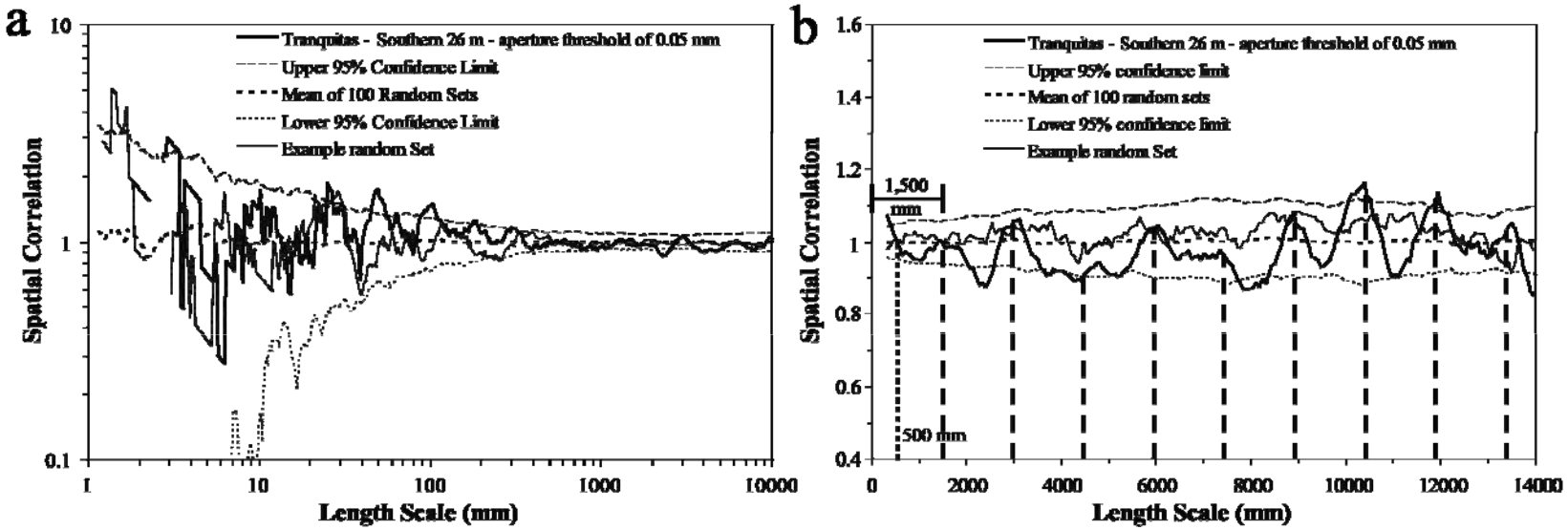

Figure 7.18 Graph of spatial correlation vs. (a) logarithmic graduations of length scale and (b) linear graduations of length scale for the southern 26 m of the Tranquitas data set (256 fractures, aperture threshold = 0.05 mm, thick continuous line). Also included an example randomized set generated with an equivalent number of fractures and scanline length (thin line). The thin discontinuous (long dashes) line represents the upper 95% confidence interval while the thin discontinuous (short dashes) line represents the lower 95% confidence interval. Thin dotted line corresponds to the mean of 100 randomized data sets. Width of length-scale bin in (a) and (b) is 9 graduations of length scale ($m = 4$). The approximately flat spatial correlation in (a) is suggestive of an arrangement that is indistinguishable from random. Evenly spaced lines every 1,500 mm in (b) match approximately the location of peaks of spatial correlation, which seem to display a regularly spaced pattern. However, only two of the seven peaks and four of the seven troughs of spatial correlation are statistically significant (Chapter 6).

7.2.3.1.2 Outcrop Scale – Northern 5 m of Tranquitas

The northern 5 m of the Tranquitas data set represents 240 fractures with a total fracture strain of 2.3%. Qualitative analysis of the fracture intensity curve for the northern 5 m may indicate periodically arranged clusters separated approximately 1.2 m (Figure 7.19). However, there does not seem to be a difference in the abundance of large fractures inside clusters than in intercluster regions. Compared with the southern 26 m along the scanline, the northern 5 m of the Tranquitas data set, exhibit several distinctive characteristics (Figures 7.15 and 7.17a). First, the northern 5 m contain a disproportionately small number of large fractures (e.g., apertures larger than 1 mm) and a disproportionately large number of small fractures (e.g., apertures smaller than 0.4 mm, Figure 7.17). Second, spatial correlation for linearly graduated length scales indicate a cluster spacing of 590 mm for the northern 5m (Figure 7.20b) and 1500 mm for the southern 26 m (Figure 7.18b). And third, independent NCC analyses using logarithmically graduated length scales for the fractures outside (southern 26 m, Figure 7.17a) and inside (northern 5 m, Figure 7.20a) the northern cluster of the Tranquitas data yielded different spatial arrangements. Fractures in the northern 5m yielded an inherited/imposed arrangement (Figures 7.3c and 7.20a) whereas fractures in the southern 26 m yielded an arrangement that is indistinguishable from random (Figures 7.3a and 7.18a).

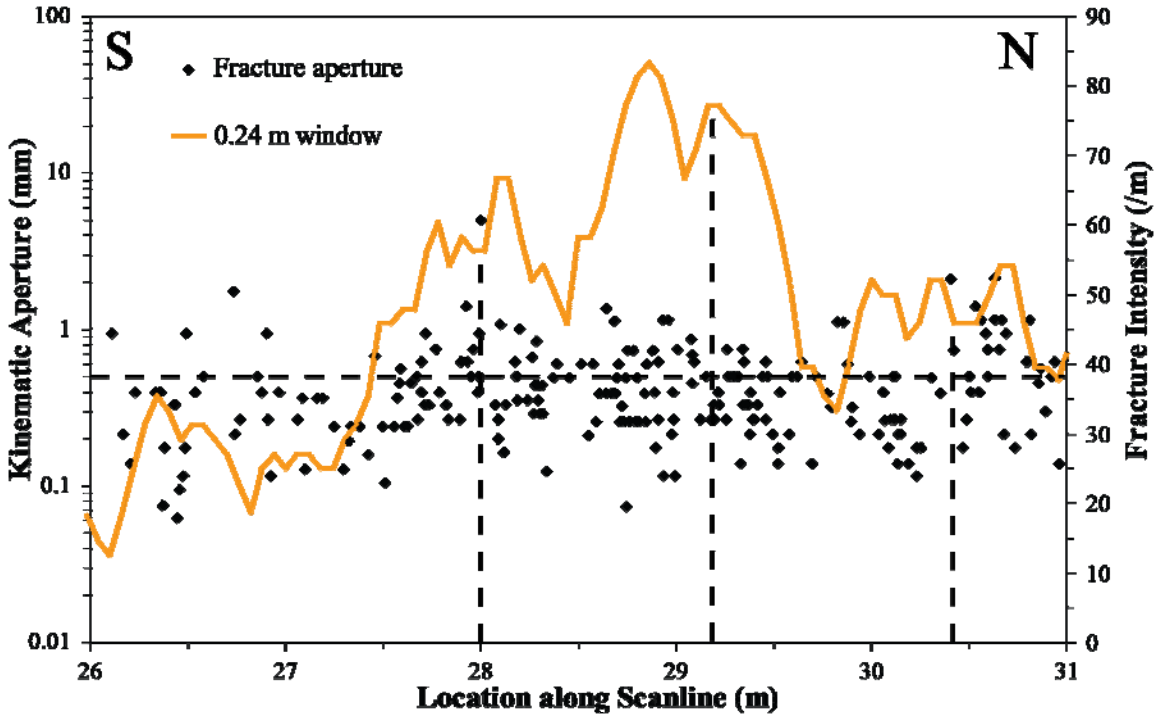

Figure 7.19 Kinematic aperture and fracture intensity versus location along scanline for the northern 5 m of Tranquitas data set. Fracture intensity was calculated inside a window with window size of 0.24 m (estimated from Figure 7.21b) and window step of 0.07 m. Fracture intensity indicates clusters approximately located at 28, 29.2, and 30.4 m, which may yield a qualitative periodic arrangement of clusters with a cluster spacing of 1.2 m. Large fractures (e.g., apertures larger than 0.5 mm, dashed line) do not seem more abundant inside clusters than in intercluster regions.

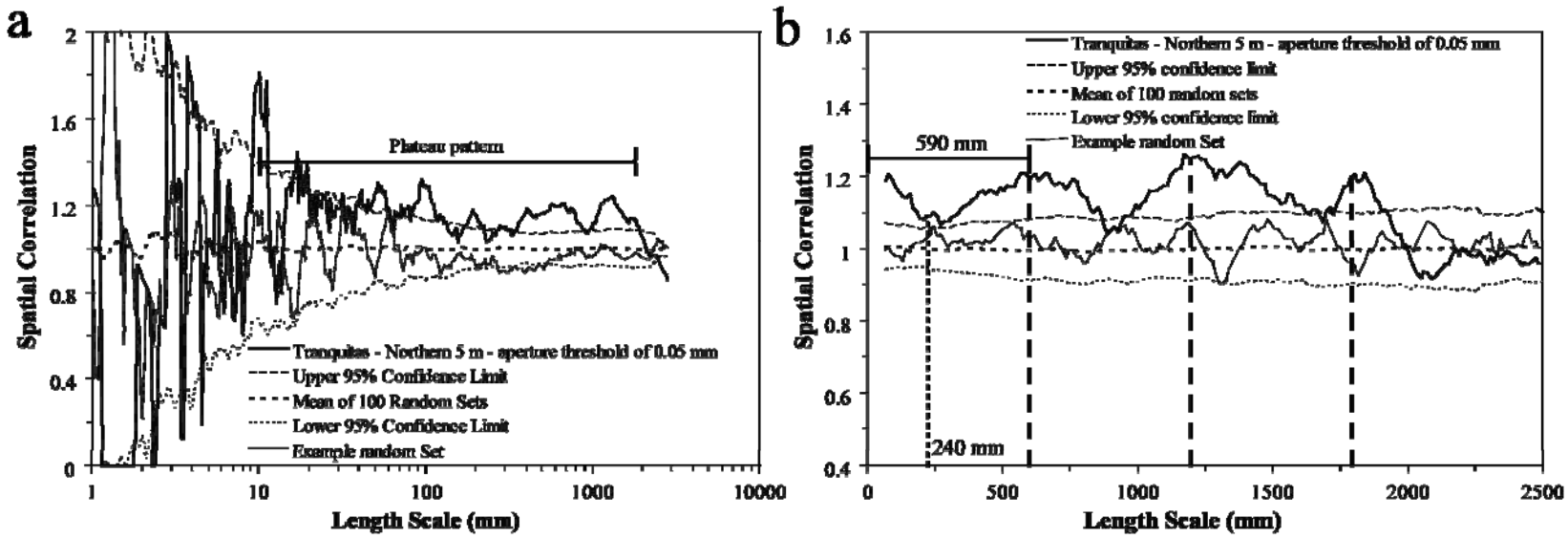

Figure 7.20 Graph of spatial correlation vs. (a) logarithmic graduations of length scale and (b) linear graduations of length scale for the northern 5 m of the Tranquitas data set (240 fractures, aperture threshold = 0.05 mm, thick continuous line). Width of length-scale bin is 9 graduations of length scale (m = 4). Linear axis of spatial correlation (instead of logarithmic) was used in (b) to facilitate the detection of patterns in curves with small differences in spatial correlation. The plateau pattern of spatial correlation in (a) indicates imposed/inherited clustering (Marrett et al., in review). Evenly spaced lines every 590 mm in (b) match approximately the location of peaks of spatial correlation, which seem to display a regularly spaced pattern, indicative of periodically arranged clusters. Cluster width is estimated in (b) as approximately 240 mm. In addition, all three peaks of spatial correlation in (b) are outside the 95% confidence interval and therefore the resulting spatial arrangement (periodically arranged clusters) is statistically significant (Chapter 6).

7.2.3.1.3 Scanline Domain and Fracture Spatial Arrangement

The two domains (northern 5 m and southern 26 m) of the Tranquitas data set display different spatial arrangements. Inside fracture clusters, the northern 5 m exhibits an inherited/imposed arrangement whereas the southern 26 m exhibits a random arrangement. Although both segments of the Tranquitas data set exhibit periodic arrangement of fracture clusters, the cluster spacing is different, 590 mm for the northern 5 m and 1500 mm for the southern 26 m.

Examination of the Tranquitas outcrop indicates that layer orientation is approximately horizontal for the entire southern 26 m of the Tranquitas scanline (Figure 7.21a), whereas layers are folded immediately north of the northern end of the scanline (Figure 7.21b). Because inherited/imposed clustering is interpreted to be caused by externally driven processes such as folding (Marrett et al., in review), I interpret the inherited/imposed fracture arrangement at the northern 5 m to be related to the folding detected only at the northern end of the scanline (Figure 7.21). In contrast, in the southern 26 m fractures do not exhibit an inherited/imposed arrangement and layer orientation does not indicate folding; therefore, I interpret the fractures in the southern 26 m to be unrelated to the folding at the northern end of the scanline and instead to be related to fracture self-organization (Marrett et al., in review).

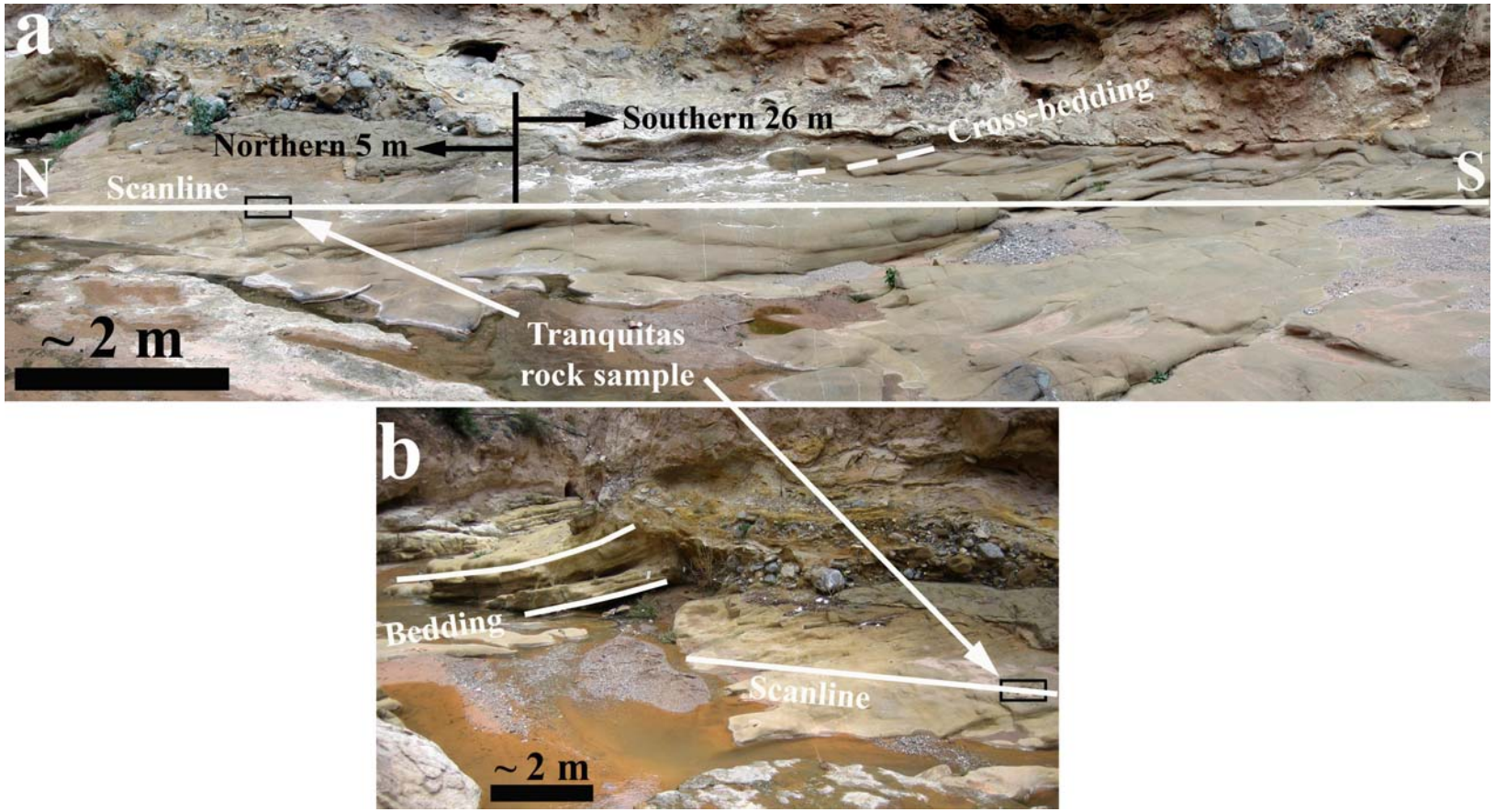

Figure 7.21 (a) Photograph of a segment of the Tranquitas scanline including the limit between the northern 5 m and the southern 26 m. Approximate location of the scanline and cross bedding are highlighted in (a). (b) Photograph of a segment of the northern 5 m of the Tranquitas scanline. Bedding is approximate horizontal in the southern 26 m, as shown in (a), but (b) shows that beds north of the northern end of the scanline are folded. Location of Tranquitas rock sample is highlighted in (a) and (b).

It is important to notice that for the southern 26 m and the northern 5 m of the Tranquitas scanline, the cluster spacing estimated qualitatively from graphs of location along scanline versus fracture intensity was approximately twice the cluster spacing obtained in graphs of spatial correlation versus length scale. This is likely the result of the inability of quantitative techniques that do not take into account fracture position, such as fracture intensity, to detect more subtle spatial arrangements, which in turn highlights the need for more rigorous quantitative techniques, such as NCC, to characterize the spatial arrangement of fractures.

Finally, the difference in the patterns of spatial correlation between the entire Tranquitas data set (Figure 7.16) and the two domains of the scanline (Figures 7.18 and 7.20) is likely the result of interference between the different spatial arrangements of the two scanline domains (Figure 7.15). The difference in spatial arrangement of fractures from the two domains of the Tranquitas scanline can be explained by different fracturing mechanisms, and therefore it is more appropriate to study the relationship between fracture size and fracture position independently for each scanline domain. The Tranquitas data set was selected for Chapter 7 because fractures are contained in a sandstone layer, which allows testing the hypothesis that large fractures are more strongly partitioned into clusters than small fractures in a lithology different from the carbonate layers of the Cupido Fm.

7.2.3.1 Rock Sample-scale Data Set

A continuous scanline that extended over eight consecutive thin sections was generated from a sample obtained along the outcrop scanline (Figure 7.21) using the methods described in Chapter 5 (Gomez and Laubach, 2006). A sample was extracted from inside the cluster located at the north end of the scanline (Figure 7.21). A total of 173 transgranular fractures were mapped in 230 mm of scanline (on SEM/CL images)

that recorded a strain of 2.59% (Table 2.3). Minimum and maximum fracture apertures measured were 0.0005 and 0.6316 mm (Figure 7.22).

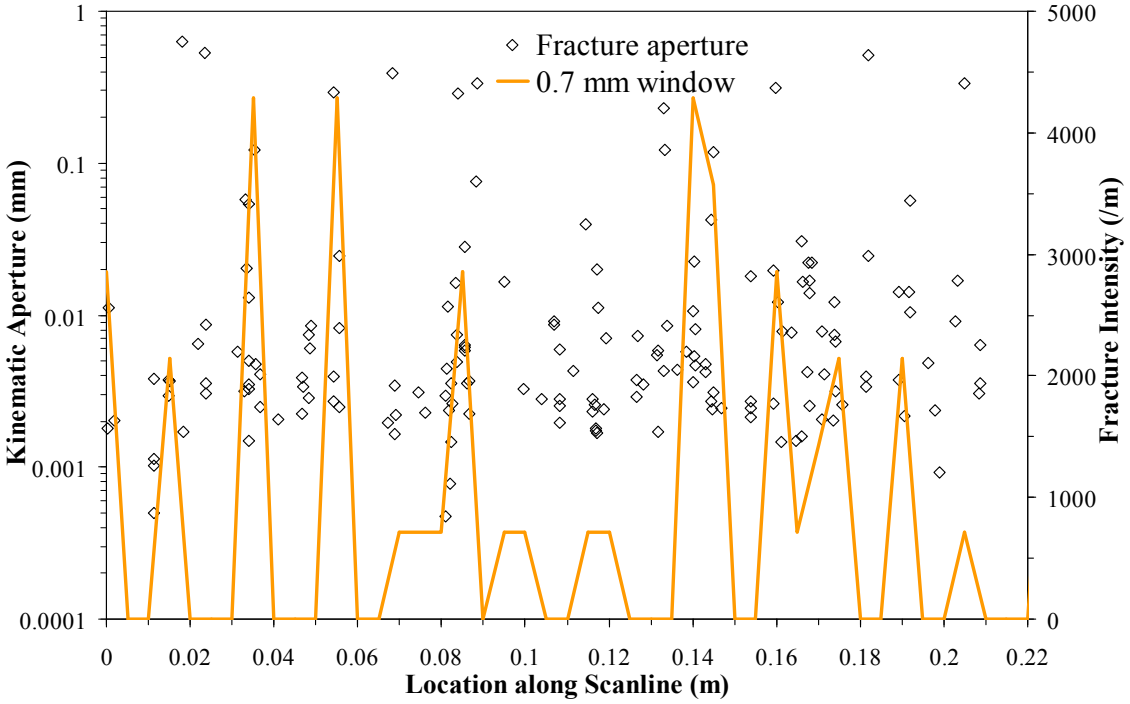

Figure 7.22 Kinematic aperture and fracture intensity versus location along scanline for the rock sample from the northern 5 m of Tranquitas data set. Fracture intensity was calculated inside a window with window size of 0.7 mm (estimated from Figure 7.21b) and window step of 5 mm. Fracture intensity suggests that clusters are regularly spaced every 0.02 m. Large fractures (e.g., apertures larger than 0.01 mm) seem more abundant inside some but not all clusters.

Fracture intensity along scanline indicates a heterogeneous arrangement of fractures, with some clusters (e.g., 0.035 and 0.055 m along scanline, Figure 7.22) having more large fractures than some intercluster domains (e.g., 0.065 to 0.08 m along scanline, Figure 7.22). Spatial correlation for logarithmically graduated length scales for the Tranquitas rock sample data set exhibit a statistically significant power-law pattern, indicating that fractures are arranged in clusters and that the clusters have internally a

fractal spatial arrangement (Figures 7.3b and 7.23a). Cluster spacing is estimated in Figure 7.23a as 0.7 mm. Spatial correlation for linearly graduated length scales for the Tranquitas rock sample data set exhibit alternating peaks and troughs outside the 95% confidence interval every 29 mm, a pattern that can be interpreted as a periodic arrangement of fracture clusters (Figures 7.3g and 7.23b). Cluster spacing is estimated in Figure 7.23b as 29 mm.

Figure 7.23 Graphs of spatial correlation (thick continuous line) vs. length scale for (a) logarithmic graduations and (b) linear graduations for the Tranquitas rock sample data set (172 fractures). In (a) and (b) the thin discontinuous line represents the upper 95% confidence limit while the thin dotted line represents the lower 95% confidence limit, and the thick discontinuous line corresponds to the mean of 100 randomized data sets. In (a) the thin continuous line represents the analytical solution of randomly arranged fractures with the same number of fractures and scanline length. In (b) the thin continuous line represents an example randomized set generated with the same number of fractures and scanline length. Width of length-scale bin in (a) is 9 (m = 4) and 23 (m = 11) graduations of length scale in (b). Spatial correlation in (a) exhibits a power-law pattern outside the 95% confidence interval, suggestive of fractal arrangement of fractures inside clusters. Cluster width in (a) is estimated at 0.7 mm. Evenly spaced lines every 29 mm in (b) match approximately peaks of spatial correlation, which can be interpreted as indicative of periodically arranged clusters.

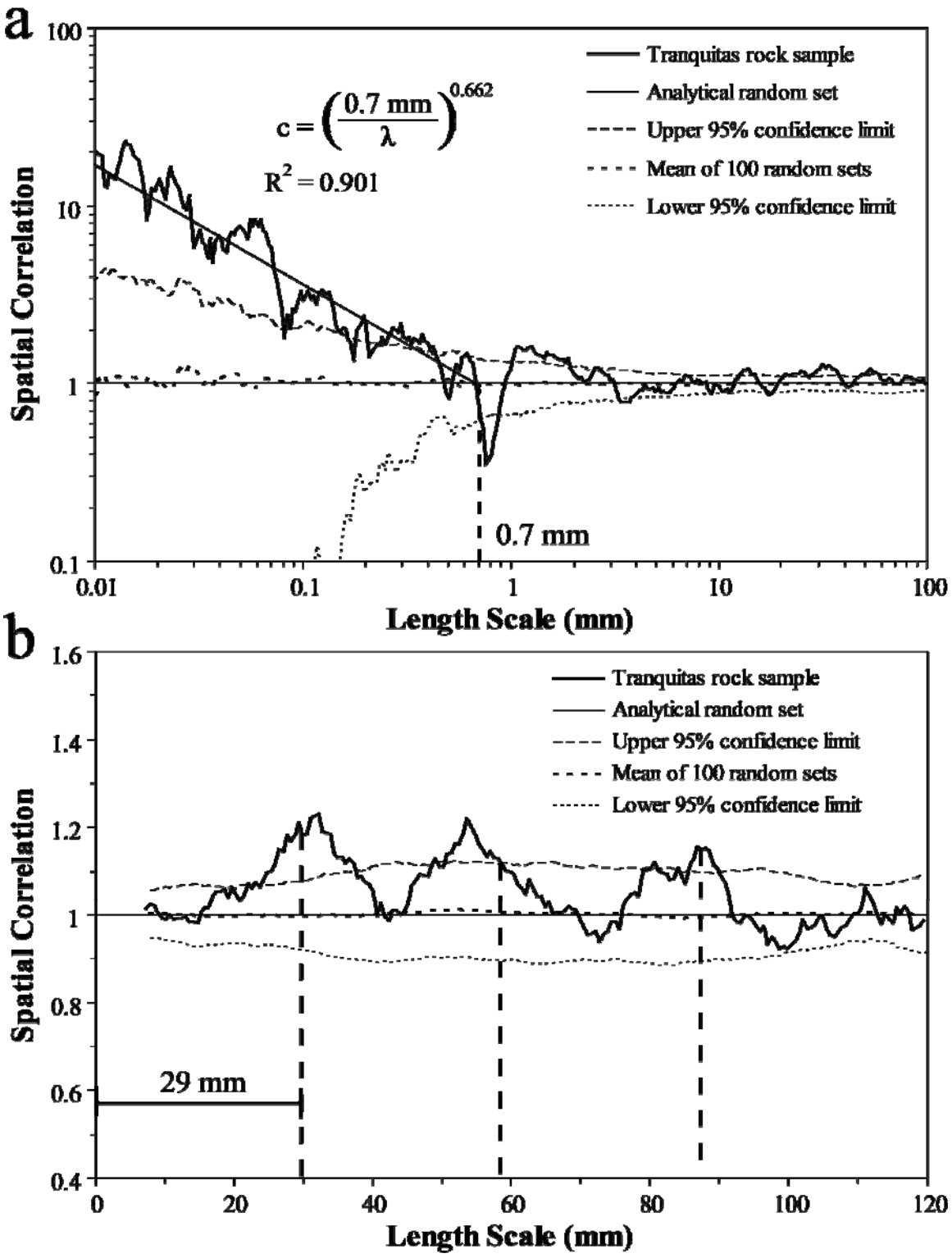
a
100
10
1
0.1
Spatial Correlation
$c = \left(\frac{0.7\ mm}{\lambda}\right)^{0.662}$
$R^2 = 0.901$
Tranquitas rock sample
Analytical random set
Upper 95% confidence limit
Mean of 100 random sets
Lower 95% confidence limit
0.7 mm
0.01
0.1
1
10
100
Length Scale (mm)
b
1.6
1.4
1.2
1
0.8
0.6
0.4
Spatial Correlation
Tranquitas rock sample
Analytical random set
Upper 95% confidence limit
Mean of 100 random sets
Lower 95% confidence limit
29 mm
0
20
40
60
80
100
120
Length Scale (mm)

7.2.4 Layer 13 at Palmas Canyon (Palmas 13)

Located a few meters stratigraphically above Layer 11, Layer 13 at Palmas canyon (Figure 7.7) is also within the Cupidito member of the Lower Cretaceous Cupido Fm. (Goldhammer, 1999; Ortega and Marrett, 2001). Using an aperture threshold of 0.14 mm, in a scanline of approximately 5.5 m I measured 459 calcite-filled veins (Figure 7.24), which display a strain of 9.16% (Table 7.1). Like the Layer 11 at Palmas canyon, the scanline of Layer 13 was positioned in the middle of the layer in a cross-sectional outcrop, as shown in Figure 7.8. Fractures of Palmas 13 layers lack porosity but most (87%) of their cement is postkinematic (13% synkinematic).

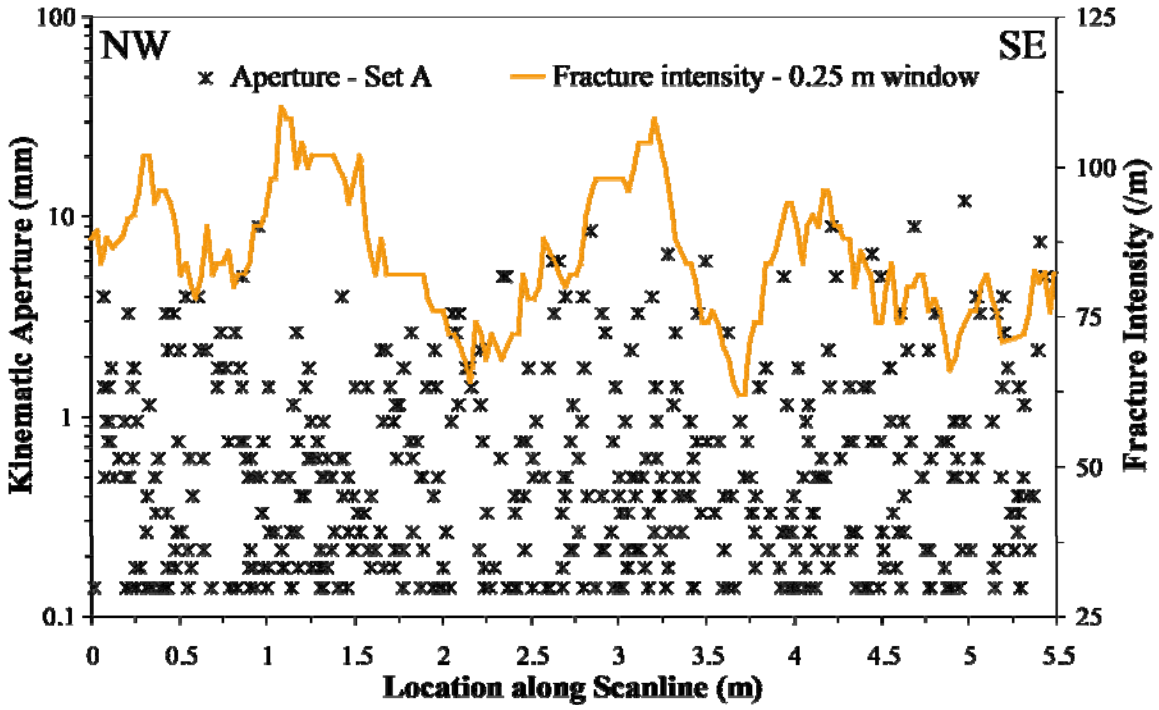

Figure 7.24 Kinematic aperture and fracture intensity versus location along scanline for the Palmas 13 data set. Fracture intensity was calculated inside a window with length (window size) of 0.25 m that was moved in increments (window step) of 0.03 m. Please note that kinematic aperture axis uses logarithmic graduations. Peaks of fracture intensity indicate clusters, but clusters do not seem regularly spaced.

Although the curve of fracture intensity indicates that the Palmas 13 data set contains clusters, there is no coincidence between the location of clusters and an unusual number of large fractures (Figure 7.24), different from what was observed in the Pedernales (Figure 7.10a), Palmas 11 LR (Figure 7.12b) and Palmas 11 HR (Figure 7.13a). In addition, the clusters detected with fracture intensity do not seem to have periodic arrangement (Figure 7.21). In addition, spatial correlation for logarithmically (Figures 7.3a and 7.25a) and linearly (Figures 7.3e and 7.25b) graduated length scales indicate arrangements that are indistinguishable from random.

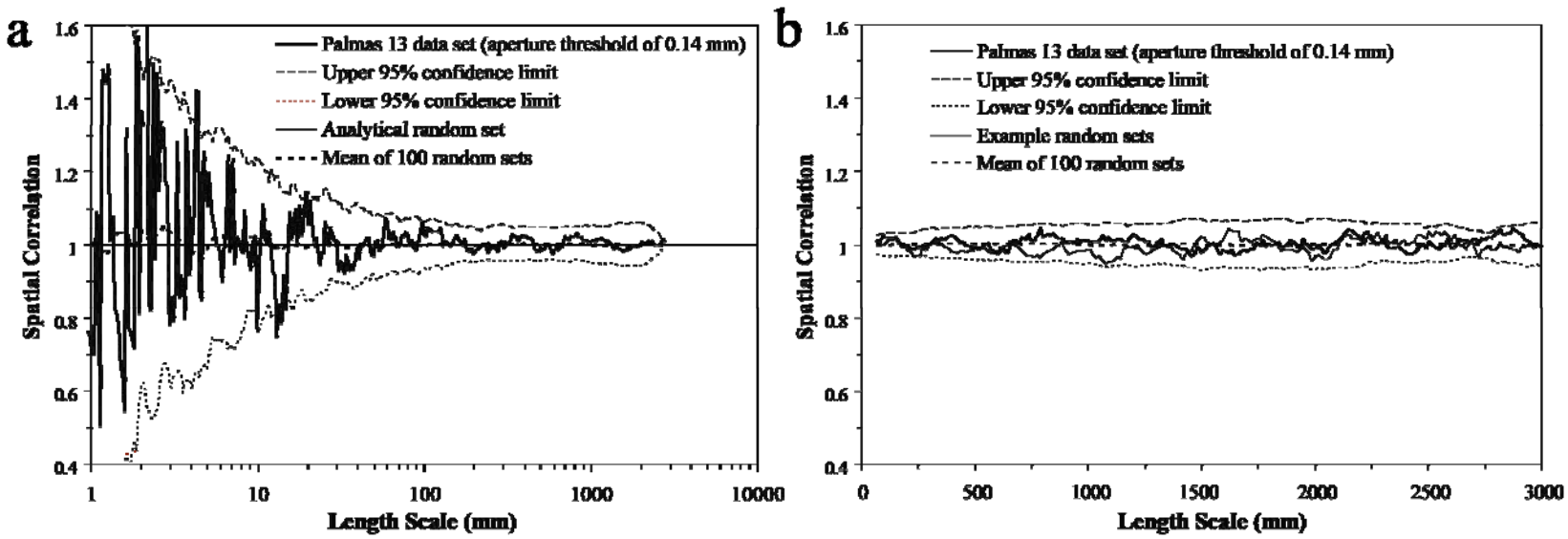

Figure 7.25 Graph of spatial correlation vs. (a) logarithmic graduations of length scale and (b) linear graduations of length scale for the Palmas 13 data set (all fractures measured, aperture threshold = 0.14 mm, thick continuous line). The thin discontinuous (long dashes) line represents the upper 95% confidence interval while the thin discontinuous (short dashes) line represents the lower 95% confidence interval. Thin dotted line corresponds to the mean of 100 randomized data sets. Width of length-scale bin is 7 graduations of length scale (m = 3). Spatial correlation in (a) and (b) follow a flat pattern of spatial correlation for most length scales and do not lie outside the 95% confidence interval, which indicates that fractures are randomly arranged at all length scales.

7.2.5 Huasteca Canyon

Unlike the Palmas 11 and Palmas 13 data sets that were measured in layers located near the top of the Cupido Formation (Appendix 3G of Ortega, 2002), I measured the Huasteca data set in a layer located near the base of the Cupido Formation (contact with the Taraises Formation, Figure 2.5). A scanline was positioned in the middle of the layer in a cross-sectional outcrop of a subvertical dolopackstone layer exposed in the Huasteca canyon, adjacent to the city of Monterrey, Mexico (Goldhammer, 1999; Ortega and Marrett, 2001). Using an aperture threshold of 0.215 mm, I measured 658 calcite-filled veins, which record a strain of 7.15%, along a 16.6 m long scanline (Figure 7.26a). Because fractures that are not perpendicular to the scanline (sets B, C, and D; Appendix 4C) account for a small portion of the fracture population (11%), I decided to leave only fractures of the A set (581 fractures, 5.74% strain), which is approximately perpendicular to scanline orientation (Table 7.1). Fractures of A set in Huasteca layer have approximately 100% of synkinematic cement.

Although the small width of the clusters (250 mm, Figure 7.27), compared with the entire scanline length (17 m, Table 7.1), obscures qualitative detection of clustering of fractures in the Huasteca data set (Figure 7.26a), peaks of fracture intensity seem to indicate the presence of relatively regularly spaced clusters with an average spacing of approximately 1050 mm (Figure 7.24a). Similar to Pedernales (Figure 7.10a) and Palmas 11 HR (Figure 7.13a), fractures with large apertures seem qualitatively more abundant inside clusters (Figure 7.26b).

Spatial correlation for logarithmically graduated length scales of set A fractures varies as a power-law of length scale (Figure 7.27), which indicates a fractal arrangement of fractures inside clusters (Figure 7.3b) with a cluster width of 250 mm. However, set A

fractures exhibit a power-law pattern of spatial correlation with an exponent near zero and therefore clusters cannot unequivocally be characterized as having a fractal (Figure 7.3b) or an inherited/imposed arrangement (Figure 7.3c). Spatial correlation for linearly graduated length scales shows a pattern of alternating peaks and troughs that is interpreted as a periodic arrangement of fracture clusters (Figures 7.3g and 7.28b).

7.2.6 Types of Spatial Arrangements

Different spatial arrangements (Marrett et al., in review) are represented by the data sets selected for this chapter (Table 7.2, Figure 7.3). NCC analysis of the Palmas 13 data set yields an arrangement of fractures that is indistinguishable from random at all length scales (Figure 7.25). Although random positioning of fractures inevitably is going to lead to some clustering (Priest and Hudson, 1976), this clustering is not statistically significant (Marrett et al., in review). In contrast to the Palmas 13 data set, the Palmas 11 LR, Palmas 11 HR data sets at outcrop scale and the Tranquitas data set at rock sample scale display what could be interpreted as a fractal arrangement of fractures inside clusters (Figures 7.11a, 7.14a, and 7.23a, respectively) and a periodic arrangement of clusters (Figures 7.11b, 7.14b, and 7.23b). Although the Pedernales data set exhibits a fractal arrangement of fractures inside clusters (Figure 7.9a), the Pedernales fractures lacks an unambiguous periodic arrangement of fracture clusters (Figure 7.9b), and therefore a pattern of periodic arrangement of fracture clusters for Pedernales can be suggested but not confirmed (Figure 7.9b).

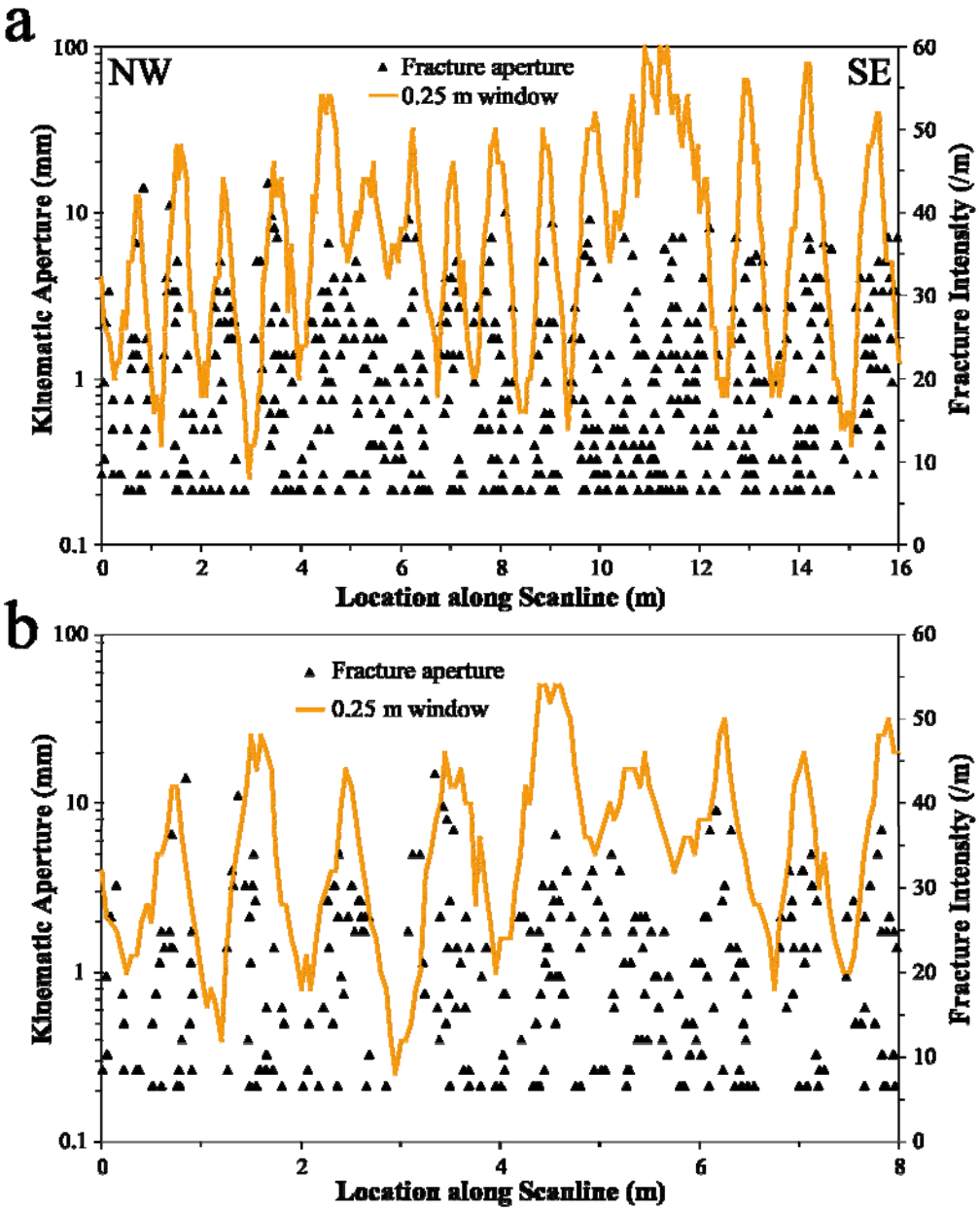

Figure 7.26 Kinematic aperture and fracture intensity versus location along scanline for the entire (a) and the first half (b) of the scanline for the Huasteca data set. Fracture intensity was calculated inside a window with window size of 0.25 m (Figure 7.26) and window step of 0.05 m. Peaks of fracture intensity indicate clusters, which appear to be regularly spaced with an average cluster spacing of 1050 mm, as shown in (a). Large fractures seem to be more abundant in clusters (peaks of fracture intensity) than in the intercluster regions (troughs of fracture intensity), as shown in (b). Please note that the kinematic aperture axis uses logarithmic graduations.

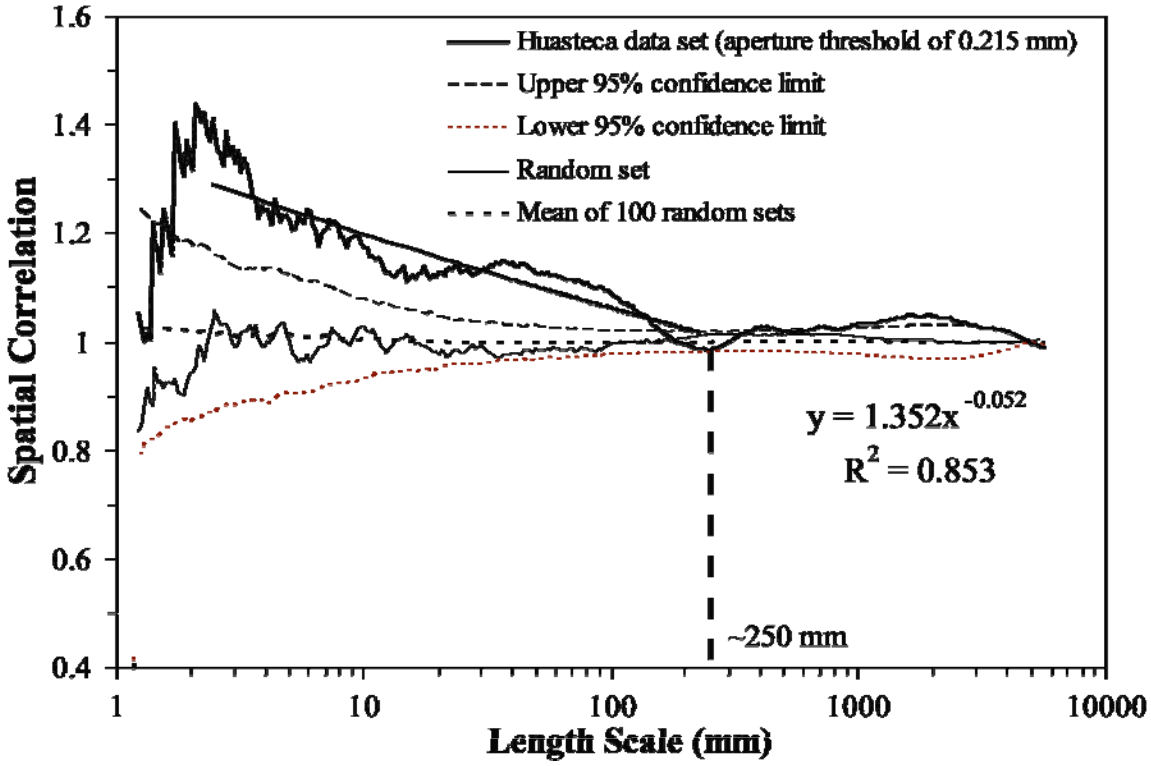

Figure 7.27 Graph of spatial correlation versus logarithmic graduations of length scale for veins of the Huasteca data set with an aperture threshold of 0.215 mm (thick line). Also included an example randomized set generated with an equivalent number of fractures and scanline length (thin line), average spatial correlation for 100 randomized data sets (short-dashed line), and upper (long-dashed line) and lower (dotted line) 95% confidence intervals. Linear axis of spatial correlation (instead of logarithmic) was used to facilitate the detection of patterns in curves with small differences in spatial correlation. Width of length-scale bin is 41 graduations of length scale (m = 20). A power-law pattern of spatial correlation is more evident than in Figure 7.27a (m = 3).

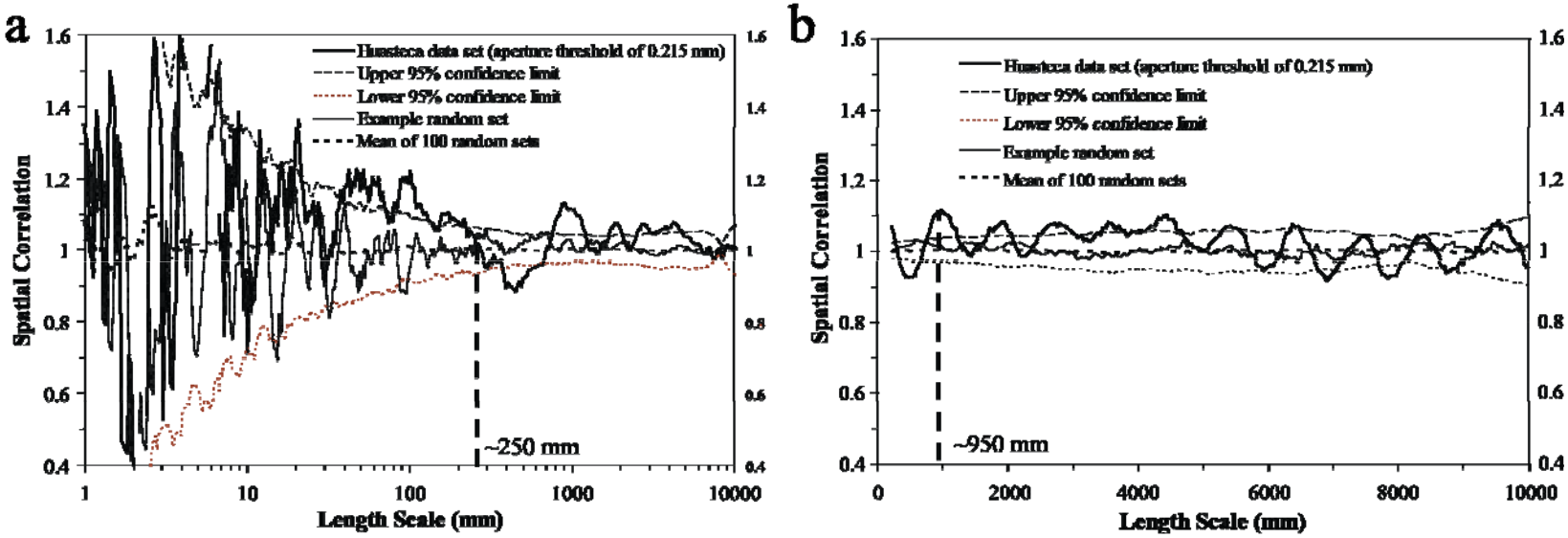

Figure 7.28 Graph of spatial correlation vs. (a) logarithmic graduations of length scale and (b) linear graduations of length scale for the Huasteca data set (set A only, 581 fractures measured, aperture threshold = 0.215 mm, thick continuous line). Analytical solution of randomly arranged fractures with an equivalent number of fractures and scanline length as veins at Huasteca (thin line). The thin discontinuous (long dashes) line represents the upper 95% confidence interval while the thin discontinuous (short dashes) line represents the lower 95% confidence interval. Thin dotted line corresponds to the mean of 100 randomized data sets. Width of length-scale bin is 7 graduations of length scale (m = 3). Alternating peaks and troughs of spatial correlation with peaks every 950 mm suggest periodically arranged clusters. Cluster width is approximately 250 mm, as indicated in (a), whereas cluster spacing is approximately 950 mm, as indicated in (b).

Fractures located in the remaining two data sets (Set A of Huasteca and southern 26 m of Tranquitas) exhibit periodic arrangement of fracture clusters (Figures7.28b and 7.18b, respectively). However, using logarithmically graduated length scales fractures of set A in Huasteca exhibit an arrangement that cannot be completely differentiated between fractal or inherited (Figure 7.27) whereas fractures in the southern 26 m of Tranquitas data set exhibit an arrangement that is indistinguishable from random (Figure 7.18a).

7.2.7 Qualitative Detection of Differential Clustering According to Fracture Size

Qualitative analysis of graphs of kinematic aperture and fracture intensity versus location along scanline suggest that of the seven data sets studied above, four (Pedernales, Palmas 11 LR, Palmas 11 HR, and set A fractures of Huasteca) display a relationship between fracture aperture and fracture position. Namely, large fractures are located mainly in clusters whereas small fractures are located both inside and in between clusters. In contrast, the remaining three fracture data sets have a dubious (southern 26 m of Tranquitas and Tranquitas rock sample) or appear to lack (Palmas 13) preferential positioning of large fractures. However, qualitative interpretation of graphs of kinematic aperture and fracture intensity versus location along scanline is not free of interpreter's bias and therefore cannot provide a conclusive answer regarding a relationship between fracture aperture and position.

Table 7.2 Characteristics of spatial arrangements using NCC technique of Marrett et al. (in review). Figure number illustrating each result is shown inside parentheses. Random = indistinguishable from random. Periodic = periodically arranged clusters. Inherited = inherited/imposed clustering.

Data set	Pedernales	Tranquitas		Huasteca (Set A only)	Palmas 11		Palmas 13
		Outcrop Southern 26 m	Rock Sample		LR	HR	
Percentage of synkinematic cement	N.A.	N.A.	N.A.	100	100	100	13%
Spatial arrangement within clusters	Fractal (7.9a)	Random (7.18a)	Fractal (7.23a)	Fractal or Inherited (7.27)	Fractal (7.11a)	Fractal (7.14a)	Random (7.25a)
Order of magnitude of power-law pattern (fractal arrangement)	~ 3	Indeterminate	~2	~2	~ 2	~1	Indeterminate
Cluster width (mm)	7200 (7.9)	500 (7.18b)	0.7 (7.23b)	250 (7.27)	220 (7.11a)	70 (7.14a)	Indeterminate
Power-law exponent (fractal arrangement)	0.17	Indeterminate	0.66	0.95	0.44	0.14	Indeterminate
Spatial arrangement between clusters	Possibly periodic (7.9)	Periodic (7.18b)	Periodic (7.23b)	Periodic (7.27b)	Periodic (7.11b)	Periodic (7.14b)	Random (7.25b)
Average distance between clusters (mm)	~19000 (7.9b)	1500 (7.18b)	29 (7.23b)	950 (7.28b)	~1100 (7.11b)	353 (7.14b)	Indeterminate

7.3. DATA ANALYSIS – TRADITIONAL TECHNIQUES

This section of Chapter 7 will explore relationship of fracture aperture and fracture spacing using analytical techniques (or variations of techniques) traditionally used to analyze fracture attributes.

7.3.1 Independent quantitative analysis of fracture aperture and spacing

Although the fracture data sets at outcrop scale presented earlier represent different geologic histories, lithologies, ages, fractures strain and types of spatial arrangement, they display relatively similar descriptive statistics. For instance, all of the outcrop fracture data sets have apertures ranging about two orders of magnitude (Table 7.1), except for the reduced range in the Palmas 11 LR data set due to a relatively large aperture threshold (0.95 mm). All fracture data sets have ranges of at least two and a half orders of magnitude for fracture spacings (Table 7.1). Although all data sets have a power-law distribution of fracture apertures (Figure 7.29a), only one the Palmas 13 data set follows a power law with an exponent smaller than one. In addition, Palmas 13 is the only data set that does not have a log-normal distribution of fracture spacings (Figure 7.29b). Instead, Palmas 13 data set displays a negative exponential distribution of fracture spacings (Figure 7.29b).

The Palmas 13 data set follows negative exponential distributions for spacing which implies that fractures might have random positioning (Chapter 6, Gomez and Marrett, in review). The log-normal distributions of all other data sets indicate that they could not have formed by random positioning. The Palmas 13 data set is also the only one with a coefficient of variation (the ratio of standard deviation over the mean, or C_v) of fracture spacing smaller than one (although close, with a value of 0.93), which suggests that veins are slightly less clustered than randomly arranged fractures (Chapter

6). All other outcrop data sets have a C_v larger than one, denoting that they are more clustered than a random arrangement of fractures (Gomez and Marrett, in review).

7.3.2 Simultaneous quantitative analysis of fracture spacing and aperture

For this section, two methods were selected to analyze simultaneously fracture spacing and aperture. The first consists of normalized plots of fracture location along scanline versus cumulative aperture, similar to the ones used by Gillespie et al. (1999). The second approach is to use crossplots of fracture aperture versus fracture spacing.

7.3.2.1 Normalized cumulative aperture vs. normalized location along scanline

In graphs of cumulative aperture versus location along scanline known as staircase plots, the location along scanline can be considered a proxy for the cumulative fracture spacing because the fracture strain of a data set is typically small (Table 7.1). Normalizing both axes by total cumulative aperture and total scanline length, respectively, allows comparison of the strain distribution along the scanline for different data sets (Figures 7.30a and 7.30b). In staircase plots, the slope is a measure of the fracture strain and the irregularity of the curve is a measure of the heterogeneity of the strain (Gillespie et al., 1999).

Figure 7.29 Cumulative frequency of (a) kinematic aperture for Tranquitas data set and (b) fracture spacing for Huasteca (triangles) and Palmas 13 (asterisks) data sets. Continuous line is power-law regression to Tranquitas data set in (a) and log-normal regression to Huasteca data set in (b). Dashed line in (b) is negative exponential regression to Palmas 13 data set. Apertures of the Tranquitas data set in (a) follow a power-law pattern for at least one order of magnitude (dashed lines).

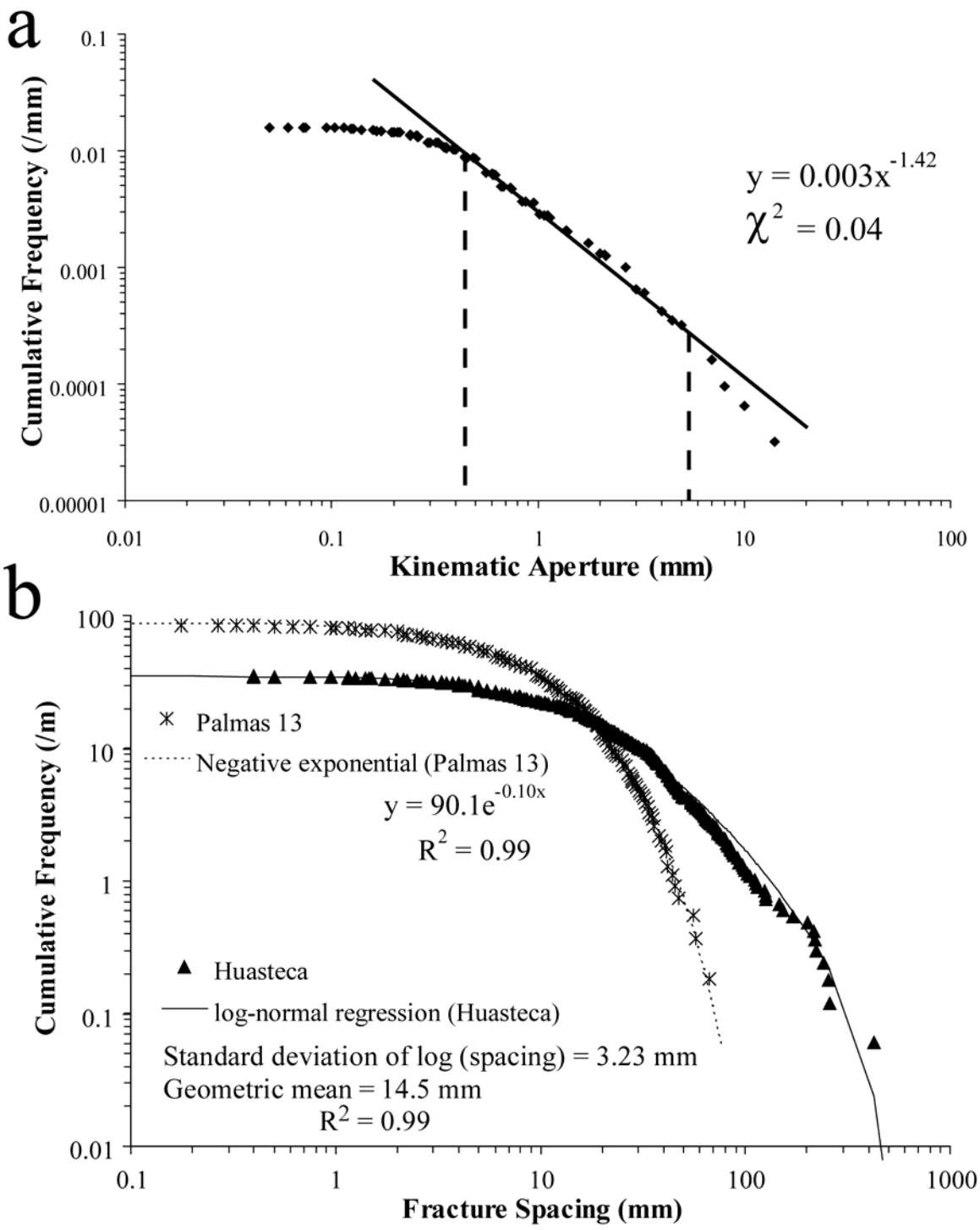
a
Cumulative Frequency (/mm)
0.1
0.01
0.001
0.0001
0.00001
0.01
0.1
1
10
100
Kinematic Aperture (mm)
y = 0.003x^-1.42
χ² = 0.04
b
Cumulative Frequency (/m)
100
10
1
0.1
0.01
Palmas 13
Negative exponential (Palmas 13)
y = 90.1e^-0.10x
R² = 0.99
Huasteca
log-normal regression (Huasteca)
Standard deviation of log (spacing) = 3.23 mm
Geometric mean = 14.5 mm
R² = 0.99
0.1
1
10
100
1000
Fracture Spacing (mm)

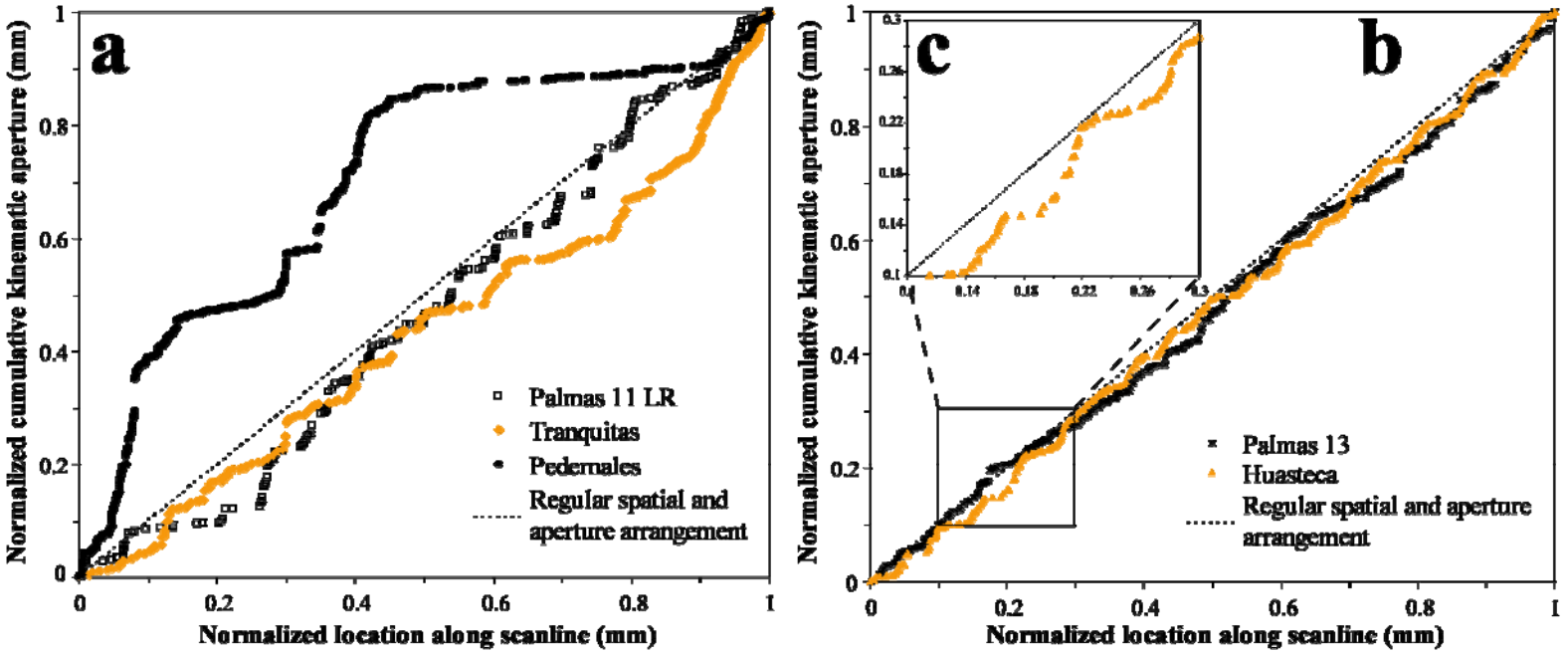

Figure 7.30 Cumulative kinematic aperture normalized by total cumulative aperture versus location along scanline normalized by total scanline length for (a) Palmas 11, Tranquitas and Pedernales data sets, (b) for Palmas 13 and Huasteca data sets, and (c) Huasteca data set between 0.1 and 0.3 of total normalized scanline length. Thin dashed line corresponds to an idealized arrangement of regularly spaced fractures with equal aperture. Data sets in (a) have a heterogeneous arrangement of fractures. However, the homogeneous arrangement of fractures of data sets in (b) is a reflection of the scale of observation, as shown in (c) for the Huasteca data set.

An approximately horizontal segment in Figures 7.30a and 7.30b represents a portion of the scanline where there is low fracture strain. Fractures could be present (e.g., Pedernales data set between 0.5 and 0.9 of total scanline length only contains 0.03% of the total cumulative aperture, Figure 7.30a) or absent (e.g., Palmas 11 LR data set between 0.24 and 0.26 of total scanline length, Figure 7.30a). In contrast, an approximately vertical segment represents a small portion of the scanline where there is high fracture strain. A vertical segment could be caused by abundant fractures in a cluster (e.g., fractures in the Palmas 11 LR data set between 0.79 and 0.8 of total scanline length contribute 10% of the total cumulative aperture, Figure 7.30a) or by a single large fracture (e.g., one fracture in the Pedernales data set at 0.08 of total scanline length contributes 6% of the total cumulative aperture, Figure 7.30a).

Pedernales, Palmas 11 LR, and Tranquitas data sets clearly display a stairway pattern, indicative of a heterogeneous arrangement of fractures, with apparent clusters and intercluster regions. In contrast, Huasteca and Palmas 13 data sets have a pattern similar to an idealized arrangement of regularly-spaced fractures with equal aperture, indicative of a homogeneous arrangement of fractures, lacking evident clustering. Nevertheless, careful observation of the Huasteca data set will show that this data set has a weak a staircase pattern (Figure 7.30b). The three data sets of Figure 7.30a contain vertical segments that display gaps inside them, confirming that they have clusters with large aperture fractures (e.g., fractures in the Pedernales data set between 0.05 and 0.09 fraction of total scanline length contribute 27% of the total cumulative aperture, or Palmas 11 LR data set between 0.26 and 0.29 fraction of total scanline length contribute 10% of the total cumulative aperture, Figure 7.30a).

Although the presence of large fractures inside clusters is qualitatively detected, a quantitative relationship between fracture size and fracture position cannot be established

using staircase plots. Namely, staircase plots cannot differentiate if the presence of large fractures inside clusters is simply due to random allocation of fracture strain or if there is a statistically meaningful relationship between fracture size and fracture position. For instance, a version of the Pedernales data set with randomized fracture aperture and without a change in the sequence of spacings (empty circles, Figure 7.31) is almost indistinguishable from the unmodified data set (filled circles, Figure 7.31).

Gillespie et al. (1999) used staircase plots to distinguish stratabound from non-stratabound fracture sets. Gillespie et al. (1999) claimed that stratabound fractures have relatively smooth staircase plots, indicative of relatively homogeneous strain, whereas non-stratabound fractures have irregular staircase plots, reflecting the heterogeneous strain (clustering) which they represent. However, Gillespie et al. (1999) failed to recognize that the irregularities in a staircase plot (e.g., Figure 7.30b) could be related to the scale of observation. Namely, that what seems as a homogeneous staircase plot at one scale could appear heterogeneous at a different scale (Figure 7.30c).

In summary, staircase plots can only generate qualitative information about the heterogeneity (presence or absence of clusters) of the spatial arrangement of a fracture data set but cannot distinguish if there is a quantitative relationship between fracture aperture and position. In addition, staircase plots are not adequate to indicate if the strain heterogeneity could be the result of random location of fracture apertures.

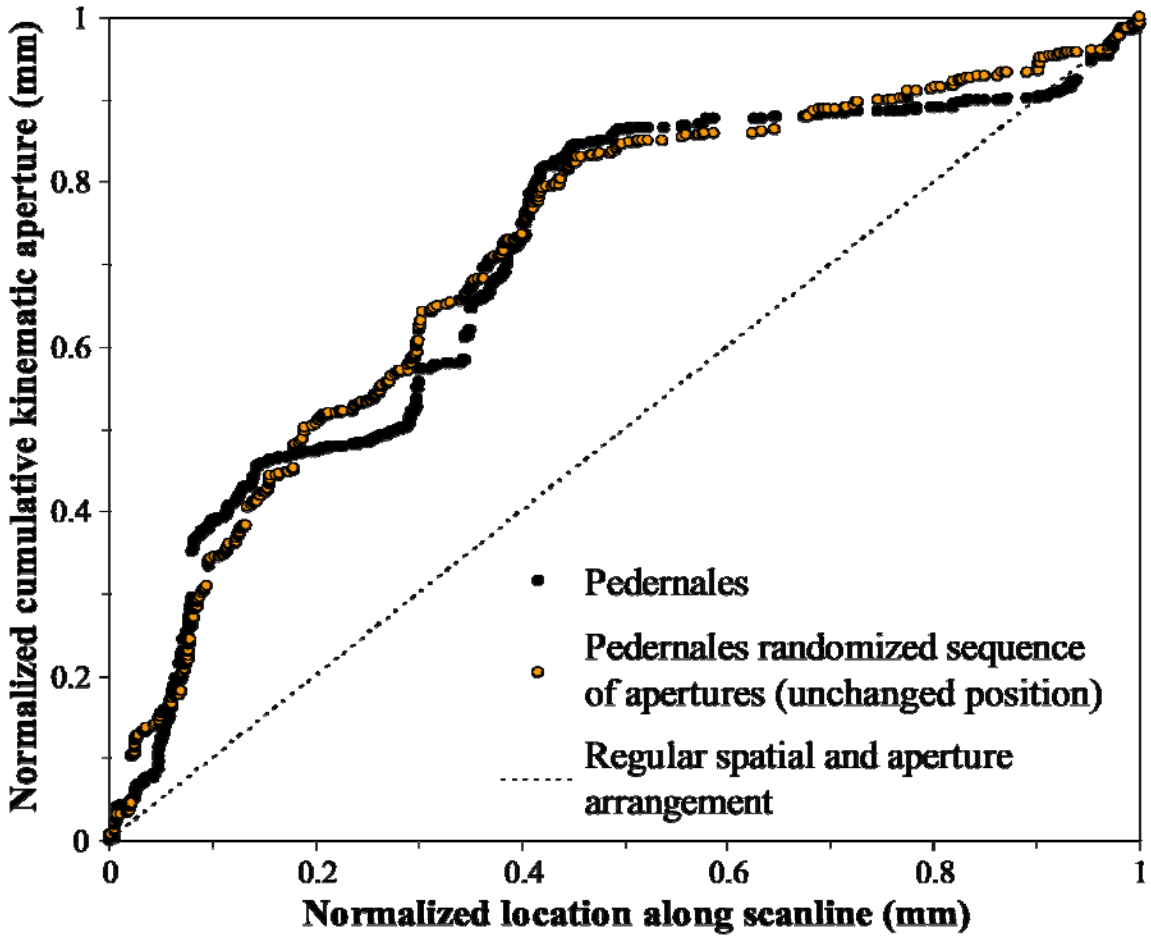

Figure 7.31 Cumulative kinematic aperture normalized by total cumulative aperture versus location along scanline normalized by total scanline length for Pedernales data set (black filled circles) and randomized sequence of apertures (unchanged sequence of fracture spacings) of the Pedernales data set (orange filled circles). Thin dashed line corresponds to an idealized arrangement of regularly spaced fractures with equal aperture.

7.3.2.2 Crossplots of fracture spacing and fracture aperture

Another approach to study the relationship between fracture aperture and spacing is to generate crossplots of both attributes like the ones created by Jolly et al. (1998) and displayed in Figure 7.7. Crossplots of kinematic aperture versus fracture spacing for two outcrop scale data set show that smaller fractures have a larger range of fracture spacings

than larger fractures (Figure 7.32). For instance, fractures of the Palmas 11 LR data set with apertures ranging from 0.95 to 2 mm have fracture spacings ranging between 0.95 to 800 mm, whereas fractures with apertures between 10 and 40 mm have spacings that range between 0.95 and 250 mm (Figure 7.32a). This indicates a trend of decreasing range of opening-mode fracture spacing with increasing aperture (Figure 7.32). This is the first time that a pattern of aperture and spacing has been detected. Perhaps the lack of crossplots of aperture with spacing in the literature on opening-mode fractures is an indicative of the lack of patterns detected by other fracture researchers (R. Ackermann, personal communication, 2005). In addition, crossplots of fracture spacing and aperture illustrate how a single value (e.g., average) of fracture aperture or fracture spacing cannot represent all the complexities in the relationship between those two fracture attributes (Figure 7.32).

Nevertheless, graphs of kinematic aperture versus maximum fracture spacing can be more indicative of a relationship between fracture spacing and fracture size (Figures 7.33 and 7.34a), akin to the kind of graphs that Jolly et al. (1998) used (Figure 7.7b). The use of a comparator in the measurement of fractures facilitates the generation of this kind of graphs because all fractures with apertures between 0.05 and 5 mm (two orders of magnitude) have predetermined apertures. For all fractures with the same aperture, only the one with the largest spacing was plotted in Figures 7.33 and 7.34. Although it is not a perfect trend, there is a pattern of maximum fracture spacing decreasing with increasing aperture for all five outcrop-scale data sets described earlier (Figures 7.33 and 7.34a).

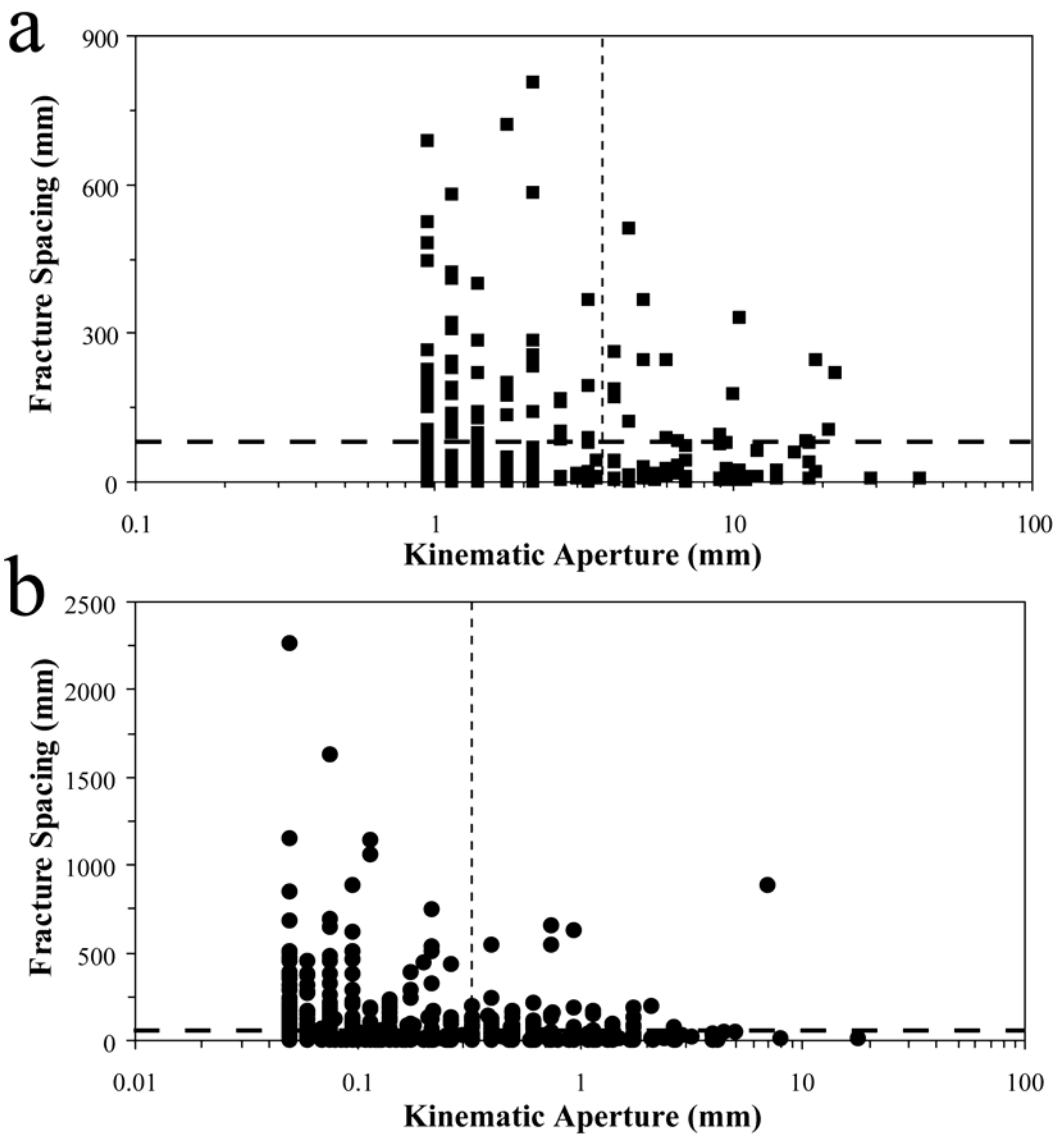

Figure 7.32 Fracture spacing versus kinematic aperture for (a) Palmas 11 LR and (b) Pedernales data sets. Of the two fracture spacings surrounding a fracture, fracture spacing plotted here corresponds to the distance between one fracture and the next fracture in the direction the scanline was measured. Horizontal dashed line indicates average spacing (Table 7.1) and vertical dashed line indicates average aperture (3.5 mm for Palmas 11 LR and 0.34 mm for Pedernales).There is a trend of decreasing the range of fracture spacings with increasing aperture. Please note that only the kinematic aperture axis use logarithmic graduations.

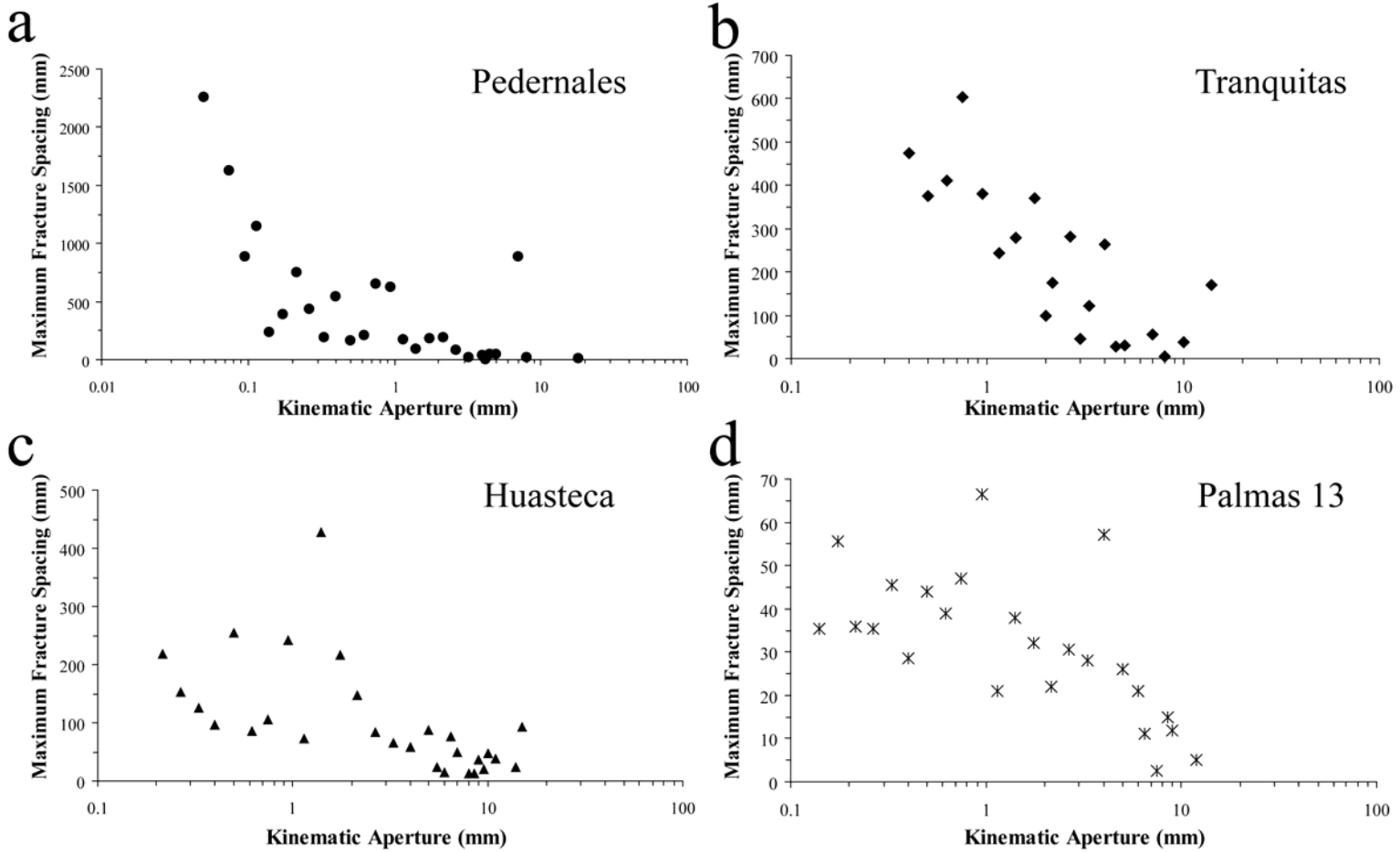

Figure 7.33 Maximum fracture spacing versus kinematic aperture for (a) Pedernales, (b) Tranquitas, (c) Huasteca and (d) Palmas 13 data sets. All four data sets display a decrease in the maximum fracture spacing with increasing kinematic aperture. Please note that only the kinematic aperture axis use logarithmic graduations.

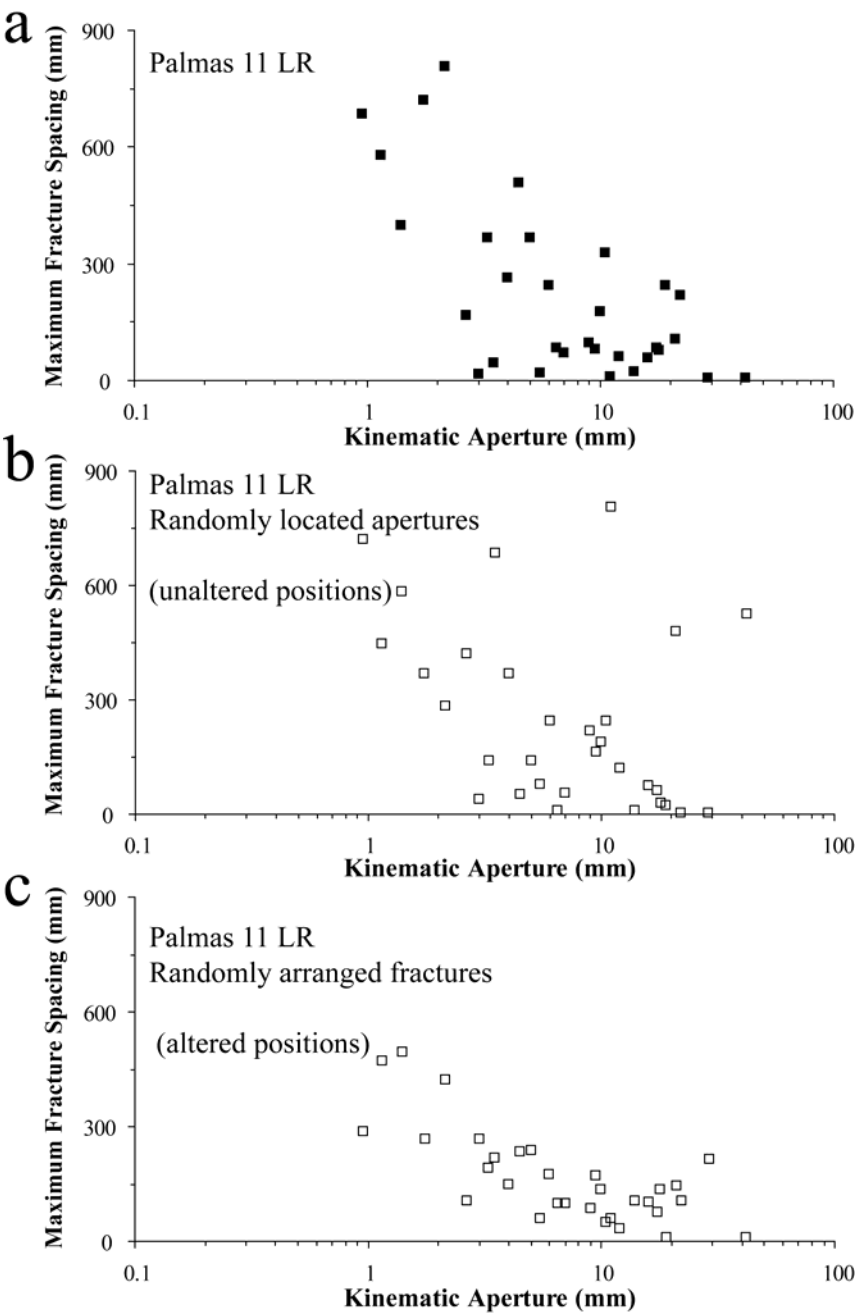

Figure 7.34 Maximum fracture spacing versus kinematic aperture for (a) Palmas 11 LR data set, b) Palmas 11 LR data set with randomly located apertures (unchanged sequence of fracture spacings), and c) Palmas 11 LR data set with randomly arranged fractures (modified sequence of fracture spacings). The quality of the pattern of decreasing maximum fracture spacing with increasing aperture in (a) remains in (c) but might not be present in (b).

The pattern of decreasing maximum spacing with increasing aperture is both clearer and opposite than the one obtained by Jolly et al. (1998) and shown in Figure 7.7b. Namely, Jolly et al. (1998) suggested that small clastic dikes tend to have other dikes only at small distances while larger clastic dikes can have surrounding dikes at small or larger distances, whereas the pattern displayed in Figures 7.33 and 7.34a implies that small fractures could have other nearest-neighbor fractures at close or large distances whereas large fractures can only have nearest-neighbor fractures at close distances. It is likely that the above difference in the patterns of spacing of structural elements (clastic dikes versus veins) of a particular aperture range is the result of different genetic processes, branching out for clastic dikes (Jolly et al., 1998) versus interaction between genetically related veins (Cladouhos and Marrett, 1996).

As mentioned earlier in this chapter, the five data sets selected cover most of the possible spatial arrangements described by Marrett et al. (in review) and yet all display a pattern of decreasing maximum fracture spacing with increasing aperture, which means that there is no relationship between patterns of maximum fracture spacing versus aperture and fracture spatial arrangement. Therefore, crossplots of aperture and spacing cannot be used to distinguish different spatial arrangements. For instance, Palmas 13 data set exhibits a spatial arrangement of fractures that in indistinguishable from random inside clusters (studied with logarithmic graduations of length scales, Figure 7.25a) or between clusters (studied with linear graduations of length scales, Figure 7.25b). Nevertheless, the pattern of decreasing maximum fracture spacing with increasing aperture of Palmas 13 (Figure 7.33d) is similar to the one for Palmas 11 LR (Figure 7.34a) data set, which displays fractal arrangement of fractures inside clusters (Figure 7.11a) and periodically arranged clusters (Figure 7.11b).

Although randomization of fracture aperture without a change in the sequence of fracture spacings makes the above mentioned pattern difficult to detect (Figure 7.34b), randomizing fracture positions (altering sequence of fracture spacings) does not alter the presence of a pattern of decreasing maximum fracture spacing with increasing aperture (Figure 7.34c). Namely, crossplots of fracture aperture and spacing cannot distinguish randomly arranged from non-randomly (e.g., periodically arranged clusters) arranged fractures (Figure 7.34a versus Figure 7.34c).

Randomly arranged fractures show a pattern of decreasing maximum fracture spacing with increasing aperture probably because there are more small fractures than large fractures, as evidenced by power-law distributions of aperture (e.g., Figure 7.29a), and therefore small fractures have a higher chance of not having a nearest-neighbor fracture at close distance. However, randomly arranged fractures (Figure 7.34c) have smaller maximum fracture spacing for the smallest fracture than the natural data set (Figure 7.34a). Consequently, the fact that the Palmas 13 data set displays an aperture range similar to the other four data sets presented in this chapter, but its range of maximum fracture spacings is smaller (Table 7.1), is perhaps another indication of what NCC has indicated, that Palmas 13 data set has an organization that cannot be distinguished from random (Figure 7.25).

7.3.3 Quantitative analysis of adjacent fracture spacing and fracture aperture

The spacing between fractures is partly controlled by the interaction between the stress shadows that surround each fracture (Olson, 2004). Therefore, when studying the relationship between fracture aperture and spacing it is, in principle, relevant to study the two spacings that surround a single fracture and not simply the one that is located in the direction in which the scanline was measured. Adjacent spacing is defined as the sum of the distances from the walls of a fracture to its two nearest neighbors (J. Gale, verbal

communication, 2004). This adjacent spacing is similar to the dike spacing of Jolly et al. (1998), although they did not measured distance between immediately contiguous fracture walls but between centers of two dikes (Figure 7.7a).

All five data sets analyzed in this section display a trend of decreasing maximum adjacent spacing with increasing kinematic aperture (Figures 7.35 and 7.36a), similar to the one detected in graphs of kinematic aperture versus maximum fracture spacing (Figures 7.33 and 7.34a). For three data sets, the most isolated fracture (largest maximum adjacent spacing) is a fracture with the smallest (Tranquitas, Figure 7.35b) or close to the smallest (Pedernales, Figure 7.35a and Palmas 11 LR, Figure 7.36a) aperture. In addition, for three data sets (Pedernales, Palmas 13, and Palmas 11 LR), the largest fracture has fractures in the closest proximity (smallest maximum adjacent spacing possible); whereas for the remaining two data sets (Tranquitas and Huasteca) the smallest maximum adjacent spacing belong to a fracture close in size to the largest fracture (Figures 7.35 and 7.36a). Between those two extreme values there is a pattern of decreasing maximum adjacent spacing with increasing kinematic aperture (Figures 7.35 and 7.36a), indicating that there is a relationship between the aperture of a fracture and the probability of how isolated (large adjacent spacing) or how close (small adjacent spacing) that fracture can be.

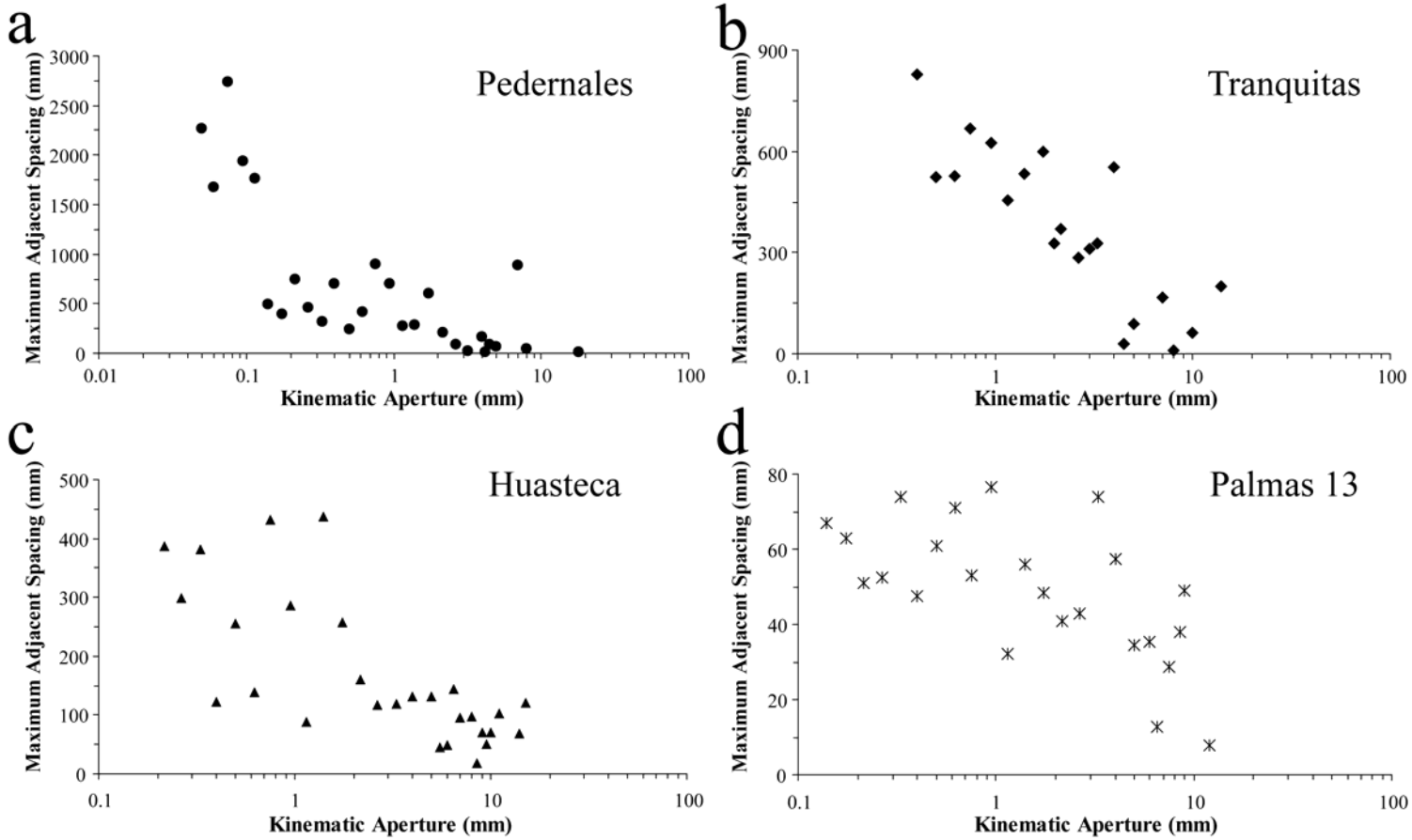

Figure 7.35 Maximum adjacent spacing versus kinematic aperture for (a) Pedernales, (b) Tranquitas, (c) Huasteca and (d) Palmas 13 data sets. Adjacent spacing was calculated by adding the two spacings around a single fracture. All four data sets display a decreasing maximum adjacent spacing with increasing kinematic aperture. Please note that only the kinematic aperture axes use logarithmic graduations.

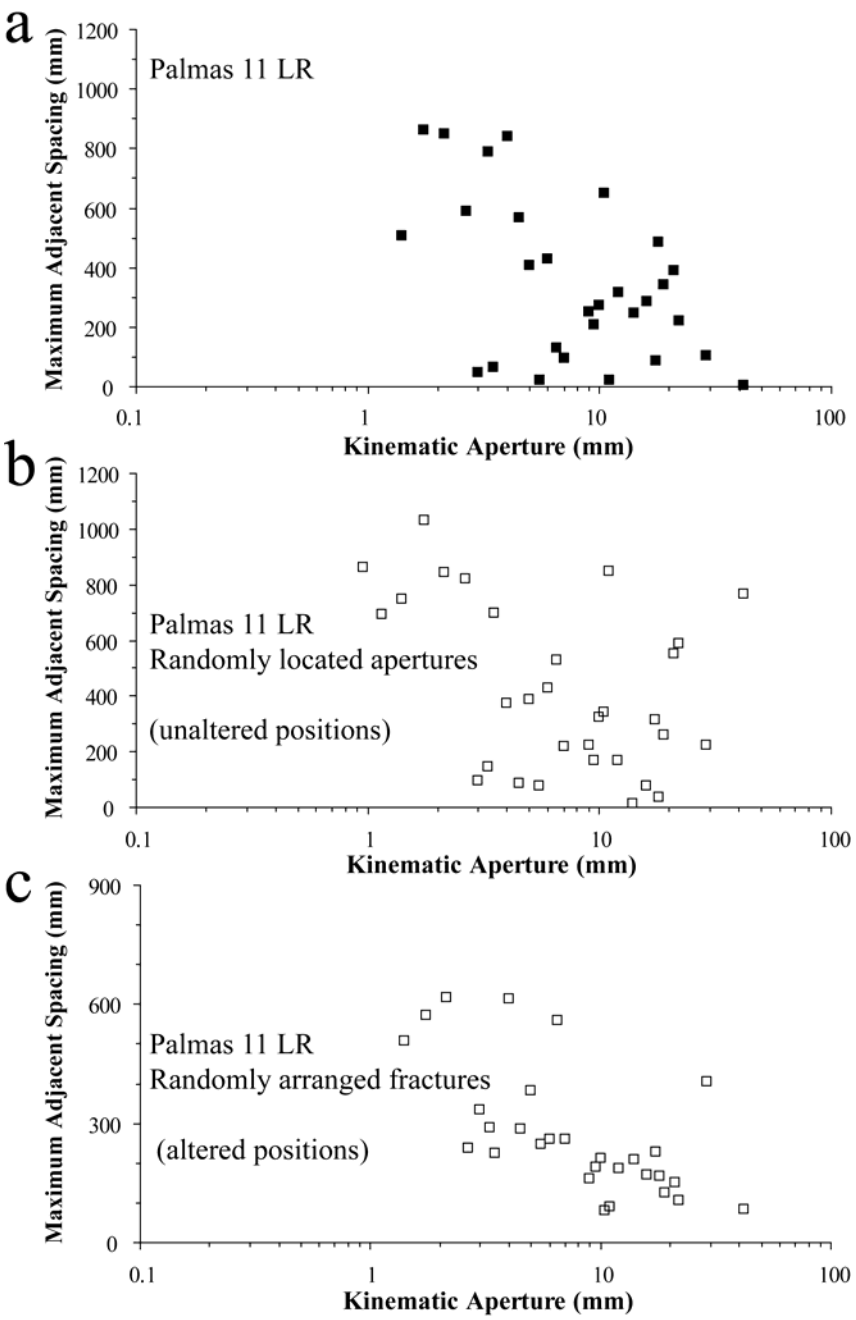

Figure 7.36 Maximum adjacent spacing versus kinematic aperture for (a) Palmas 11 LR data set, b) Palmas 11 LR data set with randomly located apertures (unchanged sequence of fracture spacings), and c) Palmas 11 LR data set with randomly arranged fractures (modified sequence of fracture spacings). The pattern of decreasing maximum adjacent spacing with increasing aperture detected in (a) is still visible in (c) but does not seem present in (b).

The pattern of decreasing maximum adjacent spacing with increasing kinematic aperture shown in Figures 7.35 and 7.36a is present in data sets that represent all possible spatial arrangements of fractures (Table 7.1) as indicated by Marrett et al. (in review), and therefore, the fraction of small fractures of a particular data set has a larger probability of having a larger adjacent spacing (being more isolated) than the fraction of large apertures of the same data set, regardless of the spatial arrangement of the data set. For instance, the Palmas 11 LR data set have clusters with an internal fractal arrangement (Figure 7.11a) that in turn are self organized in periodically arranged clusters (Figure 7.11b), and yet the Palmas 11 LR data set (Figure 7.36a) display the same pattern of decreasing maximum adjacent spacing with increasing aperture detected in the Palmas 13 data set (Figure 7.35d), which exhibits fractures randomly arranged at intra- (Figure 7.25a) and intercluster (Figure 7.25b) length scales.

Randomization of fracture apertures without a change in the sequence of fracture spacings (Figure 7.36b) does not seem to display the pattern of decreasing maximum adjacent spacing with increasing aperture detectable in the equivalent natural data set (Figure 7.36a). The lack of the above mentioned pattern indicates that the larger tendency of small natural fractures to be more isolated (larger adjacent spacing) than larger fractures cannot come from random distribution of fracture strain. In contrast, the pattern of decreasing maximum adjacent spacing with increasing aperture is still present, albeit a 50% reduction in range, when fracture position is randomized (altering sequence of fracture spacings, Figure 7.36c).

However, to investigate more deeply if patterns of maximum adjacent spacing versus kinematic aperture can or cannot distinguish random arrangement of fractures, the average adjacent spacing of 100 independently randomized versions of the Pedernales data set (e.g., Figure 7.10b) was compared with the adjacent spacing from the unmodified

data set (Figure 7.10a). Each randomized version of the Pedernales data set was created by independent randomization of fracture position, which modifies the sequence of fracture spacings. The average of the maximum adjacent spacing for the 100 randomized versions of the Pedernales data set (empty circles, Figure 7.37) also shows a pattern of decreasing maximum adjacent spacing with increasing kinematic aperture. Nevertheless, the slope of the power-law pattern for the 100 randomized versions has a lower angle than the natural data set (filled circles, Figure 7.37), indicating a fainter pattern of increasing maximum adjacent spacing with increasing aperture. In addition, at the smallest apertures (0.05 to 0.115 mm) the natural data set attains a maximum adjacent spacing larger than the average for 100 randomized versions and outside the 95% confidence interval, indicating the statistical significance of the difference in maximum adjacent spacing at equivalent apertures (Figure 7.37). Similarly, at the largest apertures (2.15 to 18 mm) the natural data set attains a maximum adjacent spacing smaller than the average for 100 randomized versions and outside the 95% confidence interval (Figure 7.34). In addition, the maximum adjacent spacing for the Pedernales data set ranges about two and a half orders of magnitude whereas the equivalent values for the 100 randomized versions range only about half order of magnitude (Figure 7.37). This reduction in the range of maximum adjacent spacing is also evident when comparing the Palmas 11 LR data set (Figure 7.36a) with its counterpart with randomized fracture positions (Figure 7.36c).

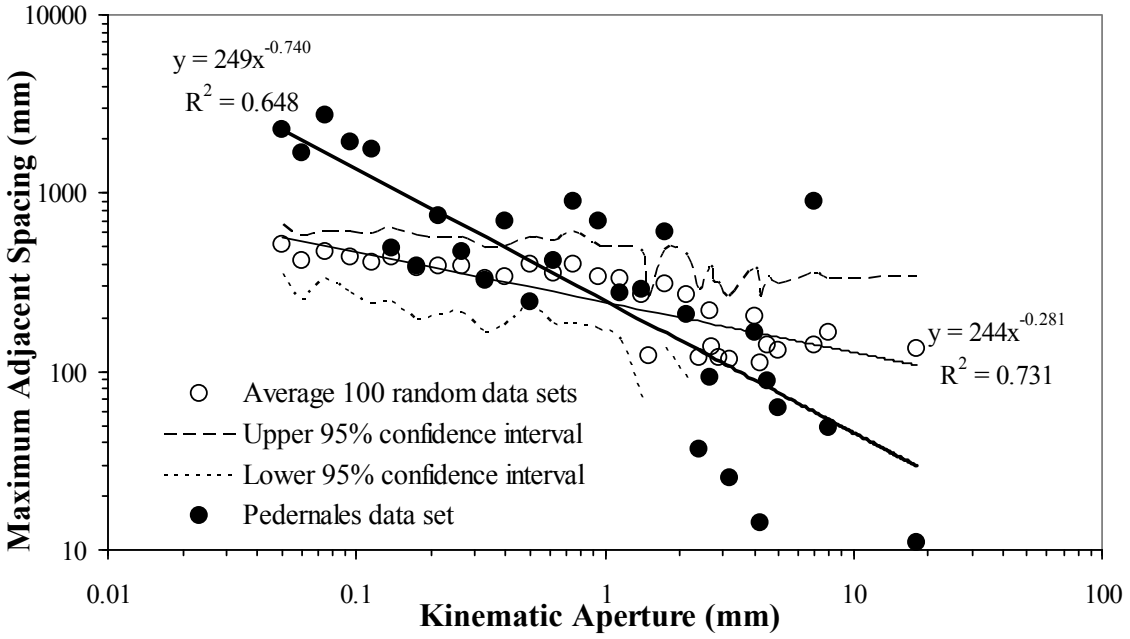

Figure 7.37 Maximum adjacent spacing versus kinematic aperture for the Pedernales data set (filled circles) and 100 versions of the Pedernales data set with randomized fracture positions (empty circles). Dashed lines are the corresponding calculated 95% confidence intervals. The pattern of decreasing maximum adjacent spacing with increasing aperture is steeper (higher power-law exponent) for the Pedernales data set (thick continuous line) that for the average of 100 randomized (randomizing fracture position) versions of the Pedernales data set (thin continuous line). Please note that both axes use logarithmic graduations.

If fractures are arranged in clusters, there should be a wide range of adjacent spacings because fractures inside clusters will have fractures at close proximity (small adjacent spacing) whereas fractures between clusters will have fractures at proportionally larger distances (large adjacent spacing). Because natural fractures data sets with both random and non-random arrangements exhibit clusters (although only non-random arrangements have statistically-significant clusters) and typically have more small than large fractures (as suggested by power-law distribution of fracture aperture), then it is logical to deduce that the abundant small fractures have a higher probability of being

inside or in between clusters than large fractures, which due to their lower abundance will have a higher probability of being in a cluster (where most fractures are) than in between clusters. Therefore, the pattern of decreasing maximum adjacent spacing with increasing aperture is a feature of all spatial arrangements that exhibit clustering, which includes all the spatial arrangements described by Marrett et al. (in review) with the exception of periodically arranged fractures arrangement (Figure 7.3f).

The difference in how rapid is the decrease of maximum adjacent spacing with increasing aperture (random arrangement having a less steep decrease, Figure 7.37) and in the range of maximum spacings (random arrangement having a smaller range) between randomly and non-randomly arranged fractures is likely the result of having statistically significant (non-random arrangements) or statistically insignificant (random arrangement) clustering. Statistically significant clusters are going to contain a much larger proportion of fractures than an equivalent data set with statistically insignificant clusters (randomly arranged) and therefore the number of small spacings is going to be larger and their sizes smaller than in statistically insignificant clustering, a pattern evident in Figure 7.37. This reasoning supports what the coefficient of variation (Table 7.1) and graphs of normalized correlation count (Figure 7.9) indicate for the Pedernales fractures: that this self-organized data set is more clustered than a random arrangement of fractures (Marrett et al., in review). In addition, the above mentioned rationalization can explain why the randomly arranged Palmas 13 data set (Figure 7.25) has a range of maximum adjacent spacings much smaller (Figure 7.35d) than the other data sets analyzed, and also explain the reduction in the range of maximum adjacent spacings when the position of fractures of the Palmas 11 LR is randomized (Figure 7.36c).

However, like some of the techniques studied in Chapter 6 (Gomez and Marrett, in review), graphs of adjacent spacing versus aperture can only detect when a array is

more clustered than a random arrangement of fractures but it cannot tell how those clusters are internally organized (e.g., in a fractal fashion) or arranged (e.g., harmonically) because they only examine the spatial relationship between three fractures (one fracture surrounded by its two nearest neighboring fractures) and ignore the spatial arrangement of fractures which can only be established by looking the sequence of fracture spacings. By ignoring the spatial arrangement of fractures, graphs of adjacent spacing versus aperture cannot fully quantify the presence of a particular aperture range inside clusters. Namely, the small adjacent spacings associated with large apertures are most likely, but not necessarily, inside a cluster.

7.4. DATA ANALYSIS – NORMALIZED CORRELATION COUNT (NCC)

The current procedure to calculate spatial correlation (the main output of normalized correlation count technique) uses as input data consecutive values of fracture aperture and spacing, the way those values are typically measured along scanlines (Chapters 2 and 6, Gomez and Marrett, in review). Although NCC is independent of fracture aperture, this technique can be used to analyze the spatial arrangement of fractures according to fracture size. For example, if fracture aperture data are available, then subsets of the data defined by aperture can be analyzed separately. Comparison of spatial correlation for different subsets of the same fracture data set with increasingly larger aperture thresholds can reveal relationships between the aperture and spatial arrangement of fractures.

7.4.1 NCC Parameters

In the current software implementation of NCC, values of length scale can have either logarithmic or linear graduations. Logarithmic graduations of length scale are skewed toward small values of length scale. Namely, the majority of length scales

analyzed are a small fraction of the total scanline length, which facilitates investigation of the spatial arrangement of fractures inside clusters (Marrett et al., in review). In contrast, consecutive values of linearly graduated length scale have constant differences, so that length scales analyzed uniformly can reach up to the entire scanline length and allow studying the spatial arrangement of fracture clusters (Marrett et al., in review). Finally, unless otherwise stated, all NCC analyses were conducted on outcrop data sets using the entire scanline available, 100 randomized versions (altered positions) and 400 graduations of length scale with the maximum length scale approximately equal to the scanline length.

7.4.2 Fractal arrangement of fractures inside clusters

The first type of spatial arrangement to be studied is the fractal arrangement of fractures inside clusters (Figure 7.3b), which is characterized by a power-law (straight line in a log-log plot) pattern of spatial correlation (Marrett et al., in review). Of the seven data sets selected for this study four (Pedernales, Palmas 11 LR, Palmas 11 HR, and rock sample from Tranquitas) clearly display a fractal arrangement of fractures inside clusters (Table 7.2).

7.4.2.1 Increasingly Larger Aperture Thresholds

When spatial correlation for the undecimated (aperture threshold used in the field) and decimated (artificially imposed aperture thresholds; Figure 7.5) subsets of the outcrop data sets are graphed together, an increase in the spatial correlation and in the slope of the power-law pattern with increasing aperture threshold can be detected at length scales smaller than cluster width (Figures 7.38, 7.39 and 7.41). An increase in spatial correlation for fractures with increasingly larger aperture indicates that larger apertures deviate more from a random arrangement than small fractures.

The increase in the slope of the power-law pattern with increasing aperture threshold (and subsequent reduction in the number of fractures) was quantified by calculating independently the exponent of the power-law equation over the same range of length scales. The slope of the power-law pattern of spatial correlation indicates the degree of clustering (Chapter 6, Marrett et al., in review) and therefore, it can be interpreted that for the Pedernales and Palmas 11 HR data sets, larger fractures are more clustered than small ones (Figure 7.38). In addition, the change in the slope of the power-law pattern does not affect the cluster width (intercept of power-law pattern with spatial correlation = 1) of the Palmas 11 HR data set (Figure 7.39) but reduces by 30% (from 7200 to 5000 mm approximately) the cluster width of the Pedernales data set (Figure 7.38). Although less evident than in outcrop-scale data sets, the power-law exponent also increases with increasing aperture threshold for data sets measured at the rock sample scale (Figure 7.41), which indicates that the difference in the degree of clustering for different fractions of fracture aperture (larger clustering for large apertures) is not limited to outcrop data sets but extends to clusters detectable at rock sample scale (typically from a few to several cm). And therefore the increased clustering of large fractures is a phenomenon of clustering that appears not to be limited by the scale of observation (Figure 7.40).

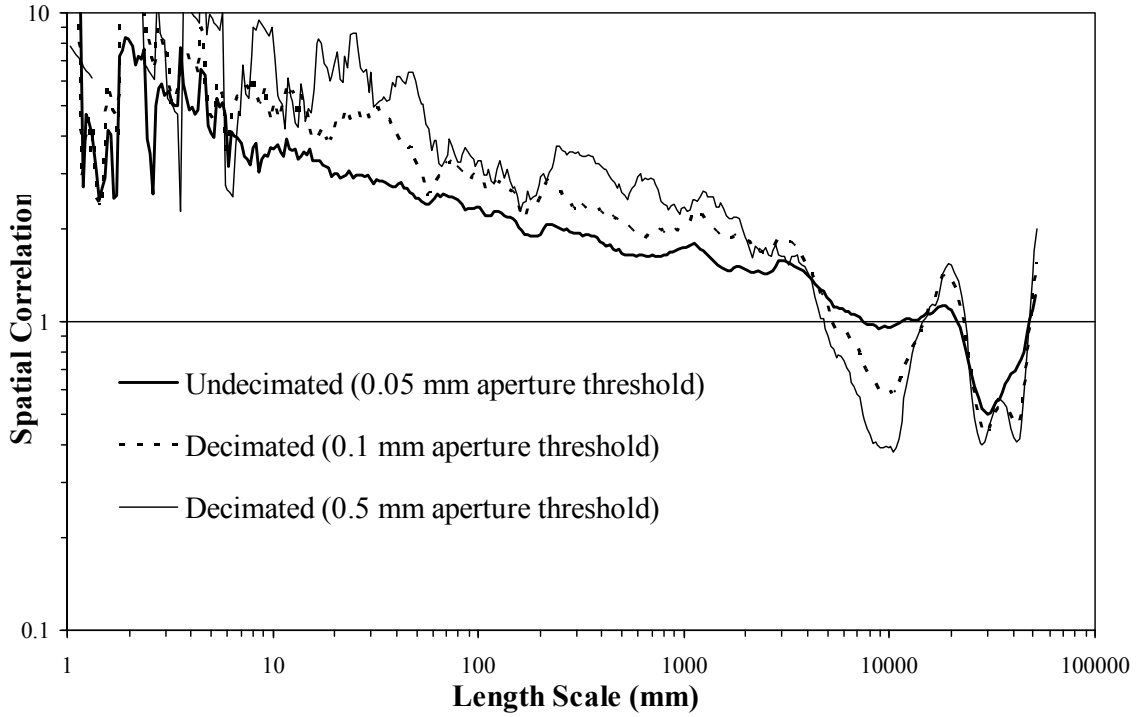

Figure 7.38 Graph of spatial correlation versus length scale for three aperture thresholds (0.05, 0.1 and 0.5 mm) using logarithmic graduations of length scale for the Pedernales data set. Width of length-scale bin is 9 graduations of length scale (m = 4). Undecimated (aperture threshold of 0.05 mm) data set contains 916 fractures whereas the decimated subsets contain 432 and 168 fractures, respectively. Power-law pattern of spatial correlation is present in all three curves. Simultaneous with an increase in the slope of power-law pattern with increasing aperture threshold it is also visible a small reduction (7,000 to 5,000 mm, approximately) in cluster width (intercept of power-law pattern with spatial correlation of 1). Spatial correlation increasingly deviate from a random arrangement of fractures (spatial correlation =1) with increasing aperture threshold.

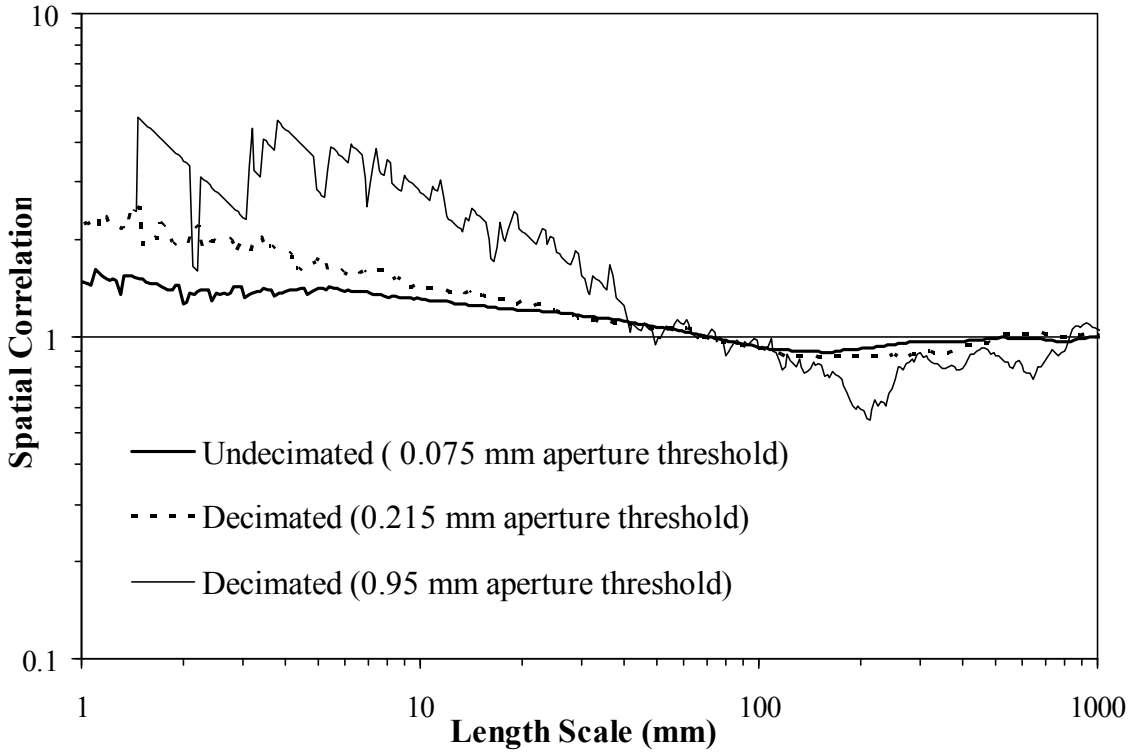

Figure 7.39 Graph of spatial correlation versus length scale for three aperture thresholds (0.075, 0.215 and 0.95 mm) using logarithmic graduations of length scale for the Palmas 11 HR data set. Width of length-scale bin is 41 graduations of length scale (m = 20). Undecimated (aperture threshold of 0.075 mm) data set contains 575 fractures whereas the decimated subsets contain 158 and 30 fractures, respectively. Power-law pattern of spatial correlation is present in all three curves. The increase in the slope of the power-law pattern with increasing aperture threshold does change the cluster width (intercept of power-law pattern with spatial correlation of 1). Spatial correlation increasingly deviate from a random arrangement of fractures (spatial correlation =1) with increasing aperture threshold.

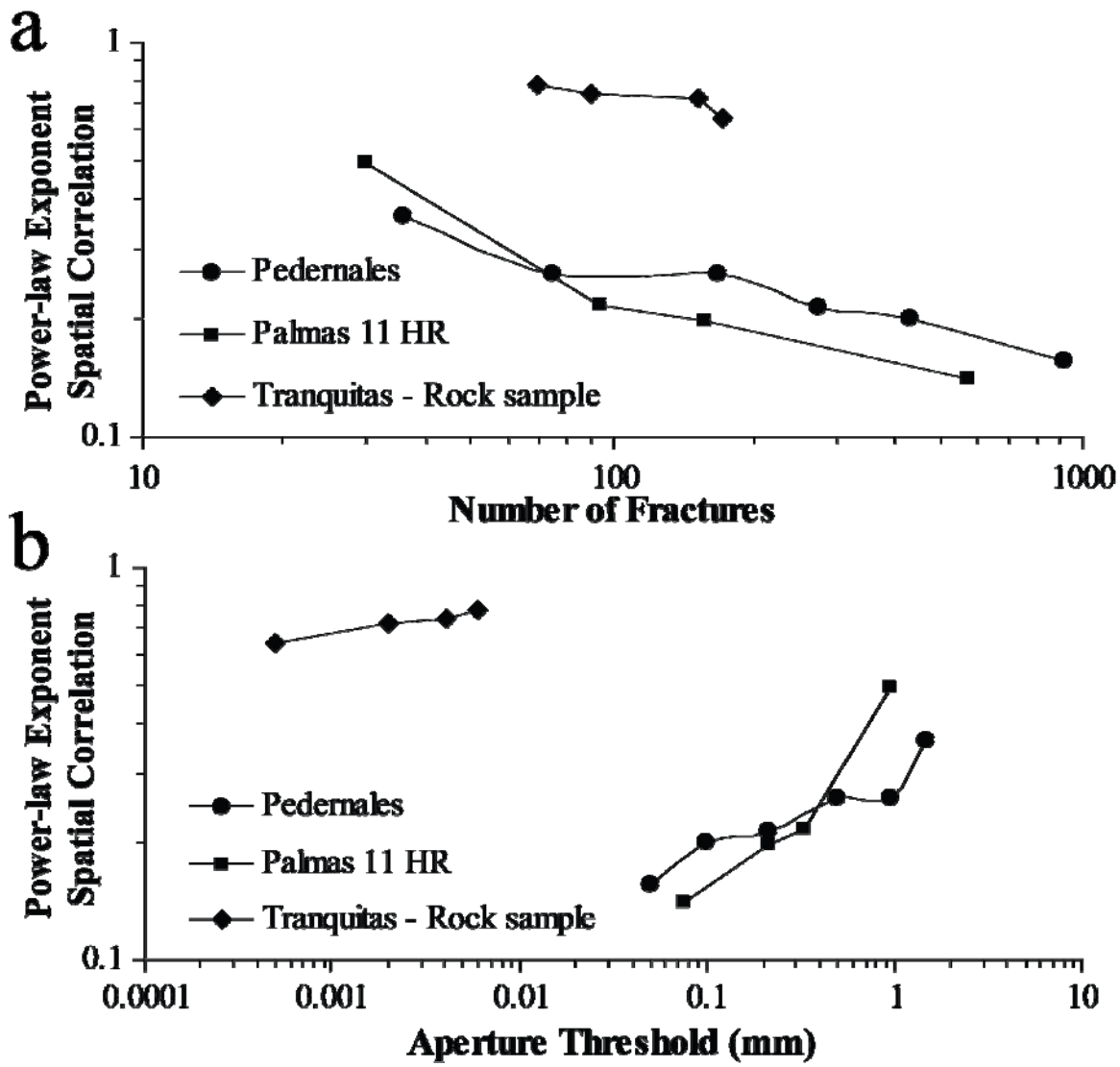

Figure 7.40 Graph of power-law exponent versus (a) number of fractures and (b) aperture threshold for the outcrop data sets at Pedernales and Palmas 11 HR, and Tranquitas at rock-sample scale. Although different for all three data sets, the power-law exponent was independently calculated for the same range of length scales. There is an increase in the degree of clustering (as indicated by the power-law exponent; Marrett et al., in review) with: an increase in aperture threshold, as shown in (a), and a decrease in number of fractures (caused by an increase in the aperture threshold), as shown in (b).

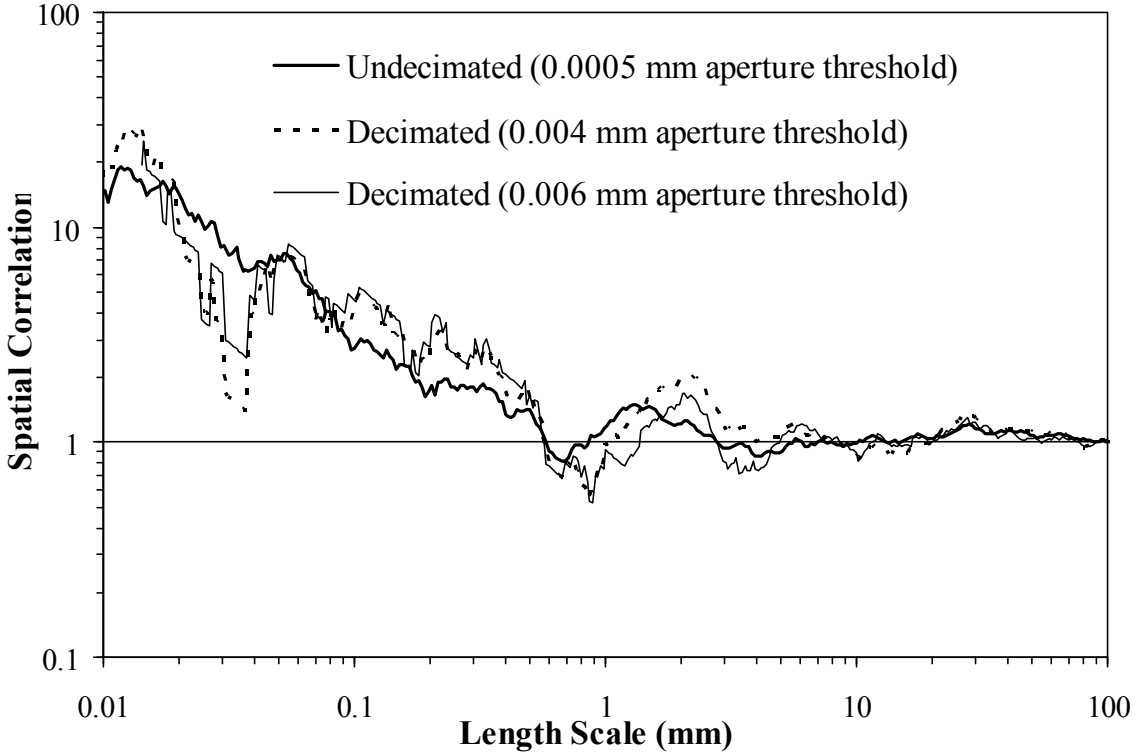

Figure 7.41 Graph of spatial correlation versus length scale for three aperture thresholds (0.0005, 0.004 and 0.006 mm) using logarithmic graduations of length scale for the Tranquitas Rock Sample data set. Width of length-scale bin is 21 graduations of length scale (m = 10). Undecimated (aperture threshold of 0.0005 mm) data set contains 172 fractures whereas the decimated subsets contain 90 and 69 fractures, respectively. Power-law pattern of spatial correlation is present in all three curves. Cluster width (intercept of power-law pattern with spatial correlation of 1) does not change with increasing aperture threshold. Spatial correlation is larger for the two decimated data sets than for the undecimated.

7.4.2.2 Mutually Exclusive Subsets

Dividing Pedernales data set in two subsets, one contains fractures with apertures larger than or equal to 0.1 mm whereas the other contains only the fractures with aperture smaller than 0.1 mm (Figures 7.6 and 7.42). As with the undecimated natural data set (Figure 7.9a), the two mutually exclusive subsets of the Pedernales data set display a power-law pattern of spatial correlation for at least three orders of magnitude of length

scale (Figure 7.42). Each of these two subsets contains approximately half of the entire data set and yet the spatial correlation for the fractures with the larger apertures (thick line, Figure 7.42) yields a higher spatial correlation than for smaller fractures (thin line, Figure 7.42), indicating, again, that for the Pedernales data set, fractures with large apertures are more clustered than small fractures.

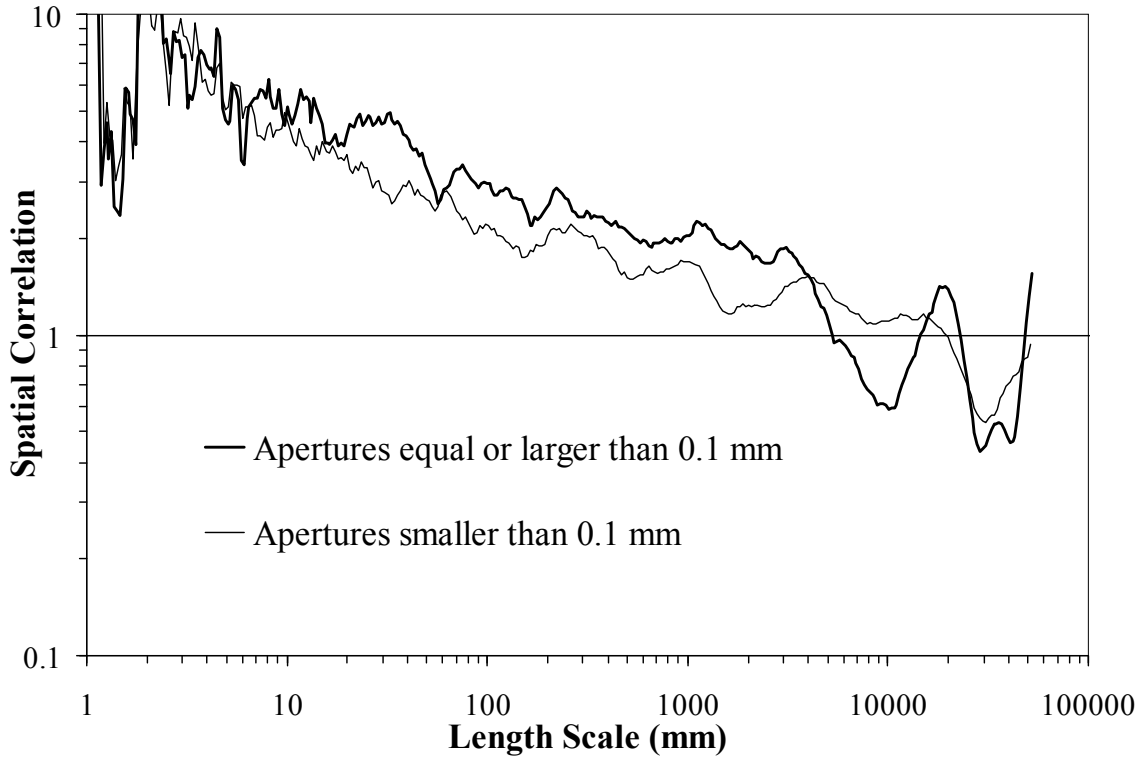

Figure 7.42 Graph of spatial correlation versus length scale for two different subsets of the Pedernales data sets using logarithmic graduations of length scale and a length-scale bin with width equal to 9 graduations of length scale ($m = 4$). One subset contains all fractures (432) with apertures larger than or equal to 0.1 mm whereas the other subset contains fractures (484) with apertures smaller than 0.1 mm. Although both subsets display a fractal arrangement of fractures (power-law pattern), fractures with apertures larger than or equal to 0.1 mm yield spatial correlations that deviate more from a random arrangement of fractures (spatial correlation =1) than fractures with apertures smaller than 0.1 mm.

7.4.2.3 Randomly Arranged Fractures

Randomly relocating all fractures changes their spatial arrangement because both the spacing and the position of each fracture changes (Gomez and Marrett, in review). After the randomization of fracture position was executed for Pedernales data set, fractures were progressively decimated using incrementally larger aperture thresholds (Figure 7.5). The curve of spatial correlation of the randomized and undecimated (aperture threshold of 0.05 mm) version of the Pedernales data set does not display the power-law pattern (Figure 7.43) clearly visible when logarithmic graduations of length scale are used Figure 7.9a). The removal of the power-law pattern indicative of a fractal arrangement is the logical consequence of randomizing fracture position (Marrett et al., in review). The decimated subsets of the randomized version of the Pedernales data set also do not show any indication of a power-law pattern (Figure 7.43). In addition, there is no coincidence between the local variations of the curve of spatial correlations from subsets with increasingly larger aperture thresholds (Figure 7.43). All last three statements suggest that for randomly arranged fractures there is not a differential clustering for different aperture fractions (large fractures are as likely to be inside clusters as small fractures). Namely, randomly arranged fractures lack a qualitative relationship between fracture aperture and fracture position (Figure 7.43).

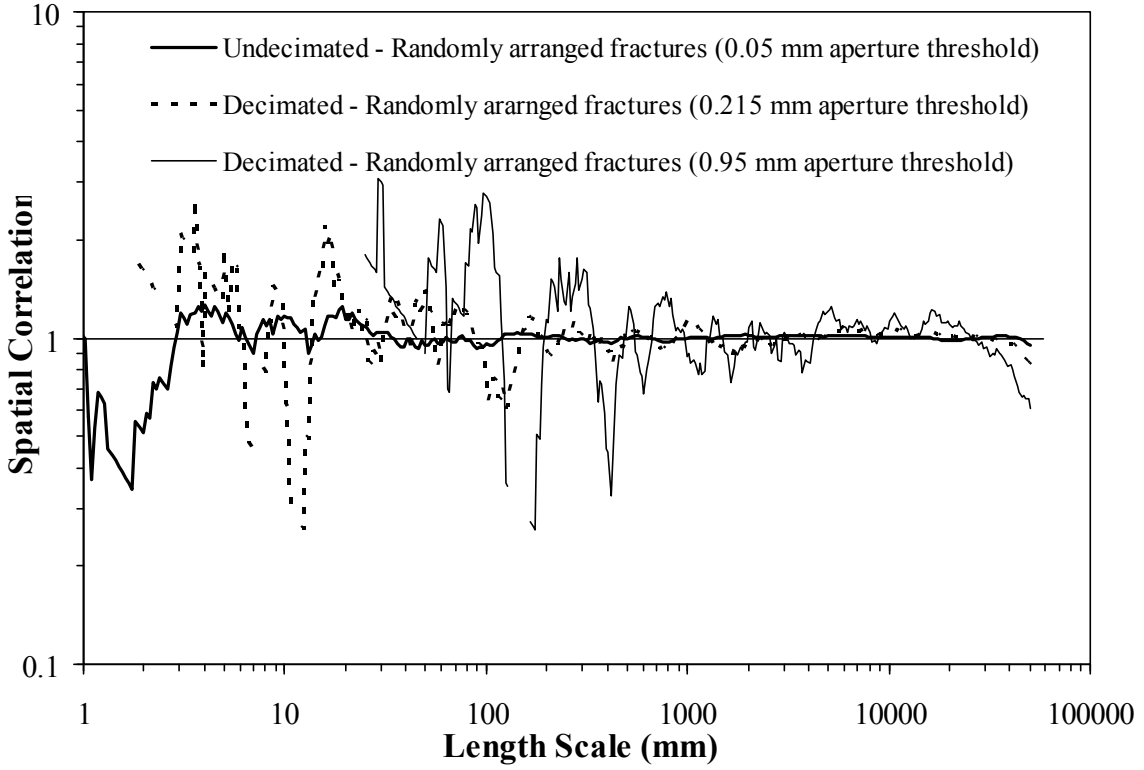

Figure 7.43 Graph of spatial correlation versus length scale for three different subsets of the Pedernales data set with different aperture thresholds and randomly arranged fractures (altered fracture positions) and using logarithmic graduations of length scale. Length-scale bin width equal to 9 graduations of length scale (m = 4). Undecimated data set contains all fractures (916) with apertures larger than or equal to 0.05 mm whereas the other subset contains fractures (274 and 75) with apertures larger than or equal to 0.215 and 0.95 mm, respectively. Undecimated data set exhibits a flat pattern of spatial correlation, which indicates an arrangement that is indistinguishable from random (Figure 7.3a). None of the three curves of spatial correlation display a power-law pattern, indicative of a fractal arrangement of fractures inside clusters.

7.4.2.4 Randomly Located Apertures

The last methodology to test the differential clustering of different fractions of fracture aperture involves randomizing fracture apertures without any change in fracture position. Using logarithmic graduations of length scale the undecimated version of the

Pedernales data set with randomly located apertures (unchanged fracture positions) displays a curve of spatial correlation (thick line, Figure 7.44) identical to the equivalent curve yielded by the undecimated and unmodified natural data set (thick line, Figure 7.38). These two data sets have an identical curve of spatial correlation because they have identical fracture positions and because NCC ignores their only difference, the organization of fracture aperture (Marrett et al., in review). Both undecimated and decimated subsets of the Pedernales data set with randomly located apertures display a power-law pattern of spatial correlation with length scale, indicative of fractures with a fractal arrangement inside clusters (Figure 7.44). However, unlike with the unmodified Pedernales data set (Figure 7.38), there is no increase of the spatial correlation with increasing aperture threshold and there is no detectable increase in the slope of the power-law pattern (Figure 7.44). On the contrary, the power-law exponent decreases slightly with increasing aperture threshold (and corresponding reduction in number of fractures (Figure 7.45). An additional difference between the unmodified and the version of the Pedernales data set with randomly located apertures is the increase in the local variation of the spatial correlation curve with increasing aperture threshold in spite of NCC using an identical width of the length-scale bin (Figures 7.38 and 7.44). Therefore, based on the Pedernales data set as an example of a fracture data set with a fractal arrangement inside clusters, it can be concluded that randomly located apertures lack a relationship between fracture aperture and fracture position (Figure 7.44). Namely, that the increased clustering of large fractures inside statistically significant clusters previously established (Figures 7.38 to 7.42) cannot be explained by random positioning of apertures along a scanline (Figures 7.44 and 7.45).

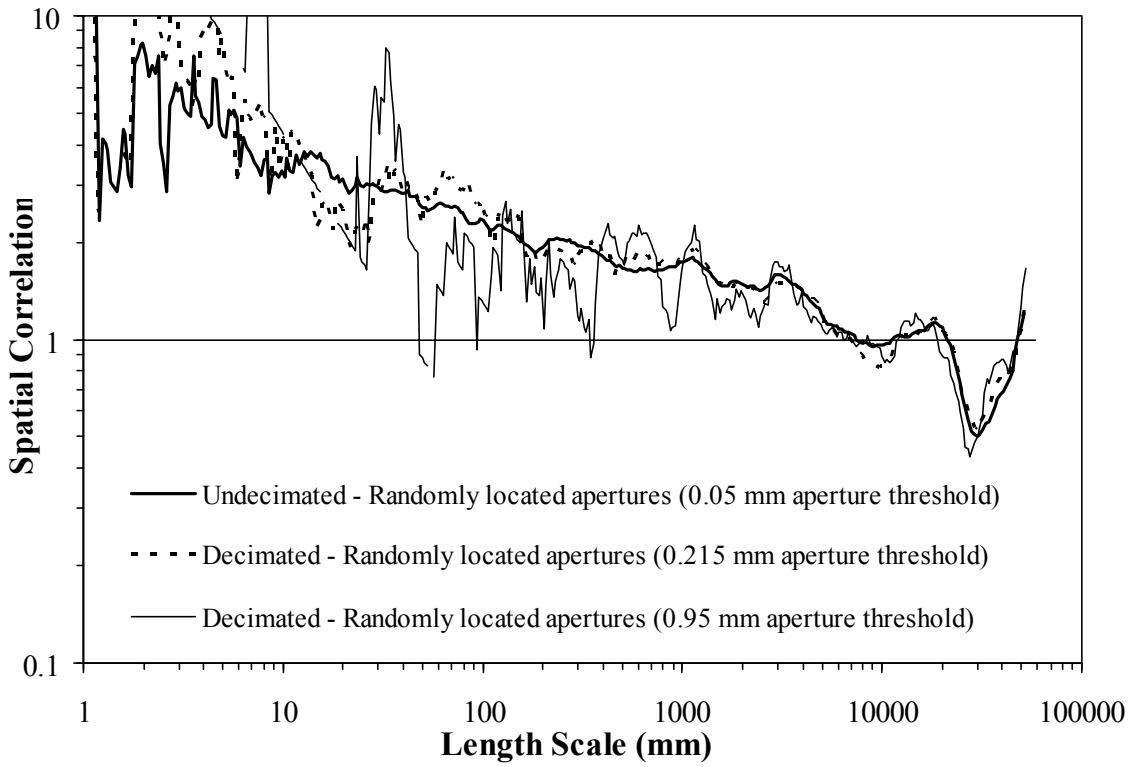

Figure 7.44 Graph of spatial correlation versus length scale for three different subsets of the Pedernales data set with different aperture thresholds and randomly located apertures (unchanged fracture positions) and using logarithmic graduations of length scale. Length-scale bin width equal to 9 graduations of length scale ($m = 4$). Undecimated data set contains all fractures (916) with apertures larger than or equal to 0.05 mm whereas the other subset contains fractures (274 and 75) with apertures larger than or equal to 0.215 and 0.95 mm, respectively. Although the three curves of spatial correlation display a power-law pattern, indicative of a fractal arrangement of fractures inside cluster, there is no substantial variation in the power-law exponent with increasing aperture threshold.

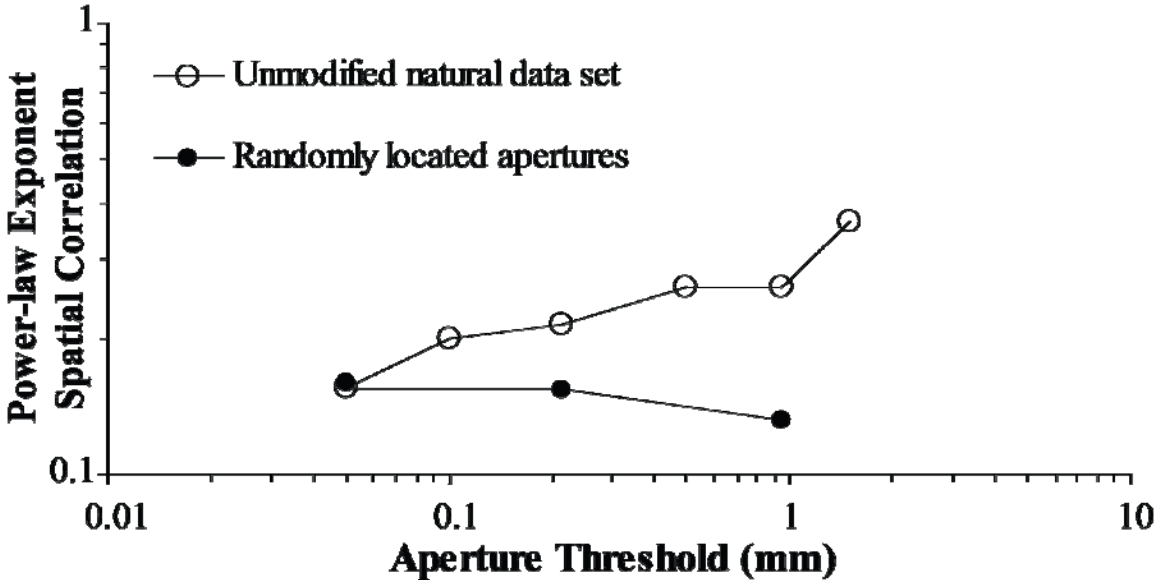

Figure 7.45 Graph of power-law exponent versus number of fractures for unmodified natural Pedernales data sets (empty circles) and equivalent data sets (same aperture threshold and number of fractures) with randomly located apertures (unchanged fracture positions). A length-scale bin of 41 was used (m = 20). Data points from the unmodified natural data set were displayed in Figure 7.40b. The increase in power-law exponent, an indicator of the degree of clustering (Marrett et al., in review) with reducing number of fractures (and corresponding increase in aperture threshold) for the unmodified natural data set is not present for the data set with randomly located apertures.

7.4.3 Periodically arranged fracture clusters

The second type of spatial arrangement to be studied is the periodically arranged fracture clusters (Figure 7.3g), which is characterized by alternating peaks and troughs of spatial correlation with peaks located at length scales multiple of the first peak (cluster spacing; Marrett et al., in review). Of the seven data sets selected for this chapter five (Palmas 11 LR, Palmas 11 HR, Huasteca, southern 26 m of Tranquitas, and rock sample from Tranquitas) display periodically arranged fracture clusters (Table 7.2). There is not complete certainty that the Pedernales data set contains periodically arranged clusters because its spatial correlation for linearly graduated length scales only yields one

statistically significant peak (Figure 7.9b), when an ideal periodic arrangement of fracture clusters should exhibit several peaks of spatial correlation at length scales multiple of the first peak (Marrett et al., in review). Nevertheless, there is value in analyzing the Pedernales data set using NCC with linear graduations of length scale because Pedernales is a data set extensively used in Chapter 6 (Gomez and Marrett, in review; Marrett et al., in review).

7.4.3.1 Increasingly Larger Aperture Thresholds

Spatial correlation for linearly graduated length scales of the undecimated (all fractures measured in the field, aperture threshold of 0.95 mm, Table 7.1) Palmas 11 LR data set clearly yields a pattern indicative of periodically arranged clusters (Figure 7.11b). Increasing the aperture threshold from 0.95 to 1.75 mm reduced by 45% the number of fractures of the Palmas 11 LR data set (from 262 to 146) and yet the pattern of spatial correlation indicative of periodically arranged fracture clusters (cluster spacing of 1100 mm) is still detectable (Figure 7.46). This pattern is still detectable in spite of further reduction of the number of fractures (from 146 to 55) of this data set by increase of the aperture threshold to 4.5 mm (Figure 7.47). Progressive removal of the 207 fractures with apertures larger than or equal to 0.95 mm but less than 4.5 mm produces no appreciable effect in the pattern of the spatial correlation curve (Figure 7.47).

Compared with the undecimated version, spatial correlation for the decimated versions of the Palmas 11 LR data set still displays the same pattern of alternating peaks (evenly spaced every 1100 mm) and troughs at the same length scales (Figure 7.47), indicating that the fraction of fractures with the largest aperture have the same periodic arrangement of fracture clusters displayed by the undecimated data set.Although the smoothness of the spatial correlation curve of the decimated versions of Palmas 11 LR data set is lower than for the undecimated, it is possible to observe that for two peaks of

spatial correlation (length scales of 4200 and 5500 mm) there is an increase in the spatial correlation with increasing aperture threshold (Figure 7.47). Likewise, in several troughs of spatial correlation (e.g., length scales of 2500, 3600, 4700, and 6400 mm) there is also a reduction in the spatial correlation with increasing aperture threshold (Figure 7.47). Increasing divergence of spatial correlation from a random arrangement of fractures (spatial correlation =1) with increasing aperture threshold indicates that clustering increases with fracture size.

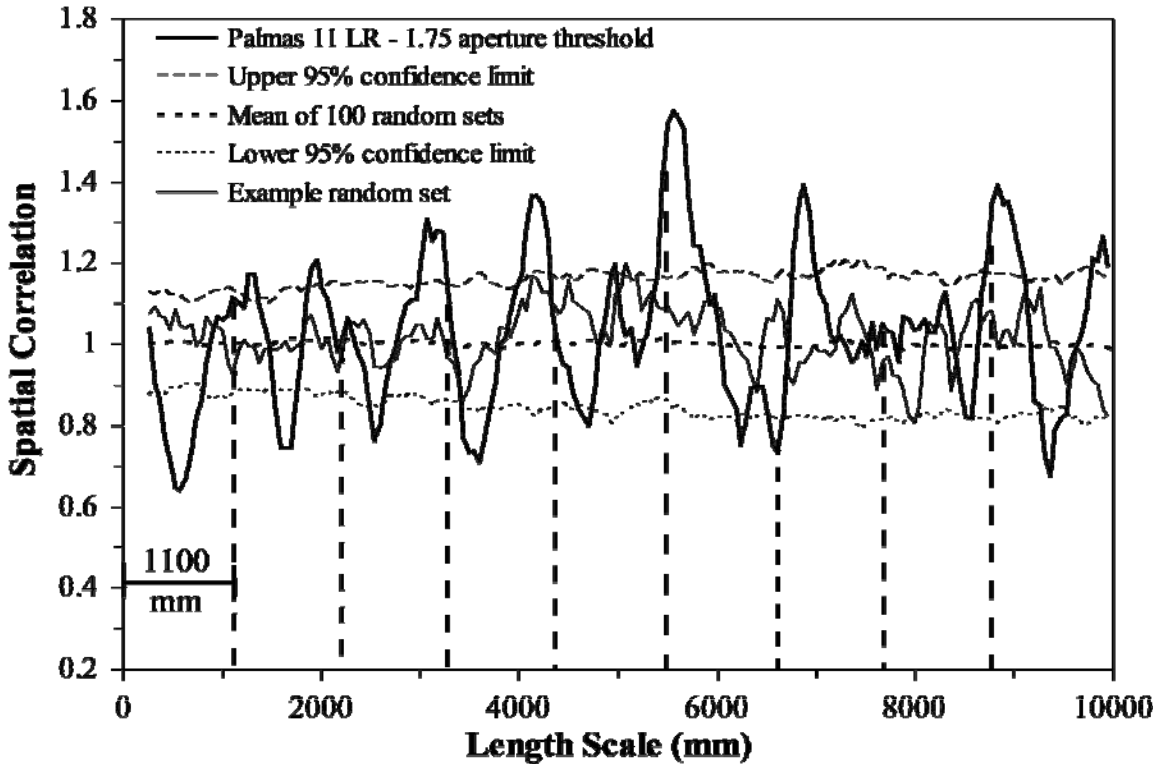

Figure 7.46 Graph of spatial correlation for linearly graduated length scales for a decimated subset (146 fractures, aperture threshold of 1.75 mm) of the Palmas 11 LR data set. Thin continuous line represents an example randomized set generated with the same number of fractures and scanline length. The thin discontinuous (long dashes) line represents the upper 95% confidence interval while the thin discontinuous (short dashes) line represents the lower 95% confidence interval. Thin dotted line corresponds to the mean of 100 randomized data sets. Width of length scale bin is 5 graduations of length scale (m = 2). Evenly spaced lines approximately every 1100 mm match approximately the location of statistically significant peaks of spatial correlation, which display a regularly spaced pattern. Only one of the expected evenly spaced peaks (~7800 mm) is not present. Please notice how the example random set does not display an alternating pattern of peaks and troughs of spatial correlation.

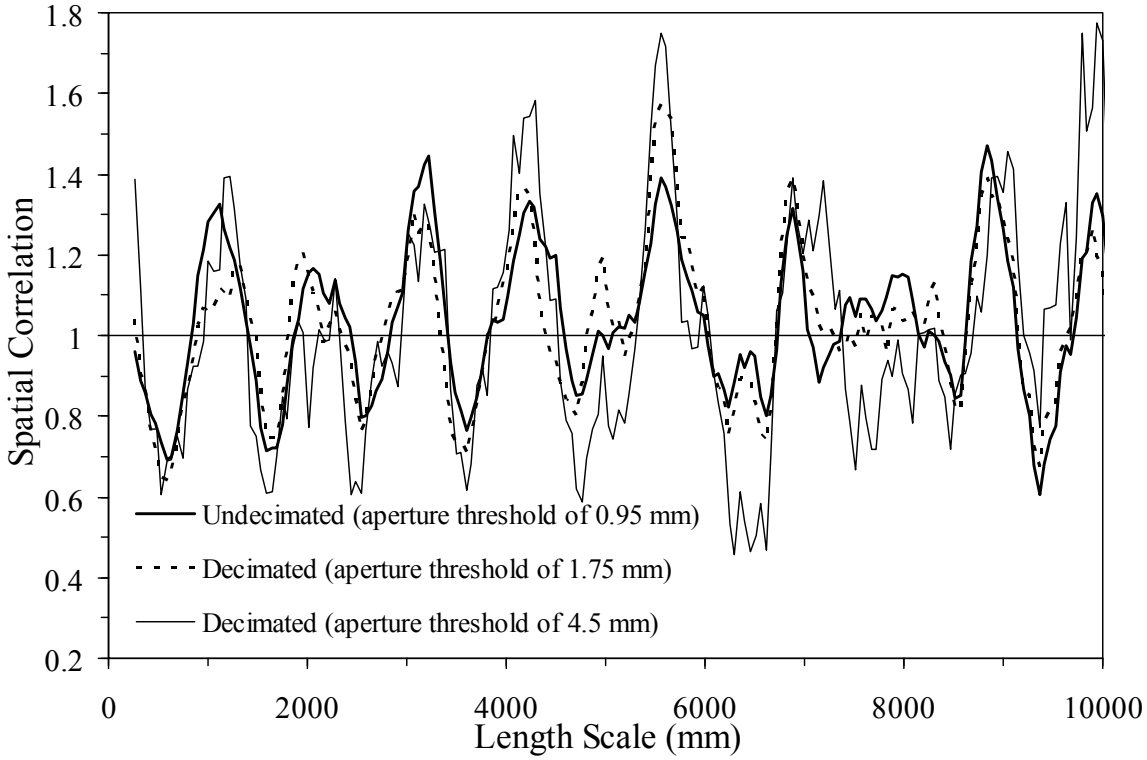

Figure 7.47 Graph of spatial correlation versus length scale for three aperture thresholds (0.95, 1.75 and 4.5 mm) using linear graduations of length scale for the Palmas 11 LR data set. Width of length-scale bin is 5 graduations of length scale (m = 2). Undecimated (aperture threshold of 0.95 mm) data set contains 262 fractures whereas the decimated subsets contain 146 and 55 fractures respectively. Curves of spatial correlation for the undecimated data set and subset with 1.75 mm of aperture threshold (with their respective 95% confidence intervals) were shown in Figures 7.11b and 7.46, respectively. Almost all peaks and troughs of spatial correlation are present in all three curves. Peaks (e.g., 4200 mm) and troughs (e.g., 3600 mm) increasingly deviate from a random arrangement of fractures (spatial correlation = 1) with increasing aperture threshold.

Increasing the aperture threshold from 0.215 to 4 mm reduced by 89% the number of fractures of the Huasteca data set (from 581 to 66) and yet the pattern of alternating peaks and troughs of spatial correlation indicative of periodically arranged fracture clusters (cluster spacing of 900 mm), is still noticeable in the highly decimated subset (Figure 7.48). When the spatial correlation of undecimated and decimated subsets is

plotted together it becomes clear that peaks and troughs of spatial correlation occur at the same length scales (Figure 7.49). In addition, increasing the aperture threshold results in an increased deviation from the spatial correlation of a random arrangement of fractures (spatial correlation = 1). This deviation from the spatial correlation of randomly arranged fractures indicates that an increase in aperture results in an increase in clustering. Namely for the Huasteca data set, large fractures are more clustered than small ones.

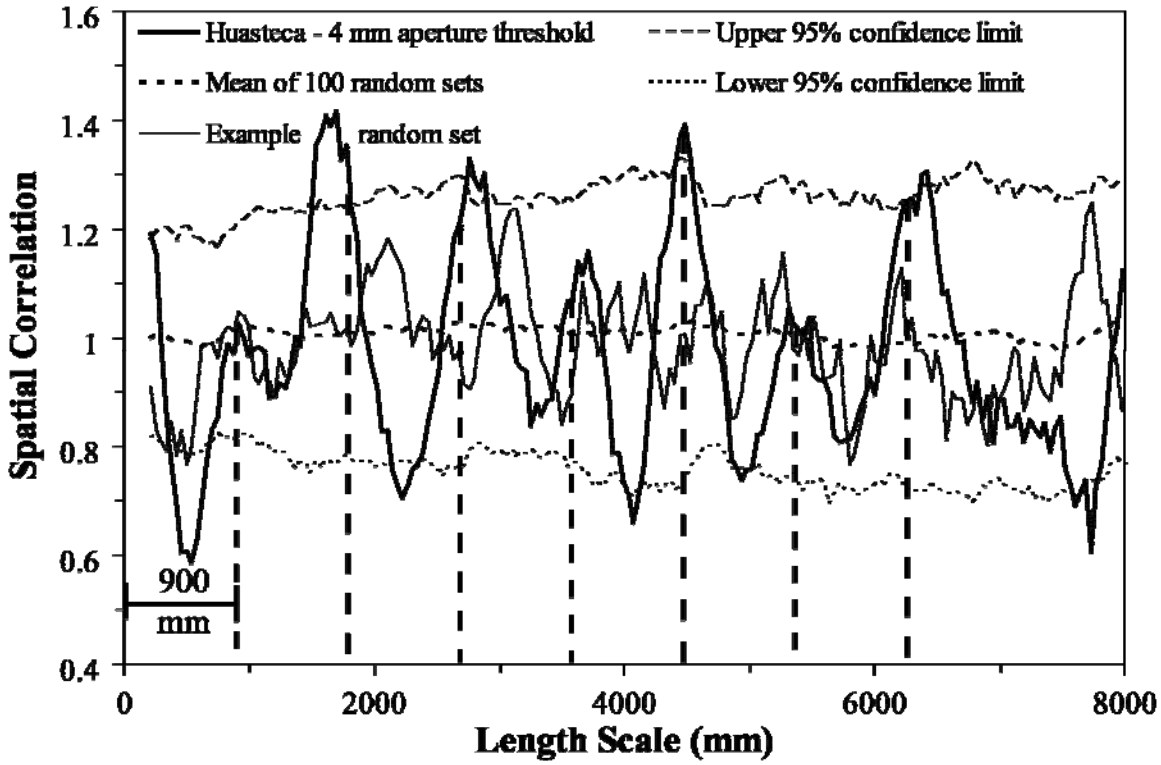

Figure 7.48 Graph of spatial correlation versus length scale for a decimated subset (66 fractures, aperture threshold of 4 mm) of the Huasteca data set. Thin continuous line represents an example randomized set generated with the same number of fractures and scanline length. The thin discontinuous (long dashes) line represents the upper 95% confidence interval while the thin discontinuous (short dashes) line represents the lower 95% confidence interval. Thin dotted line corresponds to the mean of 100 randomized data sets. Width of length scale bin is 9 graduations of length scale (m = 4). Evenly spaced lines every 900 mm match approximately peaks of spatial correlation, which display a regularly spaced pattern. Please notice that although the example random set (thin continuous line) display peaks and troughs of spatial correlation, they are not evenly spaced and they do not reach beyond the 95% confidence interval.

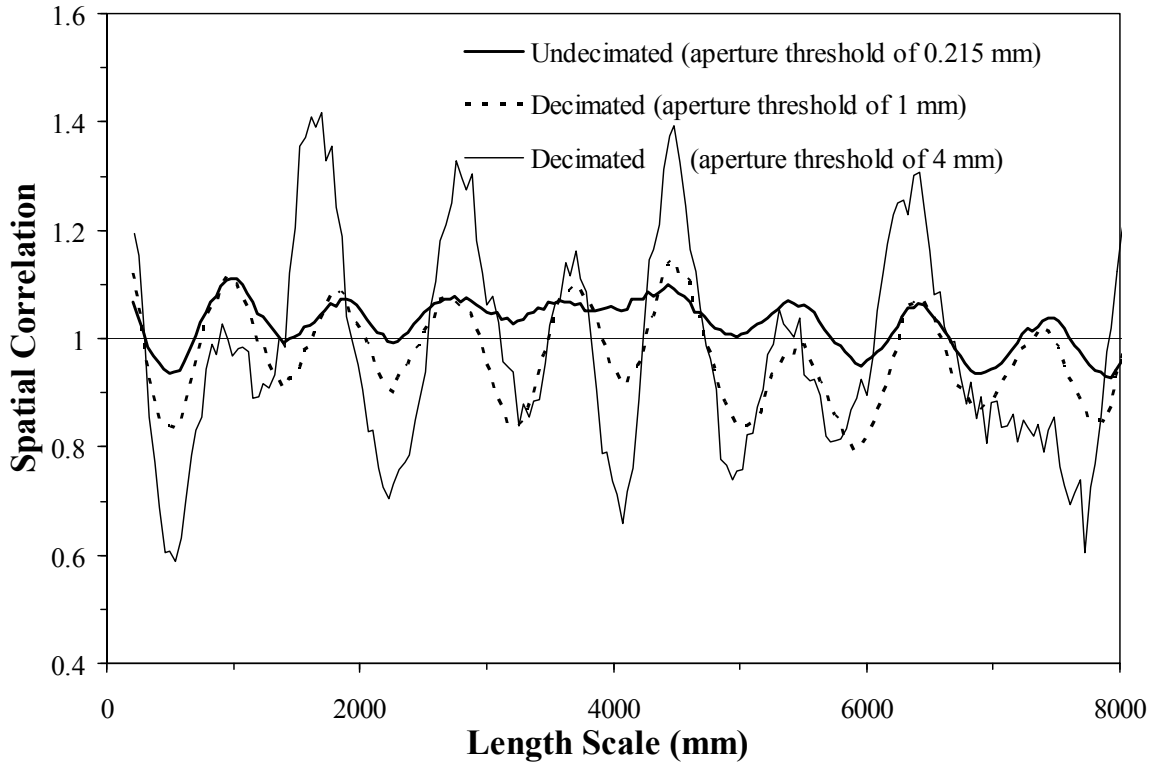

Figure 7.49 Graph of spatial correlation versus length scale for three aperture thresholds (0.215, 1 and 4 mm) using linear graduations of length scale for the Huasteca data set. Width of length-scale bin is 9 graduations of length scale (m = 4). Undecimated (aperture threshold of 0.215 mm) data set contains 581 fractures whereas the decimated subsets contain 249 and 66 fractures, respectively. Curves of spatial correlation for the undecimated data set and subset with 4 mm aperture threshold (with their respective 95% confidence intervals) were shown in Figures 7.27b and 7.48, respectively. Almost all peaks and troughs of spatial correlation are present in all three curves at the same length scales. Although there is no increase in the spatial correlation of most peaks from the undecimated (thick continuous line) to the 1 mm aperture threshold subset (dashed line), all the corresponding troughs of those two subsets display a decrease in spatial correlation with increasing aperture threshold. Nevertheless, there is a notable increase in the spatial correlation of almost all peaks from the 1 mm aperture threshold subset (dashed line) to the 4 mm aperture threshold subset (thin continuous line).

Although there is no complete certainty that the Pedernales data set has periodically arranged clusters, Pedernales data set also display a pattern of spatial

correlation indicative of statistically significant clustering (Figure 7.50) that continues to be detected in spite of a large reduction in the number of fractures (92%) resulting of an increase in the aperture threshold (from 0.05 to 0.95 mm). When the spatial correlation of this highly decimated subset is graphed together with the spatial correlation of the undecimated data set (916 fractures with aperture larger than or equal to 0.05 mm) using linear graduations of length scale, it can be noticed that the peak (19000 mm) and trough (10000 mm) of spatial correlation are at the same length scale (Figure 7.51). When a subset of the Pedernales fractures with an intermediate aperture threshold (0.215 mm, 274 fractures) is also graphed, a pattern of increasing deviation (larger peaks and smaller troughs) from the spatial correlation of randomly arranged fractures becomes apparent (Figure 7.51). Increasing spatial correlation for subsets with increasingly larger aperture threshold indicates that larger fractures are more clustered than small ones. Namely, that there is a relationship between fracture aperture and fracture position.

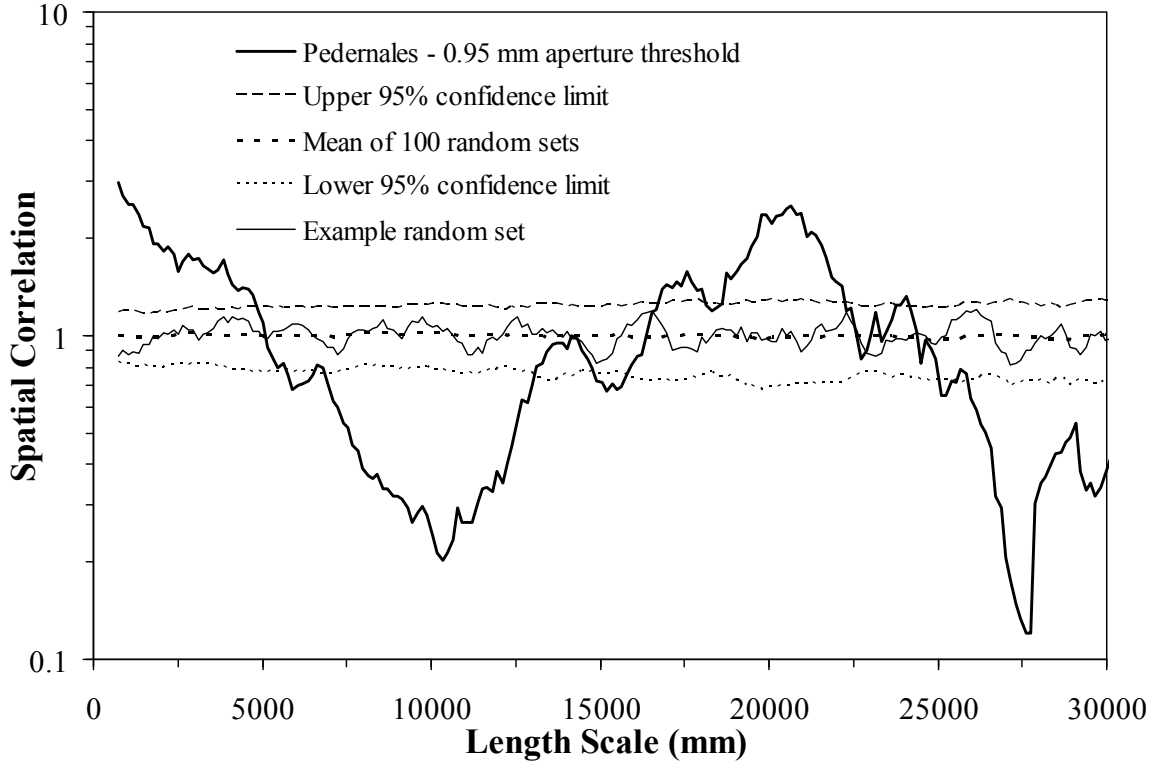

Figure 7.50 Graph of spatial correlation versus length scale for a decimated subset (75 fractures, aperture threshold of 0.95 mm) of the Pedernales data set. Thin continuous line represents an example randomized set generated with the same number of fractures and scanline length. The thin discontinuous (long dashes) line represents the upper 95% confidence interval while the thin discontinuous (short dashes) line represents the lower 95% confidence interval. Thin dotted line corresponds to the mean of 100 randomized data sets. Width of length scale bin is 9 graduations of length scale (m = 4). Peak (19000 mm) and trough (10000 mm) of spatial correlation are statistically significant (outside the 95% confidence interval). Please notice how the example random set does not yield a pattern with a spatial correlation outside the 95% confidence interval.

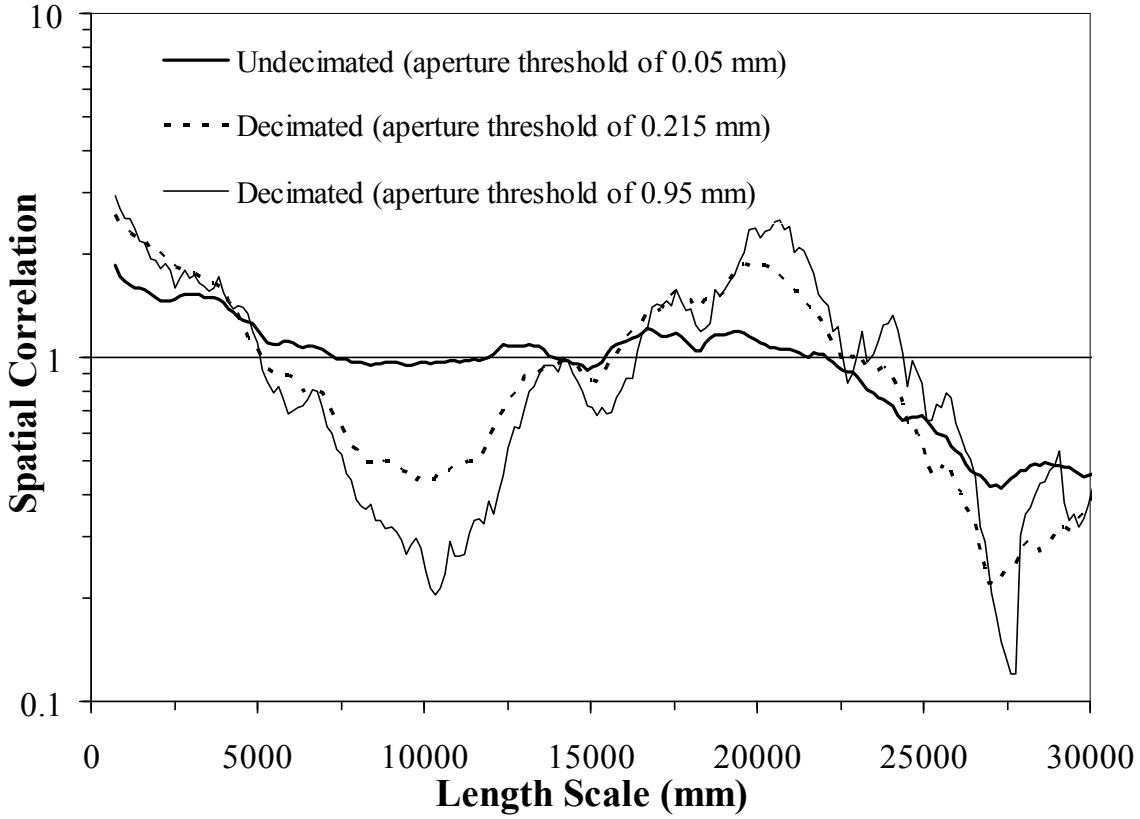

Figure 7.51 Graph of spatial correlation versus length scale for three aperture thresholds (0.05, 0.215 and 0.95 mm) using linear graduations of length scale for the Pedernales data set. Width of length-scale bin is 9 graduations of length scale (m = 4). Undecimated (aperture threshold of 0.05 mm) data set contains 916 fractures whereas the decimated subsets contain 274 and 75 fractures respectively. Curves of spatial correlation for the undecimated data set and subset with 0.95 mm aperture threshold (with their respective 95% confidence intervals) were shown in Figures 7.9b and 7.50. The peak (19000 mm) and trough (10000 mm) of spatial correlation increasingly deviate from a random arrangement of fractures (spatial correlation = 1) with increasing aperture threshold.

Increasing the aperture threshold of the southern 26 m of Tranquitas data set from 0.05 mm (undecimated) to 0.62 mm results in a 46% reduction in the number of fractures but yielded a similar pattern of alternating peaks and troughs of spatial correlation for linearly graduated length scales (Figures 7.18b and 7.52). However, the fundamental cluster spacing indicated by the decimated subset (Figure 7.52) seems to be twice that of

the one interpreted from the undecimated data set (Figure 7.18b; Table 7.2). Compiling the spatial correlation of undecimated and decimated (46% and 78% reduction in number of fractures) subsets with increasingly larger aperture threshold shows that peaks and troughs of spatial correlation every 3000 mm are present at the same length scales and increasingly deviate from the spatial correlation of a random arrangement of fractures (Figure 7.40), indicating that larger fractures are more clustered than small ones (Marrett et al., in review).

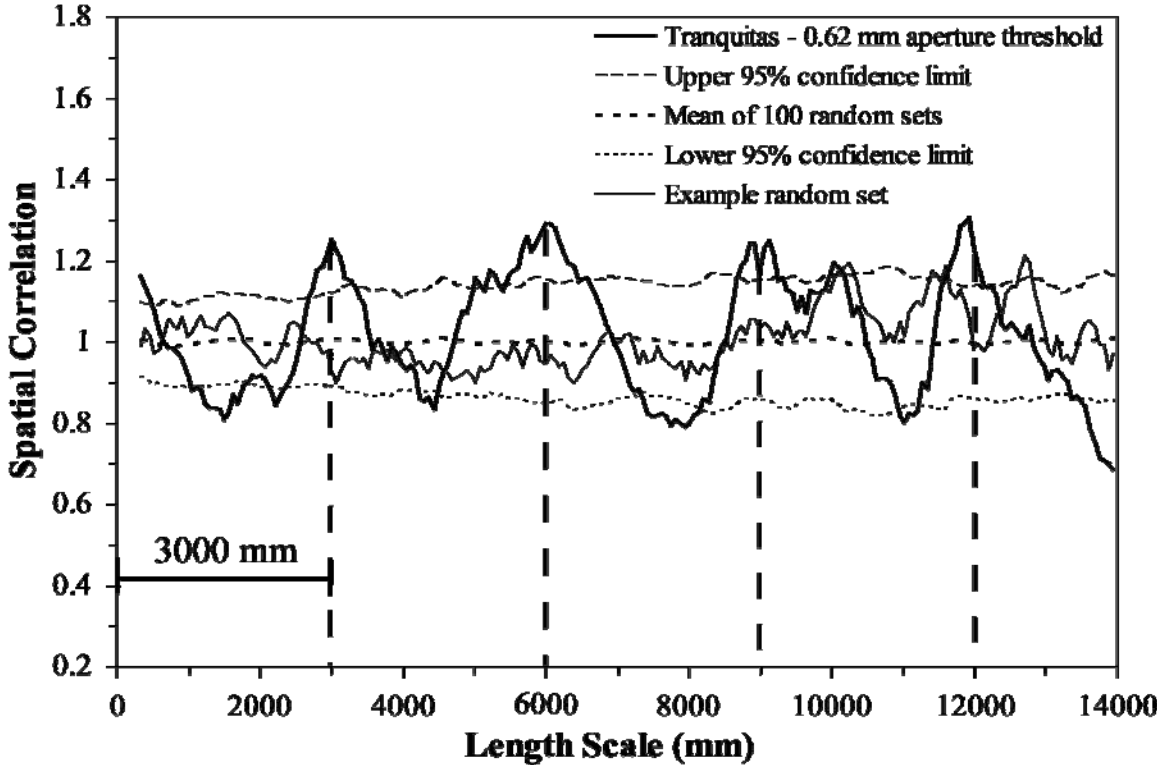

Figure 7.52 Graph of spatial correlation versus length scale for a decimated subset (138 fractures, aperture threshold of 0.62 mm) of southern 26 m of the Tranquitas data set. Thin continuous line represents an example randomized set generated with the same number of fractures and scanline length. The thin discontinuous (long dashes) line represents the upper 95% confidence interval while the thin discontinuous (short dashes) line represents the lower 95% confidence interval. Thin dotted line corresponds to the mean of 100 randomized data sets. Width of length scale bin is 9 graduations of length scale (m = 4). Evenly spaced lines every 3000 mm match approximately the location of statistically significant peaks of spatial correlation, which display a regularly spaced pattern. Please notice how the example random set does not display a pseudo-sinusoidal pattern of alternating and evenly spaced peaks and troughs.

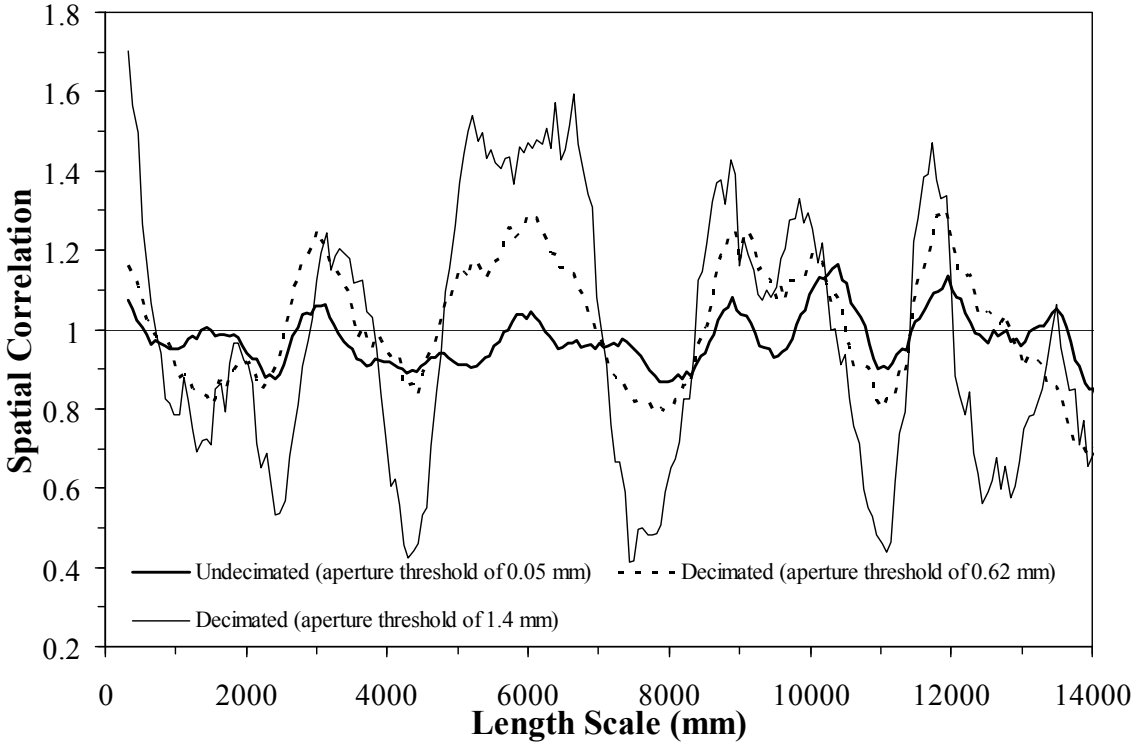

Figure 7.53 Graph of spatial correlation versus length scale for three aperture thresholds (0.05, 0.62 and 1.4 mm) using linear graduations of length scale for the southern 26 m of the Tranquitas data set. Width of length-scale bin is 9 graduations of length scale (m = 4). Undecimated (aperture threshold of 0.05 mm) data set contains 256 fractures whereas the decimated subsets contain 138 and 57 fractures respectively. Curves of spatial correlation for the undecimated data set and subset with 0.62 mm aperture threshold (with their respective 95% confidence intervals) were shown in Figures 7.18b and 7.52. Most peaks and troughs of spatial correlation are present in all three curves. Peaks (e.g., 6000 mm) and troughs (e.g., 11000 mm) increasingly deviate from a random arrangement of fractures (spatial correlation = 1) with increasing aperture threshold.

A 43% reduction in the number of microfractures due to an increase in the aperture threshold (from 0.0005 to 0.004 mm) of the Tranquitas data set at rock sample scale yielded the same pattern of alternating peaks and troughs of spatial correlation as the undecimated data set (Figure 7.54). In addition, there is an increase in the deviation from randomly arranged fractures for peaks and troughs of spatial correlation with

increasing aperture threshold (Figure 7.54), which implies that, just like for macrofractures, larger microfractures are more clustered than small ones. Namely, that differential clustering of different fractions of fracture aperture is not a phenomenon exclusive of outcrop data sets; it has also been detected at the rock sample scale.

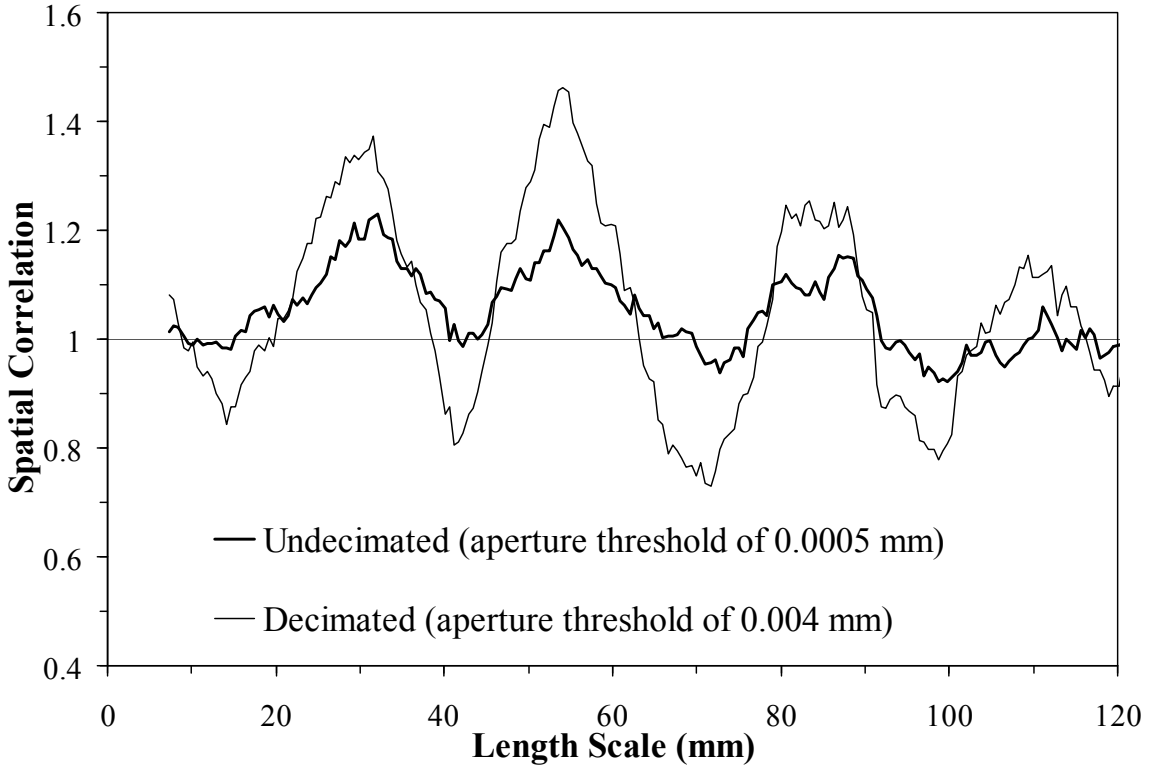

Figure 7.54 Graph of spatial correlation versus length scale for two aperture thresholds (0.0005 and 0.004 mm) using linear graduations of length scale for the Tranquitas Rock Sample data set. Width of length-scale bin is 21 graduations of length scale (m = 10). Undecimated (aperture threshold of 0.0005 mm) data set contains 172 fractures whereas the decimated subset contains 91 fractures. All peaks and troughs of spatial correlation are present in both curves. However, peaks (e.g., 55 mm) and troughs (e.g., 70 mm) increasingly deviate from a random arrangement of fractures (spatial correlation = 1) with increasing aperture threshold.

7.4.3.2 Mutually Exclusive Subsets

For this section, fractures of the Pedernales data set were separated into two mutually exclusive subsets and the spatial correlation for linearly graduated length scales was independently calculated for each subset. One subset contains all fractures with apertures larger than or equal to 0.1 mm whereas the other subset contains all fractures with apertures smaller than 0.1 mm (Figures 7.6 and 7.55). The large fraction of fracture aperture (thick line, Figure 7.55) yields a spatial correlation that deviates more from the spatial correlation of a random arrangement of fractures (spatial correlation equal to 1) than the small fraction of fracture aperture (thin line, Figure 7.55). For instance, the peak of spatial correlation at 19000 mm is larger for the large aperture fraction than for the small aperture fraction (Figure 7.55). In addition, the first trough of spatial correlation (approximately 10000 mm) is also present in both subsets but the spatial correlation is lower (smaller than one) for the large aperture fraction than for the small aperture fraction (Figure 7.55).

At a single length scale, the deviation from the spatial correlation of a random arrangement of fractures (spatial correlation = 1) is directly proportional to the number of fracture pairs separated a distance equal to the length scale (Marrett et al., in review). Therefore, the larger first peak of spatial correlation for the fraction of large apertures of Pedernales, compared with the spatial correlation for the fraction of small apertures (Figure 7.55), indicates that there are more fracture pairs inside clusters in the large aperture fraction than in the small aperture fraction. Namely, large fractures at Pedernales are more clustered than small fractures (Figure 7.55).

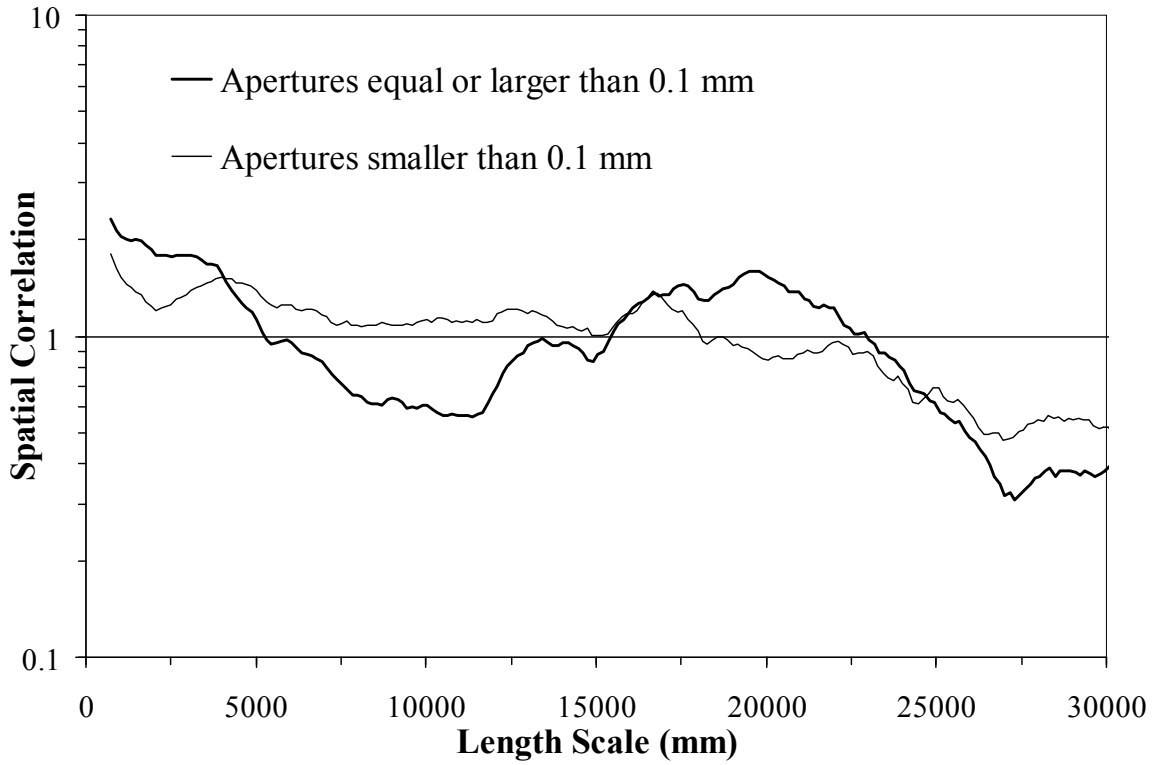

Figure 7.55 Graph of spatial correlation versus length scale for two different subsets of the Pedernales data sets using linear graduations of length scale and a length-scale bin with width equal to 9 graduations of length scale (m = 4). One subset contains all fractures (432) with apertures larger than or equal to 0.1 mm whereas the other subset contains fractures (484) with apertures smaller than 0.1 mm. Although both subsets display a peak and a trough of spatial correlation at approximately the same length scales, fractures with apertures larger than or equal to 0.1 mm yield spatial correlations that deviate more from a random arrangement of fractures (spatial correlation =1) than fractures with apertures smaller than 0.1 mm.

7.4.3.3 Randomly Arranged Fractures

Random positioning of fractures of the Palmas 11 LR data set without any change in aperture threshold removes the pattern of alternating peaks and troughs of spatial correlation (thick line, Figure 7.56) yielded by the equivalent (in number of fractures) unmodified (in fracture position) Palmas 11 LR data set (thick line, Figure 7.47). Curves

of spatial correlation for subsets of the Palmas 11 LR data set with increasingly larger aperture threshold (without any modification in fracture position) display increasingly larger peaks and troughs at the same length scales (Figure 7.47). In contrast, spatial correlation for randomly arranged fractures of Palmas 11 LR (undecimated and two decimated subsets) show peaks and troughs that do not occur at the same length scales and they do not expand with increasing aperture threshold (Figure 7.56), which indicates that in randomly arranged fractures there is no relationship between fracture aperture and fracture position. Namely, in randomly arranged fractures large fractures are as clustered as small ones (Figure 7.56).

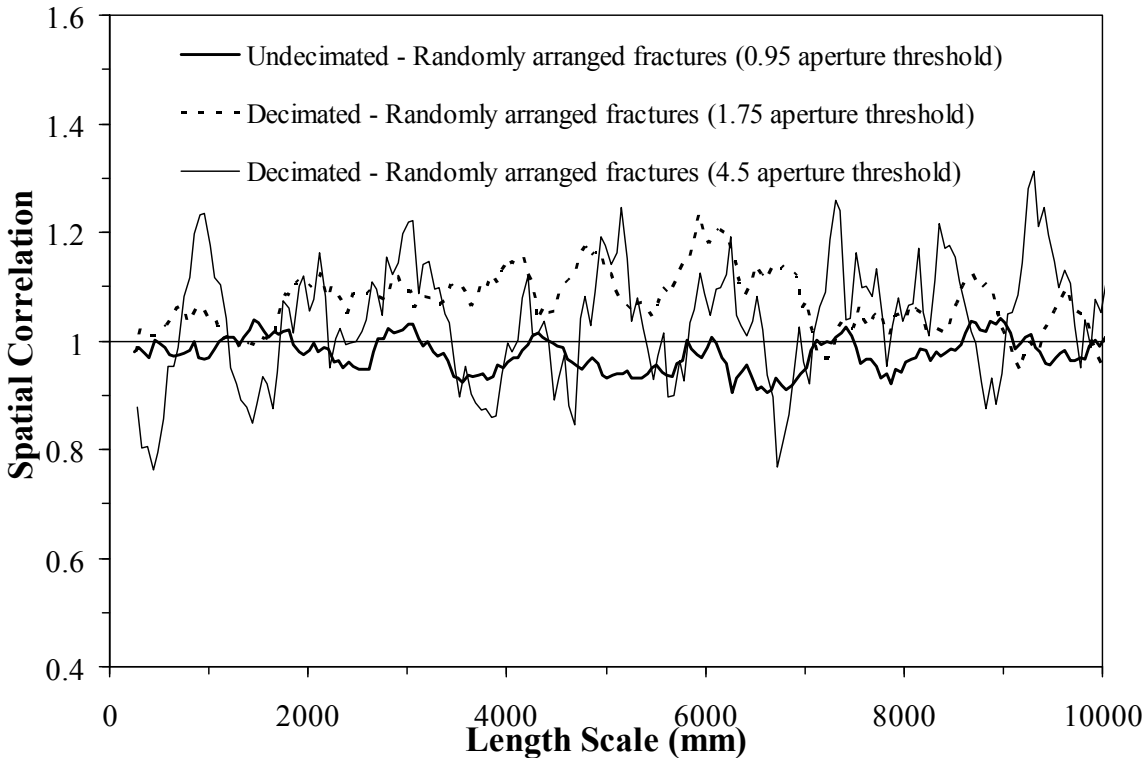

Figure 7.56 Graph of spatial correlation versus length scale for three different subsets of the Palmas 11 LR data sets with randomly arranged fractures (changed fracture positions) and using linear graduations of length scale. Length-scale bin width equal to 9 graduations of length scale (m = 4). Undecimated data set contains all fractures (262) with apertures larger than or equal to 0.95 mm whereas the other subset contains fractures (146 and 55) with apertures larger than or equal to 1.75 and 4.5 mm, respectively. Peaks and troughs of spatial correlation are not present at the same length scales for the three curves. This figure is equivalent to Figure 7.47 but for randomly arranged fractures.

7.4.3.4 Randomly Located Apertures

Spatial correlation using linearly graduated length scales for the undecimated version of the Pedernales data set with randomly located apertures (unchanged fracture positions) displays a curve of spatial correlation (thick line, Figure 7.57) identical to the equivalent curve yielded by the undecimated and unmodified natural data set (thick line, Figure 7.51). Using linear graduation of length scales, both undecimated and decimated

subsets of the Pedernales data set with randomly located apertures display a trough and a peak of spatial correlation at 10000 and 19000 respectively (Figure 7.57). However, unlike with the unmodified natural data set at Pedernales (Figure 7.51), there is no noticeable increase of the spatial correlation with increasing aperture threshold (Figures 7.57), which suggests that for the Pedernales data set, randomly locating apertures terminates the relationship between fracture aperture and clustering (larger fractures are more clustered than small ones) detected in the natural and unmodified data set (Figures 7.47, 7.49, 7.51, 7.53 to 7.56).

In addition, subsets with increasingly larger aperture thresholds of the Huasteca data set with randomly located fracture apertures (without a change in fracture position) display peaks and troughs of spatial correlation that increasingly deviate from the length scales at which the peaks and troughs are present in the undecimated data set (Figure 7.58). In contrast, the unmodified (in terms of apertures and fracture positions) subsets with increasingly larger aperture thresholds display peaks and troughs of spatial correlation at the same length scales at which the undecimated data set yields them (Figure 7.49), which suggests that fracture data sets with periodically arranged clusters display large fractures more intensely clustered those small fractures and that this relationship between fracture aperture and fracture position cannot be explained by randomly locating apertures along the scanline. Namely, randomization of fracture aperture without a change in fracture position seems to remove the qualitative relationship between fracture aperture and fracture position present in periodically arranged clusters (Figures 7.56 and 7.57).

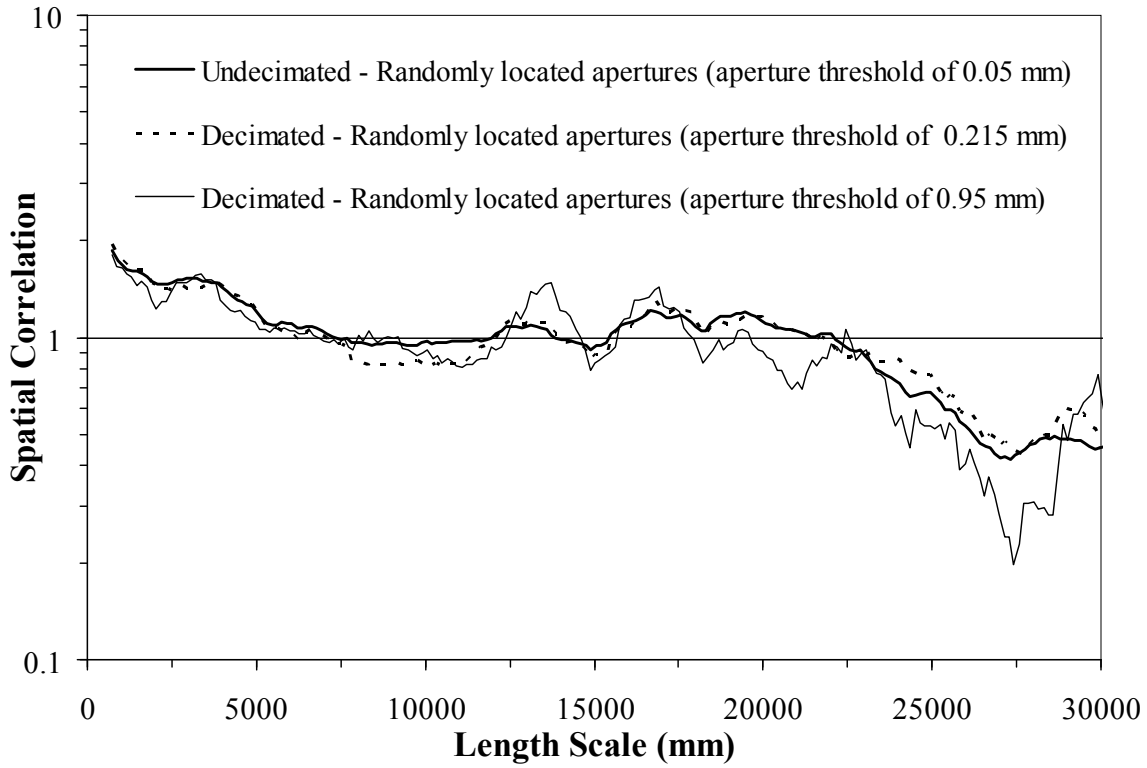

Figure 7.57 Graph of spatial correlation versus length scale for three different subsets of the Pedernales data sets with randomly located apertures (unchanged fracture positions) and using linear graduations of length scale. Length-scale bin width equal to 9 graduations of length scale (m = 4). Undecimated data set contains all fractures (916) with apertures larger than or equal to 0.05 mm whereas the other subset contains fractures (274 and 75) with apertures larger than or equal to 0.215 and 0.95 mm, respectively. All three curves of spatial correlation display one trough (~10000 mm) and one peak (~19000 mm) of spatial correlation. However, there is no change in the spatial correlation with increasing aperture threshold.

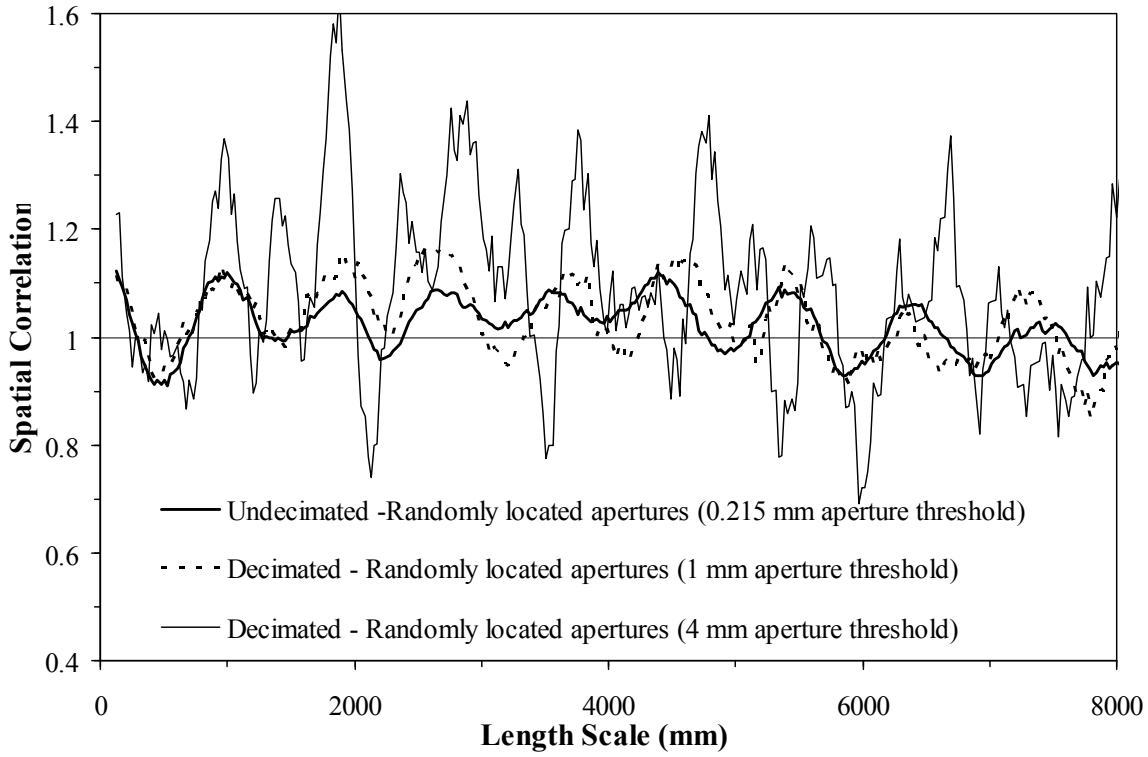

Figure 7.58 Graph of spatial correlation versus length scale for three different subsets of the Huasteca data sets with randomly located apertures (unchanged fracture positions) and using linear graduations of length scale. Length-scale bin width equal to 9 graduations of length scale (m = 4). Undecimated data set contains all fractures (581) with apertures larger than or equal to 0.215 mm whereas the other subset contains fractures (249 and 66) with apertures larger than or equal to 1 and 4 mm, respectively. Spatial correlation of subsets with increasingly larger aperture threshold yield peaks and troughs of spatial correlation at length scales that are not the same for all three curves of spatial correlation.

7.4.4 Random arrangement of fractures

Quantitative characterization of the Palmas 13 outcrop data set using NCC for both logarithmically and linearly graduated length scales (Chapter 6; Marrett et al., in review) indicates that fractures are randomly arranged or instead that their spatial organization cannot be distinguished from randomly arranged fractures (Figure 7.25). In addition, traditional techniques for the analysis of fracture spacing (Chapter 6; Gomez

and Marrett, in review) such as the coefficient of variation (near 1, Table 7.1) and the cumulative distribution of fracture spacing (negative exponential, Table 7.1) suggests that Palmas 13 fractures are randomly arranged.

Imposing an aperture threshold of 2 mm leaves the upper 15% aperture fraction of the Palmas 13 data set. Spatial correlation for fractures in the Palmas 13 data set with apertures larger than or equal to 2 mm also yield a spatial arrangement that cannot be distinguished from random (Figure 7.59). Although the curve of spatial correlation in Figure 7.59 displays peaks and troughs, they are not statistically significant (inside the 95% confidence interval), they are not evenly spaced, and they are not located at length scales equal to multiples of the first peak (dominant spacing). Comparison of the spatial correlation for linearly graduated length scales between the undecimated data set and the two subsets with artificially larger aperture thresholds shows no concurrence between the peaks and troughs (Figure 7.60b). Although the spatial correlation curves for the decimated data sets show a few peaks (e.g., 1880 mm) and troughs (e.g., 340 mm) at the same length scales (Figure 7.60b), they can be disregarded because they lack statistical significance and also are not part of a recognizable pattern (e.g., alternating peaks and troughs indicative of periodically arranged fractures or periodically arranged clusters). In addition, spatial correlation for different aperture thresholds using logarithmic graduations of length scale lacks a recognizable pattern (e.g., power law) that can be followed among the different subsets (Figure 7.60a). Spatial correlation for increasingly large fractions of fracture aperture of Palmas 13 data set indicate that when fractures have arrangements that are indistinguishable from random, there is no difference between the degrees of clustering of different aperture fractions and therefore a large fracture is as likely to be inside as it is to be outside the statistically insignificant clusters (Figure 7.60).

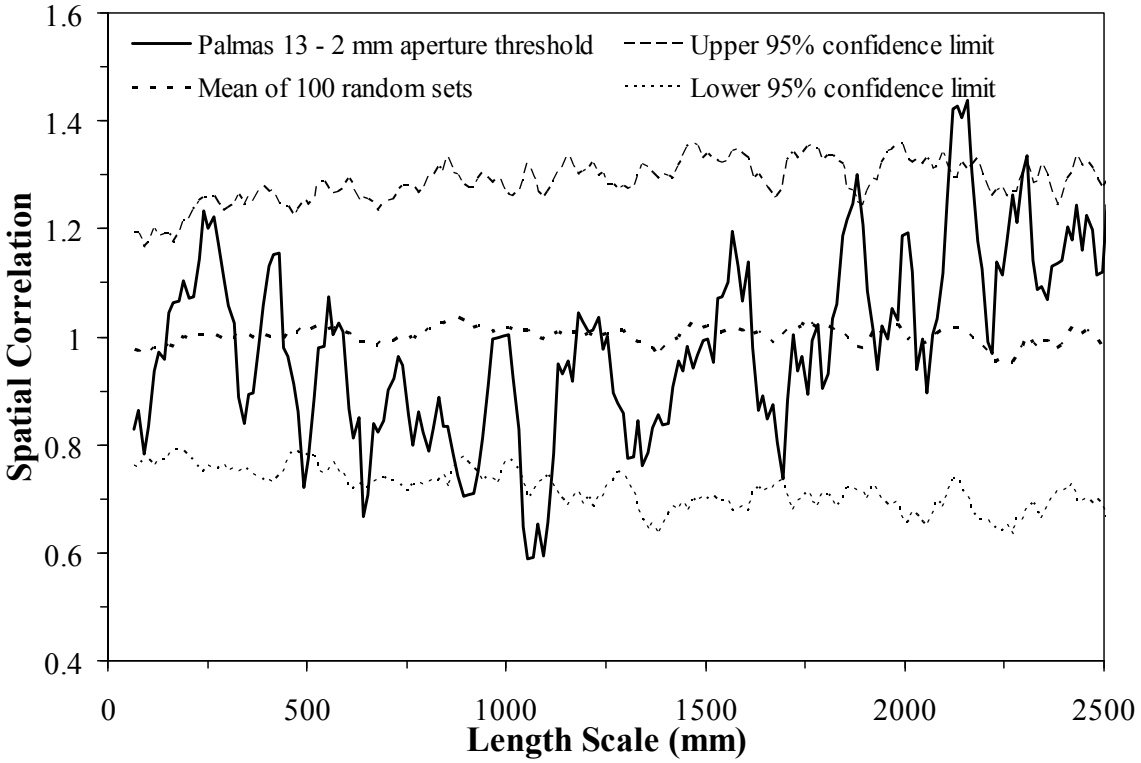

Figure 7.59 Graph of spatial correlation versus length scale for a decimated subset (62 fractures, aperture threshold of 2 mm) of the Palmas 13 data set. The thin discontinuous (long dashes) line represents the upper 95% confidence interval while the thin discontinuous (short dashes) line represents the lower 95% confidence interval. Thin dotted line corresponds to the mean of 100 randomized data sets. Width of length scale bin is 7 graduations of length scale ($m = 4$).

Figure 7.60 Graphs of spatial correlation versus length scale for three aperture thresholds (0.14, 1 and 2 mm) using (a) logarithmic and (b) linear graduations of length scale for the Palmas 13 data set. Width of length-scale bin is 7 graduations of length scale (m = 3). Undecimated (aperture threshold of 0.14 mm) data set contains 459 fractures whereas the decimated subsets contain 112 and 62 fractures respectively. Spatial correlation using linear graduations of length scale for the undecimated data set and subset with 2 mm aperture threshold (with their respective 95% confidence intervals) were shown in Figures 7.25b and 7.59. Undecimated data sets in (a) and (b) follow a flat pattern of spatial correlation, which indicates an arrangement that is indistinguishable from random. There is no consistency in either (a) or (b) on the location of the statistically insignificant peaks and troughs between the different subsets.

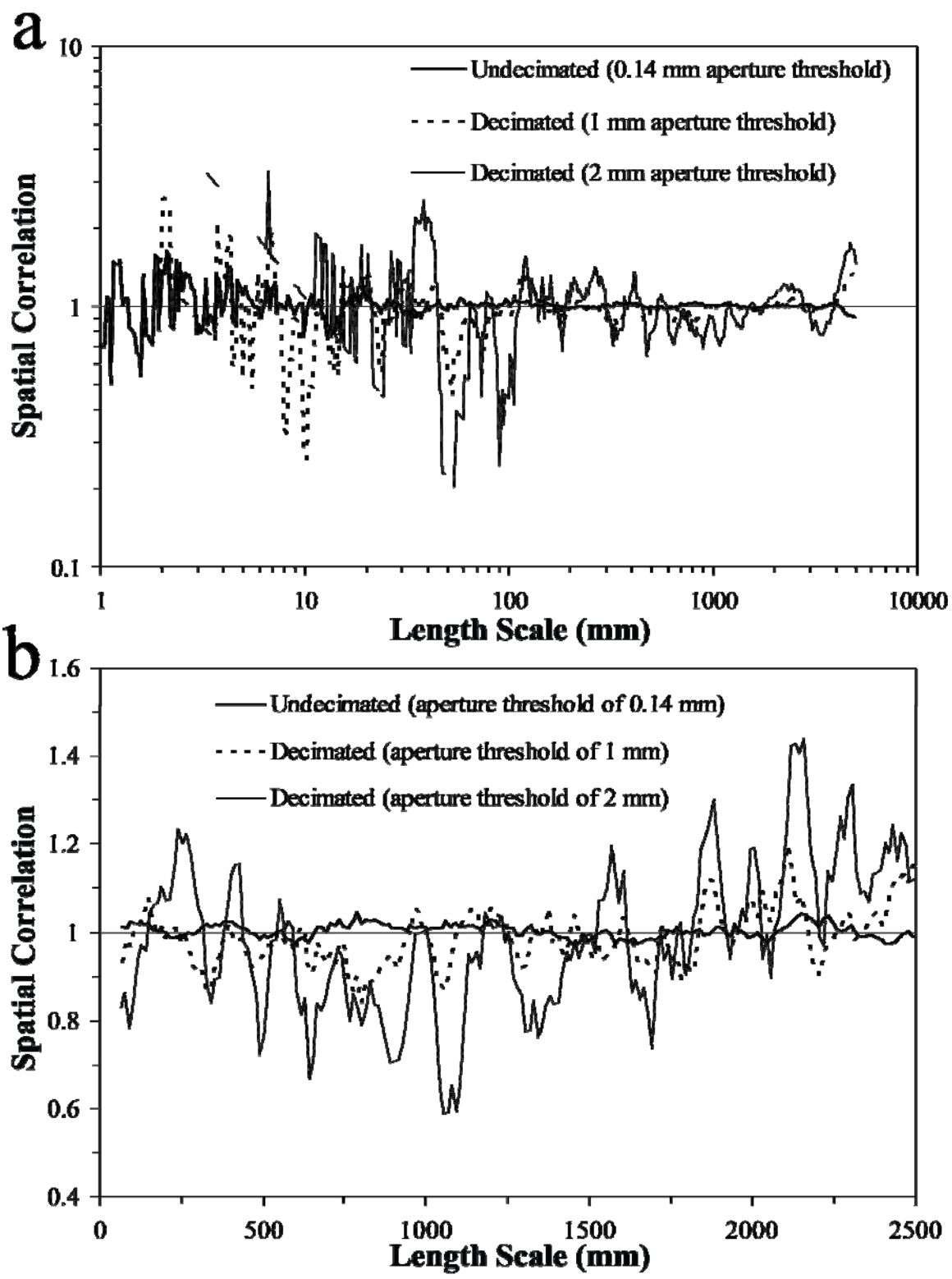
a
Undecimated (0.14 mm aperture threshold)
Decimated (1 mm aperture threshold)
Decimated (2 mm aperture threshold)
Spatial Correlation
10
1
0.1
1
10
100
1000
10000
Length Scale (mm)
b
Undecimated (aperture threshold of 0.14 mm)
Decimated (aperture threshold of 1 mm)
Decimated (aperture threshold of 2 mm)
Spatial Correlation
1.6
1.4
1.2
1
0.8
0.6
0.4
0
500
1000
1500
2000
2500
Length Scale (mm)

7.5. DISCUSSION

7.5.1 Crossplots of Fracture Size versus Fracture Spacing

Different types of crossplots of fracture size (typically aperture) and fracture spacing have been used to interpret relationships between fracture size and arrangement (e.g., Jolly et al., 1998; Gillespie et al., 1999). One type of crossplot is known as a staircase plot (Figure 7.30). Although staircase plots account for fracture position, their interpretation is only qualitative and therefore staircase plots are not free of interpreter bias. Another problem of staircase plots is that they can show different strain heterogeneity depending on the scale of analysis (Figures 7.30b and 7.30c). In addition, staircase plots cannot effectively differentiate clustering from systematic positioning of a size fraction of fractures in clusters as shown in Figure 7.31. Therefore, staircase plots are inadequate to study differential clustering of different fracture size fractions.

Another type of crossplot is a graph of fracture aperture versus fracture spacing (or some variation such as adjacent spacing). Crossplots of fracture aperture versus fracture spacing (e.g., Figure 7.33) or adjacent spacing (e.g., Figure 7.35) have a fundamental limitation: they ignore fracture position. Namely, data points from cluster and intercluster domains along the scanline (Figure 7.4) are combined indiscriminately, and therefore the points cannot be associated with a particular domain (e.g., small spacings with intracluster domains) so the technique cannot be used to test differential clustering for different fracture sizes.

Crossplots of fracture aperture versus fracture spacing exhibit a trend of decreasing fracture spacing with increasing aperture for data sets with both statistically significant (e.g., Figures 7.33a and 7.35a for Pedernales) and statistically insignificant (e.g., Figures 7.33d and 7.35d for Palmas 13) clusters. This suggests that the trend is an intrinsic characteristic of clustering, regardless of its statistical significance. A trend of

decreasing spacing with increasing aperture in data sets with clusters is probably caused by the abundance of small fractures compared with large ones (Marrett et al., 1999) because the few large fractures of a data set are most likely to be inside a cluster (where most of the fractures are) than in between clusters (Figure 7.4). Randomizing fracture position from a data set with statistically significant clusters results in a reduction, but not in a removal, of the trend of decreasing spacing with increasing aperture and in a reduction of the range of fracture spacings for identical ranges of fracture aperture, which suggests that crossplots of fracture spacing versus fracture aperture differ for arrangements with random and non-random clustering (Figure 7.37). However, even if crossplots of fracture spacing versus fracture aperture differ, they cannot quantify arrangements where fracture aperture is randomly (Figures 7.34b and 7.36b) or non-randomly located throughout the scanline (Figures 7.34a and 7.36a).

7.5.2 Normalized Correlation Count

7.5.2.1 Different Spatial Arrangements

Of all the spatial arrangements described by Marrett et al. (in review), only one, periodically arranged fractures (Figure 7.3f), lacks clusters. Arrangements that are indistinguishable from random (Figures 7.3a and 7.3e) exhibit statistically insignificant (Poissonian) clusters, whereas both fractal (Figure 7.3b), inherited/imposed arrangements (Figure 7.3c), and periodically arranged clusters exhibit statistically significant clustering. The hypothesis that a relationship between fracture size and clustering exists was tested on three distinct types of spatial arrangements, as explained by Marrett et al. (in review): fractal arrangement of fractures (Figure 7.3b), periodic arrangement of fracture clusters (Figure 7.3g), and indistinguishable from random arrangements (Figures 7.3a and 7.3e).

7.5.2.1.1 Fractal Arrangements

For fractures with a fractal arrangement inside clusters, tests using increasing aperture thresholds (Figure 7.5) indicate an increase in spatial correlation for larger fractures (Figures 7.38, 7.39, and 7.41). Mutually exclusive subsets for Pedernales (Figure 7.6), each with approximately half of the data set, also show larger spatial correlation, indicative of enhanced clustering, for larger fractures (Figure 7.42). In addition, subsets with increasing aperture thresholds show an increase in the degree of clustering (Marrett et al., in review) suggesting that in statistically significant clusters with a fractal arrangement, large fractures are more clustered than small ones (Figure 7.40b).

When positions of fractures with a fractal arrangement are randomized, the power-law pattern of spatial correlation changes to a flat pattern, suggestive of an arrangement that is indistinguishable from random (Figure 7.43). The non-systematic variation in spatial correlation with increasing aperture threshold for randomly arranged fractures (Figure 7.43) differs from the systematic variation of the natural data set with fractal arrangement (Figure 7.38). Although the aperture thresholds of Figure 7.43 are different from those of Figure 7.38, their results nevertheless show that the increase in spatial correlation and in degree of clustering exhibited by increasing fracture size with a fractal arrangement (Figure 7.38) is absent for randomly arranged fractures (Figure 7.43). Comparable non-systematic variation of spatial correlation for increasing aperture threshold results from natural fractures having indistinguishable from random arrangements (Figure 7.60a) also indicate differential clustering according to fracture size (large fractures more clustered than small ones) is absent in randomly arranged fractures.

In contrast to randomizing fracture position, randomly locating apertures without changes in fracture position and aperture threshold do not exhibit a fundamental change

for undecimated fractures (thick line of Figure 7.44, smallest aperture threshold of Figure 7.45), a result consistent with NCC ignoring fracture aperture (Marrett et al., in review). Increasing the aperture threshold for randomly located fractures results in increasing dispersion of the power-law pattern of spatial correlation (Figure 7.44) without change in the degree of clustering (Figure 7.45), in contrast to the increase in spatial correlation (Figure 7.38) and in degree of clustering (Figure 7.40b) with increasing aperture threshold exhibited by natural fractures. Therefore, randomizing fracture apertures without change in fracture position eliminates sensitivity of NCC to fracture size and supports enhanced clustering of large fractures in a fractal arrangement, which suggests non-random processes link fracture aperture with fracture position.

7.5.2.1.2 Periodic Arrangements of Fracture Clusters

Reducing the number of fractures in a data set with periodically arranged clusters by increasing the aperture threshold (Figure 7.5) resulted in identical patterns of spatial correlation that preserve alternating peaks and troughs, commonly with greater departure of spatial correlation from random (Figures 7.47, 7.49, 7.51, 7.53, and 7.54). Splitting a natural data set into two subsets with different ranges of fracture aperture also shows stronger clustering (larger spatial correlation) for large fractures and weaker clustering for small ones (Figure 7.55).

Randomizing the positions of fractures that exhibit periodically arranged clusters changes the pattern of spatial correlation (Figure 7.11b) to one indicative of an arrangement indistinguishable from random (thick line, Figure 7.56). When the positions of fractures that exhibit periodic arrangement of clusters are randomized and then an increasing aperture threshold is applied (Figure 7.5), spatial correlation between the undecimated and decimated subsets shows no systematic variations (Figure 7.56), which

suggests that randomly arranged fractures lack systematic variation in clustering with fracture size.

Randomizing fracture apertures without any change in fracture position or in aperture threshold results in nearly identical spatial correlation (thick line in Figures 7.51 and 7.57). For aperture thresholds larger than the one used in the field, the pattern of spatial correlation for randomly located apertures does not change considerably with increasing aperture threshold (Figure 7.57). In addition, the increase in spatial correlation with aperture threshold of the original data set (Figure 7.51) is not observed in the version with randomly located fractures (Figure 7.57), which suggests that the observed increase in clustering of large fractures compared with small fractures of periodically arranged clusters cannot be explained by random location of fracture apertures.

7.5.2.1.3 Arrangements Indistinguishable from Random

Natural fracture data sets that exhibit arrangements that are statistically indistinguishable from random exhibit a flat pattern of spatial correlation (Figures 7.3a and 7.3e). When increasing aperture thresholds are applied to data sets that exhibit arrangements that are indistinguishable from random, no consistent variation in spatial correlation can be observed for both logarithmically and linearly graduated length scales (Figure 7.60), which suggests that larger fractures of indistinguishable from random arrangements are not more or less clustered than small ones. Similar conclusions can be drawn from artificial randomization of non-random arrangements for both logarithmically (Figure 7.43) and linearly (Figure 7.56) graduated length scales.

7.5.2.2 Different Scales of Observation

The relationship between clustering and fracture size was explored for data sets from two scales of observation: outcrop and rock sample. Outcrop scale comprises data

sets with fracture apertures down to the smallest graduation of the comparator designed by Ortega et al. (2006), approximately 0.05 mm. In contrast, fracture apertures of data sets at rock-sample scale have apertures up to two orders of magnitude smaller (0.0005 mm) than their outcrop counterparts. In spite of the differences in scale, data sets at both outcrop and rock sample scales with periodically arranged fractal clusters exhibit the same increase of spatial correlation (e.g., Figures 7.39 and 7.41 for logarithmically graduated length scales and Figures 7.47 and 7.54 for linearly graduated length scales) and increase in degree of clustering (Figures 7.40b and 7.41) with increasing apertures, which indicates that large fractures are more clustered than small ones. Therefore, increased clustering of large fractures in non-random arrangements is a phenomenon that extends at least between typical outcrop (tens of meters) and rock sample (a few centimeters) scales of observation, suggesting that the processes that control cluster development also might affect differential clustering according to fracture size.

7.5.2.3 Different Lithologies and Loading History

Although the number of data sets studied in Chapter 7 is relatively small (Table 7.1), three sedimentary lithologies from three different geologic regions (each with a different tectonic history) were included: sandstone (below evaporite decollement, SMO), limestone (undisturbed Ouachita foreland, Central Texas), and dolostone (above evaporite decollement, SMO). Similar results of cluster variation with fracture size were obtained for different lithologies. For instance, Tranquitas rock sample (sandstone), Pedernales (limestone), and Palmas 11 HR (dolostone) data sets all show increased degree of clustering for increasing aperture thresholds (Figure 7.40b). In other examples, southern 26 m of Tranquitas (sandstone), Pedernales (limestone), and Huasteca (dolostone) data sets show similar patterns of spatial correlation (peaks and troughs at identical length scales) and increased spatial correlation with increased aperture threshold

(Figures 7.53, 7.51, and 7.49, respectively). Therefore, lithology and loading history are unlikely to be primary factors that control the development of enhanced clustering for larger fractures.

7.5.2.4 Summary

Arrangements with non-random clustering of fractures exhibit a relationship between fracture size and fracture position. Larger fractures are more clustered than small ones in statistically significant clusters (non-random arrangements), whereas in statistically insignificant clusters (indistinguishable from random arrangements) there is no difference in clustering between small and large fractures. Enhanced clustering of large fractures (compared with small ones) occurs at different scales, in different lithologies, under different loading histories and for two different spatial arrangements. An increase in the degree of clustering with increasing aperture also implies that the spatial arrangement of small fractures is closer to random than for large fractures.

7.5.3 Mechanical Interpretation

Modeling of fracture development has provided mechanical explanations for proportionality between spacing of natural fractures and layer thickness, as observed for some fracture sets (periodically arranged fractures, Figure 7.3f) although not for any considered here (e.g., Narr and Suppe, 1991; Wu and Pollard, 1995). Numerical modeling of fracture evolution has emphasized static (one fracture propagating at a time) fracture development in a cross-section plane (e.g., Rives et al., 1992) and demonstrated how the stress relief around a pre-existing fracture creates a zone (stress shadow) where stress is lower than remote stress. If fractures are close enough that stress shadows of adjacent fractures overlap, then additional extensional loading will increase the aperture of pre-existing fractures (Bai and Pollard, 2000), leading to a saturated state where no additional

fractures are allowed to grow (Wu and Pollard, 2000). Such experimental and numerical models of fracture propagation have failed to provide mechanical explanation for clusters of natural fractures (Olson, 2004). However, recent time-dependent numerical modeling of subcritical fracture propagation in a bedding-parallel plane has produced clusters similar to those observed in rocks (e.g., Olson, 1993; Olson, 2004). If subcritical fracture propagation can explain clustering of natural fractures, then it might also explain how large fractures become more clustered than small ones.

7.5.3.1 Subcritical Fracture Propagation

Fracture propagation under critical conditions (at a velocity similar to the shear elastic wave velocity of the material) occurs when opening-mode stress intensity factor (K) reaches the fracture toughness of the material (Lawn and Wilshaw, 1975). However, when long-term loading occurs, fractures can propagate at stress intensity factors lower than fracture toughness, albeit at velocities several orders of magnitude slower than the rupture velocity, in a phenomenon called subcritical crack propagation (Atkinson, 1984). K is the stress intensity factor, a linear elastic fracture mechanics parameter that quantifies the stress concentration at a fracture tip and the tendency of an opening-mode fracture to propagate (Lawn and Wilshaw, 1975). Subcritical crack growth depends on the local stress state, rock type, the chemistries of fluid and rock mass, and a reaction rate at the fracture tip that exceeds the overall strain rate (Schultz, 2000). The hypothesis of reaction rate limits to subcritical propagation provide the most accepted explanation for stress corrosion fracturing in rock (Park, 2006). The reaction rate concept is that atomic bonds in a stressed rock mass are ruptured by thermal fluctuations and accommodate displacement increase.

A log-log graph of propagation velocity versus K shows three distinct mechanisms of fracture propagation as shown in Figure 7.61 (Schultz, 2000). Subcritical

fracture propagation initiates when $K > K_0$ and occurs at sufficiently low rates of strain that the rate of propagation of the fracture tip (rate of stress corrosion) through the rock mass is limited (and governed) by the chemical reaction rates (Schultz, 2000). The subcritical index (n) is the slope in the log-log graph of fracture propagation velocity (v) versus K (Region I of Figure 7.61) that can be calculated with an empirical power-law relationship (Atkinson, 1984):

$$v = \mathrm{A}\left(\frac{K}{K_C}\right)^n \tag{1}$$

where A is a proportionality constant and K_C is fracture toughness. Subcritical index (n) is the exponent of the ratio of stress intensity factor (K) over fracture toughness (K_C). Fracture velocity in Region I is controlled by the rate of stress corrosion at the fracture tip. Subcritical fracture propagation is characterized by positive values of n and a proportional relationship between fracture propagation velocity and K (Region I, Figure 7.61). As the strain rate applied to the rock exceeds the reaction rate, chemical processes at the fracture tip cannot keep pace with the applied strain (Region II, Figure 7.61), leading to quasi-static fracture growth governed by fracture toughness or to dynamic fracture propagation ($K > K_C$, Region III, Figure 7.61). Region II of fracture propagation has been observed in some glass and ceramics but is rarely seen in rocks (Park, 2006).

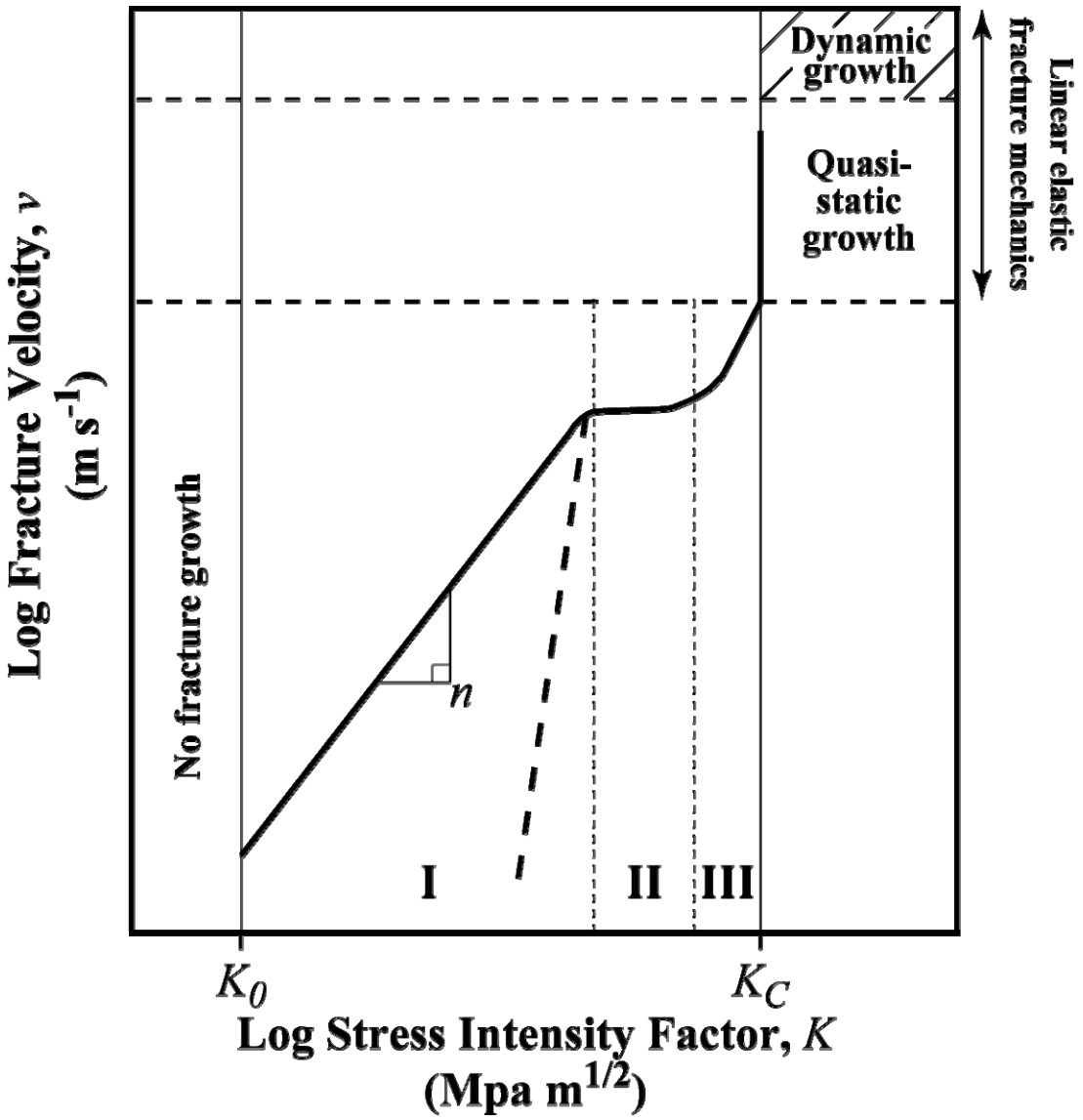

Figure 7.61 General relationship between fracture propagation velocity versus stress intensity factor (K). Region I is dominated by stress corrosion; Region II is controlled by the transport of reactive species to the fracture tip; and mechanical rupture occurs in Region III. In rocks, subcritical fracture growth occurs when K is larger than the stress corrosion limit (K_0). For $K \geq K_c$, linear elastic fracture mechanics entails either quasi-static propagation (for displacement-controlled loading) or dynamic propagation (for stress-controlled loading). Modified from Atkinson and Meredith (1987).

The subcritical index (n) quantifies the relationship between natural fracture propagation velocity and tip loading conditions only in opening-mode (Olson, et al., 2001). The propagation velocity of a fracture with constant K decreases with increasing subcritical index (Olson, 1993). The subcritical index can influence fracture clustering (e.g., Olson, 1993), cumulative frequency distributions of fracture spacing (Olson, 2001) and cumulative frequency distributions of fracture length (Olson et al., 2004). The subcritical index (n) can be measured and is postulated to depend on material properties such as porosity, grain size, and mineralogy (Holder et al., 2001). However, recent studies have shown the difficulties in isolating the influence of individual rock characteristics (e.g., porosity) on subcritical index and subcritical fracture development (Olson et al., 2002; Rijken, 2005). With increasing subcritical index (dashed line, Figure 7.61), subcritical propagation becomes less significant because very little propagation occurs before fracture toughness is reached (Olson, 2004).

Numerical modeling of subcritical crack propagation from randomly arranged flaws has generated fracture clustering similar to that observed in the field (e.g., Olson et al., 2004). When fractures are simulated with very low values of n ($n < 10$), many fractures propagate simultaneously at roughly the same velocity, penetrating the stress shadows of adjacent fractures (Olson, et al., 2001) and resulting in a somewhat irregularly spaced fracture pattern (Olson, 2004) as shown in Figure 7.62a. Intermediate values of n ($10 < n < 50$) result in somewhat regularly spaced fractures as shown in Figure 7.62b. Fractures grown at intermediate values of n propagate one at a time as a consequence of large contrast in velocity between fractures of even slightly different K. Each fracture fully develops its stress shadow before neighboring fractures begin to propagate, which impedes penetration of stress shadows from nearby fractures (Olson et al., 2004), in a similar fashion to the initial stage of development of isolated large shear

fractures surrounded (anticlustered) by small faults proposed by Ackermann and Schlische (1997). Increasing n to large values n ($n > 50$) does not result in a significant increase in the velocity contrast between adjacent fractures as suggested by early work in subcritical crack propagation on rocks (e.g., Olson, 1993). Instead, observable clusters develop through time by simultaneous propagation of clusters of small fractures in the tip region of a large fracture (Figure 7.63), in a similar manner to a process zone (Olson, 2004). Interaction between the stress shadows of initially developed clusters results in promoting cluster propagation at distances approximately equal to layer thickness and hindering fracture development in between clusters (Figure 7.62c), as suggested by Olson (2004).

Figure 7.62 Plan views of fracture patterns developed from numerical modeling of subcritical fracture growth with a layer thickness of 8.0 m, a Young's modulus of 20 GPa, a Poisson's ratio of 0.25, and a subcritical index of n = 5 (a), n = 20 (b), and n = 80 (c). Additional details about how fractures were numerically modeled are explained in Olson (2004). Axes are labeled in meters. Strain was imposed by normal displacement in the y-direction at a strain rate of 2.0×10^{-20} s^{-1} to a final extension of 9×10^{-5}. (d) Enlarged final fracture trace map of one cluster in (c). (e) Aperture map of fractures that grew in (d), showing that some fractures grew and subsequently close or never reach an observable aperture. In (e), each fracture segment modeled has an opening represented by an open circle with a proportionate diameter (aperture exaggeration is approximately 450x). Modified from Olson (2004).

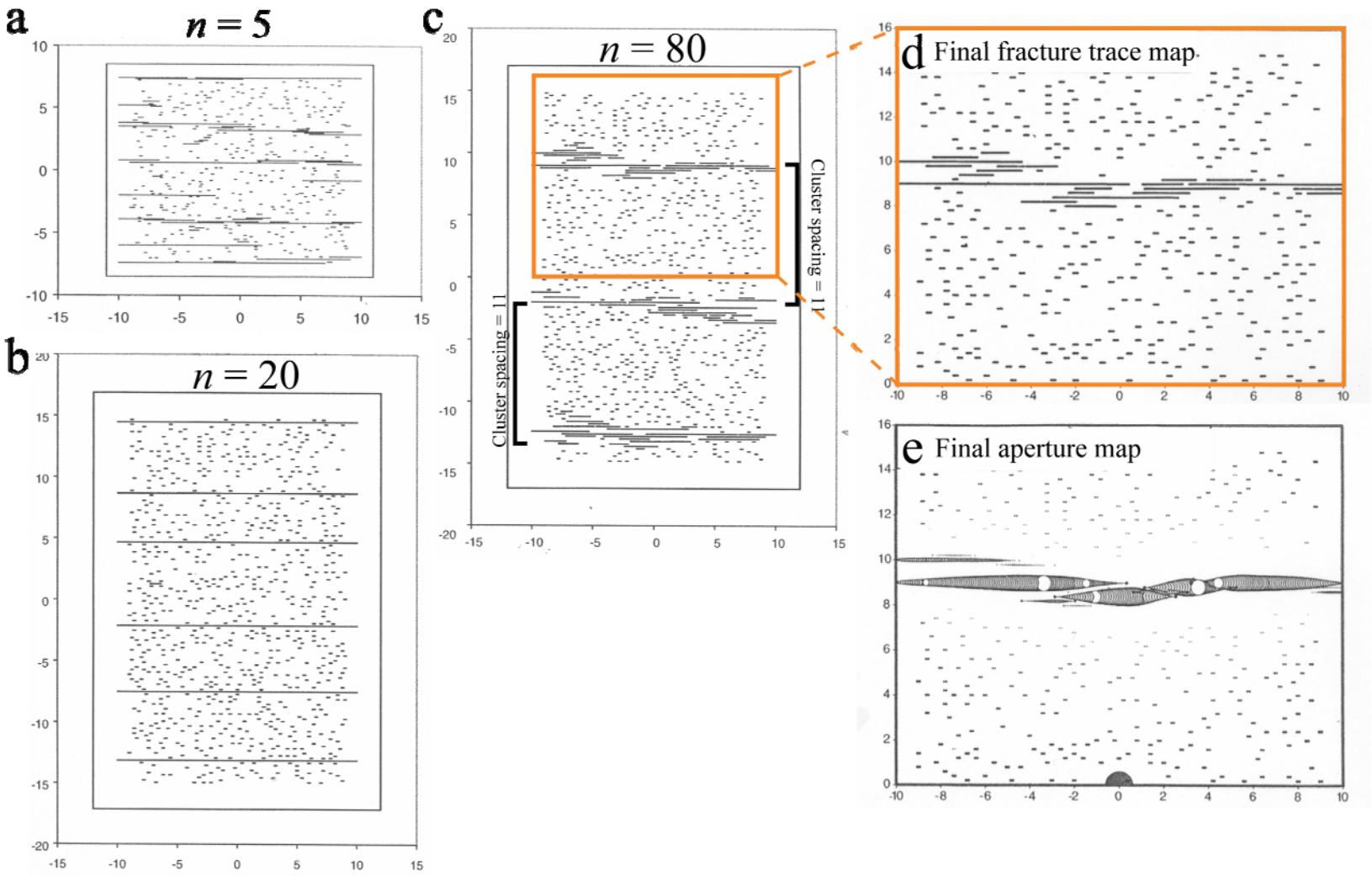
a
n = 5
b
n = 20
c
n = 80
Cluster spacing = 11
Cluster spacing = 11
d Final fracture trace map
e Final aperture map

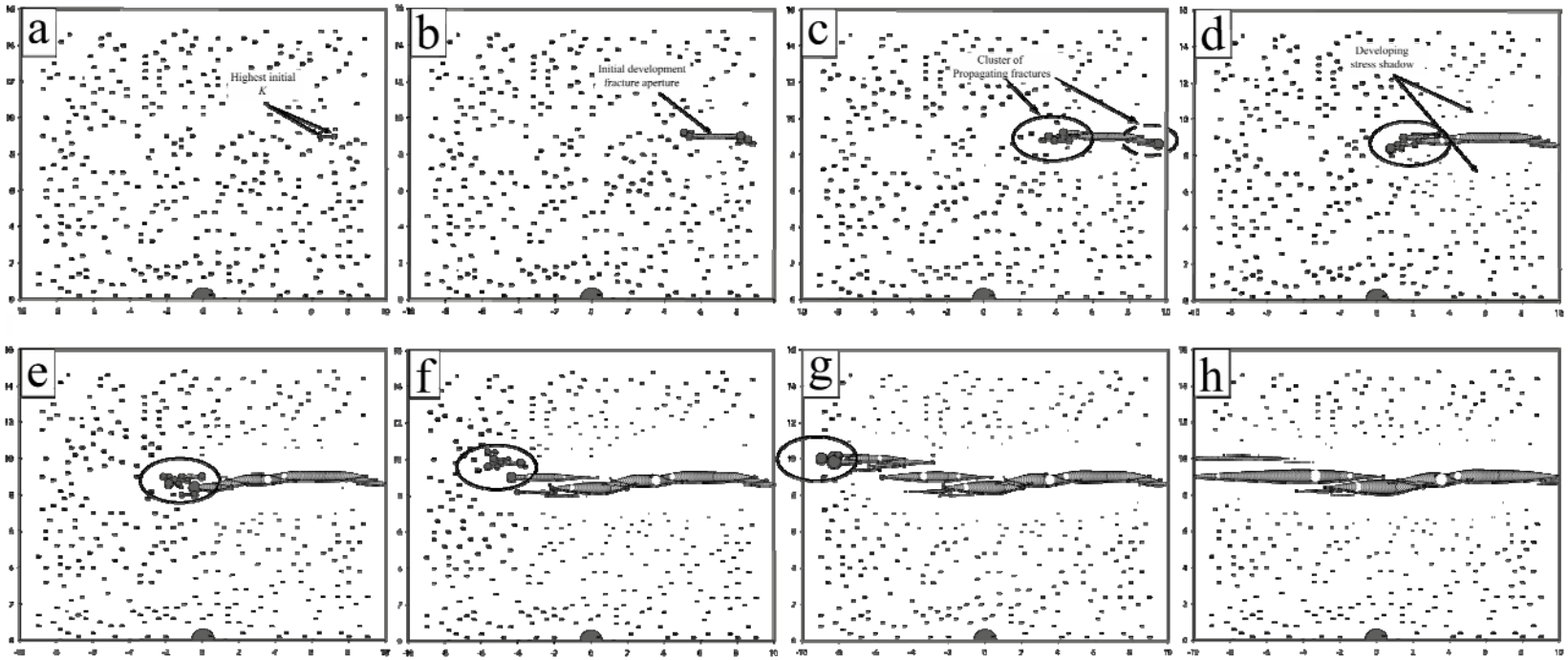

Figure 7.63 Evolution of fracture aperture and stress intensity factor (K) for the cluster of Figure 7.62e (n = 80). Axes are labeled in meters. The circle at (0,0) is the scale for K, showing the diameter appropriate for a value of 10 MPa $m^{1/2}$. K at fracture tip is represented by a shaded circle with a proportionate diameter. Each fracture segment modeled has an opening represented by an open circle with a proportionate diameter (aperture exaggeration is approximately X 450). (a) through (h) show the propagation of a fracture cluster, from an initial stage with near randomly arranged flaws (a), to a final stage with an manifest cluster (h). Notice the development of a stress shadow around cluster from (d) to (h). Also notice the cluster of propagating fractures (solid ellipse) ahead of the cluster from (c) to (g). As expected, for a given rock layer, increasing strain, from (a) to (h), applied to a body increases the total amount of fracture trace length created. Modified from Olson (2004).

7.5.3.2 Aperture Development in the Statistically-Significant Intracluster Domain

7.5.3.2.1 High Subcritical Index Simulation

Although the limited number of fractures in currently available numerical models of subcritical propagation with high n values has precluded NCC analysis of modeled fractures, models with high n values exhibit clustering that probably is statistically significant (e.g., Figure 7.62c). Monitoring the evolution of a numerically modeled cluster with high subcritical index allows detailed examination of variations of fracture aperture throughout cluster evolution (Figure 7.63). In the initial stage of a numerical model of Olson (2004), flaws of the same size (0.2 m) are elongated parallel to the X axis and randomly located (Figure 7.63a). During the early stages of fracture evolution, flaws have slightly different values of K due to random spatial location of neighboring flaws that mechanically interact with them (Olson, 2004); side-by-side arrangements of flaws decrease K whereas en echelon and tip-to-tip arrangements increase K (Olson and Pollard, 1991). In the model of Olson (2004), flaws are represented by their stress intensity factor because their apertures are negligible (Figure 7.63a).

In rocks with high n values, the power-law nature of equation (1) dictates that fracture propagation velocities are very low for fractures with K equal to K_0 (Figure 7.61). Because of low fracture propagation velocities, propagation of the flaw with the largest K is delayed until significant elastic strain has accumulated and consequently significant fracture propagation initiates at K values near K_C (Olson, 2004). At this early stage in fracture evolution only the first fracture has propagated appreciably (Figure 7.63b). As increased stress concentration is induced by the first fracture, K increases for flaws near both tips of the first fracture (solid and dashed ellipses, Figure 9.63c), initiating propagation of these flaws and marking the initiation of clusters. Interaction of

overlapping en echelon fracture tips obstructs development of the initial fracture (Figure 7.63d), as suggested by Olson and Pollard (1989), even though it has the largest aperture and length (Figure 9.63d). Rapid propagation of fractures near the tips of the first fracture acts as a pseudo process zone that iterates the increase of K in flaws ahead of each fracture tip and develops clusters that propagate along strike. Subsequent fracture evolution results in some fractures attaining apertures comparable to or larger than the first fracture and a stress shadow around the cluster that reduces the K of surrounding flaws (Figures 7.63d to 7.63g). Although fracture interaction can hinder the propagation of some of the fractures initially developed in the pseudo process zone, it can also facilitate the development of some large fractures within the cluster (Figure 7.63h). Nevertheless, some fractures developed in the pseudo process zone during the cluster evolution remain comparatively small in size (Figures 7.62d and 7.62e).

In summary, as explained by Olson (2004), the reason for clustering at high subcritical index is related to the large magnitude of K when fracture propagation occurs. The tensile stress perturbation around a crack tip is proportional to K (Lawn and Wilshaw, 1975), suggesting that with the high K values at the beginning of fracture propagation of rocks with high n (Figure 7.61), the propagation of flaws in the fracture-tip region is enhanced for high n in comparison with flaw propagation in other regions (Figure 7.63). The increased K of rocks with high n produces clusters which contain both small and large fractures, as observed in the natural datasets shown in earlier sections.

Rijken (2005) measured the subcritical index (n) of 109 different rock samples from 38 different formations and obtained an average subcritical index for sandstones (82 samples) of 62 ± 25 whereas for carbonate rocks (20 samples) subcritical index is significantly higher, averaging (120 ± 87). Although diagenetic changes suffered by the rock after fractures form can alter the rock composition, and therefore its subcritical

index, Rijken (2005) showed that lithologies like the ones examined for my dissertation (Table 7.1) can reach high ($n > 50$) values of subcritical index. If fractures in the rocks studied developed at high n, then clusters would result and contain all large aperture fractures. Although subcritical modeling of fractures at high n shows development of small fractures also only inside clusters (Figures 7.62d and 7.62e), it is reasonable to believe that during the development of natural fractures over much larger areas than the model of Figure 7.63, small fractures will develop simultaneously over many areas. Small fractures in some of those areas will later cease to develop because they would be located in intercluster domain of already developed clusters. The same authors that have reported subcritical indexes larger than 80 in rocks have shown fracture modeled with subcritical indexes only up to 80 (Olson, 2004; Rijken, 2005), which suggests that no substantial variation between models with subcritical indexes larger than 80 has been found.

7.5.3.2.2 Natural versus Modeled Clusters

Although modeling of subcritical fracture propagation generates clusters with spacing proportional to bed thickness that resemble those observed in nature, the models differ in some ways that are worth noticing. For instance, fractures in Figure 7.62c were modeled with a n of 80, in an area of 20x30 m for a 8 m thick layer that contained 800 flaws of 0.2 m long each, and the resulting clusters contain an average of 5 fractures (on a given X position) and are separated approximately 11 m. The scale of the fractures depicted in Figure 7.62c similar to a fracture set measured at outcrop scale (maximum aperture in model of Figure 7.62c is 1.7 mm). The first discernable difference between rocks and the model of Figure 7.62c is the size of the flaws. Although some rocks contain heterogeneities as large as 20 cm (e.g., fossils), constituents for most rocks have a size of few millimeters or even less (e.g., quartz grains of sand size in a sandstone, or dolomite

crystals in a dolostone). Second, the number of flaws incorporated to the initial model is probably small for the volume of rock modeled. The number of flaws has been demonstrated to have an impact on the spatial arrangement of fractures; for instance, at high values of *n*, a reduction from 800 to 400 flaws makes the clustering less evident and reduces the regularity in cluster spacing (Olson, 2004). Therefore, it is possible that by increasing the number of flaws several times more (to reflect more realistically the number of heterogeneities in rock) the modeled spatial arrangement might change. Third, the number of fractures in each model cluster is very small compared to natural clusters measured at outcrop scale (Chapter 8), with some outcrop scale clusters containing hundreds of fractures (including microfractures).

However, if the model of Figure 7.62c were considered three orders of magnitude smaller (20x30 mm, comparable in size to a rock sample), flaw size would be 0.2 mm (medium sand grain size), a size more similar to the expected size of constituents for sedimentary layers. Also, cluster spacing of the example model of Figure 7.62c would become 11 mm, comparable to those observed at rock sample scale (e.g., 29 mm for the Tranquitas rock sample; Figure 7.23b). In addition, a reduction of three orders of magnitude in the model size would result in clusters with a number of fractures comparable to what is commonly observed in clusters of microfractures at rock sample scale (e.g., clusters at 0.035, 0.055, and 0.14 m along the Tranquitas rock sample scanline; Figure 7.22).

If existing models of subcritical fracture propagation produce clusters that better represent rock sample scale than clusters at outcrop scale, then a mechanism that explains the genetic relationship between clusters at outcrop and rock-sample scales would be required. I hypothesize that first, microfractures become organized in periodically arranged clusters at rock sample scale following mechanical layering smaller than layer

thickness. Large microfractures are more clustered than small microfractures. As fracturing progresses, natural variations in fracture orientation would cause growing microfractures to intersect and coalesce into larger fractures. Large fractures inside outcrop-scale clusters within the Cupido Fm. cross layer boundaries (bottom of clusters in Figure 7.1, right end of scanline near layer top in Figure 7.8) indicating that under certain conditions fractures could develop heights larger than mechanical thickness. In addition, differential diagenesis rates between layers of differing grain size have been proposed as the cause of temporal variations of mechanical thickness (Shackleton et al., 2005). Renshaw and Pollard (1995) explained the conditions invoked by Shackleton et al. (2005) under which fracture propagation can continue across layer boundaries by reinitiating a fracture on the side of the layer boundary opposite the propagating fracture. first fractures to coalesce would secure the location of first cluster at outcrop scale (akin to cluster evolution in Figure 7.63). The stress shadow of the newly developed cluster at outcrop scale would not be related to the size of the cluster at rock-sample scale but to the size of the coalesced fractures. Subsequent outcrop-scale clusters would have to develop outside the stress shadow of the initial cluster, which could result in regularly-spaced clusters, in a similar evolution to the fracture pattern of Figure 7.62c (Chapter 8). Finally, it should be acknowledged that although subcritical fracture propagation provides some answers to the phenomenon of clustering in natural fractures, there is still a great deal of knowledge about clustering of fractures that remains to be attained.

7.5.3.3 Aperture Development for Randomly Arranged Fractures

Some natural fracture sets did not develop statistically-significant clusters and exhibit arrangements that are indistinguishable from random (e.g., Palmas 13). Numerical modeling suggests that at low values of subcritical index (n) the resulting clustering is more irregular (in size and spacing) than at high values, as shown in Figure 7.62 (Olson,

2004). The irregular clustering found in simulations with low *n* might be Poissonian and equivalent to the statistically insignificant clustering of randomly arranged fractures. In rocks with low *n*, fracture development initiates at lower values of *K* and at lower velocities than for rocks with high *n* (Figure 7.61), which results in simultaneous propagation of multiple fractures (Olson et al., 2001). If multiple fractures propagate simultaneously throughout the rock body at comparatively slow velocities, fractures that initiate early can simultaneously develop large apertures before their stress shadows start interfering with each other, resulting in a weaker organization of large fractures (Figure 7.62a).

7.5.3.4 Synkinematic Fracture Cement

One of the most common results of synkinematic precipitation of fracture cement is the development of mineral bridges (Laubach et al., 2004b). Bridges can have an impact on the development and subsequent history of fractures. For instance, bridges can help maintain the fracture open once the effective compressional stress affecting a fracture is increased by either a decrease in the pressure of fluids inside a fracture (typically caused by fluid removal) or by the development of another fracture on its vicinity (Laubach et al., 2004a). In addition, synkinematic cement tends to fill small fractures more completely than large fractures (Laubach, 2003).

Amounts of synkinematic versus postkinematic cements have not been established for Pedernales or Tranquitas data sets. However, fractures in Cupido Fm. with larger amounts of synkinematic cement exhibit non-random clustering at both outcrop (Table 7.2; Chapter 9) and rock-sample scale (Chapter 8), whereas fractures in the Cupido Fm. with smaller amounts of synkinematic cement exhibit random clustering at outcrop scale (Table 7.2; Chapter 9) and non-random clustering at rock-sample scale (Chapter 8).

For comparable ranges of fracture sizes as the ones exhibited by the outcrop data sets selected for Chapter 7 (Table 7.1), abundant synkinematic cement might have preserved the aperture of both small and large fractures that formed in the pseudo process zone ahead of the cluster preventing some of the fractures to be closed due to stress induced by adjacent and simultaneously growing fractures at both outcrop and rock-sample scale (e.g., Figures 7.62d and 7.62e). Preserving the aperture of large fractures once they developed in clusters would facilitate an increased presence of large fractures within clusters. In contrast, in layers with less abundant synkinematic cement, small fractures at rock-sample scale were probably mostly filled with synkinematic cement (Laubach, 2003), which might helped preserve their spatial organization. However, synkinematic cement was not abundant enough to bridge large fractures at outcrop scale and prevent them from partly or completely closing, eliminating existing relationships between fracture aperture and fracture position.

7.6. CONCLUSIONS

Although staircase plots have been used to distinguish between data sets with homogeneous and heterogeneous strain, qualitative interpretations of the relationship between fracture size and fracture position can change according to the scale of observation. In addition, staircase plots cannot indicate whether or not strain heterogeneity is statistically from distinguishable random. Fracture spacing, maximum fracture spacing, adjacent spacing, and maximum adjacent spacing exhibit a decreasing trend with increasing fracture aperture for random and non-random clustering of fractures. Crossplots might be used to distinguish random from non-random spatial arrangements because randomly arranged fractures exhibit a fainter trend of decreasing maximum spacing (or adjacent spacing) with increasing aperture than equivalent non-randomly arranged fractures. However, such crossplots are inadequate to study the relationship of aperture and clustering because the phenomenon of clustering implies knowledge of fracture position and crossplots of fracture spacing versus fracture aperture ignore fracture position.

Normalized correlation count, a recently developed technique that accounts for fracture position, indicates that non-random clusters of fractures exhibit a relationship between fracture size and fracture position: large fractures are more clustered than small ones. Namely, in statistically significant clusters with a fractal arrangement of fractures, the proportion of fractures in clusters (degree of clustering) increases with fracture size. An increase in the degree of clustering with increasing aperture also implies that the spatial arrangement of small fractures is closer to random than for large fractures. When periodically arranged fracture clusters are observed, artificially increasing the aperture threshold (with the subsequent reduction in number of fractures) typically results in an

increase in spatial correlation at the length scale of cluster spacing and its multiples, indicating that large fractures are more concentrated in clusters than small ones. In contrast to non-random arrangements, large fractures in arrangements that are indistinguishable from random do not exhibit clustering different than their small counterparts. Increased clustering of large fractures for non-random arrangements was detected in sedimentary rocks with different lithologies, different tectonic/diagenetic histories, and at different scales, which suggests that the phenomenon of increased clustering of large fractures is related to how and not where or when fractures propagate.

Numerical models suggest that development of spatial arrangement is strongly influenced by the mechanical interaction between neighboring fractures throughout the evolution of the fracture network. Subcritical fracture propagation at high values of subcritical index ($n > 50$) generates clusters by rapid propagation of a pseudo process zone ahead of initially developed fractures. Interaction of stress shadows for clusters results in regularly spaced clusters. Since fracture propagation is inhibited in between clusters, fractures with large apertures only develop within clusters.

The presence of abundant synkinematic cement in layers with fractures that exhibit non-random arrangements might have preserved the aperture developed by both small and large fractures inside clusters, enhancing the clustering of large fractures. In contrast, the less abundant synkinematic cement in layers with fractures that exhibit indistinguishable from random arrangements might have preferentially preserved the aperture of small fractures but allowed aperture reduction of large fractures, eliminating any relationship between fracture aperture and fracture position of indistinguishable from random arrangements.

Chapter 8: Structure of Fracture Clusters

8.1. INTRODUCTION

As stated by Ortega (2002) in the context of research on fracture apertures, studying the natural phenomenon of scaling implies describing and understanding the relationships between fractures at different scales. Chapter 8 of my dissertation aims to test the hypothesis that fracture clusters are natural fractals. Previous work has suggested that some fracture clusters at outcrop scale are fractal (Hare and Marrett, in review; Marrett et al., in review). If fracture clusters are fractal, then clusters should contain a spectrum of smaller but statistically equivalent fractal clusters. However, the internal structure of clusters of natural fractures at any scale has not been thoroughly investigated.

If fracture arrays are clustered, then the permeability of the fractured rock will be higher inside clusters than in between clusters, especially because large (and more permeable) fractures are more clustered than small fractures (Chapter 7). Therefore, understanding the internal structure of clusters could improve the numerical modeling of fluid flow in fractured reservoirs and the planning of horizontal wells (Gale, 2002). In addition, increased understanding of the phenomenon of clustering of natural fractures may provide new criteria with which to validate numerically modeled fracture systems (e.g., Olson et al., 2001).

8.1.1 Chapter Organization

Chapter 8 of my dissertation is divided in four sections. The first section introduces the hypothesis to be tested and provides a summary of the approaches taken and the methodologies used to address the hypothesis. The second and third sections introduce the data sets with and without sample analyses, respectively, selected for this chapter and presents the results from normalized correlation count, or NCC (Chapter 6),

at outcrop and subdomain scales. The fourth section discusses the results and brings the implications to bear on understanding of the evolution of natural fractures.

8.1.2 Hypothesis

Chapter 8 of my dissertation tests the hypothesis that fracture clusters described by power-law patterns of spatial correlation (from NCC analyses) are natural fractals, so they consist of smaller fractal clusters, which in turn consist of still smaller clusters, and so on. Namely, clusters of fractures with a fractal arrangement should be statistically self-similar across a broad spectrum of scales (follow fractal scaling). Hare and Marrett (in review) suggested that fractures at Pedernales Falls State Park are fractal because they show systematic fracture clustering across four orders of magnitude of wavelet wavelength (Figure 8.1). Wavelet analysis developed by Hare and Marrett (in review) show that clusters at short wavelengths coalesce into larger clusters at progressively longer wavelengths (Figure 8.1).

8.1.2.1 Concept of Fractal

Fractals are mathematically defined as geometric structures having an infinite number of nested structures that area statistically similar at all scales of observation (Schroeder, 2000). The most important feature of fractal geometry is the lack of a representative elementary volume (Bonnet et al., 2001). Although mathematical fractals are infinite, natural fractals must have upper and lower bounds (Bonnet et al., 2001). Lower bound is believed to be controlled by phenomena at grain size, whereas the upper bound is probably related to the mechanical thickness of the fractured layer (Hare and Marrett, in review). Self-similarity is a typical property of fractals. Namely, fractal geometry is exactly or approximately similar to a part of itself (Schroeder, 2000). A self-affine geometry is a fractal whose pieces are scaled by different amounts in the x- and y-

directions. A key line of evidence for fractal scaling is the absence of characteristic length scales in the fracture growth process (Bonnet et al., 2001).

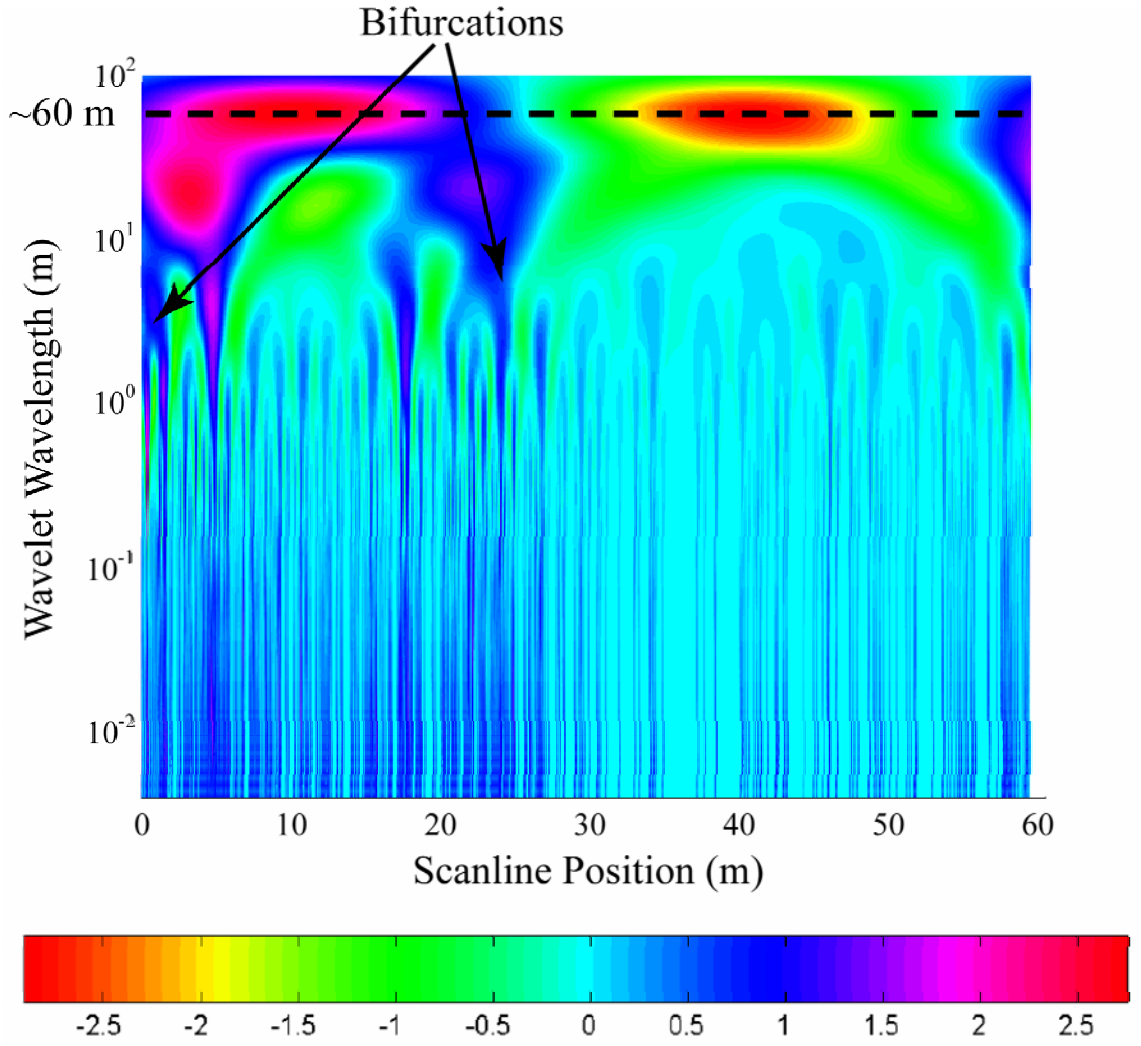

Figure 8.1 Wavelet amplitude map for fractures at Pedernales Falls State Park fracture data. Black dashed line represents the length of the scanline (~60 m). Cool colors (e.g., purple and blue) indicate areas of high amplitude, where the wavelet transform encounters areas of abundant fractures. Warm colors (e.g., yellow and red) indicate areas dominated by low amplitudes, where the wavelet transform encounters areas of low fracture intensity. Areas of high amplitude exhibit cascading bifurcations across approximately four orders of magnitude of wavelet wavelength. From Hare and Marrett (in review).

8.1.2.2 Test of Hypothesis

In order to test the hypothesis that fracture clusters follow fractal scaling, I measured fracture aperture and spacing along scanlines in outcrops (outcrop data sets) and studied the spatial arrangement of fractures using NCC. Then, I measured aperture and spacing of fractures at a higher resolution (rock sample scale) in separate domains of the outcrop scanline (e.g., inside a cluster or in between two clusters) and independently studied their spatial arrangement using NCC. Subsequently, I compared the spatial arrangement of the entire scanline at outcrop scale with the spatial arrangement of subsets of the outcrop scanline. In addition, the test was executed in data sets at outcrop scale that exhibit different types of spatial arrangement as defined by Marrett et al. (in review):

1. Random arrangement of fractures only (statistically insignificant clustering).
2. Periodic arrangement of fracture clusters, which in turn have a power-law pattern of spatial correlation (periodically arranged fractal clusters).
3. Periodic arrangement of fracture clusters, which in turn have an inherited/imposed arrangement internally.
4. Ambiguous arrangement of clusters, which in turn have a power-law pattern of spatial correlation

I devised two ways of studying the internal structure of clusters in order to test if they follow fractal clustering. The ideal approach involved extracting rock samples from layers used to collect outcrop scanline data. Then, fracture aperture and spacing of fractures (mostly microfractures) were measured and used to study the spatial arrangement of fractures within a particular domain (e.g., within a cluster). A less than ideal approach involved taking an outcrop data set and removing all fractures except for the ones located within a domain of interest (e.g., within a cluster). Then, the spatial

arrangement of the fracture subset within the domain of interest was studied. In contrast to the use of rock samples, there is no change in the resolution between the entire scanline data set and the subset under consideration. For my dissertation, I define microfractures as fractures visible only under magnification and macrofractures as fractures visible without any magnification.

The hypothesis that fracture clusters follow fractal scaling predicts that clusters at outcrop scale should in turn contain clusters that when studied independently also exhibit fractal clustering. Clusters with inherited/imposed arrangements and statistically insignificant clusters from arrangements that are indistinguishable from random will also be studied and will serve as control group for comparison. My approach to study the internal structure of fracture clusters is different from the approach of Gross and Engelder (1995). Although they measured fractures along scanlines at both outcrop and rock sample scales, they did not study the internal structure of different domains (e.g., clusters) but instead compared the amount of fracture strain and the cumulative frequency distributions of scanlines at outcrop and rock-sample scales.

8.1.3 Domains and Length Scales along Fracture Scanline

The hypothesis that fracture clusters are fractal will be tested in a variety of domains along scanlines that represent fractures exhibiting most types of spatial arrangement defined by Marrett et al. (in review). An important domain of non-random spatial arrangement of fractures is a statistically significant cluster. A fracture cluster is defined as a domain where fractures are unusually abundant. If a fracture data set exhibits statistically significant clusters that may or may not be regularly spaced (red fractures, Figure 8.2), as quantified by NCC, the intracluster domain of a scanline corresponds to part or all of a cluster (Figure 8.2). The intercluster domain refers to a part of the scanline located outside of and flanked by clusters (green fractures, Figure 8.2). The cluster-to-

cluster length scale represents a distance that is larger than the intercluster domain width and smaller than the width of clusters on each end plus intercluster width (Figure 8.2).

Existence of statistically significant clusters implies that fractures are unusually scarce in between clusters (green fractures, Figure 8.2). Although minor clusters could be located in intercluster domains, such clusters lack statistical significance with regards to the entire scanline. In addition, spatial arrangements that are indistinguishable from random also exhibit clusters, but they are not statistically significant (Marrett et al., in review).

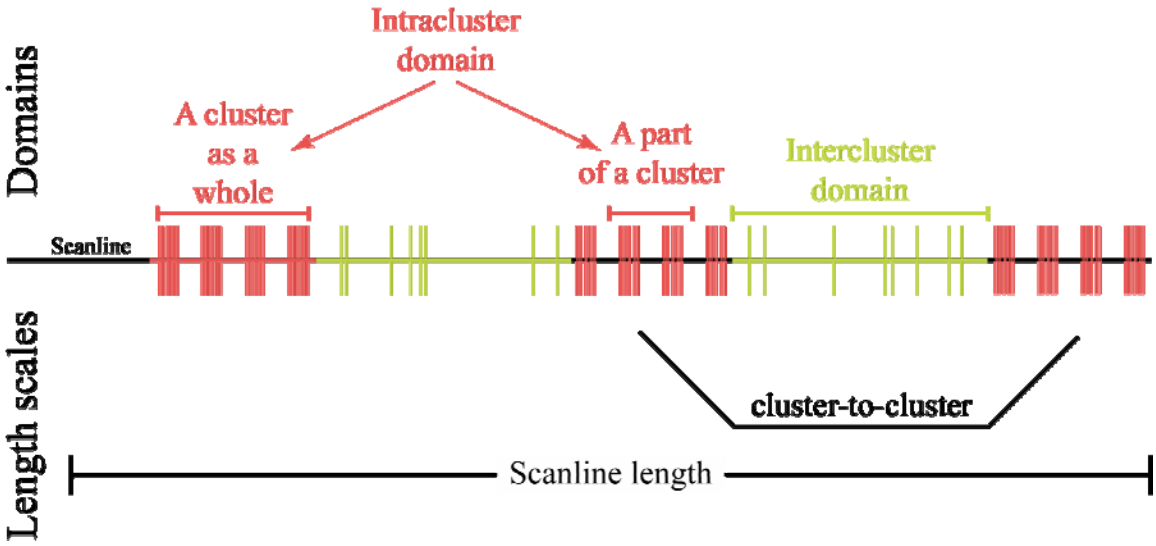

Figure 8.2 Sketch illustrating two different domains of a fracture scanline (above scanline) and two different length scales (below scanline). Fractures are represented by vertical lines of equal thickness. Data set shows three clusters (red fractures) that are regularly spaced separated by intercluster domains (green fractures). See text for definitions of terminology.

8.1.4 Methodology

I collected fracture data along scanlines in sedimentary layers that exhibit fracture arrays with different apparent spatial arrangements. Some layers exhibit evident clustering of fractures (Figure 8.3a) whereas other layers display more ambiguous

clustering of fractures (Figure 8.3b) or what seems to be regularly spaced fractures (Figure 8.3c). Although most fracture scanlines were measured in the Cupido Fm. Of the Monterrey salient, some scanlines were measured in Cuesta del Cura and Aurora Formations. Fracture data were measured only in outcrops that displayed a smooth surface, which allowed reliable measurement of fracture aperture and spacing (suitable to study the spatial arrangement of fractures using NCC), and that were long enough for measurement of a representative portion of the fracture array (Chapter 2). Along a scanline, consecutive values of kinematic aperture and fracture spacing or position were measured for fractures that are larger than a pre-determined size threshold using a hand lens and a logarithmically graduated comparator (Ortega et al., 2006). Wherever feasible, information about the type(s) of fracture cement(s) inside the fractures and fracture orientation was also acquired simultaneously and used later to separate fractures into sets. Although fracture orientation is a fracture attribute that cannot be measured in a strictly 1D line, it was acquired (or at least estimated) by following a fracture outside the scanline. In addition to the data collected for my dissertation, I used fracture data sets measured by others from the SMO (e.g., Palmas 11 LR and Tranquitas) and other areas (e.g., Pedernales and Grove Creek). Of the fracture data sets measured (Table 2.1) or made available (Table 2.2) for my dissertation, I selected ten for the study of cluster scaling (Table 8.1).

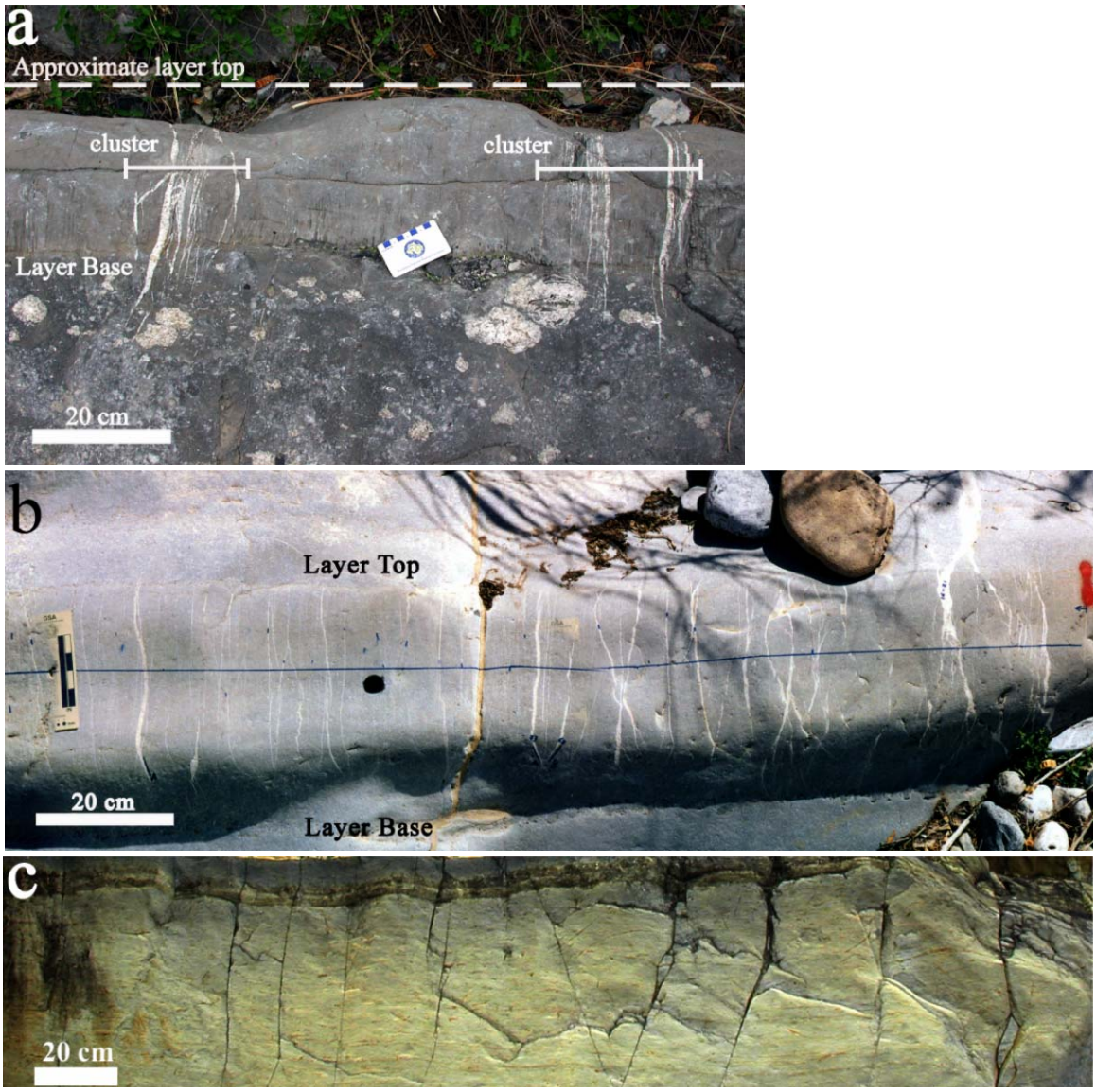

Figure 8.3 (a) Photograph of two clusters of macrofractures in cross-sectional exposure of layer Palmas 11. (b) Photograph of the northern 1.5 meters of scanline in cross-sectional exposure of layer Palmas 13. (c) Photograph of eastern 2.5 m of scanline in bedding-parallel exposure of joint outcrop (Table 2.1). Layers in (a) and (b) are from the Cupido Formation whereas layer in (c) is from the Aurora Formation. Fractures in (a) and (b) can be classified as veins whereas fractures in (c) can be classified as joints (Chapter 2). Although photographs in (a) and (b) are approximately at the same scale and both layers have a similar thickness, clustering is obvious in (a) but not in (b).

Table 8.1 Summary of geologic information and statistics for outcrop fracture data sets used to study the scaling of clustering. Shaded cells indicate outcrop data sets without rock samples (from Tables 2.1 and 2.2).

Data Set	Geographic Area	Structure Name	Structural Position	Geologic Unit	Lithology	Fracture type	Outcrop Type	Number of Fractures (all sets)		Aperture Threshold	Scanline Length	Strain
								> Aperture Threshold	< Aperture Threshold	mm	m	%
Escalera OO1	Escalera Canyon SMO, Mexico	San Blas Anticline	Anticline forelimb	Cupido Fm.	Dolostone	Veins	Cross section	680	480	0.05	3.20	13.3
Escalera OO12								1047	48		3.56	20.4
Huasteca	Huasteca Canyon, SMO, Mexico	Muertos Anticline						658	0	0.215	16.59	7.15
Palmas 11 LR	Palmas Canyon SMO, Mexico	San Blas Anticline		Cupidito Member, Cupido Fm.				262	0	0.95	21.11	4.59
Palmas 11 HR								575	0	0.075	2.49	7.62
Palmas 12								316	0	0.265	6.14	12.73
Palmas 13								459	0	0.14	5.43	9.16
Tranquitas	Galeana area SMO, Mexico	Huizachal - Peregrina Anticlinorioum	Gently-SW-dipping limb	La Boca Fm.	Sandstone		Bedding surface	496	0	0.05	31.09	1.30
Grove Creek	Near Waxahachie, North Central Texas, USA	Not Applicable	Sub-horizontal	Austin Chalk	Chalk			136	0	0.05	246.40	0.15
Pedernales	Llano uplift, Texas, USA	Not Applicable	Gently tilted bed	Marble Falls Limestone	Limestone			916	83	0.05	58.96	0.53

Total number of fracture apertures measured = 5545

Total number of fracture spacings measured = 6146

Total scanline length measured = 394.96 m

In order to make the most appropriate comparison of spatial arrangement at different scales, a rock sample should be obtained along the outcrop scanline. Where clustering was evident at outcrop scale (e.g., Figure 8.3a), an attempt to collect samples from both inside and outside clusters was made in order to test the hypothesis in question using qualitatively different domains of the outcrop-scale spatial arrangement. However, in many locations polishing of canyon walls (e.g., Figure 8.3b) by flash floods (the main reason outcrops on canyon walls are suitable for measuring fractures) complicated sampling along the scanline and only allowed sample collection from non-ideal parts of the outcrop (e.g., outside scanline).

In rock samples, the attributes of fractures (mostly microfractures) were measured using a method that I developed specifically for this purpose. A detailed explanation of the method for quantifying (aperture, spacing, length and orientation) microfracture populations in digital images was explained in Chapter 5 (Gomez and Laubach, 2006). For each sample, the first step in this method was to prepare a set of consecutive layer-parallel thin sections (without gap between adjacent thin sections) parallel to the outcrop face where the scanline was located. The motivation for developing a method that generates a set of contiguous rock chips (without gap between them) was to quantify microfractures along uninterrupted scanlines that span more than one thin section (Gomez and Laubach, 2006).

The second step in quantifying microfracture populations was to acquire overlapping digital images from the thin sections in a direction perpendicular to fracture strike using a petrographic or a scanning electron microscope (SEM). When the SEM was used, cathodoluminescence (CL) images were collected. If the rock sample contained calcite, imaging was done using the technique described by Reed and Milliken (2003). Digital images from an individual rock sample were later edited and stitched into an

image mosaic using image editing software (Photoshop®), as shown in Figure 8.4a. The third step included calibrating the image mosaic, drawing the scanline and mapping all fractures that intercepted the scanline using digitizing software (Didger®), as shown in Figure 8.4b. The last step comprised exporting the coordinates of the points that outline each fracture and importing those coordinates into a spreadsheet template called GoMezure™ that I developed. This template was used to calculate automatically attributes (i.e., aperture, length, spacing, and relative azimuth) of the outlined fractures and to rapidly generate graphs of cumulative distribution (Chapter 5; Gomez and Laubach, 2006).

Once a fracture data set from a rock sample was obtained, the spatial arrangement of fractures at both outcrop and rock sample scales was analyzed independently using NCC. There is no difference between how NCC was used to analyze outcrop and rock sample data sets. The only differences between the two types of data sets are due to the scale of data collection. For instance, outcrop data sets usually have different aperture thresholds than rock sample data sets. Typically, outcrop data sets have a predetermined aperture threshold (e.g., one of the fracture widths in the comparator of Ortega et al., 2006), whereas the aperture threshold of rock sample data sets depends mainly on the resolution of the digital images and the magnification used. In addition, total scanline length for outcrop data sets is typically at least a few meters long (Table 8.1) whereas for rock sample data sets it is typically a few centimeters to half a meter long (Table 8.2).

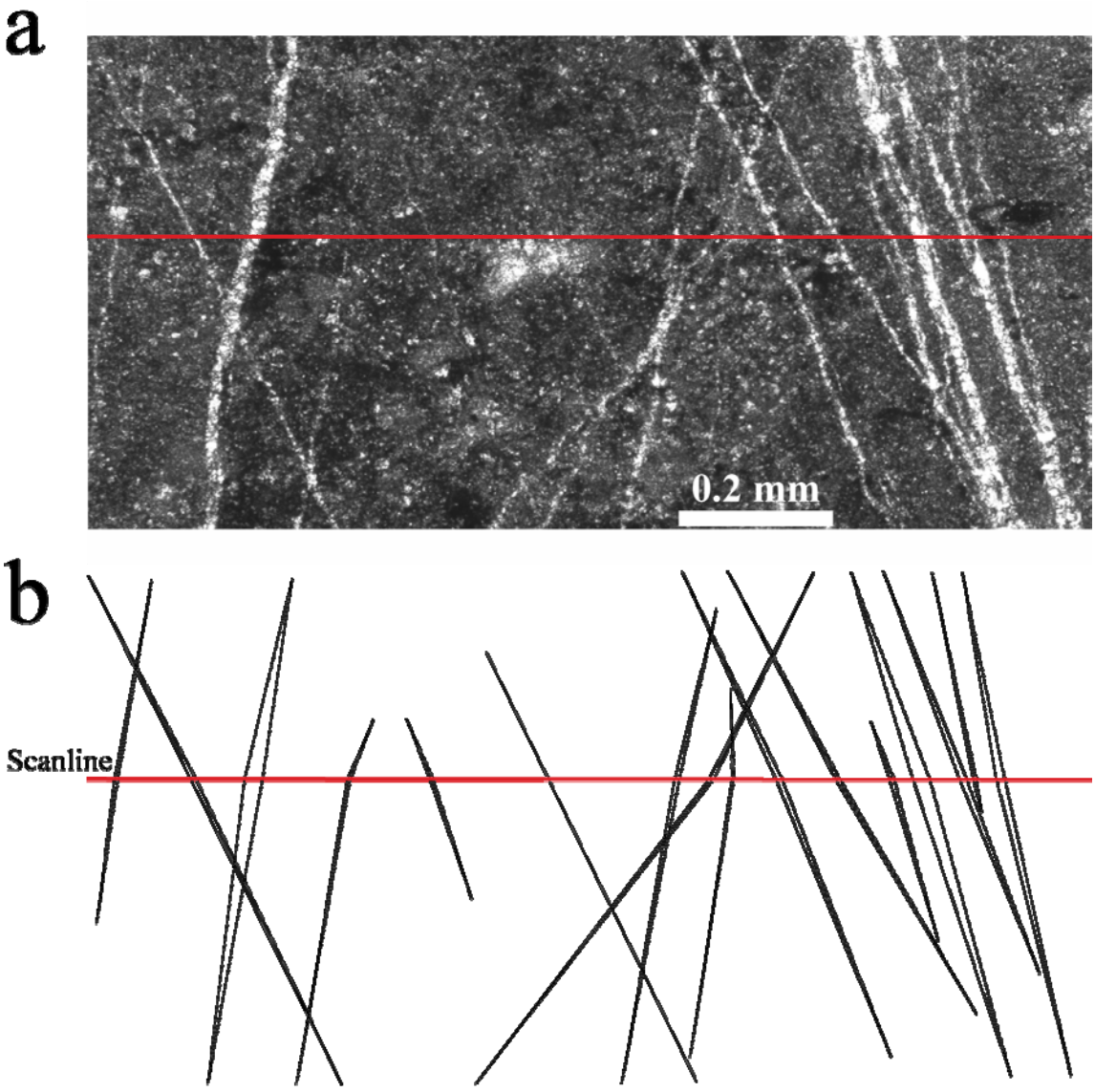

Figure 8.4 Example of image collage and fracture map used to quantify attributes of fractures in thin sections, as explained in Chapter 5 (Gomez and Laubach, 2006). (a) Portion of photomicrograph collage of thin section 02LG13-1E. (b) Microfractures mapped in (a) following methodology described in Chapter 5 (Gomez and Laubach, 2006). Scanline drawn as red line in both (a) and (b).

Table 8.2 Summary of geologic information and statistics for all the fracture data sets measured in thin sections. All thin sections are approximately parallel to bedding. SEM = Scanning Electron Microscope, CL = Cathodoluminescence.

Layer Name	Sample		Number of Consecutive Thin Sections	Thin Section Sizes	Microscope Type	Imaging			Scanline Information			Transgranular Fracture Aperture		
	Name	Location in Outcrop				Individual Images	Magnification	Image Collages	Scanline Length	Number of Fractures	Number of Transgranular Fractures	Minimum	Maximum	Strain
				(in)					(mm)			(µm)		(%)
Escalera OO1	02LG11	Inside cluster Along scanline	1	2 x 3	Petrographic	47	5X	2	65.44	60	52	3.59	3795	9.82
	02LG12	Inside cluster Outside scanline Layer base	2			85		4	110.61	94	94	1.50	1299	13.2
			1		SEM	69 (only CL)	150X	2	45.88	35	29	2.77	1254	14.4
Escalera OO12	02LG13	Inside cluster Along projected scanline	4		Petrographic	101	5X	7	148.74	484	484	0.63	12355	20.0
Palmas 12	02LG15	Along scanline	2			88		4	101.45	31	29	8.06	8590	14.6
Palmas 13	02LG16	Along scanline	5			186		10	290.32	208	175	4.55	4023	8.08
Huasteca	03LG26	Along scanline Edge of a cluster	2			77		2	121.54	38	34	3.60	136	0.918
Palmas 11 LR	PA11JG	Outside cluster Near layer base	2	1 x 2		43		2	63.72	156	156	3.50	424	14.6
			1	2 x 3		N.A.	2.5X	1	38.25	86	86	20.2	377	15.6
Tranquitas	04GA01LG	Along scanline Inside cluster	8	1 x 2	SEM	660 (only CL)	150X	16	229.77	201	173	0.48	632	2.59

Total number of thin sections = 28

Total number of digital images = 1356

Total scanline length measured = 1.22 m

Total number of fracture apertures measured = 1393

Total number of transgranular fractures used for spatial arrangement analysis = 1312

In addition to comparing the spatial arrangement of fracture data sets from the same layer but at different scales (outcrop versus rock sample), three data sets without rock samples were studied (Grove Creek, Pedernales, and Palmas 11 HR, Table 8.1). The three data sets without rock samples were selected because they exhibit obvious clusters at outcrop scale and exhibit the same patterns of spatial correlation for logarithmically and linearly graduated length scales: power-law pattern inside clusters that may or may not be periodically arranged, respectively. Of the three data sets without rock samples, two (Grove Creek and Pedernales) were collected outside the Monterrey salient (Table 8.1). Studying the spatial arrangement of the fractures located exclusively inside a cluster (or clusters) was considered a proxy for studying the spatial arrangement of macrofractures inside a rock sample that would have been obtained from the same position along the outcrop scanline.

8.1.4.1 Normalized Correlation Count (NCC)

Normalized correlation count is a statistical technique that quantifies the frequency of pairs of opening-mode fractures (e.g., or other discrete structures such as deformation bands) as a function of distance between fractures (λ_k or length scale), normalized by the number of fracture pairs for an equivalent (in terms of number of fractures and scanline length) random arrangement of fractures. Consecutive values of fracture aperture and spacing along a scanline are the typical input data for NCC, whereas the resulting normalized frequency of NCC is called spatial correlation. Spatial correlation is typically plotted in the Y axis and length scale is plotted in the X axis (Chapter 6; Marrett et al., in review).

NCC is a discrete technique in the sense that spatial correlation is estimated independently for each range of length scales considered. Namely, NCC quantifies the frequency of fracture pairs separated a distance larger than one length scale and smaller

than another. Different graduations of length scale can be used to study different types of spatial arrangement. For instance, logarithmic graduations of length scale are most effective at detecting power-law patterns of spatial correlation inside clusters, whereas linear graduations of length scale are better to identify periodic arrangements (Marrett et al., in review). Numerically randomized versions of each data set (position along scanline for each fracture is randomly assigned) are used to calculate the 95% confidence intervals for random arrangements. If the pattern of spatial correlation for a natural data set is outside the 95% confidence interval, then the corresponding spatial arrangement is significantly different from random (Marrett et al., in review). The average spatial correlation for randomized versions also serves to validate the analytical equation used to normalize the correlation count (Marrett et al., in review).

Variation of spatial correlation across a spectrum of length scales can show patterns that indicate different spatial arrangements (Figure 8.5). Using logarithmic graduations of length scale, three patterns can be distinguished. A flat-line pattern of spatial correlation (slope = 0; correlation = 1) indicates no statistically significant organization (Figure 8.5a). A power-law pattern of spatial correlation (slope < 0) as shown in Figure 8.5b. A plateau pattern of spatial correlation (slope = 0; correlation > 1) indicates statistically significant clustering due to some process other than self organization (e.g., externally imposed control or inherited pattern) as shown in Figure 8.5c. Using linear graduations of length scale, three patterns can be distinguished. A flat-line pattern of spatial correlation (slope = 0; correlation = 1) with linear graduations of length scales indicates no statistically significant organization (Figure 8.5e). Patterns of alternating peaks and troughs of spatial correlation with peaks at length scale multiples of the first peak indicate periodically arranged fractures (Figure 8.5f) or periodically arranged clusters (Figure 8.5g), depending on the presence or absence, respectively, of

decreasing spatial correlation for most length scales smaller than the first peak of spatial correlation. Combinations of any or all of these patterns can occur, with different patterns characterizing different ranges of length scale. For self-organized or inherited clusters, the length scale at which spatial correlation drops to one indicates cluster width (Figures 8.5b to 8.5d). Similarly, in periodically arranged fractures or periodically arranged clusters, the length scale of the first peak is indicative of fracture spacing (Figure 8.5f) or cluster spacing (Figure 8.5g).

8.1.4.2 Spectral Analysis of Spatial Correlation for Linearly Graduated Length Scales

Although NCC independently quantifies spatial correlation for each length scale considered, distinctive patterns of spatial correlation indicative of different spatial arrangements are visible across a range of length scales (Figure 8.5). This approach is suitable for recognizing patterns of fracture arrangement indicating periodically arranged clusters, because it generates an oscillatory variation of spatial correlation for linearly graduated length scales (Figures 8.5f and 8.5g). As a consequence, a periodic pattern should have spatial correlation that is comparable to random for many length scales and that differs most from random at the few length scales corresponding to dominant fracture or cluster spacing and its multiples (spatial correlation > 1), and at length scales equal to one half of dominant spacing and its odd multiples (spatial correlation < 1). Most length scales, considered in isolation, might show spatial correlation that is statistically indistinguishable from random. Therefore, establishing statistical significance of a periodic pattern requires a test for oscillatory variation of spatial correlation with length scale, instead of a test for specific values of spatial correlation at certain length scales. However, the confidence limits calculated by NCC technique are estimated independently for each length scale (Chapter 6).

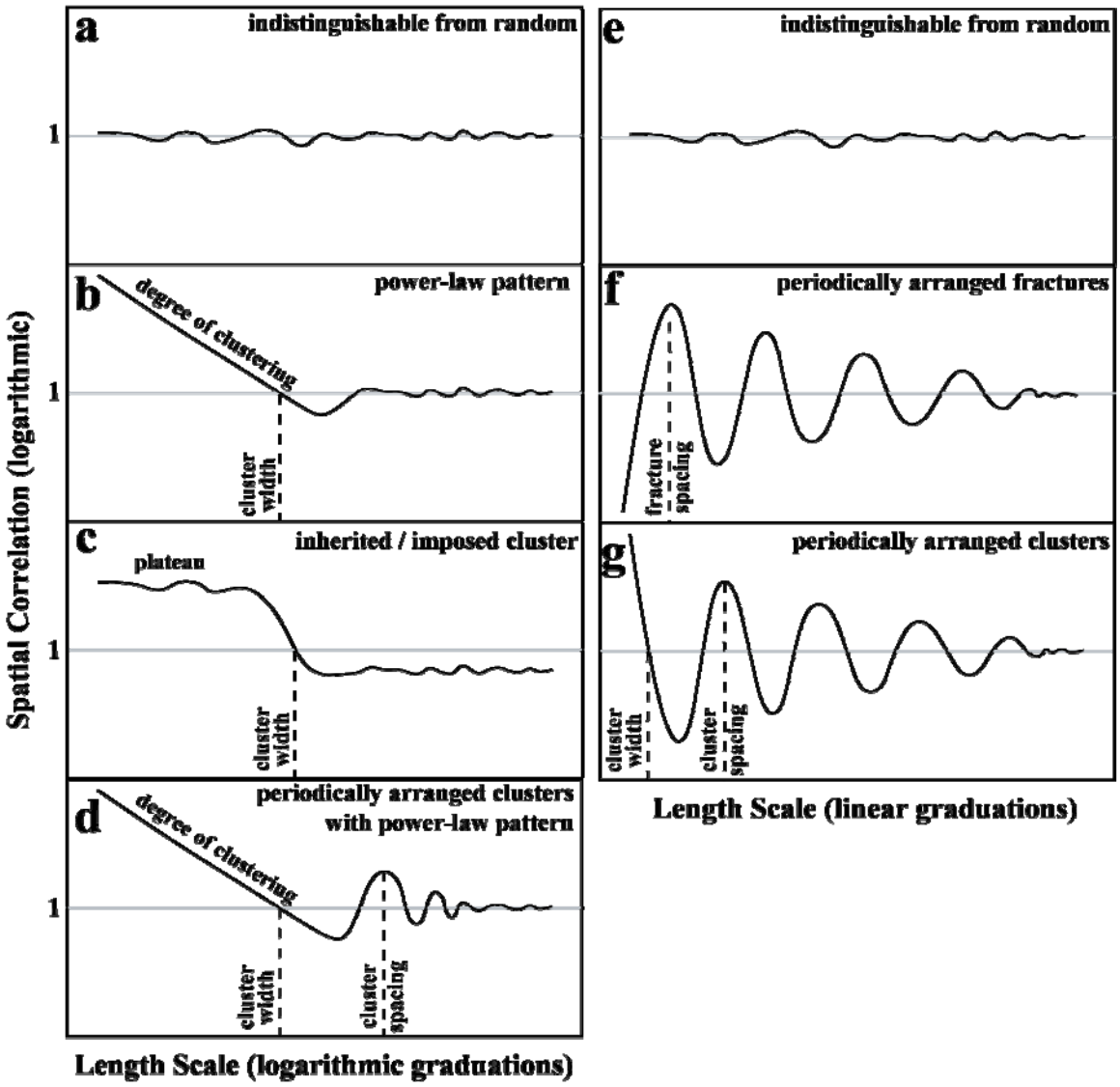

Figure 8.5 Patterns of spatial correlation versus length scale, as defined in Marrett et al. (in review), each one indicating a distinctive spatial arrangement. Using logarithmic graduations of length scale, three spatial arrangements can be distinguished (left column): (a) indistinguishable from random, (b) power-law pattern, (c) inherited or imposed clustering due to some process other than self organization (e.g., folding or faulting). Using linear graduations of length scale, three different spatial arrangements can be distinguished (right column): (e) indistinguishable from random, (f) periodically arranged fractures, (g) periodically arranged clusters. Combinations of any or all of these patterns can occur (d), with different patterns characterizing different ranges of length scale.

The statistical test established by the 95% confidence interval calculated by NCC technique is likely to be excessively hard to pass (to be statistically significant) because the pattern we are testing extends over a range of length scales but the confidence interval is calculated independently for each length scale (Chapter 6). Namely, the development of a statistically significant pattern of spatial correlation such as the one exhibited by periodically arranged clusters over a range of length scales (Figure 8.5g) is less probable to occur than a statistically significant spatial correlation at one length scale. A statistical technique that calculates confidence intervals of spatial correlation over a range of length scales is not currently available. In addition, deciding whether a pattern of spatial correlation is or is not indicative of periodically arranged clusters involves a degree of interpretation, and therefore it is subject to interpreter's bias. For instance, a "less than ideal" pattern might have alternating peaks and troughs with peaks separated by the same difference in length scale (cluster spacing) but for the most part those peaks and troughs do not leave the 95% confidence interval. So could this above mentioned pattern be periodic but not statistically significant? Another example could be a pattern of spatial correlation that has peaks and troughs outside the 95% confidence interval but the difference in length scales between those peaks is not the same for all pairs of peaks. So, is this last pattern statistically significant but not indicative of periodically arranged clusters? Finally, sometimes the peak indicating cluster spacing is broad enough that there is not an unequivocal length scale that could be called cluster spacing.

A spectral analysis technique can estimate the fundamental frequency of the pattern of spatial correlation, which is a more adequate (lacking interpreter's bias) quantification of cluster spacing. In addition, comparison of the power spectrum with the equivalent red noise would allow for an estimation of whether that fundamental

frequency is statistically significant, and therefore whether the periodicity in the pattern of spatial correlation is statistically significant or statistically insignificant.

The Fourier series technique is a common spectral analysis tool for quantifying the extent to which a variable oscillates in time or space. Fourier series have been used to address periodicity in many geological problems. For instance, Hinnov and Goldhammer (1991) compared the efficacy of different methods of spectral analysis for the study of cyclicity of thickness variations within fifth order stratigraphic cycles in the Middle Triassic Latemar limestone, and found the Blackman-Tukey method of Fourier analysis to be superior. The study of Budd et al. (2006), which examined five-point averages of petrophysical properties (e.g., porosity) in order to find oscillatory patterns along bedding, is similar to my dissertation, in the sense that the search for an oscillatory variation was done on a statistical quantity (like spatial correlation) and not on a directly measurable rock attribute (like bed thickness for Hinnov and Goldhammer, 1991). The two studies mentioned above compared the power spectra of natural datasets with "red noise" to test whether peaks of power spectral density were statistically significant.

Spectral analysis is the name given to all quantitative methods for studying periodicities in noisy time series data from the point of view provided by the frequency domain. In time series data, a cycle occurs when a variable takes the same value at constant intervals of time (called the period). In the frequency domain, Fourier analysis represents a time series as the sum of many sinusoids and cosinusoids with different amplitudes, phases and frequencies. A common purpose of Fourier analysis is to quantify the dominant periodicities. For my dissertation, the input data for Fourier analysis are represented by spatial correlation measured at approximately uniformly-graduated length scales.

For my dissertation, I calculated the Fourier power spectrum using the Blackman-Tukey method implemented in the software POWGRAF2 (Pardo-Igúzquiza and Rodríguez-Tovar, 2004). For comparison, POWGRAF2 generates the power spectrum of red noise and its 95% confidence interval (e.g., Figure 8.6). Nevertheless, independently implementing the periodogram method (as described by Hinnov and Goldhammer, 1991) validated the power spectrum results from POWGRAF2. Red noise is a model calculated from the input data using the data adaptive time series called autoregressive AR1 (Schulz and Mudelsee, 2002). Power spectral density of the red noise model has a continuous decrease with increasing frequency (or decreasing period) and represents the frequency distribution of the natural data set were it follow a random autoregressive process (Hinnov and Goldhammer, 1991). The expression for the autoregressive process AR1 is given in Pardo-Igúzquiza and Rodríguez-Tovar (2004). Randomizing the positions of natural fractures yielded power spectral density that largely did not reach the 95% confidence interval of red noise (e.g., thin line, Figure 8.6), validating its use to assess whether or not a natural data set is statistically different from a stochastic origin, as is done in studies of cyclicity in stratigraphy (e.g., Hinnov and Goldhammer, 1991). In contrast to the power spectral density of a randomized data set, the natural data set has a peak (e.g., thick line, Figure 8.6) with a power spectral density several times that for the 95% confidence interval of the red noise at the same length scale. Statistically significant frequencies indicate cluster spacing (e.g., 1089 mm for Palmas 11 LR; Figure 8.6).

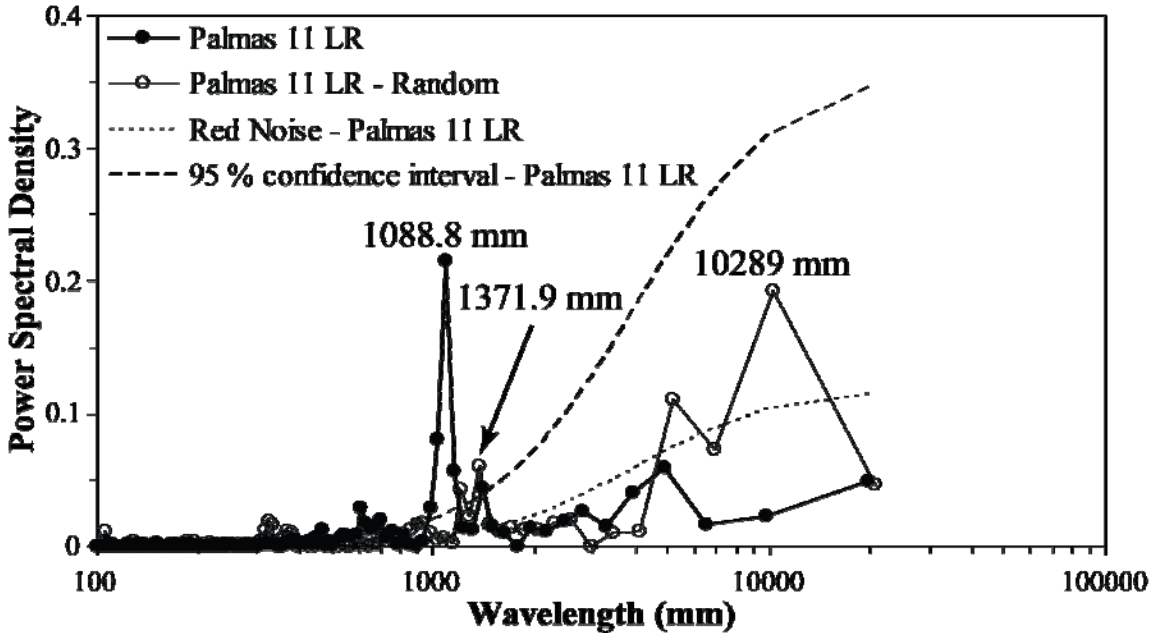

Figure 8.6 Power spectrum for the spatial correlation curve of Palmas 11 LR data set with linearly graduated length scales (thick, solid line), the spatial correlation curve of a randomly arranged version of the Palmas 11 LR data set (thin, solid line), the equivalent red noise (short dashed line) and its corresponding 95% confidence interval (long dashed line) for the Palmas 11 LR data set. Natural data set exhibits a peak of power spectral density at a wavelength of 1089 mm, which is outside the 95% confidence interval. In contrast, the equivalent (in terms of number of fractures and total scanline length) data set with randomly arranged fractures exhibits peaks with power spectral density (e.g., 10289 mm) similar to the natural data set (e.g., 1088.8 mm) but inside the 95% confidence interval, or barely outside the 95% confidence interval (e.g., 1371.9 mm).

8.1.4.3 Scanning Electron Microscope (SEM)

SEM-based cathodoluminescence systems (SEM-CL) allow higher magnification (up to 50 times more than an optical microscope; Passchier and Trouw, 1998), more stable operating conditions and better detection of weak luminescence than optical-microscope mounted CL instruments (Reed and Milliken, 2003). Details about the SEM-CL instrument that I used at BEG are described by Reed and Milliken (2003). Reed and Milliken (2003) explained the method used to overcome the image-quality problems

caused by the persistent luminescence of carbonate minerals. In brief, this method uses a UV-blue filter to image only short wavelengths while blocking the orange-red wavelength luminescence commonly found in carbonates. The SEM at the BEG also generates X-ray element maps and secondary electron images (SEI). An SEI is obtained by measuring the emission of secondary electrons produced when the SEM electron beam interacts with the sample surface (Kearsley and Wright, 1988). In addition, a SEI appears three-dimensional and therefore detects porosity (Kearsley and Wright, 1988).

8.1.5 Fracture Categories

Seven of the ten layers selected for the study of cluster scaling belong to the Cupido Fm. (Table 8.1). Fractures within the Cupido Fm. exhibit characteristics that allowed me to assign them into three distinct categories defined by petrographic attributes (Table 8.3). The most important attributes analyzed are fracture trace (straight or irregular), the mineralogy (calcite, dolomite or quartz), texture, and timing relative to fracture opening (pre-, syn, and postkinematic) of fracture cements (Laubach, 2003; Laubach et al., 2004b). Postkinematic cements precipitate after fracture opening whereas synkinematic cements precipitate concurrently with fracture opening (Laubach, 2003).

The main characteristics of fractures of category X are locally irregular trace, the presence of euhedral and translucent crystals of synkinematic dolomite cement forming bridges and pillars occasionally with bands of fluid inclusions, evidence for an emergent threshold for dolomite cement, and the lack of quartz cement (Table 8.3). Microfractures of X category also exhibit a ghost texture which makes them hard to detect (Table 8.3). X fractures exhibit only random arrangement of fractures at outcrop scale and are interpreted to have occurred before the regional D2 dolomitization event (Chapter 9).

Y fractures have either irregular (similar to X fractures) or straight traces (Table 8.3). In layers where Y macrofractures exhibit irregular traces, Y microfractures have

ghost textures. Layers that exhibit Y macrofractures with straight traces do not have Y microfractures with ghost textures (Table 8.3). In addition, Y fractures exhibit abundant fibrous dolomite crystals (perpendicular to fracture walls) that line the fracture walls, or subhedral bridges of dolomite. In contrast to X and Z fractures, Y fractures consistently display quartz cement in the form of subhedral bridges in microfractures or euhedral bridges in macrofractures. Quartz cement bridges in Y macrofractures exhibit crack-seal texture when imaged with SEM/CL (Table 8.3). Y fractures that exhibit irregular traces and microfractures with ghost texture are interpreted to have developed before regional D2 dolomitization, whereas Y fractures that exhibit straight traces are interpreted to have developed after D2. Y fractures only exhibit power-law patterns of spatial correlation inside clusters, clusters which in turn are periodically arranged (Chapter 9).

The most distinctive characteristic of Z fractures is a halo formed by dolomite crystals similar to, but more abundant than, the ones in the rock matrix (Chapter 9). Z fractures have highly irregular traces and do not exhibit bridges of dolomite or quartz cement (Table 8.3). Z fractures are interpreted to have developed simultaneously with the regional dolomitization D2 (Chapter 9). Like X fractures, Z fractures only exhibit random arrangement of fractures at outcrop scale (Chapter 9). All X, Y, and Z fractures are completely sealed with postkinematic calcite cement that filled remnant porosity. However, only in Y fractures does calcite cement seem to have partly replaced the euhedral bridges of quartz in macrofractures.

Table 8.3 Typical characteristics of X, Y, and Z fractures. A more detailed description of the characteristics of each fracture category is included in Chapter 9. Chapter 9 also includes the genetic interpretation of fracture cements with respect to fracture opening.

	Fracture trace	Dolomite cement	Calcite cement	Quartz cement
Category Z	Irregular 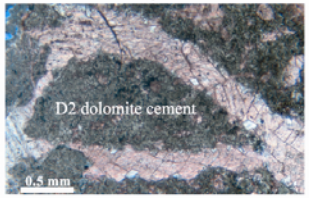 Microfractures show ghost (relic) texture 	Rhombohedral crystals form bridges and pillars perpendicular to fracture wall, and contain bands of fluid inclusions parallel to fracture wall 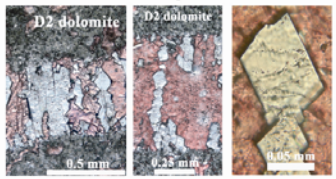 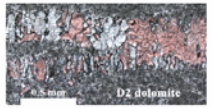 Displays emergent threshold	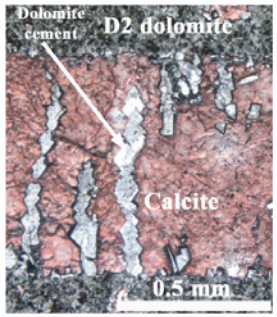 Filling fracture porosity	Not detected
Category Y	Straight 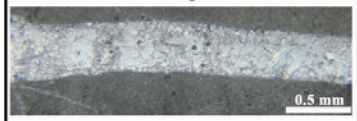 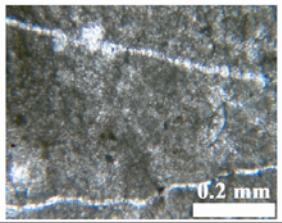	Fibrous crystals perpendicular to fracture wall Subhedral bridges perpendicular to fracture wall 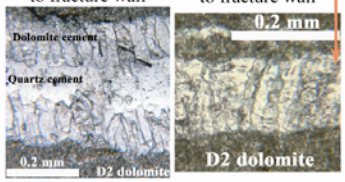  Trails of solid inclusions in quartz bridges	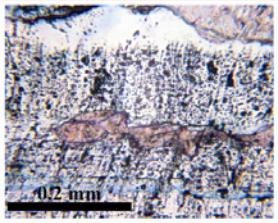 Replacing quartz and filling fracture porosity (see quartz cement)	Subhedral bridges parallel to dolomite bridges (see dolomite cement) 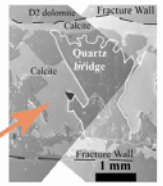 Isolated bridges Crack-seal texture inside euhedral crystals 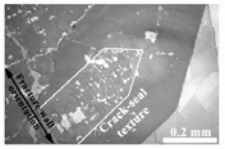
Category X	Macrofractures show highly irregular trace 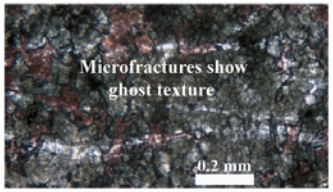	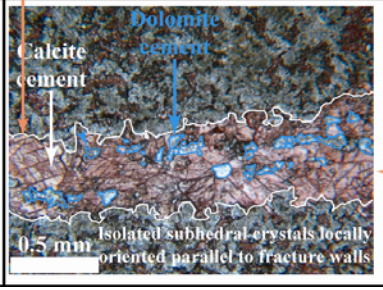	Replacing quartz and filling fracture porosity (see dolomite cement)	Not detected

8.2. DATA SETS WITH ROCK SAMPLE

Three criteria were used to select data sets for this study of the internal structure of fractal clusters of opening-mode fractures. The first criterion was the availability of fracture data along an outcrop scanline (outcrop scale) suitable for the study of the spatial arrangement of fractures. The second criterion was the availability of rock samples along a scanline. And the third criterion was the availability of fracture data suitable for the study of the spatial arrangement of fractures at rock sample scale. Of the seventeen fracture data sets at outcrop scale suitable for the study of the spatial arrangement of fractures (Tables 2.1 and 2.2), only seven (Escalera OO1, Escalera OO12, Palmas 11, Palmas 12, Palmas 13, Huasteca, and Tranquitas) satisfied the criteria (Table 8.2). All seven data sets with adequate rock samples are located in the Monterrey salient: six from the Cupido Fm. and one (Tranquitas) from the La Boca Fm. (Table 8.1). There is no rock sample available from the other three data sets (Grove Creek, Palmas 11 HR and Pedernales) selected for the study of cluster scaling.

Although I obtained rock samples (and generated thin sections) for the twelve layers in which I measured fracture data at outcrop scale (Table 2.1), samples from only five layers (Escalera OO12, Escalera OO1, Palmas 12, Palmas 13, and Huasteca) were conducive to the study of the spatial arrangement of fractures (Table 8.1). For instance, the samples from layers Escalera 1, Escalera 2 and Escalera 3 (Table 2.3) were deemed too small to generate a meaningful microfracture population, whereas the samples from the Oliverio anticline and Claxon syncline were collected on meter-scale folds of the Cuesta de Cura Fm. where there is no knowledge about the geologic history of the opening-mode fractures. Some preliminary knowledge about the timing and structural diagenesis of opening-mode fractures is required to verify that the microfractures

measured at rock sample scale are genetically related to macrofractures measured at outcrop scale. Of the six layers with scanline data at rock sample scale, one (Escalera Joints) yielded a fracture population too small (only three fractures, Table 2.3) to asses spatial arrangement. The small population of microfractures in the Escalera Joint sample could be due to a failure of the microscopic techniques (optical microscopy and SEM/CL) used to detect and measure microfractures but also could be a reflection of the paucity of microfractures in the rock volume.

Samples were made available to me for three (Palmas 11 LR, Tranquitas and Pedernales) of the five data sets (Palmas 11 LR and Palmas 11 HR data sets were measured in the same layer) at outcrop scale measured by others (Table 2.2). Of the three layers with samples collected by others, only two (Palmas 11 LR and Tranquitas) satisfied the criteria for selecting data sets for this study. Rock samples from Pedernales yielded enough microfracture data to generate cumulative frequency of fracture aperture (Marrett et al., 1999), but gaps between the previously-made thin sections did not allow measurement of a continuous scanline across the sample (Chapter 5, Gomez and Laubach, 2006). In addition, SEM/CL imaging of the sample from Pedernales failed to detect microfractures due to the strong luminescence of the calcite, even when appropriate methods were attempted (Reed and Milliken, 2003).

In the seven pairs (outcrop and rock sample scales) of data sets selected, independent analysis of fractures with common orientation (grouped in a set) was conducted (Table 8.4). However, if different fracture sets display the same spatial arrangement as the undivided version (all sets combined) of the data set, then all measured fractures, regardless of orientation, were included in a single analysis. In the following pages I will present the spatial arrangement of each of the seven data sets selected (Escalera OO1, Escalera OO12, Huasteca, Palmas 11, Palmas 12, Palmas 13, and

Tranquitas) at both outcrop and rock sample scale. In addition, some information about each data set, such as fracture strain, number of fractures, and scanline length, will be presented (Table 8.5).

Table 8.4 Orientation (right-hand rule strike and dip) of bedding and veins for all outcrop fracture sets (each set with a characteristic fracture orientation). Number of fractures for each set is included within parentheses. Only orientation of sets A, B, and C in Escalera OO1 and Escalera OO12 matches the orientation of similarly named sets in Ortega and Marrett (2001) and Ortega (2002). Sets with similar orientation and in the same location are highlighted with the same color.

		Field Categorization of Fractures			
Outcrop Data Set	**Bedding**	**Set A**	**Set B**	**Set C**	**Set D**
Escalera OO1	305/66	220/38 (127)	205/31 (853)	220/90 (24)	156/46 (156)
Escalera OO12	316/79	231/40 (1023)	203/60 (82)		
Grove Creek	Sub-horizontal	70/90 (81)			
Huasteca	285/90	30/41 (581)	297/80 (19)	204/25 (54)	338/54 (4)
Palmas 11 (LR and HR)	299/44	45/73 (91)	175/70 (55)	208/85 (116)	
Palmas 12	297/46	75/52 (190)	192/61 (126)		
Palmas 13	301/50	64/61 (286)	200/60 (173)		
Pedernales	36/15	270/90			
Tranquitas	266/3	275/90	140/90	215/90	165/90

Table 8.5 Quantitative attributes of fracture data sets. Cumulative frequency distributions (e.g., power law, negative exponential, etc.) were selected based on the best coefficient of determination. A perfect distribution has a R^2 coefficient of one and a χ^2 coefficient of zero. * = including fractures with apertures smaller than threshold.

Outcrop data sets	**Escalera OO1**	**Escalera OO12**	**Palmas 11 LR**	**Palmas 12**	**Palmas 13**
Layer Thickness (cm)	80	24.5	27	47	24
Number of Fractures	1160*	1095*	262	460	614*
Length of Scanline (m)	3.20	3.56	21.1	6.14	5.43
Fracture Strain (%)	13.3	20.4	4.59	12.7	9.16
Aperture Threshold (mm)	0.05	0.05	0.95	0.265	0.14
Maximum Aperture (mm)	48	64	42	60	12
Range of Fracture Aperture (orders of magnitude)	3	3.1	1.6	2.4	1.9
Cumulative Frequency Distribution of Apertures (fractures/mm)	Power-law $y = 0.028\ b^{-1.24}$	Power-law $y = 0.028\ b^{-0.97}$	Power-law $y = 0.015\ b^{-1.2}$	Power-law $y = 0.04\ b^{-1.2}$	Power-law $y = 0.022\ b^{-0.7}$
Chi square (χ^2)	0.112	0.146	0.0885	0.0983	0.101
Range of Fracture Spacings	0.062 – 252*	0.05 – 37.0*	0.075 – 806	0.215 – 109.5	0.175 – 66.5
(mm, orders of magnitude)	3.6*	2.8*	4.1	2.9	2.5
Average Fracture Spacing (mm)	2.43*	2.82*	76.73	17.2	10.85
Coefficient of Variation	3.50*	1.33*	1.72	1.07	0.93
Cumulative Frequency Distribution	Power-law*	Logarithmic*	Log-normal	Negative exponential	Negative exponential
of Spacings (R^2)	0.988	0.941	0.981	0.995	0.998
Average Spacing for fractures with apertures ≥ 0.95 mm (mm)	38.5	39.8	80.6	43.2	40.6

Continuation Table 8.5

Outcrop data sets	Huasteca	Tranquitas	Grove Creek	Palmas 11 HR	Pedernales
Layer Thickness (cm)	70	N.A.	N.A.	27	~10000
Number of Fractures	658	496	136	575	916
Length of Scanline (m)	16.59	31.09	246.4	2.49	58.96
Fracture Strain (%)	7.15	1.3	0.15	7.62	0.53
Aperture Threshold (mm)	0.215	0.05	0.05	0.075	0.05
Maximum Aperture (mm)	53	14	100	17.5	18
Range of Fracture Aperture (orders of magnitude)	2.3	2.5	4	2.4	2.5
Cumulative Frequency Distribution of Apertures (fractures/mm)	Log-normal / Power-law $y = 0.12\ b^{-2.1}$	Power-law $y = 0.003\ b^{-1.42}$	Power-law $y = 0.00011\ b^{-0.45}$	Power-law $y = 0.0126\ b^{-1.15}$	Power-law $y = 0.0011\ b^{-1.2}$
Chi square (χ^2)	0.260	0.040	0.018	0.035	0.018
Coefficient of Determination (R^2)	0.9884				
Range of Fracture Spacings (mm, orders of magnitude)	0.4 – 242 / 2.8	0.46 – 603 / 3.2	1 – 18640 / 4.1	0.095 – 115 / 3.1	0.08 - 2260 / 4.3
Average Fracture Spacing (mm)	23.54	61.87	1822.41	4.01	14.38
Coefficient of Variation	1.23	1.39	1.82	1.67	2.43
Cumulative Frequency Distribution of Spacings (R^2)	Log-normal / 0.994	Log-normal / 0.998	Logarithmic / 0.993	Log-normal / 0.998	Log-normal / 0.997
Average Spacing for fractures with apertures ≥ 0.95 mm (mm)	50.74	277.6	7948.27	5.18	786.1

8.2.1 Layer OO1 at Escalera Canyon (Escalera OO1)

8.2.1.1 Outcrop Scale

Escalera OO1 layer was initially studied by Ortega (2002), who only measured fracture apertures. Escalera OO1 layer is a dolostone (100% dolomite) with mud-supported intraclasts (intraclast-breccia, Ortega, 2002) from the Cupido Formation (Goldhammer, 1999; Ortega and Marrett, 2001). Escalera OO1 is located 139 m above the base of the stratigraphic column measured in the forelimb of San Blas anticline at Escalera canyon by Ortega (2002). I measured 1160 veins, of which 680 have apertures greater than or equal to 0.05 mm. For the 480 veins with apertures smaller than 0.05 mm, only spacing was recorded. The scanline has a length of approximately 3.2 m, was positioned 30 cm from the top of the layer (thickness is 80 cm) and recorded a strain of 13.3% (Table 8.1; Figure 8.7). Fractures with apertures greater than or equal to 0.05 mm exhibit spacings that follow power-law distribution and yield a coefficient of variation of 3.50 (Table 8.5). Fractures were assigned to four different sets depending on their orientation (Table 8.3). 11% of the fractures measured represent set A, 74% represent set B, 2% represent set C, and 13% represent set D (Table 9.3). However, orientation of set A (220/38) is similar to orientation of set B (205/31), and perhaps fractures of sets A and B are part of a single set. Because the spatial analysis with and without fractures not perpendicular to scanline orientation (sets B, C, and D containing 26% of the data set) did not yield different results, all analyses of the Escalera OO1 data set will include all fractures measured regardless of orientation.

Escalera OO1 scanline can be divided in two domains, each containing fractures with different characteristics. In the eastern 1.6 m of scanline (Figure 8.7) fractures tend to span the entire layer and are not related to faults (Figure 8.8a). In contrast, fractures in

the western 1.5 m of scanline do not span the entire layer, are arranged in en echelon patterns and occur near faults (Figure 8.8b). Both domains of Escalera OO1 exhibit all measured fracture orientation (Table 8.4, Figure 8.7). In thin sections from the eastern 1.6 m, fractures of sets A, B and C exhibit the typical features of Y fractures (Table 8.3). Although fractures of sets A and B in the western domain exhibit the same cements (with the same textures) as fractures in the eastern domain, the orientation of crystals is not perpendicular to fracture wall, supporting its association with faulting.

Fracture intensity indicates clusters that do not seem be regularly spaced, which indicates a heterogeneous arrangement of fractures (Figure 8.7). Although the graph of spatial correlation versus logarithmic graduations of length scale for the Escalera OO1 outcrop data set displays a power-law pattern, the slope of the power law is close to zero and therefore this pattern could also be interpreted as inherited/imposed clustering (Figure 8.9a). Inherited/imposed clustering typically displays a drastic drop of spatial correlation at the large length-scale end of the plateau pattern (Figures 8.5c and 8.9a). Spatial correlation versus linear graduations of length scale for the Escalera OO1 data set exhibits a pattern that has peaks and troughs of spatial correlation, but peaks are not at length scale multiples of the first peak, a prerequisite for interpreting a periodic arrangement of fracture clusters (Figures 8.5g and 8.9b). Power spectrum of spatial correlation for linearly graduated length scales exhibits three peaks outside the 95% confidence interval for red noise, which suggests superposition of more than one statistically-significant periodic arrangement of clusters (Figure 8.9c).

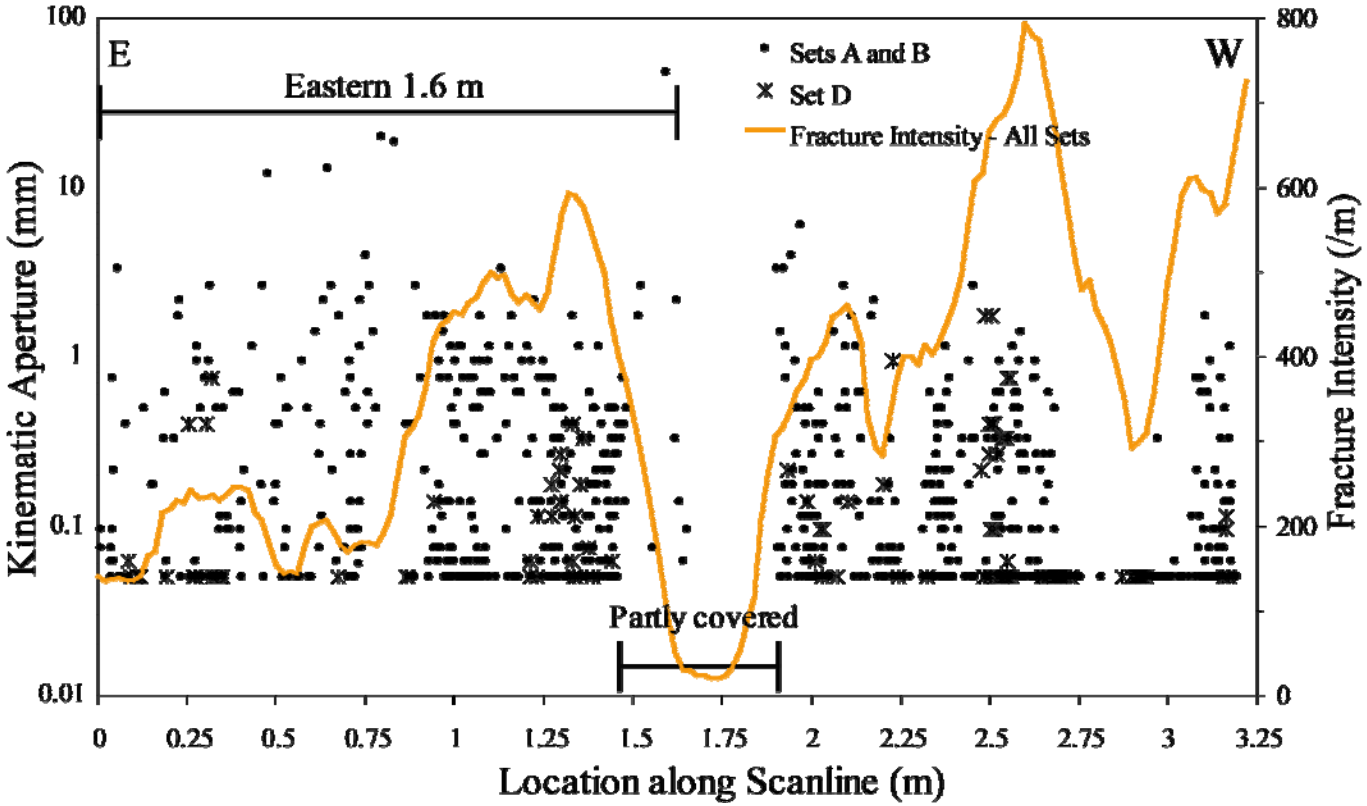

Figure 8.7 Kinematic aperture (circles for sets A and B, asterisks for set D) and fracture intensity (thick orange line) versus location along scanline for the Escalera OO1 data set. Note that kinematic aperture axis uses logarithmic graduations. Fracture intensity was calculated inside a moving window with width (window size) of 0.15 m that was moved in increments (window step) 0.02 m. Peaks of fracture intensity indicate clusters at 0.25, 1.3, 2.1, and 2.6 m, but clusters do not seem regularly spaced. Please note that kinematic aperture axis use logarithmic graduations. Although 1160 fractures were used to calculate fracture intensity, only the aperture of the 656 fractures of sets A, B, and D (fractures of set C were not included) was plotted.

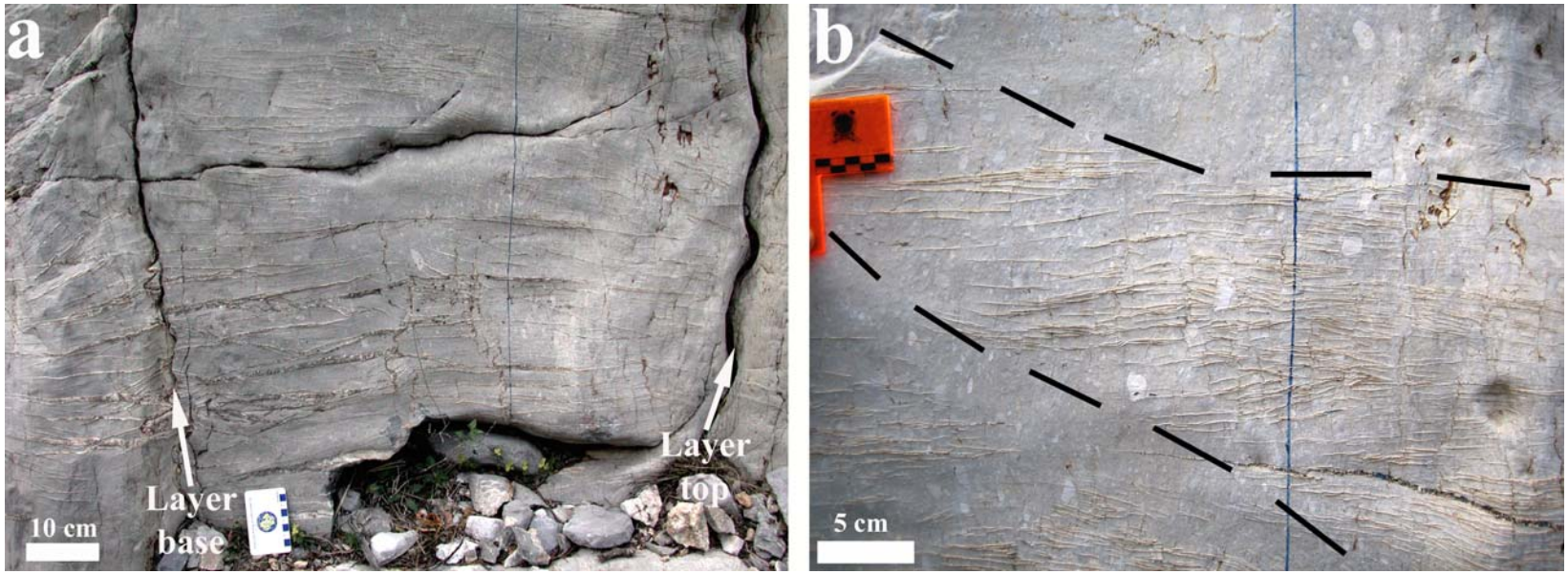

Figure 8.8 Photographs of domains the scanline in layer OO1 from Escalera canyon. (a) Photograph of fractures typical of the eastern 1.6 m of scanline (topographically lower). Fractures tend to span the entire layer. Bedding parallel stylolites cross cut these fractures. (b) Photograph of fractures typical of the western 1.5 m of scanline (topographically higher). Fractures tend to span only part of the layer, display en-echelon patterns, which terminate outside the layer in faults.

Figure 8.9 Graphs of spatial correlation vs. length scale (thick continuous line) for (a) logarithmic graduations and (b) linear graduations for the Escalera OO1 data set (1160 fractures, all fracture sets combined, aperture threshold of 0.05 mm). In (a) and (b) the thin discontinuous line represents the upper 95% confidence limit while the thin dotted line represents the lower 95% confidence limit, and the thick discontinuous line corresponds to the mean of 100 randomized data sets. In (a) and (b) the thin continuous line represents the analytical solution of randomly arranged fractures with the same number of fractures and scanline length. Width of length-scale bin in (a) and (b) is 5 (m = 2) graduations of length scale. Power law in (a) was calculated using spatial correlation between length scales of 2 and 60 mm. Cluster width is estimated in (a) to be approximately 110 mm. Evenly spaced lines every 195 mm in (b) only match a few peaks of spatial correlation, which indicate that fracture clusters might not be periodically arranged. (c) Power spectrum of spatial correlation from (b). Of the four peaks of power spectral density in (c), three (242, 314 and 524 mm) are outside the 95% confidence interval for red noise, possibly indicating multiple periodic arrangement of clusters, all of which have different cluster spacings and are statistically significant.

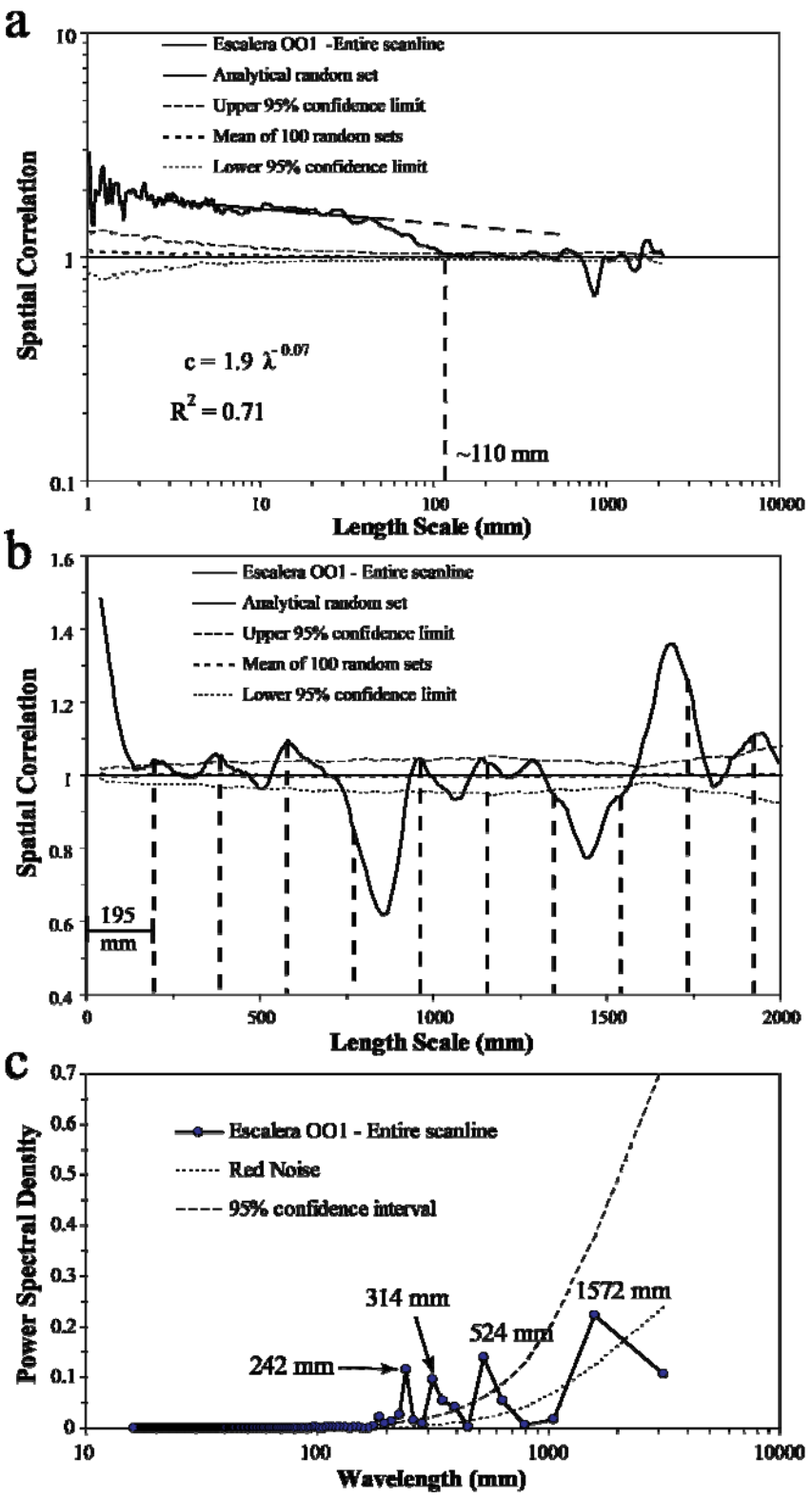
a
Escalera OO1 -Entire scanline
Analytical random set
Upper 95% confidence limit
Mean of 100 random sets
Lower 95% confidence limit
Spatial Correlation
c = 1.9 λ^-0.07
R^2 = 0.71
~110 mm
Length Scale (mm)
b
Escalera OO1 - Entire scanline
Analytical random set
Upper 95% confidence limit
Mean of 100 random sets
Lower 95% confidence limit
Spatial Correlation
195 mm
Length Scale (mm)
c
Escalera OO1 - Entire scanline
Red Noise
95% confidence interval
Power Spectral Density
314 mm
524 mm
1572 mm
242 mm
Wavelength (mm)

The spatial arrangements of the eastern 1.6 m and western 1.5 m of the Escalera OO1 data set were analyzed independently using both logarithmic and linear graduations of length scale (Figures 8.10 and 8.11). Using logarithmic graduations of length scale, the spatial arrangement of fractures inside clusters is similar to that displayed by the entire data set (Figures 8.9a, 8.10a, and 8.11a). Namely, both domains of the Escalera OO1 data set exhibit a power-law pattern of spatial correlation with an exponent near zero and therefore clusters cannot unequivocally be characterized as having a power-law pattern (Figure 8.5b) or an inherited/imposed arrangement (Figure 8.5c). In contrast, using linear graduations of length scales, there are differences between the spatial arrangement of the entire Escalera OO1 outcrop data set and the spatial arrangement of the two domains. The eastern 1.6 m of scanline yields a clear pattern of periodically arranged clusters (Figure 8.5g) because all three peaks of spatial correlation are multiples of 340 mm and therefore it can be interpreted as indicative of periodically arranged fracture clusters (Figure 8.10b). Compared with the entire data set (Figure 8.9b), power spectrum of spatial correlation for linearly graduated length scales for the eastern 1.6 m exhibits only one significant peak at 334 mm with a magnitude several times the corresponding 95% confidence interval for red noise, which supports periodically arrangement with a cluster spacing of 334 mm (Figure 8.10c).

Spatial correlation using linear graduations of length scale for the western 1.5 m of scanline displays a pattern that cannot be interpreted as periodically arranged clusters (Figure 8.11b). Although the two local maxima of spatial correlation (185 and 560 mm) are multiples, there is no peak of spatial correlation for the intermediate peak (370 mm), and therefore a pattern indicative of a periodic arrangement of fracture clusters (Figure 8.5g) cannot be interpreted (Figure 8.11b). In addition, power spectrum of spatial correlation of linearly graduated length scales exhibits wavelengths between 183 and 431

mm with power spectral density outside the 95% confidence interval for red noise, which suggests that more than one periodic arrangement of clusters are in the western 1.5 m of the scanline in layer Escalera OO1 (Figure 8.11c). Because my dissertation is only concerned with the spatial arrangement of opening-mode fractures and not with shear-mode fractures, only the eastern 1.6 m of layer Escalera OO1 data set will be considered further for analysis.

Figure 8.10 Graphs of spatial correlation vs. length scale (thick continuous line) for (a) logarithmic graduations and (b) linear graduations for the eastern 1.6 m of scanline of the Escalera OO1 data set (492 fractures, all fracture sets, aperture threshold of 0.05 mm). In (a) and (b) the thin discontinuous line represents the upper 95% confidence limit while the thin dotted line represents the lower 95% confidence limit, and the thick discontinuous line corresponds to the mean of 100 randomized data sets. In (a) and (b) the thin continuous line represents the analytical solution of randomly arranged fractures with the same number of fractures and scanline length. Width of length-scale bin in (a) and (b) is 5 (m = 2) graduations of length scale. Power law in (a) was calculated using spatial correlation between length scales of 2 and 60 mm. Although evenly spaced lines every 340 mm in (b) match all peaks of spatial correlation, only one peak is outside the 95% confidence interval, which may indicate that fracture clusters are periodically arranged. (c) Power spectrum of spatial correlation from (b). A noticeable peak of power spectra at 334 mm is outside the 95% confidence interval for red noise, indicating a periodic arrangement of fractures that is statistically significant and with a cluster spacing of 334 mm. Although for length scales larger than 500 mm the power spectral density for the natural data set is outside the 95% confidence interval for red noise, the trends for both the natural data set and the 95% confidence interval for red noise are similar, as shown in (c).

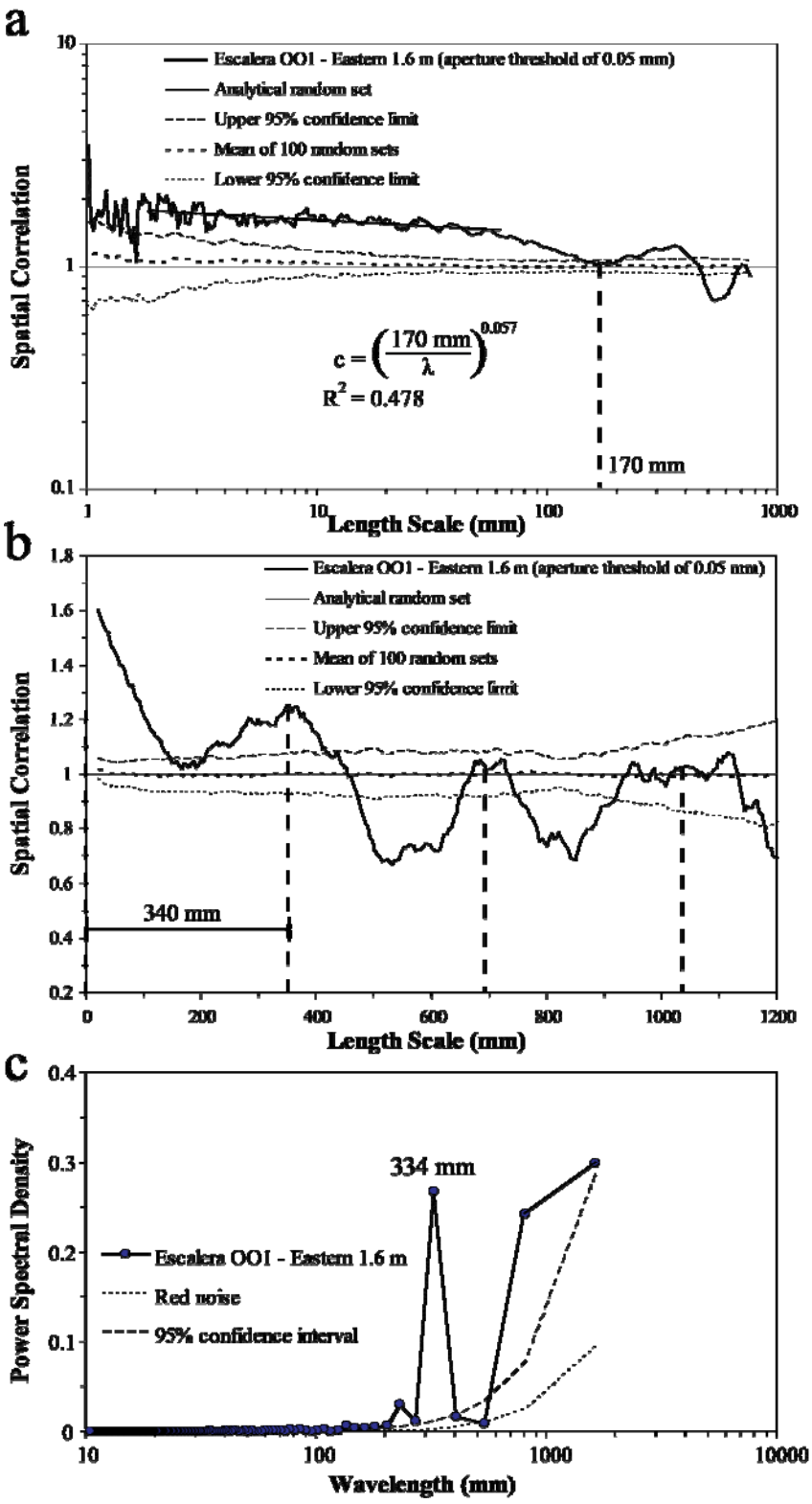
a
Escalera OO1 - Eastern 1.6 m (aperture threshold of 0.05 mm)
Analytical random set
Upper 95% confidence limit
Mean of 100 random sets
Lower 95% confidence limit
Spatial Correlation
$c = \left(\frac{170\ mm}{\lambda}\right)^{0.057}$
$R^2 = 0.478$
170 mm
Length Scale (mm)
b
Escalera OO1 - Eastern 1.6 m (aperture threshold of 0.05 mm)
Analytical random set
Upper 95% confidence limit
Mean of 100 random sets
Lower 95% confidence limit
Spatial Correlation
340 mm
Length Scale (mm)
c
334 mm
Escalera OO1 - Eastern 1.6 m
Red noise
95% confidence interval
Power Spectral Density
Wavelength (mm)

Figure 8.11 Graphs of spatial correlation vs. length scale (thick continuous line) for (a) logarithmic graduations and (b) linear graduations for the western 1.5 m of scanline of the Escalera OO1 data set (668 fractures, all fracture sets, aperture threshold of 0.05 mm). The thin discontinuous line represents the upper 95% confidence limit while the thin dotted line represents the lower 95% confidence limit, and the thick discontinuous line corresponds to the mean of 100 randomized data sets. In (a) and (b) the thin continuous line represents the analytical solution of randomly arranged fractures with the same number of fractures and scanline length. Width of length-scale bin is 5 (m = 2) graduations of length scale for (a) and (b). Power law in (a) was calculated using spatial correlation of Escalera OO1 data set between length scales of 2 and 90 mm. Two peaks (185 and 560 mm) of spatial correlation in (b) are outside the 95% confidence interval. Although the second peak of spatial correlation (560 mm) is approximately a multiple of the first peak (185 mm, dashed line), there is no evidence of an intermediate multiple (370 mm), which suggest that arrangement is not periodic. (c) Power spectrum of spatial correlation from (b). Although there seems to be a peak of spatial correlation at 185 mm in (b), a peak at 431 mm is not evident.

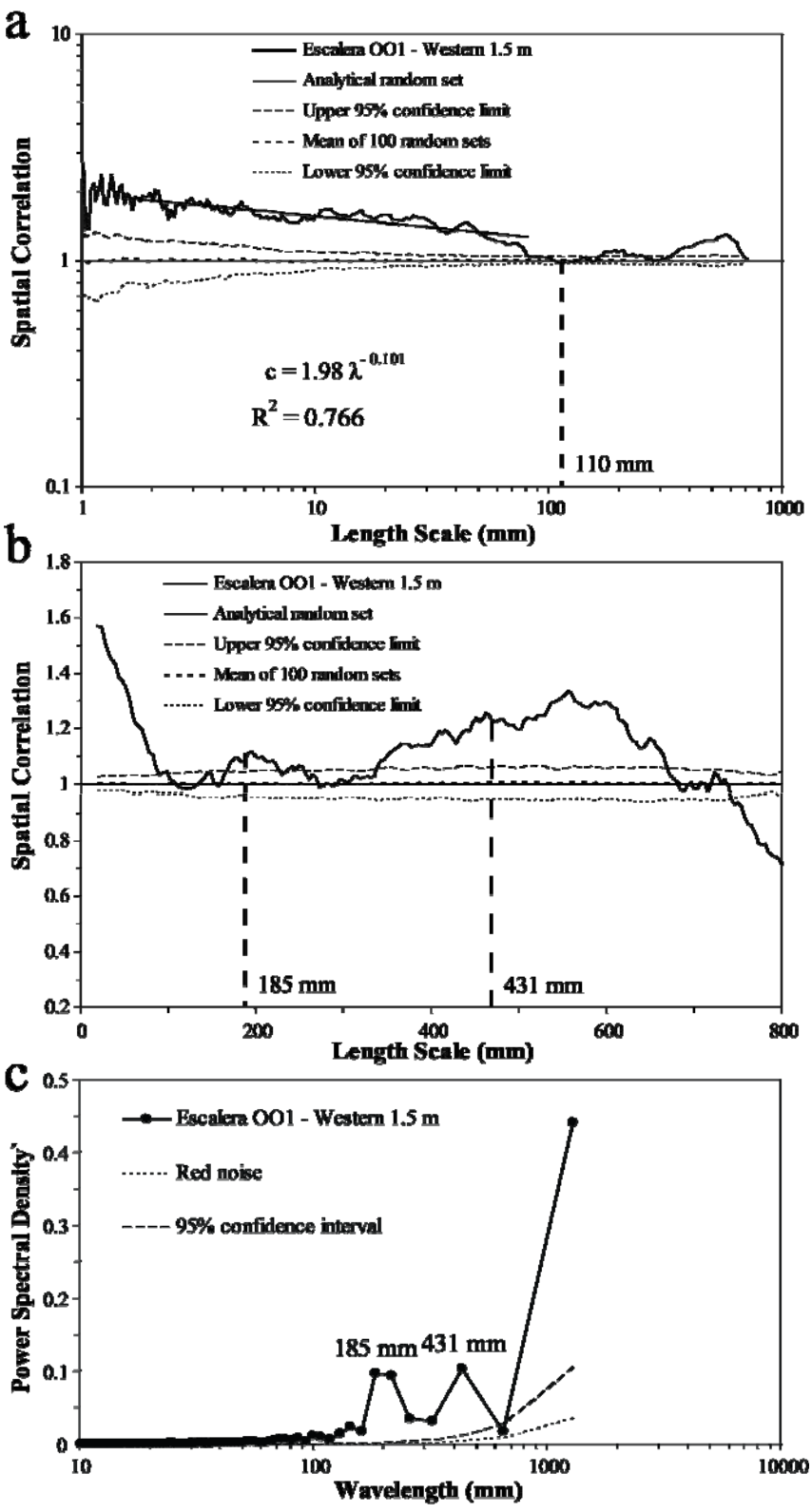
a
Escalera OO1 - Western 1.5 m
Analytical random set
Upper 95% confidence limit
Mean of 100 random sets
Lower 95% confidence limit
Spatial Correlation
c = 1.98 λ^-0.101
R^2 = 0.766
110 mm
Length Scale (mm)
b
Escalera OO1 - Western 1.5 m
Analytical random set
Upper 95% confidence limit
Mean of 100 random sets
Lower 95% confidence limit
Spatial Correlation
185 mm
431 mm
Length Scale (mm)
c
Escalera OO1 - Western 1.5 m
Red noise
95% confidence interval
Power Spectral Density
185 mm
431 mm
Wavelength (mm)

8.2.1.2 Rock Sample Scale – Sample 1

Two sets of thin sections were obtained from samples extracted from the Escalera OO1 layer (Figure 8.12, Table 8.2). Qualitatively speaking, sample 1 (02LG11) was obtained at the eastern end of the scanline (Figure 8.12), along the outcrop scanline and outside of any outcrop cluster (Figure 8.7). This sample contained fractures typical of the eastern domain of the scanline (Figure 8.8a). Sample 1 generated one thin section that allowed collection of a 66 mm scanline along which 52 transgranular fractures (9.82% strain) were measured in petrographic photomicrographs (Table 8.2). Minimum and maximum fracture apertures measured were 0.0036 and 3.7952 mm.

Spatial correlation for logarithmic graduations of length scale for sample 1 (02LG11) of the Escalera OO1 layer displays isolated peaks but no systematic pattern with length scale, which indicates an arrangement of fractures indistinguishable from random (Figures 8.5a and 8.13a). Spatial correlation for linear graduation of length scales for the same data set makes alternating small peaks and troughs, which might indicate a periodic arrangement of clusters (Figures 8.5g and 8.13b). However, only two of the eight peaks of spatial correlation are statistically significant (Chapter 6), which casts doubt of the statistical significance on the spatial correlation pattern of Figure 8.13b. Power spectrum shows a statistically significant peak of power spectral density at a wavelength of 3.6-4.1 mm, indicating that the periodic arrangement of fracture clusters of Figure 8.13b is statistically significant (Figure 8.13c). Although cluster width is typically estimated in graphs of logarithmically graduated length scales, cluster width can also be estimated using linearly graduated length scales (e.g., Figure 8.5g), which for the sample 1 of Escalera OO1 is approximately 2 mm (Figure 8.13b).

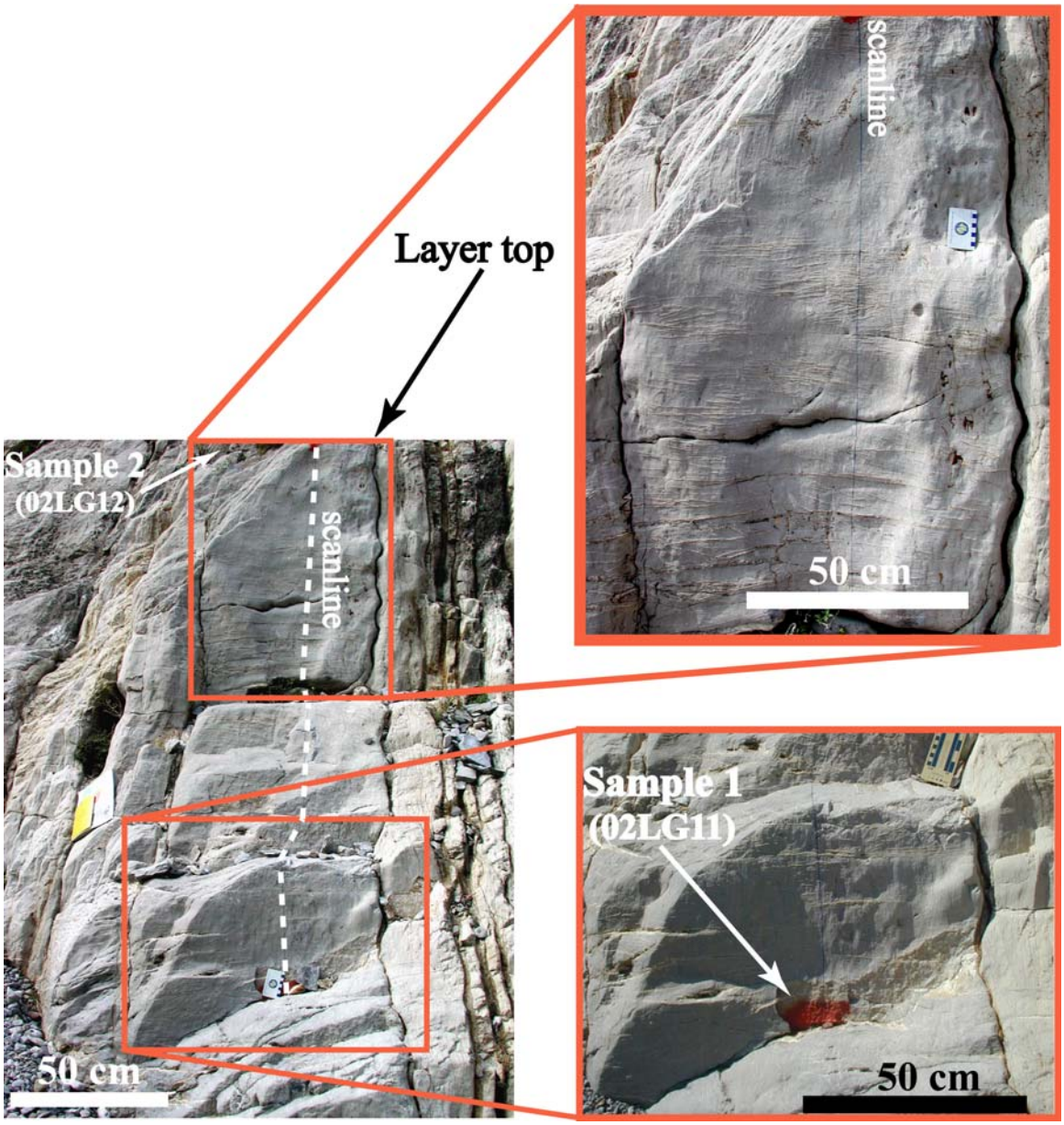

Figure 8.12 Photograph of the entire scanline in layer OO1 from Escalera canyon. Detailed view of outcrop (lower right photo) shows location of sample 1 (02LG11, Table 8.2) along scanline.

Figure 8.13 Graphs of spatial correlation vs. length scale (thick continuous line) for (a) logarithmic graduations and (b) linear graduations for the sample 02LG11 from the Escalera OO1 rock sample data set (52 fractures). In (a) and (b) the thin discontinuous line represents the upper 95% confidence limit while the thin dotted line represents the lower 95% confidence limit, and the thick discontinuous line corresponds to the mean of 100 randomized data sets. In (a) and (b) the thin continuous line represents the analytical solution of randomly arranged fractures with the same number of fractures and scanline length. Width of length-scale bin in (a) is 15 (m = 7) and 23 (m = 11) graduations of length scale for (b). Spatial correlation in (a) does not exhibit a recognizable (e.g., power law) pattern outside the 95% confidence interval. Evenly spaced lines every 4.1 mm in (b) match peaks of spatial correlation. However, only one of possibly eight peaks of spatial correlation is outside the 95% confidence interval. Cluster spacing is estimated at 4.1 mm. (c) Power spectrum of spatial correlation from (b). A peak of power spectral density is outside the 95% confidence interval for red noise, as shown in (c), which indicate that the corresponding wavelengths (3.6 to 4.1 mm) are statistically significant. Statistically significant wavelengths in (c) match cluster spacing in (b), which indicates that the periodic arrangement of clusters suggested in (b) is statistically significant.

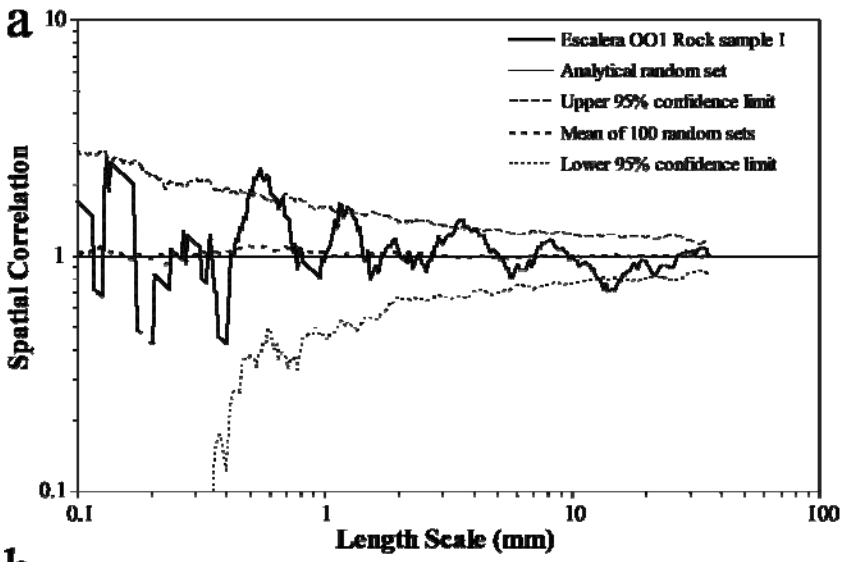
a
Escalera OO1 Rock sample 1
Analytical random set
Upper 95% confidence limit
Mean of 100 random sets
Lower 95% confidence limit
Spatial Correlation
Length Scale (mm)
10
1
0.1
0.1
1
10
100

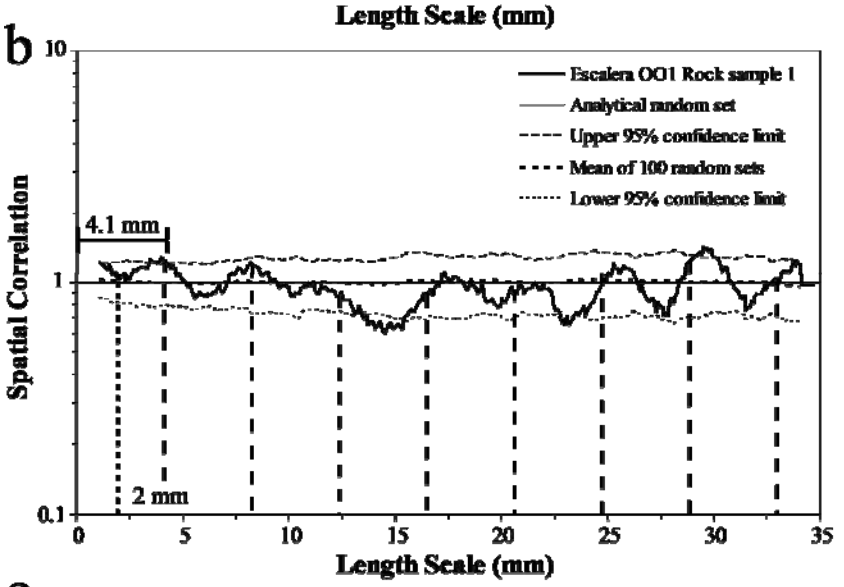
b
Escalera OO1 Rock sample 1
Analytical random set
Upper 95% confidence limit
Mean of 100 random sets
Lower 95% confidence limit
4.1 mm
2 mm
Spatial Correlation
Length Scale (mm)
10
1
0.1
0
5
10
15
20
25
30
35

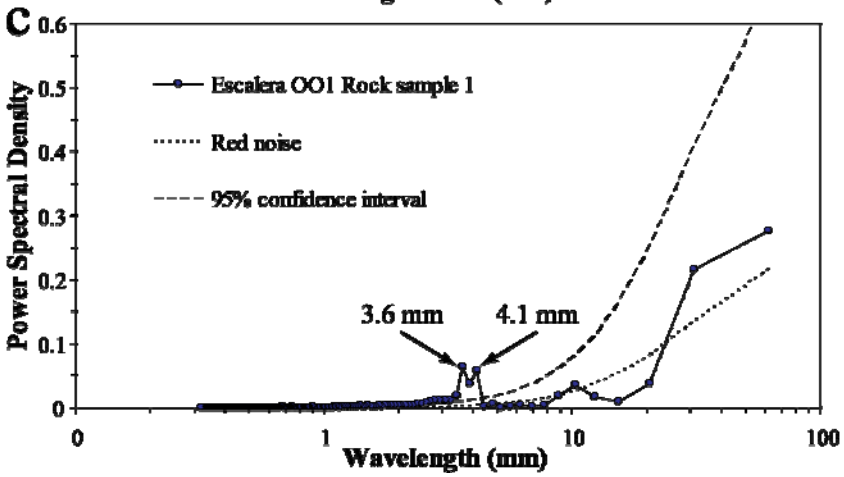
c
Escalera OO1 Rock sample 1
Red noise
95% confidence interval
3.6 mm
4.1 mm
Power Spectral Density
Wavelength (mm)
0.6
0.5
0.4
0.3
0.2
0.1
0
0
1
10
100

8.2.1.3 Rock Sample Scale – Sample 2

Sample 2 (02LG12) from Escalera OO1 layer was obtained from a macrofracture cluster and mostly contains fractures typical of the western 1.5 m of scanline (Figure 8.8b). However, the second sample was not obtained along the outcrop scanline but instead it was extracted near the layer base (Figure 8.12). Two scanlines were measured from sample 2. One scanline was 111 mm long and recorded 94 transgranular fractures (13.2% strain) in petrographic photomicrographs (Table 8.2). Minimum and maximum fracture apertures measured on the first scanline were 0.0015 and 1.2985 mm. The second scanline (49 mm) was obtained using SEM cathodoluminescence images and recorded 29 transgranular fractures with a total strain if 14.4% strain (Table 8.2). Minimum and maximum fracture apertures measured on the second scanline were 0.0028 and 1.2538 mm. Elongated dolomite and quartz crystals at an oblique angle to fracture wall confirms the association of fractures in the western 1.5 m of scanline to faults (Chapter 9).

Spatial correlation for logarithmic graduations of length scale for both scanlines in sample 2 (02LG12) of the Escalera OO1 layer display no systematic pattern with length scale, which indicates an arrangement of fractures indistinguishable from random (Figures 8.5a, 8.14a and 8.15a). Spatial correlation for linear graduations of length scale for both scanlines in sample 2 of the Escalera OO1 layer also can be interpreted as indicative of an arrangement that is indistinguishable from random (Figures 8.5e, 8.14b and 8.15b). Spatial correlation for linear graduations of length scale for the scanline obtained from petrographic images exhibit two pair of alternating peaks and troughs, which might indicate a periodic arrangement of clusters (Figures 8.5g and 8.14b). However, power spectrum of spatial correlation of Figures 8.14b and 8.15b exhibits no statistically significant peak of power spectral density, which indicates that spatial correlation of both scanlines in sample 2 (02LG12) cannot be interpreted as periodically

arranged clusters but as indistinguishable from random (Figures 8.14c and 8.15c, respectively).

Figure 8.14 Graphs of spatial correlation vs. length scale (thick continuous line) for (a) logarithmic graduations and (b) linear graduations for the sample 02LG12 from the Escalera OO1 rock sample data set (94 fractures). Fractures were mapped on images obtained from a petrographic microscope. In (a) and (b) the thin discontinuous line represents the upper 95% confidence limit while the thin dotted line represents the lower 95% confidence limit, and the thick discontinuous line corresponds to the mean of 100 randomized data sets. In (a) and (b) the thin continuous line represents the analytical solution of randomly arranged fractures with the same number of fractures and scanline length. Width of length-scale bin in (a) is 9 (m = 4) and 21 (m = 10) graduations of length scale for (b). Spatial correlation in (a) does not exhibit a recognizable (e.g., power law) pattern outside the 95% confidence interval. Variations of spatial correlation with length scale in (b) cannot be conclusively interpreted as periodically arranged clusters. (c) Power spectrum of spatial correlation from (b). The power spectral density for the natural data set exhibits the same trend as the red noise, as shown in (c). Although power spectral density at wavelengths of 26 and 35 mm in (c) are larger than equivalent values for red noise, power spectral density is not larger than the 95% confidence interval for red noise.

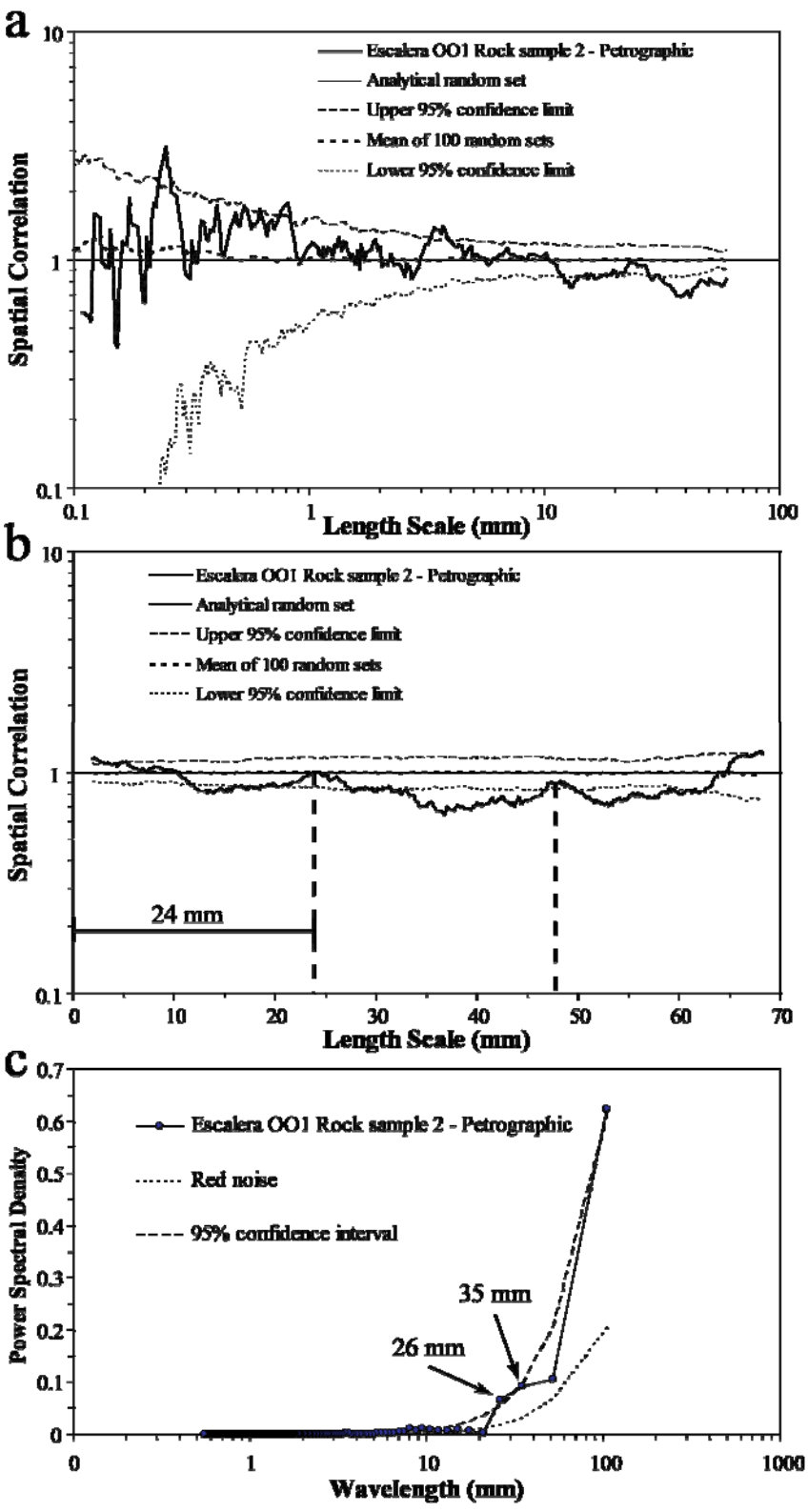
a
Escalera OO1 Rock sample 2 - Petrographic
Analytical random set
Upper 95% confidence limit
Mean of 100 random sets
Lower 95% confidence limit
Spatial Correlation
Length Scale (mm)
b
Escalera OO1 Rock sample 2 - Petrographic
Analytical random set
Upper 95% confidence limit
Mean of 100 random sets
Lower 95% confidence limit
Spatial Correlation
24 mm
Length Scale (mm)
c
Escalera OO1 Rock sample 2 - Petrographic
Red noise
95% confidence interval
35 mm
26 mm
Power Spectral Density
Wavelength (mm)

Figure 8.15 Graphs of spatial correlation vs. length scale (thick continuous line) for (a) logarithmic graduations and (b) linear graduations for the sample 02LG12 from the Escalera OO1 rock sample data set (29 fractures). Fractures were mapped on cathodoluminescence images obtained from a SEM. In (a) and (b) the thin discontinuous line represents the upper 95% confidence limit while the thin dotted line represents the lower 95% confidence limit, and the thick discontinuous line corresponds to the mean of 100 randomized data sets. In (a) and (b) the thin continuous line represents the analytical solution of randomly arranged fractures with the same number of fractures and scanline length. Width of length-scale bin in (a) is 9 (m = 4) and 21 (m = 10) graduations of length scale for (b). Spatial correlation in (a) and (b) do not exhibit a recognizable (e.g., power law) pattern outside the 95% confidence interval. (c) Power spectrum of spatial correlation from (b). The power spectral density for the natural data set exhibits the same trend as the red noise, as shown in (c). Although the natural data set exhibits a peak outside the 95% confidence interval for red noise at a wavelength of 1.4 mm, the power spectral density is small when compared with other data sets (e.g., Eastern 1.6 m of Escalera OO1 data set, Figure 9.10c).

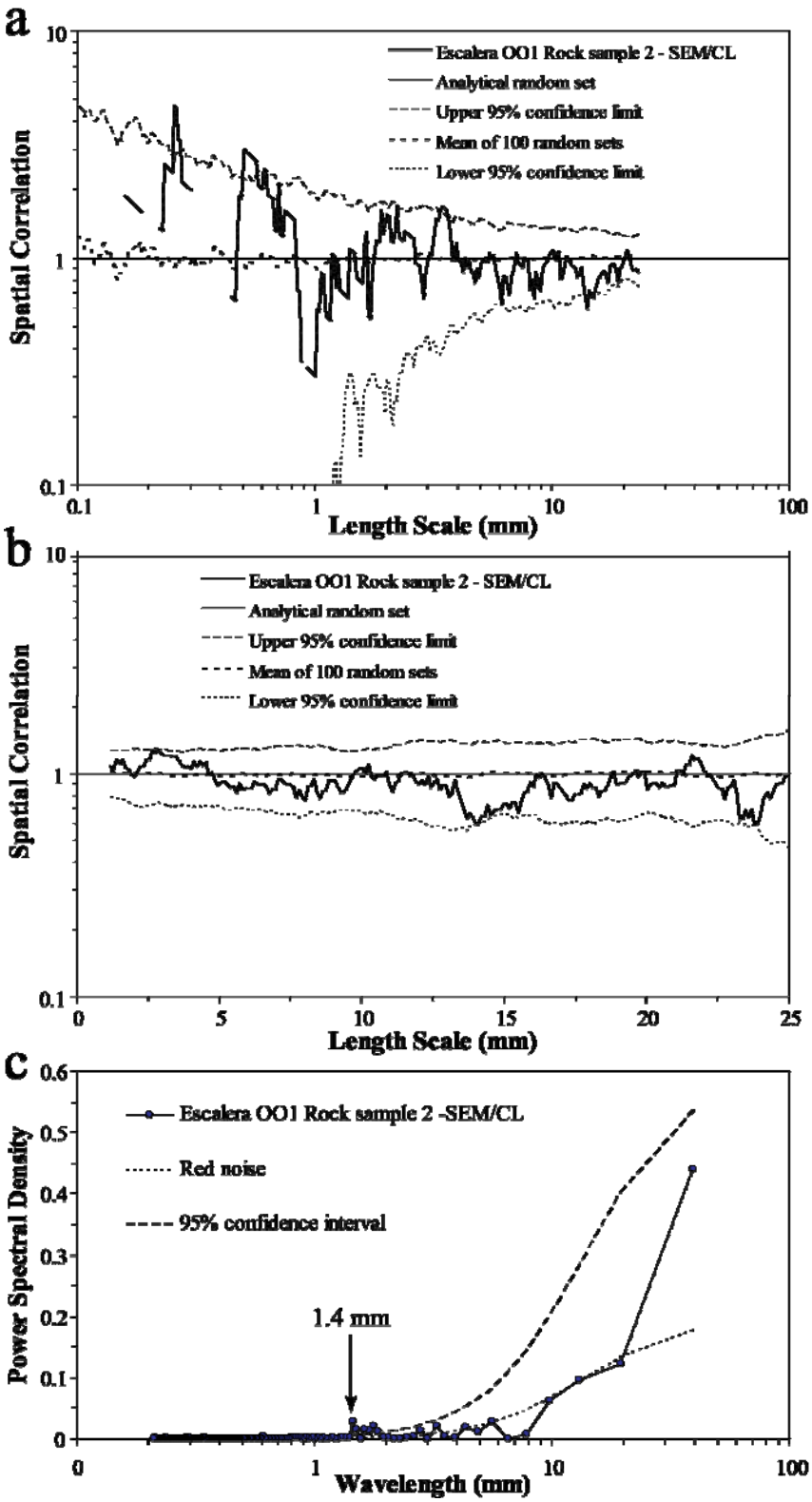
a
Escalera OO1 Rock sample 2 - SEM/CL
Analytical random set
Upper 95% confidence limit
Mean of 100 random sets
Lower 95% confidence limit
Spatial Correlation
Length Scale (mm)
b
Escalera OO1 Rock sample 2 - SEM/CL
Analytical random set
Upper 95% confidence limit
Mean of 100 random sets
Lower 95% confidence limit
Spatial Correlation
Length Scale (mm)
c
Escalera OO1 Rock sample 2 -SEM/CL
Red noise
95% confidence interval
1.4 mm
Power Spectral Density
Wavelength (mm)

8.2.2 Layer OO12 at Escalera Canyon (Escalera OO12)

8.2.2.1 Outcrop Scale

Like Escalera OO1, Escalera OO12 layer is located in the forelimb of San Blas anticline, which is exposed in the Escalera canyon (Figure 2.7), and was studied by Ortega (2002). Escalera OO12 is 24.5 cm thick and is a dolopackstone that suffered widespread recrystallization. Escalera OO12 is located 2 m above the base of the stratigraphic column measured in the forelimb of San Blas anticline by Ortega (2002). I measured 1095 veins, of which 1047 have apertures greater than or equal to 0.05 mm along a 3.5 m long scanline length positioned in the middle of a cross-section outcrop (Table 8.1; Figure 8.16). For the 48 veins with apertures smaller than 0.05 mm only spacing was recorded (Tables 8.1 and 8.5). Because veins of this size were recorded at one end of the scanline but ignored elsewhere, they were removed for spatial arrangement analysis. The strain measured along the scanline is 20.4% (Table 8.5).

The spacings between fractures exhibit a logarithmic distribution and a coefficient of variation of 1.33 (Table 8.5). Fractures with apertures greater than or equal to 0.05 mm at Escalera OO12 exhibit a power-law distribution of apertures (Table 8.5). Fractures were assigned to two different sets (A and B) depending on their orientation (Table 8.4). 93% of the fractures measured represent set A and 7 % represent set B. As with layer Escalera OO1, set A and set B of Escalera OO12 have similar orientations (231/40 and 203/60, respectively) and therefore might be part of a single set (Table 8.4). In thin sections fractures of sets A and B exhibit features of Y fractures such as straight traces, fibrous dolomite lining fracture walls, bridges of quartz with crack-seal texture, and calcite precipitated between quartz bridges and also replacing quartz (Table 8.3).

A crossplot of fracture aperture versus position along scanline shows that fractures in the Escalera OO12 data set display a heterogeneous arrangement of fractures

(Figure 8.16). Peaks of fracture intensity indicate the presence of clusters whereas low fracture intensity highlights areas with few fractures that do not seem be regularly spaced (Figure 8.16). Spatial correlation for all fracture sets of Escalera OO12 varies as a power-law of length scale (Figures 8.5b and 8.17a), with a cluster width of 150 mm. Spatial correlation for linearly graduated length scales for all fracture sets of Escalera OO12 shows a pattern of alternating peaks and troughs (Figure 8.17b). Most peaks and troughs of spatial correlation for linearly graduated length scales are outside the 95% confidence interval, which indicates a periodic arrangement of fracture clusters (Figure 8.5g) with a cluster spacing of 850 mm (Figure 8.17b). Power spectrum of the spatial correlation for linearly graduated length scales exhibits a peak at 867 mm that is outside the 95% confidence interval for red noise (Figure 8.17c), which supports the statistical significance of the periodic arrangement of fracture clusters with cluster spacing of 850 mm indicated by spatial correlation.

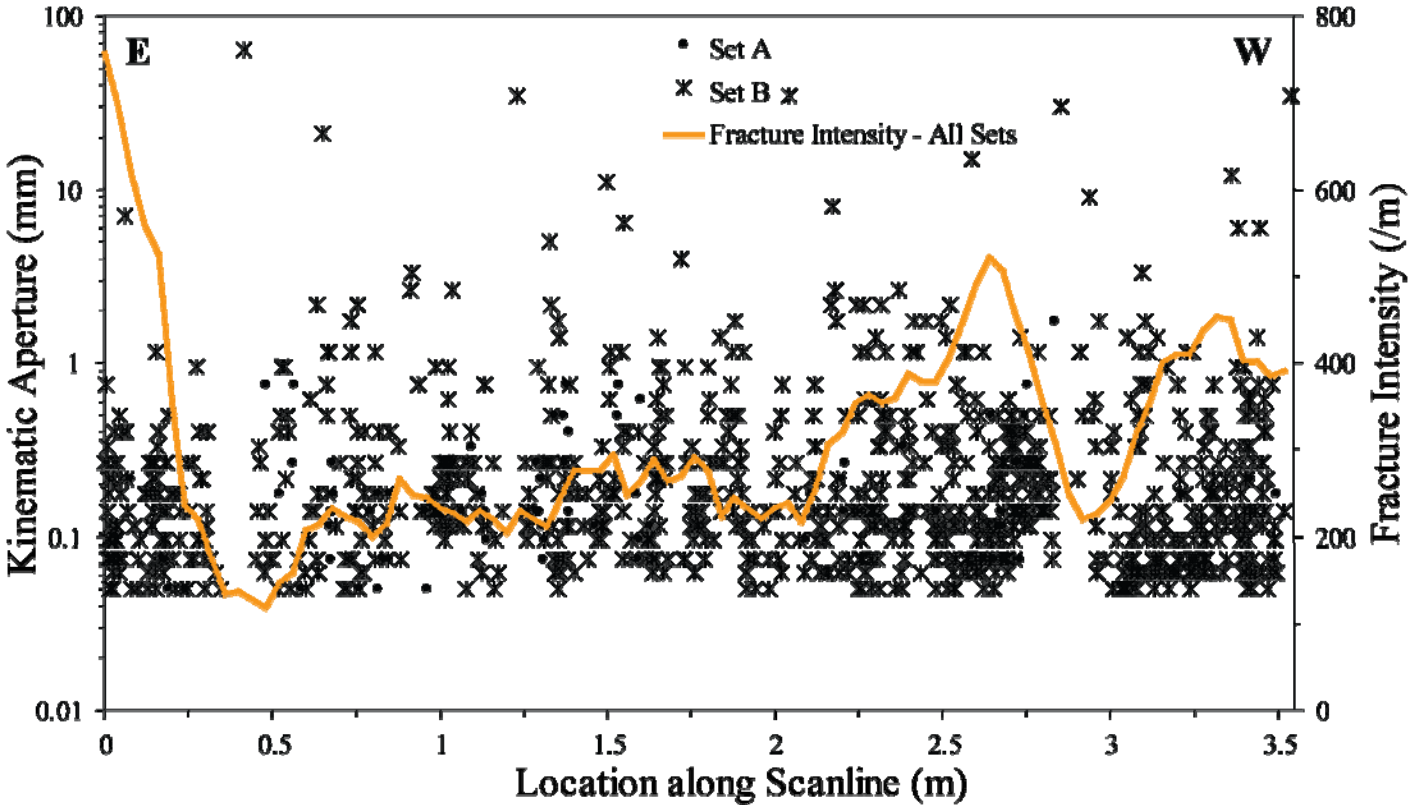

Figure 8.16 Kinematic aperture (circles for set A, and asterisks for set B) and fracture intensity (orange thick line) versus location along scanline for the Escalera OO12 data set. Note that kinematic aperture axis uses logarithmic graduations. Fracture intensity was calculated inside a moving window with width (window size) of 0.16 m that was moved in increments (window step) 0.04 m. Peaks of fracture intensity indicate clusters at 0, 2.6, and 3.3 m, but clusters do not seem regularly spaced. Although 1095 fractures were used to calculate the curve of fracture intensity, only the aperture of the 1047 fractures of sets A and B with apertures equal or larger than 0.05 mm was plotted.

Figure 8.17 Graphs of spatial correlation vs. length scale (thick continuous line) for (a) logarithmic graduations and (b) linear graduations for fractures with apertures equal or larger than 0.05 mm of the Escalera OO12 Outcrop data set (1047 fractures, aperture threshold of 0.05 mm). In (a) and (b) the thin discontinuous line represents the upper 95% confidence limit while the thin dotted line represents the lower 95% confidence limit, and the thick discontinuous line corresponds to the mean of 100 randomized data sets. In (a) and (b) the thin continuous line represents the analytical solution of randomly arranged fractures with the same number of fractures and scanline length. Width of length-scale bin is 7 (m = 3) for (a) and 13 (m = 6) for (b). A power-law pattern of spatial correlation is observed in (a). Peaks of spatial correlation are approximately evenly spaced every 850 mm (thick dashed lines), as shown in (b), and are indicative of periodically arranged clusters. (c) Power spectrum of spatial correlation from (b). A relatively broad peak with power spectral density that is several times the equivalent for the 95% confidence interval for red noise is visible in (c) at 867 mm, indicating a non-random periodic arrangement of fractures with a cluster spacing of approximately 867 mm. Another peak of power spectral density at a wavelength of 400 mm is outside the 95% confidence interval for red noise, but the difference between the peak and the 95% confidence interval is small when compared with other data sets (e.g., Eastern 1.6 m of Escalera OO1 data set, Figure 9.10c).

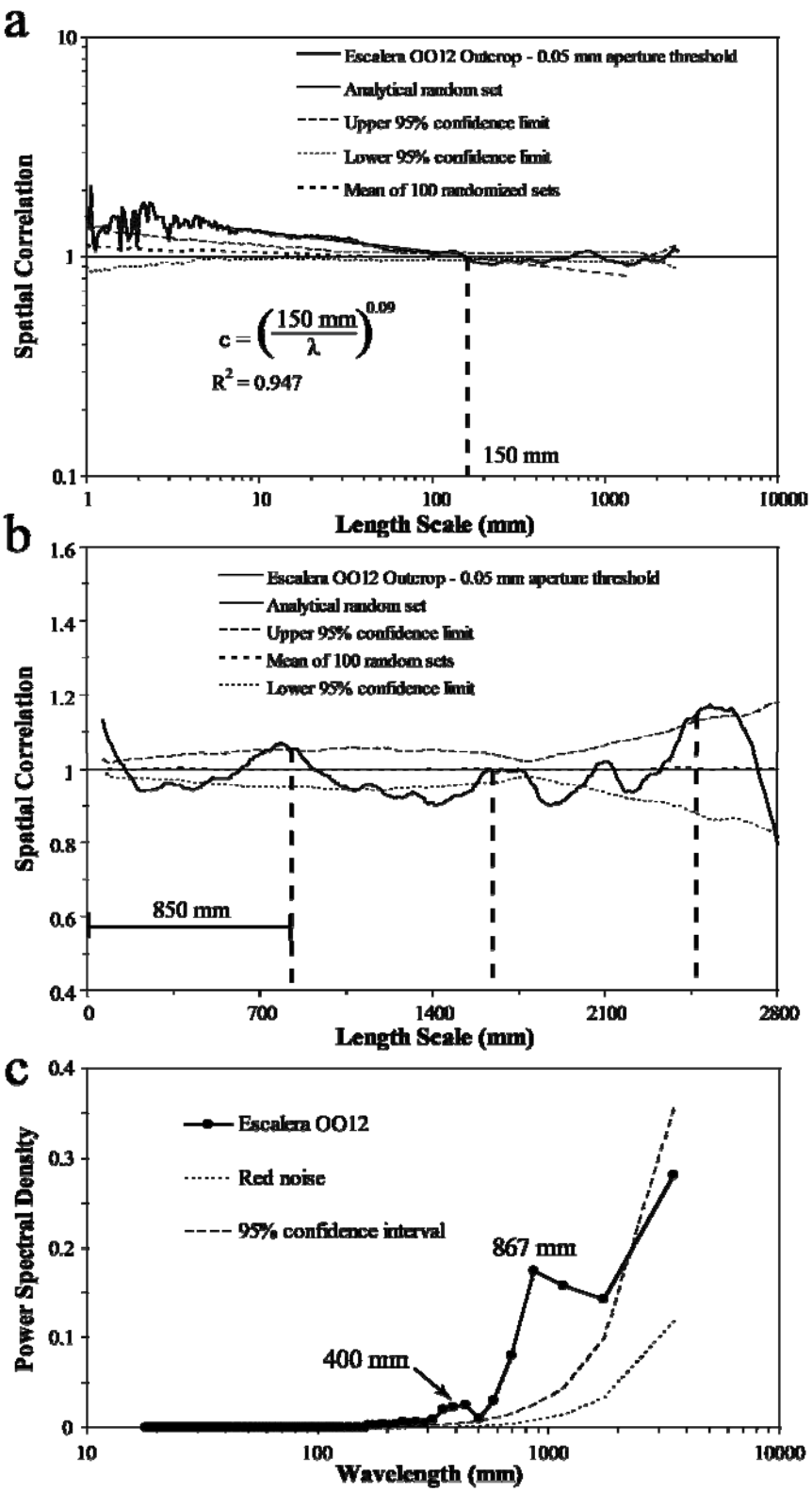
a
Escalera OO12 Outcrop - 0.05 mm aperture threshold
Analytical random set
Upper 95% confidence limit
Lower 95% confidence limit
Mean of 100 randomized sets
Spatial Correlation
$c = \left(\frac{150\ mm}{\lambda}\right)^{0.09}$
$R^2 = 0.947$
150 mm
Length Scale (mm)
b
Escalera OO12 Outcrop - 0.05 mm aperture threshold
Analytical random set
Upper 95% confidence limit
Mean of 100 random sets
Lower 95% confidence limit
Spatial Correlation
850 mm
Length Scale (mm)
c
Escalera OO12
Red noise
95% confidence interval
Power Spectral Density
867 mm
400 mm
Wavelength (mm)

8.2.2.2 Rock Sample Scale

Four consecutive thin sections were generated from a sample that was obtained along the outcrop scanline and that contained most of an outcrop cluster (Table 8.2). A total of 484 transgranular fractures were mapped in 149 mm of scanline that recorded a strain of 20% (Table 8.2). Minimum and maximum fracture apertures measured were 0.0007 and 1.4206 mm. NCC analysis of the Escalera OO12 rock sample data set display similar patterns of spatial correlation to the outcrop data set (Figures 8.17 and 8.18). Namely, spatial correlation for logarithmic graduations of length scale yielded a power-law pattern, and a cluster width of approximately 8 mm (Figures 8.5b and 8.18a). Spatial correlation for linear graduation of length scales yields a pattern of alternating peaks and troughs (all of which are outside the 95% confidence interval) that is interpreted as a periodic arrangement of fracture clusters (Figure 8.5g) with a cluster spacing of 44mm (Figure 8.18b). Power spectrum of spatial correlation for linearly graduated length scales supports the statistical significance of the periodic arrangement of fracture clusters by exhibiting a peak of power spectral density at 44 mm (Figure 8.18c).

Figure 8.18 Graphs of spatial correlation vs. length scale (thick continuous line) for (a) logarithmic graduations and (b) linear graduations for the Escalera OO12 rock sample data set (484 fractures). In (a) and (b) the thin discontinuous line represents the upper 95% confidence limit while the thin dotted line represents the lower 95% confidence limit, and the thick discontinuous line corresponds to the mean of 100 randomized data sets. In (a) and (b) the thin continuous line represents the analytical solution of randomly arranged fractures with the same number of fractures and scanline length. Width of length-scale bin is 7 ($m = 3$) for (a) and (b). The power-law pattern of spatial correlation in (a) was calculated between 0.18 and 7 mm. Power law in (a) was extended (dashed line) to facilitate its detection. Peaks of spatial correlation are approximately evenly spaced every 44 mm (thick dashed lines), as shown in (b), and are indicative of periodically arranged clusters. (c) Power spectrum of spatial correlation from (b). A relatively broad peak with power spectral density that is several times the equivalent for the 95% confidence interval for red noise is visible in (c) at 44 mm, indicating a non-random periodic arrangement of fractures with a cluster spacing of approximately 44 mm.

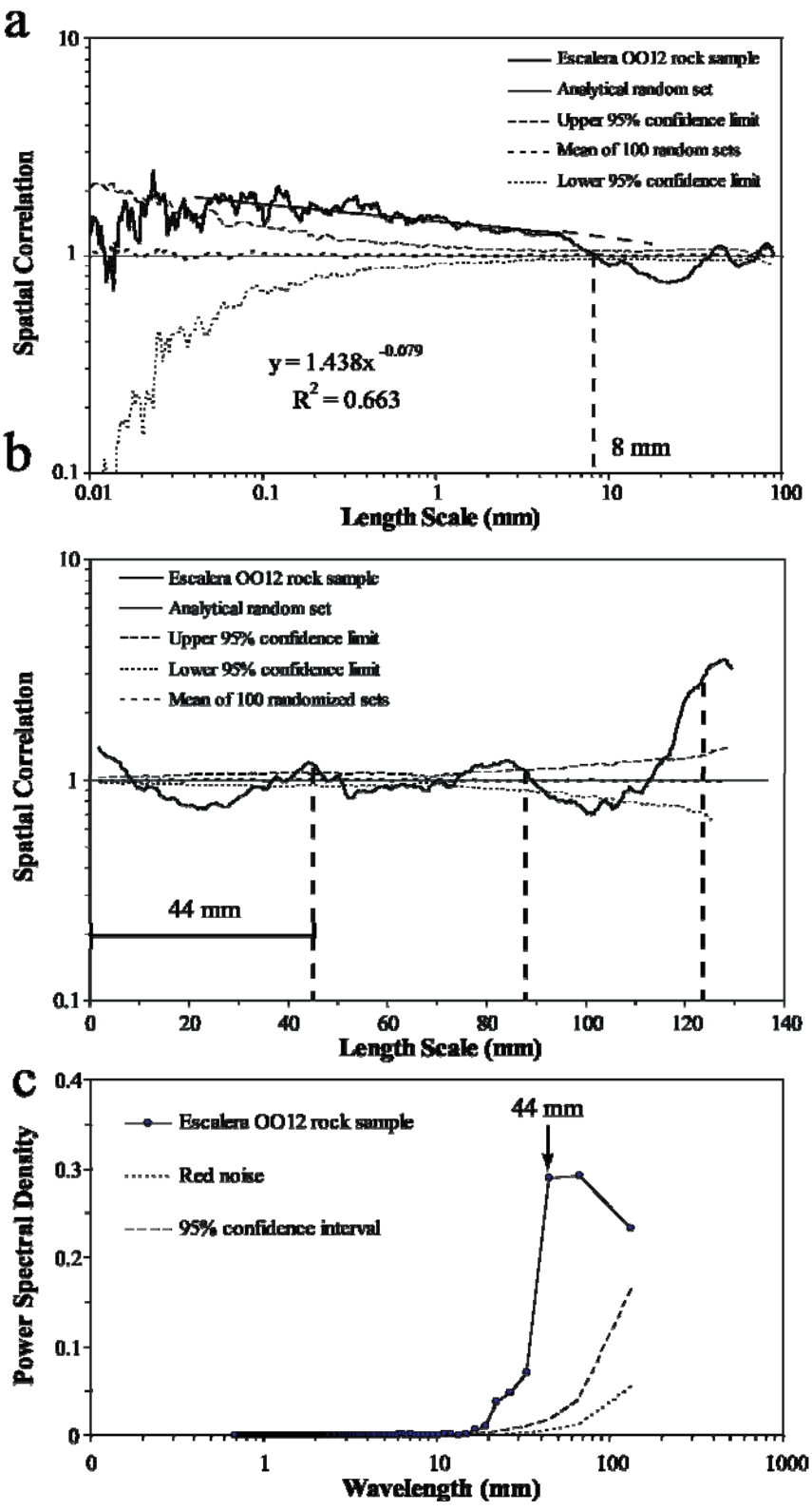
a
Escalera OO12 rock sample
Analytical random set
Upper 95% confidence limit
Mean of 100 random sets
Lower 95% confidence limit
Spatial Correlation
y = 1.438x^-0.079
R^2 = 0.663
8 mm
Length Scale (mm)
b
Escalera OO12 rock sample
Analytical random set
Upper 95% confidence limit
Lower 95% confidence limit
Mean of 100 randomized sets
Spatial Correlation
44 mm
Length Scale (mm)
c
Escalera OO12 rock sample
Red noise
95% confidence interval
44 mm
Power Spectral Density
Wavelength (mm)

8.2.3 Huasteca Canyon

8.2.3.1 Outcrop Scale

The layer studied at Huasteca canyon is located in the forelimb of the leading anticline (Muertos) inside Huasteca Park near the city of Santa Catarina, a suburb of the city of Monterrey, Mexico (Figure 8.19a). Fractures of Huasteca data set were measured in a cross sectional exposure (Figure 8.19b) along a 16.6 m long scanline (Table 8.1, Figure 8.20a). The layer at Huasteca canyon is a 70-cm thick dolopackstone that suffered partial dedolomitization. Using an aperture threshold of 0.215 mm I measured 658 veins and recorded a strain of 7.15% (Table 8.5). Four sets (A, B, C, and D) of fractures were recorded in the Huasteca layer (Table 8.4). 88% of the fractures measured represent set A, 3% represent set B, 8% represent set C, and 1% represent set D (Table 8.4). Unlike all the other data sets selected for this chapter, fracture apertures of the Huasteca data set do not follow a power-law distribution, but instead follow a log-normal distribution (Table 8.5). Chi square of fracture aperture for a power-law distribution for Huasteca is 0.2596, 50% larger than the second largest Chi square of any other data set (0.1460, Escalera OO12, Table 8.5). Fracture spacings of the Huasteca layer follow a log-normal distribution, and have a coefficient of variation of 1.23 (Table 8.5). In thin sections, fractures of sets A and B exhibit most of the typical features of Y fractures such as straight traces, microfractures that occasionally anastomose, bridges of subhedral dolomite and quartz (Table 8.3). Qualitative study of intersections between fractures of sets A and B in the field and in thin sections revealed mutually crosscutting relationships, likely indicating that fracture sets developed simultaneously.

Figure 8.19 (a) Panoramic photograph of the area near the entrance to the Huasteca canyon looking east. Approximate location of (b) is highlighted with an orange rectangle. A small car is located at the base of the photograph for scale. However, the wide angle lens used in (a) created noticeable distortion in photograph. (b) Photograph of the entire outcrop of layer and surrounding layers. Approximate location of entire scanline is drawn as a white line. Approximate location of (c) is highlighted with a green rectangle in (b). A person is located at the base of the photograph for scale. (c) Photograph of a portion of Huasteca scanline, which includes a cluster. Location of sample 03LG26 is at edge of cluster. Most of layer thickness is included in photograph. Notice the approximate equal spacing of macrofractures in (c). Scale in (c) is in centimeters.

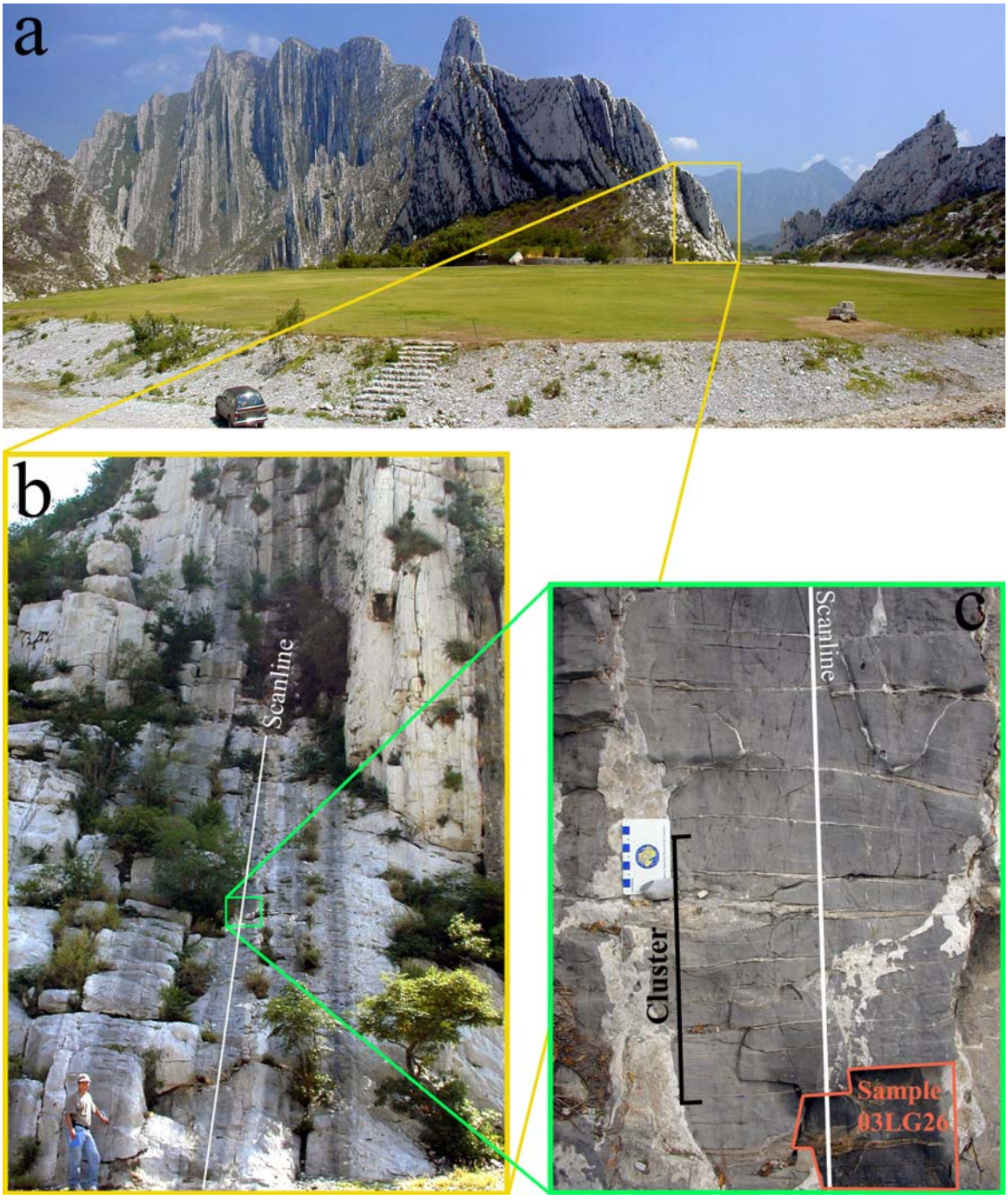
a
b
Scanline
c
Scanline
Cluster
Sample
03LG26

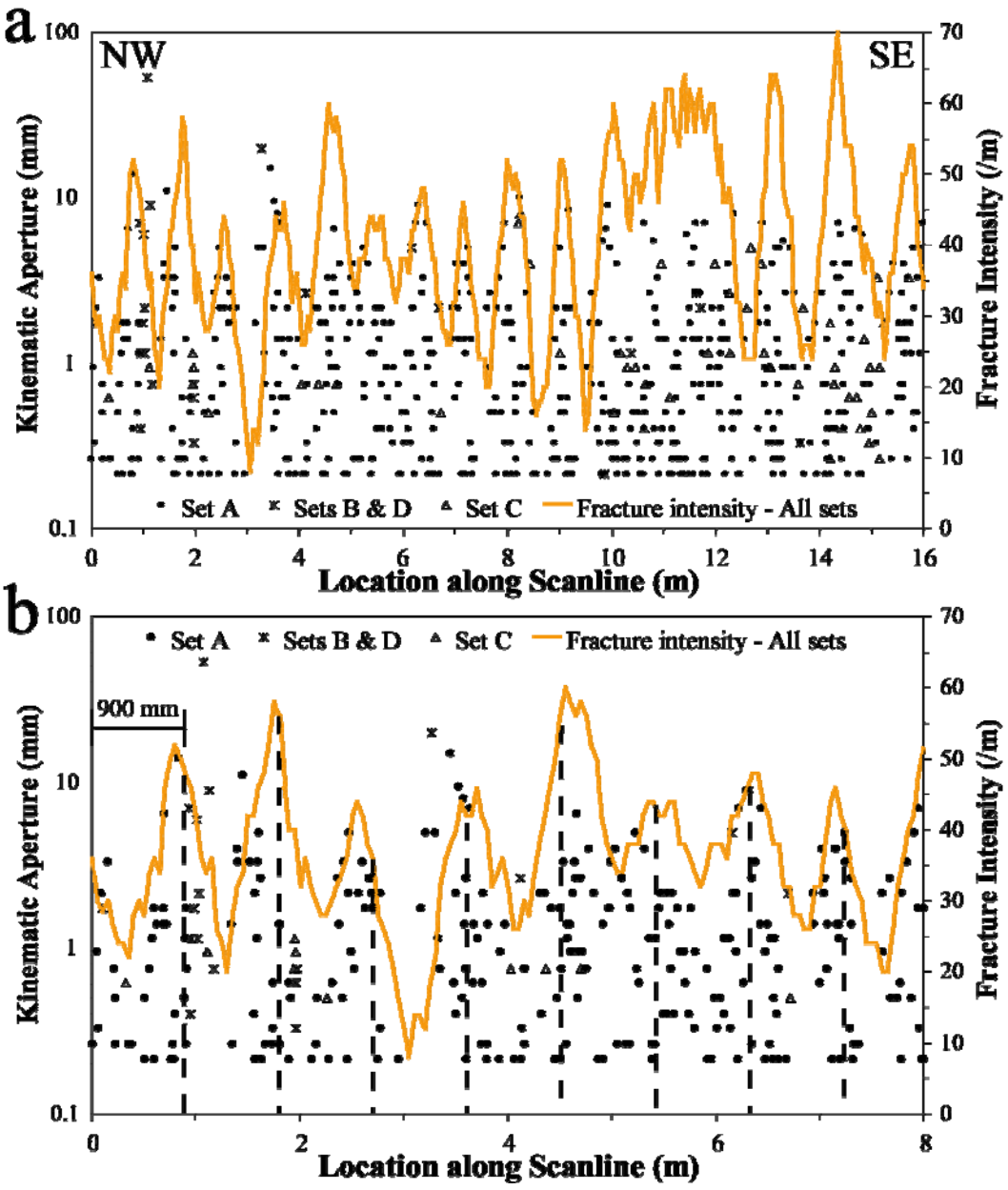
a
NW
SE
Kinematic Aperture (mm)
Fracture Intensity (/m)
Set A
Sets B & D
Set C
Fracture intensity - All sets
Location along Scanline (m)
b
900 mm
Kinematic Aperture (mm)
Fracture Intensity (/m)
Set A
Sets B & D
Set C
Fracture intensity - All sets
Location along Scanline (m)

Figure 8.20 Kinematic aperture (circles for set A, asterisks for sets B and D, and triangles for set C) and fracture intensity (thick orange line) versus location along scanline for all (a) and NW half (b) of the Huasteca data set. Fracture intensity was calculated inside a moving window with width (window size) equal to cluster width as estimated by NCC (0.25 m, Figure 8.21a) that was moved in increments (window step) equal of 0.05 m. Note that only the kinematic aperture axis use logarithmic graduations. Clusters are more easily detected in (b) than in (a) because cluster width is larger compared with the plotted scanline.

Spatial correlation for logarithmically graduated length scales of set A fractures varies as a power-law of length scale (Figures 8.5b and 8.21a) with a cluster width of 250 mm. However, set A fractures exhibit a power-law pattern of spatial correlation with an exponent near zero and therefore clusters cannot unequivocally be characterized as having a power-law pattern (Figure 8.5b) or an inherited/imposed arrangement (Figure 8.5c). Spatial correlation for linearly graduated length scales shows a pattern of alternating peaks and troughs that is interpreted as a periodic arrangement of fracture clusters (Figure 8.5g). Although the statistical significance of a periodic arrangement of fractures is not in question (most peaks are outside the 95% confidence interval), cluster spacing is slightly uncertain because some peaks are not at exact length scale multiples (dashed lines, Figure 8.21b) of the first peak of spatial correlation at 960 mm. The power spectrum of spatial correlation for linearly graduated length scales exhibit a broad peak outside the 95% confidence interval for red noise centered at a wavelength of 1001 mm (Figure 8.21c), which indicates a cluster spacing of 1001 mm. NCC results for all fracture sets combined exhibit the same patterns of spatial correlation as when set A is analyzed independently, most likely the result of set A fractures representing 88% of the Huasteca fractures. Fracture intensity indicates that the Huasteca data set contains clusters that are regularly spaced with a cluster spacing of approximately 900 mm (Figure 8.20b), which confirms the findings of NCC. However, the success of the curve of fracture intensity is

partly due to the selection of window with length approximately equal to cluster width (Chapter 6).

Spatial correlation for fractures of sets B and D combined varies as a power-law of length scale for logarithmically graduated length scales (Figure 8.5b) with a cluster width of 250 mm (Figure 8.22a), a similar cluster width estimated for fractures of set A (Figure 8.21a). Spatial correlation for linearly graduated length scales yields a pattern of alternating peaks and troughs at length scales that are multiples of the first peak (Figure 8.22b), which indicates a periodic arrangement of fracture clusters (Figure 8.5g). However, only one peak is statistically significant, which cast doubts about interpreting a periodic arrangement of clusters. In addition, cluster spacing is the same for set A and sets B and D combined (1000 mm, Figure 8.22b). To verify the statistical significance of the pattern of spatial correlation with length scale of sets B and D combined, a power spectral analysis was performed. The power spectrum of spatial correlation for linearly graduated length scales exhibits a peak at a wavelength of 1001 mm outside the 95% confidence interval for red noise (Figure 8.22c), which suggests that the periodic arrangement of fracture clusters indicated by spatial correlation is statistically significant. A difference between the spatial arrangement of fractures of set A and fractures of sets B and D is the degree of clustering, which is quantified by the power-law exponent. Fractures of set A have an exponent of 0.052 whereas fractures of sets B and D have an exponent of 0.793.

Fractures of set C also exhibit a power-law pattern of spatial correlation for logarithmically graduated length scales (Figures 8.5b and 8.23a). Spatial correlation for linearly graduated length scales of fractures of set C exhibits alternating peaks which are multiples of the first peak of spatial correlation (Figure 8.23b), which indicates that clusters are periodically arranged (Figure 8.5g). However, cluster width and spacing for

set C are much larger than for the other sets of Huasteca data set. Cluster width is estimated at 900 mm (Figure 8.23a), about four times larger than estimated for set A and sets B and D combined (250 mm). Cluster spacing is estimated at 2100 mm (Figure 9.70b), twice the spacing for sets A and for sets B and D combined (approximately 1000 mm). Power spectrum of spatial correlation for linearly graduated length scales confirms that the periodic arrangement of clusters for set C (Figure 8.23c) is statistically significant because peak power spectral density at a wavelength of 2105 mm is outside the 95% confidence interval for red noise.

Figure 8.21 Graphs of spatial correlation (thick continuous line) vs. length scale for (a) logarithmic graduations and (b) linear graduations for fractures of set A of the Huasteca outcrop data set (581 fractures, aperture threshold of 0.215 mm,). In (a) and (b) the thin discontinuous line represents the upper 95% confidence limit while the thin dotted line represents the lower 95% confidence limit, and the thick discontinuous line corresponds to the mean of 100 randomized data sets. In (a) and (b) the thin continuous line represents an example randomized set generated with the same number of fractures and scanline length. Width of length-scale bin is 21 (m = 10) in (a) and 5 (m = 2) graduations of length scale in (b). Power law in (a) was calculated using spatial correlation between length scales of 2.3 and 250 mm. Cluster width is approximately 250 mm, as shown in (a). Evenly spaced lines every 960 mm in (b) match most peaks of spatial correlation, which display a regularly spaced pattern. (c) Power spectrum of spatial correlation from (b). A broad and noticeable peak centered at a wavelength of 1001 (910 to 1093) mm has a power spectral density that is several times the equivalent for the 95% confidence interval for red noise, indicating a periodic arrangement of fractures that is statistically significant and with a cluster spacing of 1001 mm. Although the natural data set exhibits a peak of power spectral density at a wavelength of 5463 mm, this peak is not outside the 95% confidence interval for red noise, and therefore is not statistically significant.

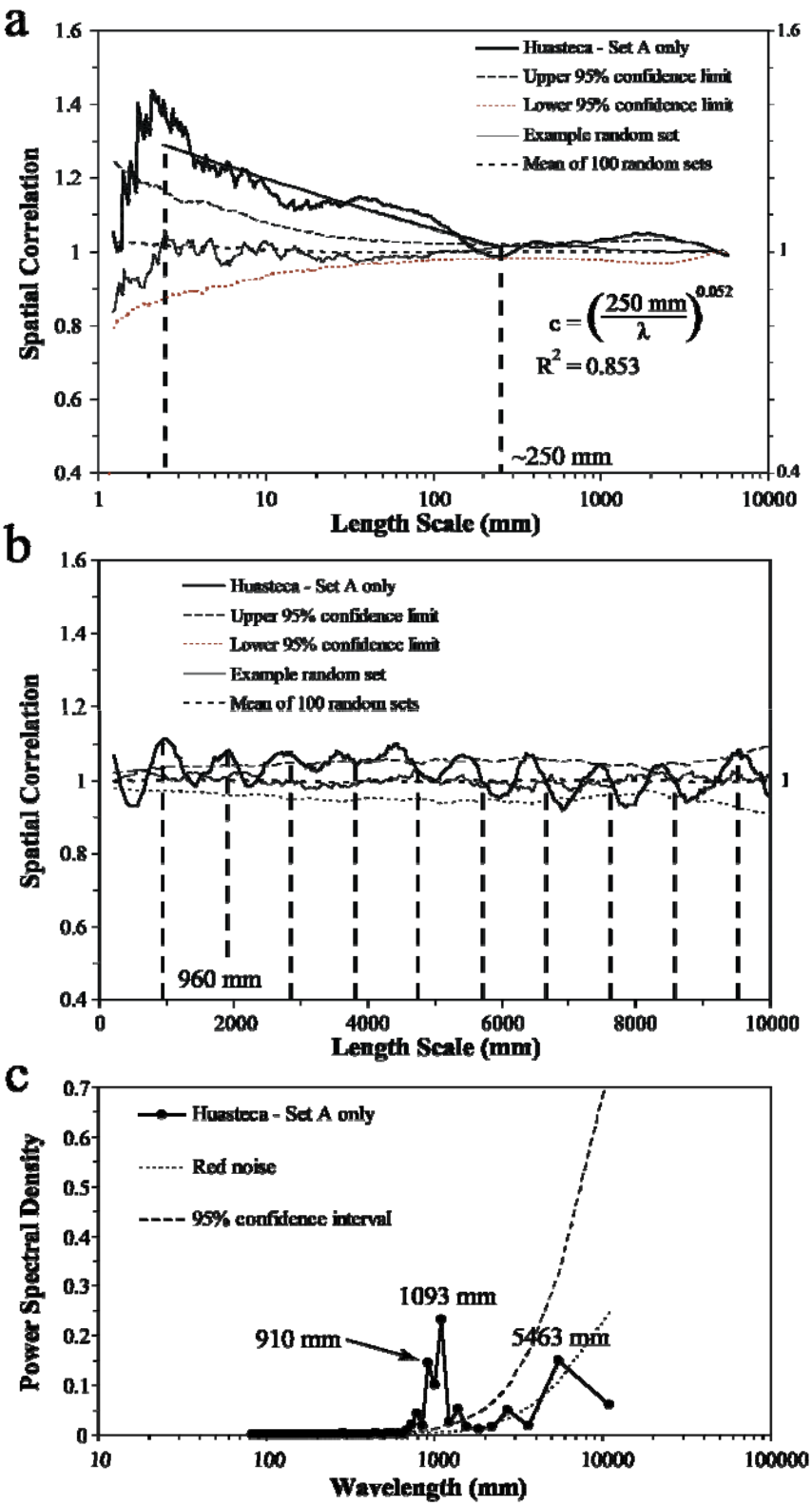
a
Spatial Correlation
Length Scale (mm)
Huasteca - Set A only
Upper 95% confidence limit
Lower 95% confidence limit
Example random set
Mean of 100 random sets
$c = \left(\frac{250\ mm}{\lambda}\right)^{0.052}$
$R^2 = 0.853$
~250 mm
b
Spatial Correlation
Length Scale (mm)
Huasteca - Set A only
Upper 95% confidence limit
Lower 95% confidence limit
Example random set
Mean of 100 random sets
960 mm
c
Power Spectral Density
Wavelength (mm)
Huasteca - Set A only
Red noise
95% confidence interval
1093 mm
910 mm
5463 mm

Figure 8.22 Graphs of spatial correlation (thick continuous line) vs. length scale for (a) logarithmic graduations and (b) linear graduations for fractures of sets B and D combined of the Huasteca outcrop data set (23 fractures, aperture threshold of 0.215 mm). In (a) and (b) the thin discontinuous line represents the upper 95% confidence interval while the thin dotted line represents the lower 95% confidence interval, and thick discontinuous line corresponds to the mean of 100 randomized data sets. In (a) the thin continuous line represents the analytical solution of randomly arranged fractures with the same number of fractures and scanline length. In (b) the thin continuous line represents an example randomized set generated with the same number of fractures and scanline length. Width of length-scale bin is 13 (m = 6 in (a) and 11 (m = 5) graduations of length scale in (b). Power law in (a) was calculated using spatial correlation between length scales of 16 and 250 mm. Evenly spaced lines every 1000 mm in (b) match approximately peaks of spatial correlation, which display a regularly spaced pattern, indicative of periodically arranged clusters. (c) Power spectrum of spatial correlation from (b). A noticeable peak at 1001 mm has a power spectral density that is several times the equivalent for the 95% confidence interval for red noise, indicating a periodic arrangement of fractures that is statistically significant and with a cluster spacing of 1001 mm.

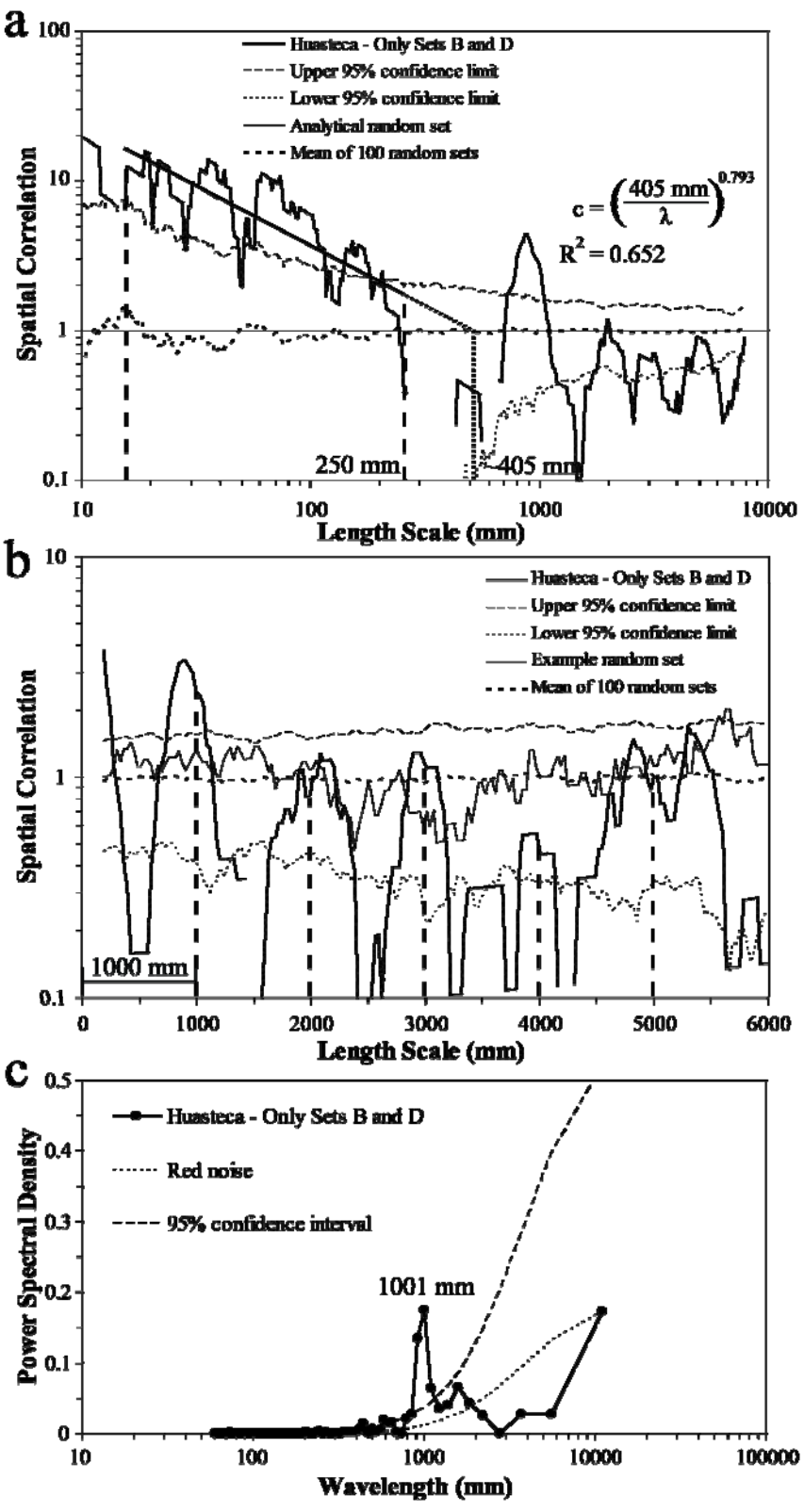
a
Huasteca - Only Sets B and D
Upper 95% confidence limit
Lower 95% confidence limit
Analytical random set
Mean of 100 random sets
$c = \left(\frac{405\ mm}{\lambda}\right)^{0.793}$
$R^2 = 0.652$
250 mm
405 mm
Spatial Correlation
Length Scale (mm)
b
Huasteca - Only Sets B and D
Upper 95% confidence limit
Lower 95% confidence limit
Example random set
Mean of 100 random sets
1000 mm
Spatial Correlation
Length Scale (mm)
c
Huasteca - Only Sets B and D
Red noise
95% confidence interval
1001 mm
Power Spectral Density
Wavelength (mm)

Figure 8.23 Graphs of spatial correlation (thick continuous line) vs. length scale for (a) logarithmic graduations and (b) linear graduations for fractures of set C of the Huasteca outcrop data set (54 fractures, aperture threshold of 0.215 mm,). In (a) and (b) the thin discontinuous line represents the upper 95% confidence interval while the thin dotted line represents the lower 95% confidence interval, and the thick discontinuous line corresponds to the mean of 100 randomized data sets. In (a) the thin continuous line represents the analytical solution of randomly arranged fractures with the same number of fractures and scanline length. In (b) the thin continuous line represents an example randomized set generated with an equivalent number of fractures and scanline length. Width of length-scale bin is 15 graduations of length scale (m = 7) in both (a) and in (b). Power law in (a) was calculated for spatial correlation between length scales of 73 and 900 mm. Cluster width is approximately 900 mm, as shown in (a). Evenly spaced lines every 2100 mm in (b) match approximately peaks of spatial correlation, which display a regularly spaced pattern, indicative of periodically arranged clusters. (c) Power spectrum of spatial correlation from (b). A noticeable peak at 2105 mm has a power spectral density that is several times the equivalent for the 95% confidence interval for red noise, indicating a periodic arrangement of fractures that is statistically significant and with a cluster spacing of 2105 mm.

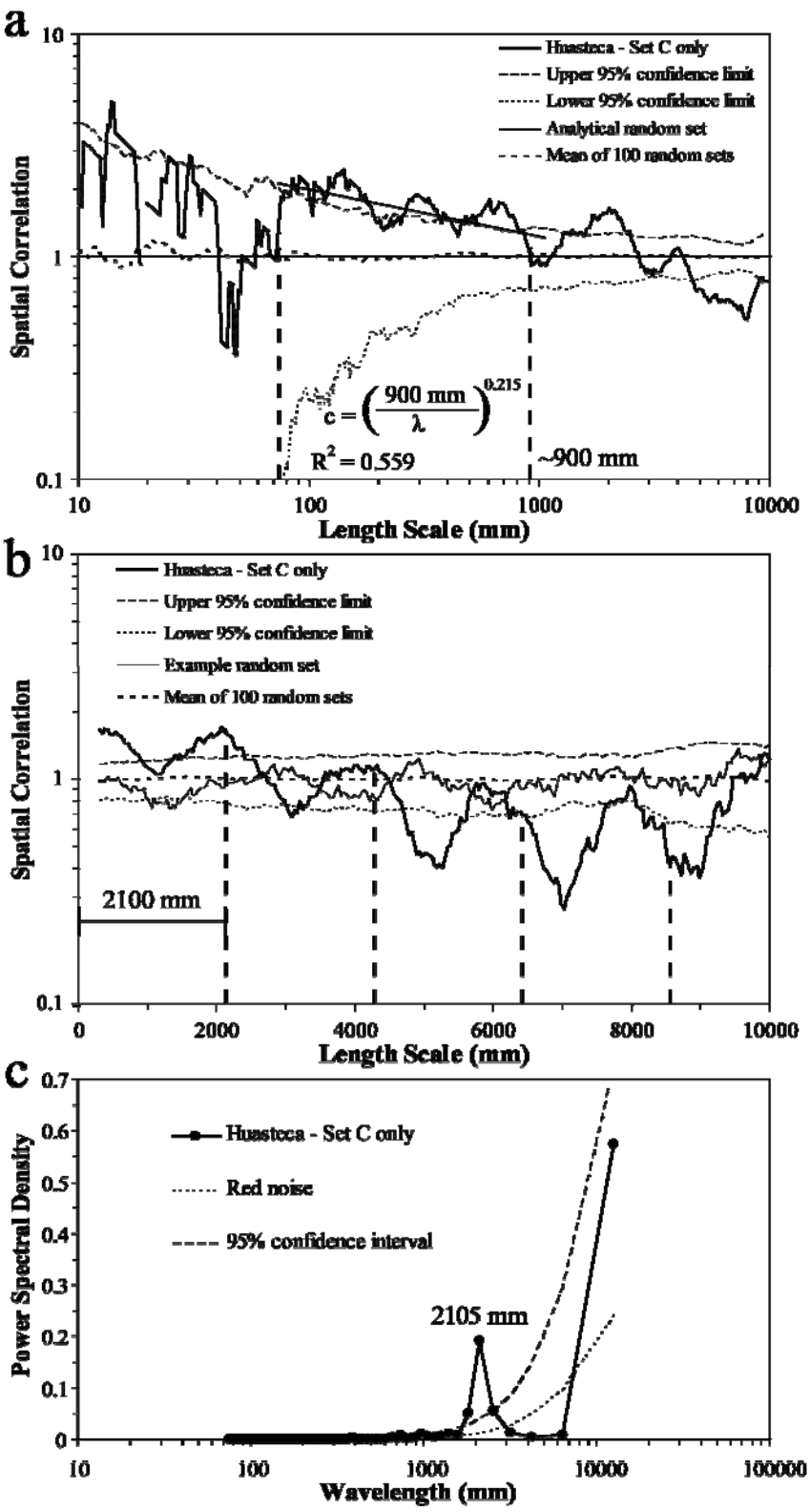
a
Huasteca - Set C only
Upper 95% confidence limit
Lower 95% confidence limit
Analytical random set
Mean of 100 random sets
Spatial Correlation
$c = \left(\frac{900\ mm}{\lambda}\right)^{0.215}$
$R^2 = 0.559$
~900 mm
Length Scale (mm)
b
Huasteca - Set C only
Upper 95% confidence limit
Lower 95% confidence limit
Example random set
Mean of 100 random sets
Spatial Correlation
2100 mm
Length Scale (mm)
c
Huasteca - Set C only
Red noise
95% confidence interval
Power Spectral Density
2105 mm
Wavelength (mm)

8.2.3.2 Rock Sample Scale

Two consecutive thin sections were generated from a sample obtained along the outcrop scanline (Figure 8.19c; Table 8.2). Although clusters were qualitatively detectable at outcrop scale, it was not possible to obtain a sample that contains an entire cluster, only part of a cluster. Macrofractures within clusters at Huasteca appear to be regularly spaced (Figure 8.19c). A total of 34 transgranular fractures were mapped in 122 mm of scanline that recorded a strain of 0.92% (Table 8.2). Minimum and maximum fracture apertures measured were 0.0036 and 0.1363 mm.

Spatial correlation for logarithmically graduated length scales of the Huasteca rock sample data set yields a non-systematic pattern, which indicates arrangement of fractures is indistinguishable from random (Figures 8.5a and 8.24a). Spatial correlation for linearly graduated length scales shows alternating shallow peaks and troughs, which might indicate either a periodic arrangement of fractures (Figure 8.5f) or a periodic arrangement of fracture clusters (Figure 8.5g). However, the statistical significance of the periodic arrangement of clusters is questionable because no peak of spatial correlation is outside the 95% confidence interval (Figure 8.24b). Power spectrum of spatial correlation for linearly graduated length scales yields a peak of power spectral density outside the 95% confidence interval for red noise at a wavelength of 29 mm (Figure 8.24c), which indicates the periodic arrangement of clusters with a cluster spacing of 29 mm of Huasteca rock sample data set is statistically significant.

Figure 8.24 Graphs of spatial correlation vs. length scale (thick continuous line) for (a) logarithmic graduations and (b) linear graduations for the Huasteca rock sample data set (34 fractures). Fractures were mapped on images obtained from a petrographic microscope. In (a) and (b) the thin discontinuous line represents the upper 95% confidence limit while the thin dotted line represents the lower 95% confidence limit, and the thick discontinuous line corresponds to the mean of 100 randomized data sets. In (a) and (b) the thin continuous line represents the analytical solution of randomly arranged fractures with the same number of fractures and scanline length. Width of length-scale bin in (a) is 17 (m = 8) and 33 (m = 16) graduations of length scale for (b). Spatial correlation in (a) does not exhibit a recognizable (e.g., power law) pattern outside the 95% confidence interval. Variations of spatial correlation with length scale in (b) could be interpreted as indicative of periodically arranged fracture clusters with a cluster spacing of 29 mm. (c) Power spectrum of spatial correlation from (b). The power spectrum for the natural data set exhibits a peak of power spectral density outside the 95% confidence interval for red noise at a wavelength equal to the cluster spacing estimated in (b), which indicates that the periodic arrangement of fracture clusters in (b) is statistically significant.

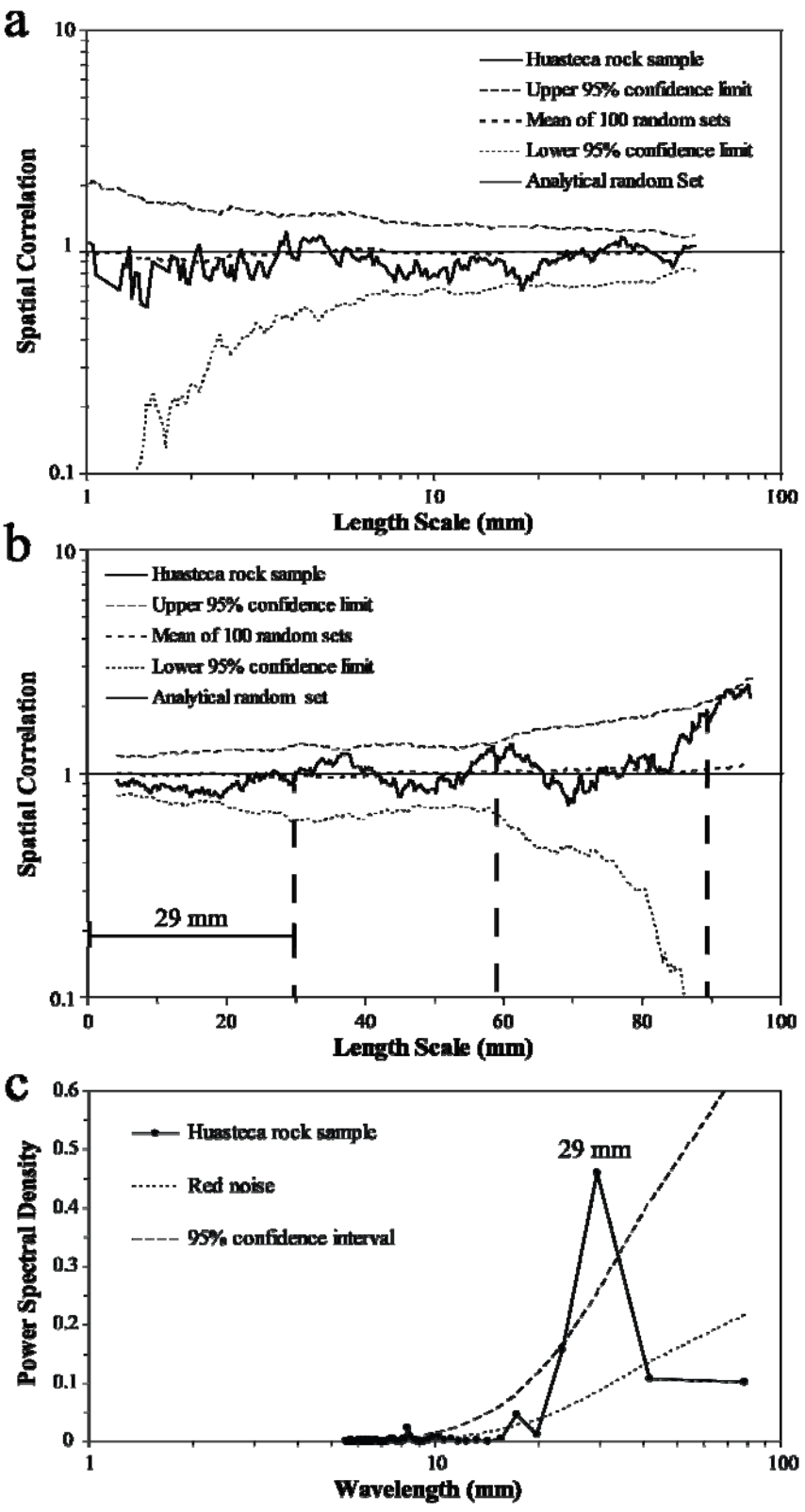
a
Huasteca rock sample
Upper 95% confidence limit
Mean of 100 random sets
Lower 95% confidence limit
Analytical random Set
Spatial Correlation
Length Scale (mm)
b
Huasteca rock sample
Upper 95% confidence limit
Mean of 100 random sets
Lower 95% confidence limit
Analytical random set
29 mm
Spatial Correlation
Length Scale (mm)
c
Huasteca rock sample
Red noise
95% confidence interval
29 mm
Power Spectral Density
Wavelength (mm)

8.2.4 Layer 11 at Palmas Canyon (Palmas 11 LR)

8.2.4.1 Outcrop Scale

Two data sets with different resolutions were measured by Dr. J. Gale in the layer Palmas 11. Palmas 11 LR data set has an aperture threshold of 0.95 mm, whereas the Palmas 11 HR data set has an aperture threshold of 0.075 mm. Palmas 11 is a 27 cm thick lime dolowackstone that suffered dedolomitization. Palmas 11 is located 84 m above the base of the stratigraphic column measured by Ortega (2001) in the forelimb of San Blas anticline at Palmas canyon and is located 20 m above the lower boundary of the Cupidito member of the Cupido Formation (Ortega, 2002). The Palmas 11 LR data set was measured in a cross sectional exposure along a 21.1 m long scanline (Table 8.1). Three sets (A, B, and C) of fractures were recorded in Palmas 11 LR (Table 8.4). 44% of the fractures measured represent set A, 35% represent set B, and 21% represent set C (Table 8.4). The Palmas 11 LR data set consists of 262 veins, which record a strain of 4.59% (Table 8.1). Fractures of the Palmas 11 LR data set exhibit a power-law distribution of apertures, a log-normal distribution of spacings, and a coefficient of variation for spacings of 1.72 (Table 8.5). In thin sections, fractures exhibit most of the typical features of Y fractures such as straight traces, microfractures that occasionally anastomose, fibrous dolomite crystals lining fracture walls, bridges of subhedral dolomite and quartz, and calcite precipitated between bridges (Table 8.3).

The Palmas 11 LR data set displays a heterogeneous arrangement of fractures in space, as shown by fracture intensity in Figure 8.25 (Marrett et al., 2004). Although clustering is obscured by cluster width that is small compared with the scanline length (Figure 8.25a), NCC shows a power-law pattern of spatial correlation for logarithmically graduated length scales (Figures 8.5b and 8.26a), which in turn have a periodic arrangement (Figures 8.5g and 8.26b). , a combination of spatial arrangements described

in Figure 8.5d (Marrett et al., in review). Cluster width and cluster spacing are 220 mm (Figure 8.26a) and 1100 mm (Figure 8.26b), respectively. The power spectrum of spatial correlation for linearly graduated length scales displays a significant peak at a wavelength of 1089 mm, which indicates a statistically significant periodic arrangement of clusters spaced at 1089 mm (Figure 8.26c). Although power spectrum also yielded a peak at a wavelength of 4900 mm, this peak has a power spectral density smaller than randomly arranged fractures and therefore cannot be considered statistically significant (Figure 8.26c).

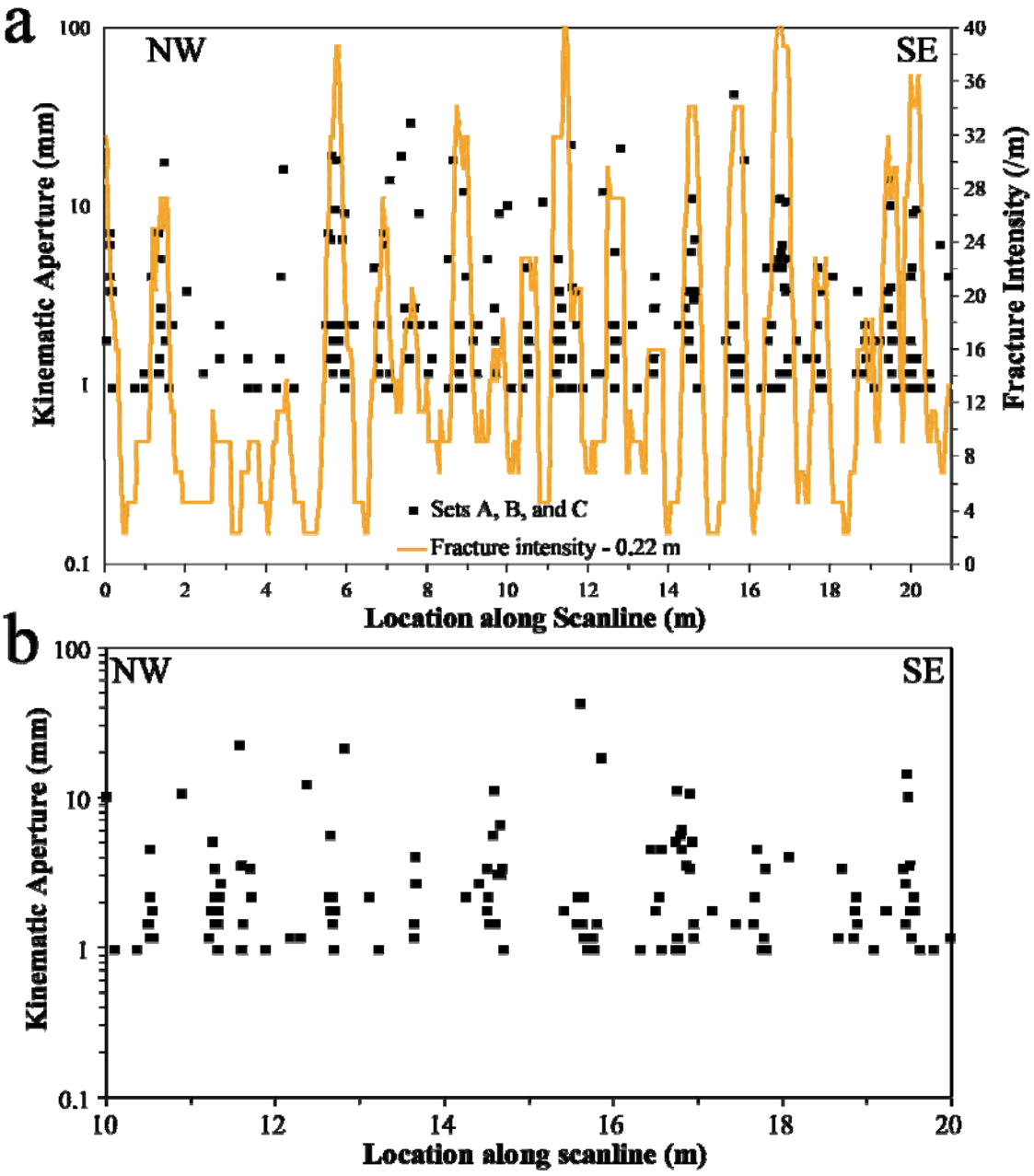

Figure 8.25 Kinematic aperture (squares) and fracture intensity (orange thick line) versus location along scanline for all (a) and part (b) of the Palmas 11 LR data set. Fracture intensity was calculated inside a moving window with width (window size) equal to cluster width as estimated by NCC (0.22 m, Figure 8.26a) that was moved in increments (window step) of 0.05 m. Please note that only the kinematic aperture axis use logarithmic graduations. Clusters are more easily detected in (b) than in (a) because cluster width is larger compared with the plotted scanline.

Figure 8.26 Graphs of spatial correlation (thick continuous line) vs. length scale for (a) logarithmic graduations and (b) linear graduations for the Palmas 11 LR data set (262 fractures, all fracture sets combined, aperture threshold of 0.95 mm). In (a) and (b) the thin discontinuous line represents the upper 95% confidence limit while the thin dotted line represents the lower 95% confidence limit, and the thick discontinuous line corresponds to the mean of 100 randomized data sets. In (a) and (b) the thin continuous line represents an example randomized set generated with the same number of fractures and scanline length. Width of length-scale bin in (a) and (b) is 5 graduations of length scale ($m = 2$). Spatial correlation in (a) follows a power-law pattern. Power law equation in (a) was calculated using spatial correlation of Palmas 11 LR data set between length scales of 12 and 664 mm. Cluster width is approximately 220 mm, as shown in (a). Evenly spaced lines every 1100 mm in (b) match approximately peaks of spatial correlation, which display a regularly spaced pattern, indicative of periodically arranged clusters with a cluster spacing of approximately 1100 mm. (c) Power spectrum of spatial correlation from (b). A noticeable peak at a wavelength of 1089 mm has a power spectral density that is several times the equivalent for the 95% confidence interval for red noise, indicating a periodic arrangement of fractures that is statistically significant and with a cluster spacing of 1089 mm.

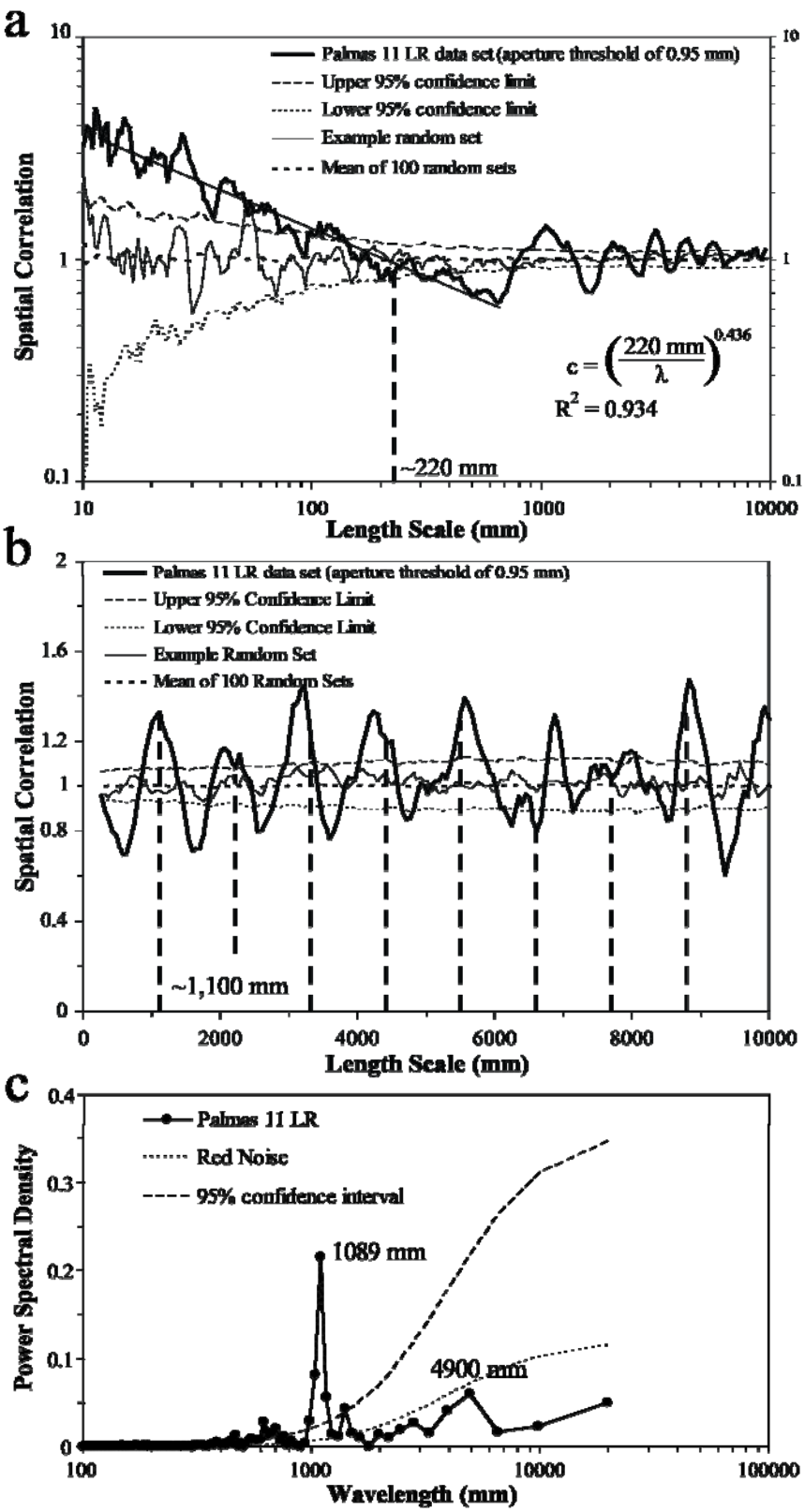
a
Palmas 11 LR data set (aperture threshold of 0.95 mm)
Upper 95% confidence limit
Lower 95% confidence limit
Example random set
Mean of 100 random sets
Spatial Correlation
$c = \left(\frac{220\ mm}{\lambda}\right)^{0.436}$
$R^2 = 0.934$
~220 mm
Length Scale (mm)
b
Palmas 11 LR data set (aperture threshold of 0.95 mm)
Upper 95% Confidence Limit
Lower 95% Confidence Limit
Example Random Set
Mean of 100 Random Sets
Spatial Correlation
~1,100 mm
Length Scale (mm)
c
Palmas 11 LR
Red Noise
95% confidence interval
Power Spectral Density
1089 mm
4900 mm
Wavelength (mm)

8.2.4.2 Rock Sample Scale

Two sets of thin sections were generated from a single sample (PA11JG), which was extracted outside of the clearly visible clusters at outcrop scale (J. Gale, personal communication, 2005). The first set contains two consecutive thin sections from which a 64 mm scanline crossing 156 transgranular fractures was measured (Table 8.2). The second set comprises only one thin section, which allowed measurement of 86 fractures along a 38 mm scanline (Table 8.2). The recorded strain for the two scanlines of Palmas 11 rock sample is 14.6% and 15.6%, respectively (Table 8.2). Minimum and maximum fracture apertures measured for the first set were 0.0035 and 0.4241 mm. Minimum and maximum fracture apertures measured for the second set were 0.0202 and 0.3771 mm.

Both scanlines from Palmas 11 yielded non-systematic patterns of spatial correlation for logarithmically graduated length scales, which indicates an arrangement of fractures that is indistinguishable from random (Figures 8.5a, 8.27a and 8.28a). Spatial correlation for linearly graduated length scales for both Palmas 11 rock sample scanlines yielded similar patterns, alternating peaks and troughs that are suggestive of periodical arrangements. However, peaks of spatial correlation are not multiples of the first peak and are smaller than the 95% confidence interval (Figures 8.27b and 8.28b), which indicates that fractures have an arrangement that is indistinguishable from random (Figure 8.5e). Evenly spaced peaks at length scale multiples of the first peak is a requisite for interpreting a periodic arrangement of fracture clusters (Marrett et al., in review). Power spectra of spatial correlation for linearly graduated length scales show peaks of power spectral density that are slightly outside (wavelength of 12 mm, Figure 8.27c) or barely reaching the 95% confidence interval for red noise (wavelengths of 5 and 9 mm, Figure 8.28c), which suggest that the periodic arrangement of clusters suggested by spatial correlation is not statistically significant.

Figure 8.27 Graphs of spatial correlation (thick continuous line) vs. length scale for (a) logarithmic graduations and (b) linear graduations for the Palmas 11 LR rock sample data set 1 (156 fractures). In (a) and (b) the thin discontinuous line represents the upper 95% confidence limit while the thin dotted line represents the lower 95% confidence limit, and the thick discontinuous line corresponds to the mean of 100 randomized data sets. In (a) and (b) the thin continuous line represents the analytical solution of randomly arranged fractures with the same number of fractures and scanline length. Width of length-scale bin in (a) is 7 (m = 3) and 5 (m = 2) graduations of length scale in (b). Spatial correlation in (a) does not follow a pattern. Although two (perhaps three) peaks of spatial correlation can be interpreted in (b) at length scales of 13 and 23 mm, those two peaks are smaller than the 95% confidence interval and do not seem to be approximately evenly-spaced; a fundamental requirement to interpret a pattern indicative of a periodic arrangement of fracture clusters. (c) Power spectrum of spatial correlation from (b). The power spectral density for the natural data set exhibits the same trend as the red noise, as shown in (c). The natural data set exhibits a peak at a wavelength of 12 mm, which has a power spectral density slightly larger than the 95% confidence interval for red noise, but the difference between the peak and the 95% confidence interval is small when compared with other data sets (e.g., Eastern 1.6 m of Escalera OO1 data set, Figure 9.10c).

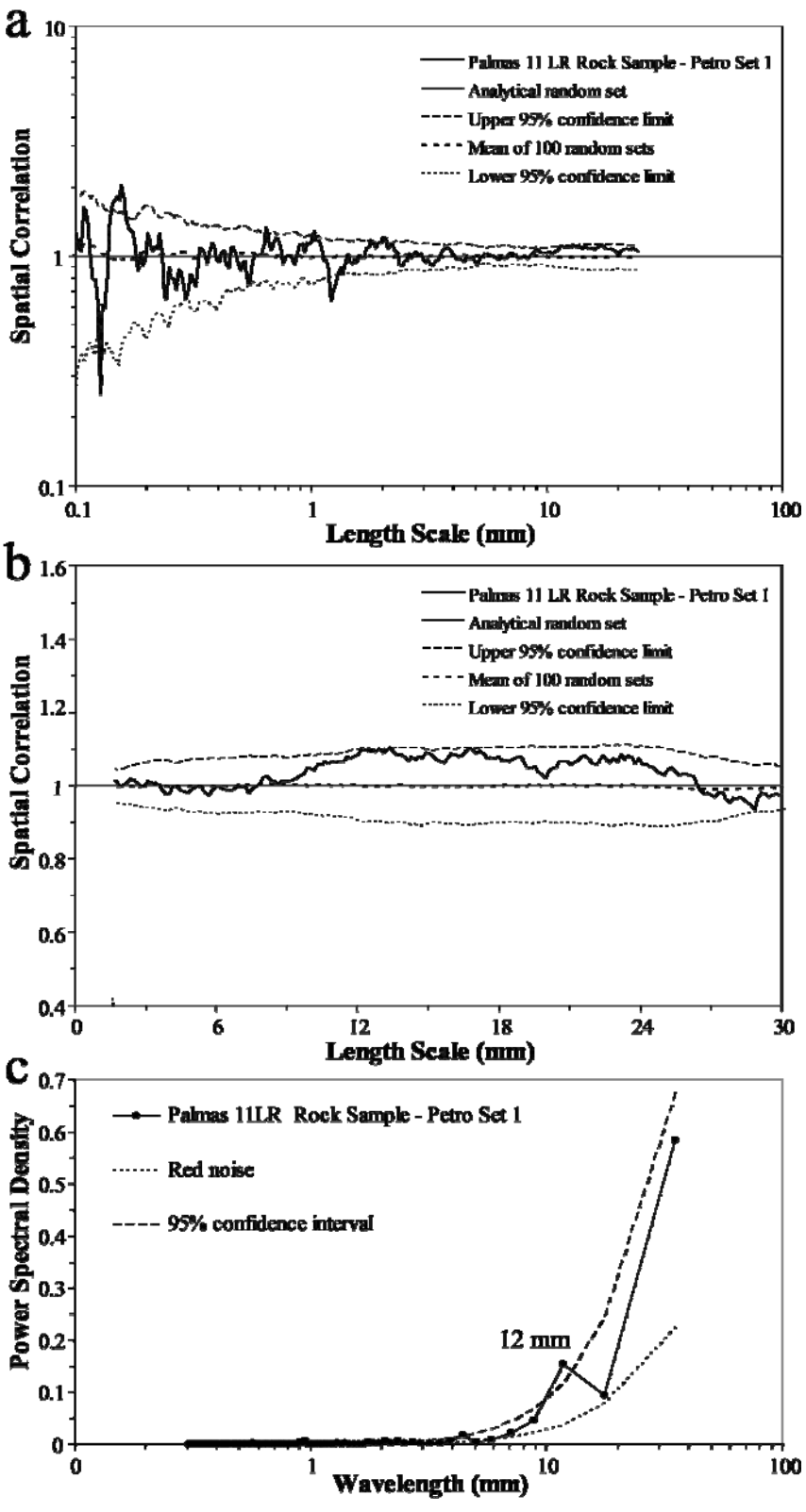
a
Palmas 11 LR Rock Sample - Petro Set 1
Analytical random set
Upper 95% confidence limit
Mean of 100 random sets
Lower 95% confidence limit
Spatial Correlation
Length Scale (mm)
b
Palmas 11 LR Rock Sample - Petro Set 1
Analytical random set
Upper 95% confidence limit
Mean of 100 random sets
Lower 95% confidence limit
Spatial Correlation
Length Scale (mm)
c
Palmas 11LR Rock Sample - Petro Set 1
Red noise
95% confidence interval
12 mm
Power Spectral Density
Wavelength (mm)

Figure 8.28 Graphs of spatial correlation (thick continuous line) vs. length scale for (a) logarithmic graduations and (b) linear graduations for the Palmas 11 LR rock sample data set 2 (86 fractures). In (a) and (b) the thin discontinuous line represents the upper 95% confidence limit while the thin dotted line represents the lower 95% confidence limit, and the thick discontinuous line corresponds to the mean of 100 randomized data sets. In (a) and (b) the thin continuous line represents the analytical solution of randomly arranged fractures with the same number of fractures and scanline length. Width of length-scale bin in (a) is 7 (m = 3) and 21 (m = 10) graduations of length scale in (b). Spatial correlation in (a) does not follow a pattern. Although three peaks of spatial correlation can be interpreted in (b) at length scales of 9, 14 and 18 mm, those two peaks are smaller than the 95% confidence interval and may or may not be approximately evenly-spaced; a fundamental requirement to interpret a pattern indicative of a periodic arrangement of fracture clusters. (c) Power spectrum of spatial correlation from (b). The power spectral density for the natural data set exhibits the same trend as the red noise, as shown in (c). The natural data set exhibits two peaks at wavelength of 5 and 9 mm, which have power spectral density equal or slightly smaller than the 95% confidence interval for red noise, and therefore are likely not statistically significant.

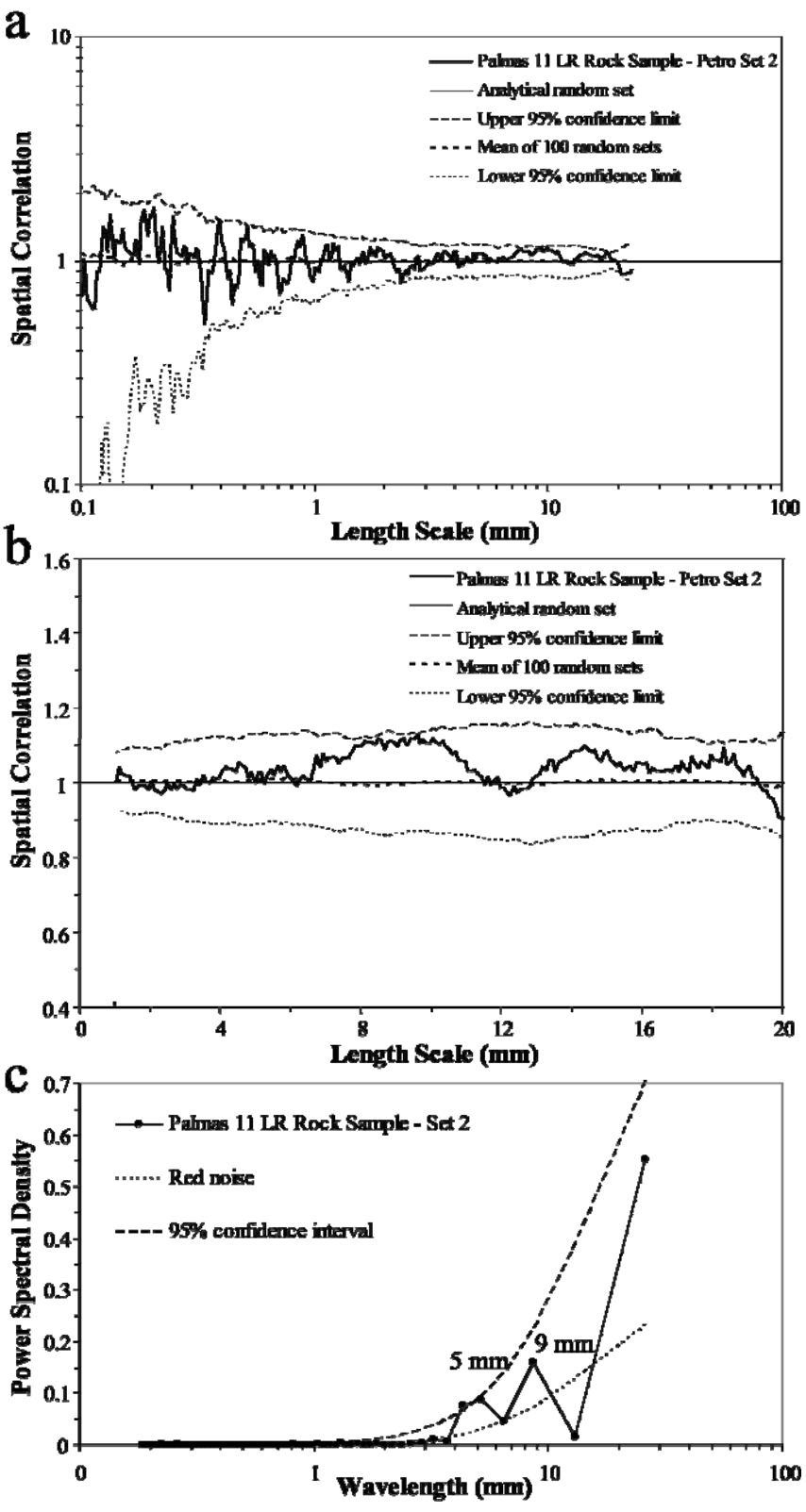
a
Palmas 11 LR Rock Sample - Petro Set 2
Analytical random set
Upper 95% confidence limit
Mean of 100 random sets
Lower 95% confidence limit
Spatial Correlation
Length Scale (mm)
b
Palmas 11 LR Rock Sample - Petro Set 2
Analytical random set
Upper 95% confidence limit
Mean of 100 random sets
Lower 95% confidence limit
Spatial Correlation
Length Scale (mm)
c
Palmas 11 LR Rock Sample - Set 2
Red noise
95% confidence interval
5 mm
9 mm
Power Spectral Density
Wavelength (mm)

8.2.5 Layer 12 at Palmas Canyon (Palmas 12)

8.2.5.1 Outcrop Scale

Palmas 12 layer is located stratigraphically between layers 11 and 13, two other layers from Palmas canyon. Palmas 12 is located approximately 7 m stratigraphically above the layer Palmas 11, above the stratigraphic column measured by Ortega (2002) in the forelimb of the San Blas anticline, and therefore is also within the Cupidito member of the Cupido Formation. Palmas 12 is a 47-cm thick lime dolowackstone. Using a threshold of 0.265 mm, I measured 316 calcite-filled veins in a scanline of approximately 6.1 m, and recorded a strain of 12.7% (Figure 8.29; Table 8.1). Palmas 12 fractures exhibit a power-law distribution of apertures, a negative exponential distribution of spacings, and a coefficient of variation for spacings of 1.07 (Table 8.5). 60% of the fractures measured represent set A and 40% represent set B (Table 8.4). In thin sections, fractures of sets A and B exhibit typical features of X fractures such as irregular traces, microfractures with ghost or relic textures, euhedral and translucent bridges of dolomite with local bands of fluid inclusions, and calcite precipitated between dolomite bridges (Table 8.3). Like Layers 11 and 13 at Palmas canyon, the scanline of Layer 12 was positioned in the middle of a cross-sectional outcrop (Table 8.1).

Qualitative examination of a photograph of the Palmas 12 outcrop reveals no relationship between aperture and clustering (Figure 8.30). In contrast a graph of kinematic aperture and fracture intensity versus location along scanline suggests the clusters (as indicated by fracture intensity) might be regularly-spaced betwen 1.1 and 1.5 m (Figure 8.29). Outcrop data set from Palmas 12 yielded a non-systematic pattern of spatial correlation for logarithmically graduated length scales, which indicates an arrangement of fractures that is indistinguishable from random (Figures 8.5a and 8.31a). Spatial correlation for linearly graduated length scales makes alternating low amplitude

peaks and troughs, which might indicate a periodic arrangement of clusters (Figures 8.5g and 8.31b). A peak of power spectral density outside the 95% confidence interval suggests that clusters might be periodically arranged with a spacing of approximately 461 mm (Figure 8.31c), which is a cluster spacing similar to the one suggested by NCC (dashed lines, Figure 8.31b). However, three reasons indicate the pattern of spatial correlation is best interpreted as indistinguishable from random (Figure 8.5e). First, none of the peaks of spatial correlation are statistically significant (outside the 95% confidence interval). Second, the amplitude between peaks and troughs of spatial correlation is smaller than the 95% confidence interval (Figure 8.31b). And third, the peak of power spectral density at 461 mm is only slightly above the 95% confidence interval for red noise (Figure 8.31c).

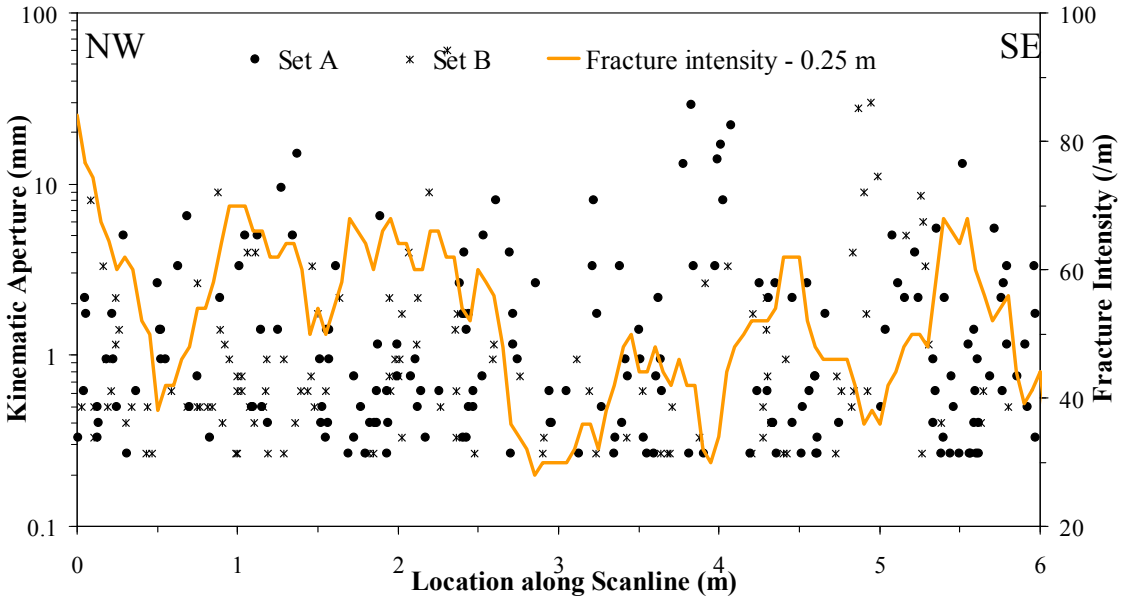

Figure 8.29 Kinematic aperture (circles for set A, asterisks for set B) and fracture intensity versus location along scanline for the Palmas 12 data set. Note that kinematic aperture axis uses logarithmic graduations. Fracture intensity was calculated inside a moving window with width (window size) of 0.25 m that was moved in increments (window step) 0.03 m. Peaks of fracture intensity could indicate statistically significant clusters at 1, 2.5, 3.4, 4.5, and 5.6 m.

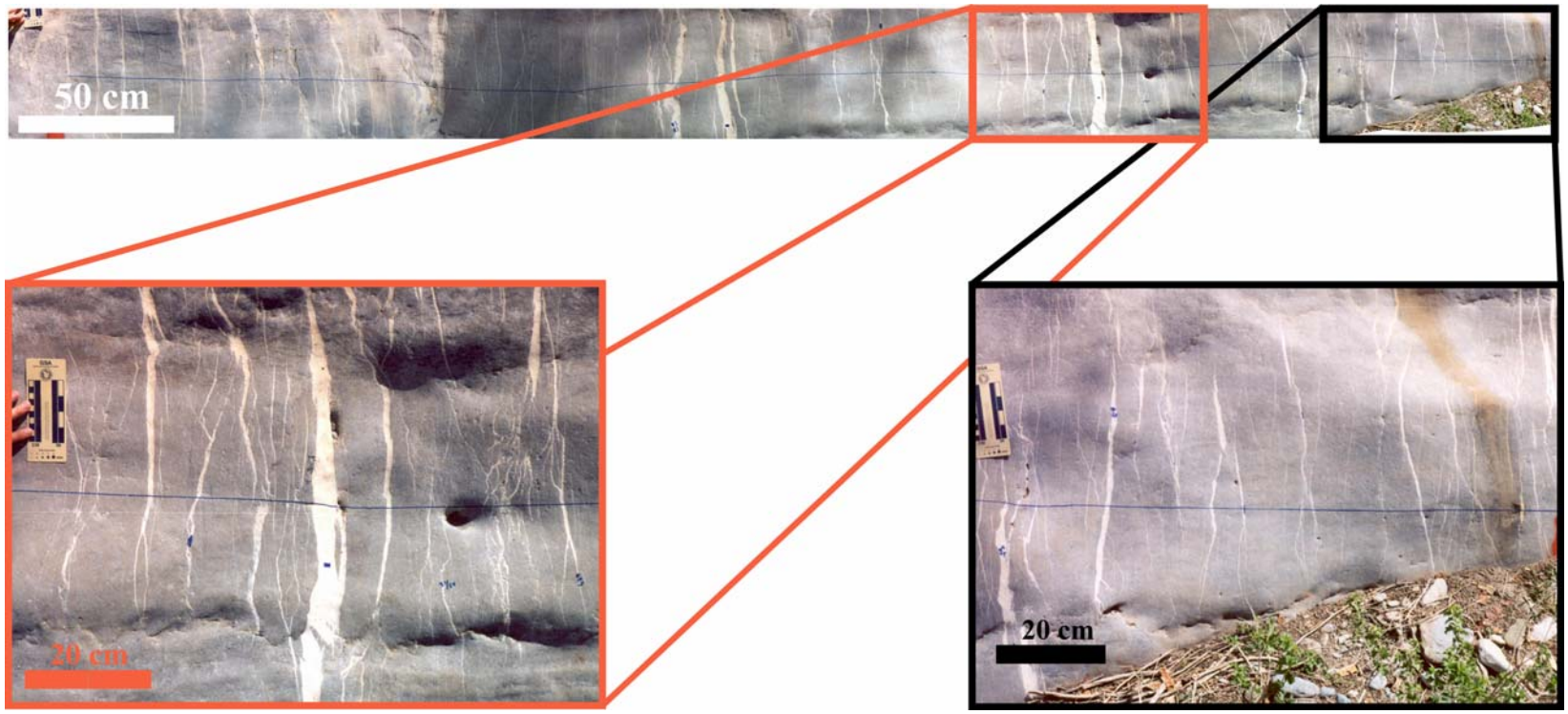

Figure 8.30 Photograph of most of the scanline on layer 12 from Palmas canyon (dark line is scanline). Insets at bottom of figure show detail views of the outcrop. No apparent clustering is qualitatively detectable on this layer. Notice the variation if fracture aperture and spacing encountered along the scanline.

Figure 8.31 Graphs of spatial correlation vs. length scale (thick continuous line) for (a) logarithmic graduations and (b) linear graduations for fractures of the Palmas 12 data set (316 fractures, all fracture sets combined, aperture threshold of 0.265 mm). In (a) and (b) the thin discontinuous line represents the upper 95% confidence limit while the thin dotted line represents the lower 95% confidence limit, and the thick discontinuous line corresponds to the mean of 100 randomized data sets. In (a) and (b) the thin continuous line represents the analytical solution of randomly arranged fractures with the same number of fractures and scanline length. Width of length-scale bin in (a) and (b) is 11 graduations of length scale (m = 5). There is no pattern of spatial correlation that can be identified (e.g., power law) outside the 95% confidence interval in (a). Variations of spatial correlation with length scale in (b) cannot be conclusively interpreted as periodically arranged clusters. (c) Power spectrum of spatial correlation from (b). The power spectral density for the natural data set exhibits the same trend as the red noise, as shown in (c). The natural data set exhibits a peak at a wavelength of 461 mm, which has a power spectral density slightly larger than the 95% confidence interval for red noise, but the difference between the peak and the 95% confidence interval is small when compared with other data sets (e.g., Eastern 1.6 m of Escalera OO1 data set, Figure 9.10c).

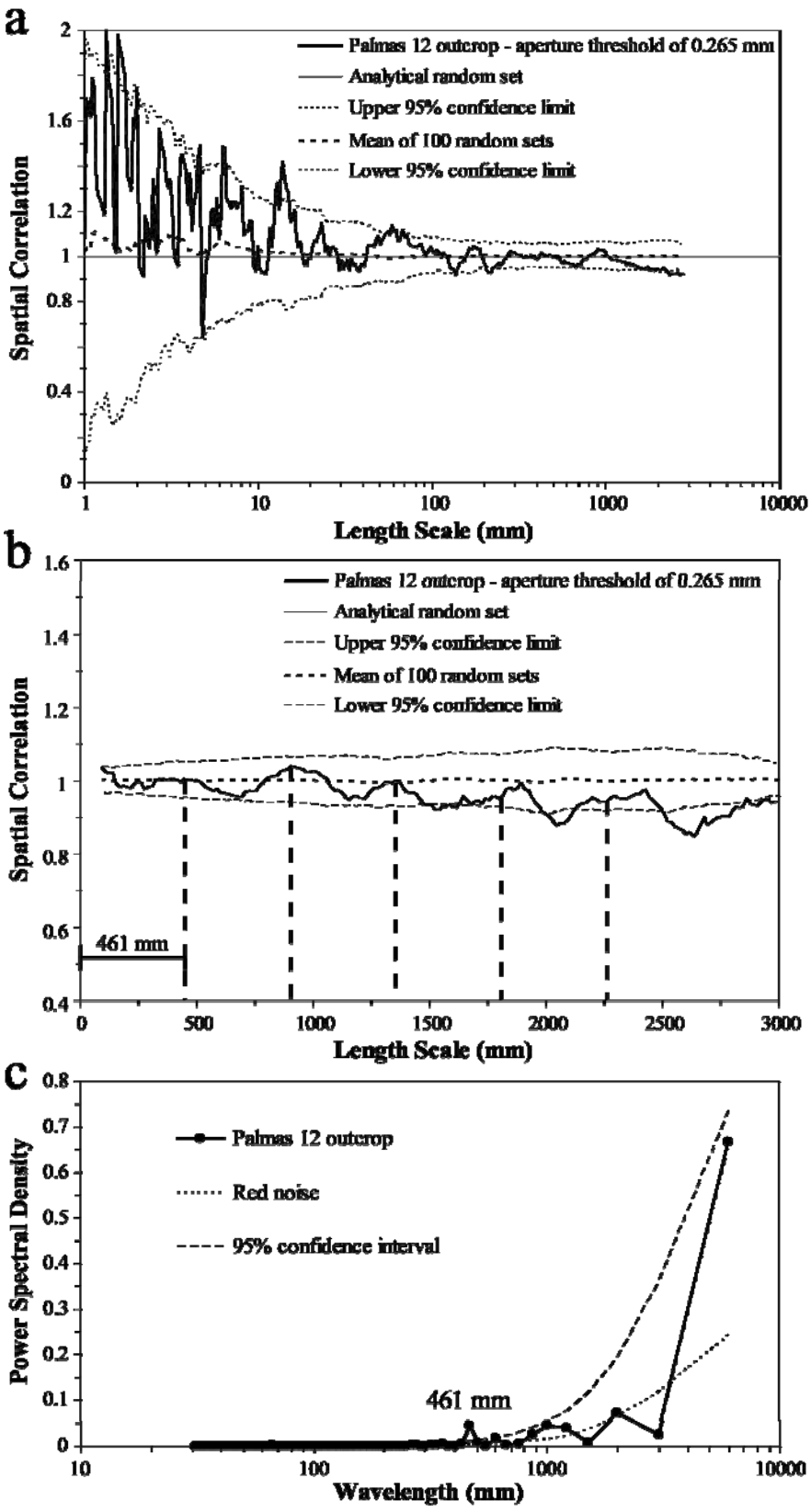
a
Palmas 12 outcrop - aperture threshold of 0.265 mm
Analytical random set
Upper 95% confidence limit
Mean of 100 random sets
Lower 95% confidence limit
Spatial Correlation
Length Scale (mm)
b
Palmas 12 outcrop - aperture threshold of 0.265 mm
Analytical random set
Upper 95% confidence limit
Mean of 100 random sets
Lower 95% confidence limit
Spatial Correlation
461 mm
Length Scale (mm)
c
Palmas 12 outcrop
Red noise
95% confidence interval
Power Spectral Density
461 mm
Wavelength (mm)

8.2.5.2 Rock Sample Scale

Two consecutive thin sections were generated from the Palmas 12 rock sample (Table 2.3). A total of 29 transgranular fractures were mapped in 101 mm of scanline that recorded a strain of 14.6% (Table 2.3). Minimum and maximum fracture apertures measured were 0.0081 and 8.590 mm. Spatial correlation for logarithmically graduated length scales of Palmas 12 rock sample does not follow a pattern with length scale, which indicates an arrangement of fractures indistinguishable from random (Figures 8.5a and 8.32a). Spatial correlation for linearly graduated length scales shows alternating peaks and troughs separated 9.5 mm, suggesting periodically arranged fracture clusters and a cluster spacing of 9.5 mm (Figures 8.5g and 8.32b). However, none of peaks and troughs of spatial correlation in Figure 8.32b are outside the 95% confidence interval, indicating that the periodic arrangement of fracture clusters might not be statistically significant. Power spectrum of spatial correlation for linearly graduated length scales shows a peak of power spectral density at 9.5 mm, supporting a periodic arrangement of clusters with a cluster spacing of 9.5 mm (Figure 8.32c).

As explained by Marrett et al. (in review), cluster width is typically estimated at the crossover between the power-law pattern and a horizontal line defined by spatial correlation of 1 (Figure 8.5b) or at the crossover between the lower length scale of the inherited/imposed pattern with a horizontal line defined by spatial correlation of 1 (Figure 8.5c). Although less certain, another method to estimate cluster width is to observe the smallest length scale smaller than cluster spacing (Figure 8.5g). For rock sample of Palmas 12 cluster width is estimated at 2 mm (Figure 8.35b).

Figure 8.32 Graphs of spatial correlation vs. length scale (thick continuous line) for (a) logarithmic graduations and (b) linear graduations for fractures of the Palmas 12 rock sample data set (29 fractures). In (a) and (b) the thin discontinuous line represents the upper 95% confidence limit while the thin dotted line represents the lower 95% confidence limit, and the thick discontinuous line corresponds to the mean of 100 randomized data sets. In (a) and (b) the thin continuous line represents the analytical solution of randomly arranged fractures with the same number of fractures and scanline length. Width of length-scale bin in (a) and (b) is 17 graduations of length scale (m = 9). There is no pattern of spatial correlation in (a) that can be identified (e.g., power law) outside the 95% confidence interval in (a). Evenly spaced lines every 9.5 mm in (b) match approximately peaks of spatial correlation, which could be interpreted as indicative of periodically arranged clusters. (c) Power spectrum of spatial correlation from (b). A noticeable peak at a wavelength of 9.5 mm has a power spectral density that is twice the equivalent for the 95% confidence interval for red noise, indicating a periodic arrangement of fractures that is statistically significant and with a cluster spacing of 9.5 mm. Periodicity at wavelengths of 31.6 mm, as indicated by peak of power spectral density in (c), is not evident in (b).

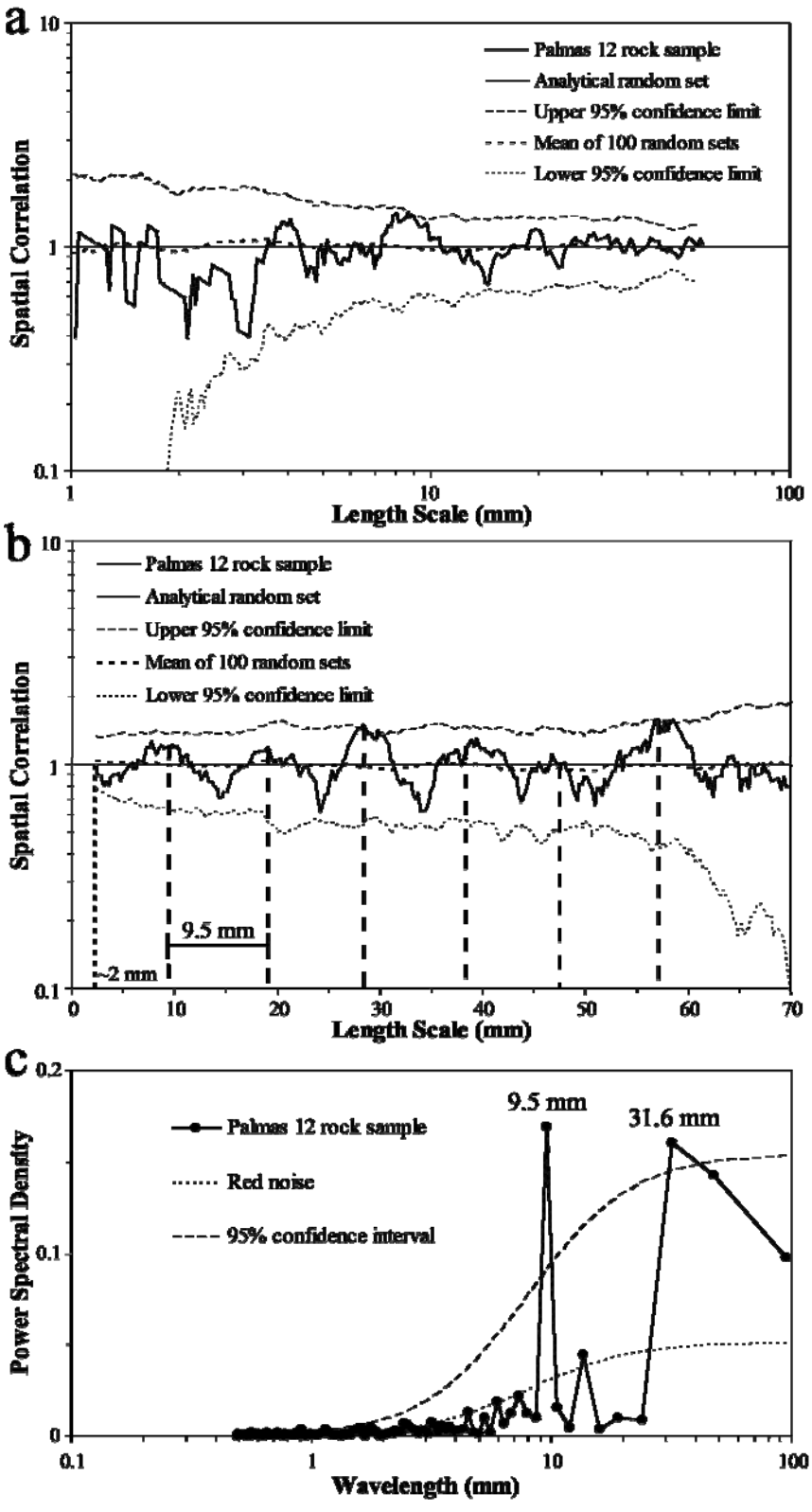
a
Palmas 12 rock sample
Analytical random set
Upper 95% confidence limit
Mean of 100 random sets
Lower 95% confidence limit
Spatial Correlation
Length Scale (mm)
b
Palmas 12 rock sample
Analytical random set
Upper 95% confidence limit
Mean of 100 random sets
Lower 95% confidence limit
Spatial Correlation
9.5 mm
2 mm
Length Scale (mm)
c
Palmas 12 rock sample
Red noise
95% confidence interval
9.5 mm
31.6 mm
Power Spectral Density
Wavelength (mm)

8.2.6 Layer 13 at Palmas Canyon (Palmas 13)

8.2.6.1 Outcrop Scale

Palmas 13 is a 24-cm thick dolowackstone located 11 m stratigraphically above layer Palmas 11, above the stratigraphic column measured by Ortega (2002) in the forelimb of the San Blas anticline, and therefore is within the Cupidito member of the Cupido Formation. Palmas 13 scanline was positioned in the middle of the layer in a cross-sectional outcrop (Figure 8.3b). Using an aperture threshold of 0.14 mm, in a scanline of approximately 5.5 m (Figure 8.33), I measured 459 veins, which display a strain of 9.16% (Table 8.1). Fractures at Palmas 13 exhibit a power-law distribution of apertures, a negative exponential distribution of spacings, and a coefficient of variation for spacings of 0.93 (Table 8.5). The two sets of fractures measured in Palmas 13 (A and B) have the same orientations as similarly named sets in Palmas 12 (Table 8.4). 62% of the fractures measured represent set A and 38% represent set B (Table 8.4). In thin sections, fractures of sets A and B exhibit the typical features of X fractures such as irregular traces, emergent threshold, euhedral and translucent bridges of dolomite that locally exhibit bands of fluid inclusions, and calcite precipitated between dolomite bridges (Table 8.3).

Spatial correlation for logarithmically graduated length scales did not yield a systematic pattern, which indicates an arrangement that is indistinguishable from random (Figures 8.5a and 8.34a). Spatial correlation for linearly graduated length scales lacks any recognizable pattern suggesting an arrangement that is indistinguishable from random (Figures 8.5e and 8.34b). In addition, the power spectrum of the spatial correlation for linearly graduated length scales shows a trend similar to red noise, which supports a spatial arrangement that is indistinguishable from random (Figure 8.34c). Spatial

correlation suggests that although Palmas 13 contains clusters (Figure 8.33), those clusters are not statistically significant.

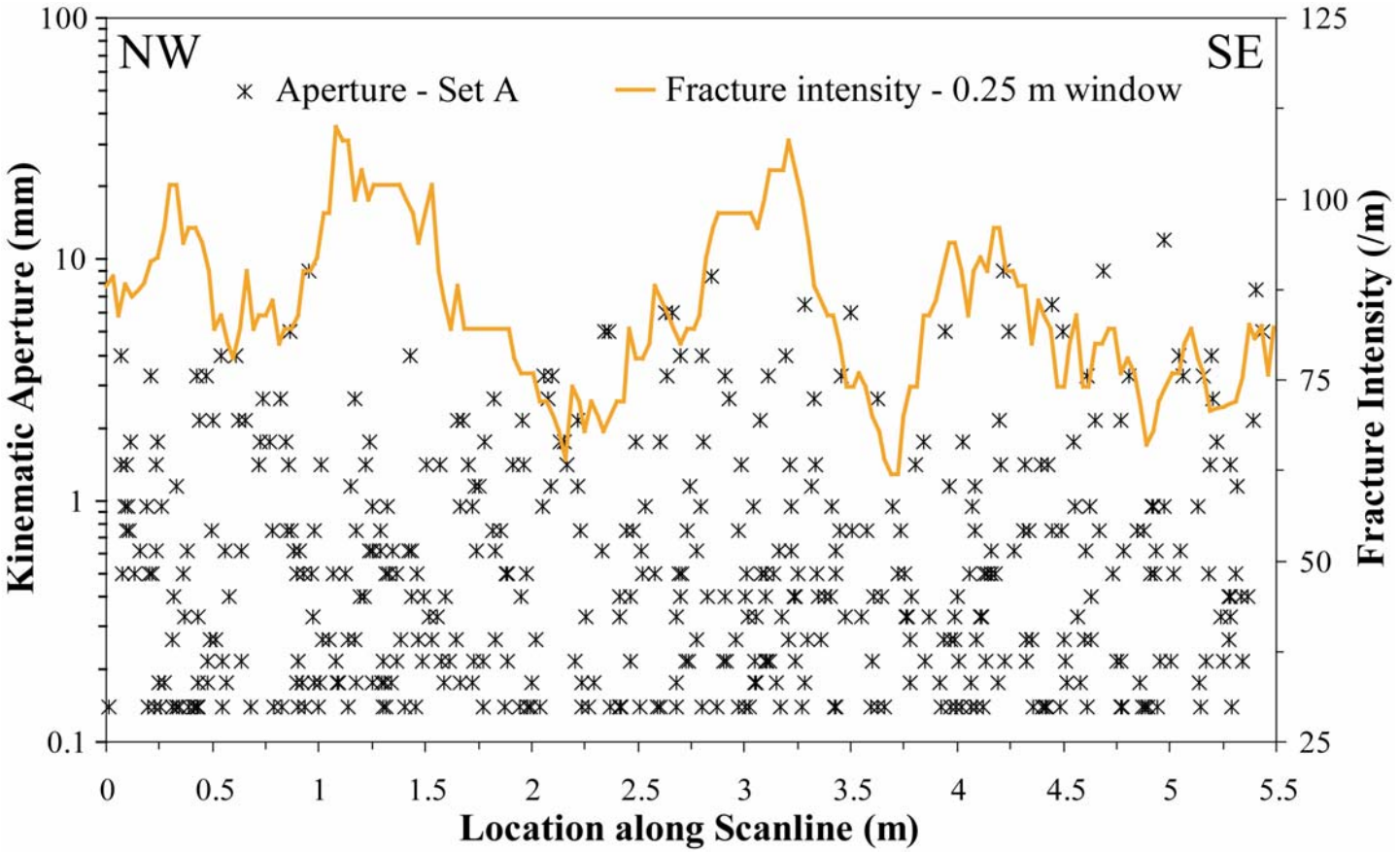

Figure 8.33 Kinematic aperture (asterisk) and fracture intensity (thick orange line) versus location along scanline for the Palmas 13 data set. Note that kinematic aperture axis uses logarithmic graduations. Fracture intensity was calculated inside a moving window with width (window size) of 0.25 m that was moved in increments (window step) 0.03 m. Peaks of fracture intensity indicate clusters at 0.25, 1.25, 3.25, and 4 m, but clusters do not seem regularly spaced.

Figure 8.34 Graphs of spatial correlation (thick continuous line) vs. length scale for (a) logarithmic graduations and (b) linear graduations for the Palmas 13 data set (459 fractures, all fractures sets, aperture threshold of 0.14 mm). In (a) and (b) the thin discontinuous line represents the upper 95% confidence limit while the thin dotted line represents the lower 95% confidence limit, and the thick discontinuous line corresponds to the mean of 100 randomized data sets. In (a) the thin continuous line represents the analytical solution of randomly arranged fractures with the same number of fractures and scanline length. In (b) the thin continuous line represents an example randomized set generated with the same number of fractures and scanline length. Width of length-scale bin in (a) and (b) is 7 graduations of length scale (m = 3). There is no pattern of spatial correlation that can be identified for logarithmic graduations of length scale (e.g., power law) in (a) or for linear graduations of length scale (e.g., regularly-spaced peaks) in (b). For all values of length scale, spatial correlation in both (a) and (b) remains within the 95% confidence interval, which indicates that spatial arrangements are indistinguishable from random. (c) Power spectrum of spatial correlation from (b). The power spectral density for the natural data set exhibits the same trend as the red noise, as shown in (c). The natural data set exhibits a peak at a wavelength of 380 mm, which has a power spectral density slightly larger than the 95% confidence interval for red noise, but the difference between the peak and the 95% confidence interval is small when compared with other data sets (e.g., Eastern 1.6 m of Escalera OO1 data set, Figure 9.10c).

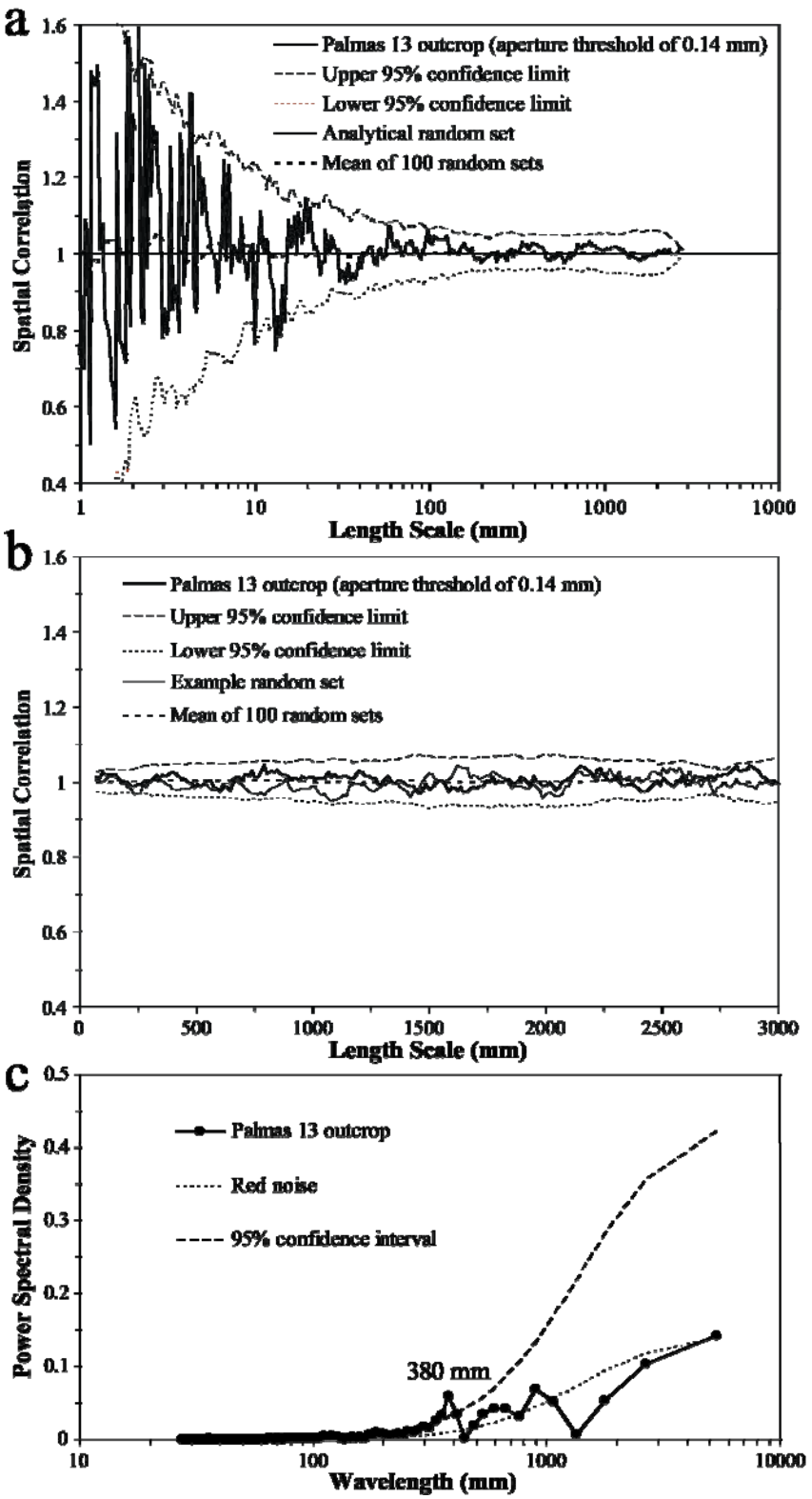
a
Palmas 13 outcrop (aperture threshold of 0.14 mm)
Upper 95% confidence limit
Lower 95% confidence limit
Analytical random set
Mean of 100 random sets
Spatial Correlation
Length Scale (mm)
b
Palmas 13 outcrop (aperture threshold of 0.14 mm)
Upper 95% confidence limit
Lower 95% confidence limit
Example random set
Mean of 100 random sets
Spatial Correlation
Length Scale (mm)
c
Palmas 13 outcrop
Red noise
95% confidence interval
380 mm
Power Spectral Density
Wavelength (mm)

8.2.6.2 Rock Sample Scale

Five consecutive thin sections were generated from Palmas 13 rock sample (Table 2.3). A total of 175 transgranular fractures recorded a strain of 8.08% along a 290 mm long scanline (Table 2.3). Minimum and maximum fracture apertures measured were 0.0046 and 4.0228 mm. Spatial correlation for logarithmically graduated length scales did not exhibit a systematic pattern outside the 95% confidence interval, which indicates a fracture arrangement that is indistinguishable from random (Figures 8.5a and 8.35a). In contrast, spatial correlation for linearly graduated length scales exhibits alternating peaks and troughs every 17 mm, which indicates a periodic arrangement of fracture clusters (Figures 8.5g and 8.35b). However, the pattern cannot be strictly interpreted as a periodic arrangement of fracture clusters (Marrett et al., in review) because only a small fraction of the peaks (20%) and troughs (0%) are outside the 95% confidence interval. However, power spectrum analysis of spatial correlation for linearly graduated length scales exhibits a peak of power spectral density at 17 mm outside the 95% confidence interval for red noise (Figure 8.35c), which indicates that the periodic arrangement of fracture clusters suggested by NCC is statistically significant.

Cluster width is typically estimated at the crossover between the power-law pattern and a horizontal line defined by spatial correlation of 1 (Figure 8.5b) or at the crossover between the lower length scale of the inherited/imposed pattern with a horizontal line defined by spatial correlation of 1 (Figure 8.5c). Although less certain, another method to estimate cluster width is to observe the smallest length scale smaller than cluster spacing (Figure 8.5g). For rock sample of Palmas 13 cluster width is estimated at 9 mm (Figure 8.35b).

Figure 8.35 Graphs of spatial correlation (thick continuous line) vs. length scale for (a) logarithmic graduations and (b) linear graduations for the Palmas 13 rock sample data set (175 fractures). In (a) and (b) the thin discontinuous line represents the upper 95% confidence limit while the thin dotted line represents the lower 95% confidence limit, and the thick discontinuous line corresponds to the mean of 100 randomized data sets. In (a) and (b) the thin continuous line represents the analytical solution of randomly arranged fractures with the same number of fractures and scanline length. Width of length-scale bin in (a) and (b) is 9 graduations of length scale (m = 4). There is no pattern of spatial correlation that can be identified in (a) or for linear graduations of length scale (e.g., regularly-spaced peaks) in (b). Evenly spaced lines every 17 mm in (b) match approximately peaks of spatial correlation, which could be interpreted as indicative of periodically arranged clusters with a cluster spacing of approximately 17 mm. (c) Power spectrum of spatial correlation from (b). A noticeable peak at a wavelength of 17 mm has a power spectral density that is several times the equivalent for the 95% confidence interval for red noise, indicating a periodic arrangement of fractures that is statistically significant and with a cluster spacing of 17 mm. Periodicity at wavelengths of 46 mm, as indicated by peak of power spectral density in (c), is not evident in (b).

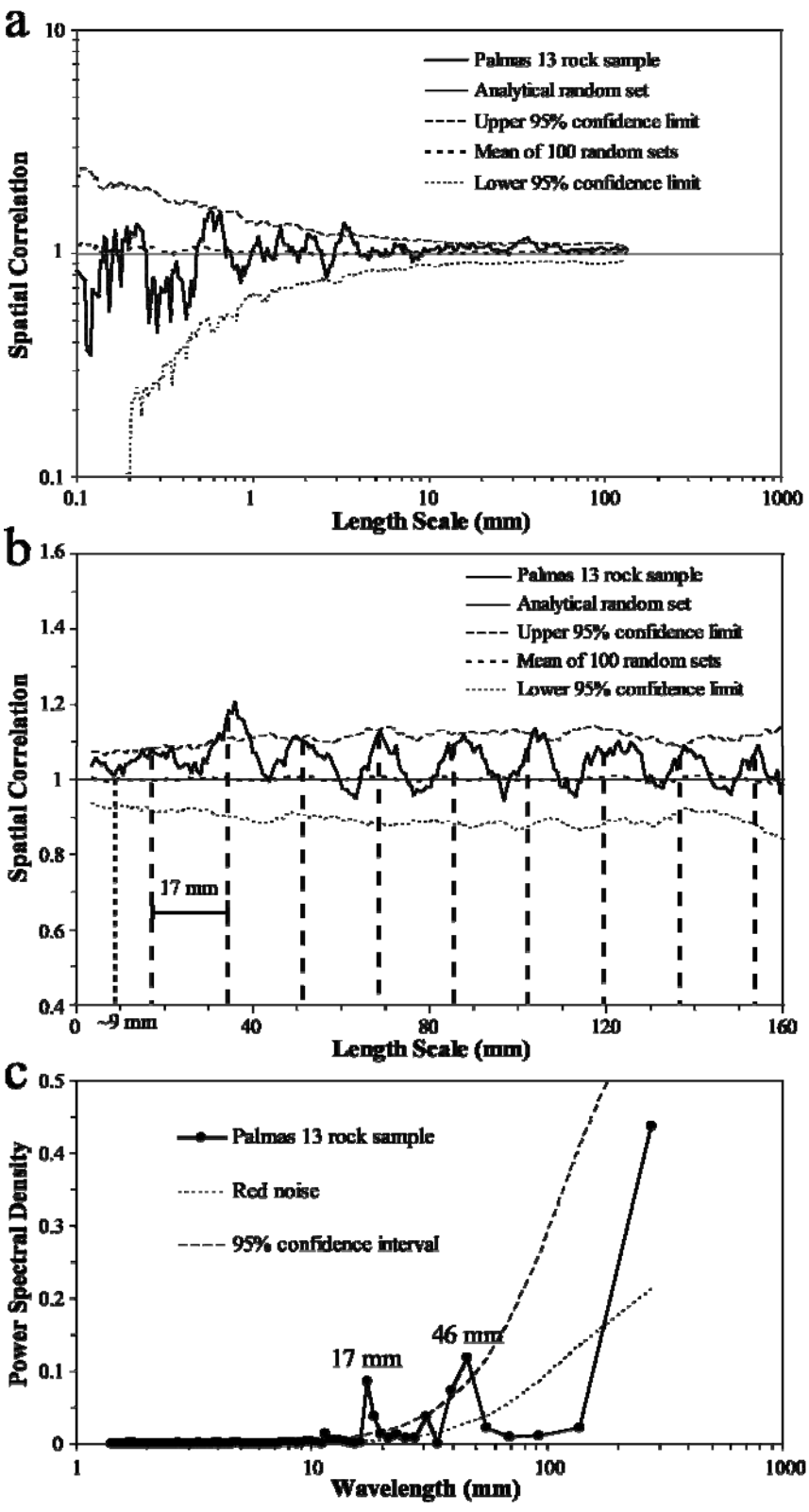
a
Palmas 13 rock sample
Analytical random set
Upper 95% confidence limit
Mean of 100 random sets
Lower 95% confidence limit
Spatial Correlation
Length Scale (mm)
b
Palmas 13 rock sample
Analytical random set
Upper 95% confidence limit
Mean of 100 random sets
Lower 95% confidence limit
Spatial Correlation
17 mm
~9 mm
Length Scale (mm)
c
Palmas 13 rock sample
Red noise
95% confidence interval
Power Spectral Density
17 mm
46 mm
Wavelength (mm)

8.2.7 Tranquitas Canyon

The Tranquitas outcrop of the La Boca Fm. is located in the Sierra Madre Oriental, approximately 100 km south of the Monterey salient near the town of Galeana (Davis, 2005). La Boca Fm. deposited Middle Triassic to Lower Jurassic and is part of Huizachal Group Red Beds deposited in extensional to transtensional basins associated with opening of the Gulf of Mexico (Barboza-Gudino et al., 1999). In the Monterrey salient an evaporite decollement separates two different structural domains. The domain above the decollement comprises the gigantic isoclinal folds that affected the Cupido Formation (Marrett and Aranda-Garcia, 2001), whereas the domain below the decollement comprises open folds with faults and basement involvement below (Marrett and Aranda, 2001). Near Galeana, La Boca sandstones are affected by an open, basement involved fold (Zhou et al., 2006) and are affected by numerous small normal and reverse faults (Davis, 2005).

8.2.7.1 Outcrop Scale – Entire Scanline

The Tranquitas data set I analyzed resulted from merging the A1 and A2 scanlines of Ward (in preparation), which were measured in what Laubach and Ward (2006) called the Canyon outcrop. The Tranquitas data set was obtained in a bedding-parallel outcrop by M. Ward (Table 8.1) for her M.Sc. thesis (Ward, in preparation) and was graciously provided for my dissertation. The Tranquitas data set represents 496 quartz- and calcite-filled veins measured along a scanline of approximately 31 m and record a strain of 1.3% (Table 8.1; Figure 8.36). Veins at the Tranquitas location are partially or completely filled with synkinematic quartz and, locally, postkinematic calcite (Ward, in preparation). Fractures of Tranquitas exhibit a power-law distribution of apertures, a log-normal distribution of spacings and a coefficient of variation for spacings of 1.39 (Table 8.5).

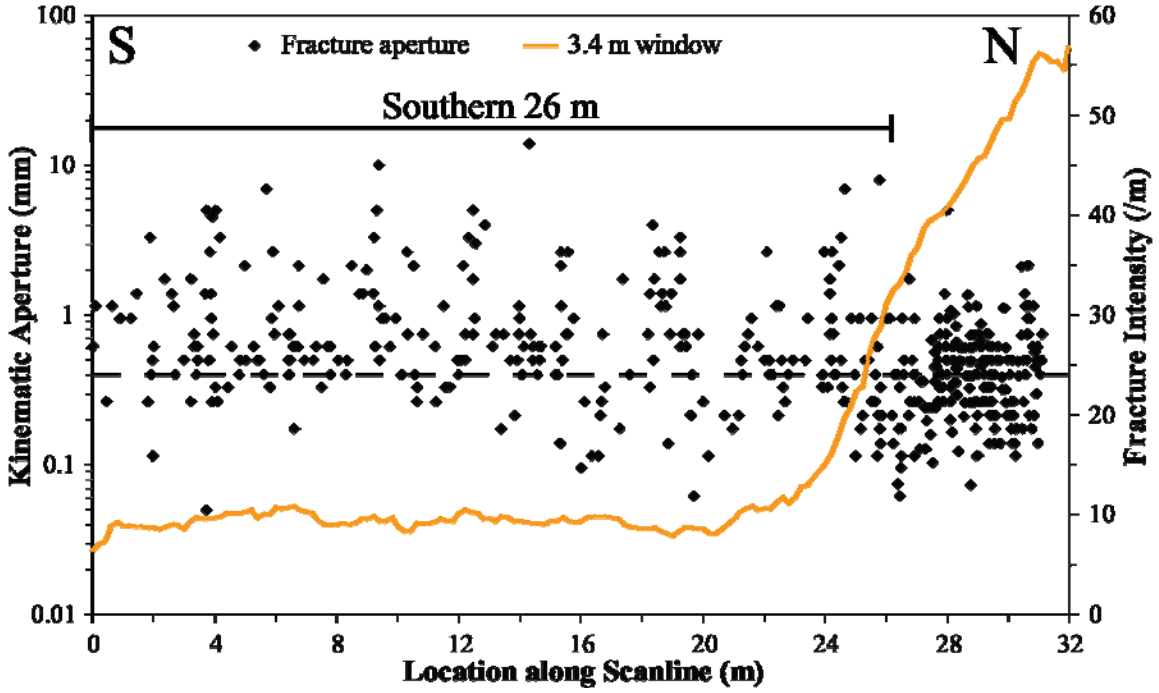

Figure 8.36 Kinematic aperture and fracture intensity versus location along scanline for all the Tranquitas data set. Fracture intensity was calculated inside a window with length (window size) of 3.4 m, the cluster width as measured by NCC (Figure 8.37a) that was moved in increments (window step) 0.2 m. Small fractures (e.g., apertures smaller than 0.4 mm, dashed line) are more abundant in the northern 5 m of scanline. In contrast, large fractures (e.g., apertures larger than 1 mm) are more abundant in the southern 26 m of scanline. Note that kinematic aperture axis uses logarithmic graduations.

Spatial correlation for logarithmically graduated length scales for the entire Tranquitas data set displays a plateau pattern that can be interpreted as inherited or imposed clustering for about two orders of magnitude (20 to 2000 mm) of length scale and with a cluster width of about 3400 mm (Figures 8.5c and 8.37a). Spatial correlation for linearly graduated length scales and its corresponding power spectrum does not exhibit a pattern, suggesting an arrangement that is indistinguishable from random (Figures 8.37b and 8.37c).

The Tranquitas data set displays a heterogeneous arrangement of fractures in space, with the largest fracture cluster located in the northern 5 m of the scanline (Figure 8.36). Closer inspection of fracture intensity reveals the possibility of regularly-spaced clusters (cluster spacing of about 3 m) in the southern 26 m (Figure 8.38a). A periodic arrangement of fracture clusters in the southern 26 m of the Tranquitas scanline does not seem to be present in the northern 5 m (Figure 8.38b). Another difference between the southern 26 m and the northern 5 m of the Tranquitas scanline is the abundance of small fractures (e.g., apertures smaller than 0.4 mm, dashed line in Figure 8.36) and the scarcity of large fractures (e.g., apertures larger than 1 mm) in the northern 5 m of scanline (Figure 8.38b) compared with the southern 26 m (Figure 8.38a). Because the differences between the southern 26 m and the northern 5 m might indicate differences in the spatial arrangement of fractures, these two domains of the Tranquitas scanline will be analyzed separately using NCC.

Figure 8.37 Graphs of spatial correlation (thick continuous line) vs. length scale for (a) logarithmic graduations and (b) linear graduations for the Tranquitas outcrop data set (496 fractures, all fracture sets combined aperture threshold of 0.05 mm, thick continuous line). In (a) and (b) the thin discontinuous line represents the upper 95% confidence limit while the thin dotted line represents the lower 95% confidence limit, and the thick discontinuous line corresponds to the mean of 100 randomized data sets. In (a) and (b) the thin continuous line represents the analytical solution of randomly arranged fractures with the same number of fractures and scanline length. Width of length-scale bin in (a) and (b) is 7 (m = 3) graduations of length scale in (b). A plateau pattern of spatial correlation can be identified outside the 95% confidence interval in (a). Power-law in (a) was calculated using spatial correlation of Tranquitas data set between length scales of 16 and 1410 mm. Cluster width is estimated in (a) at 3400 mm. Notice the low exponent of the power law, indicative of an almost horizontal line. (c) Power spectrum of spatial correlation from (b). The power spectral density for the natural data set exhibits the same trend as the red noise, as shown in (c). The natural data set exhibits a peak at a wavelength of 7600 mm, which has a power spectral density slightly larger than the 95% confidence interval for red noise, but the difference between the peak and the 95% confidence interval is small when compared with other data sets (e.g., Eastern 1.6 m of Escalera OO1 data set, Figure 9.10c).

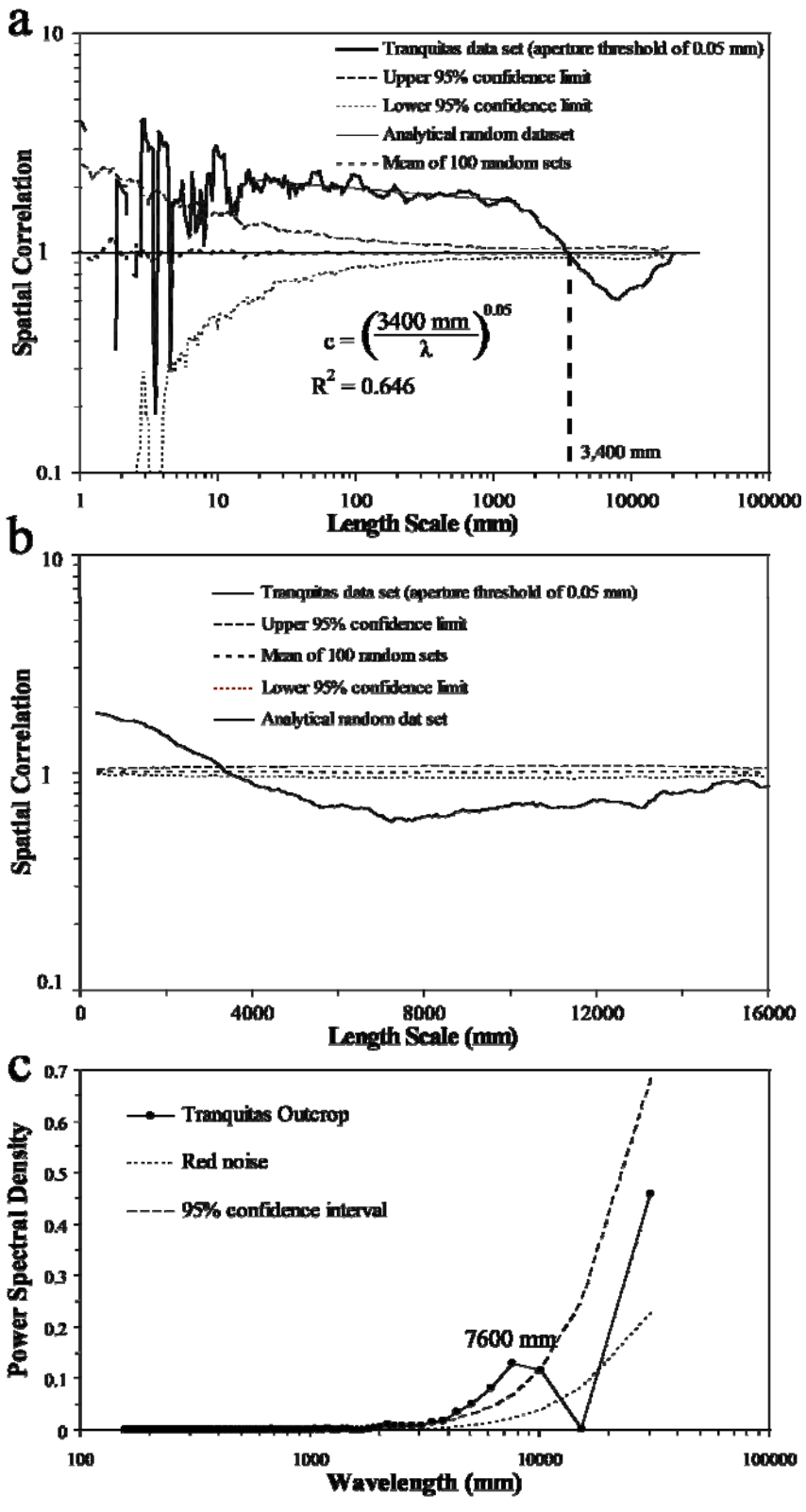
a
Tranquitas data set (aperture threshold of 0.05 mm)
Upper 95% confidence limit
Lower 95% confidence limit
Analytical random dataset
Mean of 100 random sets
Spatial Correlation
$c = \left(\frac{3400\ mm}{\lambda}\right)^{0.05}$
$R^2 = 0.646$
3,400 mm
Length Scale (mm)
b
Tranquitas data set (aperture threshold of 0.05 mm)
Upper 95% confidence limit
Mean of 100 random sets
Lower 95% confidence limit
Analytical random dat set
Spatial Correlation
Length Scale (mm)
c
Tranquitas Outcrop
Red noise
95% confidence interval
Power Spectral Density
7600 mm
Wavelength (mm)

Figure 8.38 Kinematic aperture and fracture intensity versus location along scanline for (a) the southern 26 m and (b) the Northern 5 m of Tranquitas data set. Note that in both (a) and (b) only the kinematic aperture axis uses logarithmic graduations. In (a) fracture intensity was calculated inside a window with width of 0.5 m and window step of 0.2 m. In (b) fracture intensity was calculated inside a window with size of 0.24 m (estimated from Figure 8.40a) and window step of 0.07 m. Fracture intensity in (a) indicates clusters approximately located at 3.8, 6.6, 9.5, 12.3, 15.2, 19, 22.3, and 24.5 m, which yields a qualitative periodic arrangement of clusters with an approximate cluster spacing of 3 m. Fracture intensity in (b) indicates clusters approximately located at 28, 29.2, and 30.4 m, which may yield a qualitative periodic arrangement of clusters with a cluster spacing of 1.2 m.

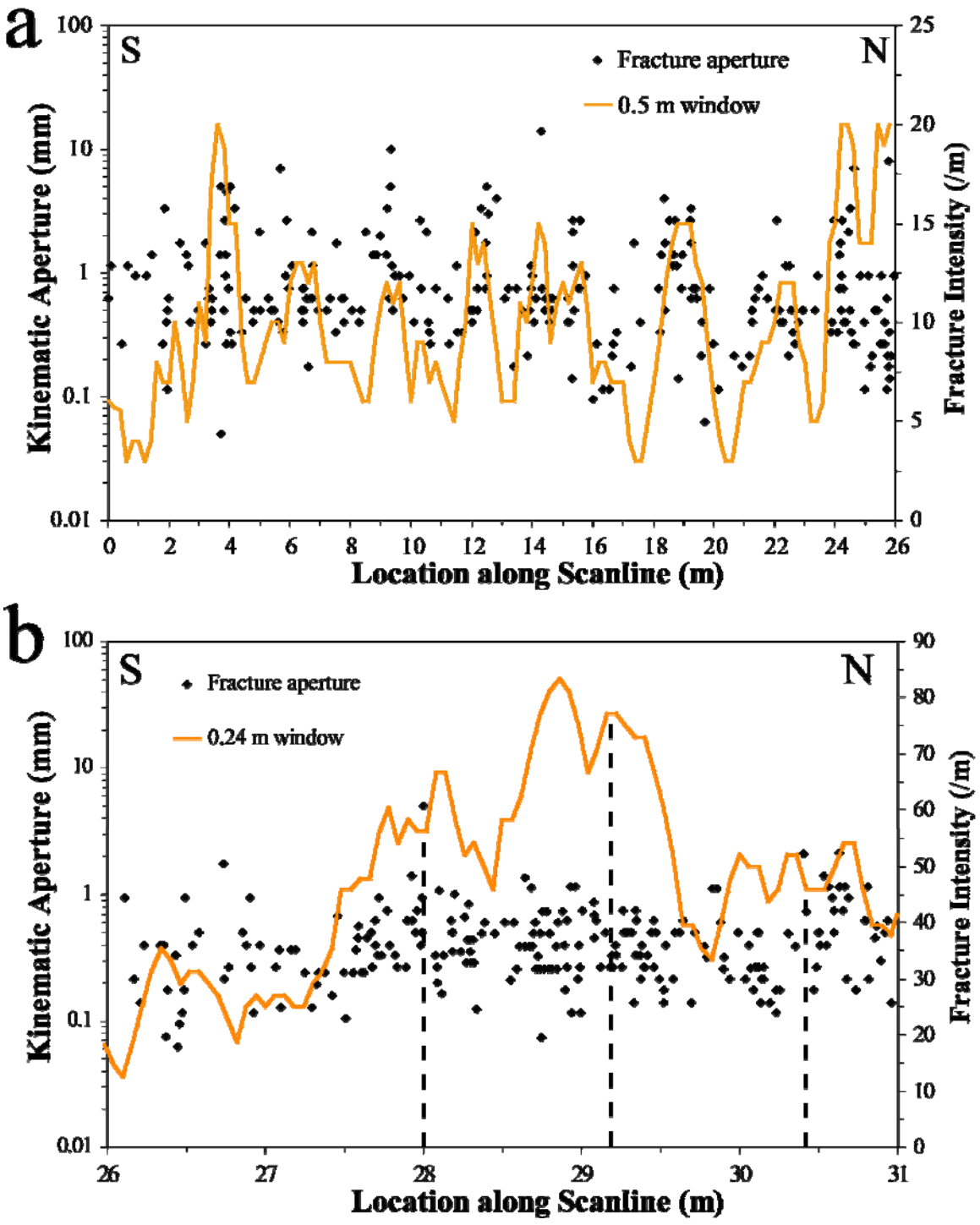
a
S
N
Fracture aperture
0.5 m window
Kinematic Aperture (mm)
Fracture Intensity (/m)
Location along Scanline (m)
b
S
N
Fracture aperture
0.24 m window
Kinematic Aperture (mm)
Fracture Intensity (/m)
Location along Scanline (m)

8.2.7.2 Outcrop Scale – Southern 26 m of Tranquitas

The southern 26 m of the Tranquitas data set represents 256 fractures with a total fracture strain of 1.1%. Qualitative analysis of the fracture intensity curve indicates 8 clusters that seem to be periodically arranged (Figure 8.38a) with a cluster spacing of 3 m. Spatial correlation for logarithmically graduated length scales for the southern 26 m did not yield a systematic pattern outside the 95% confidence interval, suggestive of an arrangement that is indistinguishable from random (Figures 8.5a and 8.39a). Spatial correlation for linearly graduated length scales for the southern 26 m of Tranquitas data set displays a pattern of alternating peaks and troughs, indicative of periodically arranged fracture clusters (Figures 8.5g and 8.39b). However, only some of the peaks and troughs of spatial correlation are outside the 95% confidence interval, suggesting that the periodic arrangement of fracture clusters might not be statistically significant. Power spectrum exhibits peak of power spectral density outside the 95% confidence interval for red noise at approximately 1500 mm (1489 mm, Figure 8.39c), which indicates that the periodic arrangement of fracture clusters of Figure 8.39b is statistically significant. Cluster width and spacing are estimated at 500 and 1500 mm (Figure 8.39b).

Figure 8.39 Graphs of spatial correlation (thick continuous line) vs. length scale for (a) logarithmic graduations and (b) linear graduations for fractures of the southern 26m of Tranquitas data set (256 fractures, all fracture sets combined aperture threshold of 0.05 mm, thick continuous line). In (a) and (b) the thin discontinuous line represents the upper 95% confidence limit while the thin dotted line represents the lower 95% confidence limit, and the thick discontinuous line corresponds to the mean of 100 randomized data sets. In (a) and (b) the thin continuous line represents an example randomized set generated with the same number of fractures and scanline length .Width of length-scale bin in (a) and (b) is 9 (m = 4) graduations of length scale in (b). There is no pattern of spatial correlation that can be identified (e.g., power law) outside the 95% confidence interval in (a). Although a cluster width cannot be estimated in (a), spatial correlation pattern in (b) may indicate a cluster width of 500 mm. Evenly spaced lines (thick dashed lines) every 1500 mm in (b) match some peaks of spatial correlation, which indicate that fracture clusters may or may not be periodically arranged. Of nine possible peaks of spatial correlation at length scales multiple of 1500 mm, only two are outside the 95% confidence interval. (c) Power spectrum of spatial correlation from (b). Several peaks of power spectral density are outside the 95% confidence interval. The two peaks with largest power spectral density are at 1489 and 1688 mm, which suggests that the periodic arrangement of clusters with cluster spacing of 1500 mm suggest in (b) is statistically significant. Two other peaks of power spectral density are outside the 95% confidence interval (wavelengths of 3164 and 5063 mm). However, periodicity at corresponding wavelengths is not evident in (b).

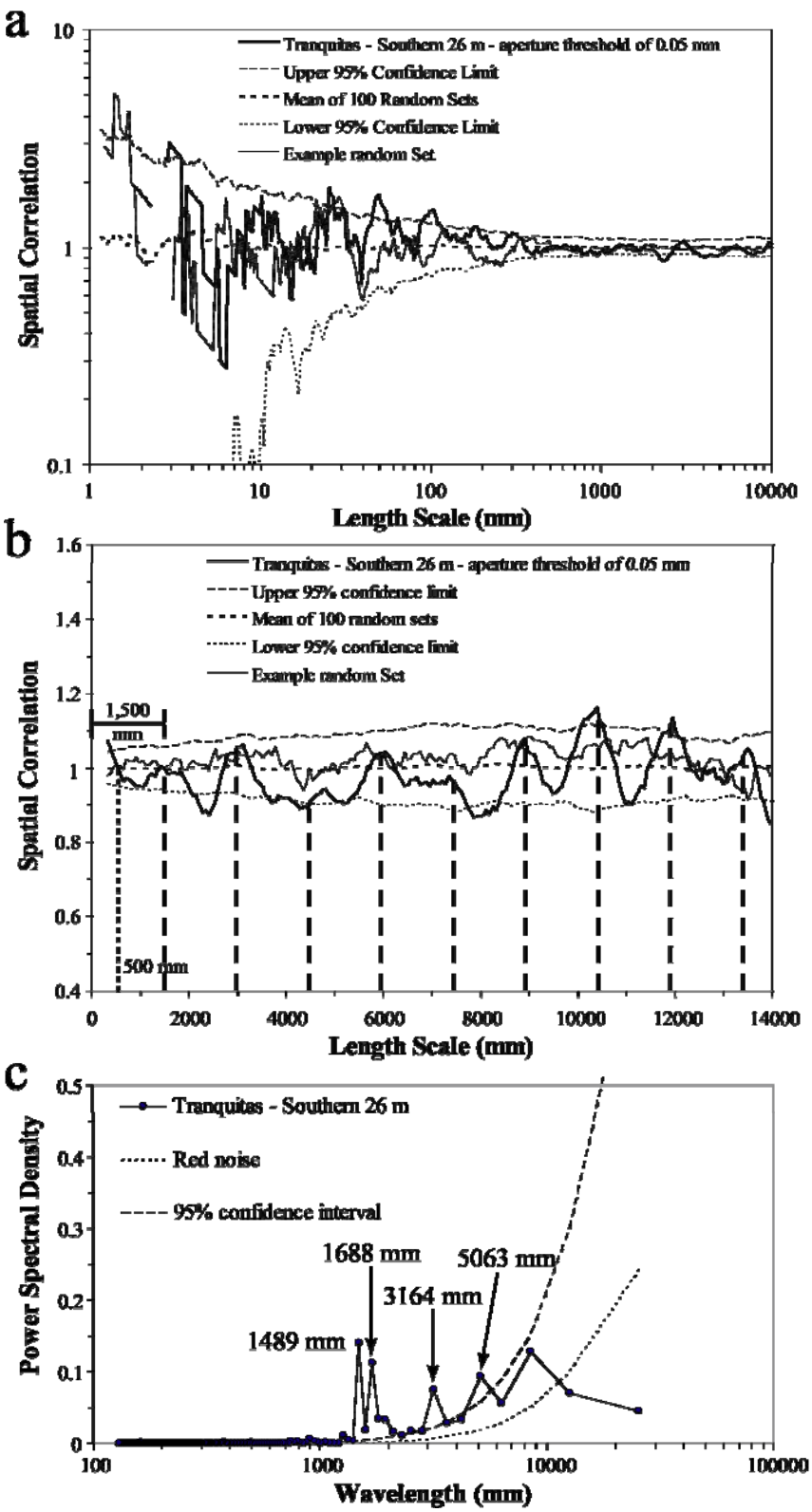
a
Tranquitas - Southern 26 m - aperture threshold of 0.05 mm
Upper 95% Confidence Limit
Mean of 100 Random Sets
Lower 95% Confidence Limit
Example random Set
Spatial Correlation
Length Scale (mm)
b
Tranquitas - Southern 26 m - aperture threshold of 0.05 mm
Upper 95% confidence limit
Mean of 100 random sets
Lower 95% confidence limit
Example random Set
1,500 mm
500 mm
Spatial Correlation
Length Scale (mm)
c
Tranquitas - Southern 26 m
Red noise
95% confidence interval
1688 mm
5063 mm
3164 mm
1489 mm
Power Spectral Density
Wavelength (mm)

8.2.7.3 Outcrop Scale – Northern 5 m of Tranquitas

The northern 5 m of the Tranquitas data set represents 240 fractures with a total fracture strain of 2.3%. Qualitative analysis of the fracture intensity curve for the northern 5 m may indicate periodically arranged clusters separated approximately 1.2 m (Figure 8.38b). Spatial correlation for logarithmically graduated length scales for fractures inside the northern 5 m of the Tranquitas scanline (Figure 8.40a) yields the same spatial arrangement as the complete data set (Figure 8.37a), an inherited or imposed clustering (Figure 8.5c; Marrett et al., in review). For the northern 5 m, the plateau pattern of spatial correlation, typical of inherited/imposed clustering is present for at least 3 orders of magnitude of length scale (10 to 1800 mm, Figure 8.40a). Large variations of spatial correlation between length scales of 10 to 1800 mm could cast doubt over the interpreted plateau pattern (Figure 8.40a). However, increasing the length-scale bin (Chapter 6) allows identification of about one order of magnitude of length scale (12-80 mm) without significant variation of spatial correlation and outside the 95% confidence interval (Figure 8.41).

Spatial correlation for linearly graduated length scales for fractures in the northern 5 m of Tranquitas does not yield an arrangement indistinguishable from random, the arrangement exhibited by the entire Tranquitas scanline (Figure 8.37b). Instead, the northern 5 m yielded a pattern of alternating peaks and troughs of spatial correlation outside the 95% confidence interval, indicative of a periodic arrangement of fractures with a cluster spacing of 590 mm (Figure 8.40b). Power spectrum for linearly graduated length scales of the northern 5 m yielded a statistically significant peak at 546 mm (Figure 8.40c), a wavelength similar to the cluster spacing estimated with NCC, and thereby supporting the statistical significance of the periodic arrangement of fracture clusters interpreted in Figure 8.40b. In addition, cluster width for fractures in the northern

5 m is estimated to be 240 mm wide (Figure 8.40b) whereas cluster width for the entire Tranquitas scanline is estimated at 3400 mm (Figure 8.37a).

One possible explanation for the differences in spatial arrangement (Figures 8.39 and 8.40), fracture strain, and range of fracture aperture (Figure 8.36) between the southern 26 m and the northern 5 m of the Tranquitas scanline is the presence of a fold or a fault that affected the Tranquitas layers immediately beyond the northern end of the Tranquitas scanline (Figure 8.42). Fractures associated with a fold or a fault could explain both the inherited/imposed spatial arrangement and the larger fracture strain (compared with the southern 26 m) of fractures in the northern 5 m of the Tranquitas scanline.

Figure 8.40 Graphs of spatial correlation (thick continuous line) vs. length scale for (a) logarithmic graduations and (b) linear graduations for the northern 5 m of the Tranquitas data set (240 fractures, all sets combined, aperture threshold = 0.05 mm, thick continuous line). In (a) and (b) the thin discontinuous line represents the upper 95% confidence limit while the thin dotted line represents the lower 95% confidence limit, and the thick discontinuous line corresponds to the mean of 100 randomized data sets. In (a) and (b) the thin continuous line represents an example randomized set generated with the same number of fractures and scanline length. Width of length-scale bin in (a) and (b) is 9 graduations of length scale ($m = 4$). A plateau pattern of spatial correlation can be interpreted for logarithmic graduations of length scale in (a). Evenly spaced lines every 590 mm in (b) match the location of peaks of spatial correlation, which seem to display a regularly spaced pattern. Although a cluster width cannot be reliably interpreted in (a), a cluster width is estimated in (b) as approximately 240 mm. (c) Power spectrum of spatial correlation from (b). Largest peak of power spectral density is outside the 95% confidence interval for red noise at a wavelength of 546 mm, which suggests the statistical significance of the pattern of periodically arranged fracture clusters suggested in (b). Although there is a peak of power spectral density at a wavelength of 335 mm, the spatial correlation curve in (b) does not exhibit an evident periodicity at that wavelength.

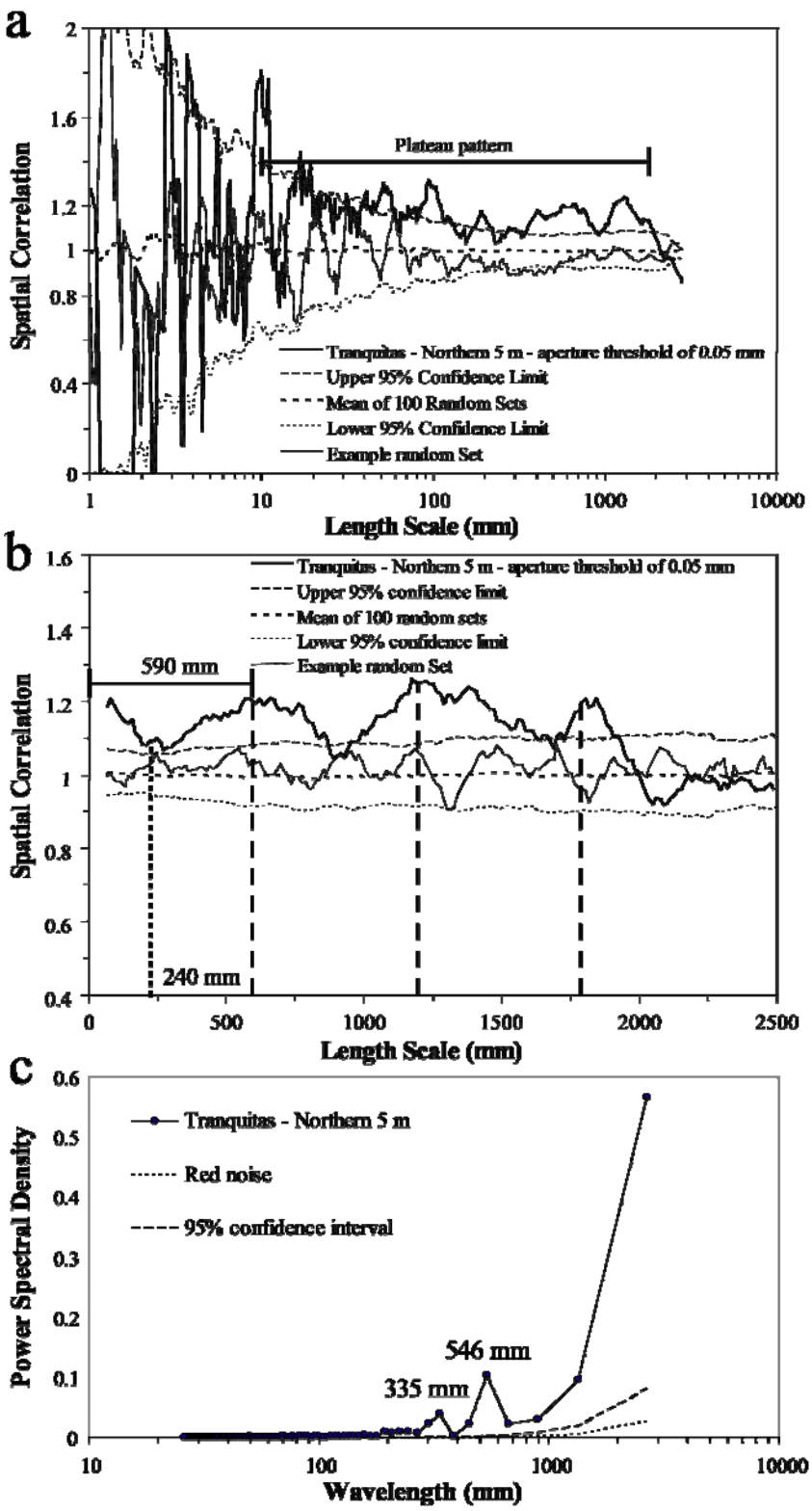
a
Spatial Correlation
Plateau pattern
Tranquitas - Northern 5 m - aperture threshold of 0.05 mm
Upper 95% Confidence Limit
Mean of 100 Random Sets
Lower 95% Confidence Limit
Example random Set
Length Scale (mm)
b
Spatial Correlation
Tranquitas - Northern 5 m - aperture threshold of 0.05 mm
Upper 95% confidence limit
Mean of 100 random sets
Lower 95% confidence limit
Example random Set
590 mm
240 mm
Length Scale (mm)
c
Power Spectral Density
Tranquitas - Northern 5 m
Red noise
95% confidence interval
546 mm
335 mm
Wavelength (mm)

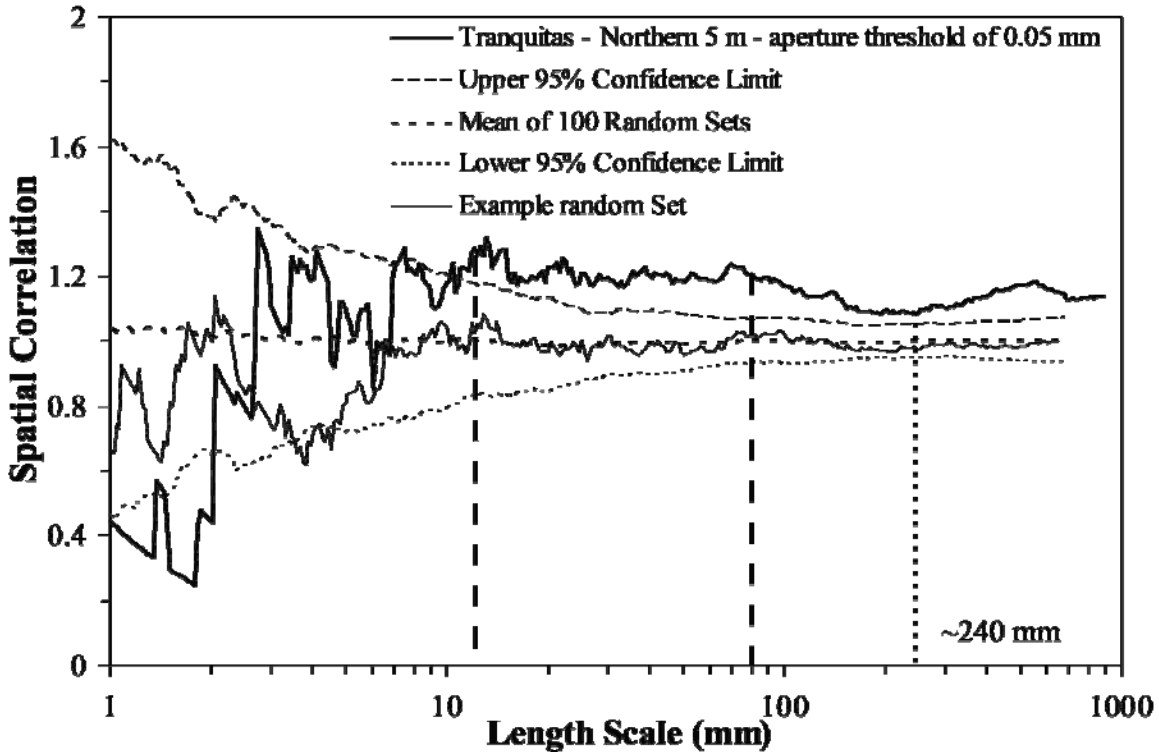

Figure 8.41 Graph of spatial correlation versus logarithmic graduations of length scale for the northern 5 m of the Tranquitas data set (240 fractures, aperture threshold = 0.05 mm, thick continuous line). Width of length-scale bin is 41 graduations of length scale (m = 20). The pattern of spatial correlation indicates inherited clustering (Marrett et al., in review) between 11 and 80 mm and a cluster width of approximately 240 mm. The spatial correlation curve for the same data set but with a smaller length-scale bin (9 graduations of length scale) was presented in Figure 8.40a.

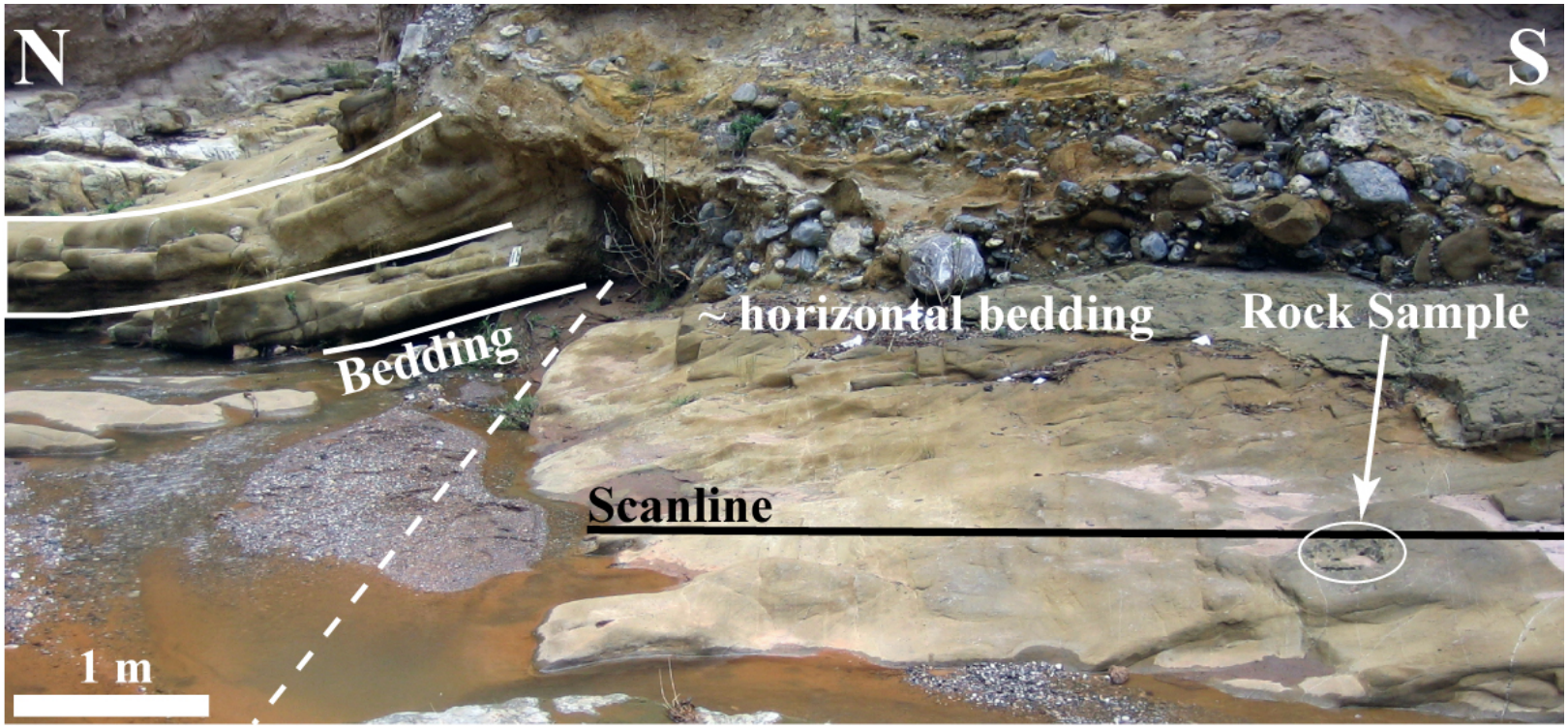

Figure 8.42 Photograph of northern 5 m of Tranquitas scanline (Black line). Scanline was located on an approximate horizontal (83/4, right-hand rule) bedding plane. Near the northern end of scanline bedding changes rapidly from horizontal (right of dashed line) to inclined (dipping to the NNW) and then gradually returns to horizontal (right end of photograph). Change in bedding could be due to either a fault or a fold. Due to the limited amount of layers exposed, it was not possible to correlate layers from different dip domains.

8.2.7.4 Rock Sample Scale

Eight consecutive thin sections were generated from a sample obtained along the outcrop scanline (Table 8.2) from inside the cluster located at the north end of the scanline (Figure 8.36). The imaging of these eight thin sections was done by acquiring cathodoluminescence images in a SEM using the automated method described in Chapter 5 (Gomez and Laubach, 2006). A total of 173 transgranular fractures were mapped in 230 mm of scanline that recorded a strain of 2.59% (Table 8.2). Minimum and maximum fracture apertures measured were 0.0005 and 0.6316 mm.

Spatial correlation for logarithmically graduated length scales for the Tranquitas rock sample data set exhibit a statistically significant power-law pattern, indicating that fractures are arranged in clusters 0.7 mm wide (Figures 8.5b and 8.43a). Spatial correlation for linearly graduated length scales for the Tranquitas rock sample data set exhibit alternating peaks and troughs outside the 95% confidence interval every 29 mm, a pattern that can be interpreted as a periodic arrangement of fracture clusters with cluster spacing of 29 mm (Figures 8.5g and 8.43b). Power spectrum of spatial correlation for linearly graduated length scales exhibits a peak of power spectral density outside the 95% confidence interval and centered at approximately 29 mm (Figure 8.43c), supporting that the periodic arrangement of fracture clusters interpreted in Figure 8.43b is statistically significant.

Figure 8.43 Graphs of spatial correlation (thick continuous line) vs. length scale for (a) logarithmic graduations and (b) linear graduations for the Tranquitas rock sample data set (172 fractures). In (a) and (b) the thin discontinuous line represents the upper 95% confidence limit while the thin dotted line represents the lower 95% confidence limit, and the thick discontinuous line corresponds to the mean of 100 randomized data sets. In (a) the thin continuous line represents the analytical solution of randomly arranged fractures with the same number of fractures and scanline length. In (b) the thin continuous line represents an example randomized set generated with the same number of fractures and scanline length. Width of length-scale bin in (a) is 9 (m = 4) and 23 (m = 11) graduations of length scale in 9b). Spatial correlation in (a) exhibits a power-law pattern outside the 95% confidence interval. Cluster width in (a) is estimated at 0.7 mm. Evenly spaced lines every 29 mm in (b) match approximately peaks of spatial correlation, which can be interpreted as indicative of periodically arranged clusters. (c) Power spectrum of spatial correlation from (b). A noticeable peak of power spectral density between wavelengths of 27 and 34 mm is outside the 95% confidence interval for red noise, indicating a periodic arrangement of fractures that is statistically significant with a cluster of approximately 30.5 mm.

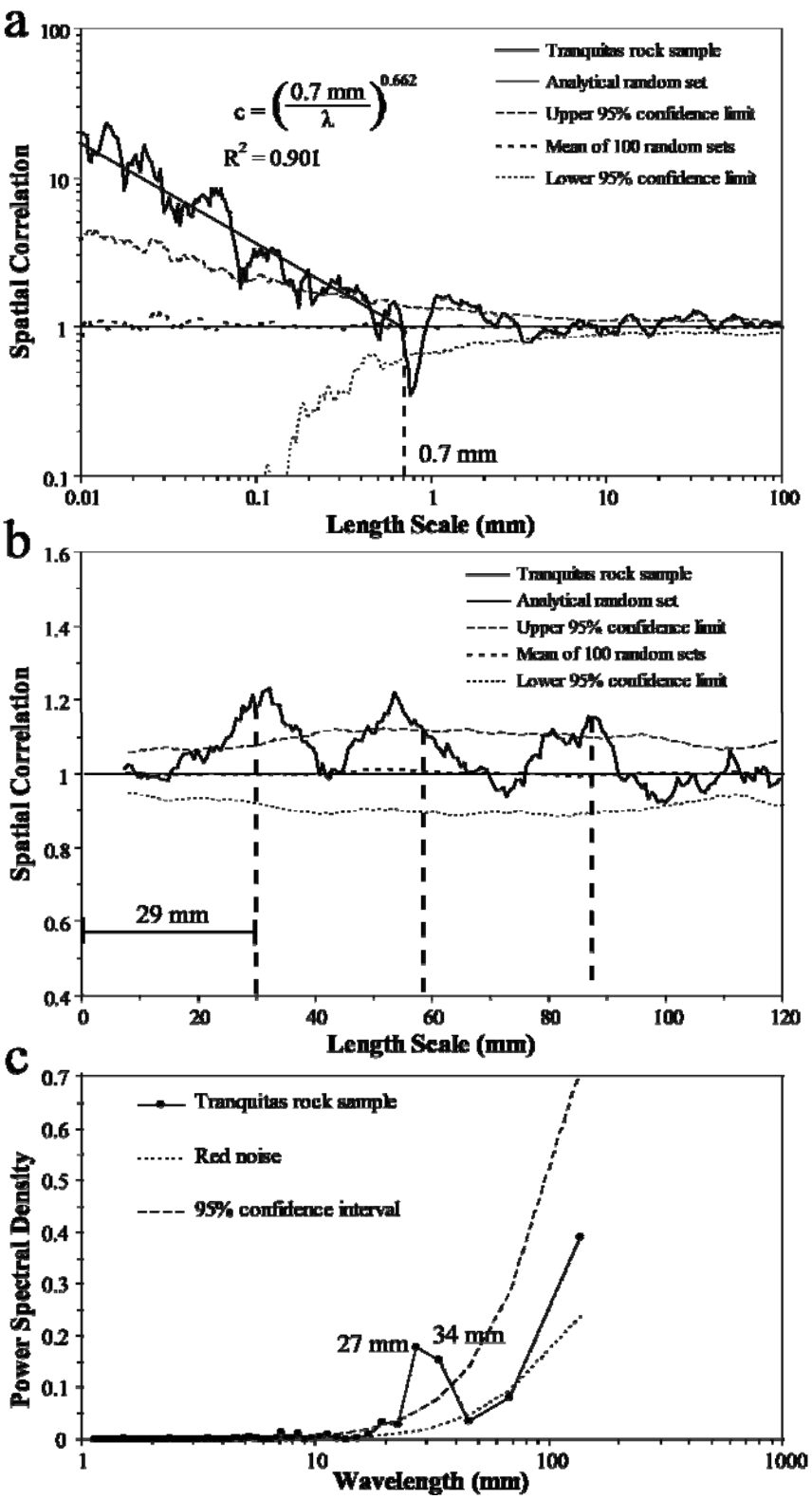
a
Tranquitas rock sample
Analytical random set
Upper 95% confidence limit
Mean of 100 random sets
Lower 95% confidence limit
$c = \left(\frac{0.7\ mm}{\lambda}\right)^{0.662}$
$R^2 = 0.901$
0.7 mm
Spatial Correlation
Length Scale (mm)
b
Tranquitas rock sample
Analytical random set
Upper 95% confidence limit
Mean of 100 random sets
Lower 95% confidence limit
29 mm
Spatial Correlation
Length Scale (mm)
c
Tranquitas rock sample
Red noise
95% confidence interval
27 mm
34 mm
Power Spectral Density
Wavelength (mm)

8.2.8 Comparison of Spatial Arrangements at Outcrop and Rock-Sample Scales

NCC results from data sets at outcrop and rock sample scales are compiled in Table 8.6. NCC analysis of fracture data sets at outcrop scale presented in Chapters 6 and 7 have quantitatively illustrated most of the spatial arrangements defined by Marrett et al. (in review) and Sheperd et al. (1981). My dissertation is the first study showing that fractures (mostly microfractures) measured in rock samples using microscopy (petrographic and SEM/CL) yield the same diversity of spatial arrangements (Figure 8.5; Table 8.6). For instance, fracture data sets at rock sample scale yielded spatial arrangements (Table 8.6) that are indistinguishable from random for both logarithmically (i.e., Huasteca, Palmas 11 LR, Palmas 12, Palmas 13, and eastern 1.6 m of Escalera OO1) and linearly (e.g., Palmas 11 LR) graduated length scales (Figures 8.5a and 8.5e). Fracture data sets from rock samples also yielded power-law patterns of spatial correlation (Figure 8.5b) using logarithmically graduated length scales (i.e., Escalera OO12 and northern 5 m of Tranquitas), and periodically arranged clusters (Figure 8.5g) using linearly graduated length scales (i.e., Huasteca, Palmas 12, Palmas 13, eastern 1.6 m of Escalera OO1, Escalera OO12 and northern 5 m of Tranquitas). Non-random spatial arrangements of fractures measured in rock samples suggest that the processes by which fractures become organized affect not only macrofractures (approximately 0.1 mm of aperture and greater) but also microfractures (between approximately 0.0005 and 0.1 mm of aperture).

Combining information about the spatial arrangement of fractures at outcrop and rock sample scale shows that some data sets exhibit the same spatial arrangement at both scales (i.e., Escalera OO12, Table 8.6), whereas other data sets show the same spatial arrangement for only one of the two types of length scale graduations used (e.g., Huasteca, Palmas 12, Palmas 13, Escalera OO1, and Tranquitas; Table 8.6). Only spatial

arrangements of Palmas 11 LR differ for both logarithmically and linearly graduated length scales at both outcrop and rock sample scales (Table 8.6). To facilitate rapid comparison between data sets at outcrop and rock sample scales, I also compiled attributes of the entire data set such as number of fractures, fracture strain and scanline length as well as attributes of the spatial arrangement such as cluster width, power-law exponent of spatial correlation, and cluster spacing (Table 8.7). In the following pages I will investigate the internal arrangement of fracture clusters using samples that represent different domains of the outcrop (Figure 8.2).

Table 8.6 Type of spatial arrangement for data sets studied in this chapter at both outcrop and rock sample scale. Figure number illustrating each result is shown inside parentheses. Figure numbers of data set at rock sample scale are displayed in *italics*. When the type of spatial arrangement at different scales is the same, the adjacent cells are merged. Power = Power-law pattern. Random = indistinguishable from random. Periodic = periodically arranged clusters.

Graduations of Length Scale	**Observation Scale**	**Data Sets**						
		Huasteca Set A	**Palmas 12**	**Palmas 13**	**Palmas 11 LR**	**Escalera OO1 E 1.6 m**	**Escalera OO12**	**Tranquitas (N 5 m)**
Logarithmic	**Outcrop**	Power, Inherited? (8.21a)	Random (8.31a) *(8.32a)*	Random (8.34a) *(8.35a)*	Power (8.26a)	Power, Inherited? (8.10a)	Power (8.17a) *(8.18a)*	Inherited (8.40a)
	Rock Sample	Random *(8.24a)*			Random *(8.27a, 8.28a)*	Random *(8.13a)*		Power *(8.43a)*
Linear	**Outcrop**	Periodic (8.21b) *(8.24b)*	Random? Periodic? (8.31b)	Random (8.34b)	Periodic (8.26b)	Periodic (8.10b) *(8.13b)*	Periodic (8.17b) *(8.18b)*	Periodic (8.40b) *(8.43b)*
	Rock Sample		Periodic *(8.32b)*	Periodic *(8.35b)*	Random *(8.27b, 8.28b)*			

Table 8.7 Compilation of spatial arrangement attributes for data sets with rock samples at outcrop and rock sample scale. Power-law exponent obtained using logarithmic graduations of length scales. Numbers in *italics* indicate values that are not statistically significant. N.A. = Not Available.

Data Set Attribute	Observation Scale	Huasteca Set A	Palmas 12	Palmas 13	Palmas 11 LR	Escalera OO1 (E 1.6 m)	Escalera OO12	Tranquitas (N 5 m)
Number of fractures	Outcrop	581	460	614	262	492	1095	240
	Rock Sample	34	29	175	156, 86	52	484	173
Scanline length (mm)	Outcrop	16590	6140	5430	21100	1654	3560	5146
	Rock Sample	122	101	290	38, 64	65	149	230
Fracture strain (%)	Outcrop	5.7	12.7	9.2	4.6	13.3	20.4	2.4
	Rock Sample	0.9	14.6	8.1	14.6, 15.6	9.8	20.0	2.6
Power-law exponent	Outcrop	0.05	N.A.	N.A.	0.44	0.06	0.09	N.A.
	Rock Sample	N.A.			N.A.	N.A.	0.08	0.76
Cluster width (mm)	Outcrop	250	N.A.	N.A.	220	170	150	240
	Rock Sample	N.A.	*2*	*9*	N.A.	*2*	8	0.7
Cluster spacing (mm)	Outcrop	1001	*461*	N.A.	1090	340	850	570
	Rock Sample	29	9.5	17	N.A.	4.1	43	29

8.2.8.1 Periodically Arranged Clusters at Outcrop Scale

8.2.8.1.1 Escalera OO12

Fractures from the Escalera OO12 layer at both outcrop and rock sample scales exhibit the same arrangements for logarithmically and linearly graduated length scales (Table 8.6; Figure 8.44). Fractures of Escalera OO12 exhibit periodically arranged clusters with a power-law pattern of spatial correlation at both outcrop and rock sample scale (Figure 8.5d), and the rock sample was extracted from an outcrop-scale cluster (Table 8.2), which suggests that periodically arranged clusters with power-law pattern at rock sample scale are inside periodically arranged clusters with power-law pattern at outcrop scale (Figure 8.44). It should be noted that the outcrop data set probably contains four clusters (scanline length ≈ 4∗cluster width + 3∗cluster spacing), and therefore its spatial correlation for length scales smaller than cluster width was calculated from fracture pairs located in four clusters.

The difference in strain between the outcrop and rock sample data sets from the Escalera OO12 is minimal (Table 8.7). Scanline length for the rock sample data set is also approximately equal to cluster width for the outcrop data set (Table 8.7). Although the difference between the power-law exponent of spatial correlation between outcrop and rock sample scale is small, there is reduction in spatial correlation from outcrop to rock sample scale (Table 8.7; Figure 8.45). In addition, there is a drastic reduction of approximately 95% in both cluster width and cluster spacing from outcrop to sample scale (Table 8.7). Extrapolating the power-law of spatial correlation from rock sample indicates a cluster width of approximately 90 mm (Figure 8.45), which corresponds to 70% of the cluster width (150 mm) estimated from the outcrop scale data set (Table 8.7).

Figure 8.44 Sketches illustrating the Escalera OO12 data set (left) and the corresponding NCC analyses using logarithmic and linear graduations of length scale (right) for (a) outcrop scale, and (b) rock sample scale. Fractures in both (a) and (b) exhibit a power-law pattern of spatial correlation inside clusters (Figures 8.17a and 8.18a) with approximately the same degree of clustering (power-law exponent). Fractures in both (a) and (b) exhibit periodically arranged clusters (Figures 8.17b and 8.18b). Fractures inside clusters exhibit a power-law pattern of spatial correlation and are red whereas fractures in the intercluster domains are green. Input data in (a) are macrofractures along the entire scanline at outcrop scale. Input data in (b) are fractures (both microfractures and macrofractures) in rock sample. Maximum length scale in (a) is equal to outcrop scanline length (A). Maximum length scale in (b) is equal to sample length, which is approximately equal to cluster width at outcrop scale (C). Cluster width at rock sample scale (E) is different that cluster width at outcrop scale (C), and extrapolating the power law at rock sample scale yielded a cluster width slightly smaller than to cluster width at outcrop scale, as shown in (b). Periodically arranged clusters in (b) exhibit distinctive cluster spacing (D), which is smaller than cluster spacing (B) in (a).

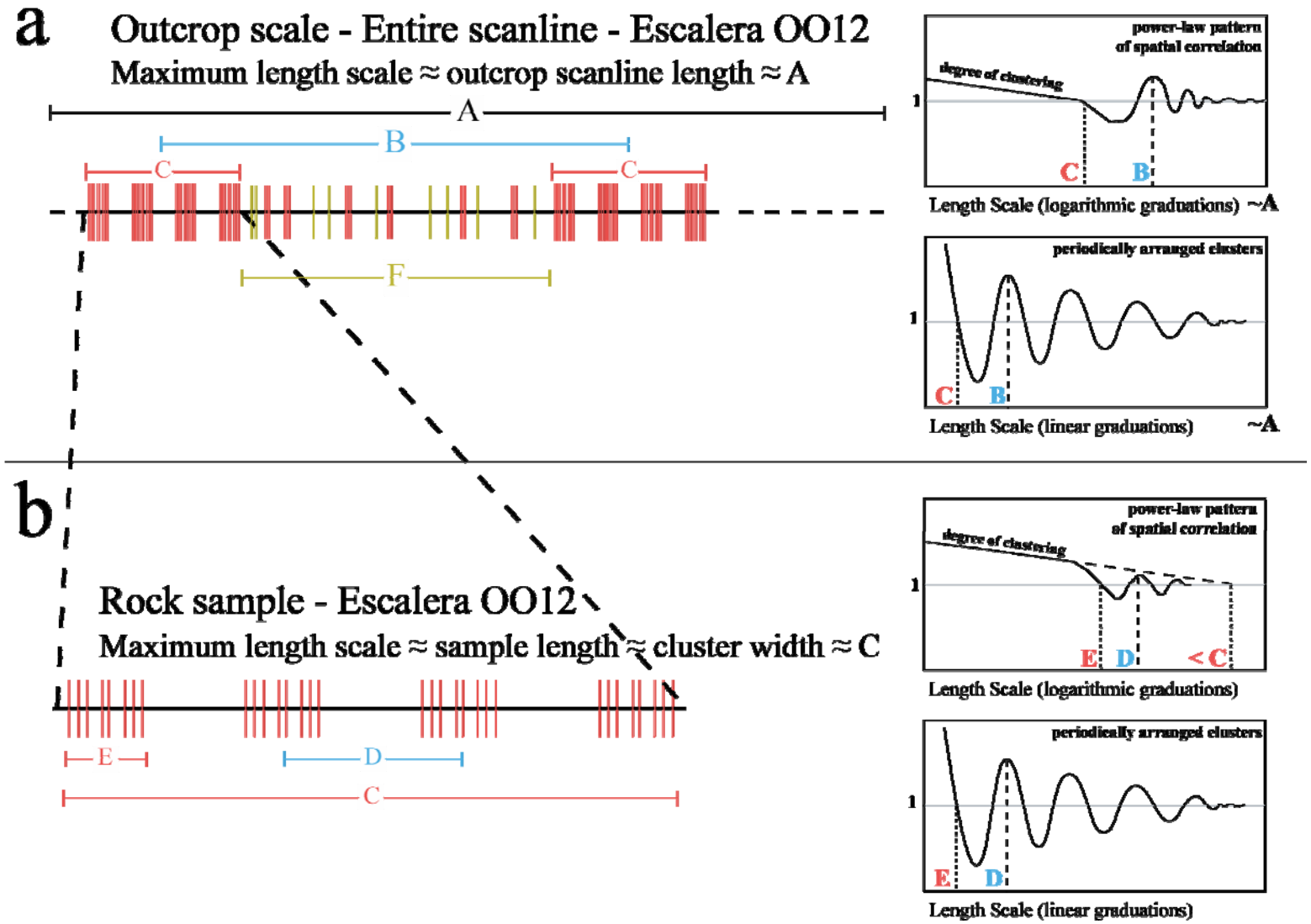
a
Outcrop scale - Entire scanline - Escalera OO12
Maximum length scale ≈ outcrop scanline length ≈ A
A
B
C
C
F
power-law pattern of spatial correlation
degree of clustering
1
C
B
Length Scale (logarithmic graduations) ~A
periodically arranged clusters
1
C
B
Length Scale (linear graduations) ~A
b
Rock sample - Escalera OO12
Maximum length scale ≈ sample length ≈ cluster width ≈ C
E
D
C
power-law pattern of spatial correlation
degree of clustering
1
E
D
< C
Length Scale (logarithmic graduations)
periodically arranged clusters
1
E
D
Length Scale (linear graduations)

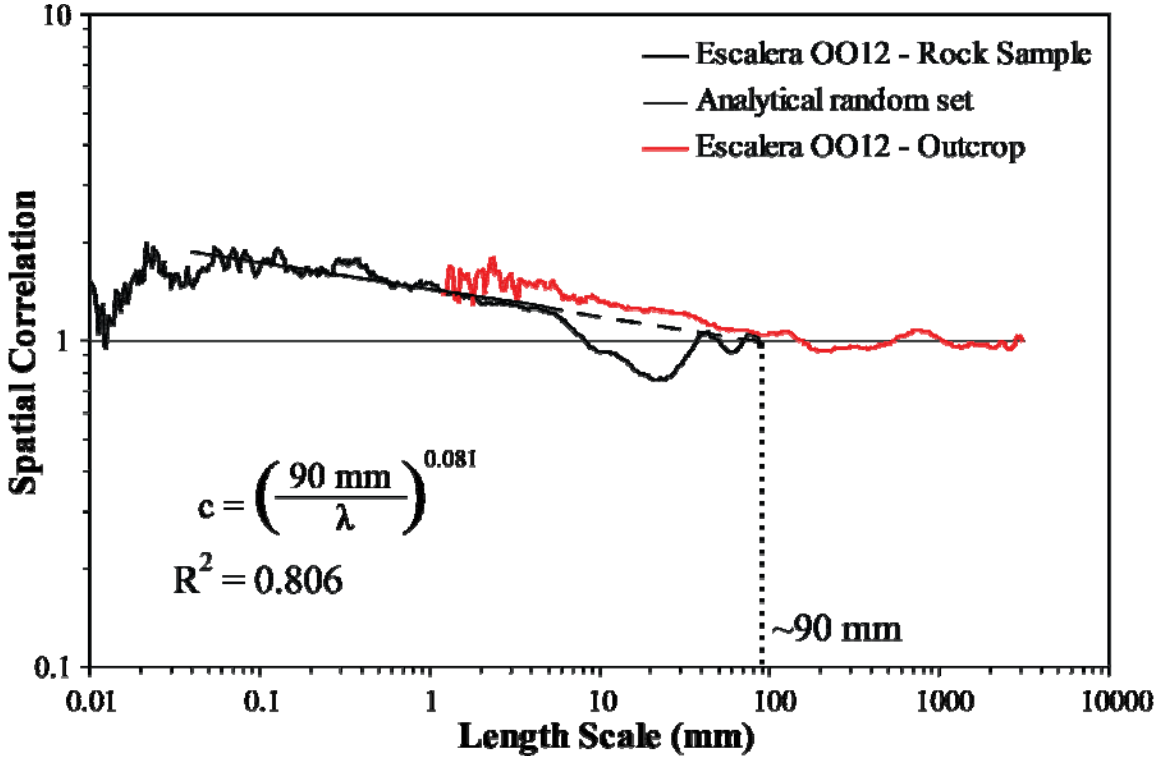

Figure 8.45 Graph of spatial correlation versus logarithmic graduations of length scale for the outcrop (red line) and rock sample (black line) scanlines of Escalera OO12 (from Figures 8.17a and 8.18a). Width of length-scale bin is 13 (m = 6) graduations of length scale for both outcrop and rock sample. Power-law regression (thick black line) was calculated for length scales of rock sample between 0.04 and 5.2 mm and extrapolated (thick dashed line) to indicate a cluster of approximately 90 mm (dotted line).

8.2.8.1.2 Northern 5 m of Tranquitas

Fractures from the northern 5 m of Tranquitas at both outcrop and rock sample scales exhibit the same type of arrangement for linearly graduated length scales,

periodically arranged clusters (Table 8.6; Figure 8.46). Using logarithmically graduated length scales, fractures of the northern 5 m of Tranquitas at outcrop scale exhibit inherited/imposed clustering whereas the rock sample counterpart exhibits a power-law pattern of spatial correlation (Figure 8.46). The rock sample was obtained along the scanline inside an outcrop cluster (Table 8.2), indicating that periodically arranged clusters at rock sample scale form periodically arranged clusters at rock sample scale (Figure 8.46). The outcrop data set contains approximately seven clusters (scanline length ≈ 7∗cluster width + 6∗cluster spacing), and therefore its spatial correlation for length scales smaller than cluster width was calculated from fracture pairs located in all seven clusters.

The difference in strain between the outcrop and rock sample data sets from the northern 5 m of Tranquitas is minimal (Table 8.7). Scanline length for rock sample data set is also approximately equal to cluster width for outcrop data set (Table 8.7). In addition, there is a drastic reduction of approximately 99% in cluster width and a 95% reduction in cluster spacing between the outcrop and the rock sample data sets (Table 8.7).

Figure 8.46 Sketches illustrating the northern 5 m of Tranquitas data set (left) and the corresponding NCC analyses using logarithmic and linear graduations of length scale (right) for (a) outcrop scale, and (b) rock sample scale. Fractures at outcrop scale exhibit an inherited/imposed arrangement of fractures for logarithmically graduated length scales (Figure 8.40a) and periodically arranged clusters for linearly graduated length scales (Figure 8.40b). Fractures at rock sample scale exhibit a power-law pattern of spatial correlation inside clusters using logarithmically graduated length scales (Figure 8.43a) and periodically arranged clusters using linear graduations of length scale (Figure 8.43b). Fractures inside clusters with a power-law pattern of spatial correlation are red whereas fractures in the intercluster domains are green. Input data in (a) are macrofractures along the entire scanline at outcrop scale. Input data in (b) are fractures (both microfractures and macrofractures) in rock sample. Maximum length scale in (a) is equal to outcrop scanline length (A). Maximum length scale in (b) is equal to sample length, which is approximately equal to cluster width at outcrop scale (C). Cluster width at rock sample scale (E) is smaller that cluster width at outcrop scale (C). Periodically arranged clusters in (b) exhibit distinctive cluster spacing (D), which is smaller than cluster spacing (B) in (a).

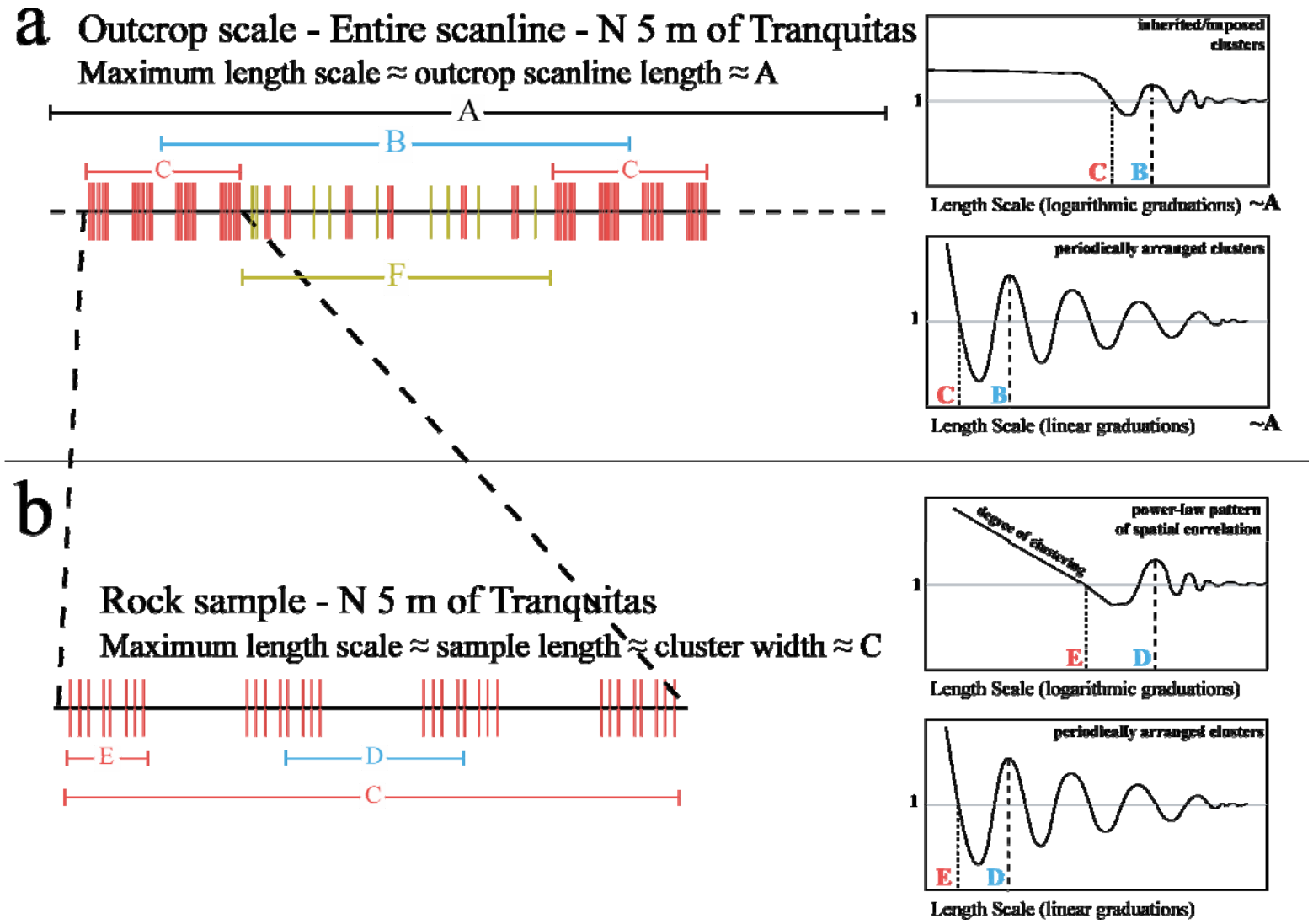
a
Outcrop scale - Entire scanline - N 5 m of Tranquitas
Maximum length scale ≈ outcrop scanline length ≈ A
A
B
C
C
F
inherited/imposed clusters
1
C
B
Length Scale (logarithmic graduations)
~A
periodically arranged clusters
1
C
B
Length Scale (linear graduations)
~A
b
Rock sample - N 5 m of Tranquitas
Maximum length scale ≈ sample length ≈ cluster width ≈ C
E
D
C
power-law pattern of spatial correlation
degree of clustering
1
E
D
Length Scale (logarithmic graduations)
periodically arranged clusters
1
E
D
Length Scale (linear graduations)

8.2.8.1.3 Huasteca and Escalera OO1

Fractures from the Huasteca and Escalera OO1 layers exhibit the same spatial arrangements at outcrop scale, periodically arranged clusters with a power-law pattern of spatial correlation inside clusters (Table 8.6; Figure 8.47a). Similarly, the Huasteca and Escalera OO1 data sets at rock sample scale exhibit the same arrangements, indistinguishable from random for logarithmically graduated length scales and periodically arranged clusters for linearly graduated length scales (Table 8.6; Figure 8.47b). Another similarity is that rock samples from both Huasteca and Escalera OO1 layers were obtained along the scanline and cover approximately half of an outcrop cluster (Tables 8.2 and 8.7), indicating that periodically arranged clusters with power-law pattern of spatial correlation at outcrop scale are formed, at least in part, by smaller periodically arranged clusters (Figure 8.47). In addition, there is a drastic reduction in the amount of strain (84%), and cluster spacing (97%) from outcrop to rock sample scale for the Huasteca data set (Table 8.7). Compared with the Huasteca data set, the Escalera OO1 exhibits a smaller reduction in strain (26%), but comparable reductions in cluster width (99%) and cluster spacing (99%) are comparable (Table 8.7).

There are two possible explanations about why fracture data sets from rock samples that are smaller than outcrop-scale cluster width (Huasteca and Escalera OO1, Table 8.7) yielded a periodic arrangement of clusters with linear graduation of length scales, but yielded indistinguishable from random arrangements with logarithmic graduations of length scale (Table 8.6; Figure 8.47). One possible explanation is that clusters that are periodically arranged at rock sample scale inside an outcrop-scale cluster do not exhibit power-law patterns of spatial correlation. However, another possible explanation is that by sampling only a portion of the outcrop-scale cluster, the scanline at

rock sample scale has enough clusters to detect a periodic arrangement of clusters (with linearly graduated length scales) but lacks enough fractures per cluster to detect a non-random arrangement using logarithmic graduations of length scale (Figure 8.47). Perhaps a longer microfracture population resulting from a longer rock sample would have yielded a non-random arrangement of fractures for logarithmically graduated length scales.

Figure 8.47 Sketches illustrating the Huasteca, Escalera OO1, and Tranquitas data sets (left) and the corresponding NCC analyses using linear graduations of length scale (right) for (a) outcrop scale, and (b) rock sample scale. Rock samples extracted from the intracluster domain of outcrop data set. Fractures for all three data sets exhibit periodically arranged clusters in both (a) and (b) (Table 8.6). Fractures inside clusters are red whereas fractures in the intercluster domains are green. Input data in (a) are macrofractures along the entire scanline at outcrop scale, whereas in (b) are fractures (both microfractures and macrofractures) in rock sample. Maximum length scale in (a) is equal to outcrop scanline length (A). Maximum length scale in (b) is equal to sample length, which is smaller than cluster width at outcrop scale (C). Cluster spacing at rock sample scale (D) is different that cluster spacing at outcrop scale (B).

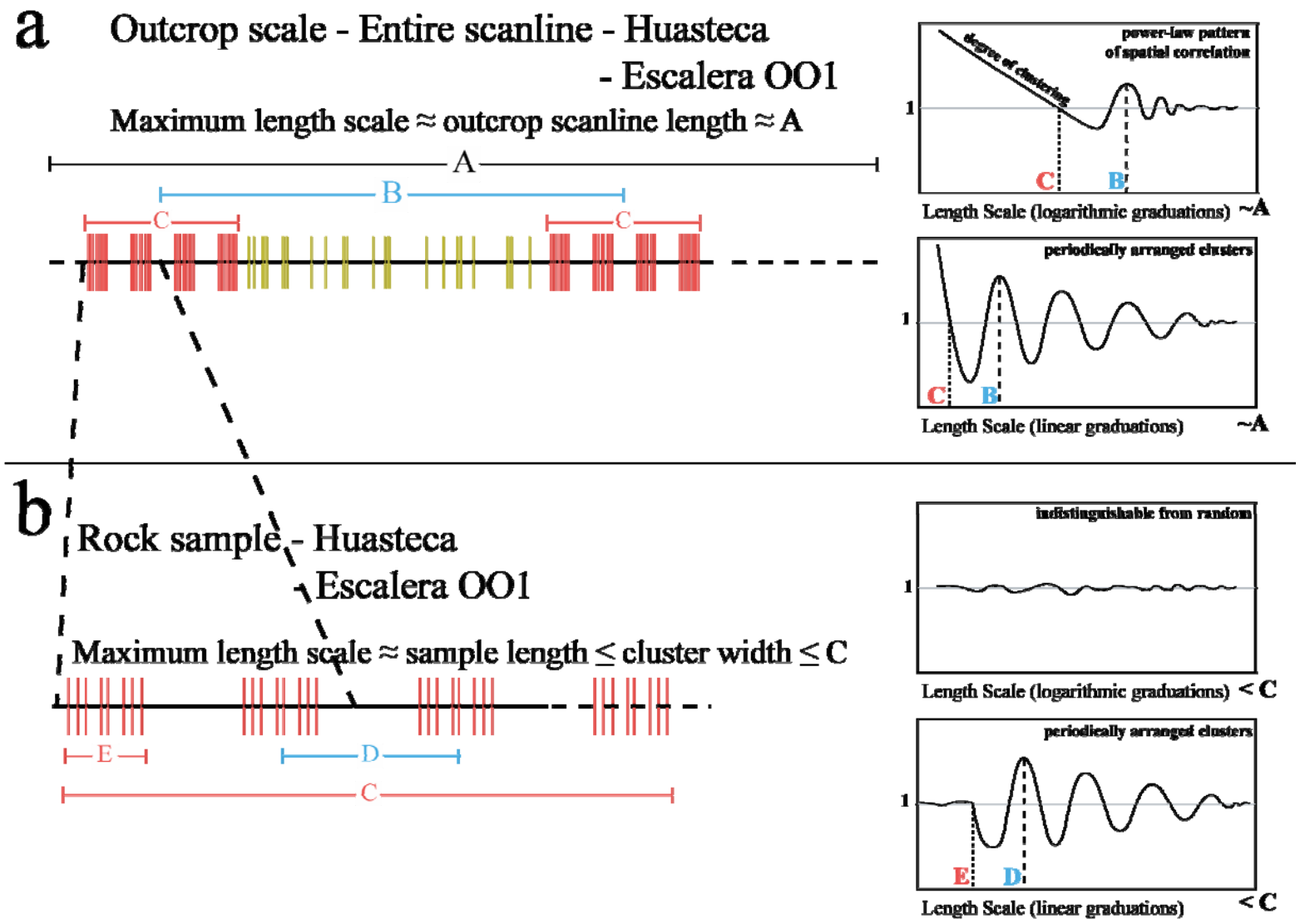
a
Outcrop scale - Entire scanline - Huasteca
- Escalera OO1
Maximum length scale ≈ outcrop scanline length ≈ A
A
B
C
C
power-law pattern
of spatial correlation
degree of clustering
1
C
B
Length Scale (logarithmic graduations)
~A
periodically arranged clusters
1
C
B
Length Scale (linear graduations)
~A
b
Rock sample - Huasteca
Escalera OO1
Maximum length scale ≈ sample length ≤ cluster width ≤ C
E
D
C
indistinguishable from random
1
Length Scale (logarithmic graduations)
< C
periodically arranged clusters
1
E
D
Length Scale (linear graduations)
< C

8.2.8.1.4 Palmas 11 LR

One outcrop data set that exhibits similar spatial arrangements as the Huasteca, Escalera OO1, Escalera O12 and Tranquitas outcrop data sets is the Palmas 11 LR data set, which displays periodically arranged clusters with a power-law pattern of spatial correlation (Figures 8.5d and 8.26). However, the two rock sample data sets from Palmas 11 yielded arrangements that are indistinguishable from random for both logarithmically and linearly graduated length scales (Table 8.6). Three features of the rock sample from Palmas 11 are different from rock samples of other layers that exhibit periodically arranged clusters with a power-law of spatial correlation (Escalera OO12 and Huasteca) or periodically arranged clusters (Escalera OO1 and Tranquitas). First, the rock sample from Palmas 11 was not extracted from an outcrop-scale cluster, but instead from the intercluster domain (Figure 8.2, Table 8.2). Second, the rock sample from Palmas 11 was not extracted along the scanline, or a position on the projected scanline, but instead was extracted near the layer base (Figure 8.48, Table 8.2). And third, the length of the rock sample (39 mm) is the smallest of all samples and much smaller than the outcrop cluster width (220 mm) and cluster spacing (1090 mm, Table 8.7).

Figure 8.48 Sketches illustrating the Palmas 11 LR data set (left) and the corresponding NCC analyses using logarithmic and linear graduations of length scale (right) for (a) outcrop scale, and (b) rock sample scale. Rock sample extracted from the intercluster domain of outcrop data set and near layer base (Table 8.2). Fractures in (a) exhibit a fractal arrangement of fractures, clusters that in turn are periodically arranged (Figure 8.5d), whereas fractures in (b) only exhibit arrangements that are indistinguishable from random (Figures 8.5a and 8.5e). Fractures inside clusters with a fractal arrangement are red whereas fractures in the intercluster domains are green. Input data in (a) are fractures along the entire scanline at outcrop scale, whereas in (b) are fractures (both microfractures and macrofractures) in rock sample. Maximum length scale in (a) is equal to outcrop scanline length (A). Maximum length scale in (b) is equal to sample length ($I << F$).

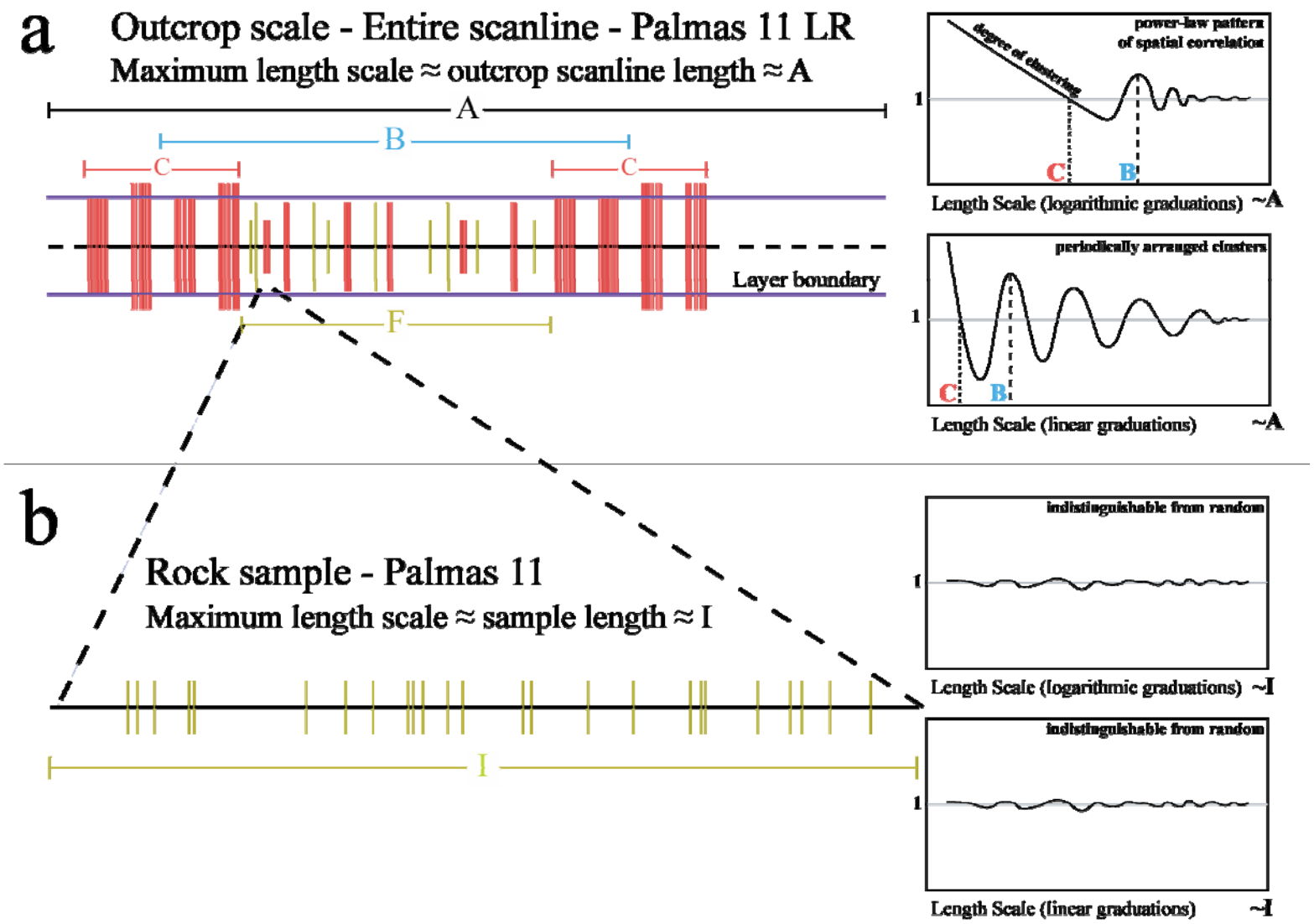
a
Outcrop scale - Entire scanline - Palmas 11 LR
Maximum length scale ≈ outcrop scanline length ≈ A
A
B
C
C
Layer boundary
F
power-law pattern of spatial correlation
degree of clustering
1
C
B
Length Scale (logarithmic graduations) ~A
periodically arranged clusters
1
C
B
Length Scale (linear graduations) ~A
b
Rock sample - Palmas 11
Maximum length scale ≈ sample length ≈ I
I
indistinguishable from random
1
Length Scale (logarithmic graduations) ~I
indistinguishable from random
1
Length Scale (linear graduations) ~I

8.2.8.2 Indistinguishable from Random Arrangements at Outcrop Scale

Data sets at outcrop scale from Palmas 12 and 13 exhibit spatial arrangements that are indistinguishable from random for both logarithmic and linear graduations of length scale (Table 8.6). Therefore, they lack statistically significant clusters, which implies that rock samples cannot represent statistically significant clusters at outcrop scale. Rock samples from Palmas 12 and Palmas 13 were taken along outcrop scanlines (Table 8.2), and yielded fractures with arrangements that are indistinguishable from random for logarithmically graduated length scales (Table 8.6; Figure 8.49). In contrast, scanlines in rock samples from Palmas 12 and Palmas 13 yielded periodic arrangement of fracture clusters for linearly graduated length scales (Figures 8.32b and 8.35b), indicating that at rock sample scale fractures (mostly microfractures) of Palmas 12 and Palmas 13 exhibit a non-random arrangement (Table 8.7; Figure 8.49).

Fractures at outcrop scale were measured with aperture thresholds of 0.265 and 0.14 mm for Palmas 12 and Palmas 13, respectively (Table 8.1). Only 14% (5 fractures) and 17% (24 fractures) of the rock sample data sets have apertures greater than or equal to outcrop threshold. Macrofractures at outcrop scale alone only yielded an arrangement of fractures indistinguishable from random even when length scales comparable to the rock sample are used (e.g., Figures 8.34 and 8.50), which suggests that although microfractures are organized, the fracture organization does not reach outcrop scale.

Figure 8.49 Sketches illustrating the Palmas 12 and Palmas 13 fracture data set (left) and the corresponding NCC analyses using logarithmic and linear graduations of length scale (right) for (a) outcrop scale, and (b) rock sample scale. For logarithmically graduated length scales, both (a) and (b) exhibit arrangements that are indistinguishable from random (Figure 8.5a). For linearly graduated length scales, (a) exhibits arrangements that are indistinguishable from random (Figure 8.5e) or that suggests some periodicity but without statistically significance, whereas for (b) fractures are organized in periodically arranged clusters (Figure 8.5g). Rock samples were extracted along the outcrop scanline, but because fractures do not exhibit statistically significant clustering at outcrop scale (Table 8.6), it is uncertain whether samples were extracted from intra- or intercluster domains. Fractures inside clusters that do not exhibit a power-law pattern of spatial correlation are blue whereas all other fractures are green. Input data in (a) are fractures along the entire scanline at outcrop scale, whereas in (b) are fractures (both microfractures and macrofractures) in rock sample. Maximum length scale in (a) is equal to outcrop scanline length (A). Maximum length scale in (b) is equal to sample length (I). Periodically arranged clusters in (b) exhibit cluster spacing (H).

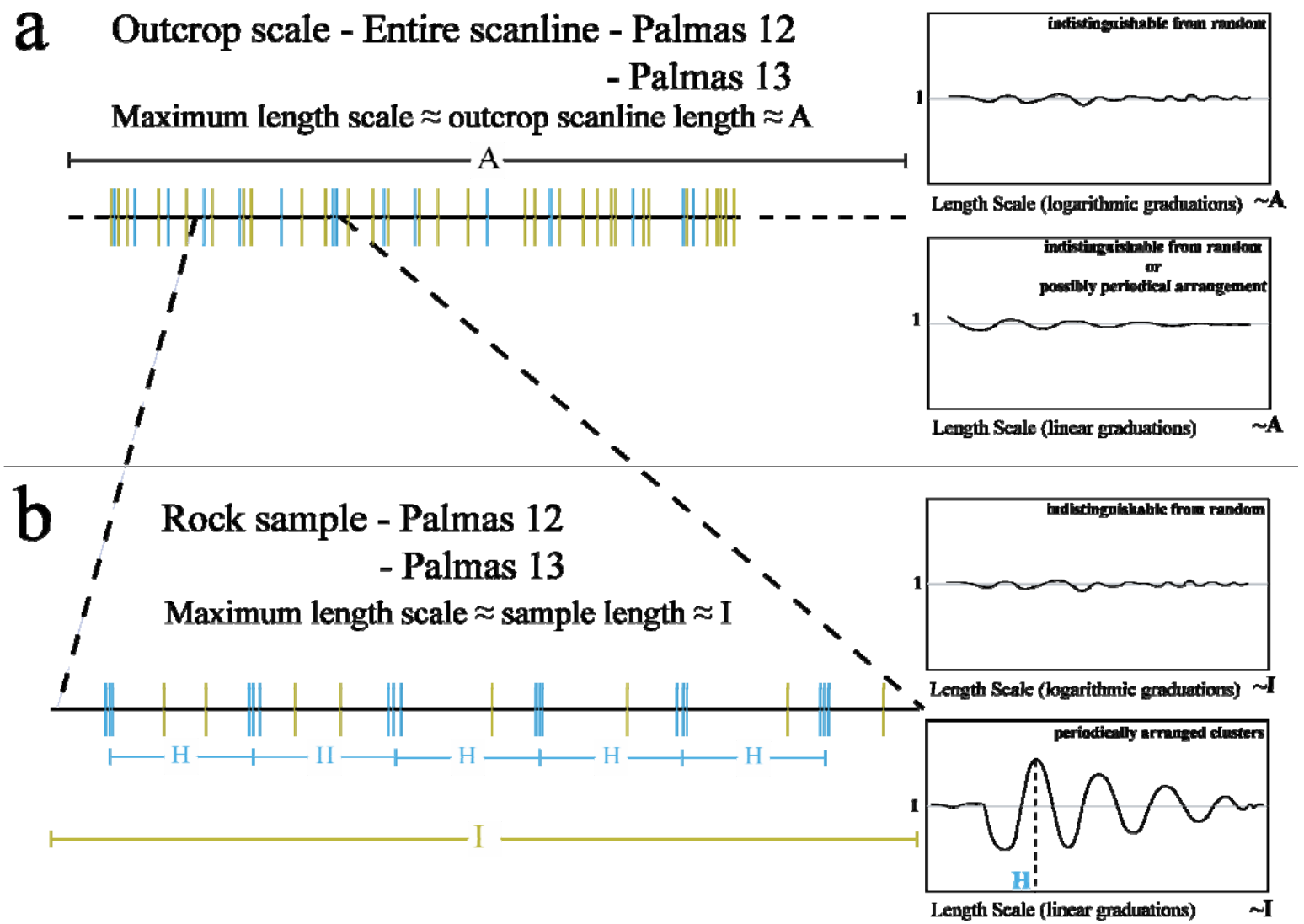
a
Outcrop scale - Entire scanline - Palmas 12
- Palmas 13
Maximum length scale ≈ outcrop scanline length ≈ A
A
indistinguishable from random
1
Length Scale (logarithmic graduations) ~A
indistinguishable from random
or
possibly periodical arrangement
1
Length Scale (linear graduations) ~A
b
Rock sample - Palmas 12
- Palmas 13
Maximum length scale ≈ sample length ≈ I
H
H
H
H
H
I
indistinguishable from random
1
Length Scale (logarithmic graduations) ~I
periodically arranged clusters
1
H
Length Scale (linear graduations) ~I

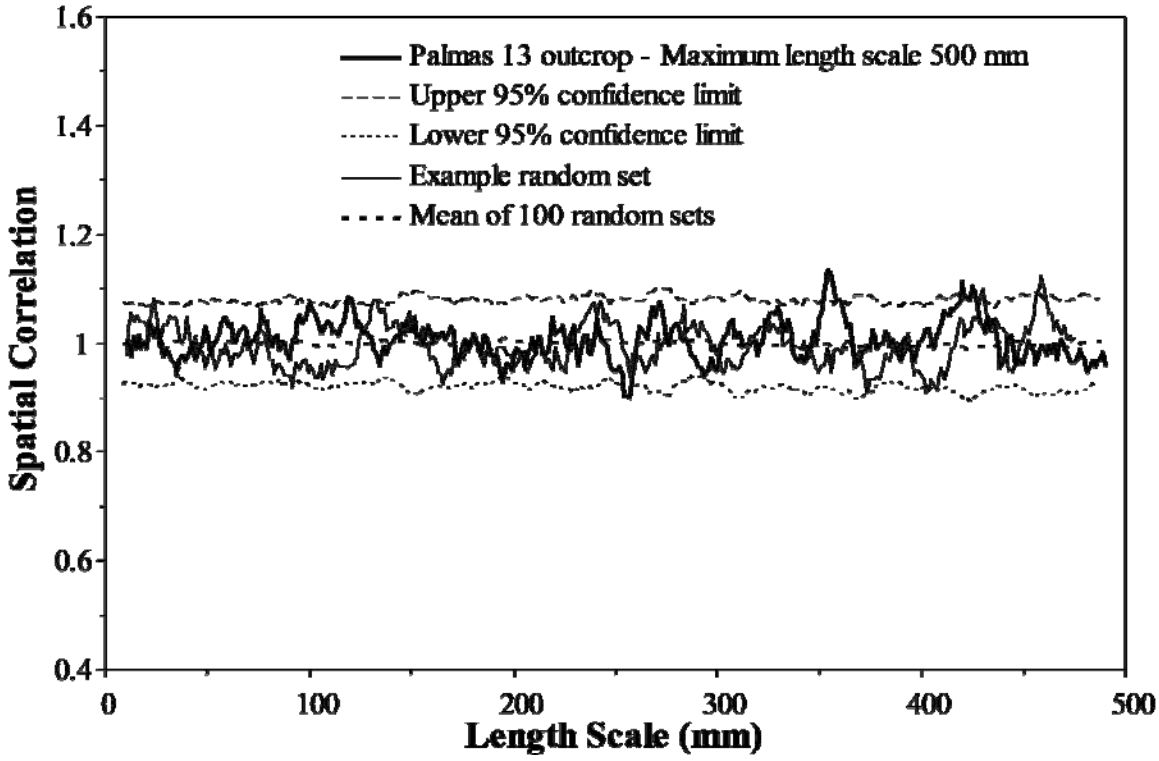

Figure 8.50 Graph of spatial correlation (thick continuous line) versus logarithmic graduations of length scale for the entire outcrop scanline at Palmas 13 data set (459 fractures, all fractures sets, aperture threshold of 0.14 mm). Thin discontinuous line represents the upper 95% confidence limit while the thin dotted line represents the lower 95% confidence limit, and the thick discontinuous line corresponds to the mean of 100 randomized data sets. Thin continuous line represents an example randomized set generated with the same number of fractures and scanline length. Width of length-scale bin is 13 graduations of length scale (m = 6). There is no pattern of spatial correlation that can be identified with length scale, suggesting that fractures at length scales smaller than 500 mm are indistinguishable from random.

8.3. DATA SETS WITHOUT ROCK SAMPLE

In addition to the seven pairs of data sets at outcrop and rock sample scale, three outcrop data sets (Grove Creek, Pedernales and Palmas 11 LR, Table 8.1) were selected for study of the internal structure of fracture clusters using subsets of outcrop data. The data sets were selected because they each exhibit a power-law pattern of spatial correlation with length scale and in graphs of kinematic aperture versus location along scanline they exhibit what qualitatively can be interpreted as clusters formed in turn by smaller clusters. For the purpose of comparing fracture clusters at different scales, an alternative method to studying rock samples is to compare the spatial correlation of different subsets of an outcrop scanline, as if a part of the outcrop scanline had been obtained by measuring fractures in thin section. For instance, the spatial arrangement of macrofractures located within a single cluster at outcrop scale is analogous to data collected in thin section from a sample within the cluster. In practice, studying the spatial arrangement of a subset of an outcrop scanline involves two steps. First, the removal of all fractures outside the domain of the outcrop data set under analysis and second, adjusting the length of the outcrop scanline (equal to the maximum length scale to be analyzed) to the length of the subset.

8.3.1 Grove Creek Outcrop Data Set

The Grove Creek outcrop of the Upper Cretaceous Austin Chalk Fm. is located near Waxahachie, north central Texas (Gale, 2002). The Grove Creek scanline was measured by Dr. J. Gale in a chalk layer (Stowell, 2001) and was graciously provided for my dissertation. The Grove Creek outcrop data set represents 136 fractures measured on a bedding-parallel outcrop along 246 m of scanline (Table 8.1). Fractures at Grove Creek

exhibit a power-law distribution of apertures, a logarithmic distribution of spacings and a coefficient of variation for fracture spacings of 1.82 (Table 8.5).

8.3.1.1 Entire Scanline

The Grove Creek data set exhibits a heterogeneous spatial arrangement of fractures (Figure 8.51a). Gale (2002) suggested that the largest (in width and proportion of total number of fractures) cluster in the Grove Creek data set contains smaller clusters that are regularly-spaced (Figure 8.51b). Spatial correlation for logarithmically graduated length scales for the entire Grove Creek data set displays a power-law pattern of fractures inside clusters (Figures 8.5b and 8.52a) with a cluster width of approximately 16000 mm. The power-law pattern is statistically significant (outside the 95% confidence interval) for more than 3 orders of magnitude of length scale (Figure 8.52a), which indicates that the interpreted arrangement is statistically significant.

Spatial correlation for linearly graduated length scales for the entire Grove Creek data set displays a pattern of alternating peaks and troughs of spatial correlation (Figure 8.52b), which could be interpreted as indicative of periodically arranged clusters with a cluster spacing estimated at 50000 mm (Figure 8.5g). Power spectrum of spatial correlation for linearly graduated length scales exhibits a statistically significant (outside the 95% confidence interval for red noise) peak at a wavelength of 47700 mm, supporting the interpretation of cluster spacing between 47.6 and 50 m (Figure 8.52c). Spatial correlation for linearly graduated length scales cannot be unequivocally interpreted as periodically arranged clusters, because the number of peaks of spatial correlation (indicative of the number of fracture clusters) is relatively small compared with other data sets such as fractures of set A at Huasteca canyon (Figure 8.21).

Figure 8.51 (a) Kinematic aperture and fracture intensity versus location along scanline for the entire Grove Creek data set. Fracture intensity was calculated inside a moving window with width (window size) of 15.5 m (equal to cluster width, Figure 8.52a) that was moved in increments (window step) 3 m. (b) Kinematic aperture versus location along scanline for the largest cluster of the Grove Creek data set. Figure in (b) was modified from Gale (2002). Notice in (b) the clusters (represented by a vertical alignment of data points) located approximately at 143, 146, 147, 149, 150.5, 152.5, 155, 156.5, and 159.5 m along the scanline.

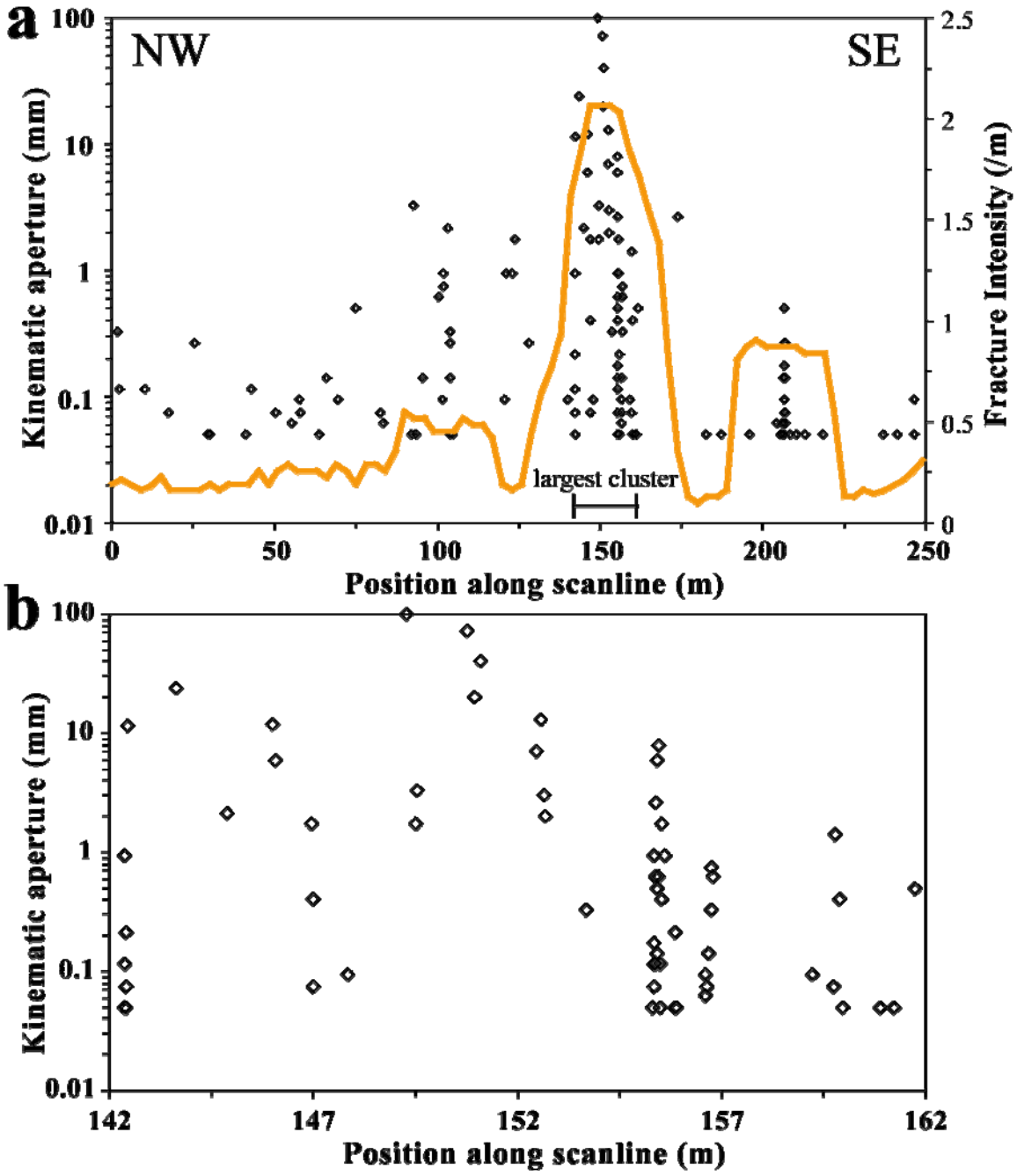
a
NW
SE
Kinematic aperture (mm)
Fracture Intensity (/m)
largest cluster
Position along scanline (m)
b
Kinematic aperture (mm)
Position along scanline (m)

Figure 8.52 Graphs of spatial correlation (thick continuous line) vs. length scale for (a) logarithmic graduations and (b) linear graduations for the Grove Creek data set (136 fractures, aperture threshold of 0.05 mm). In (a) and (b) the thin discontinuous line represents the upper 95% confidence limit while the thin dotted line represents the lower 95% confidence limit, and the thick discontinuous line corresponds to the mean of 100 randomized data sets. In (a) and (b) the thin continuous line represents the analytical solution of randomly arranged fractures with the same number of fractures and scanline length. Width of length-scale bin in (a) and (b) is 11 graduations of length scale (m = 5). Spatial correlation in (a) follows a power-law pattern. Power law equation in (a) was calculated using spatial correlation of Grove Creek data set between length scales of 10 and 20000 mm. Cluster width is estimated at 16000 mm, as shown in (a). Evenly spaced lines every 50000 mm in (b) match approximately peaks of spatial correlation, which display a regularly spaced pattern, indicative of periodically arranged clusters with a cluster spacing of approximately 50000 mm. (c) Power spectrum of spatial correlation from (b).

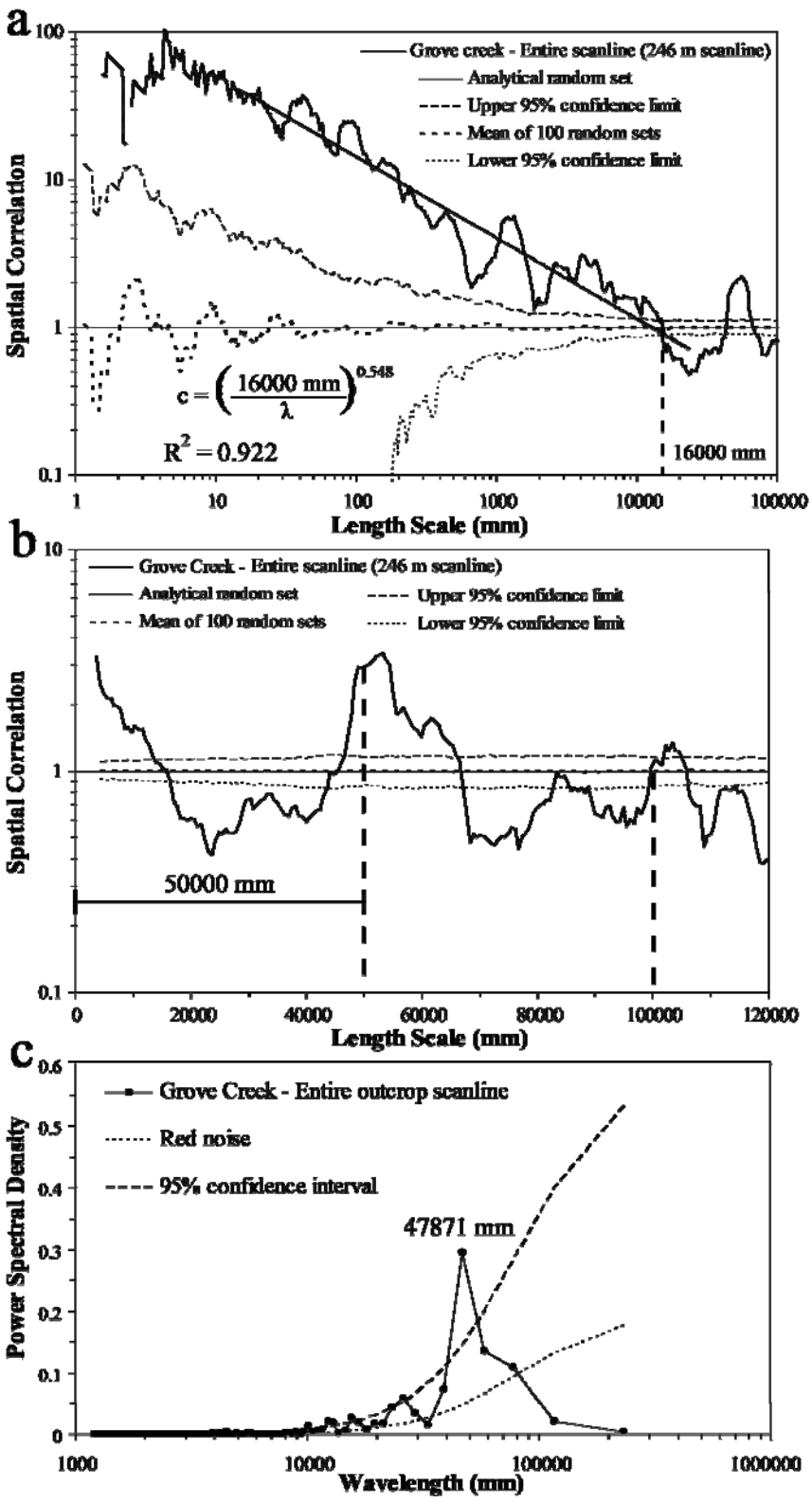
a
Grove creek - Entire scanline (246 m scanline)
Analytical random set
Upper 95% confidence limit
Mean of 100 random sets
Lower 95% confidence limit
Spatial Correlation
$c = \left(\frac{16000\ mm}{\lambda}\right)^{0.548}$
$R^2 = 0.922$
16000 mm
Length Scale (mm)
b
Grove Creek - Entire scanline (246 m scanline)
Analytical random set
Upper 95% confidence limit
Mean of 100 random sets
Lower 95% confidence limit
Spatial Correlation
50000 mm
Length Scale (mm)
c
Grove Creek - Entire outcrop scanline
Red noise
95% confidence interval
47871 mm
Power Spectral Density
Wavelength (mm)

8.3.1.2 Intracluster Domain

The largest (in width and proportion of total number of fractures) cluster in the Grove Creek data set is located between 142 and 162 m along the scanline (Figure 8.51a). The largest cluster in Grove Creek data set exhibits a fracture strain of 1.67% and contains 47% of all measured fractures. Independent NCC analyses of fractures only within the largest cluster at Grove Creek yielded same type of spatial arrangement as the entire data set. Namely, spatial correlation for logarithmically graduated length scales for the largest cluster of Grove Creek data set displays a power-law pattern with a cluster width of approximately 240 mm (Figures 8.5b and 8.53a). The power-law pattern is statistically significant (outside the 95% confidence interval) for more than one order of magnitude of length scale (Figure 8.53a), which indicates that the interpreted arrangement is statistically significant.

Spatial correlation for linearly graduated length scales for the largest cluster of Grove Creek data set displays a pattern of alternating peaks and troughs of spatial correlation (Figure 8.53b), which can be interpreted as indicative of periodically arranged clusters (Figure 8.5g). Cluster spacing is estimated at 1430 mm. Power spectrum of spatial correlation for linearly graduated length scales exhibits a statistically significant peak at a wavelength of 1430 mm, supporting the interpretation of a periodic arrangement of fracture clusters that is statistically significant with a cluster spacing of 1430 mm (Figure 8.53c). Although a peak of power spectral density is visible at a wavelength of 4000, this peak does not reach outside the 95% confidence interval for red noise and therefore is not statistically significant (Figure 8.53c). A statistically significant periodic arrangement of clusters inside the largest cluster of Grove Creek, as interpreted by NCC, validates the suggestion of Gale (2002) that the largest cluster in the Grove Creek data set is formed by smaller clusters that are regularly-spaced (Figure 8.51b).

Figure 8.53 Graphs of spatial correlation (thick continuous line) vs. length scale for (a) logarithmic graduations and (b) linear graduations for the largest cluster of Grove Creek data set (142 to 162 m along scanline, 63 fractures, aperture threshold of 0.05 mm). In (a) and (b) the thin discontinuous line represents the upper 95% confidence limit while the thin dotted line represents the lower 95% confidence limit, and the thick discontinuous line corresponds to the mean of 100 randomized data sets. In (a) and (b) the thin continuous line represents the analytical solution of randomly arranged fractures with the same number of fractures and scanline length. Width of length-scale bin in (a) and (b) is 11 graduations of length scale (m = 5). Spatial correlation in (a) follows a power-law pattern. Power law equation in (a) was calculated using spatial correlation o between length scales of 9 and 200 mm. Cluster width is estimated at 240 mm, as shown in (a). Evenly spaced lines every 1430 mm in (b) match approximately peaks of spatial correlation, which display a regularly spaced pattern, indicative of periodically arranged clusters with a cluster spacing of approximately 1430 mm. (c) Power spectrum of spatial correlation from (b).

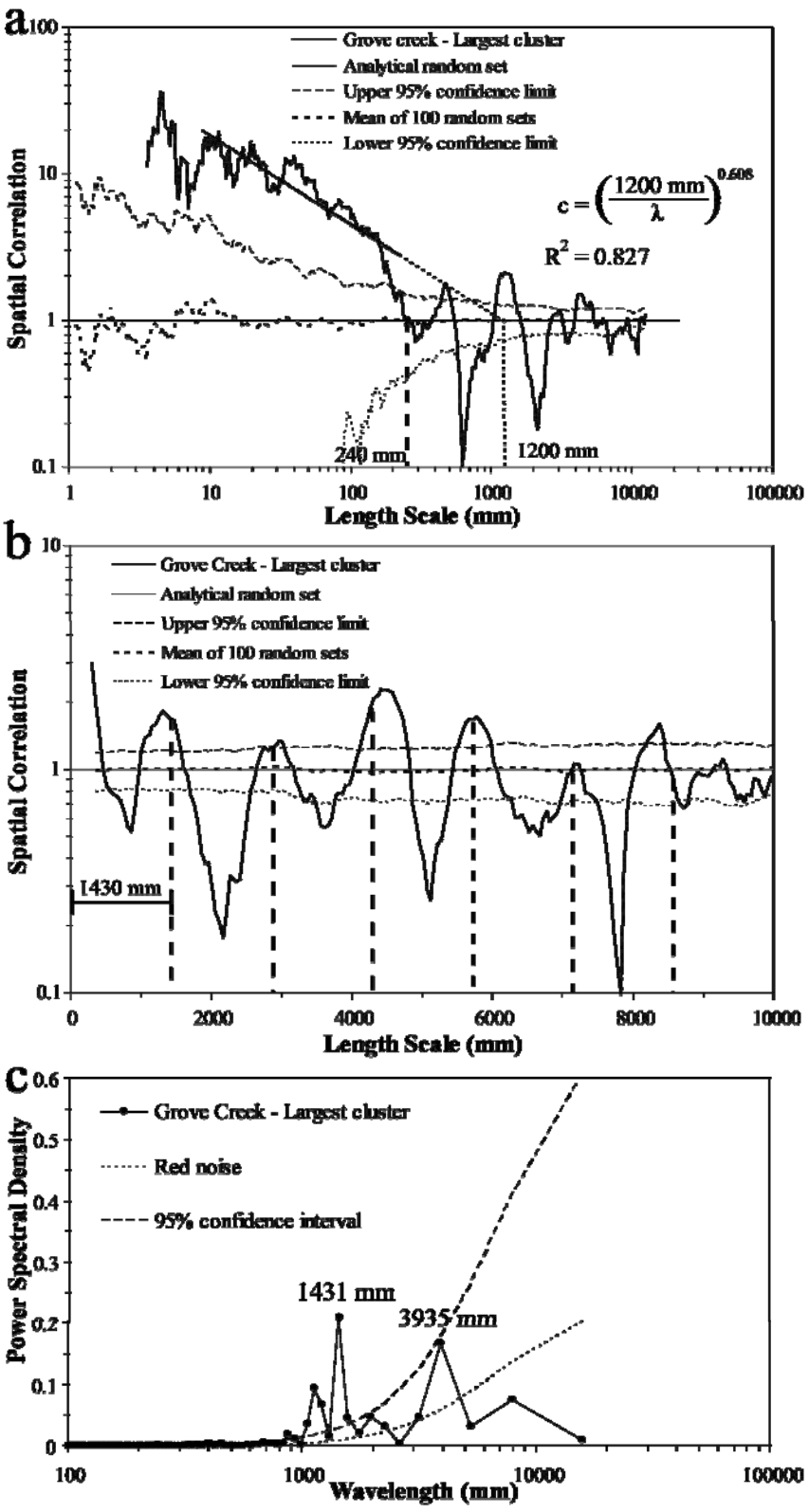
a
Grove creek - Largest cluster
Analytical random set
Upper 95% confidence limit
Mean of 100 random sets
Lower 95% confidence limit
$c = \left(\frac{1200\ mm}{\lambda}\right)^{0.608}$
$R^2 = 0.827$
240 mm
1200 mm
Spatial Correlation
Length Scale (mm)
b
Grove Creek - Largest cluster
Analytical random set
Upper 95% confidence limit
Mean of 100 random sets
Lower 95% confidence limit
1430 mm
Spatial Correlation
Length Scale (mm)
c
Grove Creek - Largest cluster
Red noise
95% confidence interval
1431 mm
3935 mm
Power Spectral Density
Wavelength (mm)

8.3.1.3 Intercluster Domains

The largest cluster in the Grove Creek data set is located between 142 and 162 m along scanline, as indicated by fracture intensity (Figure 8.51a). The largest cluster in Grove Creek data set occupies approximately 10% of the scanline and contains 47% of the measured fractures. Although other clusters are suggested by peaks of fracture intensity, they are smaller than the largest cluster in width and in number of fractures. For instance, the second largest cluster at Grove Creek is located at 208 m along scanline (Figure 8.51a), occupies 0.5% of the scanline and contains 13% of the measured fractures. Because there are no clusters comparable in width or number of fractures to the largest cluster, all domains outside the area occupied by the largest cluster will be considered intercluster (Figure 8.2).

8.3.1.3.1 Northwest of Largest Cluster

The largest intercluster domain for the Grove Creek data set is located between 0 and 142 m along the scanline (Figure 8.51a). Between 0 and 142 m, Grove Creek scanline exhibits a fracture strain of only 0.011%. Fractures of the intercluster domain located northwest of the largest cluster were analyzed independently using NCC. Spatial correlation for logarithmically graduated length scales for fractures located between 0 and 142 m did not yield a systematic pattern, which is indicative of an arrangement that is indistinguishable from random (Figures 8.5a and 8.54a). Spatial correlation for linearly graduated length scales for fractures in the intercluster domain displays a pattern of alternating peaks and troughs of spatial correlation (Figure 8.54b) that might represent periodically arranged clusters (Figure 8.5g) with a cluster spacing of approximately 8800 mm. The periodicity of fracture clusters in the intercluster domain is questionable because only two peaks of spatial correlation are statistically significant (Figure 8.54b). Power spectrum of spatial correlation for linearly graduated length scales exhibits two

statistically significant (outside the 95% confidence interval for red noise) peaks at wavelengths of 8800 an 13000 mm (Figure 8.54c). The shortest wavelength with a statistically significant power spectral density (Figure 8.54c) is almost identical to the cluster spacing estimated using NCC (Figure 8.54b), which supports the interpretation of a periodic arrangement of fracture clusters that is statistically significant with a cluster spacing of approximately 8800 mm. Although cluster width is typically estimated using logarithmically graduated length scales (Figures 8.5b to 8.5d), cluster width for fractures between 0 and 142 m along the scanline appears to be around 4000 mm (Figure 8.54b).

Figure 8.54 Graphs of spatial correlation (thick continuous line) vs. length scale for (a) logarithmic graduations and (b) linear graduations for the domain of the Grove Creek data set between the beginning of the scanline and the largest cluster (0 to 142 m along scanline, 39 fractures, aperture threshold of 0.05 mm). In (a) and (b) the thin discontinuous line represents the upper 95% confidence limit while the thin dotted line represents the lower 95% confidence limit, and the thick discontinuous line corresponds to the mean of 100 randomized data sets. In (a) and (b) the thin continuous line represents the analytical solution of randomly arranged fractures with the same number of fractures and scanline length. Width of length-scale bin in (a) and (b) is 15 (m = 7) graduations of length scale. Spatial correlation in (a) does not follow a systematic pattern. Evenly spaced lines every 9000 mm in (b) match approximately peaks of spatial correlation, which display a regularly spaced pattern, indicative of periodically arranged clusters. (c) Power spectrum of spatial correlation from (b). A noticeable peak at a wavelength of 8755 mm has a power spectral density outside the 95% confidence interval for red noise.

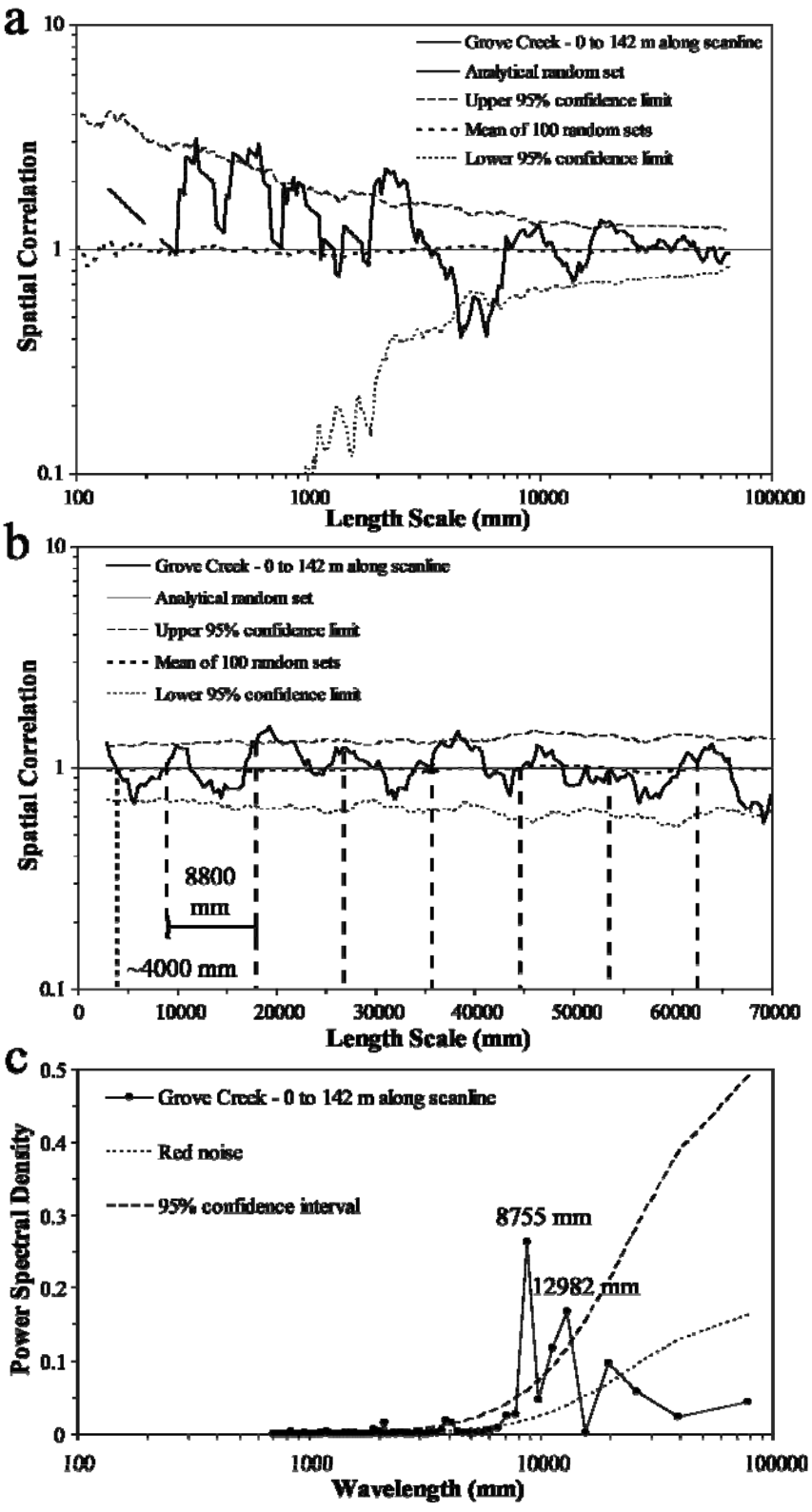
a
Grove Creek - 0 to 142 m along scanline
Analytical random set
Upper 95% confidence limit
Mean of 100 random sets
Lower 95% confidence limit
Spatial Correlation
Length Scale (mm)
b
Grove Creek - 0 to 142 m along scanline
Analytical random set
Upper 95% confidence limit
Mean of 100 random sets
Lower 95% confidence limit
Spatial Correlation
8800 mm
~4000 mm
Length Scale (mm)
c
Grove Creek - 0 to 142 m along scanline
Red noise
95% confidence interval
8755 mm
12982 mm
Power Spectral Density
Wavelength (mm)

8.3.1.3.2 Southeast of Largest Cluster

The domain of the Grove Creek scanline located southeast of the largest cluster (180 to 246 m along scanline, Figure 8.51a) is considered intercluster (Figure 8.2) because it includes a cluster that is much smaller (in width and number of fractures) than the largest cluster (142 to 162 m along scanline, Figure 8.51a). The second largest cluster at Grove Creek is located at 208 m along scanline (Figure 8.51a), occupies 0.5% of the scanline and contains 13% of the measured fractures.

Fractures between 180 and 246 m along Grove Creek scanline exhibits a fracture strain of only 0.005%. Independent NCC analyses of fractures located between 180 and 246 m yielded the same type of spatial arrangements as the entire data set (Figure 8.52) and the largest cluster (Figure 8.53). Namely, spatial correlation for logarithmically graduated length scales displays a power-law pattern inside clusters (Figure 8.5b) with a cluster width of approximately 2900 mm (Figure 8.55a). The power-law pattern is statistically significant (outside the 95% confidence interval) for about two orders of magnitude of length scale (Figure 8.55a), indicating that the interpreted arrangement is statistically significant. Spatial correlation for linearly graduated length scales for fractures between 180 and 246 m displays a pattern of alternating peaks (mostly statistically significant) and troughs of spatial correlation (Figure 8.55b), indicating periodically arranged clusters (Figure 8.5g). Cluster spacing is estimated at 5850 mm. Power spectrum of spatial correlation for linearly graduated length scales exhibits two statistically significant (outside the 95% confidence interval for red noise) peaks at wavelengths of 3832 an 5747 mm (Figure 8.55c). The longest wavelength with a statistically significant power spectral density (Figure 8.55c) is almost identical to the cluster spacing estimated using NCC (Figure 8.55b), which supports the interpretation of

a periodic arrangement of fracture clusters that is statistically significant with a cluster spacing of approximately 5800 mm.

Figure 8.55 Graphs of spatial correlation (thick continuous line) vs. length scale for (a) logarithmic graduations and (b) linear graduations for the second largest cluster of Grove Creek data set (180 to 246 m along scanline, 31 fractures, aperture threshold of 0.05 mm). In (a) and (b) the thin discontinuous line represents the upper 95% confidence limit while the thin dotted line represents the lower 95% confidence limit, and the thick discontinuous line corresponds to the mean of 100 randomized data sets. In (a) and (b) the thin continuous line represents the analytical solution of randomly arranged fractures with the same number of fractures and scanline length. Width of length-scale bin in (a) is 17 (m = 8) and in (b) is 15 (m = 7) graduations of length scale. Spatial correlation in (a) follows a power-law pattern. Power law equation in (a) was calculated using spatial correlation o between length scales of 70 and 2900 mm. Cluster width is estimated at 2900 mm, as shown in (a). Evenly spaced lines every 5850 mm in (b) match approximately peaks of spatial correlation, which display a regularly spaced pattern, indicative of periodically arranged clusters with a cluster spacing of approximately 5850 mm. (c) Power spectrum of spatial correlation from (b).

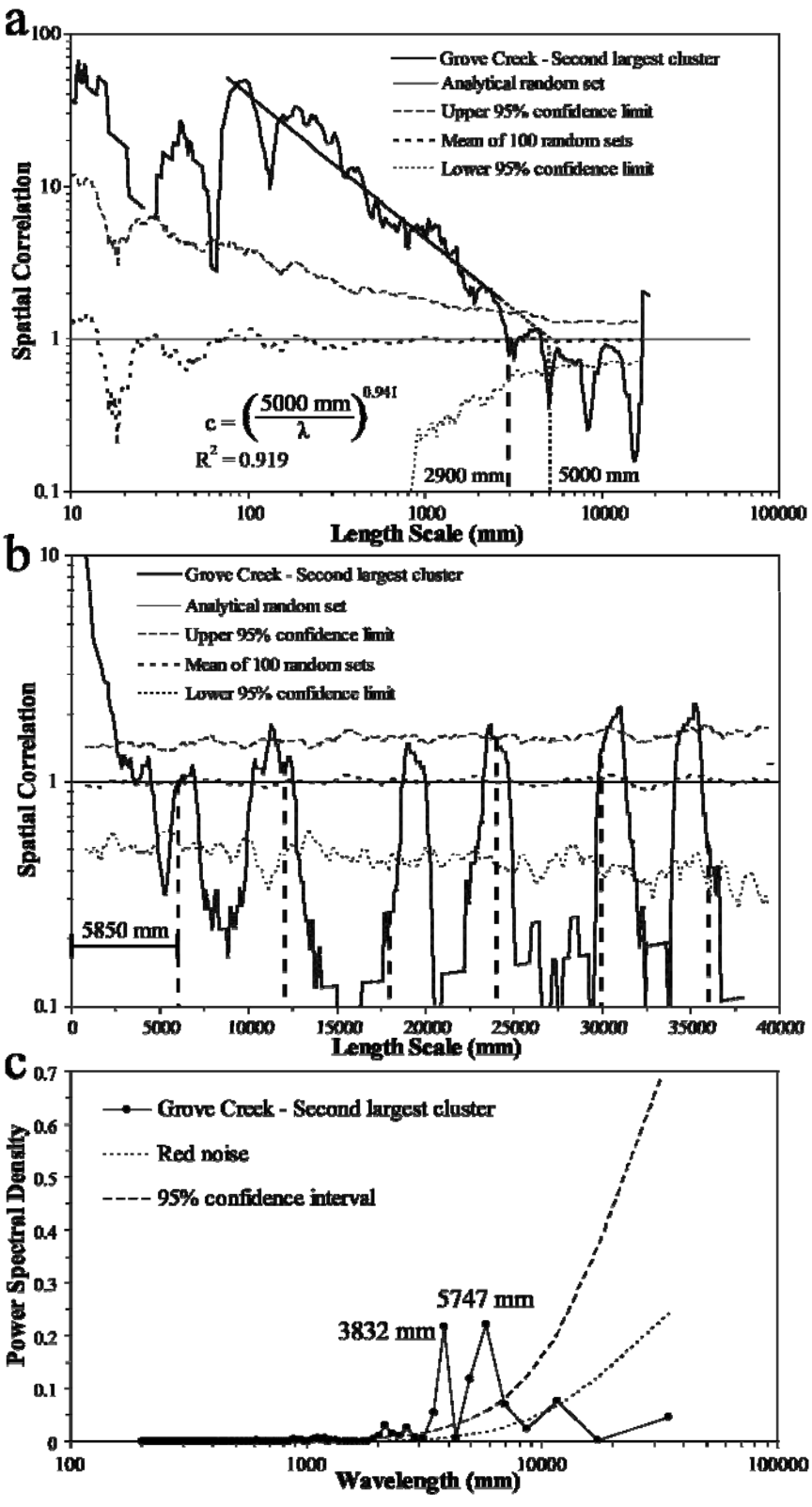
a
Grove Creek - Second largest cluster
Analytical random set
Upper 95% confidence limit
Mean of 100 random sets
Lower 95% confidence limit
Spatial Correlation
$c = \left(\frac{5000\ mm}{\lambda}\right)^{0.941}$
$R^2 = 0.919$
2900 mm
5000 mm
Length Scale (mm)
b
Grove Creek - Second largest cluster
Analytical random set
Upper 95% confidence limit
Mean of 100 random sets
Lower 95% confidence limit
Spatial Correlation
5850 mm
Length Scale (mm)
c
Grove Creek - Second largest cluster
Red noise
95% confidence interval
Power Spectral Density
5747 mm
3832 mm
Wavelength (mm)

8.3.2 Pedernales Outcrop Data Set

The Pedernales fracture data set was measured in a bedding-parallel outcrop of a limestone layer belonging to the Upper Member of the Marble Falls Limestone by several researchers of the Department of Geological Sciences of The University of Texas at Austin, and was graciously provided for my dissertation. Using an aperture threshold of 0.05 mm, a total of 916 fractures were measured at Pedernales in a 59 m long scanline (Table 8.1). Fractures at Pedernales exhibit a power-law distribution of apertures, a log-normal distribution of spacings and a coefficient of variation for spacings of 2.43 (Table 8.5). A more complete description of the Pedernales outcrop was provided in Chapter 2.

8.3.2.1 Entire Scanline

The Pedernales data set exhibits a heterogeneous spatial arrangement of fractures (Figure 8.56a). Pedernales fractures exhibit three clusters centered at 3, 22, and 57 m along the scanline. Spatial correlation for logarithmically graduated length scales for the entire Pedernales data set displays a power-law pattern inside clusters with a cluster width of approximately 7200 mm (Figures 8.5b and 8.57a). The power-law pattern is statistically significant (outside the 95% confidence interval) for about 3 orders of magnitude of length scale, which indicates that the interpreted arrangement is statistically significant (Figure 8.57a). Spatial correlation for linearly graduated length scales for the entire Pedernales data set displays a pattern of peaks (12500 and 19000 mm) and troughs of spatial correlation that are statistically significant (Figure 8.57b). Fractures at Pedernales do not exhibit the pattern of alternating peaks and troughs that is interpreted to indicate periodically arranged clusters (Figure 8.5g). The uncertainty in interpreting periodically arranged clusters at Pedernales might be caused by the relatively short length of the scanline (59 m) compared with the cluster spacing (19 m, Figure 8.57c) and cluster width (7 m), which only allowed three clusters, which are not regularly spaced, to be

measured (Figure 8.56a). Power spectrum of spatial correlation for linearly graduated length scales exhibits two statistically significant (outside the 95% confidence interval for red noise) peaks at wavelengths of 4112 and 19190 mm (Figure 8.57c). However, the difference between the highest peak and the 95% confidence interval is small when compared with other data sets (e.g., eastern 1.6 m of Escalera OO1 data set, Figure 8.10c). Because the wavelength of 19200 matches the largest peak of spatial correlation (Figure 8.57b), it is interpreted that cluster spacing is 19200 mm between the southern and middle clusters.

Figure 8.56 Kinematic aperture and fracture intensity versus location along scanline for (a) entire Pedernales scanline and (b) between 12 and 32 m along the scanline of the Pedernales data set. Fracture intensity in (a) was calculated inside a window with width equal to 7 m (estimated cluster width in Figure 8.57a and 8.57b) moved 0.1 m. Fracture intensity in (b) was calculated inside a window with width equal to 0.45 m moved in increments of 0.2 m. Please note that only the kinematic aperture axis use logarithmic graduations in (a) and (b). In (a) and (b) bars indicate the different domains of the Pedernales scanline that were independently analyzed with NCC.

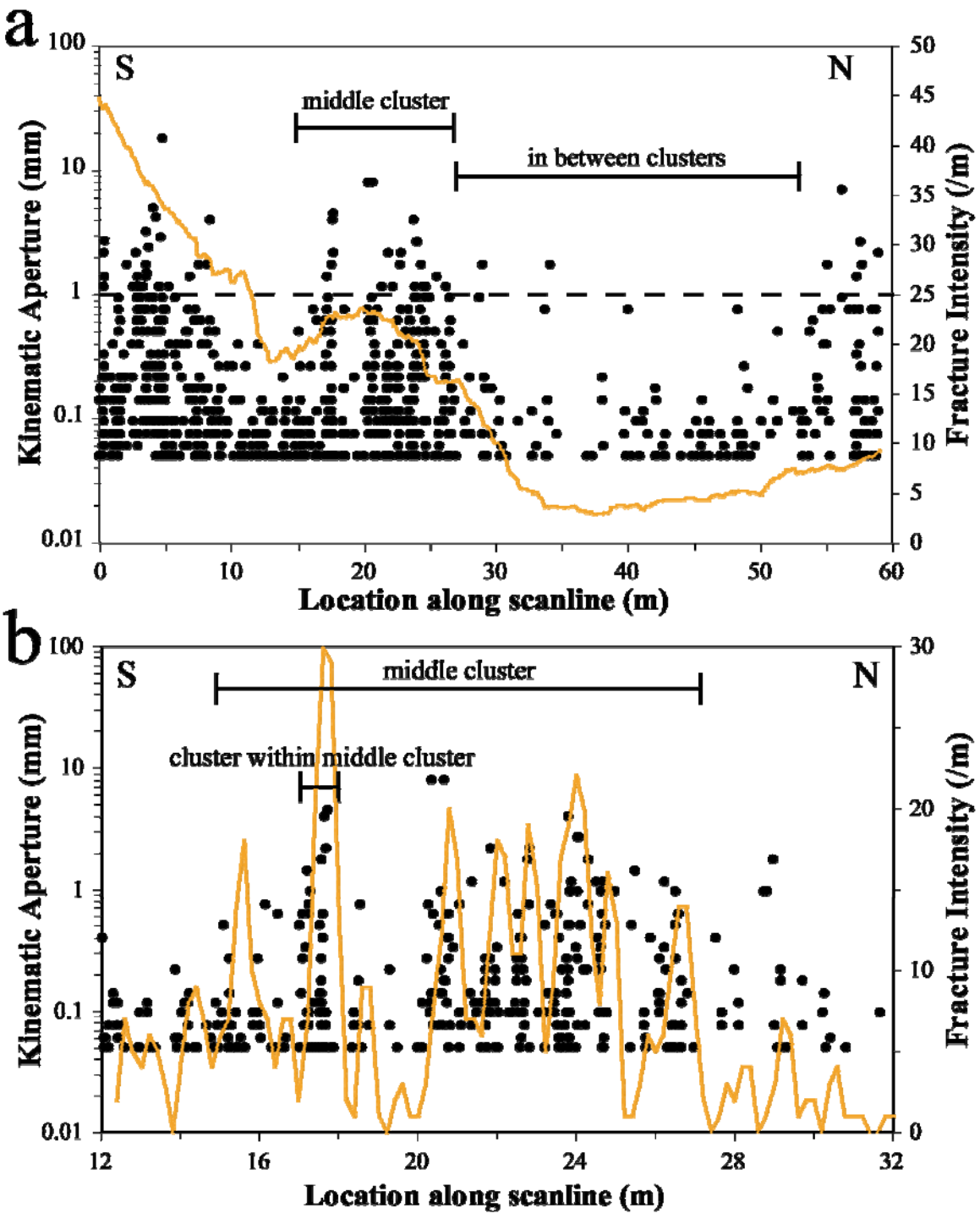
a
S
N
middle cluster
in between clusters
Kinematic Aperture (mm)
Fracture Intensity (/m)
Location along scanline (m)
b
S
N
middle cluster
cluster within middle cluster
Kinematic Aperture (mm)
Fracture Intensity (/m)
Location along scanline (m)

Figure 8.57 Graphs of spatial correlation (thick continuous line) vs. length scale for (a) logarithmic graduations and (b) linear graduations for the entire Pedernales data set (59 m of scanline, 916 fractures, aperture threshold of 0.05 mm). In (a) and (b) the thin discontinuous line represents the upper 95% confidence limit while the thin dotted line represents the lower 95% confidence limit, and the thick discontinuous line corresponds to the mean of 100 randomized data sets. In (a) the thin continuous line represents the analytical solution of randomly arranged fractures with the same number of fractures and scanline length. In (b) the thin continuous line represents an example randomized set generated with the same number of fractures and scanline length. Width of length-scale bin in (a) and (b) is 9 ($m = 4$) graduations of length scale. Spatial correlation in (a) follows a power-law pattern. Power law equation in (a) was calculated using spatial correlation between length scales of 9 and 17000 mm. Cluster width is estimated at 7200 mm, as shown in (a) and (b). Two statistically significant peaks at 13000 and 18000 mm are shown in (b). (c) Power spectrum of spatial correlation from (b).

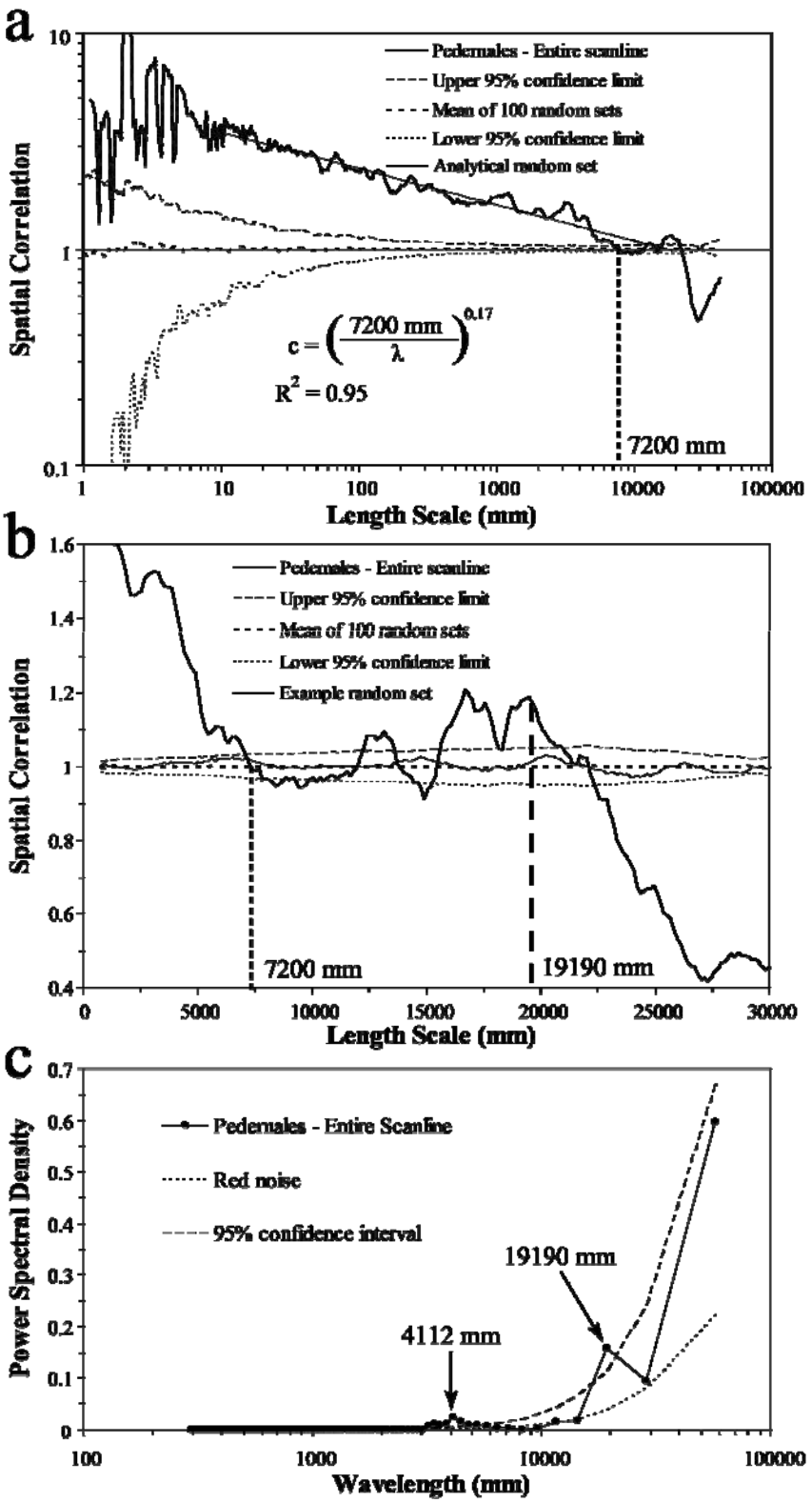
a
Pedernales - Entire scanline
Upper 95% confidence limit
Mean of 100 random sets
Lower 95% confidence limit
Analytical random set
Spatial Correlation
c = (7200 mm / λ)^0.17
R^2 = 0.95
7200 mm
Length Scale (mm)
b
Pedernales - Entire scanline
Upper 95% confidence limit
Mean of 100 random sets
Lower 95% confidence limit
Example random set
Spatial Correlation
7200 mm
19190 mm
Length Scale (mm)
c
Pedernales - Entire Scanline
Red noise
95% confidence interval
Power Spectral Density
19190 mm
4112 mm
Wavelength (mm)

8.3.2.2 Intracluster Domains

8.3.2.2.1 Middle Cluster

Pedernales data set exhibits three clusters at outcrop scale (Figure 8.56a). The boundaries of the middle cluster, which seems the widest, can be approximately located at 15 and 27 m along scanline (Figure 8.56). The middle cluster exhibits a fracture strain of 0.94%. Spatial correlation for logarithmically graduated length scales for middle cluster (Figures 8.5b and 8.58a) yielded the same type of spatial arrangements, a power-law pattern, as the entire data set (Figure 8.57a). The middle cluster at Pedernales exhibits a cluster width of approximately 470 mm (Figure 8.58a). The power-law pattern is statistically significant (outside the 95% confidence interval) for at least two orders of magnitude of length scale (Figure 8.58a), which indicates that the interpreted arrangement is statistically significant. Spatial correlation for linearly graduated length scales for fractures in the middle cluster at Pedernales displays a pattern of alternating peaks (mostly statistically significant) and troughs of spatial correlation (Figure 8.58b), which can be interpreted as periodically arranged clusters (Figure 8.5g). Cluster spacing is estimated at 1010 mm using NCC (Figure 8.58b). Power spectrum of spatial correlation for linearly graduated length scales exhibits two statistically significant (outside the 95% confidence interval for red noise) peaks at wavelengths of 972 and 2917 mm (Figure 8.58c). The shortest wavelength with a statistically significant power spectral density (Figure 8.58c) is almost identical to the cluster spacing estimated using NCC (Figure 8.58b), which supports the interpretation of a periodic arrangement of fracture clusters that is statistically significant with a cluster spacing of approximately 1000 mm. The longest wavelength (2917 mm) has a larger power spectral density and is also a multiple of the shortest wavelength (972 mm), which suggests that they expressions of the same periodic arrangement.

Figure 8.58 Graphs of spatial correlation (thick continuous line) vs. length scale for (a) logarithmic graduations and (b) linear graduations for the middle cluster of Pedernales data set (15 to 27 m along scanline, 302 fractures, aperture threshold of 0.05 mm). Location of position along scanline for middle cluster is shown in Figure 8.54. In (a) and (b) the thin discontinuous line represents the upper 95% confidence limit while the thin dotted line represents the lower 95% confidence limit, and the thick discontinuous line corresponds to the mean of 100 randomized data sets. In (a) and (b) the thin continuous line represents the analytical solution of randomly arranged fractures with the same number of fractures and scanline length. Width of length-scale bin in (a) is 15 (m = 7) and in (b) is 7 (m = 3) graduations of length scale. Spatial correlation in (a) follows a power-law pattern. Power law equation in (a) was calculated using spatial correlation o between length scales of 2.5 and 400 mm. Cluster width is estimated at 470 mm, as shown in (a). Evenly spaced lines every 1010 mm in (b) match approximately peaks of spatial correlation, which display a regularly spaced pattern, indicative of periodically arranged clusters. (c) Power spectrum of spatial correlation from (b).

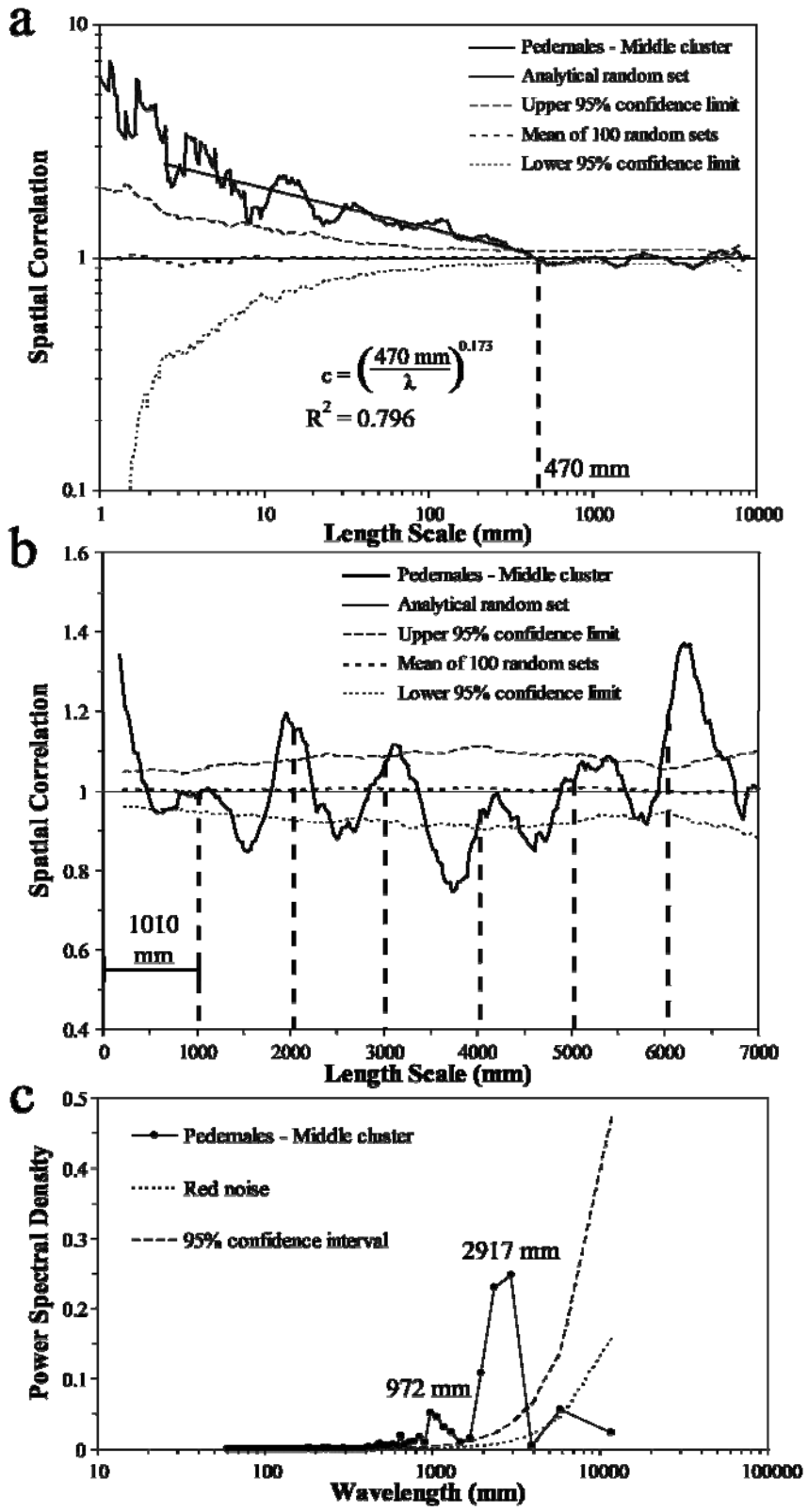
a
Pedernales - Middle cluster
Analytical random set
Upper 95% confidence limit
Mean of 100 random sets
Lower 95% confidence limit
Spatial Correlation
$c = \left(\frac{470\ mm}{\lambda}\right)^{0.173}$
$R^2 = 0.796$
470 mm
Length Scale (mm)
b
Pedernales - Middle cluster
Analytical random set
Upper 95% confidence limit
Mean of 100 random sets
Lower 95% confidence limit
Spatial Correlation
1010 mm
Length Scale (mm)
c
Pedernales - Middle cluster
Red noise
95% confidence interval
2917 mm
972 mm
Power Spectral Density
Wavelength (mm)

8.3.2.2.2 Sub-Cluster within Middle Cluster

Fracture intensity suggests that there are sub-clusters (peaks of fracture intensity) within the middle cluster at Pedernales (Figure 8.56b). The boundaries of one sub-cluster can be approximately located between 17 and 18 m along scanline (Figure 8.56b). The sub-cluster exhibits a fracture strain of 2.62%. Spatial correlation for logarithmically graduated length scales for sub-cluster yielded the same type of spatial arrangement as the entire data set (Figure 8.57a) or the middle cluster alone (Figure 8.58a), a power-law pattern with a cluster width of approximately 8.5 mm (Figures 8.5b and 8.59a). The power-law pattern is statistically significant (outside the 95% confidence interval) for about half an order of magnitude of length scale (Figure 8.59a), which suggests that the interpreted arrangement is statistically significant. Spatial correlation for linearly graduated length scales for fractures in the sub-cluster within the middle cluster at Pedernales displays an evident pattern of alternating peaks (mostly statistically significant) and troughs of spatial correlation (Figure 8.59b), which can be interpreted as periodically arranged clusters (Figure 8.5g). Cluster spacing is estimated at 37 mm using NCC (Figure 8.59b). Power spectrum of spatial correlation for linearly graduated length scales exhibits one statistically significant (outside the 95% confidence interval for red noise) peak at a wavelength of 37 mm, supporting statistically significance of the periodic arrangement of fracture clusters with a cluster spacing of 37 mm interpreted with NCC (Figure 8.59c).

Figure 8.59 Graphs of spatial correlation (thick continuous line) vs. length scale for (a) logarithmic graduations and (b) linear graduations for the a cluster within the middle cluster of Pedernales data set (17 to 18 m along scanline, 51 fractures, aperture threshold of 0.05 mm). Location of position along scanline for sub-cluster within middle cluster is shown in Figure 8.54. In (a) and (b) the thin discontinuous line represents the upper 95% confidence limit while the thin dotted line represents the lower 95% confidence limit, and the thick discontinuous line corresponds to the mean of 100 randomized data sets. In (a) and (b) the thin continuous line represents the analytical solution of randomly arranged fractures with the same number of fractures and scanline length. Width of length-scale bin in (a) is 21 (m = 10) and in (b) is 15 (m = 7) graduations of length scale. Spatial correlation in (a) follows a power-law pattern. Power law equation in (a) was calculated using spatial correlation between length scales of 1.5 and 8.5 mm. Cluster width is estimated at 8.5 mm, as shown in (a). Evenly spaced lines every 37 mm in (b) match approximately peaks of spatial correlation, which display a regularly spaced pattern. (c) Power spectrum of spatial correlation from (b). A noticeable peak at a wavelength of 37 mm has a power spectral density several times the 95% confidence interval for red noise.

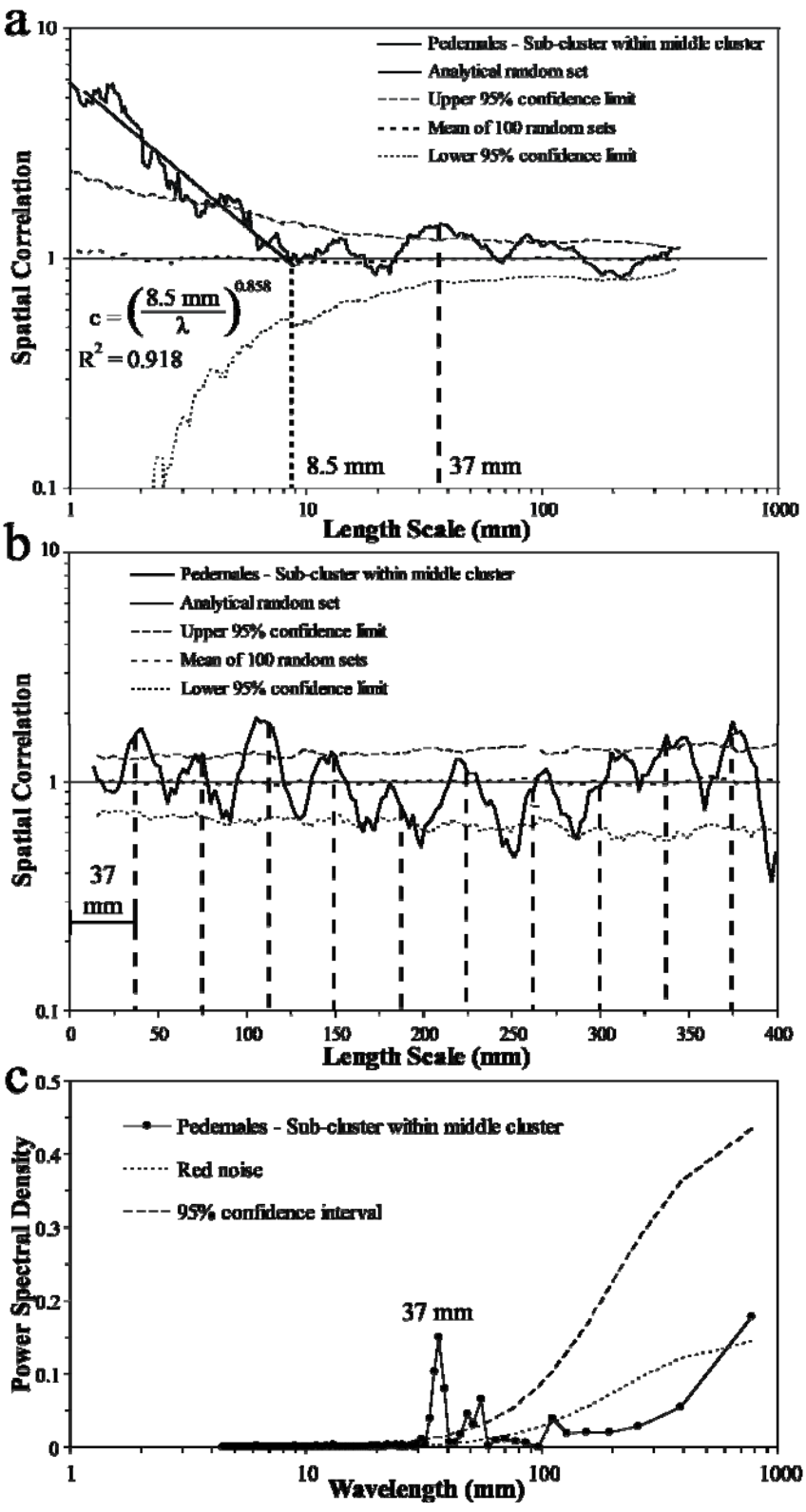
a
Pedernales - Sub-cluster within middle cluster
Analytical random set
Upper 95% confidence limit
Mean of 100 random sets
Lower 95% confidence limit
Spatial Correlation
$c = \left(\frac{8.5\ mm}{\lambda}\right)^{0.858}$
$R^2 = 0.918$
8.5 mm
37 mm
Length Scale (mm)
b
Pedernales - Sub-cluster within middle cluster
Analytical random set
Upper 95% confidence limit
Mean of 100 random sets
Lower 95% confidence limit
Spatial Correlation
37 mm
Length Scale (mm)
c
Pedernales - Sub-cluster within middle cluster
Red noise
95% confidence interval
Power Spectral Density
37 mm
Wavelength (mm)

8.3.2.3 Intercluster Domain

Fracture intensity calculated using a window size equal to cluster width is an objective way to distinguish intracluster from intercluster domains along a scanline (Chapter 6). For the entire scanline at Pedernales, the largest intercluster (Figure 8.2) domain occurs between 27 and 53 m (Figure 8.56a). Fracture intensity of the intercluster domain indicates clusters (Figure 8.60). The fracture strain for the intercluster domain at Pedernales between 27 and 53 m is 0.07%.

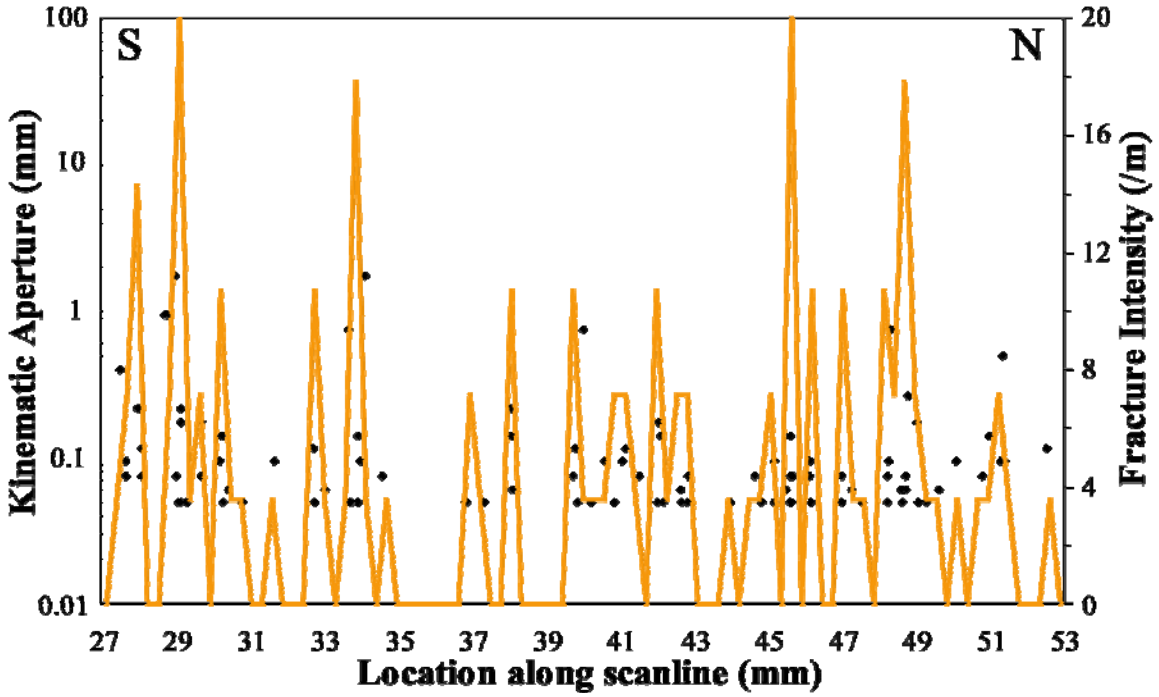

Figure 8.60 Kinematic aperture and fracture intensity versus location along scanline for Pedernales scanline between 27 and 53 m. Fracture intensity was calculated inside a window with width equal to 0.14 m (estimated cluster width in Figure 8.61a) moved 0.3 m. Please note that only the kinematic aperture axis use logarithmic graduations. Peaks of fracture intensity indicate clusters.

Spatial correlation for logarithmically graduated length scales for the largest intercluster domain at Pedernales yielded the same type of spatial arrangements as the entire data set (Figure 8.57a), the middle cluster alone (Figure 8.58a), and the sub-cluster within the middle cluster (Figure 8.59a), a power-law pattern with a cluster width of approximately 140 mm (Figures 8.5b and 8.61a). The power-law pattern is statistically significant (outside the 95% confidence interval) for about two orders of magnitude of length scale (Figure 8.61a), which suggests that the interpreted arrangement is statistically significant. Spatial correlation for linearly graduated length scales for fractures in the largest intercluster domain at Pedernales do not display a systematic pattern (Figure 8.61b), which can be interpreted as a spatial arrangement that is indistinguishable from random (Figure 8.5e). Power spectrum of spatial correlation for linearly graduated length scales confirms the lack of a statistically significant pattern of spatial correlation (Figure 8.61c).

Figure 8.61 Graphs of spatial correlation (thick continuous line) vs. length scale for (a) logarithmic graduations and (b) linear graduations for a portion of the Pedernales data set located in between clusters (27 to 53 m along scanline, 106 fractures, aperture threshold of 0.05 mm). In (a) and (b) the thin discontinuous line represents the upper 95% confidence limit while the thin dotted line represents the lower 95% confidence limit, and the thick discontinuous line corresponds to the mean of 100 randomized data sets. In (a) and (b) the thin continuous line represents the analytical solution of randomly arranged fractures with the same number of fractures and scanline length. Width of length-scale bin in (a) is 31 (m = 15) and 11 (m = 5) graduations of length scale in (b). A power-law pattern of spatial correlation is observed in (a). Cluster width is estimated to be 140 mm, as shown in (a). (c) Power spectrum of spatial correlation from (b). The power spectral density for the natural data set exhibits the same trend as the red noise, as shown in (c). The natural data set exhibits a peak at a wavelength of 1487 mm, which has a power spectral density slightly larger than the 95% confidence interval for red noise, but the difference between the peak and the 95% confidence interval is small when compared with other data sets (e.g., Eastern 1.6 m of Escalera OO1 data set, Figure 8.10c).

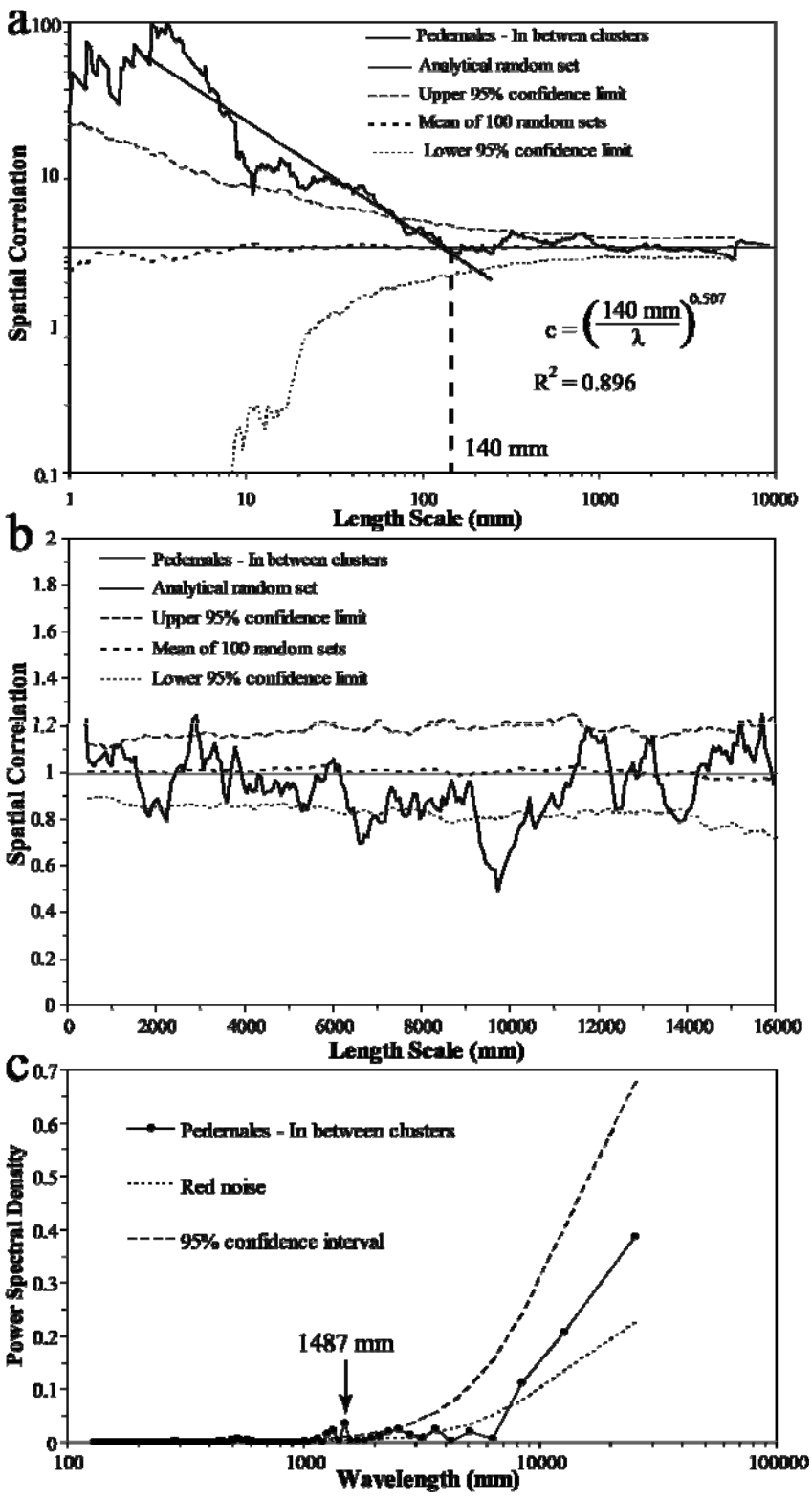
a
Pedernales - In between clusters
Analytical random set
Upper 95% confidence limit
Mean of 100 random sets
Lower 95% confidence limit
Spatial Correlation
$c = \left(\frac{140\ mm}{\lambda}\right)^{0.507}$
$R^2 = 0.896$
140 mm
Length Scale (mm)
b
Pedernales - In between clusters
Analytical random set
Upper 95% confidence limit
Mean of 100 random sets
Lower 95% confidence limit
Spatial Correlation
Length Scale (mm)
c
Pedernales - In between clusters
Red noise
95% confidence interval
Power Spectral Density
1487 mm
Wavelength (mm)

8.3.3 Palmas 11 HR Outcrop Data Set

The outcrop-scale Palmas 11 HR (high resolution) data set overlaps with the Palmas 11 LR (low resolution) data set. The Palmas 11 HR data set was measured along the NW end of the Palmas 11 LR data set, but a smaller aperture threshold (0.075 and 0.95 mm, respectively) was used. The Palmas 11 HR outcrop data set represents 575 fractures measured in a 2.49 m long scanline. The Palmas 11 HR scanline was measured by Dr. J. Gale and was graciously provided for my dissertation. Fractures of Palmas 11 HR exhibit a power-law distribution of aperture, a log-normal distribution of spacings and a coefficient of variation for spacings of 1.67 (Table 8.5).

8.3.3.1 Entire Scanline

The Palmas 11 HR data set exhibits a heterogeneous spatial arrangement of fractures (Figure 8.62). Fractures along the Palmas 11 HR scanline exhibit clusters that might be regularly spaced (Figure 8.62). Spatial correlation for logarithmically graduated length scales for the entire Palmas 11 HR data set displays a power-law pattern inside clusters with a cluster width of approximately 70 mm (Figures 8.5b and 8.63a). The power-law pattern is statistically significant (outside the 95% confidence interval) for about 1 order of magnitude of length scale (Figure 8.63a). Spatial correlation for linearly graduated length scales for the entire Palmas 11 HR data set displays a pattern of peaks and troughs of spatial correlation, some of which are statistically significant (Figure 8.63b). The pattern of spatial correlation of Figure 8.63b can be interpreted as indicative of periodically arranged fracture clusters (Figure 8.5g). Power spectrum of spatial correlation for linearly graduated length scales exhibits a few statistically significant (outside the 95% confidence interval for red noise) peaks. The peak with the largest power spectral density occurs at a wavelength of 353 mm (Figure 8.63c), which matches

approximately the estimate of cluster spacing from NCC (first peak of spatial correlation, Chapter 6).

Palmas 11 HR yielded the same type of spatial arrangement as Palmas 11 LR (periodically arranged clusters with a power-law pattern of spatial correlation). Although Palmas 11 HR intercepted two clusters present in Palmas 11 LR, the cluster width and cluster spacing exhibited by the Palmas 11 HR (70 and 353 mm, respectively) are smaller (69% reduction) than those of Palmas 11 LR data set (220 and 1100 mm), which suggests that there is an organization at a scale smaller than outcrop scale.

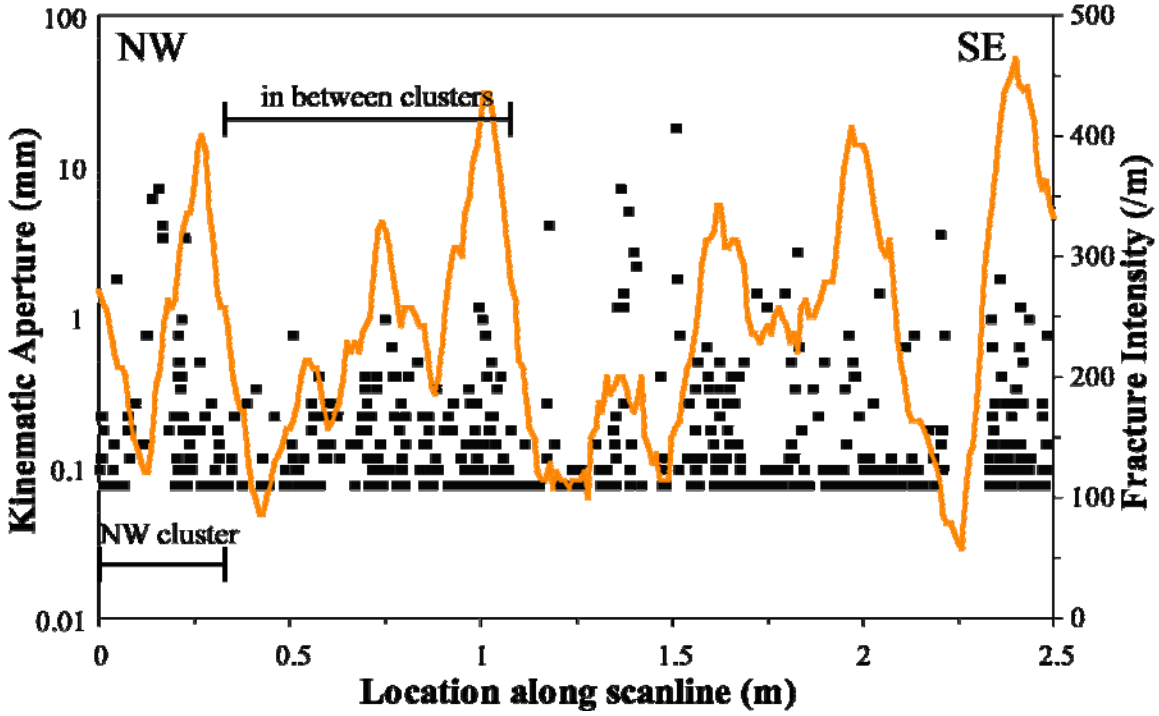

Figure 8.62 Kinematic aperture and fracture intensity versus location along scanline for entire Palmas 11 HR scanline. Fracture intensity was calculated inside a window with width equal to 0.07 m (estimated cluster width in Figure 8.63a) moved 0.01 m. Please note that only the kinematic aperture axis uses logarithmic graduations.

Figure 8.63 Graphs of spatial correlation (thick continuous line) vs. length scale for (a) logarithmic graduations and (b) linear graduations for the entire Pedernales data set (2.5 m of scanline, 575 fractures, aperture threshold of 0.075 mm). In (a) and (b) the thin discontinuous line represents the upper 95% confidence limit while the thin dotted line represents the lower 95% confidence limit, and the thick discontinuous line corresponds to the mean of 100 randomized data sets. In (a) the thin continuous line represents the analytical solution of randomly arranged fractures with the same number of fractures and scanline length. In (b) the thin continuous line represents an example randomized set generated with the same number of fractures and scanline length. Width of length-scale bin in (a) is 21 (m = 10) and in (b) is 9 (m = 4) graduations of length scale. Spatial correlation in (a) follows a power-law pattern. Power law equation in (a) was calculated using spatial correlation between length scales of 5 and 90 mm. Cluster width is estimated at 70 mm, as shown in (a). Evenly spaced lines every 353 mm in (b) match approximately peaks of spatial correlation, which display a regularly spaced pattern, indicative of periodically arranged clusters. (c) Power spectrum of spatial correlation from (b). Two largest peaks (wavelengths of 353 and 800 mm) of power spectral density are outside the 95% confidence interval for red noise. Dashed lines in (b) indicate multiples of cluster spacing (353 mm).

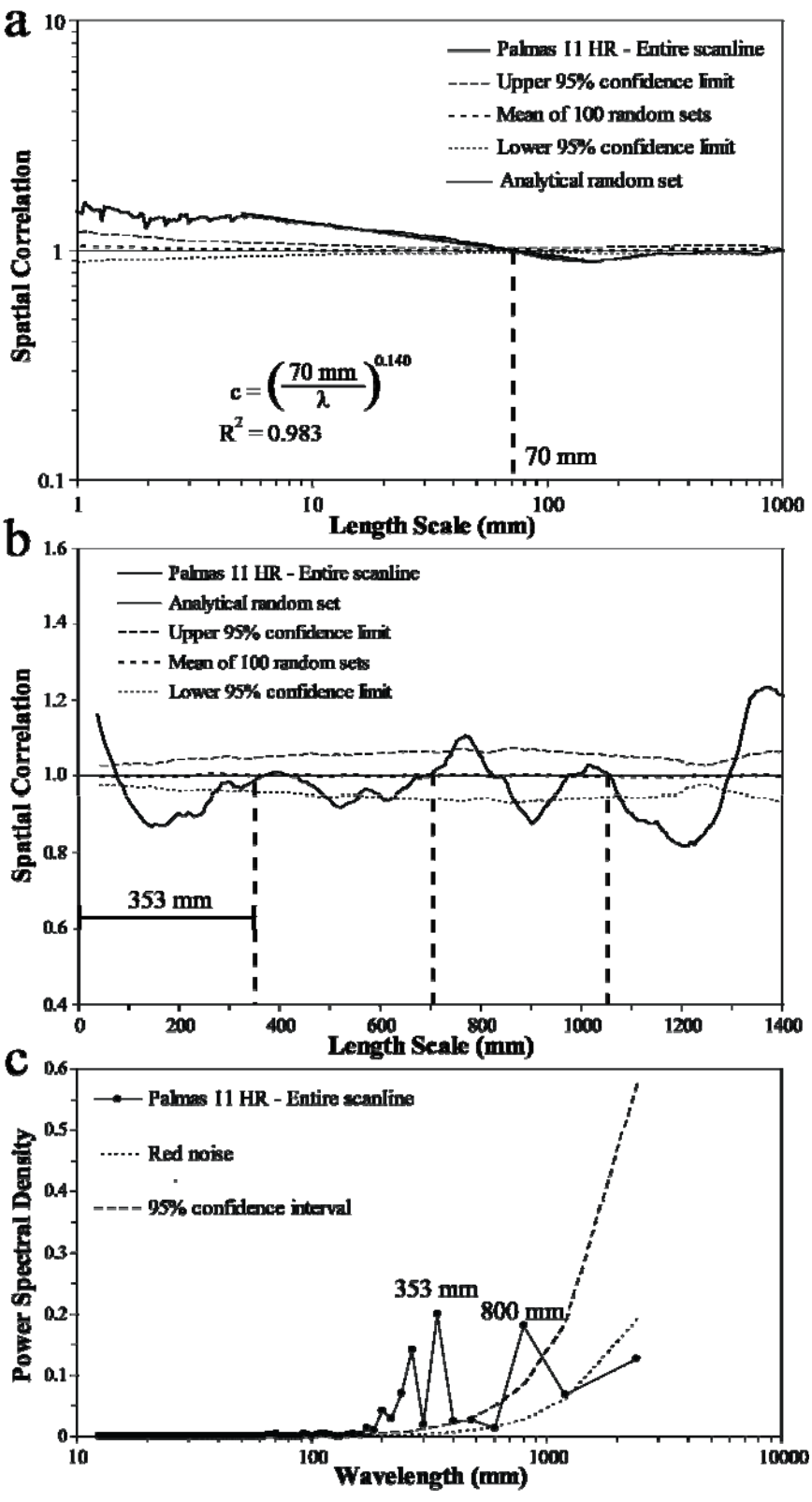
a
Palmas 11 HR - Entire scanline
Upper 95% confidence limit
Mean of 100 random sets
Lower 95% confidence limit
Analytical random set
Spatial Correlation
$c = \left(\frac{70\ mm}{\lambda}\right)^{0.140}$
$R^2 = 0.983$
70 mm
Length Scale (mm)
b
Palmas 11 HR - Entire scanline
Analytical random set
Upper 95% confidence limit
Mean of 100 random sets
Lower 95% confidence limit
Spatial Correlation
353 mm
Length Scale (mm)
c
Palmas 11 HR - Entire scanline
Red noise
95% confidence interval
Power Spectral Density
353 mm
800 mm
Wavelength (mm)

8.3.3.2 Intracluster Domain

8.3.3.2.1 Northwestern Cluster

There is a cluster in the northwestern end of the Palmas 11 HR scanline between approximately 0 and 0.32 m, which exhibits a fracture strain of 14.3%, almost twice the strain of the entire Palmas 11 HR outcrop data set (Figure 8.62). Spatial correlation for logarithmically graduated length scales for northwestern cluster of Palmas 11 HR yielded the same type of spatial arrangements as the entire data set (Figure 8.57a), a power-law pattern with a cluster width of approximately 20 mm (Figures 8.5b and 8.64a). The power-law pattern is statistically significant (outside the 95% confidence interval) for at least one order of magnitude of length scale (Figure 8.64a), which indicates that the interpreted arrangement is statistically significant. Spatial correlation for linearly graduated length scales for fractures in the northwestern cluster at Palmas 11 HR displays a pattern of alternating shallow peaks and troughs, most of which are not statistically significant (Figure 8.64b). Power spectrum of spatial correlation for linearly graduated length scales exhibits one broad peak barely outside 95% confidence interval centered at a wavelength of 36 mm (Figure 8.64c). Although pattern of spatial correlation suggests a periodic arrangement of fracture clusters with a cluster spacing of approximately 36 mm, the statistical significance of that wavelength in power spectrum is not robust enough to justify interpretation of a periodic arrangement of clusters.

Figure 8.64 Graphs of spatial correlation (thick continuous line) vs. length scale for (a) logarithmic graduations and (b) linear graduations for the northwestern cluster of Palmas 11 HR data set (0 to 320 mm, along scanline, 81 fractures, aperture threshold of 0.075 mm). Location of position along scanline for middle cluster is shown in Figure 8.62. In (a) and (b) the thin discontinuous line represents the upper 95% confidence limit while the thin dotted line represents the lower 95% confidence limit, and the thick discontinuous line corresponds to the mean of 100 randomized data sets. In (a) and (b) the thin continuous line represents the analytical solution of randomly arranged fractures with the same number of fractures and scanline length. Width of length-scale bin in (a) is 17 (m = 8) and in (b) is 13 (m = 6) graduations of length scale. Spatial correlation in (a) follows a power-law pattern. Power law equation in (a) was calculated using spatial correlation o between length scales of 2.5 and 30 mm. Cluster width is estimated at 20 mm, as shown in (a). (c) Power spectrum of spatial correlation from (b). Two peaks of power spectral density are slightly outside the 95% confidence interval for red noise, one centered at 36 mm and the other one at 71 mm. However, the difference between the peak and the 95% confidence interval is small when compared with other data sets (e.g., eastern 1.6 m of Escalera OO1 data set, Figure 8.10c).

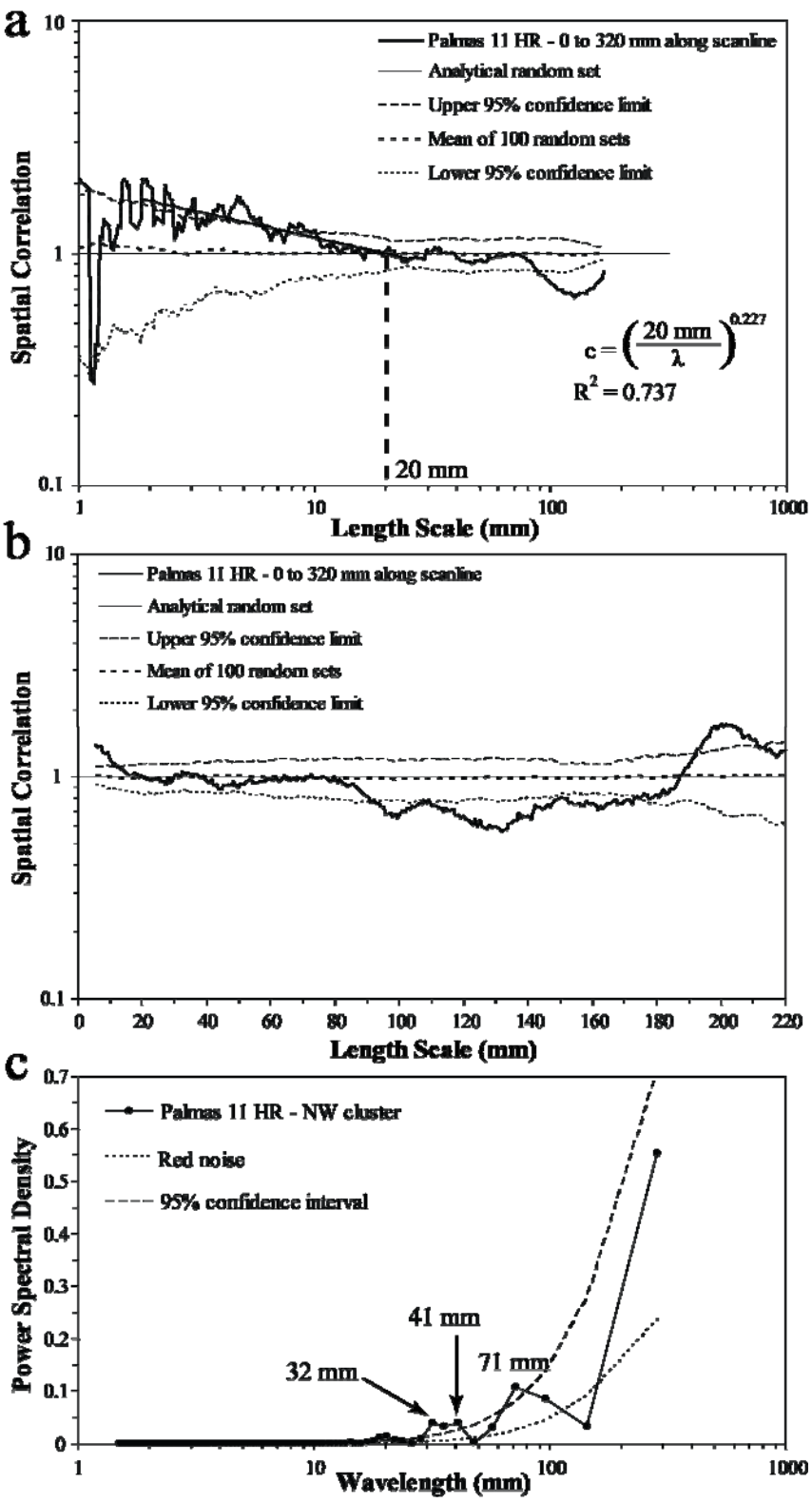
a
Palmas 11 HR - 0 to 320 mm along scanline
Analytical random set
Upper 95% confidence limit
Mean of 100 random sets
Lower 95% confidence limit
Spatial Correlation
Length Scale (mm)
20 mm
$c = \left(\frac{20\ mm}{\lambda}\right)^{0.227}$
$R^2 = 0.737$
b
Palmas 11 HR - 0 to 320 mm along scanline
Analytical random set
Upper 95% confidence limit
Mean of 100 random sets
Lower 95% confidence limit
Spatial Correlation
Length Scale (mm)
c
Palmas 11 HR - NW cluster
Red noise
95% confidence interval
Power Spectral Density
Wavelength (mm)
41 mm
32 mm
71 mm

8.3.3.3 Intercluster Domain

Cluster spacing for the Palmas 11 LR was estimated at 1100 mm (Figure 8.26). Therefore, if the northwestern-most cluster of Palmas 11 HR is centered at approximately 200 mm along the scanline, the nearest cluster towards the NE should be located at approximately 1300 mm. However, at 1300 mm along the scanline fracture intensity is smaller than between 320 and 1250 mm, which may suggest that a cluster was not detected (Figure 8.62). Although the number of fractures between 1250 and 1500 mm along the scanline does not indicate a cluster with fracture intensity similar to the one at the NW end of the scanline, there is an unusual abundance of large fractures at the same location along the scanline. Because large fractures in Palmas 11 are statistically more clustered than small fractures (Chapter 7), I interpreted a cluster to be centered near 1350 mm and defined an intercluster domain between 320 and 1100 mm (Figure 8.62). The fracture strain for the intercluster domain at Palmas 11 HR between 320 and 1100 mm is 4.13%.

Spatial correlation for logarithmically graduated length scales for the intercluster domain at Palmas 11 HR (Figure 8.65a) yielded the same type of spatial arrangement as the entire data set (Figure 8.63a) or the northwestern cluster (Figure 8.64a). Namely, the intercluster region between 320 and 1100 mm exhibits a power-law pattern inside clusters (Figure 8.5b), with a cluster width of approximately 41 mm (Figure 8.65a). However, the power-law pattern is barely outside the 95% confidence for less than one order of magnitude of length scale (Figure 8.65a), which suggests that the interpreted arrangement is barely statistically significant. Spatial correlation for linearly graduated length scales for fractures in the northwestern intercluster domain at Palmas 11 HR display a systematic pattern of alternating peaks and troughs (Figure 8.65b), which can be interpreted as indicative of periodically arranged clusters (Figure 8.5g). Power spectrum

of spatial correlation for linearly graduated length scales supports the statistically significance of the pattern of spatial correlation by exhibiting a peak of power spectral density outside the 95% confidence interval at a wavelength of 89 mm, equal to cluster spacing (Figure 8.65c).

Figure 8.65 Graphs of spatial correlation (thick continuous line) vs. length scale for (a) logarithmic graduations and (b) linear graduations for the northwestern intercluster domain of Palmas 11 HR data set (320 to 1100 mm, along scanline, 182 fractures, aperture threshold of 0.075 mm). Location of position along scanline for middle cluster is shown in Figure 8.62. In (a) and (b) the thin discontinuous line represents the upper 95% confidence limit while the thin dotted line represents the lower 95% confidence limit, and the thick discontinuous line corresponds to the mean of 100 randomized data sets. In (a) and (b) the thin continuous line represents the analytical solution of randomly arranged fractures with the same number of fractures and scanline length. Width of length-scale bin in (a) and (b) is 9 (m = 4) graduations of length scale. Spatial correlation in (a) follows a power-law pattern. Power law equation in (a) was calculated using spatial correlation o between length scales of 6 and 42 mm. Cluster width is estimated at 41 mm, as shown in (a). Evenly spaced lines every 89 mm in (b) match peaks of spatial correlation, which display a regularly spaced pattern, indicative of periodically arranged clusters. (c) Power spectrum of spatial correlation from (b). Two peaks of power spectral density are outside the 95% confidence interval for red noise, one at 89.3 mm and the other one at 238mm.

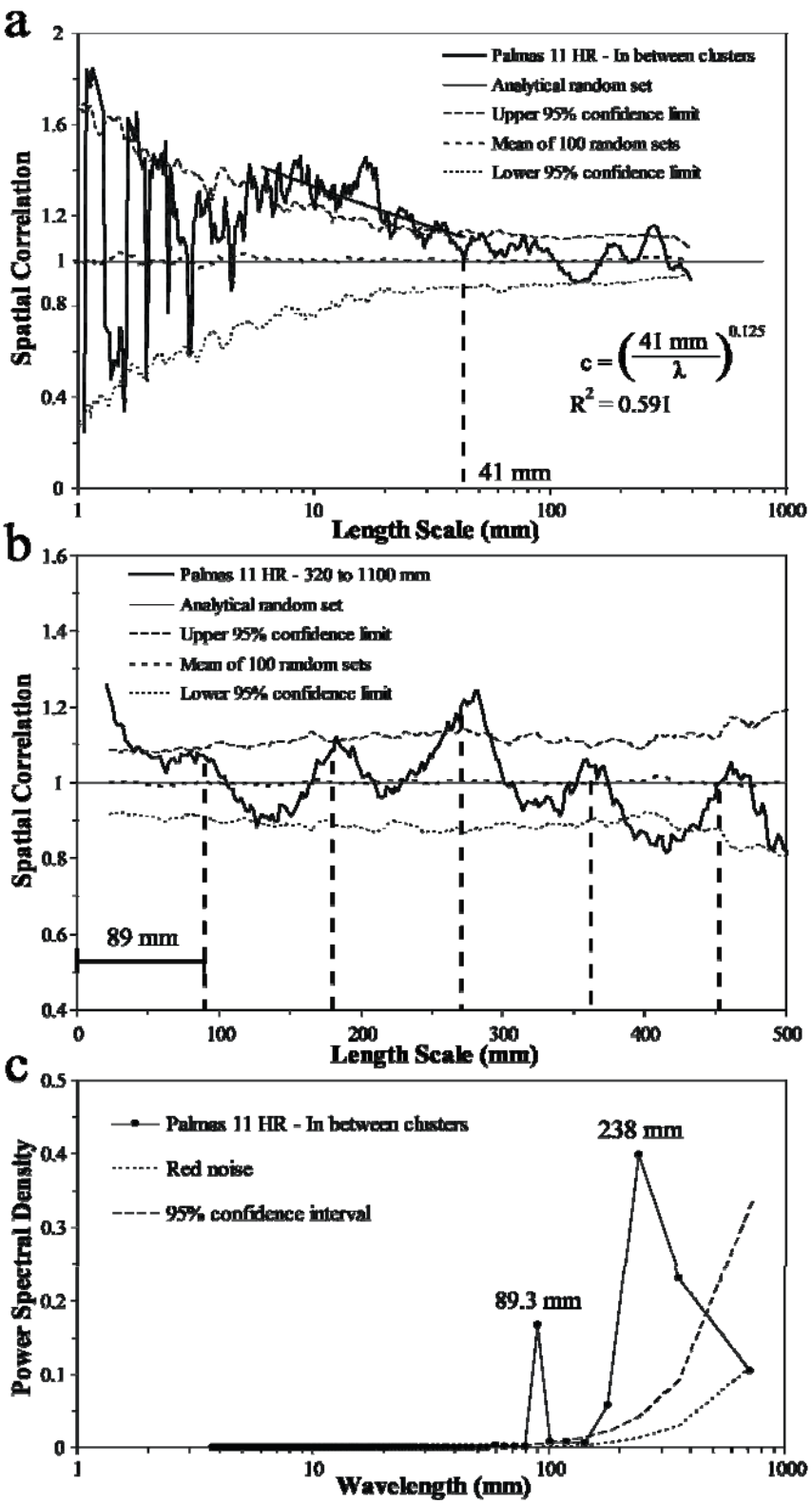
a
Palmas 11 HR - In between clusters
Analytical random set
Upper 95% confidence limit
Mean of 100 random sets
Lower 95% confidence limit
Spatial Correlation
$c = \left(\frac{41\ mm}{\lambda}\right)^{0.125}$
$R^2 = 0.591$
41 mm
Length Scale (mm)
b
Palmas 11 HR - 320 to 1100 mm
Analytical random set
Upper 95% confidence limit
Mean of 100 random sets
Lower 95% confidence limit
Spatial Correlation
89 mm
Length Scale (mm)
c
Palmas 11 HR - In between clusters
Red noise
95% confidence interval
238 mm
89.3 mm
Power Spectral Density
Wavelength (mm)

8.3.4 Spatial Arrangement of Intracluster versus Intercluster Domains

After introducing the spatial arrangement of different domains (Figure 8.2) of three outcrop data sets without rock samples (Grove Creek, Pedernales and Palmas 11 HR), I will compare and contrast the spatial arrangement of fractures among the data sets and between other outcrop data sets and their rock sample counterparts.

8.3.4.1 Entire Scanlines

Logarithmically graduated length scales for Grove Creek, Pedernales and Palmas 11 HR data sets exhibit power-law patterns of spatial correlation inside clusters (Figure 8.5b) for the entire scanline data sets (Figures 8.52a, 8.57a, and 8.63a respectively), which indicates that clusters in all three data sets probably were not formed simply by random arrangement of fractures (Marrett et al., in review). However, linearly graduated length scales show that the Grove Creek and Pedernales data sets do not yield the same spatial arrangement as Palmas 11 HR. Fractures along the entire Grove Creek and Pedernales scanlines are suggestive of periodically arranged clusters, but this type of arrangement cannot be conclusively determined (Figures 8.52b, 8.52c, 8.57b, and 8.57c). In contrast, the periodic arrangement of fracture clusters in the Palmas 11 HR data set is statistically significant (Figures 8.63b and 8.63c).

8.3.4.2 Intracluster Domains

When the spatial arrangements of fractures inside the largest clusters of Grove Creek (Figure 8.53) and Pedernales (Figure 8.58) are analyzed independently, both exhibit periodically arranged clusters with a power-law pattern of spatial correlation inside clusters (Figure 8.5d). For the Palmas 11 HR data set, logarithmically graduated length scales exhibit a power-law pattern of spatial correlation, but linearly graduated length scales exhibit a pattern suggestive of periodically arranged clusters but without

statistical significance (Figure 8.63). Independent analysis of the second largest cluster of Grove Creek also exhibits periodically arranged clusters with a power-law pattern of spatial correlation inside clusters (Figure 8.54). For the Pedernales data set, clusters are nested on at least three different scales (Figures 8.57, 8.58 and 8.59). Namely, the entire scanline is formed by clusters that exhibit a power-law pattern of spatial correlation and may be periodically arranged (Figure 8.66a), with the largest cluster formed by smaller and closely spaced clusters with the same spatial arrangement (Figure 8.66b), and with one cluster within the largest cluster formed again by smaller and closely spaced clusters with identical spatial arrangement (Figure 8.66c).

The discovery that some periodically arranged clusters (which in turn exhibit internally power-law patterns of spatial correlation) at the outcrop scale are formed by smaller clusters with identical arrangement was also indicated by rock samples of length equal to cluster width (Figures 8.44 and 8.46) or most of cluster width (Figure 8.47). If large periodically arranged clusters are formed in turn by smaller periodically arranged clusters, then cluster width and cluster spacing should decrease, a hypothesis that is validated by the Pedernales and Grove Creek data sets. For both Pedernales and Grove Creek data sets cluster width and cluster spacing always decrease with examination of smaller and smaller intracluster domains, even if the power-law exponent of spatial correlation does not change (Figure 8.67, Table 8.8). In addition, comparison of spatial correlation from different domains of Pedernales scanline suggests that local variations within power-law pattern of spatial correlation of a larger domain (black solid line, Figure 8.67) might be indicative of variations of spatial correlation at smaller scales (blue solid lines, Figure 8.67).

Figure 8.66 Sketches illustrating the outcrop-scale Grove Creek and Pedernales fracture data sets (left) and the corresponding NCC analyses using logarithmic and linear graduations of length scale (right) for (a) entire scanline, (b) only fractures from largest cluster (intracluster domain, Figure 8.2), and (c) only fractures from one cluster located inside largest cluster (only for Pedernales). Fractures in (a), (b) and (c) exhibit a power-law pattern of spatial correlation inside clusters (Figure 8.5b), clusters that in turn are periodically arranged (Figure 8.5g). Fractures inside clusters with a power-law pattern of spatial correlation are red whereas fractures in the intercluster domains are green. Input data in (a) are fractures along the entire scanline at outcrop scale. Input data in (b) are only the fractures inside largest cluster. Input data in (c) are fractures of cluster within largest cluster only. Maximum length scale in (a) is equal to outcrop scanline length (A). Maximum length scale in (b) is equal to width of largest cluster at outcrop scale (C), maximum length scale in (c) is equal to width of cluster within largest cluster (E). Periodically arranged clusters in (b) exhibit distinctive cluster spacing (D) and width (E). Periodically arranged clusters in (c) exhibit distinctive cluster spacing (K) and width (J).

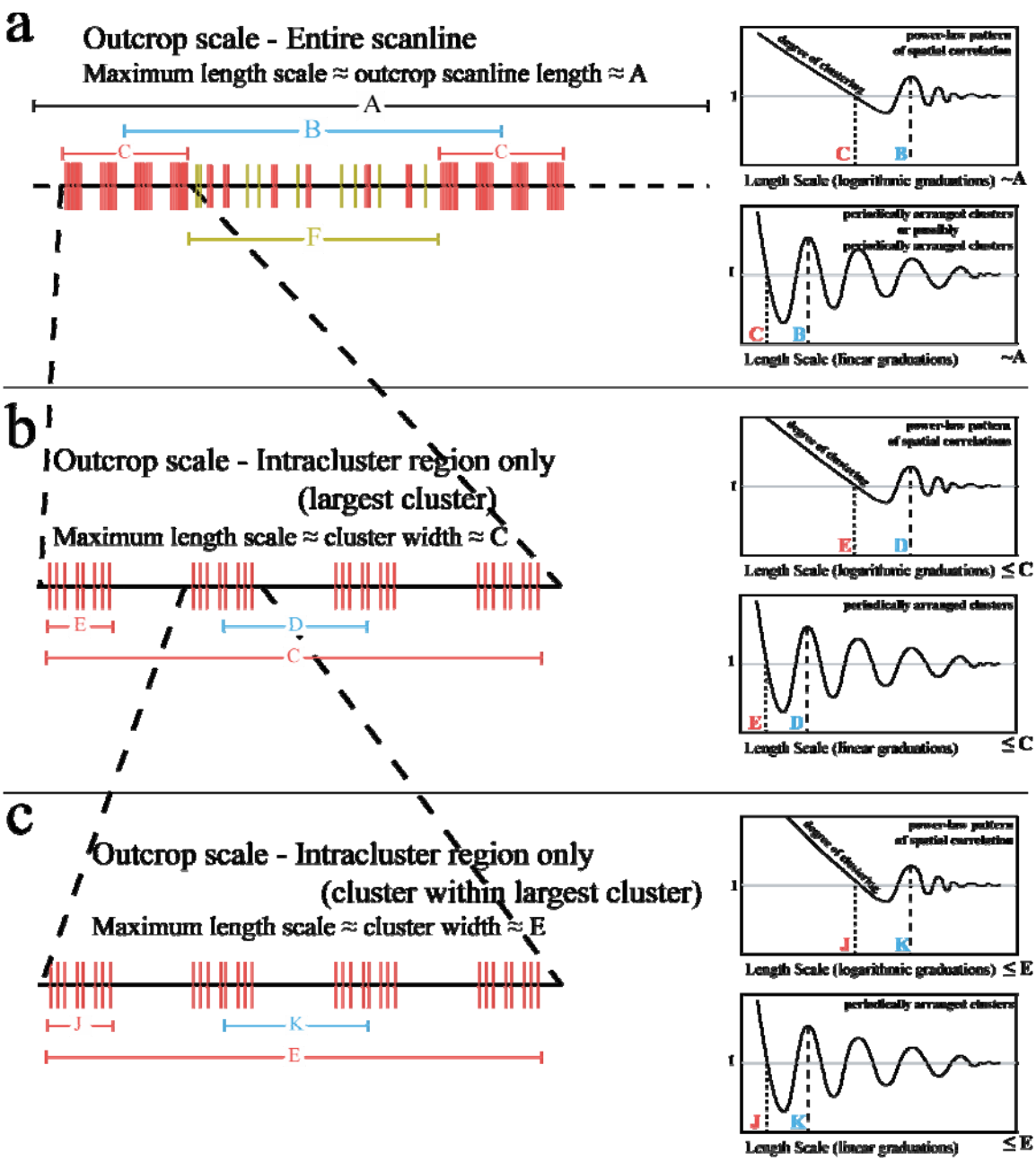
a
Outcrop scale - Entire scanline
Maximum length scale ≈ outcrop scanline length ≈ A
A
B
C
C
F
power-law pattern of spatial correlation
degree of clustering
1
C
B
Length Scale (logarithmic graduations) ~A
periodically arranged clusters or possibly periodically arranged clusters
1
C
B
Length Scale (linear graduations) ~A
b
Outcrop scale - Intracluster region only (largest cluster)
Maximum length scale ≈ cluster width ≈ C
E
D
C
power-law pattern of spatial correlation
degree of clustering
1
E
D
Length Scale (logarithmic graduations) ≤ C
periodically arranged clusters
1
E
D
Length Scale (linear graduations) ≤ C
c
Outcrop scale - Intracluster region only (cluster within largest cluster)
Maximum length scale ≈ cluster width ≈ E
J
K
E
power-law pattern of spatial correlation
degree of clustering
1
J
K
Length Scale (logarithmic graduations) ≤ E
periodically arranged clusters
1
J
K
Length Scale (linear graduations) ≤ E

Table 8.8 Compilation of spatial arrangement attributes for data sets only at outcrop scale (without rock samples) Power-law exponent obtained using logarithmic graduations of length scales. Numbers on *italics* indicate values that are not statistically significant. N.A. = Not Available.

Data Set	Attribute	Entire Scanline	Largest Cluster	2nd Largest Cluster	Cluster within Largest Cluster	Intercluster Domain
Grove Creek	**Scanline length (m)**	246	20 (142 - 162)	66 (180 – 246)	N.A.	142 (0 – 142)
	Fracture Strain (%)	0.15	1.67	0.005		0.011
	Cluster width (mm)	15500	240	2900		*4000*
	Power-law exponent	0.55	0.61	0.94		N.A.
	Cluster Spacing (mm)	49000	1430	5800		8800
Palmas 11 HR	**Scanline length (m)**	2.49	0.32 (0 – 0.32)	N.A.		0.78 (0.32 – 1.1)
	Fracture Strain (%)	7.62	14.31			4.13
	Cluster width (mm)	70	20			41
	Power-law exponent	0.14	0.227			0.125
	Cluster Spacing (mm)	353	*36*			89.3
Pedernales	**Scanline length (m)**	59	12 (15 - 27)		1 (17 – 18)	26 (27 – 53)
	Fracture Strain (%)	0.53	0.94		2.62	0.07
	Cluster width (mm)	7200	470		8.5	140
	Power-law exponent	0.17	0.17		0.86	0.5
	Cluster Spacing (mm)	*19200*	1010		37	N.A.

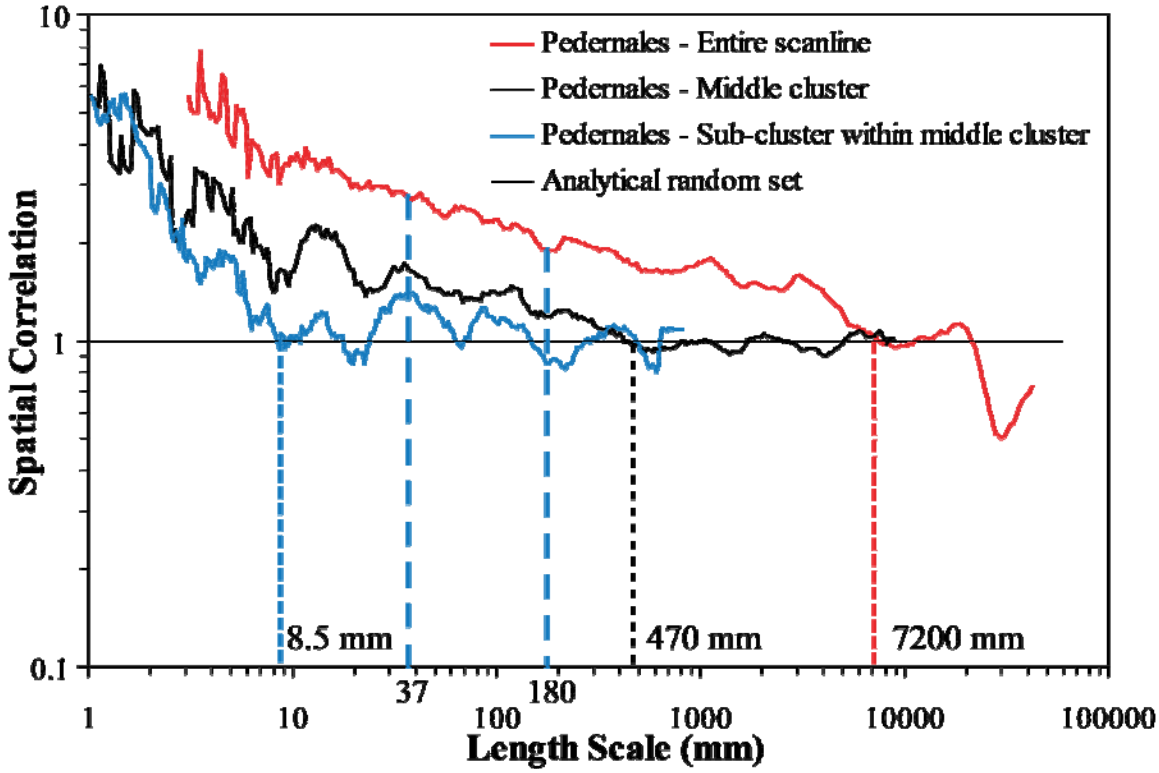

Figure 8.67 Compilation of spatial correlation for logarithmically graduated length scales of entire scanline at Pedernales (red dotted line), middle (largest) cluster from Pedernales (black dotted line), and sub-cluster within middle cluster (blue dotted line). Spatial correlation from Figures 8.57a, 8.58a, and 8.59a. Notice the progressive reduction in cluster width with an increase in power-law exponent. Spatial correlation peak at 37 mm (dashed blue line) is indicative of sub-cluster spacing at smallest cluster. A peak of spatial correlation at 37 mm is also observed for middle cluster (black solid line)

8.3.4.3 Intercluster Domains

When the entire outcrop scanlines of Grove Creek, Pedernales and Palmas 11 HR are studied, they exhibit intercluster domains. For instance, intercluster domains are located between 27 and 59 m along the Pedernales scanline (Figures 8.56a and 8.60), between 0 and 142 m along the Grove Creek scanline (Figure 8.51a), or between 320 and 1100 mm along the Palmas 11 HR scanline (Figure 8.62). Although there are clusters

within an intercluster domain of an entire scanline (e.g., Figure 8.60), such clusters are much narrower than the clusters that defined the intercluster domain. For instance, peaks of fracture intensity within one intercluster domain of Pedernales are about one meter wide (Figure 8.60), whereas peaks of fracture intensity for the entire scanline are several meters wide (Figure 8.56a).

Fractures in the intercluster domains studied earlier did not exhibit arrangements that are indistinguishable from random for both logarithmically and linearly graduated length scales. Specifically, fractures within the widest intercluster domain of Pedernales yielded a power-law pattern of spatial correlation inside clusters (Figures 8.61a and 8.68b). However, clusters are not periodically arranged but instead exhibit an arrangement that is indistinguishable from random (Figures 8.61b and 8.68b). However, it should be noted that the power-law pattern of spatial correlation of the Pedernales intercluster domain only appeared when using a comparatively large width of length scale bin (31, m = 15), which suggests that the number of fractures might be too small to reliably detect a power-law pattern. Intercluster domains of Grove Creek exhibit periodically arranged clusters (Figures 8.54b and 8.55b), but the clusters internally exhibit either a power-law of spatial correlation (Figure 8.55a) or an arrangement that is indistinguishable from random (Figures 8.54a and 8.69b). Fractures in the intercluster domain of Palmas 11 HR exhibit patterns similar those of Grove Creek, but the power-law pattern is barely statistically significant (Figures 8.65 and 8.70). Therefore, compared with intracluster domains at the same scale (Figure 8.66), intercluster domains have fractures that are less organized based on the fact that they either exhibit statistically significant (non-random) clusters that are not periodically arranged (Pedernales, Figure 8.68) or clusters that are periodically arranged but lack internal organization (Grove Creek and Palmas 11 HR; Figures 8.69 and 8.70, respectively).

Figure 8.68 Sketches illustrating the outcrop-scale Pedernales fracture data set (left) and the corresponding NCC analyses using logarithmic and linear graduations of length scale (right) for (a) entire scanline, and (b) fractures in intercluster domain (in between) of outcrop data set (Figure 8.2) only. Fractures inside clusters in (a) exhibit a power-law pattern of spatial correlation (Figure 8.5b), clusters that in turn are periodically arranged (Figure 8.5g). Fractures inside clusters in (b) exhibit also a power-law pattern of spatial correlation (Figure 8.5b), but clusters exhibit an arrangement that is indistinguishable from random (Figure 8.5e). Fractures inside clusters with power-law pattern of spatial correlation are red whereas fractures in the intercluster domains are green. Input data in (a) are fractures along the entire scanline at outcrop scale, whereas in (b) are only fractures in intercluster domain between 27 and 53 m along scanline. Maximum length scale in (a) is equal to outcrop scanline length (A). Maximum length scale in (b) is equal to distance between adjacent edges of two adjacent clusters at outcrop scale (F). Periodically arranged clusters in the intercluster domain at outcrop scale in (b) exhibit cluster width (G).

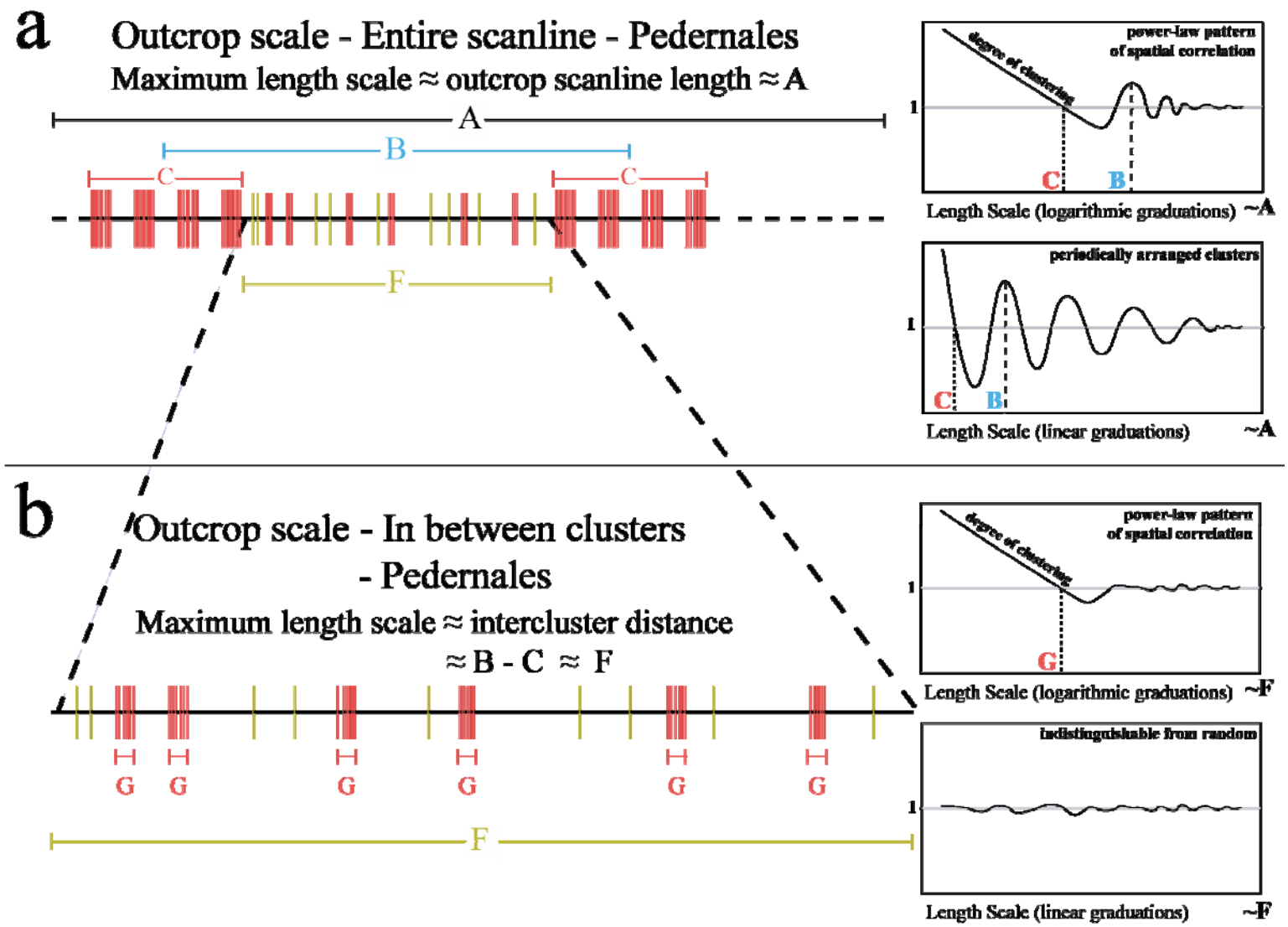
a
Outcrop scale - Entire scanline - Pedernales
Maximum length scale ≈ outcrop scanline length ≈ A
A
B
C
C
F
power-law pattern of spatial correlation
degree of clustering
1
C
B
Length Scale (logarithmic graduations)
~A
periodically arranged clusters
1
C
B
Length Scale (linear graduations)
~A
b
Outcrop scale - In between clusters - Pedernales
Maximum length scale ≈ intercluster distance ≈ B - C ≈ F
H G
F
power-law pattern of spatial correlation
degree of clustering
1
G
Length Scale (logarithmic graduations)
~F
indistinguishable from random
1
Length Scale (linear graduations)
~F

Figure 8.69 Sketches illustrating the outcrop-scale Grove Creek fracture data set (left) and the corresponding NCC analyses using logarithmic and linear graduations of length scale (right) for (a) entire scanline, and (b) fractures in intercluster domain of outcrop data set only (Figure 8.2). Fractures inside clusters in (a) exhibit a power-law pattern of spatial correlation (Figure 8.5b), clusters that in turn are periodically arranged (Figure 8.5g). Fractures in (b) exhibit an indistinguishable from random arrangement for logarithmically graduated length scales (Figure 8.5a) and periodically arranged clusters for linearly graduated length scales (Figure 8.5g). Fractures inside clusters with a power-law pattern of spatial correlation are red, fractures inside statistically insignificant clusters arrangement are blue, and fractures in the intercluster domains are green. Input data in (a) are fractures along the entire scanline at outcrop scale, whereas in (b) are only fractures between 0 and 142 m along scanline. Maximum length scale in (a) is equal to outcrop scanline length (A). Maximum length scale in (b) is equal to distance between edge of scanline and edge of largest cluster at outcrop scale (F). Periodically arranged clusters in the intercluster domain at outcrop scale in (b) exhibit cluster spacing (H).

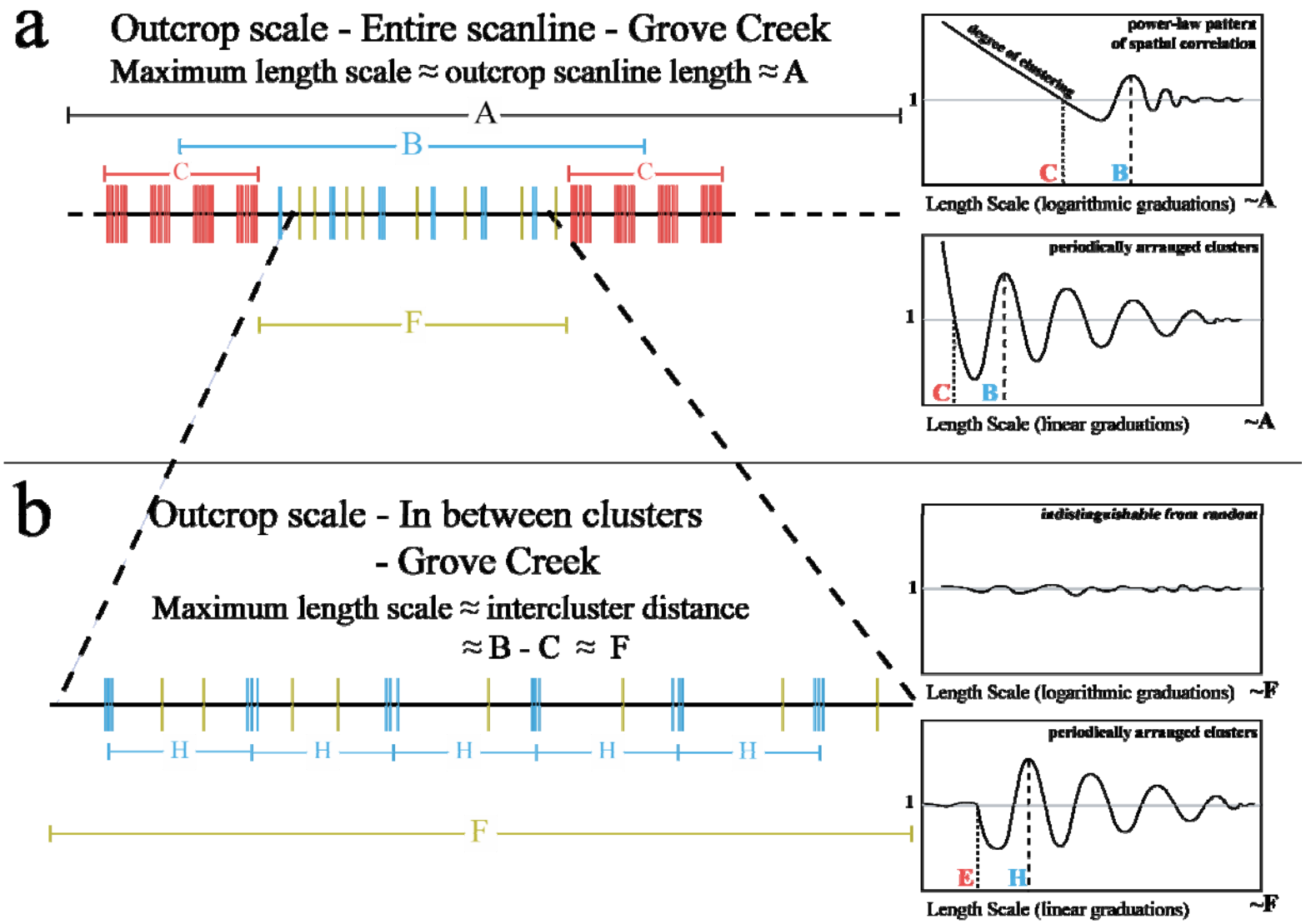
a
Outcrop scale - Entire scanline - Grove Creek
Maximum length scale ≈ outcrop scanline length ≈ A
A
B
C
C
F
power-law pattern of spatial correlation
degree of clustering
1
C
B
Length Scale (logarithmic graduations)
~A
periodically arranged clusters
1
C
B
Length Scale (linear graduations)
~A
b
Outcrop scale - In between clusters
- Grove Creek
Maximum length scale ≈ intercluster distance
≈ B - C ≈ F
H
H
H
H
H
F
indistinguishable from random
1
Length Scale (logarithmic graduations)
~F
periodically arranged clusters
1
E
H
Length Scale (linear graduations)
~F

Figure 8.70 Sketches illustrating the outcrop-scale Palmas 11 HR fracture data set (left) and the corresponding NCC analyses using logarithmic and linear graduations of length scale (right) for (a) entire scanline, and (b) fractures in intercluster domain of outcrop data set only (Figure 8.2). Fractures inside clusters in (a) and (b) exhibit power-law pattern of spatial correlation (Figure 8.5b), clusters that in turn are periodically arranged (Figure 8.5g). However, the statistical significance of power-law pattern in (b) is questionable. Fractures inside clusters with a power-law pattern of spatial correlation are red, and fractures in the intercluster domains are green. Input data in (a) are fractures along the entire scanline at outcrop scale, whereas in (b) are only fractures between 320 and 1100 mm along scanline. Maximum length scale in (a) is equal to outcrop scanline length (A). Maximum length scale in (b) is equal to distance between nearest edged of adjacent statistically significant clusters at outcrop scale (F). Periodically arranged fractal clusters in the intercluster domain at outcrop scale in (b) exhibit cluster width (G) and cluster spacing (H).

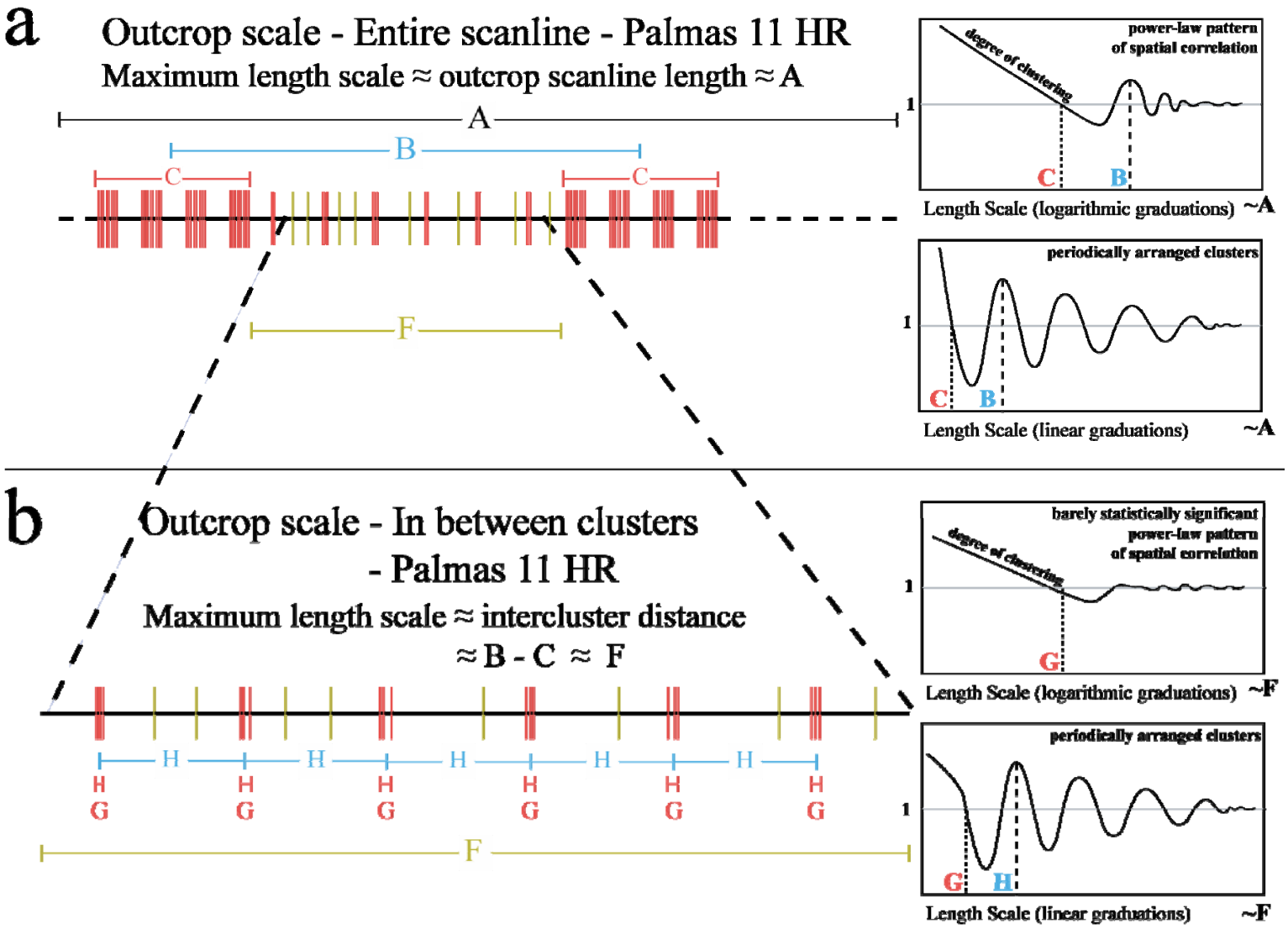
a
Outcrop scale - Entire scanline - Palmas 11 HR
Maximum length scale ≈ outcrop scanline length ≈ A
A
B
C
C
F
power-law pattern
of spatial correlation
degree of clustering
1
C
B
Length Scale (logarithmic graduations)
~A
periodically arranged clusters
1
C
B
Length Scale (linear graduations)
~A
b
Outcrop scale - In between clusters
- Palmas 11 HR
Maximum length scale ≈ intercluster distance
≈ B - C ≈ F
H
H
H
H
H
H
H
G
H
G
H
G
H
G
H
G
H
G
F
barely statistically significant
power-law pattern
of spatial correlation
degree of clustering
1
G
Length Scale (logarithmic graduations)
~F
periodically arranged clusters
1
G
H
Length Scale (linear graduations)
~F

8.3.4.4 Selection of Domains

The selection of intra- and intercluster domains for Grove Creek, Pedernales and Palmas 11 HR was done semi-quantitatively. Namely, NCC was used to quantify cluster width (e.g., Figure 8.57a), which was subsequently used to calculate fracture intensity (e.g., Figure 8.56). Afterward, peaks of fracture intensity were used to estimate the boundaries along the scanline of intra- and intercluster domains.

Although the process of locating boundaries for intra- and intercluster domains might seem inconsequential, in reality it was crucial for detection of periodically arranged fractal clusters. Namely, when the boundaries of a domain are not selected properly and fractures represent a mixture of intra-and intercluster domains at a particular scale (e.g., outcrop scale), then the resulting spatial correlation cannot unravel the spatial organization that might be present in one of those domains (e.g., intracluster domains; Figure 8.66). For instance, the 12 m long intracluster domain between 15 and 27 m along the Pedernales scanline (Figure 8.56a) yielded well-defined patterns of spatial correlation identical in type of spatial arrangement to the entire scanline (Figures 8.52 and 8.53) but with smaller cluster width and cluster spacing (Table 8.8). If a scanline with identical length (12 m) but with only half of its length within the intracluster domain is analyzed, the NCC results fail to indicate periodically arranged clusters (Figure 8.71). Fracture intensity indicates that fractures between 21 and 33 m contain half of the largest cluster in Pedernales and 20% of intercluster domain between 27 and 53 m (Figure 8.56a).

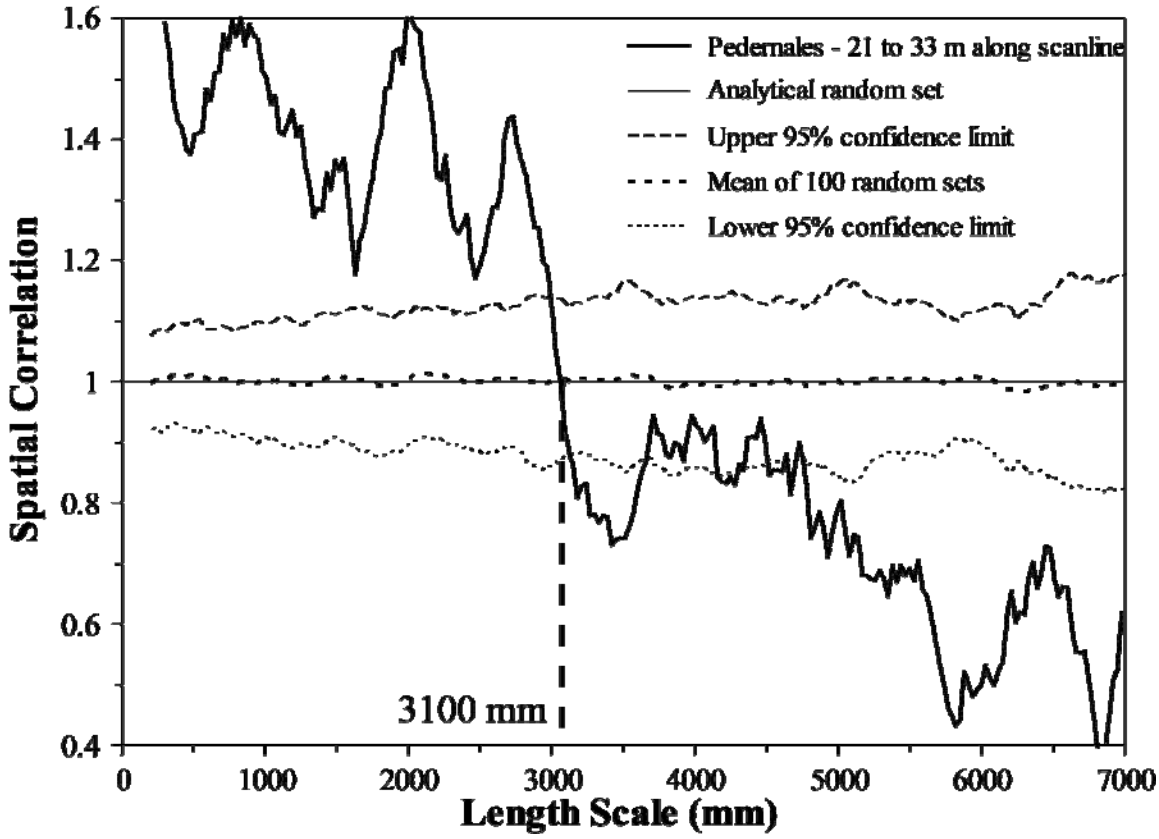

Figure 8.71 Graph of spatial correlation (thick continuous line) vs. length scale for linear graduations for fractures located between 21 and 33 m along the Pedernales outcrop data set (192 fractures, aperture threshold of 0.05 mm). Location of position along scanline is shown in Figure 8.55. The thin discontinuous line represents the upper 95% confidence limit while the thin dotted line represents the lower 95% confidence limit, and the thick discontinuous line corresponds to the mean of 100 randomized data sets. The thin continuous line represents the analytical solution of randomly arranged fractures with the same number of fractures and scanline length. Width of length-scale bin is 7 (m = 3) graduations of length scale. Cluster width is estimated at 3100 mm.

8.4. DISCUSSION

Now that NCC analyses of data sets with and without rock samples have been described, I will use them to test the hypothesis that clusters with power-law variation of spatial correlation with length scale are fractal. Afterwards, I will explore relationships between attributes of fracture spatial arrangements, such as cluster width, cluster spacing, and degree of clustering, with characteristics of the fracture populations and the fractured layers, such as fracture strain and layer thickness. Subsequently, I will speculate about a mechanical evolution that might explain the evidence and relationships.

8.4.1 Internal Structure of Outcrop-Scale Clusters with a Power-Law Pattern of Spatial Correlation

Marrett et al. (in review) suggested that clusters that exhibit a power-law pattern of spatial correlation have a fractal arrangement (Figure 8.5b), because fractal geometries are typically characterized by a power-law (Schroeder, 2000). A power-law of spatial correlation (Figure 8.5b) implies that the number of fracture pairs separated by a given distance will vary in inverse proportion to a power of length scale regardless of the scale of observation. For instance, with a cluster width of 100 mm (spatial correlation of 1) and a power-law exponent of 0.5, spatial correlation at a length scale of 1 mm (two orders of magnitude lower) is 10 (one order of magnitude higher).

Hare and Marrett (in review) showed that fracture clusters can contain smaller fracture clusters on a range of length scales (multi-scaled clusters) and suggested that multi-scaled fracture clusters are required by fractal arrangement of locations. However, the definition of fractal implies that there is a continuum of fracture clustering, as suggested by an uninterrupted power-law of spatial correlation. Although my dissertation has demonstrated that statistically significant clusters are formed by smaller, periodically

arranged, statistically significant clusters with (e.g., Escalera OO12 and Tranquitas; Table 8.6) or without (e.g., Huasteca and Escalera OO1; Table 8.6) power-law patterns of spatial correlation, periodic arrangement breaks the continuous spectrum of clustering. Instead, fracture clusters consist of a cascade of smaller clusters at discrete length scales (Figure 8.44, 8.46, and 8.66), and therefore the hypothesis that clusters of fractures with a power law of spatial correlation are fractal clusters is incorrect. Although Hare and Marrett (in review) observed bifurcations of high values of amplitude (cool colors) with decreasing wavelet wavelengths, indicative of clusters coalescing into larger clusters (Figure 8.1), their analysis did not reveal the discrete length scales of clusters that my analyses imply.

8.4.1.1 Range of Fracture Clustering

Marrett et al. (in review) indicated that NCC detected clustering at Pedernales on length scales from tens of meters to millimeters and hypothesized that clustering may continue to scales that only microscopic studies could reveal. My dissertation examined the spatial arrangement of microfractures in thin sections using both optical and cathodoluminescence techniques and demonstrated that microfractures with apertures as small as 0.0005 mm (0.5 μm) exhibit statistically significant clusters. Microfracture clusters show a power-law pattern of spatial correlation and periodic spacing (Table 8.6).

Microfractures with apertures as small as 0.28 μm have been measured using SEM/CL imaging (Chapter 4; Gomez et al., 2003) and are about half the smallest aperture measured along microscopic scanlines, which suggests that my scanlines reached close to the maximum resolution of current SEM imaging techniques for microfracture interpretation (Robert Reed, personal communication, 2005). For comparison, grains of sand have diameters between 0.0625 (62.5 μm) and 2 mm and clay is smaller than 3.9 μm, which means that the smallest microfractures measured for my dissertation have

apertures smaller than the grain size of all rocks studied. Although smaller fractures might indeed exist, my dissertation did not uncover the spatial organization of fractures with apertures smaller than maximum SEM resolution.

8.4.1.2 Variations in Spatial Correlation within Power-law Patterns

Although small variations in spatial correlation within a power-law pattern could be dismissed as statistically insignificant, they might reflect variations of spatial arrangement in the intracluster domain (Figure 8.67). For instance, one of the nested clusters inside the middle cluster at Pedernales exhibits variations of spatial correlation that are also present in larger domains (e.g., entire middle cluster) at length scales larger than cluster width (>8.5 mm, Figure 8.67). Since alternating peaks and troughs of spatial correlation indicative of periodically arranged clusters occur at length scales larger than cluster width, it is possible that variations in spatial correlation within a power-law pattern reflect the periodic arrangement of small clusters in the intracluster domain (Figure 8.72a). For instance, spatial correlation for the entire scanline at Pedernales exhibits a power-law pattern with local variations (Figures 8.57a and 8.73a). However, refined length scale graduations (obtained by reducing the maximum length scale) reveal a power-law pattern of spatial correlation on which are superimposed alternating peaks and troughs every 1020 mm (Figure 8.73b), almost identical to the separation between peaks of spatial correlation for the middle cluster analyzed alone (Figure 8.58b). The alternating peaks and troughs of spatial correlation along the power-law pattern of Pedernales shown in Figure 8.73b were not observed in Figure 8.57b, even though the input data are the same (entire scanline at Pedernales), because of aliasing.

Figure 8.72 Sketches illustrating the development of a power-law pattern of spatial correlation for a fracture data set that contains statistically-significant clusters that individually analyzed yield periodically arranged clusters with a power-law pattern of spatial correlation. (a) Sketches of spatial correlation versus logarithmic (left) and linear (right) graduations of length scales for the entire scanline, which yield periodically arranged clusters, clusters that in turn exhibit a power-law pattern. (b) Sketch of fractures that would generate (a). (c) Graphs of spatial correlation versus logarithmically (left) and linearly (right) graduated length scales for intracluster domains in (b). Cluster width (length scale = C) in (a) is the maximum length scales used in (c). Separation between local variations for length scales smaller than cluster width for linearly graduated length scales in (a) are similar to cluster spacing in (b).

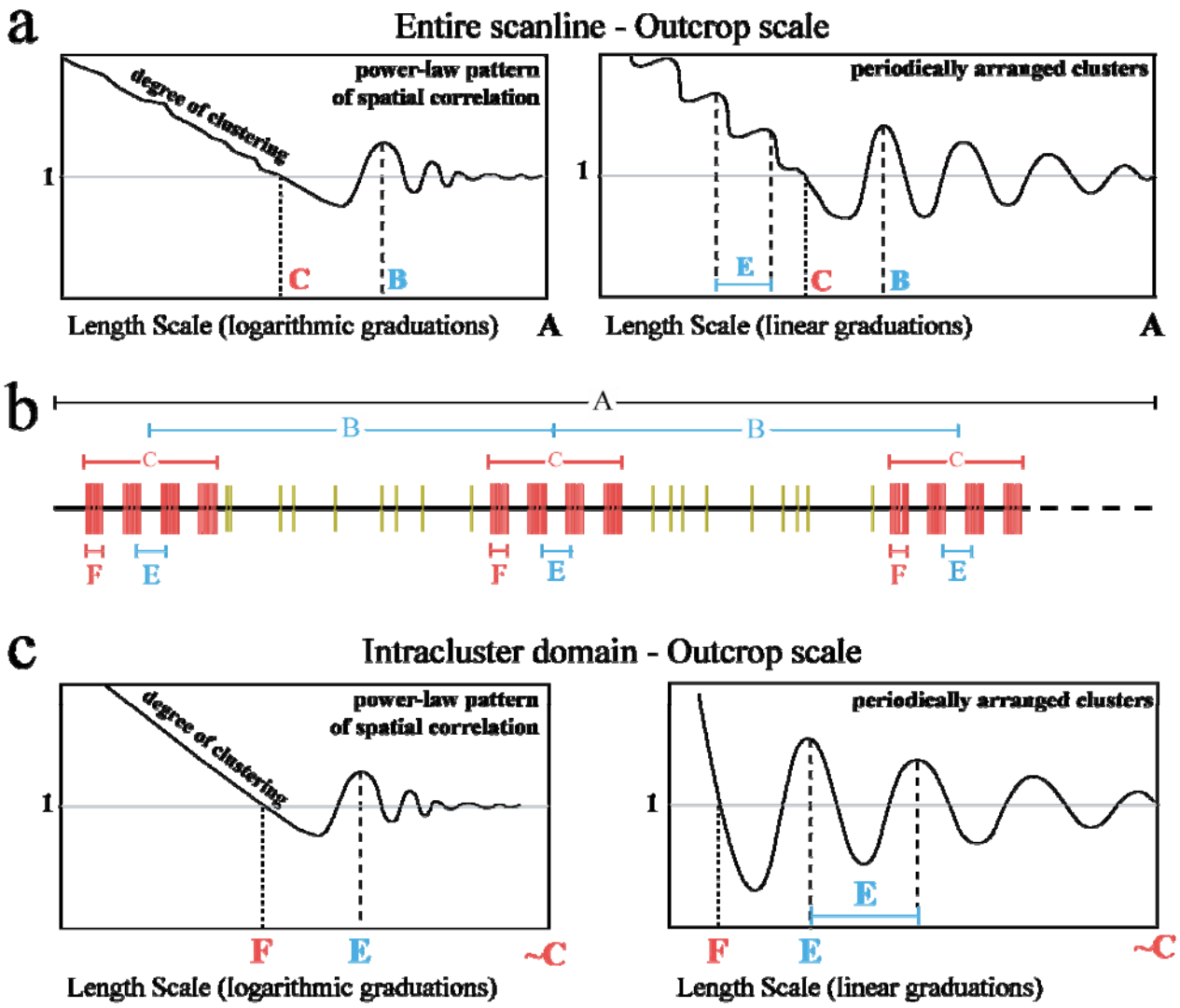
a
Entire scanline - Outcrop scale
power-law pattern
of spatial correlation
degree of clustering
1
C
B
Length Scale (logarithmic graduations)
A
periodically arranged clusters
1
E
C
B
Length Scale (linear graduations)
A
b
A
B
B
C
C
C
F
E
F
E
F
E
c
Intracluster domain - Outcrop scale
power-law pattern
of spatial correlation
degree of clustering
1
F
E
~C
Length Scale (logarithmic graduations)
periodically arranged clusters
1
E
F
E
~C
Length Scale (linear graduations)

Figure 8.73 Graphs of spatial correlation (thick continuous line) vs. length scale for (a) logarithmic graduations and (b) linear graduations for the entire Pedernales data set (59 m of scanline, 916 fractures, aperture threshold of 0.05 mm). Instead of using a maximum length scale equal to scanline length as in Figures 8.57a and 8.57b, a maximum length scale of 12 m was used. In (a) and (b) the thin discontinuous line represents the upper 95% confidence limit while the thin dotted line represents the lower 95% confidence limit, and the thick discontinuous line corresponds to the mean of 100 randomized data sets. In (a) and (b) the thin continuous line represents an example randomized set generated with the same number of fractures and scanline length. Width of length-scale bin in (a) and (b) is 9 (m = 4) graduations of length scale. Spatial correlation in both (a) and (b) follow a power-law pattern. Power law equation in (a) was calculated using spatial correlation between length scales of 5 and 7000 mm. Power-law regression is the same of similar range of length scales for the same data set with a maximum length scale equal to total scanline length (Figure 8.57a). Cluster width is estimated at 7200 mm (dotted line), as shown in (a) and (b). Cluster width is the same as estimated using a maximum scanline length equal to 60 m, the total scanline length. Peaks of spatial correlation every 1020 mm in (b) are not resolved in (a) due to the logarithmic graduations of length scales.

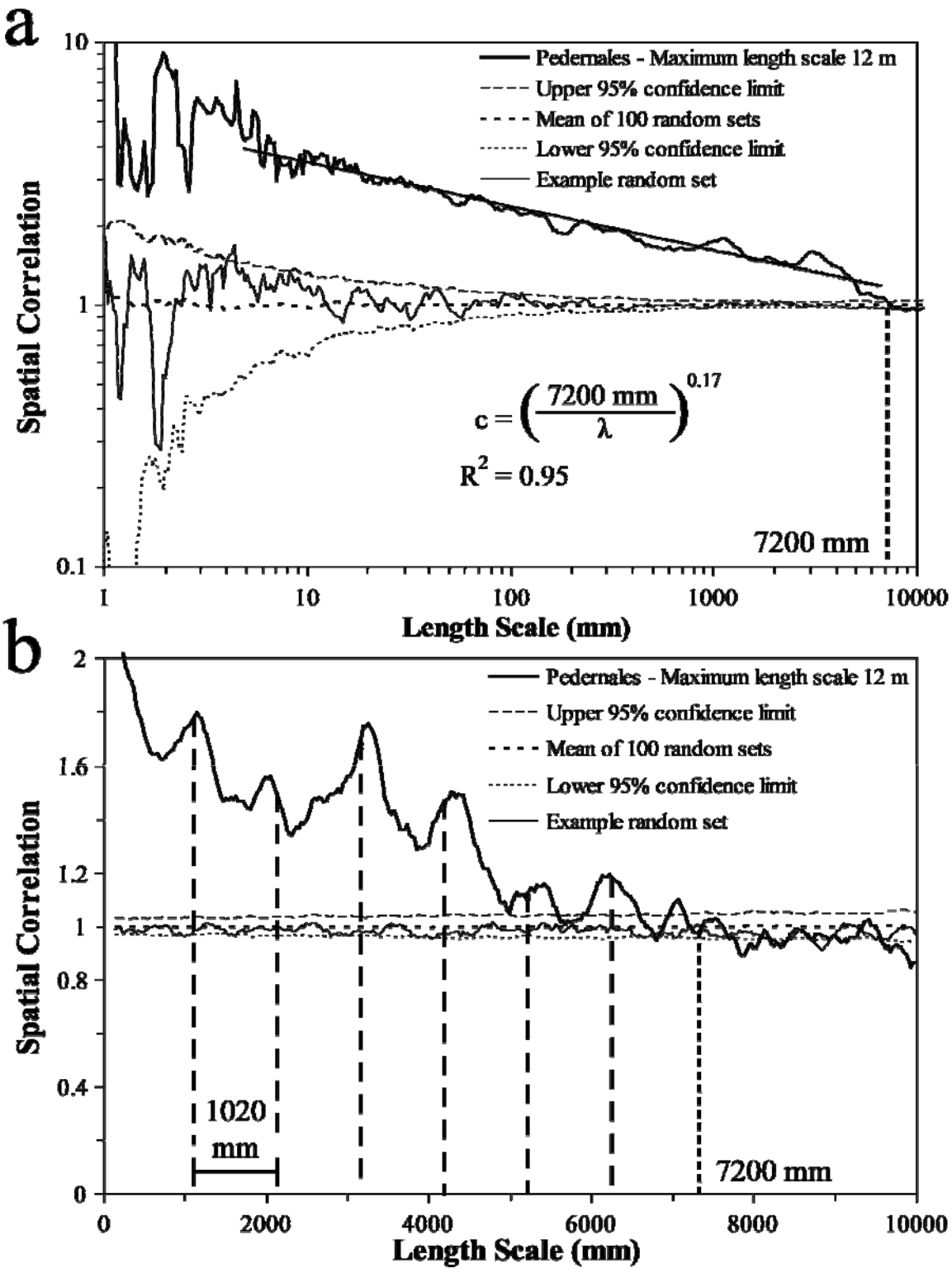
a
Pedernales - Maximum length scale 12 m
Upper 95% confidence limit
Mean of 100 random sets
Lower 95% confidence limit
Example random set
Spatial Correlation
10
1
0.1
$c = \left(\frac{7200\ mm}{\lambda}\right)^{0.17}$
$R^2 = 0.95$
7200 mm
1
10
100
1000
10000
Length Scale (mm)
b
Pedernales - Maximum length scale 12 m
Upper 95% confidence limit
Mean of 100 random sets
Lower 95% confidence limit
Example random set
Spatial Correlation
2
1.6
1.2
1
0.8
0.4
0
1020 mm
7200 mm
0
2000
4000
6000
8000
10000
Length Scale (mm)

8.4.2 Internal Structure of Outcrop-Scale Intercluster Domains

Fractures inside statistically significant clusters at outcrop scale exhibit non-random arrangements at most length scales; they commonly exhibit, internally, statistically significant clusters that are periodically arranged (Figures 8.44, 8.46, and 8.66). However, the arrangement of fractures in between highly organized clusters is not completely random. Compared with intracluster domains, fractures in between statistically significant clusters (intercluster domains) exhibit a weaker, but still measurable, degree of organization. For instance, they might have clusters with a power-law pattern of spatial correlation that do not exhibit a periodic arrangement (Figure 8.68), or periodically arranged clusters that lack a statistically significant internal arrangement (Figure 8.69). An early indication that intercluster domains have some form of internal organization can be seen in the wavelet amplitude map of Pedernales by Hare and Marrett (in review) and shown in Figure 8.1. In the intercluster region of Pedernales (27 to 53 m, Table 8.8) there are positive wavelet amplitudes indicative of abundant fractures at wavelet wavelengths of 1 to 10 cm (Figure 8.1). Although weaker than for fractures in intercluster domains, at similar scales both the intra- and intercluster domains seem to show spatial organization at similar length scales. For instance, cluster width in the intercluster domain of Pedernales is 140 mm, whereas in the middle (largest) outcrop-scale cluster it is 470 mm (Table 8.8). Also, cluster width and cluster spacing in the intercluster domain of Palmas 11 HR are 41 and 89 mm, respectively, whereas in the NW cluster they are 20 and 36 mm (Table 8.8).

8.4.3 Scaling of Cluster Width with Cluster Spacing

When cluster width is graphed against cluster spacing for all data sets with periodically arranged clusters (both outcrop, Table 8.8, and rock sample scale, Table 8.7) studied in this chapter (entire scanline or only a domain) a linear pattern (power-law with

an exponent of 1) emerges (Figure 8.74). Cluster width is proportional to cluster spacing in spite of the fact that layers studied are in different geologic regions (Chapter 2), rocks have different lithologies (Table 8.1), fracture data sets have different attributes (Table 8.5), clusters are located in both intra- and intercluster domains, and clusters have power-law patterns of spatial correlation (Pedernales, Grove Creek, Palmas 11, Huasteca, Escalera OO1, and Escalera OO12), random (rock samples from X fractures) or inherited (northern 5 m of Tranquitas) arrangements inside clusters (Table 8.6). For fractures within the Cupido Fm., only fractures at outcrop scale of category Y exhibit periodically arranged fractal clusters (Figure 8.5d). However, at rock sample scale, X fractures exhibited patterns of spatial correlation indicative of periodically arranged clusters (Figure 8.5g), which in turn have intracluster arrangement that is indistinguishable from random (Figure 8.5a). Cluster width at rock sample scale for X fractures was determined using linear graduations of length scale (Figure 8.5g).

The only similarity between all of the fracture data sets included in Figure 8.74 is that they have or are suspected to have periodically arranged clusters (Table 8.6). Cluster width follows a linear relationship in terms of cluster spacing (power law with an exponent of 1 and a coefficient of 0.4), which suggests that cluster width is about 40% of cluster spacing (Figure 8.74). Because cluster spacing is considered a measurement between the centers of adjacent clusters, a cluster width equal to 40% of cluster spacing means that the distance between adjacent edges of two different clusters is equal to 150% of cluster width. The fact that fractures probably formed under different geologic conditions nevertheless follow a single relationship of cluster width with cluster spacing suggests that when periodically arranged clusters emerge, a single mechanism controls their width and spacing during growth.

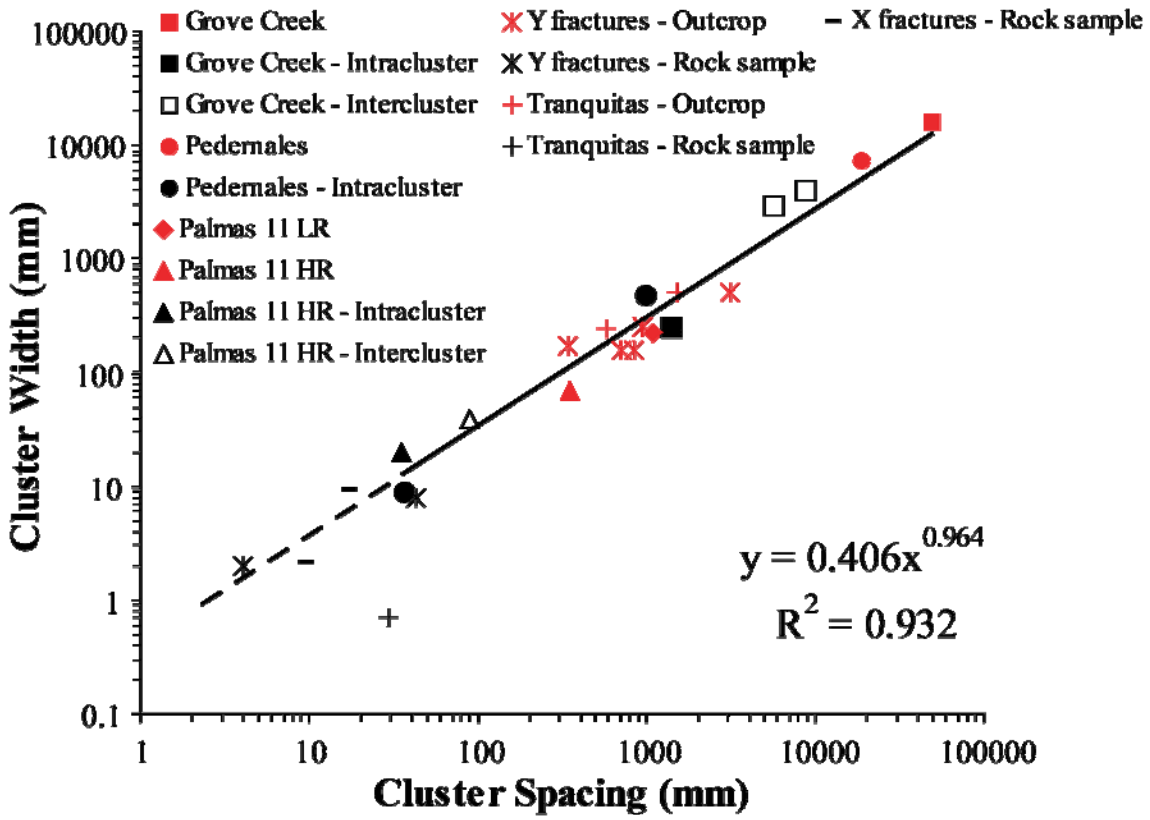

Figure 8.74 Cluster width versus cluster spacing for data sets without rock sample (left column), and for data sets with rock sample (center and right columns). Red symbols indicate entire outcrop data sets. For data sets without rock sample, black solid symbols indicate intracluster domains whereas black empty symbols indicate intercluster domains. For data sets with rock samples, results at outcrop scale (entire scanline) and rock sample were plotted independently. Power-law regression was calculated (solid line) using only data points from outcrops and extrapolated (dashed line) toward smaller clusters.

Although the two outcrop data sets at Tranquitas (northern 5 m and southern 26 m) follow the line of cluster width versus cluster spacing exhibited by all the other data sets studied, data from the Tranquitas rock sample do not follow the pattern (black plus sign, Figure 8.74). Two characteristics distinguish the Tranquitas rock sample from all other fracture data sets included in Figure 8.74. First, Tranquitas is the only siliciclastic layer whereas calcite or dolomite is the main mineral composing all other layers. And

second, the rock sample at Tranquitas was obtained from the northern 5 m (Figure 8.36), the only scanline with a well-defined inherited/imposed spatial arrangement (Figure 8.41) likely caused by a fold or a fault at the northern end of the scanline (Figure 8.42). In contrast, all other data sets exhibit fractal arrangement of fractures for logarithmically graduated length scales. It is possible that an externally imposed fracturing mechanism altered the scaling of periodically arranged fractal clusters at the northern end of Tranquitas scanline.

8.4.4 Clustering Characteristics

Now I will explore the relationship of clustering with parameters that characterize layers containing fractures, such as layer thickness, or that characterize a fracture population such as strain, fracture intensity and power-law exponent of spatial correlation.

8.4.4.1 Comparing Different Layers (Entire Scanline)

8.4.4.1.1 Fracture Intensity– Outcrop Scale

Intensity was calculated for fractures with aperture greater than or equal to 1 mm (Ortega et al., 2006). In spite of the differences (geologic regions, fracture data set attributes, spatial arrangement inside clusters) between the outcrop data sets, graphs of fracture intensity versus cluster width and cluster spacing show a power-law pattern of decreasing fracture intensity with increasing cluster width and cluster spacing (Figure 8.75). Namely, fracture data sets at outcrop scale with increasing cluster widths are separated larger distances (Figure 8.74) and exhibit smaller intensities (Figure 8.75).

However, linear trends of decreasing fracture intensity with increasing cluster width and cluster spacing emerged mainly because the Grove Creek and Pedernales data sets extended the range of fracture intensity, cluster width and cluster spacing for more

than about two orders of magnitude compared with data sets from the SMO (Figure 8.75). If measurements from those two data sets were incorrect or not considered, then there would not be a significant trend. In addition, a crossplot of intensity for fractures with aperture greater than or equal to 1 mm versus scanline length also yielded a inverse trend of fracture intensity with scanline length, which makes the trend of fracture intensity with cluster width and cluster spacing suspicious, since scanline length is not a fracture attribute (Figure 8.76). In addition, it is possible that the longest scanlines are obtainable in the lowest intensity fractured rock because high fracture intensity typically makes more broken outcrops. One approach to verify the reliability of the inverse trend of fracture intensity with cluster width and cluster spacing, would be to measure fractures arranged in clusters with widths and spacings larger than the ones exhibited by data sets from the SMO (Cupido Fm. and Tranquitas) but smaller than Pedernales.

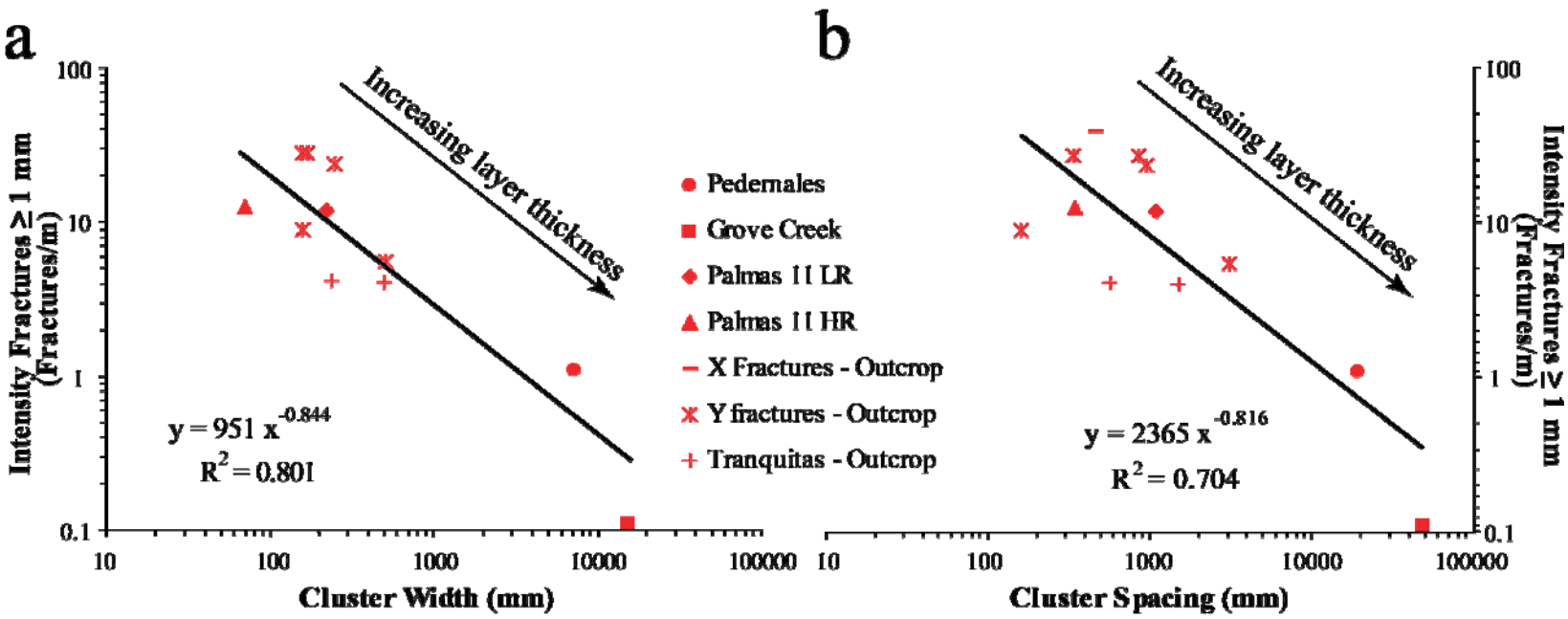

Figure 8.75 Intensity for outcrop scale fractures with aperture larger than or equal to 1 mm versus (a) cluster width and (b) cluster spacing. Each data point included in (a) and (b) corresponds to an entire outcrop scanline. Although X fractures show only random arrangements of fractures, one data set at outcrop scale (Palmas 12) showed statistically insignificant cluster spacing, which was nevertheless included. Power-laws were calculated for all data points included in each graph. Layer thickness increases with cluster width and cluster spacing.

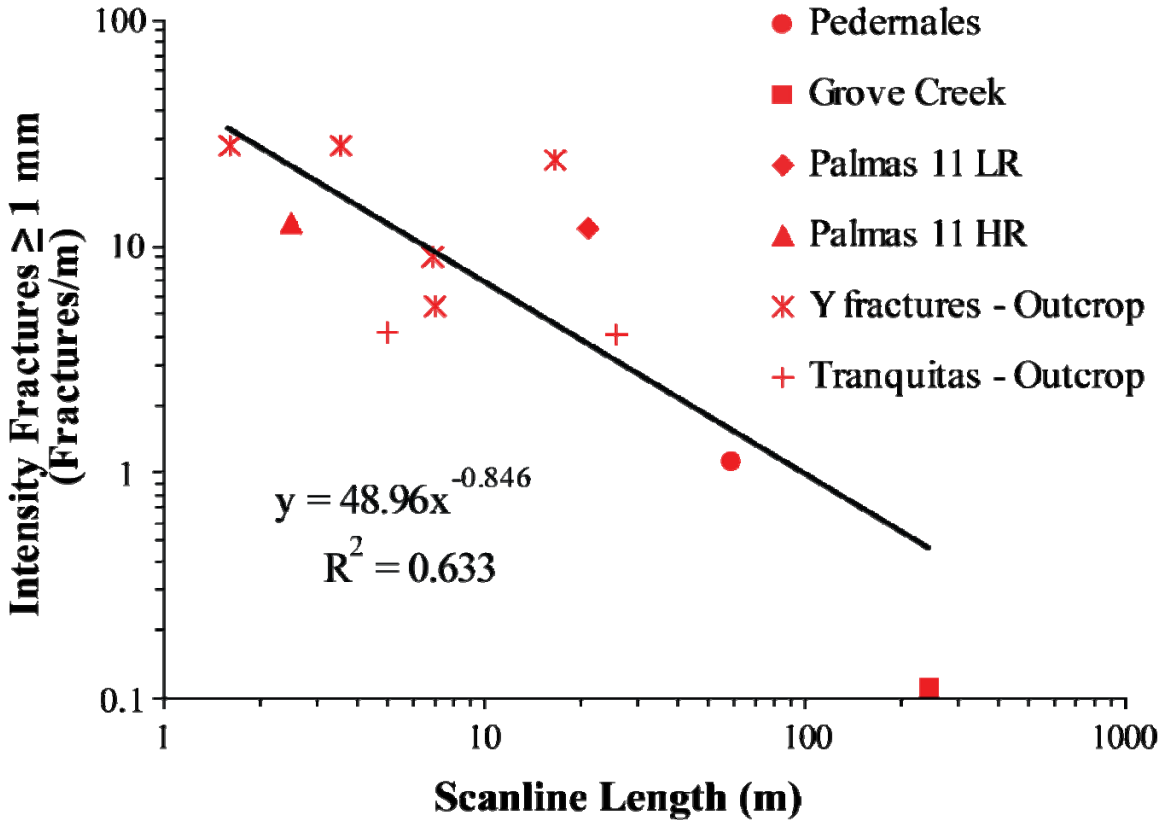

Figure 8.76 Fracture intensity for fractures with aperture larger than or equal to 1 mm versus scanline length for outcrop data sets. Red symbols indicate entire outcrop data sets (as in Figures 9.74 and 9.75). Power-law regression was calculated (solid line) using only all data points.

8.4.4.1.2 Fracture Strain

For fracture data sets at outcrop scale there is a linear relationship (power law with an exponent of 1) between fracture intensity and fracture strain (Figure 8.77). Because fracture intensity is inversely proportional to cluster width and cluster spacing (Figure 8.75), an increase in fracture strain with time should produce a decrease in both cluster width and cluster spacing. Indeed, graphs show a systematic decrease of cluster spacing and cluster width with increasing fracture strain (Figures 8.78a and 8.78b, respectively).

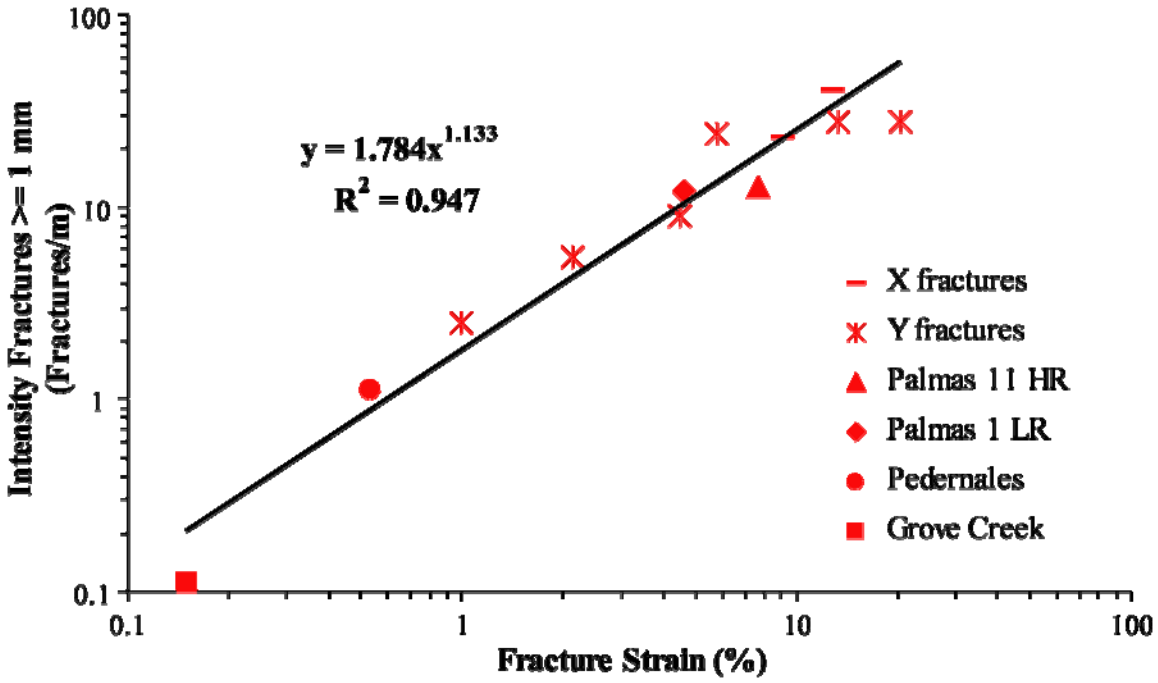

Figure 8.77 Fracture intensity for fractures with aperture larger than or equal to 1 mm versus fracture strain for outcrop data sets. Red symbols indicate entire outcrop data sets (as in Figures 9.74 and 9.75). Power-law regression was calculated (solid line) using only all data points.

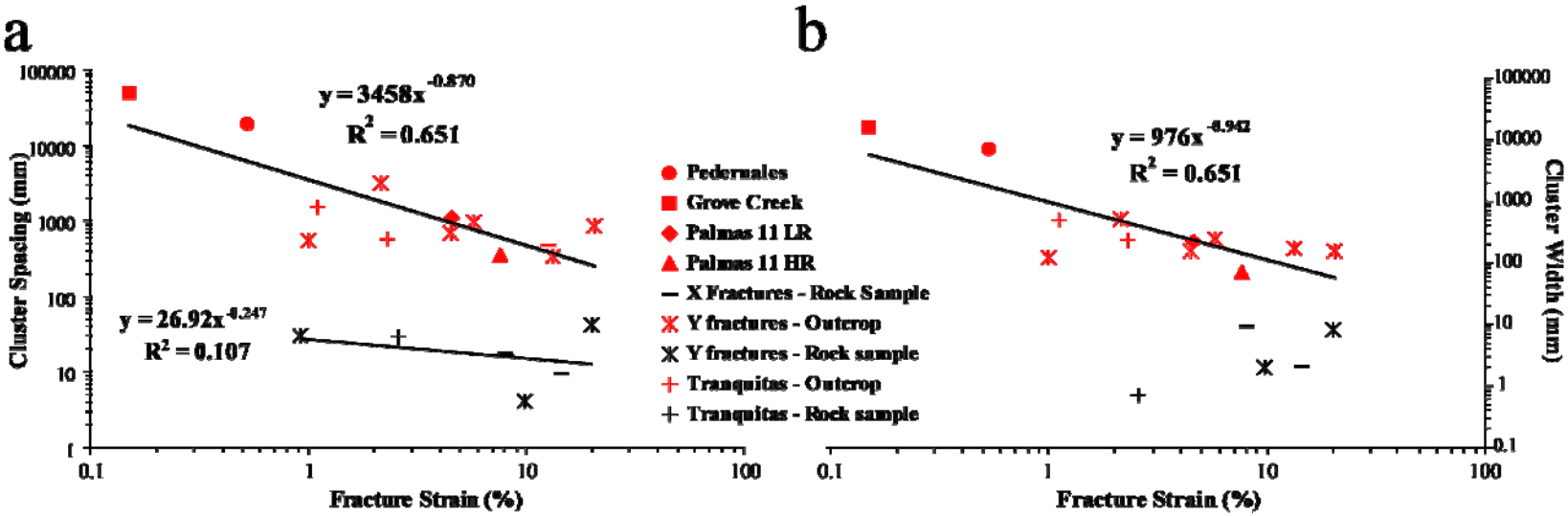

Figure 8.78 Cluster spacing (a) and cluster width (b) versus fracture strain. Red symbols indicate entire outcrop data sets. For data sets with rock samples, results at outcrop scale (entire scanline) and rock sample were plotted independently. Power-law regression was calculated (solid line) using only data points from outcrop data sets. Although X fractures show only random arrangements of fractures at outcrop scale, one data set (Palmas 12) showed statistically insignificant cluster spacing, which was nevertheless included. .There a systematic reduction in cluster spacing and cluster width for outcrop data sets with increasing fracture strain.

Although there is a small decrease in cluster spacing with increasing fracture strain (Figure 8.77b) for rock sample scale data sets, the coefficient of determination for least squares regression is only 0.11, which suggests that variations in cluster spacing cannot account for observed differences in fracture strain at rock sample scale.

8.4.4.1.3 Layer Thickness

The mechanical layer thickness of Pedernales is probably on the order of a hundred meters, as suggested by Hare and Marrett (in review). However, even if the estimate of Hare and Marrett (in review) is incorrect, direct observation of fractures at Pedernales indicates that fractures span at least a few meters (Chapter 2), a layer thickness larger than any of Cupido Fm. layers studied (0.24 to 0.89 m), suggesting a relationship between cluster width and cluster spacing with layer thickness (Figures 8.74 and 8.75). Namely, thicker layers exhibit wider clusters that are spaced farther apart. However, when cluster spacing and cluster width are graphed against measured layer thickness (only available for Cupido Fm. layers) a pattern is not observed (Figures 8.79a and 8.79b, respectively). The coefficients of determination for least-squares regression to cluster spacing and cluster width are close to zero, suggesting that variations in thickness for Cupido Fm. layers cannot account for variations in cluster width and cluster spacing (Figure 8.79).

The apparent contradiction between the results of Figure 8.75 and those of Figure 8.79 can be explained with the following three arguments. First, layers from the Cupido Fm. in the SMO (Table 8.5) have thicknesses that vary barely a half an order of magnitude, so a much larger range of layer thicknesses might be needed to detect a trend with cluster width and cluster spacing. Second, some fractures in the Cupido Fm. do not seem to be confined by layer boundaries, as shown in Figure 8.3a. If the rheological contrast between contiguous layers in the Cupido Fm. during the time Y fractures

developed was not at current lithologic boundaries, then measurements of fracture characteristics might not change systematically with layer thickness. And third, the layer thickness measured today may not be the thickness that layers had during the time fractures developed. Bedding-parallel stylolites in layers of the Cupido Fm. are common (Ortega and Marrett, 2001; Monroy-Santiago et al., 2001) and therefore layers probably are thinner than they were at the time fractures developed. In summary, there are reasons to question the lack of a recognizable trend in Figure 8.79 and to instead believe the trend of increasing cluster spacing and cluster width with increasing layer thickness (Figure 8.75), which agrees with numerical modeling that follows subcritical crack propagation (e.g., Olson, 2004). In addition, current models of subcritical crack propagation do not conjecture about variations of cluster width with layer thickness, and therefore my finding that cluster width increases with layer thickness neither supports nor contradicts fracture mechanics.

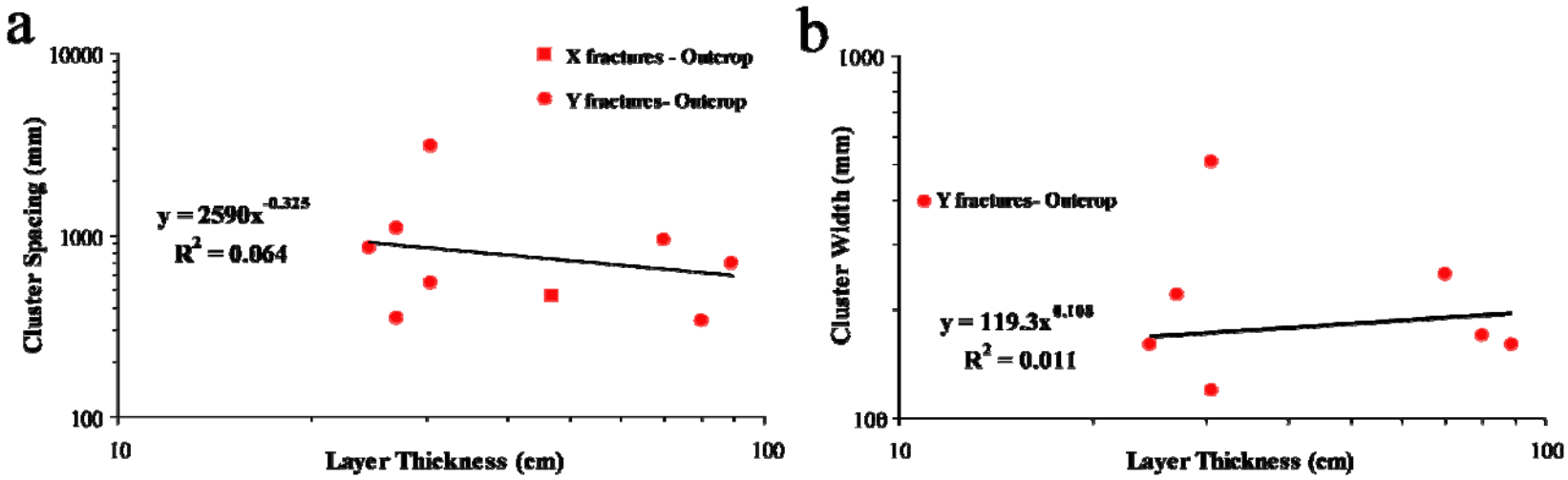

Figure 8.79 Cluster spacing (a) and cluster width (b) versus layer thickness for outcrop fracture data sets (entire scanline) in the SMO. Although X fractures show only random arrangements of fractures, one data set at outcrop scale (Palmas 12) showed statistically insignificant cluster spacing, which was included to test the similarity or dissimilarity of X fractures with Y fractures. Power-law regressions were calculated for Y fractures only. Coefficients of determination for power laws in both (a) and (b) are close to zero.

8.4.4.1.4 Degree of Clustering

When fractures exhibited a power-law pattern of spatial correlation (Figure 8.5b), the power-law exponent, which is indicative of the degree of clustering of a fracture data set (Marrett et al., in review; Chapter 6), was calculated. Although cluster width is estimated from the same power-law pattern as degree of clustering (Figure 8.5b; Marrett et al., in review), there is only a weak reduction in cluster width with increasing power-law exponent for independently analyzed Y fracture data sets. The weak correlation suggests that clusters with a higher degree of clustering are narrower (Figure 8.80a), more closely spaced (Figure 8.74) and have higher strain (Figure 8.78) and fracture intensity (Figure 8.75). In addition, there is an even weaker decrease in cluster spacing with increasing power-law exponent (Figure 8.80b).

The characteristics of clusters from the same layers but at different scales (outcrop versus rock sample) were also graphed against each other. Although the number of data points is very limited and a conclusive trend cannot be established, it is possible to state that layers with clusters of similar size at outcrop scale can have significantly different cluster sizes at rock sample scale (Figure 8.80c). In contrast, there is a systematic increase in cluster spacing at rock sample scale with increase in cluster spacing at outcrop scale, as reflected by a coefficient of determination of 0.946 (Figure 8.80d). Namely, if two rock samples from different layers yielded different cluster spacings, the layer with the largest cluster spacing at rock sample scale would have the largest cluster spacing at outcrop scale (Figure 8.80d). Cluster spacing at rock sample scale increases faster than cluster spacing at outcrop scale, as indicated by a power-law exponent larger than 1 (Figure 8.80d).

Figure 8.80 Cluster width (a) and cluster spacing (b) versus power-law exponent from NCC for Y fractures in Cupido Fm. (c) Cluster width for rock samples versus cluster width for outcrop data sets in the SMO. (d) Cluster spacing for rock samples versus cluster spacing for outcrop data sets in the SMO. In (a) and (b) solid symbols indicate outcrop data sets whereas empty symbols indicate rock sample data sets. Negative exponential regressions in (a) and (b) were calculated for outcrop data sets only. Power-law regression in (d) was calculated for all data points. Coefficient of determination for negative exponential distributions in (b) is close to zero, whereas the ones in (d) are relatively close to one. Cluster spacing at rock sample grows systematically with cluster spacing at outcrop scale, as shown in (d).

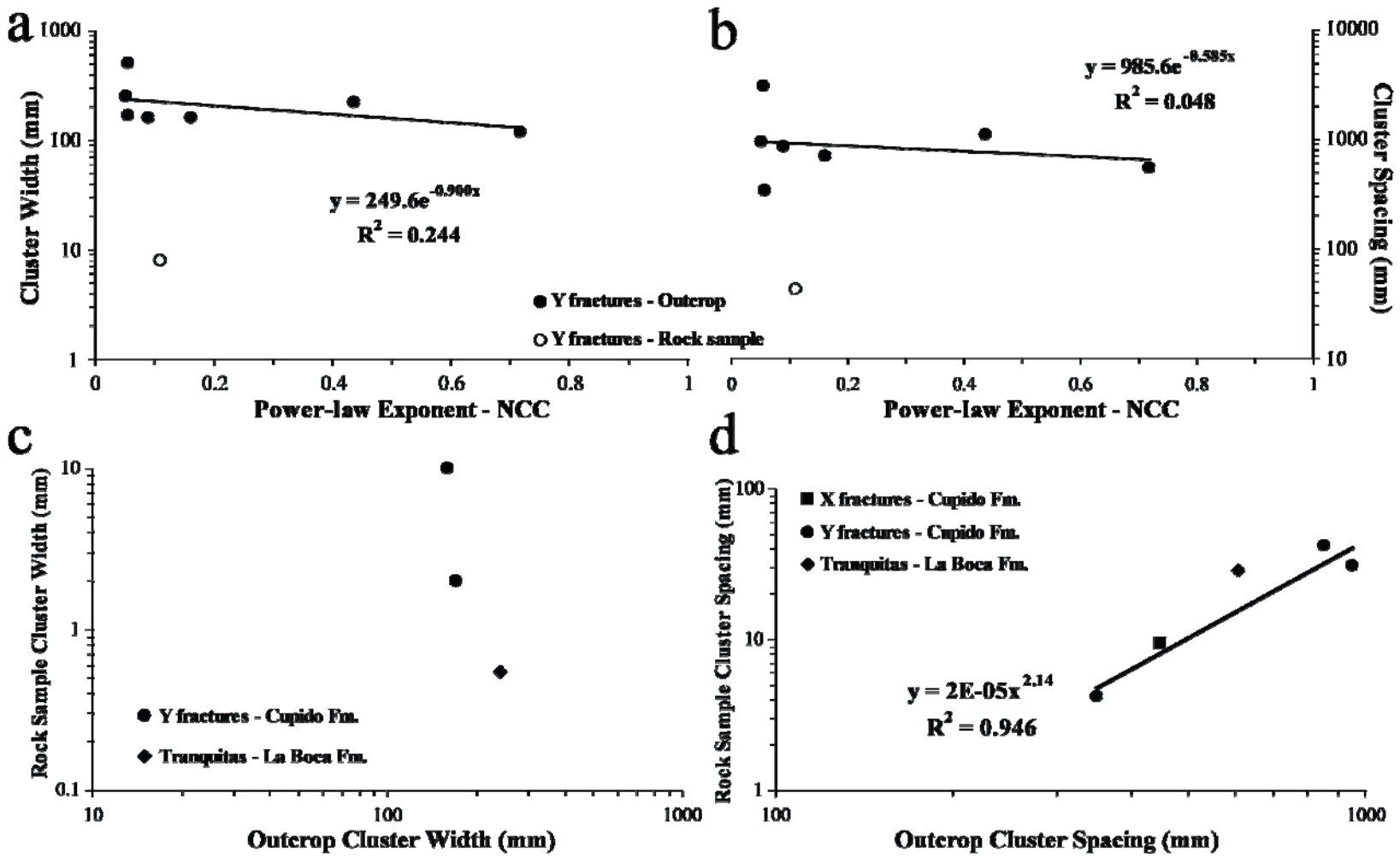
a
Cluster Width (mm)
1000
100
10
1
0
0.2
0.4
0.6
0.8
1
y = 249.6e^-0.900x
R^2 = 0.244
Y fractures - Outcrop
Y fractures - Rock sample
Power-law Exponent - NCC
b
Cluster Spacing (mm)
10000
1000
100
10
y = 985.6e^-0.585x
R^2 = 0.048
Power-law Exponent - NCC
c
Rock Sample Cluster Width (mm)
10
1
0.1
10
100
1000
Y fractures - Cupido Fm.
Tranquitas - La Boca Fm.
Outcrop Cluster Width (mm)
d
Rock Sample Cluster Spacing (mm)
100
10
1
100
1000
X fractures - Cupido Fm.
Y fractures - Cupido Fm.
Tranquitas - La Boca Fm.
y = 2E-05x^2.14
R^2 = 0.946
Outcrop Cluster Spacing (mm)

8.4.4.2 Comparing Domains of Same Layer (Outcrop Scale)

For Pedernales, Grove Creek, Palmas 11 LR, and Palmas 11 HR outcrop-scale data sets, cluster spacing and cluster width for fractures along the entire scanline and in intracluster domains decreases systematically with increasing fracture strain (solid symbols, Figures 8.81a and 8.81b). The power-law decrease of cluster width and cluster spacing with increasing fracture strain is similar (although with a smaller power-law exponent) to the trend observed for combined intra- and intercluster domains (Figure 8.78). Although the inversely proportional power-law trends of cluster width and cluster spacing with fracture intensity and fracture strain for combined domains (entire scanline) are somewhat suspicious due to the spread of data points (Figures 8.75 and 8.78), the trends with fracture strain for different domains of individual data sets are more coherent, which suggests a more reliable pattern (Figures 8.81a and 8.81b). Small periodically arranged clusters have to be narrower, more closely spaced, and exhibit larger strains than the larger cluster that they form (Figure 8.66), and therefore the trends of Figures 8.81a and 8.81b are somewhat expected. However, what is interesting about graphs of cluster width and cluster spacing versus strain at outcrop scale is that they show that clusters in the intercluster domains do not follow the same trend (Figures 8.81a and 8.81b).

Both individually considered and combined, intra- and intercluster domains of Pedernales and the Palmas 11 HR data sets show that cluster width and cluster spacing might systematically decrease with increasing power-law exponent from NCC analysis (Figures 8.81c and 8.81d), which suggests for some data sets, narrower clusters might be more clustered than wide ones as previously inferred for Pedernales clusters (Figure 8.67). Consequently, there is indication that for some data sets, small (narrow) periodically arranged clusters, some of which have a power-law pattern of spatial

correlation, might be more clustered, more closely spaced, and contain more strain than the larger (and also periodically arranged) clusters that they form (Figure 8.66). Fractures from intercluster domains exhibit weaker spatial organization than intracluster domains. Cluster widths and cluster spacing similar to the ones of intracluster domains but with strain a few orders of magnitude smaller (empty symbols, Figures 8.81a and 8.81b), which may be due to large fractures being preferentially located in intracluster domains (Chapter 7).

Figure 8.81 Cluster width (a) and cluster spacing (b) versus fracture strain, and cluster width (c) and cluster spacing (d) versus power-law exponent from NCC for outcrop data sets without rock samples (Pedernales, Grove Creek and Palmas 11 HR). Although Palmas 11 LR has a rock sample, it was included in these graphs because Red symbols indicate entire outcrop data sets. Black solid symbols indicate intracluster domains whereas black empty symbols indicate intercluster domains. Power-law regressions (solid line) in (a) and (b) were calculated using all but the data points from intercluster domains. The two power-laws reflect a trend of decreasing cluster width and decreasing cluster spacing with increasing fracture strain for fractures within a single layer. The negative exponential regressions in (c) and (d) were independently calculated for Pedernales (dashed line) and Palmas 11 HR (dotted line) data sets. For fractures of a single outcrop data set, cluster width and possibly cluster spacing decreases with increasing power-law exponent from NCC, as shown in (c) and (d), respectively.

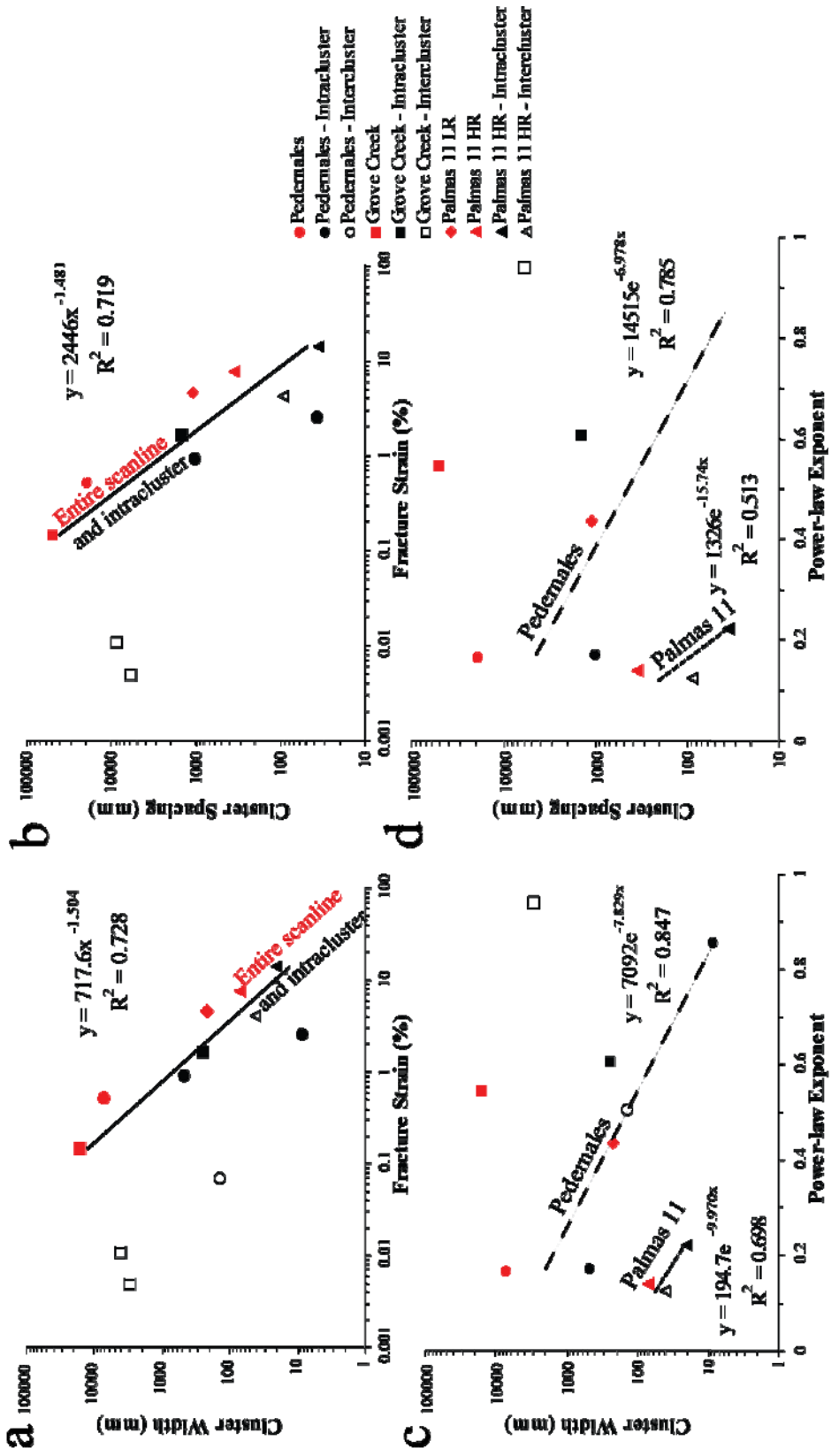
a
b
c
d
Cluster Width (mm)
Cluster Spacing (mm)
Fracture Strain (%)
Power-law Exponent
y = 717.6x^-1.504
R2 = 0.728
Entire scanline and intracluster
y = 2446x^-1.481
R2 = 0.719
y = 194.7e^-9.970x
R2 = 0.698
Pedernales
Palmas 11
y = 7092e^-7.829x
R2 = 0.847
y = 14515e^-6.978x
R2 = 0.785
y = 1326e^-15.74x
R2 = 0.513
Pedernales
Pedernales - Intracluster
Pedernales - Intercluster
Grove Creek
Grove Creek - Intracluster
Grove Creek - Intercluster
Palmas 11 LR
Palmas 11 HR
Palmas 11 HR - Intracluster
Palmas 11 HR - Intercluster

8.4.5 Spatial Arrangement near Layer Base

Of all the scanlines (at outcrop scale) measured in layers with rock samples (Tables 8.1 and 8.2), only the one at Tranquitas might not have been measured in the middle of the layer. Of all the layers with rock samples and scanlines measured in the middle of the layer (e.g., Palmas 13 scanline; Figure 8.3b) two had rock samples extracted near the layer base whereas all other samples were extracted along the scanline. Fractures from the two rock samples collected near the layer base (western 1.5 m of Escalera OO1 and Palmas 11) were the only ones at rock-sample scale yielding arrangements that are indistinguishable from random (Figures 8.14, 8.15, 8.27, and 8.28).

The Palmas 11 sample was extracted from an intercluster region and yielded arrangements that are indistinguishable from random (Figures 8.27 and 8.28). In contrast, fractures from other intercluster domains exhibit non-random arrangements, as shown for the Pedernales (Figure 8.61a), Grove Creek (Figures 8.54b and 8.55), and Palmas 11 HR (Figure 8.65) data sets. Although the two scanlines from the Palmas 11 rock sample are the shortest (38 and 64 mm; Table 8.7), the number of fractures measured in the scanlines (86 and 156, Table 8.7) is several times the number of fractures that display non-random arrangements in some other cases (e.g., 34 fractures from Huasteca sample yield periodic arrangement of clusters; Tables 8.6 and 8.7). In addition, cluster spacings at rock sample scale from other comparable layers (in terms of layer thickness and fracture strain) in the Cupido Fm. is smaller than scanline length from Palmas 11 sample. Therefore, scanline length and number of fractures from the Palmas 11 sample probably do not account for the indistinguishable from random arrangement (Table 8.6).

A similar situation occurs for the rock sample from the western 1.5 m of Escalera OO1 layer (sample 02LG12; Table 8.2). However, there are two differences between

rock-sample scale fractures from the western 1.5 m of Escalera OO1 with respect to the equivalent fractures from the Palmas 11 layer. The rock sample from the western 1.5 m of Escalera OO1 was extracted from a cluster and fractures exhibit evidence of a component of shear displacement (Chapter 9; Figure 9.26). With the exception of the rock sample from the western 1.5 m of Escalera OO1, all other rock samples extracted from outcrop-scale clusters yielded non-random arrangements (Tables 8.2 and 8.6).

The most important common threads between fractures at rock-sample scale from Palmas 11 and western 1.5 m of Escalera OO1 are that both exhibit indistinguishable from random arrangements and both samples were obtained near the layer base, and not in the center of the layer where most outcrop-scale scanlines were measured and where rock samples yielding non-random arrangements were extracted. Therefore, it is possible that the position of rock samples with respect to layer boundaries could explain why fractures yielded indistinguishable from random arrangements in domains and observational scales where other data sets yielded non-random arrangements. Namely, the spatial arrangement of fractures might vary within a layer, so that fractures along the layer center exhibit non-random arrangements and fractures near the layer boundaries exhibit indistinguishable from random arrangements. It is possible that only some of the fractures that form a statistically significant cluster at the center of the layer have a height larger than or equal to layer thickness. If this is the case, then fractures with heights as large as layer thickness may represent only a fraction of the statistically significant cluster, a fraction that in isolation lacks a non-random arrangement (Figure 8.48).

A possible answer to the question of whether the spatial arrangement of fractures that reach layer boundaries is different from fractures that do not reach layer boundaries would be to measure scanlines at different stratigraphic levels within a layer and to study independently the spatial arrangement of fractures from each scanline. At least one

scanline in the middle of the layer and another one near the layer base or near the layer top would be needed. Another test of whether spatial arrangement of fractures changes with stratigraphic level in a layer would be to extract rock samples from intra- and intercluster domains at different positions with respect to layer boundaries and to study independently the spatial arrangement of fractures at rock-sample scale. For example, one could study the spatial arrangement of fractures in one rock sample from the middle of the layer and one rock sample from near the layer boundary.

8.4.6 Prediction of Clustering at Outcrop Scale from Clustering in Rock Samples

Microfractures from rock samples have been used to predict the orientation (e.g., Laubach, 1997; Ortega and Marrett, 2000) and intensity (Marrett et al., 1999; Ortega and Marrett, 2000; Gomez et al., 2003a; Ortega et al., 2006) of genetically related macrofractures. In layers with periodically arranged clusters at outcrop scale, fractures (mostly microfractures) from rock samples inside intracluster domains (Figures 8.44, 8.46, and 8.47) or macrofractures inside intercluster domains (Figures 8.69 and 8.70) exhibit periodic arrangement of clusters. In layers with indistinguishable from random arrangements at outcrop scale (statistically insignificant clusters), microfractures from rock samples also yielded periodic arrangement of clusters (Figure 8.49). Therefore, finding periodic arrangement of microfracture clusters in rock samples cannot predict whether fractures at outcrop scale have statistically significant or statistically insignificant clusters.

8.4.7 Hypothetical Fracture Cluster Evolution

When measured along the center of a layer, fractures at outcrop scale that exhibit periodically arranged clusters also exhibit non-random arrangements inside both intra- and intercluster domains. Nevertheless, the internal organization of fractures in

intercluster domains is weaker than observed in adjacent intracluster domains. In addition, layers with fractures at outcrop scale with indistinguishable from random arrangements contain fractures at rock sample scale (mostly microfractures) that exhibit periodic arrangement of fracture clusters. Therefore, any evolutionary path proposed for natural fractures should account for the fact that spatial organization of fractures is present throughout a layer and at different scales.

One possible evolutionary path for the development of non-random clustering is that periodically arranged clusters at outcrop scale developed first and later fractures in between clusters formed. However, as shown by subcritical fracture modeling (Olson, 2004), the stress shadow of a cluster would prevent the later development of any fractures in intercluster domains, and therefore this evolutionary path cannot explain the non-random arrangements of fractures observed in intercluster domains.

An alternative evolutionary path is that statistically significant clustering starts at a scale smaller than outcrop, perhaps even smaller than rock-sample scale, throughout the entire layer being strained and not exclusively in domains that eventually become clusters at outcrop scale. Periodic arrangement of statistically significant clusters at a scale smaller than outcrop might develop following subcritical propagation at high values of subcritical index (Chapter 7), as shown in Figure 7.63. Cluster width and cluster spacing for early periodically arranged clusters might be at millimeter scale, as observed in fractures at rock sample scale (minimum cluster width and cluster spacing measured are 0.7 and 4.1 mm, respectively; Table 8.7). Periodic arrangement of clusters is believed to develop when fractures reach mechanical layer boundaries and cluster spacing is thought to be proportional to mechanical thickness (Olson, 2004), which suggests that when statistically significant clustering develops at rock-sample scale, fractures follow mechanical layering smaller than stratigraphical layer thickness (Figure 8.82a). A

periodic arrangement of clusters is believed to result from the interaction between the stress shadows of clusters during growth (Olson, 2004).

Only recently the issue of variation of mechanical stratigraphy with time has begun to be investigated. Shackleton et al. (2005) postulated that differences in diagenetic rates between individual layers with different grain sizes produced changes in the mechanical stratigraphy between two independent fracture events. However, the study of Shackleton et al. (2005) is not directly applicable to my dissertation because they addressed joint propagation across different layers instead of veins within a single layer. Mechanical layering smaller than stratigraphic layer thickness that varies during fracture evolution has not been postulated to occur and it has not been appropriately investigated. An investigation of mechanical layering smaller than stratigraphic layer thickness or systematic changes in fracture height with fracture position was not conducted for my dissertation. Nevertheless, some layers in the Cupido Fm. exhibit clusters with fractures that reach layer boundaries as well as smaller fractures with heights (and apertures) smaller than layer thickness that seem to end at compositional bands (Figure 8.83a). In addition, fractures with heights of a few cm within otherwise unfractured rock were observed in the Cupido Fm. (Figure 8.83b), suggesting that rheological differences within an individual layer might exert control on fracture development. In addition, it is possible that evidence of compositional or textural differences responsible for the development of fractures with mechanical thicknesses smaller than stratigraphical layer thickness had been erased during diagenetic evolution of rock.

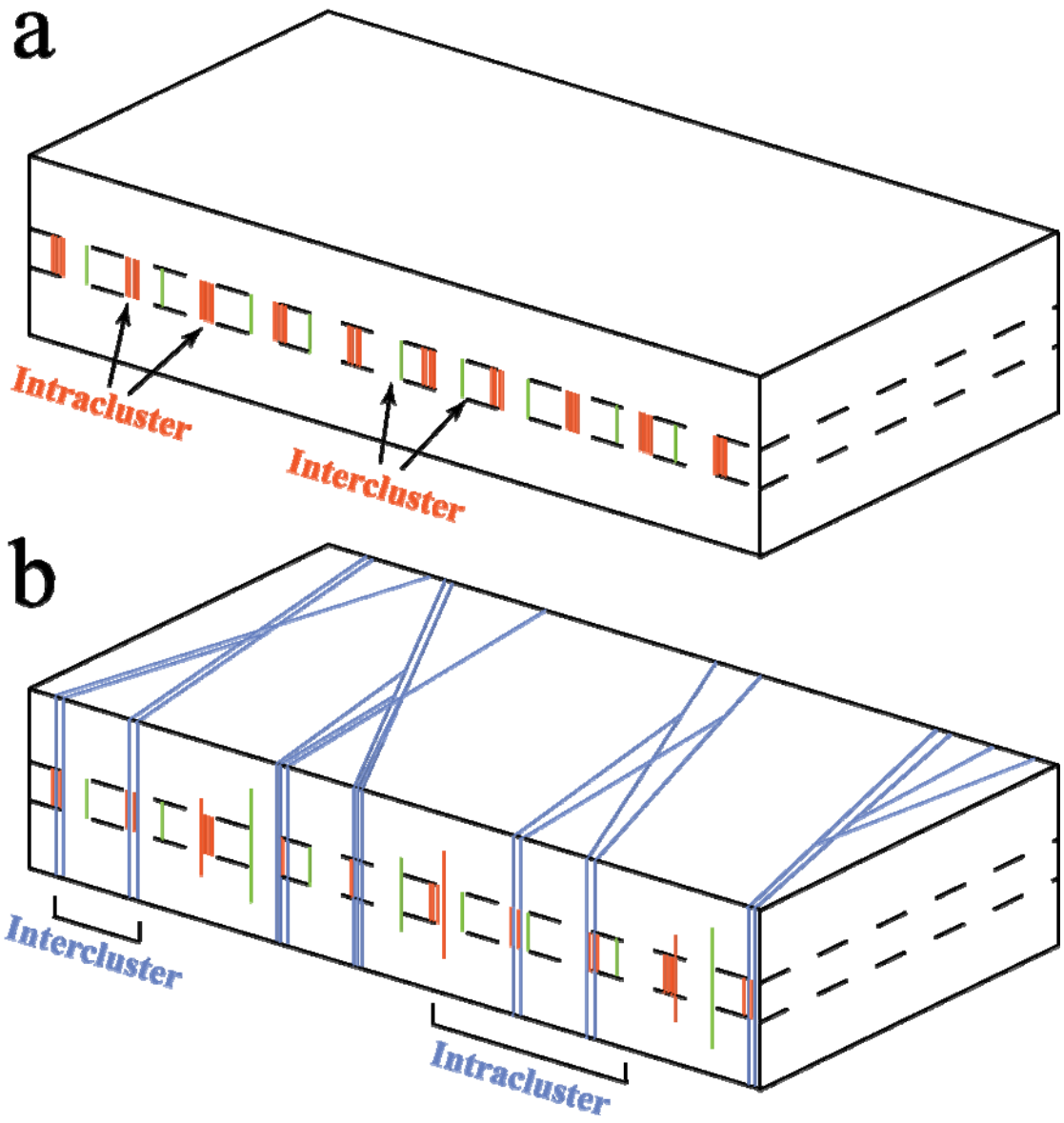

Figure 8.82 Sketches illustrating the suggested evolution of clustering through different mechanical thicknesses. In (a), periodically arranged clusters develop following mechanical thickness smaller than layer thickness. Further fracture development occurs in (b), when clusters at a larger scale grow from previously developed clusters at a smaller scale and with a larger mechanical thickness. Some fracture development in the intercluster domain of (b) could occur. Red (a) and blue (b) fractures are inside statistically significant clusters whereas green fractures formed in the intercluster domain of (a). Intracluster domain in (b) contains periodically arranged clusters developed in (a). Cluster spacing is slightly larger than mechanical thickness.

Figure 8.83 (a) Photograph of fractures in Huasteca layer with different heights, and (b) photograph of inside a layer (layer boundaries outside photograph) in the Escalera canyon showing fractures restricted to a mechanical layering smaller than layer thickness. Larger fractures in (a) form a cluster and exhibit fracture heights equal to layer thickness (green ellipse). Smaller fractures in (a) seem to terminate along compositional bands parallel to bedding (orange ellipses). Although compositional banding is not observed in (b), fractures seem to terminate at stylolites parallel to bedding. Scale of fracture spacing in (b) is similar to cluster spacing measured in rock samples from layers of the Cupido Fm. (Table 8.7). Bedding plane (dotted white line) is approximately horizontal in (a) and (b). Scale in (a) and (b) is in centimeters.

b
Tectonics Special Research Centre

a

The sketch of Figure 8.82b suggests that the spatial arrangement of fractures along a scanline on a bedding plane could be different from fractures along a scanline located half-way between the two bedding planes that form an individual layer. Spatial arrangement of fractures along a scanline located on one of the bedding planes would exhibit, in principle, only the periodically arranged clusters developed with a mechanical layering equal to stratigraphical layer thickness and very little to none in between clusters. In contrast, fractures along a scanline located half-way between the two bedding planes (cross section view) that form an individual layer would exhibit periodic arrangement for fractures developed with different mechanical layering (red fractures versus blue fractures, Figure 8.82b), with non-random spatial arrangements in the intercluster domains of fractures that developed with mechanical layering equal to stratigraphic layering. In order to test the validity of the above mention inference, independent measurements of fracture aperture and spacing along scanlines in both cross section and top of layer (bedding parallel) should be obtained and analyzed using NCC. Unfortunately none of the outcrops currently studied in the Monterrey salient are suitable for the above mentioned test, and therefore exploration for new outcrops should be conducted first.

An effective increase in thickness of mechanical layering during fracture evolution requires a mechanism that explains how some fractures (or clusters of fractures) develop heights larger than initial mechanical layering and then continue propagation under an enlarged mechanical layering. Before such mechanisms are explained, it should be noted that large fractures at outcrop scale within the Cupido Fm. commonly exhibit heights that exceed layer thickness (e.g., fractures within clusters of Figure 8.3a, or large fracture to the right end of the scanline in Figure 8.3b). So, the

question should not be whether such mechanism(s) exist but what they are and how they operate.

Two mechanisms might explain fractures (or clusters of fractures) propagating beyond the mechanical layer in which they nucleated. The first mechanism conjectures that the opening-mode stress intensity factor (K) developed by fractures formed in different rheological bands of the same layer could, if they coincide in position and are large enough, develop into a single fracture by linking vertically (Figure 8.84a), similar to what appears to have occurred in the Huasteca layer (Figure 8.83a). The bands that define mechanical banding within a single bed could be of compositional and/or textural origin.

The second mechanism, compressional crossing (Renshaw and Pollard, 1995), hypothesizes that while periodic arrangement of fracture clusters is developing at rock-sample scale, the fractures of some clusters might link due to natural variations in fracture orientation. The propagating fracture cluster resulting from linkage of smaller fractures would attain a length and height larger than fractures in the surrounding clusters at rock-sample scale and a K larger than the surrounding fractures. An enhanced K would increase stress near the tip of the propagating cluster to the point where propagation is reinitiated on the side of the interface opposite to the propagating fracture (Renshaw and Pollard, 1995) as shown in Figure 8.84b. Reinitiation most likely would occur at a small asperity along the mechanical layering before a fracture cluster reaches layer boundary (Figure 8.84b). The successful test of compressional crossing by Renshaw and Pollard (1995) was based on the assumption that compressional crossing "will occur if the magnitude of the compression acting perpendicular to the frictional interface is sufficient to prevent slip along the interface at the moment when the stress ahead of the fracture tip is sufficient to initiate a fracture in the opposite side of the interface". If the mechanical layer boundary is defined by a stylolite (Figure 8.83b), slip would be less likely than for

other planar boundaries due to the irregular nature of a sylolitic plane. In addition, compressional crossing was tested with equations that assume that materials on both side of the mechanical boundary have the same elastic properties, which could be the case for compositional and/or textural bands within the same layer or for internal mechanical layering defined by stylolite planes. However, compressional crossing has difficulty explaining the developed periodicity because a cluster could develop a height taller than mechanical thickness before the periodicity is fully developed.

Once the mechanical layering at rock sample scale is exceeded, subsequent fracture propagation would continue controlled by a larger mechanical thickness, directed in turn for thicker rheological bands parallel to bedding (Figure 8.83a) or by the entire layer thickness (Figure 8.82b). Subsequent clusters might initiate from clusters at rock sample scale (Figure 8.85) and develop outside the stress shadow of the newly developed cluster at outcrop scale. Interaction between clusters in the thicker mechanical layer would result in periodically arranged clusters (Figure 8.85). The discrete length scales of nested periodically arranged clusters might be a result of complex rheological layering during the time of fracture development.

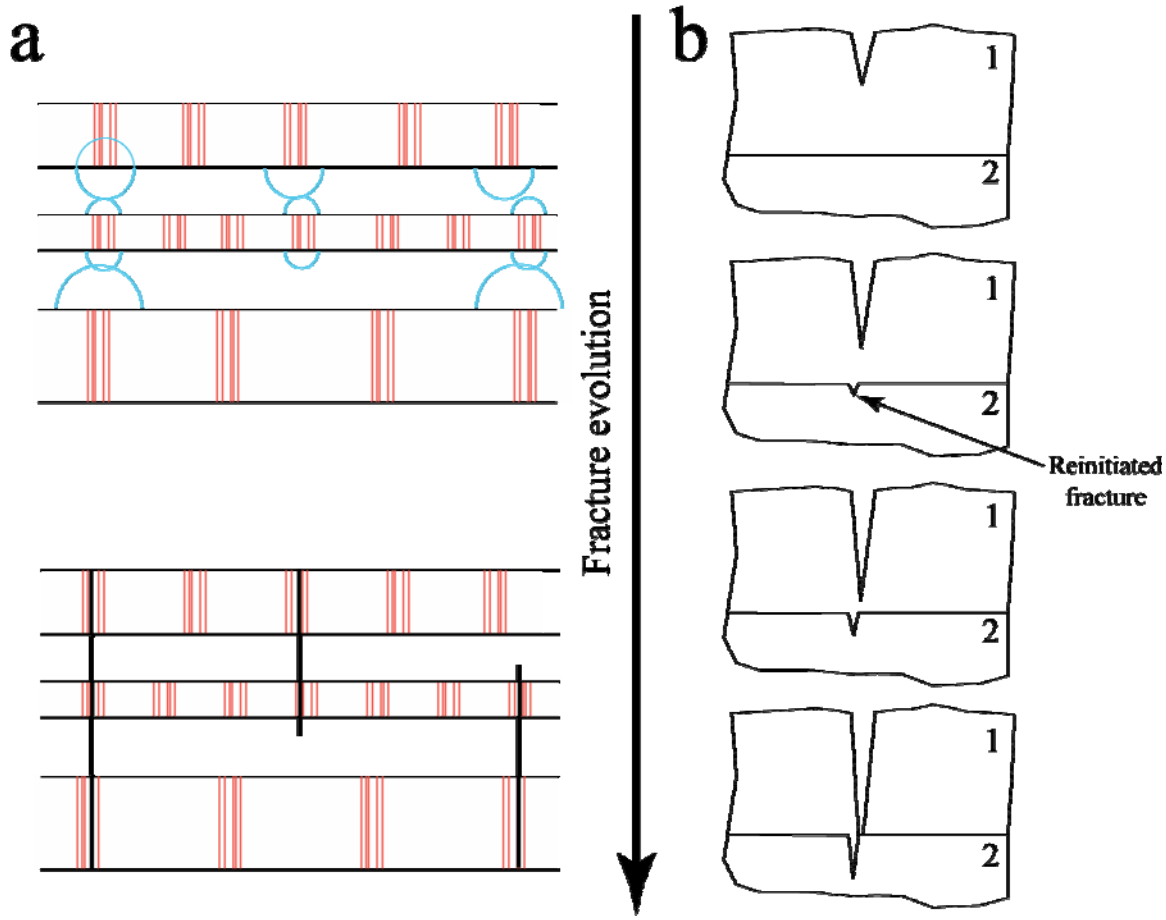

Figure 8.84 Sketches illustrating two possible mechanism of fracture propagation that might explain fractures (or clusters of fractures) at rock-sample scale developing heights larger than their initial mechanical layering. Sketches represent cross sections across (a) a layer and (b) part of a layer. (a) Of the five compositional bands within a single layer, three develop periodic arrangement of clusters. The opening-mode stress intensity factor (K) for each fracture cluster increases the stress above and below every cluster (blue circle). When clusters coincide (left) a new fracture joining the independently developed clusters might form. Partial alignment of clusters might not allow for complete fracture propagation across the entire layer (center and right). (b) Under adequate conditions, compressional crossing of an interface can occur by reinitiation of a propagating fracture at the side of the mechanical boundary opposite to the propagating fracture. (b) Modified from Renshaw and Pollard (1995).

In intercluster domains between large clusters there would be remnants of non-random clustering developed at smaller scale (Figure 8.82b). Fracture strain would have increased in the newly developed clusters but not in intercluster domains (strain directed away from intercluster domains and propagating under smaller mechanical layering), which could explain the dissimilar scaling of cluster width and spacing with fracture strain for intra- and intercluster domains (Figures 8.81a and 8.81b). However, it is unclear at this time the reason why smaller statistically significant clusters have a higher degree of clustering than larger ones. If synkinematic cement is present during fracture development, then it could preferentially preserve the aperture of small fractures such as the ones in the intercluster domain (Figure 8.82b).

The evolution of fracture clustering proposed in Figure 8.82 suggests that cluster width and cluster spacing increase through time in response to a thicker mechanical layer, which seems to contradict the inverse trend of fracture strain with cluster width and cluster spacing (Figure 8.78). However, the evolution of fracture clustering presented in Figure 8.82 shows the final stage of each episode of cluster development, when fracture clustering reaches saturation and no more clusters can be added because the stress shadows of already existing clusters impede it (Figure 8.85d). Numerical modeling of subcritical cluster propagation suggests that one cluster propagates at a time (Olson, 2004). Therefore, before the state of cluster saturation is reached, cluster spacing must progressively decrease with increasing applied strain (Figure 8.84). It is unclear at this time if cluster width changes before cluster saturation is reached.

Figure 8.85 Sketches illustrating the suggested evolution, from (a) through (d), of clustering for a single mechanical layer. Although cluster width and cluster spacing increases proportional to mechanical thickness (Figure 8.82), cluster spacing at conditions for the same mechanical thickness likely decrease with increasing applied strain. Red (a) and blue (b) fractures are inside statistically significant clusters whereas green fractures formed in the intercluster domain of (a). Cluster saturation is reached in (d).

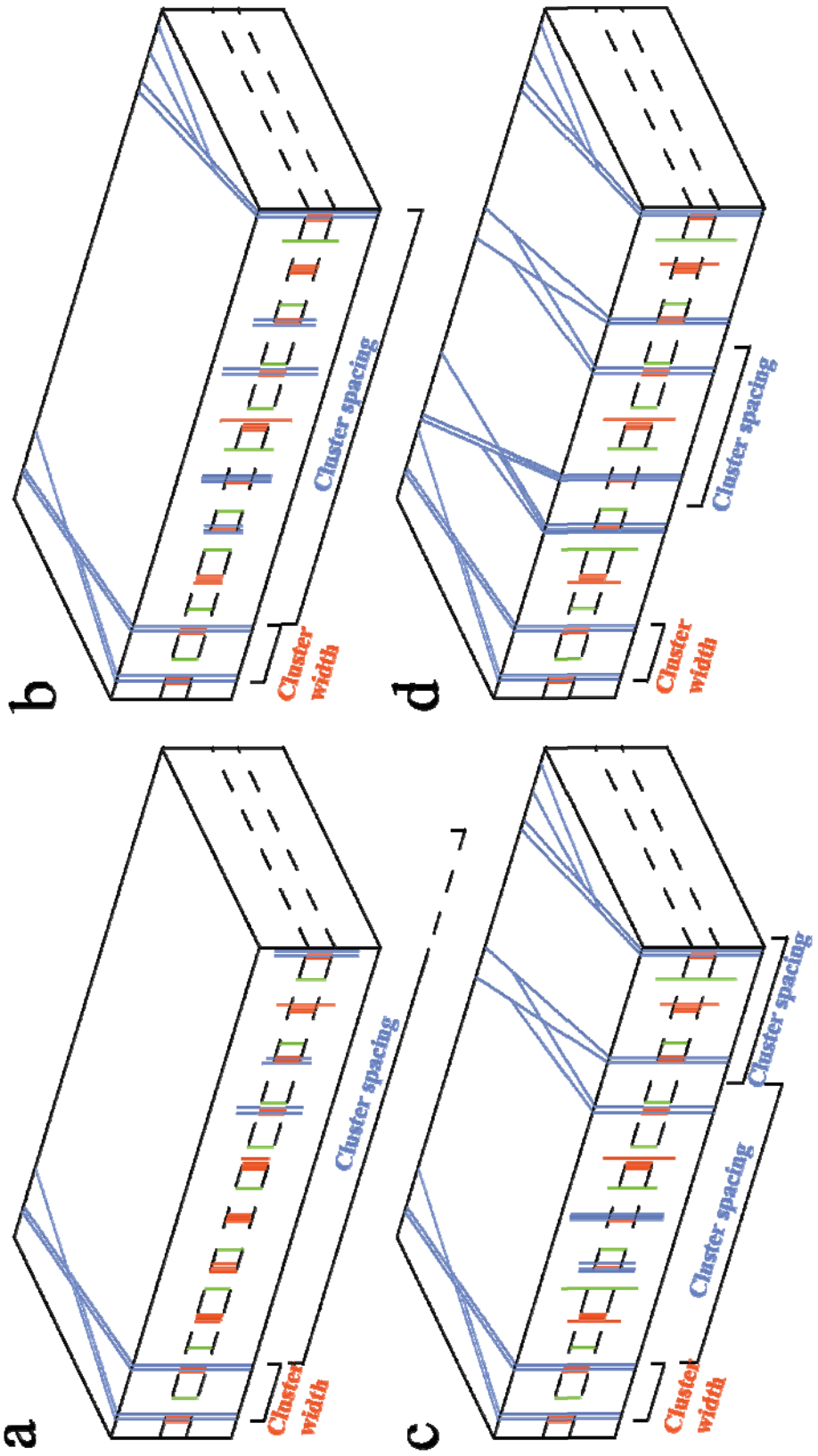
a
Cluster width
Cluster spacing
b
Cluster width
Cluster spacing
c
Cluster width
Cluster spacing
Cluster spacing
d
Cluster width
Cluster spacing

Fracture data sets measured for my dissertation were selected in part because they exhibited well developed spatial arrangements. Namely, clusters were well developed and a periodic arrangement of clusters was qualitatively recognized (Figure 8.3a), or clusters seemed ambiguous but fracture apertures and total strain were comparable to data sets with distinct clustering (Figure 8.3b). Therefore, it is possible that the data sets with distinct clustering represent fractures that had reached cluster saturation. The well-developed linear trend of cluster width versus cluster spacing of Figure 8.74 seems to confirm that the data sets measured for my dissertation reached saturation, because all the data points plot near the maximum ratio of cluster width to cluster spacing. Cluster width must be less than cluster spacing because if cluster width reaches cluster spacing, then adjacent clusters merge and clustering would no longer be apparent (Figure 8.86). Clusters that have reached saturation (e.g., Figure 8.85d) would plot near the limiting ratio (Figure 8.86). Clusters that have not reached saturation (Figures 8.85a to 8.85c) would have narrower width and/or wider spacing than at cluster saturation (Figure 8.86). During evolution of fracture clustering within the same mechanical layering (Figure 8.85), clusters will migrate through time towards the region of cluster saturation (Figure 8.86).

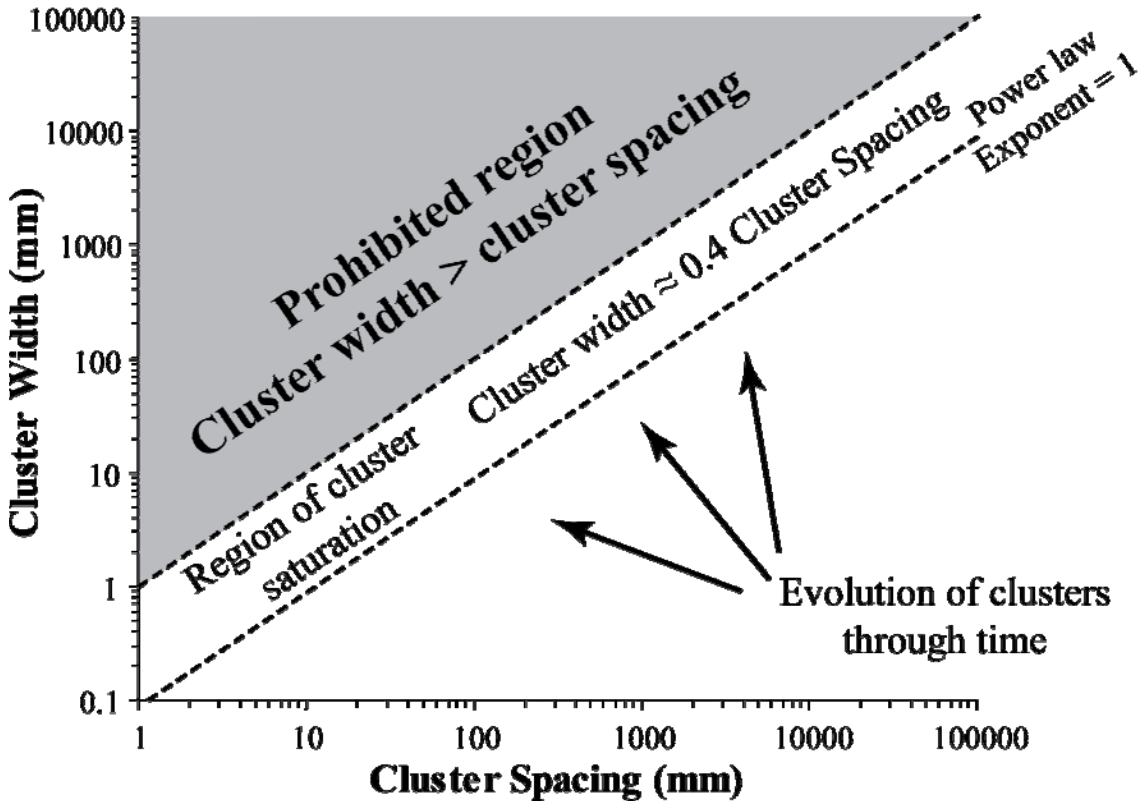

Figure 8.86 Schematic diagram of cluster width versus cluster spacing showing prohibited region (grey fill) where cluster width is larger than cluster spacing. Boundary of prohibited region is a line with cluster width equal to spacing. Region of cluster saturation is located between the lower limit of the prohibited region and a power-law regression with coefficient and exponent of 1. Exact width of region of cluster saturation is unknown. Cluster width seems to be 0.4 times the cluster spacing from data shown in Figure 8.74.

8.5. CONCLUSIONS

Normalized correlation count (NCC) has allowed quantification of the spatial arrangement of fractures and differentiation of statistically significant from statistically insignificant clustering. Previous studies detected power-law patterns of spatial correlation with length scale and suggested that they indicate fractal arrangements. I demonstrated that fracture clusters with power law variation of spatial correlation with length scale are not strictly natural fractals. Statistically significant clusters with a power law of spatial correlation can be formed by smaller clusters with a power law of spatial correlation that are also periodically arranged. However, the internal structure of statistically significant clusters is inconsistent with a fractal arrangement because clusters occur in a cascade at discrete values of length scale and not in a semi-continuous fashion.

At rock sample scale microfractures with apertures as small as 0.5 μm in both siliciclastic and carbonate lithologies show three (fractal, random and periodic) of the four fracture arrangements described by Marrett et al. (in review). However, spatial arrangements of fractures (mostly microfractures) from rock samples cannot predict spatial arrangement of genetically related fractures (mostly macrofractures) at outcrop scale because fractures at rock-sample scale from layers with both statistically significant and statistically insignificant clustering at outcrop scale exhibit periodically arranged clusters at rock sample scale.

Fractures inside statistically significant clusters at outcrop scale exhibit non-random arrangements at most length scales, and commonly contain statistically significant clusters that are periodically arranged. In contrast, intercluster domains at outcrop scale exhibit statistically weaker spatial arrangements. When clustering reaches

saturation, cluster width scales linearly with cluster spacing and approximates 40% of cluster spacing.

I propose an evolutionary model that accounts for some clustering attributes. The most important finding that this model attempts to account for is the fact that periodic clustering in outcrop scale intercluster domains occurs at short length scales similar to intracluster domains at the same scale. The model proposes that clustering initiates at rock-sample scale, or smaller, with mechanical banding smaller than layer thickness. At or near cluster saturation at rock-sample scale, fractures in some clusters propagate beyond mechanical banding and continue propagation into thicker mechanical banding. The discrete length scales of nested periodically arranged clusters might be the result of complex rheological layering during the evolution of fracture clusters. Although cluster spacing increases with mechanical layering, during the development of cluster saturation at one particular scale of mechanical layering, cluster spacing decreases. Finally, spatial arrangement of fractures from rock samples taken near layer boundaries also suggests that spatial arrangement might vary with stratigraphic level in a layer, although samples indicate more organized arrangements in the center of a bed than near layer boundaries.

Chapter 9: Diagenesis and Spatial Arrangement of Opening-mode Fractures in the Cupido Formation, Monterrey Salient, Mexico

9.1. INTRODUCTION

Structural diagenesis aims to develop an understanding of how fracture propagation and diagenetic processes interact. Theoretically, all the parameters that influence how fractures grow, such as rock properties (e.g., Young's modulus, porosity) and environmental conditions (e.g., fluid pressure, magnitude and direction of stresses), might affect how fractures are spatially arranged. In particular diagenetic processes contemporaneous with fracture growth might modulate the spatial arrangement of fractures. One advantage of studying diagenetic processes during fracture development, in contrast to other environmental conditions such as stress, is that diagenetic processes commonly leave a record in the rocks. In addition, if more than one fracture set is developed in the same rock but at different times and under different diagenetic conditions, compositional and textural evidence of different diagenetic processes can help distinguish different fracture events. The advantage of studying spatial arrangement of fractures, in contrast to other fracture attributes such as aperture, is that the spatial arrangement of fractures is less ephemeral than some other fracture attributes, which can change with time. For instance, variations of fluid pressure in the subsurface can, in principle, increase or decrease the aperture of a pre-existing fracture that has not been filled with cement, but it cannot change where that pre-existing fracture is located, or its position with respect to the other pre-existing fractures.

Diagenetic processes can affect the permeability of fractures and therefore understanding diagenesis in fractures has practical significance regarding subsurface fluid flow. For instance, the precipitation of cements after fracture opening (postkinematic

cement, as defined by Laubach, 2003) can greatly reduce fracture porosity and fracture permeability. Cements that precipitate during fracture opening (synkinematic cement, as defined by Laubach, 2003) commonly develop bridges, which can assist the preservation of fracture porosity and fracture permeability. Previous work has not succeeded in realistically modeling fluid flow partly because the link between diagenesis and fracturing has not been adequately studied (Gale et al., 2005). For instance, recent research has only started to address how diagenesis affects the porosity and permeability of fracture networks in sandstones (e.g., Laubach et al., 2004; Eichhubl and Flodin, 2005) and dolostones (e.g., Gale et al., 2004, Gale et al., 2005; Gale et al., 2006).

Through changes in the mineral composition (e.g., dolomitization of a limestone layer) and the porosity of rocks, diagenesis modifies mechanical properties, which in turn can impact how fractures develop and what quantitative attributes the resulting fracture networks have (Lorenz et al., 1997; Shackleton et al., 2005), including how fractures are arranged in space. Therefore, understanding the relationship between diagenetic processes and quantitative attributes of a fracture network might explain the genesis of some patterns of natural fractures. For instance, modeling conducted by Olson (personal communication, 2005) suggests that cumulative frequency distributions of aperture and length are affected by synkinematic fracture cementation.

Spatial arrangement of fractures can impact subsurface fluid flow. Due to the natural variation of fracture orientation, fractures that are closely spaced (forming clusters) are more likely to be connected than fractures that are widely spaced (Chapter 1). Better description and understanding of the spatial arrangement of fractures would facilitate more realistic numerical modeling of natural fracture networks for simulation subsurface fluid flow (Adler and Thovert, 1999). Another practical incentive for studying the spatial arrangement of fractures is estimation of the minimum length required for a

horizontal well to be economically feasible (Gale, 2002). Other factors being equal, regularly spaced fractures require a longer horizontal wellbore than fractures that are clustered (Chapter 1). Although diagenesis can affect fractures, fractures also affect diagenesis by enhancing circulation of diagenetic fluids. Nevertheless, all previous studies of spatial arrangements of fractures have ignored diagenesis. For instance, Rives et al. (1992) used physical and numerical modeling to evaluate the evolution of the cumulative distribution of fracture spacings with increasing applied strain. Another example is Olson (2004), who showed how subcritical fracture growth can influence fracture clustering.

This chapter of my dissertation is the first attempt to relate diagenetic processes in natural fractures with specific types of spatial arrangement. To address the relationship between diagenesis and the spatial arrangement of fractures, I independently assessed the spatial arrangement of fractures and the diagenetic processes that affected fractures in the Cupido Formation in the Monterrey salient. Afterwards, I independently classified fracture sets according to diagenetic processes and spatial arrangement and compared classifications to establish correlations. Diagenetic processes were analyzed through compositional and textural evidence (e.g., crack-seal texture in quartz cement) in both fractures and rock matrix, which can be used to indicate relative timing and prevalent conditions of diagenetic processes (Tucker and Wright, 1990). The spatial arrangement of fractures was studied using a recently developed technique (normalized correlation count, or NCC; Marrett et al., in review) that overcomes the main deficiencies of traditional techniques (Gomez and Marrett, in review).

9.1.1 Previous Studies

Although there is no publication exploring the relationship between the diagenesis and the spatial arrangement of fractures, some work has been done to relate average

fracture spacing with rock lithology and bed thickness. For instance, it is widely believed that dolostones are more intensely fractured (and therefore have a lower average spacing) than limestones (Safko and Hickey, 1992) and clastic rocks (Lorenz et al., 1997; Nelson, 2001). However, very little published data support this statement perhaps due to the difficulty in obtaining data that can be adequately compared (e.g., layers with equal thickness, same deformation history). In a recent study, Lorenz et al. (1997) noted that fracture intensity (the inverse of average fracture spacing) does not exhibit a relationship with layer thickness but increases with mud content of the Lisburne Group both in the subsurface (Lisburne field, Prudhoe Bay) and in outcrops found along the northeastern Brooks Range in Alaska. Ortega (2002) showed that fracture intensity does not correlate with bed thickness but increases with the degree of dolomitization in layers of the Cupido Fm. in the Monterrey salient. Although Ortega (2002) took into account some of the diagenetic processes affecting the rocks where natural fractures are found, both Lorenz et al. (1997) and Ortega (2002) only used the average spacing (or its inverse) to quantify how fractures are arranged in space. As explained in Chapter 6 (Gomez and Marrett, in review), average spacing does not account for fracture position and therefore it cannot adequately quantify spatial arrangement of fractures.

9.1.2 Paragenesis of the Cupido Formation

Monroy-Santiago (in preparation) developed a new workflow to understand the relationship between fracture evolution and diagenetic processes in carbonate rocks and applied it to the Cupido Fm. The workflow included petrographic interpretation of the paragenetic sequence for each sample (about a hundred were used for the Cupido Fm.), comparison of results from all samples for a given locality (Figure 2.7) and synthesis of a single paragenetic sequence that includes not only diagenetic processes like cementation, but also the timing of fracturing events relative to other processes. Lastly, paragenetic

sequences from different localities were correlated by Monroy-Santiago (in preparation) to recognize regional diagenetic patterns for the Cupido Fm. across the entire Monterrey salient. This part of the workflow allowed Monroy-Santiago (in preparation) to infer not only which diagenetic processes and fracturing events reached across the Monterrey salient, but also to map variation of the events. Two of the three field areas of Cupido Fm. used for my dissertation (Escalera and Palmas) were included in work by Monroy-Santiago (in preparation).

The paragenetic sequence of Monroy-Santiago (in preparation) for carbonate rocks of the Cupido Fm. is based on preliminary results of Monroy-Santiago et al. (2001) and includes a wide range of diagenetic processes (e.g., dolomitization, recrystallization, calcite cementation) and six fracturing events. Geochemical signatures of fracture filling cements indicate that events occurred under a variety of geological conditions (Monroy-Santiago et al., 2001; Monroy-Santiago, in preparation). In addition, diagenetic processes occurred during and between different fracturing events. For instance, Monroy-Santiago (in preparation) interpreted that fracturing occurred before, during and after the regionally significant dolomitization called D2 (Figure 9.1).

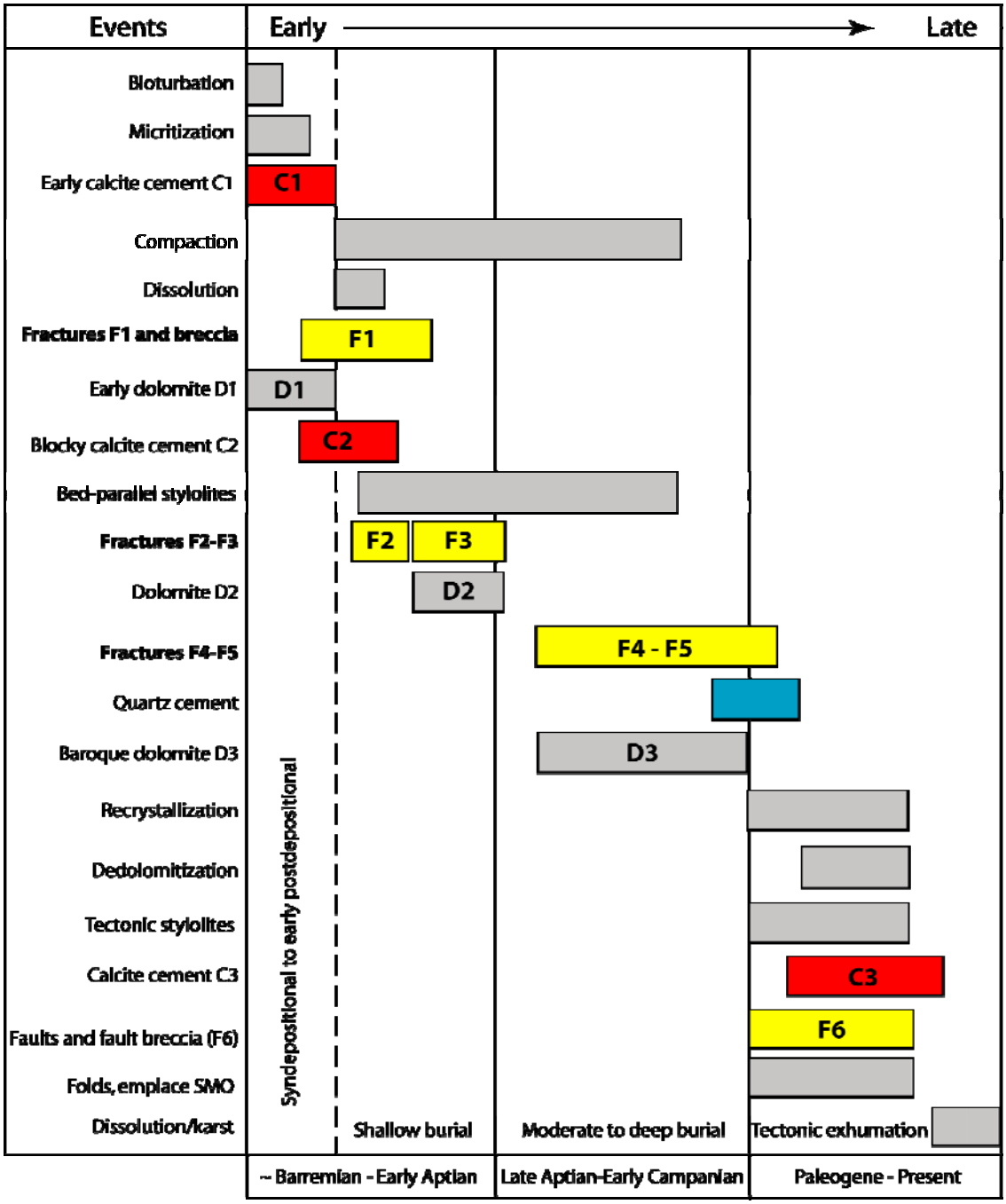

Figure 9.1 Condensed paragenetic sequence of the carbonate rocks of the Cupido Fm. in the Monterrey salient. Bars represent fracture events and diagenetic processes. Fracture events F4 to F5 were interpreted to have occurred before D2 dolomite cement by Monroy-Santiago et al. (2001) but are now interpreted to have occurred after D2 dolomitization. Absolute start-stop times are conjectural. Modified from Monroy-Santiago et al. (2001).

Monroy-Santiago (in preparation) used relative timing of a particular fracturing event with respect to other structures to constrain the paragenetic sequence of Cupido Fm. (Figure 9.1). Namely, some fractures of the first event are present in clasts of evaporite-solution-collapse breccias that formed near the surface, implying that the fracture event occurred at an early stage in the evolution of the Cupido Fm. (Monroy-Santiago et al., 2001), whereas the last fracture event produced mainly faults (including bedding-parallel slip horizons) during folding of the Sierra Madre Oriental. In contrast, fractures of intermediate events are not confined to breccia clasts and mainly have opening displacement. Monroy-Santiago et al. (2001) discriminated those intermediate fracture events into four individual events, one before, one during and two after D2 (Figure 9.1). However, information about each fracturing event (and their corresponding synkinematic cements) available in Monroy-Santiago et al. (2001) and Ortega and Marrett (2001) is relatively limited, especially regarding the cements inside fractures and their timing with respect to fracture opening.

9.1.2.1 Regionally significant D2 dolomitization

D2 dolomitization partially or completely replaced the original carbonate material in some layers of the Cupido Formation with non-ferroan dolomite (Figure 9.2), while preserving some of the original rock textures. Dolomite crystals of the D2 event replaced rock matrix, allochems and previously precipitated cements (from at least one episode of calcite cementation), are anhedral in shape, and range in size from 10 to 50 μm (Monroy-Santiago, in preparation). In addition, D2 dolomite cement was distinguished from earlier D1 dolomite cement by Monroy-Santiago (in preparation) based on the lack of association with evaporites or algal-mat laminations (present in D1) and from D1 and D3 by grain size difference (D1 crystals are smaller than 10 μm whereas D3 crystals range between 25 and 2000 μm). Moreover, Ortega (2002) concluded that dolomite abundance

increases toward the upper parts of fifth order depositional cycles in platformal facies of the Cupido Formation. Although Ortega (2002) did not interpret which dolomite cement of Monroy-Santiago (2001) varies cyclically, it is likely D2 dolomite of Monroy-Santiago (in preparation) because the Ortega (2002) only studied the dolomite in the matrix, which Monroy-Santiago (in preparation) observed almost exclusively in the matrix.

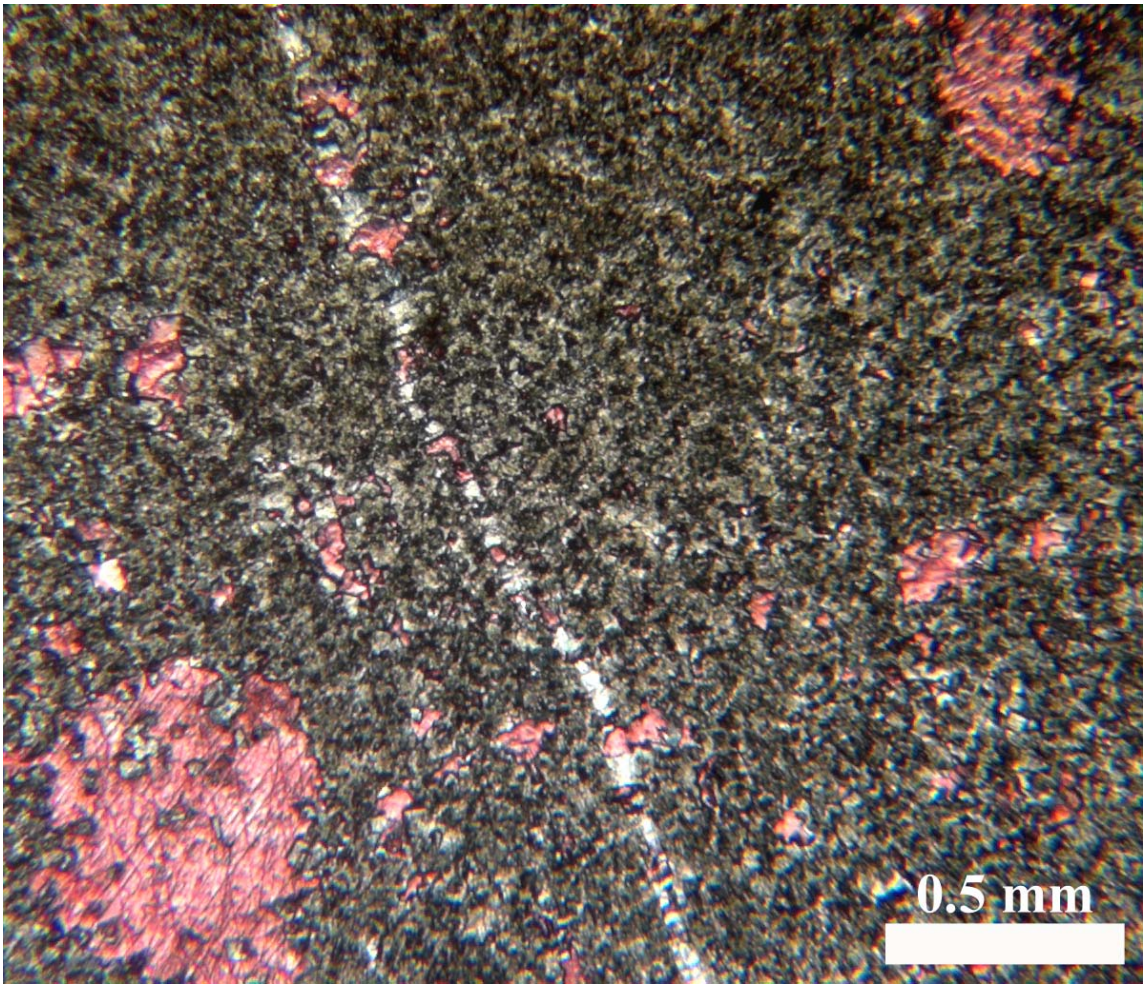

Figure 9.2 Photomicrograph of rock matrix mainly composed of D2 dolomite. Pore in lower left corner is mostly filled with calcite which was partly replaced by D2 dolomite. Fracture is filled mostly with dolomite crystals that are more translucent and larger than D2 dolomite crystals in matrix. Plane light of thin section 02LG16-1A from layer Palmas 13 (Tables 9.1 and 9.2), stained for calcite.

9.1.2.2 Changes to the Paragenetic Sequence of Monroy-Santiago et al. (2001)

It should be highlighted that the preliminary paragenetic sequence of Monroy-Santiago et al. (2001) has been modified in Monroy-Santiago (in preparation). The most important changes are as follows (F. Monroy-Santiago, personal communication, 2005):

1. The total number of fracture events has been reduced from seven to six.
2. Fracture events F4 to F5 are no longer interpreted to have occurred before D2 dolomitization but are currently interpreted to have occurred after the precipitation of D2 dolomite cement.
3. D1 dolomitization is now associated with deposition of evaporites and algal mats, instead of being the result of local replacement of rock matrix. D1 dolomite is typically finely laminated.
4. D2 replaced D1 dolomite as the most abundant dolomite cement.
5. D2 dolomitization is now interpreted to have occurred at shallow burial conditions instead of moderate to deep burial conditions.
6. Baroque dolomite cement (D3) is now recognized throughout most of the Monterrey salient and is interpreted to have occurred mainly before quartz cementation and simultaneously with part of F4 and F5 fracture events.
7. Quartz cement was primarily associated with bed-parallel and vertical stylolites but now it also is interpreted as synkinematic cement in veins.
8. Both dedolomitization and recrystallization are recognized to have occurred at relatively late stages in the paragenetic sequence.

Unfortunately, at the time this dissertation was written, a final version of the paragenetic sequence of Monroy-Santiago (in preparation) was not available. Because the studies of Monroy-Santiago (in preparation) are still unfinished, it is possible that some

diagenetic interpretations mentioned in the previous pages will undergo additional changes.

9.1.3 Scope of This Chapter

The total thickness of the Cupido Fm. has been estimated between 700 to 900 m (Goldhammer and Lehmann, 1991), and the thickness of individual layers within the Cupido Fm. is not uniform. For instance, Marrett et al. (1999) estimated the thickness of individual layers of the Cupido Fm. in the Huasteca canyon (Figure 2.7) to be between 0.5 and 1 m. In another example, Ortega and Marrett (2001) measured a stratigraphic column in the Cupido Fm. totaling 85 m in the Boquilla Corral de Palmas locality (Palmas canyon, Figure 2.7) and found that layer thickness varies from a few cm to slightly more than 2 m. Calculating the average thickness of the 42 layers studied by Ortega and Marrett (2001) yields an average thickness of about 0.7 m. Therefore, it is likely that the Cupido Fm. contains at least several hundred to slightly more than a thousand layers. This chapter utilizes data obtained from only nine layers, which represent about 1% of layers within the Cupido Fm. In addition, the nine layers were not selected with the intention of representing variations in lithology, lithofacies (as described by Goldhammer and Lehmann, 1991), stratigraphic position or layer thickness. The layers were selected on the basis of abundant opening-mode fractures and high quality outcrop, which allowed measurement of a scanline as described in Chapter 2. Consequently, the nine layers studied are not representative of the Cupido Fm., and the conclusions of this study probably do not apply to the entire Cupido Fm. This study only aims to illustrate the existence of a relationship between fracture diagenesis and how fractures are spatially arranged. A study of the relationship between fracture diagenesis and the spatial arrangement of fractures in the entire Cupido Fm. is beyond the scope of

my dissertation, and would require data that represent internal variations throughout the Cupido Fm.

9.1.4 Chapter Organization

The remaining part of Chapter 9 is divided in four sections. The first of those four sections explains the most important methods used to study the diagenetic evidence preserved in fractures, introduces the reader to some of the most common terminology to be used on this chapter, and presents a summary of the paragenesis of the Cupido Fm. in the Monterrey salient, as reported by Monroy-Santiago (in preparation). The second section shows the diagenetic evidence that supports differentiating categories of fractures in layers of the Cupido Fm. and presents an interpretation of the relative timing of the different cements with respect to fracture opening and with respect to the most pervasive diagenetic event. The third section introduces all the fracture data sets mentioned in this chapter, emphasizing the spatial arrangement of each data set at outcrop scale. Finally, the fourth section presents my interpretation of the relative timing of the fracture cements described in the second section with respect to fracture opening. The fourth section establishes the relationship between different fracture categories and types of spatial arrangement, and also elaborates on the rationale behind opening-mode fractures with different characteristics having distinctive spatial arrangements.

The second section of this chapter shows in detail the differences in roughness of fracture trace (i.e., irregular vs. straight), fracture cements (i.e., calcite, dolomite, and quartz), and texture of those fracture cements (e.g., bridges, crack-seal texture) for distinctive categories of fractures in carbonate layers of the Cupido Fm. Although the second section of this chapter shows evidence of different diagenetic processes that affected opening-mode fractures, the objective of the second section is not to create an exhaustive understanding of the paragenetic sequence of the Cupido Fm. Instead, the

objective is primarily to establish the evidence that allows distinguishing fractures that may have occurred at different stages of the geologic evolution of the Cupido Fm. in the Monterrey salient. This evidence would facilitate hypothesizing about the conditions during the different times of fracture growth.

The timing of the diagenetic processes that affected the Cupido Fm. in the Monterrey salient is based on the paragenetic sequence developed by Monroy-Santiago (in preparation), which is an update of the diagenetic history presented in Monroy-Santiago et al. (2001). A summary of the more relevant aspects of the updated version of the paragenesis of the Cupido Fm., including evidence about the most abundant dolomite cement (D2) in the carbonate rocks of the Cupido Formation, was taken from Monroy-Santiago (in preparation) and presented in the first section of this chapter. Although most petrographic analyses were conducted using an optical microscope, cathodoluminescence (CL) and element mapping using a scanning electron microscope (SEM) were also performed on selected thin sections. In addition, most thin sections analyzed exclusively in the optical microscope were stained for calcite using alizarin red.

The spatial arrangements of fracture data sets presented in the third section were analyzed using normalized correlation count (NCC) technique, as described in Chapter 6. A compilation of the different kinds of spatial arrangements (as defined by Marrett et al., in review) exhibited by all the fracture data sets analyzed is also included in the third section of this chapter. Finally, the fourth section of this chapter provides an interpretation for the observations presented in the second section for each of the two fracture categories studied. This interpretation include explanations about the relationships between the documented fracture cements and their textures and fracture opening (i.e., prekinematic, synkinematic or postkinematic). The fourth section also includes an interpretation of the timing of the two fracture categories relative to the

paragenetic sequence of the Cupido Fm. in the Monterrey salient. The fourth section establishes the relationship between fracture category and a particular type of spatial arrangement as defined by Marrett et al. (in review). The fourth section also aims to integrate the findings of the previous three sections into a single hypothesis of how the difference geologic conditions at the time fractures are developing, including diagenetic, can influence the spatial arrangement of opening-mode fractures.

9.2 METHODOLOGY

I collected fracture scanline data (or obtained data collected by Dr. J. Gale, C. Hare, C. Kelsey, Dr. R. Marrett, and M. Ward) from layers of the Cupido Fm. that exhibit fracture arrays with different apparent spatial arrangements. Some layers where fracture data were measured exhibit evident clustering of fractures (Figure 9.3a) whereas other layers display more ambiguous clustering of fractures (Figure 9.3b) or what seems to be regularly spaced fractures (Figure 9.3c). In addition, fracture data were measured only on outcrops that displayed a smooth surface allowing reliable measurement of fracture aperture and spacing, and that were long enough for the measurement of a representative portion of the fracture array (Chapter 2). Along a scanline, consecutive values of kinematic aperture and fracture spacing or position were measured for fractures that are larger than a pre-determined size threshold using a hand lens and a logarithmically graduated comparator (Ortega et al., 2006). Wherever feasible, information about the type(s) of fracture cement(s) present inside the fractures and fracture orientation was also acquired simultaneously and used to separate fractures into sets. Although fracture orientation is a fracture attribute that cannot be measured in a strictly 1D line, it was acquired (or at least estimated) by following a fracture outside the scanline.

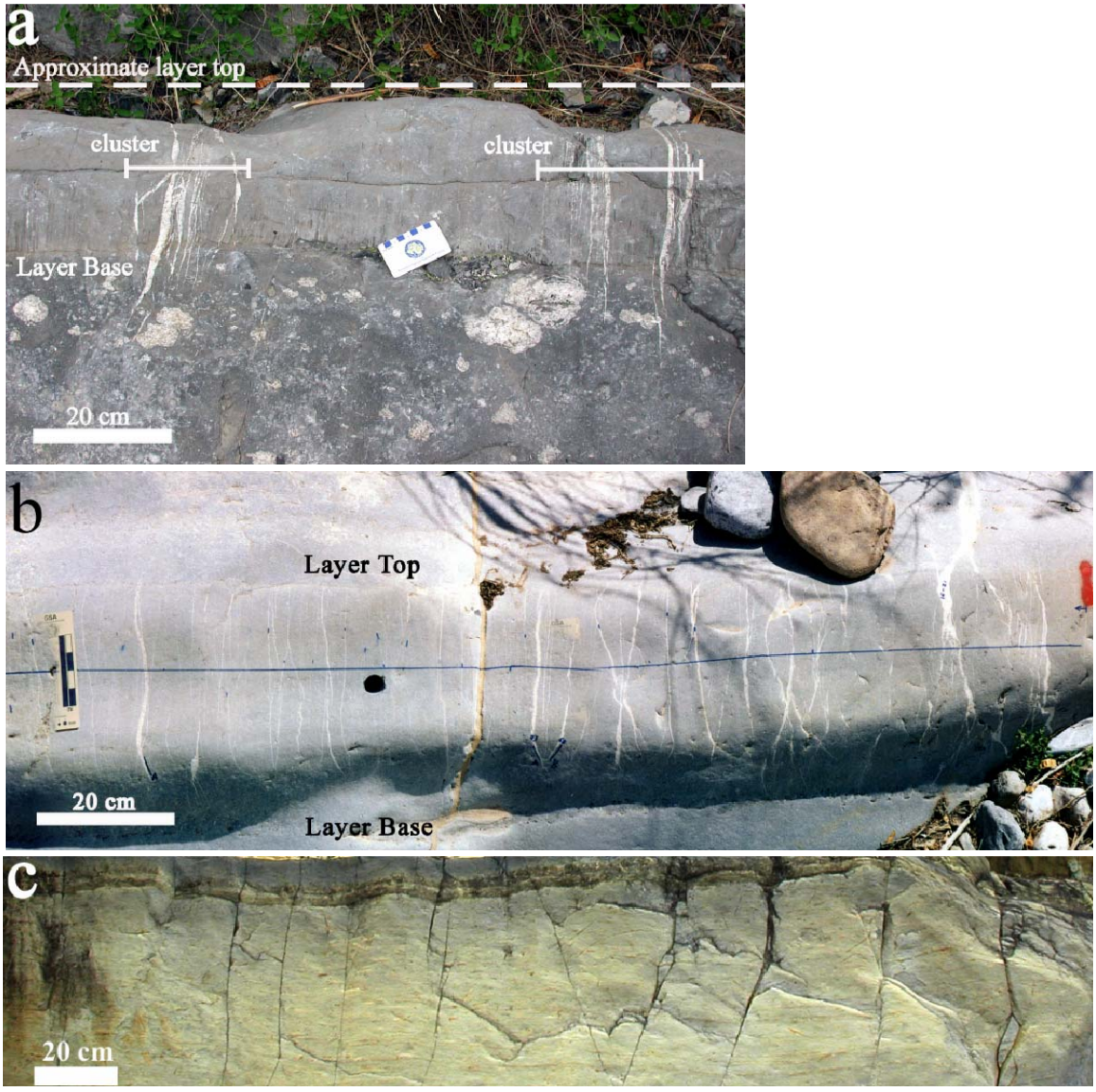

Figure 9.3 Fractures with qualitatively different spatial arrangements. (a) Photograph of two clusters of macrofractures in cross-sectional exposure of layer Palmas 11. (b) Photograph of the northern 1.5 m of scanline in cross-sectional exposure of layer Palmas 13. (c) Photograph of eastern 2.5 m of scanline in bedding-parallel exposure of joint outcrop (Table 2.1). Layers in (a) and (b) are from the Cupido Formation whereas layer in (c) is from the Aurora Formation. Fractures in (a) and (b) can be classified as veins whereas fractures in (c) can be classified as joints (Chapter 2). Although photographs in (a) and (b) are approximately at the same scale and both layers have a similar thickness, clustering is obvious in (a) but not in (b).

From all the fracture data sets available for my dissertation (Tables 2.1 and 2.2), I selected for this chapter only data sets from layers with oriented rock samples (Tables 9.1 and 9.2). An ideal rock sample should satisfy two conditions. The first condition is for the sample to be obtained along the outcrop scanline, which allows diagenetic study of fractures measured along the outcrop scanline. Studying a rock sample from outside the outcrop scanline carries the risk of encountering a diagenetic history different from the fractures along the scanline. The second condition is for the sample to contain both macrofractures and microfractures. Both macrofractures and microfractures are needed because different size fractions of fractures can provide different information about the diagenetic processes that affect fractures (Laubach, 2003; Laubach et al., 2004). Nevertheless, samples that do not completely satisfy these two conditions were used for this study. If a rock sample could not be obtained along the outcrop scanline, the sample was collected so as to contain macrofractures from the scanline, which ensures that the rock sample represents at least some fractures measured along the scanline. A sample that contains only microfractures does not necessarily provides erroneous diagenetic evidence, but instead the diagenetic history recorded only in macrofractures (if present) cannot be deciphered.

Table 9.1 Summary of geologic information and statistics for outcrop fracture data sets used to study the relationship between diagenesis and spatial arrangement of fractures (from Tables 2.1 and 2.2).

Data Set	Geographic Area	Structure Name	Structural Position	Geologic Unit	Lithology	Fracture type	Outcrop Type	Number of Fractures (all sets)		Aperture Threshold	Scanline Length	Strain
								> Aperture Threshold	< Aperture Threshold	mm	m	%
Escalera OO1	Escalera Canyon SMO, Mexico	San Blas Anticline	Anticline forelimb	Cupido Fm.	Dolostone	Veins	Cross section	680	480	0.05	3.20	13.3
Escalera OO12								1047	48		3.56	20.4
Escalera 1			Anticline backlimb				Bedding surface	460	0		7.03	7.02
Escalera 2							Cross section	568	46		6.15	7.73
Escalera 3								293	0	0.095	6.93	4.46
Huasteca	Huasteca Canyon, SMO, Mexico	Muertos Anticline	Anticline forelimb					658	0	0.215	16.59	7.15
Palmas 11 LR	Palmas Canyon SMO, Mexico	San Blas Anticline						262	0	0.95	21.11	4.59
Palmas 12								316	0	0.265	6.14	12.7
Palmas 13								459	0	0.14	5.43	9.16

Total number of fracture spacings measured = 5308

Total number of fracture apertures measured = 4734

Total scanline length measured = 76.13 m

Table 9.2 Summary of information for thin sections used to study the relationship between diagenesis and spatial arrangement of fractures. All thin sections are approximately parallel to bedding. SEM = Scanning Electron Microscope, CL = Cathodoluminescence.

Layer	Rock Sample		Number of Thin Sections	Microscope Type
	Name	Location in Outcrop		
Escalera OO1	02LG11	Inside cluster, along scanline	1	Petrographic
			1	SEM/CL
	02LG12	Inside cluster, outside scanline at layer base	2	
			7	Petrographic
Escalera OO12	02LG13	Inside cluster, along projected scanline	7	
Escalera 1	03LG16	Outside scanline	2	
	03LG17		2	
Escalera 2	8A01	Outside scanline	1	
Escalera 3	801	Outside scanline	2	
	03LG20	Along scanline, edge of cluster	2	
	03LG21	Along scanline, outside cluster	2	
Huasteca	03LG26	Along scanline, edge of cluster	2	
Palmas 11	JS002	Outside cluster, outside scanline at layer base	2	
	PA11JG		2	
Palmas 12	02LG15	Along scanline	2	
Palmas 13	02LG16	Along scanline	5	

Total number of thin sections = 42

Thin sections from six layers (Escalera OO1, Escalera OO12, Huasteca, Palmas 11, Palmas 12, and Palmas 13) were used to obtain microfracture scanline data and to characterize diagenesis in fractures (Table 2.3). In addition, thin sections from the other layers (Escalera 1, Escalera 2, and Escalera 3) were used to characterize fracture diagenesis (Table 9.2). Although scanline data (aperture and spacing, Chapters 2 and 6) were obtained at both outcrop and rock sample scales for the first six layers mentioned above (Chapter 8), only outcrop scanline data are available for the last three layers. The original objective of sampling layers with fracture scanline data was not to relate the diagenetic processes with the spatial arrangement of fractures. Sampling of the layers was done with the intention of quantifying the spatial arrangement of microfractures inside rock samples and studying possible relationships between the spatial arrangement of macrofractures (at outcrop scale) and microfractures within a rock sample (Chapter 8). Therefore, sampling focused on obtaining a rock sample with fractures of the most abundant set (each set grouping fractures with a similar orientation) measured in the outcrop scanline, which explains why some of the fracture sets of some layers were not sampled.

If possible, thin sections were prepared from oriented samples. Marks on a rock sample can be used to orient it after removal from the outcrop (Passchier and Trouw, 1998). Photographs were taken before and after removal of each rock sample from the outcrop. Photographs of a rock sample in the outcrop, together with marks on the sample indicating the orientation of macrofracture sets, ensured that the same fracture sets could be characterized independently in the resulting thin sections. If a rock sample broke during extraction, the pieces were put together and the resulting ensemble was impregnated with blue epoxy. Photographs were taken before and after impregnation in order to help track fracture sets. Additional photographs were taken of rock chips just

before thin section preparation. Photographs of the rock chips were later compared with scanned images of the corresponding thin sections to ensure thin section orientation.

Additional thin sections obtained by Ortega (2002) and Monroy-Santiago (in preparation) from about fifty layers were made available for my dissertation. Although their thin sections were obtained from layers in the same localities selected for my study (Figures 2.4 and 2.7), there are no scanline data adequate to study the spatial arrangement of fractures (only aperture data were collected by Ortega, 2002). However, thin sections from Ortega (2002) and Monroy-Santiago (in preparation) corroborated characterization of fracture categories described in section two. Conversely, photomicrographs depicting evidence of diagenetic processes were taken exclusively from the thin sections generated for my dissertation (Tables 2.3 and 9.2). Photomicrographs of specific diagenetic evidence were taken mainly from thin sections of layers that did not suffer late diagenetic processes described by Monroy-Santiago (in preparation), such as dedolomitization and recrystallization. These late diagenetic processes can overprint textures and obscure interpretation.

9.2.1 Normalized Correlation Count (NCC)

Normalized correlation count is a statistical technique that quantifies the frequency of pairs of opening-mode fractures (e.g., or other discrete structures such as deformation bands) as a function of distance between fractures (λ_k or length scale), normalized by the number of fracture pairs for an equivalent (in terms of number of fractures and scanline length) random arrangement of fractures. Consecutive values of fracture aperture and spacing along a scanline are the typical input data for NCC, whereas the resulting normalized frequency of NCC is called spatial correlation, which is typically plotted in the Y axis, with length scale plotted in the X axis (Chapter 6; Marrett et al., in review).

NCC is a discrete technique in the sense that spatial correlation is estimated independently for each range of length scales considered. Namely, NCC quantifies the frequency of fracture pairs separated a distance larger than one length scale and smaller than another. Different graduations of length scale can be used to study different types of spatial arrangement. For instance, logarithmic graduations of length scale are most effective at detecting fractal arrangement of fractures inside clusters, whereas linear graduations of length scale are better to identify periodic arrangements (Marrett et al., in review). Numerically randomized versions of each data set (position along scanline for each fracture is randomly assigned) are used to calculate the 95% confidence intervals for random arrangements. The lack of statistical significance of the pattern might indicate that the fracture clustering exhibited by the data set can be reached by a random arrangement of fractures. In contrast, if the pattern of spatial correlation for a natural data set is outside the 95% confidence interval, then the corresponding spatial arrangement is significantly different from random (Marrett et al., in review). The average spatial correlation for randomized versions also serves to validate the analytical equation used to normalize the correlation count (Marrett et al., in review).

Variation of spatial correlation across a spectrum of length scales can show patterns that indicate different spatial arrangements (Figure 9.4). Using logarithmic graduations of length scale, three patterns can be distinguished. A flat-line pattern of spatial correlation (slope = 0; correlation = 1) indicates no statistically significant organization (Figure 9.4a). A power-law pattern of spatial correlation (slope < 0) indicates fractal clustering (self-organization) as shown in Figure 9.4b. A plateau pattern of spatial correlation (slope = 0; correlation > 1) indicates statistically significant clustering due to some process other than self organization (e.g., externally imposed control or inherited) as shown in Figure 9.4c. Using linear graduations of length scale,

three patterns can be distinguished. A flat-line pattern of spatial correlation (slope = 0; correlation = 1) with linear graduations of length scales indicates no statistically significant organization (Figure 9.4e). Patterns of alternating peaks and troughs of spatial correlation with peaks at length scale multiples of the first peak indicate periodically arranged fractures (Figure 9.4f) or periodically arranged clusters (Figure 9.4g), depending on the presence or absence, respectively, of decreasing spatial correlation for most length scales smaller than the first peak of spatial correlation. Combinations of any or all of these patterns can occur, with different patterns characterizing different ranges of length scale. The most common combination of patterns for natural fractures studied previously is clusters that are periodically arranged, and internally have a fractal arrangement (Figure 9.4d). In self-organized or inherited clustering spatial arrangements, the length scale at which spatial correlation drops to one indicates the cluster width (Figures 9.4b to 9.4d). Similarly, in periodically arranged fractures or periodically arranged clusters, the length scale of the first peak is indicative of fracture spacing (Figure 9.4f) or cluster spacing (Figure 9.4g).

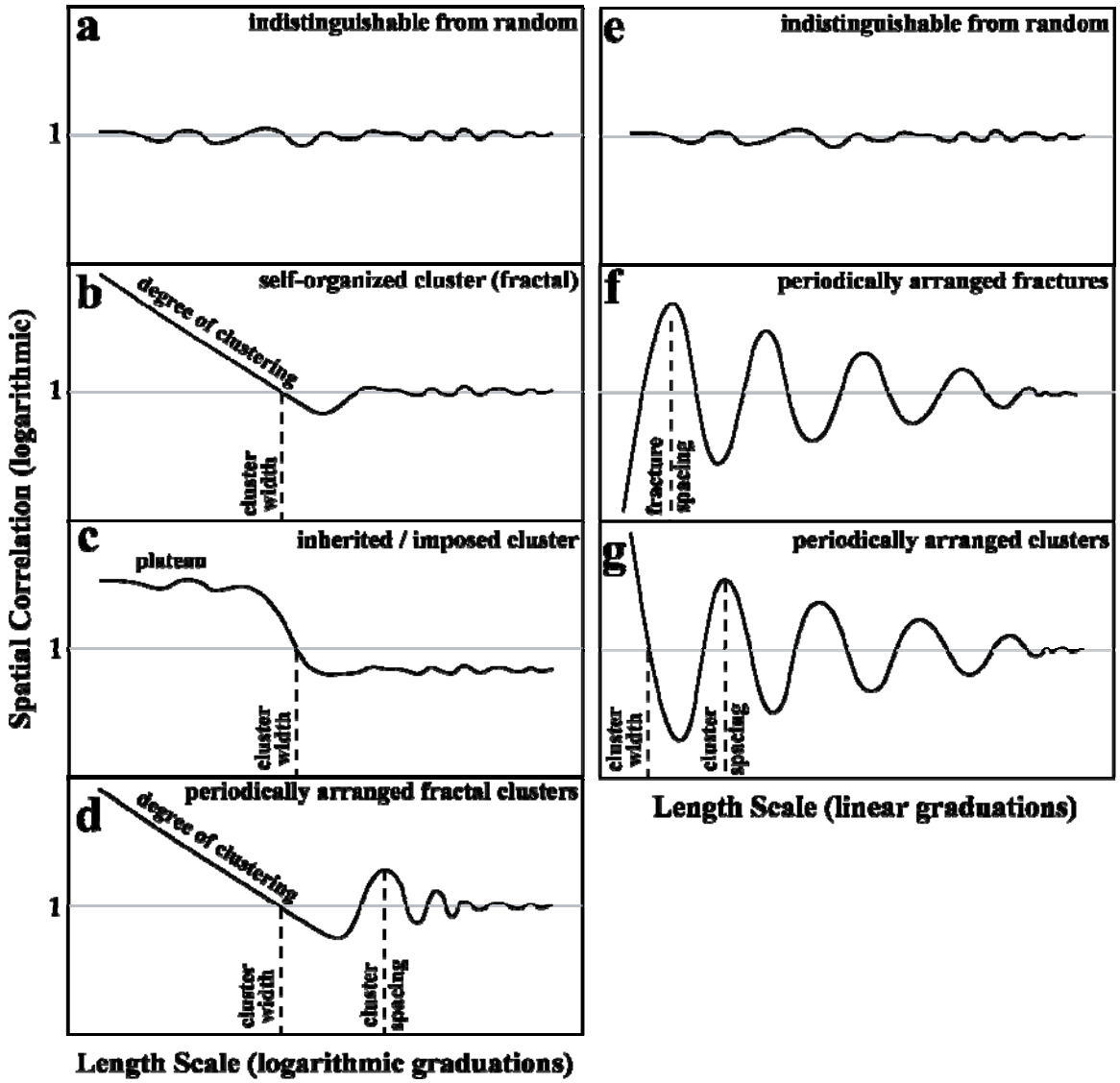

Figure 9.4 Patterns of spatial correlation versus length scale, as defined in Marrett et al. (in review), each one indicating a distinctive spatial arrangement. Using logarithmic graduations of length scale, three spatial arrangements can be distinguished (left column): (a) indistinguishable from random, (b) fractal clustering (self-organization), (c) inherited or imposed clustering due to some process other than self organization (e.g., folding or faulting). Using linear graduations of length scale, three different spatial arrangements can be distinguished (right column): (e) indistinguishable from random, (f) periodically arranged fractures, (g) periodically arranged clusters. Combinations of any or all of these patterns can occur (d), with different patterns characterizing different ranges of length scale.

9.2.2 Spectral Analysis of Spatial Correlation for Linearly Graduated Length Scales

Nonrandom patterns of fracture arrangement are characterized by systematic variation of spatial correlation across a range of length scales. However, the normalized correlation count technique independently quantifies spatial correlation for each length scale considered. Likewise, confidence limits are estimated independently for each length scale. This approach is suitable for recognizing patterns of fracture arrangement within clusters, because clustering produces a monotonic variation of spatial correlation from one length scale to the next. At length scales smaller than cluster width, spatial correlation commonly diverges far from expected values for random arrangement and demonstrates statistical significance.

Periodic patterns of fracture arrangement produce oscillatory variation of spatial correlation rather than monotonic variation. As a consequence, a periodic pattern should have spatial correlation that is comparable to random for many length scales and that differs most from random at the few length scales corresponding to dominant fracture or cluster spacing and its multiples (spatial correlation > 1), and at length scales equal to one half of dominant spacing and its odd multiples (spatial correlation < 1). Most length scales, considered in isolation, might show spatial correlation that is statistically indistinguishable from random. Therefore, establishing statistical significance of a periodic pattern requires a test for oscillatory variation of spatial correlation with length scale, instead of a test for specific values of spatial correlation at certain length scales.

Spectral analysis provides a variety of tools for quantifying the extent to which a variable oscillates in time or space. The Fourier series technique is a classic approach for addressing periodicity in many contexts, including geological problems. For instance, Hinnov and Goldhammer (1991) compared the efficacy of different methods of spectral analysis for the study of cyclicity of thickness variations within fifth order stratigraphic

cycles in the Middle Triassic Latemar limestone and found the Blackman-Tukey method of fourier analysis to be superior. The study of Budd et al. (2006), which examined five-point averages of petrophysical properties (e.g., porosity) in order to find oscillatory patterns of those properties along bedding, is similar to my dissertation, in the sense that the search for an oscillatory variation was done on a statistical quantity (like spatial correlation) and not directly on a rock attribute (like bed thickness for Hinnov and Goldhammer, 1991). The two studies mentioned above compared the power spectra of natural datasets with "red noise" to test whether peaks of power spectral density were statistically significant.

Spectral analysis is the name given to all quantitative methods for studying periodicities in noisy time series data from the point of view provided by the frequency domain. In time series data, a cycle occurs when a variable takes the same value at constant intervals of time (called the period). In the frequency domain, fourier analysis represents a time series as the sum of many sinusoids and cosinusoids with different amplitudes, phases and frequencies. A common purpose of fourier analysis is to quantify the dominant periodicities. For my dissertation, the input data for fourier analysis are represented by spatial correlation measured at approximately uniformly-spaced length scales, each one with its corresponding.

The software POWGRAF2 (Pardo-Igúzquiza and Rodríguez-Tovar, 2004) was used to calculate the fourier power spectrum using the Blackman-Tukey method. For comparison, the program generates the power spectrum of red noise and its 95% confidence interval (e.g., Figure 9.5). Nevertheless, independently implementing the periodogram method (as described by Hinnov and Goldhammer, 1991) validated the power spectrum results from POWGRAF2. Red noise is a model calculated from the input data under consideration using the data adaptive time series called autoregressive

AR1 (Schulz and Mudelsee, 2002). Power spectral density of the red noise model has a continuous decrease with increasing frequency (or decreasing period) and represents the frequency distribution of the natural data set were it follow a random autoregressive process (Hinnov and Goldhammer, 1991). The expression for the autoregressive process AR1 is given in Pardo-Igúzquiza and Rodríguez-Tovar (2004). Randomizing the positions of natural fractures yielded power spectral density that largely did not reach the 95% confidence interval of red noise (e.g., thin line, Figure 9.5), validating its use to assess whether or not a natural data set is statistically different from a stochastic origin, as is done in studies of cyclicity in stratigraphy (e.g., Hinnov and Goldhammer, 1991). In contrast to the power spectral density of a randomized data set, the natural data set has a peak (e.g., thick line, Figure 9.5) with a power spectral density several times that for the 95% confidence interval of the red noise at the same length scale.

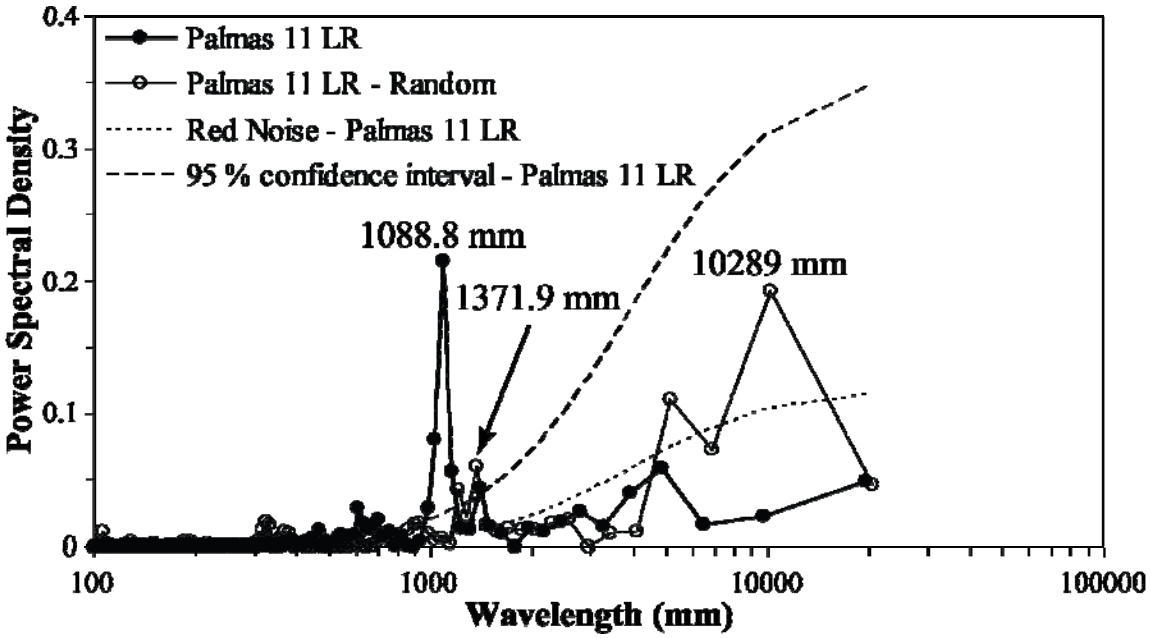

Figure 9.5 Power spectrum for the spatial correlation curve of Palmas 11 LR data set with linearly graduated length scales (thick, solid line), the spatial correlation curve of a randomly arranged version of the Palmas 11 LR data set (thin, solid line), the equivalent red noise (short dashed line) and its corresponding 95% confidence interval (long dashed line) for the Palmas 11 LR data set. Natural data set exhibits a peak of power spectral density at a wavelength of 1089 mm, which is outside the 95% confidence interval. In contrast, the equivalent (in terms of number of fractures and total scanline length) data set with randomly arranged fractures exhibits peaks with power spectral density (e.g., 10289 mm) similar to the natural data set (e.g., 1088.8 mm) but inside the 95% confidence interval, or barely outside the 95% confidence interval (e.g., 1371.9 mm).

9.2.3 Scanning Electron Microscope (SEM)

SEM-based cathodoluminescence systems (SEM-CL) allow higher magnification (up to 50 times more than an optical microscope; Passchier and Trouw, 1998), more stable operating conditions and better detection of weak luminescence than optical-microscope mounted CL instruments (Reed and Milliken, 2003). Details about the SEM-CL instrument that I used at BEG are described by Reed and Milliken (2003). Reed and Milliken (2003) explained the method used to overcome image-quality problems caused

by the persistent luminescence of carbonate minerals. In brief, this method uses a UV-blue filter to image only short wavelengths while blocking the orange-red wavelength luminescence commonly found in carbonates.

The SEM at the BEG also generates X-ray element maps and secondary electron images (SEI). A SEI is obtained by measuring the emission of secondary electrons produced when the SEM electron beam interacts with the sample surface (Kearsley and Wright, 1988). A SEI appears three-dimensional and therefore reveals porosity (Kearsley and Wright, 1988). The energy dispersive X-ray analysis tool of an SEM measures the energy of X-rays emitted by the irradiated sample, and uses that energy to map elements that occur in the sample (Passchier and Trouw, 1998). With this tool, the chemical composition of a sample can be determined in a semi-quantitative way and displayed in a grey-scale image (called an element map) where the grey tone indicates the relative abundance of an element (the grey tone becomes lighter with increasing abundance of the mapped element). False-color element maps (image made by assigning different colors to intensities of 3 different elements) are generated by digitally combining three element maps (R. Reed, personal communication, 2005). For carbonate rocks typically Si, Mg and Ca are mapped with Si represented as red, Mg represented green, and Ca represented as blue, such that intensity of color qualitatively measures the concentration of elements. Other elements were mapped but not used for my dissertation.

9.2.4 Fluid and Solid Inclusions

Fluid inclusions are nm to mm sized cavities filled with fluid inside crystals (Blenkinsop, 2000). Fluid inclusions are believed to be samples of the liquids that were present in the rock during mineral growth, deformation, or metamorphism (Passchier and Trouw, 1998). The most common fluids are aqueous, saline or CO_2-dominated, with possible mixtures of N_2, CH_4 or more complex hydrocarbons (Blenkinsop, 2000).

Commonly inclusions contain gas bubbles or solid phases, which can be used to estimate the density of the inclusion (Passchier and Trouw, 1998). Fluid inclusions are most commonly studied in quartz, but can be found in many minerals. Minerals with a strong mineral cleavage such as calcite and micas are less suitable for fluid inclusion analysis since inclusions are likely to have leaked and minerals could have reacted with water or CO_2 inside the inclusion (Passchier and Trouw, 1998). Primary fluid inclusions are inclusions that were captured when the grain in which they lie grew from a solution and typically are arranged in euhedral crystal forms that do not cross crystal growth features (Blenkinsop, 2000). In contrast, planes of fluid inclusions are thought to represent healed fractures in which fluid has been present, and are known as secondary fluid inclusions (Laubach, 1997). Planes of inclusions (fluid or solid) that are parallel to vein walls are called inclusion bands whereas planes of inclusions at high angles to vein walls are called inclusion trails (as shown in Figure 1 of Laubach et al., 2004, and Figure 5 of Ramsay, 1980).

Occasionally during the growth of a crystal, crystals of the same or other mineral phases become trapped. It is common for such trapped solid inclusions to cause simultaneous trapping of some surrounding fluid as well (Roedder, 1984). Some solid inclusions nucleate on crystal surfaces, whereas others settle out of fluid. Commonly, those that settle out act as nuclei for further growth. Planes of fluid inclusions typically parallel vein walls whereas planes of solid inclusions may parallel the opening direction of a vein, or occur in planes parallel to the vein walls (Passchier and Trouw, 1998).

9.2.5 Fracture Diagenesis Terminology

Since this chapter describes the evidence for diagenetic processes, it is convenient to introduce some terminology commonly used to relate diagenesis and fracture evolution (e.g., Laubach et al., 2004). Bridges (also called stretched crystals by Ramsay, 1980) are

defined as “cement deposits that span fractures and that are surrounded by fracture porosity or by later cements” (Laubach et al., 2004), whereas the term pillar is used to describe cement deposits that are elongated transverse to a fracture but do not connect the two walls. Nevertheless, some pillars are probably bridges that are not completely exposed due to the thin section not being precisely parallel to the bridge.

Synkinematic cement is defined as cement that precipitated concurrently with fracture opening whereas postkinematic cement is the cement that precipitated after fracture opening has ended (Laubach 1997; 2003). Crack-seal texture is “marked by lamination parallel to fracture walls defined by wall-rock inclusions, broken cement inclusions, cement zoning cut by fractures and fluid inclusion planes” (Laubach, 2003). Crack-seal texture is interpreted as the result of repeated fracturing with cement at least locally filling in the fracture between opening increments (Laubach et al., 2004). synkinematic cement tends to fill small fractures more completely than large fractures (Laubach, 2003). An emergent threshold results in fractures (or segments of fractures) with less complete fill by synkinematic cement (and therefore higher porosity or postkinematic cement) than in slightly smaller fractures (Laubach, 2003). Renewal of fracture surface area in bridges accounts for concentration of synkinematic cement in bridges instead of uniform distribution along the fracture (Lander et al., 2004). To quantify the percentage of synkinematic (or postkinematic) cement inside a fracture, individual thin sections were scanned at high resolution and the resulting images were imported into a digitizing software such as Didger®. Once images were calibrated, the trace of every fracture that spanned the entire thin sections was digitized and the area of each fracture was automatically calculated by Didger®. Then the area of the fracture occupied by either synkinematic of postkinematic cement was also digitized and

calculated, allowing estimation of the percentage of the fracture area occupied by both synkinematic and postkinematic cements.

9.2.6 Carbonate Diagenesis Terminology

Since the majority of Cupido Fm. layers can be classified as carbonate rocks, it is convenient to define the most important diagenetic processes that affected the Cupido Fm. in the Monterrey salient. Dolomitization is defined as a diagenetic process in which the calcium carbonate minerals aragonite and calcite are replaced by the mineral dolomite. Dolomitization can obscure or even obliterate all or part of the original carbonate rock textures and structures (Tucker and Wright, 1999). Recrystallization refers to changes in crystal size without any change of mineralogy whereas dedolomitization refers to replacement of dolomite by calcite (Tucker, 1991; Tucker and Wright, 1999).

9.2.7 Fibrous Veins

Fibrous fill in veins is common and forms by incremental opening at a rate comparable with the rate of cement crystallization (Blenkinsop, 2000). There are four types of fiber growth recognized in veins. Syntaxial growth indicates growth from the vein walls towards the vein center (Ramsay and Huber, 1983). A typical vein with syntaxial growth exhibits two separate bands of fibers on opposite sides of a median suture. In addition, fiber widths generally increase in the direction of growth (towards vein center) due to growth rate competition between adjacent crystal fibers (Blenkinsop, 2000). In contrast, antitaxial growth occurs from within the vein towards the vein walls, and may occur symmetrically on both sides of the vein or asymmetrically on only one side (Ramsay and Huber, 1983). Antitaxial growth is usually associated with synkinematic cement of a mineral that is not the main constituent of the rock matrix (Ramsay and Huber, 1983; Passchier and Trouw, 1998). The key characteristic of antitaxial growth is fiber continuity across the vein (Blenkinsop, 2000). Symmetric

antitaxial growth may result in a weak median line defined by small grains of the cement mineral or fragments of the wall rock indicating the initial nucleation site of the cement fibers (Passchier and Trouw, 1998), whereas asymmetric antitaxial growth may result in fiber widths increasing unidirectionally across the vein (Blenkinsop, 2000). Composite growth histories have both syntaxial and antitaxial components and are believed to reflect more than one synkinematic mineral phases (Ramsay and Huber, 1983). Finally, non-systematic growth, also known as ataxial growth (Passchier and Trouw, 1998), is marked by repeated fracture opening and fiber growth at irregular sites in the vein. Ataxial growth results in the lack of directional growth indicators (e.g., fiber widening) and fibers lacking a median line (Blenkinsop, 2000).

9.3. STRUCTURAL DIAGENESIS

An important goal of structural diagenesis is to develop an understanding of how fracture growth and diagenetic processes interact and influence each other. This section of Chapter 9 presents the diagenetic evidence that supports fracture categorization. In addition, this section presents my interpretation of the different diagenetic evidence of each fracture category. For example, I will use diagenetic evidence to postulate the timing of each cement with respect to fracture opening, and explore different alternative hypotheses about the origins of irregular traces.

9.3.1 Fracture Categorization

Although a fracture set groups all fractures with common attributes (e.g., timing, orientation, cement fill), orientation is typically the only attribute used for categorizing fractures, perhaps because fracture orientation is relatively easy to observe and quantify (Nelson, 2001). Fractures are grouped in sets because fractures with common attributes are believed to be genetically related. Because opening-mode fractures in isotropic materials propagate in directions perpendicular to the local least compressive stress (Pollard and Aydin, 1988), a common assumption behind the categorization of fractures based on orientation is that each fracture set represents one fracturing event (Bai et al., 2002). However, recent fracture mechanics modeling has indicated that an initial isotropic strain can lead to fractures growing in multiple directions at the same time (Olson et al., 2006), and that stress relief between parallel fractures can change the local principal stress direction by 90º, which can result in orthogonal fracture patterns (Bai et al., 2002). In addition, two different fracture events can occur at different geologic times and under different conditions and yet coincidentally produce fractures with a common orientation. The lack of a scientifically-based reasoning for how much variation of

fracture orientation is considered adequate for a single fracture event also reduces the reliability of fracture orientation as a criterion for fracture categorization. Therefore, fracture orientation may or may not be a useful criterion for recognizing different fracture events.

Although the orientation of each fracture was not measured for my dissertation, fractures were assigned to a particular set in the field partly based on orientation (Table 9.3). The orientations of a representative number of fractures from each set was measured and used to estimate the mean orientation for each fracture set (Table 9.3). On cross section outcrops, fractures were assigned to a set based on their systematic dip relationship with respect to bedding as defined by Ortega (2002). In addition to orientation, the criteria used in this chapter to categorize fractures were compositional and textural evidence of diagenetic processes such as roughness of fracture trace (irregular or straight), fracture cement composition (mainly dolomite and quartz), cement morphology (e.g., bridges of euhedral and translucent dolomite) and timing of fracture-cement precipitation relative to fracture opening (e.g., crack-seal texture indicating synkinematic cement). Three fracture categories (X, Y and Z) were established following the criteria detailed above. The advantage of using compositional and textural evidence of diagenetic processes to complement fracture categorization by orientation is that diagenetic processes record conditions under which fractures formed different than orientation of local least compressive stress such as composition of subsurface fluid and temperature. Fractures from different diagenetic categories were only detected in the same thin sections from the layer Escalera 1, which is the only layer studied in an outcrop parallel to bedding (Table 9.1).

Table 9.3 Orientation (right-hand rule strike and dip) of bedding and veins for all fracture sets (each set with a characteristic fracture orientation) in layers of the Cupido Fm. Number of fractures for each set is included within parentheses. Only orientation of sets A, B, and C in Escalera OO1 and Escalera OO12 matches the orientation of similarly named sets in Ortega and Marrett (2001) and Ortega (2002). Sets with similar orientation and in the same location are highlighted with the same color.

		Field Categorization of Fractures			
Outcrop Data Set	**Bedding**	**Set A**	**Set B**	**Set C**	**Set D**
Escalera OO1	305/66	220/38 (127)	205/31 (853)	220/90 (24)	156/46 (156)
Escalera OO12	316/79	231/40 (1023)	203/60 (82)		
Escalera 1	110/74	7/78 (156)	196/60 (183)	214/30 (83)	335/60 (38)
Escalera 2			189/68 (547)	193/32 (67)	
Escalera 3		11/75 (293)			
Huasteca	285/90	30/41 (581)	297/80 (19)	204/25 (54)	338/54 (4)
Palmas 11	299/44	45/73 (91)	175/70 (55)	208/85 (116)	
Palmas 12	297/46	75/52 (190)	192/61 (126)		
Palmas 13	301/50	64/61 (286)	200/60 (173)		

9.3.2 Characterization of X Fractures

9.3.2.1 Roughness of Fracture Trace

Since a thin section offers a two-dimensional view of rock, the roughness of a fracture can only be studied by examining the trace of fracture walls. Fracture roughness has typically been studied for the purpose of quantifying and modeling variations in fracture aperture (e.g., Chen et al., 2000; Lanaro, 2000) or mechanical rock properties (e.g., Jiang et al., in press; McWilliams et al., 1990), with little or no attention to grain size (e.g., Backersa et al., 2003). At the typical observational scale of a petrographic microscope, X fractures have highly irregular traces (Monroy-Santiago, in preparation). Individual deflections in the trace of X fractures are typically much larger than individual matrix crystals and do not follow stylolites (Figures 9.6 to 9.8). However, irregularity varies along the trace of many X fractures. For instance, fracture walls nearly touch in some places along an X fracture, whereas a few mm away the individual deflections in the fracture trace are several times smaller than fracture aperture (e.g., Figures 9.6 and 9.7). In addition, X microfractures are typically less visible than X macrofractures because walls are indistinct (e.g., two images of X fractures in Figure 9.9a), and in some places a texture is present that could be interpreted as ghost or relic (also called “fuzzy” fracture walls by Passchier and Trouw, 1998) of a microfracture (inset, Figure 9.9a).

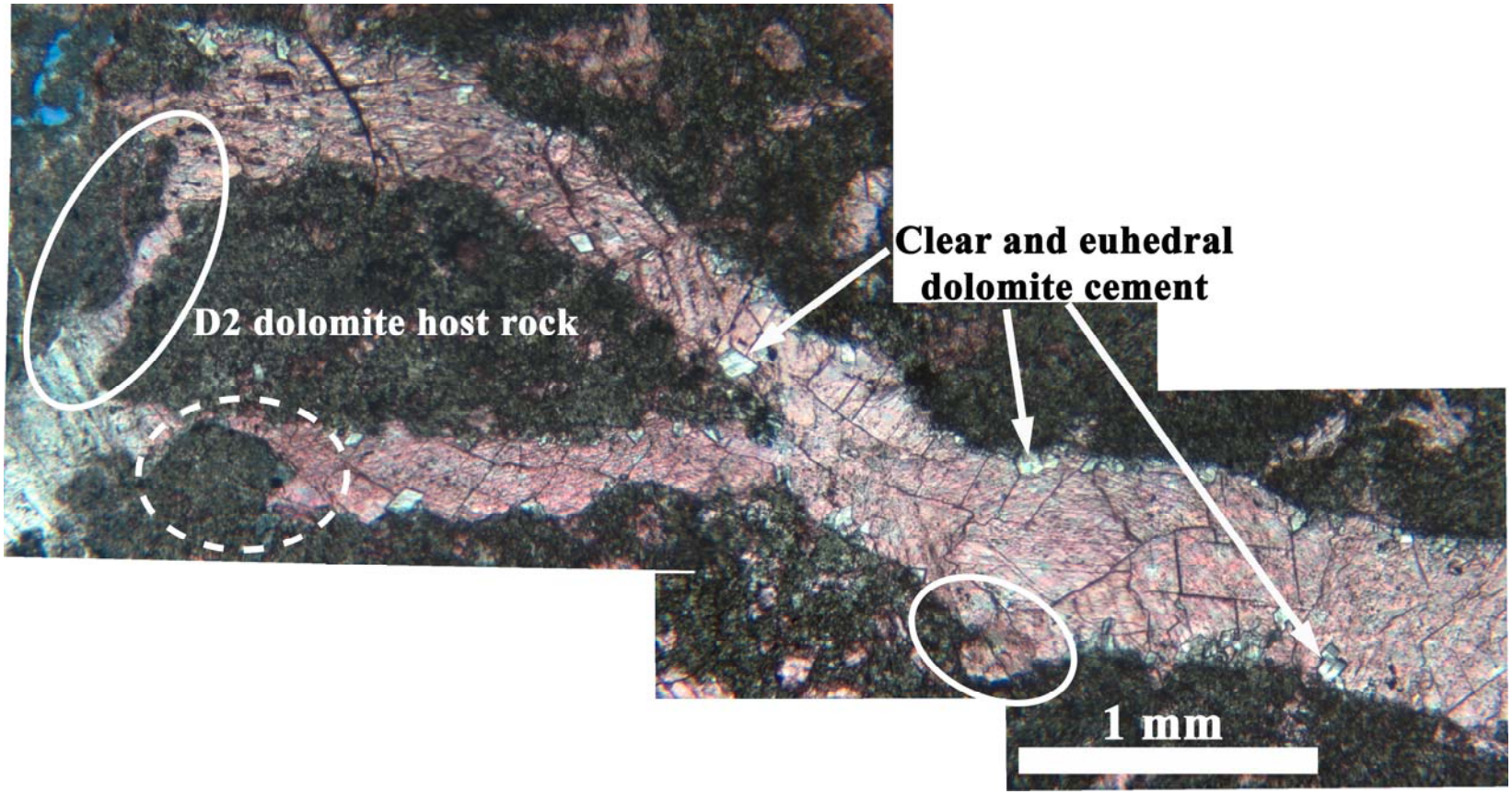

Figure 9.6 Photomicrograph of irregular traces of many calcite-filled X fractures. Most rock matrix is composed of D2 dolomite. Notice host rock almost extends across fracture on both fractures (dashed ellipses). Deflections in fracture trace can be much larger than individual matrix grains (solid ellipse). Notice the clear and euhedral dolomite cement lining fracture walls. Plane light of thin section 02LG15-1A from layer Palmas 12 (Tables 9.1 and 9.2), stained for calcite.

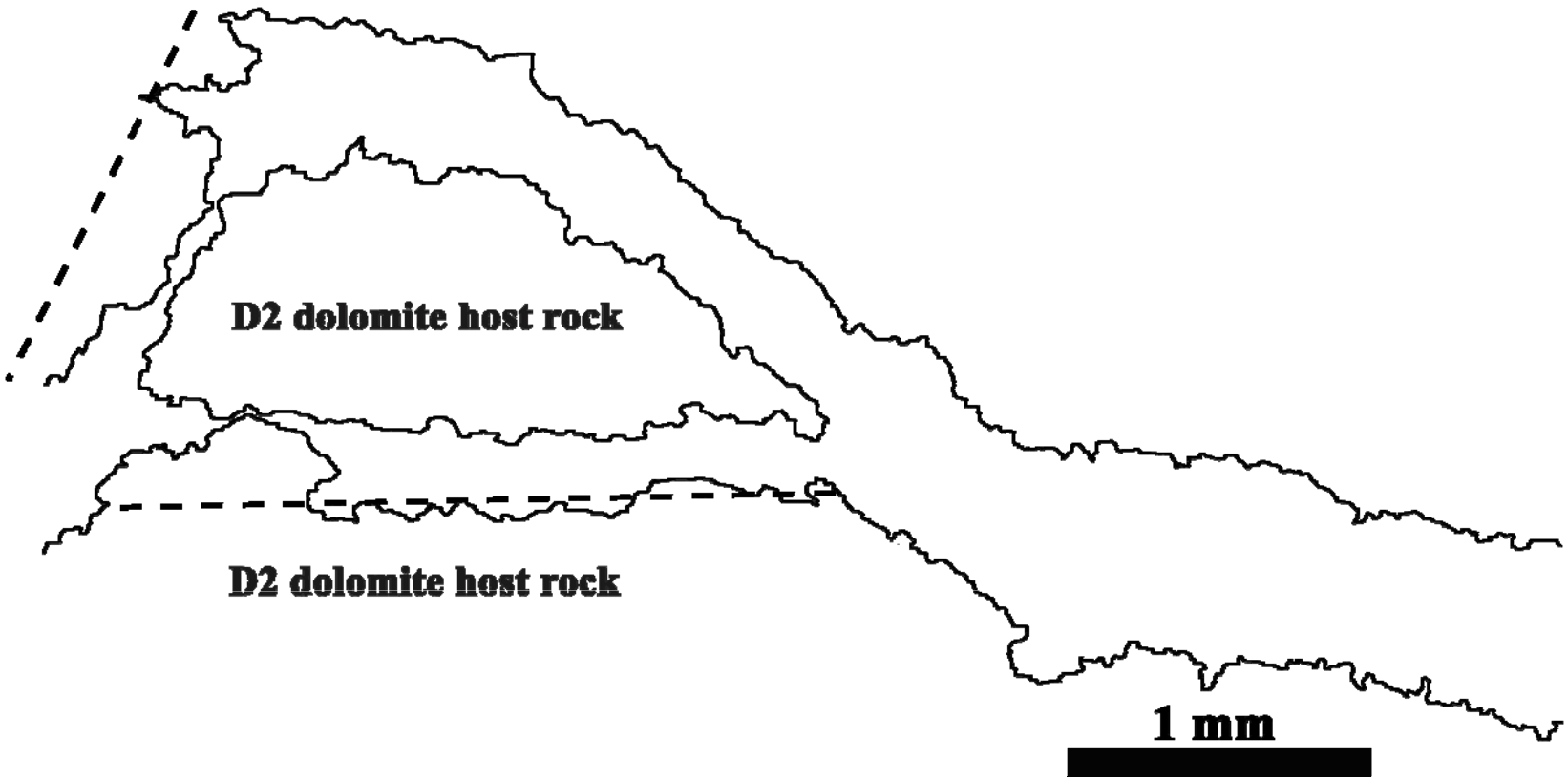

Figure 9.7 Trace of fracture walls in Figure 9.6. Notice that individual deflections in the trace of X fractures are more irregular in some parts of the fracture (e.g., left half of fracture) than in others. For comparison , dashed lines indicate the of the overall orientation of fracture walls.

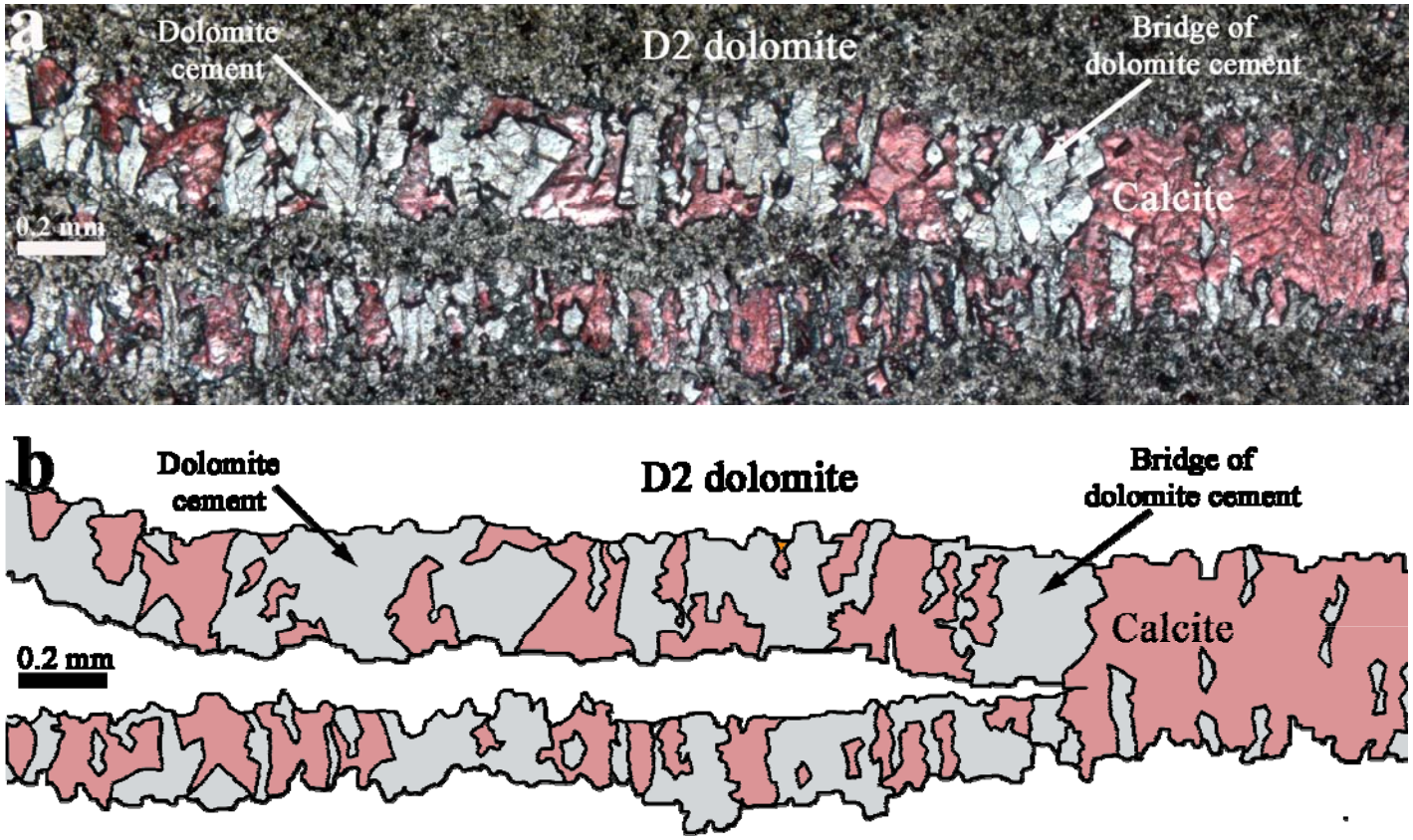

Figure 9.8 a) Photomicrograph of two coalesced X fractures (or one branched X fracture) with irregular walls and cement containing pillars and bridges of translucent and euhedral dolomite. Rock matrix mainly composed of D2 dolomite. Plane light of thin section 02LG16-1A from layer Palmas 13 (Tables 9.1 and 9.2), stained for calcite. b) Traces of fracture walls and dolomite cement in (a). Calcite cement filled remnant fracture porosity between dolomite bridges based on decrease of dolomite cement in the fracture with increasing aperture. Notice that bridges are absent where aperture is largest.

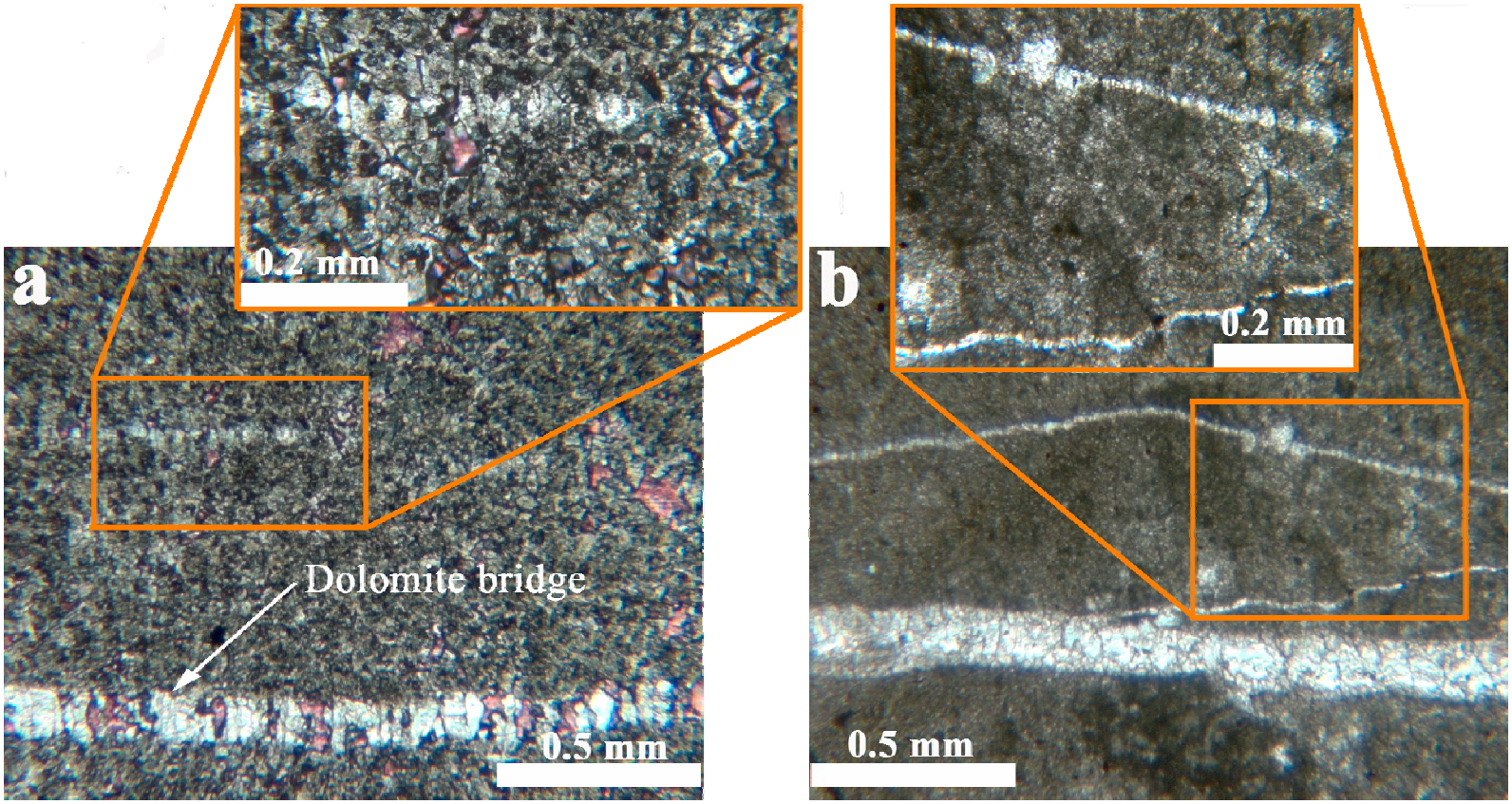

Figure 9.9 Photomicrographs of two X fractures (a) and two Y fractures (b) using plane light. Bottom photos are at the same magnification. Insets show detailed view of part of bottom photo. Both bottom photos show fractures with approximately the same aperture, and yet trace of X fracture in (a) is more irregular than trace of Y fracture in (b). Insets show a microfracture smaller than in bottom photos, and although microfracture in (a) is slightly larger than the one in (b), fracture trace is more visible in (b). Rock matrix of both rocks mainly composed of D2 dolomite. Thin section 02LG15-1A from layer Palmas 12 in (a) and thin section 02LG11-2 from layer Escalera OO1 in (b) (Tables 9.1 and 9.2), both stained for calcite.

9.3.2.2 Fracture Cements

X fractures are partially filled by euhedral and translucent dolomite cement that commonly forms bridges and pillars oriented at a high angle to fracture walls (e.g., Figures 9.8, 9.10 and 9.11). Some bridges exhibit fracture-parallel bands of fluid inclusions (e.g., Figures 9.12 and 9.13), which suggests synkinematic dolomite precipitation. Although dolomite bridges in X fractures commonly have a texture different from D2 dolomite in the matrix (e.g., Figures 9.8, 9.10 and 9.11), Monroy-Santiago (in preparation) reported finding locally bridges of dolomite in X fractures with a similar texture (although slightly larger grain size). Decrease in amount of dolomite cement (and corresponding increase of calcite) toward the right end of fracture in Figure 9.8 compared with the smaller-aperture left end illustrates the presence of an emergent threshold in some fractures of X category. The largest amount of synkinematic dolomite cement measured in X fractures is about 40%.

In contrast to the bridges and pillars of highly euhedral dolomite crystals inside X fractures (Figures 9.10 to 9.13), calcite cement in X fractures lacks crack-seal texture, does not display obvious crystal boundaries in plane light and filled remnant fracture porosity left by earlier dolomite cement (e.g., Figures 9.6, 9.8, 9.10 to 9.12), which suggests that calcite cement is postkinematic. There is no variation in the abundance of calcite cement in the rock matrix with distance to X fractures, so it is impossible to tell if fluids that deposited calcite moved through fractures and into rock matrix or vice versa (e.g., Figures 9.6 and 9.11).

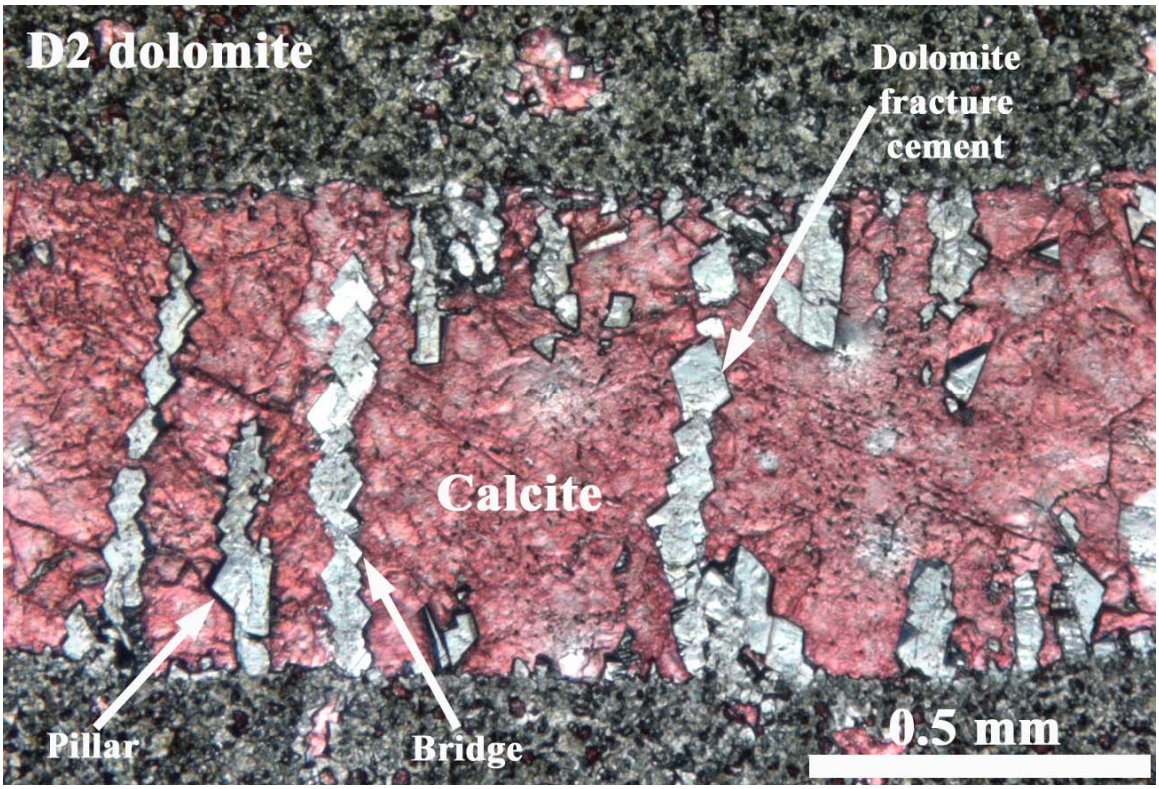

Figure 9.10 Photomicrograph of a typical X fracture with pillars and bridges of translucent euhedral dolomite cement. The dolomite crystals inside fracture are larger and more translucent than the D2 dolomite, which comprises most of the rock matrix. Note that some pillars and apparent floating crystals of dolomite probably owe to bridges and thin section plane not being precisely parallel. Of the two fracture cements (calcite and dolomite), only dolomite displays well developed euhedral crystals. Plane light of thin section 02LG16-1A from layer Palmas 13 (Tables 9.1 and 9.2), stained for calcite.

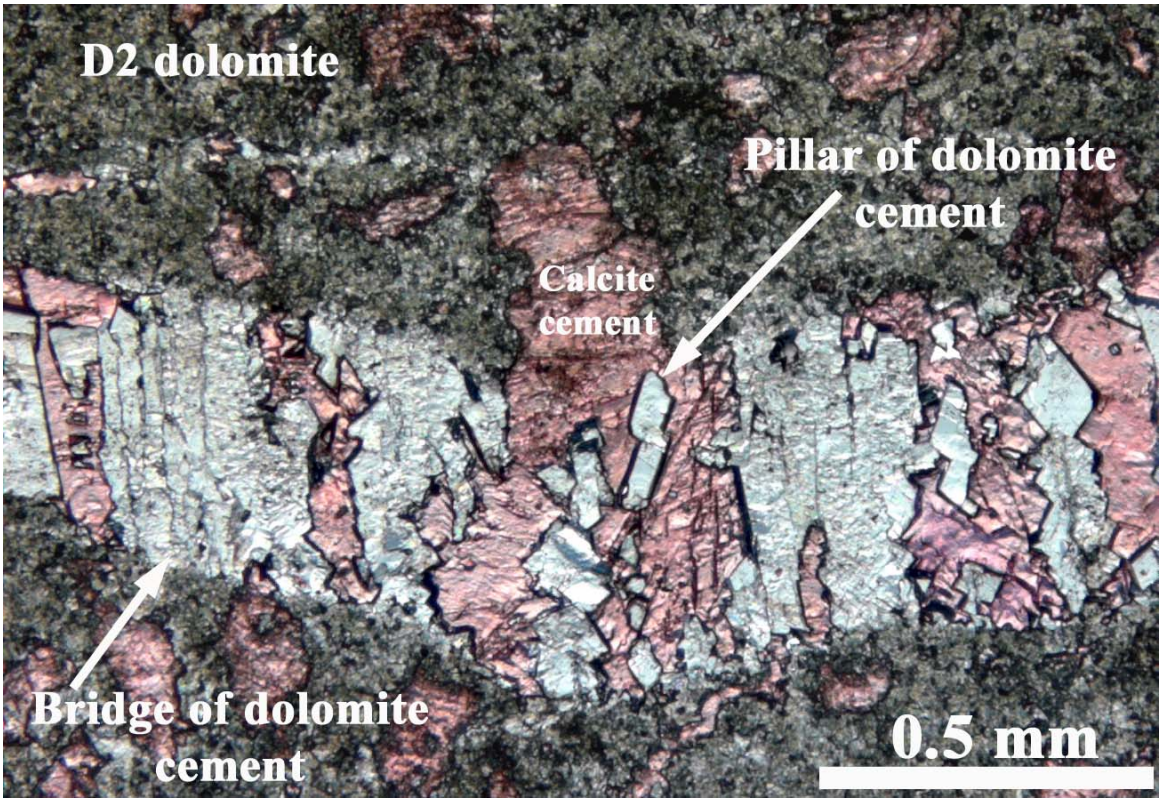

Figure 9.11 Photomicrograph of typical pillars and bridges of translucent euhedral dolomite cement in X fractures. These bridges seem to have formed by coalescing bridges like the ones depicted in Figure 9.9. The dolomite crystals inside fracture are larger and more translucent than the matrix D2 dolomite, which comprises most of the rock matrix. Plane light of thin section 02LG15-1A from layer Palmas 12 (Tables 9.1 and 9.2), stained for calcite.

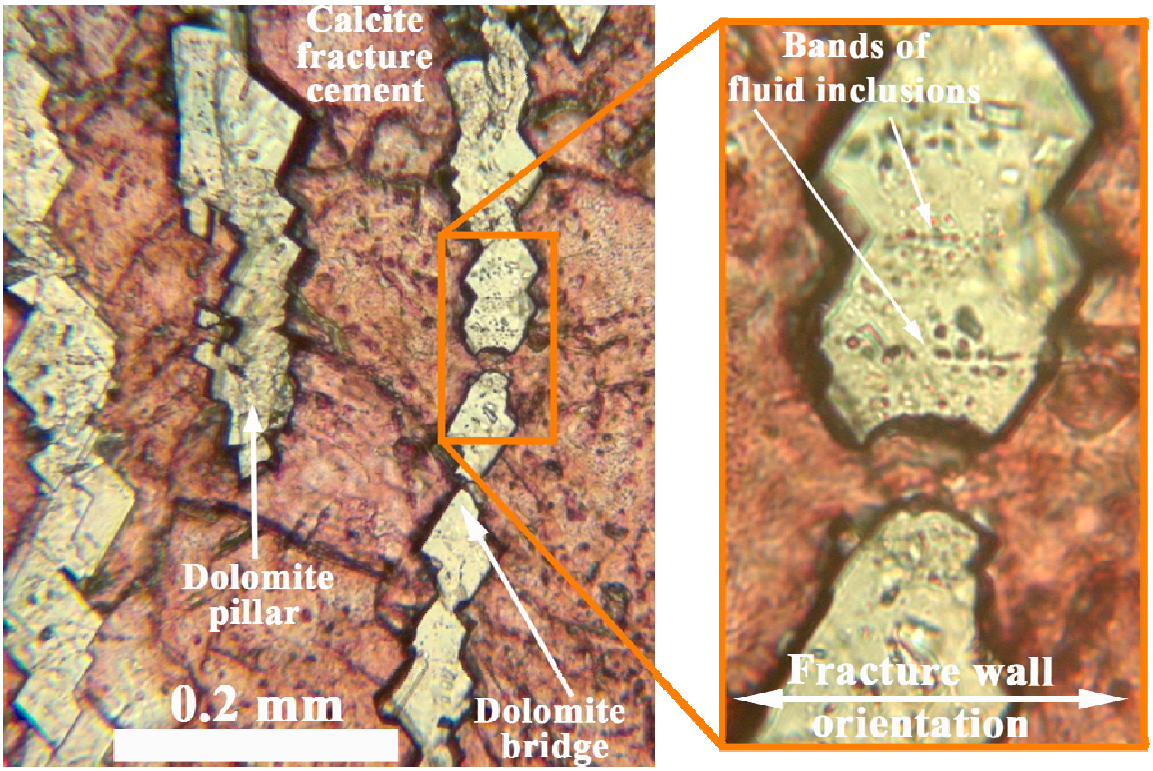

Figure 9.12 Photomicrograph of bands of fluid inclusions parallel to fracture wall inside a bridge of translucent euhedral dolomite cement in X fracture. Notice that the two pieces of dolomite bridge seem to fit together (right image), which could indicate that precipitation of dolomite cement ceased while the fracture was still opening. Plane light of thin section 02LG16-1A from layer Palmas 13 (Tables 9.1 and 9.2), stained for calcite.

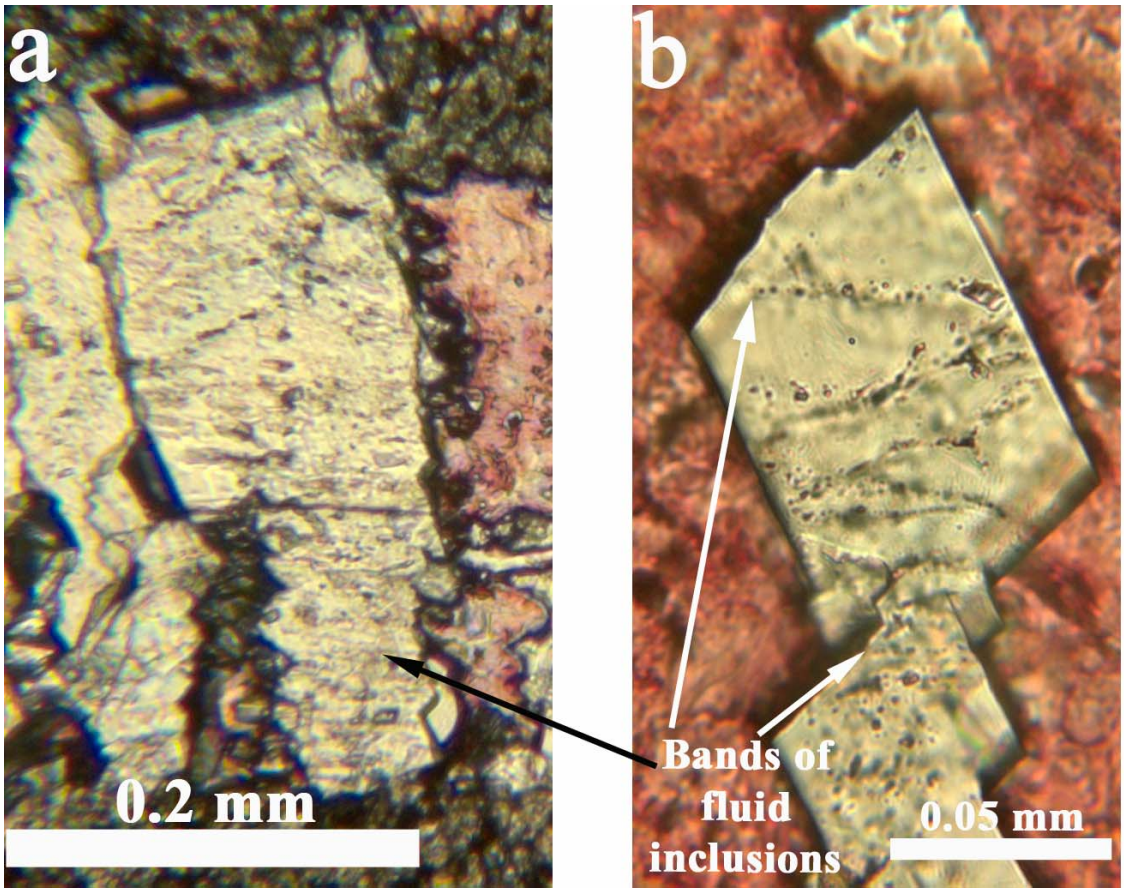

Figure 9.13 Photomicrographs of bands of fluid inclusions parallel to fracture wall inside bridges of translucent euhedral dolomite cement in X fractures. Fracture walls in both (a) and (b) are approximately horizontal. Plane light of thin section 02LG16-1A from layer Palmas 13 (Tables 9.1 and 9.2), stained for calcite.

9.3.3 Characterization of Y Fractures

9.3.3.1 Roughness of Fracture Trace

Unlike X fractures, which have only exhibited irregular traces, Y fractures are characterized by either comparatively straight fracture traces (even in layers with matrix almost completely replaced by D2 dolomite) as shown in Figure 9.14, or by irregular traces similar to the ones exhibited by X fractures, as shown in Figure 9.15. Although the number of outcrops studied for my dissertation is relatively limited, Y fractures with straight traces seem more abundant. Y fractures with straight traces were observed in three (forelimb of San Blas anticline in Escalera canyon, Huasteca, and Palmas) of the four outcrops selected for my dissertation, whereas Y fractures with irregular traces were only observed in one (backlimb of San Blas anticline in Escalera canyon).

Microfractures also exhibit traces both similar and different than X fractures. Some microfractures exhibit ghost textures (e.g., Figure 9.16c) similar to fractures of category X (e.g., Figure 9.9a), whereas others of similar size have sharper walls (e.g., Figures 9.9b, .16a and 9.16b). In addition, clusters of Y microfractures locally anastomose to form a single fracture (e.g., Figures 9.16a and 9.16b). The only outcrop where Y macrofractures with irregular traces are observed is also the only outcrop where Y microfractures with ghost (also called “fuzzy” by Passchier and Trouw, 1998) texture are observed.

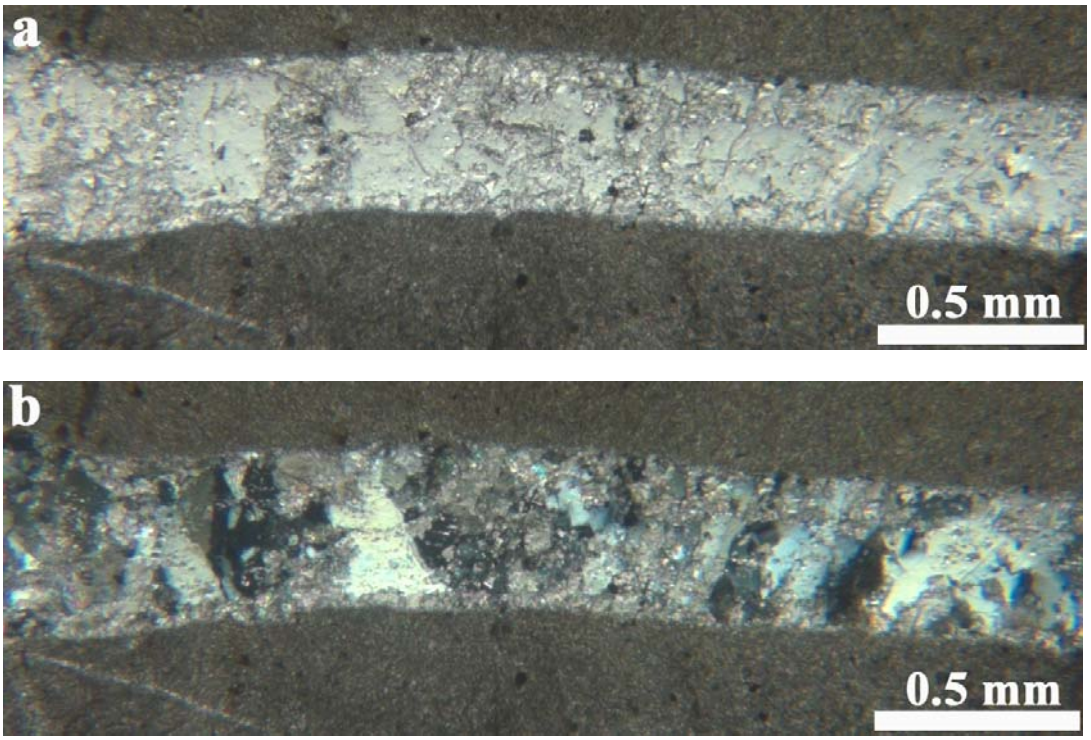

Figure 9.14 Photomicrograph of a Y fracture, a) plane light, and b) cross-polarized light. Notice that magnification is similar to Figure 9.6 and yet fracture trace is less irregular (almost straight). Notice in (a) the clear and fibrous dolomite cement lining fracture walls, and in (b) that quartz crystals are elongated perpendicular to fracture wall. D2 dolomite composes approximately 100% of matrix (Ortega, 2002). Thin section 02LG11-2 from layer Escalera OO1 (Tables 9.1 and 9.2), stained for calcite.

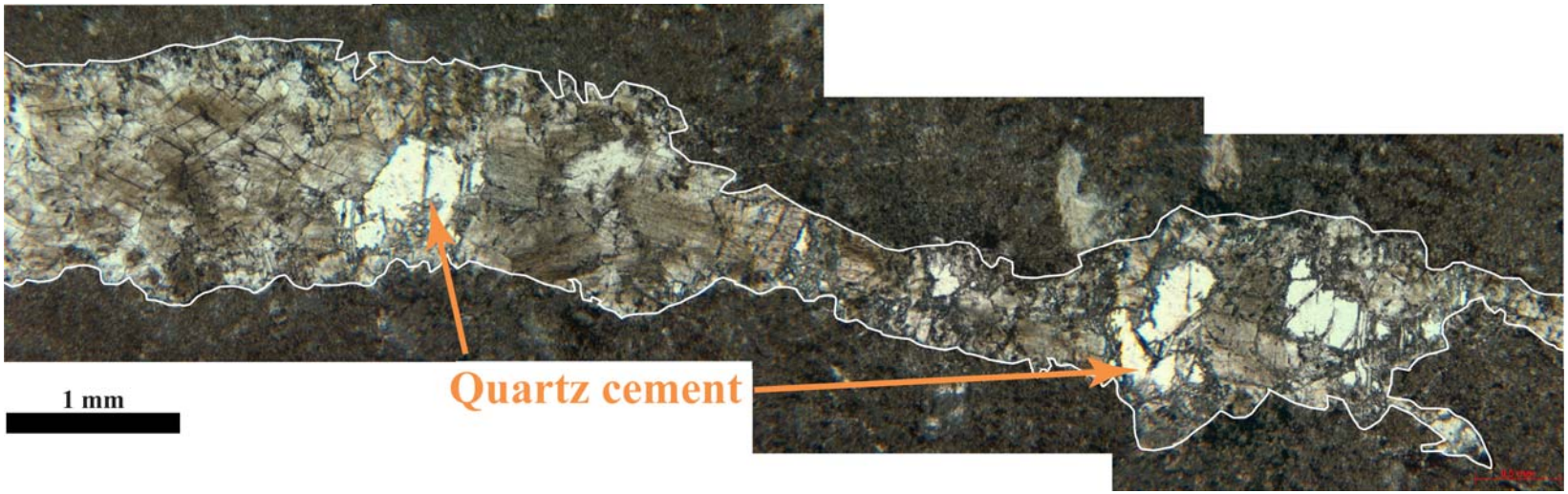

Figure 9.15 Photomicrograph of a Y macrofracture with a highly irregular trace. Notice subhedral quartz crystals in Y fracture Rock matrix mainly composed of D2 dolomite. Thin section 03LG21-1B from layer Escalera 3 (Tables 9.1 and 9.2), stained for calcite, plane light.

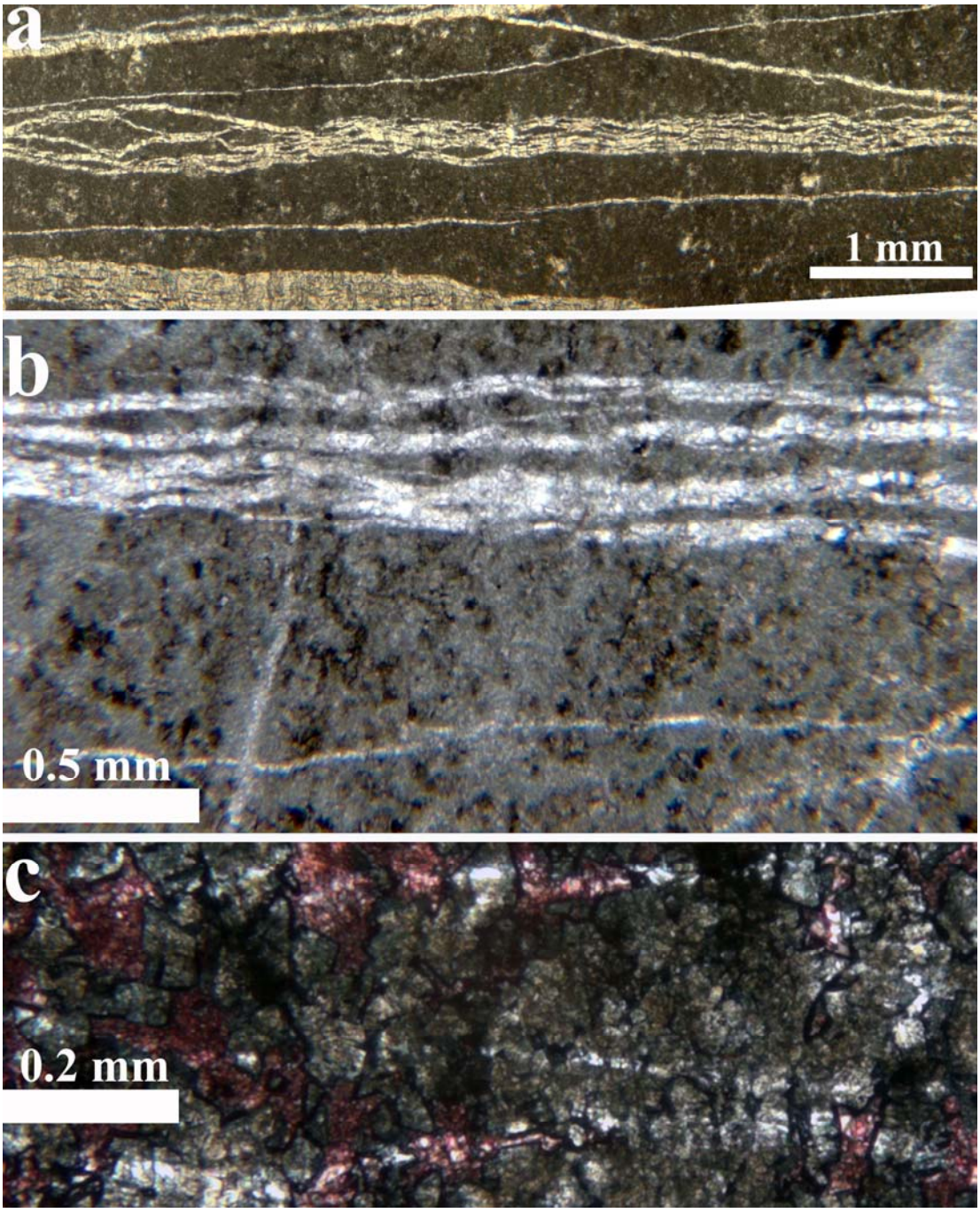

Figure 9.16 (a) and (b) Photomicrograph of clusters of Y microfractures that locally are anastomosed. (c) Photomicrograph of Y microfractures exhibiting a ghost trace. (a) Thin section PA11JG from layer Palmas 11, (b) and (c) from thin sections 03LG20-1A and 03LG21-1B, respectively, both from layer Escalera 3 (Tables 9.1 and 9.2).

9.3.3.2 Fracture Cements

Dolomite bridges in Y fractures lack euhedral shapes commonly observed in X fractures and shown in Figures 9.8, 9.10 and 9.11. Instead, Y fractures contain at least three other forms of dolomite crystals. The dolomite fracture cement most commonly exhibit by Y fractures precipitated as fibrous and translucent crystals that are approximately parallel to one another, have lengths up to approximately 0.15 mm perpendicular to fracture wall, and line fracture walls (Figures 9.17 and 9.18). Another form of dolomite fracture cement precipitated as subhedral and translucent bridges and oriented approximately perpendicular to fracture walls (e.g., Figure 9.19). The least abundant dolomite fracture cement in Y fractures is baroque dolomite (Tucker and Wright, 1999) that Monroy-Santiago (in preparation) called D3 (e.g., Figure 9.18). The bridges of dolomite in Y microfractures differ from those in X fractures in that they are typically accompanied by parallel quartz bridges (e.g., Figure 9.19).

Unlike X fractures, Y fractures contain abundant quartz cement. In Y macrofractures, quartz is found mainly in relatively isolated pillars or bridges of euhedral crystals (e.g., Figure 9.20). In some Y microfractures, quartz cement is present as bridges (e.g., Figure 9.19), but in other Y fractures quartz is present as anhedral crystals. Such quartz crystals are elongated perpendicular to fracture walls and are separated from fracture walls by dolomite lining (e.g., Figures 9.14 and 9.17). Quartz bridges in Y microfractures have irregular edges and are parallel to bridges of dolomite (e.g., Figure 9.19).

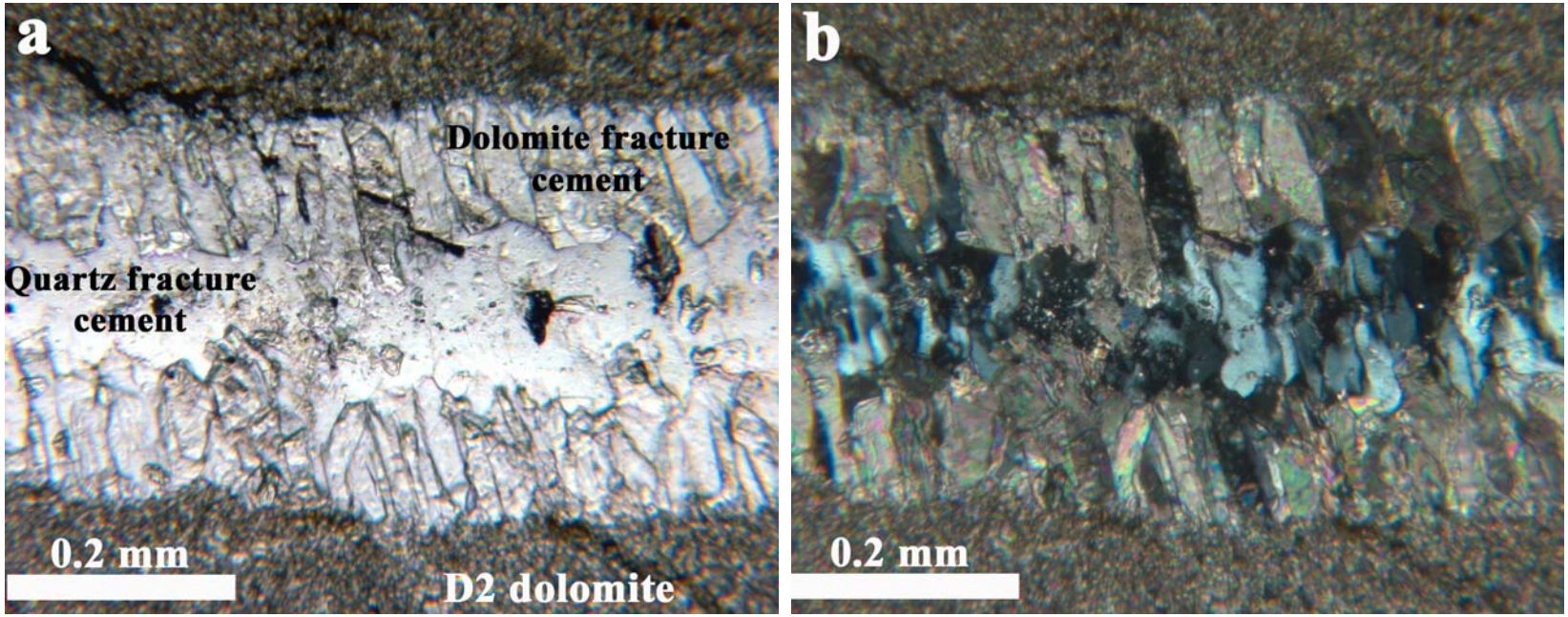

Figure 9.17 Photomicrograph of a Y microfracture using a) plane light, and b) cross-polarized light. Images show detailed views of fibrous and subhedral dolomite crystals oriented approximately perpendicular to fracture wall, and lining the walls of a typical Y fracture. Anhedral quartz crystals in center of Y fracture are elongated in the same direction as dolomite fibers. Both dolomite lining and anhedral quartz do not exhibit bands of fluid inclusions typically associated with crack-seal texture. Rock matrix mainly composed of D2 dolomite. Thin section 02LG11-2 from layer Escalera OO1 (Tables 9.1 and 9.2), stained for calcite.

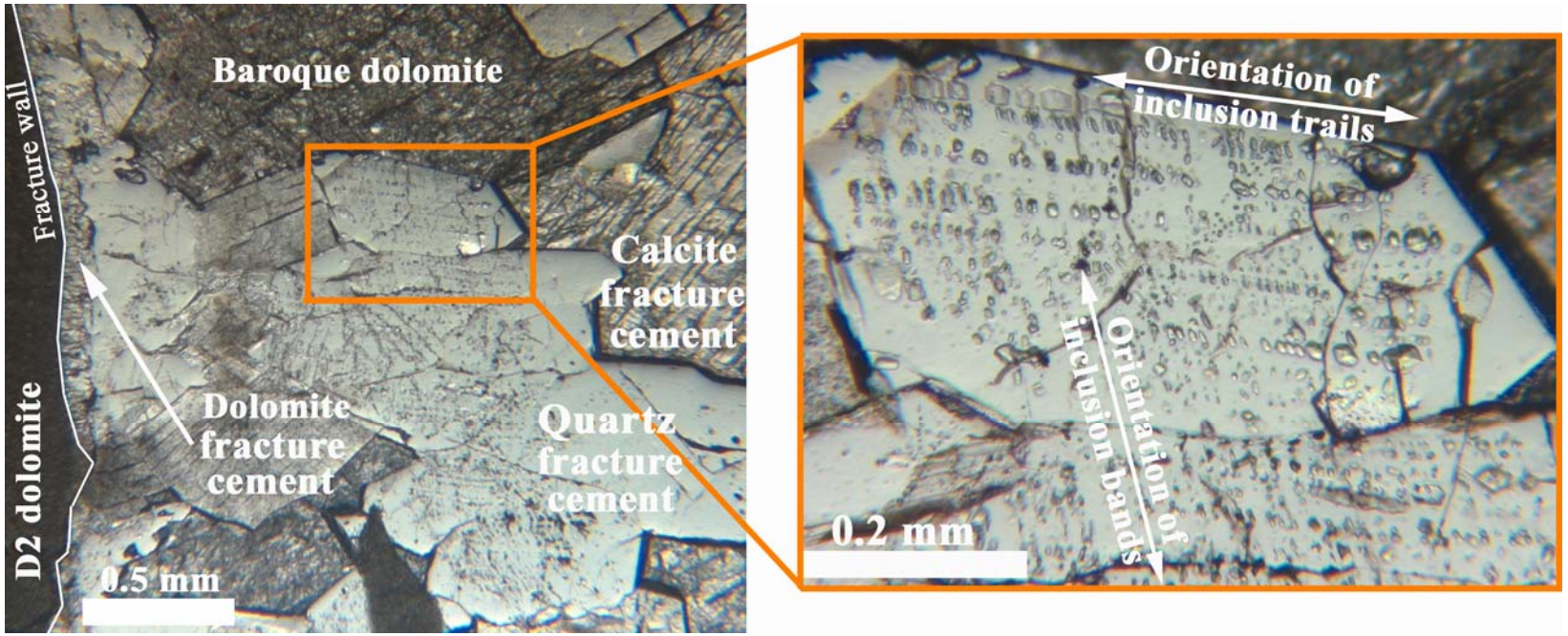

Figure 9.18 Photomicrograph of three different crystalline cements (dolomite, quartz and calcite) inside a Y macrofracture. Fibrous dolomite crystals similar to the ones depicted in Figure 9.17, line the fracture wall (white line). The next cement towards fracture center is quartz. Euhedral quartz crystals contain inclusions that are aligned parallel (bands) and approximately perpendicular (trails) to fracture wall (see inset), typical of crack-seal texture. Baroque dolomite and calcite surround euhedral quartz crystals. Thin section 02LG11-2 from layer Escalera OO1 (Tables 9.1 and 9.2), stained for calcite, plane light.

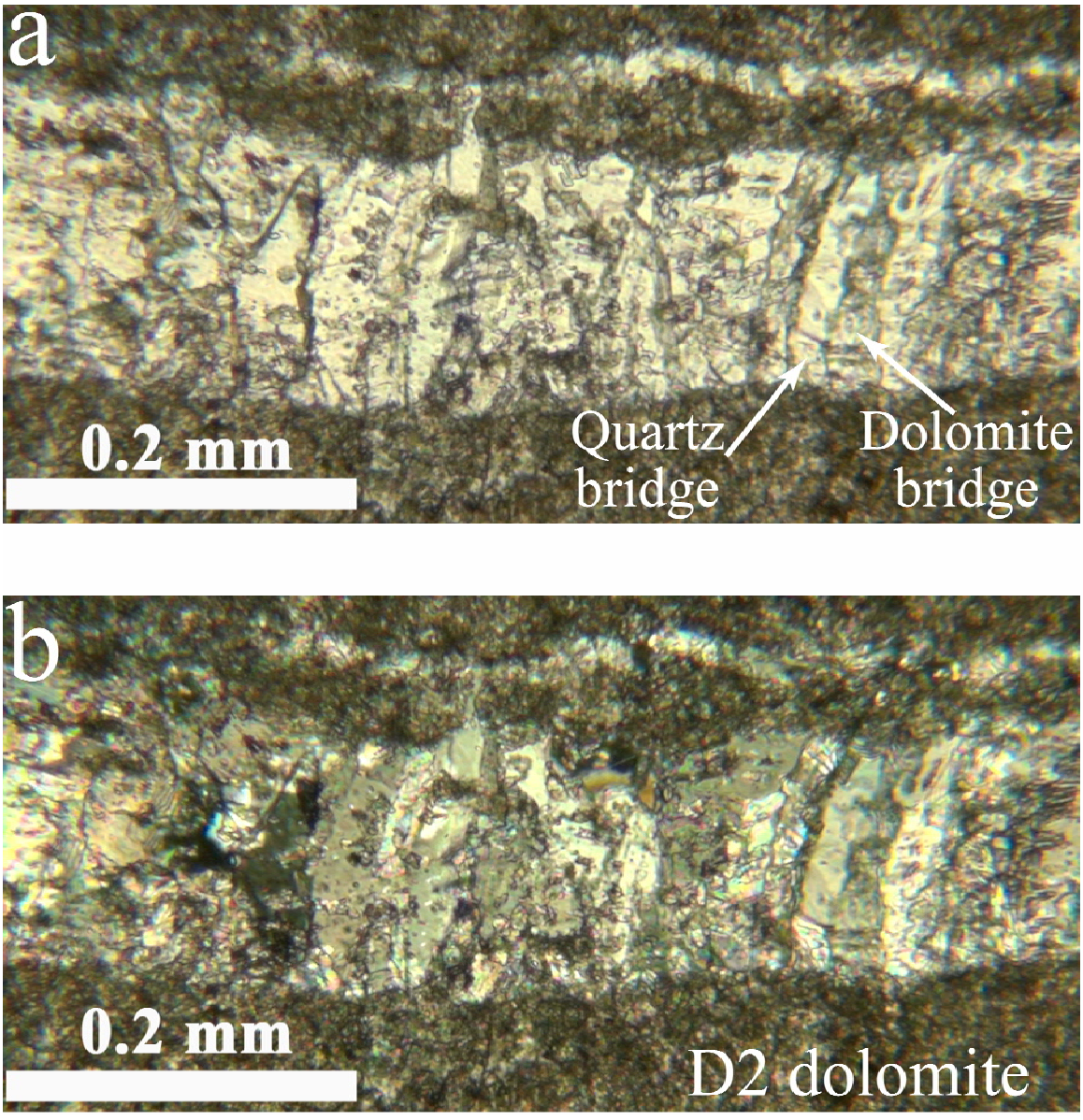

Figure 9.19 Photomicrograph of subhedral bridges of quartz and dolomite in a Y fracture using a) plane light, and b) cross-polarized light. Bridges of quartz and dolomite are parallel to each other. Bridges do not display euhedral edges like dolomite bridges in category X fractures. Rock matrix mainly composed of D2 dolomite. Thin section JS002b from layer Palmas 11 (Tables 9.1 and 9.2), stained for calcite.

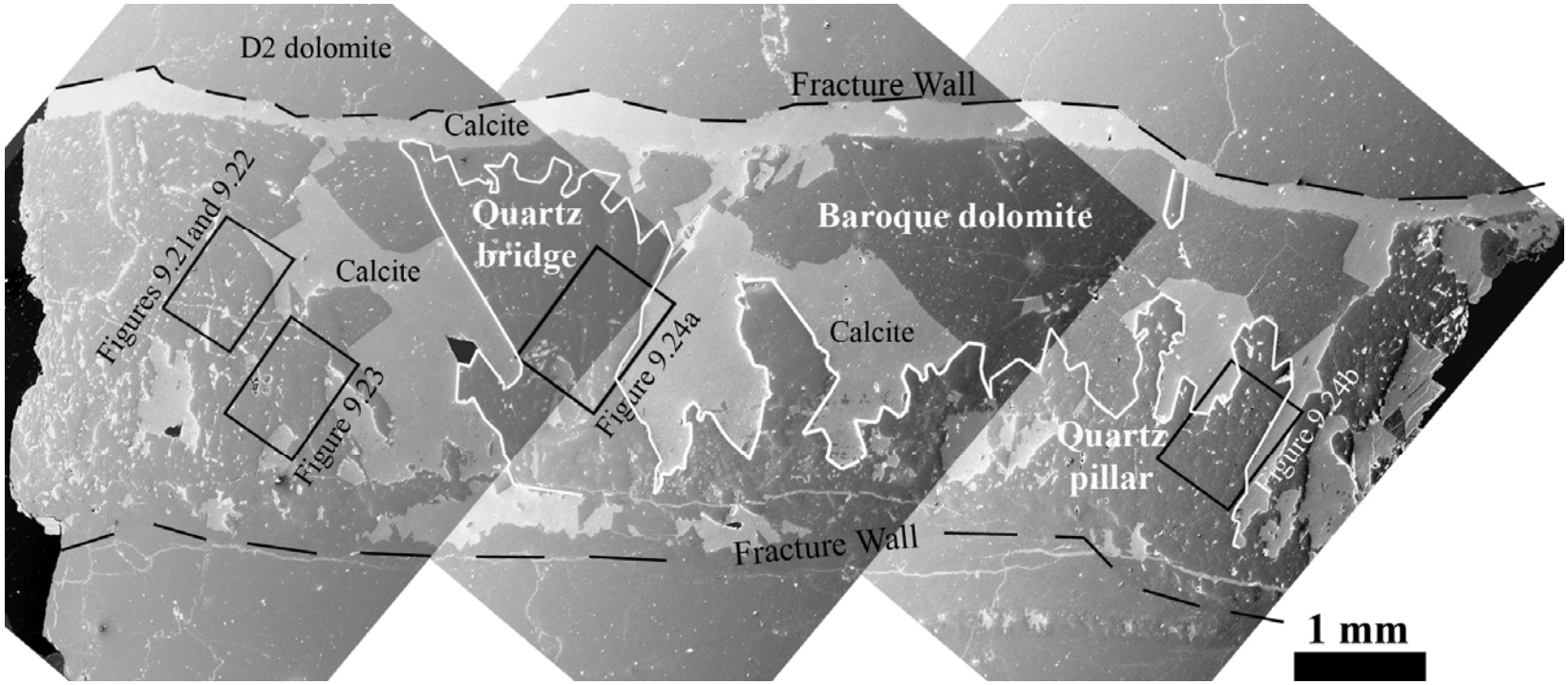

Figure 9.20 Panoramic collage of three Secondary Electron Images (SEI) from Scanned Electron Microscope (SEM) along a macrofracture categorized as Y. Calcite is light grey. White line is outline of quartz in center and right portion of image. Squares in collage indicate location of photomicrograph in Figure 9.21, element maps in Figures 9.22 and 9.23, and CL images of Figures 9.24a and 9.24b. Dashed black lines indicate location of fracture walls. Baroque dolomite occurs between quartz pillars and fracture walls. Notice how calcite precipitated between bridges and pillars of quartz (white line) and also along one of the fracture walls. Thin section 02LG11-1 from layer Escalera OO1 (Tables 9.1 and 9.2).

Some of the features commonly associated with crack-seal texture in petrographic images are such as observed in quartz cement inside Y macrofractures of the Cupido Formation. For instance, crack-seal texture is commonly associated with bands of fluid inclusions as shown in Figures 9.18 (inset), 9.21 and 9.25. Other features of crack-seal texture detected on petrographic images are inclusion trails and bridges oriented at high angles to fracture walls, as shown in Figures 9.18, 9.20, 9.24b, and 9.25. Crack-seal texture in quartz is also characterized in SEM/CL images by bands with different luminescence, as shown in Figures 9.22a, 9.23a, and 9.24. Luminescence variations that are not observed in element maps, like the ones shown in Figure 9.22 and 9.23, do not reflect different minerals but slight differences in trace-element composition and mineral structure (Pagel et al., 2000).

Where crack-seal texture is present in Y fractures, inclusions typically occur only in cores of euhedral quartz crystals (Figures 9.21 to 9.24). Linear arrays of inclusions in quartz cement of Y fractures are oriented both parallel to fracture walls (in bands) and parallel to crystal fibers or bridges (in trails) as shown in Figure 9.18. Bands mainly contain relatively small and featureless inclusions, some of which contain gas bubbles (P. Eichhubl, personal communication, 2006), and tend to be slightly elongated in a direction parallel to fracture wall (e.g., Figures 9.18 and 9.21). These small and featureless inclusions are not observed in SEM/CL images or element maps, as shown in Figures 9.22 and 9.23, which indicate that inclusions are fluid because element maps only reflect the composition of the sample surface (Pagel et al., 2000).

In contrast, some trails (perpendicular to fracture wall) mainly contain larger inclusions (e.g., Figure 9.21) that locally display rhombohedral shapes (e.g., Figures 9.23 and 9.24). Trails of inclusions are detected on SEM/CL images (e.g., Figures 9.22a, 9.23a and 9.24), which indicate that they are mainly solid because cathodoluminescence images

only reflect the composition of the sample surface (Pagel et al., 2000). In addition, element maps indicate that trails of solid inclusions in quartz cement within Y fractures are rich in magnesium (e.g., Figures 9.22b and 9.23b), and therefore are interpreted to be dolomite.

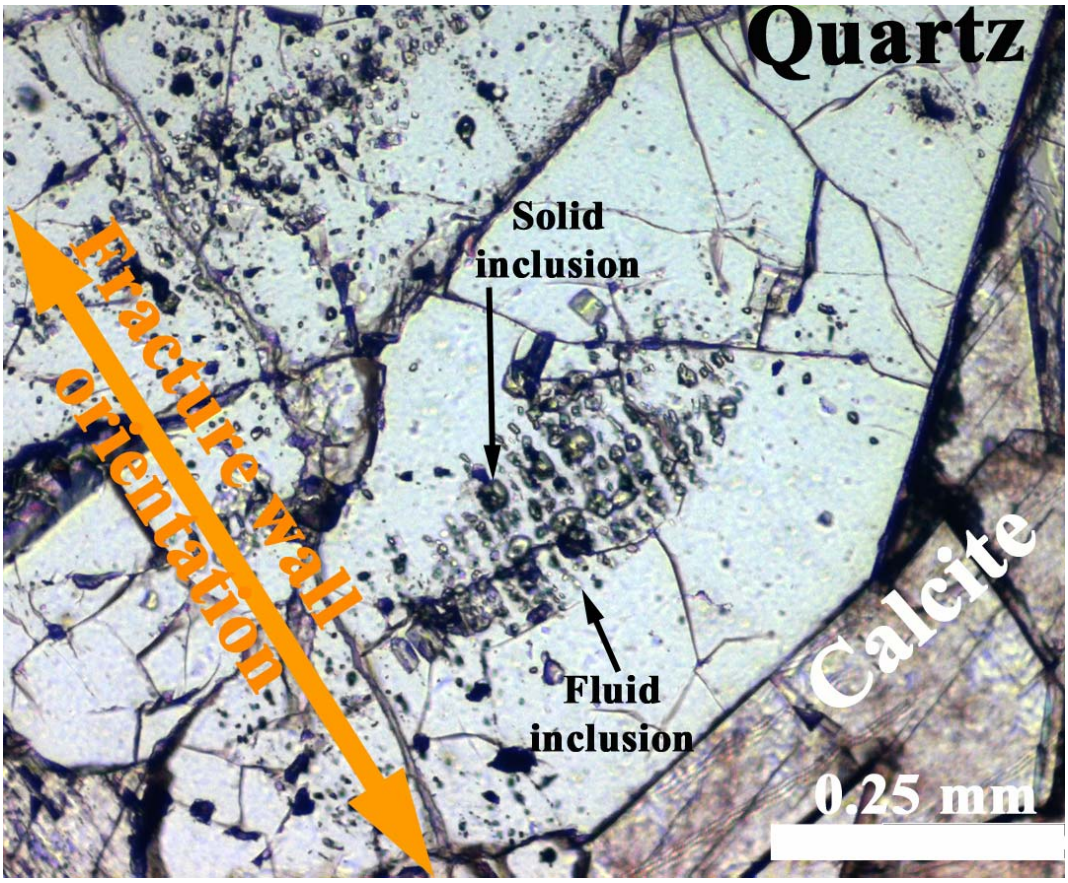

Figure 9.21 Photomicrograph of quartz crystal inside a Y macrofracture. Bands of inclusions typically associated with crack-seal texture do not extend to the edges of the quartz crystal. Solid and fluid inclusions are visible (see text and Figure 9.22 for further explanation). Thin section 02LG11-1 from layer Escalera OO1 (Tables 9.1 and 9.2), stained for calcite, plane light.

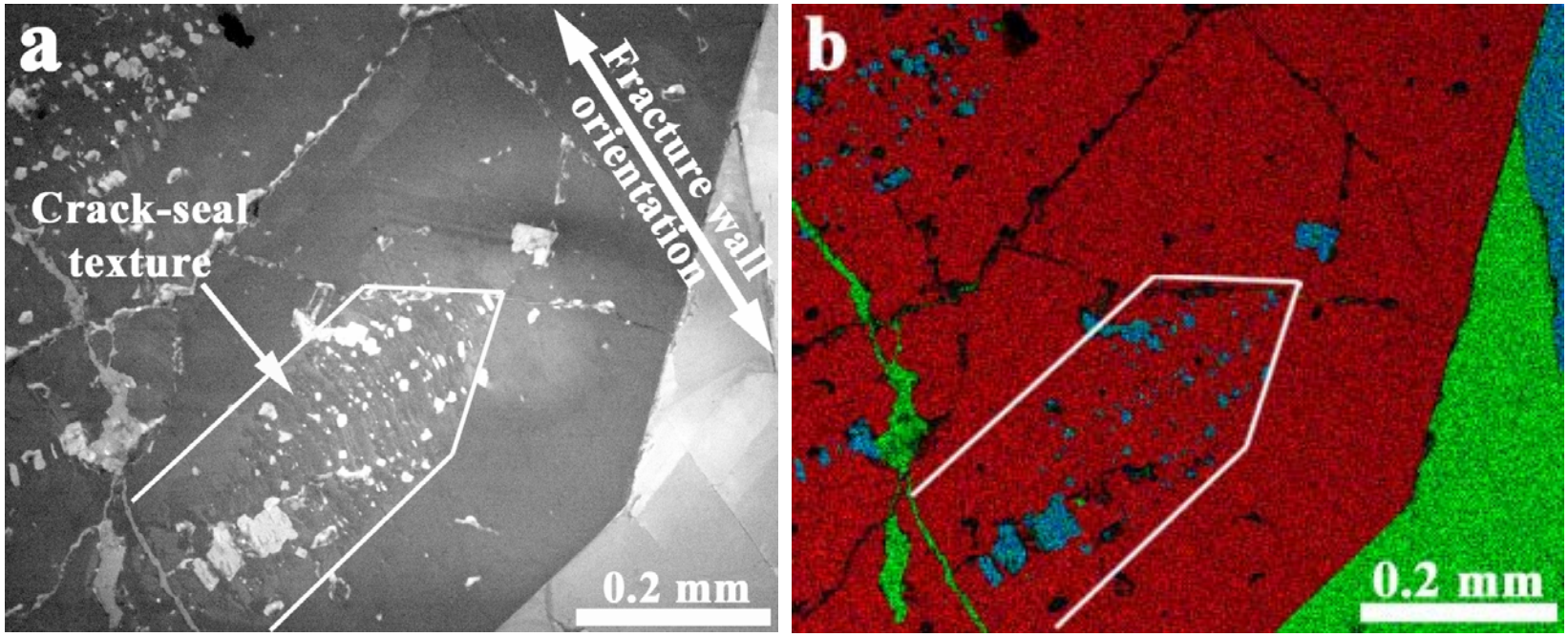

Figure 9.22 a) Cathodoluminescence (CL) image and b) element map of quartz crystal in Figure 9.21. CL image obtained using a blue filter (Reed and Milliken, 2003). Colors in element map are as follow: blue is dolomite (mg), green is calcite and red is quartz. Location of this figure is shown in Figure 9.20. Bands with different luminescence in (a) are interpreted to indicate crack seal texture, which defines a smaller euhedral quartz crystal (white line) surrounded by quartz lacking crack-seal texture. Crack-seal bands are approximately parallel to fracture wall and were not visible in petrographic image (Figure 9.21), whereas small inclusions are visible in the petrographic image but not in the cathodoluminescence image. Element map indicates that large inclusions are dolomite crystals and that crack-seal bands are composed of quartz. In element map calcite surrounds euhedral quartz faces and crosscuts quartz crystals, indicating that calcite precipitated after quartz. Thin section 02LG11-1 from layer Escalera OO1 (Tables 9.1 and 9.2).

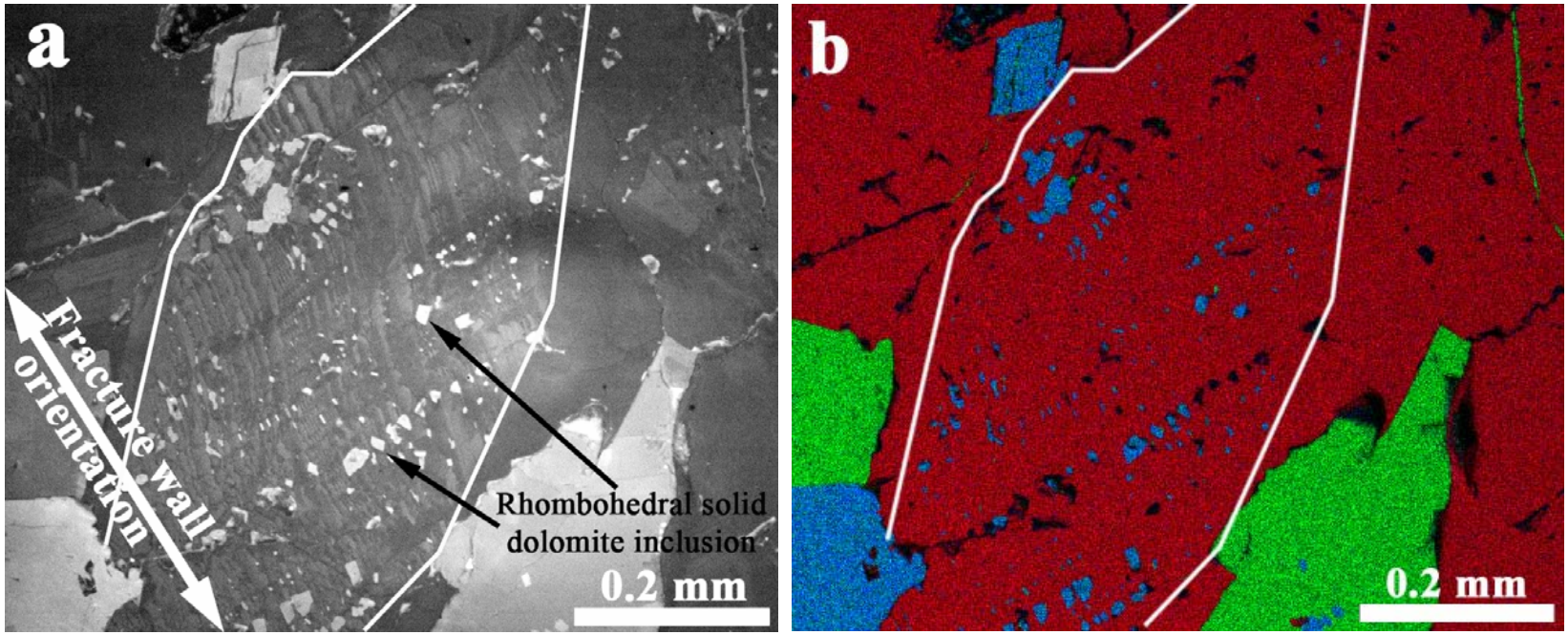

Figure 9.23 a) Cathodoluminescence (CL) image and b) element map of quartz crystal inside Y macrofracture. CL image obtained using a blue filter. Colors in element map are as follow: blue is dolomite (Mg), green is calcite and red is quartz. Location of this figure is shown in Figure 9.20. As in Figure 9.22, bands with different luminescence in (a) are interpreted to indicate crack seal texture, which defines a smaller euhedral quartz crystal core (white line) surrounded by quartz without crack-seal. Crack-seal bands are approximately parallel to fracture wall and composed of quartz. The element map indicates that the large inclusions are dolomite crystals aligned in trails perpendicular to fracture wall. Occasionally the solid inclusions of dolomite cement display a slightly rhombohedral shape. Thin section 02LG11-1 from layer Escalera OO1 (Tables 9.1 and 9.2).

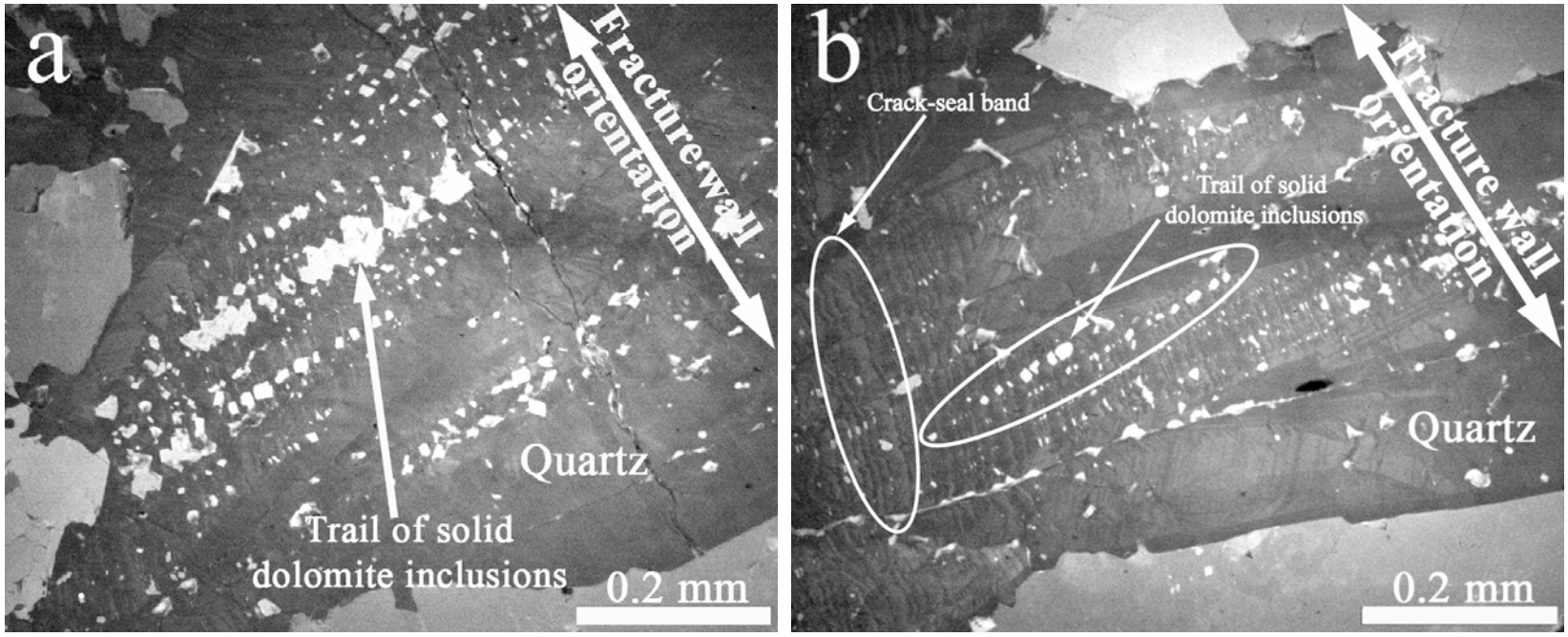

Figure 9.24 Cathodoluminescence (CL) images of two different quartz crystals inside a Y macrofracture. CL images acquired using a blue filter (Reed and Milliken, 2003). Location of these images is shown in Figure 9.20. Bands with different luminescence in (a) and (b) are interpreted to indicate crack seal texture, Crack-seal bands of quartz and trails of solid inclusions of dolomite cement (very light gray) are visible. Some of the solid inclusions of dolomite cement are not separated and/or display a slightly rhombohedral shape. Thin section 02LG11-1 from layer Escalera OO1 (Tables 9.1 and 9.2).

As indicated by Laubach et al. (2004), inclusion trails represent grain fragments that were separated by successive increments of fracture opening, and tend to parallel the wall-rock displacement direction. Solid dolomite inclusions are organized in trails oriented approximately perpendicular to fracture wall, likely indicating fracture opening direction (Ramsay, 1980). However, solid dolomite inclusions inside quartz crystals do not resemble grains broken repeatedly because the facing sides of adjacent inclusions typically do not have shapes that match (e.g., Figures 9.22a, 9.23a and 9.24). Instead, some inclusions are in contact with each other (e.g., Figure 9.24a).

As with X fractures, calcite cement in Y fractures can be interpreted as postkinematic because it lacks morphology of bridges, lacks crack-seal texture, does not display obvious crystal boundaries in plane light and locally surrounds euhedral quartz (e.g., Figures 9.21 and 9.23) and dolomite crystals (e.g., Figure 9.19). In addition, Y fractures exhibit calcite cement that might have replaced some quartz cement, as evidenced by calcite cement that disrupts the fracture-parallel bands of fluid inclusions (typically associated with crack-seal texture) inside quartz bridges (e.g., Figure 9.25). The highest percentage of postkinematic calcite measured in individual Y fractures was about 20% whereas in X fractures it was nearly 100%.

One layer (Escalera OO1, Table 9.1) exhibits some Y fractures with dolomite, quartz and calcite cement, in which crystals of dolomite and quartz are oriented obliquely to fracture walls (Figure 9.26 and 9.27). Fibrous dolomite crystals that line such fractures are unusually large (e.g., Figure 9.26), reaching lengths of up to 0.5 mm instead of the maximum size of 0.15 mm reached by the equivalent crystals oriented perpendicular to walls of other fractures (e.g., Figure 9.17). Fractures with cement crystals oblique to fracture walls also typically have additional dolomite cement at the center of the fracture with a less evident crystallographic orientation (Figures 9.26 and 9.27). Y fractures with

obliquely oriented crystals were found in one of the two samples (02LG12, Table 9.2) of Escalera OO1 layer along an en-echelon pattern likely resulting from incipient faulting. A more detailed explanation of the characteristics of the different fractures in layer Escalera OO1 is presented later.

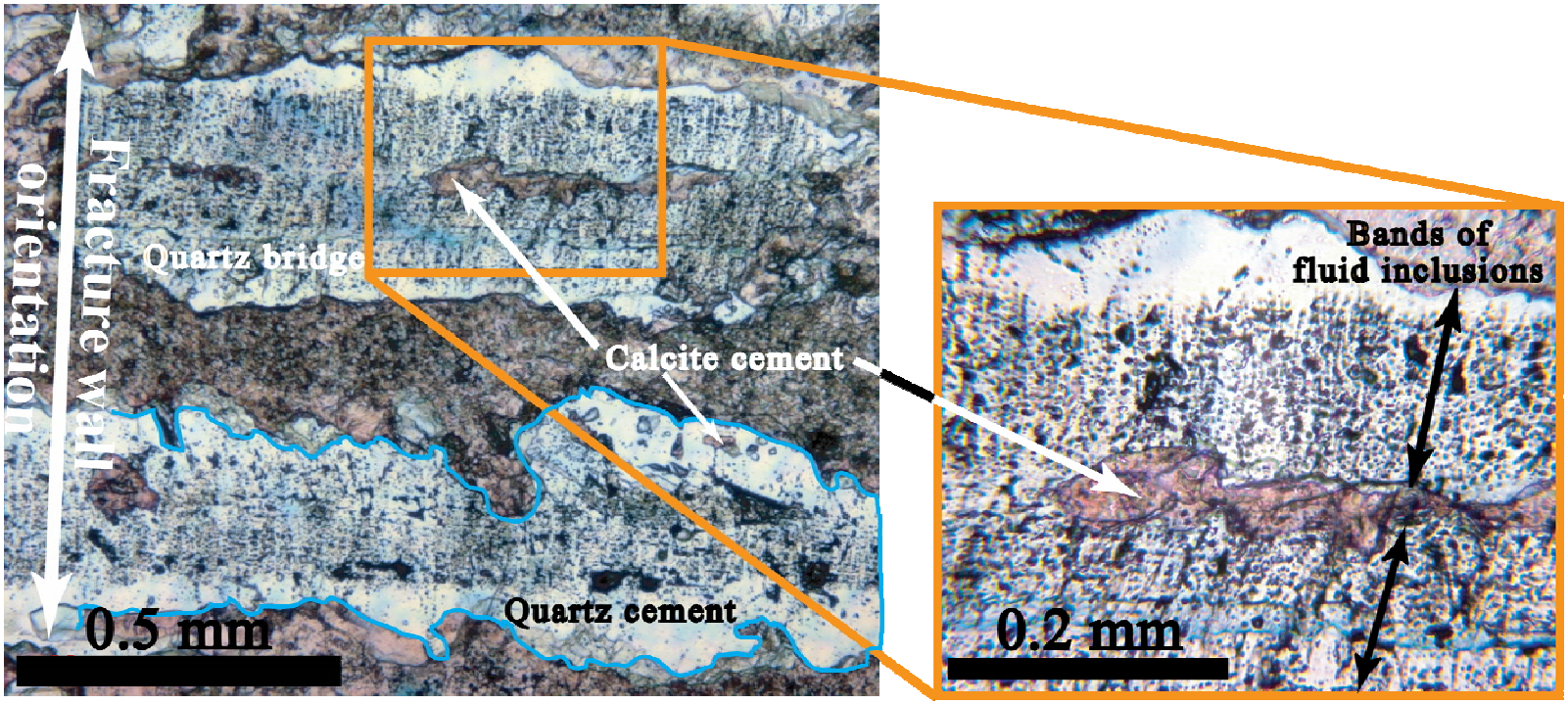

Figure 9.25 Photomicrograph of two bridges of quartz inside a macrofracture of category Y. There is calcite cement between and around (left image), but also inside (more noticeable on inset) these two bridges. Edges of quartz bridges are highly irregular (thin orange line, left image), possibly indicating calcite replaced quartz. Inside bridges, abundant bands of fluid inclusions are parallel to fracture wall, do not reach bridge margins (similar to Figure 9.21), and in some places are disrupted by calcite cement, with the last characteristic suggesting that calcite replaced quartz. Thin section 02LG13-2B from layer Escalera OO12 (Tables 9.1 and 9.2).

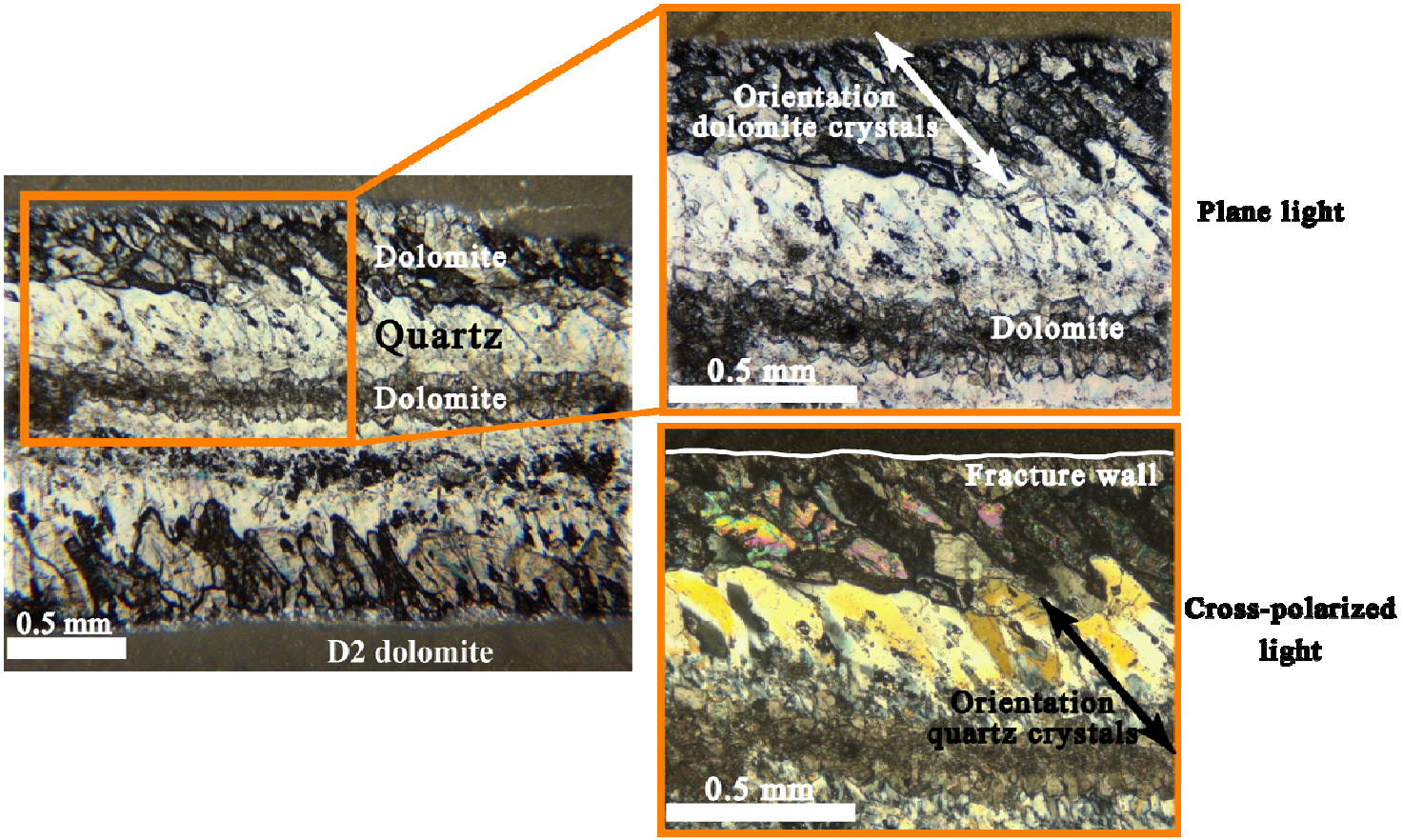

Figure 9.26 Photomicrograph of a macrofracture of category Y that displays crystals of dolomite and quartz cement that are not perpendicular to fracture wall. Notice similarity of the cements (morphology and position with respect to fracture wall) in this Y fracture with another Y fracture of the same layer (Figure 9.17), the main differences being the oblique angle of fracture cement crystals with respect to fracture wall (perpendicular in Figure 9.17), and the dolomite cement in the center of fracture (absent in Figure 9.17). Thin section 02LG12-1G from layer Escalera OO1 (Tables 9.1 and 9.2).

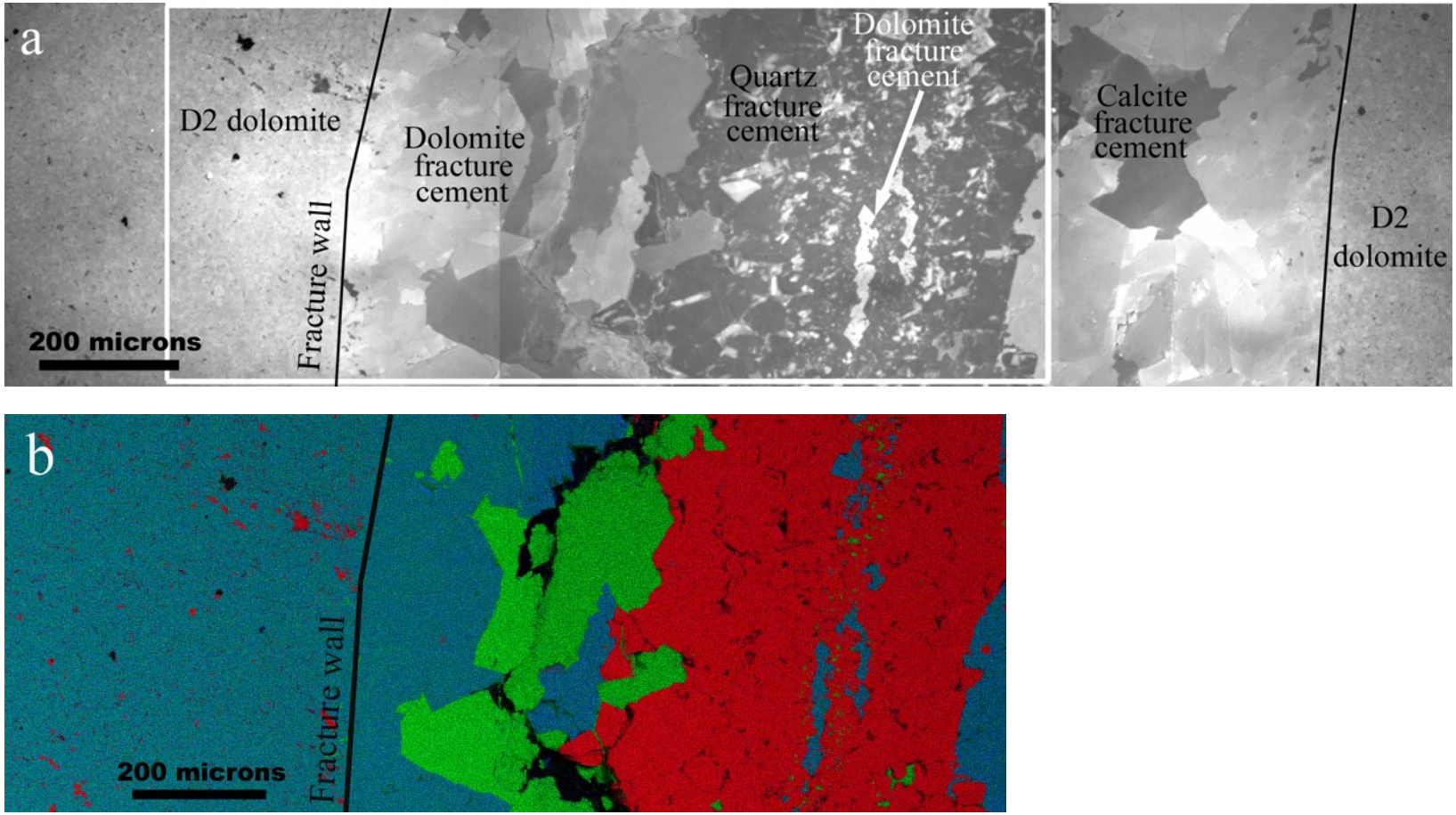

Figure 9.27 a) Cathodoluminescence (CL) images from Scanned Electron Microscope (SEM) using a blue filter (Reed and Milliken, 2003). b) Element map of part of Y macrofracture depicted in (a). Blue is dolomite (mg), green is calcite and red is quartz. Black lines indicate approximate locations of fracture walls. Square in CL image indicates location of element map. Rock matrix mainly composed of D2 dolomite. Thin section 02LG12-1F from layer Escalera OO1 (Tables 9.1 and 9.2).

9.3.4 Characterization of Z Fractures

9.3.4.1 Roughness of Fracture Trace

The most distinctive feature of Z fractures is a halo of dolomite crystals in the rock matrix around (both sides) each fracture (e.g., Figure 9.28). This halo is formed by an increase of the D2 dolomite crystals that are in rock matrix (e.g., Figure 9.29a). Although quantitative data is not currently available to verify it, the size of this halo tends to be proportional to the fracture aperture. Similar to X fractures, Z fractures have irregular traces. However, irregularity of Z fractures does not vary along trace, and individual deflections in the trace of X fractures are typically comparable in size with individual matrix crystals (e.g., Figure 9.30). Z fractures are less abundant than X or Y fractures. Currently Z fractures have only been detected in three layers (Escalera 1, Escalera 2 and Escalera 3; Table 9.1) in the backlimb of the San Blas anticline. In addition, qualitative inspection of the only outcrop where Z fractures are present indicates that Y fractures are crosscut by Z fractures (Figure 9.28).

9.3.4.2 Fracture Cements

Because of the limited presence of Z fractures and the difficulty in sampling the polished outcrops typical of canyons in the Sierra Madre Oriental (Chapter 2), it was not possible to obtain large macrofractures which typically contain a more complete suite of fracture cements than genetically related microfractures (Laubach, 2003; Laubach et al., 2004). Nevertheless, samples available show that Z fractures lack quartz cement but contain both dolomite and calcite cement. Dolomite cement in Z fractures exhibit different features than dolomite cements in X and Y fractures. Dolomite cement in Z fractures lacks bridge (or pillar) or fibrous geometries and does not exhibit trails of fluid or solid inclusions (Figure 9.30). In contrast, Z fractures exhibit individual or small

groups of dolomite crystals that tend to parallel fracture trace (Figures 9.29a and 9.30), which may indicate that dolomite cement in Z fractures is postkinematic. Calcite cement in Z fractures lacks crack-seal texture, does not display obvious crystal boundaries in plane light and filled remnant fracture porosity left by earlier dolomite cement (e.g., Figures 9.28, 9.29a, and 9.30), which suggests that calcite cement is also postkinematic. The highest percentage of postkinematic calcite measured in individual Z fractures was about 90% whereas in X and Y fractures it was about 100% and 20% respectively.

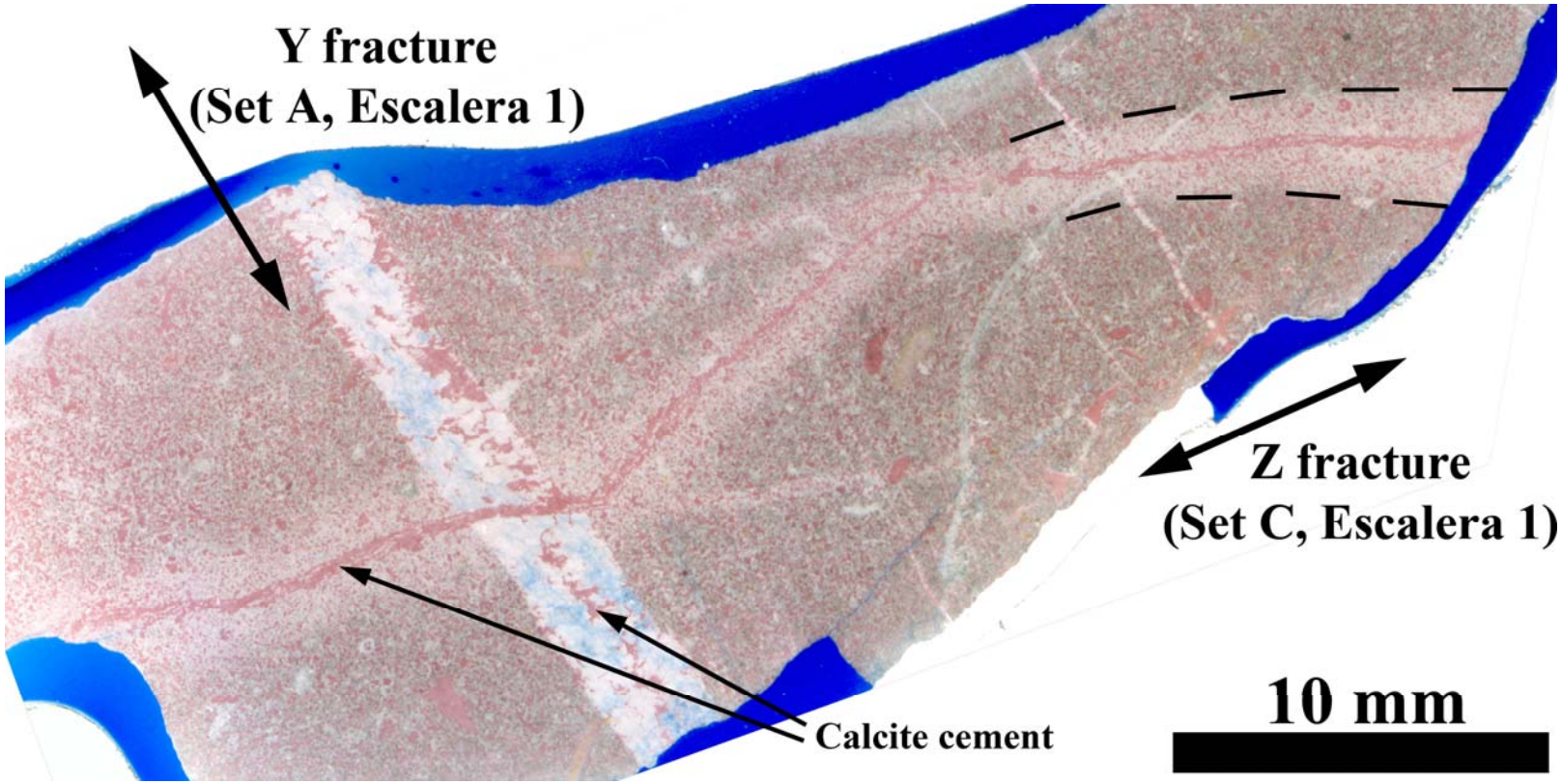

Figure 9.28 Photograph of two macrofractures from Y and Z categories on layer Escalera 1 (bedding-parallel outcrop). Fracture orientation is approximate the same as in field. Z fracture exhibits a halo (dashed line) composed of D2 dolomite crystals of the same size, but more abundant, than equivalent dolomite crystals in rock matrix. Fractures of both categories exhibit calcite cement. Notice calcite cement along Z fracture on intersection with Y fracture, which indicates that Z fracture postdates Y fracture. Rock matrix color is reddish due to photographic enhancement to highlight calcite cement in fractures. Thin section 03LG16-1A from Escalera 1 layer (Tables 9.1 and 9.2), stained for calcite, plane light.

Figure 9.29 (a) Photomicrograph of a Z fracture (vertical) intersecting several Y microfractures (approximately horizontal). Notice the halo of dolomite crystals surrounding the Z fracture; this halo is formed by more abundant D2 dolomite crystals like the ones present in rock matrix. Notice how trace of Y microfractures becomes less visible inside the halo of Z fracture. There is no evidence of Y microfractures crossing calcite cement in Z fracture, which indicates that Z fracture postdates Y microfractures. Z fracture belongs to set B whereas Y fractures belong to set A or layer Escalera 1 (Table 9.3). (b) Inset of (a). Notice on (b) the ghost texture of Y microfractures. (c) Photomicrograph of a bivalve shell (horizontal). Notice on (c) how D2 dolomite crystals from rock matrix grew from outside towards inside making more irregular the shell's trace. (a) and (b) from thin section 03LG21-1B (Escalera 3), and (c) from thin section 03LG16-1A (Escalera 1), stained for calcite, plane light (Tables 9.1 and 9.2).

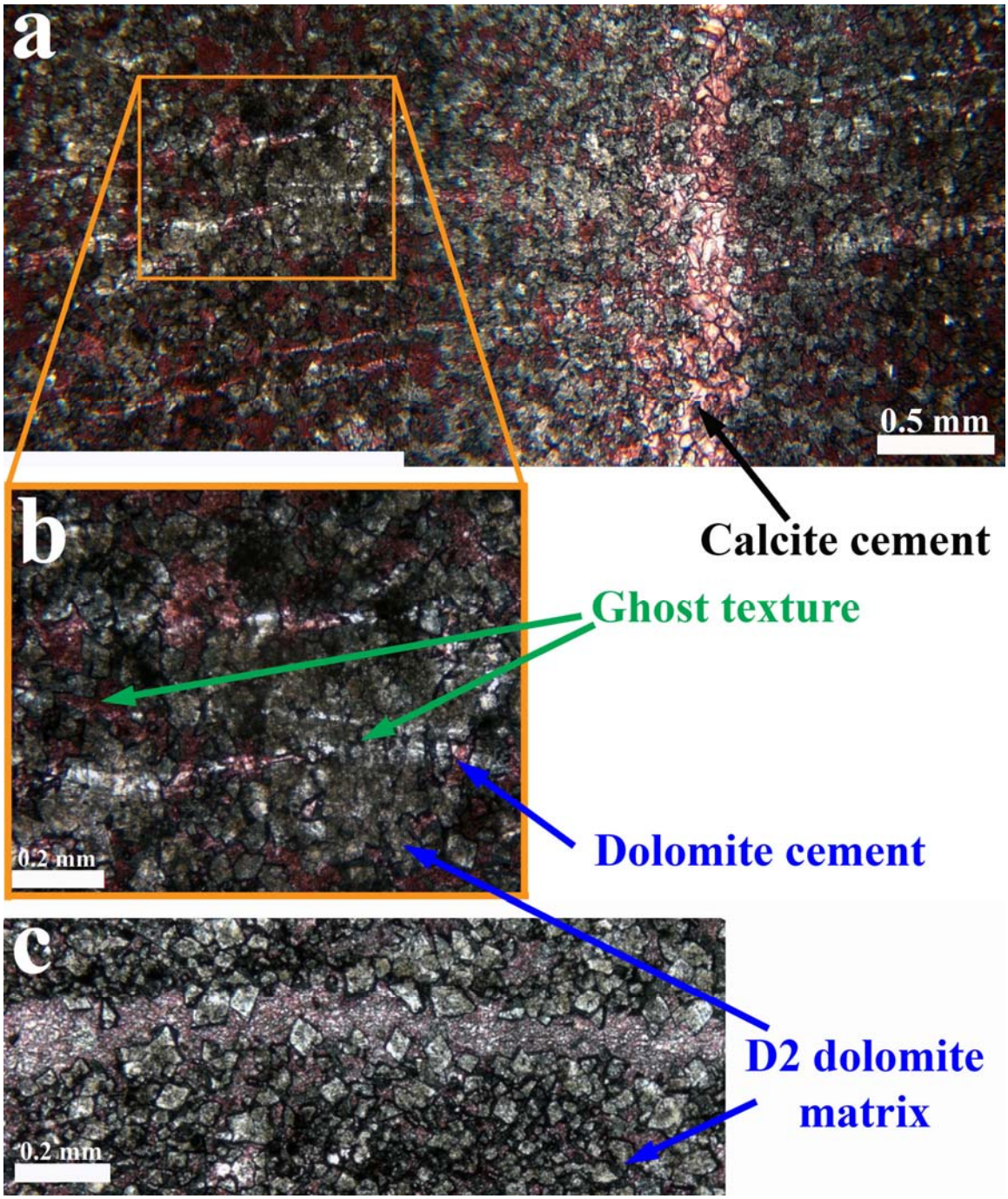
a
0.5 mm
Calcite cement
b
Ghost texture
0.2 mm
Dolomite cement
c
D2 dolomite
matrix
0.2 mm

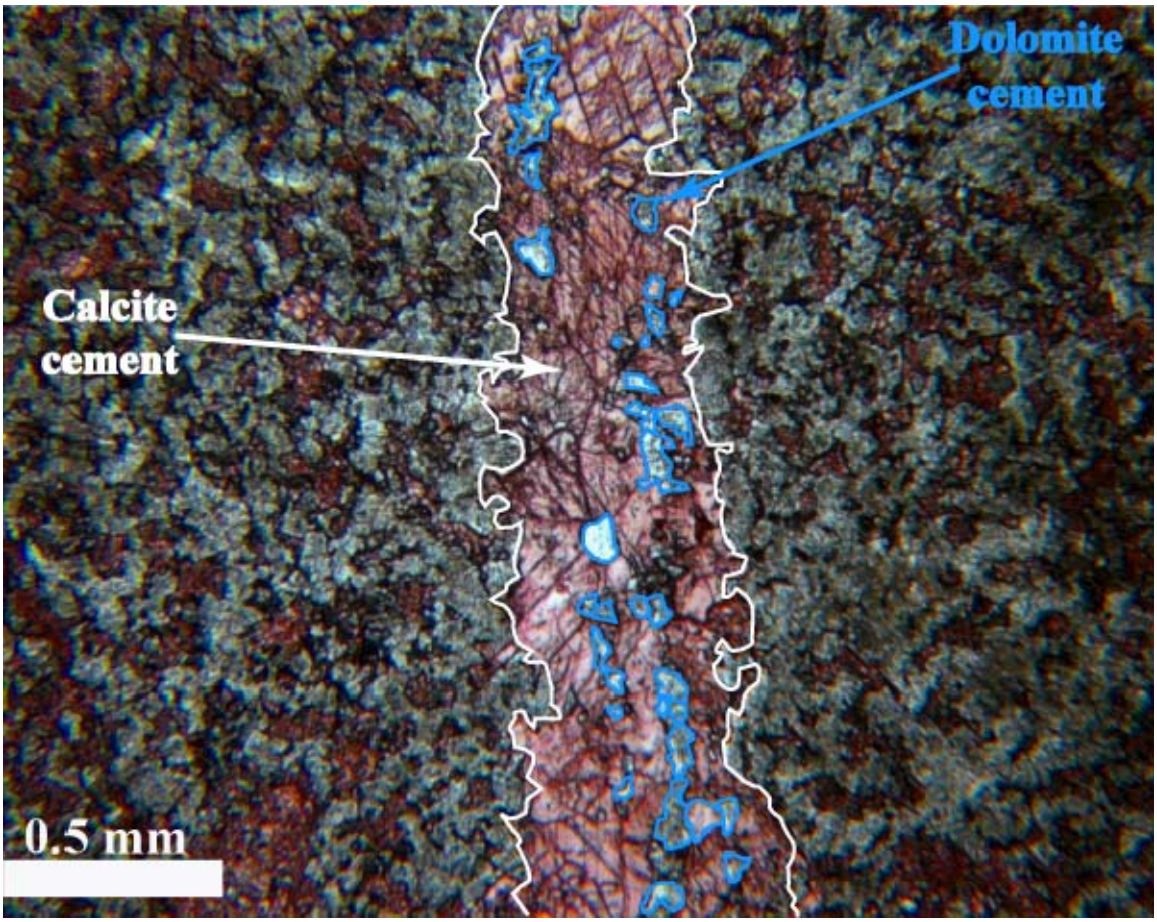

Figure 9.30 Photomicrograph of a Z fracture (vertical). Notice the irregular trace of Z fracture (white line) and the crystals of dolomite (blue lines) surrounded by calcite cement inside fracture. Crystals of dolomite cement are isolated, not connected to fracture wall, lacking bridge morphology, and of size and color similar to D2 dolomite crystals in rock matrix. From thin section 03LG21-1B (Escalera 3), stained for calcite, plane light (Tables 9.1 and 9.2).

9.3.5 Late Diagenetic Processes

Diagenetic processes that can change the composition, texture and/or crystal size of minerals in rock, such as recrystallization and dedolomitization, affected the Cupido Fm. (Monroy-Santiago et al, 2001). These two processes complicated the proper identification of fracture cements and their textures (e.g., Figure 9.31) because they occurred after all opening-mode fracturing events (Figure 9.1; Monroy-Santiago, in preparation). However, recrystallization and dedolomitization, the most important and abundant of the late diagenetic processes added some difficulty but did not preclude me from identifying the main diagenetic evidence used to categorize fractures (e.g., fracture trace, compositional and textural characteristics of fracture cements).

Some late diagenetic processes affected only rock matrix such as dedolomitization (e.g., Figure 9.31a) whereas others affected both rock matrix and fracture cements (e.g., recrystallization, Figure 9.31b). The most prevalent late diagenetic processes that affected fratures in the Monterrey Salient is recrystallization (Monroy-Santiago, in preparation), and yet fractures with apertures equal or larger than the smallest aperture threshold used in the field (0.05 mm) have fracture walls sharp enough that the fracture can be distinguished from the rock matrix (e.g., Figure 9.31b), which suggest that recrystallization did not affect measurements of fracture aperture and spacing at outcrop scale. If quantification of fracture aperture and spacing along a scanline at outcrop scale was not affected by recrystallization, then the spatial arrangement of fractures from recrystallized layers would not be affected.

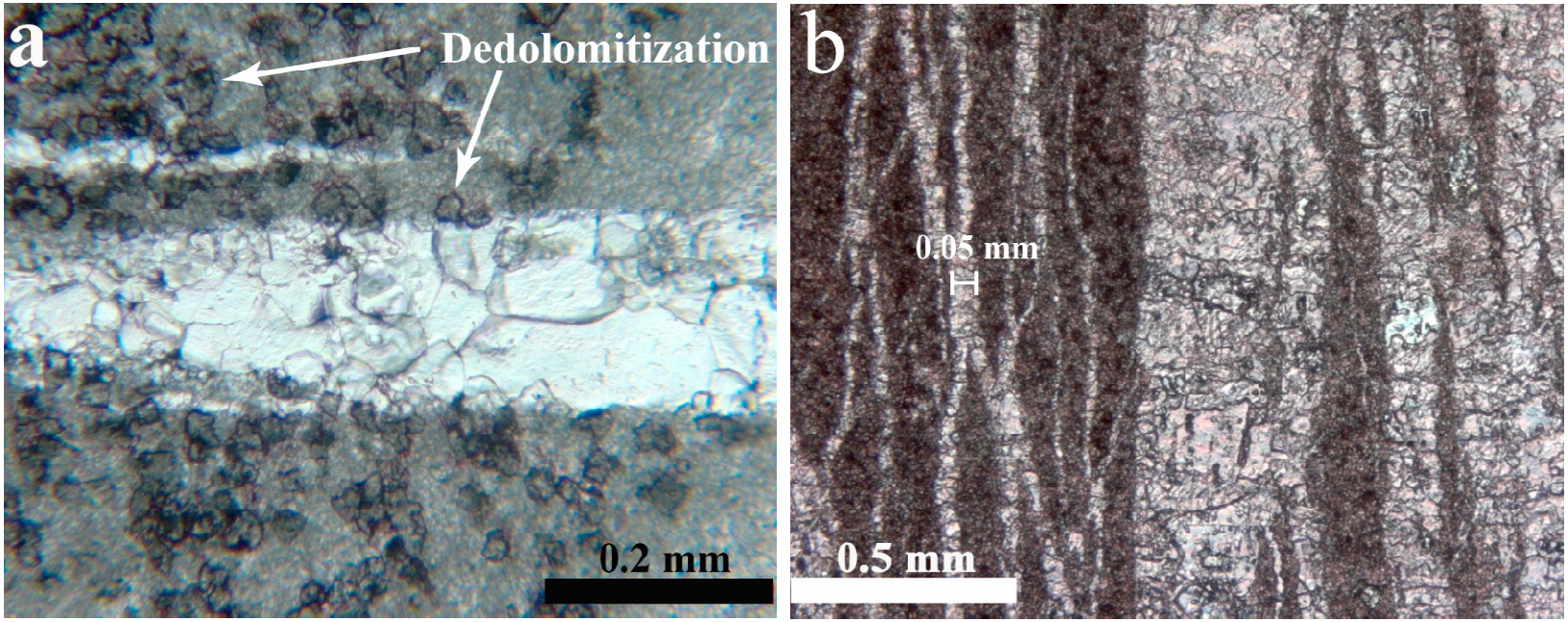

Figure 9.31 Photomicrographs of rocks affected by (a) dedolomitization and (b) intense recrystallization. Dedolomitization in (a) is evidenced by corroded dolomite crystals replaced by calcite. Notice in (a) how dedolomitization does not seem to have affected the Y fractures. Notice in (b) the difficulty in detecting crystal boundaries of crystalline cements inside fractures compared with other Y fractures (e.g., Figures 9.9 and 9.18). A fracture with aperture equal to the smallest aperture threshold used in the field (0.05 mm) can still be reliably quantified. Thin sections JS001b (a) and 02LG13-2B (b) from Palmas 11 and Escalera OO12 layers respectively (Tables 9.1 and 9.2), stained for calcite, plane light.

9.3.6 Interpretation of X Fractures

9.3.6.1 Roughness of Fracture Trace

Fractures that follow grain boundaries develop a tortuous trace and are thought to occur when rocks are not tightly cemented (Laubach, 1988). In contrast, transgranular fractures in sandstones (Laubach, 1997; Gomez et al., 2003) would be expected if natural fractures had broken abundant rock cement typical or highly consolidated rocks (Laubach, 1988). A transgranular fracture is defined as a fracture that crosses several to tens of grains and intervening cement (Laubach, 1997). In dolostones from geologic units different than the Cupido formation, fracture traces have been documented to be either straight and transgranular (e.g., Figure 4a and 4c of Gale et al., 2004) or irregular with indistinct walls that follow grain boundaries (e.g., Figure 12 of Gomez et al., 2001). In the Cupido Formation, X fractures have irregular traces and yet the individual bends are much larger than the sizes of individual matrix crystals (e.g., Figure 9.8). Some X fractures display abrupt lateral changes in aperture that almost result in fracture closure (e.g., Figure 9.6 and 9.7). In addition, X microfractures commonly exhibit ghost textures commonly associated with replacement of minerals (e.g., Figure 9.9a).

Six alternative hypotheses could be formulated in an attempt to explain the irregular trace of X fractures. In the following pages I will conjecture how each of these six hypotheses could or could not explain the irregular trace of X fractures and the ghost texture of X microfractures. The first hypothesis is that irregular fracture traces and the mismatch between opposing fracture walls (Figure 9.32) are the result of fracture shear opening, or mode II (different than non-perpendicular to fracture trace, or mode I). If dolomite cement is judged to be synkinematic with X fractures, as evidenced by euhedral

bridge morphology (e.g., Figures 9.8b, 9.10, and 9.11) and bands of fluids inclusions (e.g., Figures 9.12 and 9.13), then it could be expected for synkinematic dolomite to register the direction of fracture opening, as documented for Y fractures in Figure 9.26. Nevertheless, all X fractures exhibited mode I opening, which invalidates the hypothesis of irregular traces caused by shear fracture opening. Although it could be argued that shear fracture opening in a direction perpendicular to the thin section plane would exhibit an apparent mode I opening, it also should be noted that X fractures of two different sets (each set with a different orientation; Table 9.3) were studied in thin section and yet the expected variation between natural fractures did not reveal any fracture with shear opening. Because it is highly unlikely that all the thin sections prepared for my dissertation, for Ortega's (2002), and for Monroy-Santiago (in preparation) were cut in the only orientation that would conceal synkinematic fracture cement in mode II opening, the hypothesis of irregular traces caused by shear fracture opening is considered invalid.

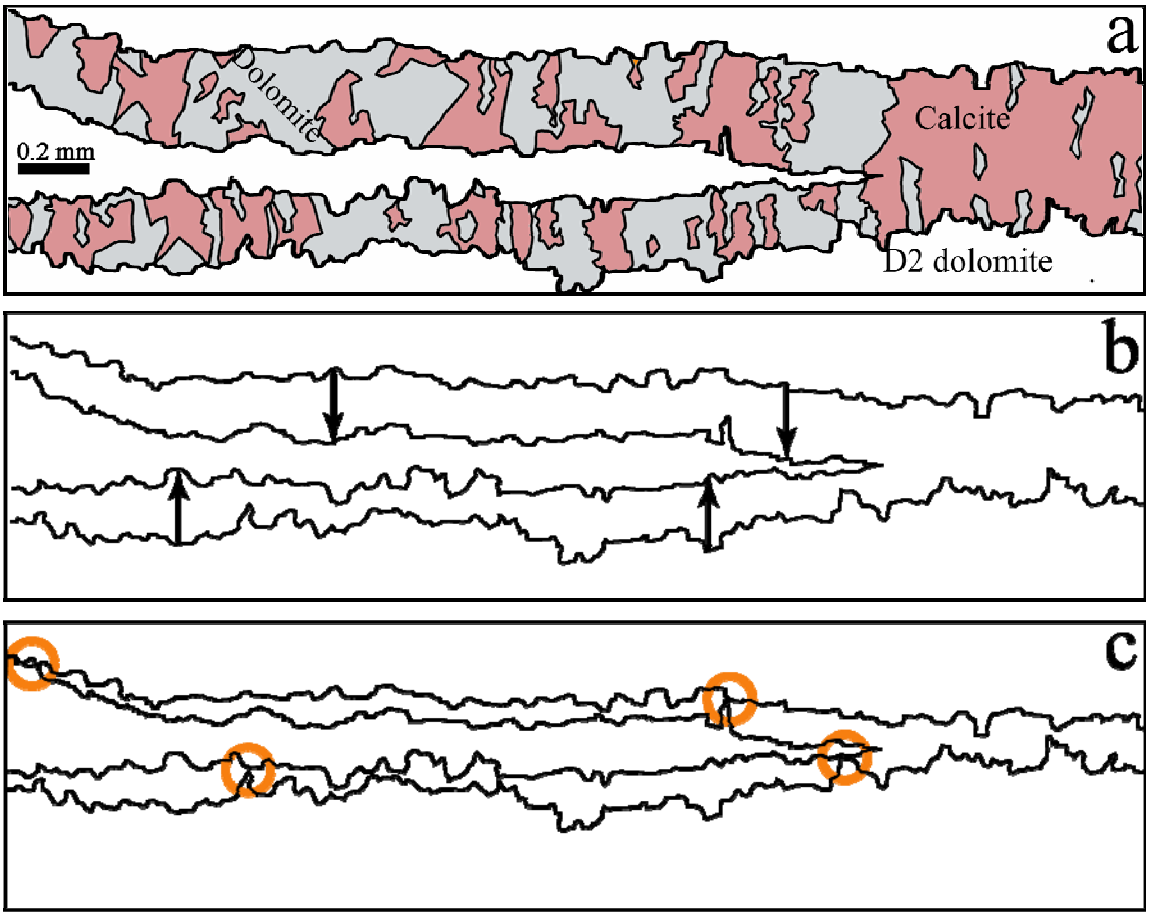

Figure 9.32 Progressive reduction of the aperture of sketch of X fracture depicted in Figure 9.8a. Sketch in (a) is a duplicate of sketch in Figure 9.8b. Sketches in (b) and (c) represent a reduction in fracture aperture by moving the two outer fracture walls towards the center of sketch, as indicated by arrows in (b). Orange circles in (c) indicate the points where the two fracture walls first come into contact with each other. Although the shape of fractures walls is similar, the abundant bends in fracture walls preclude the complete removal of fracture aperture. Removal of fracture opening in any direction along the plane of the figure will not allow for complete removal of fracture aperture.

The second hypothesis that might explain the irregular trace of X fractures is that fracture propagation occurred along individual crystal boundaries. The individual bends along walls of X fractures are much larger than the sizes of individual matrix crystals (e.g., Figure 9.8). One approach to test the second hypothesis is to take a fracture that has

been documented to propagate along (not across) grains boundaries and to shrink those grains to a size comparable to the average size of the matrix grains of Cupido Fm. layers. If the irregularities along the reduced fracture trace are comparable to the typical bends along X fractures, then it might be possible to explain the irregular trace of X fractures through fracture propagation along grain boundaries. However, the irregularities along the reduced fracture trace selected for this test (from Laubach, 1988) are much smaller than the typical bends along X fractures (Figure 9.33), invalidating the hypothesis of propagation along grain boundaries as a possible explanation for the irregular trace of X fractures. In addition, variations in the trace of X fractures can locally reach variations in fracture orientations of up to 90˚ (e.g., lower left corner of Figure 9.6). And although the simultaneous development of orthogonal fractures during the same fracturing event has been explained through subcritical propagation (Olson et al., 2004), there is still not an explanation for abrupt variations within a single fracture such the ones exhibited by X fractures.

A third hypothesis attempts to elucidate the irregular trace of typical X fractures by dissolution of an initial straight trace, probably by fluids present inside X fractures (Passchier and Trouw, 1998). Although dissolution of fracture walls between dolomite bridges can explain pore spaces in rock matrix that are connected to X fractures (e.g., Figures 9.11, 9.34d), it cannot explain bridges of dolomite connecting highly irregular fracture walls such as the ones portrayed in the left part of Figure 9.8. Namely, if dolomite cement in X fractures is believed to be synkinematic (as suggested by its crystallization as bridges, bands of fluid inclusions and exhibiting an emergent threshold), then dissolution of fracture walls would either create pillars out of bridges by dissolving preferentially one fracture wall (e.g., right end of Figure 9.34d), or irregular fracture traces connected by dolomite bridges that preserved the original fracture trace (e.g.,

bottom of Figure 9.34d). In addition, dissolution along fracture walls would have increased the aperture of microfractures making them more visible, but X microfractures instead exhibit are less visible than their Y counterparts and display a ghost texture (e.g., inset Figure 9.9a), further discrediting dissolution as the cause for the irregular trace of X fractures.

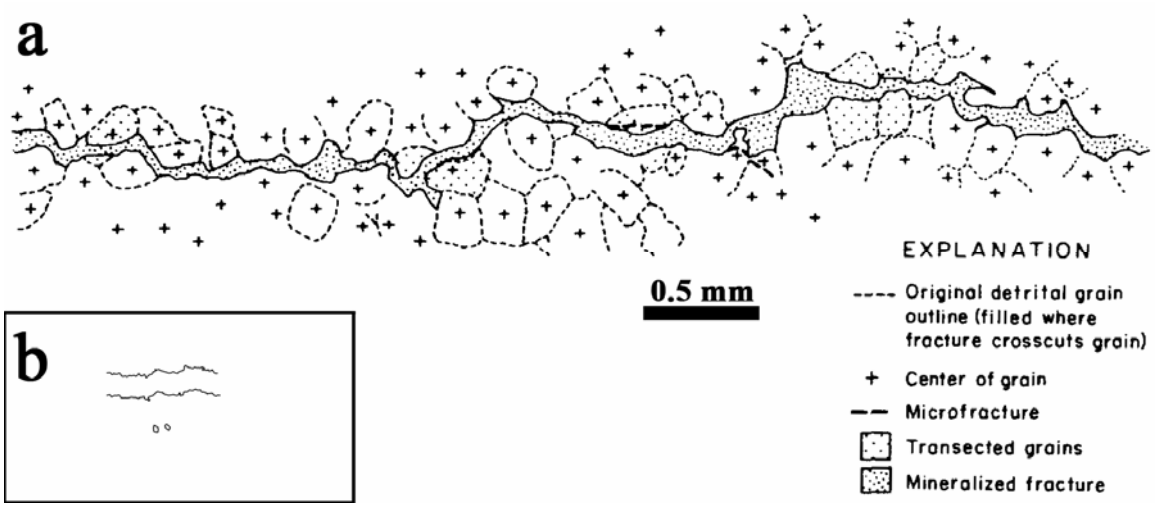

Figure 9.33 Sketches illustrating how fracture propagation along grain boundaries cannot explain the roughness displayed typically by X fractures. (a) Sketch of fracture cross-section from photomicrograph montage illustrating fracture along grain boundaries, Mobil-Cargill No. 14 well, Harrison County, Texas, depth 1879 m. Modified from Laubach (1998). (b) Sketch of a scaled (10% of original size in a) version of the fracture walls and two grains of upper sketch, scaled fracture has a larger aperture.

Figure 9.34 Sketches illustrating proposed evolution of two X fractures (or one branching) when dissolution is assumed to explain irregular trace of X fractures. (a) Final stage of fracture development of an X fracture with synkinematic dolomite cement (light grey) precipitating in bridges. Trace in (a) is still relatively straight. (b) Subsequent stage when fracture development had ceased and dissolution (represented by green arrows) along fracture walls has started to alter fracture trace. (c) Further dissolution along fracture walls has increased aperture and trace irregularity along the entire fracture. On upper fracture branch dissolution occurred mainly on upper fracture wall, resulting in the separation of bridges from fracture wall. On lower branch, dissolution occurred mainly between bridges. (d) Final stage of fracture evolution after increased dissolution of fracture wall and subsequent precipitation of postkinematic calcite cement. Dissolution between bridges on lower branch resulted in an enlarged fracture aperture between bridges and in the preservation of the original straight fracture trace underneath bridges.

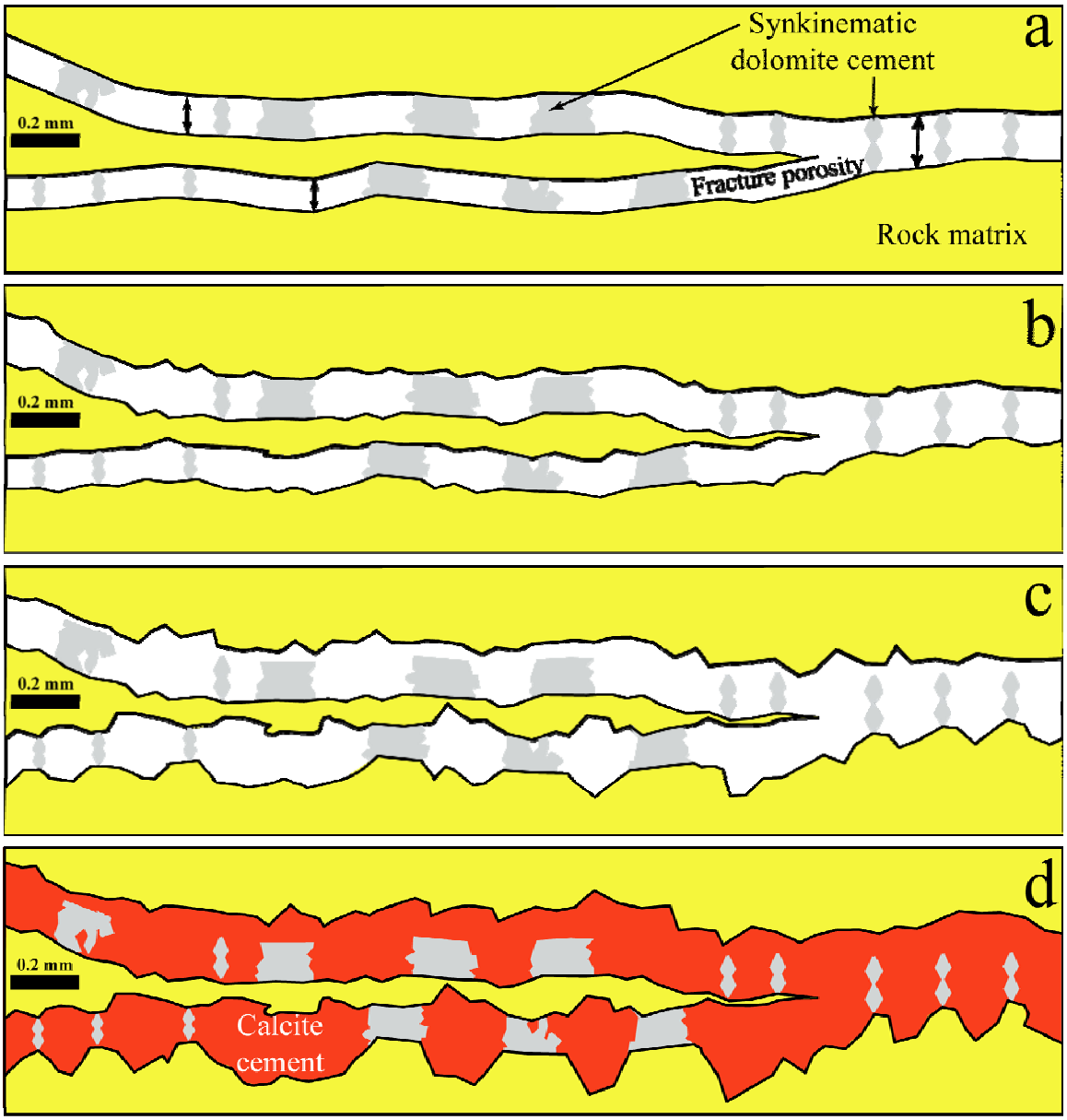
a
Synkinematic
dolomite cement
0.2 mm
Fracture porosity
Rock matrix
b
0.2 mm
c
0.2 mm
d
0.2 mm
Calcite
cement

A fourth hypothesis explains the irregular trace of X fractures and the ghost texture of X microfractures through recrystallization of the entire rock. Recrystallization has been documented in Cupido Formation layers in the Monterrey Salient (Monroy-Santiago, et al., 2001). Although intensely recrystallized carbonate rocks exhibit microfractures with textures that could be interpreted as ghost (e.g., microfractures with apertures smaller than 0.05 mm in Figure 9.31b), cement within macrofractures in recrystallized rocks also exhibit manifest recrystallization (e.g., largest fractures in Figure 9.31b). Because recrystallization was not observed in X macrofractures, the hypothesis that recrystallization is responsible for irregular trace of X fractures and ghost texture of X microfractures is not considered valid.

A fifth hypothesis to explain the irregular trace of X fractures follows Gale et al. (2004) suggestion that "if dolomitization post-dates a fracture event, then fracture walls may be modified substantially". This fifth hypothesis suggests that the irregular traces of X fractures might be the result of D2 dolomitization occurring after fractures developed (Figure 9.35). Namely, fractures grew with relatively straight traces and synkinematic bridges of dolomite when host rock was still mainly composed of calcite (Figures 9.35a and 9.35b) and subsequent D2 dolomitization changed fracture trace into an irregular one by chemical replacement of minerals from the matrix into fractures (Figures 9.35d and 9.35e). D2 replacing both rock matrix and fracture cements also explains the ghost texture commonly observed on X microfractures (e.g., inset Figure 9.9a). Replacement of fracture cements near a fracture wall by D2 dolomite is going to reduce by a larger percentage the aperture of a microfracture than a macrofracture, making X microfractures harder to detect than X macrofractures.

Figure 9.35 Idealized sketch representing evolution of an X fracture with a trace identical to the fracture depicted in Figure 9.8a, as proposed by the fourth hypothesis explained in text. Different colors represent different minerals formed at different times. In (a) fracture development has initiated with synkinematic dolomite cement forming bridges, but final aperture is only reached in (b). Black arrows in (a) and (b) indicate direction of fracture opening. Calcite cement (red) precipitated predominantly within X fractures in (c). D2 dolomitization starts in (d), extending from the matrix into pre-existing X fractures (green arrows) replacing fracture cements near fracture wall with the consequent alteration of the fracture wall. By (e) the matrix has become richer in D2 dolomite and the trace of fracture wall has become highly irregular, which likely resulted in a decrease in fracture aperture.

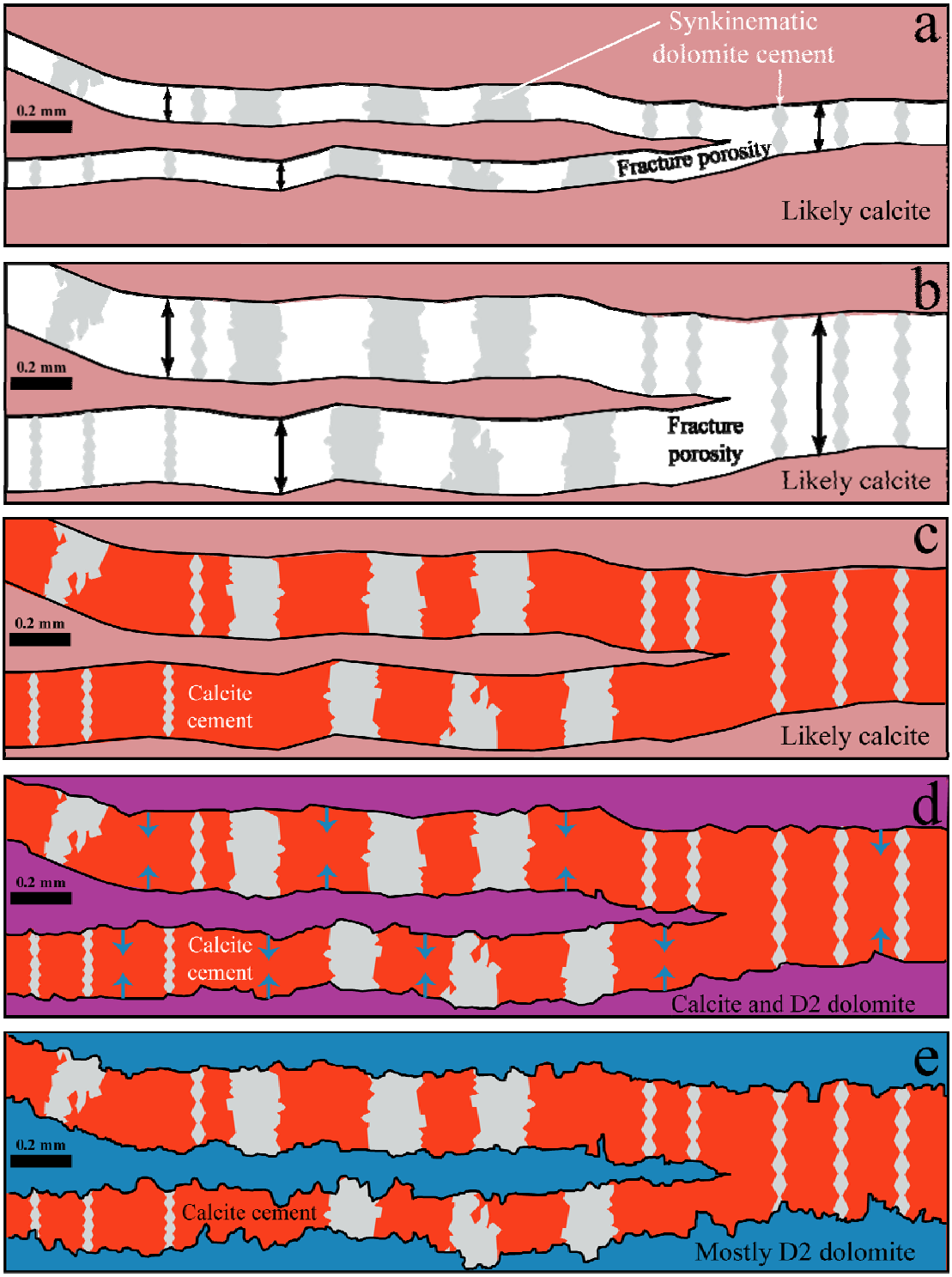
a
Synkinematic
dolomite cement
0.2 mm
Fracture porosity
Likely calcite
b
0.2 mm
Fracture
porosity
Likely calcite
c
0.2 mm
Calcite
cement
Likely calcite
d
0.2 mm
Calcite
cement
Calcite and D2 dolomite
e
0.2 mm
Calcite cement
Mostly D2 dolomite

Evidence for the original straight trace of X fractures such as a change in size of D2 dolomite crystals along fracture trace or a ghost texture were not observed. Lack of evidence for the original straight trace of X fractures could suggest that fractures were completely filled at the time of D2 dolomitization (Figure 9.35c) because D2 dolomite crystals along an open fracture could have developed a larger size due to the availability of open space compared with equivalent crystals within the rock matrix. The relatively small amount of synkinematic dolomite found in individual X fractures (2 to 40%) suggests that X fractures had significant porosity at the end of their development. The interpretation that calcite cement precipitated postkinematically in X fractures before D2 dolomitization is partly supported by the paragenesis of Cupido Formation developed by Monroy-Santiago (in preparation) as shown in Figure 9.1 (calcite cement C2 is partly contemporaneous with Pre-D2 fracture event F2). Assuming that X fractures were completely filled by the time D2 dolomitization started helps to support the hypothesis of D2 dolomitization changing rock texture and composition from the rock matrix toward X fractures (Figures 9.35d and 9.35e). Namely, if X fractures were mostly filled before D2 dolomitization, it would have been easier for Mg-rich fluids to move through the rock using the pore space between grains than through the X fractures. Evidence of D2 dolomitization changing the original (Pre-D2) trace of other carbonate rock constituents such as a bivalve (skeletal grain, Tucker and Wright, 1999) is shown in Figure 9.29c. The hypothesis of irregular fracture traces caused by fracturing before D2 dolomitization was initially proposed by Monroy-Santiago (in preparation) using petrographic examination as well as stable isotope analysis of minerals in matrix and fractures, and is the hypothesis adopted in my dissertation.

A sixth, and last, hypothesis for the origin of the irregular trace of typical X fractures is the result of propagation of a fracture around porosity (S. Laubach, personal

communication, 2005). Although an irregular fracture trace can, in principle, be the result of propagation around porosity present at the time of fracture development, current rocks show no evidence of such abundant porosity along or next to X fractures (e.g., Figure 9.9a). The lack of porosity along or next to X fractures could be also explained by D2 dolomitization occurring after fracture development, which would have replaced porosity with dolomite crystals, thereby validating also the hypothesis that X-fractures predate D2 dolomitization.

9.3.6.2 Fracture Cements

Crack-seal texture can be interpreted as evidence of synkinematic cementation (Laubach, 2003; Laubach, et al., 2004). Although bridges and pillars of euhedral (rhombohedral) dolomite cement in X fractures could not be successfully imaged with SEM/CL to test the presence of crack-seal texture, bands (parallel to fracture wall) of fluid inclusions (e.g., Figures 9.12 and 9.13) and bridge morphology detected in X fractures (e.g., Figures 9.8, 9.10 and 9.11) resemble similar structures in fractured sandstones with synkinematic quartz cement (Lander et al., 2002), suggesting that dolomite cement in X fractures is synkinematic. In addition, numerical modeling of dolomite precipitation in opening fractures has indicated that rhombohedral bridges of dolomite are formed when opening rates are comparable or slightly slower than the rate of dolomite growth (Gale et al., 2006).

Another indication that dolomite in X fractures is synkinematic is the presence of an emergent threshold (Laubach, 2003). An emergent threshold is observed when there is a small proportion of synkinematic cement (translucent and euhedral dolomite for X fractures) and corresponding large proportion of postkinematic cement (calcite for X fractures) where aperture is large compared to where aperture is small (e.g., Figure 9.8). Therefore, I agree with Monroy-Santiago (in preparation) in that the translucent and

euhedral dolomite cement that formed bridges and pillars inside X fractures can be interpreted as synkinematic. In addition, if euhedral and translucent dolomite cement in X fractures is interpreted as synkinematic and D2 dolomitization is interpreted to have occurred after X fracturing event, then it can be interpreted that dolomite cement in X fractures precipitated before D2 dolomitization. Isolated euhedral bridges and pillars of translucent dolomite commonly found in X fractures (e.g., Figures 9.10, 9.12, and 9.13b) suggest that dolomite cement grew unrestricted in an open fracture. However, in certain X fractures, bridges of translucent dolomite seem to have grown adjacent to each other, which precluded them from being perfectly euhedral (e.g., Figures 9.8, 9.11, and 9.13a).

Calcite cement is abundant in X fractures, lacks planes of fluid inclusions, and seems to have filled fracture porosity left by earlier euhedral dolomite cement (e.g., Figures 9.8, 9.10 to 9.13), which suggests that calcite precipitated after fracture opening in a post-kinematic manner (as interpreted by Monroy-Santiago, in preparation). Although it could be argued that locally it is not possible to distinguish if an X fracture contains bridges of dolomite surrounded or calcite or bridges of calcite surrounded by dolomite (for instance leftmost portion of fractures in Figure 9.8), careful examination of the same fracture along its trace showed locations where it is more evident that the bridges are made of euhedral dolomite and not of calcite (e.g., Figure 9.10). There is evidence of calcite affected by the dolomitization (D2) that affected the matrix of rocks with X fractures (e.g., large pore in lower left corner of Figure 9.2), which helps support the interpretation of postkinematic calcite cement precipitating also before the D2 dolomitization.

Monroy-Santiago (in preparation) observed bridges of dolomite in X fractures with color and texture similar to the D2 dolomite crystals in matrix, and thereby suggested that synkinematic dolomite cement in X fractures formed at the same time

(from the same fluid) that replacement of matrix by D2 dolomite was occurring. Monroy-Santiago (in preparation) argued that differences in crystal size, color and texture between the dolomite crystals in the matrix and in the fractures might indicate that they formed at different times from different fluids, but also it could reflect the difference in dolomite that replaced calcite compared with dolomite that precipitated in open fracture porosity. Since the objective of my dissertation was not to generate a detailed paragenetic sequence of the Cupido formation, I did not pursue studies which could have better clarified the timing of D2 dolomitization with respect to X fracturing such as stable isotopes. Therefore, I accept the possibility that some D2 dolomitization (or in some layers) could have also occurred during X fracturing. Hopefully, once the stable isotope studies of Monroy-Santiago (in preparation) are concluded, the precise timing of D2 dolomitization with respect to X fracture opening will be established more precisely.

9.3.7 Interpretation of Y Fractures

9.3.7.1 Roughness of Fracture Trace

In contrast to X fractures which only exhibit irregular traces (e.g., Figure 9.8), Y fractures exhibit commonly straight (e.g., Figure 9.14) but on one outcrop they exhibited irregular traces (e.g., Figure 9.15). Like for X fractures, Y fractures with irregular traces exhibit locally drastic lateral variations in fracture aperture (e.g., Figure 9.15). In addition, layers that exhibit Y fractures with irregular traces (Escalera 1, Escalera 2, and Escalera 3) also exhibit Y microfractures with a ghost texture (e.g., Figure 9.29b). Y fractures with straight traces display bends that are less frequent and smaller than those in X or Y fractures with irregular traces, and exhibit morphologies that are more similar to what has been typically reported under petrographical examination (e.g., Gross and Engelder, 1995; Gale et al., 2004). In addition, layers with Y fractures that exhibit Y

traces with straight traces (Escalera OO1, Escalera OO12, Huasteca, and Palmas 11) exhibit microfractures lacking ghost textures and instead have sharp edges (e.g., Figure 9.9b). Therefore, based on the hypothesis selected to explain the irregular traces of X fractures and ghost texture of X microfractures, I interpret that Y fractures with irregular traces developed before D2 dolomitization (Pre-D2) whereas Y fractures with straight traces developed after D2 dolomitization (Post-D2).

9.3.7.2 Fracture Cements

The most important difference between X and Y fractures is the presence of quartz cement, which was observed in Y fractures with both irregular (e.g., Figure 9.16) and straight (e.g., Figure 9.18) traces. The largest volume of quartz cement in Y fractures is represented by bridges and pillars with abundant bands and trails of fluid inclusions (e.g., Figures 9.18 and 9.20) that under SEM/CL imaging show to be display crack-seal texture (Figures 9.22 to 9.24), as revealed in sandstones by Laubach et al. (2004), which indicate that quartz in Y fractures has a synkinematic origin. Bridges and pillars of quartz helped the temporary preservation of fracture porosity (e.g., Figure 9.20).

Crack-seal texture in Y fractures is mainly present in euhedral cores of euhedral quartz crystals (e.g., Figures 9.21 and 9.22). A pattern similar was described by Laubach (1988), who suggested that quartz precipitated synkinematically only for a limited period of time, and that later quartz precipitated postkinematically (Laubach et al., 2004; Lander et al., 2004). Quartz that precipitated synkinematically generated the euhedral crystals with crack-seal texture whereas postkinematic quartz precipitated around the synkinematic quartz after fracture opening had ceased and therefore lacks crack-seal texture, as shown in Figures 9.22a.

Euhedral cores of crack-seal texture can also be encased with micro-scale veneer of quartz lacking crack-seal instead of a euhedral quartz crystal, as is perhaps suggested

in Figure 9.23a, which could also indicate that the quartz around the euhedral core of crack-seal texture is postkinematic (Laubach et al., 2004). However, recent numerical modeling of quartz growth has shown that bridges of synkinematic quartz crystals with the c-axis oriented parallel to fracture opening are likely to develop a thin veneer of synkinematic quartz surrounding the crack-seal texture due to quartz growth parallel to the a or b axes (R. Lander, personal communication, 2006). Regardless of which interpretation is best for the timing of crack-seal-free quartz with respect to fracture opening, both explanations suggest the presence of synkinematic quartz.

Y fractures, like X fractures exhibit dolomite cement. However, Y fractures do not exhibit the euhedral bridges of dolomite commonly shown their X counterparts. Instead, Y fractures exhibit fibrous and translucent dolomite crystals lining both fracture walls and oriented perpendicular to fracture wall (e.g., Figures 9.17 and 9.18). Fibrous dolomite cement commonly lining fracture walls has been interpreted to indicate a fracture opening rate that exceed the rate of synkinematic dolomite growth (Gale et al., 2006), and therefore fibrous lining of dolomite in Y fractures can also be interpreted as synkinematic.

Microfractures of category Y commonly also exhibit bridges of quartz next to bridges of dolomite (e.g., Figure 9.19). Bridges of these two minerals display subhedral edges and without any porosity or mineral precipitated between them, which could indicate simultaneous growth of both minerals (Tucker and Wright, 1999). Simultaneous synkinematic growth of bridges of quartz and dolomite might have impeded quartz from developing euhedral bridges like the ones shown Y macrofractures and shown in Figures 9.18 and 9.20. Because both dolomite and quartz exhibit evidence of independent synkinematic growth (see paragraphs above) simultaneous synkinematic growth could be possible. However, bridges of subhedral quartz next to subhedral bridges of dolomite

could also indicate that one of those two minerals grew synkinematically (developing bridges) whereas the other mineral precipitated postkinematically between bridges of the earlier formed mineral. Petrographic examination of subhedral bridges of dolomite and quartz failed to yield convincing evidence of crack-seal texture (e.g., persistent bands of fluid inclusions), but perhaps SEM/CL imaging could detect crack-seal texture and provide more evidence for dolomite, quartz, or both having synkinematic growth when they develop contiguous subhedral bridges.

Another justification for suspecting the simultaneous synkinematic precipitation of dolomite and quartz inside Y fractures is the characteristics of some solid dolomite inclusions aligned in trails within quartz crystals (e.g., Figures 9.23a and 9.24a). Trails of solid inclusions have been detected to initiate at the boundaries of grain fragments (Ramsay, 1980; Laubach et al., 2004) and also to have sigmoidal patterns in horizontal veins (Hilgers and Urai, 2005). However, trails of solid dolomite inclusions in Y fractures lack both characteristics. Although trails of solid dolomite inclusions are of the same mineral as the rock matrix they do not seem connected to the rock matrix as shown in Figure 9.36 (Figure 5 from Ramsay, 1980) and instead are found only inside euhedral cores of quartz crack-seal texture (e.g., Figures 9.18, 9.21 to 9.24). Some solid inclusions of dolomite in a single trail are in optical continuity (inset, Figure 9.18) and have adjacent sides that match (e.g., concave-convex) as shown by the largest dolomite inclusions in Figure 9.22a, in a pattern similar to the inclusions in trails C_{i2} and C_{i3} of Figure 9.36, whereas other solid dolomite inclusions in trails have inclusions with adjacent sides that do not match (e.g., convex-convex), or exhibit rhombohedral shapes (e.g., Figure 9.23a) or are in contact with each other (Figure 9.24a). An alternative interpretation for the patterns of solid dolomite inclusions exhibited in Y fractures is that solid dolomite inclusions originated from a dolomite crystal in the rock matrix at the initial stages of

syntaxial fracture opening (occurring at fracture center) as suggested by Ramsay (1980), but subsequent opening of the fracture was antitaxial (occurring at fracture walls), which allowed for trails of solid dolomite inclusions to separate from fracture wall. In addition, simultaneous precipitation of synkinematic quartz and synkinematic dolomite allowed for solid inclusions oriented favorable to rapid grow (Ramsay, 1980), which resulted in solid dolomite inclusions developing rhombohedral shapes or colliding into each other to become a single elongated inclusion similar to inclusion trail C_{i4} in Figure 9.36 (e.g., Figure 9.24a). Antitaxial fracture growth was documented in X macrofractures by postkinematic calcite cement precipitating along one fracture wall (e.g., upper wall in Figure 9.20). Although the morphology of some cements in Y fractures is suggestive of what Ramsay and Huber (1983) called composite growth (e.g., Figure 9.17), Y fractures do not exhibit all of the documented characteristics of composite fractures. Namely, there is no median line at the center of Y fractures, or increased fiber width from the center towards walls, two of main indicators of the antitaxial part of a fracture with composite growth, which indicates a complex fracture evolution.

Two additional cements in Y fractures were observed by Monroy-Santiago (in preparation), baroque dolomite and calcite. Monroy-Santiago (in preparation) interpreted baroque dolomite in Y fractures to be synkinematic. However, thin sections analyzed for my dissertation show that baroque dolomite does not exhibit some of the common features associated with synkinematic cements, such as bands of fluid inclusions, crack-seal texture, and bridges (e.g., Figures 9.18 and 9.20), and therefore I cannot conclusively interpret baroque dolomite to be exclusively synkinematic or postkinematic. Finally, calcite cement in Y fractures, like in X fractures, seems to be postkinematic because filled remnant porosity left by earlier euhedral quartz cement (Figure 9.20 and 9.23) and crosscut quartz cement (e.g., Figure 9.22a), and lacks trails or bands of inclusions or any

other evidence of crack-seal texture, which makes likely that calcite cement precipitated after fracture opening ceased, namely, to be postkinematic (Laubach, 2003).

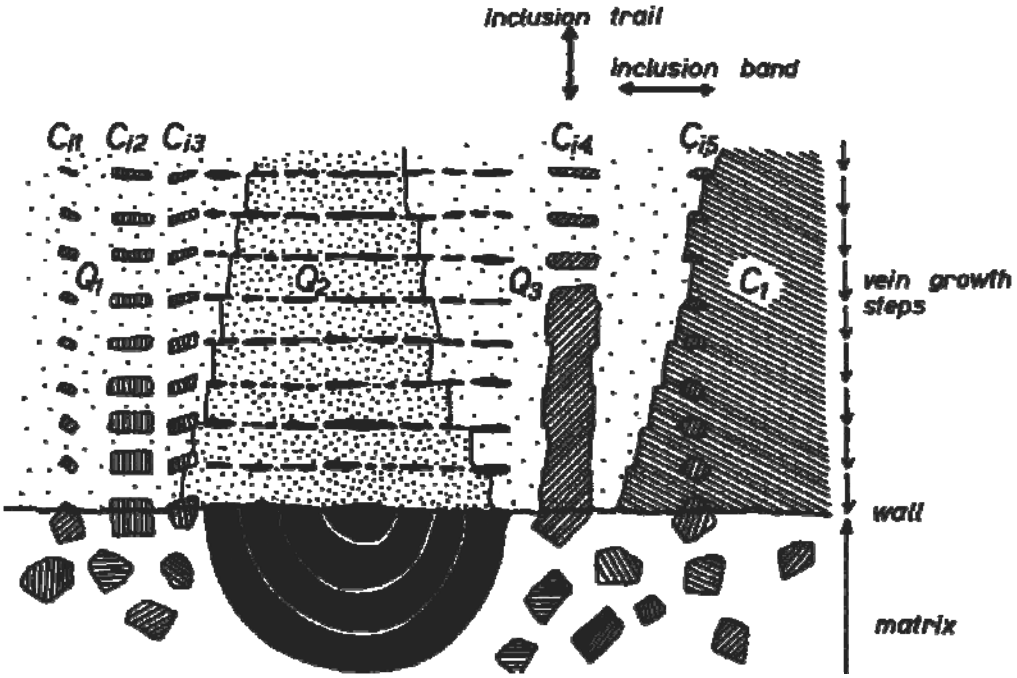

Figure 9.36 Sketch showing the main features of inclusion bands and inclusion trails and bridges of calcite (C, ruled pattern) and quartz (Q, dotted pattern) cement in the Windgällen veins. This sketch illustrates how some trails of solid inclusions remain shape related (adjacent sides match, trails C_{i2} and C_{i3}) whereas others seem to have coalesced into a single inclusion (bottom part of trail C_{i4}). Solid dolomite inclusions associated with crack-seal texture in quartz bridges of Y fractures are organized in trails perpendicular to fracture wall, like the trails displayed in this figure, but trails of inclusions in Y fractures do not exhibit an evident relationship with a grain fragment in rock matrix as the trails in this figure suggest. From Ramsay (1980).

9.3.8 Interpretation of Z Fractures

The study of Z fractures in my dissertation might be hampered by the limited sampling of these fractures. Although Z fractures were detected in only one outcrop of the four outcrops selected for my dissertation (backlimb of San Blas Anticline on Escalera canyon), it is possible that Z fractures are more commonly distributed

throughout the Monterrey salient. Almost invariably, Z fractures display a halo composed of more abundant (compared with rock matrix) dolomite crystals of similar sizes than the surrounding D2 dolomite crystals in matrix (e.g., Figures 9.29a and 9.30). Z fractures also commonly have dolomite cement with a texture similar to the dolomite cement present in the above mentioned halo and lack bridge morphology or bands of fluid inclusions (e.g., Figures 9.29a and 9.30). I interpret the halo surrounding Z fractures to reflect the precipitation of the diagenetic fluids that caused D2 dolomitization in rock matrix, and therefore Z fractures can be interpreted to have developed simultaneous (Syn-D2) with D2 dolomitization. The interpretation of Z fractures as Syn-D2 is also supported by the tortuous trace of Z fractures (Figure 9.30), a likely product of recrystallization around the fracture walls (Gale et al., 2004). Z fractures also exhibit calcite cement which lacks bridge morphology, bands of fluid inclusions and seem to have precipitated in the porosity left after precipitation of dolomite cement (e.g., Figure 9.28 to 9.30) and therefore calcite cement in Z fractures is interpreted to be postkinematic. In addition, Z fractures commonly cross cut Y fractures in the Escalera 1 outcrop (Figure 9.36b), a pattern also observed in thin section, which indicates that Z fractures could postdate Y fractures (e.g., Figures 9.28, 9.29a).

9.3.9 Stratigraphy and the Spatial Arrangement of Opening-mode Fractures

Each fracture category studied here has separate evidence for different diagenetic processes, which was used to suggest timing of fracture cement precipitation with respect to fracture opening and to interpret relative timing with respect to the main dolomitization episode D2. Fractures from each category also exhibit a particular type(s) of spatial arrangement (Table 9.7). Could the stratigraphic position of layers be related in any way to the fracture categories they contain and therefore to the type(s) of spatial arrangement they exhibit? All layers selected for the study on the relationship between diagenesis and

spatial arrangement of fractures are within the platformal facies of the Cupido Fm. All but the three layers in Palmas canyon are within the Cupidito member of the Cupido Fm. However, knowing that layers are from platformal facies and knowing which layers are in the Cupidito member does not establish a relationship between fracture categories and stratigraphic position but perhaps the position of individual layers within parasequences could, as suggested by Ortega (2002) for fracture intensity and dolomite content (Figure 9.37).

Although detailed stratigraphic columns were not measured for my dissertation, they were available for two of the three canyons (Escalera and Palmas) where I conducted research in the spatial arrangement of fractures through the research conducted in recent years by graduate students at the University of Texas at Austin (Ortega, 2002; Monroy-Santiago, in preparation). However, some layers were outside those columns (Palmas 12 and Palmas 13) and therefore their position relative to parasequences is not known. An important difficulty in using parasequences is that the stratigraphic columns were measured and interpreted by different researchers. Palmas canyon and Escalera forelimb were measured by Ortega (2002) where as Escalera backlimb was measured by Monroy-Santiago (in preparation). Since the interpretation of stratigraphic cycles is not an exact science, it is unlikely that Ortega (2002) and Monroy-Santiago (in preparation) would have interpreted exactly the same parasequences and therefore the position of individual layers within parasequences from different researchers should be avoided. Indeed, field examination by Monroy-Santiago (in preparation) of Ortega (2002) stratigraphic columns on Escalera canyon has already shown differences in interpretation of stratigraphic cycles (F. Monroy-Santiago, personal communication, 2002). In addition, the maximum number of layers within parasequences interpreted by the same researcher is 3; Ortega (2002) provided the position within fifth order cycles of Escalera OO1,

Escalera OO12 and Palmas 11 whereas Monroy-Santiago (in preparation) did it for Escalera 1, Escalera 2 and Escalera 3. Therefore, at this time it is not possible to study the relationship between cyclostratigraphy and spatial arrangement of fractures.

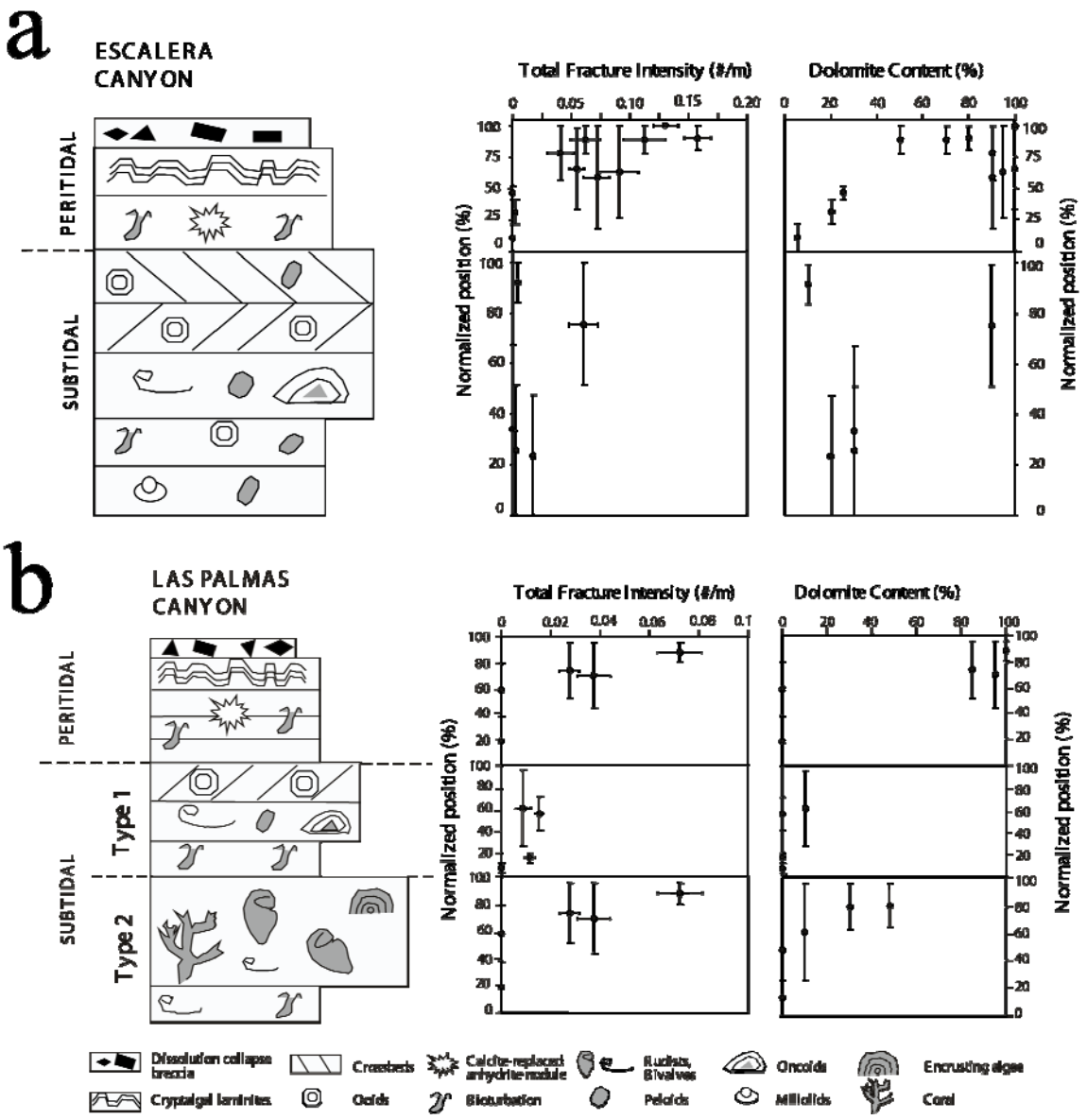

Figure 9.37 Schematic distribution of fracture intensity and degree of dolomitization in peritidal and subtidal parasequences at (a) Escalera and (b) Palmas canyon. Notice the increase in dolomite content and the increase in fracture intensity at the parasequence top. However, Ortega (2002) noted that some sequence stratigraphic cycles do not show this behavior, typically when peritidal facies are absent at the parasequence top. Ortega (2002) explained that two kinds of subtidal cycles are present at Las Palmas locality: subtidal cycles capped by grainstone shoal deposits, and subtidal cycles capped by bioherms or bivalve banks.Fracture intensity was calculated as the total number of fractures with aperture larger than 0.2 mm per meter of scanline. From Ortega (2002). Type cycles after Goldhammer et al. (1991).

9.4. DATA SETS

The previous section of Chapter 9 presented the diagenetic evidence that supports fracture categorization. The following section presents the quantitative characteristics, with emphasis in the spatial arrangement, of the selected data sets (Table 9.1). By examining the characteristics of fractures on thin sections from all layers, fracture sets of each layer were interpreted to belong to one of the two fracture categories (X or Y) described earlier (Table 9.4).

9.4.1 Fracture Categories in Rock Samples

There are at least three possible explanations about the presence of only one fracture category (X, Y and Z, as defined earlier) in thin sections from layers with cross-sectional outcrop (Table 9.4). The only layer exhibiting fractures from different categories (Escalera 1) has a bedding-parallel exposure (Table 9.1). One possible explanation is that only Escalera 1 layer exhibits a particular characteristic that allowed different fracture categories to develop. However, no single attribute of Escalera 1 such as lithology (dolopackstone), layer thickness (30.5 cm), or percentage of D2 dolomite (90%) is particularly different from the attributes of all other layers (Table 9.5), and therefore there is no known reason for Escalera 1 layer to be the only layer with fractures from different categories.

Another possible explanation is that the difficulties in obtaining rock samples from polished outcrops limited not only the size and abundance of rock samples (Chapter 2) but also how representative are the fractures present in those rock samples. However, rock samples from five (Escalera OO1, Escalera OO12, Huasteca, Palmas 12, and Palmas 13) of the eight layers included in Table 9.1 were large enough to generate groups of thin sections suitable for quantification of the spatial arrangement of microfractures (Chapters 5 and 8), and yet only fractures from one category were found in them.

Table 9.4 Fracture category (X or Y) for all sets (each set with a characteristic fracture orientation) in layers of the Cupido Fm. N.A. = Not Available, which indicates fracture sets that were not sampled.

Outcrop Data Set	Set(s)	Fracture Category (X or, Y)	Photomicrographs
Escalera OO1	A, B	Y	9.14, 9.17, 9.18, 9.20, 9.21, 9.22, 9.23, 9.24, 9.26, 9.27
	C, D	N.A.	
Escalera OO12	A, B	Y	9.25, 9.31b
Escalera 1	A, D	Y	9.28, 9.29c
	B, C	Z	9.28
Escalera 2	B	N.A.	
	C	Z	
Escalera 3	A	Y	9.15, 9.16b, 9.16c, 9.29a, 9.29b, 9.30
Huasteca	A, B	Y	
	C, D	N.A.	
Palmas 11	A, B, C	Y	9.16a, 9.19, 9.31a
Palmas 12	A, B	X	9.6, 9.7, 9.9a, 9.11
Palmas 13	A, B	X	9.2, 9.8, 9.10, 9.12, 9.13

A third explanation for the lack of fractures from different categories in layers with cross-sectional exposure is that outcrop orientation favored observation and sampling of some fracture sets in detriment of less-favorably oriented fracture sets. Fractures oriented orthogonally with respect to the outcrop have a higher probability of

being observed. In addition, fractures with different orientations on a bedding parallel plane but same angle with respect to bedding (typically 90˚) cannot be distinguished on the basis of their orientation on a cross-sectional exposure alone. If a fracture set that is not favorably oriented for cross-sectional exposure has different diagenetic evidence (and therefore can be assigned to a different fracture category, as defined earlier) than a fracture set favorably oriented, then, it is probable that fractures from the earlier set remained unnoticed, and therefore scanline measurements and sampling were designed to study only the latter set.

Most likely, however, there is not a single explanation about why only fractures from one category were observed in rock samples from layers with cross-sectional exposure. Some layers perhaps have only fractures with same diagenetic evidence whereas other layers have fractures from more than one category but they remained undetected due to unfavorable exposure. Finally, there is no reason to believe that the geological processes that allowed the layer Escalera 1 to develop more than one fracture category are limited to that layer exclusively.

9.4.2 Quantitative Characterization

Traditional techniques for the analysis of fracture spacings such as average and cumulative frequency distributions (Chapter 6; Gomez and Marrett, in review) have been used to detect differences or similarities between fracture sets in a single layer or an individual geologic body. For instance, three of the four sets of fractures (each one with its own distinctive orientation) measured by Wines and Lilly (2002) display a negative exponential distribution of fracture spacings and yet their average spacing in a direction perpendicular to fracture set orientation differs up to more than 100%. However, it is difficult to detect common features on the nine data sets selected for the study about different fracture events and the spatial arrangement of fractures that allows for a

categorization (Table 9.5). For instance, all but one (Huasteca) data set exhibit a power-law distribution of fracture apertures (Table 9.5). On another example, both the Escalera 3 (Y fractures) and the Palmas 13 (X fractures) data sets exhibit a negative exponential distribution of fracture spacings and yet they have the largest (103.5 mm) and close to smallest (40.56 mm), average spacing for fractures with apertures equal or larger than 0.95 mm, respectively (Table 9.5). In addition, the different scanline lengths and aperture thresholds does not allow for a reliable comparison between some data sets. For instance between the Escalera OO12 data set (3.56 m of scanline, aperture threshold of 0.05 mm) and the Palmas 11 LR (21.11 m of scanline, aperture threshold of 0.95 mm).

But even if some pattern were established using traditional techniques of quantifying fracture spacing, those traditional techniques are unable to distinguish different spatial arrangements (Chapter 6; Gomez and Marrett, in review) and therefore differences or similarities between different sets of fractures established by traditional techniques may be deceiving. For instance, veins of sets A and D of the Escalera 1 outcrop data set have average spacings that differ about 400% (41 mm for set A and 160 mm for set D) and yet they display the same spatial arrangement of fractures inside (fractal, Table 9.6) and between clusters (periodic, Table 9.6). In contrast, sets A and B of the same outcrop data set have average spacings that differ only 15 % (35 mm for set B) and yet they have different spatial arrangements inside and between clusters (random for set B, Table 9.6).

Table 9.5 Quantitative attributes of selected fracture data sets selected for this study. Cumulative frequency distributions (e.g., power-law, negative exponential, etc.) were selected based on the best coefficient of determination. A perfect distribution has a R^2 coefficient of one and a χ^2 coefficient of zero. * = including fractures with apertures smaller than threshold.

Outcrop data sets	Escalera OO1	Escalera OO12	Escalera 1	Escalera 2	Escalera 3
Layer Thickness (cm)	80	24.5	30.5	18	89
Percentage D2 dolomite in matrix	100	95	90	90	85
Number of Fractures	1160*	1095*	460	614*	293
Length of Scanline (m)	3.20	3.56	7.03	6.15	6.93
Fracture Strain (%)	13.29	20.44	7.02	7.73	4.46
Aperture Threshold (mm)	0.05	0.05	0.05	0.05	0.095
Maximum Aperture (mm)	48	64	17	31	17.2
Range of Fracture Aperture (orders of magnitude)	3	3.1	2.5	2.8	2.2
Cumulative Frequency Distribution of Apertures (fractures/mm)	Power-law $y = 0.028\ b^{-1.24}$	Power-law $y = 0.028\ b^{-0.97}$	Power-law $y = 0.02\ b^{-1.3}$	Power-law $y = 0.015\ b^{-1.08}$	Power-law $y = 0.009\ b^{-0.85}$
Chi square (χ^2)	0.112	0.146	0.024	0.092	0.027
Range of Fracture Spacings (mm, orders of magnitude)	0.062 – 252* 3.6*	0.05 – 37.0* 2.8*	0.265 – 131.5 2.9	0.05 – 70* 3.2*	0.115 – 173 2.9
Average Fracture Spacing (mm)	2.43*	2.82*	14.27	9.29*	22.66
Coefficient of Variation	3.50*	1.33*	1.23	1.00*	1.30
Cumulative Frequency Distribution of Spacings (R^2)	Power-law* 0.988	Logarithmic* 0.941	Negative exponential 0.961	Negative exponential 0.989	Negative exponential 0.985
Average Spacing for fractures with apertures ≥ 0.95 mm (mm)	38.5	39.8	53.6	58.5	104

Continuation Table 9.5

Outcrop data sets	Huasteca		Palmas 11 LR	Palmas 12	Palmas 13
Layer Thickness (cm)	70		27	47	24
Percentage D2 dolomite in matrix	100		65	65	95
Number of Fractures	1160*		1095*	460	614*
Length of Scanline (m)	16.59		21.11	6.14	5.43
Fracture Strain (%)	7.15		4.59	12.70	9.16
Aperture Threshold (mm)	0.215		0.95	0.265	0.14
Maximum Aperture (mm)	53		42	60	12
Range of Fracture Aperture (orders of magnitude)	2.3		1.6	2.4	1.9
Cumulative Frequency Distribution of Apertures (fractures/mm)	Log-normal	Power-law $y = 0.12\ b^{-2.1}$	Power-law $y = 0.015\ b^{-1.2}$	Power-law $y = 0.04\ b^{-1.2}$	Power-law $y = 0.022\ b^{-0.7}$
Chi square (χ^2)		0.260	0.089	0.098	0.101
Coefficient of Determination (R^2)	0.9884				
Range of Fracture Spacings (mm, orders of magnitude)	0.4 – 242 2.8		0.075 – 806 4.1	0.215 – 109.5 2.9	0.175 – 66.5 2.5
Average Fracture Spacing (mm)	23.54		76.73	17.2	10.85
Coefficient of Variation	1.23		1.72	1.07	0.93
Cumulative Frequency Distribution of Spacings (R^2)	Log-normal 0.994		Log-normal 0.981	Negative exponential 0.995	Negative exponential 0.998
Average Spacing for fractures with apertures ≥ 0.95 mm (mm)	50.7		80.6	43.2	40.6

To select the cumulative frequency distribution of fracture apertures and spacings for each data set, four types of distributions (linear, logarithmic, negative exponential and power law) were generated with Microsoft Excel® software and the distribution with the largest coefficient of determination R^2 (indicating how closely the estimated values of the distribution are to the data; Burt and Barber, 1996.) was selected as the distribution that closest represent the cumulative frequency data (Table 9.4). In addition, the coefficient of determination R^2 of a log-normal distribution was independently generated for each fracture attribute using a custom-designed Excel® spreadsheet (R. Marrett, personal communication, 2004). If a power-law distribution exhibited the largest R^2 coefficient, then another custom-designed Excel® spreadsheet was used to estimate a power-law equation that takes into account the truncation and censoring effects commonly present at the lower and upper ends of the cumulative frequencies of fracture attributes (R. Marrett, personal communication, 2003).

All the data sets selected for this chapter have information about fracture orientation (Table 9.3). Typically, fracture sets were determined in the field by measuring the different fracture orientations before scanline data was acquired and noting the angle between the scanline and the representative fracture orientation of each set. When the aperture of a fracture was measured, this fracture was assigned to one of the already determined fracture sets based on the fracture orientation and/or the angle between the fracture and the scanline. To test whether fractures of different sets (each set containing fractures with a common orientation) have different spatial arrangements, independent analysis of the spatial arrangement of each set was conducted using NCC (Chapter 6 Marrett et al., in review). Only spatial arrangements of distinct fracture sets within a single layer (as defined in Table 9.3) that differ among themselves will be shown. If an outcrop data set exhibits the same spatial arrangement for individual fracture sets and also

for all fracture sets combined, only the spatial arrangement for all fractures combined will be shown. One exception are the fractures of sets B and D of Huasteca layer because the number of fractures on each set (17 and 4, respectively) are likely too small to generate meaningful results of NCC. However fractures of sets B and D of Huasteca were combined on a single analysis. Another exception is the Escalera 3 data set because all other data sets analyzed in this chapter contain fractures of more than one orientation. For the Escalera 3 data set only fractures of one orientation (Set A, Table 9.3) were measured in the field, and fractures of all other orientations were ignored. Finally, unless otherwise stated, all NCC analysis were conducted on outcrop data sets using the entire scanline available, 100 randomized versions (altered positions) and 400 graduations of length scale with the maximum length scale approximately equal to the scanline length.

9.4.3 Layer 1 at Escalera Canyon (Escalera 1)

The Escalera 1 layer is located in the backlimb of San Blas anticline exposed in the Escalera canyon (Figure 2.7). Unlike all other outcrop data sets measured in the Cupido Fm., the Escalera 1 data set was measured in an outcrop surface that is parallel to bedding (Figure 9.38). Compared with a cross-section outcrop, a bedding-parallel outcrop greatly facilitates classification of fractures into different sets (Figure 9.39, Table 9.3). Escalera 1 is 30.5 cm thick, and is located 135 m below the top of the stratigraphic column measured at the backlimb of the San Blas Anticline by Monroy-Santiago (in preparation). Lithologically, the Escalera 1 layer is a dolopackstone. Using an aperture threshold of 0.05 mm, I measured 460 veins in a scanline of approximately 7 m, and recorded a strain of 7% (Figure 9.40, Table 9.5). Fractures of the Escalera 1 outcrop data set exhibit a power-law distribution of fracture apertures, a negative exponential distribution of fracture spacings, and a coefficient of variation of fracture spacing of 1.23 (Table 9.5). Each fracture was assigned to one of the four sets based on orientation

(Figures 9.38 and 9.39, Table 9.3). 34% of the measured fractures represent set A, 40% represent set B, 18% represent set C, and 8% represent set D (Table 9.3).

In addition to having distinctive orientations, fracture sets of Escalera 1 also display different characteristics at outcrop scale and were assigned to different fracture categories. For instance, fractures of set D seem to consist of coalesced echelon fractures of set A (Figure 9.41a) and exhibit small amounts of shear displacement, with fractures of both sets A and D exhibiting the typical characteristics of Y fractures such as a straight trace, bridges of subhedral dolomite and subhedral quartz approximately perpendicular to fracture wall (Table 9.4). In addition, fractures of sets C commonly abut against fractures of set B and vice versa (Figure 9.42), which suggests that both sets are contemporaneous. Fractures of sets B and C crosscut fractures of sets A and D (Figures 9.28 and 9.41a), which indicates that sets B and C are younger. Fractures of sets B and C exhibit the typical characteristics of Z fractures (Table 9.4) such as a halo around each fracture (Figure 9.28), an irregular trace, dolomite cement in small crystals with texture similar to D2 dolomite in matrix, and abundant calcite cement (e.g., Figure 9.28).

Qualitative examination of variation of aperture and fracture intensity along the scanline indicates a heterogeneous arrangement of fractures (Figure 9.40). Spatial correlation for fractures of all four sets combined varies as a power law with length scale (Figure 9.43a), which indicates a fractal arrangement of fractures inside clusters (Figures 9.4b). However, the fractal spatial arrangement is barely statistically significant because the power law pattern is almost horizontal (slope of 0.06) and is scarcely larger than the 95% confidence interval (Figure 9.43a). Although the graph of spatial correlation for linearly graduated length scales for the same data displays peaks outside the 95% confidence interval (at length scales of 2500 and 3700 mm, Figure 9.43b), the pattern of spatial correlation cannot be interpreted as a periodic arrangement of fracture clusters

(Figure 9.4e) because peaks do not occur at length scales representing multiples of the first peak (cluster spacing, Chapter 6). However, the power spectrum of spatial correlation for linearly graduated length scales exhibits a peak outside the 95% confidence interval for red noise at a wavelength of 3434 mm, which indicate that periodic arrangement of clusters with cluster spacing of approximately 3434 mm is statistically significant (Figure 9.43c).

Fracture sets of Escalera 1 layer exhibit different orientations (Table 9.3) and characteristics (Figures 9.41 and 9.42) and therefore the spatial arrangement of each set should be studied separately. When analyzed independently, fracture sets display different spatial arrangements. Spatial correlation for fractures of set A varies as a power-law of length scale (Figure 9.4b), which indicates a fractal arrangement of fractures inside clusters with a cluster width of approximately 400 mm (Figure 9.44a). Spatial correlation shows one broad peak that is centered at a length scale of approximately 3100 mm (Figure 9.44b), which could indicate a periodic arrangement of fracture clusters (Figure 9.4g). To be certain that a pattern of spatial correlation with linearly graduated length scales indicates a periodic arrangement of clusters, more than one peak at length scales multiple of the first peak is needed (Figure 9.4g), and therefore the spatial arrangement of clusters of set A is indeterminate. Power spectrum of the spatial correlation for linearly graduated length scales exhibits a noticeable peak at a wavelength of 3217 mm outside the 95% confidence interval for red noise, which suggests that the periodic arrangement of fracture clusters indicated by spatial correlation is statistically significant (Figure 9.44c).

Like with fractures of set A, spatial correlation for logarithmically graduated length scales of set D fractures also varies as a power-law of length scale (Figure 9.45a), which indicates a fractal arrangement of fractures inside clusters (Figure 9.4b). However,

the cluster width of set D fractures is approximately 110 mm (Figure 9.45a). Spatial correlation for linearly graduated length scales of set D fractures show several peaks, some of which are outside the 95% confidence interval (Figure 9.45b). Peaks of spatial correlation for fractures of set D appear to be every 530 mm (Figure 9.45b), which indicate a periodic arrangement of clusters (Figure 9.4g) with a cluster spacing of 530 mm. Power spectrum of the spatial correlation for linearly graduated length scales exhibits a peak outside the 95% confidence interval for red noise at a wavelength of 528 mm, which confirms that the periodic arrangement of fracture clusters indicated by spatial correlation is statistically significant (Figure 9.45c). Close inspection of the position of fractures of set D along scanline shows clusters located that contain smaller clusters spaced 530 mm apart (Figure 9.46).

Spatial correlation for logarithmically graduated length scales of sets B and C fractures (analyzed independently) yield no recognizable pattern outside the 95% confidence interval (Figures 9.47a and 9.48a respectively), which are interpreted to indicate spatial arrangements indistinguishable from random (Figure 9.4a). Spatial correlation for linearly graduated length scales of sets B and C fractures (analyzed independently) also yield no recognizable pattern outside the 95% confidence interval (Figures 9.47b and 9.48b respectively), which are also interpreted to indicate spatial arrangements indistinguishable from random (Figure 9.4e). Power spectrum of spatial correlation for linearly graduated length scales of sets B and C follow the trend of the 95% confidence interval for red noise (Figures 9.47c and 9.48c respectively) without noticeable peaks outside the 95% confidence interval. Although the power spectral densities of both sets B and C exhibit a peak outside the 95% confidence interval (489 and 2118 mm, Figures 9.47c and 9.48c respectively), both peaks are small when compared with other data sets.

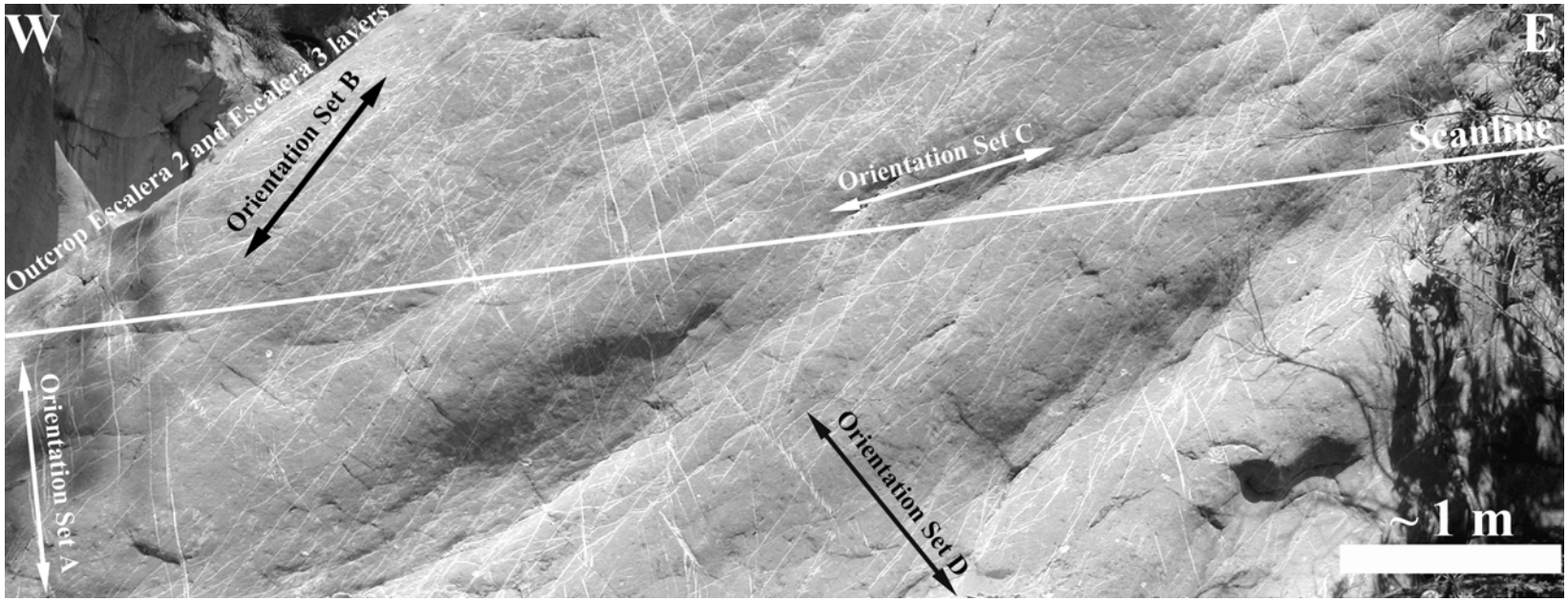

Figure 9.38 Photograph of the bedding plane outcrop along which the Escalera 1 data set was measured. White line indicates location of scanline. Four fracture sets (A, B, C, and D), each one with a distinctive orientations (Table 9.3) can be recognized. The average orientation in outcrop for each set is highlighted with an arrow. The name of each fracture set only reflects the order in which they were measured. On the upper left corner the position of outcrop of layers Escalera 2 and Escalera 3 is highlighted.

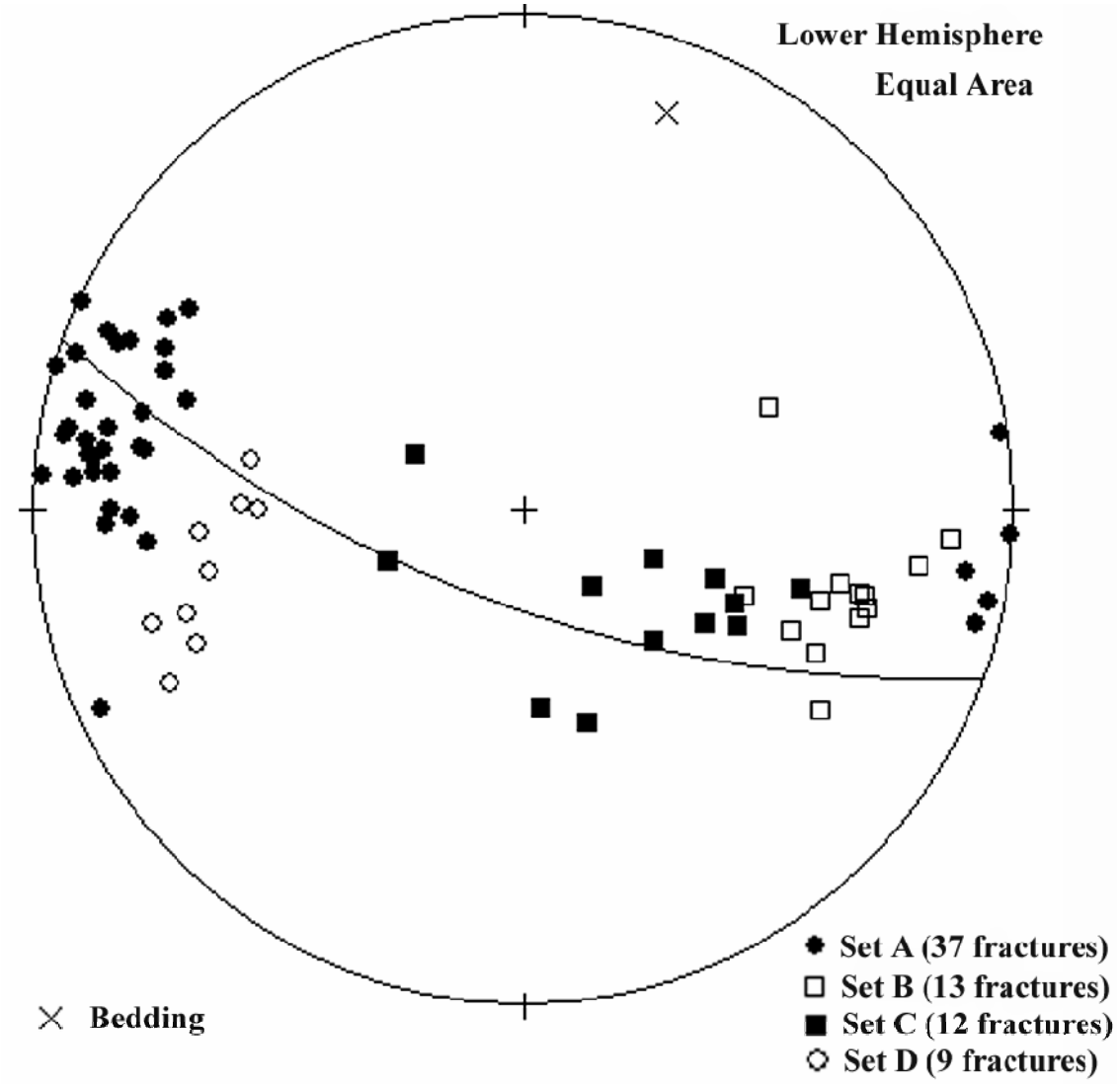

Figure 9.39 Equal area stereographic projection of bedding and poles to fractures for all four fracture sets on layer Escalera 1. The name of each fracture set does not indicate relative timing of fracture development; it only reflects the order in which they were measured.

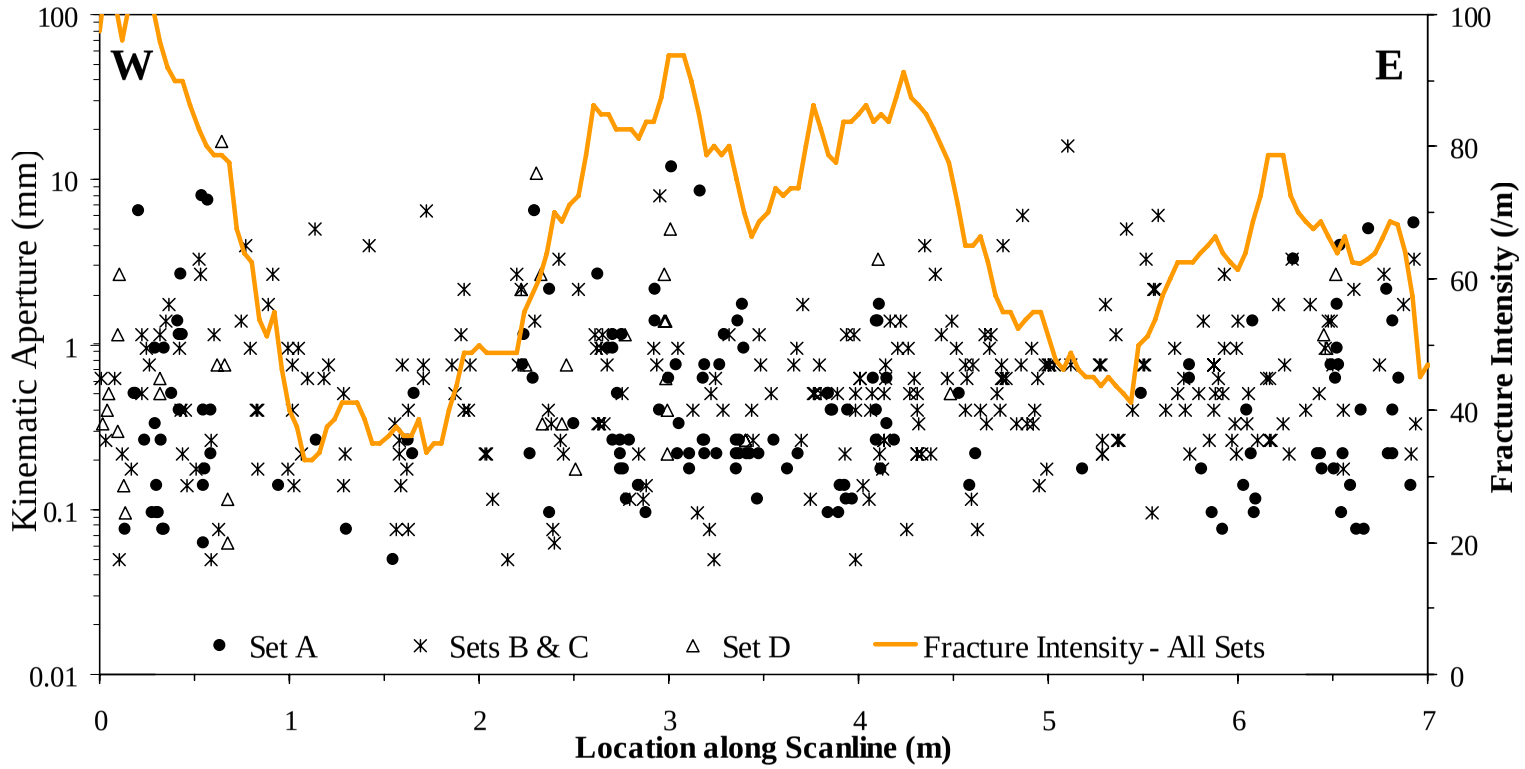

Figure 9.40 Kinematic aperture (circles for set A, asterisks for sets B and C, and triangles for set D) and fracture intensity (thick orange line) versus location along scanline for the Escalera 1 data set. Note that kinematic aperture axis use logarithmic graduations. Fracture intensity for fractures of all four sets was calculated inside a moving window with width (window size) of 0.4 m that was moved in increments (window step) of 0.04 m. Fractures of sets A (filled circles) and D (empty triangles) seem more heterogeneously arranged than fractures of sets B and C (asterisks). Most fractures of sets A and D are located in clusters (high values of fracture intensity) centered at 0.5, 3.5 and 6.5 m along the scanline.

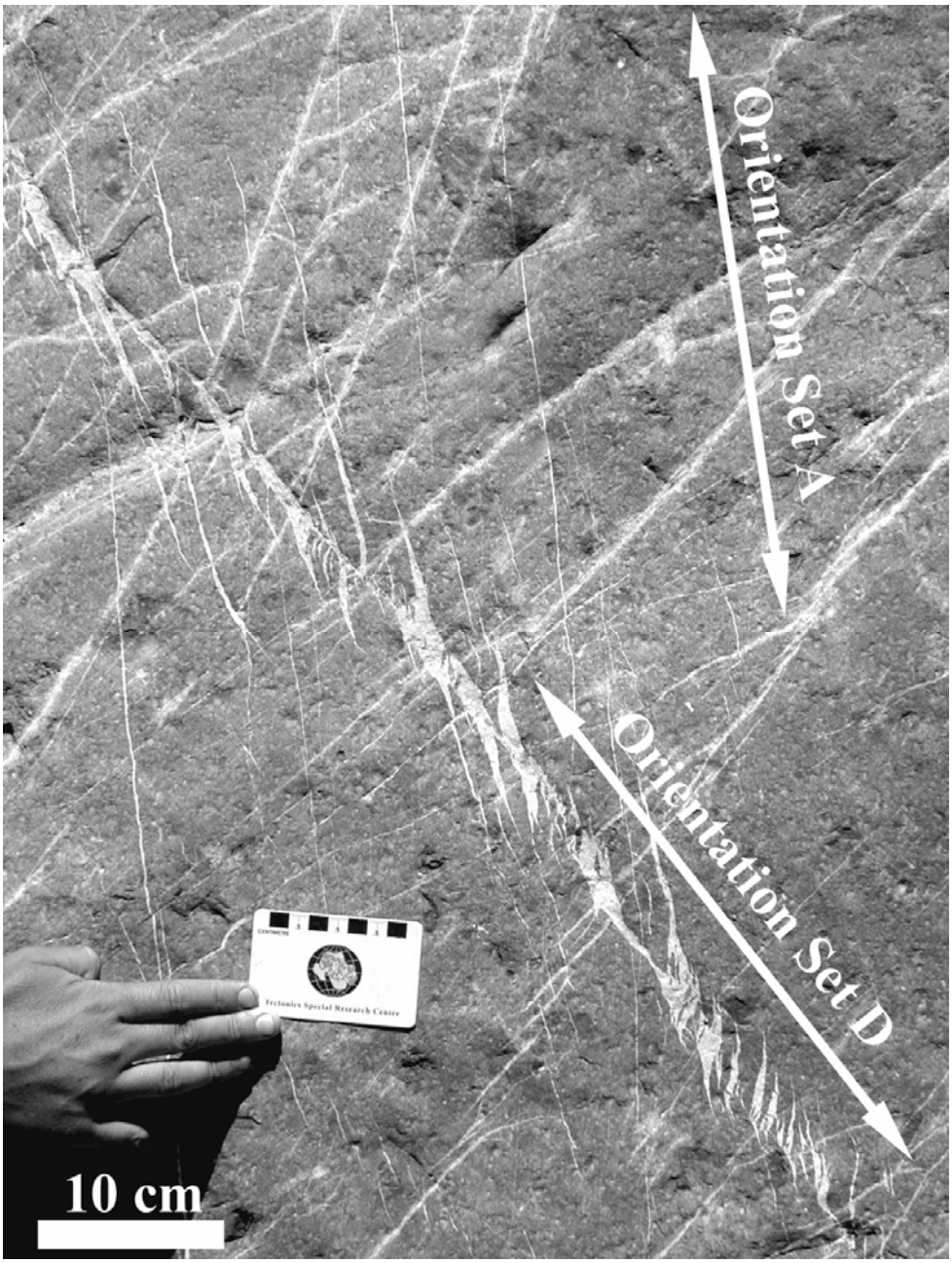

Figure 9.41 Photograph of Escalera 1 outcrop depicting a fracture of set D. Fractures of set D seem to consist of coalesced echelon arrays of fractures of set A.

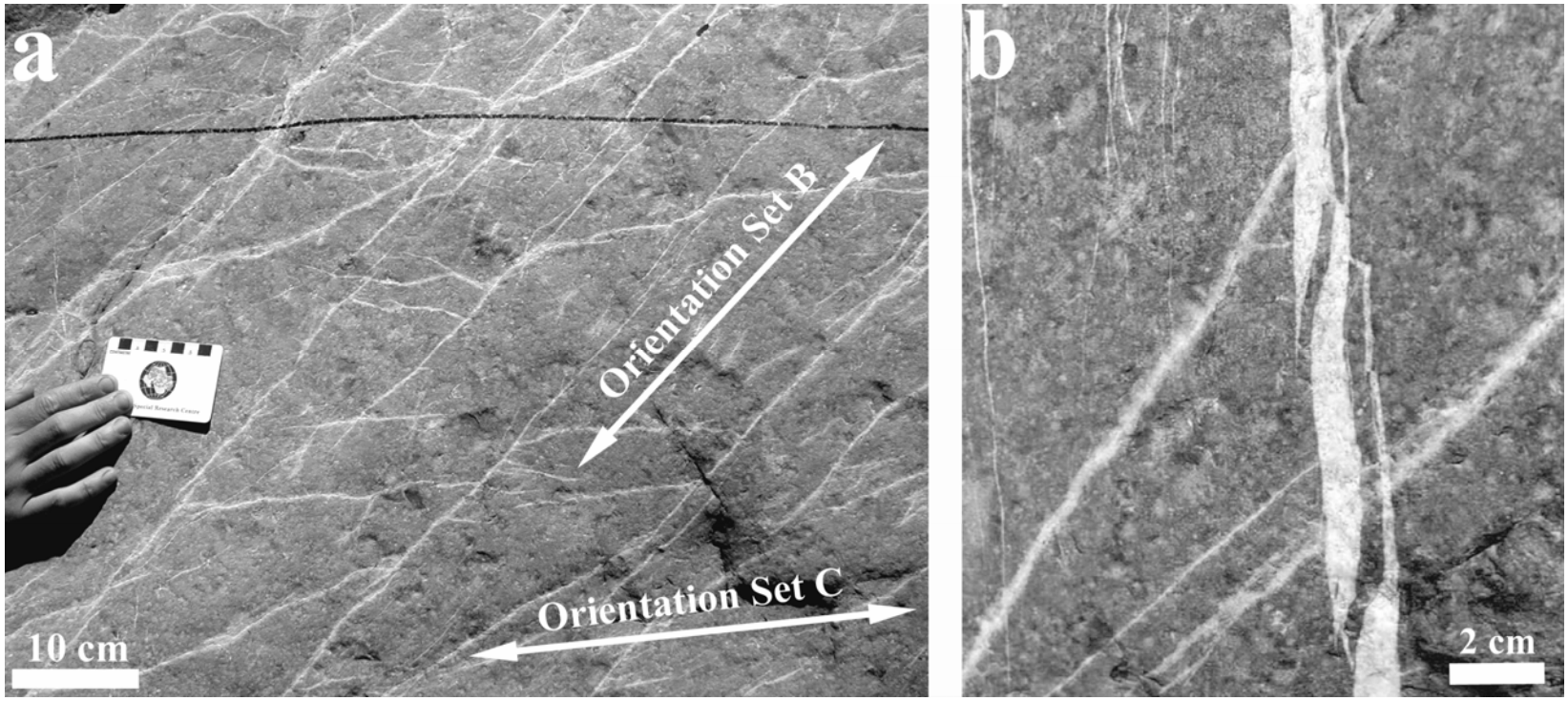

Figure 9.42 (a) Photograph of Escalera 1 outcrop depicting several fractures of sets B and C. (b) Detailed photograph of fractures of Set A (vertical) and Set B (diagonal). Note in (a) how fractures of set C commonly abut in fractures of set B. Note in (b) the halo that fractures of sets B and C commonly display is absent around fractures of set A. In addition, fracture geometries in (b) seem to indicate that fractures of set B crosscut fractures of set A.

Figure 9.43 Graphs of spatial correlation vs. length scale (thick continuous line) for (a) logarithmic graduations and (b) linear graduations for fractures of all four fracture sets combined of the Escalera 1 outcrop data set (460 fractures, aperture threshold = 0.05 mm). In (a) and (b), the thin discontinuous line represents the upper 95% confidence limit while the thin dotted line represents the lower 95% confidence limit, and the thick discontinuous line corresponds to the mean of 100 randomized data sets. In (a) and (b) the thin continuous line represents the analytical solution of randomly arranged fractures with the same number of fractures and scanline length. Width of length-scale bin in (a) and (b) is 11 graduations of length scale (m = 5). A power-law pattern of spatial correlation in (a) indicates a fractal arrangement of fractures with a cluster width of approximately 400 mm. Although it may look that the power-law distribution in (a) follows a straight line, in fact it follows a convex line. There are two peaks of spatial correlation outside the 95% confidence interval (2500 and 3050 mm) in (b). (c) Power spectrum of spatial correlation from (b). A peak of power spectral density at 3434 mm in (c) is outside the 95% confidence interval for red noise, which indicates a periodic arrangement of fracture clusters that is statistically significant and has a cluster spacing of 3434 mm.

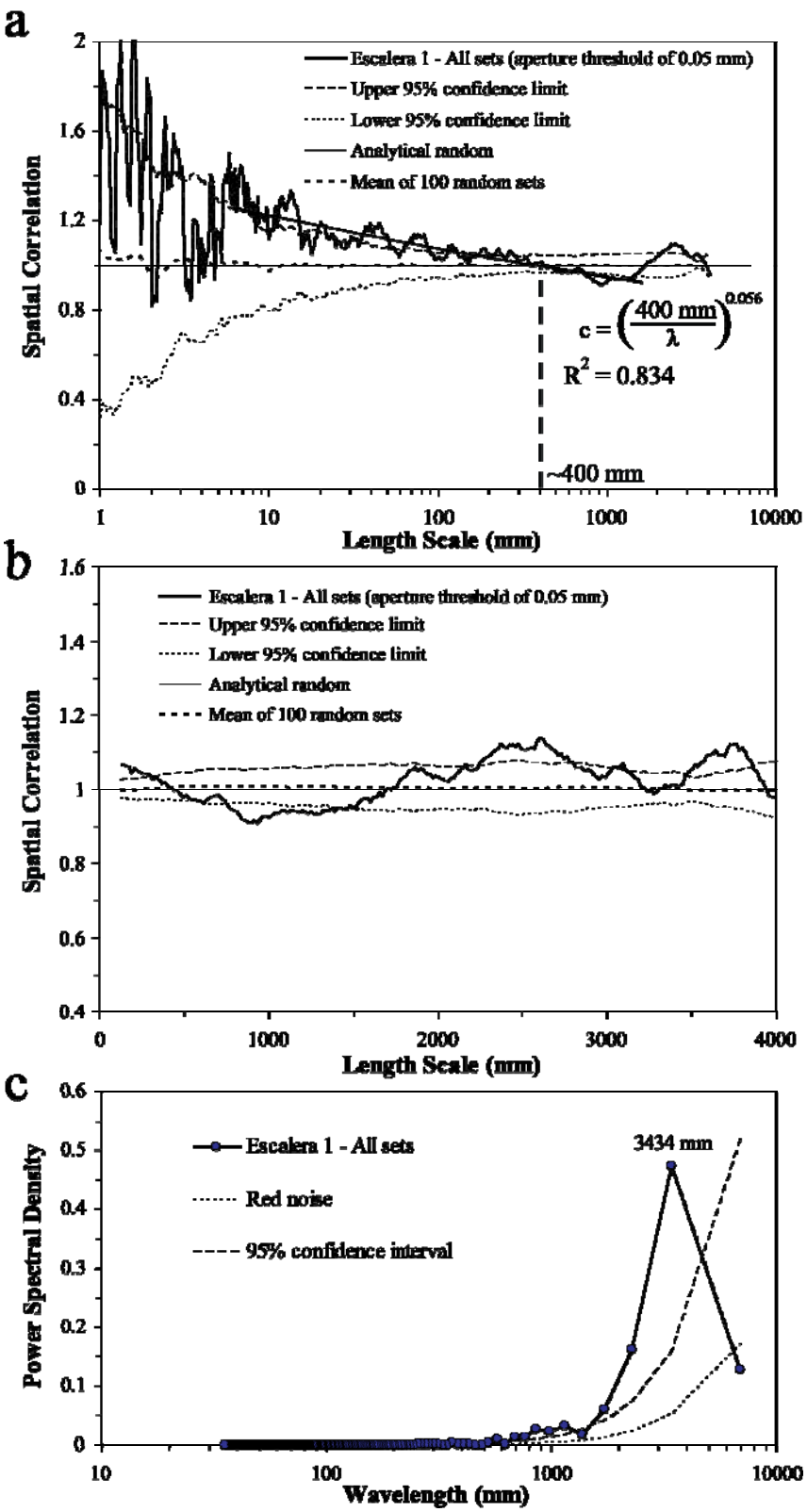
a
Escalera 1 - All sets (aperture threshold of 0.05 mm)
Upper 95% confidence limit
Lower 95% confidence limit
Analytical random
Mean of 100 random sets
Spatial Correlation
$c = \left(\frac{400\ mm}{\lambda}\right)^{0.056}$
$R^2 = 0.834$
~400 mm
Length Scale (mm)
b
Escalera 1 - All sets (aperture threshold of 0.05 mm)
Upper 95% confidence limit
Lower 95% confidence limit
Analytical random
Mean of 100 random sets
Spatial Correlation
Length Scale (mm)
c
Escalera 1 - All sets
Red noise
95% confidence interval
3434 mm
Power Spectral Density
Wavelength (mm)

Figure 9.44 Graphs of spatial correlation vs. length scale (thick continuous line) for (a) logarithmic graduations and (b) linear graduations for fractures of set A of the Escalera 1 outcrop data set (156 fractures, aperture threshold = 0.05 mm). In (a) and (b) the thin discontinuous line represents the upper 95% confidence limit while the thin dotted line represents the lower 95% confidence limit, and the thick discontinuous line corresponds to the mean of 100 randomized data sets. In (a) the thin continuous line represents the analytical solution of randomly arranged fractures with the same number of fractures and scanline length. In (b) the thin continuous line represents an example randomized set generated with the same number of fractures and scanline length. Width of length-scale bin in (a) and (b) is 11 graduations of length scale (m = 5). A fractal arrangement of fractures with a cluster width of approximately 400 mm is detected in (a). A periodic arrangement of clusters could be interpreted in (b) but more than one peak of spatial correlation is needed to confirm it. Cluster spacing is estimated in (b) at 3100 mm. (c) Power spectrum of spatial correlation from (b). Peak of power spectral density at a wavelength of 3217 mm in (c) is several times the power spectral density for the 95% confidence interval for red noise, indicating a non-random periodic arrangement of fractures with a cluster spacing of 3217 mm.

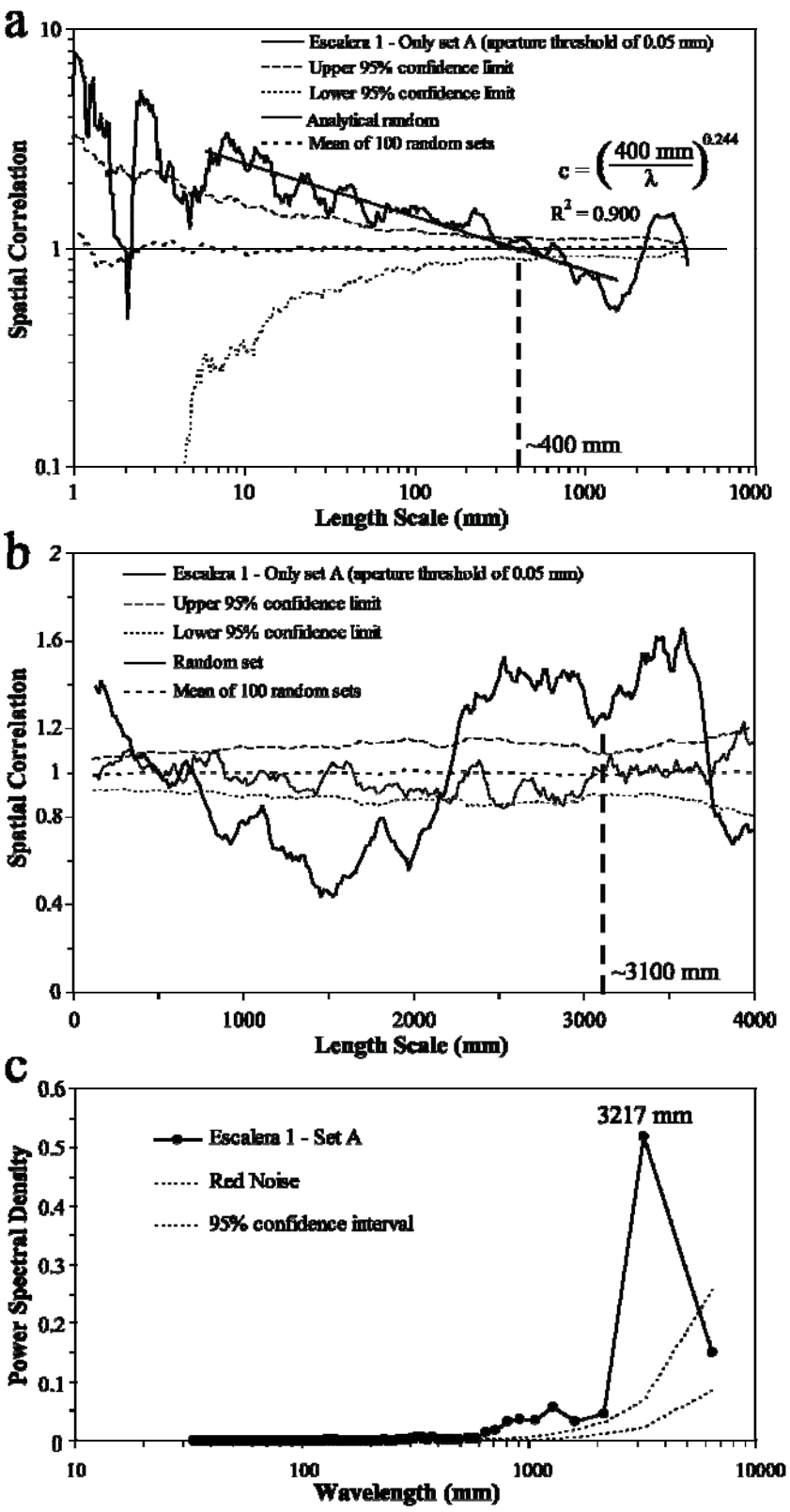
a
Escalera 1 - Only set A (aperture threshold of 0.05 mm)
Upper 95% confidence limit
Lower 95% confidence limit
Analytical random
Mean of 100 random sets
$c = \left(\frac{400\ mm}{\lambda}\right)^{0.244}$
$R^2 = 0.900$
~400 mm
Spatial Correlation
Length Scale (mm)
b
Escalera 1 - Only set A (aperture threshold of 0.05 mm)
Upper 95% confidence limit
Lower 95% confidence limit
Random set
Mean of 100 random sets
~3100 mm
Spatial Correlation
Length Scale (mm)
c
3217 mm
Escalera 1 - Set A
Red Noise
95% confidence interval
Power Spectral Density
Wavelength (mm)

Figure 9.45 Graphs of spatial correlation vs. length scale (thick continuous line) for (a) logarithmic graduations and (b) linear graduations for fractures of set D of the Escalera 1 outcrop data set (38 fractures, aperture threshold = 0.05 mm). In (a) and (b) the thin discontinuous line represents the upper 95% confidence limit while the thin dotted line represents the lower 95% confidence limit, and the thick discontinuous line corresponds to the mean of 100 randomized data sets. In (a) the thin continuous line represents the analytical solution of randomly arranged fractures with the same number of fractures and scanline length. Width of length-scale bin in (a) and (b) is 11 graduations of length scale (m = 5). A power-law pattern of spatial correlation in (a) indicates a fractal arrangement of fractures with a cluster width of approximately 110 mm. Peaks of spatial correlation are approximately evenly spaced every 530 mm (thick dashed lines), as shown in (b), an indication that clusters are periodically arranged with a cluster spacing of 530 mm. Four of the seven peaks of spatial correlation in (b) are outside the 95% confidence interval. (c) Power spectrum of spatial correlation from (b). Although two peaks of power spectral density are visible in (c), only the peak at 528 mm is outside the 95% confidence interval for red noise, indicating a non-random periodic arrangement of fractures with a cluster spacing of 528 mm.

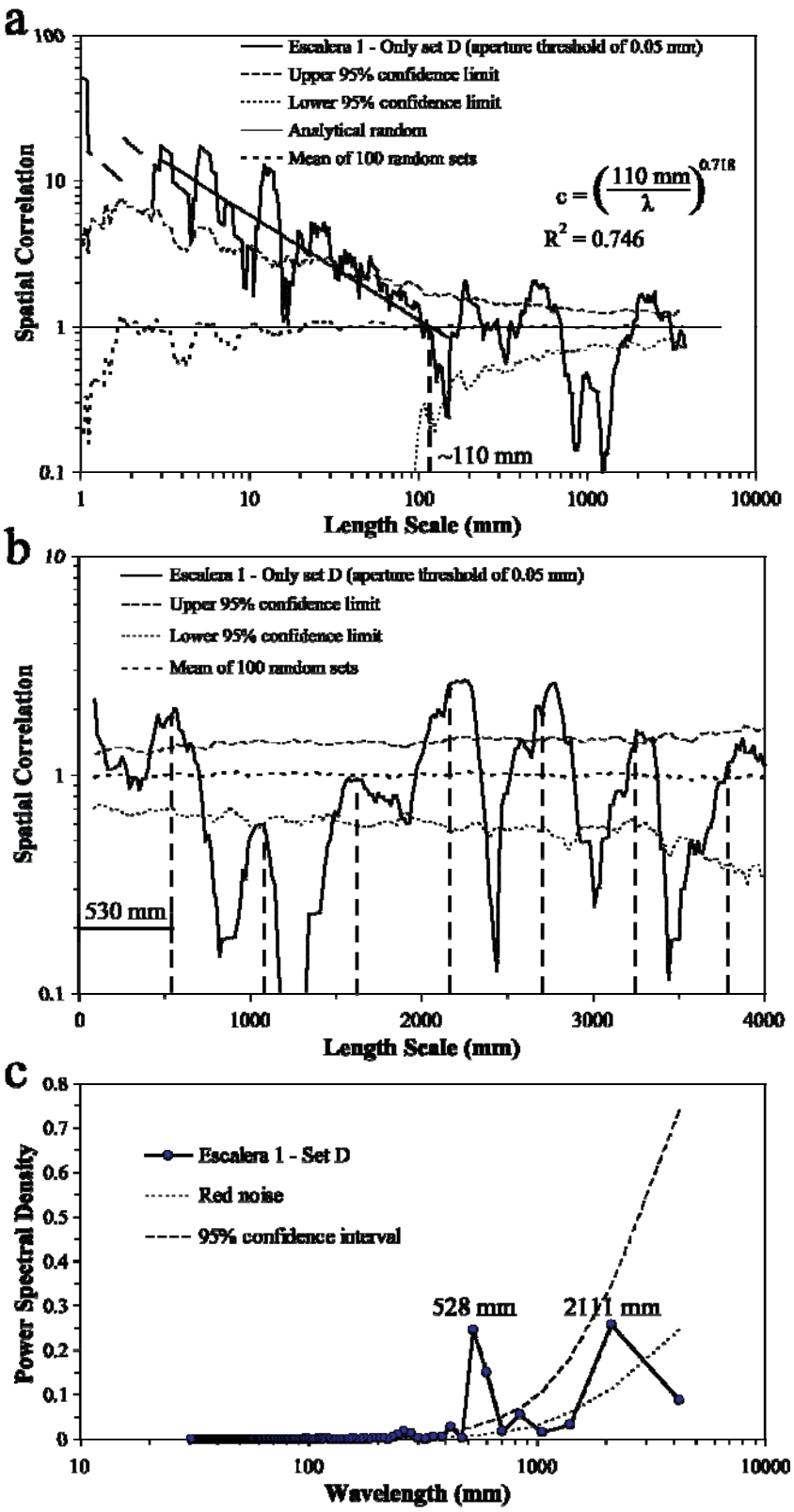
a
Escalera 1 - Only set D (aperture threshold of 0.05 mm)
Upper 95% confidence limit
Lower 95% confidence limit
Analytical random
Mean of 100 random sets
$c = \left(\frac{110\ mm}{\lambda}\right)^{0.718}$
$R^2 = 0.746$
~110 mm
Spatial Correlation
Length Scale (mm)
b
Escalera 1 - Only set D (aperture threshold of 0.05 mm)
Upper 95% confidence limit
Lower 95% confidence limit
Mean of 100 random sets
530 mm
Spatial Correlation
Length Scale (mm)
c
Escalera 1 - Set D
Red noise
95% confidence interval
528 mm
2111 mm
Power Spectral Density
Wavelength (mm)

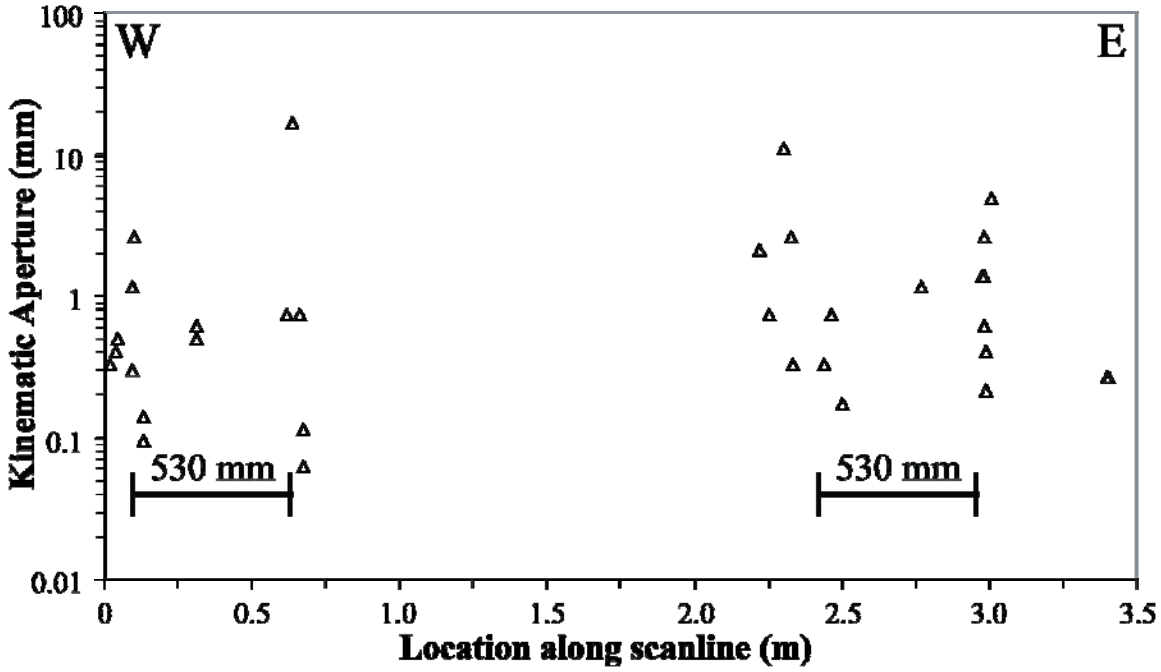

Figure 9.46 Kinematic aperture (triangle) versus location along scanline for set D fractures of the most western 3.5 m for the Escalera 1 outcrop data set. Fractures of set D inside clusters centered at 0.5 and 3 mm seem to be formed by smaller clusters separated approximately 530 mm.

Figure 9.47 Graphs of spatial correlation vs. length scale (thick continuous line) for (a) logarithmic graduations and (b) linear graduations for fractures of set B of the Escalera 1 outcrop data set (183 fractures, aperture threshold = 0.05 mm). In (a) and (b) the thin discontinuous line represents the upper 95% confidence limit while the thin dotted line represents the lower 95% confidence limit, and the thick discontinuous line corresponds to the mean of 100 randomized data sets. In (a) and (b) the thin continuous line represents an example randomized set generated with the same number of fractures and scanline length. Width of length-scale bin in (a) and (b) is 11 graduations of length scale (m = 5). Spatial correlation in both (a) and (b) do not display a systematic pattern outside the 95% confidence interval, which indicates a spatial arrangement that is indistinguishable from random. (c) Power spectrum of spatial correlation from (b). The power spectral density for the natural data set exhibits the same trend as the 95% confidence interval for red noise, as shown in (c). Although one peak of power spectral density is outside the 95% confidence interval for red noise (489 mm), the difference in power spectral density between the natural data set and the 95% confidence interval is small when compared with other data sets (e.g., set D of Escalera 1, Figure 9.45c).

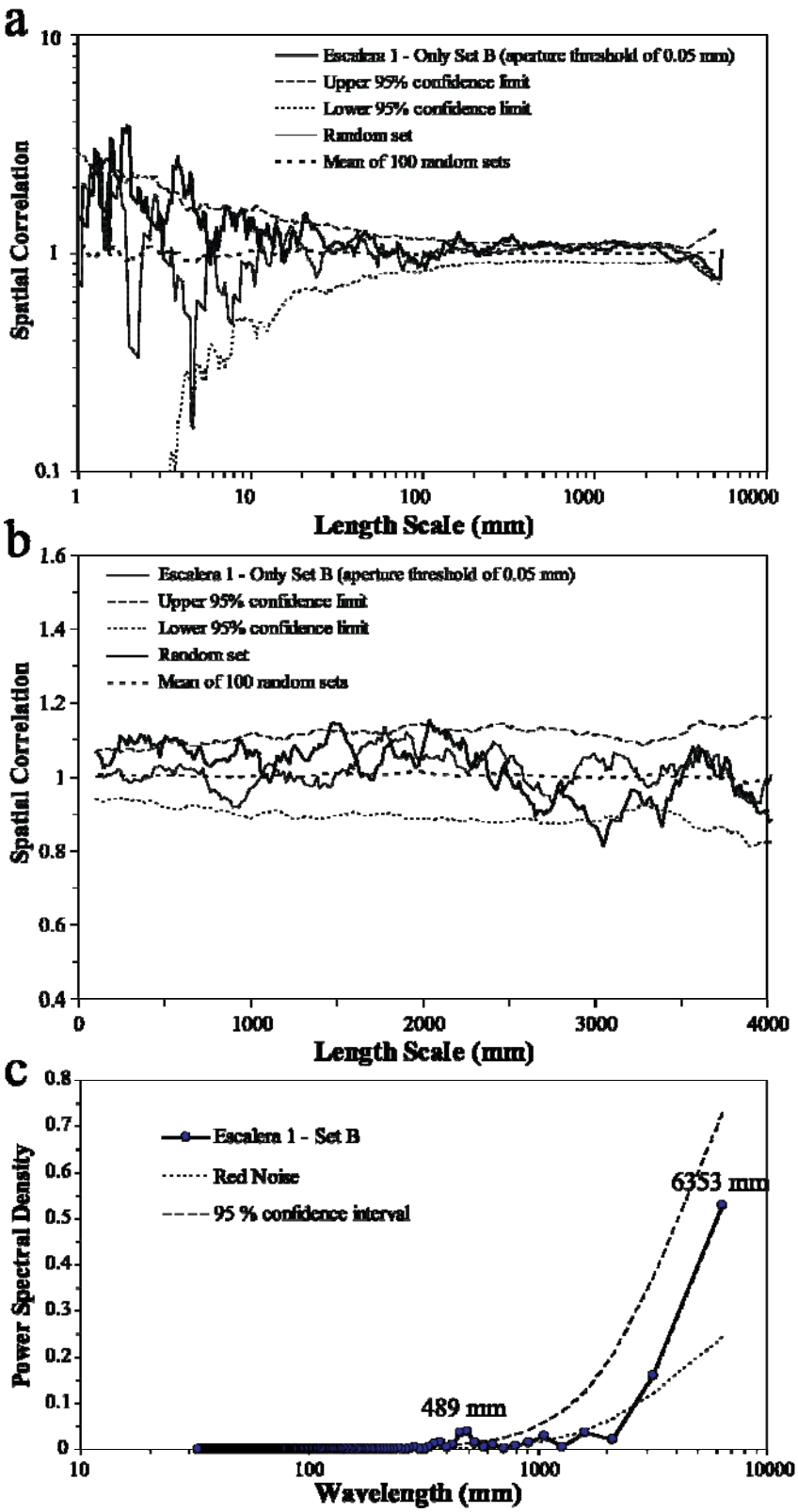
a
Escalera 1 - Only Set B (aperture threshold of 0.05 mm)
Upper 95% confidence limit
Lower 95% confidence limit
Random set
Mean of 100 random sets
Spatial Correlation
Length Scale (mm)
b
Escalera 1 - Only Set B (aperture threshold of 0.05 mm)
Upper 95% confidence limit
Lower 95% confidence limit
Random set
Mean of 100 random sets
Spatial Correlation
Length Scale (mm)
c
Escalera 1 - Set B
Red Noise
95 % confidence interval
6353 mm
489 mm
Power Spectral Density
Wavelength (mm)

Figure 9.48 Graphs of spatial correlation vs. length scale (thick continuous line) for (a) logarithmic graduations and (b) linear graduations for fractures of set C of the Escalera 1 outcrop data set (83 fractures, aperture threshold = 0.05 mm). In (a) and (b) the thin discontinuous line represents the upper 95% confidence limit while the thin dotted line represents the lower 95% confidence limit, and the thick discontinuous line corresponds to the mean of 100 randomized data sets. In (a) and (b) the thin continuous line represents an example randomized set generated with the same number of fractures and scanline length. Width of length-scale bin in (a) and (b) is 11 graduations of length scale (m = 5). Spatial correlation in both (a) and (b) do not display a systematic pattern outside the 95% confidence interval, which indicates a spatial arrangement that is indistinguishable from random. (c) Power spectrum of spatial correlation from (b). The power spectral density for the natural data set exhibits the same trend as the 95% confidence interval for red noise up to a length scale of 2118 mm, as shown in (c). Although the peak of power spectral density at 2118 mm is outside the 95% confidence interval for red noise, the difference in power spectral density between the natural data set and the 95% confidence interval is small when compared with other data sets (e.g., set D of Escalera 1, Figure 9.45c).

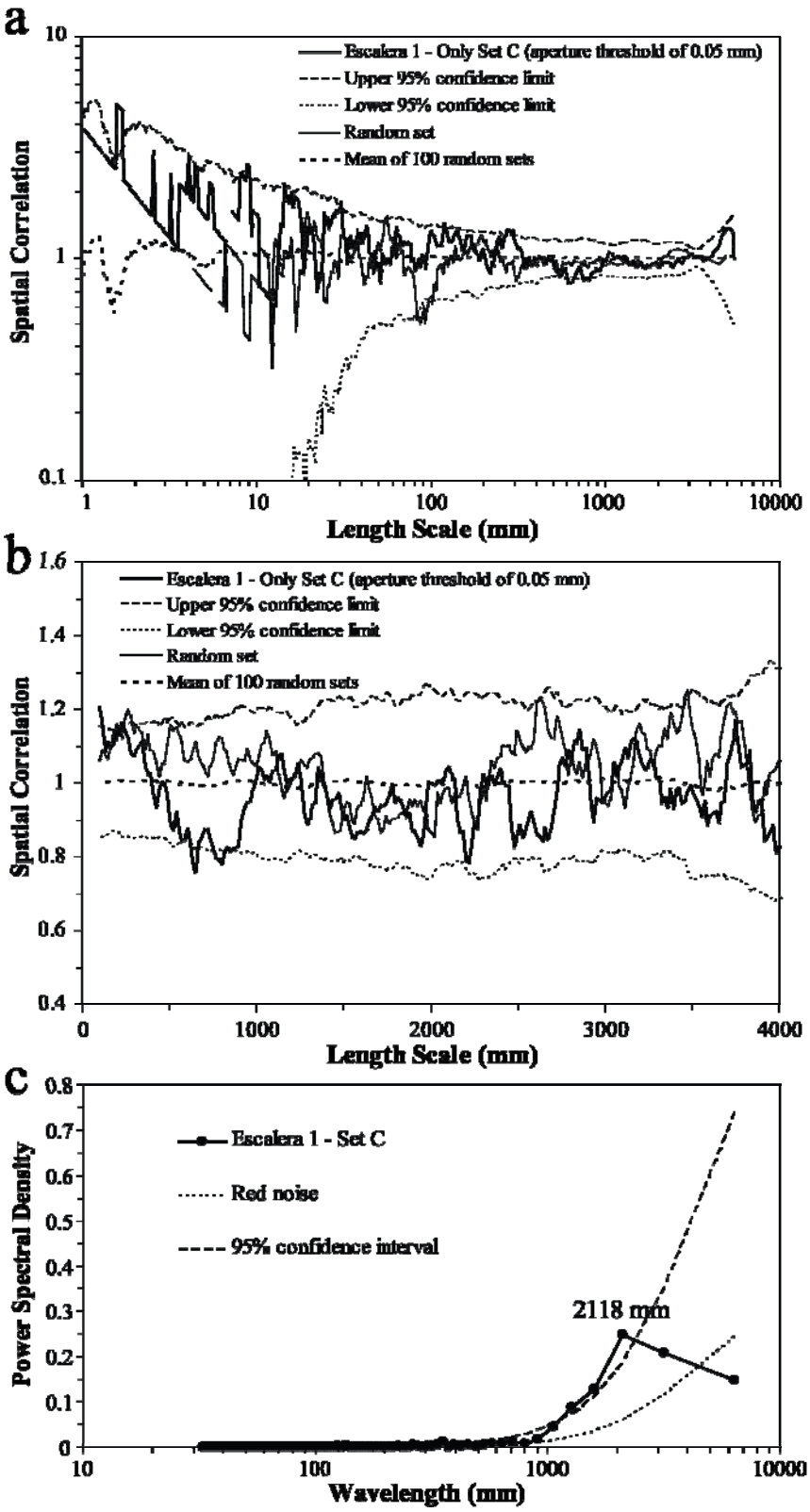
a
Escalera 1 - Only Set C (aperture threshold of 0.05 mm)
Upper 95% confidence limit
Lower 95% confidence limit
Random set
Mean of 100 random sets
Spatial Correlation
Length Scale (mm)
b
Escalera 1 - Only Set C (aperture threshold of 0.05 mm)
Upper 95% confidence limit
Lower 95% confidence limit
Random set
Mean of 100 random sets
Spatial Correlation
Length Scale (mm)
c
Escalera 1 - Set C
Red noise
95% confidence interval
2118 mm
Power Spectral Density
Wavelength (mm)

9.4.4 Layer 2 at Escalera Canyon (Escalera 2)

Although located stratigraphically below the layer Escalera 1, the Escalera 2 layer was not measured in a bedding-parallel outcrop but in a cross-sectional exposure (Table 9.1, Figures 9.38 and 9.49). Escalera 2 is 18 cm thick, and lithologically is a dolopackstone and is located stratigraphically within the Cupido Formation. Using an aperture threshold of 0.05 mm, I measured 614 veins in a scanline of approximately 6.2 m, and recorded a strain of 7.7% (Tables 9.1 and 9.5). Of the 614 fractures measured at the Escalera 2 layer, 568 fractures have an aperture equal or larger than 0.05 mm. For the 46 fractures with apertures smaller than 0.05 mm only their position was recorded (Table 9.1). The 568 fractures with apertures equal or larger than 0.05 mm exhibit a power-law distribution of fracture apertures (Table 9.5). Spacings between the 614 fractures of the Escalera 2 outcrop data set exhibit a negative exponential distribution and a coefficient of variation of 1 (Table 9.5). 89% of the measured fractures represent set B and 11% represent set C (Table 9.3). Compared with the immediately adjacent layers Escalera 1 and Escalera 3, the matrix of layer Escalera 2 exhibits a much lighter gray color, which made more difficult the detection and measurement of small fractures (< 0.5 mm approximately). Examination of the single sample available from Escalera 2 layer (Table 9.2) only allowed for categorization of set C fractures, which display characteristics typical of Z fractures (Table 9.4) such as irregular traces, dolomite cement in isolated crystals without bridge morphology and sizes similar to D2 dolomite in matrix and calcite cement. Set C fractures in Escalera 1 has the same orientation of set C fractures in Escalera 2 and also were categorized as Z (Table 9.4).

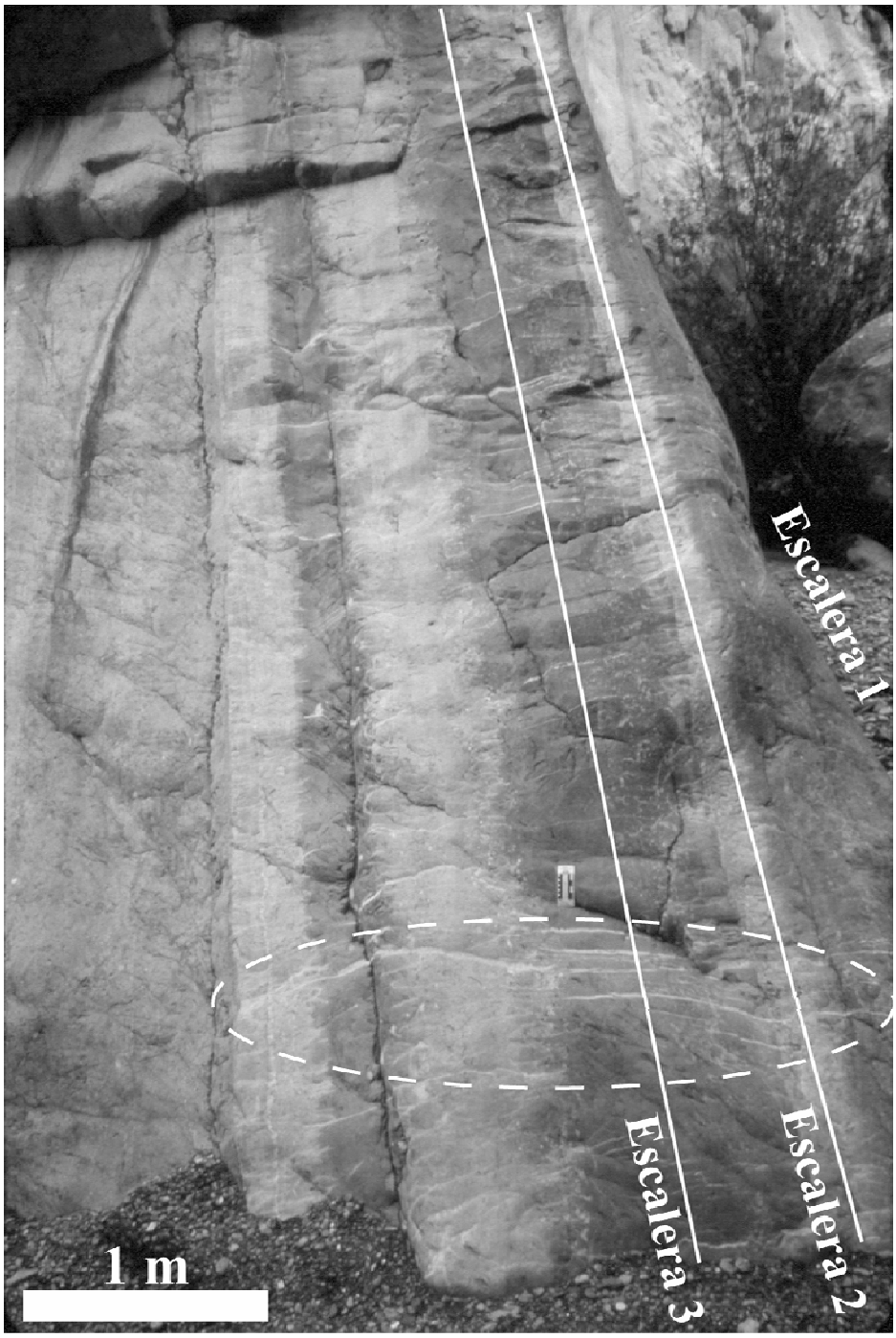

Figure 9.49 Photograph of the cross-sectional exposure of layers Escalera 2 and Escalera 3 (Cupido Formation). Notice bedding-parallel exposure of Escalera 1 layer. Solid lines indicate position of scanlines. Dashed oval indicates en-echelon pattern of set D fractures which displaces a few mm the boundary between Escalera 2 and Escalera 3 layers.

Although the orientation of fracture sets in Escalera 2 is approximately the same as in Escalera 1 and Escalera 3 (Table 9.3), only fractures of sets B and C were recorded in Escalera 2. In addition, Escalera 3 outcrop is approximately parallel and of equal size to Escalera 2 outcrop and yet almost 300 fractures of set A were measured in Escalera 3 and none were detected in Escalera 2. There are four reasons to suspect the classification of fractures of set B on Escalera 2 data set. First, the cross-section outcrop of Escalera 2 layer is approximately parallel to set B fractures and has a high angle (~60 degrees) to set A fractures (Figure 9.38), which would decrease the probability of observing set B fractures and increase the probability of observing A fractures. Second, it was not possible to use the angle between the fractures and the scanline to classify each measured fracture into different sets (as explained by Ortega, 2002) because the above mentioned angle was almost identical for fractures of both set A and set B. Third, the much lighter color of rock matrix made impossible to detect the halo around fractures of sets B and C commonly seen in Escalera 1 layer and used to differentiate fractures of set A, which do not exhibit a halo. And fourth, the Escalera 2 was the first data set that I measured, and therefore it is possible that the lack of experience in measuring fractures along a scanline have allowed for errors in classifying fractures into set B.

Kinematic aperture and fracture intensity indicates that fractures at Escalera 2 have a heterogeneous arrangement of fractures (Figure 9.50). Spatial correlation for all fracture sets combined varies as a power law of length scale (Figure 9.51a), which indicates a fractal arrangement of fractures inside clusters (Figure 9.4b). However, the power-law has a very small exponent, which indicates almost no variation of spatial correlation with length scale, a feature of an inherited/imposed clustering of fractures (Figure 9.4c). Spatial correlation for all fracture sets combined remains approximately constant between 0 and 2900 mm of length scale, indicating an inherited/imposed

arrangement of fractures (Figure 9.51b). In addition, spatial correlation for all Escalera 2 fracture sets combined is barely outside the 95% confidence interval for both logarithmic (Figure 9.51a) and linear (Figure 9.51b) graduations of length scale, which indicates that the interpreted spatial arrangements are hardly statistically significant. Power spectrum of spatial correlation for linearly graduated length scales shows a trend that is similar to the 95% confidence interval for red noise. In addition, the power spectrum exhibits an peak outside the 95% confidence interval (wavelength of 410 mm), the peak of power spectral density is only slightly above the 95% confidence interval for red noise (Figure 9.51c).

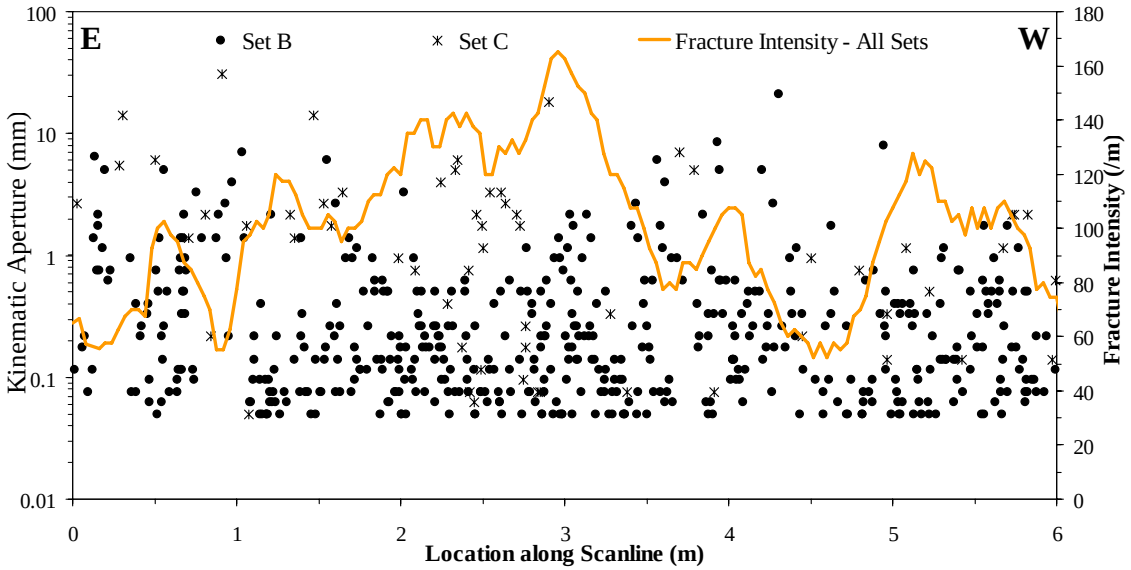

Figure 9.50 Kinematic aperture versus location along scanline and fracture intensity for the Escalera 2 data set. Fracture intensity for fractures of all two sets was calculated inside a moving window with width (window size) equal to 0.2 m that was moved in increments (window step) equal to 0.04 m. Note that kinematic aperture axis uses logarithmic graduations.

When analyzed independently using logarithmic graduation of length scales, fractures of set B (Figure 9.52a) yield a spatial correlation that resemble those for all sets combined (Figure 9.51a). Namely, a power-law pattern of spatial correlation with a very

small exponent (0.01) that is barely outside the 95% confidence interval, which can be interpreted as an inherited/imposed arrangement (Figure 9.4c) that is hardly statistically significant (Marrett et al., in review). Spatial correlation for linearly graduated length scales of fractures of set B exhibit a pattern with peaks at length scales of 510, 1020, 1740, 2250, and 2760 mm that are outside the 95% confidence interval (Figure 9.52b), which may be interpreted as a periodic arrangement of fracture clusters (Figure 9.4g). However, only the second peak is a multiple of the first peak (cluster spacing, or 510 mm of length scale), and although the difference in length scale between the third, fourth and fifth peaks is 510 mm, the difference in length scale between the second and third peak of spatial correlation is 720 mm (Figure 9.52b). For a pattern of spatial correlation to be unequivocally interpreted as indicative of periodically arranged clusters, all peaks of spatial correlation should be located at length scales that are approximate multiple values of cluster spacing (Figure 9.4g). In addition, the difference between peaks and troughs of spatial correlation is smaller than the 95% confidence interval, reducing the likelihood of the spatial correlation pattern of Figure 9.52b to be interpreted as periodic arrangement of clusters. Power spectrum of spatial correlation for linearly graduated length scales follows the trend of the 95% confidence interval for red noise and does not exhibit noticeable peaks, which does not yield an interpretation of periodically arranged clusters and instead indicates fractures have an arrangement that is indistinguishable from random (Figure 9.52c). Although two peaks are outside the 95% confidence interval for red noise (820 and 1912 mm, Figure 9.52c), the difference of power spectral density between the two peaks and the 95% confidence interval is small when compared with other data sets (e.g., set D of Escalera 1, Figure 9.45c).

Figure 9.51 Graphs of spatial correlation vs. length scale (thick continuous line) for (a) logarithmic graduations and (b) linear graduations for all fracture sets of the Escalera 2 data set (614 fractures, aperture threshold of 0.05 mm). In (a) and (b) the thin discontinuous line represents the upper 95% confidence limit while the thin dotted line represents the lower 95% confidence limit, and the thick discontinuous line corresponds to the mean of 100 randomized data sets. In (a) and (b) the thin continuous line represents an example randomized set generated with the same number of fractures and scanline length. Width of length-scale bin in (a) and (b) is 11 graduations of length scale (m = 5). The power-law of spatial correlation in (a) was calculated for length scales between 9 and 2900 mm. The exponent of power-law in (a) is almost zero (0.007), which indicates a negligible variation of spatial correlation with length scale. Although it may look that the power-law distribution in (a) follows a straight line, in fact it follows a convex line. Spatial correlation in (b) does not display a systematic pattern outside the 95% confidence interval. Spatial correlation for all fracture sets combined are barely statistically significant (outside the 95% confidence interval) in both (a) and (b). (c) Power spectrum of spatial correlation from (b). The power spectral density for the natural data set exhibits the same trend as the 95% confidence interval for red noise up to a length scale of 1495 mm, as shown in (c). Although the power spectra for length scales smaller than 1495 mm is outside the 95% confidence interval for red noise, the difference in power spectra between the natural data set and the 95% confidence interval is small when compared with other data sets (e.g., set D of Escalera 1, Figure 9.45c).

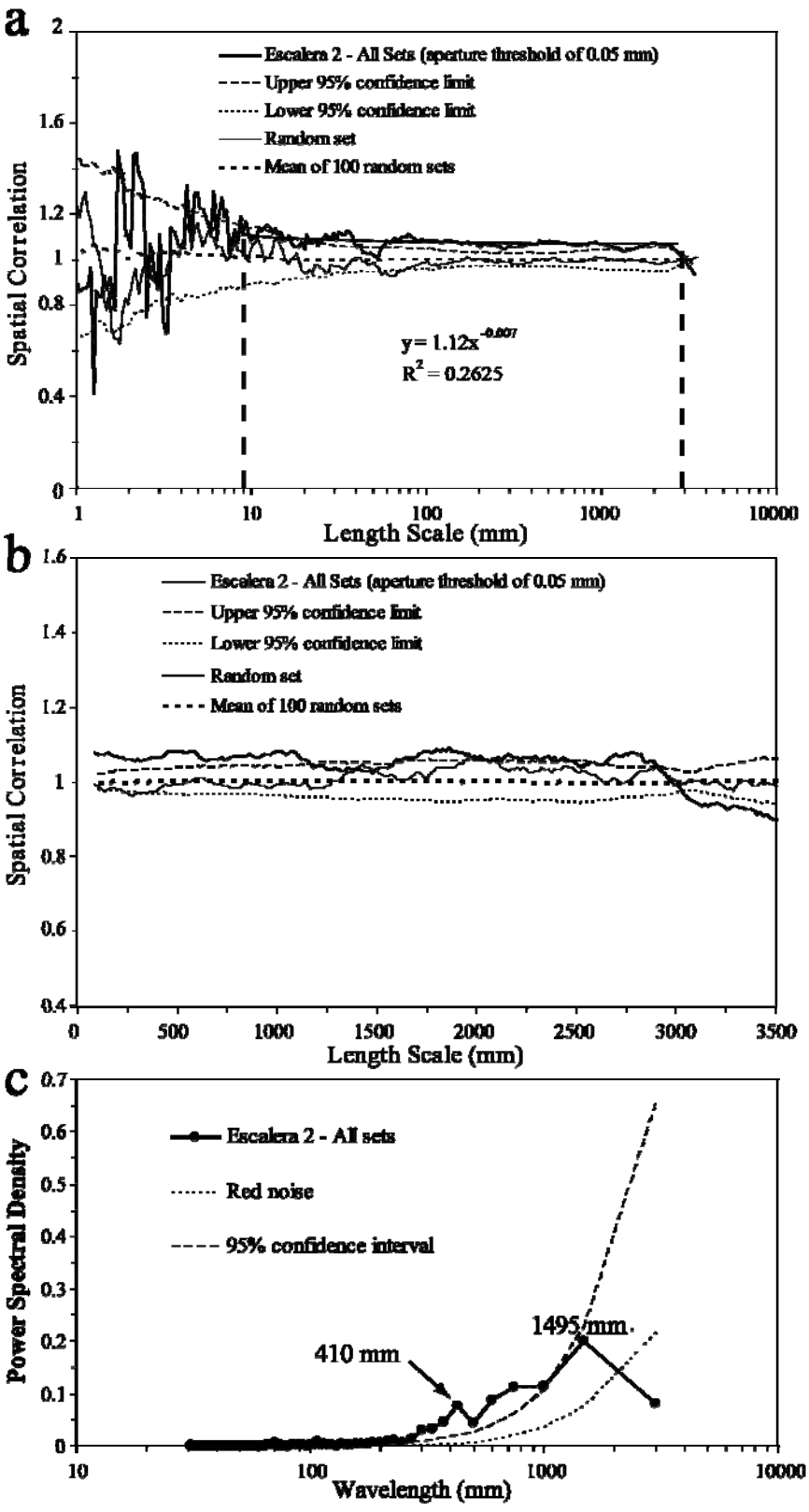
a
Escalera 2 - All Sets (aperture threshold of 0.05 mm)
Upper 95% confidence limit
Lower 95% confidence limit
Random set
Mean of 100 random sets
Spatial Correlation
y= 1.12x^-0.007
R^2 = 0.2625
Length Scale (mm)
b
Escalera 2 - All Sets (aperture threshold of 0.05 mm)
Upper 95% confidence limit
Lower 95% confidence limit
Random set
Mean of 100 random sets
Spatial Correlation
Length Scale (mm)
c
Escalera 2 - All sets
Red noise
95% confidence interval
Power Spectral Density
410 mm
1495 mm
Wavelength (mm)

Figure 9.52 Graphs of spatial correlation vs. length scale (thick continuous line) for (a) logarithmic graduations and (b) linear graduations for fractures of set B of the Escalera 2 data set (546 fractures, aperture threshold of 0.05 mm). In (a) and (b) the thin discontinuous line represents the upper 95% confidence limit while the thin dotted line represents the lower 95% confidence limit, and thick discontinuous line corresponds to the mean of 100 randomized data sets. In (a) and (b) the thin continuous line represents an example randomized set generated with the same number of fractures and scanline length. Width of length-scale bin in (a) and (b) is 11 graduations of length scale (m = 5). The power-law pattern of spatial correlation in (a) was calculated for length scales between 9 and 2800 mm, is almost horizontal and barely outside the 95% confidence interval. Peaks of spatial correlation outside the 95% confidence interval can be identified in (b). (c) Power spectrum of spatial correlation from (b). The power spectral density for the natural data set exhibits the same trend as the 95% confidence interval for red noise, as shown in (c). Although the power spectra for length scales smaller at 512 and 1912 mm is outside the 95% confidence interval for red noise, the difference in power spectra between the natural data set and the 95% confidence interval is small when compared with other data sets (e.g., set D of Escalera 1, Figure 9.45c).

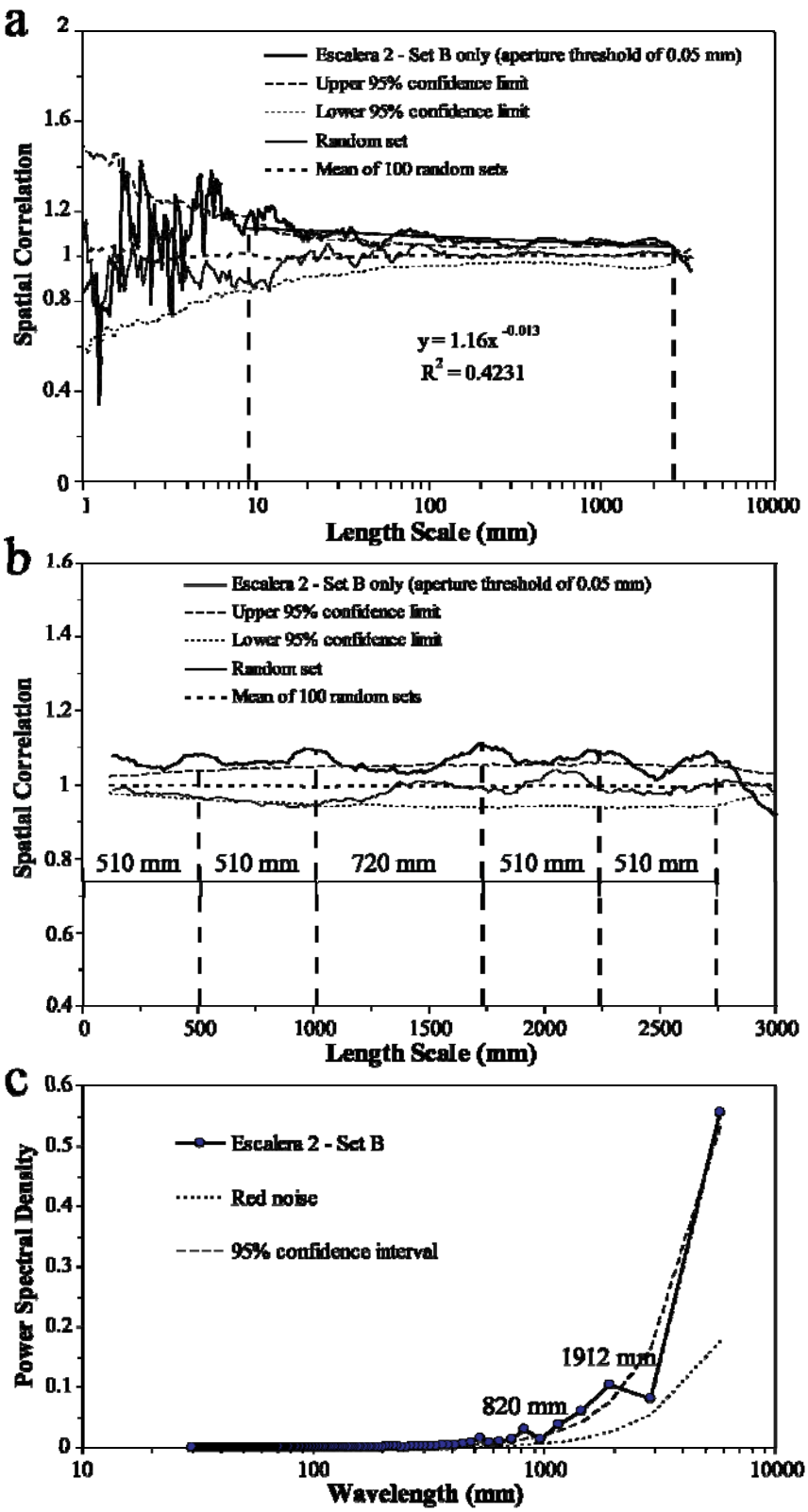
a
Escalera 2 - Set B only (aperture threshold of 0.05 mm)
Upper 95% confidence limit
Lower 95% confidence limit
Random set
Mean of 100 random sets
y = 1.16x^-0.013
R^2 = 0.4231
Spatial Correlation
Length Scale (mm)
b
Escalera 2 - Set B only (aperture threshold of 0.05 mm)
Upper 95% confidence limit
Lower 95% confidence limit
Random set
Mean of 100 random sets
510 mm
510 mm
720 mm
510 mm
510 mm
Spatial Correlation
Length Scale (mm)
c
Escalera 2 - Set B
Red noise
95% confidence interval
1912 mm
820 mm
Power Spectral Density
Wavelength (mm)

Spatial correlation for fractures in the Palmas 12 outcrop does not follow a systematic pattern with length scale (e.g., power-law), which indicates an arrangement of fractures indistinguishable from random (Figures 9.4a and 9.53a). Spatial correlation for linearly graduations of length scale also shows no recognizable pattern (Figure 9.53b), which is interpreted to indicate a spatial arrangement indistinguishable from random (Figure 9.4e). In addition, power spectrum of spatial correlation for linearly graduated length scales follows the trend of the 95% confidence interval for red noise and does not exhibit peaks outside the 95% confidence interval for red noise, which confirms the interpretation of a spatial arrangement that is indistinguishable from random (Figure 9.52c).

Figure 9.53 Graphs of spatial correlation vs. length scale (thick continuous line) for (a) logarithmic graduations and (b) linear graduations scale for fractures of set C of the Escalera 2 data set (67 fractures, aperture threshold of 0.05 mm). In (a) and (b) the thin discontinuous line represents the upper 95% confidence limit while the thin dotted line represents the lower 95% confidence limit, and the thick discontinuous line corresponds to the mean of 100 randomized data sets. In (a) and (b) the thin continuous line represents an example randomized set generated with the same number of fractures and scanline length. Width of length-scale bin in (a) and (b) is 11 graduations of length scale (m = 5). There is no pattern of spatial correlation that can be identified for logarithmic graduations of length scale (e.g., power law) in (a) or for linear graduations of length scale (e.g., regularly-spaced peaks) in (b). For all values of length scale, spatial correlation in both (a) and (b) remains within the 95% confidence interval, which indicates that spatial arrangement is indistinguishable from random in both (a) and (b). (c) Power spectrum of spatial correlation from (b). The power spectral density for the natural data set exhibits the same trend as the 95% confidence interval for red noise, as shown in (c). Although there are peaks of power spectral density (e.g., 365, 1564 and 4691 mm), no peak reaches amplitudes larger than the 95% confidence interval for red noise.

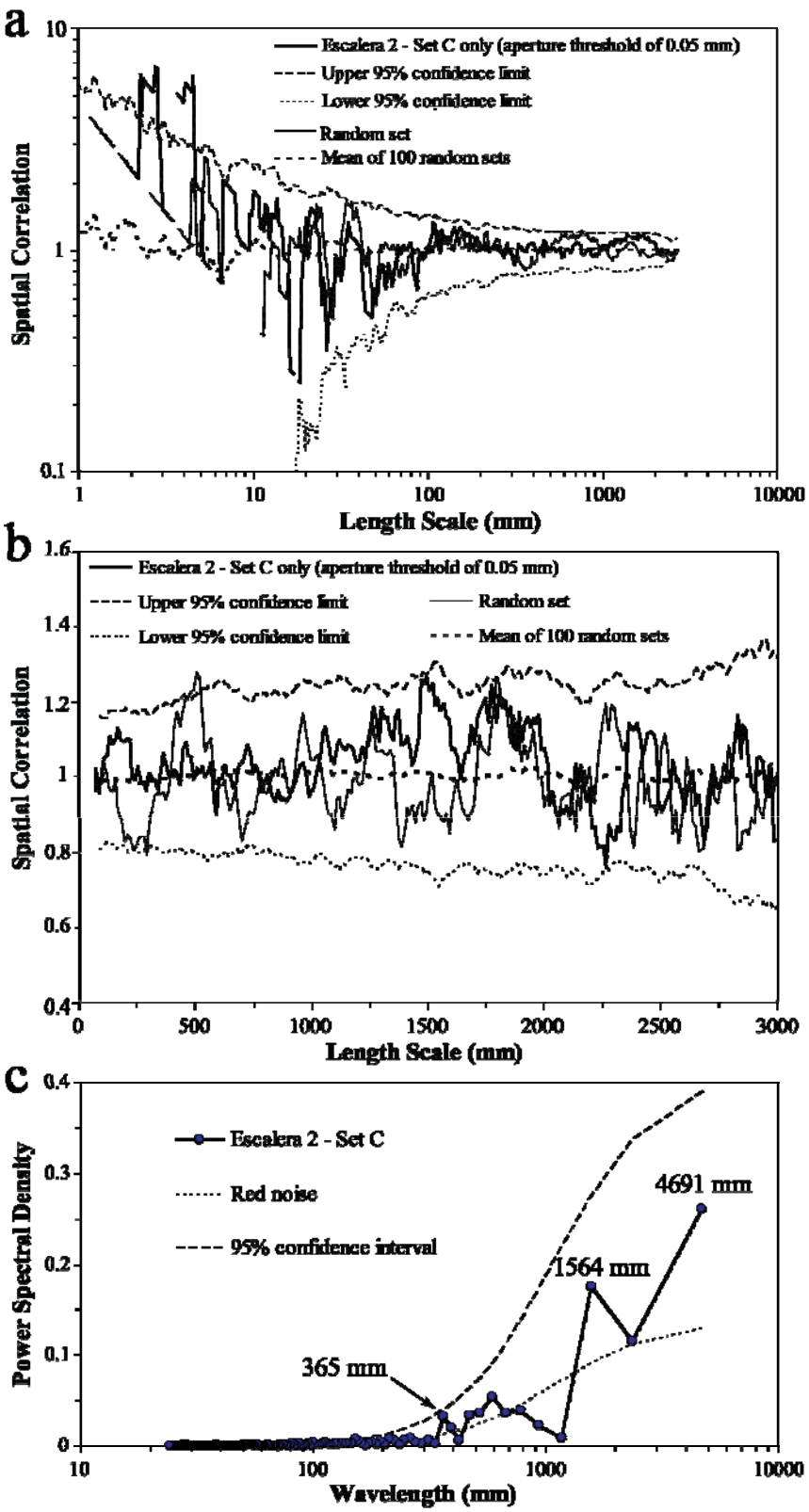
a
Escalera 2 - Set C only (aperture threshold of 0.05 mm)
Upper 95% confidence limit
Lower 95% confidence limit
Random set
Mean of 100 random sets
Spatial Correlation
Length Scale (mm)
b
Escalera 2 - Set C only (aperture threshold of 0.05 mm)
Upper 95% confidence limit
Lower 95% confidence limit
Random set
Mean of 100 random sets
Spatial Correlation
Length Scale (mm)
c
Escalera 2 - Set C
Red noise
95% confidence interval
4691 mm
1564 mm
365 mm
Power Spectral Density
Wavelength (mm)

9.4.5 Layer 3 at Escalera Canyon (Escalera 3)

The Escalera 3 layer is exposed in a cross-sectional exposure (Table 9.1), and is located immediately below layer Escalera 2 (Cupido Formation). Escalera 3 is 89 cm thick, and lithologically is a dolowackstone. Using an aperture threshold of 0.095 mm, I measured 293 veins of a single set (Set A) in a scanline of approximately 7 m (Figure 9.54), and recorded a strain of 4.5% (Table 9.5). Fractures of Escalera 3 exhibit a power-law distribution of fracture apertures and a negative exponential distribution of fracture spacings (Table 9.5). The coefficient of variation of fracture spacings is 1.3 (Table 9.5). Fractures with orientation different from the dominant orientation of set A were ignored (Table 9.3). In thin section fractures of set A exhibit typical features of Y fractures such as straight traces (e.g., Figure 9.16b), microfractures that occasionally anastomose (e.g., Figure 9.16b), subhedral bridges of dolomite, and subhedral bridges of quartz with bands of fluids inclusions (Table 9.4).

Spatial correlation for fractures in the Escalera 3 outcrop data set varies as a power-law of length scale (Figure 9.55a), which indicates a fractal arrangement of fractures inside clusters (Figure 9.4b). Cluster width is approximately 160 mm. Spatial correlation shows alternating peaks and troughs (Figure 9.55b), which indicates a periodic arrangement of fracture clusters (Figure 9.4g). However, the statistical significance of a periodic arrangement of fracture clusters is questionable because only two of the five peaks of spatial correlation are statistically significant (outside the 95% confidence interval, Figure 9.55b). The power spectrum of spatial correlation for linear graduations of length scale exhibits peaks outside the 95% confidence interval for red noise for wavelengths of 680 to 968 mm, which suggests that the periodic arrangement of fracture clusters indicated by spatial correlation is statistically significant (Figure 9.55c).

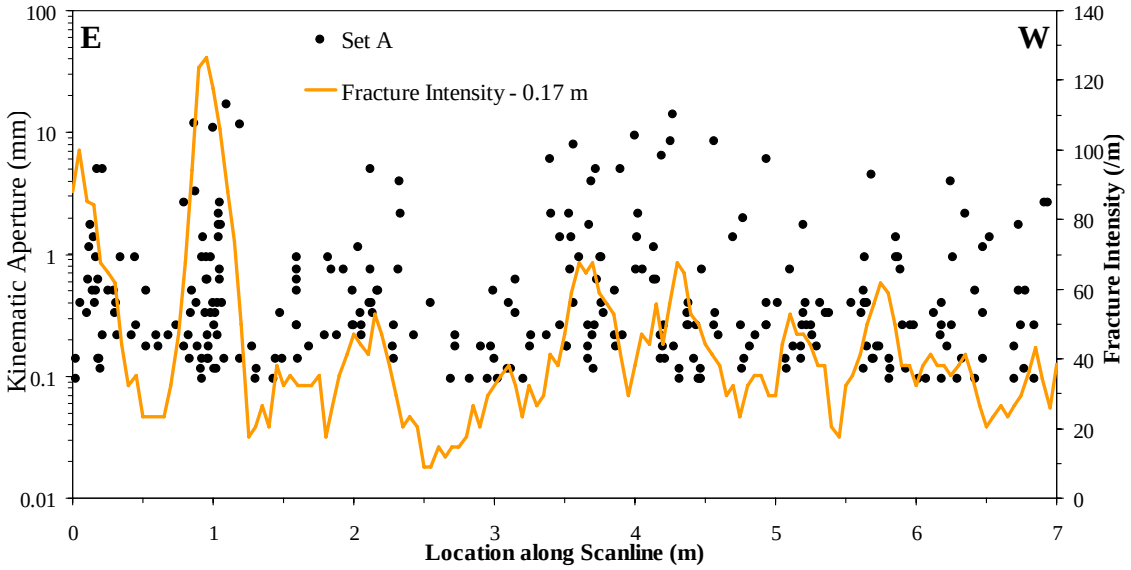

Figure 9.54 Kinematic aperture (circles) and fracture intensity (orange line) versus location along scanline for the Escalera 3 data set. Note that only kinematic aperture axis uses logarithmic graduations. Fracture intensity was calculated inside a moving window with width (window size) equal to cluster width (0.17 m) as determined by NCC (Figure 9.55a). Window for calculating fracture intensity was moved in increments (window step) equal to 0.05 mm.

Figure 9.55 Graph of spatial correlation (thick continuous line) vs. length scale using (a) logarithmic graduations and (b) linear graduations for fractures of set A of the Escalera 3 data set (293 fractures, aperture threshold of 0.095 mm). The thin discontinuous line represents the upper 95% confidence limit while the thin dotted line represents the lower 95% confidence limit, and thick discontinuous line corresponds to the mean of 100 randomized data sets. In (a) the thin continuous line represents the analytical solution of randomly arranged fractures with the same number of fractures and scanline length. In (b) the thin continuous line represents an example randomized set generated with the same number of fractures and scanline length. Width of length-scale bin is 11 graduations of length scale (m = 5). Cluster width is estimated in (a) to be approximately 160 mm. (c) Power spectrum of spatial correlation from (b). A relatively broad peak of power spectral density outside the 95% confidence interval for red noise is visible in (c) between 680 and 968 mm (centered at 827 mm), indicating a non-random periodicity of spatial correlation and a cluster spacing of approximately 827 mm.

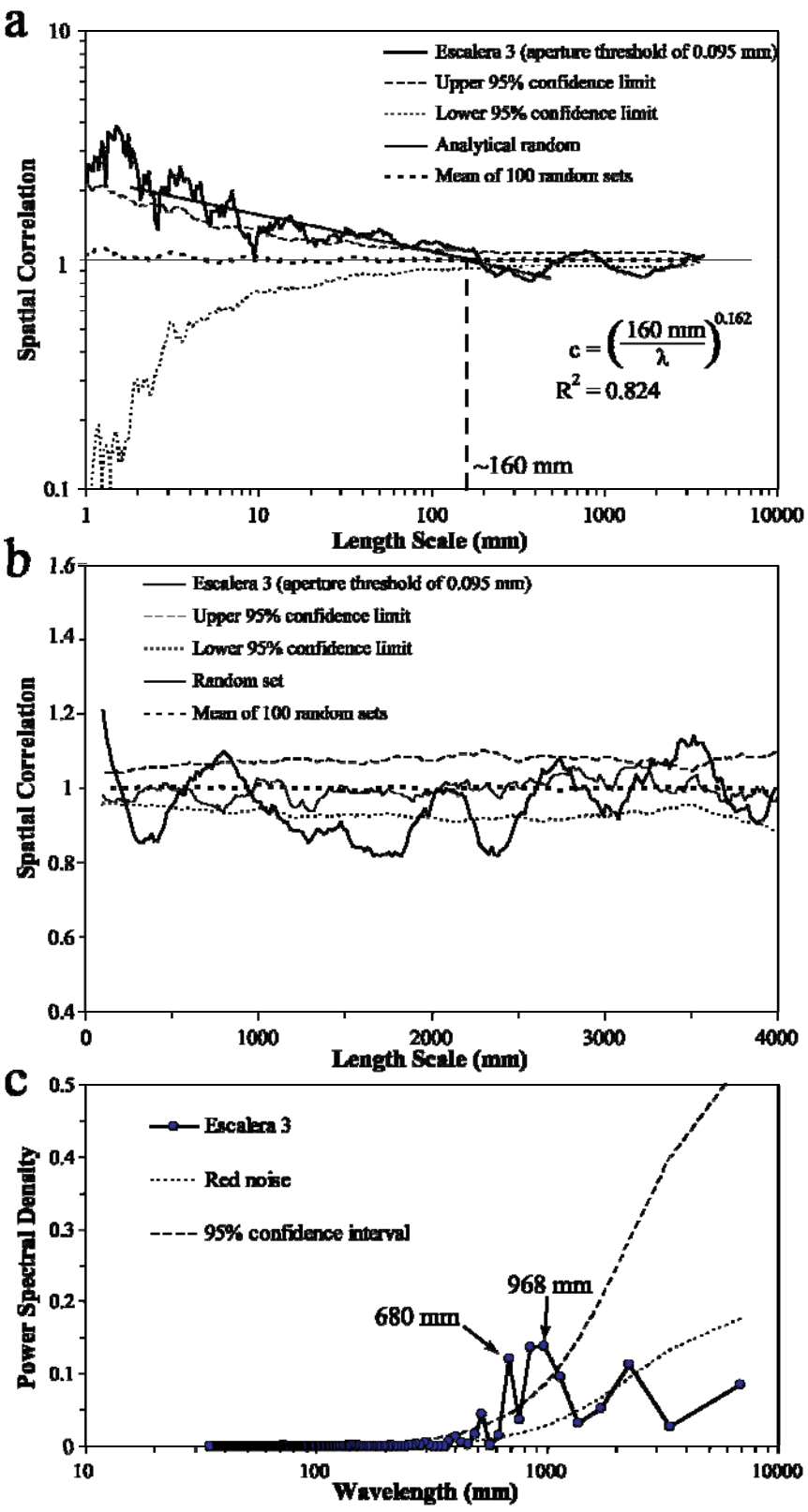
a
Escalera 3 (aperture threshold of 0.095 mm)
Upper 95% confidence limit
Lower 95% confidence limit
Analytical random
Mean of 100 random sets
Spatial Correlation
$c = \left(\frac{160\ mm}{\lambda}\right)^{0.162}$
$R^2 = 0.824$
~160 mm
Length Scale (mm)
b
Escalera 3 (aperture threshold of 0.095 mm)
Upper 95% confidence limit
Lower 95% confidence limit
Random set
Mean of 100 random sets
Spatial Correlation
Length Scale (mm)
c
Escalera 3
Red noise
95% confidence interval
968 mm
680 mm
Power Spectral Density
Wavelength (mm)

9.4.6 Layer OO1 at Escalera Canyon (Escalera OO1)

In contrast to Escalera 1, Escalera 2 and Escalera 3, which are located in the backlimb of San Blas anticline, Escalera OO1 layer is located in the forelimb (Figure 2.7). Escalera OO1 was initially studied by Ortega (2002), who only measured fracture apertures. Escalera OO1 is 80 cm thick, and is a dolostone (100% dolomite) with mud-supported intraclasts (intraclast-breccia, Ortega, 2002) from the Cupido Formation (Goldhammer, 1999; Ortega and Marrett, 2001). Escalera OO1 is located 139 m above the base of the stratigraphic column measured in the forelimb of San Blas anticline at Escalera canyon by Ortega (2002). I measured 1160 veins, of which 680 have apertures greater than or equal to 0.05 mm (Figure 9.56). For the 480 veins with apertures smaller than 0.05 mm, only spacing was recorded. The scanline has a length of approximately 3.2 m, was positioned 30 cm from the top of the layer and recorded a strain of 13.3% (Table 9.5). Spacings between fractures with apertures greater than or equal to 0.05 mm exhibit a power-law distribution and a coefficient of variation of 3.50 (Table 9.5). Fractures were assigned to four different sets depending on their orientation (Table 9.3). 11% of the fractures measured represent set A, 74% represent set B, 2% represent set C, and 13% represent set D (Table 9.3). However, orientation of set A (220/38) is similar to orientation of set B (205/31), and perhaps fractures of sets A and B are part of a single set.

The scanline in layer Escalera OO1 can be divided in two domains, each one containing fractures with different characteristics. In the eastern 1.6 m of scanline (Figure 9.56) fractures tend to span the entire layer and are not related to faults (Figure 9.57a). In contrast, fractures in the western 1.5 m of scanline do not span the entire layer, are arranged in en echelon patterns and occur near faults (Figure 9.57b). Fractures of all sets (Table 9.3) are present in both domains of Escalera OO1 (Figure 9.56).

In thin sections from the eastern 1.6 m of Escalera OO1 layer, fractures of sets A, B and C exhibit the typical features of Y fractures such as straight traces (e.g., Figure 9.14), fibrous dolomite lining fracture walls (e.g., Figures 9.17 and 9.18), quartz cement in anhedral crystals (e.g., Figure 9.17) or in bridges of quartz with crack-seal texture (e.g., Figures 9.21 to 9.24), and calcite precipitated between quartz bridges and also replacing quartz (e.g., Figure 9.20). In thin sections from the western 1.5 m of Escalera OO1 layer, fractures of sets A, B and C exhibit some of the typical features of Y fractures such as straight traces (e.g., Figure 9.26), and calcite precipitating around bridges of quartz. Although fractures of sets A and B in the western domain of Escalera OO1 layer exhibit the same cements (with the same textures) as fractures in the eastern domain, the orientation of crystals is not perpendicular to fracture wall (e.g., Figures 9.26 and 9.27), supporting its association with faulting. Fractures of sets C and D were not present in samples collected from Escalera OO1 layer (Table 9.4).

Fractures in Escalera OO1 display a heterogeneous arrangement of fractures (Figure 9.56). Fracture intensity indicates clusters that do not seem be regularly spaced (Figure 9.56). Spatial correlation for all fracture sets combined varies as a power law of length scale (Figure 9.58a), which indicates a fractal arrangement of fractures inside clusters (Figure 9.4b) with a cluster width of 100 mm (Figure 9.58a). However, the power-law pattern of spatial correlation has a relatively small exponent that indicates the possibility of fractures having inherited/imposed clusters (Figure 9.4c). Spatial correlation versus linear graduations of length scale for all fracture sets of the Escalera OO1 data set yields a pattern that although it has peaks and troughs of spatial correlation, has peaks that are not at length scales multiples of the first peak, a prerequisite for interpreting a periodic arrangement of fracture clusters (Figure 9.58b). Power spectrum of spatial correlation for linearly graduated length scales exhibits three peaks outside the

95% confidence interval for red noise, which suggests superposition of more than one statistically-significant periodic arrangement of clusters t (Figure 9.58c).

When the spatial arrangements of the eastern 1.6 m and western 1.5 m of the Escalera OO1 data set are analyzed independently using logarithmic graduations of length scales (Figures 9.59a and 9.60a), the spatial arrangement of fractures inside clusters is similar to that displayed by the entire data set (Figure 9.58a). Namely, both domains of Escalera OO1 exhibit a power-law pattern of spatial correlation with an exponent near zero and therefore cannot unequivocally be differentiated between a fractal (Figure 9.4b) or an inherited/imposed arrangement (Figure 9.4c). However, using linear graduations of length scales, there are differences between the spatial arrangement of the entire data set and the spatial arrangement of the two domains described earlier. Compared with the entire data set (Figure 9.58b), the eastern 1.6 m of scanline yields a clearer pattern of periodically arranged clusters (Figure 9.4g) because all three peaks of spatial correlation are multiples of by 340 mm and therefore it can be interpreted as indicative of periodically arranged fracture clusters (Figure 9.59b). In addition, power spectrum of spatial correlation for linearly graduated length scales exhibits a significant peak at 334 mm with a magnitude several times the corresponding 95% confidence interval for red noise, which supports periodically arranged with a cluster spacing of 334 mm (Figure 9.59c).

In contrast to fractures in the eastern 1.6 m of scanline, NCC analysis using linear graduations of length scale for the western 1.5 m of scanline displays a pattern that cannot be interpreted as periodically arranged clusters because, although it has statistically significant peaks of spatial correlation at 185 and 560 mm, and 560 mm is an approximate multiple of 185 mm, the intermediate length scale (370 is not present), a characteristic of periodic arrangements (Figure 9.60b). In addition, power spectrum of

spatial correlation of linearly graduated length scales exhibits two significant peaks at 185 and 431 mm outside the 95% confidence interval for red noise, which suggests that two periodic arrangements of clusters (both statistically significant) are in the western 1.5 m of the scanline in layer Escalera OO1 (Figure 9.60c). Because my dissertation is only concerned about the spatial arrangement of opening-mode fractures and not with shear-mode fractures, only the eastern domain of layer Escalera OO1 will be considered for analysis.

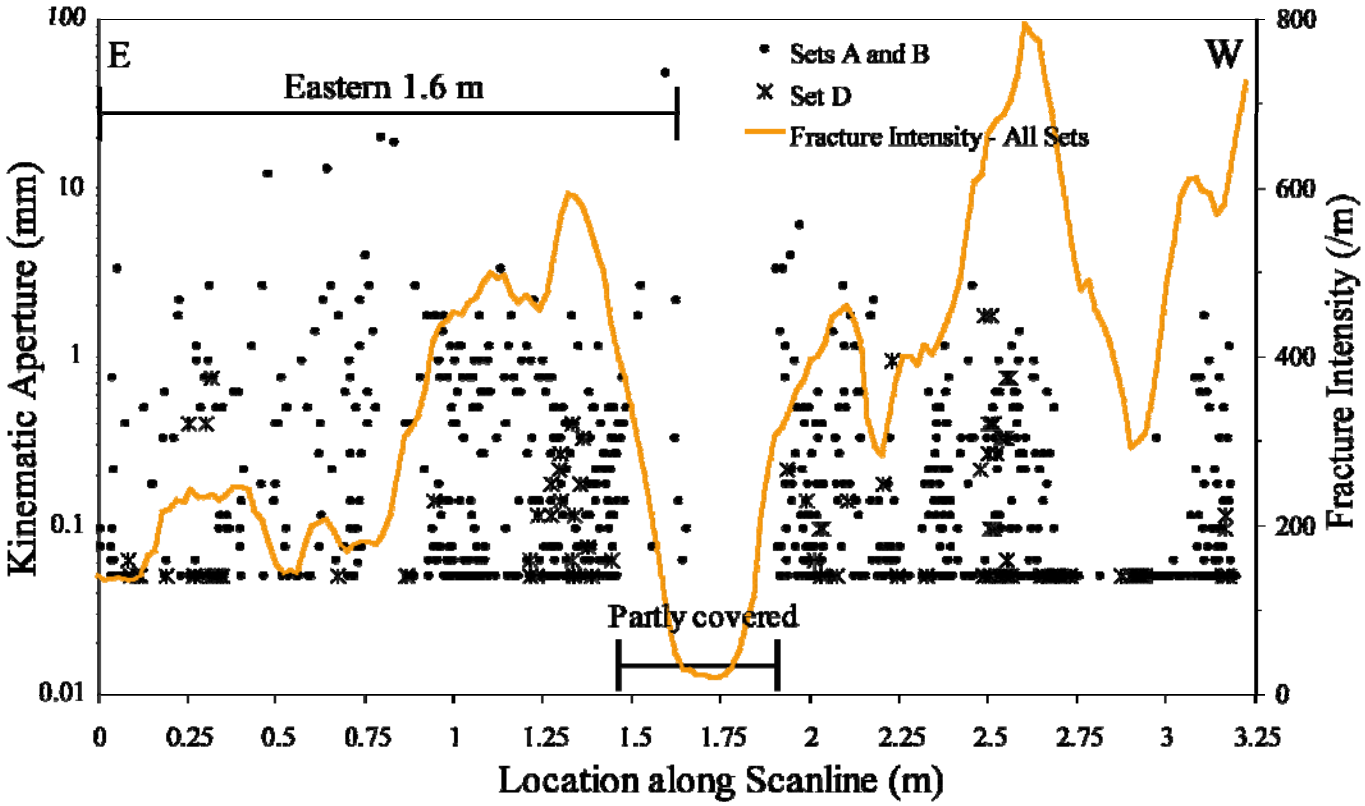

Figure 9.56 Kinematic aperture (circles for sets A and B, asterisks for set D) and fracture intensity (thick orange line) versus location along scanline for the Escalera OO1 data set. Note that kinematic aperture axis uses logarithmic graduations. Fracture intensity was calculated inside a moving window with width (window size) of 0.15 m that was moved in increments (window step) 0.02 m. Peaks of fracture intensity indicate clusters at 0.25, 1.3, 2.1, and 2.6 m, but clusters do not seem regularly spaced. Please note that kinematic aperture axis use logarithmic graduations. Although 1160 fractures were used to calculate fracture intensity, only the aperture of the 656 fractures of sets A, B, and D (fractures of set C were not included) was plotted.

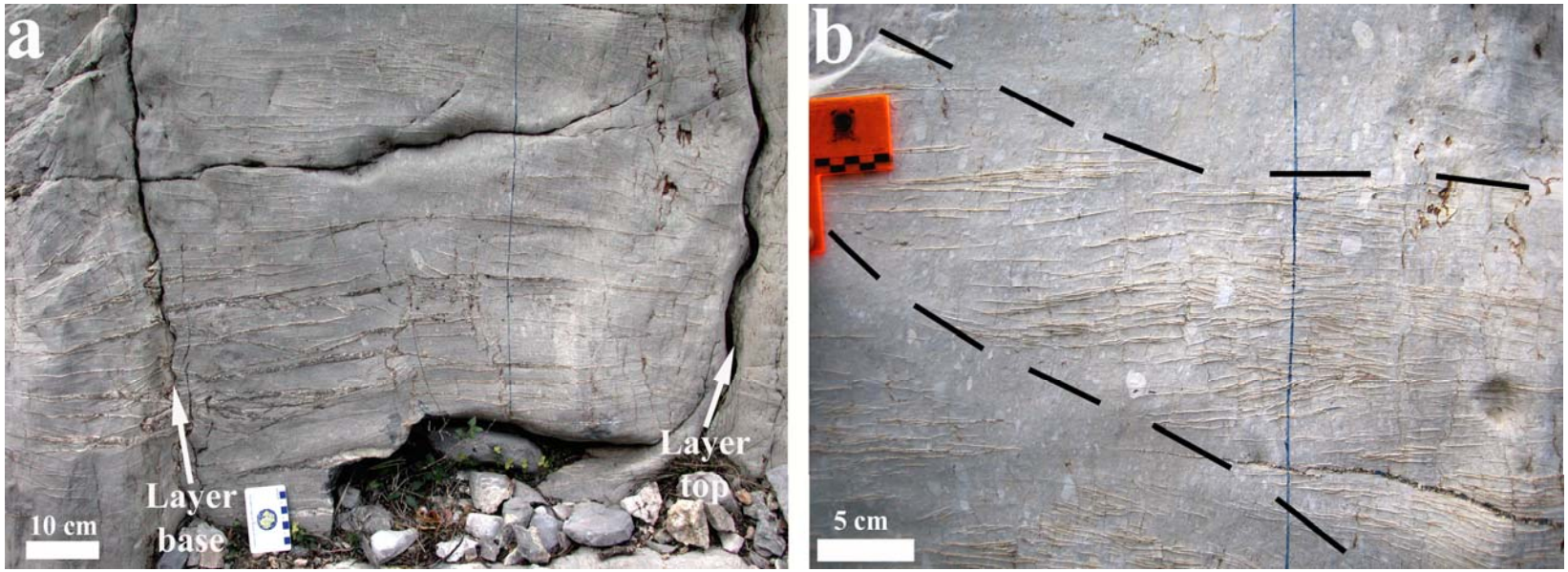

Figure 9.57 Photographs of two domains of scanline in layer OO1 from Escalera canyon. (a) Photograph of fractures typical of the eastern 1.6 m of scanline (topographically lower). Fractures tend to span the entire layer. Bedding parallel stylolites cross cut these fractures. (b) Photograph of fractures typical of the western 1.5 m of scanline (topographically higher). Fractures tend to span only part of the layer, display en-echelon patterns, which terminate outside the layer in faults.

Figure 9.58 Graphs of spatial correlation vs. length scale (thick continuous line) for (a) logarithmic graduations and (b) linear graduations for the Escalera OO1 data set (1160 fractures, all fracture sets combined, aperture threshold of 0.05 mm). In (a) and (b) the thin discontinuous line represents the upper 95% confidence limit while the thin dotted line represents the lower 95% confidence limit, and the thick discontinuous line corresponds to the mean of 100 randomized data sets. In (a) and (b) the thin continuous line represents the analytical solution of randomly arranged fractures with the same number of fractures and scanline length. Width of length-scale bin in (a) and (b) is 5 (m = 2) graduations of length scale. Power law in (a) was calculated using spatial correlation between length scales of 2 and 60 mm. Cluster width is estimated in (a) to be approximately 110 mm. Evenly spaced lines every 195 mm in (b) only match a few peaks of spatial correlation, which indicate that fracture clusters may not be periodically arranged. (c) Power spectrum of spatial correlation from (b). Of the four peaks of power spectral density in (c), three (242, 314 and 524 mm) are outside the 95% confidence interval for red noise, possibly indicating multiple periodic arrangement of clusters, all of which have different cluster spacings and are statistically significant.

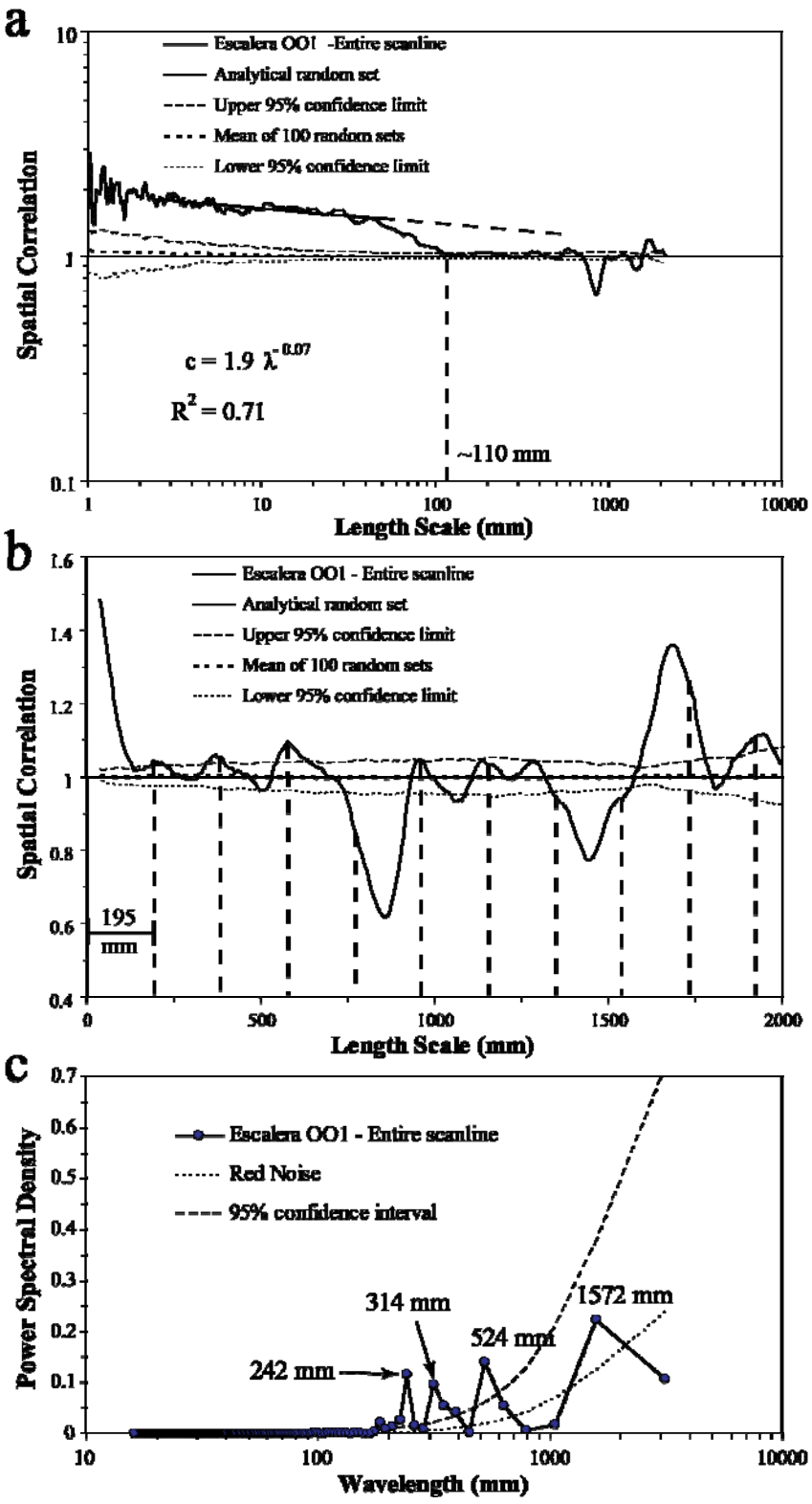
a
Escalera OO1 -Entire scanline
Analytical random set
Upper 95% confidence limit
Mean of 100 random sets
Lower 95% confidence limit
Spatial Correlation
c = 1.9 λ^-0.07
R^2 = 0.71
~110 mm
Length Scale (mm)
b
Escalera OO1 - Entire scanline
Analytical random set
Upper 95% confidence limit
Mean of 100 random sets
Lower 95% confidence limit
Spatial Correlation
195 mm
Length Scale (mm)
c
Escalera OO1 - Entire scanline
Red Noise
95% confidence interval
Power Spectral Density
314 mm
524 mm
1572 mm
242 mm
Wavelength (mm)

Figure 9.59 Graphs of spatial correlation vs. length scale (thick continuous line) for (a) logarithmic graduations and (b) linear graduations for the eastern 1.6 m of scanline of the Escalera OO1 data set (492 fractures, all fracture sets, aperture threshold of 0.05 mm). In (a) and (b) the thin discontinuous line represents the upper 95% confidence limit while the thin dotted line represents the lower 95% confidence limit, and the thick discontinuous line corresponds to the mean of 100 randomized data sets. In (a) and (b) the thin continuous line represents the analytical solution of randomly arranged fractures with the same number of fractures and scanline length. Width of length-scale bin in (a) and (b) is 5 (m = 2) graduations of length scale. Power law in (a) was calculated using spatial correlation between length scales of 2 and 60 mm. Although evenly spaced lines every 340 mm in (b) match all peaks of spatial correlation, only one peak is outside the 95% confidence interval, which may indicate that fracture clusters are periodically arranged. (c) Power spectrum of spatial correlation from (b). A noticeable peak of power spectra at 324 mm is outside the 95% confidence interval for red noise, indicating a periodic arrangement of fractures that is statistically significant and with a cluster spacing of 324 mm. Although for length scales larger than 500 mm the power spectral density for the natural data set is outside the 95% confidence interval for red noise, the trends for both the natural data set and the 95% confidence interval for red noise are similar, as shown in (c).

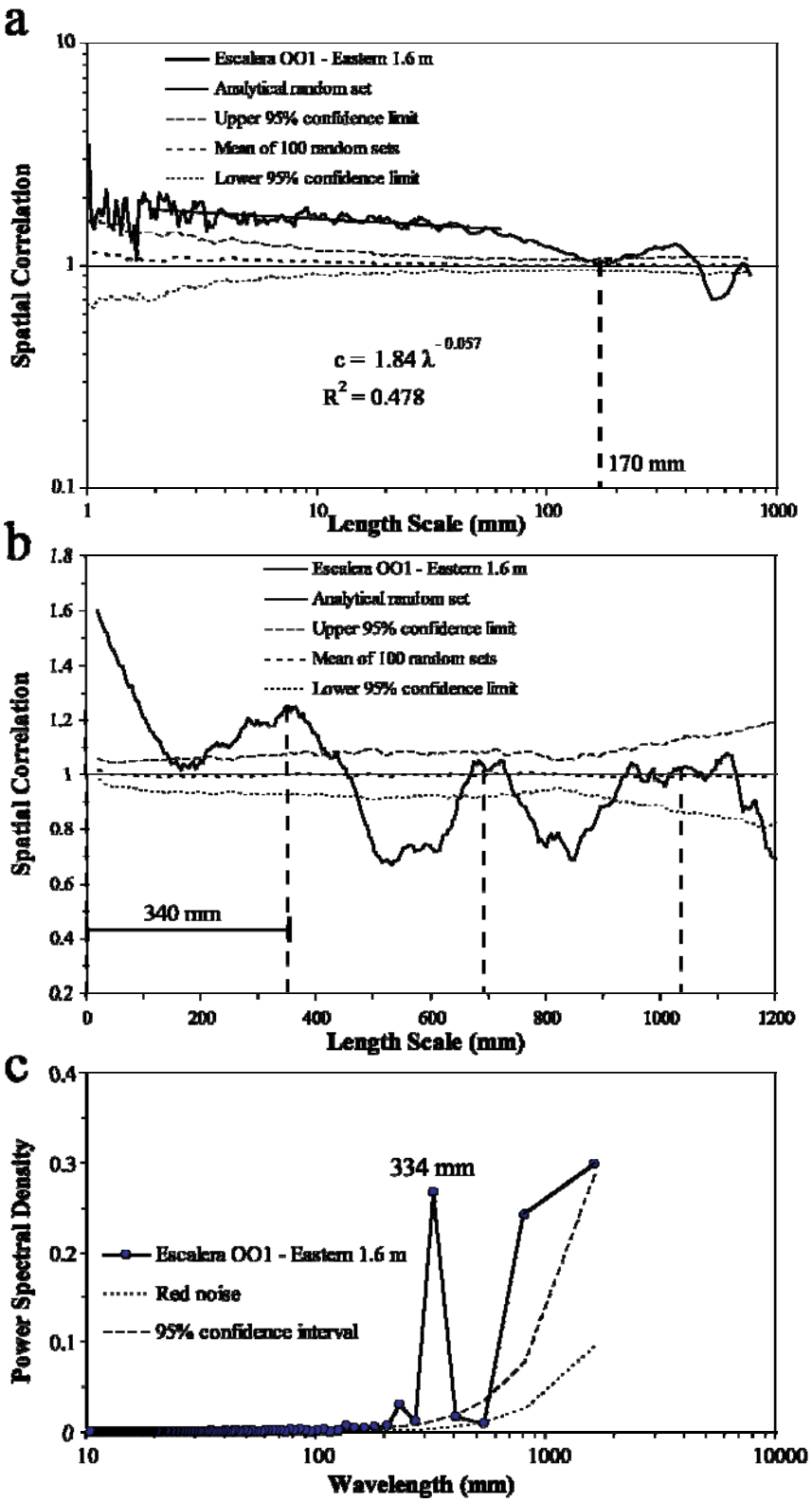
a
Escalera OO1 - Eastern 1.6 m
Analytical random set
Upper 95% confidence limit
Mean of 100 random sets
Lower 95% confidence limit
Spatial Correlation
c = 1.84 λ^-0.057
R^2 = 0.478
170 mm
Length Scale (mm)
b
Escalera OO1 - Eastern 1.6 m
Analytical random set
Upper 95% confidence limit
Mean of 100 random sets
Lower 95% confidence limit
Spatial Correlation
340 mm
Length Scale (mm)
c
334 mm
Escalera OO1 - Eastern 1.6 m
Red noise
95% confidence interval
Power Spectral Density
Wavelength (mm)

Figure 9.60 Graphs of spatial correlation vs. length scale (thick continuous line) for (a) logarithmic graduations and (b) linear graduations for the western 1.5 m of scanline of the Escalera OO1 data set (668 fractures, all fracture sets, aperture threshold of 0.05 mm). The thin discontinuous line represents the upper 95% confidence limit while the thin dotted line represents the lower 95% confidence limit, and the thick discontinuous line corresponds to the mean of 100 randomized data sets. In (a) and (b) the thin continuous line represents the analytical solution of randomly arranged fractures with the same number of fractures and scanline length. Width of length-scale bin is 5 (m = 2) graduations of length scale for (a) and (b). Power law in (a) was calculated using spatial correlation of Escalera OO1 data set between length scales of 2 and 90 mm. Two peaks (185 and 560 mm) of spatial correlation in (b) are outside the 95% confidence interval. Although the second peak of spatial correlation (560 mm) is approximately a multiple of the first peak (185 mm, dashed line), there is no evidence of an intermediate multiple (370 mm), which suggest that arrangement is not periodic. (c) Power spectrum of spatial correlation from (b). The natural data set exhibits two peaks (185 and 431 mm) in (c) with power spectral density that is several times the 95% confidence interval for red noise, possibly indicating two periodic arrangement of clusters, both statistically significant and each one with a distinctive cluster spacings. Although there seems to be a peak of spatial correlation at 185 mm in (b), a peak at 431 mm is not evident.

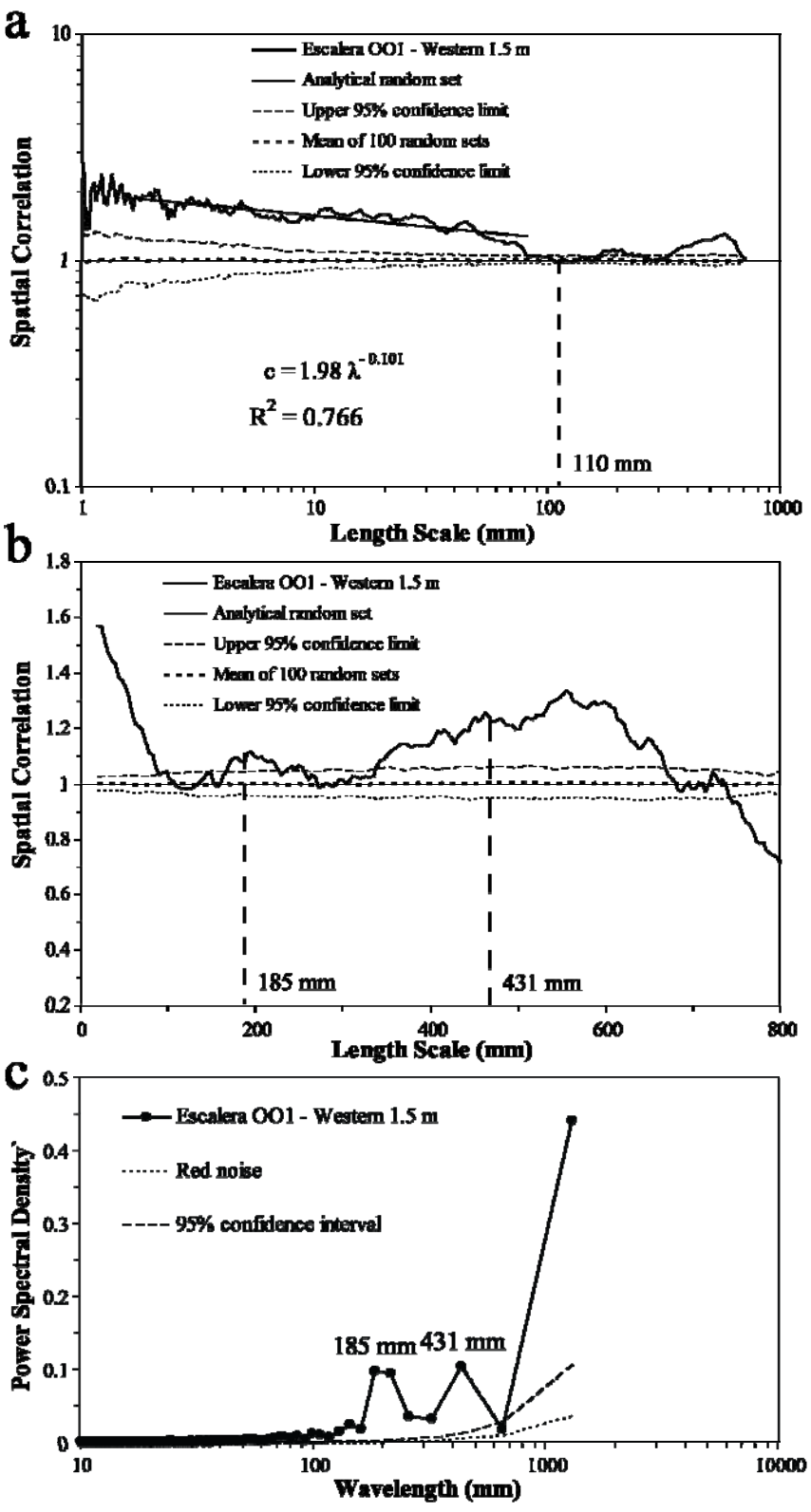
a
Escalera OO1 - Western 1.5 m
Analytical random set
Upper 95% confidence limit
Mean of 100 random sets
Lower 95% confidence limit
Spatial Correlation
c = 1.98 λ^-0.101
R^2 = 0.766
110 mm
Length Scale (mm)
b
Escalera OO1 - Western 1.5 m
Analytical random set
Upper 95% confidence limit
Mean of 100 random sets
Lower 95% confidence limit
Spatial Correlation
185 mm
431 mm
Length Scale (mm)
c
Escalera OO1 - Western 1.5 m
Red noise
95% confidence interval
Power Spectral Density
185 mm
431 mm
Wavelength (mm)

Restoring bedding to horizontal allows comparison of the orientation of fracture sets from opposing limbs of San Blas anticline at Escalera canyon (Figure 9.61). Set A shows a similar orientation in both limbs once bedding is restored to horizontal. In addition, fractures of set A in both limbs exhibit the typical characteristics of Y fractures (Table 9.4). Although fractures of set B in both forelimb and backlimb were classified as Y fractures (Table 9.4), interpretation of their orientation in both limbs is less clear. Orientation of restored set B in the forelimb from one layer (Escalera OO1) is relatively close to the restored orientation of set A in the same limb (Figure 9.61a), which could indicate that fractures of set B of Escalera OO1 could be part of set A. In contrast, restored set B for layer Escalera OO12 in the forelimb (Figure 9.61a) exhibits an orientation more similar to the restored set B in the backlimb (Figure 9.61b). Restored fractures of set C in the backlimb (categorized as Z fractures, Table 9.4) do not seem to be in the forelimb. Likewise, restored fractures of set D in the forelimb do not appear to be in the backlimb (Figure 9.61).

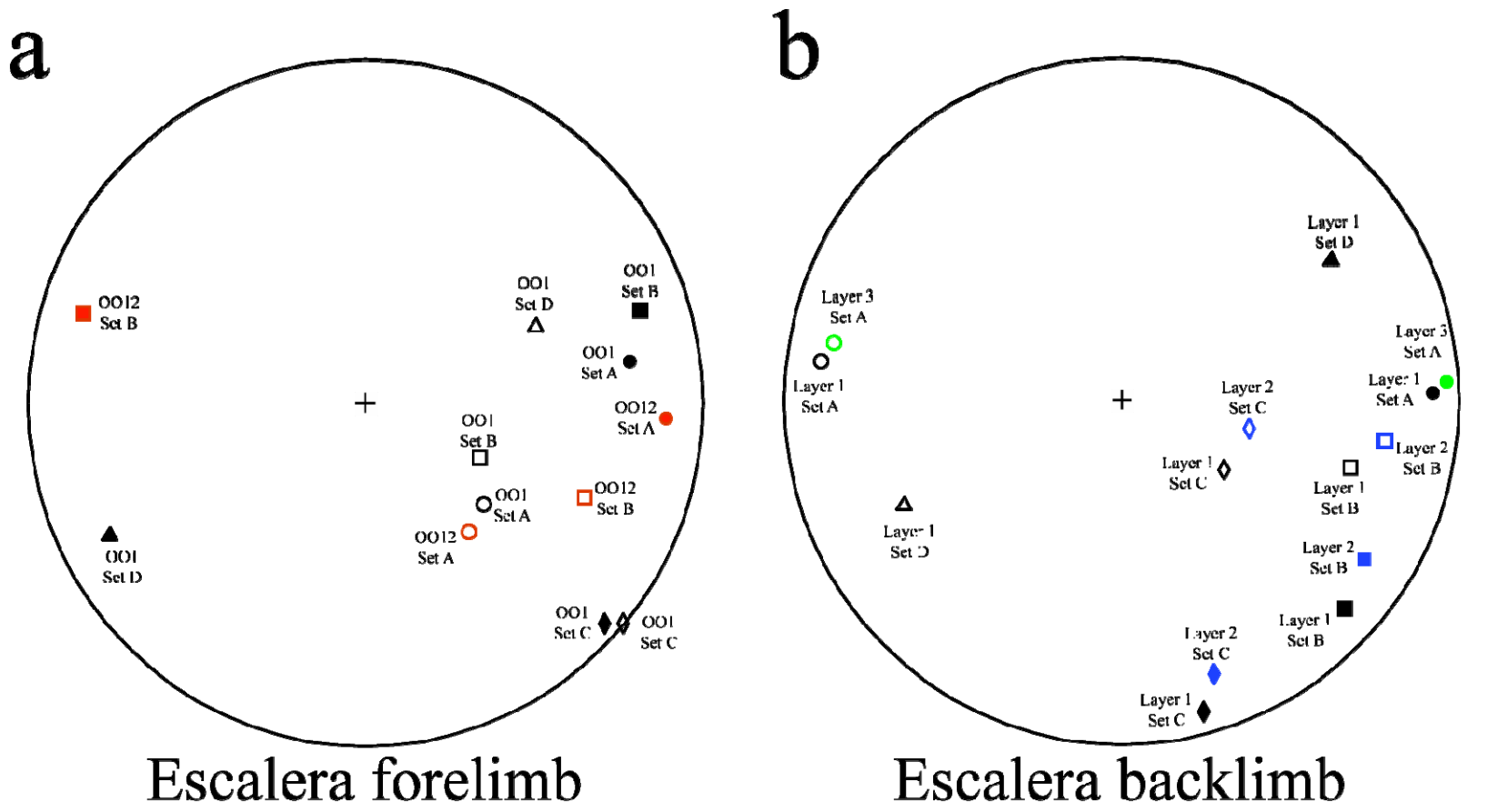

Figure 9.61 Equal area stereographic projection of poles to fractures for (a) forelimb of San Blas anticline at Escalera canyon and (b) backlimb of San Blas anticline at Escalera canyon. Fracture orientation as measured in field is represented by hollow symbols whereas fracture orientation with bedding restored to horizontal is represented by filled symbols. Color of symbols indicate the layer name, whereas different symbols indicate different fracture set (circle for set A, square for set B, diamond for Set C, and triangle for set D).

9.4.7 Layer OO12 at Escalera Canyon (Escalera OO12)

Like Escalera OO1, Escalera OO12 is located in the forelimb of San Blas anticline exposed in the Escalera canyon (Figure 2.7). Fracture apertures on Escalera OO12 were measured by Ortega (2002). Escalera OO12 is 24.5 cm thick and is a dolopackstone that suffered widespread recrystallization (e.g., Figure 9.31b). Escalera OO12 is located 2 m above the base of the stratigraphic column measured in the forelimb of San Blas anticline by Ortega (2002). I measured 1095 veins, of which 1047 have apertures greater than or equal to 0.05 mm. For the 48 veins with apertures smaller than 0.05 mm only spacing was recorded (Table 9.1). Because these 48 veins were recorded at one end of the scanline their presence in the scanline is biased and therefore they will be removed for subsequent spatial arrangement analysis.

The scanline has a length of 3.56 m, was positioned in the middle of the layer and recorded a strain of 20.44%. The 1047 fractures with apertures equal to or larger than 0.05 mm at Escalera OO12 exhibit a power-law distribution of fracture apertures (Table 9.5). Spacings between the 1095 fractures exhibit a logarithmic distribution and a coefficient of variation of 1.33 (Table 9.5). Fractures were assigned to two different sets depending on their orientation (Table 9.3). Fracture sets A and B of layer Escalera OO12 have the same orientation as similarly named sets of layer Escalera OO1 (Table 9.3). 93% of the fractures measured represent set A and 7 % represent set B (Table 9.3). As with layer Escalera OO1, sets A and B of Escalera OO12 have similar orientations (231/40 and 203/60, respectively) and therefore might be part of a single set. In thin sections (Table 9.2), fractures of sets A and B exhibit features of Y fractures such as straight traces (e.g., Figure 9.31b), fibrous dolomite lining fracture walls, bridges of quartz with crack-seal texture (e.g., Figure 9.25), and calcite precipitated between quartz bridges and also replacing quartz (e.g., Figure 9.25).

Fractures in the Escalera OO12 data set display a heterogeneous arrangement of fractures (Figure 9.62). Fracture intensity indicates clusters and areas with few fractures that do not seem be regularly spaced (Figure 9.62). Spatial correlation for all fracture sets at Escalera OO12 varies as a power-law of length scale (Figure 9.63a), which indicates a fractal arrangement of fractures (Figure 9.4b) inside clusters with a cluster width of 150 mm. Spatial correlation for linearly graduated length scales for all fracture sets of Escalera OO12 shows a pattern of alternating peaks and troughs (two peaks are outside the 95% confidence interval) that is interpreted as a periodic arrangement of fracture clusters (Figure 9.4g) with a cluster spacing of 850 mm (Figure 9.63b). Power spectrum of the spatial correlation for linearly graduated length scales exhibits a peak at 867 mm that is outside the 95% confidence interval for red noise (Figure 9.63c), which confirms the statistical significance of the periodic arrangement of fracture clusters with cluster spacing of 850 mm indicated by spatial correlation.

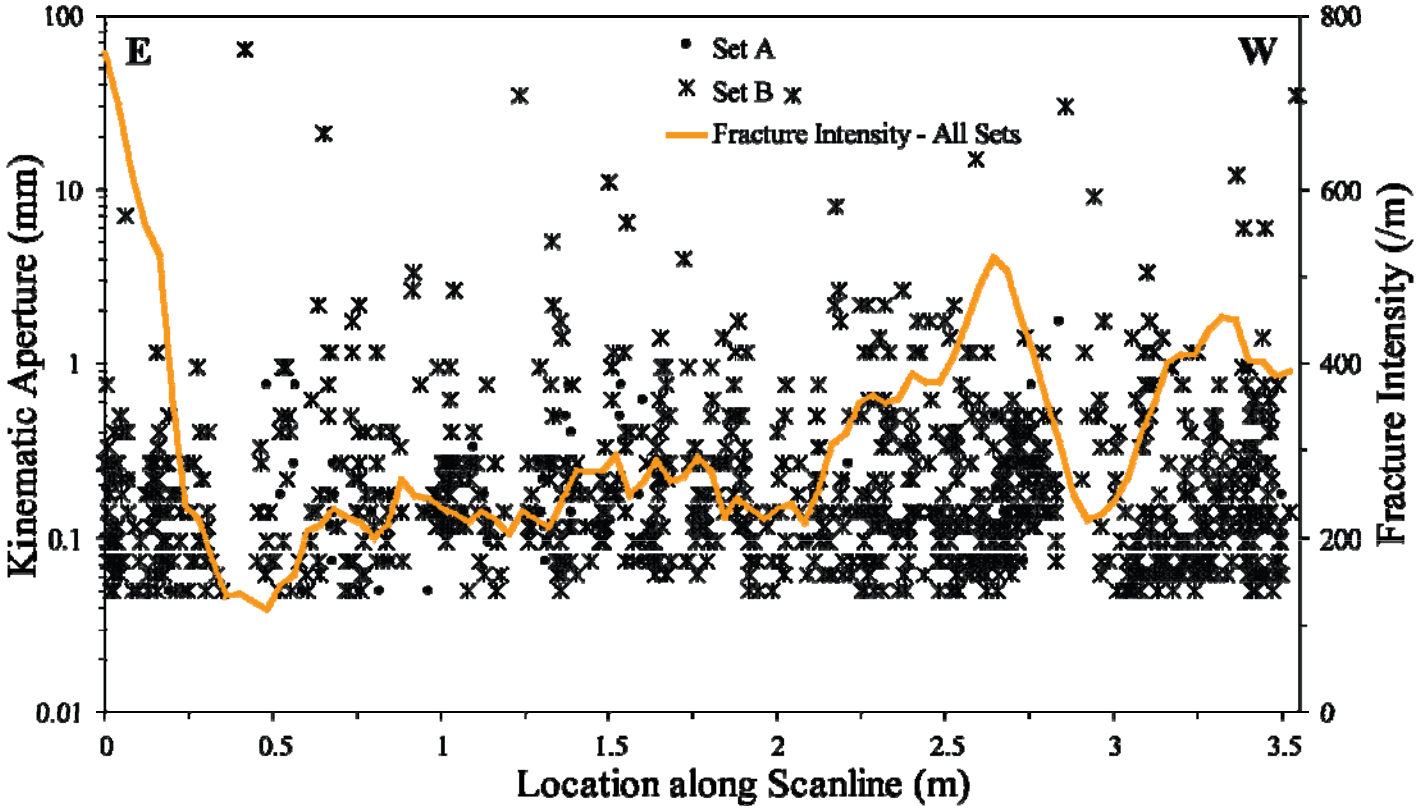

Figure 9.62 Kinematic aperture (circles for set A, and asterisks for set B) and fracture intensity (orange thick line) versus location along scanline for the Escalera OO12 data set. Note that kinematic aperture axis uses logarithmic graduations. Fracture intensity was calculated inside a moving window with width (window size) of 0.16 m that was moved in increments (window step) 0.04 m. Peaks of fracture intensity indicate clusters at 0, 2.6, and 3.3 m, but clusters do not seem regularly spaced. Although 1095 fractures were used to calculate the curve of fracture intensity, only the aperture of the 1047 fractures of sets A and B with apertures equal or larger than 0.05 mm was plotted.

Figure 9.63 Graphs of spatial correlation vs. length scale (thick continuous line) for (a) logarithmic graduations and (b) linear graduations for fractures with apertures equal or larger than 0.05 mm of the Escalera OO12 Outcrop data set (1047 fractures, aperture threshold of 0.05 mm). In (a) and (b) the thin discontinuous line represents the upper 95% confidence limit while the thin dotted line represents the lower 95% confidence limit, and the thick discontinuous line corresponds to the mean of 100 randomized data sets. In (a) and (b) the thin continuous line represents the analytical solution of randomly arranged fractures with the same number of fractures and scanline length. Width of length-scale bin is 7 (m = 3) for (a) and 13 (m = 6) for (b). The power-law pattern of spatial correlation in (a) indicates that fractures inside clusters have a fractal spatial arrangement and that cluster width is approximately 150 mm. Peaks of spatial correlation are approximately evenly spaced every 850 mm (thick dashed lines), as shown in (b), and are indicative of periodically arranged clusters. (c) Power spectrum of spatial correlation from (b). A relatively broad peak with power spectral density that is several times the equivalent for the 95% confidence interval for red noise is visible in (c) at 867 mm, indicating a non-random periodic arrangement of fractures with a cluster spacing of approximately 867 mm. Another peak of power spectral density at a wavelength of 400 mm is outside the 95% confidence interval for red noise, but the difference between the peak and the 95% confidence interval is small when compared with other data sets (e.g., set D of Escalera 1, Figure 9.45c).

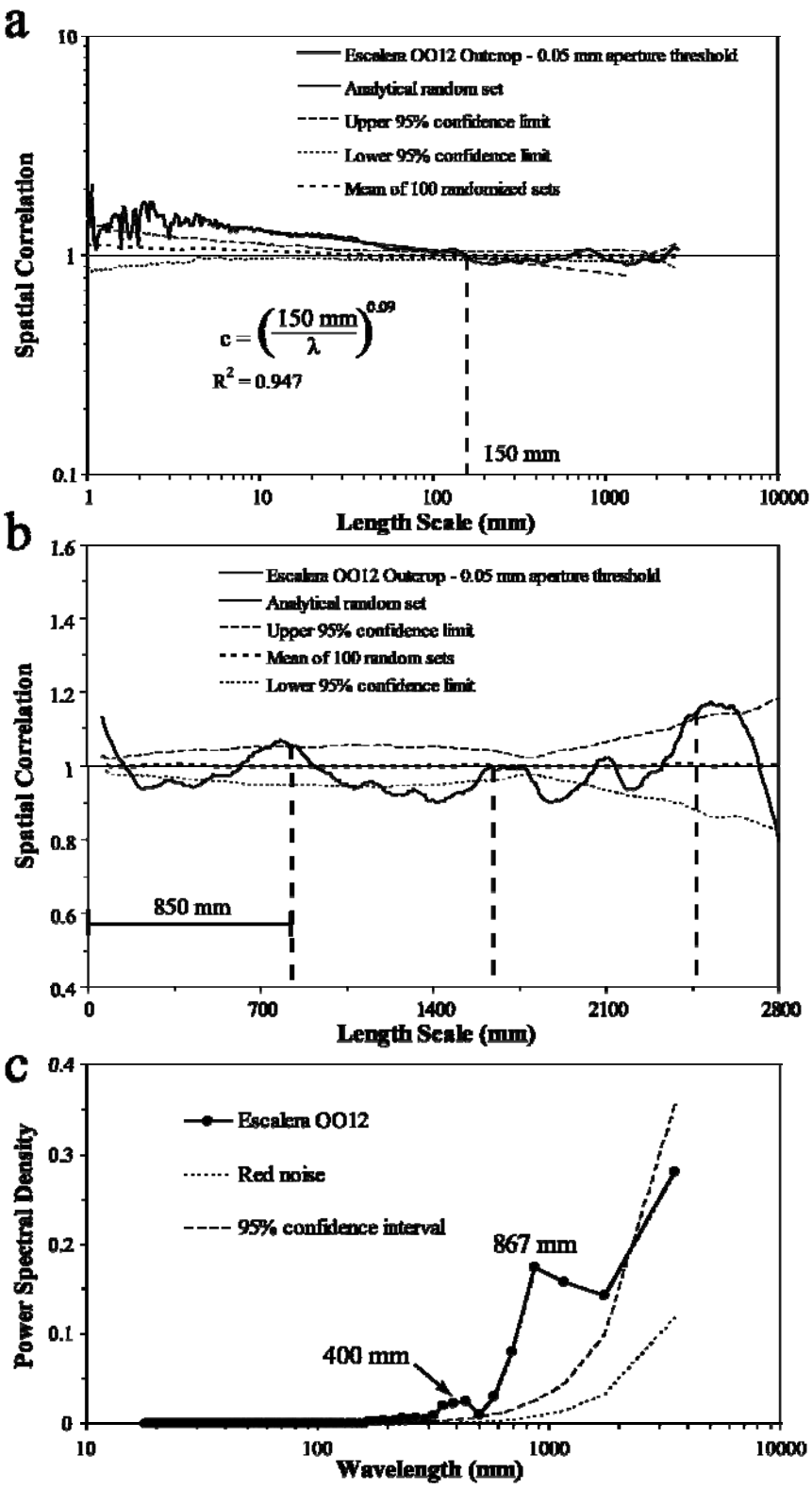
a
Escalera OO12 Outcrop - 0.05 mm aperture threshold
Analytical random set
Upper 95% confidence limit
Lower 95% confidence limit
Mean of 100 randomized sets
Spatial Correlation
$c = \left(\frac{150\ mm}{\lambda}\right)^{0.09}$
$R^2 = 0.947$
150 mm
Length Scale (mm)
b
Escalera OO12 Outcrop - 0.05 mm aperture threshold
Analytical random set
Upper 95% confidence limit
Mean of 100 random sets
Lower 95% confidence limit
Spatial Correlation
850 mm
Length Scale (mm)
c
Escalera OO12
Red noise
95% confidence interval
867 mm
400 mm
Power Spectral Density
Wavelength (mm)

9.4.8 Layer 11 at Palmas Canyon (Palmas 11 LR)

Two data sets (High Resolution, or HR, and Low Resolution, or LR) with different aperture thresholds (0.075 and 0.95 mm, respectively) were measured in layer 11 at Palmas canyon (Figure 2.7). The Palmas 11 LR data set was measured in a cross sectional exposure along a 21.1 m long scanline (Table 9.1). Palmas 11 is 27 cm thick lime dolowackstone that suffered dedolomitization (Figure 9.31a). Palmas 11 is located 84 m above the base of the stratigraphic column measured by Ortega (2001) in the forelimb of San Blas anticline at Palmas canyon and is located 20 m above the lower boundary of the Cupidito member of the Cupido Formation (Ortega, 2002). Three sets (A, B, and C) of fractures were recorded in Palmas 11 (Table 9.3) by Dr. J. Gale, who measured 262 veins using an aperture threshold of 0.95 mm, and recorded a strain of 4.59% (Table 9.5). Fractures of the Palmas 11 LR data set exhibit a power-law distribution of fracture apertures, a log-normal distribution of fracture spacings, and a coefficient of variation of fracture spacings of 1.72 (Table 9.5). 44% of the fractures measured represent set A, 35% represent set B, and 21% represent set C (Table 9.3). In thin sections (Table 9.2), fractures exhibit most of the typical features of Y fractures such as straight traces (e.g., Figure 9.16a), microfractures that occasionally anastomose (e.g., Figure 9.16a), fibrous dolomite crystals lining fracture walls, bridges of subhedral dolomite and quartz (e.g., Figure 9.19), and calcite precipitated between bridges (Table 9.4). However, the only rock sample available could not be oriented and therefore fractures could not be assigned to specific fracture sets.

The Palmas 11 LR data set displays a heterogeneous arrangement of fractures in space, as shown by fracture intensity in Figure 9.64 (Marrett et al., 2004). Although the small width of clusters, compared with the scanline length (21 m, Table 9.5), obscures clustering of fractures in the Palmas 11 LR data set (Figure 9.64a), NCC shows a fractal

arrangement inside clusters (Figures 9.4b and 9.65a), which in turn have a periodic arrangement (Figures 9.4g and 9.65b). Cluster width and cluster spacing are 220 mm (Figure 9.65a) and 1100 mm (Figure 9.65b), respectively. The power spectrum of spatial correlation for linearly graduated length scales displays a significant peak at a wavelength of 1089 mm with several times the magnitude of the 95% confidence interval for red noise, which indicates a statistically significant periodic arrangement of clusters spaced at 1089 mm (Figure 9.65c). Although power spectrum also yielded a peak at a wavelength of 4900 mm, the power spectral density of a wavelength of 4900 mm is smaller than the equivalent for randomly arranged fractures and therefore cannot be considered statistically significant (Figure 9.65c).

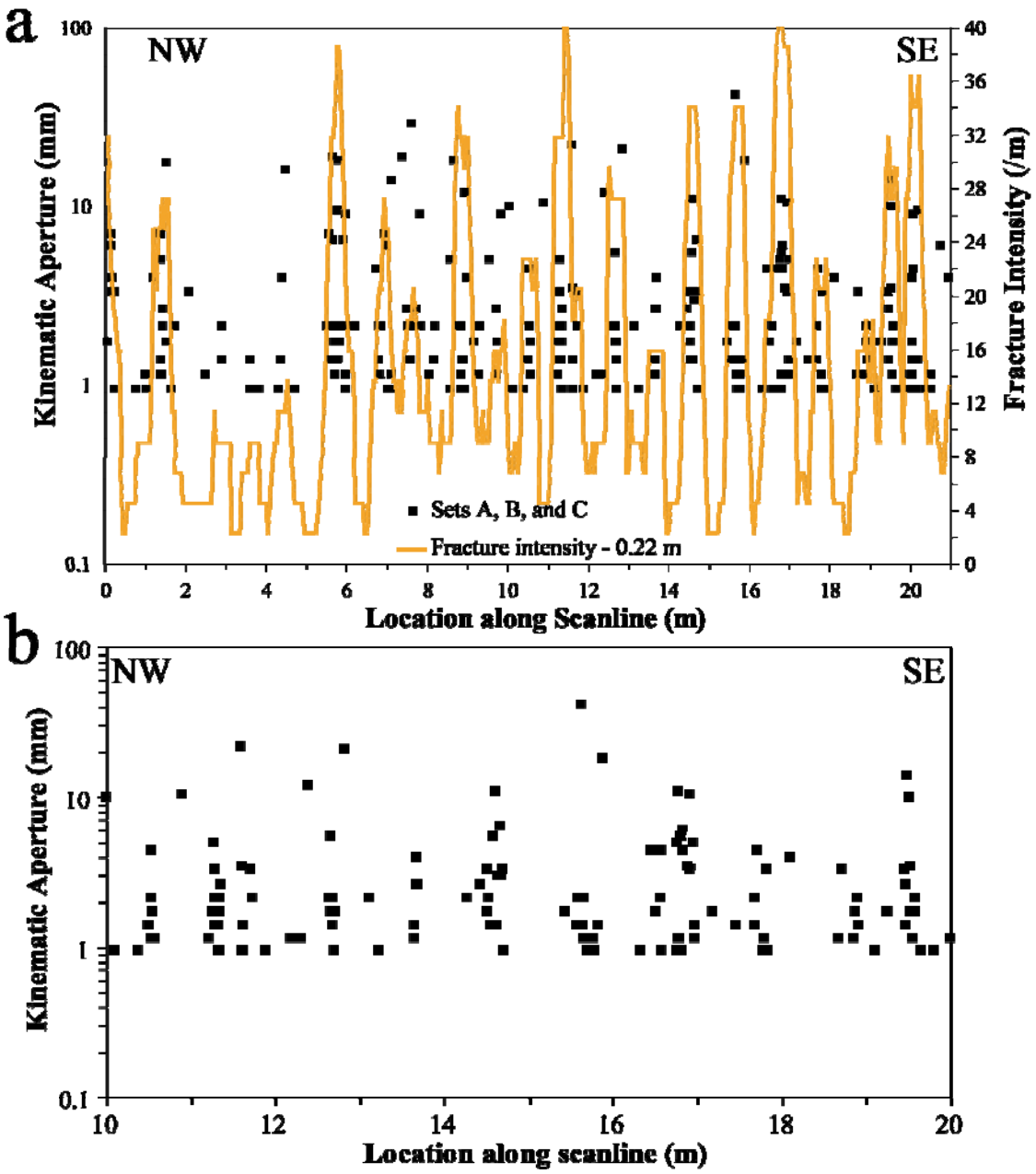

Figure 9.64 Kinematic aperture (squares) and fracture intensity (orange thick line) versus location along scanline for all (a) and part (b) of the Palmas 11 LR data set. Fracture intensity was calculated inside a moving window with width (window size) equal to cluster width as estimated by NCC (0.22 m, Figure 9.65a) that was moved in increments (window step) of 0.05 m. Please note that only the kinematic aperture axis use logarithmic graduations. Clusters are more easily detected in (b) than in (a) because cluster width is larger compared with the plotted scanline.

Figure 9.65 Graphs of spatial correlation (thick continuous line) vs. length scale for (a) logarithmic graduations and (b) linear graduations for the Palmas 11 LR data set (262 fractures, all fracture sets combined, aperture threshold of 0.95 mm). In (a) and (b) the thin discontinuous line represents the upper 95% confidence limit while the thin dotted line represents the lower 95% confidence limit, and the thick discontinuous line corresponds to the mean of 100 randomized data sets. In (a) and (b) the thin continuous line represents an example randomized set generated with the same number of fractures and scanline length. Width of length-scale bin in (a) and (b) is 5 graduations of length scale (m = 2). Spatial correlation in (a) follows a power-law pattern. Power law equation in (a) was calculated using spatial correlation of Palmas 11 LR data set between length scales of 12 and 664 mm. Cluster width is approximately 220 mm, as shown in (a). Evenly spaced lines every 1100 mm in (b) match approximately peaks of spatial correlation, which display a regularly spaced pattern, indicative of periodically arranged clusters with a cluster spacing of approximately 1100 mm. (c) Power spectrum of spatial correlation from (b). A noticeable peak at a wavelength of 1089 mm has a power spectral density that is several times the equivalent for the 95% confidence interval for red noise, indicating a periodic arrangement of fractures that is statistically significant and with a cluster spacing of 1089 mm.

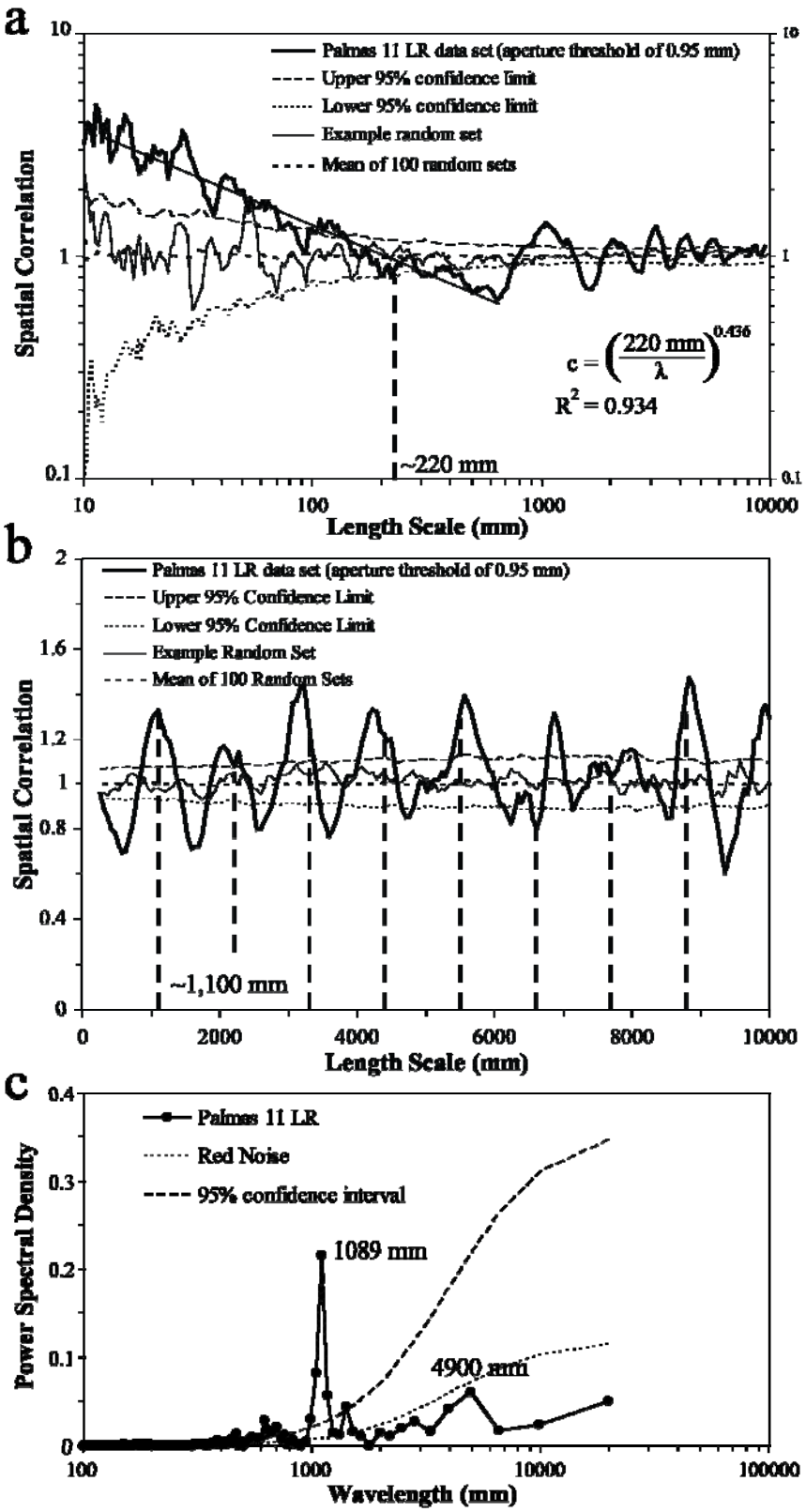
a
Palmas 11 LR data set (aperture threshold of 0.95 mm)
Upper 95% confidence limit
Lower 95% confidence limit
Example random set
Mean of 100 random sets
Spatial Correlation
$c = \left(\frac{220\ mm}{\lambda}\right)^{0.436}$
$R^2 = 0.934$
~220 mm
Length Scale (mm)
b
Palmas 11 LR data set (aperture threshold of 0.95 mm)
Upper 95% Confidence Limit
Lower 95% Confidence Limit
Example Random Set
Mean of 100 Random Sets
Spatial Correlation
~1,100 mm
Length Scale (mm)
c
Palmas 11 LR
Red Noise
95% confidence interval
Power Spectral Density
1089 mm
4900 mm
Wavelength (mm)

9.4.9 Layer 12 at Palmas Canyon (Palmas 12)

As its name indicates, Palmas 12 layer is located stratigraphically between layers Palmas 11 and Palmas 13. Palmas 12 is a 47-cm thick lime dolowackstone. Palmas 12 is located approximately 7 m stratigraphically above the layer Palmas 11, above the stratigraphic column measured by Ortega (2002) in the forelimb of the San Blas anticline, and therefore is also within the Cupidito member of the Cupido Formation. Fractures in Palmas 12 were measured in the middle of the layer in a cross sectional exposure along a 6.1 m long scanline (Figure 9.66). Two sets of fractures (A and B) were recorded in Palmas 12 (Table 9.3). Using an aperture threshold of 0.265 mm, I measured 316 veins and recorded a strain of 12.7% (Table 9.5). The fractures of Palmas 12 exhibit a power-law distribution of fracture apertures, a negative exponential distribution of fracture spacings, and a coefficient of variation of fracture spacings of 1.07 (Table 9.5). 60% of the fractures measured represent set A and 40% represent set B (Table 9.3). In thin sections (Table 9.2), fractures of sets A and B exhibit typical features of X fractures (Table 9.4) such as irregular traces (Figures 9.6, 9.7, and 9.9a), microfractures with ghost or relic textures (inset, Figure 9.9a), euhedral and translucent bridges of dolomite (Figure 9.11) with local bands of fluid inclusions, and calcite precipitated between dolomite bridges (Figures 9.9a and 9.11). Qualitative study of intersections between fractures of sets A and B in the field and in thin section revealed mutually crosscutting relationships, likely indicating that fracture sets developed simultaneously.

Spatial correlation for logarithmically graduated length scales of fractures in the Palmas 12 outcrop does not follow a systematic pattern with length scale, which indicates an arrangement of fractures indistinguishable from random (Figures 9.4a and 9.67a). Position along scanline of Palmas 12 fractures might suggest clusters that are regularly-spaced between 1.1 and 1.5 m (Figure 8.66). Although spatial correlation for linearly

graduated length scales also suggests periodic arrangement of clusters (because the presence of alternating small peaks and troughs), suggested cluster spacing is 461 mm (Figures 9.4g and 9.67b). A peak of the power spectrum outside the 95% confidence interval suggests that clusters might be periodically arranged with a spacing of approximately 461 mm (Figure 9.67c), which is a cluster spacing similar to the one suggested by NCC (dashed lines, Figure 9.67b). However, there are three reasons that the pattern of spatial correlation is best interpreted as indistinguishable from random (Figure 9.4e). First, none of the peaks of spatial correlation are statistically significant. Second, the amplitude between peaks and troughs of spatial correlation is smaller than the 95% confidence interval (Figure 9.67b). And third, the peak of power spectral density at 461 mm is only slightly above the 95% confidence interval for red noise (Figure 9.67c).

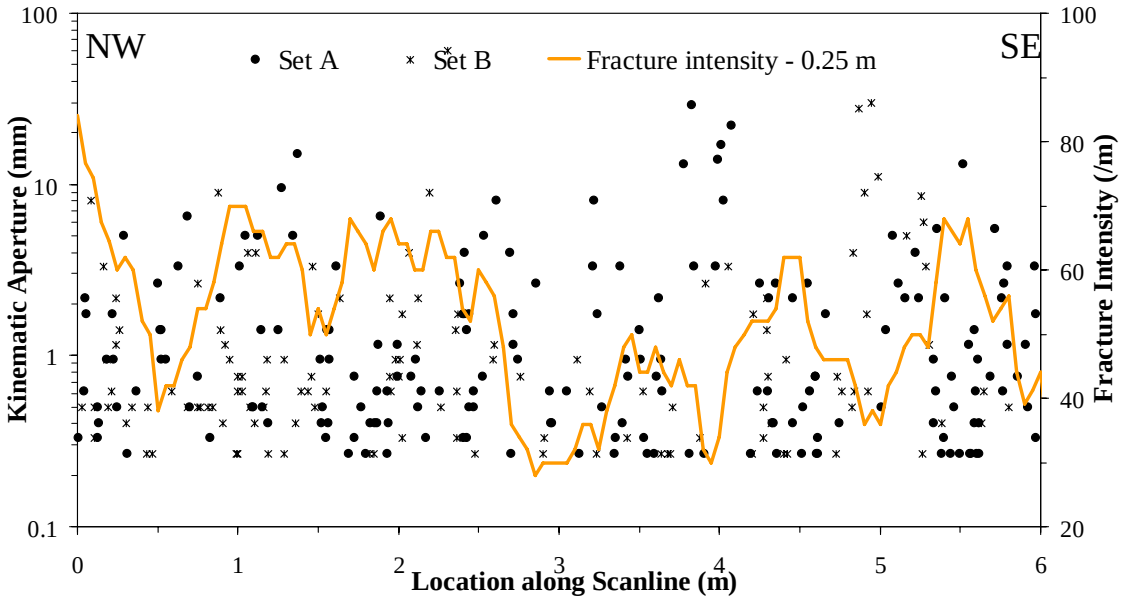

Figure 9.66 Kinematic aperture (circles for set A, asterisks for set B) and fracture intensity versus location along scanline for the Palmas 12 data set. Note that kinematic aperture axis uses logarithmic graduations. Fracture intensity was calculated inside a moving window with width (window size) of 0.25 m that was moved in increments (window step) 0.03 m. Peaks of fracture intensity could indicate statistically significant clusters at 1, 2.5, 3.4, 4.5, and 5.6 m.

Figure 9.67 Graphs of spatial correlation vs. length scale (thick continuous line) for (a) logarithmic graduations and (b) linear graduations for fractures of the Palmas 12 data set (316 fractures, all fracture sets combined, aperture threshold of 0.265 mm). In (a) and (b) the thin discontinuous line represents the upper 95% confidence limit while the thin dotted line represents the lower 95% confidence limit, and the thick discontinuous line corresponds to the mean of 100 randomized data sets. In (a) and (b) the thin continuous line represents the analytical solution of randomly arranged fractures with the same number of fractures and scanline length. Width of length-scale bin in (a) and (b) is 11 graduations of length scale (m = 5). There is no pattern of spatial correlation that can be identified (e.g., power law) outside the 95% confidence interval in (a). Variations of spatial correlation with length scale in (b) cannot be conclusively interpreted as periodically arranged clusters. (c) Power spectrum of spatial correlation from (b). The power spectral density for the natural data set exhibits the same trend as the red noise, as shown in (c). The natural data set exhibits a peak at a wavelength of 461 mm, which has a power spectral density slightly larger than the 95% confidence interval for red noise, but the difference between the peak and the 95% confidence interval is small when compared with other data sets (e.g., set D of Escalera 1, Figure 9.45c).

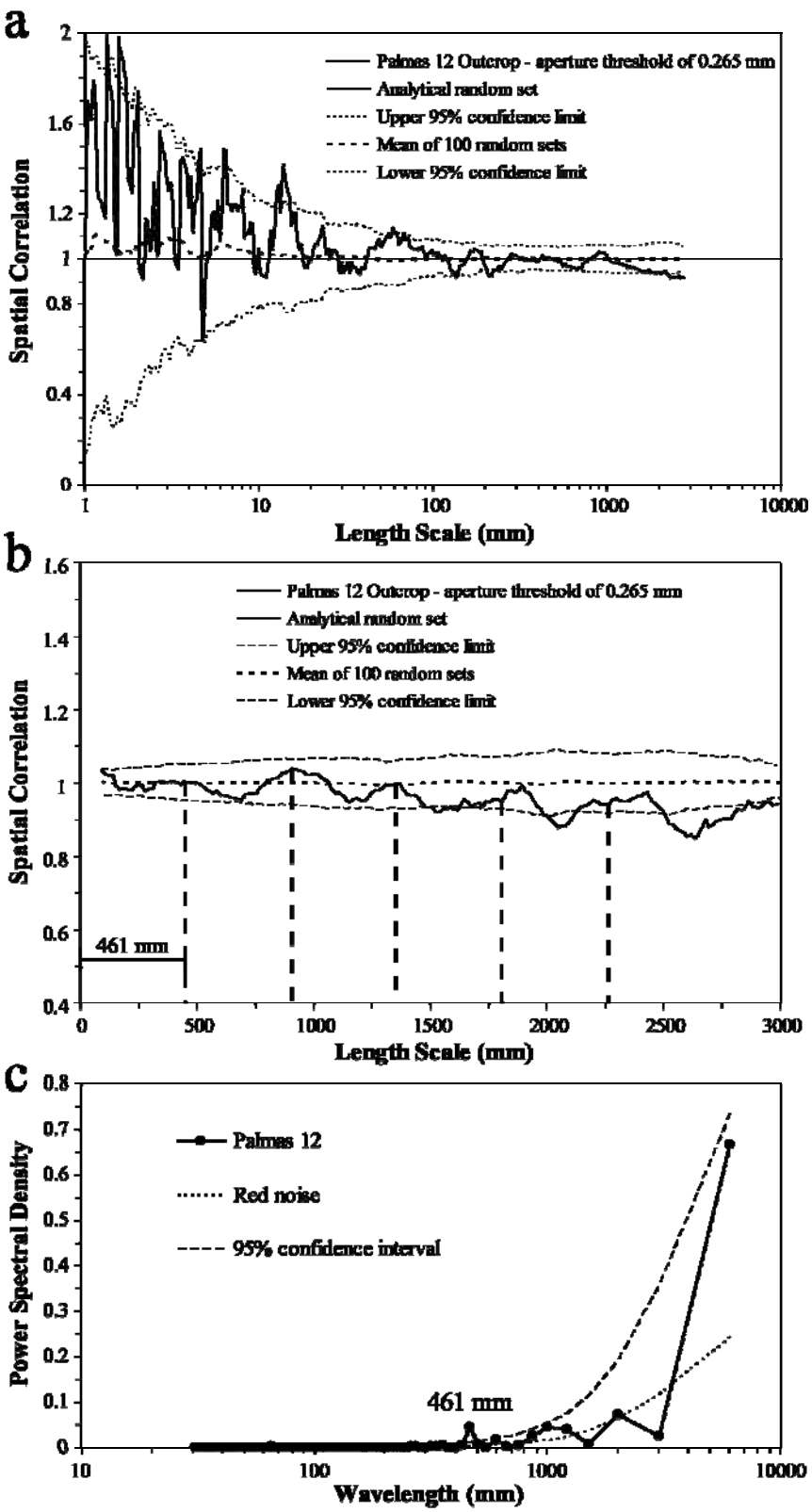
a
Palmas 12 Outcrop - aperture threshold of 0.265 mm
Analytical random set
Upper 95% confidence limit
Mean of 100 random sets
Lower 95% confidence limit
Spatial Correlation
Length Scale (mm)
b
Palmas 12 Outcrop - aperture threshold of 0.265 mm
Analytical random set
Upper 95% confidence limit
Mean of 100 random sets
Lower 95% confidence limit
Spatial Correlation
461 mm
Length Scale (mm)
c
Palmas 12
Red noise
95% confidence interval
Power Spectral Density
461 mm
Wavelength (mm)

9.4.10 Layer 13 at Palmas Canyon (Palmas 13)

Palmas 13 is located 11 m stratigraphically above layer Palmas 11, above the stratigraphic column measured by Ortega (2002) in the forelimb of the San Blas anticline, and therefore is within the Cupidito member of the Cupido Formation. Palmas 13 is a 24-cm thick dolowackstone (Figure 9.68). The two sets of fractures measured in Palmas 13 (A and B) have the same orientations as sets in Palmas 12 (Table 9.3). Using an aperture threshold of 0.14 mm, in a scanline of approximately 5.5 m, I measured 459 calcite-filled veins, which display a strain of 9.16% (Tables 9.1 and 9.5). Scanline at Palmas 13 was positioned in the middle of the layer in a cross-sectional outcrop (Figure 9.68). Fractures at Palmas 13 exhibit a power-law distribution of fracture apertures, a negative exponential distribution of fracture spacings, and a coefficient of variation of fracture spacings of 0.93 (Table 9.5). 62% of the fractures measured represent set A and 38% represent set B (Table 9.3). In thin sections (Table 9.2), fractures of sets A and B exhibit the typical features of X fractures (Table 9.4) such as irregular traces (Figure 9.8), emergent threshold (Figure 9.8), euhedral and translucent bridges of dolomite (Figures 9.8 and 9.10) that locally exhibit bands of fluid inclusions (Figure 9.12 and 9.13), and calcite precipitated between dolomite bridges (Figures 9.8, 9.10, 9.12 and 9.13). Qualitative study of intersections between fractures of sets A and B in the field and in thin sections revealed mutually crosscutting relationships, likely indicating that fracture sets developed simultaneously.

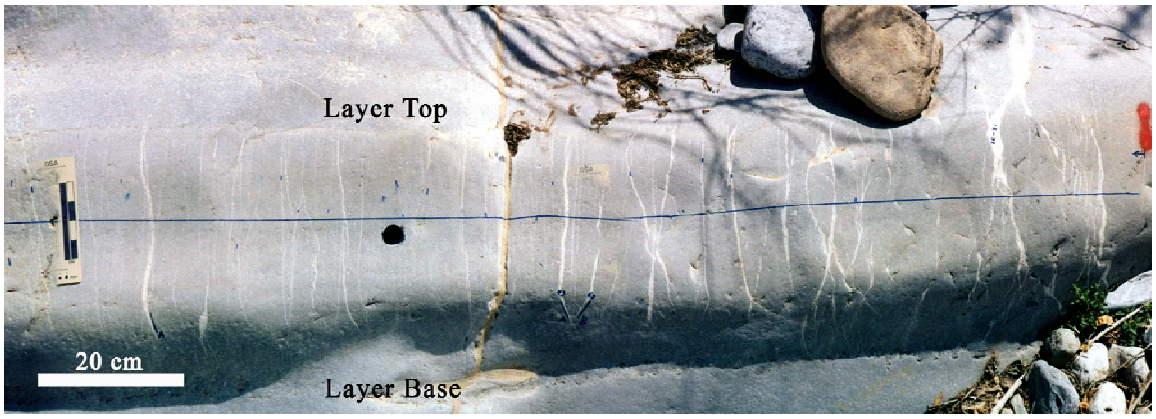

Figure 9.68 Photograph of the northern 1.5 meters of scanline in cross-sectional exposure of layer 13 from Palmas canyon (Cupido Fm.). Scanline was located approximately half-way between top and base of layer. Notice that most fractures are confined between layer boundaries and that obvious fracture clusters are lacking.

Fracture intensity indicates that the Palmas 13 data set exhibits clusters that might not be regularly spaced (Figure 9.69). This interpretation of the fracture intensity along the scanline is in agreement with NCC analyses of the data set (Figure 9.70). Spatial correlation versus length scale for logarithmic (Figure 9.70a) and linear (Figure 9.70b) graduations of length scale for fractures in the Palmas 13 outcrop data set yield a non-systematic pattern, which indicate arrangement of fractures is indistinguishable from random (Figures 9.4a and 9.4e) and that clusters, when present, are not statistically significant. In addition, the power spectrum of the spatial correlation for linearly graduated length scales shows a trend similar to red noise, which supports a spatial arrangement that is indistinguishable from random (Figure 9.70c).

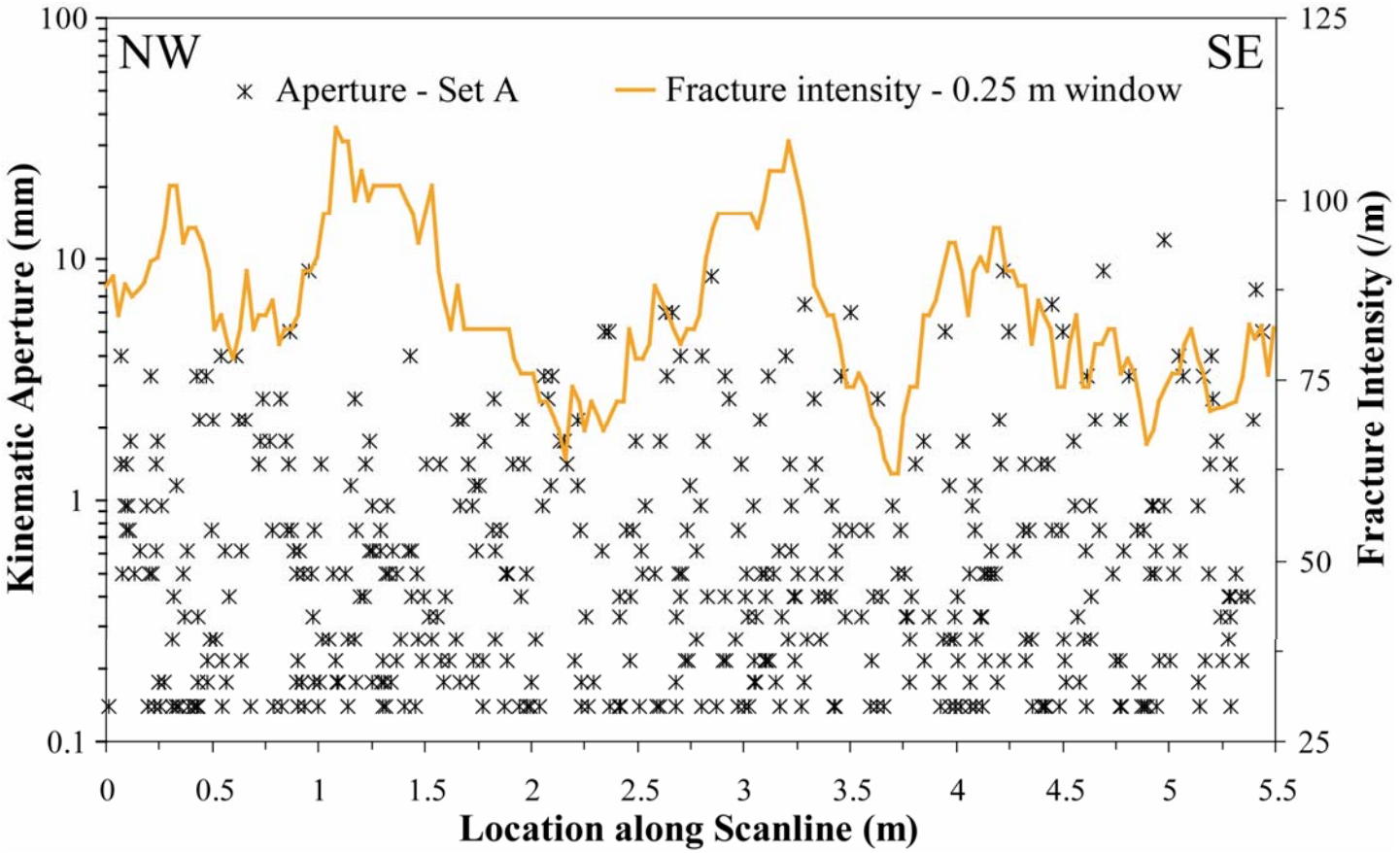

Figure 9.69 Kinematic aperture (asterisk) and fracture intensity (thick orange line) versus location along scanline for the Palmas 13 data set. Note that kinematic aperture axis uses logarithmic graduations. Fracture intensity was calculated inside a moving window with width (window size) of 0.25 m that was moved in increments (window step) 0.03 m. Peaks of fracture intensity indicate clusters at 0.25, 1.25, 3.25, and 4 m, but clusters do not seem regularly spaced.

Figure 9.70 Graphs of spatial correlation (thick continuous line) vs. length scale for (a) logarithmic graduations and (b) linear graduations for the Palmas 13 data set (459 fractures, all fractures sets, aperture threshold of 0.14 mm). In (a) and (b) the thin discontinuous line represents the upper 95% confidence limit while the thin dotted line represents the lower 95% confidence limit, and the thick discontinuous line corresponds to the mean of 100 randomized data sets. In (a) the thin continuous line represents the analytical solution of randomly arranged fractures with the same number of fractures and scanline length. In (b) the thin continuous line represents an example randomized set generated with the same number of fractures and scanline length. Width of length-scale bin in (a) and (b) is 7 graduations of length scale (m = 3). There is no pattern of spatial correlation that can be identified for logarithmic graduations of length scale (e.g., power law) in (a) or for linear graduations of length scale (e.g., regularly-spaced peaks) in (b). For all values of length scale, spatial correlation in both (a) and (b) remains within the 95% confidence interval, which indicates that spatial arrangements are indistinguishable from random. (c) Power spectrum of spatial correlation from (b). The power spectral density for the natural data set exhibits the same trend as the red noise, as shown in (c). The natural data set exhibits a peak at a wavelength of 380 mm, which has a power spectral density slightly larger than the 95% confidence interval for red noise, but the difference between the peak and the 95% confidence interval is small when compared with other data sets (e.g., set D of Escalera 1, Figure 9.45c).

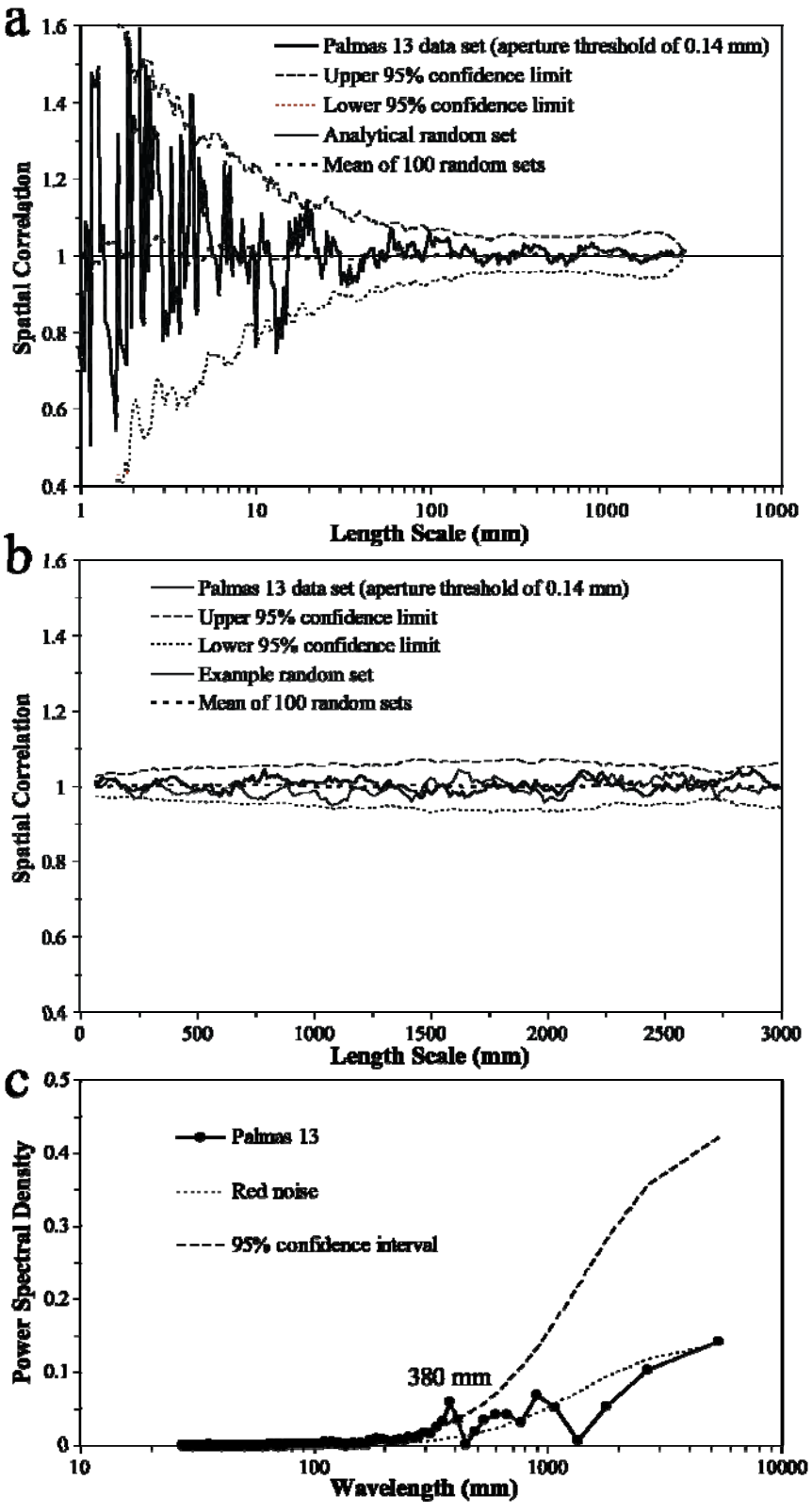
a
Palmas 13 data set (aperture threshold of 0.14 mm)
Upper 95% confidence limit
Lower 95% confidence limit
Analytical random set
Mean of 100 random sets
Spatial Correlation
Length Scale (mm)
b
Palmas 13 data set (aperture threshold of 0.14 mm)
Upper 95% confidence limit
Lower 95% confidence limit
Example random set
Mean of 100 random sets
Spatial Correlation
Length Scale (mm)
c
Palmas 13
Red noise
95% confidence interval
380 mm
Power Spectral Density
Wavelength (mm)

Orientation of fractures in layers 11, 12 and 13 in Palmas canyon shows consistency before (as measured in the field) and after restoring bedding to horizontal (Figure 9.71). Fractures of set A (circles, Figure 9.71) show more variation once restored to horizontal than fractures of set B (squares, Figure 9.71) and set C (diamonds, Figure 9.71).

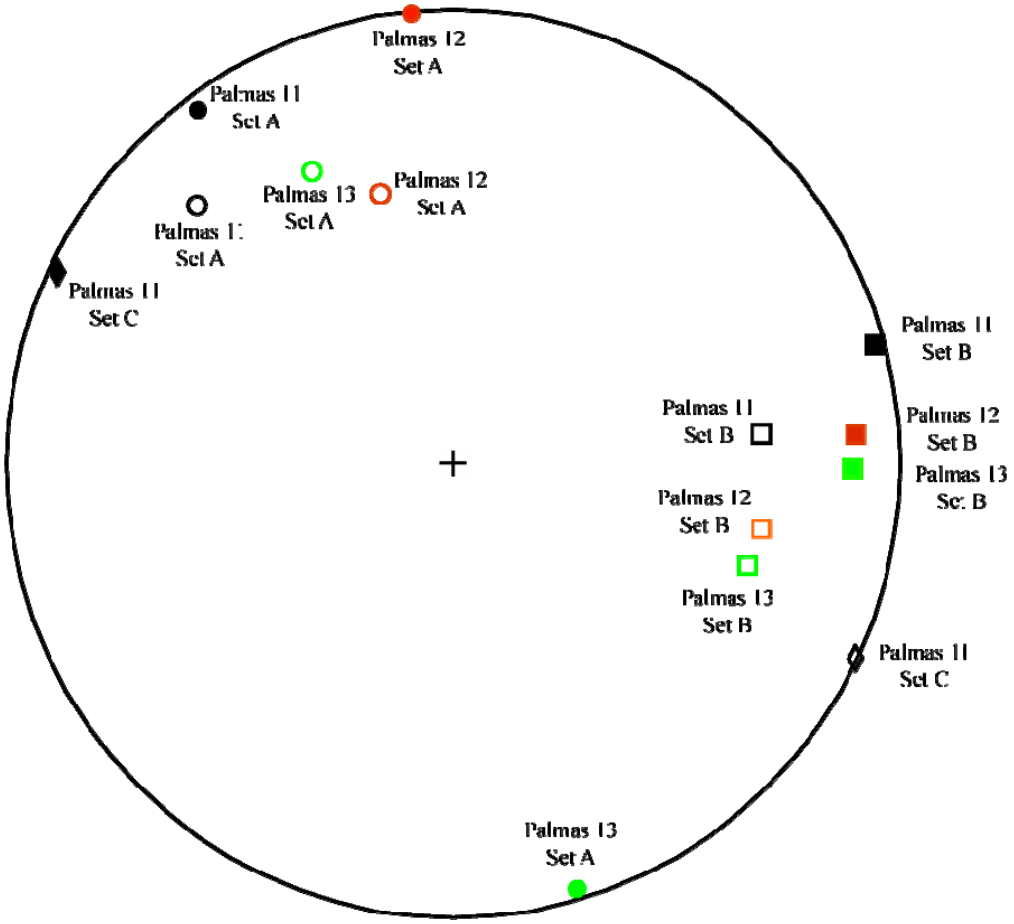

Figure 9.71 Equal area stereographic projection of poles to fractures for (a) forelimb of San Blas anticline at Escalera canyon and (b) backlimb of San Blas anticline at Escalera canyon. Fracture orientation as measured in field is represented by hollow symbols whereas fracture orientation with bedding restored to horizontal is represented by filled symbols. Color of symbols indicate the layer name, whereas different symbols indicate different fracture set (circle for set A, square for set B, and diamond for Set C). Orientation of restored set B in Palmas canyon matches with orientation of restored set A in Escalera canyon (Figure 9.60).

9.4.11 Huasteca Canyon

The layer at Huasteca canyon is a 70-cm thick dolopackstone that suffered partial dedolomitization. The layer at Huasteca canyon is located in the forelimb of the leading anticline (Figure 9.72a). Fractures of Huasteca data set were measured in a cross sectional exposure (Figure 9.72b) along a 16.6 m long scanline (Table 9.1, Figure 9.73). Four sets (A, B, C, and D) of fractures were recorded in the Huasteca layer (Table 9.3). Using an aperture threshold of 0.215 mm I measured 658 veins and recorded a strain of 7.15% (Table 9.5). Unlike all the other data sets selected for this chapter that follow a power-law distribution of fracture apertures, fractures of the Huasteca data set seem to follow a log-normal distribution (Table 9.5). Chi square for a power-law distribution of fracture aperture for Huasteca is 0.2596, which about 50% larger than the second largest coefficient for another data set (0.1460, Escalera OO12, Table 9.5). Fracture spacings of the Huasteca layer follow a log-normal distribution and have a coefficient of variation of 1.23 (Table 9.5). 88% of the fractures measured represent set A, 3% represent set B, 8% represent set C, and 1% represent set D (Table 9.3). In thin sections (Table 9.2), fractures of set A and B exhibit most of the typical features of Y fractures such as straight traces, microfractures that occasionally anastomose, bridges of subhedral dolomite and quartz. However, samples with fractures of sets C, and D from the Huasteca layer could not be obtained. Qualitative study of intersections between fractures of sets A and B in the field and in thin sections revealed mutually crosscutting relationships, likely indicating that fracture sets developed simultaneously.

Figure 9.72 (a) Panoramic photograph of the area near the entrance to the Huasteca canyon looking east. Approximate location of (b) is highlighted with an orange rectangle. A small car is located at the base of the photograph for scale. However, the wide angle lens used in (a) created noticeable distortion in photograph. (b) Photograph of the entire outcrop of layer and surrounding layers. Approximate location of entire scanline is drawn as a white line. Approximate location of (c) is highlighted with a green rectangle in (b). A person is located at the base of the photograph for scale. (c) Photograph of most of layer in Huasteca canyon (layer top and layer bottom outside photograph). Notice the approximate equal spacing of macrofractures in (c). Scale in (c) is in centimeters.

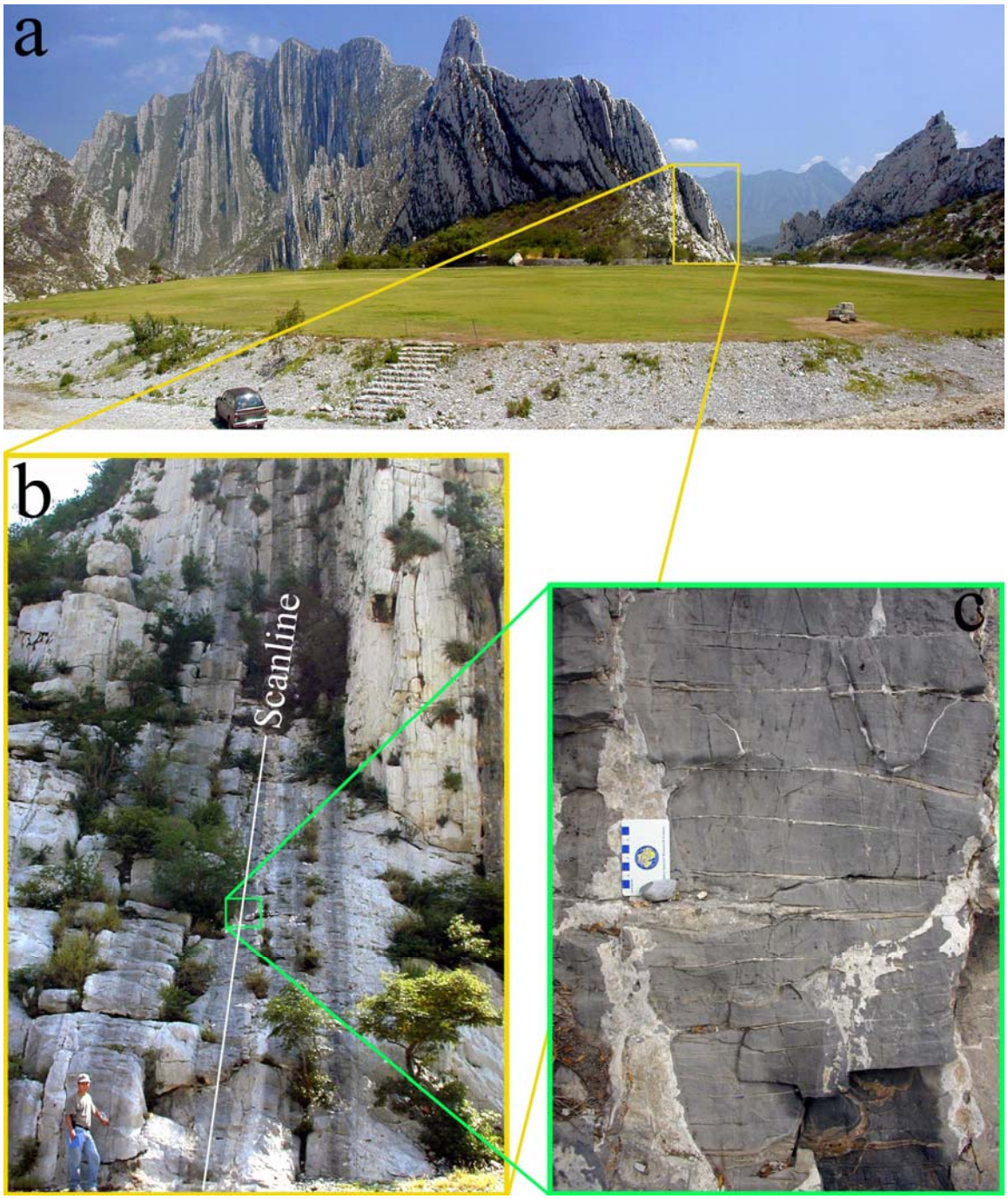
a
b
Scanline
c

Spatial correlation for fractures of set A of the Huasteca data set varies as a power-law of length scale (Figure 9.74a), which indicates a fractal arrangement of fractures inside clusters (Figure 9.4b) with a cluster width of 250 mm. However, power-law exponent is very small, possibly indicating an inherited/imposed arrangement of fractures (Figure 9.4c). Spatial correlation shows a pattern of alternating peaks and troughs that is interpreted as a periodic arrangement of fracture clusters (Figure 9.4g). Although the statistical significance of a periodic arrangement of fractures is not in question (most peaks are outside the 95% confidence interval), cluster spacing is slightly uncertain because some peaks are not at exact length scale multiples (dashed lines, Figure 9.74b) of the first peak of spatial correlation at 960 mm. The power spectrum of spatial correlation for linearly graduated length scales exhibit a broad peak outside the 95% confidence interval for red noise centered at a wavelength of 1001 mm (Figure 9.74c), which indicates a cluster spacing of 1001 mm. NCC results for all fracture sets combined of Huasteca data set exhibit the same patterns of spatial correlation as when the set A is analyzed independently (Figure 9.74), most likely because most of the Huasteca data set is composed of set A fractures (88%).

Similarly to fractures of set A, spatial correlation for fractures of sets B and D combined also varies as a power-law of length scale (Figure 9.75a), indicative of a fractal arrangement of fractures inside clusters (Figure 9.4b). However, the power-law exponent of set A fractures is near zero and therefore clusters cannot unequivocally be characterized as having a fractal (Figure 9.74a) whereas for fractures of sets B and D exponent is near one (Figure 9.75a), leaving no doubt about the fractal character of the arrangement. Spatial correlation for linearly graduated length scales yields a pattern of alternating peaks and troughs at length scales that are multiples of the first peak (Figure 9.75b), which indicates a periodic arrangement of fracture clusters (Figure 9.4g).

However, only one peak is statistically significant, which cast doubts about interpreting spatial correlation as indicative of a periodic arrangement of clusters. It is a testament of the robustness of NCC that only 23 fractures (sets B and D combined) in more than 16 m of scanline can yield clear patterns of spatial correlation (Figures 9.75a and 9.75b). The power spectrum of spatial correlation for linearly graduated length scales exhibits a peak at a wavelength of 1001 mm outside the 95% confidence interval for red noise (Figure 9.75c), which suggests that the periodic arrangement of fracture clusters indicated by spatial correlation is statistically significant. In addition, cluster spacing is the same for set A (Figure 9.74c) and sets B and D combined (1000 mm, Figure 9.75c).

Fractures of set C also exhibit a power-law pattern of spatial correlation for logarithmically graduated length scales (Figure 9.76a), indicative of a fractal arrangement of fractures inside clusters (Figure 9.4b). Spatial correlation for linearly graduated length scales of fractures of set C exhibits alternating peaks which are multiples of the first peak of spatial correlation (Figure 9.76b), which indicates that clusters are periodically arranged (Figure 9.4g). However, cluster width and spacing for set C are much larger than for the other sets of Huasteca data set. Cluster width is estimated at 900 mm (Figure 9.76a), about four times the cluster width estimated for set A or sets B and D combined (250 mm). Cluster spacing is estimated at 2100 mm (Figure 9.76b), twice the spacing for sets A, and sets B and D combined (1000 mm). Power spectrum of spatial correlation for linearly graduated length scales confirms that the periodic arrangement of clusters for set C (Figure 9.76c) is statistically significant because peak of power spectral density at a wavelength of 2105 mm is outside the 95% confidence interval for red noise.

Fracture intensity indicates that the Huasteca data set contains clusters (peaks of fracture intensity) that are regularly spaced with a cluster spacing of approximately 900 mm (Figure 9.73), which confirms the findings of NCC. However, the success of the

curve of fracture intensity is partly due to the selection of window with length approximately equal to cluster width (Chapter 6).

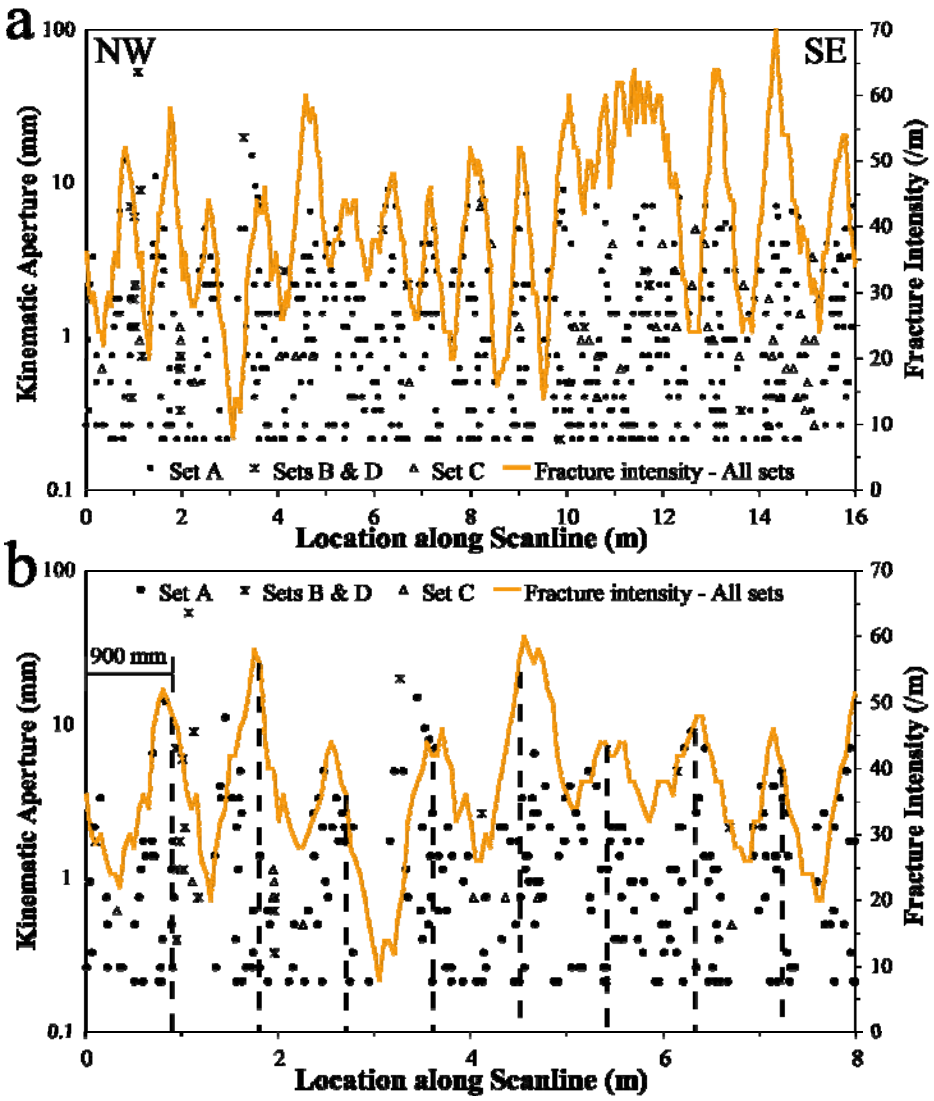

Figure 9.73 Kinematic aperture (circles for set A, asterisks for sets B and D, and triangles for set C) and fracture intensity (thick orange line) versus location along scanline for all (a) and NW half (b) of the Huasteca data set. Fracture intensity was calculated inside a moving window with width (window size) equal to cluster width as estimated by NCC (0.25 m, Figure 9.74a) that was moved in increments (window step) equal of 0.05 m. Clusters are more easily detected in (b) than in (a) because cluster width is larger compared with the plotted scanline. Note that only the kinematic aperture axis use logarithmic graduations.

Figure 9.74 Graphs of spatial correlation (thick continuous line) vs. length scale for (a) logarithmic graduations and (b) linear graduations for fractures of set A of the Huasteca outcrop data set (581 fractures, aperture threshold of 0.215 mm,). In (a) and (b) the thin discontinuous line represents the upper 95% confidence limit while the thin dotted line represents the lower 95% confidence limit, and the thick discontinuous line corresponds to the mean of 100 randomized data sets. In (a) and (b) the thin continuous line represents an example randomized set generated with the same number of fractures and scanline length .Width of length-scale bin is 21 (m = 10) in (a) and 5 (m = 2) graduations of length scale in (b). Power law in (a) was calculated using spatial correlation between length scales of 2.3 and 250 mm. Cluster width is approximately 250 mm, as shown in (a). Evenly spaced lines every 96 mm in (b) match most peaks of spatial correlation, which display a regularly spaced pattern. (c) Power spectrum of spatial correlation from (b). A broad and noticeable peak centered at a wavelength of 1001 (910 to 1093) mm has a power spectral density that is several times the equivalent for the 95% confidence interval for red noise, indicating a periodic arrangement of fractures that is statistically significant and with a cluster spacing of 1001 mm. Although the natural data set exhibits a peak of power spectral density at a wavelength of 5463 mm, this peak is not outside the 95% confidence interval for red noise, and therefore is not statistically significant.

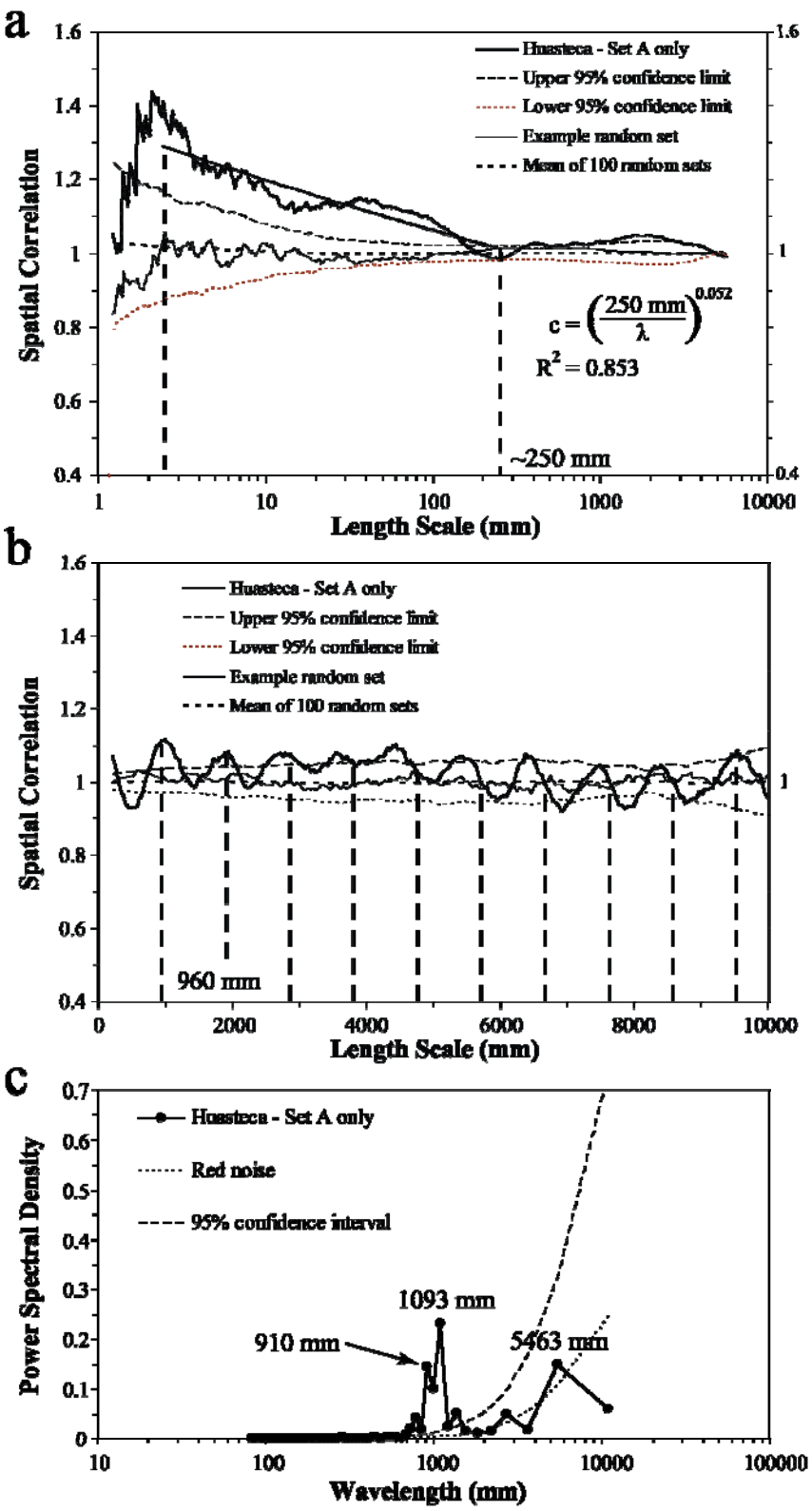
a
Huasteca - Set A only
Upper 95% confidence limit
Lower 95% confidence limit
Example random set
Mean of 100 random sets
Spatial Correlation
Length Scale (mm)
$c = \left(\frac{250\ mm}{\lambda}\right)^{0.052}$
$R^2 = 0.853$
~250 mm
b
Huasteca - Set A only
Upper 95% confidence limit
Lower 95% confidence limit
Example random set
Mean of 100 random sets
Spatial Correlation
Length Scale (mm)
960 mm
c
Huasteca - Set A only
Red noise
95% confidence interval
Power Spectral Density
Wavelength (mm)
1093 mm
910 mm
5463 mm

Figure 9.75 Graphs of spatial correlation (thick continuous line) vs. length scale for (a) logarithmic graduations and (b) linear graduations for fractures of sets B and D combined of the Huasteca outcrop data set (23 fractures, aperture threshold of 0.215 mm). In (a) and (b) the thin discontinuous line represents the upper 95% confidence interval while the thin dotted line represents the lower 95% confidence interval, and thick discontinuous line corresponds to the mean of 100 randomized data sets. In (a) the thin continuous line represents the analytical solution of randomly arranged fractures with the same number of fractures and scanline length. In (b) the thin continuous line represents an example randomized set generated with the same number of fractures and scanline length. Width of length-scale bin is 13 (m = 6) in (a) and 11 (m = 5) graduations of length scale in (b). Power law in (a) was calculated using spatial correlation between length scales of 16 and 250 mm. Evenly spaced lines every 1000 mm in (b) match approximately peaks of spatial correlation, which display a regularly spaced pattern, indicative of periodically arranged clusters. (c) Power spectrum of spatial correlation from (b). A noticeable peak at 1001 mm has a power spectral density that is several times the equivalent for the 95% confidence interval for red noise, indicating a periodic arrangement of fractures that is statistically significant and with a cluster spacing of 1001 mm.

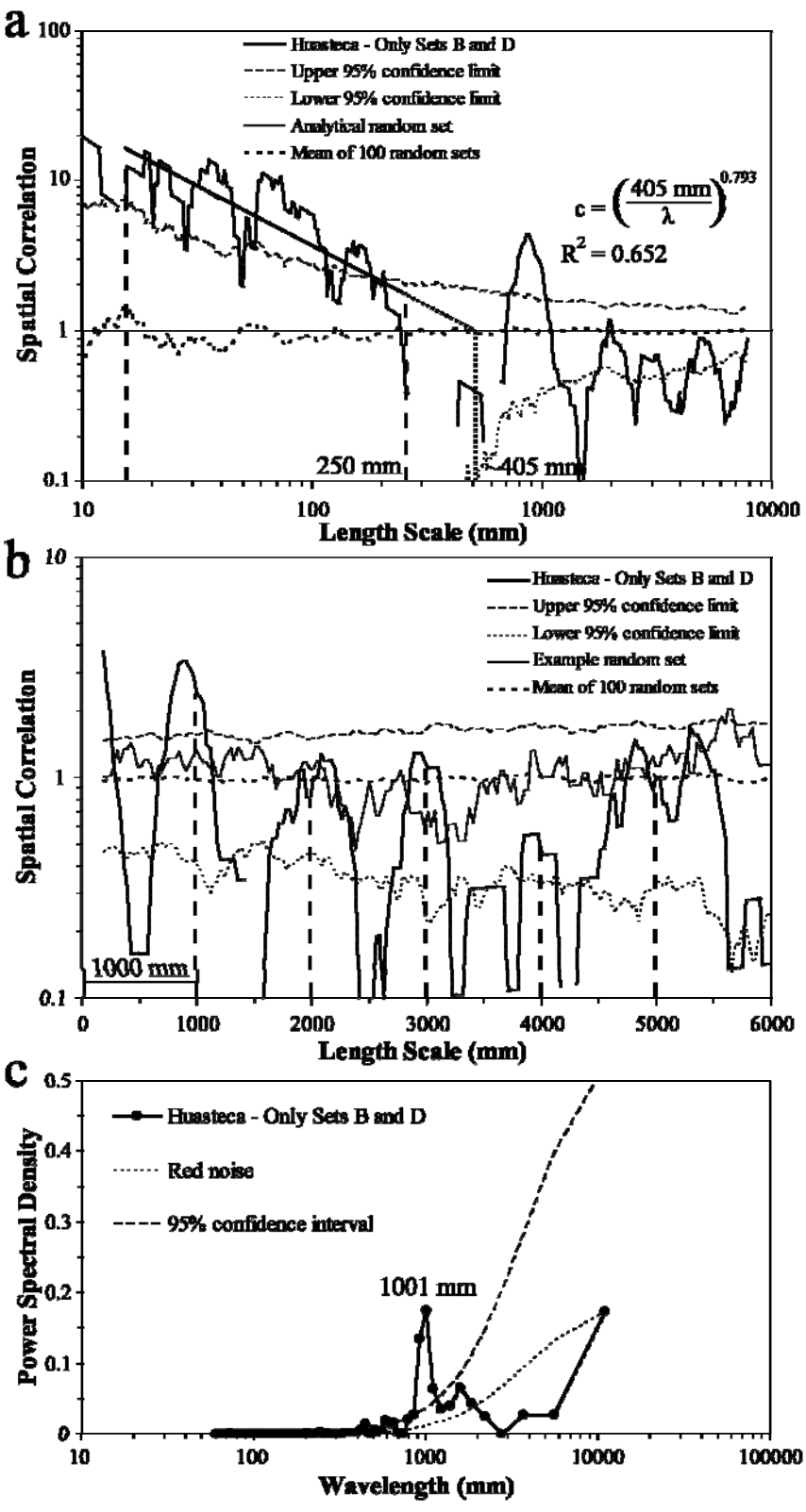
a
Huasteca - Only Sets B and D
Upper 95% confidence limit
Lower 95% confidence limit
Analytical random set
Mean of 100 random sets
$c = \left(\frac{405\ mm}{\lambda}\right)^{0.793}$
$R^2 = 0.652$
250 mm
405 mm
Spatial Correlation
Length Scale (mm)
b
Huasteca - Only Sets B and D
Upper 95% confidence limit
Lower 95% confidence limit
Example random set
Mean of 100 random sets
1000 mm
Spatial Correlation
Length Scale (mm)
c
Huasteca - Only Sets B and D
Red noise
95% confidence interval
1001 mm
Power Spectral Density
Wavelength (mm)

Figure 9.76 Graphs of spatial correlation (thick continuous line) vs. length scale for (a) logarithmic graduations and (b) linear graduations for fractures of set C of the Huasteca outcrop data set (54 fractures, aperture threshold of 0.215 mm,). In (a) and (b) the thin discontinuous line represents the upper 95% confidence interval while the thin dotted line represents the lower 95% confidence interval, and the thick discontinuous line corresponds to the mean of 100 randomized data sets. In (a) the thin continuous line represents the analytical solution of randomly arranged fractures with the same number of fractures and scanline length. In (b) the thin continuous line represents an example randomized set generated with an equivalent number of fractures and scanline length. Width of length-scale bin is 15 graduations of length scale (m = 7) in both (a) and in (b). Power law in (a) was calculated for spatial correlation between length scales of 73 and 1000 mm. Cluster width is approximately 900 mm, as shown in (a). Evenly spaced lines every 2100 mm in (b) match approximately peaks of spatial correlation, which display a regularly spaced pattern, indicative of periodically arranged clusters. (c) Power spectrum of spatial correlation from (b). A noticeable peak at 2105 mm has a power spectral density that is several times the equivalent for the 95% confidence interval for red noise, indicating a periodic arrangement of fractures that is statistically significant and with a cluster spacing of 2105 mm.

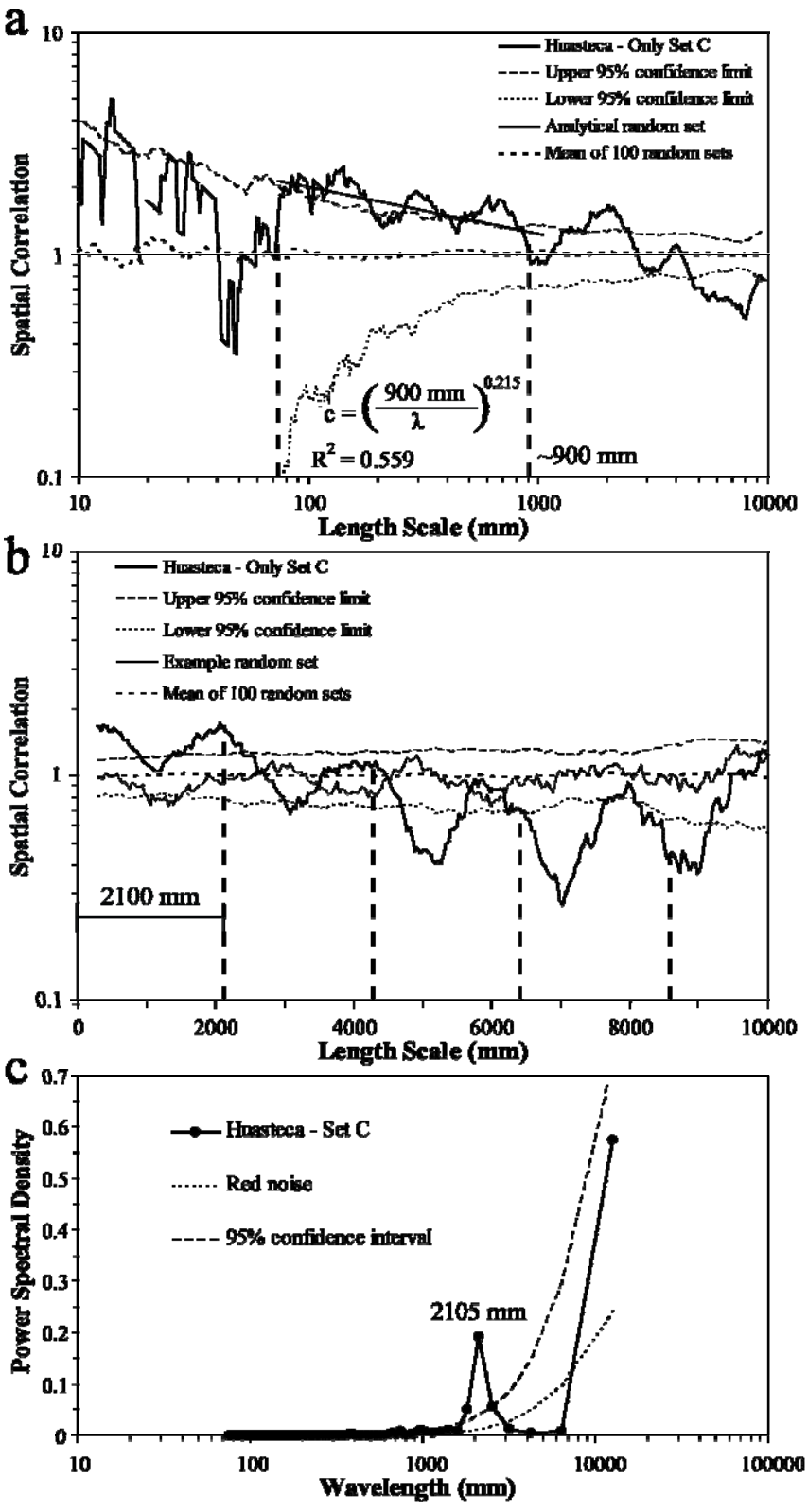
a
Husteca - Only Set C
Upper 95% confidence limit
Lower 95% confidence limit
Analytical random set
Mean of 100 random sets
Spatial Correlation
$c = \left(\frac{900\ mm}{\lambda}\right)^{0.215}$
$R^2 = 0.559$
~900 mm
Length Scale (mm)
b
Husteca - Only Set C
Upper 95% confidence limit
Lower 95% confidence limit
Example random set
Mean of 100 random sets
Spatial Correlation
2100 mm
Length Scale (mm)
c
Husteca - Set C
Red noise
95% confidence interval
Power Spectral Density
2105 mm
Wavelength (mm)

Table 9.6 Types of spatial arrangements for outcrop data sets of the Cupido Fm. selected for this chapter. Types of spatial arrangements as defined by Marrett et al. (in review). Fractal = Self-organized cluster, Inherited = Inherited/imposed cluster, Periodic = Periodically arranged clusters, Random = indistinguishable from random.

Outcrop	**Fracture Set(s)**	**Spatial Arrangement**		**Fracture Strain (%)**
		Logarithmic Graduations	**Linear Graduations**	
Escalera OO11 Eastern 1.6 m	A, B, C, D	Fractal / Inherited (9.59a)	Periodic (9.59b)	13.3
Escalera OO12	A, B	Fractal (9.63a)	Periodic (9.63b)	20.4
Escalera 1	A	Fractal (9.44a)	Indeterminate, possibly periodic (9.44b)	2.1
	B	Random (9.47a)	Random (9.47b)	2.1
	C	Random (9.48a)	Random (9.48b)	1.8
	D	Fractal (9.45a)	Periodic (9.45b)	1.0
Escalera 2	B	Inherited?, Fractal? (9.52a)	Periodic? (9.52b)	3.8
	C	Random (9.53a)	Random (9.53b)	3.9
Escalera 3	A	Fractal (9.55a)	Periodic? (9.55b)	4.5
Huasteca	A, B and D	Fractal (9.74a, 9.75a)	Periodic (9.74b, 9.75b)	5.7, 1.0
	C	Fractal (9.76a)	Periodic (9.76b)	0.5
Palmas 11 LR	A, B, and C	Fractal (9.65a)	Periodic (9.65b)	4.6
Palmas 12	A and B	Random (9.67a)	Random? (9.67b)	12.7
Palmas 13	A and B	Random (9.70a)	Random (9.70b)	9.2

9.5. DISCUSSION

The previous two sections of Chapter 9 categorized fracture sets in the Cupido Fm. according to structural diagenesis and spatial arrangement. In this section, I will establish a relationship between the diagenetic categories and types of spatial arrangement, and I will test different hypotheses about the origin of the relationship between spatial arrangement and fracture categories.

9.5.1 Diagenesis and the Spatial Arrangement of Opening-mode Fractures

Compiling data provided in Tables 9.4 and 9.6 into a single table (Table 9.7) indicates a correspondence between the fracture category and the type of spatial arrangement of outcrop data sets. Using both logarithmic and linear graduations of length scales spanning the entire scanline length, the arrangement of category X and Z fractures cannot be distinguished from random (Table 9.7). In contrast, fractures of category Y display periodically (or suspected to be periodic) arranged clusters which in turn have internally a fractal arrangement (Table 9.7). Of all the layers studied, only one (Escalera 1) exhibit fractures from more than one category. Escalera 1 is the only layer with a bedding-parallel outcrop.

Spatial arrangement of fractures (mostly microfractures) measured along scanlines in rock samples was also compiled (Table 8.6). Details about the attributes of fractures at rock sample scale as well as NCC results (cross-plots of spatial correlation versus length scale) are included in Chapter 8. With one exception (Palmas 11), rock-sample scale fractures of category Y exhibit periodic arrangement of clusters for linearly graduated length scales and random or fractal arrangements for logarithmically graduated length scales (Table 9.7). The Palmas 11 rock sample was the only one extracted from near the layer base instead of the center, and therefore it is possible that the random

arrangement indicates that spatial arrangement varies with stratigraphic level in the layer (Chapter 8). Category X fractures at rock–sample scale also exhibit periodic arrangements of clusters for linearly graduated length scales and random arrangements for logarithmically graduated length scales (Table 9.7). It is interpreted that the random arrangement of fractures within clusters at rock sample scale is either due to the small number of fractures per cluster and/or the small number of clusters at rock sample scale (Chapter 8).

Table 9.7 Summary of spatial arrangements for the three fracture categories studied in this chapter. Types of spatial arrangements as defined by Marrett et al. (in review) are described in Table 9.6. Names of fracture sets were independently named for each outcrop and also do not reflect timing (e.g., set A is not necessarily earlier than set B). Log = Logarithmic. Ind = Indeterminate.

<table>
<tr><th rowspan="4">Fracture Category (X, Y or Z)</th><th colspan="2">Outcrop Data Set</th><th colspan="4">Spatial Arrangement</th></tr>
<tr><th rowspan="3">Layer Name</th><th rowspan="3">Fracture Set(s)</th><th colspan="2">Outcrop Scale</th><th colspan="2">Rock-Sample Scale</th></tr>
<tr><th colspan="2">Graduations</th><th colspan="2">Graduations</th></tr>
<tr><th>Log</th><th>Linear</th><th>Log</th><th>Linear</th></tr>
<tr><td rowspan="2">X</td><td>Palmas 12</td><td>A, B</td><td colspan="2" rowspan="2">Random</td><td rowspan="2">Random</td><td rowspan="2">Periodic</td></tr>
<tr><td>Palmas 13</td><td>A, B</td></tr>
<tr><td rowspan="8">Y</td><td rowspan="2">Escalera 1</td><td>A</td><td rowspan="8">Fractal</td><td>Ind.</td><td colspan="2" rowspan="2">Not Available</td></tr>
<tr><td>D</td><td rowspan="7">Periodic or possibly periodic</td></tr>
<tr><td>Escalera 3</td><td>A</td><td colspan="2">Not Available</td></tr>
<tr><td>Escalera OO1 (Eastern 1.6 m)</td><td>A, B</td><td>Random</td><td>Periodic</td></tr>
<tr><td>Escalera OO12</td><td>A, B</td><td>Fractal</td><td>Periodic</td></tr>
<tr><td>Huasteca</td><td>A, B</td><td>Random</td><td>Periodic</td></tr>
<tr><td>Palmas 11</td><td>A, B, C</td><td colspan="2">Random</td></tr>
<tr><td rowspan="3">Z</td><td rowspan="2">Escalera 1</td><td>B</td><td colspan="2" rowspan="2">Random</td><td colspan="2" rowspan="2">Not Available</td></tr>
<tr><td>C</td></tr>
<tr><td>Escalera 2</td><td>C</td></tr>
</table>

9.5.2 Relative Timing of Fracture Development

My dissertation did not attempt to elucidate the complete diagenetic and burial history of the Cupido Fm. (an objective closer to Monroy-Santiago, in preparation) and, therefore, studies which could have helped constrain the temperature range or depth at which a particular synkinematic cement precipitated were not pursued (e.g., stable isotopes, fluid inclusions). Because of the absence of tools that can provide quantitative information about the conditions under which fractures developed, any attempt made in my dissertation to speculate about those conditions is based on published (Monroy-Santiago et al., 2001; Marrett and Laubach, 2001; Ortega, 2002) and unpublished (Monroy-Santiago, in preparation) data and on the findings presented earlier in this chapter.

Orientation of fracture sets A, B and C of layers Escalera OO1 and OO12 (Table 9.3; Figure 9.61a) in the forelimb of the San Blas Anticline match the orientation of similarly named sets in Ortega and Marrett (2001). Ortega and Marrett (2001) used crosscutting relationships with other structures such as stylolites and collapse breccias to interpret that sets A and B developed before folding and set C during early folding of the SMO. In addition, Marrett and Laubach (2001) noted that "in the present-day geographic reference frame, veins in forelimbs do not parallel those in backlimbs but rotate into alignment upon restoration of bedding to horizontal, suggesting veins predate folding". Although for the layers I measured in the San Blas anticline there is not a dramatic difference in orientation between forelimb and backlimb (Figures 9.61a and 9.61b), similarity in orientation between forelimb and backlimb fractures increases when bedding is restored to horizontal (Figure 9.77), which suggest that fractures I studied in Escalera canyon also predate folding. The similarity in fracture orientation (Table 9.3; Figure 9.77), layer thicknesses (Table 9.5), lithology, percentage of D2 dolomite in matrix

(Table 9.5), and quantitative fracture attributes (e.g., size distribution of apertures), make it likely that fractures from Palmas and Huasteca canyon also predate folding.

Ortega and Marrett (2001) and Ortega (2002) noted that in platformal strata of the Cupido Fm. (all Cupido layers of my dissertation are interpreted to be platformal), fractures filled with calcite and dolomite are preferentially located (have higher fracture intensity) in layers with higher dolomite content at the top of fifth-order sequence stratigraphic cycles, which they indicate is suggestive of a shallow burial (pre-folding) origin (Figure 9.37). Although Ortega and Marrett (2001) and Ortega (2002) did not explicitly relate the dolomite cement that varies within fifth order sequence stratigraphic cycles with a specific dolomitization event of Monroy-Santiago (2001), most likely they were referring to D2 dolomitization. Monroy-Santiago (in preparation) indicated that D2 dolomite precipitation was the main diagenetic process and occurred during shallow to moderate burial. In addition, Marrett and Laubach (2001) suggested that both platform and basinal facies of the Cupido Fm. developed veins "essentially the same time as deposition of the Barremian-Aptian sedimentary section"; namely that rocks lithified and fractured during early burial. Veins are unrelated to the isoclinal folds present in the Monterrey salient and instead owe their origin to "gravitational spreading from platform margins toward adjacent basins." Although it can be interpreted that fractures lacking synkinematic quartz cement (X and Z categories) developed in shallow to moderate burial conditions (<300 m, Ortega and Marrett, 2001), fractures that contain synkinematic quartz (Y category) must have developed at depths with temperatures of 80˚C (approximately the minimum temperature required to precipitate quartz, Worden and Morad, 2000) or higher. Following the burial-history analysis of the SMO by Gray et al. (2001), it can be inferred that 80˚C would have been reached at a depth of approximately 2 km, implying that Y fractures developed at depths of at least 2 km. Ortega and Marrett

(2001) and Monroy-Santiago et al. (2001) recognized that some fracture sets developed at depths larger than 300 m but they did not realize that some fractures probably developed at much deeper conditions, because they did not recognized that quartz cement was abundant and of synkinematic origin.

The correspondence between diagenesis and spatial arrangement of fractures at outcrop scale (Table 9.7) is complemented with similarities between fractures of different categories that have similar orientations and identical spatial arrangements (Figure 9.77). For instance, orientation of one set of Z fractures (after restoration of bedding to horizontal, set C of Escalera 1 layer; Figure 9.77b) is approximately the same (~85°/>85°, right-hand rule) as a set of X fractures in another canyon (set A of Palmas 13 layer, Figure 9.77c) and both X and Z fractures at outcrop scale exhibit random arrangement of fractures using logarithmic and linear graduations of length scales (Table 9.7). Fractures of category Y in different outcrops (Palmas 11 set B, Figure 9.77c; set A of Escalera 1 and Escalera 3, Figure 9.77b; set A of Escalera OO1 and Escalera OO12, Figure 9.77a) have almost identical orientation (bedding restored to horizontal, ~0°/>80°) and identical spatial arrangement (fractal arrangement inside clusters, periodic arrangement of clusters; Table 9.6).

Although there is a clear pattern relating diagenesis and spatial arrangement of fractures at outcrop scale (Table 9.7), a simple genetic model that consistently explains fracture orientation, fracture category, relative timing among fracture categories and D2 dolomitization, could not be conceived at this time. For instance, crosscutting relationships at outcrop (Figure 9.42b) and rock sample scale (Figures 9.28 and 9.29a) indicate that Z fractures are syn-D2 and postdate Y fractures, and Y fractures contain synkinematic quartz. This suggests that Z fracturing and D2 dolomitization should have occurred on certain locations at depths larger than approximately 2 km, contradicting

inferences from burial history and about D2 dolomitization, believed to indicate only reflux of marine waters rich in magnesium at shallow conditions (<300 m, Ortega and Marrett, 2001). A second example of the difficulties of a genetic model based on current knowledge of Cupido Fm. are the restored orientations of fractures from different categories (Figure 9.77). Namely, Y fractures in the forelimb of San Blas anticline along Escalera canyon (hollow blue squares, Figure 9.77a) have approximately the same orientation (~0°/>80°) as Y fractures in the backlimb (filled blue squares, Figure 9.77b), and yet Y fractures in the forelimb are interpreted to be Post-D2 whereas Y fractures in the backlimb are interpreted to be Pre-D2. A third example illustrating the complexity of fracture evolution in the Cupido Fm. is the fact that fractures from different categories in Palmas canyon (set B of layers Palmas 11, Palmas 12, and Palmas 13; Figure 9.77c) have almost identical orientations but different spatial arrangements (random for X fractures, fractal and periodic for Y fractures) and are stratigraphically separated only a few meters.

The difficulty in generating a single genetic model that encompasses all the evidence for fractures in the Cupido Fm. probably arises because of incomplete knowledge on diagenetic and structural evolution of the Cupido Fm. Perhaps the greatest limitation on current knowledge is the inadequate constraints on spatial and temporal variations of diagenetic processes and what role each fracture category played in the movement of diagenetic fluids. For instance, it is unclear why D2 dolomitization seems to have occurred at different times with respect to Y fractures that have the same orientation (Figure 9.77).

Figure 9.77 Equal area stereographic projection of restored-to-horizontal poles to fractures for (a) forelimb of San Blas anticline at Escalera canyon, (b) backlimb of San Blas anticline at Escalera canyon, and (c) forelimb of San Blas anticline at Palmas canyon. Different symbols indicate different fracture categories (circle for X fractures, squares for Y fractures, and triangles for Z fractures). Color of symbols indicates the types of spatial arrangement exhibited by each fracture set with logarithmic and linear graduations of length scales. Black symbols indicate fracture sets that exhibit random arrangements with both logarithmic and linear graduations of length scales, whereas blue symbols indicate fracture sets that exhibit fractal arrangements with logarithmic graduations of length scale and periodically arranged clusters with linear graduations of length scale. Filled and hollow squares represent Y fractures interpreted to have developed earlier (Pre-D2) and later (Post-D2) than the D2 regional dolomitization.

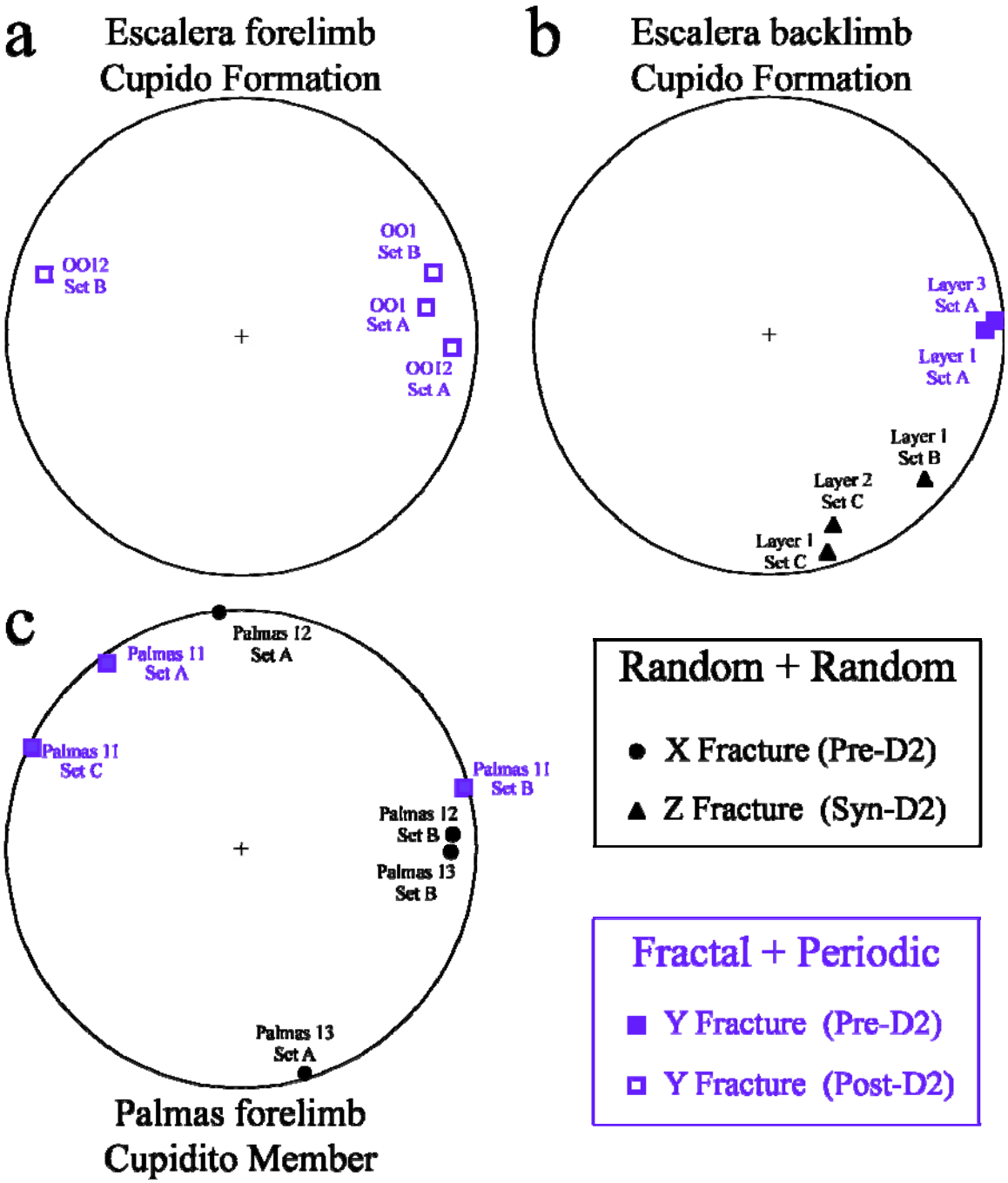
a
Escalera forelimb
Cupido Formation
OO12
Set B
OO1
Set B
OO1
Set A
OO12
Set A
b
Escalera backlimb
Cupido Formation
Layer 3
Set A
Layer 1
Set A
Layer 1
Set B
Layer 2
Set C
Layer 1
Set C
c
Palmas 12
Set A
Palmas 11
Set A
Palmas 11
Set C
Palmas 11
Set B
Palmas 12
Set B
Palmas 13
Set B
Palmas 13
Set A
Palmas forelimb
Cupidito Member
Random + Random
X Fracture (Pre-D2)
Z Fracture (Syn-D2)
Fractal + Periodic
Y Fracture (Pre-D2)
Y Fracture (Post-D2)

Lastly, postkinematic calcite precipitated in the porosity left by synkinematic cements in X, Y and Z categories. The paragenetic sequence of Monroy-Santiago (in preparation) includes three episodes of calcite precipitation, two before the Pre-D2 fracture events and one after the Post-D2 fracture event (Figure 9.1). Assuming that the paragenetic sequence of Monroy-Santiago (in preparation) contains all the diagenetic episodes, only the last episode of calcite cementation could be postkinematic relative to fractures studied for this dissertation. However, my dissertation cannot unequivocally confirm the suggestion that postkinematic calcite cement in Pre-D2 fractures is the same observed in Post-D2 fractures. On the contrary, the absence of synkinematic quartz cements inside X (Pre-D2) fractures suggests that some calcite cement precipitated after the development of X fractures and sealed them from later diagenetic fluids rich in silica, fluids present during the development of Y fractures. A less plausible alternative interpretation is that networks of X fractures (with remnant porosity) were not connected to the networks of Y fractures and therefore remained isolated from fluids that precipitated quartz inside Y fractures, but at the same time, X fractures were connected to the source of calcium carbonate-rich fluids that carried the last postkinematic cement. On-going (e.g., Monroy-Santiago, in preparation) or future research using stable isotopes might test the two hypotheses or provide a new one that fits the data available.

9.5.3 Processes Controlling the Spatial Arrangement of Fractures

If the timing, geographic location, and stratigraphic position of different fracture categories do not offer a completely reliable explanation for the relationship between fracture categories and spatial arrangement (Table 9.7), perhaps an explanation can be generated through comparison of the types of spatial arrangement with parameters that are thought to influence fracture development. Among the parameters to be tested are layer thickness, fracture strain, fracture intensity, percentage of D2 dolomite in matrix, and amount of synkinematic cement within fractures.

9.5.3.1 Mechanical Parameters

Previous work has argued that fractures in well-layered strata commonly are arranged periodically in space, with a dominant fracture spacing that is comparable to layer thickness (e.g., Bai and Pollard, 2000). Because average fracture spacing is the inverse of fracture intensity (Ortega et al., 2006), an inverse trend of fracture intensity with layer thickness would be expected if average spacing increases with layer thickness. In addition, recent numerical modeling of subcritical fracture propagation has indicated that cluster spacing might also be proportional to layer thickness (Olson, 2004). In addition, if layer thickness had an impact on the type of spatial arrangement developed by fractures in the Cupido Fm., then fractures that exhibit random arrangements (X and Z categories) should exhibit different trends of fracture intensity or fracture strain versus layer thickness from fractures that exhibit non-random arrangements (Y category).

When layer thickness is plotted against fracture intensity for fractures with apertures greater than or equal to 1 mm (using methodology described by Ortega et al., 2006), results suggest little to no correlation for different fracture categories (Figure 9.78a). Lack of correlation between layer thickness and fracture intensity indicates that variations in thickness cannot account for observed differences in fracture intensity,

similar to the conclusion of Ortega and Marrett (2001). Similarly, when layer thickness is plotted against fracture strain, results suggest little to no correlation for different fracture categories (Figure 9.78b). If fractures from one category (with one particular type of spatial arrangement) exhibited systematic differences in the amount of fracture strain compared with other categories, then it could be speculated that spatial arrangement of fractures would change during fracture development (with the expected increase in fracture strain). However, different fracture categories exhibit similar ranges of fracture strain, suggesting that as fracture strain increases during fracture development there is no variation in the type of spatial arrangement (Figures 9.78b, 9.79).

When fracture intensity is plotted against fracture strain, a well defined power-law pattern with an exponent of approximately 0.9 emerges for all fracture categories combined. If this represents an evolutionary trend, then new fractures were reaching the aperture threshold at a rate slightly lower than the rate of aperture increase of pre-existing fractures (Figure 9.79). The fact that fractures of both random and non-random spatial arrangements follow the same pattern of fracture intensity with fracture strain indicates that rate of fracture growth did not have a dominant impact on the spatial arrangement of fractures (Figure 9.79).

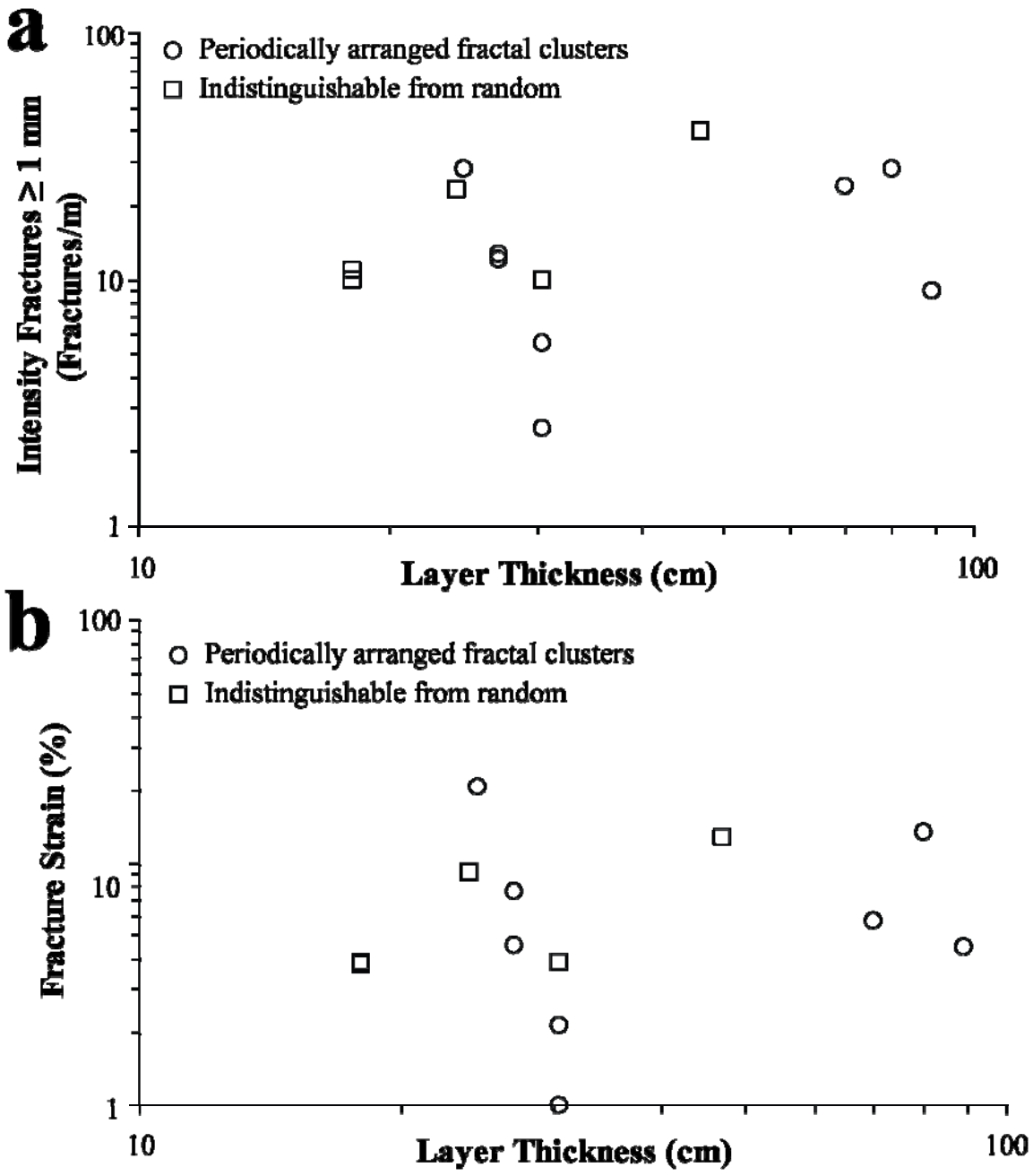

Figure 9.78 (a) Intensity for fractures with apertures larger than or equal to 1 mm versus layer thickness. (b) Fracture strain versus layer thickness.

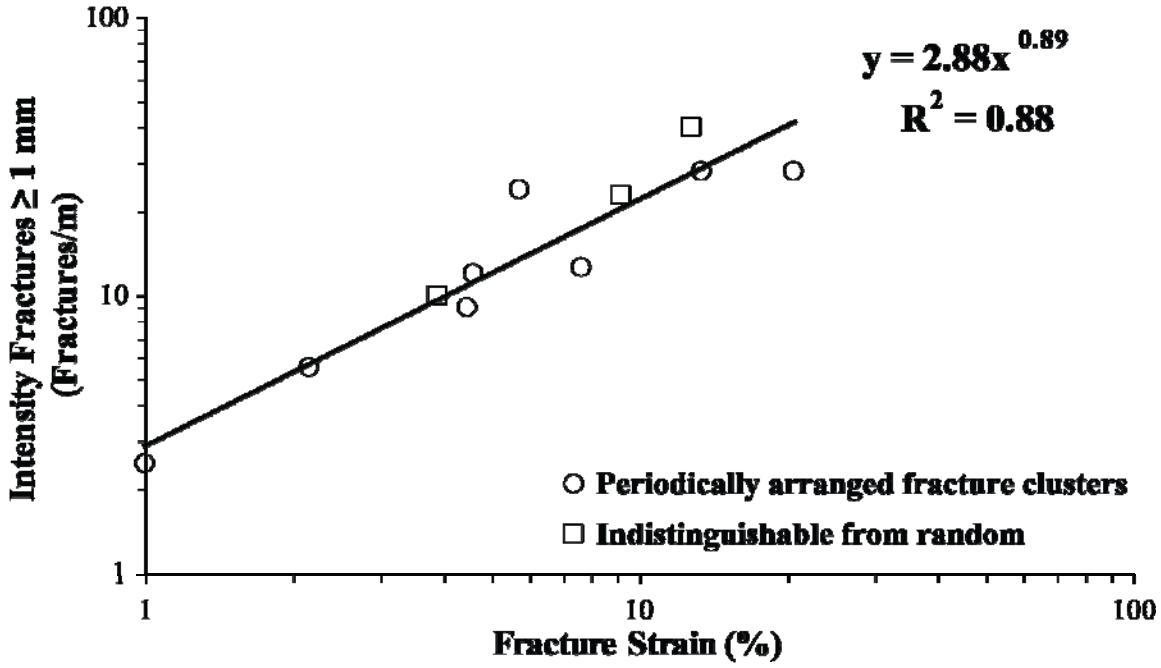

Figure 9.79 Fracture intensity for fractures with aperture larger than or equal to one mm versus fracture strain for fracture sets with periodically arranged fracture clusters (Y fractures) and fracture sets with arrangements that are indistinguishable from random (X and Z fractures). Power-law distribution was calculated for fractures of all categories combined. A power-law exponent of 0.88 indicates that fracture strain increases at a slightly faster rate that the number of fractures with apertures equal or larger than 1 mm. The power-law distribution only for Y fractures is similar to the one for all fracture categories combined.

Subcritical crack propagation has been associated with variations in the spatial arrangements of natural fractures (Olson, 1993; Olson et al., 2001). In addition, recent improvements in sample preparation and testing have allowed for reliable measurement of the subcritical index (partly a rock property and partly a reflection of chemical environment) of natural rocks (Holder et al., 2001). However, the subcritical index depends on rock microstructure and chemical environment, both of which are expected to change through time (Rijken, 2005). Therefore, for rocks that have suffered such a complex diagenetic history as the Cupido Fm. (Figure 9.1), it is very unlikely that a

subcritical index measured today, from exposed rocks, would be the same that rocks had when fractures of categories X, Y and Z were developed, particularly because several diagenetic changes occurred after fracture development (Figure 9.1). For these reasons, conclusions drawn from current measurements of subcritical index might not be valid, and therefore measuring the subcritical index was not attempted.

9.5.3.2 Diagenetic Parameters

9.5.3.2.1 Percentage of D2 Dolomite in Matrix

Previous work has suggested that the dolomite content in rock matrix exerts a control on fracture intensity in the Cupido Fm. (Ortega and Marrett, 2001; Ortega, 2002). If D2 dolomite also governed spatial arrangement (random or non-random) of fractures, then graphs of fracture intensity versus percentage of matrix composed of D2 dolomite should exhibit different patterns for random and non-random fracture arrangements. Instead, fractures with different spatial arrangements are found in layers having similar amounts of D2 dolomite, which suggests that the amount of D2 dolomite in matrix does not control how fractures are arranged into space (Figure 9.80a).

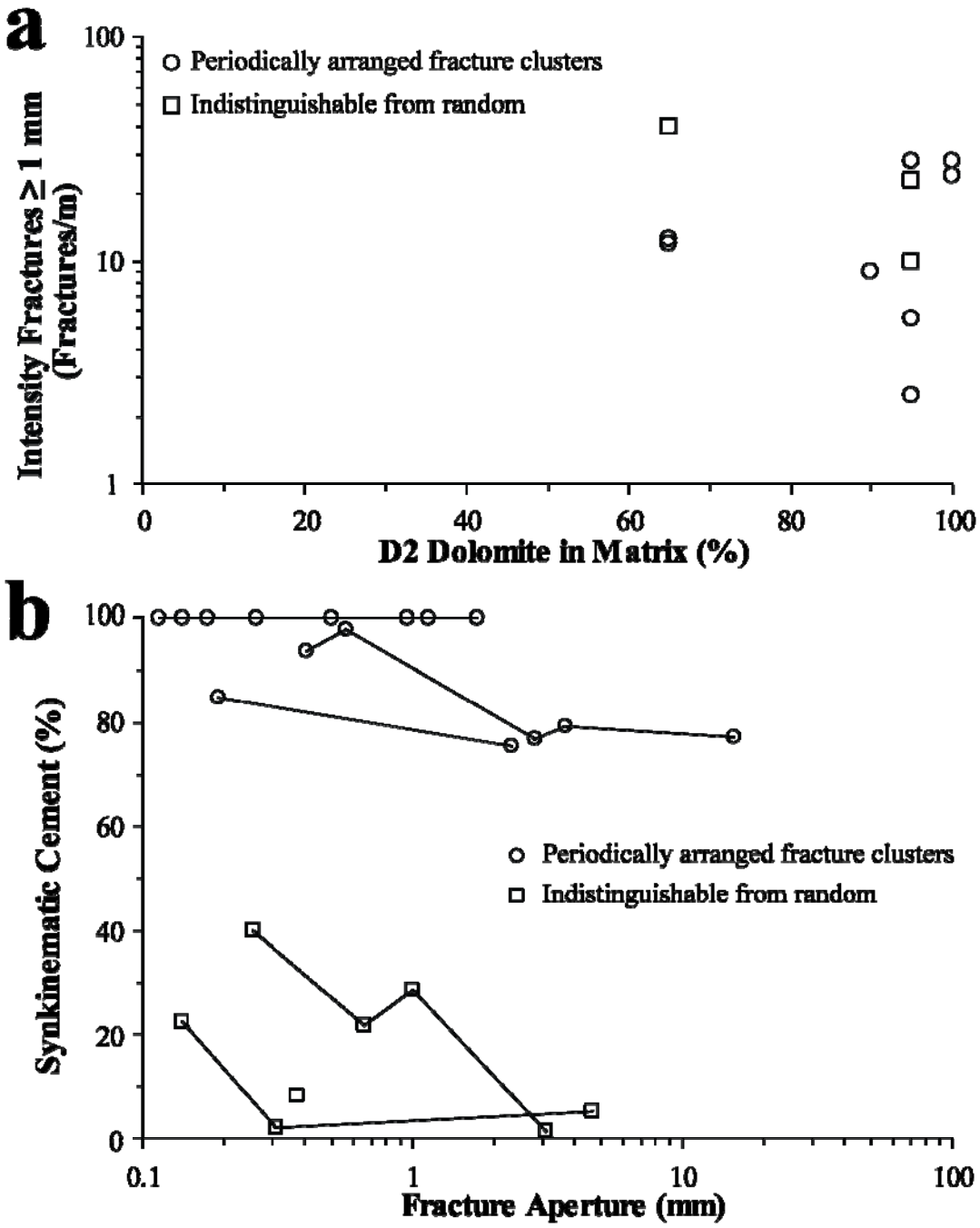

Figure 9.80 Cross-plots of percentage of cements in rock matrix and fracture versus mechanical parameters indicative of fracture evolution. (a) Fracture intensity for fractures with apertures larger than or equal to 1 mm versus percentage of D2 dolomite in matrix (a), and percentage of synkinematic cement in fractures versus fracture aperture (b), for fractures with random and non-random arrangements.

9.5.3.2.2 Percentage of Synkinematic Cement(s) in Fracture

Synkinematic cement has been shown to affect the length distribution and permeability of fractures numerically-modeled under subcritical propagation (Olson et al., 2004). Therefore, it is possible that synkinematic cement also has an impact on the spatial arrangement of fractures (Olson et al., 2007). Synkinematic cement tends to fill small fractures more completely than large fractures (Laubach, 2003), so graphs of percentage of synkinematic cement versus fracture aperture might indicate the emergent threshold, or the minimum aperture in which synkinematic cement did not completely fill fracture porosity (Laubach, 2003). Consequently, such graphs could detect different emergent thresholds for fractures that exhibit random (X and Z categories) and non-random (Y category) arrangements. If different trends for different spatial arrangements are observed, then the implication is that synkinematic cement had an impact on how fractures developed a spatial organization.

When fracture aperture is plotted against proportion of fracture filled by synkinematic cement, a decrease on the amount of synkinematic cement with increasing aperture is observed for both randomly and non-randomly arranged fractures (Figure 9.80b), which is indicative of emergent threshold, a characteristic of synkinematic fracture cements (Laubach, 2003). In addition, there is a significant difference in the amount of synkinematic cement between fractures that developed random arrangements compared with fractures that developed non-random arrangements (Figure 9.80b). Namely, fractures with random arrangements (X and Z categories) exhibit systematically smaller (0-40%) amounts of synkinematic cement than Y fractures (80-100%), as shown in Figure 9.80b. Virtually all fractures studied for my dissertation have no porosity, which implies that the amount of synkinematic cement is inversely proportional to the

amount of postkinematic cement (% synkinematic cement + % postkinematic cement = 100 %).

9.5.3.3 Synkinematic Cement and Spatial Arrangement of Fractures

How does precipitation of abundant synkinematic cement during fracture development lead to non-random spatial arrangements (periodically arranged fractal clusters) and scarce synkinematic cement lead to random spatial arrangements, both at outcrop scale?

9.5.3.3.1 Composition of Synkinematic Cements

Fractures that exhibit random arrangements of fractures at outcrop scale contain relatively small (0-40%) amounts of synkinematic dolomite whereas fractures that exhibit periodically arranged fractal clusters contain large (80-100%) amounts of synkinematic quartz and dolomite cements, as a consequence, both cement amount and composition distinguish fracture arrangement types. There are no data at this time to test the hypothesis that the composition of the synkinematic cement is more important than the amount of synkinematic cement for the spatial arrangement of fractures. Also, no previous study has addressed the question of whether fluids with different compositions (e.g., Si-rich versus Mg-rich) impact the spatial arrangement of fractures. Therefore, at this time no conclusions can be made regarding the possible role of synkinematic cement composition on fracture spatial arrangements.

9.5.3.3.2 Synkinematic Cements and Rheological Properties of Host Rock

The modified equation of Pollard and Segal (1987) for the incremental change in maximum fracture aperture depends on the inverse of Young's modulus (E), and is proportional to the incremental change in opening mode driving stress (absolute value of internal fluid pressure minus remote normal stress perpendicular to fracture), as explained by Olson (2003). Simultaneous precipitation of synkinematic cement in rock matrix and

within fractures is expected to stiffen the host rock (increasing Young's modulus), increasing the compressive stress required to close the fracture (Figure 9.81), which potentially could have an impact on the spatial arrangement of fractures (Olson et al., 2004; 2007).

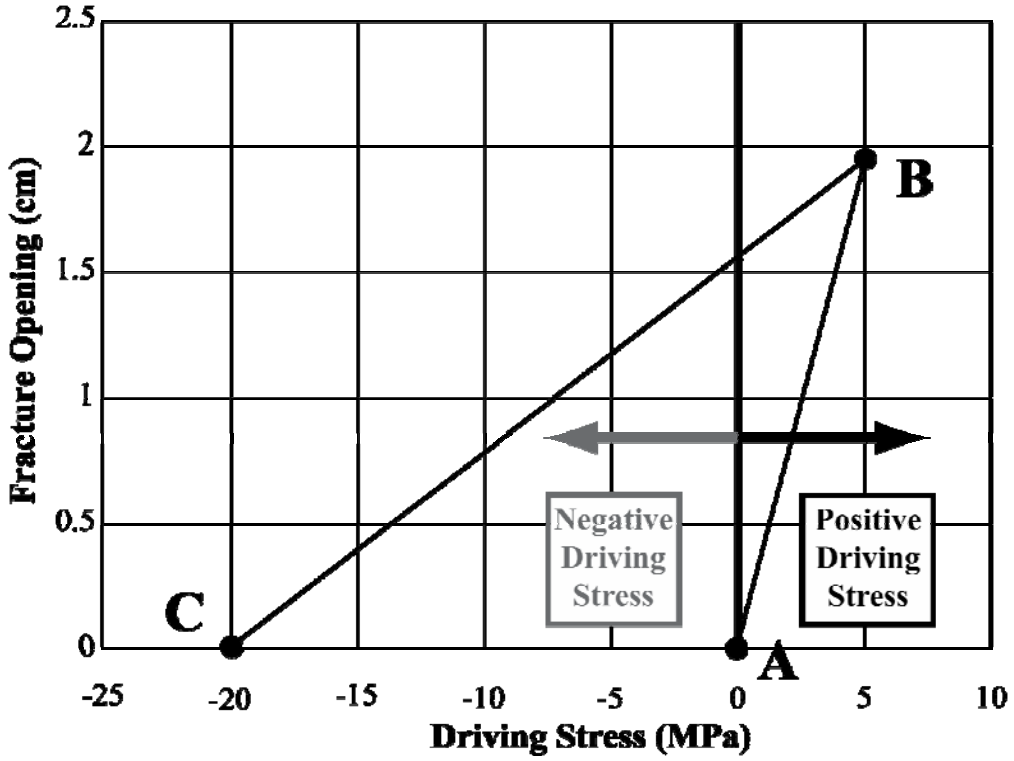

Figure 9.81 Crossplots of fracture opening versus driving stress showing the influence of cement precipitation on the stress required to close a fracture. The line from A to B represents fracture opening at low Young's modulus (E=0.5 GPa). At point B cement precipitates in both rock matrix and fracture while the fracture is open, increasing Young's modulus by a factor of 5 (E=5 GPa). The line from B to C reflects the change in driving stress required to close the fracture at the higher Young's modulus. Loss of driving stress to close the fracture can occur by reduction in fluid pressure after and/or as a result of the fracturing event, or by a subsequent increase in the compressive stress due to tectonics or other causes. From Olson et al. (2007).

However, synkinematic fracture cements (dolomite and quartz) have only a minor presence in rock matrix of Cupido Fm. layers and therefore it is unlikely that the amount

of synkinematic cement present only inside fractures could have changed drastically the Young's modulus of the entire layer because fracture porosity ranges between 4.5 and 20.5% (Table 9.5). Although it is possible that synkinematic dolomite that precipitated in X (Pre-D2) fractures was later replaced by D2 dolomite and is no longer observed in rock matrix, it is unlikely that this occurred because if there was enough synkinematic cement to precipitate abundantly in the rock matrix, there should be abundant synkinematic cement in the fractures which were open during the time of cement precipitation. Therefore, changes in Young's modulus are unlikely to have occurred due to the precipitation of synkinematic cement.

9.5.3.3.3 Changes in Rheological Properties of Host Rock

Another possible explanation is that the different amounts of synkinematic cement are not *per se* responsible for the different spatial arrangement of fractures but that they merely reflect that the rheological properties of the rock changed between the different fracturing events. However, layers that exhibit both random and non-random arrangements of fractures at outcrop scale exhibit periodic arrangement of clusters at rock sample scale (Table 9.7). Since fractures at both outcrop (mostly macrofractures) and rock sample (mostly microfractures) scale are genetically related there is no reason to assume that the conditions under which outcrop scale fractures develop is different from the ones experimented by fractures at rock-sample scale. Therefore, rheological properties and mechanical parameters (e.g., subcritical index) were similar enough that fractures at rock-sample scale yielded periodically arranged clusters.

9.5.3.3.4 Internal Structure of Randomly Arranged Fractures at Outcrop Scale

Rock samples revealed that randomly arranged fractures at outcrop scale are not completely random at rock scale (Chapter 8; Table 9.7). Namely, in layers with randomly-arranged fractures at outcrop scale, fractures at rock sample scale along the

same scanline exhibit periodically arranged clusters that lack an internal organization (Figure 9.82). Of all the fracture data sets from the Cupido Fm. analyzed (Table 9.1), the two data sets that exhibit random arrangements at outcrop scale and periodically arranged clusters at rock sample scale also are the only two data sets that were categorized as X fractures (Palmas 12 and Palmas 13, Table 9.7). X fractures contain synkinematic cements in much lower amounts than Y fractures, with Y fractures exhibiting non-random arrangements at outcrop scale (Table 9.7).

9.5.3.3.5 Emergent Threshold and Spatial Arrangement of Fractures

Fractures with apertures below the emergent threshold will tend to be completely filled with synkinematic cement whereas fractures with apertures above the emergent threshold will tend to be partially filled with bridges of synkinematic cement (Laubach, 2003). A common feature of synkinematic cement in fractures above the emergent threshold are bridges of synkinematic cement that connect both fracture walls (Laubach et al., 2004b). If bridges are abundant enough, they can impact on the evolution of fracture aperture. For instance, bridges can help maintain the fracture open once the effective compressional stress affecting a fracture is increased by (Laubach et al., 2004a). Emergent threshold is commonly in the range of about 0.01–1 mm in siliciclastic rocks and dolomite (Laubach, 2003).

Because synkinematic cement precipitates during fracture opening, synkinematic cement will help preserving the fracture aperture developed during fracture propagation for fractures with apertures below the emergent threshold. Namely, fractures with aperture below the emergent threshold would be completely filled with cement immediately (in geologic times, perhaps faster than fracture propagation) after their opening, and therefore if local stress become compressive due to propagation of nearby fractures ahead of a fracture cluster (Olson and Pollard, 1991; Olson, 2004), fracture

could no be closed due to the synkinematic cement now occupying the space created by the fracture. In contrast, fractures above the emergent threshold are not completely filled with synkinematic cement, and therefore there is a possibility that bridges across the fracture walls are not pervasive enough to prevent partial fracture closure. Additionally, bridges of synkinematic cement have high spatial anisotropy along fracture walls, and could be more abundant on fracture tips (Laubach, 2003), which would allow fracture closure in the center of the fracture but preclude closure towards fracture tips.

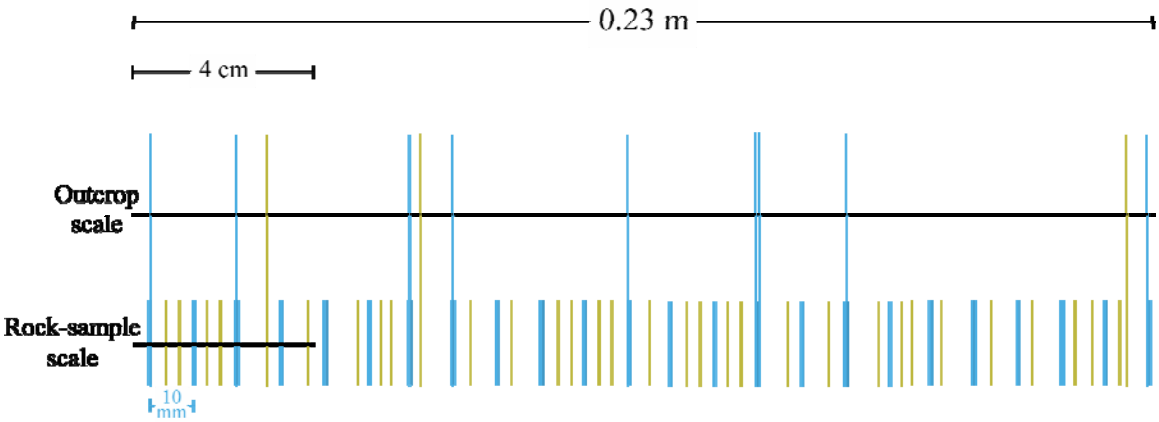

Figure 9.82 Sketch illustrating how two scanlines along the same fractures but at different scales can have different spatial arrangements. At rock sample scale fractures are organized in periodically arranged clusters (blue lines) that internally do not exhibit a statistically significant arrangement. Periodically arranged clusters at rock sample scale are separated 10 mm (Palmas 12 data set has clusters separated 9.5 mm, Table 8.7). There are fractures (green lines) in between clusters at rock-sample scale. Macrofractures (tall lines) can be observed at both outcrop and rock sample scale. However, microfractures (short lines) can only be observed at rock-sample scale (through magnification). A 4 cm long rock sample (two 1”x2”thin sections) would intercept four clusters at rock sample scale. Macrofractures measured along a 0.23 m long scanline do not exhibit a statistically significant arrangement.

Numerical modeling of subcritical fracture development has suggested that precipitation of synkinematic cement affects fracture aperture and length distributions (Olson et al., 2004; 2007). Fracture aperture distribution changes when synkinematic

cement is modeled because small fractures become preferentially filled with synkinematic cement (indicative of an emergent threshold, Laubach, 2003) and are precluded from closing due to the stress shadow effects of larger fractures that are propagating nearby (Olson, 2004). Precipitation of synkinematic cement would affect not only aperture changes but also fracture propagation, as the bridges formed during fracture development can change the stress field in the body, changing stress intensity factors and propagations velocities (Olson et al., 2007).

One evolutionary model for fractures that could explain fractures at outcrop scale with random arrangements, fractures at rock sample scale with periodic arrangements of clusters, and scarce synkinematic cement is based on the hypothesis that initial fracture development occurred at mechanical layering smaller than layer thickness (Chapter 8; Figure 9.83). Initially, fracture development occurred under subcritical propagation with high values of subcritical index (Olson, 2004), and mechanical layering smaller than layer thickness, which results in clusters of microfractures periodically arranged with cluster spacing proportional to mechanical layering (Chapter 8). Clusters of microfractures developed with enough synkinematic cement to fill them completely, which results in preservation of the spatial arrangement developed at rock sample scale (Figure 9.83a). Subsequent fracture development results in some clusters at rock sample scale intercepting each other and developing heights larger than the initial mechanical thickness (Figure 9.83b). At this stage fractures are now propagating under a larger mechanical thickness, perhaps equal to layer thickness (Figure 9.83b). This newly formed fracture or cluster of fractures would be larger than the fractures or clusters of fractures of which it originated, which would increase stress intensity factor (K) at fracture tip and result in subsequent aperture development to preferentially occurring at this newly developed fracture or cluster. At this stage the aperture of the fracture is no longer

smaller than emergent threshold, and therefore fracture aperture could decrease due to interaction with the stress shadow of other fractures propagating in the same cluster (Olson et al., 2007). Further development results in non-systematic reduction or fracture aperture and/or non-systematic closure of fractures with apertures (Figures 9.83b to 9.83e).

For layers with abundant synkinematic cement, initial development of fracture clusters at rock-sample scale would be identical to layers with scarce synkinematic cement because most fractures in both cases would have aperture smaller than the emergent threshold (Figure 9.83a). Namely, fractures would arrange into periodic clusters with cluster spacing proportional to the initial mechanical thickness. Subsequent fracture development would be different for layers with abundant synkinematic cement because the aperture of fractures in periodically arranged clusters at outcrop scale would be preserved and the periodic arrangement of clusters at a larger scale would be detected (Figure 9.83f).

In addition, it is also possible that scarce synkinematic cement allowed for linkage of fractures that coalesce to form progressively larger open fractures (with larger stress shadows), which can suppress the development of clusters around those fractures. If small fractures are not allowed to grow, there is going to be a small number of fractures growing simultaneously, which would result in little interaction between fractures, and the likelihood of positive feedback responsible for non-random arrangements is going to be smaller. In contrast, linkage of fractures when abundant synkinematic cement is being precipitated would generate smaller fractures than when synkinematic cement is scarce (because linking typically occurs at fracture tips), which in turn would not suppress cluster development and allow for interaction between a larger number of fractures which can result in non-random arrangement of fractures (Marrett et al., in review). Although

fracture clusters with an apparent periodic arrangement have been numerically modeled without inclusion of synkinematic cement (Olson, 2004), the periodicity of clusters does not appear in all numerical models, which could indicate that interaction between fractures inside clusters when synkinematic cement is not present is not always large enough to develop a level of positive feedback between fractures capable of generating periodically arranged clusters. As Olson et al. (2007) stated: “if a rock slightly fractures, then cements, then fractures some more, the fracture pattern may be very different than if the fracturing event happens all at once and cementation occurs at the end of the deformation“.

Figure 9.83 Sketches illustrating the suggested evolution of fractures in layers with scarce synkinematic cement. In (a), mechanical layering is smaller than layer thickness, and fractures are small enough to be below the emergent threshold, resulting in preservation of the periodic arrangement of clusters. From (b) to (e) there is progressive development of fracture clustering with mechanical layering equal to layer thickness but with non-systematic reduction of fracture aperture and closure of fractures, which precludes the development of periodically arranged clusters at outcrop scale. (f) Periodically arranged clusters at outcrop scale resulting with larger amounts of synkinematic cement.

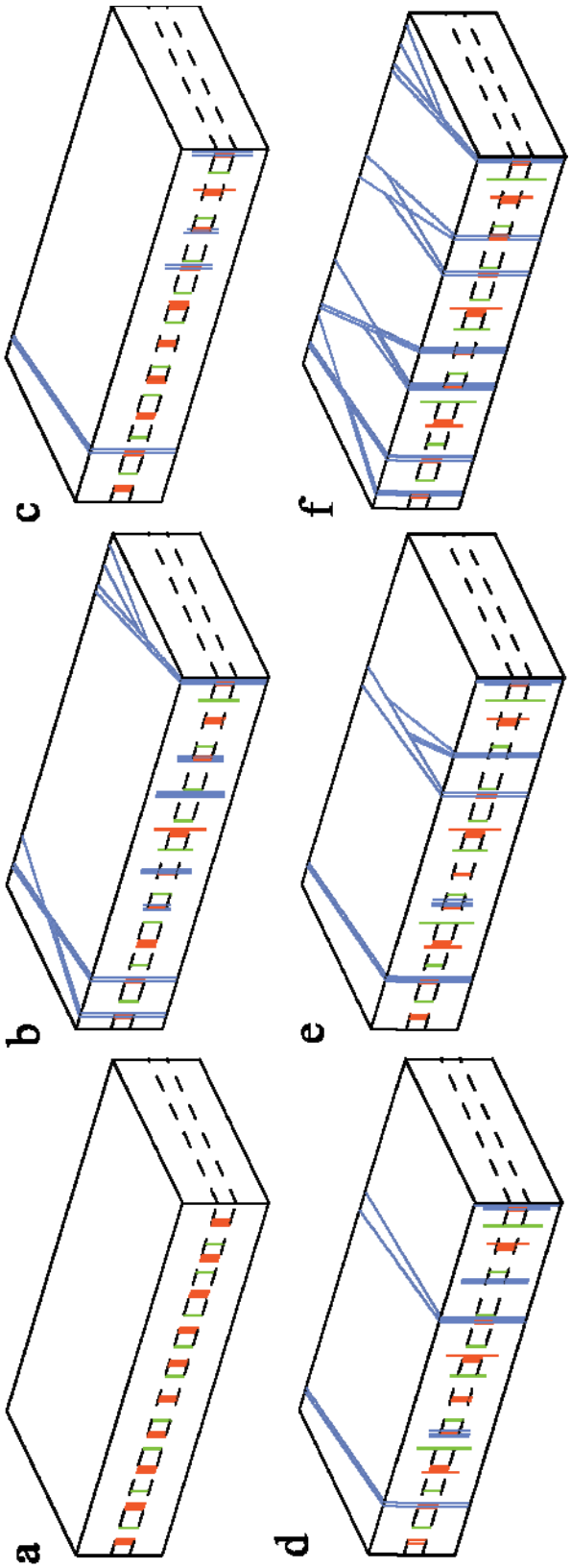
a
b
c
d
e
f

9.6. CONCLUSIONS

Using criteria different than fracture orientation, three distinctive categories of fractures were recognized in layers of the Cupido Fm. in the Monterrey salient. Each fracture category has traces with different degrees of roughness, different cements, different timing of fracture cements with respect to fracture opening, and different timing with respect to the regional D2 dolomitization. Relative timing of fractures with respect to diagenetic episodes can be obtained by studying the characteristics of fractures and the cements that precipitated in them. One fracture category (X) has irregular traces, postkinematic calcite, and euhedral bridges of synkinematic dolomite. A second fracture category (Y) groups fractures with irregular or straight traces, have fibrous synkinematic dolomite, abundant bridges of synkinematic quartz that exhibit crack-seal texture, and postkinematic calcite. A third category (Z), groups fractures that have highly irregular traces, halos of abundant D2 dolomite crystals, lacks any bridges and contains postkinematic calcite. X fractures and Y fractures with irregular traces are interpreted to have developed before the regional D2 dolomitization event whereas Z fractures are interpreted to have developed simultaneously with D2 dolomitization and have helped moved the diagenetic fluids that caused D2 dolomitization. Y fractures with straight traces are believed to have developed after D2 dolomitization. Although calcite is interpreted to have precipitated after the development of the three fracture categories mentioned above, it was not possible to distinguish if this postkinematic calcite belongs or not to a single diagenetic episode. A relationship between fracture category (and their respective spatial arrangement) and stratigraphic position could not be established because of the limited number of layers available for this study.

In addition, normalized correlation count for logarithmic and linear graduation of length scales indicates that fractures from different categories exhibit different spatial arrangements. At outcrop scale X and Z fractures exhibit only arrangements that are indistinguishable from random whereas Y fractures (regardless if interpreted as Pre- or Post-D2) exhibit fractal clusters might be periodically arranged. At rock sample scale, X and Y categories exhibit a non-random arrangement: mostly periodically arranged clusters. Layer thickness, fracture strain and fracture intensity do not seem to control the type of spatial arrangement is exhibited by fractures of different categories. Fracture intensity versus fracture strain for different fracture categories exhibits a power-law pattern with an exponent of 0.9, which suggests that during fracture evolution new fractures were being added at a slightly slower rate than fracture aperture was being increased in pre-existing fractures. Unlike what has been previously proposed for average spacing, the amount of D2 dolomite in matrix does not seem to control the spatial arrangement of fractures. However, the amount of synkinematic cements showed a strong correlation with spatial arrangement of fractures. Fractures with low (0-40%) amounts of synkinematic cement exhibit only random arrangement at outcrop scale and periodically arranged clusters at rock sample scale, whereas fractures with abundant synkinematic cement (80-100%) show fractal arrangement inside clusters occasionally with periodic arrangements at outcrop scale and periodically arranged clusters at rock sample scale. I speculate that aperture preservation for fractures with apertures smaller than the emergent threshold “freezes” the development of periodically arranged clusters at rock-sample scale and mechanical layering smaller than layer thickness for both abundant and scarce synkinematic cement. These clustering develops under subcritical fracture propagation with high subcritical index. However, when fractures or cluster of fractures link and mechanical layering increases, fractures develop apertures larger than emergent

threshold. For layers with scarce synkinematic cement, the aperture of those fractures is not preserved and results in non-systematic alteration of fracture aperture and/or fracture closure. For layers with abundant synkinematic cement, periodic spatial arrangement at both outcrop and rock sample scale is “frozen” by the abundance of synkinematic cement.

Appendices

Paper copies of this dissertation are kept at the Walter Geology Library, Jackson School of Geosciences, The University of Texas at Austin and the Perry Castañeda Library, The University of Texas at Austin. These paper copies contain a CD with the appended data in digital form. Most appendices in this CD are in Portable Digital Format (PDF) or in Excel®. PDF files are viewable with Acrobat Reader, which is available for free at: http://www.adobe.com. Most other files are digital images (JPEG or TIF formats) or files from Excel® format (widely available Microsoft software) or Didger® (commercially available digitizing software). Additional copies of the appendices in paper and digital form are kept by Dr. Randall Marrett (Supervisor, Department of Geological Sciences), archives of the Fracture Research and Application Consortium (http://www.beg.utexas.edu/indassoc/fraccity/public/recntevnt.htm), Bureau of Economic Geology, The University of Texas at Austin, and the author.

APPENDIX 1: TEMPLATES AND EXAMPLES OF FILES USED TO QUANTIFY THE SPATIAL ARRANGEMENT OF FRACTURES IN DIGITAL IMAGES

Appendix 1 encloses a set of digital templates needed to quantify fractures in new digital image collages as explained in Chapter 5 (Gomez and Laubach, 2006). This appendix also contains all the files generated during the quantification of fractures in microscopic images taken in a coordinated set of thin sections from a layer in the Cupido Formation (Chapter 5, Gomez and Laubach, 2006).

Appendix 1A: GoMezure excel® template

Appendix 1A contains the Excel® template designed to compile and analyze the attributes (aperture, orientation, length and spacing) of fractures digitized in images as explained in Chapter 5 (Gomez and Laubach, 2006). Although GoMezure was designed for digital image mosaics from thin sections, GoMezure can be readily applied to any kind of digital image (e.g., air photos).

Appendix 1B: GoMezure instructions

Appendix 2B contains the PDF file with the instructions on how to use the GoMezure template (Chapter 5). Among the directions included are instructions on: how to digitize fractures in Didger®; how the BNA files (from Didger®) organize the coordinates of points that form a digitized fracture; how to import the point coordinates of all fractures into GoMezure; how to calculate and import the scanline length (for 1D analysis); how to verify that imported fractures are represented by the correct number of points; how to specify if the analysis is 1D or 2D; how to correct fracture aperture and

spacing for scanlines that are non-perpendicular to fracture strike; how to generate cumulative frequencies of fracture attributes (aperture, length or spacing) using macros present in a worksheet; and how to generate consecutive values of fracture aperture and spacing for a subset (based on fracture type) of fractures.

Appendix 1C: GoMezure example, rock sample and thin section photos

Appendix 1C contains photos of the different stages during the preparation of sets of coordinated thin sections from rock samples as explained in Chapter 5 (Gomez and Laubach, 2006). This appendix includes photos of rock samples, rock slabs, and scans of thin sections. Rock sample is from layer Escalera OO12, Monterrey Salient, Sierra Madre Oriental, Mexico.

Appendix 1D: GoMezure example, individual image files

Appendix 1D contains the TIF files of individual, but contiguous, images from one thin section taken in a petrographic microscope. Together, the images form a long and narrow band that extends across an entire thin section (Appendix 1E).

Appendix 1E: GoMezure example, image mosaic

Appendix 1E contains the image mosaic (TIF file) formed by joining the adjacent images included in Appendix 1D. Because of limitation in the number of pixels that image editing software (e.g., Photoshop®) can handle, typically more than one image mosaic is needed to traverse an individual thin section. Image mosaics can be formed with digital images from any source, including petrographic microscope and SEM.

Appendix 1F: GoMezure example, interpreted didger® file

Appendix 1F contains the Didger® file containing the fractures mapped on the image mosaic included in Appendix 1E. The fractures on each image mosaic (Appendix 1E) were mapped in individual Didger® files.

Appendix 1G: GoMezure example, executed GoMezure template for interpreted didger® file

Appendix 1G contains the GoMezure Excel® file for rock sample included in Appendix 1C.

APPENDIX 2: SOFTWARE, TEMPLATES AND EXAMPLES OF FILES USED FOR NCC ANALYSIS

Appendix 2 contains the digital files (software, input and output files and Excel® template) used to calculate and display NCC results (Chapter 6).

APPENDIX 2A: NORMALIZED CORRELATION COUNT SOFTWARE, JAVA EXECUTABLE

Appendix 2A contains file (cc.jar) containing the Java® executable designed to calculate the Normalized Correlation Count of a particular fracture data set as explained in Chapter 6 (Marrett et al., in review). It runs in both PC and Macintosh computers.

APPENDIX 2B: NORMALIZED CORRELATION COUNT SOFTWARE, EXAMPLE OF INPUT AND OUTPUT FILES

Appendix 2B contains a collection of files used for input and generated as output for cc.jar executable (Appendix 2A).

APPENDIX 2C: NORMALIZED CORRELATION COUNT SOFTWARE, EXCEL® TEMPLATE

Appendix 2C contains the Excel® template used to create the input data for cc.jar (Appendix 2A) and graph Normalized Correlation Count results (after importing output files, Appendix 2B, into template).

APPENDIX 3: QUANTITATIVE AND QUALITATIVE DATA OF ALL OUTCROP DATA SETS MEASURED FOR MY DISSERTATION

Appendix 3 compiles all the quantitative (e.g., orientation, unedited field aperture and spacing measurements, cumulative frequency distributions of fracture spacing, graph of fracture location vs. aperture, NCC results) and qualitative (e.g., location, outcrop photo) data for each data set that I measured in outcrop (Chapters 7 and 8).

APPENDIX 3A: OUTCROP PHOTOGRAPHS

Appendix 3A contains photographs of outcrops for layers with scanline data measured on them.

APPENDIX 3B: QUANTITATIVE FRACTURE ATTRIBUTES, OUTCROP SCANLINE DATA

Appendix 3B contains an Excel® file for each scanline measured in outcrop containing the unaltered field data, descriptive statistics of fracture apertures and spacings and a common collection of figures describing the quantitative characteristics of the fracture outcrop data set. Those figures are: location along scanline vs. aperture, normalized location along scanline vs. normalized cumulative kinematic aperture, cumulative number of fractures vs. fracture aperture, cumulative number of fractures vs. fracture spacing, fracture aperture vs. adjacent spacing (Chapter 7), location along scanline vs. number of fractures and location along scanline vs. fracture indicator (Chapter 6, Gomez and Marrett, in review).

APPENDIX 3C: OUTCROP FRACTURE ORIENTATION DATA

Appendix 3C contains files with orientation data (Excel® and Geoplot®) for all structures (bedding, fractures and stylolites) measured in outcrop and their corresponding stereograms (Illustrator®).

APPENDIX 3D: NCC – LOGARITHMIC GRADUATION OF LENGTH SCALES – OUTCROP SCANLINE DATA

Appendix 3D contains Excel® files with the Normalized Correlation Count template using a logarithmic graduation of length scales for all fracture outcrop data sets described in Table 2.1 and some of the outcrop fracture data sets described in Table 2.2.

APPENDIX 3E: NCC – LINEAR GRADUATION OF LENGTH SCALES – OUTCROP SCANLINE DATA

Appendix 3E contains Excel® files with the Normalized Correlation Count template using a linear graduation of length scales for all fracture outcrop data sets described in Table 2.1 and some of the outcrop fracture data sets described in Table 2.2.

APPENDIX 4: QUANTITATIVE AND QUALITATIVE DATA OF ALL DATA SETS MEASURED FOR MY DISSERTATION ON ROCK SAMPLES

Appendix 4 is similar to Appendix 3 but compiles data from data sets measured in coordinated sets of thin sections from rock samples. Among the data included in Appendix 4 are the NCC results for coordinated sets of thin sections (for both logarithmic and linear graduations of length scales) used in Chapters 7 and 8.

Appendix 4A: Photo of sample location in outcrop

Appendix 4A contains, if available, a digital photo of the location in the outcrop of each rock sample.

Appendix 4B: Photo of intact rock sample and rock chips

Appendix 5B contains the photographs of all collected samples, regardless of whether or not they were used to collect scanline data (Table 2.3). All rock samples were photographed after arrival from the field. If coordinated sets of thin sections were generated, this appendix will also includes photos of the rock chips from where thin sections were obtained.

Appendix 4C: Scan of individual thin sections

Appendix 4C contains the image files for all thin sections generated for this dissertation (one image file per thin section).

Appendix 4D: Individual image files and image mosaics

Appendix 4D contains all the individual images and image mosaics generated for this dissertation whether or not they were used later to collect scanline data (Table 2.3). Thin sections used to obtain scanline data at rock sample scale were imaged using a petrographic microscope or a SEM. As explained in Chapter 5, individual digital images were joined to form image mosaics that can be used to quantify the attributes of the fracture array present in the rock sample.

Appendix 4E: Interpreted Didger® files

Appendix 4E contains the Didger® files for all thin sections (or coordinated sets of thin sections from a single rock sample) where 1D scanline fracture data was acquired. The mapping of fractures on image mosaics was conducted using a digitizing software called Didger®.

Appendix 4F: GoMezure Excel® files

Appendix 4F contains the GoMezure files for all thin sections (or sets of coordinated thin sections from a single rock sample) where 1D scanline fracture data was obtained (Table 2.3).

Appendix 4G: NCC – logarithmic graduation of length scales – rock sample data

Appendix 4G contains Excel® files with the Normalized Correlation Count template using a logarithmic graduation of length scales for all the thin sections (or coordinated sets of thin sections from a single rock sample) where 1D scanline fracture data was obtained (Table 2.3).

Appendix 4H: NCC – linear graduation of length scales – rock sample data

Appendix 4H contains Excel® files with the Normalized Correlation Count template using a linear graduation of length scales for all the thin sections (or coordinated sets of thin sections from a single rock sample) where 1D scanline fracture data was obtained (Table 2.3).

APPENDIX 5: QUANTITATIVE DATA FOR ALL DATA SETS (AT BOTH OUTCROP AND ROCK SAMPLE SCALES) WITH DIFFERENT FRACTURE APERTURES

Appendix 5 groups all the Excel® files containing the NCC results for fracture data sets (from both outcrop and rock sample) with different aperture thresholds used in Chapter 7.

Appendix 5A: Excel® files – different aperture thresholds

Appendix 5A contains Excel® files (one file per data set) with the recalculated spacings at different aperture thresholds for all fracture data sets where analysis of NCC at different aperture thresholds was practiced.

Appendix 5B: NCC – logarithmic graduation of length scales – different aperture thresholds

Appendix 5B contains Excel® files (one file per data set and per aperture threshold) with the Normalized Correlation Count results using logarithmic graduations of length scales.

Appendix 5C NCC – linear graduation of length scales – different aperture thresholds

Appendix 5C contains Excel® files (one file per data set and per aperture threshold) with the Normalized Correlation Count results using linear graduations of length scales.

Appendix 5D: Compilation of NCC results – logarithmic graduation of length scales – Different Aperture Thresholds

Appendix 5D contains Excel® files (one file per data set) compiling the Normalized Correlation Count curve (curve of length scale vs. spatial correlation) using logarithmic graduation of length scales (excluding the curves for the analytical random, the average, and the upper and lower 95% confidence interval of the randomized versions of the data set under analysis) at different values of using linear graduations of length scales. No input or intermediate data is included.

Appendix 5E: Compilation of NCC results – linear graduation of length scales – Different Aperture Thresholds

Appendix 5E contains Excel® files (one file per data set) compiling the Normalized Correlation Count curve (curve of length scale vs. spatial correlation) using linear graduation of length scales (excluding the curves for the analytical random, the average, and the upper and lower 95% confidence interval of the randomized versions of the data set under analysis) at different values of using linear graduations of length scales. No input or intermediate data is included.

References

Ackermann, R.V., and Schlische, R.W., 1997. Anticlustering of small normal faults around larger faults. Geology 25, 1127-1130.

Adler, P.M., and Thovert, J.F., 1999. Fracture and Fracture Networks. Kluwer Academic Publishers, Dordrecht.

Altobi, Y., in preparation. Sequence stratigraphic control on early dolomite distribution within subtidal/intertidal carbonate strata, the Cupido Formation, Sierra Madre Oriental, NE Mexico. Ph.D. dissertation, The University of Texas at Austin.

Atkinson, B.K., 1984. Subcritical Crack Growth in Geologic Materials. Journal of Geophysical Research 89 B6, 4077-4114.

Atkinson, B.K., and Meredith, P.G., 1987. The theory of subcritical crack growth with applications to minerals and rocks. In Atkinson, B.K. (ed.): Fracture mechanics of rock. New York: Academic Press, 66-111.

Avenius, C.G., 1982. Tectonics of the Monterrey salient, Sierra Madre Oriental, northeastern Mexico. American Association of Petroleum Geologists Bulletin 66, 544.

Backersa, T., Fardinb, N., Dresena, G., and Stephansson, O., 2003. Effect of loading rate on Mode I fracture toughness, roughness and micromechanics of sandstone. International Journal of Rock Mechanics & Mining Sciences 40, 425-433.

Bai, T., Maerten, L., Gross, M.R., and Aydin, A., 2002. Orthogonal cross joints: do they imply a regional stress rotation? Journal of Structural Geology 24, 77-88.

Bai, T., Pollard, D.D., 2000. Fracture spacing in layered rocks: a new explanation based on the stress transition. Journal of Structural Geology 22, 43-57.

Barboza-Gudino, J.R., Tristán-González, M., and Torres-Hernández, T.R., 1999. Tectonic setting of pre-Oxfordian units from central and northeastern Mexico: A review. In Bartolini, C., Wilson, J. L., and Lawton, T. F. (eds.): GSA Special Paper 340, Mesozoic sedimentary and tectonic history of north-central Mexico, 197-210.

Barton, C.C., and Hsieh, P.A., 1989. Physical and hydrologic-flow properties of fractures: Washington, D.C., American Geophysical Union, 28th International Geological Congress Field Trip Guidebook T385.

Barton, C.C., and Larsen, E., 1985. Fractal geometry of two-dimensional fracture networks at Yucca Mountain, southwestern Nevada. In Stephansson, O. (ed.): Proceedings of the International symposium on fundamentals of rock joints, 77-84.

Biegel, R.L., Sammis, C.G., Dieterich, J.H., 1989. The frictional properties of a simulated gouge having a fractal particle distribution. Journal of Structural Geology 11, 827-846.

Bonnet, E., Bour, O., Odling, N.E., Davy, P., Main, I., Cowie, P., and Berkowitz, B., 2001. Scaling of fracture systems in geological media. Reviews of Geophysics 29, 347-383.

Böse, E., and O.A. Cavins, 1927. The Cretaceous and Tertiary of southern Texas and northern Mexico. University of Texas Bulletin 2748, 7-142.

Bour, O., and Davy, P., 1999. Clustering and size distribution of fault patterns: Theory and measurements. Geophysical Research Letters 26, 2001-2004.

Brooks, B.A., 1994. Fractal clustering of metamorphic veins-comment. Geology 22, 1147-1148.

Brooks, B.A., Allmendinger, R.W., and de la Barra, I.G., 1996. Fault spacing in the El Teniente Mine, central Chile; evidence for nonfractal fault geometry. Journal of Geophysical Research 101-B6, 13,553-13,633.

Budd, D.A., Pranter, M.J., and Reza, Z.A., 2006. Lateral periodic variations in the geophysical and chemicals properties of dolomite. Geology 34, 373-376.

Burt, J.E., and Barber, G.M., 1996. Elementary Statistics for Geographers. The Guilford Press, New York.

Camerlo, R.H., 1998. Geometric and kinematic evolution of detachment folds, the Monterrey salient, Sierra Madre Oriental, Mexico. M.Sc. thesis, The University of Texas at Austin.

Chen, Z., Narayan, S.P., Yang, Z., and Rahman, S.S., 2000. An experimental investigation of hydraulic behaviour of fractures and joints in granitic rock. International Journal of Rock Mechanics & Mining Sciences 37, 1061-1071.

Chilès, J.P., 1988. Fractal and geostatistical methods for modeling of a fracture network. Mathematical Geology 20, 631-654.

Cladouhos, T.T., and Marrett, R., 1996. Are fault growth and linkage models consistent with power-law distributions of lengths? Journal of Structural Geology 18, 281-293.

Cotton, C.B., 1966. Barnhart field. Oil and gas fields in West Texas Symposium, West Texas Geological Society Publication 66-52, 38-41.

Cruikshank, K.M., and Aydin, A., 1995. Unweaving the joints in Entrada Sandstone, Arches National Park, Utah, U.S.A. Journal of Structural Geology 17, 409-421.

Cumella, S.P., Laubach, S.E., Ortega, O., Makowitz, A., and Rijken, P., 2002. Natural fracture and diagenetic controls on producibility of low permeability, Upper Cretaceous Williams Fork Formation sandstones, Piceance Basin, Colorado (abs.). AAPG Annual Convention Program 11, A37.

de Cserna, Z., 1956. Tectónica de la Sierra Madre Oriental de México, entre Torreon y Monterrey. 20˚ Congreso Internacional.

Davis, D.M., and Engelder, T., 1985. The role of salt in fold-and-thrust belts. Tectonophysics 119, 67-88.

Davis, G.H., and Reynolds, S.J., 1996. Structural Geology of Rocks and Regions. John Wiley and Sons, New York.

Davis, M.H., 2005. The Tectonics of Tranquitas: A Field Study of Rift through Passive Margin Development and Laramide Deformation in Triassic and Jurassic Strata of the Sierra Madre Oriental, NE Mexico. M.Sc. thesis, The University of Texas at Austin.

Dershowitz, W.S., and Einstein, H.H., 1988. Characterizing rock joint geometry with joint system models. Rock Mechanics and Rock Engineering 21, 21-51.

Diaz-Tushman, K., Laubach, S.E., and Gomez, L.A., 2005. Expanding the Tectonic History of the Highlands: A Strain Study Utilizing Fractures from Cambrian Eriboll Group Sandstones (abs.). Geological Society of America Abstracts with Programs 37 (7), 235.

Dickinson, W. R. and Snyder, W. S., 1977. Plate tectonics of the Laramide orogeny. In Matthews III, V.(ed.): Laramide folding associated with basement block faulting in the western United States, Geological Society of America Memoir 151, 355-366.

Dutton, S.P., Clift, S.J, Hamilton, D.S., Hamlin, H.S., Hentz, T.F., Howard, W.E., Akhter, M.S., and Laubach, S.E., 1993. Major low-permeability sandstone gas reservoirs in the Continental United States. The University of Texas at Austin Bureau of Economic Geology Report of Investigations No. 211, 221 p.

Eichhubl, P., and Flodin, E., 2005. Brittle deformation, fluid flow, and diagenesis in sandstone at Valley of Fire State Park, Nevada. In Pederson, J., and Dehler,

C.M.(eds.): Interior Western United States, Geological Society of America Field Guides 6, 151-167.

Eguiluz de Antuñano, S. 1991. Interpretación geológica y geofísica de la Curvatura de Monterrey, en el noreste de México. Revista Ingeniería Petrolera 31, 25-39.

Ekstrom, M.P., Dahan, C.A., Chen, M., Lloyd, P.M., and Rossi, D.J., 1987. Formation imaging with microelectrical scanning arrays. The Log Analyst 28, 294-306.

Engelder, T., and Geiser, P., 1980. On the Use of Regional Joint Sets as Trajectories of Paleostress. Fields During the Development of the Appalachian Plateau, New York. Journal of Geophysical Research 85, 6319-6341.

Erlich, R.N., and Coleman, J.L., 2005. Drowning of the Upper Marble Falls carbonate platform (Pennsylvanian), central Texas: A case of conflicting signals? Sedimentary Geology 175, 479-499.

Ferrill, D.A., Morris, A.P., Stamatakos, J.A., and Simset, D.W., 2000. Crossing conjugate normal faults. American Association of Petroleum Geologists Bulletin 84, 1543-1559.

Fischer, M. P., and Jackson, P.B., 1999. Stratigraphic controls on deformation patterns in fault-related folds: a detachment fold example from the Sierra Madre Oriental, northeast Mexico. Journal of Structural Geology 21, 613-633.

Gale, J.F.W., 2002, Specifying lengths of horizontal wells in fractured reservoirs. Society of Petroleum Engineers Reservoir Evaluation and Engineering, Paper No. 78600, 266-272.

Gale, J.F.W, and Gomez, L., in review. Late opening-mode fractures in karst-brecciated dolostones of the Lower Ordovician Ellenburger Group, West Texas : recognition, characterization, and implications for fluid flow. American Association of Petroleum Geologists Bulletin.

Gale, J.F.W., Lander, R.H., Reed, R.M., 2006. Predicting Fracture and Porosity Evolution in Dolostone (abs.). AAPG Annual Convention Official Program, Houston 15, 35.

Gale, J.F.W., Laubach, S.E., Marrett, R.A., Olson, J.E., Holder, J., and Reed, R.M., 2004. Predicting and characterizing fractures in dolostone reservoirs: using the link between diagenesis and fracturing. In Braithwaite, C. J. R., Rizzi, G., and Darke, G. (eds.): The Geometry and Petrogenesis of Dolomite Hydrocarbon Reservoirs, Geological Society, London, Special Publication 235, 177-192.

Gale, J.F.W., Laubach, S.E., Olson, J.E., and Marrett, R.A., 2005. Using the Link between Diagenesis and Fracturing to Accurately Predict, Characterize, and

Model Fluid-Flow in Fractured Carbonates. SPE Latin American and Caribbean Petroleum Engineering Conference, SPE 97382, 1-7.

Gibbons, T., Marrett, R., and Gomez, L., 2005. Spatial Distribution of Deformation Bands and Processes of Formation within Porous Sandstone: Southeastern Utah. Geological Society of America Abstracts with Programs. 37, No. 7, 209.

Gillespie, P.A. Howard, C.B., Walsh, J.J., and Watterson, J., 1993. Measurement and characterization of spatial distributions of fractures. Tectonophysics 226, 114-141.

Gillespie, P.A., Johnston, J.D., Loriga, M.A., McCaffrey, K.L.W., Walsh, J.J., and Watterson, J., 1999. Influence of layering on vein systematics in line samples. In McCaffrey, K.J.W., Lonergan, L., Wilkinson, J.J. (eds.): Fractures, Fluid Flow and Mineralization. Geological Society, London, Special Publication 155, 35-56.

Gillespie, P.A., Walsh, J.J., Watterson, J., Bonson,C.G and Manzocchi, T., 2001. Scaling relationships of joint and vein arrays from The Burren, Co. Clare, Ireland. Journal of Structural Geology 23, 183-201.

Goldhammer, R.K., and Johnson, C.A., 1991. Middle Jurassic-Upper Cretaceous paleogeographic evolution and sequence-stratigraphic framework of the northwest Gulf of Mexico rim. In Bartolini, C., Buffler, R. T., and Cantú-Chapa, A. (eds.): The western Gulf of Mexico Basin: Tectonics, sedimentary basins, and petroleum systems, American Association of Petroleum Geologists Memoir 75, 45-81.

Goldhammer, R.K., 1999. Mesozoic sequence stratigraphy and paleogeographic evolution of northeast Mexico. In Bartolini, C., Wilson, J.L., and Lawton, T.F. (eds.): Mesozoic sedimentary and tectonic history of north-central Mexico: Geological Society of America Special Paper 340, 1-58.

Gomez, L., 2004. Predicting macrofracture spatial arrangement from small rock samples: testing new analytical techniques using microfracture spacing (abs). AAPG Annual Convention Official Program 13, A53.

Gomez, L., Gale, J., Laubach, S., and Cumella, S., 2003a. Quantifying fracture intensity: an example from the Piceance Basin. Rocky Mountain Association of Geologists Piceance Guidebook, on CD.

Gomez, L.A., Gale, J.F.W., Reed, R.M., Loucks, R.G., Ruppel, S.C., and Laubach, S.E., 2003b. New Techniques in Fracture Imaging and Quantification: Applications in the Ellenburger Group, West Texas.

Gomez, L.A., Gale, J.F.W., Ruppel, S.C., and Laubach, S.E., 2001. Fracture characterization using rotary-drilled sidewall cores: an example from the Ellenburger Formation, West Texas. In Viveiros, J.J., and Ingram, S. M. (eds.):

The Permian Basin: Microns to Satellites, Looking for Oil and Gas at all Scales, The West Texas Geological Society, Fall Symposium, 81-89.

Gomez, L.A., and Laubach, S.E., 2006. Rapid Digital Quantification of Microfracture Populations. Journal of Structural Geology 28, 408-420.

Gomez, L.A., and Marrett, R., 2006. Relationship between Aperture and Spatial Arrangement of Opening-mode Fractures: Preferential Positioning of Large Fractures Inside Clusters (abs.). AAPG Annual Convention Official Program, Houston 15, 38.

Gomez, L.A., and Marrett, R., in review. Spatial arrangement of fractures I – Traditional analyses. Journal of Structural Geology.

Gray, G.G., Pottorf, R. J., Yurewicz, D.A., Mahon, K.I., Pevear, D.R., and Chuchla, R.J., 2001. Thermal and chronological record of syn- to post-Laramide burial and exhumation, Sierra Madre Oriental, Mexico. In Bartolini, C., Buffler, R. T., and Cantú-Chapa, A. (eds.): The western Gulf of Mexico Basin: Tectonics, sedimentary basins, and petroleum systems, American Association of Petroleum Geologists Memoir 75, 159-181.

Gross, M.R., 1993. The origin and spacing of cross joints: examples from the Monterey Formation, Santa Barbara Coastline, California. Journal of Structural Geology 15, 737-751.

Gross, M.R., Engelder, T., 1995. Strain accommodated by brittle failure in adjacent units of the Monterrey Formation, U.S.A.: scale effects and evidence for uniform displacement boundary conditions. Journal of Structural Geology 17, 1303-1318.

Gross, M.R., Fisher, M.P., Engelder, T., and Greenfield, R.J., 1995. Factors controlling joint spacing in interbedded sedimentary rocks: integrating numerical models with field observations from the Monterey Formation, USA. In Ameen, M.S. (ed.): Fractography: fracture topography as a tool in fracture mechanics and stress analysis. Geological Society, London, Special Publication 92, 215-233.

Hansley, P.L., and Johnson, R.C., 1980. Mineralogy and diagenesis of low-permeability sandstones of Late Cretaceous age, Piceance Creek basin, northwestern Colorado. The Mountain Geologist 17, 88-129.

Hare, C.M., and Marrett, R., in review. Spatial arrangement of fractures II - Spectral analysis. Journal of Structural Geology.

Harris, C., Franssen, R., and Loosveld, R., 1991. Fractal analysis f fractures in rock: the Cantor's dust method-comment. Tectonophysics 198, 107-111.

Hilgers, C., and Urai, J.L., 2005. On the arrangement of solid inclusions in fibrous veins and the role of the crack-seal mechanism. Journal of Structural Geology 27, 481-494.

Hinnov, L.A., and Goldhammer, R.K., 1991. Spectral Analysis of the Middle Triassic Latermar Limestone. Journal of Sedimentary Petrology 61, 1173-1193.

Hoak, T., Sundberg, K., Deyhim, P., and Ortoleva, P., 1998. Fracture characterization and discrimination criteria for karst and tectonic fractures in the Ellenburger Group, West Texas: Implications for Reservoir and Exploration Models, DOE/PC/91008-23 Part 6.

Holder, J., Olson, J.E., and Philip, Z., 2001. Experimental Determination of Subcritical Crack Growth Parameters in Sedimentary Rock, Geophysical Research Letters 28, 599-602.

Holtz, M.H., and Kerans, C., 1992. Characterization and classification of West Texas Ellenburger reservoirs. In Candelaria, M.P., and Reed, C.L. (eds.): Paleokarst, karst related diagenesis and reservoir development: examples from Ordovician-Devonian age strata of West Texas and the Midcontinent: Permian Basin SEPM Publication 92-33, 45-54.

Hooker, J.N., 2004. Fault timing in the Sierra Madre Oriental, northeastern Mexico. M.Sc. thesis, The University of Texas at Austin.

Huang, Q., and Angelier. J., 1989. Fracture spacing and its relation to bed thickness. Geological Magazine 126, 355-362.

Humphrey, W.E. and Diaz, T., 2003. Jurassic and Lower Cretaceous stratigraphy and tectonics of northeast Mexico. In Wilson, J.L., and Jordan, C. (eds.): Bureau of Economic Geology Report of Investigations No. 267, 152 p.

Jiang, Y., Lib, B., and Tanabashi, Y., in press. Estimating the relation between surface roughness and mechanical properties of rock joints. International Journal of Rock Mechanics & Mining Sciences.

Jolly, R.J.H., Cosgrove, J.W., and Dewhurst, D.N., 1998. Thickness and spatial distributions of clastic dykes, northwest Sacramento Valley, California. Journal of Structural Geology 20, 1663-1672.

Kearsley, A., Wright, P., 1988. Geological applications of scanning electron cathodoluminescence imagery. Microscopy and Analysis, September, 49-51.

Kerans, C., 1990. Depositional systems and karst geology of the Ellenburger Group (Lower Ordovician), subsurface, West Texas: The University of Texas at Austin, Bureau of Economic Geology Report of Investigations No. 193, 63 p.

Kranz, R.L., 1983. Microcracks in rock: a review. Tectonophysics 100, 449-480.

La Pointe, P.R., and Hudson, J.A., 1985. Characterization and Interpretation of Rock Mass Joint Patterns. Geological Society of America, Special Paper 199.

Lanaro, F., 2000. A random field model for surface roughness and aperture of rock fractures. International Journal of Rock Mechanics & Mining Sciences 37, 1195-1210.

Lander, R.H., Gale, J.F.W., Laubach, S.E., and Bonnell, L.M., 2002. Interaction between quartz cementation and fracturing in sandstone (abs.). AAPG Annual Convention Program 11, A98-A99.

Laubach, S.E., 1988. Subsurface fractures and their relationship to stress history in East Texas basin sandstone. Tectonophysics 156, 37-49.

Laubach, S.E., 1989. Paleostress directions from the preferred orientation of closed microfractures (fluid-inclusion planes) in sandstone, East Texas basin, U.S.A. Journal of Structural Geology 11, 603-611.

Laubach, S.E., 1991. Fracture patterns in low-permeability-sandstone gas reservoir rocks of the Rocky Mountain region. Proc. Joint Society of Petroleum Engineers Rocky Mountain Regional Meeting/Low Permeability Reservoir Symposium, SPE 21877, 501-510.

Laubach, S.E., 1997. A method to detect natural fracture strike in sandstones. American Association of Petroleum Geologists Bulletin 81, 604-623.

Laubach, S.E., 2003. Practical approaches to identifying sealed and open fractures. Association of Petroleum Geologists Bulletin 87, 561-579.

Laubach, S.E., and E. Doherty, 1999, Oriented drilled sidewall cores for natural fracture evaluation: Society of Petroleum Engineers, Paper SPE 56801, 793-800.

Laubach, S.E., and Milliken, K., 1996. New fracture characterization methods for siliciclastic rocks. In Aubertin, M., Hassani, F., and Mitri, H. (eds.): Proceedings 2nd North American Rock Mechanics Symposium, Rotterdam, Balkema, 1209-1213.

Laubach, S.E., Marrett, R., and Olson, J.O., 2000. New Directions in Fracture Characterization. The Leading Edge 19, 704-711.

Laubach, S.E., Olson, J.E., and Gale, J.F.W., 2004a. Are open fractures necessarily aligned with maximum horizontal stress? Earth and Planetary Science Letters 222, 191–195.

Laubach, S.E., Reed, R.M., Olson, J.E., Lander, R.H., and Bonell, L.M., 2004b. Coevolution of crack-seal texture and fracture porosity in sedimentary rocks: cathodoluminescence observations of regional fractures. Journal of Structural Geology 26, 967-982.

Laubach, S.E., and Ward, M.E., 2006. Diagenesis in porosity evolution of opening-mode fractures, Middle Triassic to Lower Jurassic La Boca Formation, NE Mexico. Tectonophysics 419, 75–97.

Lawn, B.R., and Wilshaw, T.R., 1975. Fracture of Brittle Solids. Cambridge University Press. Cambridge.

Lehmann, C., Osleger, D.A., and Montañez, I., 2000. Sequence stratigraphy of Lower Cretaceous (Barremian-Albian) carbonate platforms of northeastern Mexico: regional and global correlations. Journal of Sedimentary Research 70, 373-391.

Lespinasse, M., 1999, Are fluid inclusion planes useful in structural geology? Journal of Structural Geology 21, 1237-1243.

Lofts, J.C., Bedford, J., Boulton, H., Van Doorn, J.A., and Jeffreys, P., 1997. Feature recognition and the interpretation of images acquired from horizontal wellbores. In Lovell, M.A and Harvey, P.K. (eds.): Developments in Petrophysics, Geological Society Special Publication. No 122, 345-365.

Lofts, J.C., and Bourke, L.B., 2000. The recognition of artifacts from acoustic and resistivity borehole imaging devices. In Thompson, L.B. (ed.): Atlas of Borehole Imagery AAPG/Datapages Discovery Series 4.

Lopez-Ramos, E., 1983. Geologia de México, Tomo III. Mexico: Tesis Resendiz, 453 p.

Lorenz, J.C., 1983. Lateral variability in the Corcoran and Cozzette blanket sandstones and associated Mesaverde rocks, Piceance Creek basin, northwestern Colorado. Society of Petroleum Engineers, SPE/DOE Paper 11608, 81-86.

Lorenz, J.C., and Finley, S.J., 1989, Differences in fracture characteristics and related production: Mesaverde Formation, Northwestern Colorado: SPE Formation Evaluation, March 1989, v. 4, 11-16.

Lorenz, J.C., and Hill, R., 1991. Subsurface fracture spacing: comparison of inferences from slant/horizontal core and vertical core in Mesaverde reservoirs in the Piceance Basin. SPE Rocky Mountain Regional Meeting/Low-Permeability Reservoir Symposium, April 15-17, 1991, Denver, SPE No. 21877, 705-716.

Lorenz, J.C., and Hill, R., 1992. Measurement and analysis of fractures in core. In Schmoker, J.W., Coalson, E.B., and Brown, C.A. (eds.): Geological studies

relevant to horizontal drilling: examples from western North America, Rocky Mountain Association of Geologists, 47-57.

Lorenz, J.C., and R. E. Hill, 1994, Subsurface fracture spacing: comparison of inferences from slant/horizontal and vertical cores: SPE Formation Evaluation, March 1994, v. 9, 66-72.

Lu, E., 2000. Orientation, timing, kinematics, and genesis of veins and stylolites in seven anticlines, Sierra Madre Oriental, Mexico. B. Sc. senior thesis, The University of Texas at Austin.

Manning, C.E., 1994. Fractal clustering of metamorphic veins. Geology 22, 335-338.

Marone, C., Scholz, C.H., 1989. Particle size-distribution and microstructures within simulated fault gouge. Journal of Structural Geology 17, 799-814.

Marrett, R., 1996. Aggregate properties of fracture populations. Journal of Structural Geology 18, 169-178.

Marrett, R., 1997. Permeability, porosity and shear-wave anisotropy from scaling of open fracture populations. In Hoak, T.E., Klawitter, A.L., and Blomquist, P. K. (eds.): Fractured Reservoirs: Characterization and Modeling Guidebook, Rocky Mountain Association of Geologists, 217-226.

Marrett, R., Ortega, O., and Kelsey, C., 1999. Extent of power-law scaling for natural fractures in rock: Geology 27, 799-802.

Marrett, R., Gale, J., and Gomez, L., 2004. New techniques for characterizing fracture spacing: examples from Northeastern Mexico and Central Texas (abs.), AAPG Annual Convention Official Program 13, A91.

Marrett, R., Gale, J.F., and Gomez, L.A., in review. Spatial arrangement of fractures III - Correlation analyses. Journal of Structural Geology.

Marrett, R.A. and Aranda-García, M., 2001. Regional structure of the Sierra Madre Oriental fold-thrust belt, Mexico. In Marrett, R.A. (ed.): Genesis and controls of reservoir-scale carbonate deformation, Monterrey salient, Mexico, Bureau of Economic Geology Guidebook 28, 31-55.

Marrett, R.A., and Laubach, S.E., 2001. Fracturing during burial diagenesis. In Marrett, R.A. (ed.): Genesis and controls of reservoir-scale carbonate deformation, Monterrey salient, Mexico, Bureau of Economic Geology Guidebook 28, 109-123.

McWilliams, P.C., Miller, S.M., and Kerkering, J.C., 1990. Fractal characterization of rock fracture roughness for estimating shear strength. In Rossmanith, H.P. (ed.):

Mechanics of jointed and faulted rock, Proceedings of the international conference. International conference on Mechanics of jointed and faulted rock, Vienna, Austria, 331-336.

Milliken, K.L., and Laubach, S.E., 2000. Brittle deformation in sandstone diagenesis as revealed by cathodoluminescence imaging with application to characterization of fractured reservoirs. In M. Pagel, Barbin, V., Blanc, P., and Ohnenstetter, D. (eds.): Cathodoluminescence in geosciences, Springer-Verlag, 225-244.

Monroy-Santiago, F., Laubach, S.E., and Marrett, R., 2001. Preliminary Diagenetic and Stable Isotope Analyses of Fractures in the Cupido Formation, Sierra Madre Oriental. In Marrett, R. (ed.): Genesis and Controls of Reservoir-Scale Carbonate Deformation, Monterrey Salient, Mexico, 83-107.

Monroy-Santiago, F., in preparation. Interrelationships between Carbonate Diagenesis and Fracture Development: Example from Monterrey Salient, Mexico and Implications for Hydrocarbon Reservoir Characterization. Ph.D. dissertation, The University of Texas at Austin.

Moros, J.G., 1999. Relationship between fracture aperture and length in sedimentary rocks. M.Sc. thesis, The University of Texas at Austin.

Narr, W., 1991. Fracture density in the deep subsurface; techniques with application to Point Arguello oil field. American Association of Petroleum Geologists Bulletin 75, 1300-1323.

Narr, W., 1996. Estimating average fracture spacing in subsurface rock. American Association of Petroleum Geologists Bulletin 80, 1565-1585.

Narr, W., and Lerche, I., 1984. A Method for Estimating Subsurface Fracture Density in Core: American Association of Petroleum Geologists Bulletin 68, 637-648.

Narr, W., and Suppe, J., 1991. Joint spacing in sedimentary rocks. Journal of Structural Geology 13, 1037-1048.

Nelson, R.A., 2001. Geologic Analysis of Naturally Fractured Reservoirs. Houston: Gulf Publishing, Boston.

Olson, J.E., 2003. Sublinear scaling of fracture aperture versus length: an exception or the rule? Journal of Geophysical Research, 108-B9, 2416-2423.

Olson, J.E., 2004. Predicting fracture swarms - the influence of subcritical crack growth and the crack-tip process zone on joint spacing in rock. In Engelder, T., and Cosgrove, J.W. (eds.): The initiation, propagation, and arrest of joints and other fractures. Geological Society, London, Special Publication 231, 73-87.

Olson, J.E., Holder, J., and Rijken, P., 2002. Quantifying the Fracture Mechanics Properties of Rock for Fractured Reservoir Characterization. Proceedings of SEP/IRSM Rock Mechanics Conference, Irving, TX, SPE 78207.

Olson, J.E., Laubach, S.E., and Lander, R.H., 2004. Improving fracture permeability prediction by combining geomechanics and diagenesis. North America Rock Mechanics Symposium (NARMS), Rock Mechanics Across Borders and Disciplines, ARMA/NARMS 04-563, 1-9.

Olson, J.E., Laubach, S.E., and Lander, R.H., 2007. Combining diagenesis and mechanics to quantify fracture aperture distributions and fracture pattern permeability. In Lonergan, L., Jolly, R. J. H., Sanderson, D. J., and Rawnsley, K. (eds.): Fractured Reservoirs. Geological Society, London, Special Publication 270, 97-112.

Olson, J.E., and Pollard, D.D., 1989. Inferring paleostresses from natural fracture patterns: A new method. Geology 13, 345-348.

Olson, J.E., Qiu, Y., Holder, J., and Rijken, P., 2001. Constraining the spatial distribution of fracture networks in naturally fractured reservoirs using fracture mechanics and core measurements. Society of Petroleum Engineers, Paper SPE 71342, 1-12.

Onash, C.M., 1990. Microfractures and their role in deformation of a quartz arenite from the central Appalachian foreland. Journal of Structural Geology 12, 883-894

Ortega, O., 2002. Fracture-size scaling and stratigraphic controls on fracture intensity. Ph.D. dissertation, The University of Texas at Austin.

Ortega, O., 2001. Type section of the Cupido Formation from the Boquilla Corral de Palmas locality. In Marrett, R. (ed.): Genesis and Controls of Reservoir-Scale Carbonate Deformation, Monterrey Salient, Mexico, plate in pocket.

Ortega, O., Marrett, R., Hamlin, H.S., Cliff, S., and Reed, R., 1998. Quantitative Macrofracture Prediction Using Microfracture Observations: A Successful Case Study in the Ozona Sandstone, West Texas. American Association of Petroleum Geologists Annual Convention Extended Abstracts 7, A503.

Ortega, O., and Marrett, R., 2000. Prediction of macrofracture properties using microfracture information, Mesaverde Group sandstones, San Juan Basin, New Mexico: Journal of Structural Geology 22, 571-588.

Ortega, O., and Marrett, R., 2001. Stratigraphic Controls on Fracture Intensity in Barremian-Aptian Carbonates, Northeastern Mexico. In Marrett, R. (ed.): Genesis and Controls of Reservoir-Scale Carbonate Deformation, Monterrey Salient, Mexico, 57-82.

Ortega, O., Marrett, R., and Laubach, S.E., 2006. A scale-independent approach to fracture intensity and average spacing measurement. American Association of Petroleum Geologists Bulletin 90, 193-208.

Padilla y Sanchez, R.J., 1985. Las estructuras de la Curvatura de Monterrey, estados de Coahuila, Nuevo León, Zacatecas y San Luis Potosí. Universidad Nacional Autonomia de México Revista - Instituto de Geología 6, 1-20.

Pagel, M., Barbin, V., Blanc, P., Ohnenstetter, D. (eds.), 2000. Cathodoluminescence in Geosciences. Springer, Berlin.

Pardo-Iguzquiza, E., and Rodriguez-Tovar, F. J. 2004. POWGRAF2: a program for graphical spectral analysis in cyclostratigraphy. Computers & Geosciences 30, 533–542.

Park, N., 2006. Discrete element modeling of fracture rock behavior: fracture toughness and time-dependent fracture growth. Ph.D. dissertation, The University of Texas at Austin.

Passchier, C.W., and Trouw, R. A. J., 1998. Microtectonics. Springer, Berlin.

Philip, Z.G., Jennings, J.W., Olson, J.E., Laubach, S.E., and Holder, J., 2005. Modeling Coupled Fracture-Matrix Fluid Flow in Geomechanically Simulated Fracture Networks. Society of Petroleum Engineers Reservoir Evaluation and Engineering, Paper No. 77340, 300-309.

Pitman, J.K., and Sprunt, E.S., 1986. Origin and distribution of fractures in Lower Tertiary and Upper Cretaceous Rocks, Piceance basin, Colorado, and their relation to the occurrence of hydrocarbons. In Spencer, C. W., and Mast, R.F. (eds.): Geology of tight gas reservoirs: AAPG Studies in Geology 24, 221-234.

Pollard, D., and Aydin, A., 1988. Progess in understanding jointing over the past century. Geological Society of America Bulletin 100, 1181-1204.

Pollard, D., and Segal, P., 1987. Theoretical displacements and stress near fractures in rock: with applications to fault, joints, veins, dikes and solution surfaces. In Atkinson, B.K. (ed.): Fracture Mechanics of Rock. Academic Press, 277-350.

Price, N.J., and Cosgrove, J.W., 1990. Analysis of Geological Structures. Cambridge University Press, Cambridge.

Priest, S.D., and Hudson, J.A., 1976. Discontinuity spacings in rock. International Journal of Rock Mechanics 13, 135-148.

Ramsay, J.G., 1980. The crack-seal mechanism of rock deformation: Nature (London) 284, no. 5752, p. 135-139.

Ramsay, J.G., and Huber, M.I., 1983. The Techniques of Modern Structural Geology. Volume 1: Strain Analysis. Academic Press, London.

Renshaw, C.E., 2000. Fracture spatial density and the anisotropic connectivity of fracture networks. In Faybishenko, B., Witherspoon, P.A., Benson, S.M. (eds.): Dynamics of fluids in fractured rocks. Geophysical Monograph 122, 203-211.

Renshaw, C.E., and Pollard, D. D., 1995. An Experimentally Verified Criterion for Propagation Across Unbounded Frictional Interfaces in Brittle, Linear Elastic Materials. International Journal of Rock Mechanics, Mining Science and Geomechanical Abstracts 32, 237-249.

Rico, L., 1999. Geometric and kinematic evolution of a complete detachment fold in a natural cross-section. M.Sc. thesis, The University of Texas at Austin.

Rijken, M. C. M., 2005. Modeling naturally fractured reservoirs: from experimental rock mechanics to flow simulation. Ph.D. dissertation, The University of Texas at Austin.

Rives, T., Razack, M., Petit, J.-P., and Rawnsley, K.D., 1992. Joint spacing: analogue and numerical simulations. Journal of Structural Geology 14, 925-937.

Rives, T., Rawnsley, K.D., and Petit, J.-P., 1994. Analogue simulation of natural orthogonal joint set formation in brittle varnish. Journal of Structural Geology 16, 419-429.

Rouleau, A., and Gale, J.E., 1985. Statistical characterization of the fracture system in the Stripa Granite, Sweden. International Journal of Rock Mechanics, Mining Science and Geomechanical Abstracts 22, 353-367.

Safko, P. S., and Hickey, J. J., 1992. A preliminary approach to the use of borehole data, including television surveys, for characterizing secondary porosity of carbonate rocks in the Floridan Aquifer System. U.S. Geological Survey Water Resources Investigation, 91-4168.

Salkind, N.J., 2004. Statistics for People Who (Think They) Hate Statistics. Sage Publishing Inc., Thousand Oaks.

Sammis, C.G., King, G., and Biegel, R.L., 1987. The Kinematics of Gouge Deformation. PAGEOPH 125, 777-812.

Sanderson, D.J., Roberts, S., and Gumiel, P., 1994. A fractal relationship between vein thickness and gold grade in drill core from La Codosera, Spain. Economic Geology 89, 168-173.

Schultz, R.A., 2000. Growth of Geologic Fracture into Large-Strain Populations: Review of Nomenclature, Subcritical Crack Growth, and Some Implications for Rock Engineering. International Journal of Rock Mechanics and Rock Engineering 37, 403-411.

Schulz, M., and Mudelsee, M. 2002. REDFIT: estimating red-noise spectra directly from unevenly spaced paleoclimate time series. Computer and Geosciences 48, 471-476.

Shepherd, J., Creasey, J. W., and Fisher, N. L., 1981. Statistical analysis of spacings between geological discontinuities in coal mines, with applications to short-range forecasting of mining conditions. Australian coal geology 3, 71-80.

Schroeder, M., 2000. Fractals, Chaos, Power Laws: Minutes from an Infinite Paradise. W.H. Freeman and Co, New York.

Simpson, G.D.H., 2000, Synmetamorphic vein spacing distributions: characterisation and origin of a distribution of veins from NW Sardinia, Italy. Journal of Structural Geology 22, 335-348.

Shackleton, J. R., Cooke, M. L., and Sussman, A.J., 2005. Evidence for temporally changing mechanical stratigraphy and effects on joint-network architecture. Geology 33, 101–104.

Sharp, J.M., Jr., 1993. Fractured Aquifers/Reservoirs: Approaches, Problems, and Opportunities, Memoirs of the 24th Congress of the IAH, Oslo, Norway.

Sheriff, R.E., 1994. Encyclopedic Dictionary of Exploration Geophysics. Society of Exploration Geophysicists, Tulsa.

Stewart, S.A., 1996. Influence of detachment layer thickness on style of thinskinned shortening. Journal of Structural Geology 18, 1271-1274.

Stowell, J.F.W., 2001. Characterization of Opening-Mode Fracture Systems in the Austin Chalk. Proceedings of Gulf Coast Association of Geological Societies, Shreveport, Louisiana, L1, 313-319.

Strachan, R.A., Smith, M., Harris, A.L., and Fettes, D. J., 2002. The northern Highland and Grampian terranes. In: Trewin, N. H. (ed.): The Geology of Scotland. The Geological Society, London, 81-148.

Suppe, J., 1985. Principles of Structural Geology, Prentice-Hall, Englewood Cliffs.

Terzaghi, R., 1965, Sources of error in joint surveys: Geotechnique 15, 287-297.

Tinker, S.W., 1985. Lithostratigraphy and biostratigraphy of the Aptian La Peña Formation, northeast Mexico and South Texas (Part 1), and the depositional setting of the Aptian Pearsall-La Peña formations, Texas subsurface and northeastern Mexico: Why is there not another Fairway Field? (Part 2). M.Sc. thesis, University of Michigan, Ann Arbor, 80 p.

Todd, R.G., and Mitchum, R. M., Jr., 1977. Seismic stratigraphy and global changes of sea level, part 8: Identification of Upper Triassic, Jurassic, and Lower Cretaceous seismic sequences in Gulf of Mexico and offshore West Africa. In Payton, C.E. (ed.): Seismic stratigraphy—applications to hydrocarbon exploration, American Association of Petroleum Geologists Memoir 26, 145-163.

Trimby, P.W., and Prior, D.J., 1999. Microstructural imaging techniques: a comparison between light and scanning electron microscopy. Tectonophysics 303, 71-81.

Twiss, R.J., and Moores, E.M., 1992. Structural Geology. W.H. Freeman, New York.

Tucker, M.E., 1991. Sedimentary Petrology, Blackwell Scientific Publications, Oxford.

Tucker, M.E., and Wright, V.P., 1999. Carbonate Sedimentology, Blackwell Science, Oxford.

Tyler, N., Bebout, D.G., Garrett, C.M., Jr., Guevara, E.H., Hocott, C.R., Holtz, M.H., Hovorka, S.D., Kerans, C., Lucia, F.J., Major, R.P., Ruppel, S.C., and Vander Stoep, G.W., 1991. Integrated characterization of Permian Basin reservoirs, University Lands, West Texas: targeting the remaining resource for advanced oil recovery: The University of Texas at Austin, Bureau of Economic Geology Report of Investigations No. 203, 136 p.

van Daalen, M., Heilbronner, R., and Kunze, K., 1999. Orientation analysis of localized shear deformation in quartz fibres at the brittle-ductile transition. Tectonophysics 303, 83-107.

Van der Pluijm, B.A., and Marshak, S., 1997. Earth Structure: An Introduction to Structural Geology and Tectonics. WCB/McGraw-Hill, Dubuque.

Vega-Vera, F.J., Mitre-Salazar, L.M., and Martinez, E., 1989. Contribucion al conocimiento de la estratigrafia del grupo Difunta (Cretacio superior-Terciario) en el noreste de México. Universidad Nacional Autonomia de México Instituto de Geología Revista 8, 179-187.

Velde, B., Dubois, J., Touchard, G., and Badri, A., 1990. Fractal analysis of fractures in rocks: the Cantor's dust method. Tectonophysics 179, 345-352.

Villaescusa, E., and Brown, E.T., 1990. Characterizing joint spatial correlation using geostatistical methods. In Barton, N., and Stephansson, O. (eds.): Rock Joints, Balkema, Rotterdam, 115-122.

Walsh, J.J., and Watterson, J., 1993. Fractal analysis of fracture patterns using the standard box-counting technique; valid and invalid methodologies. Journal of Structural Geology 15, 1509-1512.

Ward, M., in preparation. Opening History and Porosity Evolution of Fractures in Sandstone, Triassic to Jurassic La Boca Formation, Northeast Mexico. M.Sc. thesis, The University of Texas at Austin.

Warren, J.E., and Root, P.J., 1963. The behavior of naturally fractured reservoirs. Society of Petroleum Engineers Journal 3, 245-255.

Weidie, A.E., and Murray, G. E., 1967. Geology of the Parras Basin and adjacent areas of northeastern Mexico. American Association of Petroleum Geologists Bulletin 51, 678-695.

Wermund, E.G., and Barnes, V.E., 2003. Down to Earth at Pedernales Falls State Park, Texas. Bureau of Economic Geology Publication DE0005, Austin.

Wilson, J.L., 1990. Basement structural controls on Mesozoic carbonate facies in northeastern Mexico- A review. In Tucker, M., Wilson, J.L., Crevello, P.D., Sarg, J.F., and Read, J.F. (eds.): Carbonate platforms, facies, sequences, and evolution, International Association of Sedimentologists Special Publication 9, 235-255.

Wilson, J.L., and Pialli, G., 1977. Cretaceous carbonates of Texas & Mexico; applications to subsurface exploration. In Bebout, D.G., and Loucks, R.G. (eds.): The University of Texas at Austin Bureau of Economic Geology Report of Investigations No. 89, 286-294

Wines, D.R. and Lilly, P.A., 2002. Measurement and analysis of rock mass discontinuity spacing and frequency in part of the Fimiston Open Pit operation in Kalgoorlie, Western Australia: a case study. International Journal of Rock Mechanics & Mining Sciences 39, 589-602.

Worden, R.H., and Morad, S., 2000. Quartz cementation in oil field sandstones: a review of the key controversies. In Worden, R.H., and Morad, S. (eds.): Quartz cementation in sandstones, special publication 29, International Association of Sedimentologists, Blackwell Science.

Wu, H., and Pollard, D., 1995. An experimental study of the relationship between joint spacing and layer thickness. Journal of Structural Geology 17, 887-905.

Zhou, Y., Murphy, M.A., and Hamade, A., 2006. Structural development of the Peregrina-Huizachal anticlinorium, Mexico: Journal of Structural Geology 28, 494-507.

Vita

The son of Olga Torres and Leonel Gómez, Leonel Augusto Gómez was born in Bucaramanga, Colombia the 18th of January of 1969. After finishing high-school at Colegio La Salle at the age of 16, Leonel pursued a B.S. in geology at the Universidad Industrial de Santander (UIS). At UIS, Leonel was active in student organizations, including being the first editor of Facies, the geological magazine of the UIS geology students. In Facies, Leonel also had his first taste of the complexities of scientific writing. Through his undergraduate studies Leonel sponsored his photographic expeditions to the Colombian highlands by taking slides to classmates and professors. In addition to the required courses, Leonel took several classes in software programming which helped him during the year-long thesis in geophysics at the research laboratory (ICP) of the Colombian oil state company Ecopetrol. After graduating in March of 1992, Leonel went to work for Shell Oil as processing geophysicist in the cities of Bogotá and Cartagena, Colombia. After being laid off from Shell, Leonel took a month off to ride countless times his motorcycle in the roads of Pescadero Canyon. Thanks to his last boss in Shell, Leonel landed a job as wellsite geologist for Chevron Colombia. A year later Leonel became an Exploration Earth Scientist looking for oil in the foothills of the eastern cordillera in Colombia. Before moving to Austin, Leonel worked as consultant for OAS and took a two months motorcycle trip along the eastern coast of South America from Bogotá, Colombia to Puerto Montt, Chile. Leonel accepted a job at the Upstream Research Center of ExxonMobil in Houston. Leonel is still chasing his dream trip: in a motorcycle, with people that care for him, through at least one mountain range, with a tent, a geology guide and a photographic camera in the saddle bags; all while being paid.

This dissertation was typed by the author.